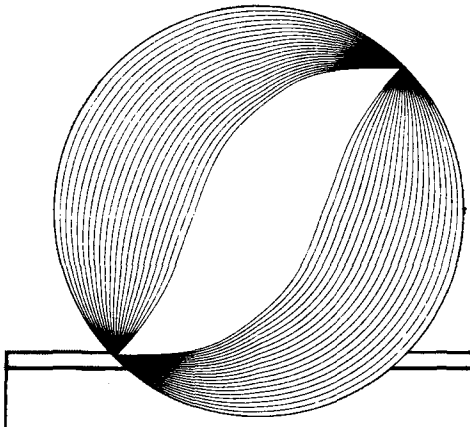
AD-A253 000

DTIC
ELECTE
JUN 4 1992
S C D



ISIF 91

PROCEEDINGS

3rd International Symposium

on

Integrated Ferroelectrics

DISTRIBUTION STATEMENT A
Approved for public release;
Distribution Unlimited

92-13566

Colorado Springs

April 3-5, 1991

COMPONENT PART NOTICE

THIS PAPER IS A COMPONENT PART OF THE FOLLOWING COMPILATION REPORT:

TITLE: Proceedings of the International Symposium on Integrated Ferroelectrics (ISIF) (3rd) Held in Colorado Springs, Colorado on 3-5 April 1991.

TO ORDER THE COMPLETE COMPILATION REPORT, USE AD-A253 000.

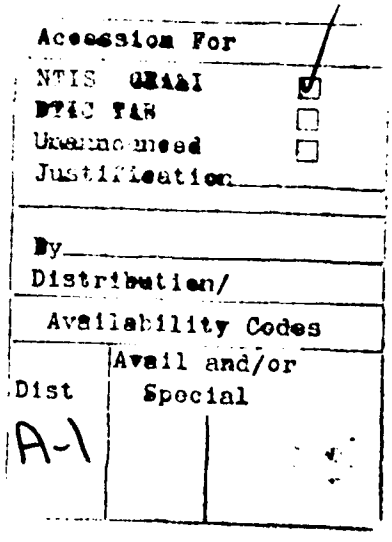
THE COMPONENT PART IS PROVIDED HERE TO ALLOW USERS ACCESS TO INDIVIDUALLY AUTHORED SECTIONS OF PROCEEDING, ANNALS, SYMPOSIA, ETC. HOWEVER, THE COMPONENT SHOULD BE CONSIDERED WITHIN THE CONTEXT OF THE OVERALL COMPILATION REPORT AND NOT AS A STAND-ALONE TECHNICAL REPORT.

THE FOLLOWING COMPONENT PART NUMBERS COMPRISE THE COMPILATION REPORT:

AD#: AD-P006 638 THRU AD#: AD-P006 694

AD#: AD#:

AD#: AD#:



DTIC FORM 463 MAR 85

OPI: DTIC-TID

ISIF-91

3rd International Syposium on Integrated Ferroelectrics

April 3, 4, and 5, 1991
Antlers Hotel, Colorado Springs, Colorado

Sponsored by:
University of Colorado at Colorado Springs
Defense Advanced Research Projects Agency (DARPA)
Gordon & Breach Science Publishers, Inc.
Naval Postgraduate School
Storage Technology Corporation
University of Colorado Foundation, Inc.



Accession For
NTIS GRA&I ☒
DTIC TAB ☐
Unannounced ☐
Justification
By
Distribution/
Availability Codes
Dist | Avail and/or Special
A-1

Statement A per telecon Dr. Wallace Smith
ONR/Code 1131
Arlington, VA 22217-5000

NWW 6/2/92

Copyright 1991
International Symposium on
Integrated Ferroelectrics

Printed in the United States of America

3rd ISIF-91 COMMITTEE

Carlos A. Paz de Araujo
SYMPOSIUM CHAIRMAN

Rudolf Panholzer
SYMPOSIUM CO-CHAIRMAN

James F. Scott
TECHNICAL PROGRAM CHAIRMAN

Alona S. Miller
SYMPOSIUM COORDINATOR

TABLE OF CONTENTS

FOREWORD
Carlos A. Paz de Araujo (chairman)

SESSION I **MATERIALS**
Chair: George W. Taylor

Ferroelectric Memory Programs in Canada 1
Michael Sayer

Recent Advances in the Deposition of Ferroelectric Thin Films 10
S.B. Krupanidhi

Advances in Processing and Properties of Perovskite Thin-Films for FRAMs, DRAMs, and Decoupling Capacitors 30
S.K. Dey, C.K. Barlingay, J. J. Lee, T.K. Gloerstad, and C.T.A. Suchicital

Fast Decay Component of the Remanent Polarization in Thin Film PZT Capacitors 44
Joseph M. Benedetto, Randall A. Moore, and F. Barry McLean

SESSION II **LASER ABLATION DEPOSITION**
Chair: Leonard Schwee

Ferroelectric $PbZr_{0.2}Ti_{0.8}O_3$ Thin Films on Epitaxial Y-Ba-Cu-O 54
R. Ramesh, A. Inam, W.K. Chan, B. Wilkens, F. Tillerot, T. Sands, J. Bullington, J. M. Tarascon, and J. Evans

Pulsed Laser Deposition (PLD) of Oriented Bismuth Titanate Films for Integrated Electronic Applications 62
H. Buhay, S. Sinharoy, M.H. Francombe, W.H. Kasner, J. Talvacchio, B.K. Park, N.J. Doyle, D.R. Lampe, and M. Polinsky

Filament-Assisted Pulsed Laser Deposition of Epitaxial $PbZr_xTi_{1-x}O_3$ Films: Morphological and Electrical Characterization 72
R.E. Leuchtner, K.S. Grabowski, D.B. Chrisey, and J.S. Horwitz

Preparation, Microstructure, and Ferroelectric Properties of Laser-Deposited Thin $BaTiO_3$ and Lead Zirconate-Titanate Films 87
P.S. Brody, B.J. Rod, K.W. Bennett, L.P. Cook, P.K. Schenck, M.D. Vaudin, W. Wong-Ng, and C.K. Chiang

Pulsed Excimer Laser Deposition of Ferroelectric Thin Films 100
S.B. Krupanidhi, D. Roy, N. Maffei, and C.J. Peng

SESSION III **DEVICE PHENOMENA**
Chair: T.S. Kalkur

Process Dependent Electrical Characteristics and Equivalent Circuit Model of Sol-Gel Based PZT Capacitors 116
T. Mihara, H. Watanabe, H. Yoshimori, C.A. Paz de Araujo, B. Melnick, and L.D. McMillan

Device Effects of Various Zr/Ti Ratios of PZT Thin-Films Prepared by Sol-Gel Method 139
H. Watanabe, T. Mihara, and C.A. Paz de Araujo

Statistical Theory of Fatigue in Ferroelectric Devices 151
C.A. Paz de Araujo, R. Zuleeg, T. Mihara, H. Watanabe, A. Carrico, L.D. McMillan, and J.F. Scott

C-V and I-V Simulations of Metal Ferroelectric Silicon Capped and Uncapped $BaMgF_4$ Devices Using Pieces II-B 169
Deng-Yuan Chen, C.A. Paz de Araujo, and L.D. McMillan

d.c. Leakage Currents in Ferroelectric Memories 176
J.F. Scott, B.M. Melnick, C.A. Paz de Araujo, L.D. McMillan, and R. Zuleeg

Preparation of $PbTiO_3$ Thin Films by Laser Ablation 185
Masanori Okuyama, Tadayuki Imai, and Yoshihiro Hamakawa

SESSION IV **EUROPEAN INTEGRATED FERROELECTRICS**
Chair: William A. Geideman

Application of Metal Alkoxides in the Synthesis of Oxides 195
M.I. Yanovskaya, E.P. Turevskaya, V.G. Kessler, I.E. Obvintseva, and N. Ya. Turova

Ferroelectric Thin Film Research in France 205
P. Gaucher, S.P. Faure, and P. Barboux

SESSION V **DETECTORS AND SENSORS: OPTICAL EFFECTS**
Chair: Gene Haertling

Thin Ferroelectric Films for Thermal Detector Applications 215
F. Ainger, A. Patel, N.M. Shorrocks, C. Trundle, and R.W. Whatmore

Sol-Gel Derived Ferroelectric Thin Films in Silicon Micromachining 231
C.-C. Hsueh, T. Tamagawa, C. Ye, A. Helgeson, and D.L. Polla

Thin Piezoelectric VDF-TrFE Copolymer Films for Data Storage 245
Peter Guthner, Joachim Glatz-Reichenbach, Doris Schilling, and Klaus Dransfeld

Photovoltages in Ferroelectric Films 251
P.S. Brody and B.J. Rod

Photoresponse from Thin Ferroelectric Films of Lead Zirconate Titanate 262
Sarita Thakoor, Anil P. Thakoor, and Stephen E. Bernacki

Study of the Optical Properties of RF Supttered Lithium Niobate Thin Films 278
Charles Hung-Jia Huang and Thomas A. Rabson

SESSION VI **THEORY**
Chair: Rainer Zuleeg

Theory of Conduction and Breakdown in Perovskite Thin Films 288
Rainer Waser and Mareike Klee

On Polarization Reversals in Ferroelectrics 306
Yoshihiro Ishibashi

Fast Reversal Process in Real Ferroelectrics 315
V. Ya. Shur, A.L. Gruverman, N. Yu. Ponomarev, E.L. Rumyantsev, and N.A. Tonkachyova

SESSION VII **THEORY AND MODELS**
Chair: Paul Beale

Numerical Analyses of Ferroelectric Characteristics for Memory Use by Using a Lattice Model 326
Masayoshi Omura, Hideo Adachi, and Yoshihiro Ishibashi

Rejuvenation of Ferroelectric Fatigue in Modified Lead Zirconate Titanate Ceramics
Near Tetragonal-Rhombohedral Morphotropic Phase Boundary 335
Wuyi Pan and Cheng-Feng Yue

A Generalized Ferroelectric Capacitor Modeling Methodology 344
Douglas E. Dunn

Characterization and Modeling of Thin-Film Ferroelectric Capacitors
Using C-V Analysis 354
Ciaran J. Brennan

SESSION VIII **TESTING**
Chair: Thomas A. Rabson

Ferroelectric Memory Evaluation and Development System 364
David W. Bondurant

Characterization of PZT Films Fatigued at Low Frequency 368
R.A. Lipeles, B.A. Morgan, and M.S. Leung

Aspects of Fatigue and Rapid Depolarization in Thin Film PZT Capacitors 376
R.D. Nasby, J.R. Schwank, M.S. Rodgers, and S.L. Miller

SESSION IX **MEMORY DEVICES**
Chair: Jane Alexander

Integration of Ferroelectric PZT Capacitors with GaAs JFET Devices 390
S.Y. Wu and Wm. A. Geideman

Anomalous Remanent Polarization in Ferroelectric Capacitors 404
Norman E. Abt

SESSION X **PROCESSING I**
Chair: James McGarrity

A High-Capacitance PZT-on-Ta_2O_5 Memory Cell with a Chemically Stable Electrode Suitable for Sub-Micron Processing 414
M. Azuma, T. Nasu, S. Katsu, T. Otsuki, and G. Kano

Improved Switching Endurance of Lead Zirconate-Titanate Capacitors for Nonvolatile Memory Applications 431
I.K. Naik, L.E. Sanchez, S.Y. Wu, and B.P. Maderic

Crack-Free PZT Thin Films Micropatterned on Silicon Substrate for Integrated Circuits 444
Motoo Toyama, Naoto Inoue, Masanori Okuyama, and Yoshihiro Hamakawa

Ferroelectric $Pb(Zr,Ti)O_3$ Thin Films Prepared by Planar Multi-Target Sputtering 453
R. Bruchhaus, H. Huber, D. Pitzer, and W. Wersing

Electrical Results of Multilevel and Homogeneous Ferroelectric Capacitors 461
J.D. Cuchiaro, B.M. Melnick, and C.A. Paz de Araujo

Ferroelectrics for Silicon VLSI 475
Sheng T. Hsu and Israel H. Kalish

SESSION XI **PIEZO-PYRO-OPTICAL INTEGRATED FERROELECTRIC DEVICES**
Chair: Henry Stadler

Integrated SAW-AO Optical Switch on Si 492
Tadashi Shiosaki, Naoki Kitamura, and Akira Kawabata

Electronic Emission by Nanosecond Switching in PLZT 501
Hartmut Gundel

SESSION XII **PROCESSING II**
Chair: Joe Evans

Ferroelectric $Pb(Zr,Ti)O_3$ Thin Films Prepared by Gas Jet Deposition 515
C.L. Hwang, B.A. Chen, T.P. Ma, J.W. Golz, Y.D. Di, B.L. Halpern, and J.J. Schmitt

Process Technology Developments for GaAs Ferroelectric Nonvolatile Memory 524
L.E. Sanchez, I.K. Naik, S.H. Watanabe, I.S. Leybovich, J. H. Madok, and S.Y. Wu

Solution Chemistry Effects in $Pb(Zr,Ti)O_3$ Thin Film Processing 535
R.W. Schwartz, B.C. Bunker, D.B. Dimos, R.A. Assink, B.A. Tuttle, D.R. Tallant, and I.A. Weinstock

Statistical Investigation of Sol-Gel Lead Titanate (PT) Processing 547
B.M. Melnick, R. Gallegos, and C.A. Paz de Araujo

Low Temperature Processing of Ferroelectric Thin-Films and Amorphous Ferroelectricity 561
Ren Xu, Yuhuan Xu, and John D. Mackenzie

Chemical Aspects of Pb-Zr-Ti Oxide Thin Film Syntheses by PE-MOCVD Below 500° C 571
William T. Petuskey, David A. Richardson, and Sandwip K. Dey

$PbTiO_3$ Thin Films Grown by Organometallic Chemical Vapour Deposition 598
G.J.M. Dormans, M. DeKeijser, and P.K. Larsen

SESSION XIII **ELECTRODING and ALTERNATIVE MATERIALS**
Chair: George Rohrer

Bottom Electrodes for Integrated $Pb(Zr,Ti)O_3$ Thin Films 612
Philip D. Hren, S.H. Rou, H.N. Al-Shareef, M.S. Ameen, O. Auciello, and A.I. Kingon

Electrical Characteristics of Aluminum-Zirconium Oxide-Barium Magnesium Fluoride-p Silicon MIS Capacitors 627
T.S. Kalkur, R.Y. Kwor, L. Levenson, and L. Kammerdiner

Thin Film Lithium Niobate for Use in Silicon Based Devices 637
Timothy A. Roet, He Lin, Thomas A. Rabeon, Robert C. Baumann, and J.M. McDavid

Electrical Switching in Lithium Niobate Thin Films 644
Timothy A. Rost, He Lin, and Thomas A. Rabeon

SESSION XIV **PROCESSING TECHNOLOGY**
Chair: Lewis Cohn

Liquid Source CVD 649
L.D. McMillan, C.A. Paz de Araujo, T. Roberts, J. Cuchiaro, M. Scott, J.F. Scott

Sputter Deposition of Ferroelectric Thin Films 658
Angus I. Kingon, H.N. Al-Shareef, K.D. Gifford, T.M. Graettinger, S.H. Rou, P.D. Hren, O. Auciello, and S. Bernacki

UHV Processing of Ferroelectric Barium Magnesium Fluoride Films and Devices 674
S. Sinharoy, D.R. Lampe, H. Buhay, and M.H. Francombe

INDEX 685

(this page blank)

PROCEEDINGS OF THE
3RD INTERNATIONAL SYMPOSIUM ON INTEGRATED FERROELECTRICS

FOREWORD

The field of Integrated Ferroelectrics has now grown to a level of activity well beyond the initial expectations of the early pioneers. In june 1955, the magazine Scientific American published an article on the possible use of ferroelectric materials in computer memories. However, the technology that finally entered the market was the ferrite core memory. After the initial success of ferrite core memories in the early sixties, attention to ferroelectric memories returned with several groups studying ways to implement ferroelectric thin-films (and single crystals) in a variety of devices. Efforts included everything, from optically addressed memories to pyroelectric focal plane arrays.

The technology driver, the nonvolatile fast access ferroelectric memory was still a primitive device based primarily on the single point array architecture used by the analogous ferrite core devices. By the early seventies, attempts to make ferroelectric field effect transistors (FETs) met with the advent of the successful developments in semiconductor devices such as the many forms of tunneling nonvolatile FETs and the first Dynamic Random Access Memories (DRAMs).

Ferroelectric thin-films were not very well understood at that time, and the lack of device physics models that could explain the parasitics encounterred in the ferroelectric storage cell, led to the virtual shut down of further activity in the field. Today, after seven years of rebirth, this field is well in its way to become part of the mainline research in integrated circuits.

Several factors contributed to this ressurgence in relevance. Firstly, after decades of growth, the semiconductor based nonvolatile memories have failed to provide endurance results beyond one hundred thousand cycles. In fact, the norm is only ten thousand cycles in most implementations of Electronically Erasable Programmable Read Only Memories (EEPROMs). Also, the erase/write times of these devices are still in the millisecond range and limitations in density still persist.

With the advent of very sophisticated synthesis and deposition techniques, ferroelectric devices are now becoming the hope for the future in the area of nonvolatile memories. But the applications, as seen in these proceedings, go way beyond nonvolatile memories. Researchers have rediscovered the utility of ferroelectrics as high dielectric constant capacitors opening new possibilities for the ability to manufacture an all planar very high density DRAM. Applications to neural networks, integrated optics, micromachines and Monolythic Microwave Integrated Circuits (MMICs) are burgeoning. The field is also expanding in the integrated sensors area, as shown in some of the papers contained herein.

This 3rd International Symposium on Integrated Ferroelectrics stands as a milestone in this field. It is here that approximately two hundred people from over ten countries confirmed the maturity of the field and the utility of further research. It is here that the lines of interdiciplinary research fused into the fundamental paradigms of materials, processes and devices which set the field on its own as a unique area of research. It is here that this field is set apart from being the vague explorations of ferroelectric materials applied to semiconductor devices of the past. For now, at least, this field is self-contained in practice and broad enough in applications to render itself worthy of scientific inquiry for the benefit of mankind.

Carlos A. Paz de Araujo
Editor

AD-P006 638

FERROELECTRIC MEMORY PROGRAMS IN CANADA

MICHAEL SAYER
Department of Physics, Queen's University, Kingston,
Ontario, Canada K7L 3N6

Abstract Thin film PZT ferroelectrics have been fabricated in Canada since 1976 by magnetron sputtering and more recently by acetate-based sol gel processing and are now being considered for implementation into commercial communications systems. Processing based on rapid thermal annealing has shown marked advantages for crystallization into the required perovskite phase. Applications based on the piezoelectric properties of PZT films are shown to have an interesting potential for a range of devices.

INTRODUCTION

Thin film lead zirconate titanate (PZT) technology began in Canada at Queen's University in 1976 through the magnetron sputtering of pressed powder targets prepared from ground sintered ceramics supplied to Queen's University through a collaboration with Almax Industries Ltd of Lindsay, ON, a company manufacturing large piezoelectric PZT ceramics for sonar transducers. Developments since that time have led to the integration of such ceramics with silicon technology on the micron scale using both physical and chemical techniques. In ferroelectrics, the potential high speed, high packing density and low switching voltage of ferroelectric random access memory (RAM) devices is of industrial interest to Northern Telecom Electronics of Ottawa, The incentive is to provide sufficient memory to personalize telephone handsets, to provide local telephone number storage, and to facilitate on-line software updates and back-up memory without the intervention of service personnel. The piezoelectric properties of such films have been adapted to a range of ultrasonic and electro-optic devices in association with the Industrial Materials Institute, Boucherville, Qu [1,2]. Work on the design aspects of ferroelectric RAM is in progress at the University of Toronto, and on chemical vapour deposition of PZT-type compounds at McMaster University.

92-16102

Ferroelectric and Piezoelectric Oxide Films

Since 1970, ferroelectric or piezoelectric materials which have been actively examined in the form of thin films include:

Piezoelectrics: ZnO, CdS, AlN, $LiNbO_3$, $PbTiO_3$:$PbZrO_3$ (PZT)
Ferroelectrics: $BaTiO_3$, $PbTiO_3$ and PZT
Electro-optic : $PbTiO_3$:$PbZrO_3$:La (PLZT)

The type of application and the principal fabrication methods used since 1970 are shown in Figure 1.

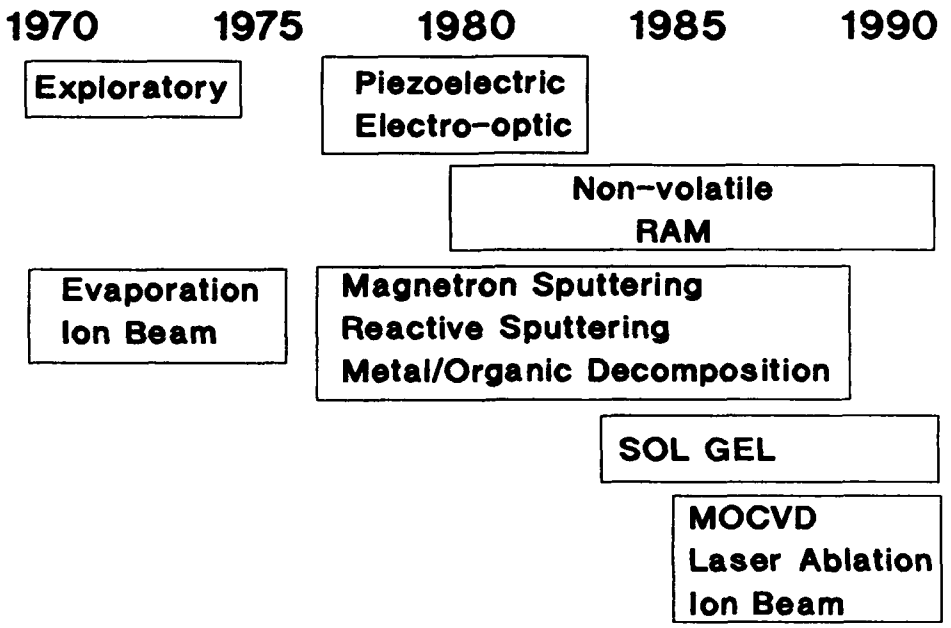


FIGURE 1 Ferroelectric film fabrication processes and applications

The earliest commercial piezoelectric applications were those by Hickernell using ZnO for surface acoustic wave substrates [3], a technology which has now been commercialised in Japan for surface acoustic wave filters for TV -IF applications. In more complex oxides it is of interest that, contrary to expectations, thin films of lithium niobate or barium titanate have not been as successful as the lead based perovskite ferroelectrics based on PZT. It is argued in this paper that this is due to the role of lead in PZT-type compounds, in that the volatility of PbO both allows the film composition to achieve stoichiometry during annealing [4], and that the structure is able to crystallise rapidly by fast diffusion processes.

Film Fabrication

In RF magnetron sputtering a disadvantage of ceramic targets is that changes in target stoichiometry occur during sputtering. Since metal targets have potentially more reproducible properties, reactive multi-element target sputtering in oxygen [5,6] has been employed using a sectored lead, zirconium and titanium target [7]. In more recent work chemical methods utilising an acetate based sol gel process have been applied with similar success [8,9]. The flow process for this method is shown in Figure 2.

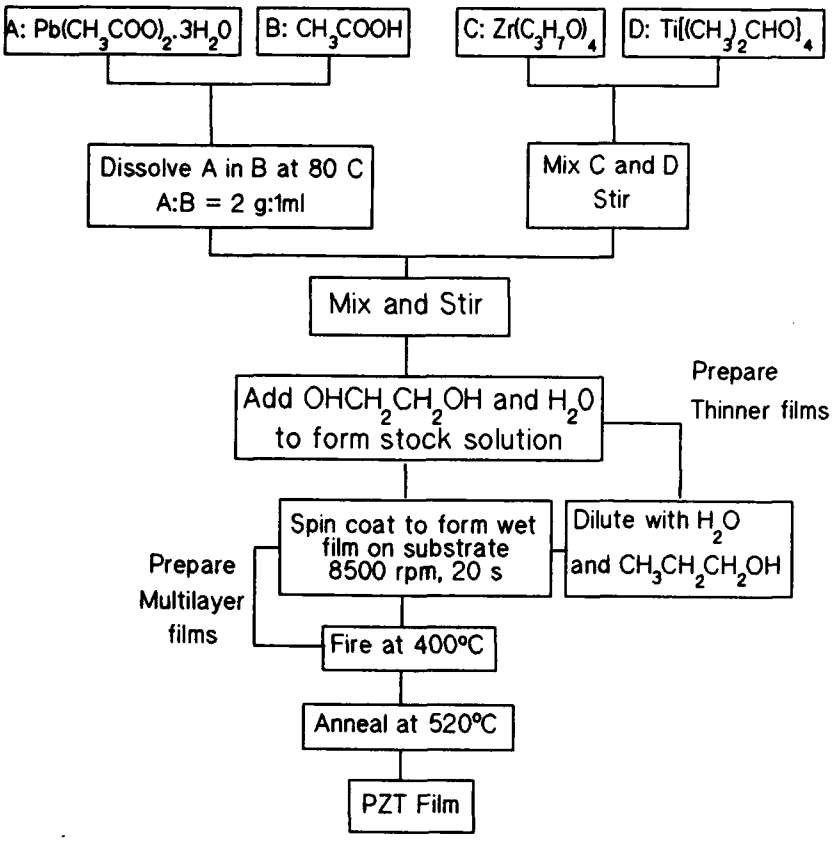


Figure 2: Flow process for acetate based sol gel PZT

The original objective for this system was to use a carboxylic acid like acetic acid to chelate alkoxides to stabilise the gel against uncontrolled hydrolysis during use, and to control the firing of the film using high boiling point organic additives to reduce crack formation and enhance adhesion. A particular feature of our current solutions is an ability to fire films to the full PZT perovskite structure and properties at relatively low temperatures. Films of thickness 0.2-0.4 μm can be fired directly on a hotplate in air at 400°C although a better process route for films of about 1 μm thickness prepared by spin or dip coating is shown in Figure 3. Three temperatures are significant, T1, at which the gel fully matures and dries, T2, when organic removal is virtually complete and an amorphous oxide film is achieved, and T3, when crystallisation into the perovskite phase is complete. For films > 0.8 μm, greater control of the process is achieved if the film is processed under vacuum in stage 1, at 0.1 atm air in stage 2 and at atmospheric pressure in stage 3. The inset indicates that rapid crystallisation to the required perovskite structure starts at 450°C and is complete at 520°C.

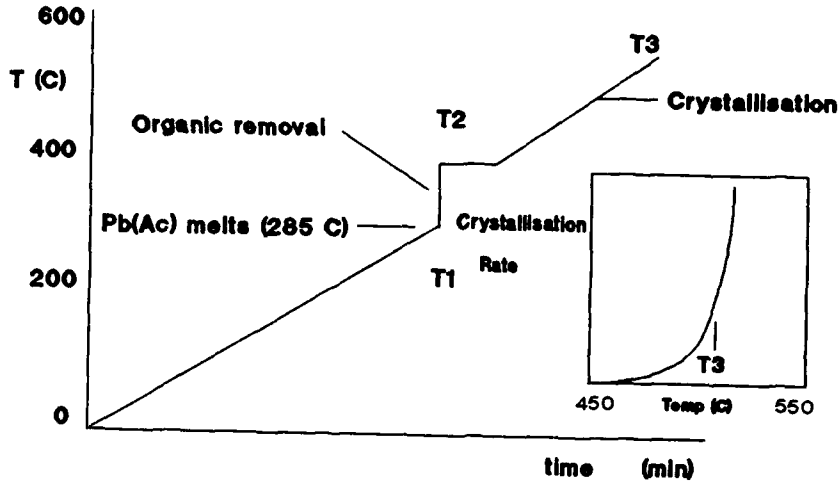


Figure 3 Process route to sol gel film crystallisation

Processing within this temperature range is of interest in that it allows crystallisation of perovskite films on aluminum metallisations. Figure 4 shows x-ray diffraction patterns for a film crystallised on aluminum. A second feature of significance is that crystallisation occurs directly into the perovskite phase with little evidence for a competing non-ferroelectric pyrochlore phase.

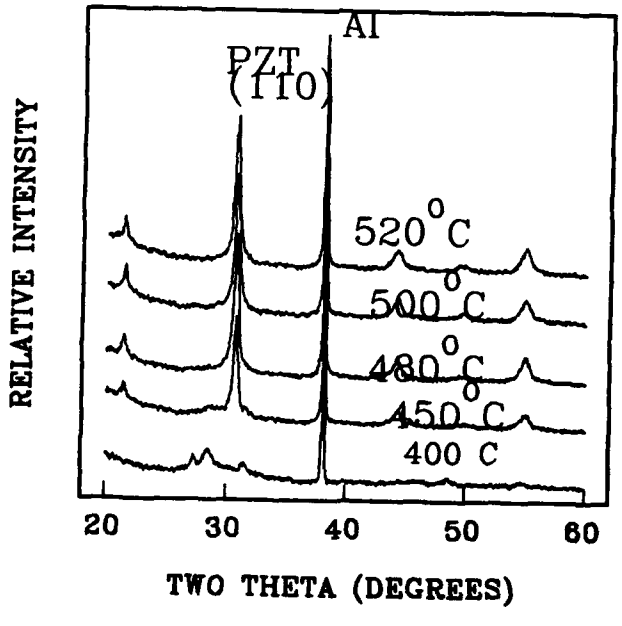


Figure 4 (a) Film crystallisation on aluminium on a hotplate at 520°C [10]. Temperature ramped from 400°C in 5 mins.

Films crystallised on aluminum tend to show similar values of polarisation to those crystallised on platinum, but generally have a

higher coercive field. This is possibly due to an oxide formation at the Al-PZT interface.

Rapid Thermal Processing

It is of importance to understand film growth and crystallisation processes in order to implement advanced processing methods for PZT films which are compatible with silicon technology. Techniques which are important for this purpose are rapid thermal processing [11] in which film annealing is accomplished by a computer controlled bank of heat lamps, and glancing angle x-ray diffraction which uses a grazing incidence x-ray beam to probe crystal structures at various depths below the surface of a film [12]. Using these techniques it has been possible to reduce processing times for PZT films from periods of hours to tens of seconds with consequent reduced degradation of underlying electrode structures, and to investigate the sequence of phases which arise during crystallisation from an amorphous film. It is also possible to deduce whether crystallisation nucleates within the bulk or at the interface with the substrate.

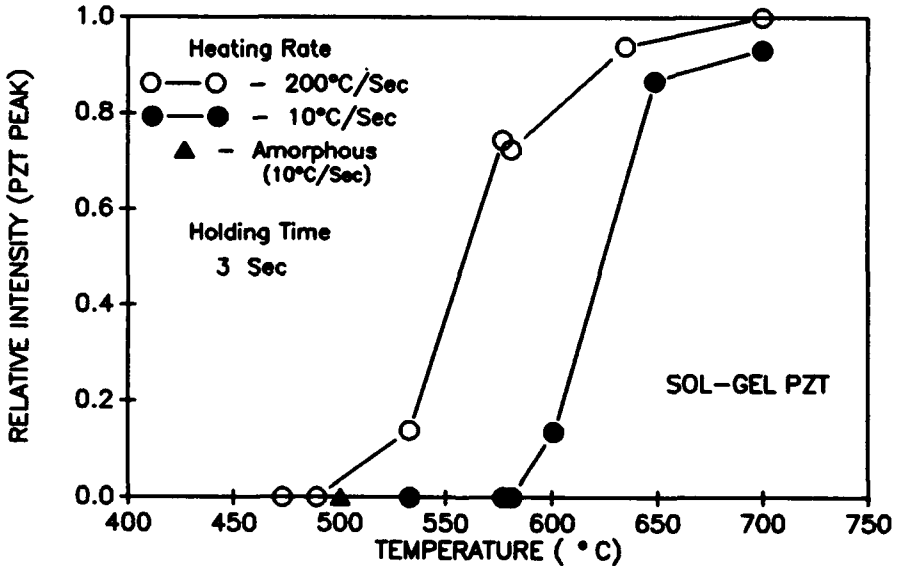


Figure 5: RTA crystallisation of alcohol based sol gel PZT films

Figure 5 shows the crystallisation kinetics of alcohol based [13] sol gel PZT films on platinum substrates in air using an AG Associates Heatpulse 410 Rapid Thermal Annealing Facility [14]. Ramp rates of 10 and 200°C/s are shown with a hold time of 3 s. The firing temperature for this alcohol based system is in the range 600 - 750°C which is possibly somewhat higher than for the acetate system given in Figure 3. but the degree to which crystallisation occurs by RTA within a

period of seconds is remarkable. XRD studies indicate that in this case, crystallisation nucleates at the interface with the substrate in contrast with sputtered films which nucleate throughout the bulk. Work is now in progress to assess the degree to which the substrate influences such crystallisation.

Kumar et al [15,16] have shown that pulsed thermal processing can provide unique information with respect to reaction sequences during crystallisation and particularly have demonstrated the crucial role of oxygen deficient lead oxides in PZT processing. Figure 6 shows the progressive changes in the x-ray diffraction patterns which occur for a sputtered PZT film which is sequentially thermally pulsed for the times and temperatures shown in the diagram.

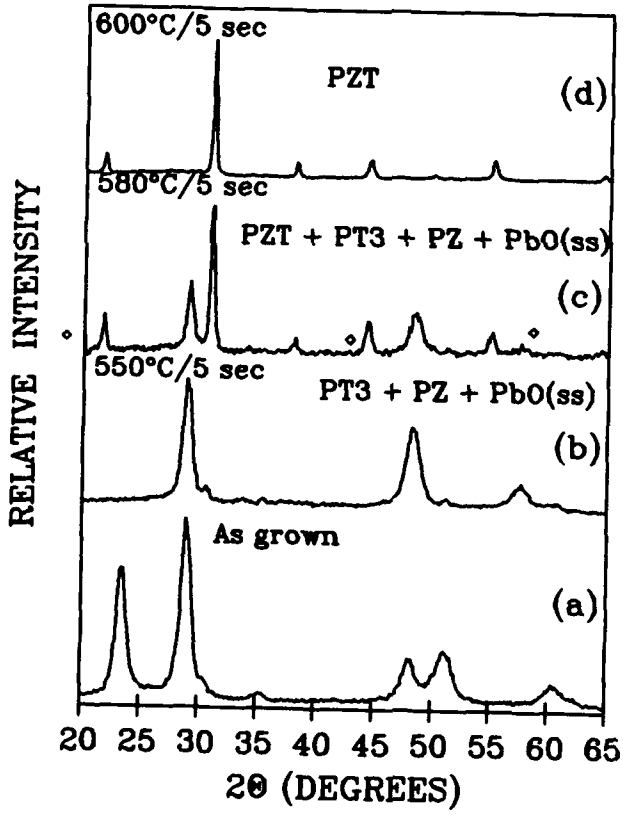


Figure 6 Pulsed Thermal Processing of PZT by RTA

A careful comparision with similar results for the individual components (PbO, $PbTiO^3$ and $PbZrO_3$) shows that the as-grown film consists of crystalline α-PbO_2 in a matrix of amorphous zirconia and titania, and the first step causes the formation of $PbTiO_3$, $PbZrO_3$ and an oxygen-deficient lead oxide $PbO_{1.44}$. The latter plays a crucial role in the subsequent steps in the formation of PZT since $PbTiO_3$ and

$PbZrO_3$ show little reactivity unless sufficient excess PbO is present to facilitate the intergrowth of the two phases. If too little is present, the reactions will not proceed to completion, if too much is present phase intergrowth is again inhibited. This kind of information is crucial in the design of processing routes towards fully crystallised PZT, and the results demonstrate that rapid thermal processing provides an unique new tool to aid in understanding the solid state reactions involved.

Substrate Selection

One of the major current problems in device development is the electrode metallisation at the silicon/PZT interface. This plays a number of roles - as a low resistance electrode, as a barrier layer to prevent the diffusion of lead into underlying silicon structures, and as a method of influencing the crystallisation of the PZT film. In the early stages of film development, stannic oxide or indium tin oxide transparent conducting coatings were selected as the bottom electrode [4,8]. While this electrode was initially chosen for its stability for high temperature processing under oxygen, it turned out that adhesion between PZT and ITO was strong and crystallisation was enhanced on substrates of this nature. Unfortunately, the resistance of the coating after processing is intrinsically higher than optimum for ferroelectric RAM, and unacceptable limitations on the frequency response are incurred as shown in the plot of dielectric constant vs frequency in Figure 7 [17]. There is also evidence of diffusion of lead into the oxide [18]. Continuing efforts are being made to define an appropriate electrode system. Platinum is currently the material of choice, but this is not particularly desirable for use in a silicon-based technology because of its potential for introducing electronic defects in silicon. The nature of the top and bottom contacts may also have significance for the aging of ferroelectric films under switched excitation. Electrical data has been seen [19] in both dielectric constant and polarisation studies which is consistent with the postulate that the effective area of the electrodes decreases with time. This has been correlated with spalling of the electrode under the high applied field and is consistent with a suggestion by Smyth [20] that oxygen release from the matrix due to the high field at the electrode could give rise to high stresses in the electrode region.

Piezoelectric Applications of Thin Film PZT

A number of interesting piezoelectric devices could expand the potential opportunities for thin film ferroelectrics. In planar

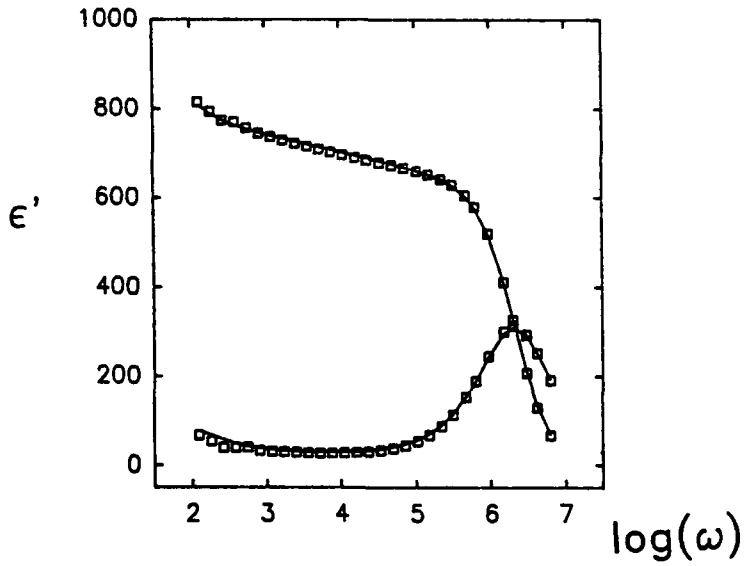


Figure 7 Frequency dispersion in ϵ' due to a high resistance electrode

geometry, sputtered electro-optic switches based on lanthanum-doped PZT are being actively explored. However multilayer sol-gel processing allows the fabrication of relatively thick PZT coatings on non-planar surfaces such as metal wires or cylinders [21] or on optical fibres [22]. In the case of wires, a range of coaxial pressure transducers and sensors has been developed for medical and biological applications [21]. In the case of optical fibres, the development of an in-line optical phase modulator is being explored in which compressive stresses imposed on a metallized fibre by an ac voltage applied to a coaxial PZT element modulates the transmission of light within the fibre [23]. It is very possible that even if the development of ferroelectric RAM is a major commercial success, fabrication will of necessity be confined to major semiconductor manufacturers having dedicated processing lines. Thin film piezoelectric devices could be the focus of significant niche markets in sensors, actuators and electronic devices. Since the requirements for electrodes and reproducibility will remain, the results of the marriage of ceramics and silicon seen in ferroelectric RAM will support this activity also.

CONCLUSIONS

It is clear that ferroelectric films can be fabricated of thickness down to less than 0.1 μm with properties which equal those of the bulk material. The lower limit on thickness seems to be a moving target while the upper limit is associated with the development of cracks within the film during processing. Processing methods are becoming of increasing reliability with techniques such as rapid thermal annealing making complex oxide film fabrication a true semiconductor technology.

The current emphasis is on sol gel processing with its advantages in simplicity, range of film thicknesses, and ease of compositional variation. However, the compatibility of sputtering with many VLSI processing methods suggests that it should not be discarded too precipitously. Further work is required on the mechanisms of gelation and crystallisation in both sol gel and sputtered films. Major niche markets are apparent not only in ferroelectric RAM, but also in piezoelectrics, transducers and electro-optic devices.

Acknowledgements

This work was supported through the Ontario Centre for Materials Research from the Premiers Technology Fund of the Government of Ontario and by the Natural Sciences and Engineering Research Council of Canada.

References

1. C.K.Jen, K.Sreenivas and M.Sayer, J.Acoust. Soc. Amer. 84,26 (1988)
2. C.K.Jen, C.Neron, G.Yi, M.Sayer, M.Castonguay and J.D.N.Cheeke, Mat. Sci. Eng. A122, 21 (1990)
3. F.S.Hickernell, Proc. 1980 IEEE Ultrasonics Symp. 1 (1980)
4. K.Sreenivas and M.Sayer, J.Appl.Phys. 64,1484 (1988)
5. K.Sreenivas, M.Sayer and P.Garrett, Thin Sol. Films 178,251 (1989)
6. E.M.Griswold, M.Sayer and I.D.Calder, Can.J.Phys (in press) (1991)
7. A.Croteau and M.Sayer in V.E.Wood (Ed.), Proc.6th IEEE Symp. on Applications of Ferroelectrics Bethlehem, PA, p606 (1986)
8. G.Yi, Z.Wu and M.Sayer, J.Appl.Phys. 64,2717 (1988)
9. G.Yi, Z.Wu, M.Sayer, C.K.Jen, and J.F.Bussiere Ceramic Thin Films, American Ceramic Society
10. G.Yi and M.Sayer, Ceram. Bull. July 1 (in press) 1991
11. C.V.R.Vasant Kumar, M.Sayer, R.Pascual, D.T.Amm, Z.Wu and D.M.Swanston, Appl.Phys.Letts. 58,1161 (1991)
12. R.Pascual, M.Sayer, C.V.R.Vasant Kumar and Li Zou, J.Appl.Phys. (in press) (1991)
13. K.D.Budd, S.K.Dey and D.A.Payne, Brit. Ceram. Proc. 36,109 (1985)
14. Z.Wu, R.Pascual and M.Sayer, Proc. Mat. Res. Soc. Sympos., San Diego 1991 (in press)
15. C.V.R.Vasant Kumar, R.Pascual and M.Sayer, J.Appl.Phys. (in press) (1991)
16. C.V.R.Vasant Kumar, R.Pascual and M.Sayer, Proc. 3rd Int. Conf. on Integrated Ferroelectrics, May 1991
17. M.Sayer, A.Mansingh, A.K.Arora and A.Lo, Ferroelectrics (submitted) 1991
18. K.Sreenivas, M.Sayer, T.Laursen, J.L.Whitton, R.Pascual, D.J.Johnson, D.T.Amm, F.I.Sproule, D.I.Mitchell, M.J.Graham, S.C.Gujrathi and K.Oxorn, Mat. Res. Soc. Proc. Ferroelectric Thin Films, 200, 255 (1990)
19. D.J.Johnson, D.T.Amm, E.Griswold, K.Sreenivas, G.Yi and M.Sayer, Mat. Res. Soc. Proc. Ferroelectric Thin Films, 200, 289 (1990)
20. D.M.Smyth, Proc. 3rd Int. Conf. on Integrated Ferroelectric (1991)
21. G.Yi, M.Sayer, Z.Wu, C.K.Jen and J.F.Bussiere, Electron. Letts 25, 907 (1989)
22. C.K.Jen, M.Sayer, G.Yi and J.F.Bussiere, US Patent #485,918
23. G.Yi, M.Sayer, C.K.Jen, J.C.H.Yu and E.L.Adler, 1989 IEEE Ultrasonics Symp. 1231 (1989)

AD-P006 639

RECENT ADVANCES IN THE DEPOSITION OF FERROELECTRIC THIN FILMS

S.B. Krupanidhi[a)]

Materials Research Laboratory, Pennsylvania State University, University Park, PA 16802.

ABSTRACT Recent developments in ferroelectric thin film deposition involving plasma based approaches, are described, which include a) multi-magnetron sputter deposition, b) Multi-ion-beam reactive sputter (MIBERS) deposition, c) Pulsed excimer laser ablation and d) ECR (Electron cyclotron resonance) plasma assisted deposition. These methods commonly prevailed intrinsic low energy ion bombardment during the growth process, which may be used for the control over composition, crystallization temperature and microstructure. A low energy (60 - 75 eV) ion bombardment of the ferroelectric $Pb(Zr,Ti)O_3$ thin films indicated a reduction in the phase formation/crystallization temperature, improved the electrical properties, microstructure and the surface smoothness. Discussion is presented exphasizing the effects of low energy bombardment in different deposition processes. Recent findings using rapid thermal annealing process are also described.

INTRODUCTION

Earlier attempts of depositing ferroelectric thin films were mostly limited by the complexities involved in depositing multi-component systems, while the application interests were only confined to developing thin film capacitors using large k materials such as barium titanate. Most recently, however, development of ferroelectric thin films has been well motivated with the latest advances in thin film growth processes and offered the opportunity to exploit phenomena such as polarization hysteresis, pyroelectricity, piezoelectricity and electrooptic activity of ferroelectric materials[1]. The application of ferroelectric films to radiation hard non-volatile memories has become quite attractive[2] (also called FERRAMS), as they offer fast read and write cycles, low switching voltages (3-5 V), non-volatility, longer endurance (10^{12} cycles)[3]. Several growth techniques were involved

---

a) Also with Dept. of Engg. Science & Mechanics

92-16103

historically to develop ferroelectric thin films, including thermal[4], flash[5] and e-beam[6] evaporations, magnetron[7] and ion beam[8] sputtering, sol-gel[9], CVD (chemical vapor deposition)[10] and MOCVD (metal-oranic chemical vapor deposition)[11]. Despite the consistent progress in the growth of ferroelectric thin films, a) low temperature processing (with films exhibiting device quality properties), b) controlled grain size and density and c) uniform homogeneity over large area still remain as major tasks of research. Present paper describes some latest growth techniques, which are being widely explored (as well as in author's laboratory at MRL/Penn State), for the deposition of ferroelectric thin films.

STATUS OF FERROELECTRIC THIN FILM GROWTH

Magnetron sputtering technique was mostly employed for the deposition of multi-component ferroelectric thin films[12]. However, recent advances in thin film growth technology made it possible to employ a vast variety of techniques, involving either physical or chemical transport of the species. Sol-gel (solution based) technique also received significant attention due to its apparent process simplicity[13]. In most of the attempts (irrespective of nature of species transport), the crystallinity was solely obtained by thermal energy (substrate heating or post-deposition annealing). However, in the plasma based techniques, either intrinsic or extrinsic energetic species bombardment during the thin film growth is believed to enhance the growth process[14] in terms of, a) reduction in growth/process temperature, b) control of properties via modifying the grain structure, density and nature of crystallinity, and c) modify the surface morphology.

The range of bombarding energies varies in different techniques and also depend on the nature of ion excitation, such that the ion bombardment assistance could be used to the benefit of modifying/controlling the properties of the ferroelectric thin films. Few selective growth processes were chosen for the comparison of intrinsic ion bombarding energies and are listed in Table.1, similar to that shown earlier[15] and the choice of techniques was done by matching with the current efforts at author's laboratory, which involve low energy bombardment during the growth of multi-component ferroelectric oxide films.

Table.I Comparison of bombarding energies in different deposition techniques.

Nature of Deposition Process	Energy of Bombarding Species (eV)	Source of Species Energy
Magnetron sputtering	100 - 1000	Substrate Biasing
Ion Beam Sputtering	50 - 1000	Ion Beam Source
Electron Cyclotron Resonance (ECR)	5 - 50	ECR plasma
Excimer Laser Ablation	10 - 100	Ablated Species

LATEST GROWTH PROCESSES FOR FERROELECTRIC THIN FILMS

Development of ferroelectric thin films pose several stringest restrictions to satisfy the requirements in the phase formation, crystallization and the microstructure development. Following techniques were devised to commensurate with the current demands and the ferroelectric phase is realized over large areas.

Multi-magnetron sputtering

Magnetron sputter deposition had been the most popular dry technique for depositing ferroelectric thin films. Majority of efforts appeared in the literature used compound ceramic targets of desired composition as the starting material[16]. Evidences of success for growing ferroelectric thin films by this technique, however, often suffered from the following drawbacks: a) limited control over the composition of the films, due to the large differences in the sputter yields and as a result the preferential deficiency of volatile elements in the films. Often, in case of Pb-based perovskites, the starting targets had to be made Pb rich to compensate for any subsequent losses during the deposition, b) the presence of negative ions during sputtering of oxide targets has been established to bombard the growing film

uncontrollably and damage the surface and influence the surface stoichiometry and the growth morphology and c) low deposition rates with oxide targets.

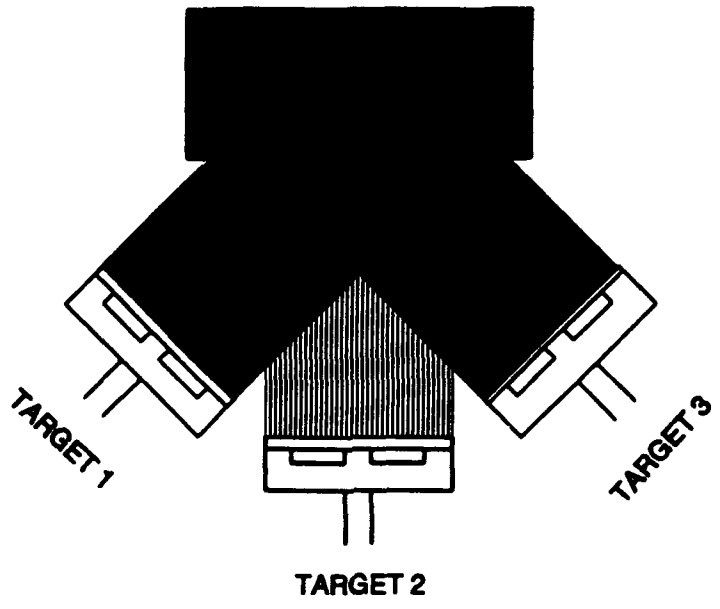


Figure 1. Schematic of multi-mangnetron sputtering system.

Reactive sputtering of multi-elemental metal targets had been attempted as an alternate approach to allow better control over film composition as well as achieving higher sputter rates[17]. However, the target has to be replenished with the most volatile component (fresh Pb metal in case of PZT) for subsequent depositions, which tends to influence the distribution of volatile species in the final film composition. Reactive magnetron sputtering with multiple targets, while each target consisting of one element in the composition, has been reported to grow excellent PLT (La modified $PbTiO_3$) thin films[18] and was considered to be a more successful alternate approach to ceramic targets, to grow good quality ferroelectric thin films for the following reasons: a) Control over the composition of the final film via the independent control of sputter rates of individual targets and allows the *in-situ* altering of composition during growth and b) offers high rates of deposition due to the reactive sputtering of metal targets.

The schematic of our multi-magnetron sputter deposition system, similar to that reported in the literature[18], is shown in Fig.1. The system consists of three magnetron cathodes of 7.5 cms diameter, vertically mounted at an angle of 20^{o} with respect to the central axis, such that all the targets are focussed to a common focal point while ensuring a large overlapping area from each target. A substrate holder was arranged in front of the target which is capable of moving in and out (for changing the target-substrate distance) and also features simultaneous rotation, dc biasing and substrate heating. As the present approach offers flexibility of varying the amounts of each component in the film composition, the effect of depositing power ratios via composition on the crystallinity of the films was examined[19]. It was observed with $PbTiO_3$ thin films that the films with excess Pb content encouraged (110) oriented growth while the presence of stoichiometric Pb content favored a preferred oreintation along (100) direction.

Multi-Ion Beam Reactive Sputter (MIBERS) Deposition

Most of the physical vapor deposition techniques prevail intrinsic energetic particle bombardment of the depositing film which has often been maneuvered to improve the film quality under controlled bombardment[20]. In plasma based deposition techniques such as magnetron sputter deposition, the flux density and the energy of the sputtered species are inseparable and limited opportunities exist to introduce controlled bombardment (e.g., substrate biasing) during the thin film growth. However, ion beam sputter deposition technique has been established to offer the following unique features:[21]

a) Independent control of flux density and energy of the sputtered species,

b) Lower operating pressures during thin film growth ensures better quality of films and

c) The possibility of concurrent low energy ion bombardment (usually with reactive oxygen species) of the growing thin films. This sort of bombardment also offers additional benefits such as increasing adatom mobility, providing extra energy to supplement thermal energy to the species during nucleation thus reducing the crystallization temperature.

Ion beam sputter deposition technique has not been explored extensively for the

growth of multi-component oxide thin films such as ferroelectrics, while most of the efforts were towards using a compound ceramic target[22]. Very recently, few alternative attempts are evident in the literature involving ion beam sputter deposition to grow ferroelectric thin films[23,24]. A multi-ion beam sputter deposition approach has been devised in our lab at MRL/ Penn State,[25] in which three independent metal targets of Pb, Zr and Ti were individually sputtered by high energy focused ion beam sources and the schematic illustration of our system is shown in Fig.2.

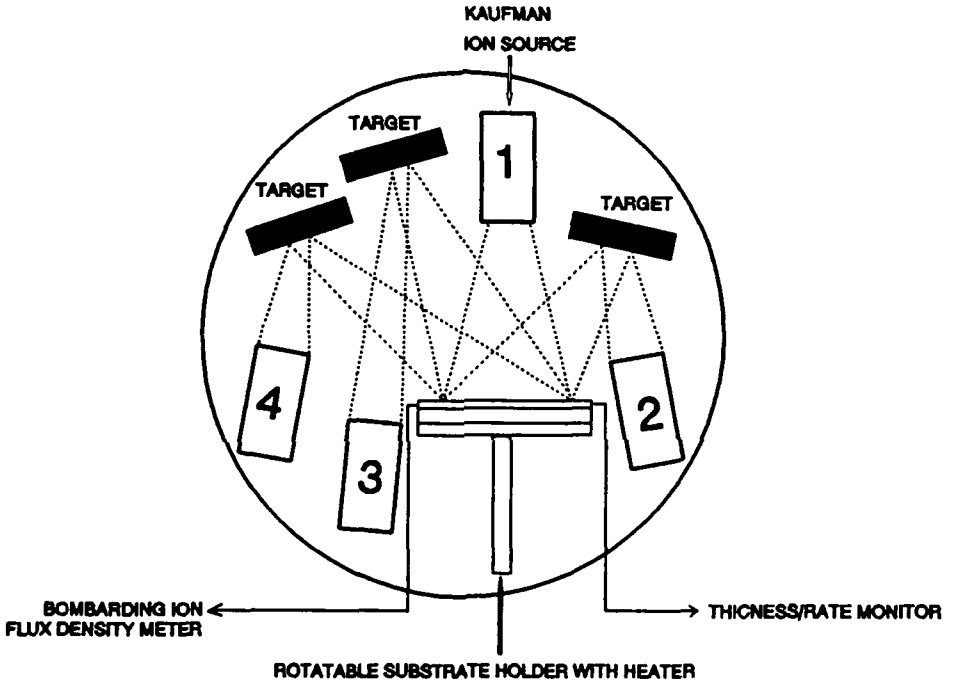


Figure 2. Schematic of MIBERS (multi-ion beam reactive sputtering system.

Three individual metal targets about 7.5 cm diameter were coordinately arranged so that a uniform profile of sputtered species was obtained. A fourth ion source was used to bombard the growing film at an incident angle of 35^{o} with respect to the normal of substrate surface. An ion flux density measurement probe was placed beside the substrates to measure the flux density of bombarding ions at the substrate. This measurement, in conjunction with the atomic flux density determined from the thickness monitor, establishes a parameter known as the ion/atom ratio which is critical to achieve reproducible bombarding effects.

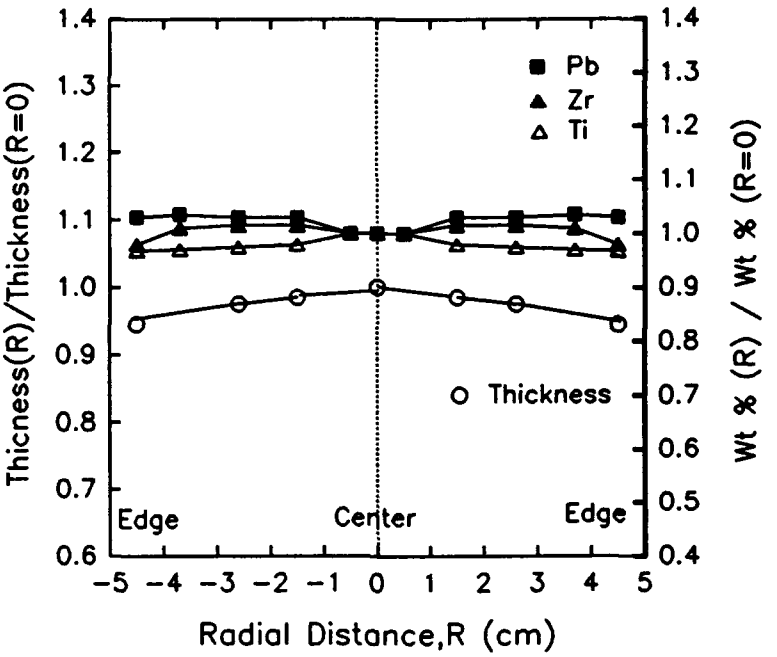


Figure 3. Radial distribution of Pb, Zr and Ti elements and thickness as well over a diameter of 4". (R is the distance from center to any point across diameter)

The deposition rates of individual targets were measured as a function of ion beam voltage, while the ion beam current and oxygen partial pressures were kept constant. The beam voltage determines the energy of the sputtered ions which is to be kept above a threshold level necessary to initiate sputtering of each metal. Small quanitites of molecular oxygen was bled into the chamber during the deposition to creaste a reactive environment for the oxidation of the sputtered metal species. By adjusting the powers on individual targets, stoichiometric PZT films could be grown and a Zr/Ti of 50/50 is mainly focused in the present work. Significantly appreciable uniformity in homogeneous distribution in the composition and thickness are achieved by this technique and is illustrated in the Fig.3. It may be seen that a variation in compositional homogeneity of < 5% and thickness by about 7% was obtained with MIBERS technique, over a diameter of 10 cm, which was observed reproducibly.

UV Excimer Laser Ablation

Pulsed laser ablation is another film deposition technique in which a plume of ionized and ejected material is produced by high intensity laser irradiation of a solid target. Most commonly, UV excimer lasers are being employed for this purpose and the wavelength of the radiation is tuned by the lasing gas composition, such as ArF (193 nm), KrF (248 nm),

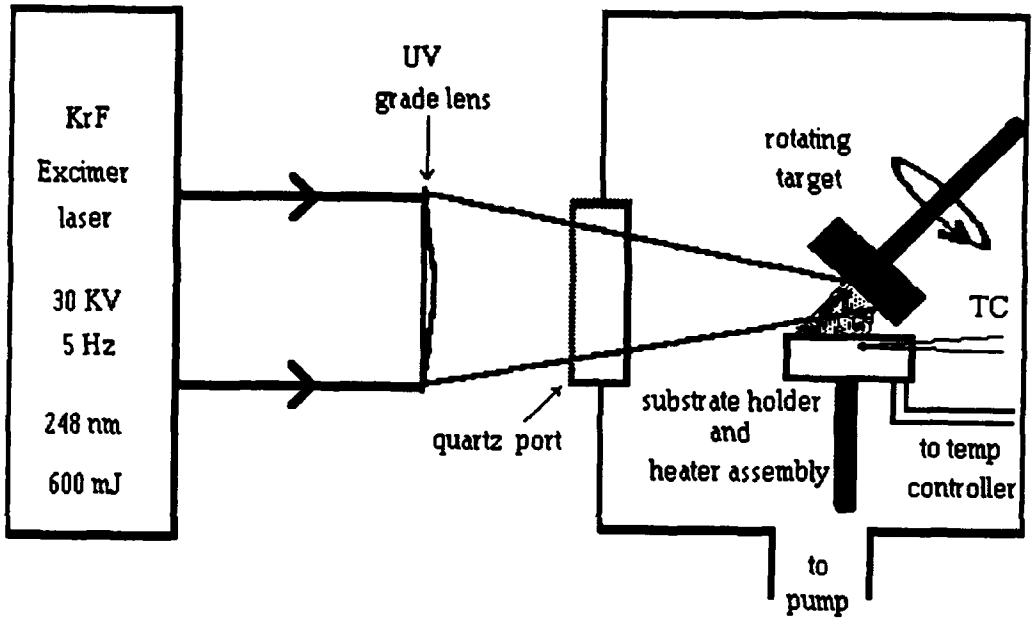


Figure 4. Schematic of UV excimer laser ablation system.

KCl (222 nm), XeF (351 nm) and XeCl (308 nm), while KrF (248 nm) has been most dominantly employed due to its high energy laser pulse output[26]. The ablation of the material is always perpendicular to target surface irrespective of the angle of incidence of laser beam and the generated plasma is composed of neutrals, ionized atomic and mostly molecular species. This technique has been popularly employed for the successful deposition of high T_c superconductors and currently being exploited for the growth of device quality *in-situ* stoichiometric ferroelectric thin films, such as $Bi_4Ti_3O_{12}$[27,28] and PZT[29,30]. Inspite of few limitations of the technique, such as the occurrence of particulates on the surface of the film and the thickness unevenness, the laser ablation offers several

advantages, such as: a) composition of the film is similar to that of target b) low crystallization temperatures because of the high excitation energy of the photo-fragments in the laser produced plasma, and c) high deposition rates.

Fig.4 shows the schematic of our laser ablation system arrangement. The output of

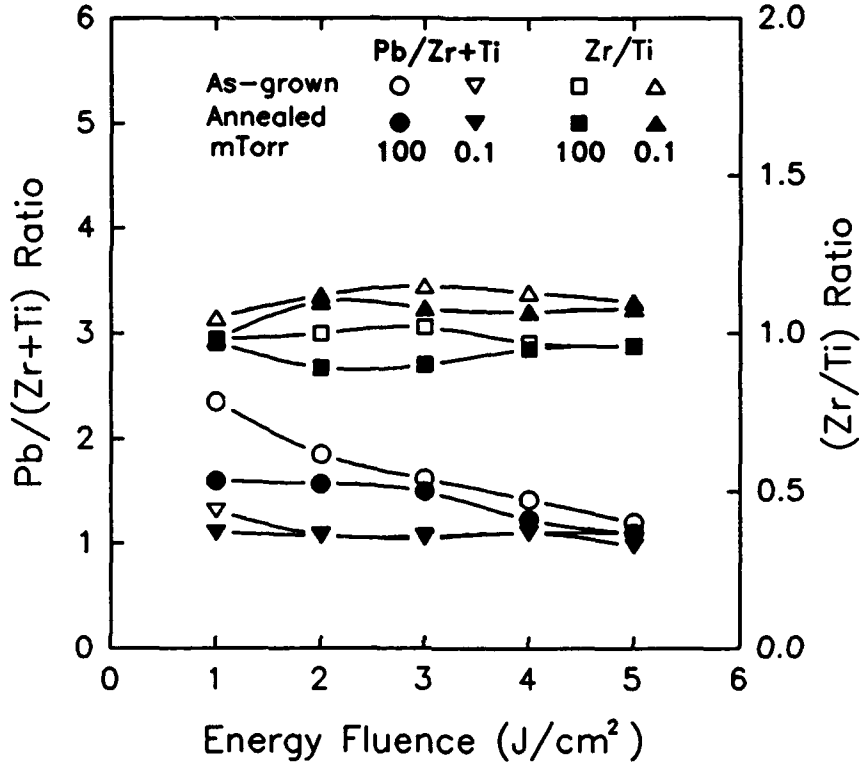


Figure 5 Variation of Pb/(Zr+Ti) and Zr/Ti ratio with laser fluence and partial pressure of oxygen in *ex-situ* crystallized films.

a KrF excimer laser beam at 5Hz and 248 nm was used in the present work. The beam is focussed by a UV grade plano-convex lens and was brought into the chamber through a quartz port. The incoming beam was incident onto the target at an angle of 45°. The beam energy density was varied by changing the laser spot size on the target. The stability of the energy of the incoming beam was regularly monitored by an energy meter. Fig.5 illustrates the results on the composition of the films deposited on silicon and platinum coated silicon substrates at ambient temperature. It can be seen that the Zr/Ti ratio remained almost same and close to that of the target. However, the films showed a persistent change in Pb content as the fluence was increased. It is apparent that below the onset of the non-thermal ablation for a certain fluence, the material is removed from the target by a thermally

assisted process which leads to preferential evaporation of lead from the target culminating in a higher amount of lead in the film. However, as the fluence level for ablation was reached (>2 J/cm^2), stoichiometric amounts of various oxides were deposited.

Electron Cyclotron Resonance (ECR) Plasma Assisted Growth

Employing plasma reactions by glow discharge has become an important research suibject in recent years,[31] while the frequency of the glow discharge has been changed from dc to microwave regions. Electron Cyclotron Resonance (ECR) plasma stream enhanced deposition is an emerging technology and allows the deposition of high quality thin films at relatively lower substrate temperatures[32]. This significant process is achieved by

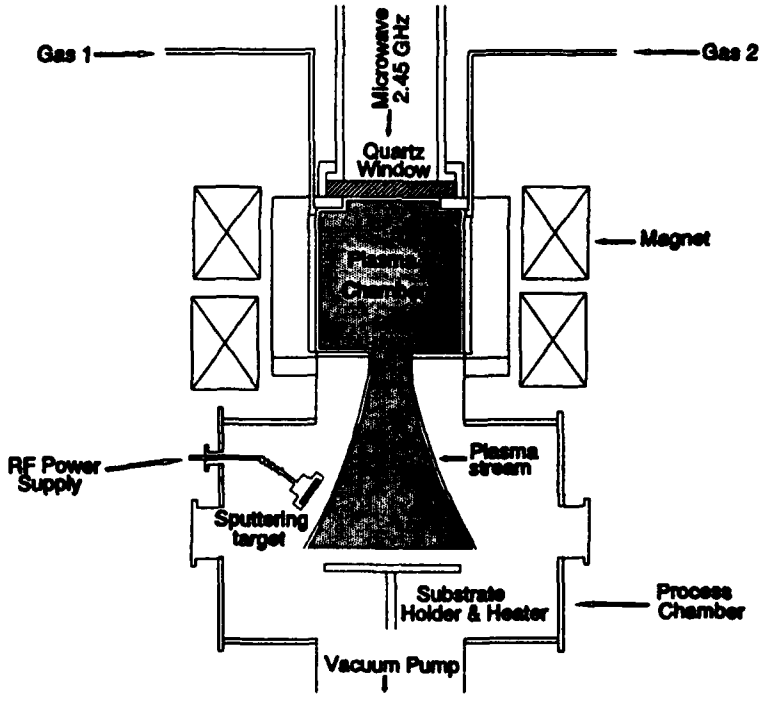


Figure 6. Schematic of ECR system coupled to magnetron sputtering.

enhancing the plasma excitation efficiency and by the acceleration effect of ions with moderate energies on the deposition reaction, using a microwave ECR source and a plasma extraction by a divergent magnetic field. Besides the efforts of depositing simple optical

oxides[33], most recently, efforts are also evident to deposit ferroelectric complex oxide thin films[34,35]. The attractive features of ECR plasma stream for the deposition of ferroelectric thin films are the following: a) enhancement of low temperature deposition process, b) even at very low pressures, the plasma density in an ECR plasma is much higher than the conventional capacitive RF plasma, c) wide operating pressure range of 10^{-5} - 10^{-1} Torr, d) ions arriving at the sample are of low energy, in the range of 5 - 50, which could be used to enhance the adatom mobility. The deposition sources (magnetrons) were arranged with an oblique angle with respect to the ECR source, as shown in Fig.6. It was observed, with such arrangement, the ECR plasma coupling enhanced the distribution of the components uniformly over large areas (15 cm diameter) as well as enhancing the ferroelectric properties of PZT thin films.

LOW ENERGY ION BOMBARDMENT INDUCED EFFECTS

It has been pointed out above that the plasma based physical vapor deposition techniques involve intrinsic low energy bombardment during the thin film growth directly or indirectly. In our attempts to gain an understanding, we have conducted the low energy ion bombardment by a Kaufman source (60-1000 eV), while the film growth was carried on by MIBERS technique. Following discussion is mostly confined to the low energy ion beam assistance and its subsequent effects on the crystallization/phase formation and electrical properties of PZT of near morphotropic phase boundary composition.

Effect on Crystallization

Normally, enhanced crystallization by energetic ion bombardment is evidenced by a reduction in either crystallization or epitaxy temperature. Similar bombardment induced crystallization enhancement was observed for PZT (50/50) thin films and the results are shown in Fig.7. Films were deposited, with near stoichiometric composition on Pt coated Si substrates.Films grown without the secondary ion bombardment assumed only pyrochlore

phase at 550°C (Fig.7a), whereas the films growrn under low energy ion (O_2^+/O^+)

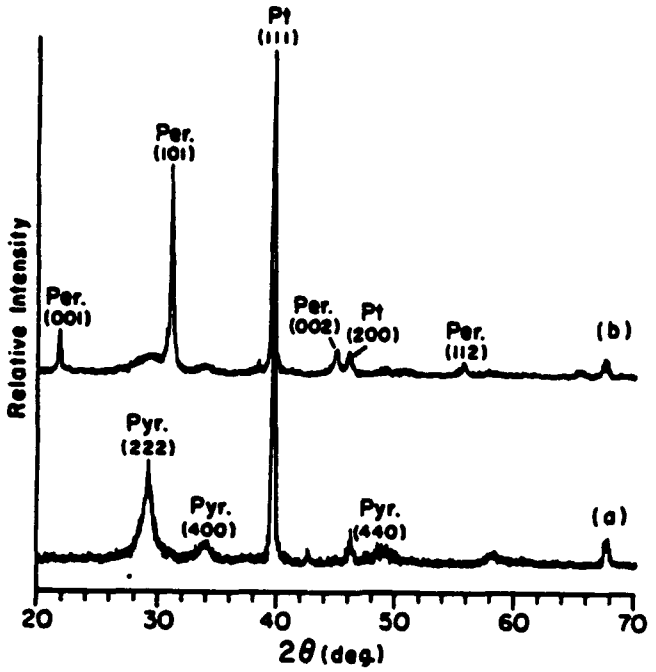


Figure 7. XRD patters of PZT films with a) no bombardment and b) bombardment.

bombardment at an energy of 75 eV and a beam current of 3 mA showed a dominant perovskite phase (Fig.7b). Considering the fact that usually temperatures in excess of 650°C were necessary to induce crystallinity by either substrate heating or post-deposition annealing, the low ion energy assistance reduced the crystallization temperature to relatively lower magnitudes.

Effect on Electrical Properties

a) Dielectric Behavior

The effect of low energy bombardment has further been examined in terms of measuring the low field dielectric constant and dissipation factors as functions of crystallization temperatures (T_c). The dielectric behavior was investigated at a frequency of 100 KHz on PZT films in MFM (Metal-Ferroelectric-Metal) configuration and the results

are shown in Fig.8. In general, after attaining the perovskite phase (T_c >600°C), these films

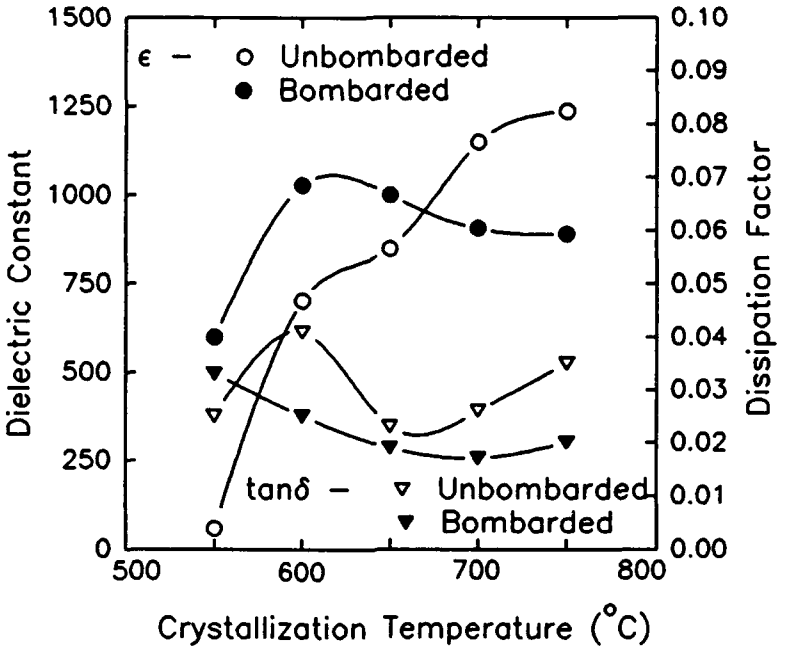


Figure 8. Effect of low energy bombardment on the dielectric behavior of MIBERS grown PZT films.

showed relatively high dielectric constant (800 - 1200) and low dissipation factors (0.02-0.03) which are comparable to those of bulk ceramic PZT of the same composition[36]. It can be seen from the figure that for T_c = 550°C, the films deposited under low energy bombardment have higher dielectric constant than the non-bombarded films, and consistent with the fact of reduction in crystallization temperature.

b) Polarization Switching

The low energy ion beam assistance further showed improvements in the polarization behavior in PZT films. The polarization switching behavior was examined in the present films using an automated modified Sawyer-Tower circuit. Typically, the ferroelectric

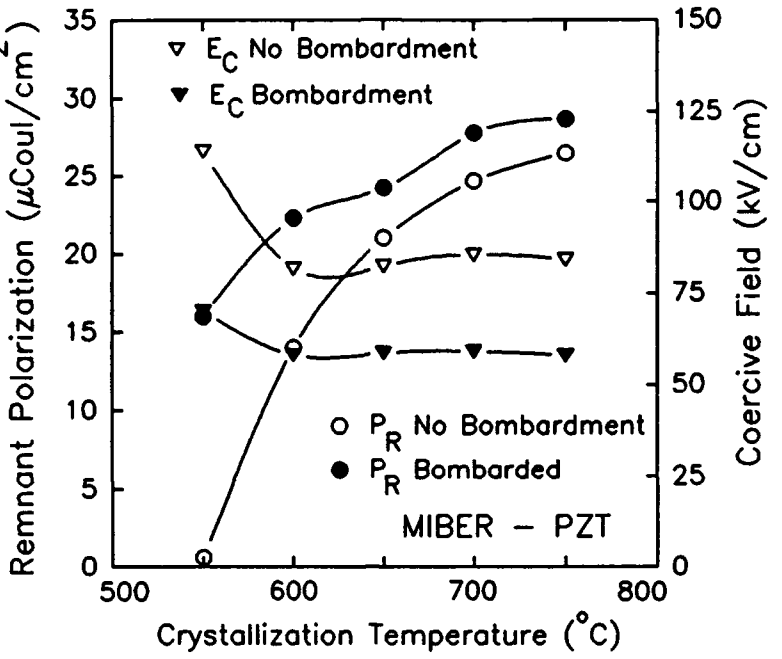


Figure 9. Effect of low energy bombardment on the polarization behavior of MIBERS grown PZT films.

hysteresis loops showed a remanent polarization of about 26 $\mu C/cm^2$ and a coercive field of about 60-70 kV/cm. However, the low energy off-normal incident ion beam appeared to improve the polarization behavior consistent with other properties and the results are shown in Fig.9. A common trend is that within the regime of crystallization temperatures, P_r showed a consistent increase with the temperature and corresponding decrease in the E_c and in case of bombardment, P_r is higher and E_c is lower for each corresponding temperature. It may be noted that the bombarded films, a) might have attained better crystallinity for each crystallization temperatures, b) gained higher degree of (001) orientation and c) might have had better electrode-film interfaces on both sides since the films had denser and smoother surfaces.

RAPID THERMAL ANNEALING PROCESS

Most recently, a rapid thermal annealing (RTA) tecvhnique using heat lamps has been

popularly applied to IC processing[37], developing low resistance ohmic contacts[38] and oxidation of silicon for growing ultra thin gate dielectrics[39]. This novel technique process to reduce the thermal budget by minimizing the processing time to only a few seconds and has recently been applied to crystallize ferroelectric thin films. Typical combination of a temperature of 600°C for about 20 sec offered pure perovskite phase PZT thin films and a systematic study of several combinations of temperature and time yielded a generalized picture, in comparison with oven annealing process, as shown in Fig.10. It may be seen that

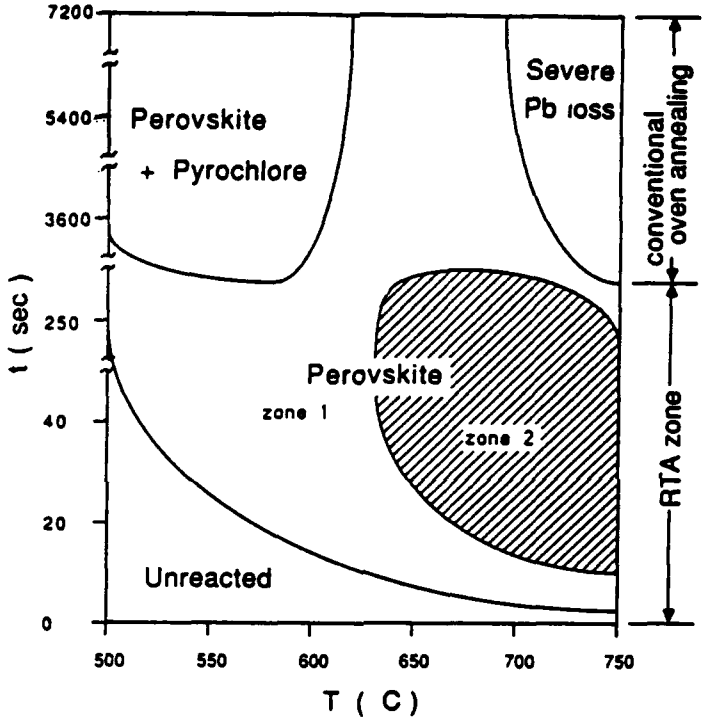


Figure 10. Generalized representation of RTA versus oven annealing effects in PZT films.

at temperatures less than 600°C, longer annealing times were necessary to attain pure perovskite phase, because in short annealing times, films showed either insufficient reaction or the presence of dominant pyrochlore phase. However, temperatures in excess of 600°C are effective in imparting pure perovskite phase even at durations as short as 10 seconds. Extended duration at these temperatures did not improve any further perovskite phase and instead, showed evidences of interface reactions. These results were compared with those obtained by conventional oven annealing and are shown in Fig.10. Upto temperatures of

600°C, even for the durations of 2 hours, PZT films showed a mixture of perovskite and pyrochlore phases and annealing beyond 700°C caused severe Pb losses. Thus for conventional furnace annealing of PZT thin films, slightly large amounts of excess Pb were needed to compensate for the loss accompanied the crystallization. These observations prompted us to notice the differences in temperature-time combinations based upon the Pb content present in the films prior to annealing.

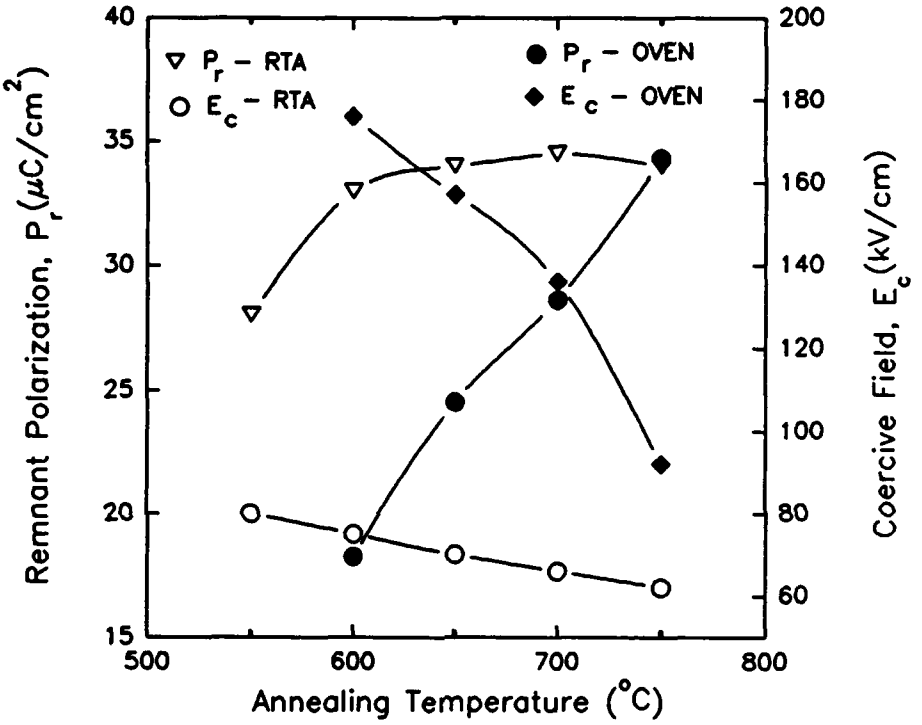


Figure 11. Ferroelectric behavior of RTA and oven annealed PZT films.

It was obsreved that the presence of excess Pb in the starting film made it relatively easier to induce perovskite phase on a reproducible basis in a wide range of temperatures and time combinations (zone 1 in Fig.10), however, exhibited a high degree of porosity due to reevaporation of excess Pb during annealing. Relatively low or stoichiometric Pb content in the as-grown films prompted more accurate control of annealing temperature-time combinations in a relatively narrower region (zone 2 in Fig.10) which repeatedly showed better morphology and dense grain structure.

The quality of RTA processed films in comparison with the oven annealed, was

further evaluated by measuring their ferroelectric properties and are shown in Fig.11. Films showed a typical dielectric constant of 700-1300 and a dissipation factor of less than 0.03 reproducibly. It may be noted that the RTA processed PZT films exhibited dielectric constants as high as 700 at annealing temperatures of 550°C while the oven annealed films showed significantly lower dielectric constant which may be attributed to the presence of pyrochlore phase. Similar property enhancement was observed for ferroelectricity in that the RTA processed films exhibited a remnant polarization of 25 $\mu C/cm^2$ at 550°C, while the oven annealed films needed higher annealing temperatures to reach those values.

In the formation of thin film PZT ceramics, a two step phase formation such as amorphous - pyrochlore and pyrochlore - perovskite during the conventional annealing process, is often reported. Such phase formation kinetics is dependent on the combination of temperature and time of annealing. However, in the present case, due to fast rise time in the RTA process, it may be realistic to assume that a single step phase formation process exists, in that a direct transition from amorphous to perovskite phase occurs, thus eliminating the pyrochlore phase formation. Besides, it may also be understood in terms of release of an instantaneous energy during the fast heating process and crystallization similar to that observed in amorphous semiconductor thin films as "explosive crystallization"[40]. Such sudden release of energy might tend to raise the local temperatures to mugh higher values than the observed and leads to an improved crystallinity at relatively lower set annealing temperatures. More studies are in progress to gain a clear understanding of phase formation and nucleation kinetics during RTA processing of ferroelectric thin films.

SUMMARY

Most recent advances in the growth processes for the deposition of ferroelectric thin films were examined. Multi-magnetron sputter deposition offers the capability of controlling the films structure via composition and reasonable uniformity in thickness and composition. The combined nature of flux and energy of species offered less flexibility of controlling properties via bombardment. Excimer laser ablation appeared to offer highest deposition rates and

stoichiometric films close to the starting target, however, the process needs more optimization for thickness and composition uniformity over large areas. Multi-ion beam reactive sputtering (MIBERS) offered excellent control over composition and thickness uniformity over large areas, reproducibly. Low energetic ion bombardment in controlled conditions, (e.g., using a Kaufman source (60-1000 eV)) offered potential to reduce the phase formation / crystallization temperature, control the orientation, modify the grain structure (finer grains) and density, and enhance the properties (crystallinity, dielectric and ferroelectric), compared to other techniques which involve no such controlled bombardment. It will be much beneficial if a better understanding of low energetic ion-surface interactions is established for multi-component ferroelectric oxide thin films. RTA process appeared to be an excellent alternate approach to induce crystallinity in the amorphous thin films of ferroelectric compositions and besides reducing the thermal budget, it also offered better dielectric and ferroelectric properties, improved density. Since RTA process has already been accepted in the existing semiconductor technology, its adaption to ferroelectric thin films processing would be quite appropriate.

ACKNOWLEDGEMENTS

The author thanks the financial assistance from DARPA (Grant # N00014-89-J-1976) for carrying out the present work and gratefully acknowledges the encouragement received from Prof. L.E. Cross.

REFERENCES

1. M.H. Francombe and S.V. Krishnaswamy, J. Vac. Sci. & Technol.A, 8, 1382 (1990).
2. J.F. Scott and C.A. Araujo, Science, 246, 1400 (1989).
3. L.E. Sanchez, S.Y. Wu and I.K. Naik, Appl. Phys. Lett. 56, 2399 (1990).
4. A. Mansingh and S.B. Krupanidhi, J. Appl. Phys., 51, 10, 5408 (1980).
5. A. Mansingh and S.B. Krupanidhi, Thin Solid Films, 80, 4, 359 (1981).
6. M. Oikawa and K. Toda, Appl. Phys. Lett., 29, 491 (1976).

7. S.B. Krupanidhi, N. Maffei, M. Sayer and K. El-Assal, J. Appl. Phys., 54, 6601 (1983).

8. R.N. Castellano and L.G. Feinstein, J. Appl. Phys., 50, 4406 (1979).

9. K.D. Budd, S.K. Dey and D. A. Payne, Br. Ceram. Proc., 36, 107 (1985).

10. M. Kojima, M. Okuyama, T. Nakagawa and Y. Hamakawa, Jpn. J. Appl. Phys., 22, Suppl.2, 14 (1983).

11. M. Okada, S. Takai, M. Amemiya and K. Tominaga, Jpn. J. Appl. Phys., 28, 1030 (1989).

12. S.B. Krupanidhi and M. Sayer, J. Vac. Sci. & Technol.A2, 2, 203, (1984).

13. S.K. Dey and R. Zuleeg, Ferroelectrics, 108, 37 (1990).

14. J.E. greene, S.A. Barnett, J.E. Sundgren, and A. Rochett, in *Ion Beam Assisted Film Growth*, edited by T. Itoh (Elsevier, Amsterdam, 1989), p.101.

15. R.Roy, K.F. Etzold, and J.J. Cuomo, MRS Symposium Proceedings, 200, (1990), p.141.

16. H. Adachi, T. Mitsuyu, O. Yamazaki, and K. Wasa, J. Appl. Phys., 60, 736 (1986).

17. K. Sreenivas and M. Sayer, J.Appl. Phys., 64, 1484 (1988).

18. K. Wasa, H. Adachi, K. Hirochi, T. Matsushima, and K. Setsune, J. Mater. Res. 6, 1595 (1991).

19. K. Terao, S. Leiphart, and S.B. Krupanidhi, Proceedings of fifth US-Japan seminar on Dielectrics and Piezoelectric Ceramics, Kyoto, Japan (1990), p.95.

20. J.M.E. Harper, J.J. Cuomo, R.J. Gambino, and H.R. Kaufman, in *Ion Bombardment Modification of Surfaces: Fundamentals and Applications*, eds. O. Auciello and R. Kelly, (Elsevier Science Publishers B.V., Amsterdam, 1984).

21. J.J. Cuomo, S.M. Rossnagel, and H.R. Kaufman, eds. Handbook of ion beam processing Technology, Noyes Publications, NJ (1990).

22. R.N. Castellano and L. G. Feinstein, J. Appl. Phys., 50, 4406 (1979).

23. A.I. Kingon, T.M. Graetinger, S.H. Rou, H.N. Al-Shareef, K.D. Gifford, P.D. Hern and O.H. Auciello, in Proceedings of fifth US-Japan Seminar on Dielectric and Piezoelectric ceramics, Kyoto, Japan, (Dec. 1990), p.324.

24. D. Xiao, Z. Xiao, J. Zhu, Y. Li and H. Guo, Ferroelectrics, 108, 59 (1990).

25. S.B. Krupanidi, H. Hu, and V. Kumar, J. Appl. Phys., (1991 In press).

26. R.K. Singh and J. Narayan, Phys. Rev. B 41, 8843 (1990).

27. H. Buhay, S.Sinharoy, W.K. Kasner, M.H. Francombe, D.R. Lampe and E. Stepke, Appl. Phys. Lett. 58, 1470 (1991).

28. N. Maffei and S.B. Krupanidhi, Appl. Phys. Lett. (1991 In Press).

29. D. Roy, S.B. Krupanidhi and J.P. Dougherty, J. Appl. Phys., 69, 7930 (1990).

30. K.L. Saengr, R.A. Roy, K.F. Etzold and J.J Cuomo, Mater. Res.Symp. Proc. 200, 115 (1990).

31. D.B. Beach, IBM J. Res. Dev. 34, 6, 795 (1990).

32. M. Ohkubo, Jpn. J. Appl. Phys., 27,7, L1271 (1988).

33. K. Machida and H. Oikawa, J. Vac. Sci. & Technol. B4, 818 (1986).

34. M. Okuyama, Y. Togani, and Y. Hamakawa, Appl. Surf. Sci., 33/34, 625 (1988).

35. Y. Masuda, A. Baba, H. Masomoto, T. Goto, M. Minakata and T. Hirai, Proceedings of fifth US-Japan meeting on Dielectric and Piezoelectric ceramics, Kyoto, Japan, (Dec. 1990), p.337.

36. B. Jaffe, W.R. Cook, and H. Jaffe, *Piezoelectric Ceramics* (Academic, New York, 1971), p.142.

37. T. Hori and H. Iwasaki, IEEE Electron Device lettrs, 10, 64 (1989).

38. L.H. Allen, L.S. Hung, K.L.Kavanagh, J.R. Phillips, A.J. Yu and J.W. Mayer, Appl. Phys. Lett. 51, 326 (1987).

39. J. Nulman, J.P. Krusius and A. Gat, IEEE Trans. Electron Device Letters, EDL-6, 205 (1985).

40. R. Messier, T. Takamori, and R. Roy, J. Non-Cryst. Solids, 8-10, 816 (1972).

AD-P006 640

ADVANCES IN PROCESSING AND PROPERTIES OF PEROVSKITE THIN-FILMS FOR FRAMs, DRAMs, AND DECOUPLING CAPACITORS

S.K. DEY, C.K. BARLINGAY, J.J. LEE, T.K. GLOERSTAD and C.T.A. SUCHICITAL.

Department of Chemical, Bio and Materials Engineering and
Centers for Solid State Science/Electronics Research,
Arizona State University, Tempe, AZ 85287-6006, U.S.A.

Abstract Highly oriented, dense, and crack-free ferroelectric and paraelectric thin-films on three inch diameter Pt / Ti / Si_3N_4 / Si (100) substrates were obtained by polymeric sol-gel processing. Ferroelectric PZT thin-films were fabricated at temperatures as low as 550°C within 15 minutes by rapid thermal annealing. The films heat treated at 700 °C for 5 minutes were single grain thick and exhibited P_r, P_{sp}, and E_c in the ranges of 29-32 $\mu C/cm^2$, 44-53 $\mu C/cm^2$, and 50-60 kV/cm, respectively, and high speed switching times below 5 ns on 30x30 μm^2 electrodes. A switching time of 2.7 ns was observed on 19x19 μm^2 area electrodes at a field of 200 kV/cm. Results of low and high field characterization on paraelectric PLT thin-films which were conventionally heat treated indicated that it has an excellent potential for use in ULSI DRAMs and as decoupling capacitors. These films showed a high charge storage density (15 $\mu C/cm^2$) and a low leakage current (0.5 $\mu A/cm^2$) at a field of 200 kV/cm. Also, the charging time for a capacitor area of 1 μm^2 at 200 kV/cm was estimated to be 0.10 ns.

INTRODUCTION

Recently, there has been increasing interest in perovskite thin-films due to their high permittivities and bistable polarization states.[1-8] The bistable nature of $PbZrO_3$-$PbTiO_3$ or PZT ferroelectric thin-films offers the potential for binary memories that are truly non-volatile and radiation hard.[1-4] Reading or writing is accomplished with a pulse of sufficient magnitude and duration.[2] Switching times below 3 ns are required for the fabrication of fast switching ferroelectric random access memories (FRAMs).[9]

For a number of high speed non-switching applications, there is a critical need for chip integrated dielectric materials with low leakage currents, high dielectric strengths, and high dielectric permittivities.[5-8,10] Ferroelectric PZT thin-films are also being explored for these unipolar applications[6-8], which in our view, present a number

92-16104

of disadvantages. The large difference between the switched polarization, P_{sp}, and the remanent polarization, P_r, in the saturation arm of the hysteresis loop, is due to the contributions of the linear capacitive charge and also from the relatively slow and time dependent polarization switching processes. These latter processes, namely, domain reorientation and phase switching, not only pose a potential fatigue problem but also can increase loss tangent, tan δ, and severely limit the charging and discharging speeds of the capacitors.[5] Therefore, non-switching cubic paraelectric (i.e., non-ferroelectric) dielectrics with extremely high permittivity, should offer significant advantages over their ferroelectric counterparts for unipolar non-switching operations such as in ULSI DRAMs and decoupling capacitors. For example, Pb-based ferroelectric perovskite can be transformed into cubic paraelectric perovskite by chemical modification. Thus, a 28 mol% lanthanum modified lead titanate (PLT) in chip integrated form would be a suitable choice for the aforementioned applications, due in part to the simple composition that would lend itself to ease of processing.

A trend towards the integration of linear and non-linear dielectric thin-films onto semiconductors has led to the progress in the understanding of organometallic precursor synthesis, thin-film fabrication, interfacial effects, and the evolution of the microstructure and their influences on electrical properties. To date, research efforts of our group have focused on the thin-film chemical processing techniques, namely polymeric sol-gel[2,3,5,12,13] and plasma enhanced chemical vapor deposition (PECVD).[14,15] These routes have a number of advantages over physical vapor deposition methods including; low processing temperature (<550 °C), excellent compositional control, thickness and lateral film homogeneity without cracking, high purity, ease of fabrication over large areas with conformal step coverage, and moderately low cost with a short processing cycle.

The processing of perovskite dielectric capacitors will be preceded by IC fabrication steps to incorporate circuit elements within the semiconductor substrate. This will impose severe restrictions on the flexibility in processing of the ferroelectric thin-films. Most critical restriction will be the heat treatment temperature, since it is necessary to preserve the structure of the underlying device. It is believed that rapid thermal annealing (RTA) of the dielectric thin-film will help maintain dopant profiles in the underlying semiconductor read/write circuits due to the reduced time and temperature of processing. Additionally, it is envisioned that dense thin-films can be obtained with the combination of densification additives and RTA.

PROCESSING AND PROPERTIES OF PEROVSKITE THIN-FILMS

This paper reports and discusses the recent developments in our laboratory on sol-gel processing along with the static and dynamic electrical properties of perovskite dielectric thin-films. In this study, two different perovskite thin-films were fabricated and electrically characterized to determine their potential for specific applications, i.e., a) a switching ferroelectric $Pb(Zr_{0.52}Ti_{0.48})O_3$ for high speed switching FRAMs, and b) a non-switching paraelectric $(Pb_{1-\alpha x}La_x)TiO_3$ (α=1.32, x=0.28) for ULSI DRAMs and decoupling capacitors. Additionally, the use of rapid thermal annealing (RTA) in achieving dense and crack-free ferroelectric thin-films, at temperatures as low as 550 °C is demonstrated.

EXPERIMENTAL

Thin-Film Fabrication

Zr (or La) and Ti methoxyethoxide were reacted with anhydrous Pb-acetate under dry nitrogen using standard Schlenk technique to synthesize the precursor Pb-Zr-Ti (or Pb-La-Ti) complex. Niobium methoxyethoxide was added in the required quantity in PZT solutions. Details of the fabrication procedure for PZT and PLT thin-films were reported previously.[2,5,12,13] The precursor solution was then hydrolyzed in the presence of basic catalyst (NH_4OH) and aged to form the spin casting solution. This solution was spin cast onto three inch diameter Pt / Ti / Si_3N_4 / Si (001) wafers at 2000 rpm for 80 seconds. A typical thickness of 1000 Å per layer was obtained. Thin-films (0.5 μm) were fabricated with multiple depositions accompanied by heating at 350 °C for 1 minute between layers and for 15 minutes after the last layer. The final crystallization and sintering of PLT thin-films was carried out by conventional tube furnace at 700 °C for 20 minutes in air. The PZT thin-films were however, heat treated at 550-700 °C for 5-15 minutes using an AG Associates Heat Pulse 610 rapid thermal annealing (RTA) furnace.

Characterization

The capacitor area was defined by top gold electrodes, which were deposited by sputtering using a laboratory scale sputter coater. Low field measurements were carried out on a HP4192 multifrequency LCR meter with an oscillation level of 15 mV (i.e., 300 V/cm). Polarization-field (P-E) properties were evaluated using the standard Sawyer-Tower circuit in conjunction with a HP54503A Digitizing Oscilloscope and

Wavetek Model 191 20MHz Pulse/Function Generator. The leakage current (I-V) characteristic was measured on a HP4145 picoampere current meter. Switching and charging times were defined as the time required for the maximum transient current to decrease by 90 percent. The switching and charging transient measurements (I-t) were done with a "Digital Signal Analyzer" (Tektronix DSA 602) and a mercury wetted relay pulse generator. The latter instrument was rated for high amplitude (50V), high current (1A) and short rise and fall times (1 ns) of the pulse.[16]

RESULTS AND DISCUSSIONS

Ferroelectric PZT Thin-Films

Densification and Microstructure

Conventional furnace sintering (at 700 °C for 0.5 hr) of PZT (52/48) with 15% excess PbO showed intergranular porosity.[2,12] This was due to the slow heating rate in the furnace that caused the removal of organics and crystallization to occur simultaneously. Incomplete densification of the amorphous gel-matrix prior to crystallization also contributed to the residual porosity. This lead to trapped pores in the rigid crystalline matrix which were difficult to remove, and therefore, required extreme thermal treatments for full densification of the polycrystalline matrix.[17]

The removal of residual organics followed by the densification of the amorphous gel-matrix in thin-films, prior to crystallization, was possible by using a rapid rate of heating (250 °C/s) in a halogen lamp RTA furnace. Additionally, the incorporation of excess PbO[13] or niobium as sintering additive was essential for the complete densification of stoichiometric thin-film products. For example, the site occupancies for niobium modified stoichiometric PZT (A/B=1) is given by equation 1:

$$PbNb_XTi_{1-X}O_{3+X/2} \text{ -----> } [Pb_{1-X/2}V''_{X/2}]_A[Nb_XTi_{1-X}]_BO_3 + X/2\ PbO \qquad (1)$$

The substitution of niobium at the B-site forms lead vacancies which expedites mass transfer and therefore, densification.[18]

An effective heat treatment schedule was comprised of an initial organic removal step followed by the densification of the amorphous films (at 500 °C for 15 minutes). Finally, dense polycrystalline microstructures developed between 550-700 °C within 5 to 15 minutes. Figure 1 illustrates a SEM micrograph of PZT(52/48) thin-film with

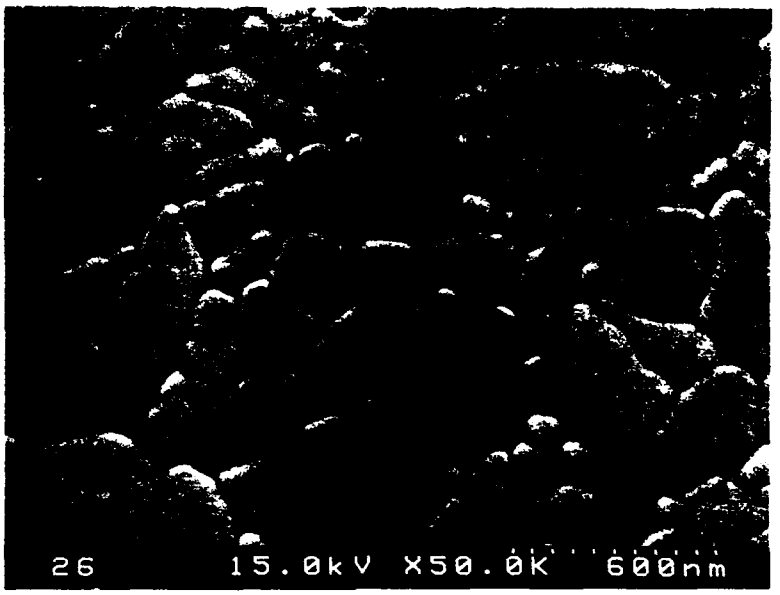


Figure 1: SEM micrograph of a 0.5 μm PZT (52/48) thin-film with 15% excess PbO additive, crystallized and sintered at 700 °C for 5 minutes.

15% excess PbO, that was crystallized and sintered in the RTA at 700 °C for 5 minutes. The film exhibited submicron grains (0.2-0.6 μm) with a columnar growth habit (Figure 2). A dense microstructure was also obtained for 2% niobium modified PZT(52/48), but with a narrow grain size (0.4-0.6 μm) distribution.[19]

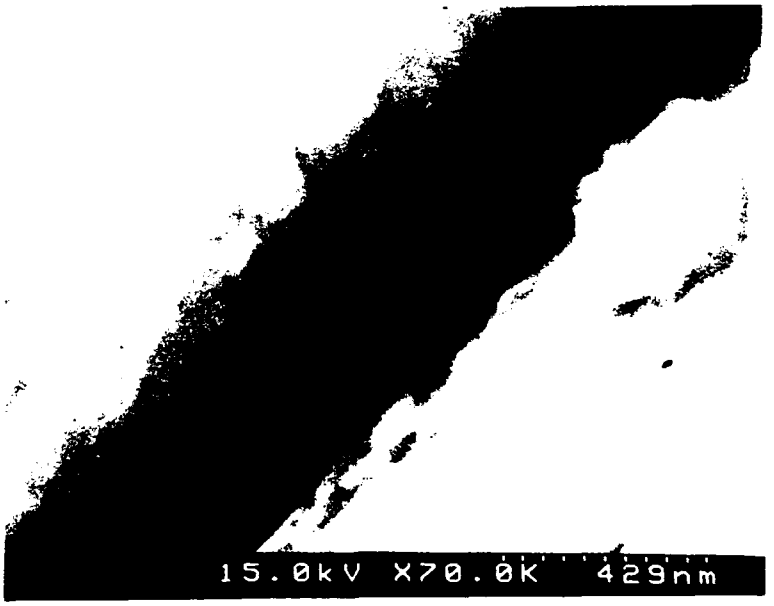


Figure 2: Cross-sectional view of 0.5 μm PZT (52/48) thin-film with 15% excess PbO additive, crystallized and sintered at 700 °C for 5 minutes; showing columnar grain growth.

Interestingly, films that were heat treated at temperatures as low as 550°C for 15 minutes also developed dense polycrystalline microstructres with grain sizes in the range of 0.4-1.0 μm. A typical microstructure of the thin-film heat treated at this low temperature is illustrated in Figure 3. X-ray diffraction carried out on all these thin-films revealed the perovskite crystal structure and absence of any other second phase. This result was surprising because in certain compositions upto 15% excess lead was added to stoichiometric PZT to expedite densification. Since there exists a narrow range of cation stoichiometry in PbO-TiO_2 and PbO-ZrO_2 systems[18], the excess lead is expected to be in the form of an amorphous or nanocrystalline second phase. High resolution TEM studies would be required to confirm this. Futhermore, highly oriented PZT (111) thin-films were observed on platinum (111) passivated silicon.



Figure 3: SEM micrograph of a 0.5 μm PZT (52/48) thin-film, sintered at 550°C for 15 minutes.

High Field Characterization

Stable 100 Hz-1KHz hysteresis loops were obtained on sub-micron PZT thin-films (with 1 mm diameter electrodes) using 10 and 15 V_P (peak voltage) sinusoidal waves. The remanent polarization (P_r), switched polarization (P_{sp}), and coercive field (E_c) for PZT(52/48) with 15% excess PbO were in the ranges of 29-32 $\mu C/cm^2$, 44-58 $\mu C/cm^2$, and 50-55 kV/cm, respectively. A well saturated hysteresis loop is illustrated in the inset of Figure 4 for PZT(52/48) with 15% excess lead oxide. The beneficial effect of PbO is clearly manifested in the improved density and therefore, the hysteresis

properties of these PZT films as the quantity of excess PbO is increased. For example, stoichiometric PZT thin-films with 0%, 5% and 15% excess lead compositions exhibited P_r and E_c in the ranges of 8-10, 14-20, 29-32 $\mu C/cm^2$ and 95-100, 75-80, 50-55 kV/cm, respectively. The niobium modified PZT(52/48) showed a very low coercive field of 30-35 kV/cm and remanent polarization of 18 $\mu C/cm^2$.

Figure 4 illustrates a 6.7 KHz pulse switching experiment result, performed on 1mm diameter PZT(52/48) thin-film capacitors with 15% excess lead additive. A full switching transient (fs) is obtained by applying a positive voltage pulse to the thin-film which was initially polarized negatively ($-P_r$) with a negative voltage pulse. Similarly a non-switching (ns) is obtained by applying a second positive voltage pulse to the thin-film which was previously polarized positively with the first positive pulse. The integrated area of the switching transient (i.e., sp, obtained by subtracting ns from fs

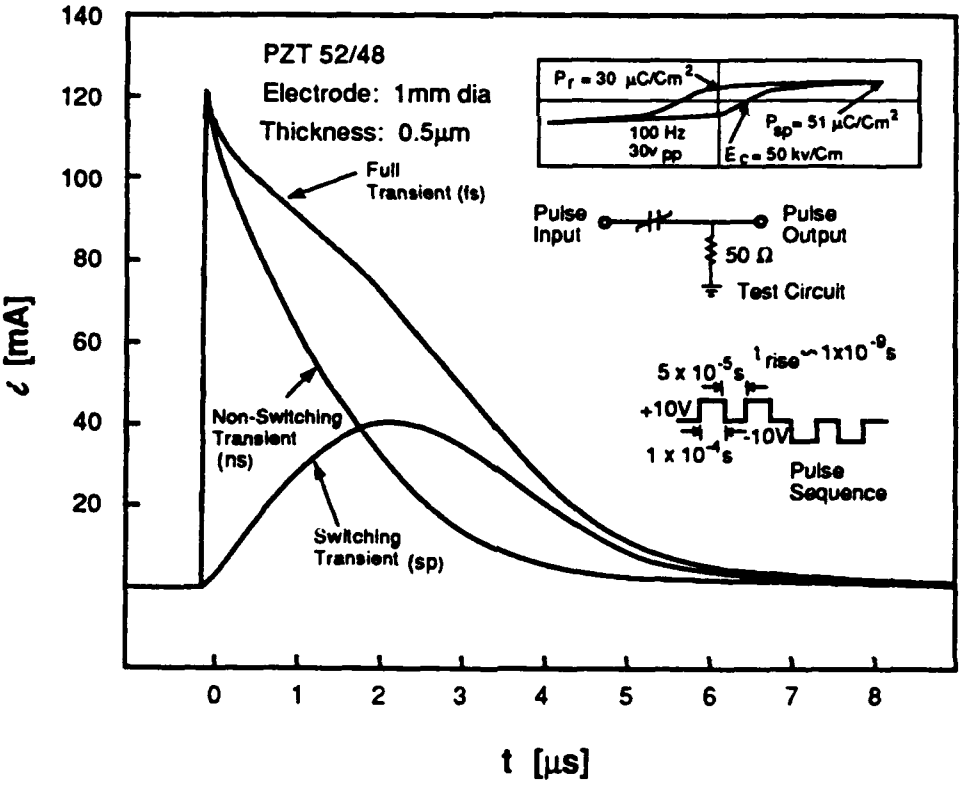


Figure 4: Circuit diagram, pulse sequence, and transient characteristics (for two positive pulses only) of 0.5 μm PZT (52/48) thin-film with 15% excess PbO. The corresponding Sawyer-Tower hysteresis loop in the inset.

transient) was found to be 0.8×10^{-7}C for a applied field of 200 kV/cm. This switched charge obtained from the pulse measurements is about 60 percent of the low frequency hysteresis P_r value. Note that the long switching time (> 5 μs) is a result of the electrical time constant of the measuring circuit. Therefore, the effect of reducing the capacitance (C) can be clearly seen in Figure 5 where the measurement was carried out on a smaller area (30x30 μm^2) electrode and a switching time below 5 ns was observed. Furthermore, a switching time of 2.7 ns was observed on 19x19 μm^2 area electrodes at a field of 200 kV/cm.

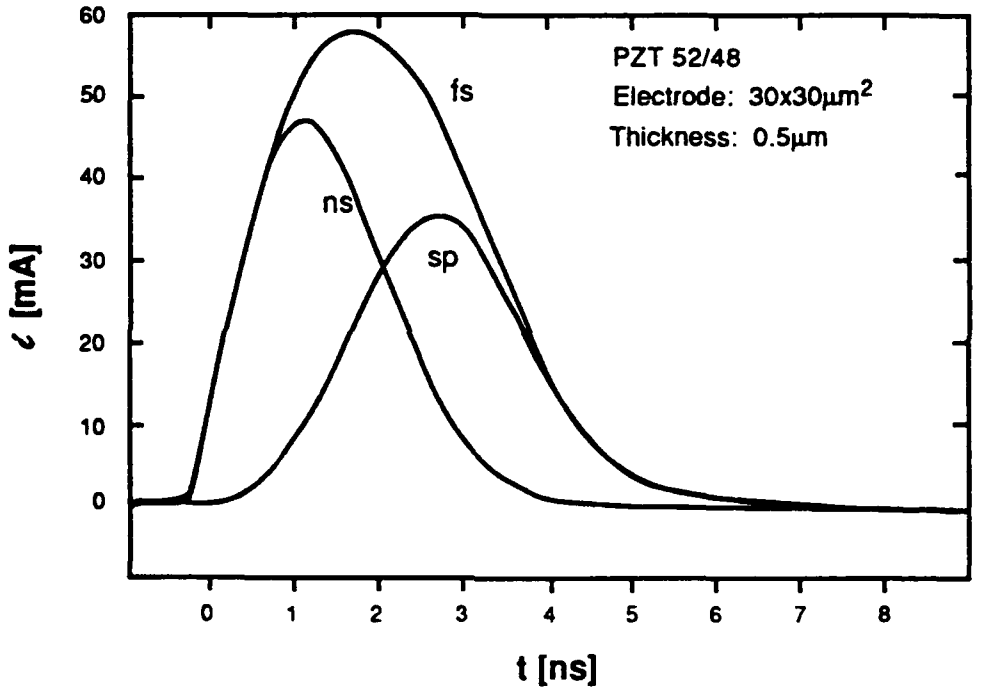


Figure 5: Full switching (fs), non-switching (ns) and switching (sp) transients obtained on 30x30 μm^2 Pt electrodes deposited on PZT(52/48) thin-film fired at 700°C for 5 minutes.

Note that the rise time (1 ns) of the pulse used to generate Figure 5, now appears to be the limiting factor for measuring the intrinsic switching speed. Scott et. al.[20] reported, switching times faster that 100 ns for PZT (54/46) thin-films but their measurements were also limited by the rise time of the input pulse. Currently, studies are underway to extract the domain dynamical parameters, and therefore the mechanisms of high speed switching in thin ferroelectric films.

Non-Switching Paraelectric PLT Thin-Films

All electrical characterization were carried out on 0.5 μm PLT(28) thin-films with the pure cubic perovskite phase which were conventional sintered at 700 °C for 20 minutes.

Low Field Properties

In the frequency range of 100 Hz to 13 MHz, polycrystalline PLT thin-films exhibited dispersionless dielectric permittivity (ε_r) and loss tangent (tan δ) values of ~1400 and 0.015 at room temperature, respectively. An area independent ε_r value was observed in the range of 438x438 μm^2 to 25x25 μm^2. The ε_r value decreased by 13 percent as the temperature was varied from 20 °C to 100 °C.[5]

Polarization-Electric Field (P-E) Characteristics

The P-E characteristics were evaluated by connecting the sample on a typical Sawyer-Tower circuit (Fig. 6(a)) with an input sine wave of 100 Hz. Fig. 6(b)-(d) illustrate the P-E characteristics of PLT(28) thin-films under different peak voltage (V_p). In Figure 6(b), with a V_P of 2V (40 kV/cm), the effective ε_r (calculated from the slope) equals 1400, and the thin-film is a linear capacitor. The corresponding polarization, or charge storage density, is 5.7 $\mu C/cm^2$. On increasing V_P (Figures 6(c) and (d)), the polarization tends towards saturation and the effective ε_r diminishes. For example, the effective ε_r is ~850 at V_P of 10V (200 kV/cm), while the polarization is 15 $\mu C/cm^2$.

Charging Time

The charge storage densities and charging times were estimated from varying amplitude pulse voltage experiments.[5,7] The field dependence of the charge storage density was in agreement with data obtained by the P-E measurements. The plots (Figure 7) of the total charging time (t_T) versus capacitor area (A_C) for different electric fields followed the relation:

$$t_T = 2.303(R_L C) + t_P = t_C + t_P \qquad (2)$$

where R_L, the load resistor, and C, the field dependent capacitance. Note that t_T is

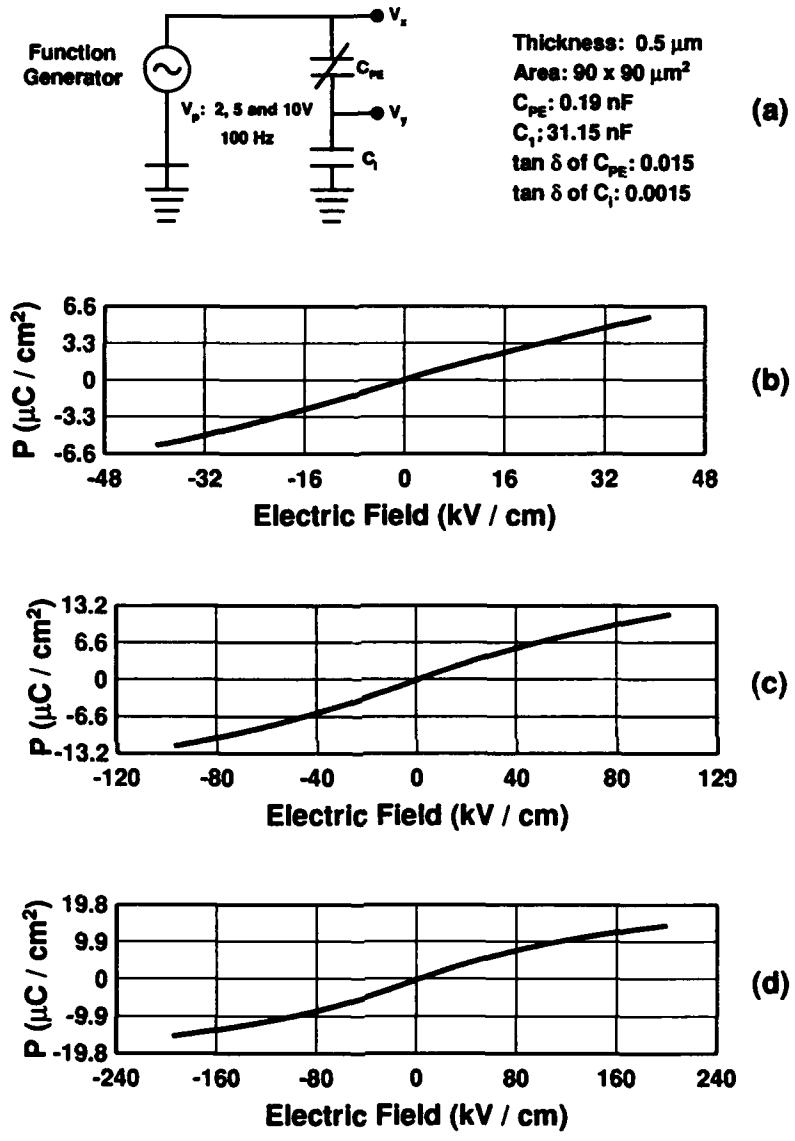


Figure 6: (a) Sawyer-Tower circuit and P-E characteristics of 0.5 μm PLT(28) thin-film at V_p of (b) 2V, (c) 5V, and (d) 10V.

comprised of the intrinsic charging time (t_C), and the test set-up parasitic capacitance (t_P). From the intercept of Figure 7, the value of t_P was determined to be 0.7 μs; which implies that t_C is ~1.4 μs (since t_T = 2.1 μs) at E=100 kV/cm for a capacitor area, A_C, of 10,000 μm^2. Simple extrapolation to dimensions of A_C ~1 μm^2, enables one to estimate a t_C of ~0.14 ns at 100 kV/cm.The charging times for different fields are tabulated in the inset of Figure 7.

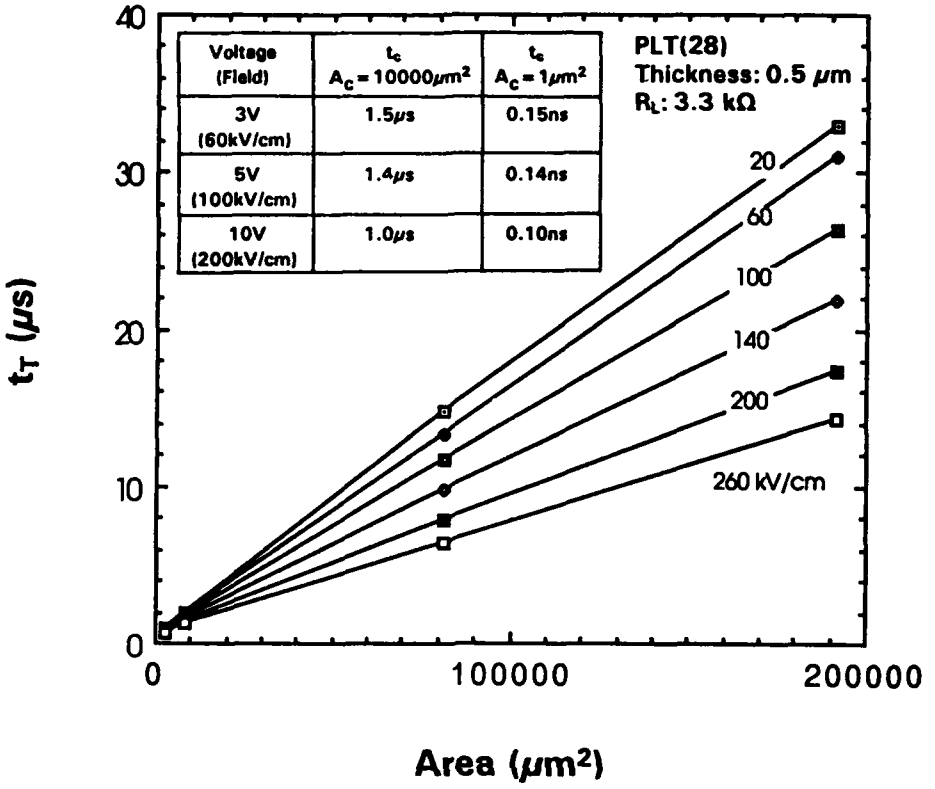


Figure 7: Charging time as a function of electrode area at different electric fields for 0.5 μm PLT(28) thin-film.

Electrical Conduction

The effective SiO_2 field is defined[5,8] as

$$E_{eff,\,SiO2} = (E_{app} \cdot \varepsilon_{r,\,diel.}) / \varepsilon_{r,SiO2} \qquad (3)$$

where E_{app} is the applied field on the dielectric thin-film, and $\varepsilon_{r,\,diel.}$ and $\varepsilon_{r,SiO2}$ are the dielectric permittivities of dielectric thin-film and SiO_2, respectively. This equation implies that dielectric thin-films with the same $E_{eff,\,SiO2}$ have the same amount of charge storage density. The leakage current density versus $E_{eff,\,SiO2}$ for a PLT thin-film is compared with SiO_2[21], Ta_2O_5[22], and ferroelectric PZT[8] thin-films in Figure 8. Since the ε_r value of PLT thin-film is high, a 3V (V_{app}) across a PLT thin-film corresponds to an effective SiO_2 field ($E_{eff,\,SiO2}$) of 20 MV/cm. In this high $E_{eff,\,SiO2}$ regime, note that the PLT thin-film exhibits superior leakage characteristic to the aforementioned dielectric

thin-films. The leakage current densities at $E_{eff, SiO2}$ of 20, 30 and 45 MV/cm (i.e., E_{app} of 60, 100 and 200 kV/cm, respectively) are 0.30, 0.38 and 0.50 μA/cm^2, respectively.

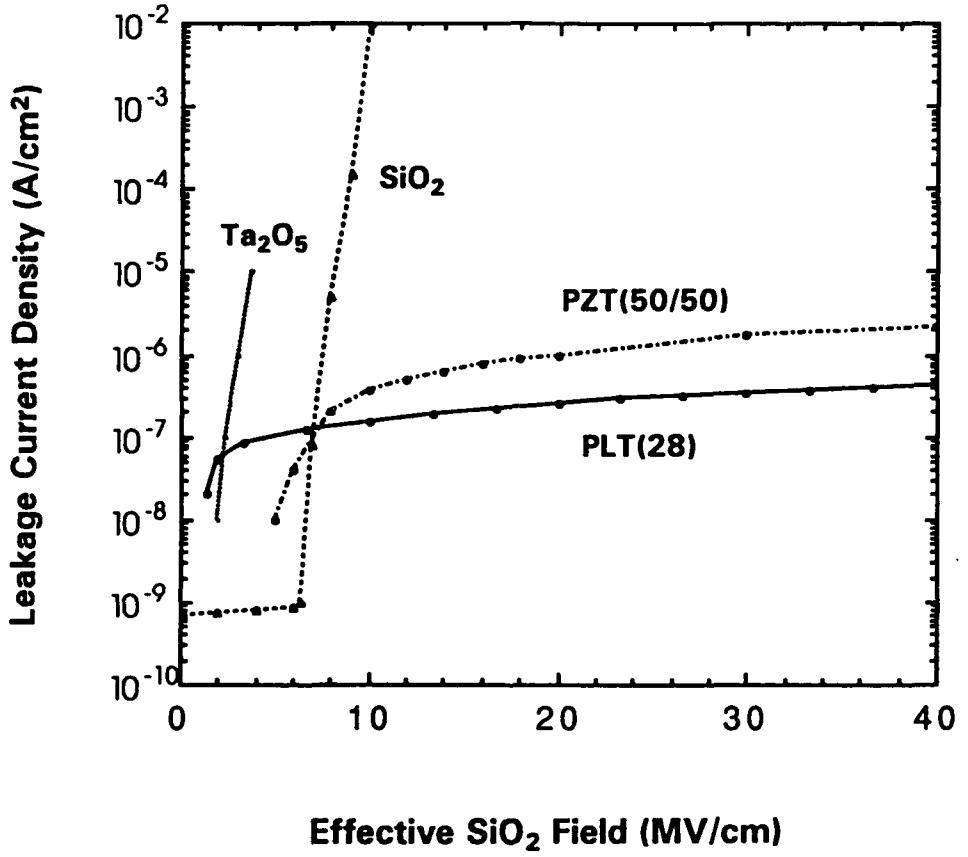


Figure 8: Comparison of leakage current density of paraelectric 5000Å PLT(28) thin-film with 200Å SiO_2[21], 640Å Ta_2O_5[22] and 4000Å ferroelectric PZT[8] thin-films.

In future, sol-gel processing of PLT thin-films coupled with RTA has the potential to obtain dense microstructures as illustrated earlier in this paper for ferroelectric PZT thin-films. Consequently, the charge storage density will increase and the leakage current density will decrease significantly for a given applied field. Furthermore, the low value of the leakage current density (e.g., 0.50 μA/cm^2) at very high $E_{eff, SiO2}$ (i.e., 45 MV/cm), gives one the freedom to reduce the thickness (<<0.5 μm) of PLT thin-films in order to obtain higher capacitances for a given area and voltage; thus increasing the potential for higher density circuits.

CONCLUSIONS

The removal of residual organics followed by the densification of the amorphous gel-matrix in thin-films, prior to crystallization, was possible by using a rapid rate of heating (250 °C/s) in a halogen lamp RTA furnace. Additionally, the incorporation of excess PbO (15%) or niobium (2%) as sintering additive was essential for the complete densification of stoichiometric PZT thin-films. The PZT(52/48) thin-films with 15% excess lead oxide additive exhibited P_r, P_{sp}, and E_c in the ranges of 29-32 $\mu C/cm^2$, 44-58 $\mu C/cm^2$, and 50-60 kV/cm, respectively. Dense and crack free PZT thin-films were obtained at temperatures as low as 550 °C. The reduced processing time and temperature using rapid thermal annealing would help maintain the dopant profiles in the underlying semiconductor read write circuits. A switching time of 2.7 ns was observed on a 19x19 μm^2 ferroelectric capacitors at a field of 200 kV/cm. These studies demonstrate that high speed switching ferroelectric memories that are non-volatile can be integrated onto Pt passivated Si wafers.

28 mol% La modified $PbTiO_3$ or PLT(28) thin-films have been successfully fabricated by the sol-gel route. A high charge storage density (15 $\mu C/cm^2$) and low leakage current density (0.50 $\mu A/cm^2$) has been illustrated in this study. Additionally, the charging time for 1 μm^2 capacitor has been estimated to be 0.1 ns at 200 kV/cm. The use of paraelectric (non-switching) PLT thin-films with linear dielectric characteristic offers significant advantages over conventional dielectrics (e.g., SiO_2 and Ta_2O_5) and is also preferable to ferroelectric thin-films for use in ULSI DRAMs and as decoupling capacitors.

ACKNOWLEDGEMENTS

This work was supported by the Defence Advanced Research Project Agency (DARPA). The authors would like to thank Brad Lawrence and Bill Roth of Hitachi, Nissei Sangyo America Limited for microstructural analysis of the films.

REFERENCES

1. J. Free, *Popular Science*, 86, April (1990).
2. S.K. Dey and R. Zuleeg, *Ferroelectrics*, **108**, 37 (1990).
3. S.K. Dey and R. Zuleeg, *Ferroelectrics*, **112**, 309 (1990).
4. The First and Second Symp. on Integrated Ferroelectrics, Eds. C. A. Araujo and G.W. Taylor, *Ferroelctrics*, **112** (1990) and **116** (1991).
5. S.K. Dey and J.J. Lee, submitted to *IEEE Trans. Electron Device* (1991).

6. L.H. Parker and A.F. Tasch, *IEEE Circuit and Devices Magazine*, 17, Jan. (1990).
7. D. Sudhama. J.C. Carrano, L.H. Parker, V. Chikarmane, J.C. Lee, A.F. Tasch, W. Miller, N. Abt and W.H. Shepherd, *Mat. Res. Soc. Sym, Proc.*, **200**, 331 (1990).
8. R. Moazzami, C. Hu and W.H. Shepherd, *IEEE Electron Device Lett.*, **11**, 454, Oct. (1990).
9. L.J. Schwee, *Ferroelectrics*, **116**, 157 (1991).
10. D.A. Chance, C.W. Ho, C.H. Bajorek and M. Sampogna, *IEEE Trans. Comp. Hybrids, Manufac. Technol.*, **CHMT-5**, 368 Dec. (1982).
11. D. Henning and K.H. Hardtl, *Phys. Stat. Sol. (a)*, **3**, 465 (1970).
12. A.R. Modak and S.K. Dey, *Ceram. Trans.* **15**, "Materials and processes for Microelectronic systems", edited by K.M. Nair, R. Pohanka and R.C. Buchanan, 477 (1990)
13. A. R. Modak, M.S. Thesis, Chem. Bio. and Mat. Engg., Arizona State University (1991).
14. W.T. Petuskey, D.A. Richardson and S.K. Dey, *Ferroelectrics*, This issue.
15. D.A. Richardson, W.T. Petuskey and S.K. Dey, *Proc. of the Symp. on Ferroelectric Films*, 93rd Annual Meeting of the American Ceramic Society, Cincinnati, Ohio, April (1991).
16. T.K. Gloerstad, L.T. Clark, R.O. Grondin and S.K. Dey, submitted to *IEEE Trans. Instrumentation and Measurement* (1991).
17. A.R. Modak and S.K. Dey, *Ferroelectrics*, This issue.
18. R.L. Holman and R.M. Fulrath, *J. Am. Ceram. Soc.*, **55**, 192 (1972)
19. C.K. Barlingay and S.K. Dey, *Proc. of the Symp. on Rapid Thermal and Integrated Processing*, MRS Spring Meeting, Anaheim CA, April (1991).
20. J. F. Scott, L. Kammerdiner, M. Parris, S. Traynor, V ottenbacher, A. Shawabkeh and W. F. Oliver *J. Appl. Phy.*, **64**, 787 (1988).
21. W. Ting, P.C. Li, G.Q. Lo, J. Lee and D.L. Kwong, *Solid State Electronics*, **34**, 38 (1991).
22. C. Hashimoto, H. Oikawa and N. Honma, *IEEE Trans. Electron Device*, **ED-36**, 14, Jan. (1989).

AD-P006 641

FAST DECAY COMPONENT OF THE REMANENT POLARIZATION IN THIN-FILM PZT CAPACITORS

JOSEPH M. BENEDETTO, RANDALL A. MOORE, AND F. BARRY McLEAN
Harry Diamond Laboratories, Adelphi, MD 20783, U.S.A.

Abstract The remanent polarization ($2P_r$) of thin-film PZT capacitors was examined using a voltage pulse method. The amount of polarization remaining after a "write" pulse was found to be a function of both the time between the write and read pulses and the duration of the write pulse. The $2P_r$ was found to decrease significantly from 3 μs to 100 ms after the initial write. In some cases the remanent polarization decayed by almost 70 percent in this time regime. The fast decay component of $2P_r$ was also observed to be dependent on the duration of the write pulse (the write pulse width). The longer the write pulse was applied the smaller the fast decay component became, leaving more measurable charge retained after 100 ms.

INTRODUCTION

Thin ferroelectric (FE) PZT films developed for use as non-volatile (NV) memory storage capacitors are expected to have read/write times of less than 100 ns, with corresponding read/write pulse widths on the order of 50 ns or less. It is generally accepted that a remanent polarization ($2P_r$) of at least 1 $\mu C/cm^2$ measured with these short read pulses will be sufficient to reliably discriminate between a stored "1" or "0." The fast read/write times of 50 ns are relatively easy to obtain on the small capacitors (approximately 100 μm^2 or less) intended for use in NV random access memories (RAMs). However, fatigue and retention data on these small devices are difficult to measure "off-chip" with an external circuit (e.g., Sawyer-Tower[1] integrating capacitor), and it is important to verify the 1-$\mu C/cm^2$ threshold under worst-case fatigue and retention conditions. In a memory circuit the polarization state will be evaluated by a differential sense amplifier and sense capacitors "on-chip," making it possible to measure the small amount of switched charge from one of these small capacitor elements.

92-16105

Because of the difficulty in performing routine measurements and also in manufacturing small capacitor elements, a large portion of the data that currently exist on the fatigue and retention behavior of thin-film ferroelectric PZT capacitors was obtained using relatively large

area shadow mask capacitors. This paper presents data from shadow mask dot capacitors which imply that results obtained from these larger area capacitors using relatively slow read/write pulses may overestimate the amount of charge available in a memory element. This is particularly true with hysteresis loop measurements, where the measured remanent polarization can be much larger than that measured by a fast pulse method on small area capacitors. The data presented in this paper show the measured $2P_r$ decreases as a function of the time between a write and read pulse for time regimes from 3 μs to 1 s, and that $2P_r$ (at a fixed read time) increases with increasing write pulse width (while holding the read pulse width constant). These results may be related to the "self reversal," or unstable partial switching first reported in certain bulk ferroelectric materials. [2-4]

EXPERIMENTAL TECHNIQUES

Three different types of sol-gel PZT ferroelectric samples were used in this work, denoted as samples A, B, and C. Sample A was a 170-nm-thick film of PZT (52/48) (zirconium/titanium) with platinum electrodes. The area for all sample A capacitors was 14.8×10^{-4} cm^2. Sample set B was the same ferroelectric PZT as set A but with 1.59×10^{-4} cm^2 area platinum electrodes deposited by the HDL Semiconductor Electronic Materials Technology Laboratory. Sample set C used a 400-nm-thick film of PZT (53/47) with the same 1.59×10^{-4} cm^2 platinum electrodes used in sample set B.

The electrical characterization of the PZT films for this work consisted of two separate voltage pulse measurements. The first was designed to measure the decay of $2P_r$ shortly after a write pulse. The second measurement was designed to examine the effects on the longer term retention as a function of the width of the write pulse. We use the terms write pulse and read pulse to be consistent with memory application. Writing a "1" was arbitrarily chosen to be a positive pulse applied to the top electrode of the sample, while a "0" would be a negative pulse to the top electrode. In all cases a positive going pulse (applied to the top electrode) was used to perform a read, and the charge was measured on an integrating capacitor. A small charge on the integrating capacitor after a read would mean the capacitor had stored

a "1" while a relatively large charge would mean a "0" had been previously written to the FE. We used a series of "set" or "pre-conditioning" pulses to "firmly" polarize the PZT into the opposite state into which it was about to be written. This was done to minimize any possible effects of the samples' previous history and to provide a worst-case condition for a write.

Fast $2P_r$ Decay Measurement

To measure the fast decay of $2P_r$ as a function of time between read/write pulses we used the pulse train shown in figure 1. The top portion of the figure shows the pulse train used to a write a "0" while the bottom portion shows the pulse train used to a write a "1." Notice that there is a series of five pulses opposite in polarity to that of the write pulse prior to the application of the write pulse. These are the set pulses as discussed above. There was a fixed delay period of 2 s between the set pulses and the write pulse. Following the write pulse there was a variable delay of between 3 μs and 1 s before the application of the read pulse (note that the read pulse was always positive regardless of the polarity of the write). The difference between the charge measured by the read pulse for a stored "1" and a stored "0" is the amount of polarization that would be available for a

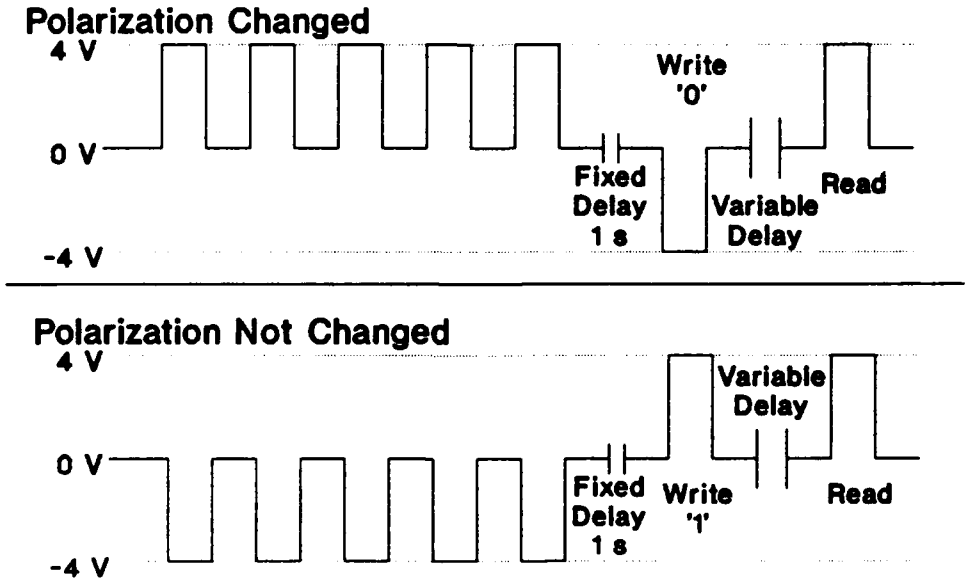


FIGURE 1 Pulse train used to measure switched (upper portion of figure) or unswitched (lower portion of figure) charge as a function of read/write time delay.

memory circuit to sense, and this difference as a function of time between read/write pulses is shown in the results section.

$2P_r$ as a Function of Write Pulse Width

Figure 2 shows the pulse train used to determine the effect of varying the width of the write pulse on $2P_r$. Similar to the fast $2P_r$ measurement discussed above, the pulse trains begin with five set pulses with opposite polarity to the write pulse. The same fixed 2-s delay between the set pulses and the write pulse was used. Notice that in this measurement the wait time between write and read pulses is fixed at 1 s, in contrast to the variable time delay discussed above, and the width of the write pulse is varied instead. Again, the data presented in the results section is the difference between a stored "0" and a stored "1". It is important to note that all of the write pulse widths were adjusted for rise time so that the width recorded was actually the time at full voltage. For example, if it took 250 ns for the voltage to rise to 95 percent of its full voltage and a 10-μs pulse was desired, the pulse width was set to 10.25 μs. This is especially important to consider for the shorter pulses, 0.5 μs and less, where the rise time is on the order of the width.

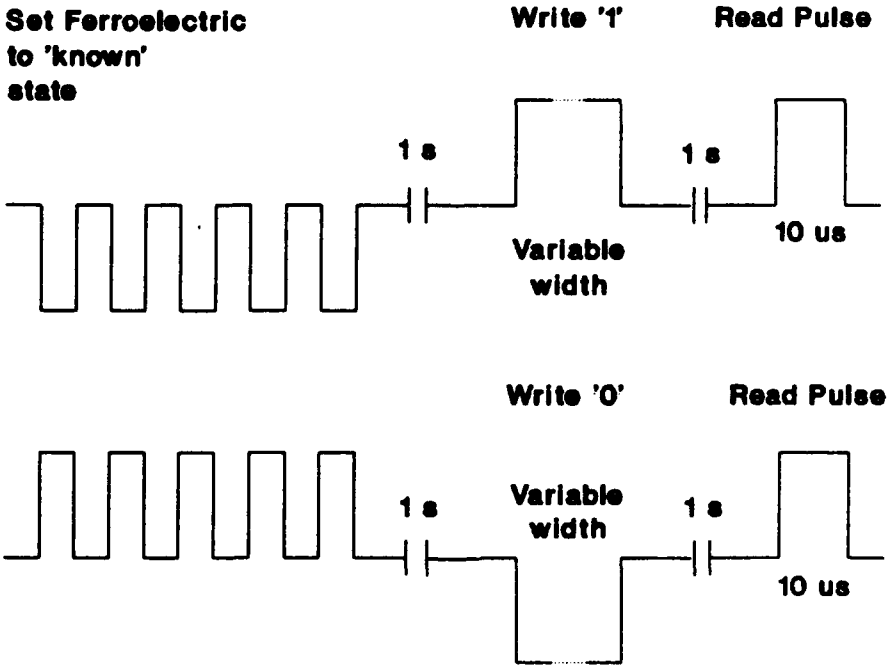
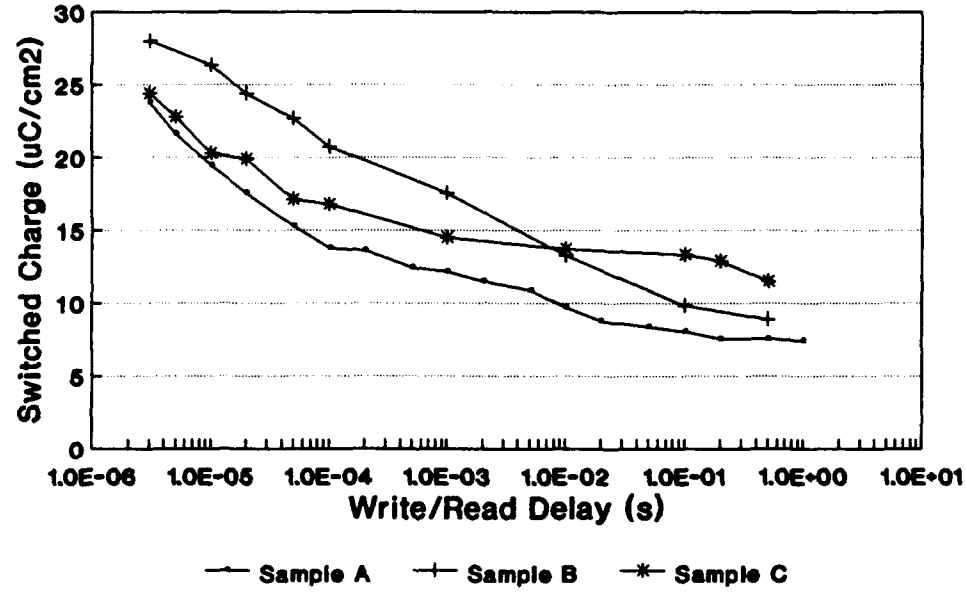


FIGURE 2 Pulse train used to measure switched (upper portion of figure) or unswitched (lower portion of figure) charge as a function of write pulse width.

RESULTS

Figures 3a and 3b show the fast remanent polarization decay for three different samples. Figure 3a shows the raw data for $2P_r$ while figure 3b shows the data normalized to their respective values at 3-μs. There is a significant loss in $2P_r$ in the time regime of 3 μs to 100 ms. For example, the $2P_r$ for sample A dropped from approximately 24 $\mu C/cm^2$ at 3 μs to only about 7 $\mu C/cm^2$ at 100 ms, and similar losses of $2P_r$ were observed for samples B and C. As the time between the read/write pulses becomes greater than 100 ms, the $2P_r$ value appears to stabilize to a



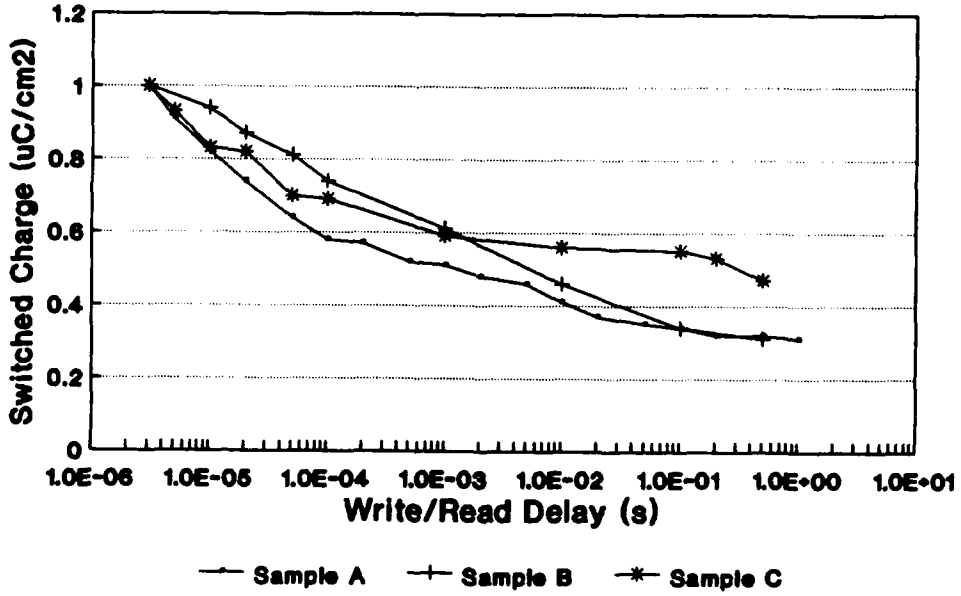


FIGURE 3 Switched charge (remanent polarization) versus write/read delay time. 3a is the raw data; 3b is data normilized to their respective values at 3 us.

long-term retention level. Measurements performed with a time delay between the read/write pulses of a few seconds to the order of a year is generally known as a retention measurement. An important implication of these results is that, in general, two different time regimes exist in the time-dependent description of $2P_r$. At times less than 1 s, the fast depolarization component dominates the polarization degradation, whereas at times greater than 1 s, the fast decay component has saturated and the long-term retention characteristics become important.

Figure 4 shows the data for sample A from figure 3a with additional data points plotted for the 1 s read/write delay time. The additional data also show $2P_r$ at 1 s for write pulse widths of 0.5 μs and 0.5 s. In all cases the read pulse was held constant at 10 μs. These data show that the amount of charge remaining 1 s after a write pulse is dependent upon the length of the write pulse. A 0.5-μs write pulse left the smallest charge (5 $\mu C/cm^2$), while a 0.5-s write pulse left significantly more charge (14 $\mu C/cm^2$) than either the 10- or 0.5-μs write pulse. At this time we are not able to determine how the write pulse width affects the fast depolarization for times less than 1 s. With improved instrumentation we hope, in future work, to further examine the fast depolarization component as a function of time beginning at 3 μs for variable write pulse widths (while holding the read pulses constant).

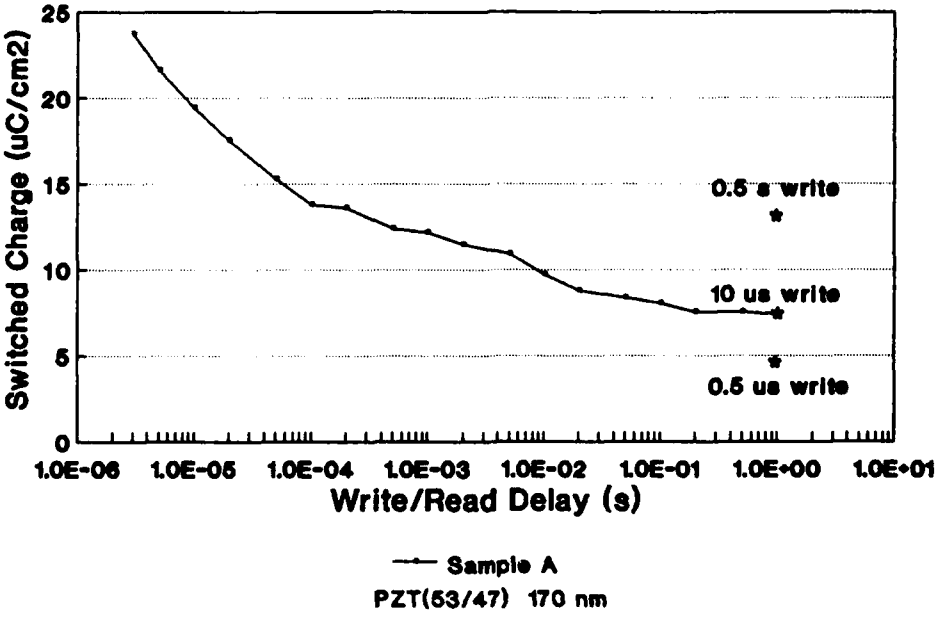


FIGURE 4 Switched charge versus write/read delay time for sample A. Three different write pulse widths are shown at 1s delay.

The write pulse width dependence on the retention at a fixed write/read delay of 1 s for samples A, B, and C is shown in figure 5. The width (which we define as the time at full voltage as discussed in the previous section) of the write pulse was varied from 0.1 μs to 0.5 s for samples B and C and from 0.5 μs to 0.5 s for sample A. The three samples consistently show a loss in the $2P_r$ as the width of the write pulse is shortened. The $2P_r$ for samples A and B show a relatively strong dependence on the write pulse width while sample C shows a somewhat smaller effect. Since we have plotted the data as a function of the time at full voltage and not just the write pulse width, these data cannot be explained by pulse rise time limitations. Further, from switching current measurements taken on these three sets of samples, we believe that "full" switching is obtained before the end of the shortest write pulse. The switching current measurements were performed by measuring the current across a resistor during the write pulse. In all cases the peak of the current pulse occurred at the leading edge of the write pulse and from the data presented in figures 4 and 5, it appears that the amount of $2P_r$ that can be measured after a write pulse is dependent both upon the time after the write pulse and on the duration of the write pulse.

DISCUSSION

There are several possible physical mechanisms that may be responsible for our observations, although with the limited amount of experimental

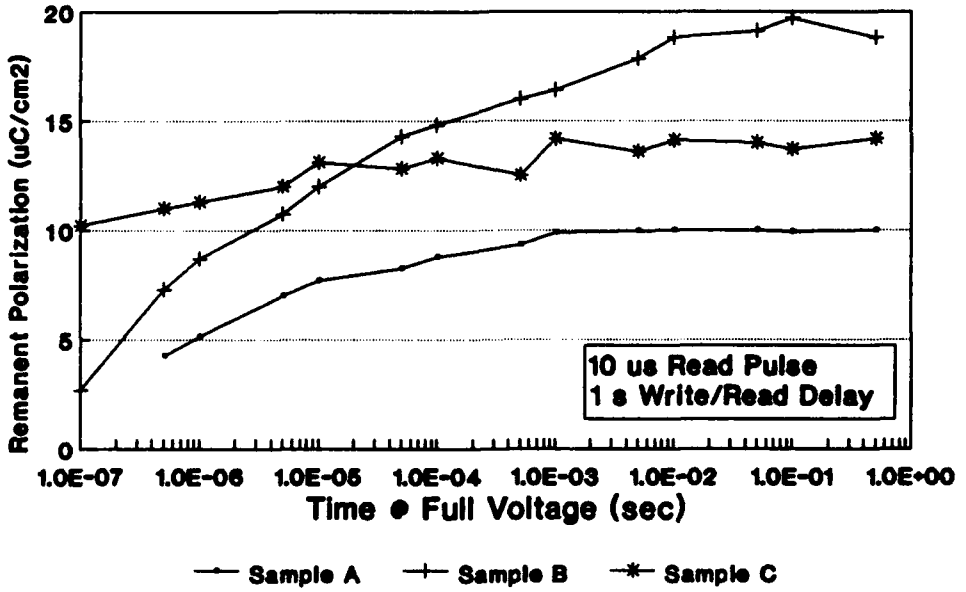


FIGURE 5 Switched charge (remanent polarization) versus write pulse width (defined as time at full voltage) for all three sample sets.

data currently available we can really do little more than offer reasonable speculations as to the underlying causes. A possible candidate mechanism underlying the rapid decay of $2P_r$--either directly or indirectly--is the buildup and then subsequent relaxation (discharge) of space charge within the PZT film or in interfacial layers near the electrodes. Possible sources of space charge buildup include: mobile charges within the bulk of the film (such as ions, oxygen vacancies, or hopping transport of trapped electronic charges)[5,6]; formation of Schottky depletion regions near the interfaces or grain boundaries; injection of charge from the electrodes into localized interface traps, or into the bulk (although it is difficult to envision achieving significant space charge buildup by charge injection into the bulk with the very short write pulses); and the reorientation of electric dipoles associated with defect/impurity complexes[5] which yields an effective space charge polarization. In all cases the space charge is induced in response to the applied switching (write) field, leading to an effective internal charge separation or polarization with the concomitant buildup of internal space charge fields. The induced internal fields would be directed opposite to the applied write field (as charge motion occurs to screen or reduce the total field seen by the charges). Then after the write field is removed there would be a relaxation (or discharge) of the internal space charge fields as the charge state of the film tends to move back toward one of charge neutralization. As the internal charge relaxes, there would be a corresponding drop in the internal fields, which may underlie the approximate log-time decay of $2P_r$, due to the coupling of the rate of space charge relaxation with the internal fields.

There are at least two possibile ways that the internal space charge buildup and subsequent relaxation could cause the observed fast depolarization. First, the space charge polarization could contribute directly to the total polarization, i.e., the space charge separation in itself contributes a significant fraction of the early time polarization (within microseconds after the end of the write pulse), which then decays with time as the space charge relaxes back toward the net neutral state. The second possibility, however, is that the space charge fields act in a more indirect fashion to effect the rapid depolarization, namely, by inducing a partial polarization reversal of

the spontaneous polarization. In this case the internal space charge fields--directed opposite to the polarization induced by the write pulse--would serve as initiation fields for polarization reversal at nucleation sites or at weakly stabilized domain walls such that reverse polarization growth is possible in response to relatively weak reverse electric fields. Again, the rate of observed polarization decay decreases in time as the internal space charge is discharged. Note that in this case the actual space charge component of the total observed polarization may be small, yet effect a large change in $2P_r$. Finally, for the case of actual reversal of the spontaneous polarization, we cannot rule out root causes other than induced space charge fields, for example, mechanical strain effects or perhaps a distribution of internal fields due to existing charged defects (not induced by the switching fields).

Within the framework of our present speculations we also offer several comments regarding the increase in polarization retention at 1 s write/read delay with increasing write pulse duration (Fig. 5). First, with increasing write pulse widths the induced space charge distributions may tend to become more stabilized, for example, an increasing fraction of mobile charges may find their way to and become trapped at various defects, grain boundaries, domain walls, or near the ferroelectric-electrode interfaces; and consequently this charge component is not able to relax upon removal of the write field. Then, if the space charge polarization constitutes some sizeable fraction of the observed $2P_r$, this portion corresponding to the trapped or stabilized charge would effectively become part of the long-term (>1 s) retained polarization. Along similar lines, domain walls that are only weakly stabilized for short write pulses may become increasingly more stabilized by the presence of trapped space charge localized near the domain walls, or perhaps by strain fields associated with the trapped charge buildup. Yet another possibility is that--even though our switching current measurements indicate that most switching occurs rapidly, before the end of the shortest write pulse--we cannot rule out a slow, continued increase in polarization with increasing write time. This increase in the switched polarization is associated with the gradual release of initially pinned domain walls during the longer write pulse times.

SUMMARY

This work has presented data that show a substantial loss in $2P_r$ in times less than 1 s after a write pulse for three different sample sets. The amount of $2P_r$ remaining 1 s after a write pulse was also found to be dependent upon the write pulse width, i.e., increasing the write pulse width increased $2P_r$. We have provided some discussion on the mechanisms that may be responsible for this behavior. The discussion is necessarily speculative in nature and more experimental data need to be obtained on the fast depolarization and retention properties, especially on the time dependence of the fast depolarization for a series of various write times, before the mechanisms can be fully understood.

The fast $2P_r$ decay and write pulse width data presented in this paper have important implications for testing FE films for use as the storage element in NV memories. In general, it appears that pulse testing will be more reliable than hysteresis loop measurements as long as a delay of >100 ms exists between the write and read pulses. Shortening the delay time could cause a large overestimation of the switched charge (Fig. 3). Also, based on the write pulse width data (Fig. 5), larger area test devices may overestimate $2P_r$ because of the longer write/read pulses that are required to drive the large capacitance compared with the shorter pulses to be used in actual memory devices.

REFERENCES

1. C. B. Sawyer and C. H. Tower, Phys. Rev. 35, 269 (1930).

2. G. W. Taylor, J. Appl. Phys. 37, 593 (1966).

3. G. W. Taylor, J. Phys. Soc. Japan 28, Supp, 389 (1970).

4. J. C. Burfoot and G. W. Taylor, Polar Dielectrics and Their Applications, Univ. California Press (1979) p. 46.

5. D. M. Smyth, Ferroelectrics 116, 117 (1991).

6. H. M. Duiker, P. D. Beale, J. F. Scott, C. A. Paz de Araujo, B. M. Melnick, J. D. Cuchiaro, and L. D. McMillan, J. Appl. Phys. 68, 5783 (1990).

AD-P006 642

FERROELECTRIC $PbZr_{0.2}Ti_{0.8}O_3$ THIN FILMS ON EPITAXIAL Y-Ba-Cu-O

R.Ramesh, A.Inam, W.K.Chan, B.Wilkens, F.Tillerot, T.Sands and J.M.Tarascon
Bellcore, Red Bank, NJ 07701.

J.Bullington and J.Evans
Radiant Technologies
Albuquerque, NM 87106.

ABSTRACT

Using a combination of pulsed laser deposition and sol-gel processing, we have fabricated epitaxial $PbZr_{0.2}Ti_{0.8}O_3$/ $YBa_2Cu_3O_{7-x}$ heterostructures on single crystalline [001] $LaAlO_3$. Rutherford back-scattering studies show the composition to be the same as the nominal starting composition. Transmission electron microscopy shows the existence of a randomly oriented polycrystalline microstructure in the PZT layer with a grain size of about 500-1000Å. Microscopic pores were also observed in the PZT layer. The PZT film exhibits ferroelectric hysteresis with a saturation polarization of 22-25$\mu C/cm^2$ (at 7.5V, 1kHz), a remanence of 5-6$\mu C/cm^2$ and a coercive field of about 40kV/cm.

92-16106

INTRODUCTION

There is now considerable interest in thin film ferroelectrics for a variety of applications that includes mainly high speed, non-volatile solid state memories[1,2]. Among many types of ferroelectric materials the lead zirconate titanate (PZT) class of

perovskites and its derivatives are being intensively examined as memory materials. Typically, sub-micron thick films are deposited onto Pt coated Si wafers using a variety of thin film deposition techniques[3-6]. Pulsed laser deposition (PLD), with its considerable success in the growth of high quality cuprate superconductor thin films, has emerged as an exciting new deposition technique for the growth of ferroelectric PZT films, although problems related to cationic stoichiometry and phase purity still remain[1,2].

In earlier papers, the growth of high quality epitaxial thin films and heterostructures of bismuth titanate ferroelectric films by PLD was demonstrated[7,8]. It was also shown that the cuprate superconductors could be used as suitable bottom electrodes at room temperature. Epitaxial cuprate superconductor/bismuth titanate heterostructures were grown in-situ on single crystal $SrTiO_3$, $LaAlO_3$[7] and on [001] Si[8] with a yttria- stabilized ZrO_2 buffer layer for this purpose. In order to test the efficacy of the $YBa_2Cu_3O_{7-x}$ (YBCO) film as the bottom electrode for other ferroelectrics, we have grown PZT films on it by conventional sol-gel processing. The motivation for such an experiment was two-fold : (i) the results obtained from these experiments can be directly compared with those obtained with conventionally prepared films, i.e., those grown on Pt electrodes ; (ii) study the role of the YBCO layer as a suitable structural and chemical template that would promote the growth of well oriented or even epitaxial PZT films by sol-gel processing, which is currently a more mature processing route for making PZT films[3,9]. In this letter, we report first results of the ferroelectric properties of $PbZr_{0.2}Ti_{0.8}O_3$ thin films grown on single crystalline c-axis oriented $YBa_2Cu_3O_7$ thin films.

1000Å of epitaxial, c-axis oriented YBCO thin films were grown on 1cm x 1cm [001] $LaAlO_3$ wafers by PLD[10]. X-ray diffraction showed these films to be c-axis oriented with a rocking angle of 0.5° for the $(005)_{YBCO}$ peak. 4000Å thick $PbZr_{0.2}Ti_{0.8}O_3$ films were grown on the epitaxial YBCO layer by acetic acid based sol-gel processing the details of which are described earlier[3,9]. The heterostructures were characterized structurally using x-ray diffraction, scanning electron microscopy(SEM), and transmission electron microscopy (TEM). The ferroelectric properties of the film were evaluated using a Sawyer-Tower circuit, a pulsed testing system (Radiant Technologies, RT 66A) and the dielectric dispersion properties were studied using a HP 4192A impedance analyzer.

X-ray diffraction spectra obtained from the heterostructure showed that there was no degradation in the crystalline quality of the YBCO layer due to the growth of the

PZT overlayer. All the "00l" lines from the c-axis oriented YBCO film are observed in the x-ray diffraction pattern. The diffraction peaks from the perovskite PZT are very weak indicating either an amorphous material or a very small grain size (along with random orientation of the grains). Diffraction peaks from the oxygen or lead deficient pyrochlore phases are not observed in the x-ray diffraction patterns. Rutherford Backscattering analysis showed that the composition of the PZT layer is close to the nominal starting stoichiometry. Auger depth analyses showed that there is very little interdiffusion between the two layers. Scanning electron microscopy of the surface showed a very smooth surface morphology, Fig.1, that was infrequently disturbed by spherical particulates. These particles are readily identified as those arising from the YBCO deposition step.

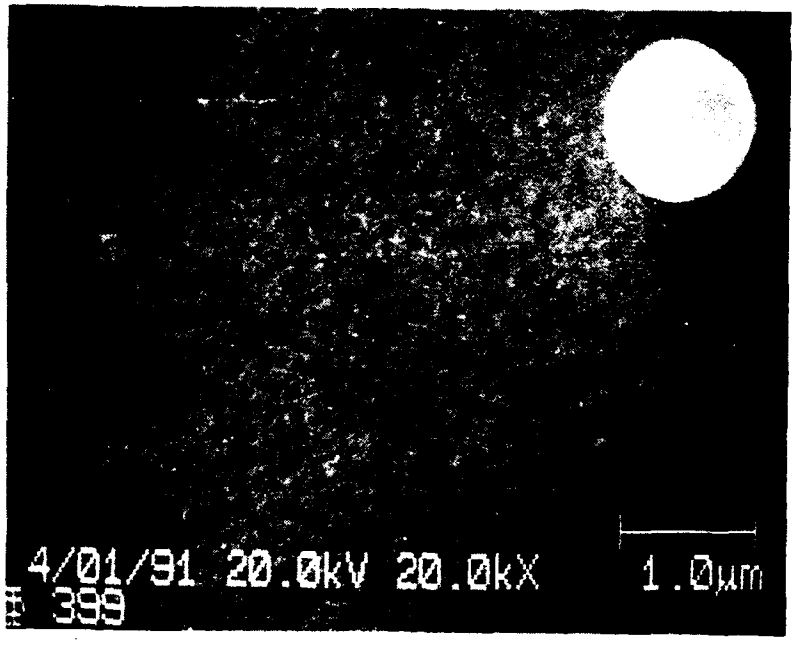


Figure 1: A scanning electron micrograph illustrating the smooth surface after the growth of the PZT layer. The large blob is an example of occasional "laser particles" from the YBCO layer.

Closer examination of the surface in the SEM as well as by planar section transmission electron microscopy revealed microscopic pin holes in the PZT layer. Planar section were prepared by Argon ion milling from the back side of the wafer, leaving an electron transparent PZT thin film. Fig.2(a) is a low magnification transmission electron micrograph of a planar section prepared from the heterostructure. A very uniform, randomly oriented polycrystalline microstructure with an average grain size of 500-1000Å was observed in the PZT layer. Selected area electron diffraction showed ring patterns, indicative of a very small grain size, polycrystalline microstructure. At higher magnifications, microscopic pin-holes were revealed, as illustrated in the micrograph in Fig.2(b). No intergranular phases were onserved in these films. interesting feature of the microstructure is the absence of the twinned structure that is generally characteristic of these ferroelectrics. It is likely that the very small grain size in these films prevents the release of the cubic-tetragonal transformation strain by twinning[11].

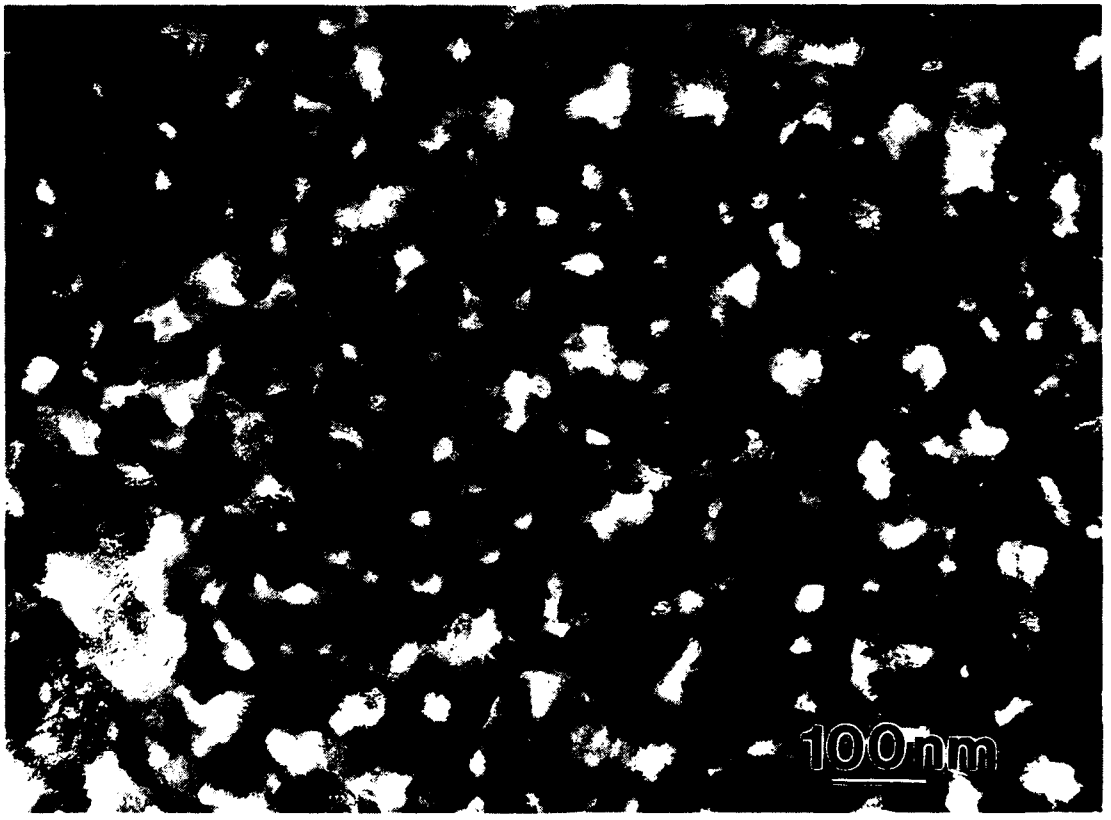


Figure 2: (a) A low magnification tramsmission electron micrograph illustrating the polycrystalline fine-grained microstructure of the PZT layer.

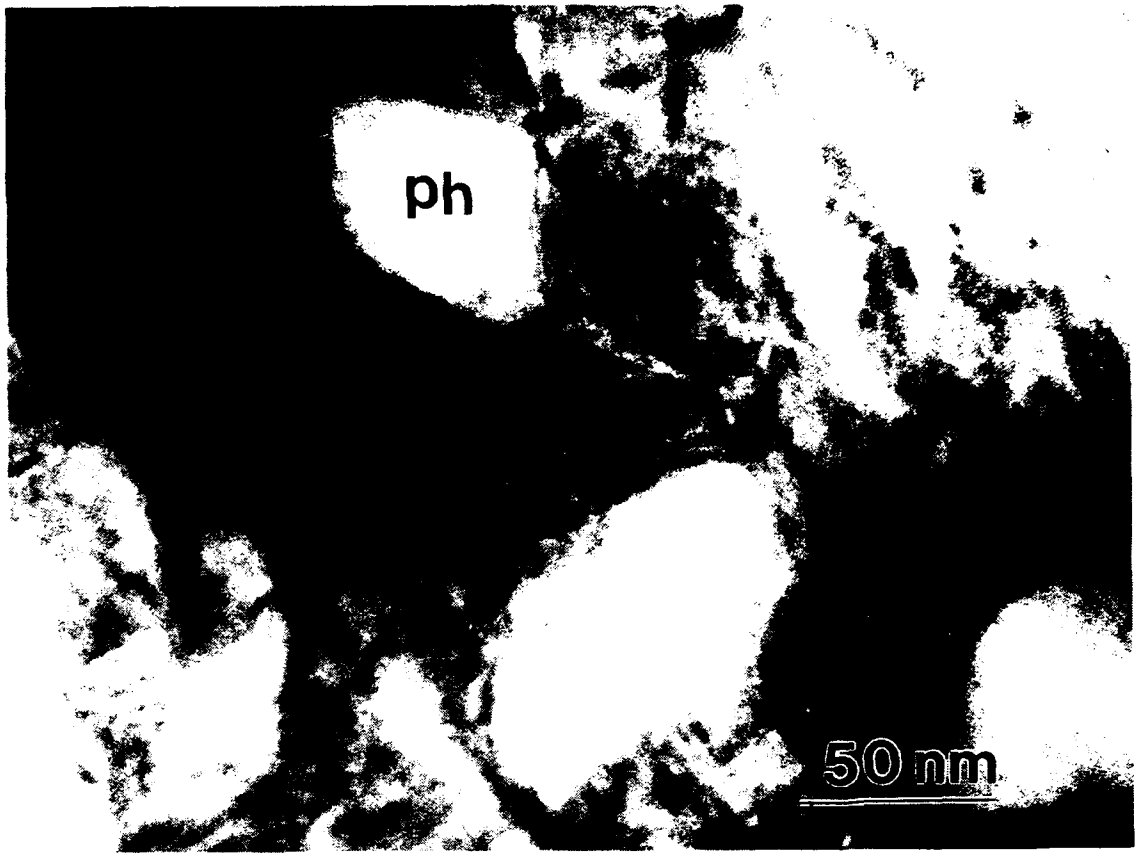
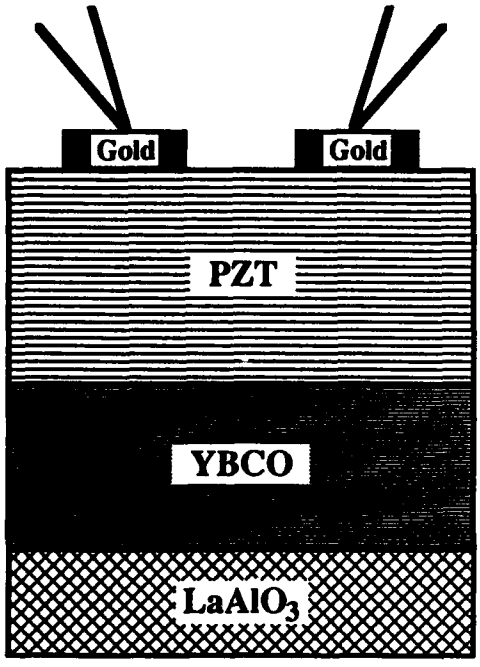


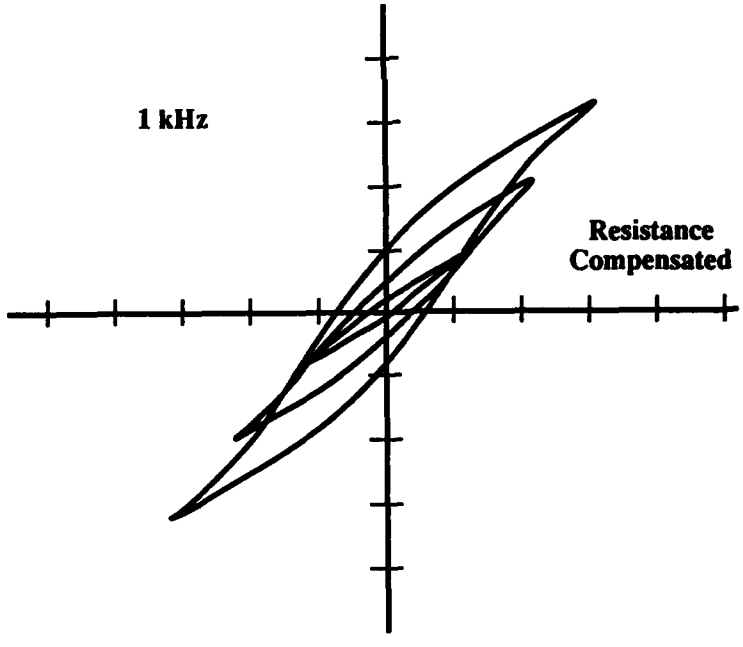
Figure 2(b) a higher magnification micrograph showing the presence of 300-500Å sized pores at the triple grain junctions of the grains. Note the absence of any transformation twins in the ferroelectric film.

Ferroelectric hysteresis loops were obtained at various frequencies and applied voltages using a Sawyer-Tower circuit as well as a pulsed testing set-up. The measurement method is schematically illustrated in Fig.3(a). Since two electrodes of the same area are used as the input and output, this acts as a 1:1 voltage divider and hence the actual applied voltage on each capacitor is half the total applied voltage. Fig.3(b) shows typical hysteresis loops obtained at a frequency of 1kHz for applied voltages of 2.5V, 5V and 7.5 V. The saturation polarization at 7.5V is 22$\mu C/cm^2$ while the remanence is 5-6$\mu C/cm^2$. The corresponding coercive field is about 40kV/cm. Data from the pulsed measurements are also presented in the inset to Fig.3. The observed DP value of 14-15 $\mu C/cm^2$ is quite sufficient for the ferroelectric to be used as a memory device. We have also carried out preliminary fatigue testing of the heterostructures at a frequency of 10kHz in an alternating field of 6Volts. The capacitors showed a 20% drop in DP after 10^7 cycles and a 40%



Virtual Ground Mode
or Sawyer-Tower Mode

Pulse Data
$\Delta P = 14.7\ \mu C / cm^2$
C = .87 nF
K(eff) = 730
$\rho = 10^7\ \Omega$·cm
$E_c = 40$ kV / cm



x-axis : 1 div = 65 kV / cm
y-axis : 1 div = 5.00 $\mu C / cm^2$

Figure 3: (a) A schematic illustration of the set-up used to test the ferroelectric properties of the heterostructures; (b) ferroelectric hysteresis loops measured using a Sawyer-Tower circuit at 1kHz for three different voltages (2.5V, 5V and 7.5V).

drop after 10^8 cycles. The shape and magnitude of the hysteresis loops do not change appreciably with frequency up to 10kHz. At higher frequencies, there is a progressive drop in the saturation and remnant polarization, due to the shrinking of the hysteresis loop.

The dielectric dispersion behaviour was examined using an impedance analyzer in the frequency range of 5Hz to 13MHz. Fig.4 shows the dielectric constant, k', and the loss tangent, tan∂, as a function of frequency. The dielectric constant is relatively unchanged up to a frequency of about 400 kHz after which it drops dramatically to a very small value. At around the same frequency, the loss tangent shows a very strong maximum, indicative of an intrinsic loss mechanism in the film. The loss tangent is typically in the range of 2-5% at lower frequencies.

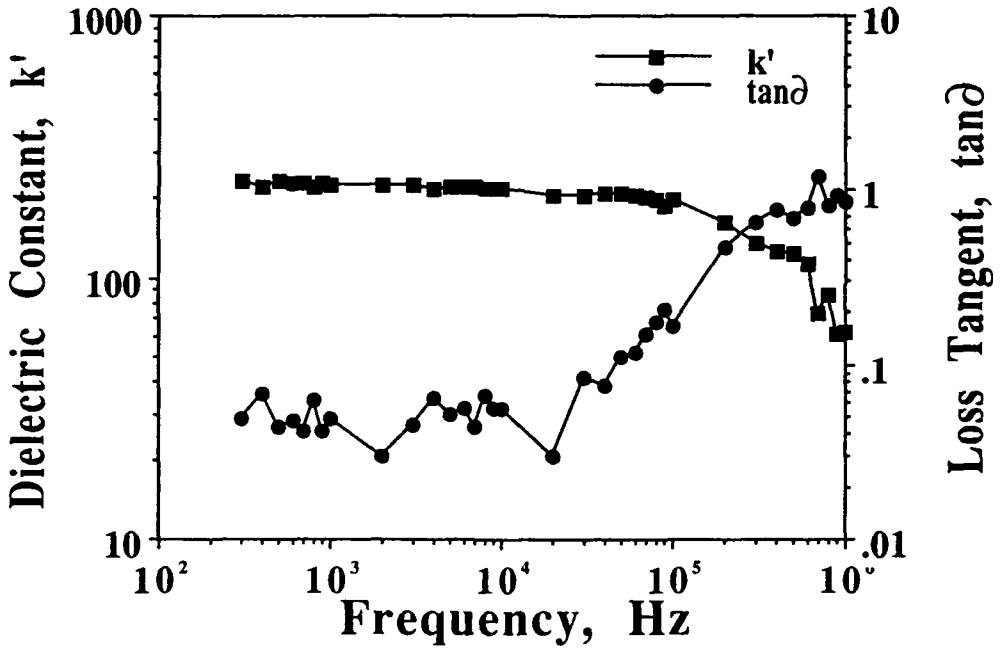


Figure 4: Frequency dependence of the dielectric constant, k', and loss tangent, tan∂ for the PZT/YBCO heterostructure.

In summary, we have demonstrated that the cuprate superconductors, specifically Y-Ba-Cu-O, can be used as epitaxial bottom electrodes for the growth of ferroelectric thin film capacitors. The epitaxial nature of the bottom electrode influences the orientation of the ferroelectric film, although the film is still polycrystalline due to the processing route (sol-gel). Further improvements in the microstructure and electrical properties should be possible by close optimization of the processing parameters.

REFERENCES

1. See for example, Proc. of Materials Research Society Spring Meeting Symposium on "Ferroelectric Thin Films", Eds. E.R.Myers and A.Kingon, Materials Research Society, Pittsburgh,PA, April 1990; G.H.Haertling, Jl. Vac. Sci. Tech., 9, 414(1991).
2. Proc. of Third Int. Symp. on Integrated Ferroelectrics, Colorado Springs, CO, April1991 (this conference).
3. S.K.Dey and R.Zuleeg, Ferroelectrics, 108, 37(1990).
4. C.A.Paz de Araujo, L.D.McMillan, B.M.Melnick, J.D.Cuchiaro and J.F.Scott, Ferroelectrics, 104, 241(1990).
5. Y.Sakashita, T.Ono, H.Segawa, K.Tominaga and M.Okada, Jl. of Appl. Phys., 69, 8352(1991); G.A.C.M.Spierings, M.J.E.Ulenaers, G.L.M.Kampschoer, H.A.M.van Hal and P.K.Larsen, Jl. of Appl. Phys., 70, 2290(1991).
6. K.Iijima, R.Takayama, Y.Tomita and I.Ueda, Jl. of Appl. Phys., 60, 2914(1986); K.Sreenivas and M.Sayer, Jl. of Appl. Phys., 64, 1484(1988).
7. R.Ramesh, A.Inam, B.Wilkens, W.K.Chan, D.L.Hart, K.Luther, and J.M.Tarascon, Science, 252, 944(1991); H.Buhay, et.al., Appl Phys. Lett., 58, 1470(1991).
8. R.Ramesh, A.Inam, B.Wilkens, W.K.Chan, T.Sands, J.M.Tarascon, J.Bullington and J.Evans, Appl. Phys. Lett., in press.
9. S.K.Dey, K.D.Budd and D.A.Payne, IEEE Trans. UFFC, 35, 80(1988); see also papers in Refs.1,2.; R.W.Vest and J.Xu, Ferroelectrics, 93, 21(1989).
10. A.Inam, et.al., Appl. Phys. Lett., 54, 908(1988).
11. B.G.Demczyk, A.G.Khatchaturyan and G.Thomas, Scripta Metallurgica, 21,967(1987).

AD-P006 643

PULSED LASER DEPOSITION (PLD) OF ORIENTED BISMUTH TITANATE FILMS FOR INTEGRATED ELECTRONIC APPLICATIONS

H. BUHAY, S. SINHAROY, M. H. FRANCOMBE, W. H. KASNER,
J. TALVACCHIO, B. K. PARK, AND N. J. DOYLE
Westinghouse Science & Technology Center
1310 Beulah Road, Pittsburgh, PA 15235

D. R. LAMPE AND M. POLINSKY
Westinghouse Advanced Technology Division
Nursery and Winterson Roads, Baltimore, MD 21203

Abstract In this paper we describe recent successes of growth of epitaxial bismuth titanate (BTO) films by pulsed laser deposition (PLD) suitable for electro-optic and electrical switching device structures, and fabrication of an improved gate structure for a ferroelectric memory FET (FEMFET). TEM and x-ray results indicate that excellent crystalline quality BTO films were achieved on $LaAlO_3$. Polarization switching was demonstrated for BTO capacitors with epitaxial superconducting $YBa_2Cu_3O_7$ as the lower electrode. Using an SiO_2 buffer layer, a BTO/Si structure was fabricated and direct charge modulation in the Si by polarization reversal in the BTO was demonstrated.

92-16107

INTRODUCTION

Since the growth of stoichiometric[1] and epitaxial[2] films of ferroelectric bismuth titanate, $Bi_4Ti_3O_{12}$ (BTO), by rf sputtering was demonstrated in these laboratories, it has become apparent that films of this material offer several important and unique application opportunities in integrated electronics. These potential applications derive from an unusual combination of several useful properties, such as high electro-optic contrast switching effects under low address fields, demonstrated feasibility of direct integration in silicon FET's as a gate dielectric, and the capability of high specific capacitance associated with low dielectric loss.

The unique electro-optic switching behaviour of BTO crystals has already been duplicated in sputtered epitaxial films to achieve an X-Y addressed display.[3] For this purpose, single-domain film

structures were required with the spontaneous polarization and optic axis lying in the plane of the film. Similarly, experimental Si-based memory structures were successfully fabricated in which switching between the "zero" and "one" states was produced by reversing the ferroelectric polarization in the BTO gate dielectric of an FET.[4] Finally, high-value (0.3 $\mu F/cm^2$) and low-loss (tan δ = 0.005) capacitors were fabricated on metallized silicon substrates at growth temperatures of about 550°C.

Despite these early successes with sputtered films of BTO, serious growth problems were often encountered due to the low deposition rates available, to the Bi_2O_3-rich composition needed in the target, and to the influence of ion bombardment at the substrate. These effects led to particle formation in the films,[1] cracking of epitaxial layers and interdiffusion with the substrate material.[4] In particular, the the interdiffusion with Si surfaces produced tunneling barriers which promoted anomalous, injection-dominated switching in ferroelectric FET memories (FEMFETs).

Recent studies by Buhay et al.[5,6] and also by Ramesh et al.[7] have demonstrated that high-quality films of BTO can be grown on a variety of substrates, and epitaxially on MgO, by pulsed laser deposition (PLD), using approaches similar to those developed for growth of oxide superconductor layers. We have shown that, unlike the situation with sputtering, stoichiometric targets can be used to yield particle-free films of excellent structural and electrical quality, displaying essentially bulk ferroelectric properties. Moreover, growth could be achieved at high rates and low substrate temperatures under conditions compatible with the processing needs of semiconductor integrated circuits. In the present paper we describe recent extensions of the PLD method to epitaxial growth of BTO films suitable for electro-optic and electrical switching device structures, and to fabrication of improved gate dielectrics for FEMFET arrays.

EXPERIMENTAL

Film deposition was carried out using a Lumonics HyperEx-460 industrial laser operating on the KrF transition at 248 nm at pulse energies up to 300 mJ, with pulse durations of 20-30 nsec and repetition rates up to 65 Hz. The films were prepared, as previously

described,[5,6] with an estimated laser fluence, on the stoichiometric BTO ceramic target, of 2 J/cm^2, laser pulse rate of 10 Hz, and oxygen flowing at a pressure of 200 mTorr. For these conditions, and for nominal substrate temperatures used in the range 500-700°C, films were grown to a typical thickness of 1 micron, at a rate of about 30 nm/min. Structural characterization was performed using X-ray diffractometry and rocking curve measurements, X-ray oscillation and Weissenberg patterns, electron diffraction and transmission electron microscopy (TEM). The composition of the layers was evaluated using electron microprobe techniques. Capacitance and conductance measurements were made over the frequency range 10-500 kHz using a Boonton bridge, and ferroelectric hysteresis studies were carried out with a modified Sawyer-Tower circuit.

The epitaxial BTO films studied here included BTO/$LaAlO_3$(001), bi-layer structures of the type BTO/YBCO/$LaAlO_3$(001) and BTO/YBCO/YSZ(100) and tri-layer structures of the type BTO/$SrTiO_3$/YBCO/$LaAlO_3$(001) and BTO/$SrTiO_3$/YBCO/YSZ(001). MIS structures involving BTO deposits on thin (100-200A) buffer layers of CaF_2 and SiO_2 on (001)Si were also prepared for electrical C-V measurements. In the bi- and tri-layer structures the epitaxial films of YBCO ($YBa_2Cu_3O_7$) and $SrTiO_3$ were pre-deposited in a separate vacuum system by rf magnetron sputtering. In the case of silicon substrates, CaF_2 and SiO_2 were pre-deposited by vacuum sublimation and thermal oxidation respectively.

RESULTS

Epitaxial Structures on (001)$LaAlO_3$ and Zirconia (YSZ) Substrates

$LaAlO_3$(001) substrates provide an excellent lattice match to the paraelectric (high-temperature) tetragonal (001) face of BTO (~1% compared to 2% for $SrTiO_3$ and 10% for MgO). BTO films were grown at nominal substrate temperatures of 600, 675, and 750°C. Examination by X-ray diffractometry indicated in each case primarily the ferroelectric orthorhombic phase with a very strong c-axis (normal) crystal orientation. X-ray Weissenberg patterns confirmed a well-oriented epitaxial structure with BTO(001) // $LaAlO_3$(001), and with a-b twinning in the (001) plane of the substrate, i.e. BTO[100] and [010] // $LaAlO_3$[110] (see Figure 1). X-ray rocking curve studies



FIGURE 1 X-ray Weissenberg pattern of BTO film grown at 750°C on $LaAlO_3$(100).

yielded FWHM values depending sensitively on growth temperature. Increasing the growth temperature from 600 through 675 to 750°C produces a dramatic improvement in film quality, with the corresponding FWHM widths changing as shown in Figure 2.

TEM studies performed on the 750°C sample gave confirmation of the twinned structure (Figure 3). Small area diffraction (SAD) measured in the twinned areas (different contrast regions in Figure 3a and 3b) showed the orientations of the a-b axes differ by 90° rotation and the twin boundaries are parallel to the film axes. Two types of boundaries observed were: (a) straight boundaries (Figure 3a) probably associated with formation of twins directly at the growth temperature near the Curie point (Tc) transition, and (b) curved boundaries (Figure 3b) tentatively attributed to formation of ferroelectric domains on cooling below Tc. These results suggest that the true film growth temperature may differ from that measured at the heater surface by as much as 60-80°C. However, single domain film structures of quality adequate for optical waveguide modulators can probably be achieved by growing further above the Tc transition.

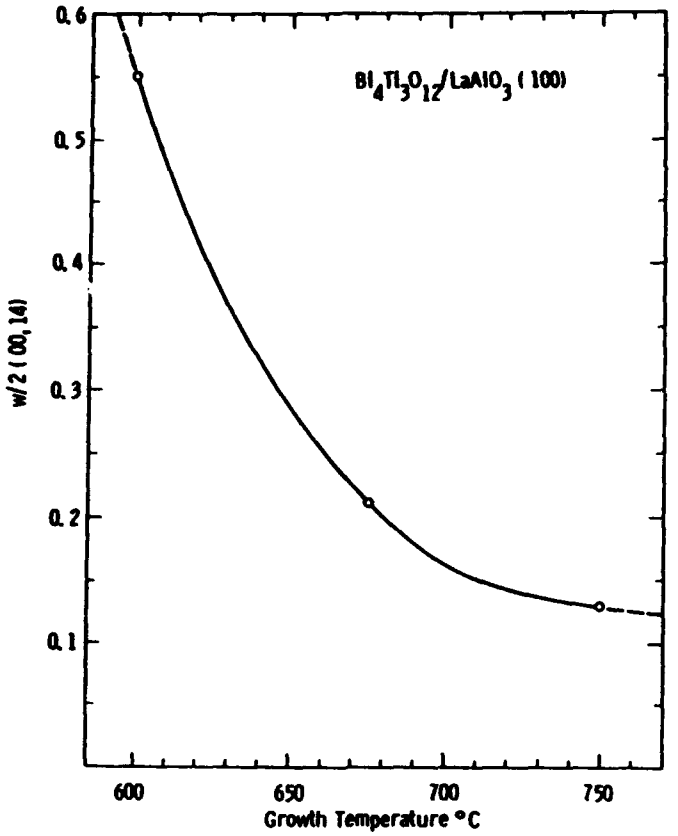


FIGURE 2 FWHM of X-ray rocking curve about (0014) versus temperature for BTO film of Figure 1.

Good-quality epitaxy of BTO was also obtained in the various bi- and tri-layer, (001) oriented samples on $LaAlO_3$ and yttria-stabilized ZrO_2. In each case, the BTO c-axis was normal to the substrate plane. In the case of the structures with YBCO, a narrow temperature window was established for BTO growth which led to ferroelectric behaviour without degradation of the superconducting transition at 90K in the YBCO. Using gold top electrodes, hysteresis loops of the type shown in Figure 4 were displayed. The measured polarization at partial saturation (4.3 $\mu C/cm^2$) agrees well with the bulk crystal value parallel to the c-axis, but the coercive field (200-300 kV/cm) is anomalously high. These structures provide a unique example of highly-ordered, lattice-matched electrode/ ferroelectric interfaces, which should possess high stability and reduced fatigue, for example, in semiconductor memory configuration.



(a)



(b)

FIGURE 3 TEMs of same BTO film of Figures 1 and 2: (a) straight twin boundaries; (b) curved twin boundaries.

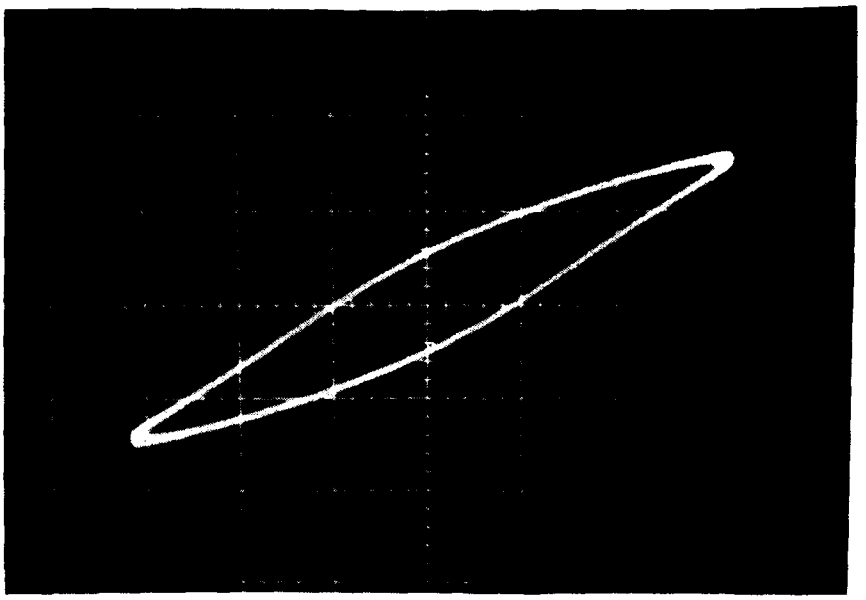


FIGURE 4 Hysteresis loop measured at 2 kHz for BTO/$SrTiO_3$/YBCO/YSZ structure. Scale: Vertical, 3.5 $\mu C/cm^2$ per large division; Horizontal, 310 kV/cm per large division.

MIS Structures on Silicon

These structures were explored with the aim of establishing whether PLD films of BTO on Si (with or without dielectric buffer layers) might exhibit switching behaviour free from the charge injection effects encountered previously with sputter-deposited BTO layers. BTO structures prepared by PLD without such buffer layers were in fact found to display injection effects, and will not be discussed further here. The results for BTO structures using CaF_2 or SiO_2 as a buffer layer are discussed further below. The BTO/CaF_2 dielectric structure was deposited on a standard VHSIC CMOS wafer (4-8 Ohm-cm p^-Si epi-layer grown on 0.005-0.02 Ohm-cm p^{++}Si substrate). The BTO/SiO_2 structure was deposited on a gridded (6 μm wide N^+ lines spaced 60 μm apart) standard wafer. In both cases a mercury probe having an area of 0.64×10^{-3} cm^2 was used as the top electrode. The BTO/CaF_2 and BTO/SiO_2 test structures and C-V plots are shown in Figures 5 and 6 respectively.

The test structure of Figure 5 was intended to simulate a FEMFET that is incorporated in a P-well CMOS VLSIC memory, i.e., an N-channel FEMFET. Thus, as the gate voltage sweeps from +5 volts to -5 volts in the C-V hysteresis curve of Figure 5, the capacitance of the gate dielectric stack increases as the depletion-region "inversion charge

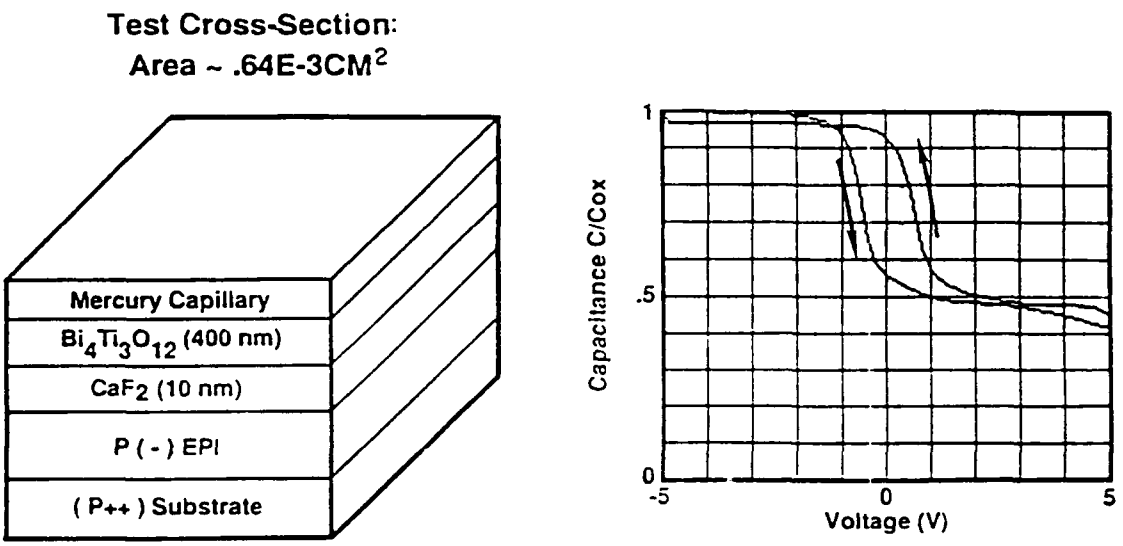


FIGURE 5 Test structure and C-V hysteresis result for a CaF_2-buffered BTO film on a standard VHSIC CMOS Si wafer.

layer" becomes an "accumulation charge layer", with the disappearance of the series depletion-region capacitance at approximately the threshold voltage. The shift of the threshold from enhancement mode toward depletion mode in response to negative programming (V_{gate} = -5 volts) indicates positive charge trapped near the semiconductor-gate-dielectric interface rather than a negative sheet of charge that would arise if the negative gate reoriented the ferroelectric dipoles to the positive end adjacent to the negative gate. Thus, the polarity of the threshold shift of the C-V plot (arrow directions shown in Figure 5) for the BTO/CaF_2 structure is consistent with the interpretation that charge is being injected from the Si surface into traps near the BTO/CaF_2 interface (injection type on/off switching).

The test structure of Figure 6 includes more of the FEMFET (namely, the NMOST source/drain implants) to greatly facilitate both pulsed and endurance C-V measurements. Consequently, in the C-V plot of Figure 6, the lower apparent capacitance is shunted back to its higher value by an inversion layer whose source of electrons is the source/drain grid implant that is shorted to the substrate. Only during the transition from an accumulation layer (arising from a negative gate bias) to the inversion layer (associated with a positive gate bias) does the gate capacitance drop to a minimum value at a gate voltage near the effective threshold voltage. Thus, from the gridded-

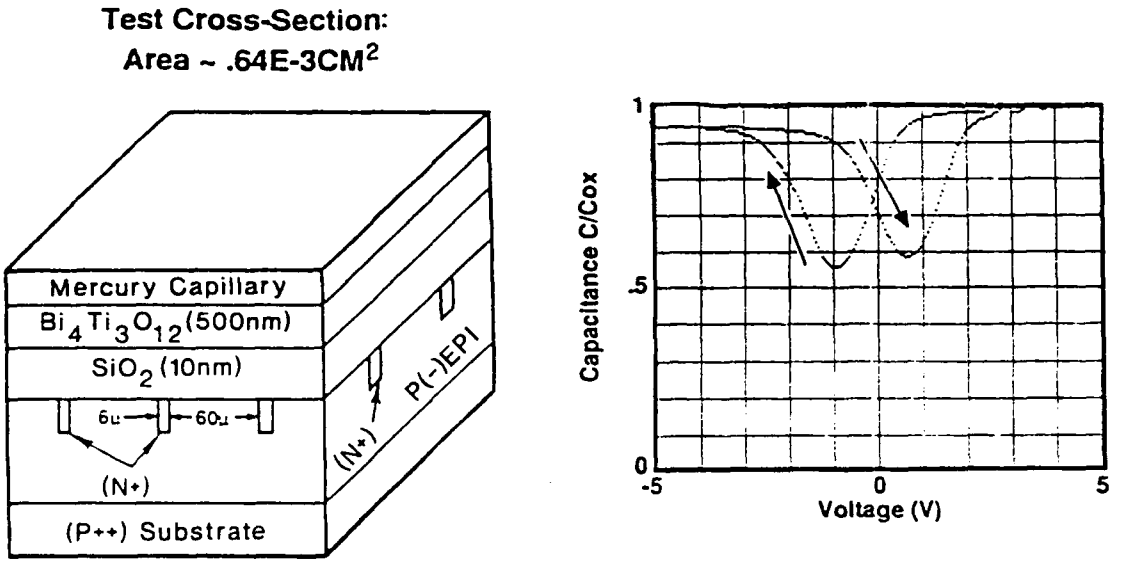


FIGURE 6 Test structure and C-V hysteresis result for a SiO_2-buffered BTO film on a gridded wafer.

wafer C-V hysteresis curve of Figure 6, the negative memory-gate programming gives the enhancement mode (normally OFF) while the positive memory gate programming gives the depletion mode (normally ON). The polarity of the threshold shift of the C-V plot (arrow directions shown in Figure 6) for the BTO/SiO_2 structure is opposite of that in Figure 5 and is indicative of ferroelectric switching. That is, for 5-volt programming, the reversible ferroelectric polarization dominated when charge tunnelling and trapping was inhibited by the good quality SiO_2 buffer layer. The CaF_2 buffer layer, however, permitted so much charge tunnelling and trapping that it completely dominated over any likely ferroelectric polarization switching. The faster BTO ferroelectric switching is the desired goal for NDRO FERRAM operation.

SUMMARY

Pulsed laser deposition has been used, in conjunction with a stoichiometric target, to deposit a variety of BTO epitaxial structures on (001) crystal substrates of $LaAlO_3$ and YSZ. By controlling the growth temperature, it was possible to form high-quality BTO capacitors with epitaxial superconducting YBCO as the lower electrode, and to demonstrate polarization switching. Using

SiO_2 buffer layers, BTO/Si MIS structures also were grown, and the feasibility of direct charge modulation in the Si by polarization reversal in the BTO was demonstrated.

ACKNOWLEDGEMENTS

The authors would like to thank B. A. Fleischmann, V. A. Toth, B. A. Blankenship, and J. Uphoff for preparing the BTO films and electrodes for ferroelectric hysteresis measurements and characterization of the superconducting films. We appreciate assistance in interpreting the x-ray and TEM results provided by W. J. Takei and J. Greggi. J. T. acknowledges support from AFOSR contract F-49620-88-C-0039 for preparation of the epi YBCO films and buffer layers.

REFERENCES

1. W. J. Takei, N. P. Formigoni and M. H. Francombe, J. Vac. Sci. Tech. 7, 442 (1970).

2. W. J. Takei, S. Y. Wu and M. H. Francombe, J. Crystal Growth 28, 188 (1975).

3. S. Y. Wu, W. J. Takei and M. H. Francombe, Ferroelectrics 10, 209 (1976).

4. S. Y. Wu, IEEE Trans. Electron Devices ED-21, 499 (1974).

5. H. Buhay, S. Sinharoy, W. H. Kasner, M. H. Francombe, D. R. Lampe and E. Stepke, Proc. 7th Int. Symp. Appl. Ferroelectrics (1990).

6. H. Buhay, S. Sinharoy, W. H. Kasner, N. H. Francombe, D. R. Lampe and E. Stepke, Appl. Phys. Lett. 58, 1470 (1991).

7. R. Ramesh, K. Luther, B. Wilkens, D. L. Hart, E. Wang, A. Inam, X. D. Wu and T. Venkatesan, Appl. Phys. Lett. 57, 1505 (1990).

AD-P006 644

Filament-Assisted Pulsed Laser Deposition of Epitaxial $PbZr_xTi_{1-x}O_3$ Films: Morphological and Electrical Characterization

R.E. Leuchtner*, K.S. Grabowski, D.B. Chrisey, and J.S. Horwitz
Code 4670, Naval Research Laboratory, Washington, D.C., 20375-5000

Abstract A modification of the conventional pulsed laser deposition technique was employed, whereby a low energy electron-emitting filament was placed between the target and the substrate (-20 V filament/substrate bias) in order to produce reactive species (O_2^- and O^-) during deposition. Using this modification, epitaxial thin films of $PbZr_xTi_{1-x}O_3$ (PZT, $0 \leq x \leq 0.6$) were prepared *in situ* on virgin (100) MgO and (100) Pt/(100) MgO substrates at a substrate temperature of 550°C and in an oxygen ambient (0.3 Torr). The topography of films prepared without a filament on virgin MgO were porous and composed of grains of about 1000 Å in diameter. As the emission current was increased from 0 to 400 μA, the grain size decreased to less than 100 Å with a concomitant decrease in the porosity. The nucleation of crystallites of other orientations was observed at emission currents greater than about 500 μA. Trilayer structures (Pt/PZT/Pt/<100>MgO) were fabricated for electrical measurements. Non-filament-assisted PZT cells usually failed because of a high probability of conductive paths through the PZT layer. Filament-assisted films were much less prone to this problem. Typical remanent polarizations and coercive fields were 15-20 $\mu C/cm^2$ and 30-50 kV/cm, respectively.

Introduction

Pulsed laser deposition or PLD is a rapidly emerging technique for the production of high quality thin films of multicomponent materials. While not new,[1] the method has gained considerable attention in the fabrication of high temperature superconductors.[2,3,4] A logical extension of these efforts is to apply the method to thin film fabrication of other perovskite materials. In the case of ferroelectrics, e.g., the lead based ceramic $PbZr_xTi_{1-x}O_3$ (PZT) and it's doped variants, high quality thin films offer great promise as non-volatile memories and highly responsive electrooptic waveguides.[5,6,7]

A fundamental but poorly understood problem with polycrystalline PZT is it's loss of remanent polarization with cycling (fatigue) and

92-16108

* - Office of Naval Technology Postdoctoral Research Associate

with time (ageing). In an effort to improve the performance of PZT as well as shed light on the mechanisms responsible for these phenomena, we have fabricated oriented, single phase films of PZT at a variety of compositions ($0 \leq x \leq 0.6$), focussing special attention near the morphotropic phase boundary ($x = 0.54$).

Results from previous investigations[8,9,10] of PZT deposition by PLD identified several key processing parameters, which include substrate material and temperature, laser fluence, and gas ambient and it's pressure. These studies indicated that congruent vaporization of the target did not ensure a stoichiometric composition of the film. In particular, an oxygen pressure 0.2 to 0.3 Torr was necessary to maintain the lead content of the film. Oriented and sometimes epitaxial perovskite films could be obtained under appropriate deposition conditions however, a non-ferroelectric metastable phase (referred to herein as pyrochlore) was frequently observed. Although it was found that pyrochlore content could be minimized when the substrate temperature was maintained between 550-575°C, it was difficult to control the relative mixture of the perovskite and pyrochlore phases within this narrow temperature window. In addition, the morphology of the films was unsuitable for electrical characterization and dielectric trilayers (Au/PZT/Pt) frequently shorted.

The present study reports on the growth of phase pure, oriented PZT films using a novel PLD experimental arrangement which employs an electron emitting filament. The filament-assisted deposition (FAD) involves the emission of low energy electrons into the oxygen ambient during deposition. Oxygen anions (O_2^- and O^-) are likely formed by attachment processes which have been well characterized.[11] The use of the filament had a profound influence on film morphology and crystal structure. Detailed crystallographic analysis of the present films and specifics on the FAD process, however will be presented elsewhere.[12] Trilayer films produced by FAD are easily amenable to electrical characterization and preliminary results demonstrate hysteretic behavior similar to that of other techniques.[13] In addition, the use of the filament has led to a substantial decrease in the occurrence of shorting compared with non-FAD films.

Experimental

The experimental apparatus has been described in detail previously.[8-10] Briefly, an excimer laser beam (30 nsec duration, 248 nm) was first spatially filtered by placing a 0.16 cm diameter orifice at the focus of 50 cm focal length lens and recollimated using a second 50 cm focal length lens. A third lens (50 cm focal length) was used to focus the laser light onto a PZT target to a spot size roughly 0.06 cm^2 in area. Typical laser beam energies were between 100 and 150 mJ/pulse (1.7 - 2.5 J/cm^2). The vaporized material was collected on a heated substrate about 4 cm away at an angle of 45° from the incident laser beam. Depositions were usually performed at a dynamic pressure of 0.3 Torr of oxygen (5-10 standard cm^3/minute). The substrate was heated to 550°C as indicated by a thermocouple placed in the substrate heater block.

For those films prepared by FAD, an electron emitting filament was inserted between the target and substrate. A 0.005" diameter platinum wire was coated with a thin film of $BaZrO_3$ to enhance emission of electrons.[14] During the deposition, the coated wire was resistively heated to incandescence and held at a constant bias potential (typically -20 V) with respect to the grounded substrate holder. Electrons were thermionically emitted and, under these oxygen pressures and fields (8-20 V/cm), should have attached to oxygen,[11,15] while concomitantly being transported toward the substrate. The identity and rates at which these anions can be produced have been well-studied under low field conditions.[16,17] While more direct experimentation is required, it is believed that a large fraction of the emitted electrons were consumed first by dissociative attachment to molecular oxygen to form O^-, which subsequently underwent a charge exchange with oxygen to form O_2^-. At these pressures, direct three-body attachment is possible at low electron energies ($\leq$ 0.1 eV).[18]

From the measurements of Kwok et. al.[19], an estimate of the number density of ablated species in the region between the filament and substrate should be less than about 1 x $10^{14}/cm^3$ while that of the ambient molecular oxygen was calculated to be between about 4 x 10^{15} and 1 x $10^{16}/cm^3$, depending upon the local temperature. Consequently, the oxygen anions (ca. 1 x $10^{14}/cm^3$) will rarely encounter the laser ablated species in the gas phase. Therefore, under the low fields employed, a

steady flux of oxygen anions (a mixture of O^- and O_2^-) arrived at the surface. In addition, due to the numerous gas phase collisions in transit, the anions arrived at the substrate surface with near thermal energies (about 0.2 eV).

Two filament geometries were employed during these investigations. A circularly shaped emitter was found to produce a relatively uniform film in terms of morphology and crystal quality. A linear filament was employed in order to understand more clearly the electrostatic field conditions, hence the flux of anions on the substrate surface. The linear filament was placed closer to the substrate surface (1 versus 2.5 cm for the circular filament) to further enhance its influence. In both cases, the substrates were centered symmetrically below the filaments.

PZT pellets were fabricated from stoichiometric quantities of PbO, ZrO_2 and $PbTiO_3$ powders, pressed and then calcined at 500 °C for one hour. Pellets were pressed with either a cold vertical press (approximately 3.5×10^4 psi) or with an isostatic press (1.0×10^5 psi). The density of the isostatically pressed targets was approximately 6.5 g/cm^3 compared to about 5.8 g/cm^3 for the vertically pressed targets (bulk PZT density is 7.9 g/cm^3). This small increase in density had a large effect on the deposition rate and yielded two to three times more material per laser shot (about 2.5 Å/shot) compared to the vertically pressed pellets. In addition, about an order of magnitude fewer particulates were observed for these denser targets.

X-ray diffraction was used to characterize the crystal structure of the deposited films. The relative amounts of the pyrochlore and perovskite phases were determined by measuring the strongest x-ray diffraction peak of each ((001) for perovskite and either (222) or (400) for pyrochlore). Elastic backscattering (EBS, 6.2 MeV He^{2+}) was used to measure the metals content of the films, and using the bulk density of PZT, allowed for the determination of the film thicknesses.

Deposited films were examined with a scanning electron microscope (SEM). This microscope was also equipped to perform energy dispersive analysis of x-ray fluorescence (EDAX). Films deposited directly on virgin MgO required a conducting layer for analysis. A thin film (100-200 Å) of Au was sputter-coated onto the PZT for this purpose.

The electrical characterization was performed using a ferroelectric test system (RT-66A, Radiant Technologies) and hysteresis measurements

were performed on trilayer samples. The Pt base electrode was typically deposited by PLD onto <100> MgO using a high purity platinum foil target. Deposition rates were typically 0.1 Å/shot and film thicknesses ranged from 750-1200 Å. Smooth, epitaxial metal films were obtained with deposition conditions of 0.05 Torr of oxygen and substrate temperatures of 450-500°C. Deposition conditions outside of this range produced Pt films of degraded crystalline and morphological quality.[20] For a few specimens, the substrate used was Pt-coated silicon,[21] where sputter deposition was used to deposit a Pt layer on top of a series of buffer layers.

The PZT middle layer was deposited on top of the Pt bottom layer. Typically, PZT films of between 0.3-1.0 μm were prepared. The samples were cooled in 760 Torr of oxygen and then removed from the chamber; 500 μm diameter dots (typically gold) were subsequently deposited at room temperature by either electron beam evaporation or sputtering. The latter technique was preferred for reproducibility and ease of use.

Results and Discussion

I. Structure and Morphology

PZT/MgO

Initial investigations of PZT depositions on MgO substrates without a filament were plagued with the presence of the metastable, non-ferroelectric fcc phase (known as pyrochlore). The variant identified by x-ray diffraction was a rather disordered form of pyrochlore which nevertheless formed with a strongly preferred orientation ((111) or (100)), as did the perovskite phase (001). The quantity of the pyrochlore relative to that of perovskite was difficult to control. The amount pyrochlore in the non-FAD films ranged from between one-fifth to 3 times the perovskite content as determined by x-ray diffraction.

A rapid decrease in the pyrochlore as a function of emission current was observed for films prepared by the FAD process. Using a circular filament, the ratio of pyrochlore to perovskite decreased by over five orders of magnitude as the emission current was varied between 0 and 600 μA. The films were completely pyrochlore-free (< 0.02%) at about 450-500 μA. For emission currents greater than about 500 μA, other orientations, e.g., (110) and (111), of PZT were observed. A

dramatic change in surface structure was observed as well.

In Figure 1, electron micrographs at four different emission currents: 0, 200, 400, and 600 μA are shown. In the case of 0 μA emission current (the filament is hot but is biased positively to prevent electron emission), the surface appears porous. EDAX analysis suggested that the intergranular regions were almost completely void of the oxide ceramic. The grains were small and had an average width of about a 1000 Å. A morphology of this nature is inappropriate for microelectronics applications since it would provide conductive paths between the top and bottom electrodes. The surface morphology and phase composition of this specimen is identical to one prepared without a filament.

At an emission current of 200 μA, no visible change in the surface structure was apparent although the amount of pyrochlore phase observed decreased by over 100 fold.[12] When the emission current was increased to 400 μA, a dramatic transition to a smooth and non-granular surface occurred. Closer inspection revealed grains with an average diameter of less than 100 Å. After the emission current was further increased to 600 μA, the surface became rougher again and additional orientations of the perovskite phase appeared. Apparently, the nucleation of randomly oriented crystallites was promoted at higher emission currents. It is interesting to note that while the film growth mechanism appears to change, the metal composition as determined by EBS remained constant and identical to that of the target.[12]

In an attempt to understand the influence of the emission current, the circular filament was replaced with a linear filament and moved closer to the substrate (about 1 cm). In Figure 2, three micrographs are shown which were taken at three different locations on the PZT film as indicated by the arrows. The film was deposited onto a 0.5 x 1 cm (100) MgO substrate centered under the filament as indicated by the dotted line in the figure.

A clear transition is evident in the morphology across the film surface perpendicular to the filament axis. Figure 2a shows the morphology near the edge of the substrate and was very similar to that of films produced at 0 and 200 μA emission current (see Figure 1). As one moves toward the central region of the substrate (section directly below the filament), a change to the smooth, non-granular surface was

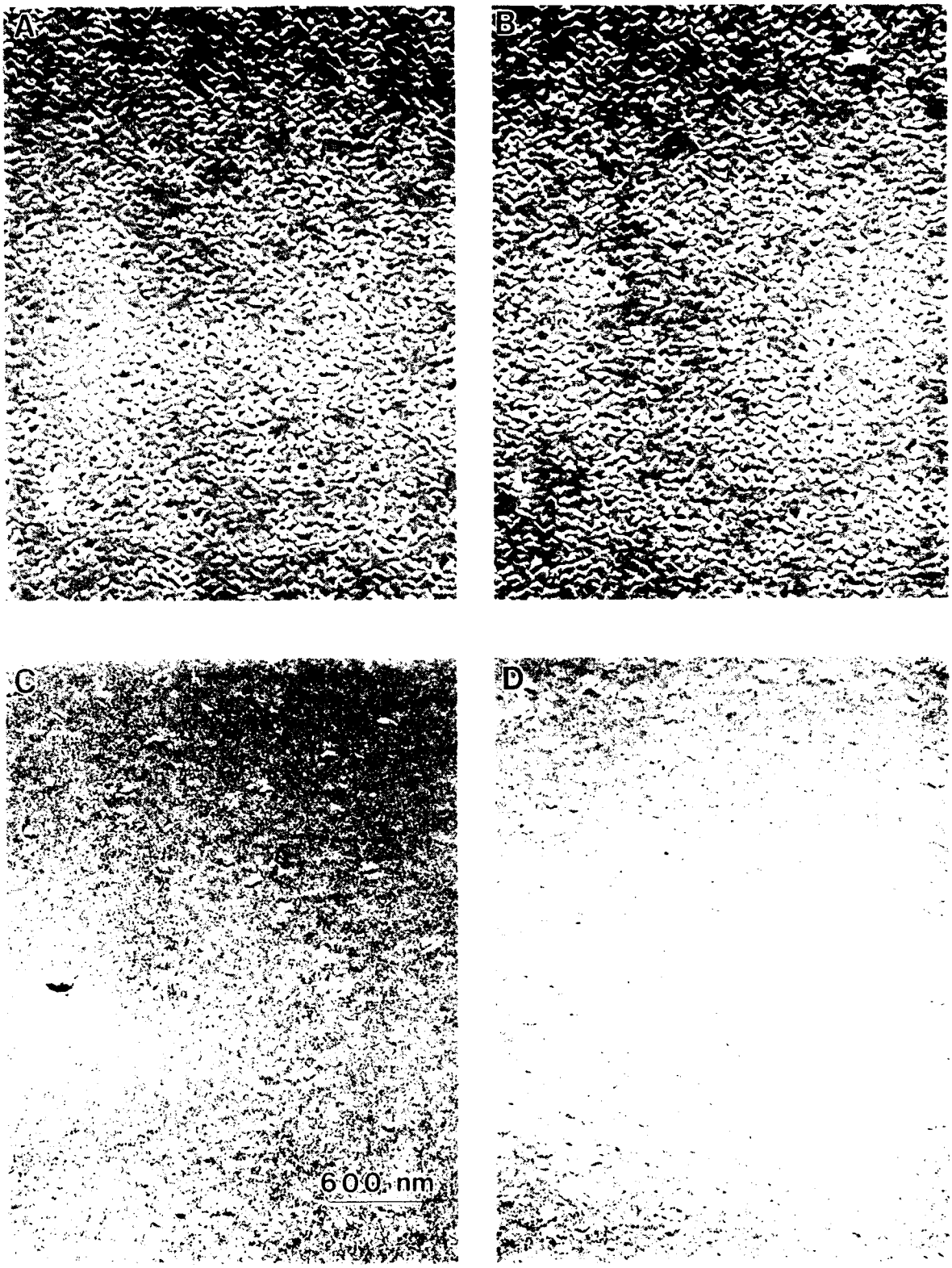


Figure 1. SEM micrographs of a PZT surface showing effects of ion bombardment of surface during deposition. (a) 0 μA, (b) 200 μA, (c) 400 μA, and (d) 600 μA.

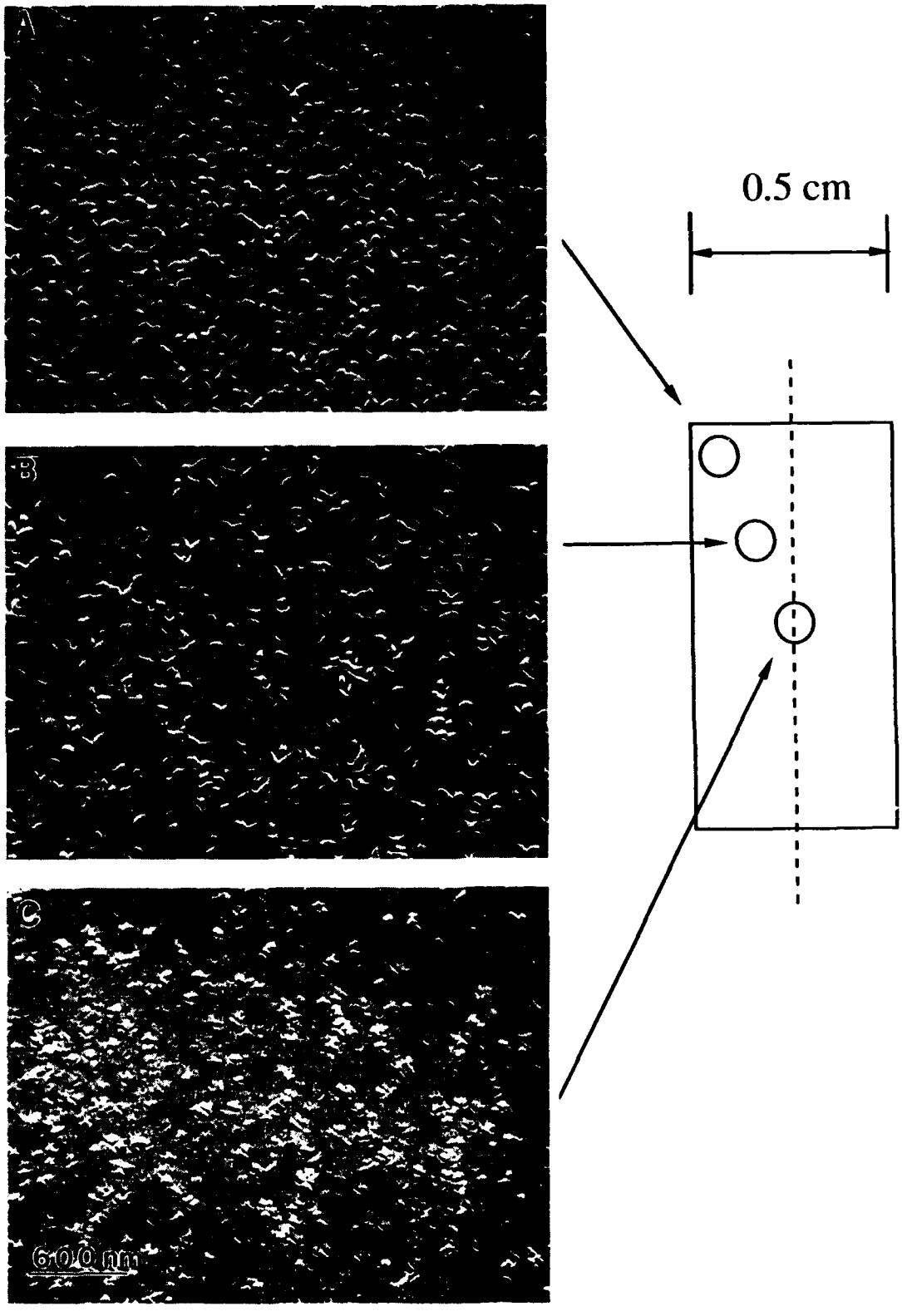


Figure 2. PZT morphology as a function of location using a linear filament geometry with 600 μA emission current. Dotted line indicates filament position over substrate, (100) MgO.

observed.

The linear geometry was expected to more clearly show the effect of the filament. Since the field-induced drift velocity of the oxygen ions is about 2-3 times greater than the transverse diffusive motion,[11,15] the oxygen anions produced will move more rapidly toward the surface under the influence of the electric field than diffusing perpendicular to it. The reaction rates for electron capture have been measured,[16,17] therefore the chemical and physical description of this system is relatively straightforward. Details of this analysis and the implications of filament shape and proximity will be presented elsewhere.[22]

Given the propensity for oxygen anion formation under these low field conditions, it is believed that these species were primarily responsible for the dramatic crystallographic and morphological changes observed. It is surprising however that ion impact of such low energy ($\leq$ 0.2 eV) can have such a tremendous influence on the film structure. It is possible that the anions make the surface more chemically reactive, which would in turn reduce the mobility of surface atoms and grain boundary segregation.

Au/PZT/Pt/MgO

Initial efforts to deposit PZT (non-FAD) for the purpose of electrical characterization used platinum-coated silicon as the substrate and yielded films composed predominantly of pyrochlore. To overcome this difficulty, PLD was used to deposit epitaxial Pt on (100) MgO.[20] The morphology of PZT grown on epitaxial Pt was also strongly influenced by FAD and showed a variety of different morphological structures compared to those films prepared on MgO. In Figure 3, the most commonly observed morphologies for PZT deposited onto (100) Pt films are presented. Figure 3a shows an FAD film in which 400 μA emission current was used during the deposition. While it was found that slightly larger emission currents were required to remove the pyrochlore phase on Pt compared to depositions on MgO,[12] the film surface became smoother as the emission current was increased from 0 to 400 μA. This was in striking contrast to the morphology of a non-FAD PZT deposition on epitaxial (100) Pt (Figure 3b) where the surface is composed of a high density (i.e. no pores present) of small grains ($\leq$

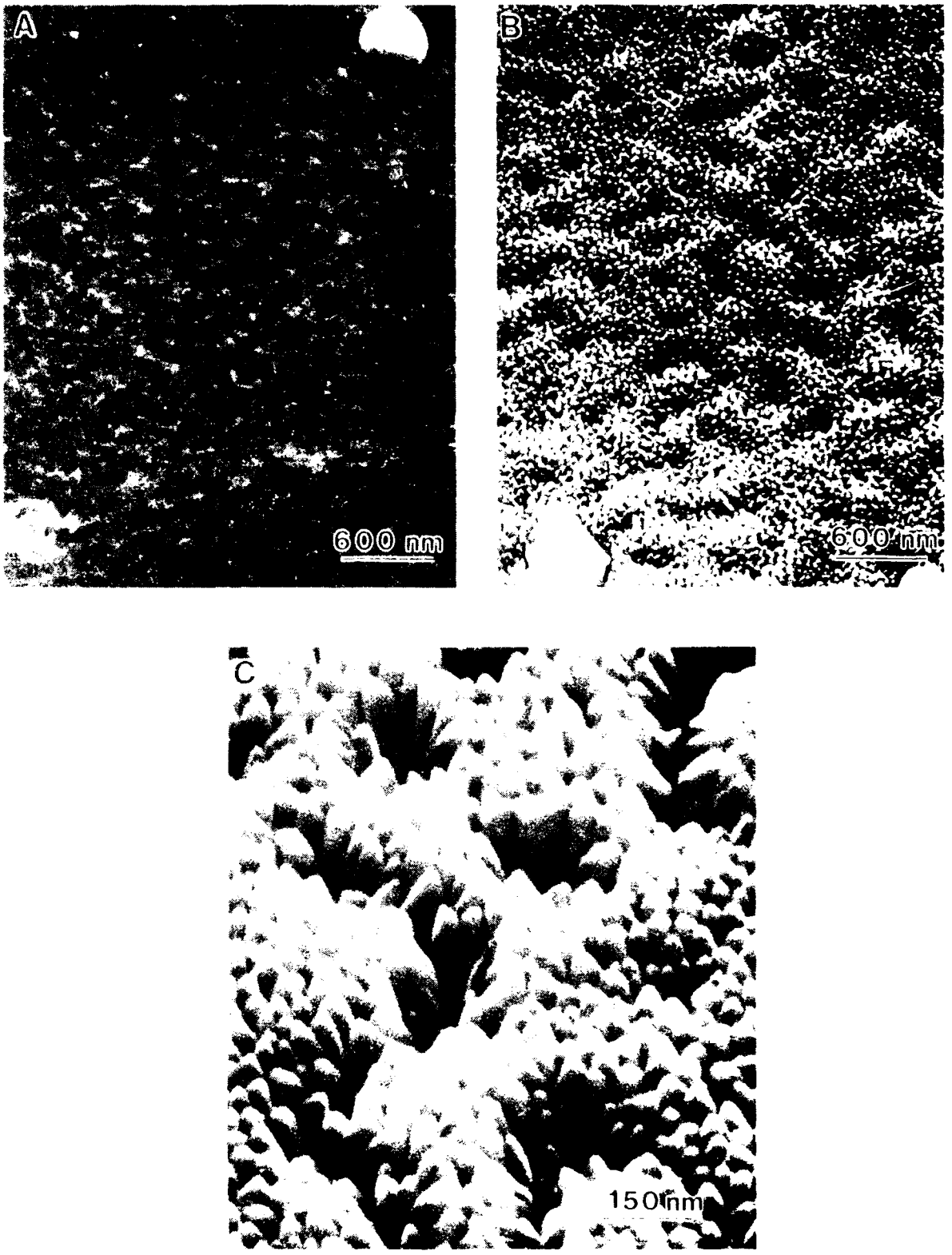


Figure 3. PZT morphology on (100) Pt/(100) MgO. (a) FAD film prepared with 300 μA emission current, (b) non-FAD film showing typical granular surface, (c) same film as (b) demonstrating columnar structure of grains.

250 Å diameter). In Figure 3c, a higher magnification of a region near that of Figure 3b shows the grains are columnar in structure. This granular structure was typical of films produced by non-FAD and was also observed in FAD films which were prepared with low emission currents.

II. Electrical Characterization

Preliminary electrical measurements on the PZT films produced by PLD were performed in order to determine typical remanent polarization, P_r, and the potential, E_c, required for switching. These results were then evaluated to determine the effect of crystal orientation. Although several of the FAD films still contained a few percent of pyrochlore, they rarely shorted, even in the presence of particulates. Non-FAD films, characterized by the granular structure shown in Figure 3b and c, frequently shorted. In addition, thinner non-FAD PZT films usually contained large intergranular regions (e.g., where the large columnar grains are visible in Figure 3c) which were attractive sites for aggregation of metal used in the top electrode.

Figure 4 shows hysteresis loops measured for four different PLD trilayers. In (a) and (b) measurements are presented for the only two non-FAD films which did not fail (2 out of several hundred). In (a), the loop is for a film on Pt-coated silicon while (b) is on (100) Pt/(100) MgO. The computed values for P_r and E_c are also included in the figure. Although these cells contained about 25-50% of the pyrochlore phase, the values of P_r and E_c are comparable to values obtained by others.[13] It should be noted that all films in Figure 4 were of similar thickness and ranged between 3400 and 4000 Å. This corresponds to coercive fields on the order of 30 to 50 kV/cm.

The lower curves, (c) and (d), are representative measurements made on 64 cells (only 2 failed) prepared using the FAD method. While more data is required to substantiate the behavior of PZT material subjected to anion bombardment, it was apparent from the measurements taken so far that the ferroelectric behavior (P_r and E_c) are similar to non-FAD produced films. More experimentation however, is required in order to determine reliable variance of P_r and E_c as a function of emission current. While these films contained some pyrochlore (between 1 and 10 %), it was surprising that their remanent polarizations were not larger since an enhancement of P_r with c-axis orientation was expected compared

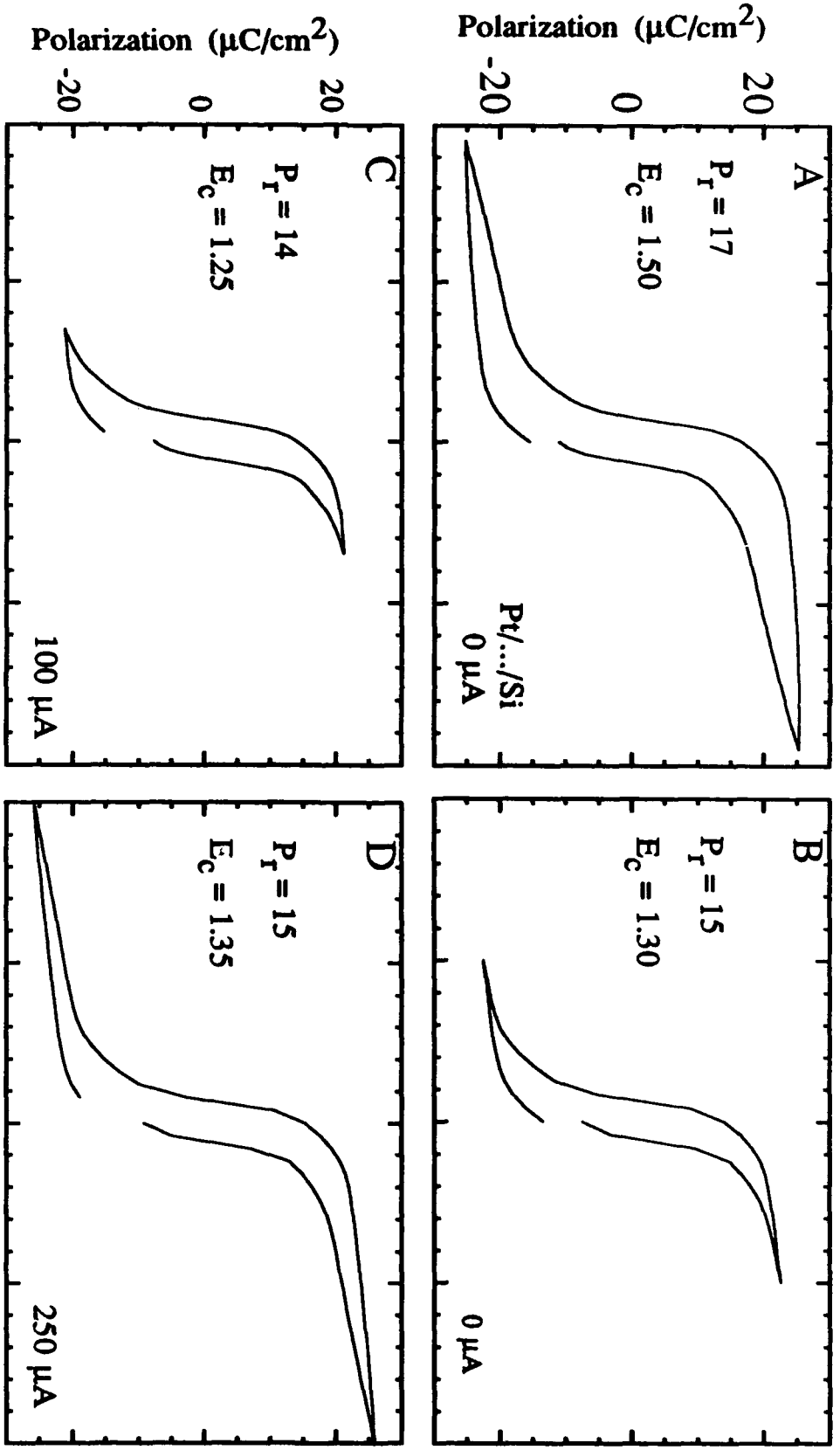


Figure 4. Hysteresis curves for PZT/Pt capacitors. (a) and (b) were prepared by non-FAD, (c) was prepared with 100 μA and (d) with 250 μA emission current.

to polycrystalline films.

Some cells (both FAD and non-FAD) had large components of non-remanent polarization and it was not possible to get saturation before electrical breakdown. Some cells were very lossy ('football' shaped hysteresis loops), while still maintaining a large dc resistivity (> 10^9 ohm-cm). In those films that had a large pyrochlore content, this may be explained by the fact that pyrochlore compounds are known to be good ionic conductors when they contain a certain degree of defects or anion disorder.[23]

One sample (12 cells) prepared at high emission currents (1200 μA), showed smaller P_r (roughly 5-8 $\mu C/cm^2$). These loops had shapes which were similar to hysteresis data presented for cells which had been aged.[13] It is possible that the anions produce defects in the films which at high fluxes, poison or degrade the ferroelectric response. Vacancy defects and space charge effects have been postulated to be partly responsible for ageing observed in oxide ferroelectrics.[24] This phenomenon becomes even more important as the grain size becomes smaller.[25]

Conclusion

An electron emitting filament was used to produce low energy oxygen anions which arrived at the substrate surface and made it more chemically reactive to the arriving atoms from the laser vaporization. These anions affected both the structure and morphology of the deposited film. On virgin MgO, a progression from a granular surface to a smooth one as the emission current increased from 0 to 500 μA was observed. At values greater than about 500 μA, the surface quality degraded. While a morphological transition was not as clear in the case of PZT films deposited on (100) Pt, a smoother film was obtained at 400 μA compared to the non-FAD film which was co sed of columnar grains.

The anions appeared to encourage the growth of the perovskite phase compared with the growth of the fcc pyrochlore phase. The ratio of pyrochlore to perovskite decreased by over five orders of magnitude with a concomitant increase in the smoothness of the film. The reasons for this enhancement are not entirely clear and require further study. Current efforts are aimed at determining the influence of defects on the growth and nucleation of the pyrochlore phase.

Preliminary determination of typical hysteretic behavior of filament-assisted films grown via pulsed laser deposition was accomplished. These films were found to be reliably short-free and give remanent polarization and coercive field values at least as good as polycrystalline PZT films produced by other methods. It is not clear why an enhancement of the remanent polarization was not observed for c-axis oriented films. This may be a consequence of excess electrons being trapped within the PZT lattice. Future investigations will pursue the long-term behavior of these films in an effort to gain insight into the role of the oxygen anions as well as to shed light on the fatigue and ageing mechanisms.

Acknowledgements

One of us (REL) would like to acknowledge financial support from the Office of Naval Technology. We wish to acknowledge the assistance of Dr. R. Gossett (NRL) for the EBS measurements, Dr. M. Kahn (NRL) for discussions concerning PZT, and Dr. S. Bernacki (Raytheon) for the Pt-coated silicon and electrical measurements on the initial non-FAD films.

References

1. H.M. Smith and A.F. Turner, Appl. Opt., 4, 147 (1965); H. Schwarz and H.A. Tourtellotte, J. Vac. Sci. 6, 373 (1968).

2. T. Venkatesan, X.D. Wu, B. Dutta, A. Inam, M.S. Hedge, D.M. Huang, C.C. Chang, L. Nazar, and B. Wilkens, Appl. Phys. Lett. 54, 581 (1989).

3. R.K. Singh, J. Narayan, A.K. Singh, and J. Krishnaswamy, Appl. Phys. Lett. 54, 2271 (1989).

4. B. Roas, L. Schultz, and G. Endes, Appl. Phys. Lett. 53, 1557 (1988).

5. J.F. Scott and C.A. Paz de Araujo, Science 246, 1400 (1989).

6. G.H. Haertling and C.E. Land, J. Am. Ceram. Soc. 54, 1 (1971); G.H. Haertling, *ibid*, 303 (1971).

7. see, e.g., R.A. Roy, K.F. Etzold, and J.J. Cuomo, in Material Research Society Symposium Proceedings, vol. 200, p. 141, E.R. Myers and A. Kingon, eds., 1990.

8. K.S. Grabowski, J.S. Horwitz, and D.B. Chrisey, Ferroelectrics 116, 19 (1991).

9. J.S. Horwitz, K.S. Grabowski, D.B. Chrisey, and R.E. Leuchtner, "*In-situ* Deposition of Epitaxial $PbZr_xTi_{1-x}O3$ Thin Films by Pulsed Laser Deposition", accepted for publication, Appl. Phys. Lett.

10. D.B. Chrisey, J.S. Horwitz, and K.S. Grabowski, in Materials Research Society Symposium Proceedings, vol. 191, p. 25, D.C. Paine and J.C. Bravman, eds., 1990.

11. Electron-Molecule Interactions and Their Applications, Vol. 1 & 2, L.G. Christophorou, ed., Academic Press, Inc., New York, N.Y., 1984 and references therein.

12. R.E. Leuchtner, K.S. Grabowski, J.S. Horwitz, and D.B. Chrisey, "Filament-Assisted Pulsed Laser Deposition of Epitaxial $PbZr_xTi_{1-x}O_3$ Films: Crystallographic and Physical Characterization", manuscript in preparation.

13. "Proceedings of the Second International Symposium on Integrated Ferroelectrics", Ferroelectrics 116 (1990); Material Research Society Symposium Proceedings, vol. 200, E.R. Myers and A. Kingon, eds., 1990.

14. D. MacNair, Rev. Sci. Instr. 38, 124 (1967).

15. The Mobility and Diffusion of Ions in Gases, E.W. McDaniel and E. A. Mason, John Wiley and Sons, New York, N.Y., 1973.

16. R.W. Crompton and M.T. Elford, Aust. J. Phys. 26, 771 (1973); I.D. Reid and R.W. Crompton, *ibid* 33, 215 (1980).

17. L.G. McKnight, Phys. Rev. A 2, 762 (1971); *ibid* 4, 1043 (1971).

18. For electron energies between about 4 and 10 eV, dissociative attachment will predominate and at energies below about 1 eV, three-body attachment will predominate in the uptake of electrons. In the regime between 1 and 4 eV, a combination of both processes is expected. See ref. 11 for more information.

19. N.H. Cheung, Q.Y. Ying, J.P. Zheng, and H.S. Kwok, J. Appl. Phys. 69, 6349 (1991).

20. R.E. Leuchtner, D.B. Chrisey, J.S. Horwitz, and K.S. Grabowski, "The Preparation of Epitaxial Platinum Films by Pulsed Laser Deposition", to be submitted to J. Coatings.

21. Samples provided by Raytheon Corporation, Lexington, Mass.

22. R.E. Leuchtner, D.B. Chrisey, J.S. Horwitz, and K.S. Grabowski, to be published.

23. P.K. Moon and H.L. Tuller, Sol. St. Ionics, 28 470 (1988); *ibid*, Mat. Sci.& Eng., B1 171 (1988).

24. M. Takahashi, Jpn. J. Appl. Phys. 9, 1236 (1970); S. Takahashi, *ibid*, 20, 95 (1980).

25. K. Okazaki and K. Nagata, J. Am. Cer. Soc. 56, 82 (1973).

AD-P006 645

PREPARATION, MICROSTRUCTURE, AND FERROELECTRIC PROPERTIES OF LASER-DEPOSITED THIN $BATIO_3$ AND LEAD ZIRCONATE-TITANATE FILMS

P. S. BRODY, B. J. ROD, K. W. BENNETT
Harry Diamond Laboratories, Adelphi, MD 20783
L. P. COOK, P. K. SCHENCK, M. D. VAUDIN, W. WONG-NG, AND C. K. CHIANG
National Institute of Standards and Technology
Gaithersburg, MD 20899

Abstract: Ferroelectric thin films of $BaTiO_3$ and lead zirconate titanate, $PbZr_{0.53}Ti_{0.47}O_3$ (PZT), have been prepared by pulsed excimer laser deposition. The microstructure and crystallography of these films have been studied by scanning electron microscopy (SEM), energy dispersive x-ray spectrometry (EDX), transmission electron microscopy (TEM), x-ray diffraction (XRD), and differential scanning calorimetry (DSC). Electrical properties, including remanent polarization, dielectric loss, and dielectric constant, have been measured. Also, switched remanent polarization has been measured under conditions of continuous cycling.

92-16109

INTRODUCTION

Interest in ferroelectric thin films has increased recently, due to the realization that the use of these materials may provide practical and improved nonvolatile silicon integrated random access memory (RAM).[1] Ferroelectric thin films have other applications as well, including optical switches and waveguides, and sensors and actuators. The tetragonally distorted perovskite forms of lead zirconate titanate (PZT) and $BaTiO_3$ are the most extensively studied and used bulk ferroelectric materials, and have also become leading candidates for thin film applications.

In a series of papers[2-10] we have described progress in the use of the laser deposition method to produce ferroelectric thin films. Our earliest studies demonstrated that PZT films could be deposited using the Nd/YAG laser.[2,3] Subsequently, we were able to show that these films, although characterized

by a rough surface morphology, could be made ferroelectric.[4,5] Next, we applied the excimer laser to thin film deposition, and were able to produce films having markedly smoother surfaces,[6] although these were not ferroelectric. Most recently, we have succeeded in producing excimer-deposited films having both improved surfaces as well as ferroelectric properties.[7-10] The present paper builds upon these results and reports new results on the characterization of PZT and $BaTiO_3$ thin films produced by the excimer laser deposition method. Laser deposition presents, we believe, a very important route for the preparation of ferroelectric thin films.

THIN FILM DEPOSITION AND PROCESSING

Pulsed laser deposition was used to prepare thin films of $BaTiO_3$ and PZT from dense stoichiometric ceramic targets. The laser was operated at 193 nm (ArF). Films were deposited on <100> silicon substrates which had been coated with a titanium bond layer about 25 nm thick, followed by a 200-nm-thick platinum layer. Depositions took place in an evacuated chamber, with a background oxygen pressure of 13.33 Pa. This pressure was maintained by a continuously metered oxygen flow combined with a differential pumping arrangement. The laser beam was brought into the chamber and onto the target at an incidence angle of ~35° through a windowed vacuum port. The laser was pulsed at 20 Hz, with 23-ns pulse duration. Fluence was ~30 J/cm^2, with 100 mJ per pulse. The substrate-to-target distance was 2 to 3 cm. The geometry of the deposition system is shown in Fig. 1. During deposition, a luminous plume was produced, the axis of which was perpendicular to the target surface. The laser beam was scanned across the rotating target by an external focusing lens, which was moved under computer control at the rate necessary to ensure comparable exposures on each area of the target. Using this arrangement it was possible to avoid production of deep troughs in the target surface, and instead, material was removed relatively evenly from the surface, thereby prolonging the useful life of the target. Deposition times ranged up to 1 hr at deposition rates of ~2 μm/hr. The as-deposited films showed optical interference fringes, indicating a variation in thickness near the edges. Rotation of the substrate during deposition promoted increased uniformity of film thickness, and resulted in films without interference fringes over a central 1 to 1.5-cm^2 region. While the use of this effect was limited by the size of our chamber, we

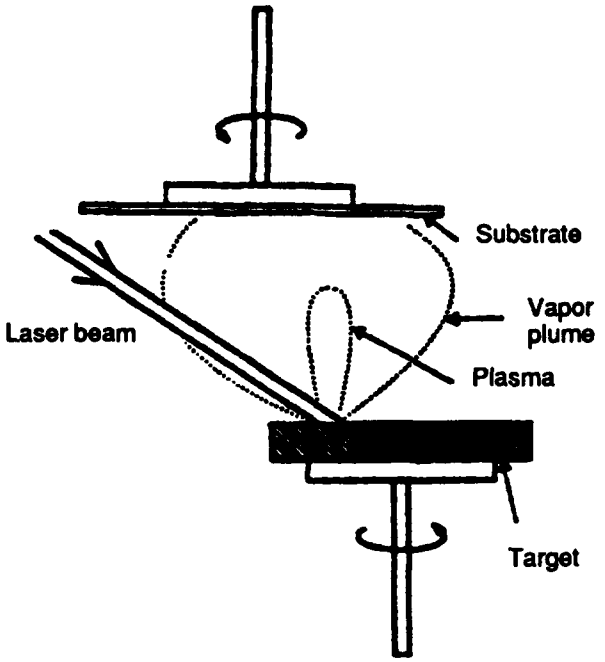


FIGURE 1. Arrangement for deposition of films using excimer laser.

believe the idea of dual nonconcentric rotation axes for target and substrate could be applied to produce films uniform over much larger areas.

In the present study films were deposited on both unheated and heated substrates. The substrate heater used a geometry similar to Fig. 1, in which the rotating Si substrate was resistively heated by passing 1.5 to 2.5 A through it at an applied potential of 6 to 12 V. The temperature was maintained during the depositions by operating the heating power source, a dc supply, in the constant current mode. At first the temperature was slowly raised to the desired point manually to avoid thermal runaway. Temperatures were estimated by optical pyrometry at incandescent temperatures (i.e., T > 550°C).

Due to Pb volatility, it was not possible to deposit PZT on substrates heated to incandescent temperatures. Instead, substrates were heated to a temperature below incandescence—estimated, as above, to be at ~400°C. Other films were deposited on unheated substrates. To complete a post-depositional annealing step for all PZT films, the wafer substrate was inserted into a preheated box furnace for times ranging from 15 min to several hr.

MICROSTRUCTURAL CHARACTERIZATION

General

Before the electrical measurements, the laser-deposited films were examined by SEM/EDX, TEM (including hot stage work), Raman scattering, profilo-

metry, and XRD (Ni-filtered Cu Ka radiation, theta/two-theta diffractometer).

In the as-deposited state on unheated substrates, all films were amorphous, based on both x-ray and electron diffraction. By comparison with films prepared by the Nd/YAG method (Fig. 2), we found the surfaces of the excimer films were relatively smooth (Fig. 3), with only a few widely scattered



FIGURE 2. Microstructure of Nd/YAG-deposited PZT film (SEM).

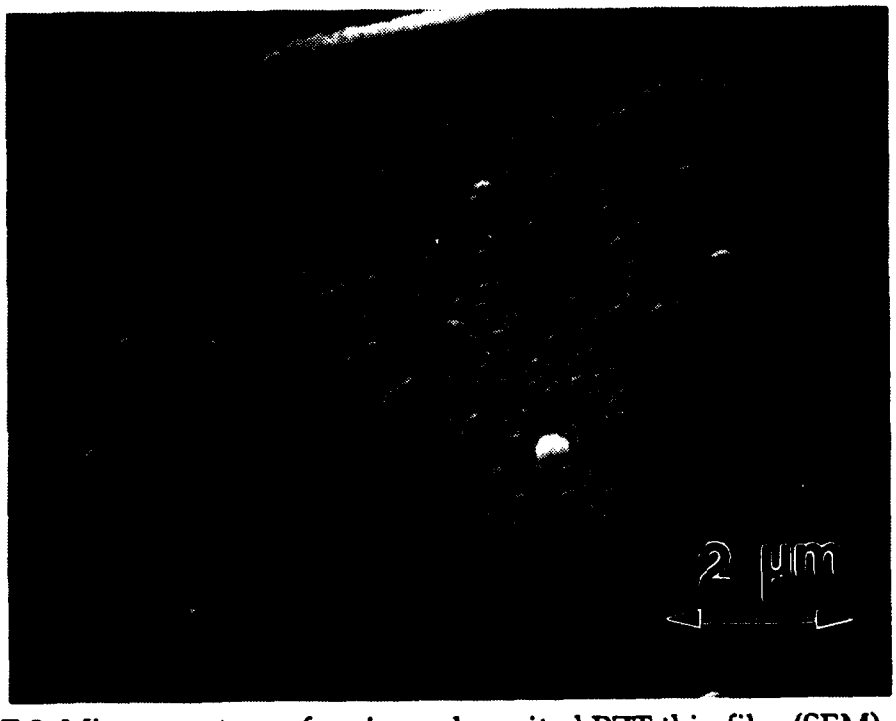


FIGURE 3. Microstructure of excimer-deposited PZT thin film (SEM).

ejecta present (e.g., at upper left of Fig. 3). Profilometry measurements on the excimer-deposited films indicated an average surface roughness of nearly 0.07 μm for both $BaTiO_3$ and PZT films. Most of this roughness was caused by a few widely scattered ejecta.

$BaTiO_3$

Excimer-deposited thin films were prepared from a dense ceramic target of a commercial formulation known as ceramic "B," which contained 5 mol% $CaTiO_3$. Preliminary TEM-hot-stage experiments were completed on very thin excimer-deposited films which had been formed directly on electron-transparent carbon substrates. Most of the results of this study have been described in ref. 6, where it was noted that, with heating, amorphous $BaTiO_3$ particulates crystallized directly to tetragonal $BaTiO_3$. On the basis of this information, we decided to deposit $BaTiO_3$ directly on a heated substrate, with the aim of causing crystallization to occur at the vapor plume/film interface, as film growth proceeded. Using the heated substrate assembly described above, we deposited a film at dull red heat, estimated at 750°C. This crystalline $BaTiO_3$ film had a very dense microstructure, and showed apparent cubic (rather than tetragonal) symmetry, on the basis of both XRD and TEM-electron diffraction. It also had considerable preferred orientation, with <100> perpendicular to the substrate surface. The grains were elongated parallel to the crystallographic alignment axis. A TEM micrograph for a section perpendicular to the alignment axis is shown in Fig. 4, where it can be seen that the average grain size in this section is in the range 25 to 50 nm. The grains were rodlike and measured at least 250 nm in the elongated direction. This film was not ferroelectric, and was found to have a dielectric constant of ~100. Another film deposited in similar fashion, although also having apparent cubic symmetry on the basis of the x-ray pattern (Fig. 5), was ferroelectric (to be described below). Raman data for this ferroelectric thin film showed that in spite of an apparently cubic x-ray pattern which did not exhibit splitting, the material had Raman lines at wavenumbers characteristic of tetragonal symmetry.[11]

PZT

To prepare PZT thin films, we used a dense ceramic of a commercial formulation known as "PZT 5A." Initial TEM studies[6] indicated lead loss due to electron beam heating, so crystallization studies were not completed in the TEM. However, noting that the as-deposited PZT films were amorphous, we carried out studies to investigate the crystallization process by DSC,[6,9] a method

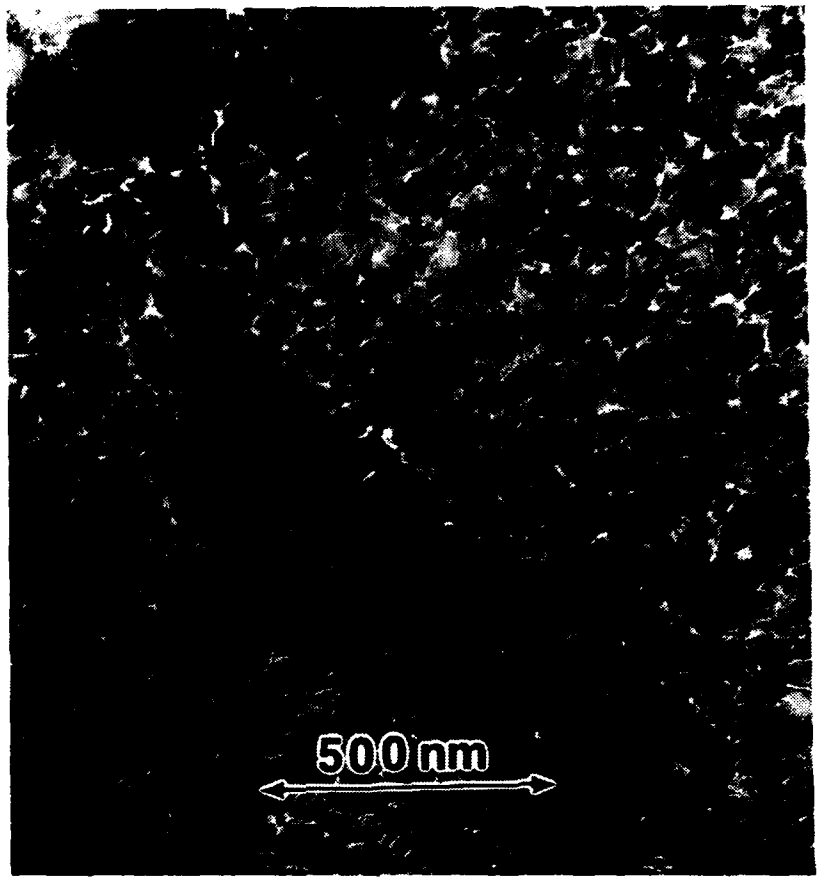


FIGURE 4. Microstructure of excimer-deposited $BaTiO_3$ thin film deposited on heated substrate (~750°C) (TEM).

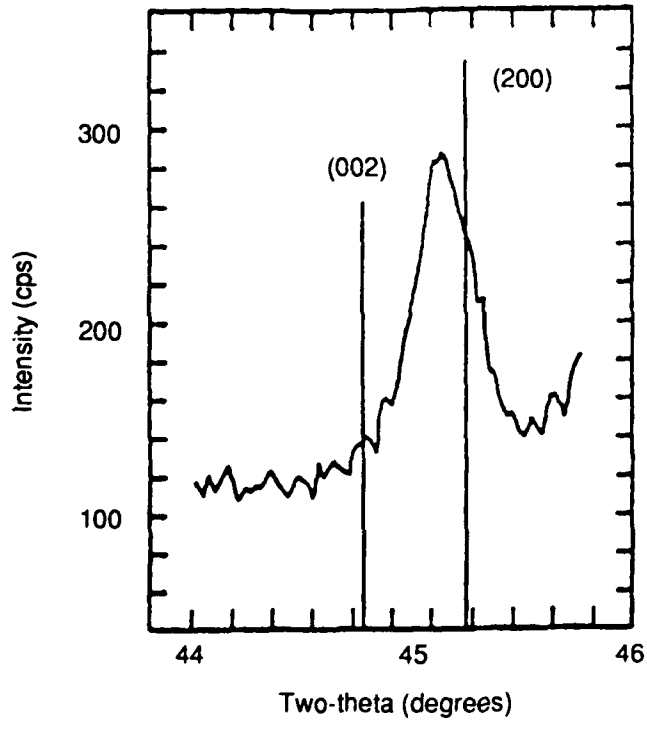


FIGURE 5. XRD data for ferroelectric excimer-deposited $BaTiO_3$ thin film. Note lack of tetragonal splitting.

commonly employed for glassy materials. The DSC data suggested a glass transition near 300°C. We then attempted to deposit films at a substrate temperature of ~400°C (i.e., above the glass transition temperature), so that the mobility of deposited material would permit good densification. Crystallization was then completed after deposition by annealing in air under isothermal conditions. Since the DSC data indicated a broad crystallization maximum near 500°C, we chose an annealing temperature of 600°C. This yielded unexpectedly large crystallites, as shown in Fig. 6, where it can be seen that the individual crystallites averaged 4 to 5 μm across. On the basis of EDX analyses, production of correct film stoichiometries using the excimer system was more of a problem for PZT than for $BaTiO_3$. The portions of the films deposited away from the vapor plume axis could not be crystallized completely; rather, they contained PZT crystals in a lead-depleted, glassy matrix. Areas of the film deposited directly in front of the plume could be crystallized completely, however, and so these areas were used for the electrical measurements reported below. XRD patterns for films prepared in this fashion were similar to those for the $BaTiO_3$, in that they showed a lack of tetragonal splitting (Fig. 7).



FIGURE 6. Microstructure of partially crystallized excimer-deposited PZT thin film (reflected light microscope).

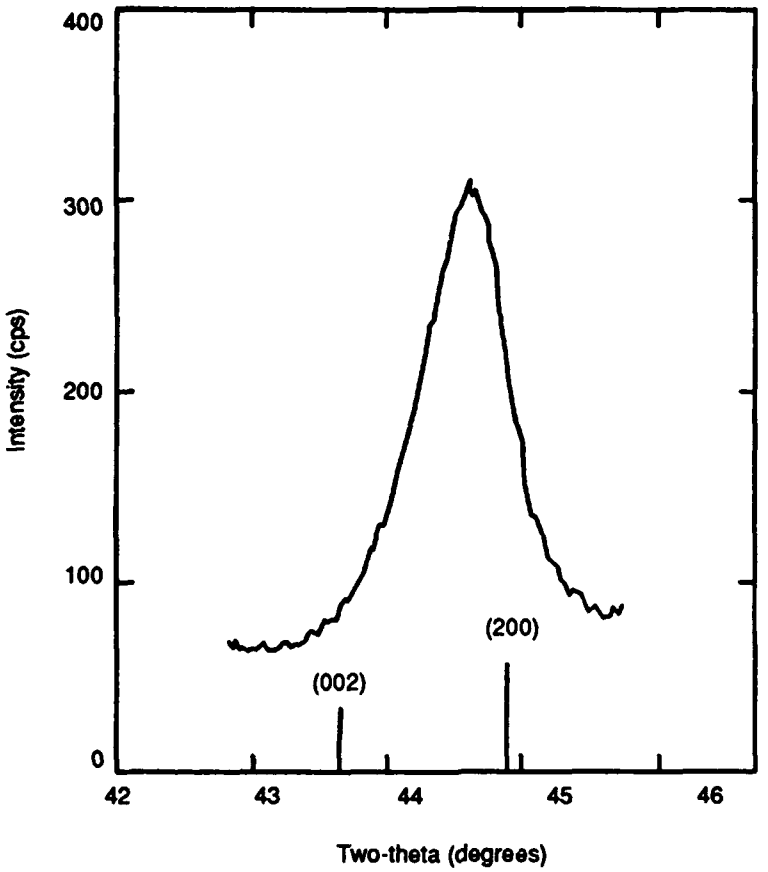


FIGURE 7. XRD data for ferroelectric excimer-deposited PZT thin film. Note again the lack of tetragonal splitting.

DIELECTRIC AND FERROELECTRIC PROPERTIES

General

Dielectric and ferroelectric properties were studied using parallel plate capacitor structures. To form these structures we deposited an array of square Pt electrodes on the surface of the film by sputtering using a shadow mask. The resulting capacitors were investigated using a Hewlett-Packard 4275A LCR meter* and a four-probe technique; capacitance and dissipation factors were measured at 1 mV. Ferroelectric hysteresis measurements for determining remanent polarization were made using a Sawyer-Tower circuit and a Hewlett-Packard 8116A pulse/function generator at sinusoidal applied voltages of ±5 V. We measured decay of remanent polarization and dielectric constant with cycling at 200 kHz.

Certain commercial equipment, instruments, or materials are identified in this paper in order to adequately specify the experimental procedure. Such identification does not imply recommendation or endorsement by the U.S. Government.

$BaTiO_3$

A 2-μm-thick $BaTiO_3$ film, with microstructural and crystallographic characteristics as described in the previous section, was measured and shown to give a ferroelectric hysteresis loop (Fig. 8) with a remanent polarization of 4.3 μC/cm^2 at an applied field of 180 kV/cm. Because of the thickness of this film it was not possible to fully investigate the dependence of remanent polarization on applied field. The dielectric constant for this film was calculated to be ~1300, a value close to the bulk dielectric constant for $BaTiO_3$ ceramic "B."

PZT

A 180-nm-thick PZT film was shown to give ferroelectric hysteresis loops as indicated in Fig. 9. There is no clear tendency for saturation of the remanent polarization in Fig. 9. Fig. 10 indicates the effect of applied field on remanent polarization. The highest measured remanent polarization was 13.5 μC/cm^2 at 600 kV/cm. The switching behavior was measured for single 8-V negative and positive pulses as shown in Fig. 11.

The remanent polarization shows no indication of decay over the time interval of Fig. 11. Fig. 12 shows decay of the switched remanent polarization as a function of switching cycles (fatigue), as determined from hysteresis loop

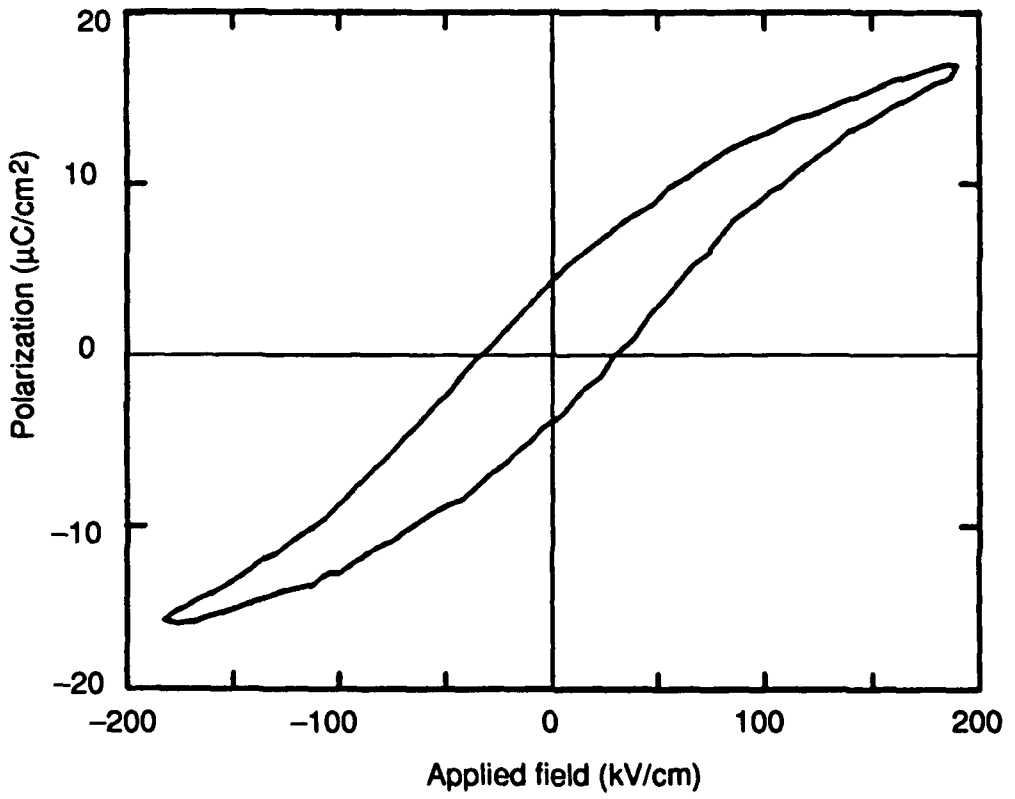


FIGURE 8. Polarization vs. applied field for 2-μm excimer-deposited $BaTIO_3$ thin film measured at 10 kHz.

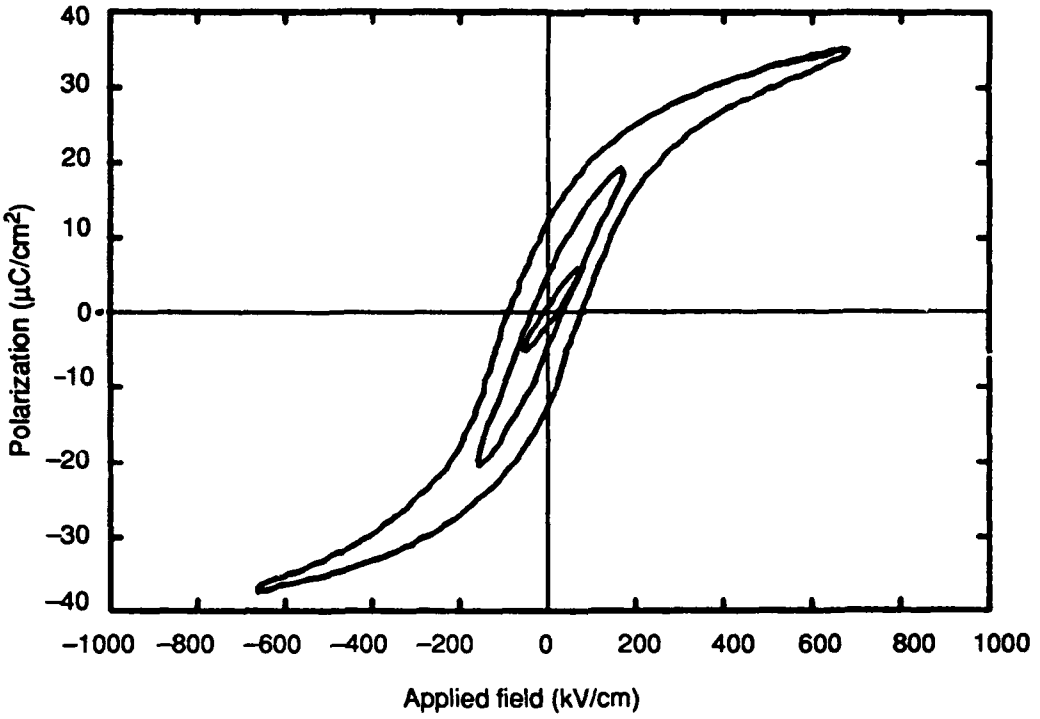


FIGURE 9. Polarization vs. applied field, showing nested hysteresis loops, for 180-nm excimer-deposited PZT film (annealed at 600°C); measured at 10 kHz.

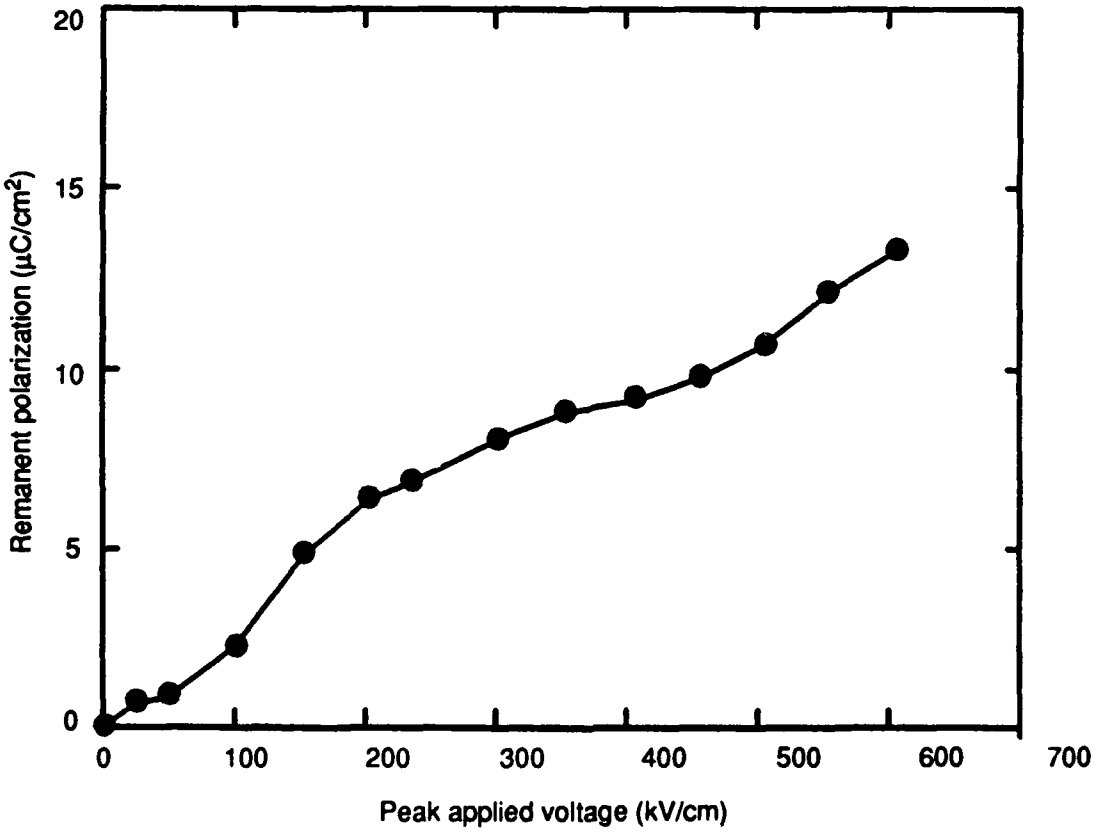


FIGURE 10. Remanent polarization vs. applied field for same film as in Fig. 9.

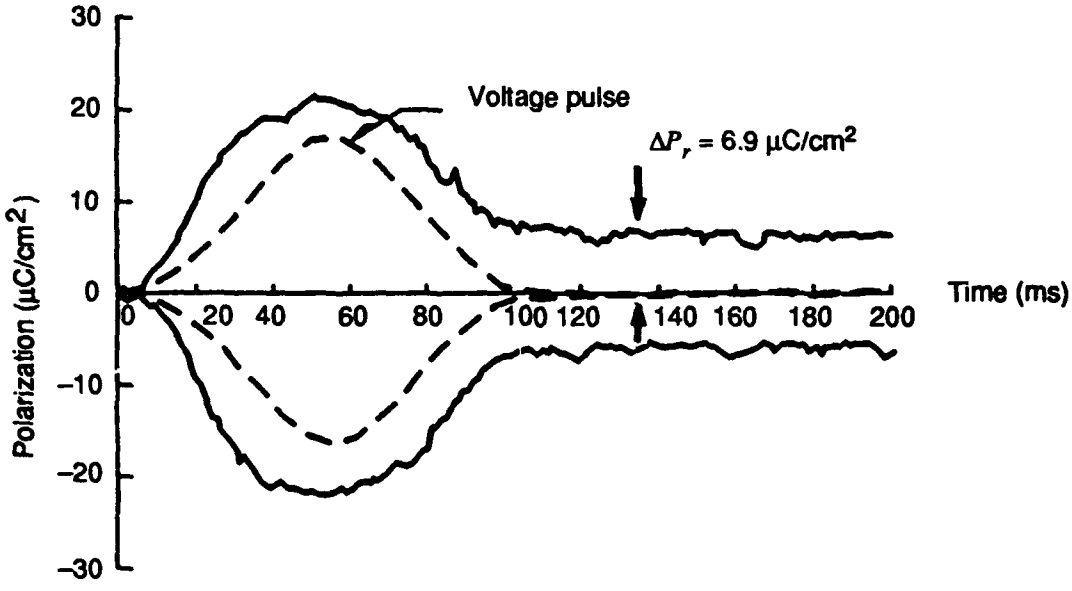


FIGURE 11. Polarization vs. time for 8-V positive and negative pulses for same film as Fig. 9.

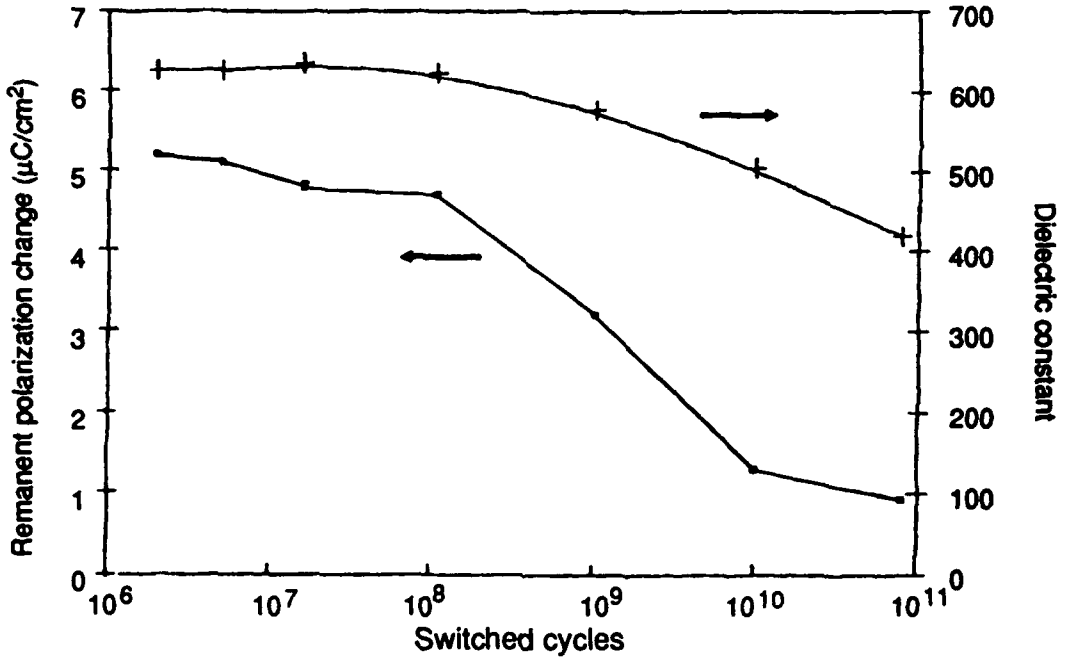


FIGURE 12. Remanent polarization and dielectric constant vs. cumulative switching cycles at 200 kHz for same film as Fig. 9.

measurements. It appears that the decay begins to level off at 10^{10} cycles. The value of the dielectric constant, as determined from the measured capacitance and by assuming a homogeneous film, also decayed with cycling (Fig. 12). The dissipation factor (Fig. 13) showed relatively less change with cycling. These fatiguing data are similar to those obtained on PZT films prepared by other methods.

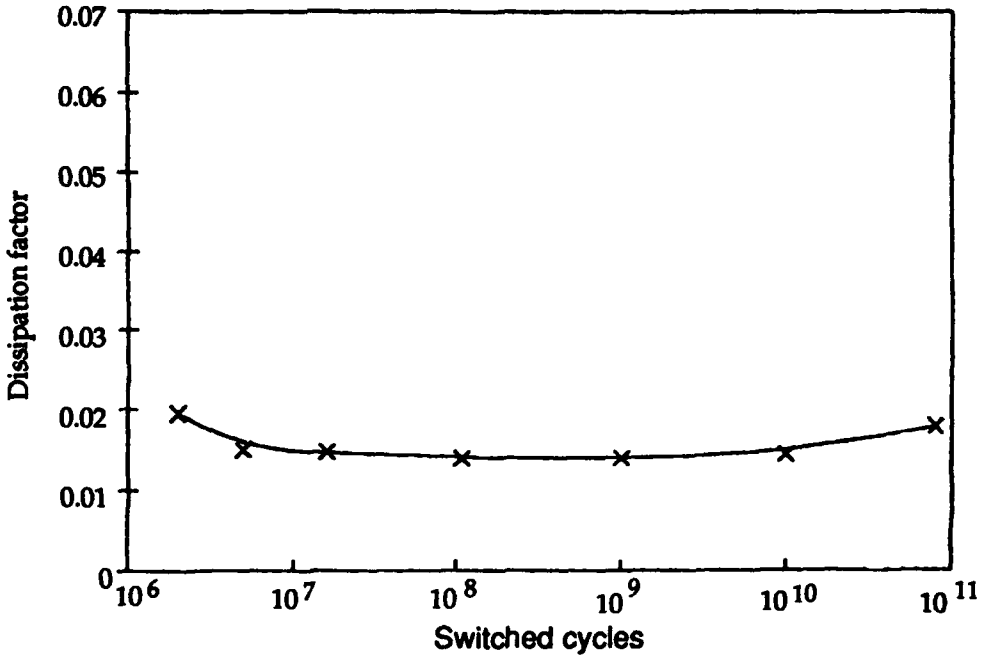


FIGURE 13. Dissipation factor as a function of cumulative switching cycles at 200 kHz for same film as in Fig. 9.

CONCLUSIONS

Dense smooth thin films of $BaTiO_3$ and PZT were prepared on Pt-coated silicon using the pulsed excimer laser deposition technique. Ferroelectric $BaTiO_3$ films can be formed directly on substrates heated at dull red heat. To produce ferroelectric PZT films, however, it was necessary to use a lower substrate deposition temperature, followed by post-deposition annealing. The PZT ferroelectric thin films have polarization/switching characteristics required for memory applications; the $BaTiO_3$ thin films have not been fully investigated. Fatigue properties of the PZT thin films are similar to those prepared by other methods.

REFERENCES

1. J. F. Scott and C. A. Paz de Aroujo, *Science*, **240** (1989), 1400.
2. L. P. Cook, P. K. Schenck, J. Zhao, E. N. Farabaugh, C. K. Chiang, and M. D. Vaudin, in *Ceramic Thin and Thick Films*, Ceramic Trans. **11**, B. V. Hiremath, editor (Amer. Ceram. Soc., Westerville, OH, 1990), 99-107.
3. P. K. Schenck, L. P. Cook, J. Zhao, J. W. Hastie, E. N. Farabaugh, C. K. Chiang, M. D. Vaudin, and P.S. Brody, in *Beam-Solid Interactions: Physical Phenomena*, Mater. Res. Soc. Symp. Proc., **157**, J. A. Knapp, P. Borgesen, and R. A. Zuhr, editors (Mater. Res. Soc., Pittsburgh, PA, 1990), 587-592.

4. P. S. Brody, J. M. Benedetto, B. J. Rod, K. W. Bennett, L. P. Cook, P. K. Schenck, C. K. Chiang, and W. Wong-Ng, "Microstructure and Ferroelectric Properties of Lead Zirconate-Titanate Films Produced by Laser Evaporation," to be published in *Proceedings of the 7th International Symposium on Applications of Ferroelectrics (ISAF)* (IEEE, Univ. Illinois, Champaign-Urbana, 6-8 June 1990).
5. C. K. Chiang, L. P. Cook, P. S. Brody, and J. M. Benedetto, in *Ferroelectric Thin Films*, Mater. Res. Soc. Symp. Proc. **200**, E. R. Myers and A. I. Kingon, editors (Mater. Res. Soc., Pittsburgh, PA, 1990), 133-138.
6. L. P. Cook, M. D. Vaudin, P. K. Schenck, W. Wong-Ng, C. K. Chiang, and P. S. Brody, in *Evolution of Thin-Film and Surface Microstructure*, Mater. Res. Soc. Symp. Proc. **202**, C. V. Thompson, J. Y. Tsao, and D. J. Srolovitz, editors (Mater. Res. Soc., Pittsburgh, PA, 1991), 241-246.
7. W. Wong-Ng, T. C. Huang, L. P. Cook, P. K. Schenck, M. D. Vaudin, C. K. Chiang, and P. S. Brody, "PZT Films Prepared by the Pulsed Laser Deposition Technique," to be published in *Proceedings of the International Conference on Materials and Process Characterization for VLSI (ICMPC '91)*, R. C. McDonald and T. C. Huang, editors.
8. L. P. Cook, W. Wong-Ng, T. Huang, P. K. Schenck, M. D. Vaudin, C. K. Chiang, and P. S. Brody, *Thermal Processing of Laser-Deposited $BaTiO_3$*, **ibid**.
9. L. P. Cook, P. K. Schenck, M. K. Vaudin, C. K. Chiang, W. Wong-Ng, "Processing of Laser-Deposited Thin Films of $BaTiO_3$ and PZT," to be published in *Ferroelectric Films*, Proc. AcerS Symp. Cincinnati, OH (April 1991), A. S. Bhalla and K. M. Nair, editors (Amer. Ceram. Soc., Westerville, OH, 1991).
10. C. K. Chiang, W. Wong-Ng, P. K. Schenck, L. P. Cook, M. D. Vaudin, P. S. Brody, B. J. Rod, and K. W. Bennett, "Characterization of Lead Zirconate-Titanate Thin Films Prepared by Pulsed Laser Deposition," to be published in *Phase Transformation Kinetics in Thin Films*, Mater. Sci. Symp. Proc. **230** , ed. by M. Chen, M. Thompson, R. Schwartz, and M. Libera (Mater. Res. Soc., Pittsburgh, PA, 1991)
11. L. H. Robins, unpublished data, NIST, 1991.

AD-P006 646

PULSED EXCIMER LASER DEPOSITION OF FERROELECTRIC THIN FILMS

S. B. Krupanidhi[a], D. Roy, N. Maffei and C. J. Peng

Materials Research Laboratory, Pennsylvania State University, University Park, PA 16802.

ABSTRACT Pulsed UV excimer laser ablation was employed to deposit multi-axial, bi-axial and uni-axial ferroelectric compositions of PZT, bismuth titanate and lead germanate respectively. In general, a fluence lower than 2 J/cm² caused a preferential evaporation of volatile components, resulting in stoichiometric imbalance. However, the fluences beyond 2 J/cm² enabled the deposition of stoichiometric thin films of multi-component oxide systems. The intrinsic bombardment due to the energetic ablated species during the thin film deposition seemed to influence the composition, structure, orientation and the electrical properties. The electrical characterization of ferroelectric films indicated a dielectric constant of 800-1000, a P_r of 32μC/cm² and E_c of 130KV/cm for polycrystalline PZT films and the corresponding quantities were measured to be 150, 7 μC/cm² and 20 KV/cm for *in-situ* crystallized *c*-axis preferred oriented bismuth titanate films. Lead germanate thin films oriented along *c*-axis (003) showed a dielectric constant of 30, a P_r of 2.5 μC/cm² and E_c of 55 KV/cm.

97-10110

INTRODUCTION

Most recent interests in ferroelectric thin films are directed towards exploring the applications in piezoelectric[1], pyroelectric[2], electro-optic[3] and radiation hard non-volatile memory devices[4]. Potential non-volatile memory applications warranted assertive attention due to its promise of high access speed, possibility of high density and low operating voltage in addition to the non-volatility and radiation hardness[4,5]. A plethora of deposition techniques have been successfully used to

[a] Also with Dept. of Engg. Science & Mechanics.

synthesize ferroelectric thin films, including RF magnetron[6-11], ion-beam sputtering[12,13] electron cyclotron resonance (ECR) plasma stream[14], metal organic decomposition (MOD)[15], metal-organic chemical vapor deposition (MOCVD)[16,17] and sol-gel synthesis[18-22].

Reproducible synthesis of stoichiometric ferroelectric films has been a hard task to execute due to larger differences in volatilites in the complex composition. The accomplishment of pulsed laser ablation in depositing high quality superconducting films is regarded to be persistent with the deposition of *in-situ* stoichiometric ferroelectric films. Most recently, successful deposition of $Bi_4Ti_3O_{12}$[23] and PZT[24] by excimer laser ablation has been reported.

Present paper highlights our attempts to apply pulsed laser ablation technique to deposit *in-situ* crystalline and stoichiometric, multi-component oxide films of ferroelectrics. Studies were done on a multi-axial Pb based perovskite, such as PZT ($PbZr_{0.52}Ti_{0.48}O_3$), a bi-axial system such as bismuth titanate ($Bi_4Ti_3O_{12}$) and a uni-axial system such as lead germanate ($Pb_5Ge_3O_{11}$).

EXPERIMENTAL

The output of a KrF excimer laser beam operating at 5Hz and 248nm wavelength was used in the present work. The ≃600mJ was focussed by a uv grade plano-convex lens of 50cm focal length and was brought into the chamber through a quartz port. The incoming beam was incident onto the target at an angle of 45°. The beam energy density or fluence was varied by changing the laser spot size on the target by altering the lens to target distance. The stability of the energy of the incoming beam was regularly monitored by an energy meter, made by Coherent (Model# Lasersure II). Attention was also drawn towards the regulation of beam shape and reproducibility of the spot size. The deposition pressure was controlled by an MKS flowmeter which operated in conjunction with a gas flow controller.

Stoichiometric sintered targets of PZT of near morphotropic phase boundary composition ($PbZr_{0.52}Ti_{0.48}O_3$), bismuth titanate ($Bi_4Ti_3O_{12}$) and lead germanate ($Pb_5Ge_3O_{11}$) were prepared by ceramic powder processing. The sintered density of the targets were about 95% of theoretical density to facilitate efficient absorption

of the laser beam. Care was taken so that the targets were monophasic which was confirmed by X-ray diffraction pattern. The targets were mounted on a copper disc with high temperature silver cement.

A freshly polished target surface was used for each deposition and the target was mounted on a motor driven rotary shaft for a continuous rotation at a constant rpm during the ablation process to ensure uniform ablation rate. Platinum coated silicon substrates were placed parallel to the target at a distance of ≈3cm. Films thus deposited at room temperature at various partial pressures of oxygen and fluences were annealed in flowing oxygen at 650°C for 2hr (*ex-situ* crystallization). Also films were grown *in-situ* crystallized by employing an electrically heated mount on which the substrates were placed and mechanically clamped for attaining uniformity of temperature.

The crystallographic structure of the films was examined by X-ray diffraction (XRD) and the chemical composition of the films was determined by energy dispersive spectroscopy (EDS) while the surface morphology was examined by scanning electron microscopy (SEM). Gold electrodes were deposited on the top surface of the films for electrical characterization and the dielectric properties were measured as a function of frequency by using a low frequency (LF) impedance analyzer. The ferroelectricity in the laser ablated films was investigated in terms of polarization hysteresis behavior by employing a computer controlled modified Sawyer-Tower circuit. The fatigue of polarization reversal was studied by combining a fast pulse generator and the automated Sawyer-Tower circuit.

RESULTS AND DISCUSSIONS

Multiaxial System (PZT)

PZT ($PbZr_{0.52}Ti_{0.48}O_3$) has a perovskite structure with a Curie temperature of 386°C and lattice parameters of $a = b = 4.036$ Å and $c = 4.146$ Å. For a composition in the vicinity of morphotropic phase boundary, the possible polarization directions are eight along <111> and six along <100>, a total of fourteen, making the system a *multi-axial* one.

The composition of the films deposited on silicon and platinum coated silicon substrates at ambient temperature, were determined using the EDS method for as grown and annealed films and the results are shown in Figure 1. It can be seen that

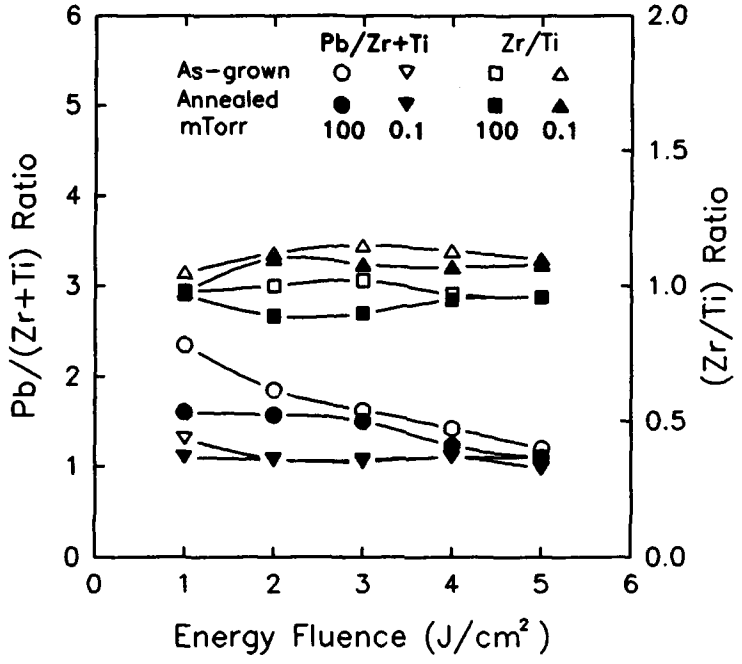


Figure 1 Variation of Pb/(Zr+Ti) and Zr/Ti ratio with laser fluence and partial pressure of oxygen in *ex-situ* crystallized films.

the Zr/Ti ratio remained almost same and close to that of the target which elucidates that the Zr/Ti ratio is almost independent of the laser fluence in the films irrespective of the oxygen pressure and the annealing temperatures of 650°C and 700°C.[24] However, the films showed a persistent change in Pb content as the fluence was increased. Slight reduction in Pb content with increasing laser fluence is consistent with earlier reports.[25,26] It is apparent that below the onset of the non-thermal ablation for a certain fluence the material is removed from the target by a thermally assisted process which leads to preferential evaporation of Pb[27] from the target culminating in a higher amount of Pb in the film. However, as the fluence level reached the ablation regime, stoichiometric amounts of various oxides were deposited onto the substrate, as may be observed from Figure 1.

Figure 2 shows the variation of Pb as a function of substrate temperature at

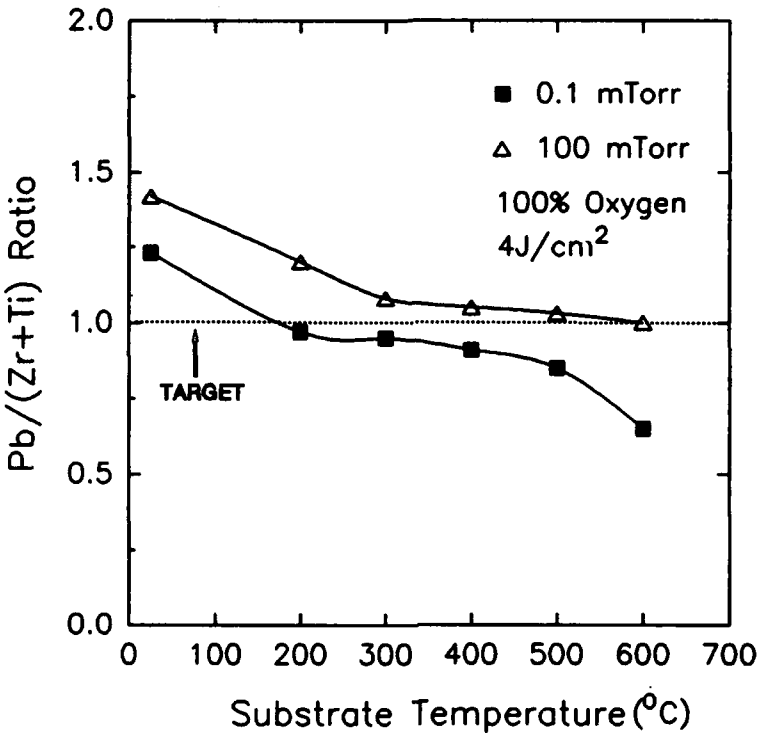


Figure 2 Variation of Pb/(Zr+Ti) ratio with partial pressure of oxygen and substrate temperature in films deposited at 4 J/cm².

different partial pressures of oxygen for the films deposited at 4 J/cm². The films deposited at 0.1 mTorr showed sharper drop in Pb content than the films deposited at 100 mTorr at temperatures above 400 °C. It may also be seen from the figure that there exists a decrease in Pb content in the films deposited at an oxygen pressure of 0.1 mTorr, while the substrate temperature was increased to 600°C. However, as the ablation pressure was raised to 100 mTorr, the Pb content in the films became almost independent of growth temperature. This behavior may be associated with the modified sticking co-efficients of Pb due to the oxidation at higher pressures and resulted in a balanced stoichiometry at elevated substrate temperatures. These observations also suggest that higher oxygen pressures in the range of 100mTorr are necessary to maintain stoichiometry in the PZT films deposited at higher temperatures and also indicates no need of higher pressures for the films deposited at room temperature.

Figure 3 shows the X-ray diffraction patterns of the annealed PZT films deposited on platinum coated Si substrates at 2-5 J/cm² fluences and 1.0 mTorr

of partial pressure of oxygen. All the patterns of the *ex-situ* crystallized films consistently evidenced polycrystallinity with mainly (100) and (110) orientation. Minor amounts of pyrochlore phase were also noticed with a perceptible trend among the films deposited at various fluences. The relative peak intensity ratio

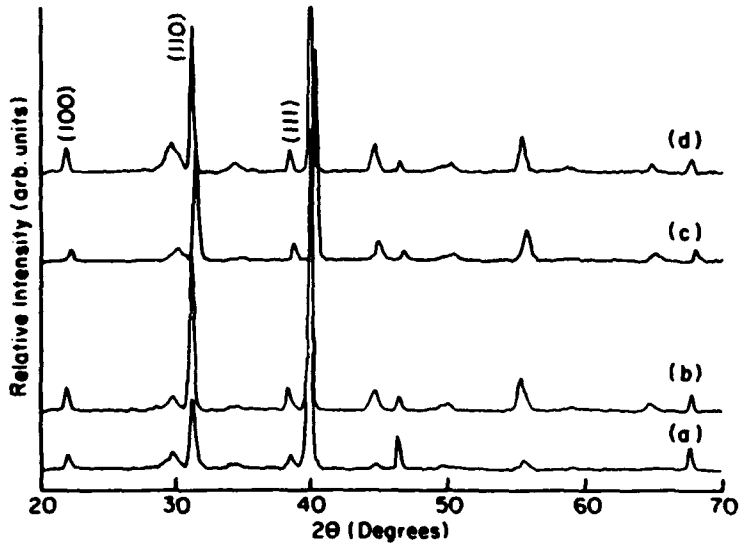


Figure 3 XRD patterns for the films deposited at different fluences at 1 mTorr of oxygen pressure and annealed at 650°C: a) 2 J/cm²; b) 3 J/cm²; c) 4 J/cm²; d)5 J/cm².

between the pyrochlore and perovskite peaks increased as the fluence was increased while the substrates were kept at room temperature. The average crystallite sizes were calculated from the peak widths at the half maxima of in the X-ray diffraction patterns by Scherrer'r formula.[28] The crystallite sizes were calculated to be 140, 215, 230 and 280 Å respectively for the films deposited at 2, 3, 4 and 5 J/cm², indicating another trend that the crystallite size of the films increased with the fluence. The proportionality between the crystallite size and fluence could be attributed to the fact that the ejected material in the plume would have higher energy (of the order of several eV)[26] as the fluence went up and tends to enhance the growth of the crystallites.

The fluence dependence of the *in-situ* crystallized PZT films is also shown in Figure 4. The films deposited at 500 °C at different energies of 2 and 4 J/cm² (fig 4c and 4d) showed pyrochlore phase. In case of 4 J/cm², the Pb deficient pyrochlore phase peak was quite strong. As the growth temperature was raised to

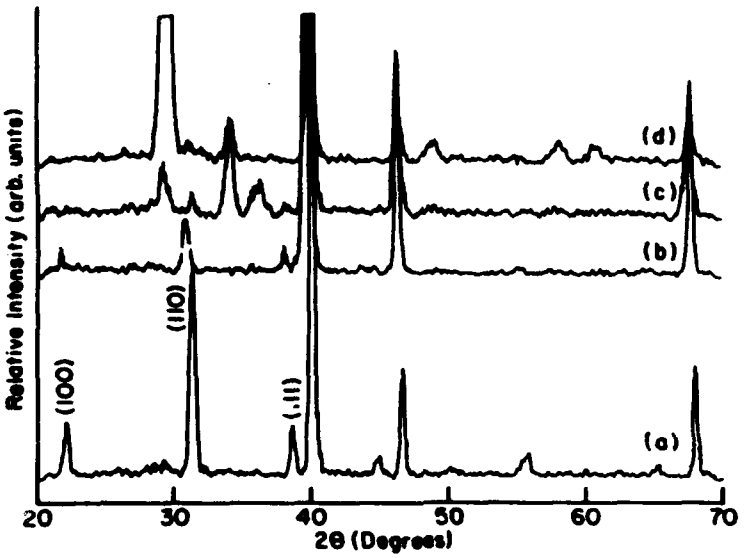


Figure 4 XRD patterns for the films deposited at: a) 2 J/cm², 1.0 mTorr, 600°C; b) 4 J/cm², 1.0 mTorr, 600°C; c) 2 J/cm², 100 mTorr, 500°C; d) 4 J/cm², 100 mTorr, 500°C.

600 °C, both the energies of 2 and 4 J/cm² offered films with perovskite phase, while the (110) peak intensities were relatively weaker in case of high energy (4 J/cm²). These results suggest the presence of several competing phenomena, including a) scattering of volatile species at low energies and low pressure; b) energetic particle bombardment at higher fluences and high substrate temperature induced Pb escape at low pressures, leading to Pb deficiency. The presence of higher pyrochlore peak (fig 4d) or lower perovskite peak (fig 4b) may also be attributed to the higher kinetic energy of the material ejected in the plume and the bombardment of the growing film causing a preferential loss of some of the constituents.

The dielectric properties were measured on the PZT films sandwiched between the bottom platinum and the top gold electrodes. The small signal dielectric data was obtained by using an HP low frequency impedance analyzer. The variation of dielectric constant and dissipation factor of the excimer laser ablated films as a function of laser fluence are shown in Figure 5. Such dependence on fluence is believed to reflect via compositional variations at lower laser fluences. The dielectric constant increased from about 400 to 1000 and the dissipation factor decreased from 0.3 to .03 as we increased the fluence from 1 to 2 J/cm². As stoichiometric amount of Pb began to be present around 2 J/cm², the dielectric

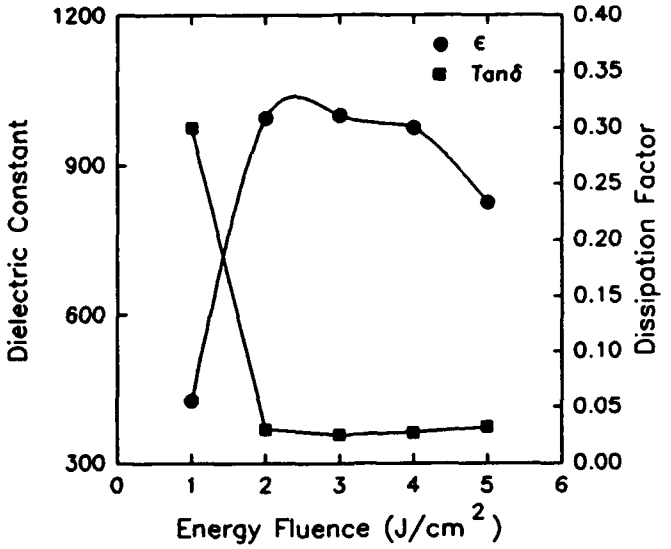


Figure 5 Dielectric constant and loss factor as a function of fluence for films with thickness of 0.5 μm.

constant rose notably and the dissipation factor improved compared to the films deposited at 1 J/cm². As the fluence approached 5 J/cm², there might be a possibility of slight departure from stoichiometry due to intrinsinc bombardment and caused slight reduction in the dielectric constant. Films of typical thickness of $\approx$0.5μm exhibited a $\varepsilon \simeq$ 800-1000 and a tanδ of 0.03 at 100KHz frequency.

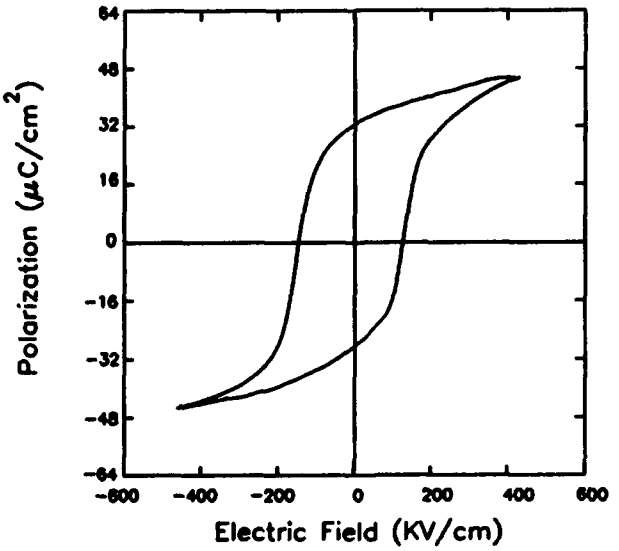


Figure 6 Ferroelectric behavior of the film deposited with 2J/cm² at 0.1 mTorr and annealed at 650°C.

The ferroelectricity was investigated by observing the polarization hysteresis

using an automated Sawyer-Tower circuit at 1 KHz frequency. The results are shown in figure 6 which indicate a remanent polarization of 32μC/cm^2 and the coercive field of 130KV/cm for the PZT films. The remanent polarization may be found close to that normally observed for bulk ceramics. The relatively higher coercive field compared to that of bulk PZT may be associated with the small grained microstructure of the films.

Bi-axial system (Bismuth Titanate)

Bismuth titanate ($Bi_4Ti_3O_{12}$) has a layered pervoskite structure consisting of Bi_2O_2 layers interleaved with $Bi_2Ti_3O_{10}$ pervoskite like layers. The Curie temperature is 676°C and the lattice parameters are a= 5.448 Å, b= 5.410 Å and c= 32.84 Å. The polarization vector in bismuth titanate is inclined at a small angle (~4°) to the a-b plane. This leads to two polarizations: one along the a-axis , P_s=50 μC/cm^2, and the other along the c-axis, P_s=4 μC/J/cm^2 and hence this composition has been termed *bi-axial*. The coercive fields are 50 kV/cm along the a-axis and 3-5 kV/cm along the c-axis.[29] The low coercive field along the c-axis makes bismuth titanate an attractive gate dielectric in ferroelectric field effect transistor.[30]

Earlier attempts to deposit device quality bismuth titanate thin films were done involving r.f. sputtering technique.[31] Excess Bi_2O_3 was needed in the sputtering target to obtain crystalline films (due to the preferential sputtering of bismuth and its high volatility). Sputtering offered low deposition rates and also resulted in interdiffusion with the substrate at the high temperatures needed for single-phase film growth. Recently, bismuth titanate thin film deposition has been reported by the pulsed laser technique.[32,33] Following presents some of our results on excimer laser ablated bismuth titanate thin films.

Figure 7 shows the XRD patterns for films deposited with different laser fluences (1-9 J/cm^2) at 600°C and in an oxygen partial pressure of 50 mTorr. It may be seen that at fluences less than 2 J/cm^2, the presence of Bi rich bismuth titanate phase ($Bi_{12}TiO_{20}$) was detected, however, such Bi rich phases were not observed in films deposited at fluences higher than 2 J/cm^2. These results suggest that at lower fluences the possible preferential evaporation of volatile component

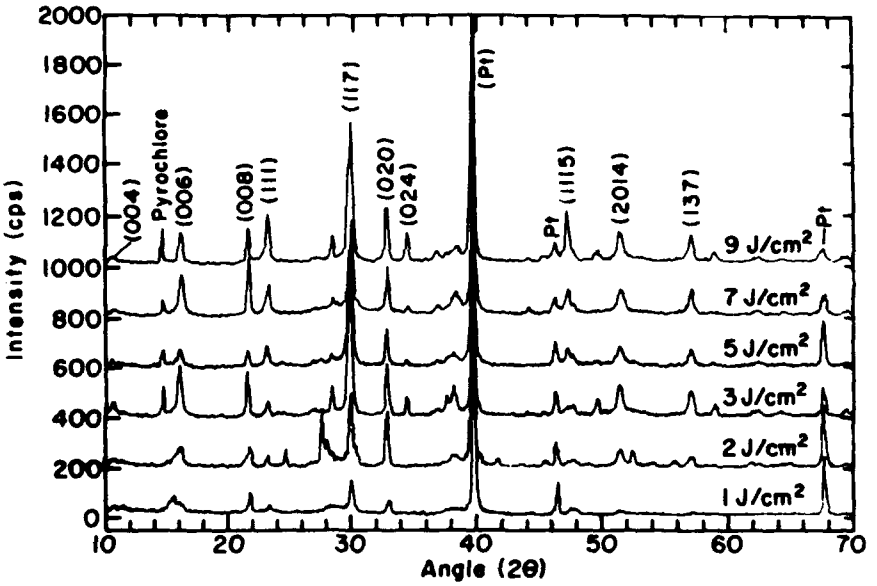


Figure 7 XRD patterns for the films deposited at various fluences at 50 mTorr and at a substrate temperature of 600°C.

(Bi in the present case) might have occurred. At higher fluences strictly the ablation regime was reached and this lead to the deposition of stoichiometric bismuth titanate thin films. It may also be pointed out that as the fluence was increased upto 7 J/cm², films attained slightly improved preferred orientation and also the crystallite size increased. However, at 9 J/cm², the presence of pyrochlore phase became more significant. These results suggest an intrinsic bombardment by the energetic ablated species assisting crystallization upto 7 J/cm² and further increase in fluence might have caused probable loss of Bi leading to the appearance of noticeable pyrochlore phase.

The room temperature permittivity and dissipation factor at 100 kHz were found 150 and 0.015 respectively, for the films deposited at 600°C, 200 mTorr oxygen partial pressure and 3 J/cm². The permittivity was comparable to that reported by others[32] and showed no dispersion with frequency indicating that the measured quantity was representative of the bulk. The dissipation factor was quite low and indicative of high resistivity of films. The ferroelectric behavior in the *c*-axis preferred oriented bismuth titanate films was estimated in terms of P_r= 7 μC/cm² at a coercive field of 20 KV/cm. Studies are in progress to obtain controlled oriented films and correlation with polarization switching behavior.

Uniaxial system (Lead Germanate)

Lead germanate ($Pb_5Ge_3O_{11}$) is another attractive candidate in which the ferroelectricity was first reported by Iwasaki et. al along with its piezoelectric, dielectric and electro-optic properties[34]. Lead germanate belongs to optically active (enantiomorphous) space group P3. The interesting feature of this material is that the optical rotatory power along the ferroelectric c-axis changes its sense by the reversal of the spontaneous polarization. In addition, it also exhibits a remanent polarization of about 4 $\mu C/cm^2$ at a coercive field of about 25 KV/cm along the *uni-axial* (003) polar direction, making it suitable as another candidate for memory applications. Thin films of lead germanate were made, in the past, by thermal evaporation[35], flash-evaporation[36] and dc reactive sputtering[37] methods. Here we present our preliminary results on lead germanate thin films prepared, for the first time, by excimer laser ablation method.

The results of the composition analysis obtained by EDS for lead germanate films are shown in Fig. 8, which were grown onto unheated substrates. It may be

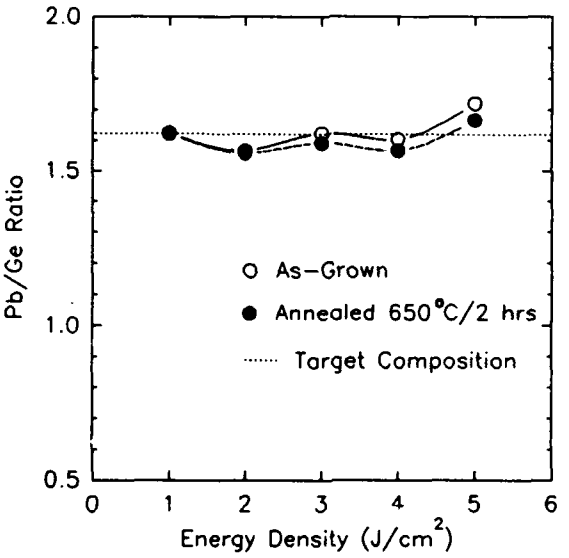


Figure 8 Compositions of as-grown and annealed lead germanate films as function of energy densities.

seen from the figure that the composition of as-grown films are quiet close to that of target and close to stoichiometry (Pb/Ge=1.67) as well. The slight increase of Pb content at 5J/cm² energy density towards more close to stoichiometric level

may be due to the energy density dependent composition variation via secondary effects such as bombarding and is consistent with the observations made for other multi-component oxides. Films deposited at various energy densities were annealed by at 650°C for 2 hrs, and despite the infinitismal Pb loss (within 0.7 mol%), the compositions were found still quite close to the target as shown in Fig. 8. The film composition after annealing seems to have been controlled by stoichiometric requirement of the compound.

The structure of the lead germanate films, deposited at different energy densities under different ablation pressures, was studied in terms of XRD. Films annealed at temperatures as high as 500°C, showed random polycrystalline structure, irrespective of the ablation energy density. However, further elevation of annealing temperatures up to 650°C, introduced a preferred orientation and the results are shown in Fig. 9. The $Pb_5Ge_3O_{11}$ films deposited onto a Pt coated silicon

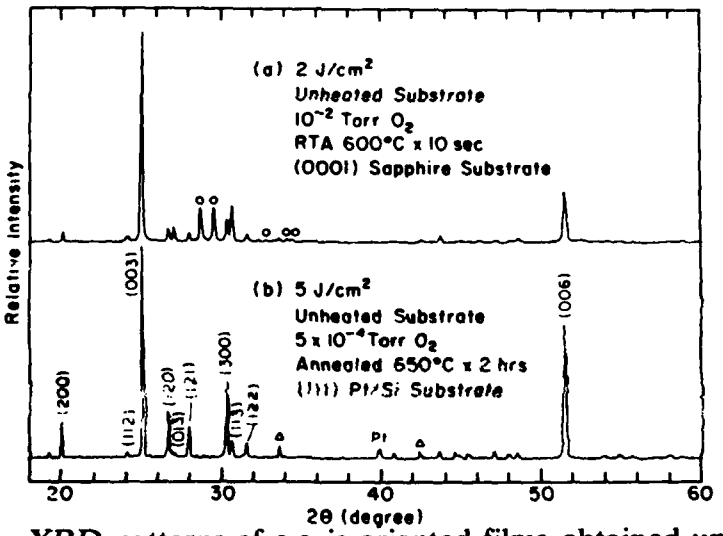


Figure 9 XRD patterns of c-axis oriented films obtained under two different growth conditions. Open circles denote Pb_3GeO_5 phase and open triangles indicate unknown phases.

substrates at an energy density of 5J/cm² attained a strong (003) preferred orientation, which also happens to be the unique spontaneous polarization axis of lead germanate.

The dielectric behavior of lead germanate films was studied on the films of both (003) and (300) orientations, in terms of small signal dielectric constant. The room temperature dielectric constant was found to be about 30 for (003) oriented

film whereas it was about 24 for the a-axis oriented (300) film. The temperature dependent dielectric behavior exhibited a clear onset of ferro-paraelectric phase transition at the Curie temperature, Tc of about 175°C for (003) oriented films consistent with the single crystal. However, such phase transition is absent in (300) oriented films as predicted for a-axis orientation.[33]

The ferroelectricity in lead germanate (003) films in terms of polarization hysteresis is shown in Fig. 10 showed a remanent polarization of about 2.5 $\mu C/cm^2$

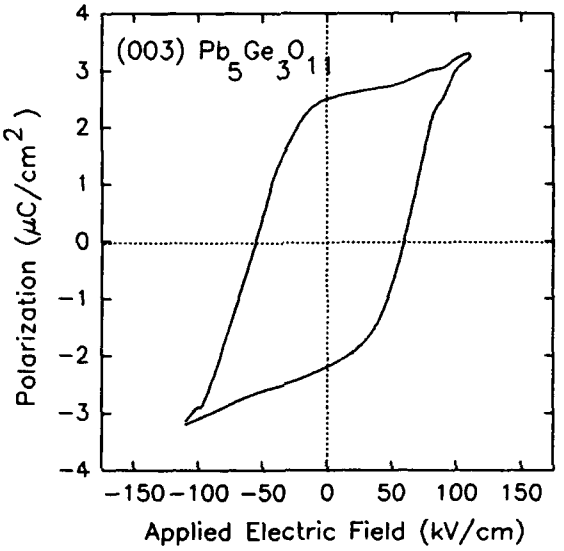


Figure 10 Ferroelectric hysteresis loop of c-axis preferred oriented $Pb_5Ge_3O_{11}$ films on Pt/Si substrate with growth conditions are the same as Fig. 9(b).

with a coercive field of 55 kV/cm. Good square polarization hysteresis loops were observed, however at relatively larger coercive fields, which may be associated with the presence of small amounts of second phase, as shown in Fig.9 and also to the probable growth stress.

IV. CONCLUSIONS

In conclusion, stoichiometric ferroelectric films of multi-axial (PZT), bi-axial (bismuth titanate) and uni-axial (lead germanate) nature were successfully prepared by pulsed excimer laser ablation of stoichiometric targets both at room and elevated substrate temperatures. The composition of the film was clearly dependent on the fluence in the low energy densities. Beyond a fluence of 2 J/cm², the

composition of the films showed no dependence on the ablation fluence. A correlation between the fluence, ablation pressure and substrate temperature has been established. In the absence of substrate temperatures, low energy and low ablation pressures seemed to offer stoichiometric films. However, in the case of elevated substrate temperatures, higher oxygen pressures for ablation were found necessary to accompany high energy densities, whereas lower energy densities (2 J/cm^2) needed only lower oxygen pressures. The intrinsic bombardment due to energetic ablated species seemed to play an important role in defining the composition of the perovskite phase as well as the grain structure.

The electrical characterization of polycrystalline PZT films indicated typical ε' of 900 and a $\tan\delta$ of 0.02. The ferroelectric properties indicated a P_r=35 μC/cm^2 and E_c=130-140 KV/cm. Similar characterization on *c*-axis preferred oriented polycrystalline bismuth titanate ($Bi_4Ti_3O_{12}$) films indicated a dielectric constant of 150, a P_r of 7 μC/cm^2 and a coercive field of 20 KV/cm. Lead germanate (Pb_5Ge_3O11) films oriented along *c*-axis (003) clearly exhibited a ferro-paraelectric phase transition at 175°C while the ferroelectricity at room temperature was observed in terms of remanent polarization of 2.5 μC/cm^2 at a coercive field of 55 kV/cm.

The overall observations made in our attempts of depositing multi-axial, bi-axial and uni-axial ferroelectric multi-component oxides, suggest that the excimer laser ablation is a viable growth technique to deposit *in-situ* stoichiometric thin films and close control over process conditions offer possibilities of tailoring the physical properties. With efforts extended to improving the uniformity of deposition over large areas, excimer laser ablation may be considered as a practical approach in developing usable ferroelectric thin films. A close process-structure-property correlation studies in a variety of ferroelectric compositions are in progress.

ACKNOWLEDGEMENTS

The authors gratefully acknowledge the financial support to DARPA grant #N00014-89-J-1976, Tetrad and Ben Franklin grants.

REFERENCES

1. M. Kojima, M. Sunagawa, H. Seto, Y. Matsui and Y. Hamakawa, Jpn. J. Appl. Phys., 22, Suppl.1, 255 (1982).
2. M. Okuyama and Y. Hamakawa, Ferroelectrics, 63, 243 (1985).
3. T. Kawaguchi, H. Adachi, K. Setsune, O. Yamazaki and K. Wasa, Appl. Opt., 23, 2187, (1984).
4. S. Y. Wu, Ferroelectrics, 11, 379 (1976).
5. C. A. Araujo, L. D. McMillan, B. M. Melnick, J. D. Cuchiaro and J. F. Scott, Ferroelectrics, 104, 241 (1990).
6. W. J. Takei, N. P. Formigoni and M. H. Francombe, J. Vac. Sc. Technol., 7, 442 (1969).
7. S. B. Krupanidhi, N. Maffei, M. Sayer and K. El-Assal, J. Appl. Phys., 54, 6601 (1983).
8. K. Iijima, Y. Tomita, R. Takayama and I. Ueda, J. Appl. Phys., 60, 361 (1986).
9. H. Adachi, T. Mitsuyu, O. Yamazaki and K. Wasa, J. Appl. Phys., 60, 736 (1986).
10. K. Sreenivas and M. Sayer, J. Appl. Phys., 64, 1484 (1988).
11. M. Matsubara, S. Miura, Y. Miyasaka and N. Sohata, J. Appl. Phys., 66, 5826 (1989).
12. R. N. Castellano and L. G. Feinstein, J. Appl. Phys., 50, 4406 (1979).
13. H. Hu, V. Kumar and S. B. Krupanidhi, Communicated to J. Appl. Phys., (1991).
14. M. Okuyama, Y. Togani and Y. Hamakawa, Appl. Surf. Sci., 33/34, 625 (1988).
15. R. W. Vest, Ferroelectrics, 102, 53 (1990).
16. M. Kojima, M. Okuyama, T. Nakagawa and Y. Hamakawa, Jpn. J. Appl. Phys., 22, Suppl.2, 14 (1983).
17. M. Okada, S. Takai, M. Amemiya and K. Tominaga, Jpn. J. Appl. Phys., 28, 1030 (1989).
18. K. D. Budd, S. K. Dey and D. A. Payne, Br. Ceram. Proc., 36, 107 (1985).

19. J. Fukushima, K, Kadaira and T. Matsushita, J. Mater. Sci., 19, 595 (1985).

20. G. Yi, Z. Wu and M. Sayer, J. Appl. Phys., 64, 2717 (1988).

21. D. A. Payne, Bull. Am. Phys. Soc., 34, 991 (1989).

22. S. K. Dey and R. Zuleeg, Ferroelectrics, 108, 37 (1990).

23. H. Buhay, S. Sinharoy, W. H. Kasner and M. H. Francombe, Proceedings of the International Symposium on Applications of Ferroelectrics, Urbana, IL, June 6-8, (1990) [IEEE Trans. Ultrason. Ferroelectr. Freq. Control (to be published)].

24. D. Roy, S. B. Krupanidhi and J. P. Dougherty, J. Appl. Phys., 69, 7932 (1991).

25. K. L. Saenger, R. A. Roy, K. F. Etzold and J. J. Cuomo, Materials Research Society Symp. Proc., 200 (1990).

26. T. Venkatesan, X. D. Wu, A. Inam, Y. Jeon, M. Croft, E. W. Chase, C. C. Chang, J. B. Wachtman, R. W. Odom, F. diBrozolo and C. A. Magee, Appl. Phys. Lett., 53, 1431 (1988).

27. A. Morimoto, S. Otsubo, T. Shimizu, T. Minamikawa, Y. Yonezawa, H Kidoh and T. Ogawa, Materials Research Soc. Symp. Proc., 200 (1990).

28. B. D. Cullity, Elements of X-ray Diffraction, 2nd Ed., Page 102, Addison-Wesley (1978).

29. M. E. Lines and A. M. Glass, Principles and Applications of ferroelectrics and Related Materials, (Oxford Univ. Press, 1977).

30. A. Mansingh and S. B. Krupanidhi, J. Appl. Phys., 52, 5274 (1981).

31. S.Y. Wu, J. Appl. Phys., 50, 4314 (1979).

32. H. Buhay, S. Sinharoy, W. K. Kasner, M. H. Francombe, D. R. Lampe, and E. Stepke, Appl. Phys. Lett., 58, 1470 (1991).

33. R. Ramesh, K. Luther, B. Wilkens, D. L. Hart, E. Wang, J. M. Tarascon, A. Inam, X. D. Wu, and T. Venkatesan, Appl. Phys. Lett., 57, 1505 (1990).

34. H. Iwasaki, S. Niyazawa, H. Koisumi, K. Sugii and N. Nizeki, J. Appl. Phys., 43, 4933 (1972).

35. A. Mansingh and S. B. Krupanidhi, J. Appl. Phys., 51, 5408(1980).

36. A. Mansingh and S. B. Krupanidhi, Thin Solid Films, 80, 359 (1981).

37. H. Schmitt, H. E. Mueser and R. Karthein, Ferroelectrics, 56, 141 (1984).

AD-P006 647

PROCESS DEPENDENT ELECTRICAL CHARACTERISTICS AND EQUIVALENT CIRCUIT MODEL OF SOL-GEL BASED PZT CAPACITORS

TAKASHI MIHARA, HITOSHI WATANABE, HIROYUKI YOSHIMORI
Olympus Optical Co., LTD. 2-3 Kuboyama-cho
Hachioji-shi, Tokyo 192, Japan

C.A. PAZ DE ARAUJO, BRAD MELNICK
University of Colorado at Colorado Springs

L. D. MCMILLAN
Symetrix Corp., 5055 Mark Dabling Blvd.
Colorado Springs CO 80918

Abstract Studies of electrical properties and an equivalent circuit model is developed for ferroelectric PZT(Ti=60%) thin film capacitors made by sol-gel spin coating with Pt electrodes. The equivalent circuit consists of two major parts: serial space charge capacitors demonstrating surface effects and parallel elements modeling the inner polycrystalline ferroelectric regions. This model is based on device physics which can demonstrate both the measured capacitance voltage characteristics and hysteresis curves. From the model fit to the data, an estimate of the space charge concentration at the surface and inner grain boundary region of $5x10^{20}$ cm^{-3} and $1x10^{18}$ cm^{-3} respectively is made. Further electrical characterizations such as pulse switching and polarization degradation (fatigue) have also been studied. Using the equivalent circuit, other characteristics such as the switching time can be studied showing its dependence on applied voltage and capacitor area. The applied voltage dependence of fatigue is shown via an empirical equation where the degradation rate is electric field activated.

92-16111

INTRODUCTION

Recently, research on solid state ferroelectric nonvolatile memories has intensified dramatically[1,2]. This level of activity has been aided by the search for properties such as nonvolatility, radiation hardness, fast switching time and so on. However, a serious obstacle to large scale production of ferroelectric memories is the limitation imposed by reliability shortcomings such as fatigue and unknown retention limit[3]. Systematic studies and measurement data are not widely available yet, but views of

the physical mechanisms which cause fatigue are available[4,5]. In order to improve degradation of retention and endurance, quantitative investigations are required using integrated device structures which posses familiar solid state effects such as surface states, space charge regions, domain pinning and domain motion control. These characterizations should be done in the same manner as with other semiconductor devices in the past. A first step may be to study device modeling or equivalent circuits of the thin film ferroelectric capacitors. These must be of great value for both circuit designers and the investigation of device physics. However, very few studies of an equivalent circuit have been proposed at this time[6,7]. Also, these models involve basic phenomenology due to the lack of qualitative and quantitative comparisons with measurement data. Presently, more refined device models are needed to explain thin-film devices in their integrated environment (e.g., parasitic devices, etc.) and effects not seen in bulk devices.

We have studied a realistic equivalent circuit model based on device physics including space charge effects. Since our model is directly connected with the concentration of space charge, we can compare it to real measurement data, such as capacitance voltage and hysteresis characteristics, and can estimate the electrical characteristics predicted by space charge effects. We have also investigated the basic electrical properties, such as switching and fatigue, in order to get some information for memory applications.

This paper consists of two parts. Part 1 describes the equivalent circuit study of our sol-gel derived thin-film ferroelectric capacitors. Part 2 summarizes switching and fatigue properties of PZT.

PART 1: EQUIVALENT CIRCUIT

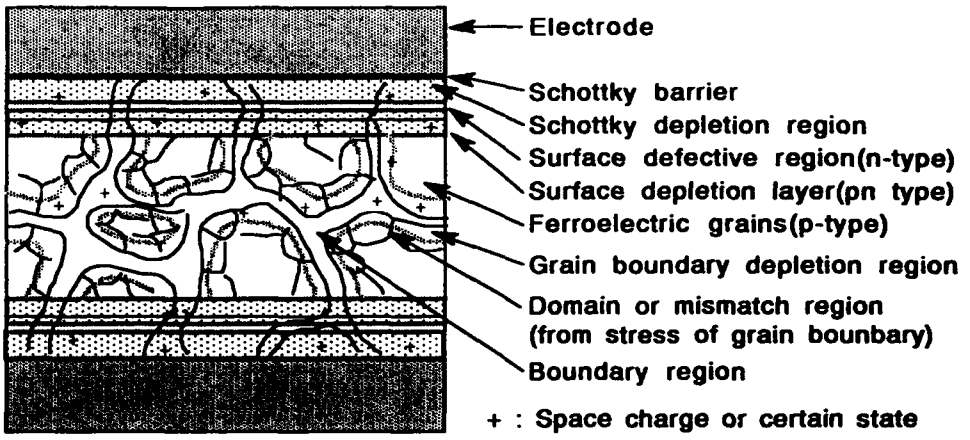
Basic Device Physics of Thin-Film Ferroelectric Capacitors

For a long time, researchers have considered that a ferroelectric material consisted of an ideal uniform polarization connected with a parallel linear

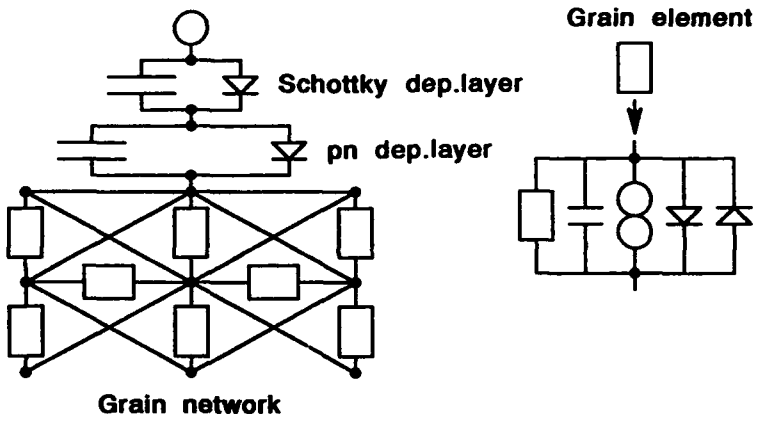
capacitor and a parallel high resistor. Several investigators considered this as a semiconductor with a large band gap and extremely low carrier mobility[8]. Recently, C.A. Paz de Araujo[6] proposed a three-capacitor serial model containing depletion capacitors, and also showed that the voltage dependence of capacitance was explained by a depletion capacitance with an index 3.0. Currently, the data show that a ferroelectric PZT thin film (made by sol-gel) contains such depletion layers. Specifically, in the case of thin film ferroelectric capacitors, it is now widely recognized that there are space charge regions at both of the surfaces facing the electrodes and at the interfaces between grain boundary regions.

Figure 1 shows the microstructure and a composite equivalent circuit network model of ferroelectric thin film. As schematically shown, the ferroelectric thin film consists of two major regions; the surface region and the internal microcrystalline region. Since the surface region is exposed to high temperature annealing, this area becomes a n-type semiconductor due to the lack of oxygen in which the excess oxygen vacancies have a shallow donor level, as recognized by Khanzig[10] and discussed in the defect chemistry literature[11,12]. The surface n-layer has been shown by several researchers using auger electron analysis which indicates a significant oxygen depletion region near the electrode region[13]. The internal region of capacitors consists of many microcrystalline grains, which are in fact internal surfaces with a high saturation of oxygen vacancies and probably a non-perovskite structure. Even if each grain forms a complete perovskite lattice, there still may be significant oxygen vacancies produced by PbO migration during annealing[11,12].

Taking into consideration this microstructure, a complex equivalent circuit network can be built as shown in Figure 1(b). The interface between the surface defective layer and the electrode is explained as a Schottky barrier. However, the interface between the surface layer (Schottky region) and the internal region which has a p-n junction like structure seems to be dominant. The internal microcrystalline region contains a set of circuit



(a) Micro structure in ferroelectric thin capacitors.



(b) The full network equivalent circuit model.

Figure-1. The microstructure and the realistic circuit model of ferroelectric thin film capacitors.

elements consisting of a resistor, a linear capacitance, an ideal polarization source and a depletion layer capacitor. However, this circuit model is too complex to analyze and make useful comparisons with the measurement data. Therefore, a simplified model is derived which can be justified in view of its remarkable agreement with measured parameters.

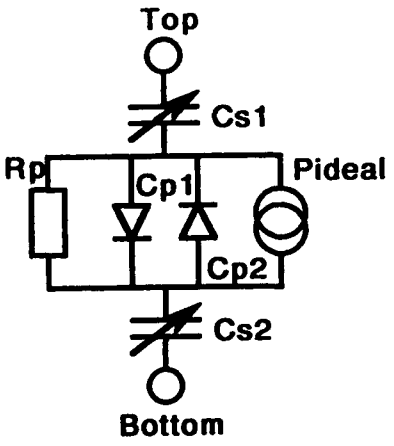
Simplified Equivalent Circuit

Figure 2 shows the simplified equivalent circuit model derived from the

complex model of Figure 1. All surface effects are compressed into two simple serial capacitors, each of which acts as a depletion capacitor whose capacitance have a specific applied voltage dependence (Cs1 and Cs2). The internal network is also compressed into one parallel circuit with four essential elements: an effective parallel resistance (Rp) including both the DC resistivity and dielectric loss, an upward parallel depletion capacitor (Cp1), a downward parallel depletion capacitor (Cp2), and an ideal polarization (Pideal) which acts as a voltage controlled current source. This source is only due to domain motion.

Electrical Characteristics of Each Elements

Each element should be explained in terms of device physics equations. These equations are written as follows:



Pideal	Ideal polarization
Rp	Resistance (Dielectric loss &R_{DC})
Cp1 Cp2	Upward parallel Downward parallel Depletion capacitors
Cs1 Cs2	Upward serial Downward serial Depletion capacitors

Figure-2. An equivalent circuit model adopted in this study.

(1) Ideal polarization

The ideal polarization source can be derived by the derivative of the Landau free energy description of a ferroelectric. In our case, this free energy does not include any contributions from space charge such as donors and acceptors which exist in actual devices because these are parasites shown

as the other elements in the circuit. Translating the standard form of the Landau electric field (i.e., the first derivative of the free energy) to a voltage-to-charge relationship, yields

$$V = k1^{*}Q + k2^{*}Q^{3} + k3^{*}Q^{5} \tag{1}$$

Where V and Q are applied voltage and accumulated charge respectively (V=Ed and Q=PA), k_1, k_2 and k_3 are all fitting parameters proportional to the standard α, β, and γ of the Landau energy.

(2) Resistance

The parallel resistor consists of two parts. A DC resistance and an AC resistance which is caused by dielectric loss induced by the energy dispersion of electronic dipoles. This can be written as

$$Rp = \frac{1}{Cp^{*}D^{*}2\pi^{*}f} + Rdc \tag{2}$$

Where D is the dielectric loss tangent factor, Cp is the equivalent parallel capacitor, f is the frequency of the applied signal and R_{dc} is DC resistance. This DC resistance is estimated by the DC leakage current over the range of applied voltage. It is very hard to show both the dielectric constant (of Cp) and R_{dc} because many effects due to the microstructure (such as interface effects[14] and grain boundary[15] effects), affect these measurements. Because the resistance is extremely large in a well built device, its effect is merely a phase shift (when the sinusoidal input is used in a Sawyer-Tower circuit) which causes a small broadening of the hysteresis curve.

(3) Depletion capacitors

All depletion capacitors act as very important elements in our study because their capacitance strongly depends on the applied voltage and controls the shape of the hysteresis loop. A standard space-charge capacitance of an abrupt junction is used.

$$Cp = \left(\frac{e_s e_o}{qN_b}\right)^{1/2} (V_{bi} \pm V)^{-(1/n)} \qquad (3)$$

Where, ϵ_s is the dielectric constant of the space charge layer, ϵ_o is the permeability of freespace, q is the unit charge, N_b is the space charge concentration, V_{bi} is the built-in potential, V is the applied voltage and n is the ideality factor determined by the space charge profile if n = 2, this is the expression of the capacitance of an abrupt p-n junction or a Schottky barrier with constant space charge concentration. In this study, it is assumed that the dependence of the space charge concentration is as shown in equation (3), because n is not expected to be ideal.

Calculation Method

The detailed calculations are eliminated from this paper due to a restriction of the number of pages. In general, a computer program calculates both the charge and voltage on each element simultaneously. In the case of the parallel circuit, the total charge of the system is the sum of the charge of each capacitor and the total applied voltage is the same across each one. In the case of the serial circuit, the voltage of the circuit from end to end is the sum of the voltage forced on each element and the charge of each elements is kept constant.

Comparison with Capacitance Voltage Characteristics

Before the comparison with the measured CV curve, the method of measurement should be discussed in order to eliminate ambiguity caused by the composite applied signal of the CV measurement itself.

An example of a CV curve from a typical sample is shown in Figure 3. Typically this is measured using an LCR meter with 10KHz frequency and a 50 mV superimposed sinusoidal signal. The sample is a thin film ferroelectric PZT capacitor made by a sol-gel spin coating method which is described elsewhere[16]. Figure 3 shows both the positive (solid line) and

negative (dashed line) sweep direction applied on the top electrode of an initially unpolled film (see extra line in the positive quadrant).

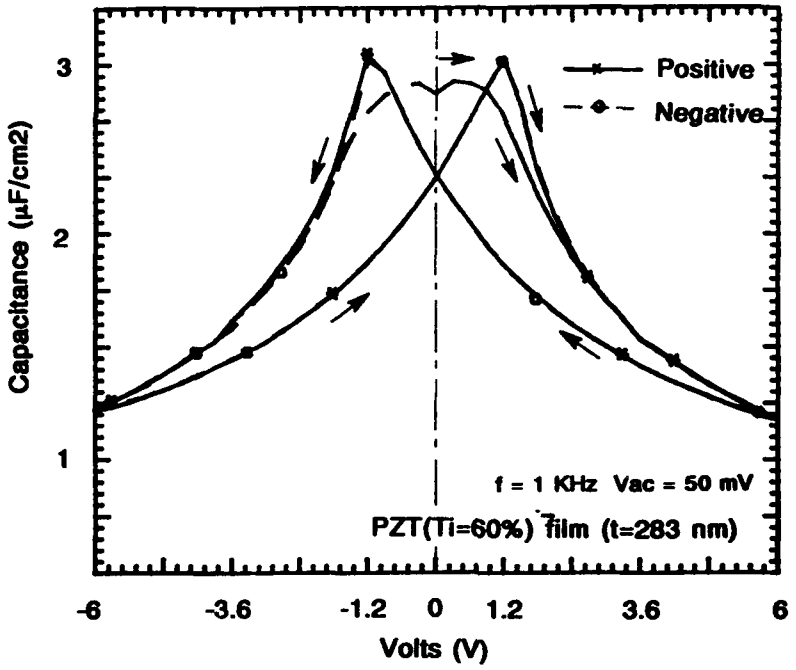


Figure-3. The CV characteristic of a ferroelectric PZT thin film capacitor.

Since the CV curves contain too much information to compare with the calculated results, we must decompose the CV data into the several parts which the equivalent circuit models consist of. Initially, it is possible to eliminate the serial surface capacitors of well saturated samples, because their capacitance must be very large in comparison with the capacitance of the internal region.

Therefore the total capacitance is the sum of each parallel element. Figure 4 shows the decomposed CV curves from Figure 3 using the parallel circuit model. The depletion capacitance in the second column is extracted as capacitance with a polarization in the same direction as the applied voltage. The capacitance due to polarization is the capacitance with a

polarization opposite to the direction of the applied voltage. The unpolled (virgin) state is the capacitance with randomly orientated state. The polarization induced capacitance may be caused by many factors such as a response to domain motion, a fraction of ionic polarization as well as space charge or some defects. However, the space charge (depletion) capacitance, can be compared with the calculated capacitance directly.

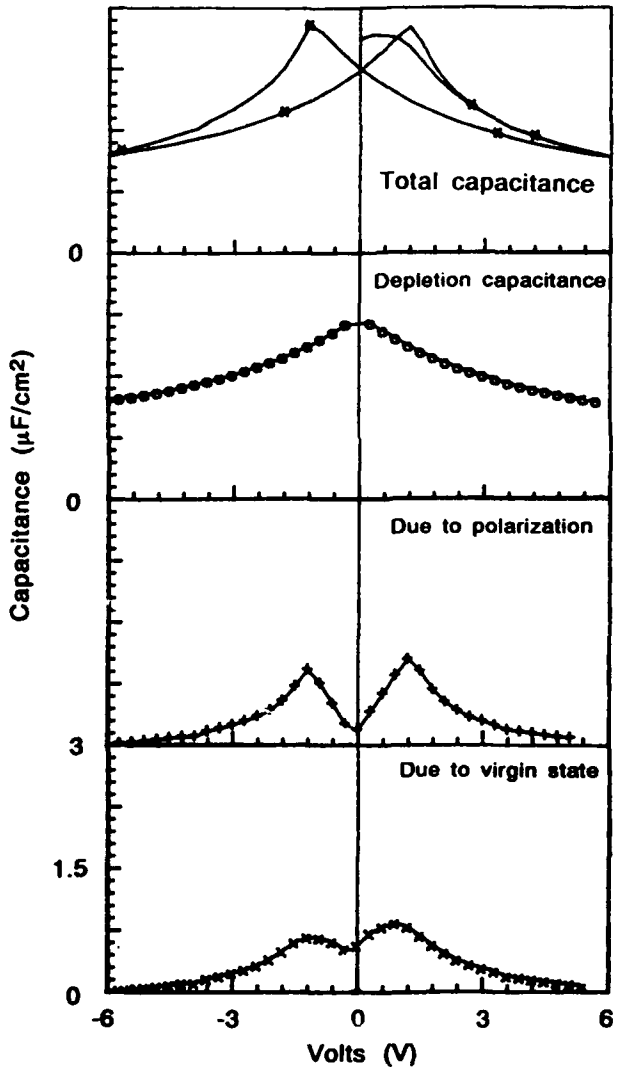


Figure-4. Extracted parallel components of a CV curve of a ferroelectric capacitor.

Figure 5 shows the comparison of measured CV data along with three calculated results which are obtained by the different models explained by (a) only an ideal polarization, (b) an ideal polarization with a parallel linear capacitor and (c) the model (an ideal polarization with parallel depletion capacitors) developed in this paper. In all cases, the zero bias dielectric constant is the dielectric constant of the parallel linear capacitor. Only the result of the model with parallel depletion capacitors can satisfy the measured data with accuracy both in the value of the capacitance and its dependence to applied voltage. The fitting parameters for PZT are the space charge concentration [N_b in equation (2)], which is about $5x10^{17}$ cm^{-3}, and the index n in equation (3), which is about 3.0. This value of the index n is exactly the same as derived before[9].

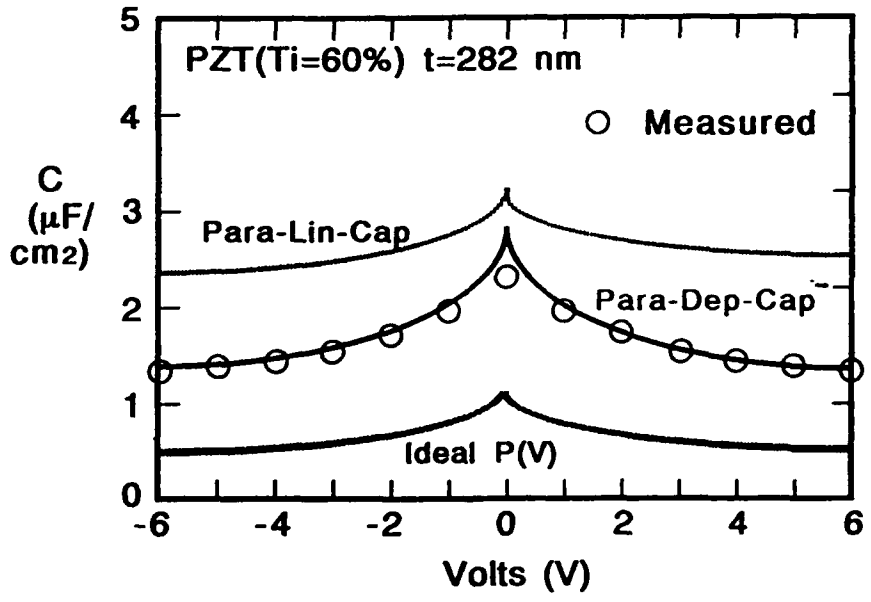


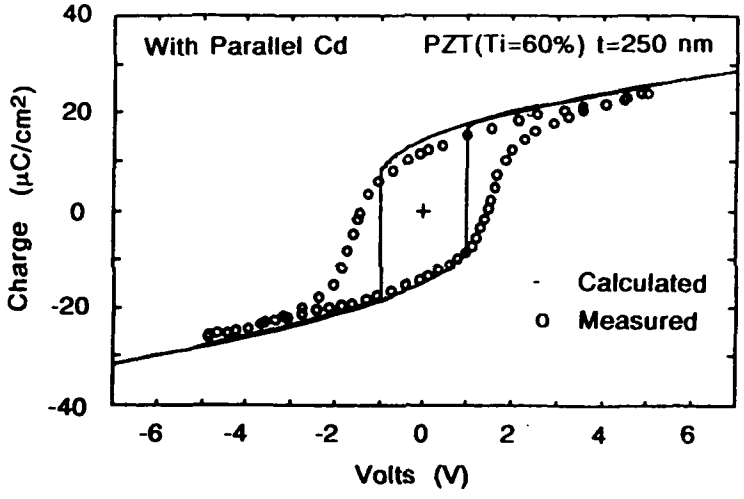
Figure-5. Calculated CV characteristics as compared with a measured data.

Comparison with Measured Hysteresis Curves

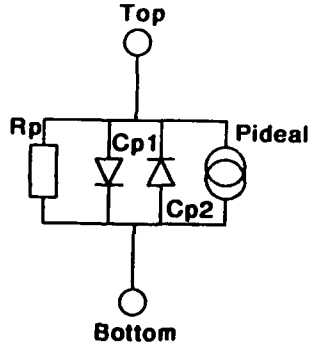
Figures 6 & 7 show the comparison with a measured hysteresis curves.

The hysteresis curves are obtained by a conventional Sawyer-Tower circuit at room temperature. The applied voltage is a sine wave with a standard frequency of 1KHz. This measuring frequency is not significant because the shape of hysteresis curves for PZT, over a wide frequency range of 100Hz up to 100KHz, are almost the same. The parallel circuit shown in Figure 6 is used to illustrate that the serial space charge capacitances on the surface are still needed to complete the fit. And contrary to other researchers, linear capacitors in any place in the equivalent circuit are insufficient to show the loss of squareness typical in thin-film devices.

Equivalent circuit Modeling



(a) Comparison with measured hysteresis curve.



Device parameters			
Ideal polarization & Rp			
k1	-2	Pr	16 μC
k2	0	D	0.02
k3	3		
Cp1,Cp2			
Nb1	8E 17		
Nb2	15E 17		
Vbi	0.8		
n	3		
e	600		

(b) Device parameters of circuit model.

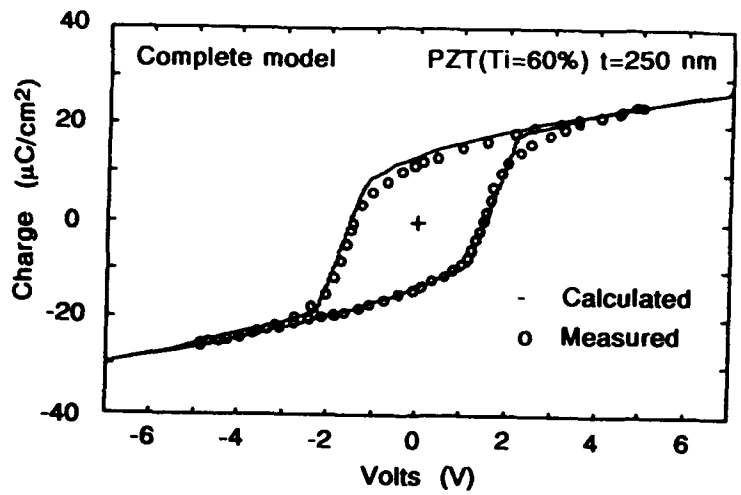
Figure-6. The calculated hysteresis curves using a parallel depletion capacitor model compared with measured data.

Figure 7, which adds the surface capacitances shows a remarkable fit to the data. Using this model, especially due to the effects of both the serial and parallel depletion capacitors, it is possible to fit not only the whole shape of the hysteresis curve, but also the space-charge effects on the hysteresis. Furthermore, the broadening of the hysteresis curve and increase in the coercive voltage is induced by the surface depletion layer. The shape of the hysteresis shoulder around zero bias is brought about by the inner depletion region around the grain boundaries. Finally, the fitting parameters of a typical hysteresis for PZT are estimated as follows: the space charge concentration at surface is about $5x10^{20}$ cm^{-3} and near the grain boundaries is about $1x10^{18}$ cm^{-3} as shown in these figures. Since we assumed the dielectric constant to be an average value of over the film, these values should be considered a rough estimated.

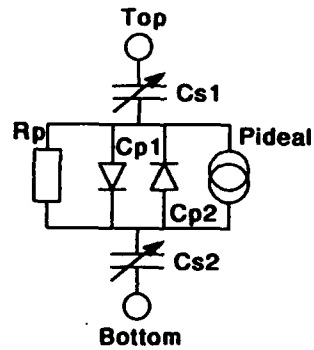
The Space Charge Dependence of Hysteresis Curve

As a final discussion to part one, we show two important calculated results which can provide some useful understanding of the effects of space charge. Figure 8 shows the surface space charge concentration dependence of the calculated hysteresis curve. The surface in our model shows a large amount of electrons (n+), therefore this has a small impact in the hysteresis because the width of the depletion layer becomes very small and the capacitance extremely large. This is expected because the high concentration of oxygen vacancies are fully ionized and a large number of electrons are emitted to the conduction band. In any case, large capacitances at the surface yields a square hysteresis loop. Figure 9 shows the internal space charge concentration dependence of a calculated hysteresis loop. In the case of internal depletion capacitance, since the amount of space charge around the grain boundary directly affects the total capacitance. The shoulder of the hysteresis and the apparent dielectric constant (the linear part of the curve) is greatly influenced by this parameter. This further elucidates the impact of the microstructure on the dielectric properties of these devices.

Equivalent circuit Modeling



(a) Comparison with measured hysteresis curve.



Device parameters			
Ideal polarization & Rp			
k1	-2	Pr	16 μC
k2	0	D	0.02
k3	3		
Cp1,Cp2		Cs1,Cs2	
Nb1	8E 17	Nb1	5E 20
Nb2	15E 17	Nb2	5E 20
Vbi	0.8	Vbi	0.8
n	3	n	3
e	600	e	600

(b) Device parameters of circuit model.

Figure-7. The calculated hysteresis curve using the complete model compared with measured data.

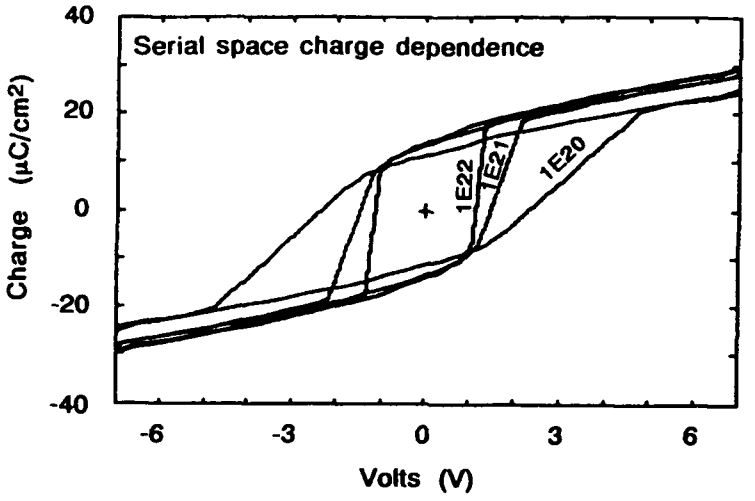


Figure-8. The surface space charge concentration dependence of the calculated hysteresis curve.

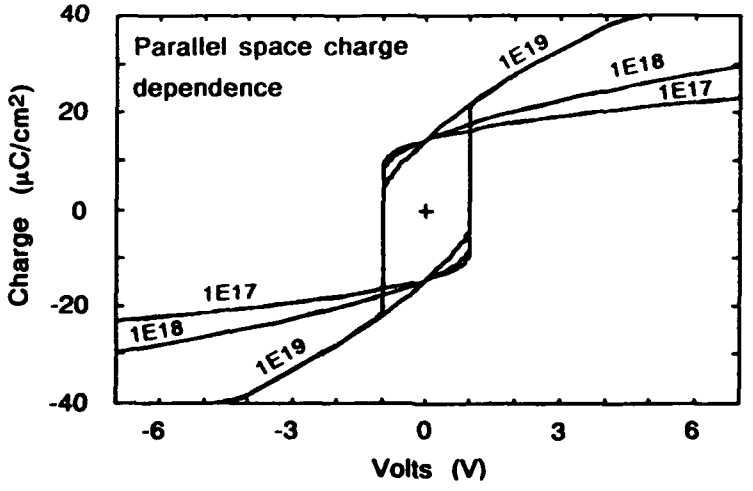


Figure-9. The internal space charge concentration dependence of the calculated hysteresis curve.

PART 2: SWITCHING AND FATIGUE IN PZT

Pulses Switching Characterization

The switching kinetics theory in ferroelectric devices have been studied successfully by the application of the earlier theory of Avrami to specific ferroelectrics[17]. Recently these theories have been applied to several ferroelectric thin films[18,19]. The shape of the switching response can be well explained by this theory. However, in spite of these efforts, in the view point of application to circuits, this theory is sometimes too complicated to be used in circuit analysis. On the other hand, very fast switching times of less than 5 nanoseconds have been observed on thin (60 nm) and small (150 μm^2) area PZT capacitors[20]. Because of such high switching speeds, the fine details of nucleation and domain growth may be ignored. Therefore, a simple characterization of switching using Merz[21] equation is sufficient for a first order circuit model. A modified version of Merz[21] equation is

$$t_s = \frac{Q_{nl} R_l A_f}{V - V_c - V_{out}} + t_R \qquad (4)$$

Where Q_{nl} is the total switching charge, R_l is the load resistance, A_f is the area of the capacitor, V_c is the coercive voltage, V_{out} is the output voltage measured across a 50 ohms series load resistor, t_r is specific raise time of input pulse which is determined by the output impedance of pulse generator used.

Figure 10 shows an example of pulse switching response of a 10x10 μm^2 PZT thin film capacitor. The definition of switching time in our evaluation is the time required to transfer 90% of the charge from the ferroelectric capacitor through the load resistance. The switching time of this sample is estimated to be 24 nanoseconds which is almost the same as the rise time of the input pulse (25 nanoseconds). Therefore, the ultimate switching time under a virtual zero rise time input signal is

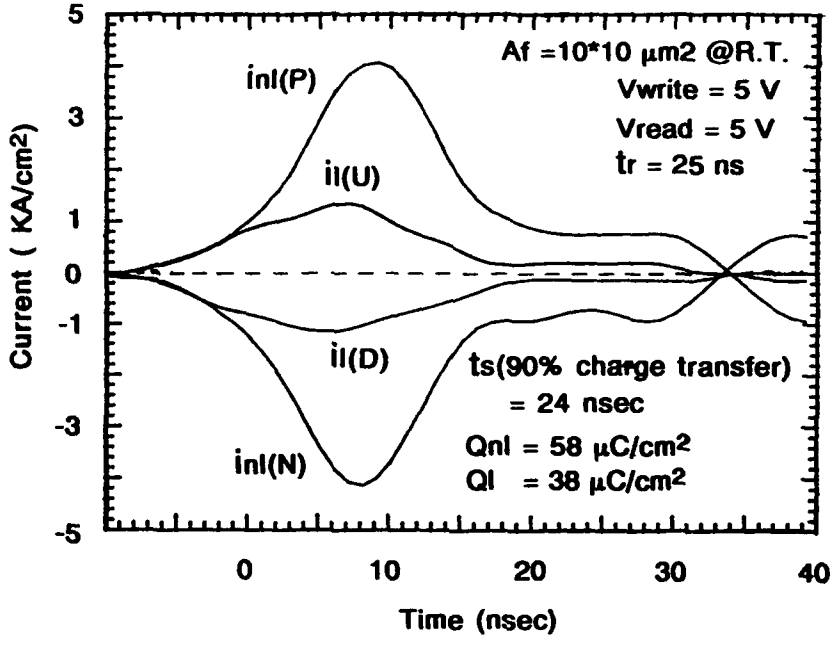


Figure-10. The switching curves on a 10x10 μ^2 capacitor.

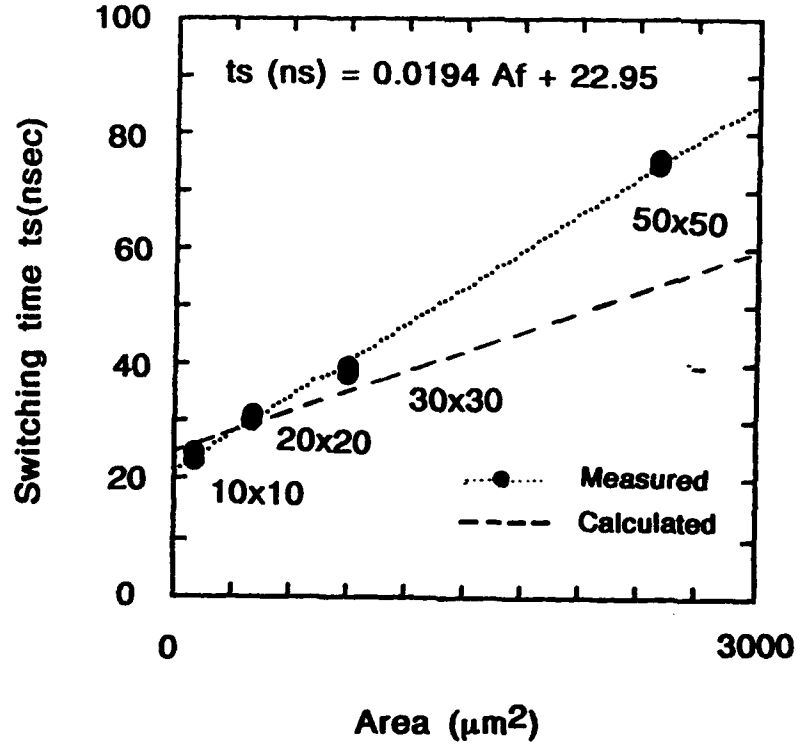


Figure-11. Area dependence of measured switching time compared with Merz[21] model.

expected to be of sub nanosecond value. Figure 11 shows the area dependence of switching time based on equation (4).

The discrepancy between the measured and calculated results is attributed to the rise time. Using these results, it can be estimated that the intrinsic switching time of a smaller capacitor of 2x2 μm^2 is expected to be less than 0.1 nanoseconds. Figure 12 shows the applied voltage dependence of switching times with calculated result. The agreement between the measurement and the theory is quite good. The switching times saturate at a voltage beyond 4 volts (for PZT).

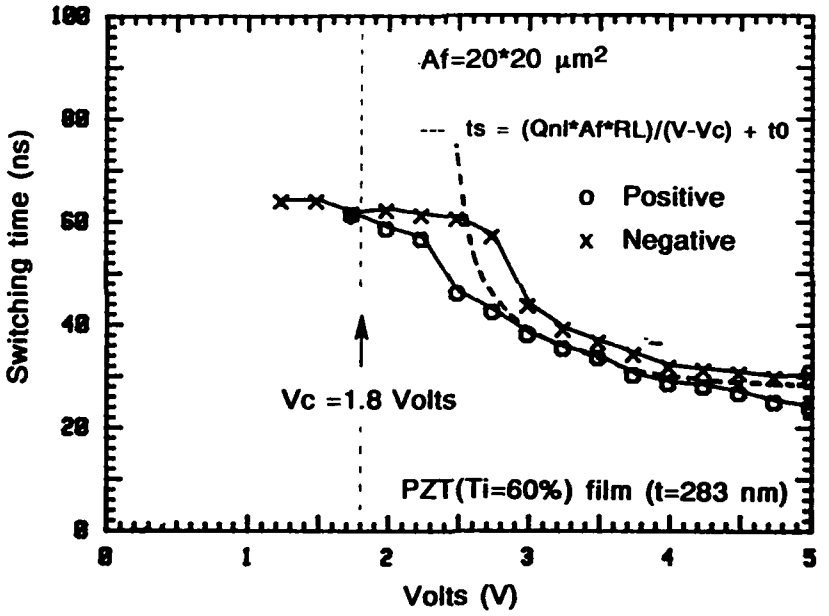


Figure-12. The pulse height dependence of measured switching times as compared with Merz[21] model.

The Degradation of Remanent Polarization by Fatigue

The purpose of this study is to empirically determine the device degradation known as fatigue. Hysteresis curves are measured after each fatigue step at which a continuous bipolar pulse train is forced into a device loaded with a 50 ohm resistor in series, instead of conventional pulse measuring[4,21]. The frequency of each fatigue cycle is 1MHz with 50% duty cycle. The reason this method was adopted in this study is that a hysteresis curve

includes useful information to study the degradation mechanism. Applied voltages and fields during the fatigue cycles are 6 volts, or an equivalent field of 212 KV/cm. Figure 13 shows the hysteresis curves after each fatigue step up to $1x10^9$ cycles along with the initial state. Each state of degradation is shown clearly in the hysteresis shape by this measurement. Figure 14 shows the shape parameters of hysteresis versus fatigue cycles on a semi-logarithmic plot. Where P_r and P_s are the remanent polarization and saturated polarization respectively. The notation (+) and (-) show positive and negative polarization direction with respect to the applied signal. Although all parameters have a logarithmic dependence, because the difference between P_r and P_s is almost constant, all major change occurs mostly to the remanent polarization. Based on the model presented in Section 1, this indicates that the active area which controls device behavior occurs near the surface regions and not in the internal region as other researchers have described[4,14].

Useful empirical equations can be derived form this fatigue data. Figure 15 shows the cycle dependence of the switching charge (equivalent to Pr(+)-Pr(-)) under several applied voltages. As expected, the degree of degradation has a significant dependence on the applied voltage. This means that the screening due to the n+ region is very significant. This also translates into a voltage dependent broadening of the depletion region into the p-type body of the device. Figure 16 shows the applied voltage dependence of the 50% degradation point, of N(50) cycle. This is the point where the remanent polarization declines to 50% of initial state. N(50) is proportional to the reciprocal of the applied voltage. Such a behavior is similar to hot electron effects in silicon field effect transistors. Using a least square approximation to this data, a useful equation which predicts the 50% point as a function of the applied voltage can be found. Thus,

$$N\,(50) = Exp\,(43.58/V_f + 11.58) \qquad (5)$$

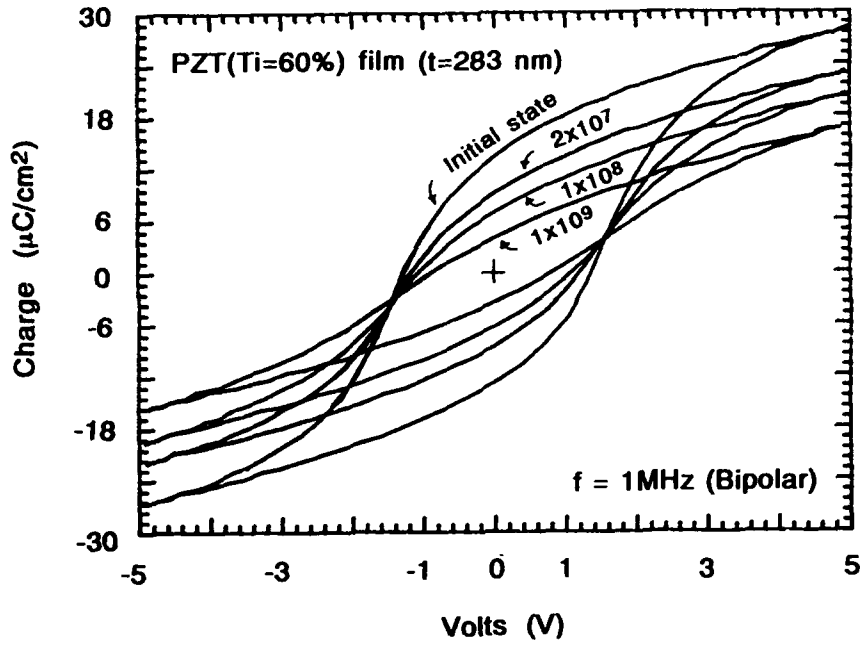


Figure-13. Hysteresis curves after each fatigue step (10^7-10^9) for PZT.

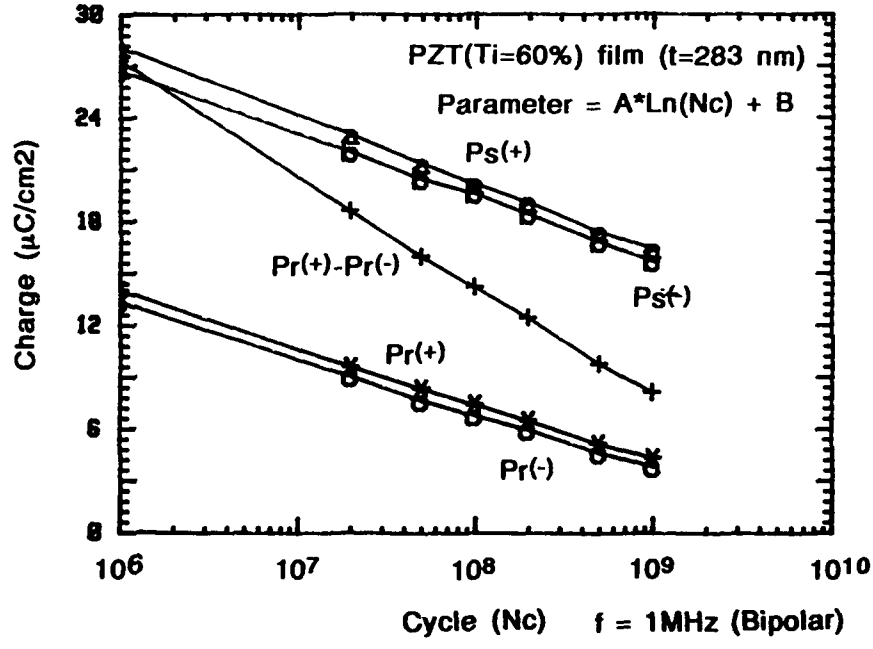


Figure-14. The cycle dependence of several hysteresis parameters.

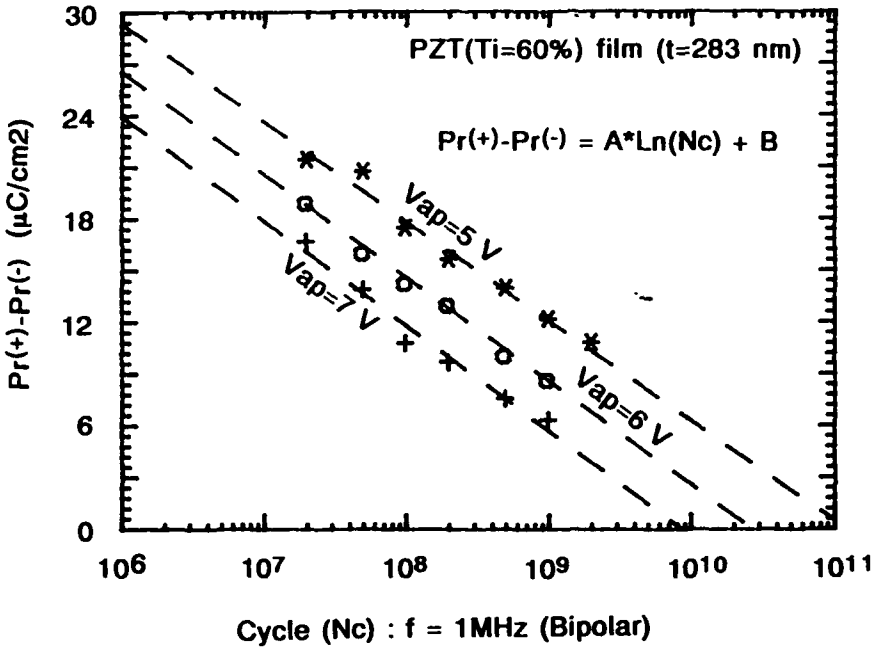


Figure-15. The cycle dependence of 2Pr (Equivalent switching charge).

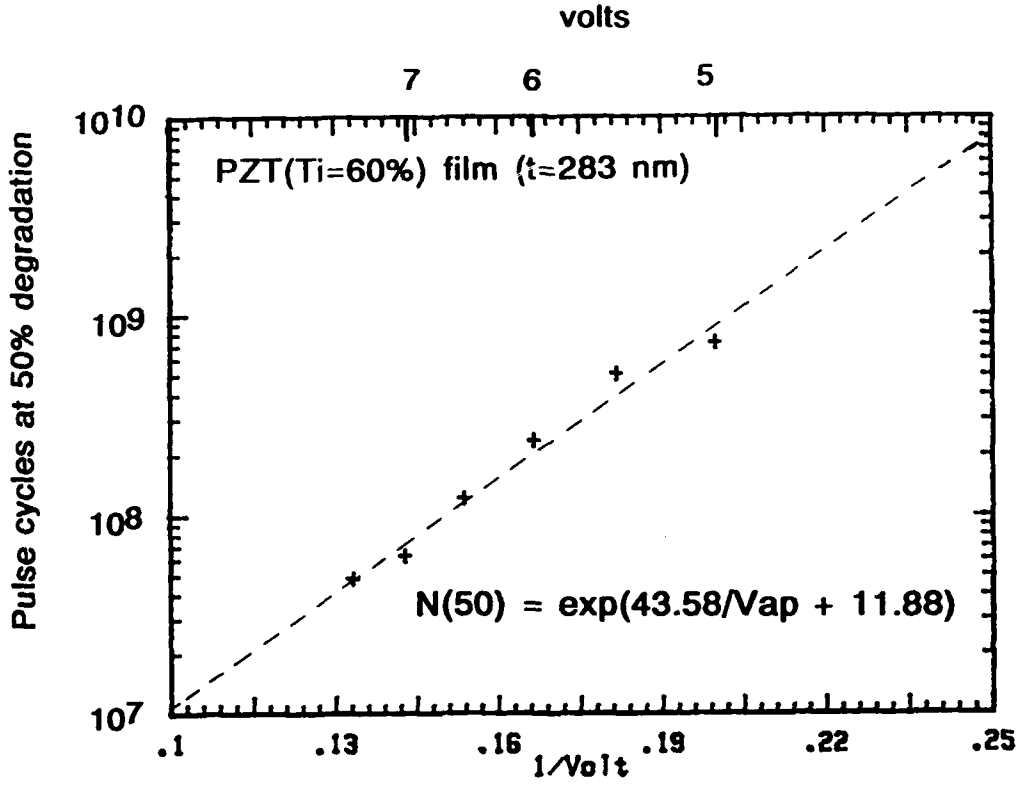


Figure-16. Applied voltage dependence of specific cycles at 50% degradation of 2Pr (Equivalent switching charge).

According to this equation, if 5.5 volts is the maximum applied voltage (TTL + 10%) N(5O) can be estimated to be $4x10^8$ cycles. On the other hand if it is required, N(5O) of up to $1x10^{11}$ cycles, the applied voltage should be designed below 3.24 volts. As a more general equation, the following empirical relation representing remanent polarization is introduced:

$$2Pr = (4.27/V_f - 3.34)\ Log\,(Nc) + 22.51/V_f + 59.21 \qquad (6)$$

Where 2Pr means Pr(+) - Pr(-). This equation contains both the number of cycles and the applied voltage. This equation is required to design the memory support analogue circuitry such as the sense amplifier. In the view point of device physics, this kind of equation is the indispensable first step for studying this degradation mechanism. Araujo, et al.[22], has proposed tow state-cluster models which derives equation 6 from first principal.

SUMMARY AND CONCLUSIONS

A study of the electrical characterization and an equivalent circuit model are described for integrated thin-film capacitors of ferroelectric PZT(Ti = 60%) for thickness circa 300 nm made via the sol-gel spin coating method using Pt electrodes. Several key results can be summarized as follows:

(1) An equivalent circuit model which consisted of space-charge capacitors comprising the surface effects and several parallel elements explaining the inner polycrystalline (grain induced) ferroelectric film behavior are studied. This model achieved remarkable accuracy in representing the measured capacitance voltage characteristics and hysteresis curves.

(2) The estimated space charge density at the surface and inner grain boundary regions of our capacitors are about $5x10^{20}$ cm^{-3} and $1x10^{18}$ cm^{-3} respectively, both control the lack of squareness of the hysteresis curve.

(3) A prediction of sub-nanosecond switching speeds with reasonable TTL compatible voltages without dielectric breakdown shows an intrinsic switching time of 0.1 nanoseconds in PZT.

(4) An empirical model of fatigue degradation shows that sol-gel PZT has a 50% charge loss of $4x10^8$ cycles (1MHz pulses) when 5.5 V (TL + 10%) is applied. A V^{-1} voltage dependence is also clearly determined by the measurements. A complete charge vs log(t) equation (including voltage dependence) is also determined.

Finally, there is strong evidence that the locus of degradation is the surface. This is clearly shown by the voltage dependence of P_r and E_c - both susceptible to the surface screening effect induced by electron emission into the conduction band via the shallow donor sites caused by oxygen vacancies.

REFERENCES

1. J.F. Scott, C.A. Paz de Araujo and L.D. McMillan Ultrasonic Symposium, 299 (1989)
2. J.F. Scott and C.A. Paz de Araujo Science, 246,1400 (1989)
3. J.T. Evans, J.M.D. Levey and J.A. Bullington, Proc of CMC89, 218, (1989)
4. H.M. Duker, P.D. Beal, J.F. Scott, C.A. Paz de Araujo, B.M. Melnick, J.D. Cuchiaro and L.D. McMillan, Applied Physics, 11, 5783 (1990)
5. D.M. Smyth, Ferroelectrics, 116,117 (1991)
6. C.A. Paz de Araujo, NVMTR, Session 3 (1989)
7. A.K. Kulkarni, G.A. Rohrer, S. Narayan, L.D. McMillan, Ferroelectrics, 116, 95 (1991)
8. V.M.Fridkin, Ferroelectric Semiconductors. (1974), Translated from Russian (1980) Consultants Bureau, New York and London
9. C.A. Paz de Araujo, (private communication) circa 1959
10. W. Kanzig, Phys. Rev., 98, 549 (1955)
11. L.L. Hench and J.K. West, Principles of Electric Ceramics, John Willy and Sons 165, (1990)
12. D.M. Smyth, Ferroelectrics, 116,117, (1991)
13. L.E. Sanches, D.T. Dion, S.Y. Wu, and I.K. Naik, Ferroelectrics, 116,1, (1991)
14. J.F. Scott, C.A. Paz de Araujo, B.M. Melnick, L.D. McMillan and R. Zuleeg (this symposium proceeding)
15. D.Y. Wang and K. Umeya J.Am.Ceram.Soc, 73,1574,(1990)
16. B.M. Melnick, J.D. Cuchiaro, L.D. McMillan, C.A. Paz de Araujo and J.F. Scott, Ferroelectrics, 109, (1990)
17. Y. Ishibashi and Y. Takagi, J.Phys.Soc. Jpn, 31, 506 (1971)

18. K. Dimmler, M. Parris, D. Butler, S. Eaton, B. Pouligny, J.F. Scott and Y. Ishibashi, J.Appl.Phys, 61, 5467 (1987)
19. J.F. Scott, L. Kammerdiner, M. Parris, S. Traynor, V. Ottenbacher, A. Schwabkeh and W.F. Oliver, J.Appl.Phys, 64, 787 (1988)
20. B.P. Maderic, L.E. Sanches and Y. Wu, Ferroelectrics, 116, 65 (1991)
21. W.J. Merz, J.Appl.Phys, 27, 938 (1956)
22. C.A. Paz de Araujo (this symposium proceeding)

AD-P006 648

DEVICE EFFECTS OF VARIOUS Zr/Ti RATIOS OF PZT THIN-FILMS PREPARED BY SOL-GEL METHOD

H. WATANABE, T. MIHARA
Olympus Optical Co Ltd., Hachioji, Tokyo, 192 Japan

C. A. PAZ DE ARAUJO
Microelectronics Research Laboratiries
University of Colorado at Colorado Springs

Abstract PZT, $PbZr_xTi_{1-x}03$, thin-films with various Zr/Ti ratios, 100/0 (lead zirconate) to 0/100 (lead titanate), were prepared by the sol-gel method. Basic electric properties, dielectric constant, tan σ, P-E hysteresis curve, switching properties were measured respectively as a function of composition. Dielectric constant indicated a specific peak value (~1100) around the morphotropic phase boundary between tetragonal and rhombohedral phase. Satisfactory low-voltage saturated hysteresis curves were observed for the compositions of PZT(90/10) through PZT(20/80). The remanent polarization and the coercive field increased as the titanium content decreased. The result of X-ray measurement showed that the lattice constants of thin-Film PZT are different from bulk ceramics for compatible compositionS. The boundary, on which the c/a ratio must be 1 (rhombohedral phase), was slightly shifted to $PbTiO_3$ side. This distortion in crystal structure is considered to be due to the thin-film effect, which the lattice mismatch between the platinum substrate and the PZT layer, restricted the ions to position into proper cites.

INTRODUCTION

Ferroelectric thin-films consisting of a perovskite structure, such as PZT, are currently being investigated as high potential materials for micro-device applications such as non-volatile random access memory[1,2], infrared detectors, surface acoustic wave devices and other optoelectronic devices.

For each of device application there is a need to ahve a corresponding variations of PZT compositions. However, there has not been many reports dealing with such a detail composition study[3-5].

Many preparation techniques for PZT thin-films have been reporteo,

92-16112

such as electron beam deposition, rf sputtering, ion beam sputtering, laser ablation, metallorganic compound thermal decomposition (MOD)[6], sol-gel[7-12] and MOCVD. Although these techniques have merits and limitations, sol-gel process has the advantage of easy control of composition and homogeneity.

In this paper, we studied electrical properties of PZT thin-film with various Zr/Ti ratios, which should be the basic information required for the many applications using the sol-gel preparation method.

EXPERIMENTAL PROCEDURE

Substrate preparation involved dc-magnetron sputter deposition of 200Å titanium layer, as an adhesive layer, and following 2,000Å platinum bottom electrode onto 5000Å silicon dioxide on (100) silicon wafer, as shown in Figure 1.

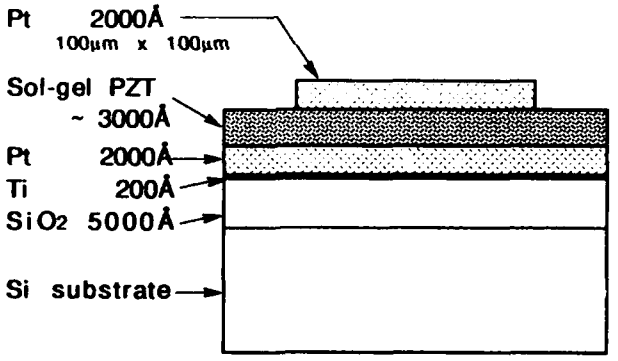


Figure 1 Device structure

Figure 2 shows preparation process for various compositions for sol-gel PZT thin films. Lead zirconate solution and lead titanate solution were prepared respectively by a conventional sol-gel method. Then, two solutions were mixed together into each ratio. The mixed solutions were hydrolized with proper amount of water and acidic solution and spun onto platinum metallized silicon substrates. Film thickness was about 3,000Å

consisting of multi-layer structure controlled by the molarity of the coating solution and spinning speed. The coated films were dried on a hot plate to remove the solvent and annealed in an electric furnace at 600 - 750°C for 1 hour in 100% oxygen ambient. Then, a platinum top electrode, with thickness of 2,000Å was deposited. Capacitors with 100 μm x 100 μm of area were patterned by ion beam etching.

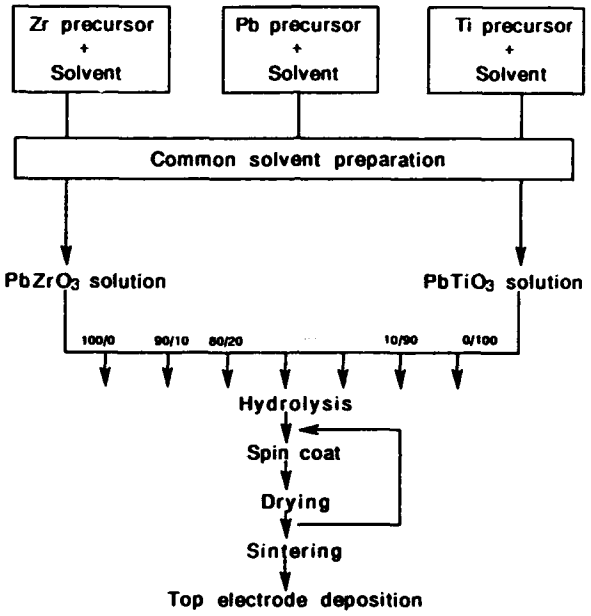


Figure 2 Sol-gel film preparation process

RESULTS

Microstructures

Crystallinity of prepared PZT films was measured by X-ray diffractometer. Figure 3 shows typical diffraction patterns of various composition of PZT thin-films, (a)PZT(O/100), (b)PZT(20/80), (c)PZT(50/50) and (d)PZT(90/10). It is well known that [111] is a preferred orientation of platinum layer deposited onto silicon dioxide. Our sol-gel PZT thin films showed polycrystalline phase on such [111] orientated platinum substrate.

Measured lattice constants of sol-gel PZT thin films were slightly different from bulk ceramics for compatible composition.

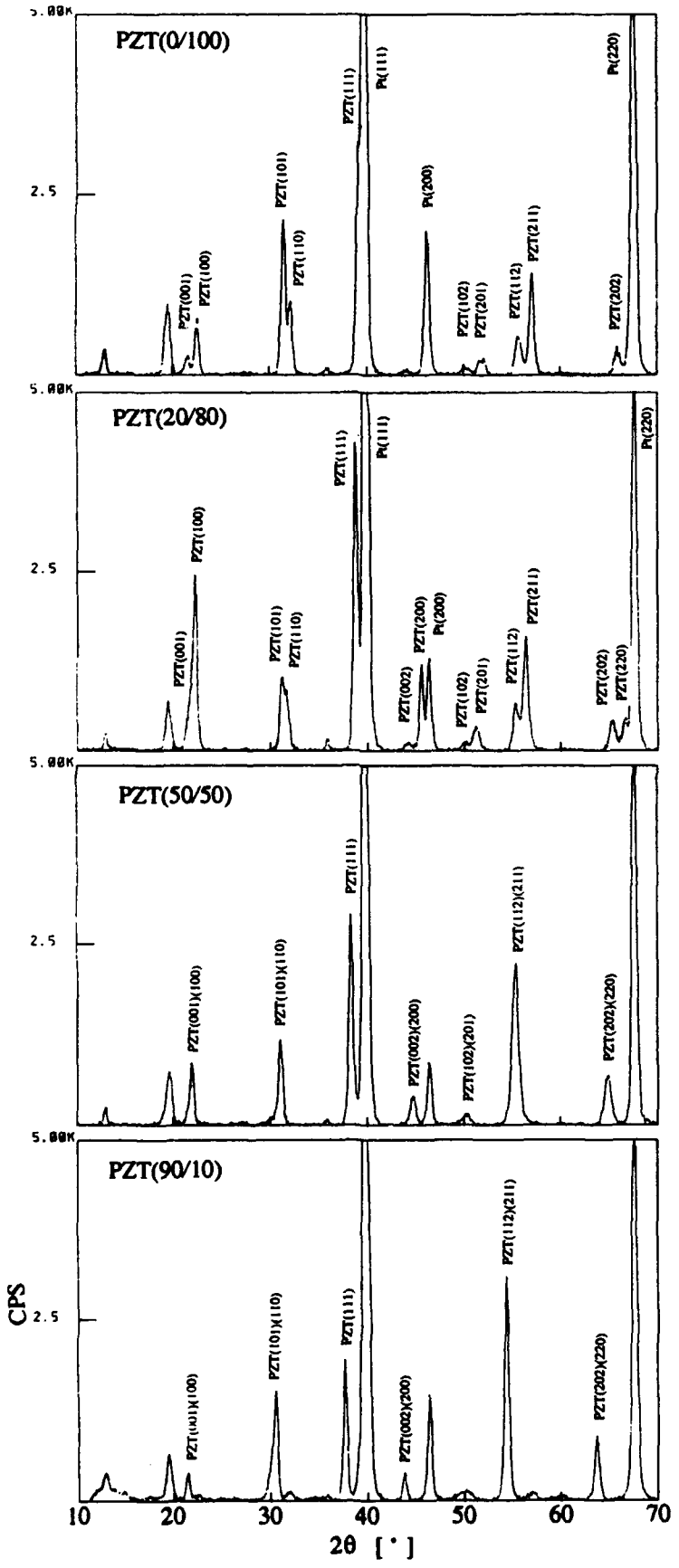


Figure 3 X-ray diffraction pattern of sol-gel PZT thin film on Pt/SiO_2/Si substrate

In Figure 4, the lattice constant of thin films are compared with bulk data[13]. The boundary between tetragonal and rhombohedral phase, on which the c/a ratio must be 1, was shifted to $PbTiO_3$ side. This distortion in PZT crystal structure is considered to be due to the thin-film effect[4], which seems to be caused by the lattice mismatch and/or thermal expansion coefficient between the platinum substrate and the PZT layer, restricting the ions to position into improper sites. In our results, this deviation in lattice parameters was larger than that reported by Tohge et al.[4] This fact indicates that relatively large mechanical stress remains in our thin films. However, there was no sign of the large stress in apparent voltage shift or asymmetrical shape of hysteresis curves. Even after long post anneals to reduce stress, our sol-gel films did not change their lattice parameters and electrical properties. Also, ICP quantitative analysis showed no composition differences between the thin films and stock solutions used in this work.

Electrical Properties

Dielectric constant (ϵ) and tan δ were measured on our PZT capacitors using an HP-4275A LCR meter. Figure 5 shows dielectric constant and tan δ for each composition at 10kHz, 100kHz and 1 MHz. The dielectric constant curve has a peak at the morphotropic phase boundary (MPB). The peak value is above 1,000. It is larger than that of bulk PZT, which usually shows 600 to 800[14] values of the dielectric constant at room temperature. The same tendency of the dielectric constant of rf-sputtered PZT thin films was reported by Ueda et al.[3] The frequency dependence of dielectric constant of each composition is shown in Figure 6. From 10 kHz to 2 MHz, all films showed constant values of ϵ.

The temperature dependence of the dielectric constant for each Zr/Ti ratio is shown in Figure 7 from room temperature to 300°C. At any temperature, the fitting curves shows a peak at the morphotropic boundary. A sign of declining Curie point with zirconium ratios is observed at the 90/10, 80/20 and 70/30.

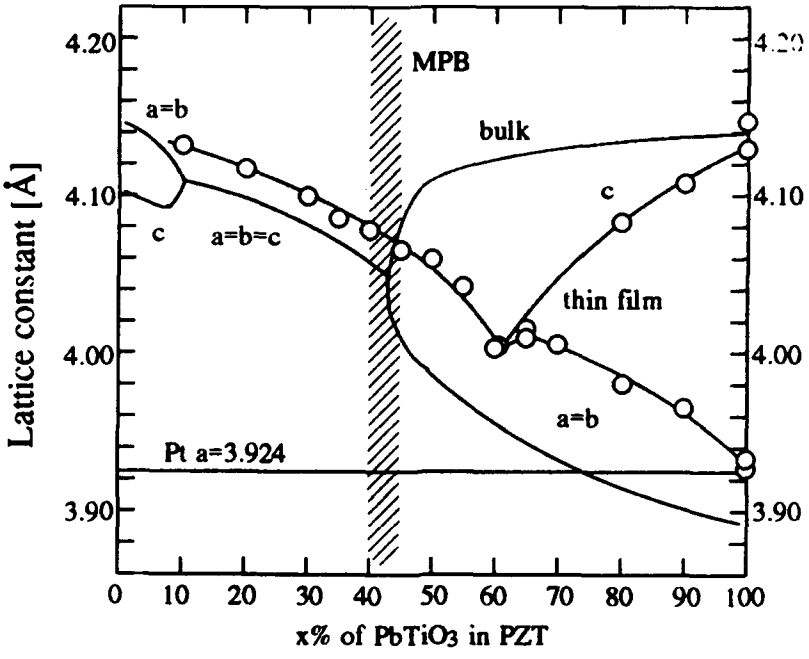


Figure 4. Lattice constant of verious Zr/Ti ratio of PZT

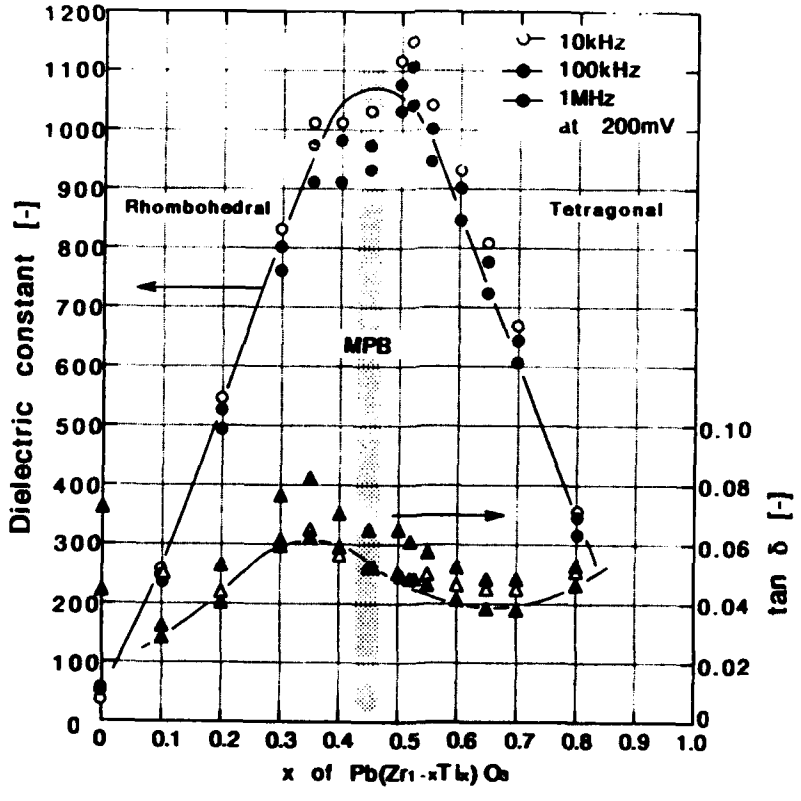


Figure 5. Dielectric parameters of sol-gel PZT thin films at room temperature

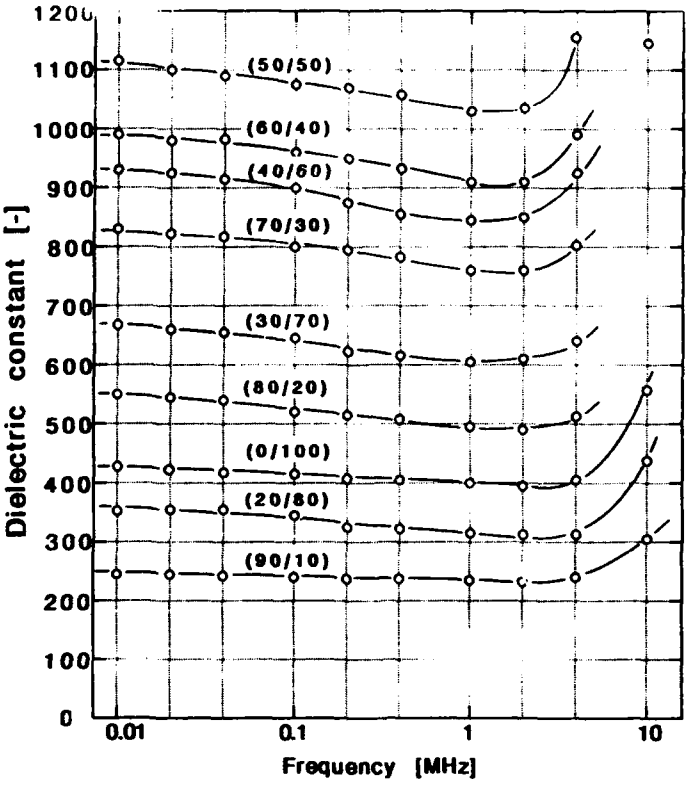


Figure 6. Frequency dependence of dielectric constant of sol-gel PZT thin films

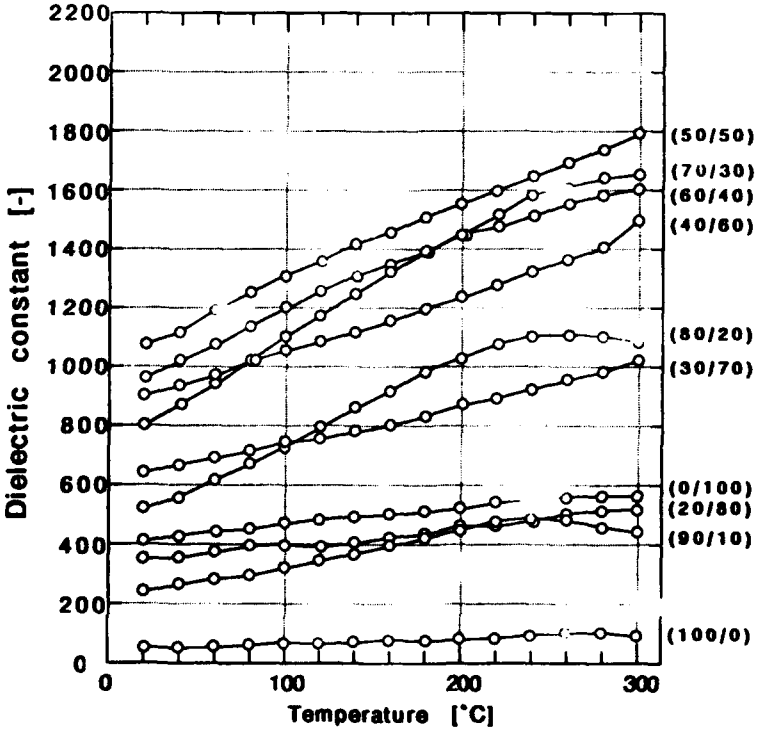


Figure 7. Temperature dependence of dielectric constant at 100 kHz

The hysteresis properties were measured by a conventional Sawyer-Tower bridge circuit with a 1 kHz sine wave. Figure 8 shows the sequential change of typical hysteresis curves of PZT(100/0) to PZT(0/100) at applied voltages of ±4 and ±6 volts. All films showed good low voltage saturation and perfect symmetry in their hysteresis curves. The remanent polarization (P_r) and coercive voltage (V_c) increased as Zr/Ti ratio decreased from 100/0. This coercive voltage is low enough to be compatible with any IC devices. However, films of PZT(20/80) to PT(0/100) extremely expanded their hysteresis shape at an applied voltage above ±10 volts. This phenomenon means that films with titanium rich compositions tend to be very leaky. It was considered that the leaky films were due to lead loss and oxygen defects in the microstructure, as the result of unsuitable preparation conditions, probably unecessarily high temperature during annealing.

Figure 9 shows the relation between P_r, E_c and PZT compositions. P_r showed a peak of 9.8 $\mu C/cm^2$ at around 35/65, and Ec increased with the titanium ratio. The meshed area, indicated in Figure 10, shows that hysteresis curves in this region were extremely leaky. The solid lines are measured data of P_r and E_c; real values may be shown by the dotted line.

Figure 10 shows the switching parameters for each composition. Applied square pulses were ±5 volts with 1 microsecond width. P_r calculated with switching charge and switching time are shown. Switching charge increased with titanium ratios and dropped from 20/80 to 100% $PbTiO_3$. The switching speed slightly increased as the total amount of switching charge.

The remanent polarization measured for our sol-gel PZT thin films was generally lower than those reported by other investigators[4-10]. Details in preparation condition supposedly caused this difference. The crystallographic distortion seen in the previously mentioned result of X-ray diffraction is considered as one of the causes for the low remanent polarization and the high coercive field.

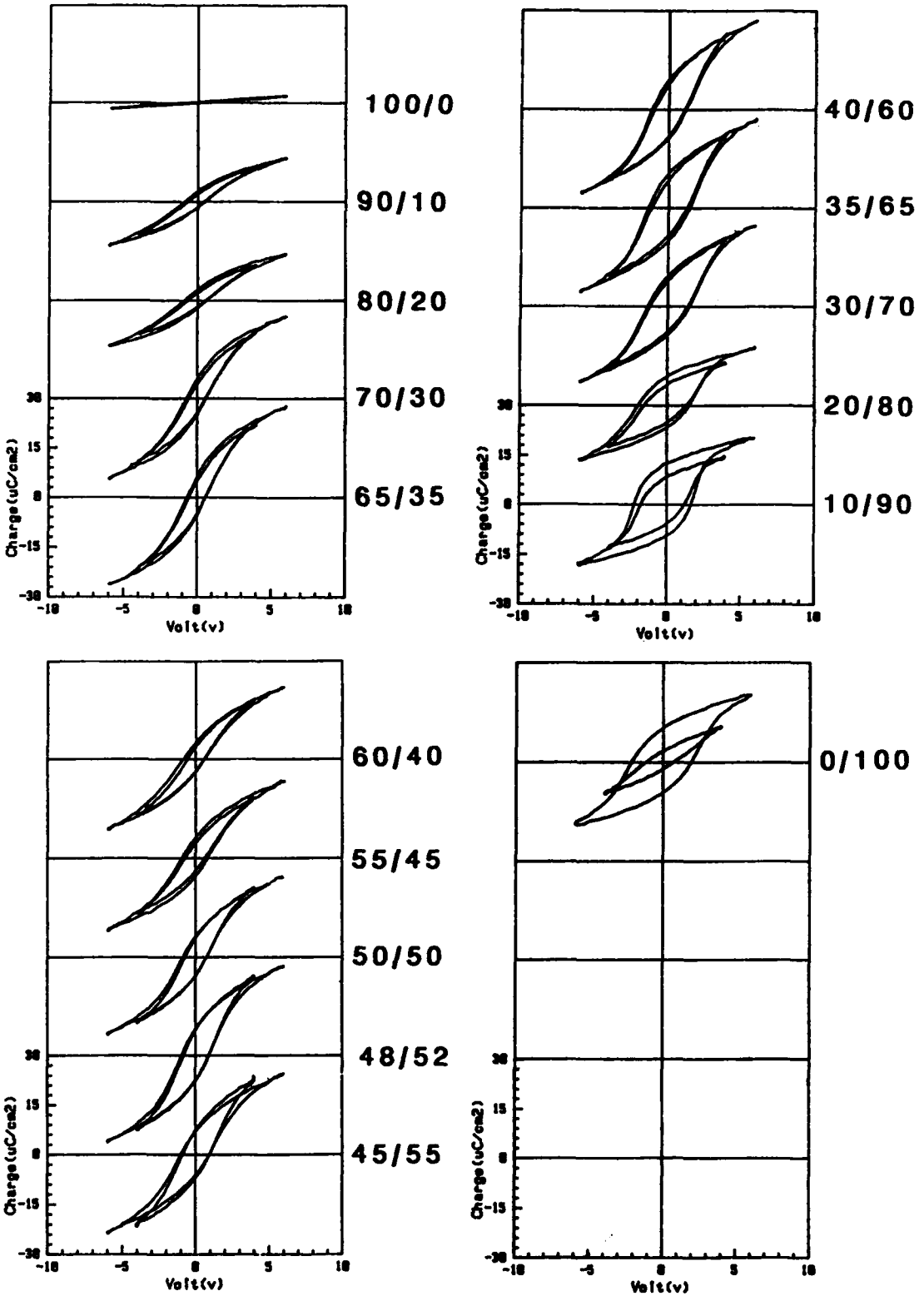


Figure 8 Hysteresis curves at ±4 and ±6 volts

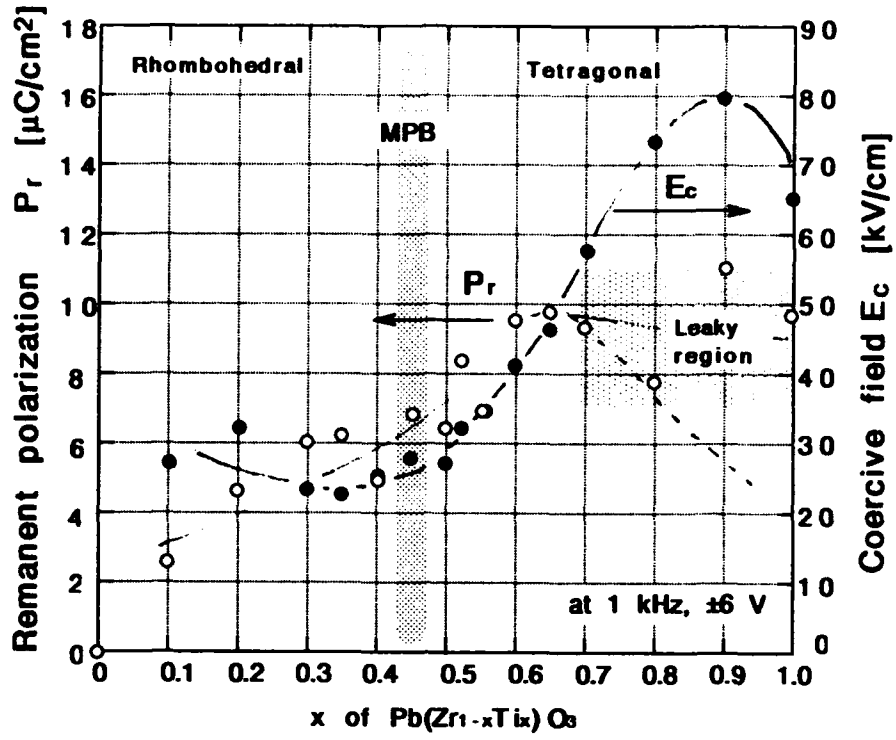


Figure 9. Hysteresis parameters of sol-gel PZT thin films

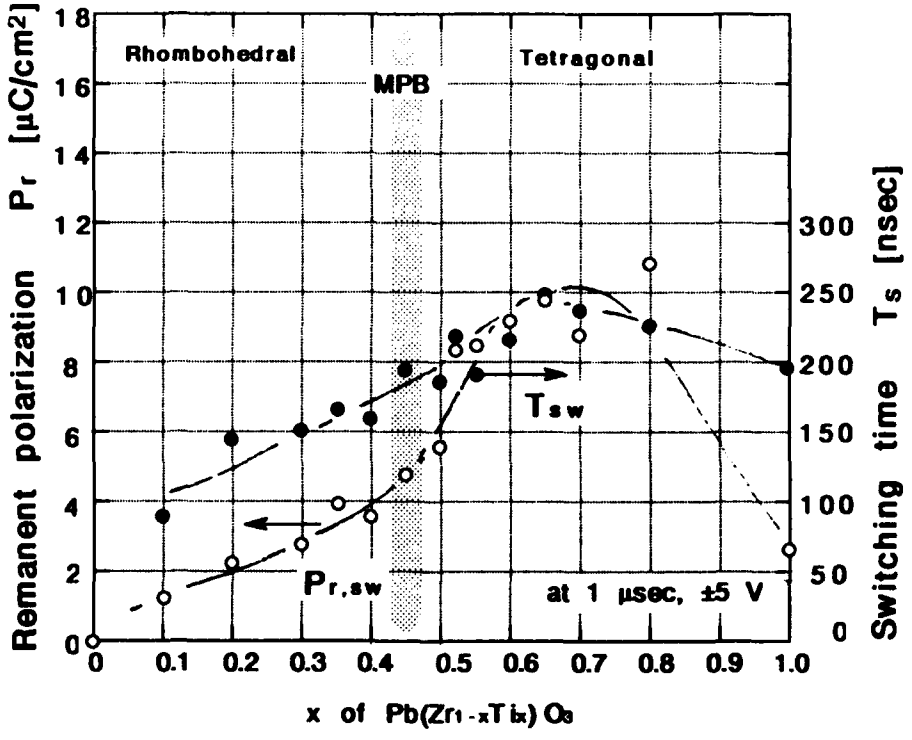


Figure 10. Switching parameters of sol-gel PZT thin films

SUMMARY

We have reported the electrical properties of PZT thin film capacitors with various composition prepared by sol-gel method in this paper. Some interesting results are summarized below.

1. $PbZr_xTi_{1-x}O_3$ thin films with various Zr/Ti ratios were easily obtained by sol-gel method.
2. PZT thin film has a larger dielectric constant (above 1,000), than bulk ceramic with a compatible composition.
3. All films showed high quality hysteresis properties with low voltage saturation and good symmetry.
4. The hysteresis properties showed a gradual transition from $PbZrO_3$ to $PbTiO_3$ without any drastic change at the morphotropic phase boundary (MPB). Electrical parameters such as dielectric constant showed a peak value at around the MPB, however, crystallographic phase diagram for our sol-gel PZT thin film significantly shifted to $PbTiO_3$ side.

REFERENCES

1. J F. Scott and C.A. Paz de Araujo, Mol Electron, (1987) 206-214
2. G.C. Messenger and F.N. Coppage, IEEE Transactions on Nuclear Science, 35[6] (1988) 1461-1466
3. I. Ueda, K. Iijima, and K. Kugiyama, Abstract of the fifth U.S.-Japan seminar on dielectric and piezoelectric ceramics, IV- 11 (1990) 316-319
4. N. Tohge, S. Takahashi, and T. Minami, J.Am.Ceram.Soc., 74[1] (1991) 67-71
5. T. Shiosaki and T. Okamura, Abstract of the fifth U.S.-Japan seminar on dielectric and piezoelectric ceramics, IV-14 (1990) 329-332
6. J. Fukushima, K. Kodaira, and T. Matsushita, J. Mater.Sci., 19 (1984) 595-598
7. K.D. Budd, S.K Day, and D.A. Payne, Proc.Brit.Ceram.Soc., 36 (1985) 107-121
8. K.D. Budd, S.K. Day, and D.A. Payne, Proc.Material Research Society Symp., 73 (1986) 71 1-716
9. C.J. Chen, E.T. Wu, Y.H. Xu, K.C. Chen, and J.D. Mackenzie, Proc.CMC (1989) 185-188
10. V.K. Seth and W.A. Schluze, Proc.CMC (1989) 175-184

11. C. Chen, D.F. Ryder,Jr., and W.A. Spurgeon, J.Am.Ceram.Soc., 72[8] (1989) 1495-1498
12. R.W. Vest and J. Xu, IEEE Transactions on Nuclear Science, 35[6] (1988)711-717
13. G. Shirane and K. Suzuki, J.Phys.Soc.Japan, 7(1952) 333
14. B. Jaffe, R.S. Roth, and S. Marzullo, J.Res.Natl.Bur.Stand.(U.S.), 55 (1955) 239

AD-P006 649

STATISTICAL THEORY OF FATIGUE IN FERROELECTRIC DEVICES

C. A. PAZ DE ARAUJO, R. ZULEEG
Microelectronics Research Laboratories, Dept. of Electrical and Computer Engineering, University of Colorado at Colorado Springs

T. MIHARA, H. WATANABE
Olympus Optical Corporation, Ltd., Tokyo, Japan

A. CARRICO
Dept. of Physics, U. Fed. do R.G. do Norte, Brazil; Microelectronics Research Laboratories, Dept. of Electrical and Computer Engineering, University of Colorado at Colorado Springs

L. D. MCMILLAN
Symetrix Corporation, Colorado Springs, Colorado

J. F. SCOTT
Dept. of Physics, University of Colorado at Boulder

Abstract A simple model of fatigue in ferroelectric thin-films is developed from first principles. The core of the model is the distribution of pinning and coercive energies due to the polycrystalline nature of the material. Also, because domain nucleation for thin-films seem to be surface dominant, and surface space-charges are usually present, the model assumes that the pinning energies are field activated due to surface screening effects. The model is based on the well known two-state cluster theory in statistical physics. Further results from the model include the log (t) dependence of fatigue as a direct consequence of a gaussian distribution of pinning energies. And, for the first time a theoretical description of the V^{-1} dependence of fatigue is also described. The model is tested using fatigue data of sol-gel derived integrated (Si) PZT capacitors.

INTRODUCTION

For many years researchers have faced three important degradation mechanisms in ferroelectric materials - fatigue, aging, and retention. The standard theoretical treatment of these phenomena stem from the original

92-16113

work of Street and Wooley in 1949[1]. In that work, it was demonstrated that domain walls in pinned states (deep wells) do not contribute to the overall polarization. That treatment was later adapted to ferroelectrics (the original was in connection to magnetic viscosity) by Mason in 1955[2]. Mason[2] related the potential energy to the elastic relaxation of domains wall in $BaTiO_3$ under residual stress.

Recently, ferroelectric thin-films operating in the high field regime with the aim of being used as non-volatile memory elements[3] has brought back the need to investigate this problem. Empirical results of fatigue (i.e. degradation in stored charge over continuous square pulse bipolar stress) show the same log (t) dependence which numerous researchers identified as aging of the dielectric properties[4,5,6,7].

While aging is a small signal measurement between long time intervals, fatigue and retention are responses to high frequency pulses with several orders of magnitude difference in amplitude. Retention is similar with aging insofar it is a response to a signal taken between very long time intervals.

This paper has the basic premise that in all cases the degradation comes from Debye relaxation of shallow wells - or even barrier free wells - and, that frozen dipoles (deeply pinned walls or single dipoles) do not fully participate in the switching-relaxation mechanism. Although this point of departure is the same as before, the model ignores the fine microscopic details of the pinning energies and assumes that the variety of shallow wells is a direct consequence of the distribution of unit cells in a polycrystalline lattice. Different charge arrangements lead to distribution in coercivity (especially in the surface and grain boundaries), which in turn lead to further pinning of free dipoles by the space-charge generated by the already pinned sites in such defective regions.

This argument becomes the basis to extend the Debye relaxation treatment over a polycrystalline matrix as described below. The tools of statistical mechanics are used to average over an infinite distribution of

coercive energies. However, the process of fatigue is shown to arrive as a consequence of a continuous relaxation current which flows whether the device is under continuous stress (fatigue) or aging (or shelf-life retention). This relaxation is derived and shown to appear in the time between pulses or small signal measurements.

Finally, this paper shows that the total energy stored in the capacitor leads to the V^{-1} dependence in the rate of fatigue and the initial charge. The model also shows explicitly the temperature dependence and the effect of space-charge in the apparent coercivity as shown in the hysteresis measurements. The surprising dependence of coercivity on applied voltage, before and after fatigue in ceramic thin-films is also easily accommodated in the theoretical treatment shown below.

THEORY

Before proceeding to develop the theoretical framework of the model, it is necessary to define some quantities and conventions. In this paper,

N = total number of dipoles per cm^3
N_+ = number of dipoles in the up (positive) position
N_- = number of dipoles in the down (negative) position
q^* = dipole charge (= Ze; where Z = atomic number)
$Q = Q_+ + Q_-$ (where $Q_{+/-} = (+/-)\, q^* N_{+/-}$) is the total stored charge.
P = Polarization (scalar) = $Q\delta$/vol, where δ = dipole displacement

With these quantities defined, the following basic equations can be easily understood:

$$P = q^* N\delta (\rho_+ - \rho_-) \qquad (1)$$

Where $\rho_+ = N_+/N$ and $\rho_- = N_-/N$ are the dipole densities.

The dipole conservation condition is

$$\rho_+ (t) + \rho_- (t) = 1 \text{ (for all times)} \tag{2}$$

and, the dipolarization (relaxation) current is

$$i_p = A \frac{dP}{dt} \tag{3}$$

where is the A electrode area.

Finally, the depolarization current can be written from (1) and (2) as,

$$i_p = Q_o \left(\frac{d\rho_+}{dt} - \frac{d\rho_-}{dt} \right) \tag{4}$$

where $Q_o = q^* NA\delta$

Equation (4) clearly shows that any change in the dipole densities ρ_+ and ρ_- lead to a depolarization current. These changes can be forced, causing one species of dipoles increase at the expense of the other (this is the case of polarization reversal) or, if both species exist there is a leakage relaxation current if the net rate of change do not equal zero (i.e. $d\rho/dt \neq 0$).

A. Two-State Model

Figure 1 shows a double well for the potential energy of dipoles that have pinning energy (deeper well) as an asymmetry. This is the point of departure of considering relaxation from the deeper well or shallow barrier (low coercivity). Whether this represents a dipole or a domain wall is unimportant at this point in view that only an energy picture of the physical situation is required. Assuming Boltzmann statistics, Ma[8] has shown that the rate equations for state transition are

$$\frac{d\rho_+}{dt} = \frac{1}{\tau}\,\rho_+(t) + \frac{1}{\tau}\exp\,(-E_p/kT)\,\rho_- \tag{5}$$

$$\frac{d\rho_-}{dt} = \frac{1}{\tau}\,\rho_+\,(t) - \frac{1}{\tau}\exp\,(-E_p/kT)\,\rho_+ \tag{6}$$

where, $E\rho$ = pinning energy

$$\frac{1}{\tau} = \frac{1}{\tau_o}\exp\,(-E_c/kT) \tag{7}$$

and E_c = coercive energy of the barrier

τ_o = barrier transit time when $T = \infty$.

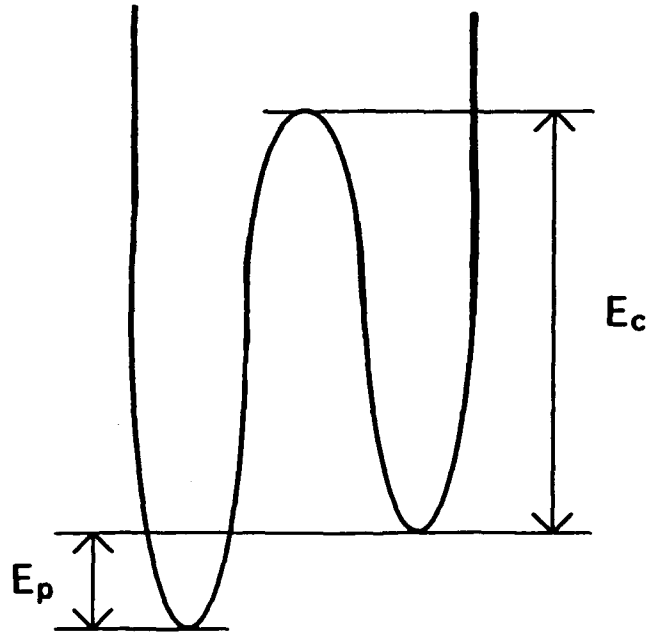


Fig. 1 - Double-well with pinning energy for a single cluster.

With the aid of equations (5) and (6) the spontaneous depolarization current can be shown to be

$$i_{p\ (spontaneous)} = \frac{-Q_1}{\tau} \tag{8}$$

where

$$Q_1 = 2Q_o\ [1 + \exp\ (-E_p/kT)]\ \rho_+\ (t) \tag{9}$$

and

$$\rho_+\ (t) = f + \Delta\ \exp\ (-rt) \tag{10}$$

is the solution of equations (5) and (6) using the conservation condition of equation (2).

The parameters in equation (10) are as follows:

$$f = 1/\ [\ \exp\ (E_p/kT)\ +1\ ] \tag{11}$$

$$\Delta = \rho_+(o)\ - f \tag{12}$$

$$r = (1/\tau_o)\ \exp\ (-E_c/kT)\ [1\ +\exp\ (E_p/kT)] \tag{13}$$

B. Two-State Clusters

So far, the depolarization current (equation (8)) shows simply an exponential decay via equations (9) and (10). We now proceed to

demonstrate the lot(t) dependence by arriving at a new form for Q_1 (equation (9)) when the polycrystalline nature of the material is taken into consideration. Again, Ma[8] provides us with a brilliant insight which has been used in magnetic rocks[9]. The total energy of the system as a function of time is described as

$$E(t) = \int_{E_c} \int_{E_p} E_p \, \rho_+ (t) \, N (E_p , E_c) \, dE_p \, dE_c + E_o (T) \tag{14}$$

Equation (14) simply states that the total energy is found by taking an average over the energy distributions due to E_p and E_c over the dipole density population. The energy $E_o(T)$ which is only temperature dependent is the energy at time equal zero - i.e., just after storage in the capacitor.

It is not clear from equation (14) how the time dependence will eventually appear in the integral. Because of the limited space, the reader is requested to refer to reference[8] for details.

Before we proceed with the results of two important conditions affecting equation (14), let us review the physical model of the ferroelectric capacitor. Figure 2 shows a ferroelectric capacitor and the description of the domains within each grain. The key point here is that each grain may have similar domains. The counting process proceeds by placing similar domains in bins called clusters (see Figure 3). The i^{th} cluster represents the set of all domains from wherever grain which have the same pinning energy and barrier energy (same E_c). In other words, each cluster is a two state system and we add the energy of all clusters.

Two limiting cases are easily grasped:

Case 1: All clusters have the same E_c and E_p (Fatigue-Free Condition)

This means that the density of states is

$$N(E_p , E_c) = \delta (E_p - E_{po}) \, \delta (E_c - E_{co}) \tag{15}$$

Where E_{po} and E_{co} is the common pinning and barrier energy for all clusters and $\delta(\bullet)$ is the delta function. In this case, the integral vanishes and

$$E(t) = E_o(T) \tag{16}$$

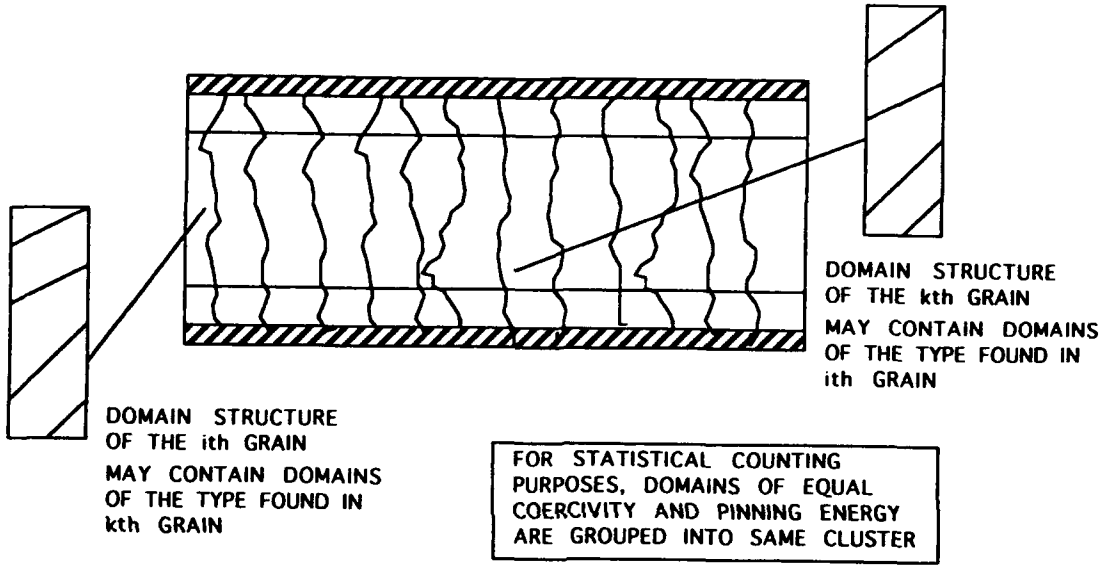


Fig. 2 - Ferroelectric capacitor showing domains of similiar E_p and E_c within each grain.

The result shown in equation (16) means that the total energy is time independent - i.e., no fatigue is possible. This is the fatigue-free condition. In a capacitor

$$E(t) = \frac{1}{2} CV^2 = \frac{1}{2} QV \tag{17}$$

Where C is the capacitance per unit area.

Equation (16) is rewritten as

$$Q(t) = \frac{2E(t)}{V} = \frac{2E_o(T)}{V} \tag{18}$$

It was discussed above that $E_o(t)$ is the time independent part of the energy integral. This is

$$E_o(T) = \int_{E_c}\int_{E_p} \frac{E_p N(E_p, E_c)}{\exp(E_p/kT) + 1}\, dE_p\, dE_c \tag{19}$$

Defining equation (18) as

$$E_o(T) = \frac{1}{2} Q_{oo}(T) V \tag{20}$$

Using equation (17) above, and considering that at time equal zero, the initial polling charge is $2P_rA$ (where P_r is the residual polarization and A is the area - the factor 2 is the full swing of the polarization reversal). Then, fatigue free condition of equation (16) can be rewritten as, (using equations (18) and (20)),

$$Q(t) = P_r A \tag{21}$$

Case 2: Clusters have a gaussian distribution of E_p and E_c (log (t) condition)

Assuming that there are mean values for E_p and E_c - namely, E_{po} and E_{co}. But, there is a normal distribution of these energies, such that:

$$N(E_p, E_c) = g_1(E_p)\, g_2(E_c) \tag{22}$$

where

$$g_1(E_p) = N_1 \exp\left[-\frac{(E_p - E_{po})^2}{2\Delta E_p^2}\right] \tag{23}$$

$$g_2(E_c) = N_2 \exp\left[-\frac{(E_c - E_{co})2}{2\Delta E_c^2}\right] \tag{24}$$

where N_1 and N_2 have the usual meaning

$(1/(\sqrt{2\pi})\ \Delta)$ *where* $\Delta = \Delta E_c\ ,\ \Delta E_p$

It is clear from (22) that the pinning energies are statistically independent of the barrier heights. This is very reasonable in view that the barrier height is due to the dipole moment of the B-site atom in an ABO_3 perovskite lattice. And, the pinning energy is due to a completely random defect site such as an oxygen vacancy.

It is only when these gaussian conditions are invoked that the total energy integral (equation (14)) reduces to

$$E(t) = [E_o(T) + b_o] - a_o \ln(t/\tau_o) \tag{25}$$

This is the log(t) dependence found in empirical fatigue and aging results. The parameters in equation (25) are:

$$a_o = E_{po}\ \rho^*(o)\left[\frac{kT}{\sqrt{2\pi}\ \Delta E_c}\right] \tag{26}$$

$$b_o = E_{po}\ \rho^*(o)\left[\frac{\sqrt{2\pi}\ \Delta E_c + E_{co}}{2\sqrt{2\pi}\ \Delta E_c}\right] \tag{27}$$

Equation (25) can be rewritten using the same arguments of equation (17) to yield Q(t) - the more familiar form of fatigue. In this case

$$Q(t) = b(V) - a(V) \ln(t/\tau_o) \tag{28}$$

where

$$b(V) = \frac{2[E_o(T) + b_o]}{V} \qquad (intercept) \tag{29}$$

and

$$a(V) = \frac{2a_o}{V} \qquad (slope\ of\ fatigue\ curve) \tag{30}$$

Equations (29) and (30) clearly show the well known experimental result that the slope and intercept of the Q(t) vs log(t) curve are dependent on 1/V. Figures 3 and 4 show this dependence of a(V) and b(V) from PZT data.

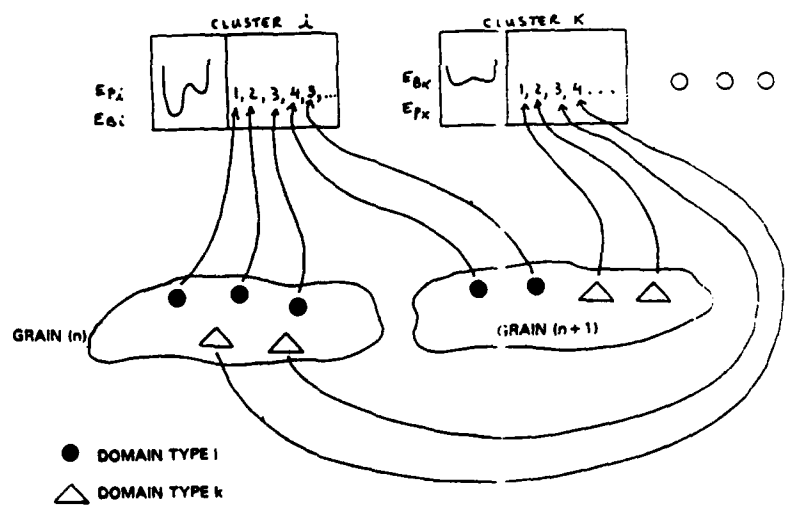


Fig. 3 - Domain bins (clusters) for counting process.

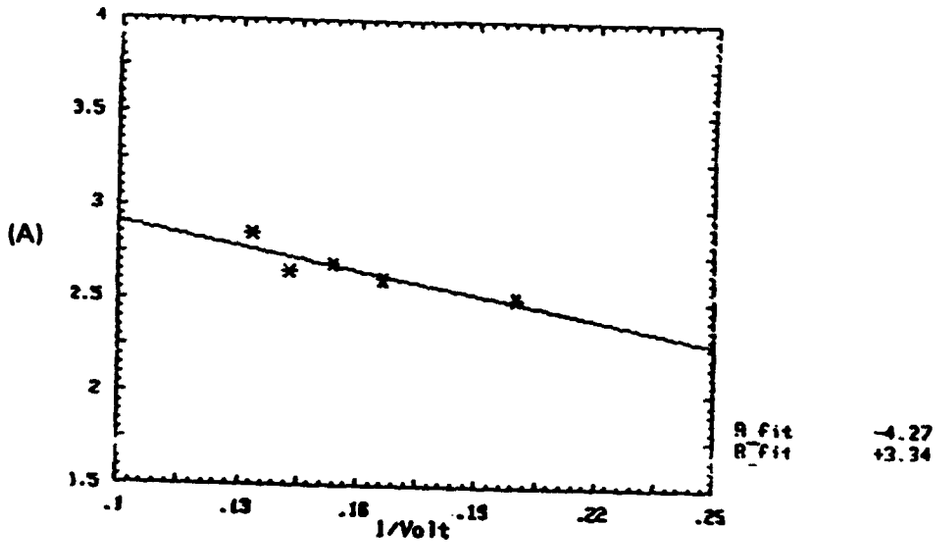


Fig. 4 - Dependence of the slope of the fatigue curve on applied voltage.

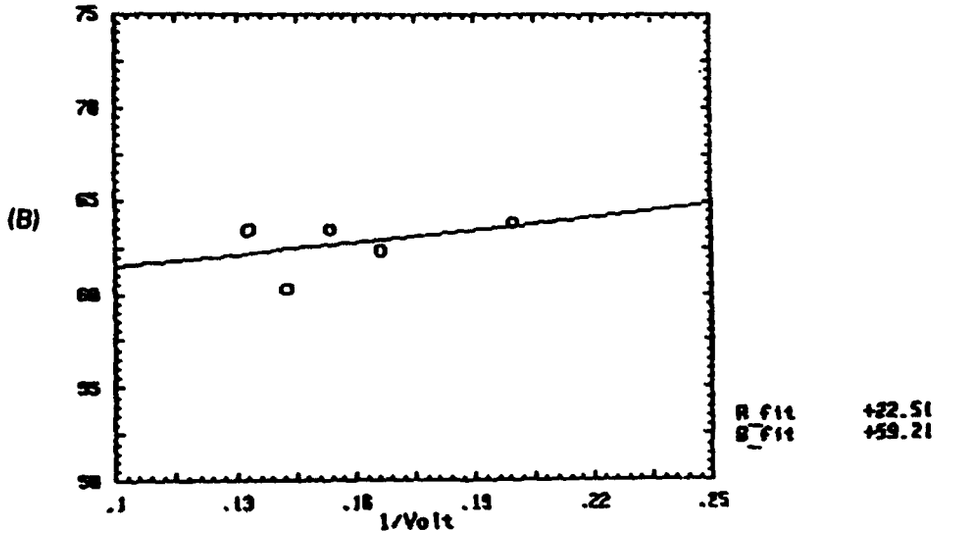


Fig. 5 - Dependence of the intercept of the fatigue curve on applied voltage.

where a(v) is as before, ln(•) was changed to log (•) and

$$b_1(V) = b(V) - a(V)\ln(\tau_c/\tau) \tag{32}$$

For the device in the data of Figures 4 and 5,

$$a(V) = \frac{4.27}{V} - 3.34 \tag{33}$$

and

$$b(V) = \frac{22.51}{V} + 59.21$$

Another way of writing the fatigue equation (equation (31)) which has the usual empirical form is,

$$2P_r(n) = (4.27/V - 3.34)\log(n) + (22.51/V + 59.21) \tag{34}$$

Using equation (34) the 50% point can be estimated at 5V to be 10^9. Or, in more general terms,

$$n_{critical} = 10^x \qquad where\ x = [b(V)/2a(V)] \tag{35}$$

which also yields the final life as $n_F = (n_{critical})^2 = 10^{18}$ cycles. (The pulse train of all this data had a frequency of 1 Mhz.)

In fact, in Figure 6, the E_c vs V curve after fatigue is a power-law with voltage. In order to appreciate the significance of this result, the reader needs to be made aware of other factors outside the subject of this paper (see [10]). However, if $E_c(V)$ is seen as the surface field of the ferroelectric in the n^+ side, it is possible to write

$$E_c = E_S \left(\frac{1-x}{W(V)}\right)^n + E_{co} \tag{36}$$

which is analogous to the potential drop across a depletion region[11], i.e.,

$$\varnothing = \varnothing_s \left(\frac{1-x}{W(V)}\right)^n \tag{37}$$

where the surface potential near the contact is

$$\varnothing_s = \frac{qN_b W(V)^2}{2\epsilon_s \epsilon_o} \tag{38}$$

E_{co} is the coercivity of the n^+ region and W(V) and N_b are the depletion layer and the background (p-type) uncompensated ion concentration in the bulk of the film.

In our case,

$$E_c \approx \varnothing/d \quad \text{and} \quad E_s \approx \varnothing_s / W(V)$$

where d = total device width.

If we assume that most of the pinning occurs at the surface (which is plausible in thin-films due to mist nucleation sites residing on the surface), the pinning energy can be written as

$$E_p = E_s \left(1 - \frac{x}{W(V)}\right)^n \tag{39}$$

or

$$E_c = E_p\,(V) + E_{co} \tag{40}$$

DISCUSSION

Figure 6 shows a charge vs ln(cycles) fatigue curve for a PZT with [Ti] = 60%. It is clear that the model is in good agreement with the data. However, we still must account for the discrete nature of the fatigue pulses.

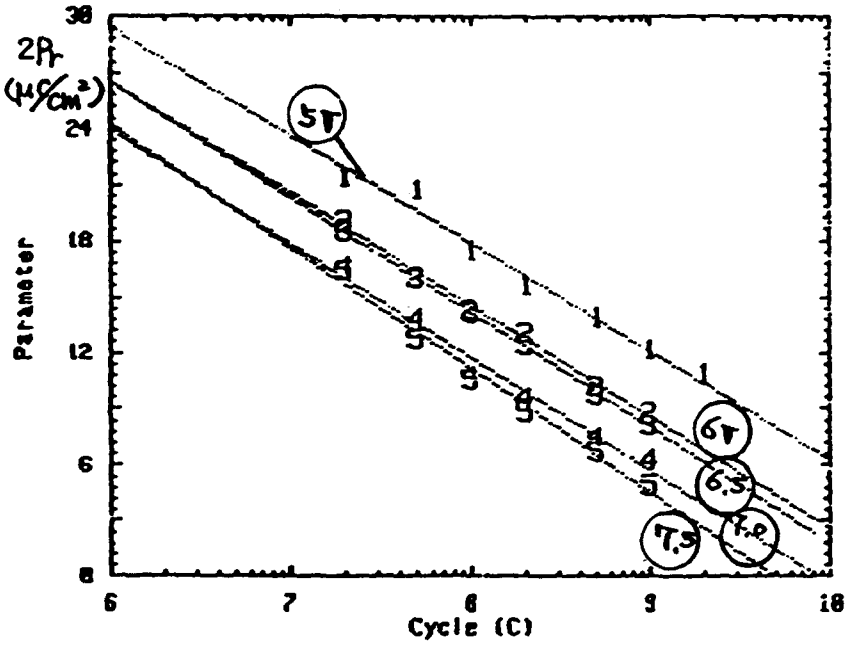


Fig. 6 - Fatigue curve for PZT showing log(t) dependence.

Assuming a continuous bipolar pulse train with zero rise time, the fatigue equations are modified as follows:

Let $t = n\tau_c$, where τ_c = pulse width, n is the cycle index, then Q(t) becomes Q(n), or:

$$Q(n) = b_1(V) - a(V)\log(n) \qquad (31)$$

The detailed analysis of the artifacts in testing due to the discreetness of the pulse train is omitted here due to the lack of space. However, the error is easily detected in the residue of the slope in equation (33) - notice the extra -3.34 term which is not accounted by the theory as shown in equation (30). The absolute error is hard to calculate because there are also experimental errors. In any case, the model does exceptionally well in showing many aspects of the data.

Voltage Activation of Pinning Energy

A final word must be added to explain our initial assertion that the pinning energy is voltage activated. Mihara, et al.[10] has shown that the surface layers of a ferroelectric thin-film capacitor is a space-charge region formed by an $n^+ - p$ junction induced by oxygen vacancies. The screening of the applied field by this surface layer is shown in Figure 7. The measured coercivity is unexpectedly voltage dependent and follows a power law similar to the voltage drop across a depletion layer capacitor in reverse bias.

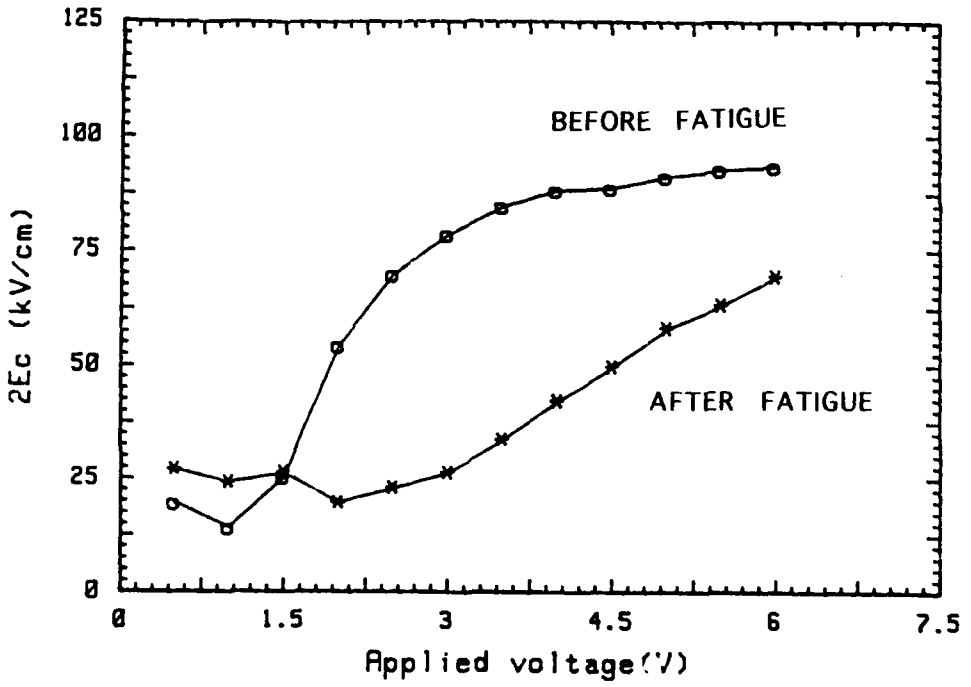


Fig. 7 - Apparent coercivity versus applied voltage. (A) Before fatiguing and (B) After Fatigue. (PZT thin-film capacitors).

Equation (39) completes the model by providing a plausible ansatz to the data of Figure 7. It is clear that after fatigue, most of the applied voltage drops across a space charge region (there are no more free switching dipoles). In this case, E_c no longer saturates. The power law curve supports the argument that E_p is voltage dependent and originates from the potential drop across the surface space charge region. In reference [10] this is further elaborated via the CV characteristic of a ferroelectric device. As the device fatigues there is a broadening of the CV neo-gaussian peaks. This means a distribution of coercivities, which in turn correlates well with a non-saturating E_c vs V curve (a broad and continuous spectrum of E_c). Thus, the pinning energy can be calculated from the E_c vs V plot of Figure 6. Further discussion on this and the built-in potential embedded in W(V), the depletion layer width will be shown elsewhere[12].

CONCLUSIONS

Fatigue in ferroelectric thin-films has been modelled using a statistical mechanic description of the material with emphasis on the surface layer. The model correctly describes the log(t) dependence of the fatigue curve. The slope and intercept 1/V dependence is also accounted for with good accuracy. Predictions for 50% duty cycle for sol-gel PZT is in agreement with the empirical results. The voltage activated pinning energy is described in terms of the potential drop across an n^+-p surface layer in agreement with the equivalent circuit model shown elsewhere[10]. The overall argument of the model is also in agreement with past theoretical results that invoke frozen states in pinning energy wells.

ACKNOWLEDGEMENTS

The authors wish to thank Ms. Linah Pritchard for typing this manuscript.

This work was supported in part by Navy SBIR Contract #N00164-89-C-0166.

REFERENCES

(1) Street, R., and Woolley, J.C., 1949, Proc. Phys. Soc. A, 62, 562.
(2) Mason, W.P., 1955, J. Acoust. Soc. America, 27, 73.
(3) Scott, J.F., and Paz de Araujo, C.A, 1991, Science, 246, 1400, 1989.
(4) Plessner, KnW., 1956, Proc. Phys. Soc.(London), 69[444B], 1261-68.
(5) McQuarrie, M.C., and Buesjen, W.R., 1955, Ceramic Bull., 34, 12, 402.
(6) Uchida, N., and Ikeda, T., 1968, Jap. J. of Appl. Phys., 7, N.10, 1219.
(7) Burkhanov, A., and Shilnikov, A., 1989, Ferroelectrics, 90, 39.
(8) Ma, S.K., Statistical Mechanics, World Scientific, Philadelphia, 1985.
(9) Dasgusta, C., Ma, S-k., and Hu, C-k., 1979 Phys. Rev.B, 20, 9, p.383.
(10) Mihara, T., Watanabe, H., Yoshimori, H., Paz de Araujo, C.A., Melnick, B., and McMillan, L.D., these proceedings.
(11) Grove, A.S., Physics and Technology of Semiconductor Devices, John Wiley and Sons, Inc., New York, 1967.
(12) To be published ISIF-92.

AD-P006 650

C–V AND I–V SIMULATIONS OF METAL FERROELECTRIC SILICON CAPPED AND UNCAPPED $BaMgF_4$ DEVICES USING PISCES II–B [1]

DENG–YUAN CHEN, C.A. PAZ DE ARAUJO, and L.D. MCMILLAN

Microelectronics Research Laboratories, University of Colorado at Colorado Springs, Colorado Springs, CO 90933–7150 and Symetrix Corporation, 5055 Mark Dabling Blvd. Suite #100, Colorado Springs, CO 80918

Abstract Simulation of $BaMgF_4$ metal–ferroelectric–silicon field effect transistors (MFSFETs) are presented based on experimentally derived CV data shown recently in the literature. A standard 2–D semiconductor device simulator (PISCES II–B) is used. The modulation of the semiconductor surface is modelled by adding the net $BaMgF_4$ (capped with ZrO_2 or not), polarization charge to the interface charge. The model correctly describes the experimental CV behavior including the sense of the CV curve (indicating pure ferroelectric modulation). The effect of threshold voltage modulation by the ferroelectric is also examined. The device model clearly shows the adaptive transistor behavior of the I_{DS} vs. $V_g(P_r)$ characteristics. These simulations are being used as tools for device design and process integration towards the development of non–destructively read ferroelectric memories.

INTRODUCTION

Metal ferroelectric silicon field effect transistor (MFSFET) has been studied since 1963 [1–12]. $BaMgF_4$ has been proposed as a prospective ferroelectric material for nondestructive readout (NDRO) and radiation hard (Rad Hard) MFSFET device [12]. PISCES II–B is a standard two–dimentional, two–carrier semiconductor simulator [13]. In this paper, an interface charge model is proposed to simulate the polarization charge of capped and uncapped $BaMgF_4$ MFSFET device. The C–V and I–V characteristics are simulated using PISCES II–B.

MFSFET DEVICE SIMULATION

[1]This research work was funded by SBIR (SDIO) DNA contract # DNA 001–90–C–0004.

92–16114

The Interface Charge Model

A basic characteristics of ferroelectric material is the hysteretic behavior relating polarization P and applied field Ea. When Ea is cut off, P does not go to zero but remains at a finite value, called the remanent polarization, P_r.

The interface charge model is that the ferroelectric material of MFSFET device is assumed the linear dielectric material with the fixed charge on both of the dielectric material interfaces. The fixed charge density Q_f is defined by

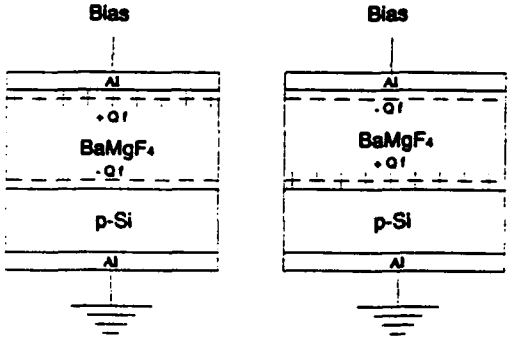
$$Q_f = \pm \frac{P_r}{q}$$

where $q = 1.602 \times 10^{-19} C$ is unit charge.

Q_f may be implemented into the "INTERFACE" card of PISCES II–B input file.

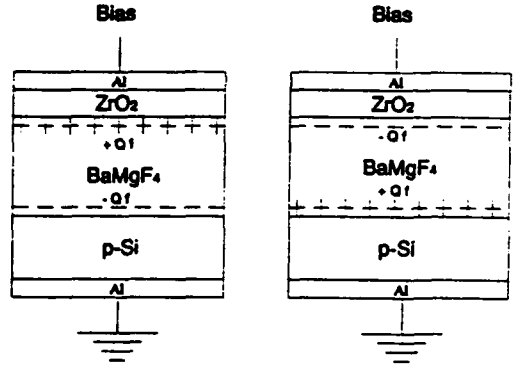
C–V Simulation

Fig. 1 and Fig. 2 show the uncapped and capped MFS structure with the interface charge model for PISCES II–B simulation.



(a) Forward Sweep (b) Reverse Sweep

Fig. 1 Metal Uncapped Ferroelectric Silicon Structure For PISCES II-B Simulation, Qf=Pr/q.



(a) Forward Sweep (b) Reverse Sweep

Fig. 2 Metal Capped Ferroelectric Silicon Structure For PISCES II-B Simulation, Qf=Pr/q.

Fig. 3 shows the effects of the thickness of ZrO_2 capping on $BaMgF_4$ on C–V curves. They are 100 Å, 300 Å, and 500 Å, respectively. The thickness of $BaMgF_4$ is 1800 Å. The dielectric constant and remanent polarization P_r of $BaMgF_4$ are assumed 8.0[11] and $0.175 \mu C/cm^2$. The dielectric constant of ZrO_2 is assumed 10. The p–type substrate doping concentration is $1.25 \times 10^{15} cm^{-3}$, and the simulation ac frequency is $1 KHz$. Fig. 3 shows that as the thickness of ZrO_2 increases the capacitance decreases

but the width of the C–V curve does not change.

Fig. 4 shows the effects of the thickness of capped $BaMgF_4$ on C–V curves. They are 1200 Å, 1800 Å, and 2400 Å, respectively. The dielectric constant and the remanent polarization P_r of $BaMgF_4$ are 8 and $0.175\mu C/cm^2$. The thickness and dielectric constant of ZrO_2 are 300 Å and 10. The p–type substrate doping concentration is $1.25 \times 10^{15} cm^{-3}$. The simulation ac frequency is $1KHz$. Fig. 4 shows that as the thickness of $BaMgF_4$ increases the capacitance decreases and the width of C–V curve becomes larger as well.

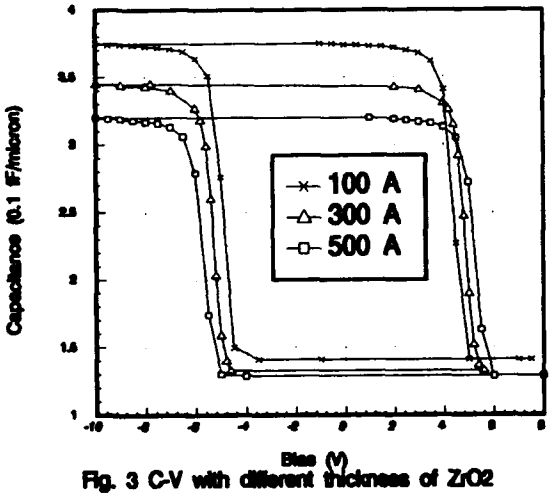


Fig. 3 C-V with different thickness of ZrO2

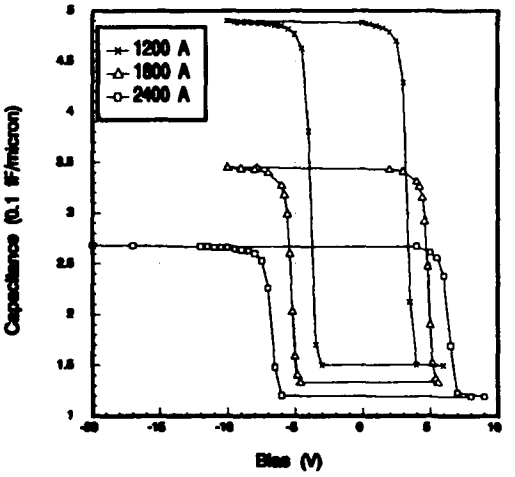


Fig. 4 C-V with different thickness of capped BaMgF4

Fig. 5 shows the effects of the thickness of uncapped $BaMgF_4$ on C–V curves. They are 1200 Å, 1800 Å, and 2400 Å, respectively. The dielectric constant and the remanent polarization P_r of $BaMgF_4$ are 8 and $0.175\mu C/cm^2$. The p–type substrate doping concentration is $1.25 \times 10^{15} cm^{-3}$. The simulation ac frequency is $1KHz$. Fig. 5 shows almost the same effect as Fig. 4 does.

Fig. 6 shows the effects of the dielectric constant of capped $BaMgF_4$ on C–V curves. they are 8, 14, and 21, respectively. The thickness and remanent polarization are 1800 Åand $0.175\mu C/cm^2$. The thickness and dielectric constant of ZrO_2 are 300 Å and 10. The p–type substrate doping concentration is $1.25 \times 10^{15} cm^{-3}$. The simulation ac frequency is $1KHz$. Fig. 6 shows that as the dielectric constant of $BaMgF_4$ increases the capacitance increases and the width of the C–V curve become smaller as well.

Fig. 7 shows the effects of the p–type substrate doping concentration on C–V curves. They are $5.0 \times 10^{14} cm^{-3}$, $1.25 \times 10^{15} cm^{-3}$, and $1.0 \times 10^{16} cm^{-3}$, respectively. The remanent polarization, the dielectric constant and the thickness of $BaMgF_4$ are

$0.175\mu C/cm^2$, 8, and 1800 Å, respectively. The dielectric constant and the thickness of ZrO_2 are 10 and 300 Å. The simulation ac frequency is $1KHz$. Fig. 7 shows that as the doping concentration increases the lower line of the C–V curve becomes higher. It seems that the shift of the C–V lower line becomes much larger as the doping concentration is higher than $1.25 \times 10^{15} cm^{-3}$.

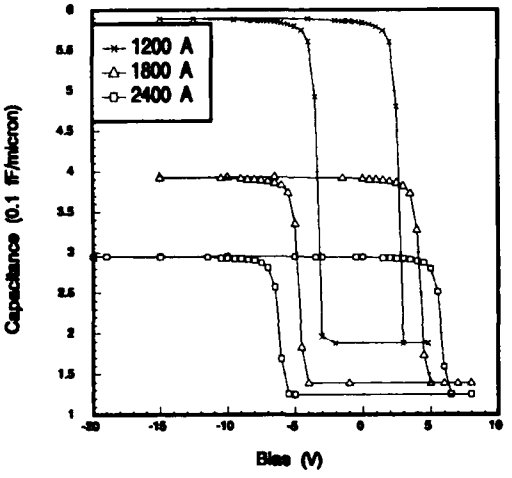


Fig. 5 C-V with different thickness of uncapped BaMgF4

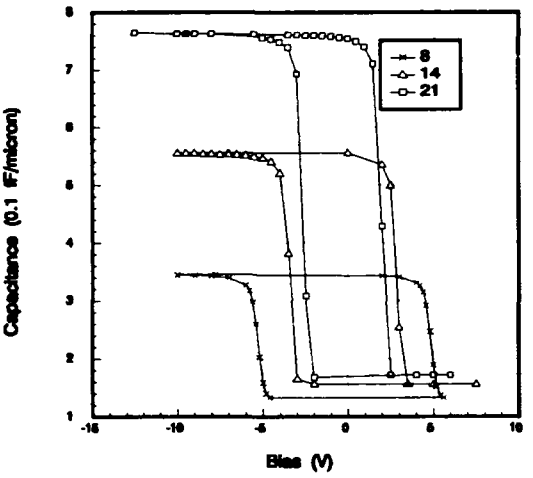


Fig. 6 C-V with different dielectric constant of BaMgF4

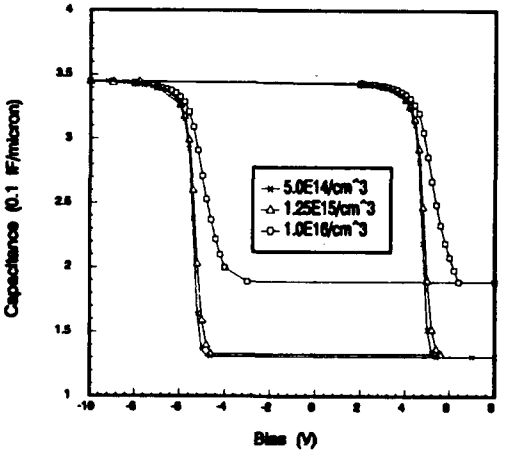


Fig. 7 C-V with different substrate concentration

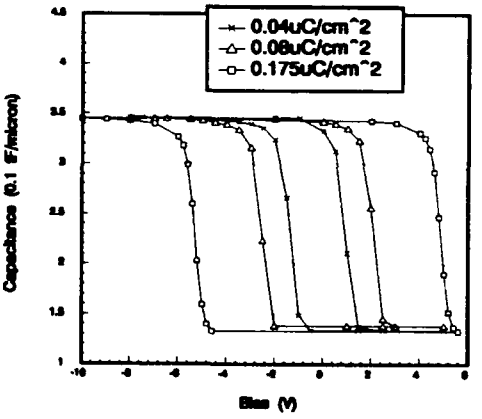


Fig. 8 C-V with different remanent polarization of BaMgF4

Fig. 8 shows the effects of the remanent polarization of $BaMgF_4$ on C–V curves. They are $0.04\mu C/cm^2$, $0.08\mu C/cm^2$, and $0.175\mu C/cm^2$, respectively. The dielectric

constant and the thickness of $BaMgF_4$ are 8 and 1800 Å. The dielectric constant and the thickness of ZrO_2 are 10 and 300 Å. The p–type substrate doping concentration is $1.25 \times 10^{15} cm^{-3}$. The simulation ac frequency is $1KHz$. Fig. 8 shows that as the remanent polarization of $BaMgF_4$ increases the capacitance does not change but the width of the C–V curve becomes larger.

Fig. 9 shows the simulation results and experimental data of C–V curve. The parameters chosen for simulation are: the dielectric constant and the thickness of ZrO_2 are 10 and 300 Å; the dielectric constant and the thickness of $BaMgF_4$ are 8 and 1800 Å; the remanent polarization of $BaMgF_4$ is $0.175 \mu C/cm^2$; the p–type substrate doping concentration is $1.25 \times 10^{15} cm^{-3}$; and the simulation ac frequency is $1KHz$. The parameters reported [11] of the experimental data are: the thickness of ZrO_2 is 300 Å; the dielectric constant and the thickness of $BaMgF_4$ are 8 and 1799 Å; the p–type substrate concentration is about $1.25 \times 10^{15} cm^{-3}$.

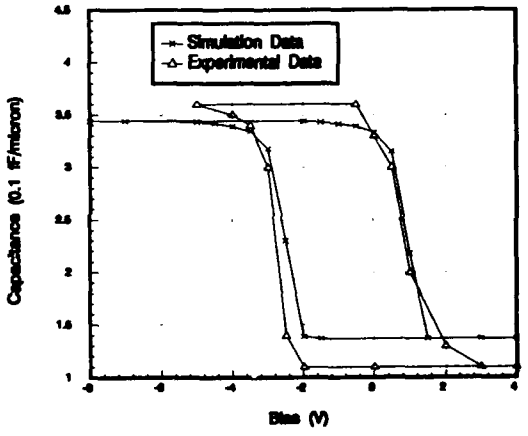


Fig. 9 C-V comparison between simulation and experimental data

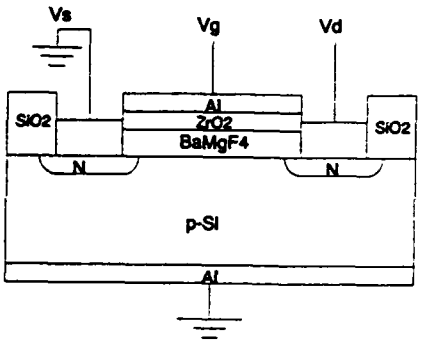


Fig. 10 Metal Capped Ferroelectric Silicon Field Effect Transistor Structure For Subthreshold Characteristics Simulation

Obviously, the interface charge model does not include: (1) the effect of non ideal contacts, (2) the effect of the substrate impurity on the properties of the ferroelectric material (i.e., $BaMgF_4$), and (3) the effect of other interface phenomena.

Subthreshold Current Simulation

Fig. 10 shows the metal capped ferroelectric silicon field effect transistor structure for subthreshold current simulation.

Fig. 11 shows the effects of the thickness of capped $BaMgF_4$ on the subthreshold characteristics. They are 900 Å, 1200 Å, 1500 Å, and 1800 Å, respectively. The dielectric

constant and the thickness of ZrO_2 are 10 and 300 Å. The dielectric constant and the remanent polarization of $BaMgF_4$ are 8 and $0.175\mu C/cm^2$. The drain voltage is 0.5 V. Fig. 11 shows that there are two threshold voltages for a MFSFET device. The threshold voltage shift is due to the polarization characteristics of the ferroelectric material. As the thickness of $BaMgF_4$ increases the shift of the threshold voltage becomes larger.

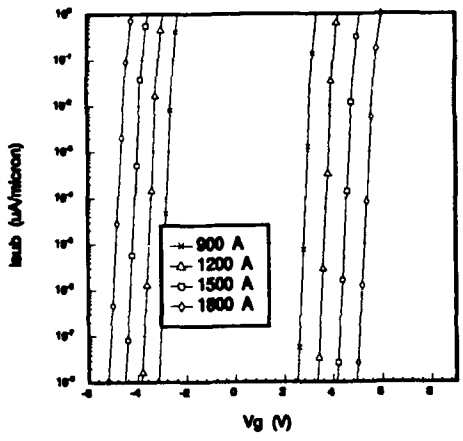


Fig. 11 Isub vs. Vg with different thickness of capped BaMgF4

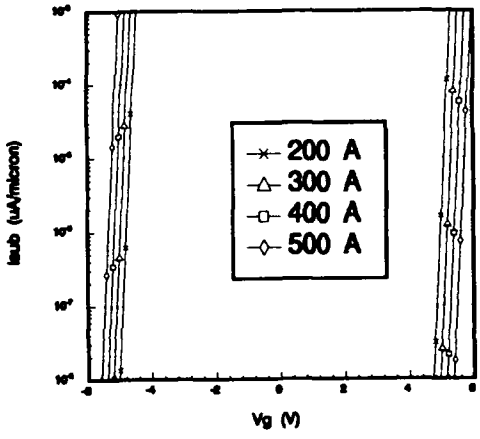


Fig. 12 Isub vs. Vg with different thickness of ZrO2

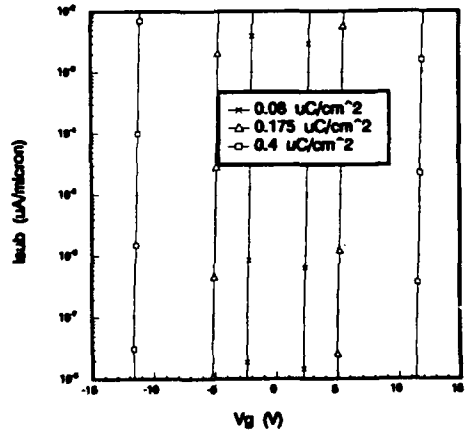


Fig. 13 Isub vs. Vg with different remanent polarization

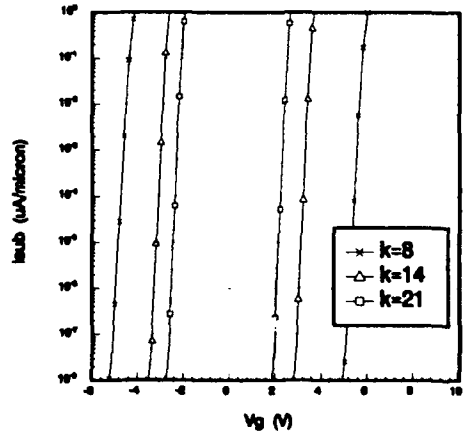


Fig. 14 Isub vs. Vg with different dielectric constant of BaMgF4

Fig. 12 shows the effects of the thickness of ZrO_2 on the subthreshold characteristics. They are 200 Å, 300 Å, 400 Å, and 500 Å, respectively. The dielectric constant

and the thickness of $BaMgF_4$ are 8 and 1800 Å. The remanent polarization of $BaMgF_4$ is $0.175\mu C/cm^2$. The dielectric constant of ZrO_2 is 10. The drain voltage is 0.5 V. Fig. 12 shows that as the thickness of ZrO_2 increases the threshold voltage shift becomes larger.

Fig. 13 shows the effects of the remanent polarization of $BaMgF_4$ on the subthreshold characteristics. They are $0.08\mu C/cm^2$, $0.175\mu C/cm^2$, and $0.4\mu C/cm^2$, respectively. The dielectric constant and the thickness of $BaMgF_4$ are 8 and 1800 Å. The dielectric constant and the thickness of ZrO_2 are 10 and 300 Å. The drain voltage is 0.5 V. Fig. 13 shows that as the remanent polarization increases the threshold voltage shift becomes larger.

Fig. 14 shows the effects of the dielectric constant of $BaMgF_4$ on the subthreshold characteristics. They are 8, 14, and 21, respectively. The remanent polarization and the thickness of $BaMgF_4$ are $0.175\mu C/cm^2$ and 1800 Å. The dielectric constant and the thickness of ZrO_2 are 10 and 300 Å. The drain voltage is 0.5 V. Fig. 14 shows that as the dielectric constant of $BaMgF_4$ increases the threshold voltage shift becomes smaller.

CONCLUSION

The C–V curve and I–V curve of MFSFET are simulated by interface charge model using PISCES II–B. The remanent polarization and dielectric constant and the thickness of the ferroelectric material ($BaMgF_4$) layer, the dielectric constant and thickness of the capping (ZrO_2) layer, and the substrate doping concentration are sensible to the simulation results. Therefore, the MFSFET device may be designed by the interface charge model using PISCES II–B simulation.

REFERENCES

[1] J.L. Moll, et al, IEEE Trans. Electron Dev., ED–10, 338 (1963)
[2] S. S. Perlman, et al, IEEE Trans. Electron Dev., ED–12, 816 (1967)
[3] G.G. Teather, et al, Solid–State Electronics, 11, 527 (1968)
[4] J.C. Crawford, et al, IEEE Trans. Electron Dev., ED–16, 525 (1969)
[5] S.Y. Wu, IEEE Trans. Electron Dev., ED–21, 499 (1974)
[6] S.Y. Wu, Ferroelectrics, 11, 379 (1976)
[7] M. Okuyama, et al, Jap. J. Appl. Phys., 18, No.6 (1979)
[8] T.A. Rabson, et al, Ferroelectrics, 109, (1990)
[9] H.B. Meadows, Master Thesis, UCCS (1986)
[10] A.R. McGowan, Master Thesis, UCCS (1986)
[11] J.R. Kulkarni, Master Thesis, UCCS (1991)
[12] Westinghouse, Proposal for Ferroelectric Thin Films for I. C. (1990)
[13] M.R. Pinto, et al, PISCES II–B User's Manual, Stanford University (1985)

AD-P006 651

d.c. Leakage Currents in Ferroelectric Memories

J. F. Scott, B. M. Melnick, C. A. Araujo,
L. D. McMillan, and R. Zuleeg
Symetrix Corp., Colorado Springs, CO 80918 and
The University of Colorado, Boulder, CO 80309-0390
and Colorado Springs, CO 80933-7150

ABSTRACT

Experimental data on d.c. leakage currents in lead zirconate titanate thin films (210 nm) are presented. The data show a flat, ohmic response up to a threshhold of approximately 2.0 V, above which they satisfy a modified Child's Law, with a perfectly quadratic dependence: $I = aV^2$. This suggests that at 5 V operation the film behaves as a fully depleted device. The difficulty in distinguishing between Frenkel-Poole, Schottky emission, and true space-charge limited currents is briefly discussed.

INTRODUCTION

The presence of and effect of space charge in ferroelectric memories has been a recent source of controversy, with some authors maintaining that there is negligible space charge and others attempting to quantify large effects in PZT thin-film memories arising from space charges at grain boundaries and/or electrode interfaces. In the most extreme case of data presented publicly, the entire switched charge in some so-called ferroelectric memories arises from space charge, in our opinion; these are purely electret effects and can be simulated by a circuit model consisting of back-to-back diodes. Such electret devices can be useful (the US Army used electret-based field telephones as late as the Korean War), but they are not useful in high-speed RAMs.

We estimate in our PZT thin-film memories that 10-20% of the switched charge is electret-like space charge, primarily at the electrode-ferroelectric interface (not at grain boundaries, since the grains in thin PZT films are columnar and often extend from one electrode to the other); 80-90% of the switched charge is displacement current due to lattice polarization.

92-16115

There are three general ways to measure space charge effects quantitatively in ferroelectric thin films: The first is capacitance C(V) data. Measurement of C(V) is normally done via a slow ramp voltage (e.g., 0 to 10V in 10 sec) on which is superimposed a low-voltage oscillation (e.g., 0.1 V at 10 kHz). For reasons discussed in many textbooks, such as Hench and West,[1] the capacitance measured in this way is a complicated function of that at the high oscillation frequency (10 kHz) plus that of the main frequency in the Fourier transform of the ramp voltage (0.1 Hz). The latter measures primarily the response of the interfacial space charge. As a result, the capacitance measured by such C(V) testing is typically larger than that determined by hysteresis loops at 60 Hz or 1 kHz. The extra capacitance in the C(V) data, compared with the hysteresis data, is due to space charge and can permit the latter to be estimated quantitatively. The second technique to measure space charge is discussed by Okazaki.[2] He measures the switching time for switching ferroelectrics from + to - and then from - to +. At equal fields one of these processes will be faster than the other -- a phenomenon known as "waiting time" effect. However, if one compares the switching at equal times rather than equal fields, the difference between the + and - fields for equally fast response is just $2E_s$, where E_s is the space-charge field. Okazaki estimates for PZT that E_s is typically about 14 kV/cm. The third technique for measuring space charge is that of current-voltage measurements, I(V). The theory for these I(V) currents is reviewed briefly in the section below.

THEORY

A rather detailed theory of I(V) currents in insulators has been published recently by Hamann et al.[3] For the case of discrete trapping energies their results are reproduced in Fig. 1 below. The principal characteristics of the log-log plot for I(V) shown in this figure are, first, that it is ohmic (slope 1.0) below a certain voltage threshhold corresponding to the lowest trap energy (in eV). Above that threshhold there is a series of discrete steps (which in practice will probably be smeared out). And finally, above the highest trap energy, the I(V) dependence is perfectly quadratic (slope 2.0 on the log-log plot), corresponding to modified Child's Law behavior. It is very important to note in this graph that the $I = aV^2$ portion of the plot does <u>not</u> extrapolate to the origin. Hence, efforts to fit I(V) data to a formula such as $I = bV + aV^2$ will generally fail and are not based upon correct physics.

In Fig. 2 we show typical I(V) data for a 216 nm thick sol-gel PZT film of about 40/60 Zr-Ti composition. This is an undoped, virgin film (not fatigued). Its response is linear (ohmic) up to about 1.8V, after which a quadratic

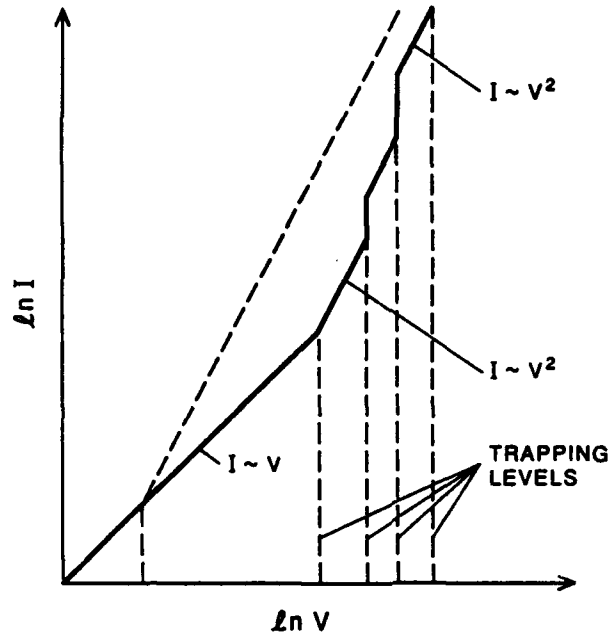


Fig. 1. Theoretical dependence of leakage current I versus applied d.c. voltage V. This log-log plot assumes a small number of discrete trap energies. Ref. 3.

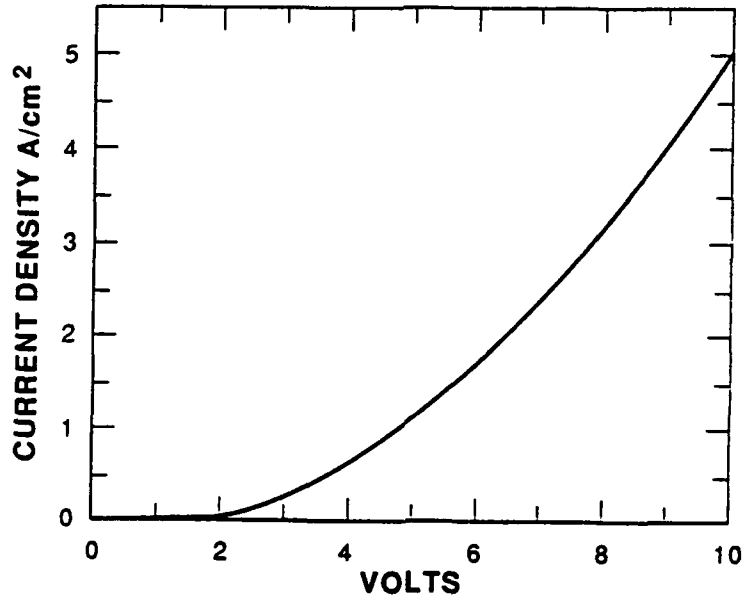


Fig. 2. Experimental dependence of d.c. leakage current I(V) for a 40/60 PZT film 210 nm thick. Note the break in slope at about 1.9 V.

dependence sets in. In Fig. 3 below we show the same data replotted on a log-log plot, which makes the linear and quadratic regimes more explicit. In all of the data sets like the ones shown here, 510 points (every 20 mV) were sampled; and the sampling time was about 40 ms per point.

It is useful to compare these results with those of other workers. Dey and Zuleeg[4] have shown by measuring I(T) temperature dependence for leakage currents that in similar sol-gel PZT films the current is characterized by Frenkel-Poole emission, with an activation energy of 1.44 eV at 5V operation. Some unpublished data were also taken at 10V, but no data were presented to permit accurate I(V) curves to be fitted to theoretically hypothesized dependences. As Sze emphasizes in his classic text, "For large space charge effect, the tunneling characteristic is found to be very similat to the Schottky-type emission."[5] In Fig. 4 we show the results of trying to fit one data set of I(V) for PZT to Schottky emission, Frenkel-Poole emission, and field (tunneling) emission. The Frenkel-Poole formula gives a reasonable fit over the entire range from 0 to 10V, but for all of our data sets, the modified Child's Law always gave a better fit; visual inspection of the data in Fig. 2 reveals a fairly sharp break in I(V) at just below 2V, above which a different (quadratic) dependence is manifest.

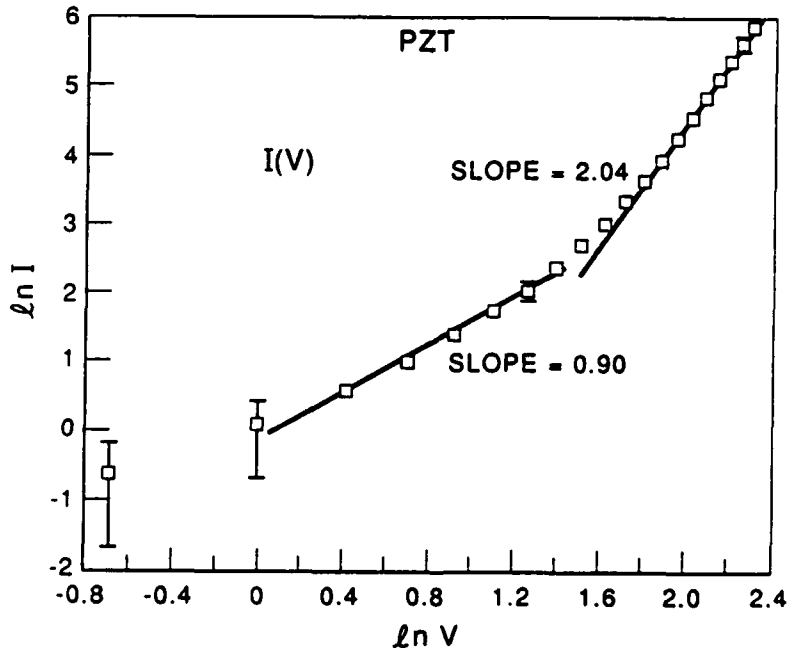


Fig. 3. Log-log plot of the I(V) data in Fig. 2, showing ohmic region below 2V, Child's Law above 2V.

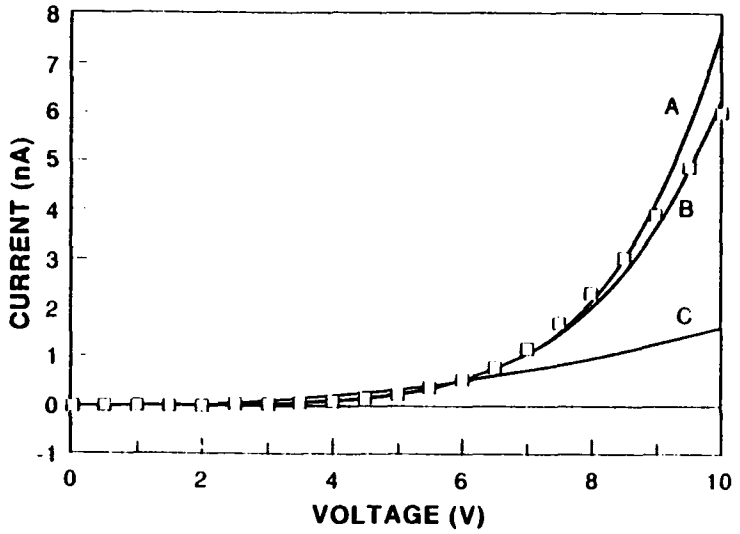


Fig. 4. Attempts to fit PZT d.c. leakage currents I(V) to Schottky emission (A), Frenkel-Poole emission (B), and field emission (C).

EXPERIMENT

Effect of Y^{3+} Doping

Doping with donors or acceptors should influence leakage current behavior. In PZT the primary d.c. conduction mechanisms involve both holes and oxygen vacancies.[6] When yttrium is doped into PZT it goes in as valence 3+ and is substitutional for both Pb^{2+} and Zr^{4+}/Ti^{4+}. As a result, it is somewhat self-compensating; but empirically we find that 1 to 2 molar % of Y will reduce the leakage current in typical sol-gel PZT films by about 100. This may be useful in extending lifetime and in particular minimizing failure due to d.c. breakdown.

Effect of Fatigue

The d.c. leakage currents in PZT films usually exhibit a remarkable change after repetitive polarization reversals: Increases of x100 in current density are noted after only 10^9 to 10^{10} cycles. We have proposed that this is due to a change in work function at the electrode-ferroelectric interface.[7,8] This hypothesis is supported by theoretical calculations[8] as well as the known change in work function for monolayer and sub-monolayer coverage of Pt [111] electrode surfaces by oxygen. Two independent tests of this hypothesis involve Auger spectroscopy (depth profiles of oxygen concentration) and the role of Ti electrodes, both of which are discussed below. The numerical value of work function change required to explain our data after 10^9 cycles is from 0.33 eV (before fatigue) to about 0.6-0.7 eV after. We ignore the role of space charge at grain boundaries (favored by Waser[9]) in our model because grains in PZT are columnar, often extending from one electrode to

the other.

Auger Data

In our most recent publication on this topic, Auger data were presented that support these ideas. Firstly, the oxygen concentration through the PZT film was shown to be highly non-uniform, with large vacancy concentrations near each electrode; although some of these vacancies will be compensated, such compensation will be incomplete, resulting in large space charge densities near the electrodes. Secondly, after fatigue this vacancy density increased. In specimens with one gold electrode and one platinum electrode the increase in oxygen vacancies was observed at only the Pt electrode. We believe that this is due to the porosity of some sputtered Pt electrodes. If the Pt were completely impervious to oxygen, the oxygen vacancy concentration in the PZT would rise as a function of fatigue but saturate at a value limited by the electrochemical steady-state. In this case we might expect the switched charge or remnant polarization P_r to decrease as a function of switching cycles, but to reach asymptotically a modest, non-zero value as cycles go to 10^{15}. However, if oxygen is continuously lost through a porous Pt electrode, the electrochemical reactions will proceed until extremely large densities of oxygen vacancies are produced, perhaps resulting in dendritic growth of conducting pathways in the PZT film. Both of these kinds of behavior have been reported in different PZT memories. We believe that the "good" memory films have impervious Pt and yield finite remnant polarizations without failure after long periods of polarization-reversal cycling; the "bad" films that "crash" to zero switched charge are probably losing oxygen through porous electrodes.

Effect of Titanium Electrodes

Many laboratories add a thin (20 - 50 nm) layer of Ti between the thick (200 nm) Pt electrode and the silicon IC. This improves mechanical adhesion and prevents peeling of the Pt off the silicon. Under optimum conditions this is a good processing step. However, if the Pt is porous, as discussed above, the Ti will worsen the failure mechanism by acting as an electrochemical sink for the diffusing oxygen. Rutile (TiO_2) can form as a reaction product at the Ti/Pt interface and thus enhance the generation rate for oxygen vacancies, causing failure.

HYPERSONIC SWITCHING

The general aim of the present study is to analyze effects that might influence the switching time and current. In particular, space charge effects do this by reducing internal electric fields and/or pinning domain walls. Therefore

it is interesting to end this paper with a consideration of the criteria involved in determining the ultimate switching speed in ferroelectric memories. Three different groups at this meeting have shown that the fundamental switching time in PZT is about 1.0 ns; Dey, Larsen, and Gundel have[9] independently measured this time via different techniques. What limits faster switching? In this section we examine the new results by Shur[10] and apply them to this practical question.

A long-standing controversy in ferroelectric switching is whether domain walls[11] can achieve supersonic or even hypersonic velocities. Evidence based upon I(t) transient responses to applied voltages definitely show that the displacement current peaks (in high fields) at a time short compared with the transit time for longitudinal or transverse sound waves.[12] In one experiment there was an abrupt change of apparent domain velocity as applied voltage was increased to a threshhold where v(domain) = v(sound).[13] In another experiment only a smooth increase in v(domain) was noted with no threshhold behavior.[14] It is impossible, however, to infer from such data that domain velocities actually exceed the speed of sound; it is equally likely, a priori, that there is instead simply extensive homogeneous or inhomogeneous nucleation throughout the ferroelectric, with only slow domain wall motion of individual domains.

In the present volume the work of V. Shur shows[10] that in lead germanate, even at very high fields E, the individual domain wall speeds never exceed v(sound). What happens instead is coherent, correlated domain nucleation in front of the leading edge of an existing domain wall. We believe that this is triggered by the Coulomb field at the domain wall. In fact, the distance from the existing wall at which nucleation occurs is a direct measure of the screening length in the ferroelectric.

The net result is that the displacement current I(t) travels across the ferroelectric not at the group velocity of the soliton-like domain wall [ca. v(sound)], but instead at the phase velocity of the correlated nucleation front, which may be much greater than v(sound).

One may contrast this situation with the case of magnetic domains, where Kreines' group in Moscow has demonstrated[15] directly that when magnetic field B is increased such that v(magnon) = v(sound), a Cerenkov-like emission of acoustic phonons occurs (in a cone whose angle is related to v[magnon]/v[sound]). In the magnetic case no coherent nucleation of domains occurs. Why do ferroelectrics not exhibit this Cerenkov emission of acoustic phonons as v(domain) → v(sound)? And why do magnets not exhibit correlated nucleation? The answer, we think, is that magnetic domain walls are spatially extended and have no Coulomb field (there are no magnetic monopoles!). Therefore, the correlated nucleation in front of a moving domain wall, which is apparently energetically favored in ferroelectrics, is inoperative in magnets.

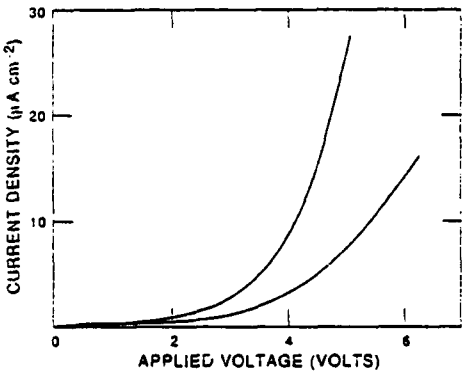


Fig. 5. Change in space-charge current I(V) as work function mismatch varies from 0.33 eV to 0.66 eV (Ref. 8).

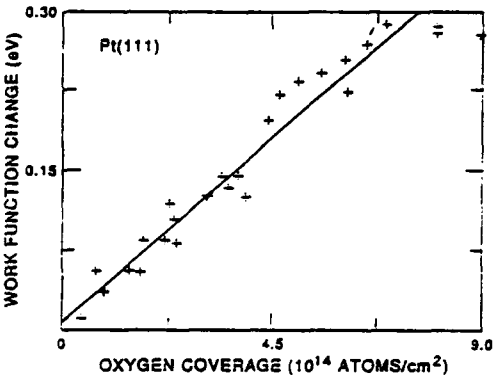


Fig. 6. Work function mismatch change at Pt [111] electrode interface with oxygen coverage (Ref. 16).

SUMMARY

We have presented some d.c. leakage current data I(V) on PZT (40/60) at ambient temperatures, together with models to fit the data. The data imply a dominance of space-charge limited current (modified Child's Law) above 2 V. However, it is not trivial to separate out contributions from Schottky and Frenkel-Poole emission. In the present system the current characteristics are modified by the electrochemical generation of oxygen vacancies that accumulate near the electrodes. This entails a concommitant release of oxygen. We believe that the oxygen ions change the work function at the Pt electrode surface (by about 0.3 eV after 10^{10} cycles); this modifies the height and shape of the Schottky barrier there. At the same time, the oxygen vacancies left behind contribute to the space charge. Therefore, for this particular model, it is impossible to separate the Schottky emission characteristics from the space-charge current characteristics; one necessarily entails the other. The particular I(V) formalism we have employed in the space-charge limited case (modified Child's Law) actually assumes ohmic contacts. In view of the preceding comments about Schottky-barrier formation at the Pt -- PZT interface, this is not correct. A correct, but more complicated description will incorporate simultaneously the change in Schottky barrier with oxygen accumulation, and the change in space charge with oxygen vacancy accumulation nearby.

Finally, some attempts have been made to explain the role of correlated domain nucleation at high fields in ferroelectric memories, to resolve an old controversy concerning the maximum switching speed in ferroelectrics. If space charge problems are minimized in PZT memories, by doping (e.g, Y^{3+}) or by optimized electroding, this is the speed which can be expected in thin-film RAMs. In PZT it is apparently about 1.0 ns.

REFERENCES

1.) L. L. Hench and J. C. West, Principles of Electronic Ceramics (Wiley, New York, 1990).
2.) K. Okazaki, H. Igarishi, K. Negata, and A. Hasegawa, Ferroelectrics 7, 153 (1974).
3.) C. Hamann, H. Burghardt, and T. Frauenheim, Electrical Conduction Mechanisms in Solids (VEB, Berlin, 1988).
4.) S. Dey and R. Zuleeg, Ferroelectrics 109, 1643 (1990).
5.) S. Sze, Physics of Semiconductor Devices (Wiley, New York, 1981).
6.) R. Waser, T. Baiatu, and K.-H. Hardtl, J. Am. Ceram. Soc. 73, 1645, 1654, 1663 (1990).
7.) J. F. Scott, B. M. Melnick, C. A. Araujo, L. D. McMillan, and R. Zuleeg, J. Appl. Phys. (in press, May 1, 1991).
8.) R. H. Tredgold, Space Charge Conduction in Solids (Elsevier, Amsterdam, 1966), pp.75-79.
9.) S. Dey, this volume; P. Larsen, this volume; H. Gundel, this volume.
10.) V. Shur, this volume.
11.) E. Fatuzzo and W. J. Merz, Ferroelectricity (North-Holland, Amsterdam, 1967).
12.) H. L. Stadler, J. Appl. Phys. 29, 1485(1958).
13.) B. Binggeli and E. Fatuzzo, J. Appl. Phys. 36, 1431 (1965).
14.) H. L. Stadler and P. J. Zachmanidis, J. Appl. Phys. 34, 3255 (1963).
15.) S. O. Demokritov, A. I. Kirilyuk, N. M. Kreines, V. I. Kudinov, V. B. Smirnov, and M. V. Chetkin, Pis'ma Zh. Eksp. Teor. Fiz. 48, 267 (1988).
16.) J. Nowotny and N. Sloma, "Work Function of Oxide Ceramic Materials," Surface and Near-Surface Chemistry of Oxide Materials, edited by J. Nowotny and L. C. Dufour (Elsevier, Amsterdam, 1988).

ACKNOWLEDGMENTS

The work at the University of Colorado was supported in part by NSF grant DMR89-18900 and by ARO grant DAAL-03-90-G0002; the work at Symetrix was supported by DARPA and by the US Naval Support Center (Crane, IN).

AD-P006 652

PREPARATION OF $PbTiO_3$ THIN FILMS BY LASER ABLATION

MASANORI OKUYAMA, TADAYUKI IMAI and YOSHIHIRO HAMAKAWA
Department of Electrical Engineering,
Faculty of Engineering Science, Osaka University,
Machikaneyama-cho 1, Toyonaka, Osaka 560

Abstract $PbTiO_3$ thin films have been deposited on Si or Pt substrates by laser ablation method using ArF excimer or YAG laser. Species evaporated in the vacuum have been studied by mass analysis, and the measured Pb and Ti are not oxidized. Spacial distributions of the deposition rates on the substrate have been studied as a parameter of laser fluence. The excimer laser gives better films than the YAG. Perovskite films have been obtained at substrate temperature ~ 400 ℃ and appropriate ambient O_2 gas pressure.

INTRODUCTION

In recent years, much attention has been gathered on ferroelectric thin films from viewpoins of their wide application to electronic devices such as nonvolatile memory, infrared sensor, ultrasonic sensor, low- threshold-voltage electroluminescent device and optoelectronic devices. Especially integrated nonvolatile memory has been developed remarkably by combining Si LSI with Pb-included perovskite films such as PZT, PLZT and $PbTiO_3$. $PbTiO_3$ shows good pyroelectric and piezoelectric properties as well as large D-E hysteresis and large dielectric constant. Ferroelectric property of $PbTiO_3$ is much better in c-axis direction than in the others as crystalline direction having large dielectric polarization is c-axis. The conventional deposition methods such as sputtering, CVD and chemical processing[1-3] damage the substrates as substrate temperature during the deposition is very

92-16116

high(~ 600 ℃) and particles having high kinetic energy impinge on growing film. Therefore, c-axis-oriented $PbTiO_3$ films are desired to be prepared at low temperature without the damage. Recently, laser ablation method has been exploited to prepare high-Tc superconducting oxide films and given good films[4-6]. The composition of the films prepared by the laser ablation is very close to that of the target, and the deposition apparatus is very simple. Moreover, it is expected that the crytstalization can occur at relatively low substrate temperature because molecules ablated from the target are highly excited. Quite recently, this laser ablation method has been also used for preparation of ferroelectric films[7-12]. In this paper, we have studied a series of experimental data of the laser ablation of $PbTiO_3$ and characterization of the prepared films.

DEPOSITION OF $PbTiO_3$ FILM

Lasers used for the ablation are Nd:YAG laser (1064nm) or ArF excimer laser (193nm). The target is $PbTiO_3$ ceramic disk of 8cm in diameter and 6mm thick, and contains excess PbO of 10 wt.%. The schematic view of the deposition apparatus is illustrated in Fig.1. Substrates of Si wafer or Pt sheet were set on the sample holder hung over the target, and the substrate face is parallel to the target face. The substrate temperature

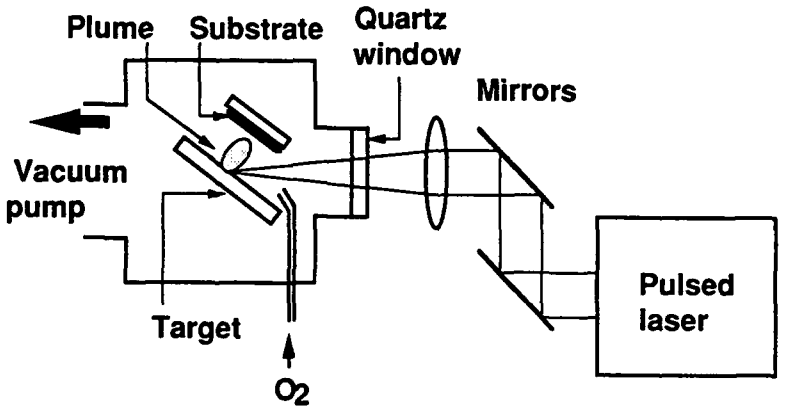


FIGURE 1. Schematic view of apparatus for laser ablation of PbTiO3.

TABLE I. Deposition condition of $PbTiO_3$ thin films

Target	$PbTiO_3$ ceramic disk containing excess PbO of 10wt.%
Substrate	Si wafer, Pt sheet
Substrate temperature	R.T. ~ 600 ℃
Gas pressure	$10^{-1} \sim 10^{-5}$Torr
Laser	YAG(1064nm), Excimer(193nm)
Repetition frequency	0.03 , 10Hz
Total shot number	100 , 5,000 times
Beam size	2.5 × 0.5 , 0.10 × 0.3cm^2
Energy	2.8 ~ 4 , 0.025 ~ 0.1J/shot
Fluence	0.5 ~ 4.0J/(cm^2 · shot)
Target-substrate distance	~ 3 , 1.2cm

during the deposition, Ts, was monitored by a thermocouple attached to the holder, and was controlled from room temperature to 600 ℃ by a heater in the holder. The chamber was evacuated to pressure of ~ 10^{-5}Torr before O_2 gas was introduced up to the pressure lower than 10^{-1}Torr. Detailed deposition condition is shown in Table I. Laser fluence(energy density) defined as energy per shot divided by irradiated area was 0.5-4.0J/(cm^2 · shot) although Otsubo et al. used ArF laser at 6.0J/(cm^2 · shot)[7]. The laser beam was focused onto the target in the vacuum chamber through a quartz lens and a window. Luminous plume was extended from the irradiated point on the target in the direction vertical to the target face. After the deposition, the film was cooled down to room temperature naturally. Film thickness was measured by a stylus instrument(DEKTAK) for the film striped by etching or deposition with a mask.

The ablated molecules were monitored by a quadru-pole mass analyzer (ULVAC MSQ-400) measuring species of mass-charge ratio of 1-400, when the ArF excimer laser was used for the deposition. The tube of the analyzer was connected with the chamber and was directed to the irradiated point at an angle of incidence of about 63 ° to the target face. A peak is found at m/e=48(Ti) in the spectra, but there are

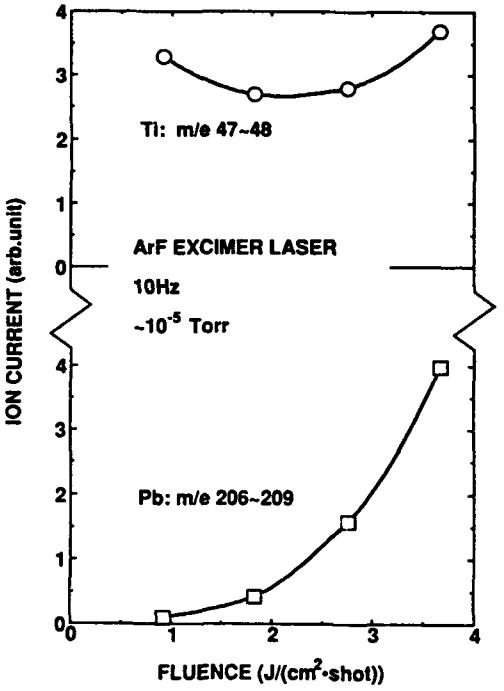


FIGURE 2. Amounts of Pb and Ti atoms evaporated by ArF laser as a function of laser fluence, measured by quadru-pole mass analyzer.

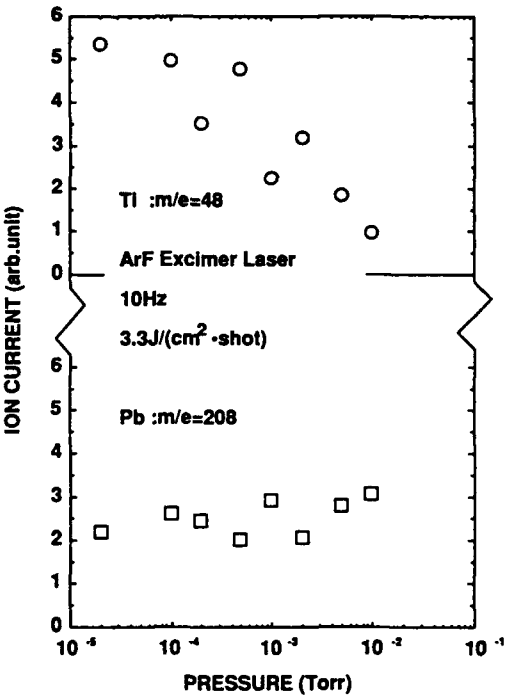
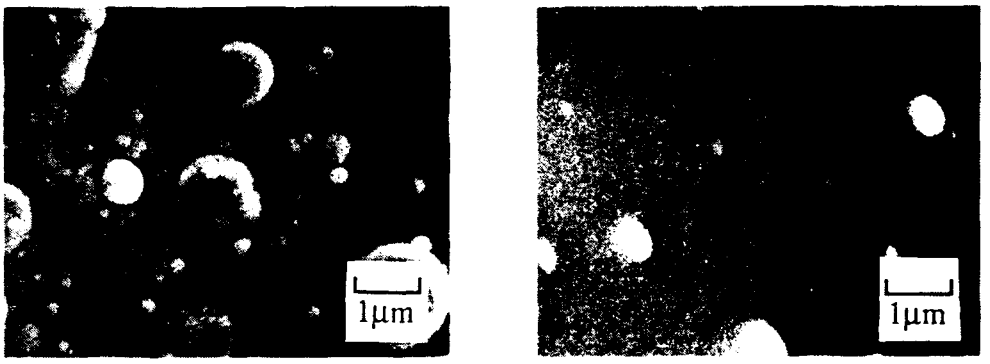


FIGURE 3. Amounts of Pb and Ti atoms evaporated by ArF laser as a function of O_2 pressure measured by quadru-pole mass analyzer.

no peaks at m/e=64(TiO) and 80(TiO_2) even at oxygen pressure 10^{-2}Torr. So the Ti is not oxidized in the vapor. Peaks are observed at some m/e of Pb isotopes, but there are no peaks corresponding to PbO and PbO_2 at 10^{-2}Torr. So Pb is not oxidized in the vapor too. Figure 2 shows amounts of Pb and Ti atoms as a function of fluence of the ArF excimer laser. The amount is a peak value of the spectrum. The amount of lead atoms increases very much with increase of the laser fluence, while that of titanium atoms doesn't change so much. These results are inconsistent to the general fact that the film composition is close to that of the target in the laser ablation, and so detailed study is required more. Figure 3 shows amounts of Ti and Pb as a function of O_2 pressure. Ti decreases abruptly with increasing O_2 pressure, but Pb is almost constant. Mass of Ti(48) is a little close to mass of oxygen



(a) (b)

FIGURE 4. SEM micrographs of the thin films deposited on Si using (a) YAG laser and (b) ArF excimer laser.

molecule(32) in comparison with that of Pb(208), and so momentum exchange induced by impact with O_2 is remarkably larger in Ti than in Pb. Therefore, Ti is easily scattered in wider direction and amount of Ti measured by mass spectrometer is reduced in high pressure region.

Figures 4 (a) and (b) show the SEM micrographs of the surface of the films deposited at about 10^{-5}Torr with the YAG laser and the ArF excimer laser, respectively. The fluence of the YAG laser and the ArF laser on the target is 2.8J/(cm^2·shot) and 3.4J/(cm^2·shot), respectively. There exist many droplets less than a couple of micrometers in the films deposited by both the lasers. The droplets are apparently fewer on the sample of the excimer laser than on one of the YAG. Better films can be prepared with the laser of shorter wave length than the YAG. This reason might be due to highly excited state of the ablated particles and large absorption coefficient of the target material in the case using ArF laser. So the experiments using the excimer laser are mainly described below.

CHARACTERIZATION OF DEPOSITED FILM

The angular dependence of quantity of the molecules ablated from the target is characteristic of the laser ablation, related to the shape of the

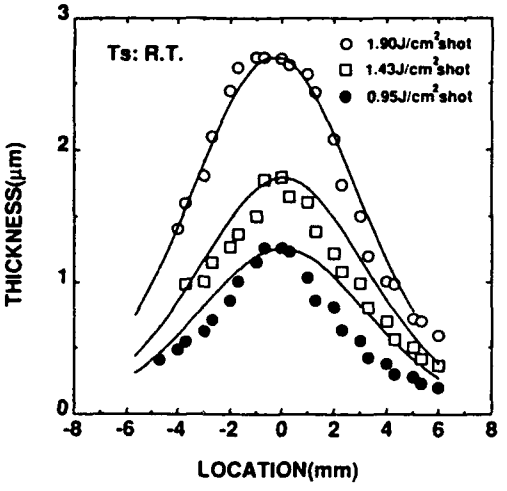


FIGURE 5. Spacial distribution of thickness of thin films deposited by ArF laser

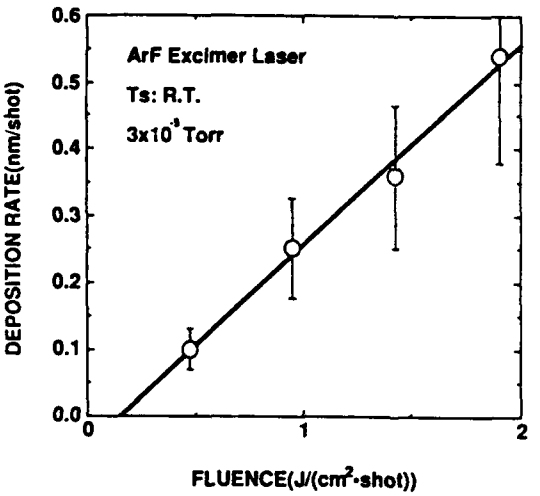


FIGURE 6. Deposition rate as a function of laser fluence deposited by ArF laser.

plume. The film thickness varies very much along with the film surface. Examples of spacial distribution of the film thickness on the substrate are shown in Fig.5. The films were deposited on Si at room temperature when the target was irradiated 5,000 times by the excimer laser. The laser spot size and fluence on the target was 3 × 1mm^2 and 0.95-1.90 J/(cm^2·shot), respectively. The solid lines in Fig.5 are the values calculated from the angular distribution function of $\cos^{11}\theta$ (θ ; deposition angle) which was obtained empirically in the laser deposition of YBCO thin films by Venkatesan et al[6]. The measured values of thickness of the film deposited at 1.90J/(cm^2·shot) fit well with the calculated values, but show a little discrepancy with the calculated when the fluence decreases. The maximum thickness is obtained at the point of the substrate vertical to the irradiated spot of the target. The maximum values normalized by number of the shots, those are defined as deposition rates, are plotted against the laser fluence in Fig. 6. The deposition rate varies linearly with the laser fluence in the range of fluence of 0.5-2.0J/(cm^2·shot), having a threshold fluence.

X-ray diffraction measurement(XRD) has been carried out using Cu-K α at room temperature. Figure 7 shows X-ray diffraction

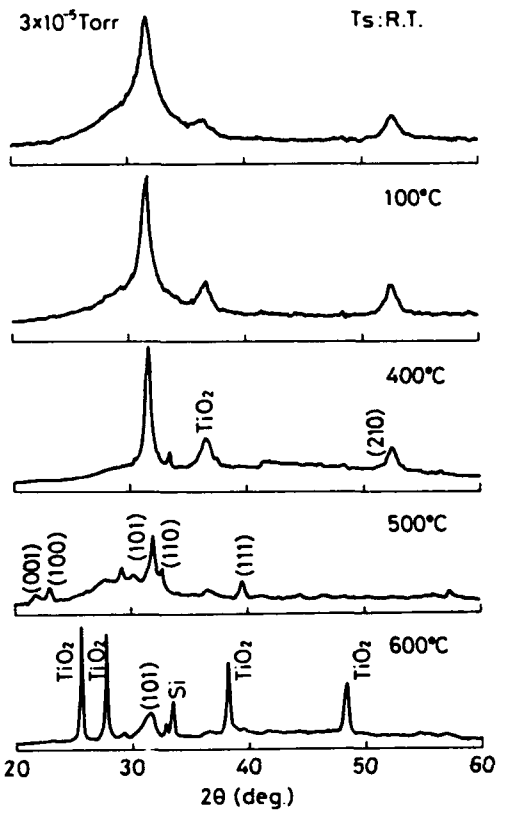


FIGURE 7. XRD patterns of films deposited by ArF laser as a parameter of substrate temperature. Gas pressure was $\sim 10^{-5}$Torr without ambient O_2.

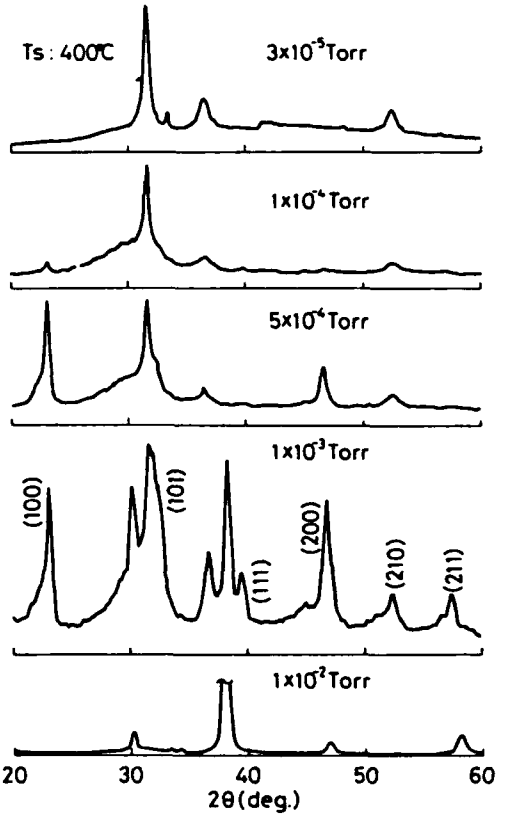


FIGURE 8. XRD patterns of films deposited by ArF laser as a parameter of O_2 gas pressure. Substrate temperature was 400 °C.

patterns of the films grown on Si substrates at several temperatures. The fluence was 1.7J/(cm^2·shot), and the total shot number was 5,000. The gas pressure was $\sim 10^{-5}$Torr and no O_2 gas was introduced. The patterns are not so different from each other in the samples grown between room temperature and 400 °C. Two peaks in the patterns correspond to (101) and (211) perovskite structure, and are also very close to the peaks of lead crystal. F.W.H.M. of the (101) peak decreases with rising temperature and has the minimum value in the film deposited at Ts $\sim$ 400 °C. Whether the films deposited at substrate temperatures lower than 400 °C with no O_2 ambient are $PbTiO_3$ and/or

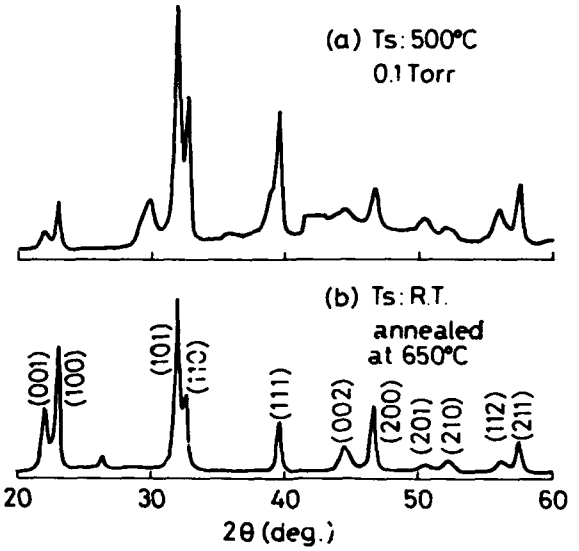


FIGURE 9. XRD patterns of the films (a) deposited at 500 °C and 0.1Torr on Si by ArF laser , and (b) deposited on Si at room temperature and $\sim 10^{-5}$ Torr and annealed at 650 °C for 3hours in O_2 ambient.

lead could not be clearly identified. But some information about atomic bonds in the films was obtained from X-ray photo-electron spectroscopy (XPS) measurement. Binding energies for Pb_{4f} and Ti_{2p} peaks of the deposited films were proven to be closer to the energies of PbO and TiO_2 rather than those of Pb and Ti, respectively. Therefore, the probability still remains that grains of $PbTiO_3$ crystal exist in the film at low substrate temperature although sensitive depth in XPS measurement is very small. The other peaks, e.g. (001) peak, appear above Ts $\sim$ 500 °C and peaks for TiO_2 are also found at Ts $\sim$ 600 °C. Lead might reevapolate from the film at high temperature. The patterns of the films grown on Pt substrates are similar to these on Si. The difference of these two substrate materials is that obvious $PbTiO_3$ perovskite phase is obtained in the films deposited at rather lower temperature on Pt substrates than on Si ones. XRD patterns in Fig. 8 show dependence of the crystallinity in O_2 atmosphere. The deposition was done at 400 °C , the target was lighted 5000 times and the fluence was 1.7J/(cm^2·shot). Non-oriented $PbTiO_3$ perovskite film is obtained at 1x10^{-3}Torr. The film deposited at 500 °C and 0.1Torr on Si shows good

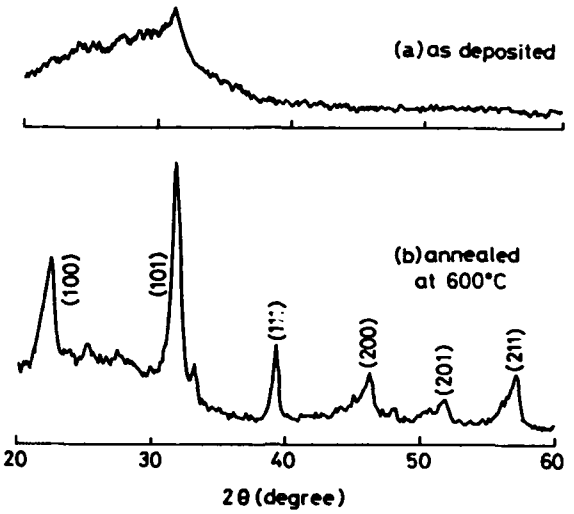


FIGURE 10. XRD patterns of the films (a) deposited at 500 °C and $\sim 10^{-5}$Torr on Si by YAG laser , and (b) annealed at 600 °C for 3hours in O_2 ambient.

crystalline property. The X-ray diffraction pattern of this film is shown in Fig. 9(a). Moreover, crystalline property of the films deposited even at room temperature in low pressure could be improved by annealing. Figure 9(b) shows X-ray diffraction pattern of the film which was deposited at room temperature and $\sim 10^{-5}$ Torr and was annealed at 650 °C for 3hours in O_2 ambient. The annealing at 400 °C improves crystalline state of the film deposited at 400 °C. The films deposited by YAG laser show the similar tendency of the crystalline state to that by ArF laser. The crystalline state of the film deposited by YAG laser is improved with increasing the substrate temperature and the annealing. Figure 10 shows XRD patterns of the films (a) deposited at $\sim 10^{-5}$ Torr and room temperature and (b) annealed at 600 °C for 3 hrs.

SUMMARY

$PbTiO_3$ thin films were prepared by laser ablation method using ArF and YAG lasers. Perovskite phase has been obtained in the film deposited in O_2 ambient of 1×10^{-3}Torr at substrate temperature of 400 °C. The annealing treatment at 650 °C is also effective to obtain

perovskite films. The amount of lead atoms emitted from the target is very much dependent on the laser fluence although the laser ablation method is known as a deposition method conserving the stoichiometric ratio. On the other hand, the amount of evaporated Ti changes a little with change of the fluence. More detailed experiments are needed to know behavior of the ablation from the target, reaction on the substrate and deposition of the film in order to obtain good quality $PbTiO_3$ thin film.

ACKNOWLEDGEMENTS

The authors wish to thank Dr. M. Nakatsuka, Dr. H. Daido, Mr. Soh and Mr. Asahara of Institute of Laser Engineering of Osaka University for their support to use YAG laser. The authors are indebted to Mr. C. Sada, Dr. K. Inoue, and H. Tabata and O. Murata for their of help.

REFERENCES

1) M. Okuyama and Y. Hamakawa: Ferroelectrics, 63 (1985) 243.
2) K. Iijima, Y. Tomita, R. Takayama and I. Ueda: J. Appl. Phys., 60 (1986) 361.
3) K. D. Budd, S. K. Dey and D. A. Payne: Br. Ceram. Proc., 36 (1985) 107.
4) D. Dijkamp, T. Venkatesan, X. D. Wu, S. A. Shaheen, N. Jisrawi, Y. H. Min-Lee, W. L. Mclean and M. Croft: Appl. Phys. Lett., 51 (1987) 619.
5) S. Witanachchi, H. S. Kwok, X. W. Wang and D. T. Shaw: Appl. Phys. Lett., 53 (1988) 234.
6) T. Venkatesan, X. D. Wu, A. Inam and J. B. Wachtman: Appl. Phys. Lett., 52 (1988) 1193.
7) S. Otsubo, T. Maeda, T. Minamikawa, Y. Yonezawa, A. Morimoto and T. Shimizu: Jpn. J. Appl. Phys., 29 (1990) L133.
8) R. Ramesh, A. Inam, W. K. Chan, B. Wilkens, D. L. Hart and J. M. Tarascon, 3rd Int. Symp. on Integrated Ferroelectrics, Colorado Springs, 1991.
9) H. Buhay, S. Sinharoy, W. H. Kasner, M. H. Francombe, B. K. Park, W. J. Takei, N. J. Doyle, D. R. Lampe and E. Stepke, 3rd Int. Symp. on Integrated Ferroelectrics, Colorado Springs, 1991.
10) D. Roy, S. B. Krupanidhi and J. P. Dougherty, 3rd Int. Symp. on Integrated Ferroelectrics, Colorado Springs, 1991.
11) K. S. Grabowski, R. E. Leuchtner, J. S. Horwitz and D. B. Chrisey, 3rd Int. Symp. on Integrated Ferroelectrics, Colorado Springs, 1991.
12) R. E. Reuchtner, K. S. Grabowski, J. S. Horwitz and D. B. Chrisey, 3rd Int. Symp. on Integrated Ferroelectrics, Colorado Springs, 1991.

AD-P006 653

APPLICATION OF METAL ALKOXIDES IN THE SYNTHESIS OF OXIDES

M.I.YANOVSKAYA, E.P.TUREVSKAYA, V.G.KESSLER,
I.E.OBVINTSEVA, N.Ya.TUROVA
L.Ya.Karpov Institute of Physical Chemistry, Obukha St.,10,
103064, Moscow, USSR.
Department of Chemistry, Moscow State University,
Lenin Hills, 117234, Moscow, USSR.

Abstract. Powders and thin films of the following simple and complex oxides have been obtained from metal alkoxides: $M^{II}TiO_3$ (M=Mg, Ca-Ba), $MM_{1/3}B_{2/3}O_3$ (M=Sr,Ba,M'=Mg-Zn; B=Nb,Ta); $MNbO_3$(M=Li,Na); $ZrTiO_4$; $PbTiO_3$; PZT, PLZT-materials; M_2BO_4 (M=Li,Na; B=Mo,W), Bi_2BO_6(B=Mo,W); Li_xWO_3,WO_3, MoO_3, Bi_2O_3-WO_3(solid solutions), $YFeO_3$,$Y_3Fe_5O_{12}$; $YBa_2Cu_3O_{7-x}$; $Bi_2Sr_2CaCu_2O_x$; $Bi_2Sr_2Ca_2Cu_3O_x$. For synthesis of metal alkoxides and solutions containing two or more elements electrochemical technique (the anodic dissolution of metals in alcohols) has been used. Analysis of different examples emphasises that considerable attention in sol-gel chemistry of oxides should be paid to decomposition of $M(OR)_n$ with elimination of ether and formation of oxoalkoxides, containing M-O-M' bonds - the basis of future oxide phases.

The present report concerns the works in the field of sol-gel technology with application of metal alkoxides as precursors which have been performed in Moscow since 1978 in two scientific centres - in Karpov Institute of Physical Chemistry and in the Moscow State University. These works are a natural continuation of the studies of chemistry of alkoxides which have been carried out at the Chair of Inorganic Chemistry of the Moscow State University since early sixties.

It is well known that hydrolysis of metal alkoxides is nowadays extensively used for preparation of oxides in the form of fine powders, glasses, films. The advantages of this method (high quality of oxide powders, their purity, homogeneity, dispersity, as well as certain versatility and ease of processing) determine special interest to this route of preparation of oxides. We were first of all concerned with the synthesis of complex oxide materials which have different applications in the form of powders and thin films. Synthesis of the following materials has been studied: $M^{II}TiO_3$(M=Mg,Ca-Ba); $MM_{1/3}B_{2/3}O_3$ (M=Sr,Ba,M=Mg,Zn; B=Nb,Ta); $MNbO_3$(M=Li,Na);$ZrTiO_4$, $PbTiO_3$; PZT, PLZT-materials; M_2BO_4(M=Li,Na;B=Mo,W), Bi_2BO_6(B=Mo,W); Li_xWO_3; Bi_2O_3-WO_3 (solid solutions); $YFeO_3$; $Y_3Fe_5O_{12}$, WO_3; MoO_3; TiO_2-RuO_2; $YBa_2Cu_3O_{7-x}$; $Bi_2Sr_2CaCu_2O_x$; $Bi_2Sr_2Ca_2Cu_3O_x$ [1-9]. The properties of the synthesized materials were compared with the properties of the same materials

92-16117

obtained by traditional techniques (e.g. precipitation from aqueous solutions) in order to find the cases were application of metalalkoxides proved really fruitful.

In all the cases formation of a complex oxide material includes three stages: 1) Preparation of mixed complex solution in organic solvent which includes all the elements of the future oxide composition; 2) Hydrolysis of the solution; 3) Heat treatment of the hydrolysis product.

It is quite clear by now that future successful application of metal alkoxides in the synthesis of oxides is impossible without comprehensive understanding of all chemical processes which ensure transformation from alkoxides to oxides.

The first problem concerns synthesis of metal alkoxides and their solutions. Usually transition metal alkoxides are synthesized by the exchange reaction [10]:

$$MCl_n + nROH + nNH_3 \longrightarrow M(OR)_n + nNH_4Cl$$

This method however has got many disadvantages: poor yields, environmental contaminations, absence of universal technique for synthesis of different alkoxides. Although it has been also used in our laboratory practice, for large scale syntheses of transition metal alkoxides highly efficient electrochemical technique which gives no wastes or environmental contaminations has been used [11-14]:

$$M + ROH \xrightarrow{\text{electrosynthesis}} M(OR)_n + nH_2$$

M = Y,Ln,Ti,Zr,Sn,Nb,Ta,Cr,Mo,W,Ni,Ca,Cu

The electrochemical technique proves especially fruitful for preparation of solutions containing two or more alkoxide derivatives. Solutions obtained by this way (e.g. the methoxyethoxide Y-Ba, Zr-Ti, Zr-Y, Ba-Zn-Nb, Ba-Zn-Ta solutions) demonstrate unique properties as precursors for thin films technology. For the metals which undergo reduction in the course of electrosynthesis the improved exchange technique has been suggested:

$$MCl_n + nNaOR \longrightarrow M(OR)_n + NaCl$$

which allows us to obtain alkoxides with quantitative yields [15].

In order to optimize the conditions for preparation of the alkoxide solution, to chose the proper alkoxide derivative and the organic solvent solubility diagrams for the tri-component systems $M(OR)_n$-$M(OR)_m$-L (L=ROH, ArH, THF) have been studied [16-20]. In many cases the knowledge of these data allowed us to simplify the technique for preparation of the complex alkoxide solution. For instance, drastic enhancement of the solubility of Mg and Al alkoxides which is due to formation of complexes in solutions allows us to obtain

solutions with the composition of $Mg[Al(OEt)_4]_2$ directly by dissolution of the two metals in EtOH without application of any catalysts (Fig.1). The spinel films

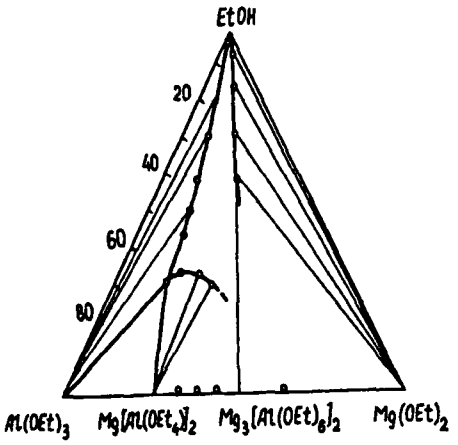


Fig.1 Solubility diagram at 20°C in the system Mg(OEt)2-Al(OEt)3-EtOH

$MgAl_2O_4$ may be obtained directly from these solutions. On the other hand $Mg[Al(OEt)_4]_2$ which is volatile even at atmospheric pressure is especially convenient precursor for the CVD of spinel films [21].

Solutions applied for synthesis of a series of perovskites were obtained by direct interaction of metals with alcoholic solutions of transition metal alkoxides (it is noteworthy that the "acidic" alkoxide plays the role of a catalyst, in its absence Mg or alkaline metals interact with alcohols very slowly):

$$Ba + Ti(OR)_4 + ROH \longrightarrow \text{"}BaTi(OR)_6\text{"} + H_2$$

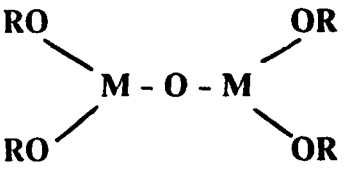
$$Ba + 1/3Mg + 2/3Ta(OBu)_5 + ROH \longrightarrow \text{"}BaMg_{1/3}Ta_{2/3}(OR)_6\text{"} + H_2$$

$$Ba + 1/3Mg + 2/3Nb(OBu)_5 + ROH \longrightarrow \text{"}BaMg_{1/3}Nb_{2/3}(OR)_6\text{"} + H_2$$

R = Et, Pr^i, Bu, $CH_3OC_2H_4OH$

Recently different authors suggested that decomposition of metal alkoxides with elimination of ether may take place at low temperature [22-24]:

$$M(OR)_n \xrightarrow{-R_2O} MO_x(OR)_{n-2x}$$



This reaction is especially characteristic in the case of simple and double alkoxides of molybdenum and tungsten. For instance interaction of sodium and tungsten or molybdenum ethoxides at low temperature results in precipitation from the solutions of highly crystalline Na_2WO_4, $NaMoO_4$ respectively in accordance with the following reactions:

$$2NaOEt + MoO_2(OEt)_2 \xrightarrow{20^oC} Na_2MoO_4 + Et_2O$$

$$2NaOEt + WO(OEt)_4 \xrightarrow{20^oC} Na_2WO_4 + Et_2O$$

Crystallization of complex oxide from solutions of alkoxides in organic solvent is a surprising fact and may be regarded as the limiting case of the above reaction (complete loss of the OR groups).

By now it is apparent that this type of decomposition which leads to the partial loss of OR is characteristic of transition metal alkoxides and usually occurs to a certain extent in their alcoholic solutions (and even sometimes in pure alkoxides on prolonged storage). Alongside with hydrolysis this reaction is responsible for the formation of M-O-M bridges in solutions, thus being a path to formation of oxo-products, the basis for the future oxide phases. Naturally this reaction plays an important role in sol-gel technology, although its significance has not yet been completely realized.

In the numerous techniques for preparation of complex oxides the alkoxide solutions are being refluxed for some hours before hydrolysis. Some authors explain the necessity of this procedure by the formation of complex metal alkoxides in the solutions [25,26]. Now it is clear that refluxing fastens reaction of decomposition with elimination of ether and formation in solution of oligomeric oxoalkoxides, continuation of refluxing sometimes leads to precipitation of oxoalkoxide polymers.

Another way of formation of oxoalkoxides lies in oxidation of $M(OR)_{n-x}$ derivatives of the lower oxidation states. The latter are formed on reduction of alkoxides by hydrogen evaluated in the course of interaction with active metals or in electrochemical processes [27]:

$$Ti(OR)_4 + [H\uparrow] \longrightarrow Ti(OR)_3 \xrightarrow{O_2} (OR)_3Ti\text{-}O\text{-}Ti(OR)_3$$

This reaction explains the higher extent of formation of oxo-complexes in the case of preparation of the complex solution by direct dissolution of metals in comparison with solutions obtained by mixing of simple alkoxides:

$$M(OR)_n + M(OR)_m \longrightarrow M(OR)_n \cdot M'(OR)_m$$

$$M + M'(OR)_m + ROH \longrightarrow MM_yO_x(OR)_{m+n-2x} + H_2$$

Among complex oxide materials studied by us special attention has been paid to $BaTiO_3$. After the classical work of Mazdiyasni [28] concerning synthesis of $BaTiO_3$ from alkoxides this method has been discussed often, however results seemed somewhat contradictory.

Solubility diagrams in the tri-component systems $Ba(OR)_2$-$Ti(OR)_4$-L(R=Et,Pr^i,Bu; L=ROH,C_6H_6) have been studied. In all the systems the most stable are the complexes of the composition $BaTi_4(OR)_{18}$. The ethoxide complex has been isolated in the form of single crystals. The data of its structural analysis

are represented in the Fig.2. In the butoxide system this complex presumably exists only in solution (which may be testified by the only branch of solubility of $Ba(OBu)_2$ which goes along the 1:4 section) (Fig.3).

At the same time in all the solutions decomposition is accompanied by formation of bimetallic oxoalkoxides:

$$Ba(OBu)_2 + Ti(OBu)_4 \longrightarrow BaTiO_x(OBu)_{6-2x} + Bu_2O$$

The rate and the depth of this decomposition increases with dilution of the solution and enhancement of Ba:Ti ratio in it.

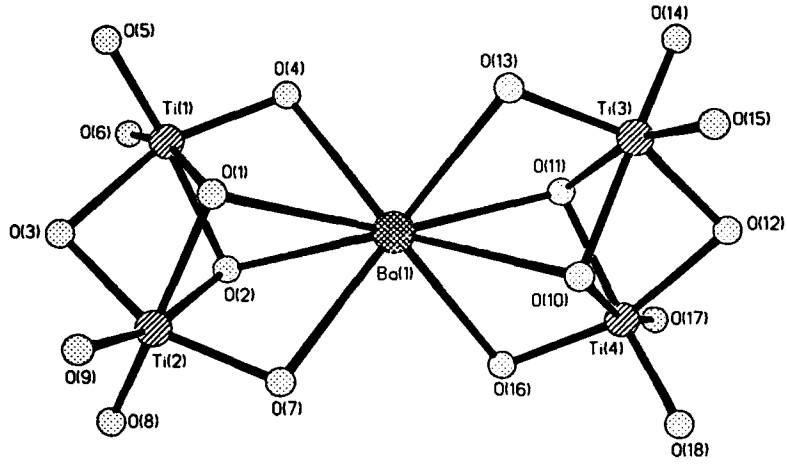


Fig.2 Molecular structure of $BaTi_4(OEt)_{18}$

X-ray structural analysis of the crystals $Ba_4Ti_4O_4(OPr^i)_{16} \cdot 3.5\ Pr^iOH$ which have been isolated in accordance with the following reaction:

$$Ba + Ti(OPr^i)_4 + Pr^iOH \longrightarrow BaTiO(OPr^i)_4 \cdot 7/8Pr^iOH$$

allows us to make certain assumptions concerning the structures of oxoalkoxides (Fig.4). The basis of the molecule is a distorted cube with the alternating Ba and O atoms. The O atoms are bonded to the five-coordinated Ti atoms. Thus the Ba-O-Ti bonds (with the very short Ti-O bonds) are formed already on the stage of the oxoalkoxide, which ensures homogeneity of distribution of metals in the future complex oxide phase.

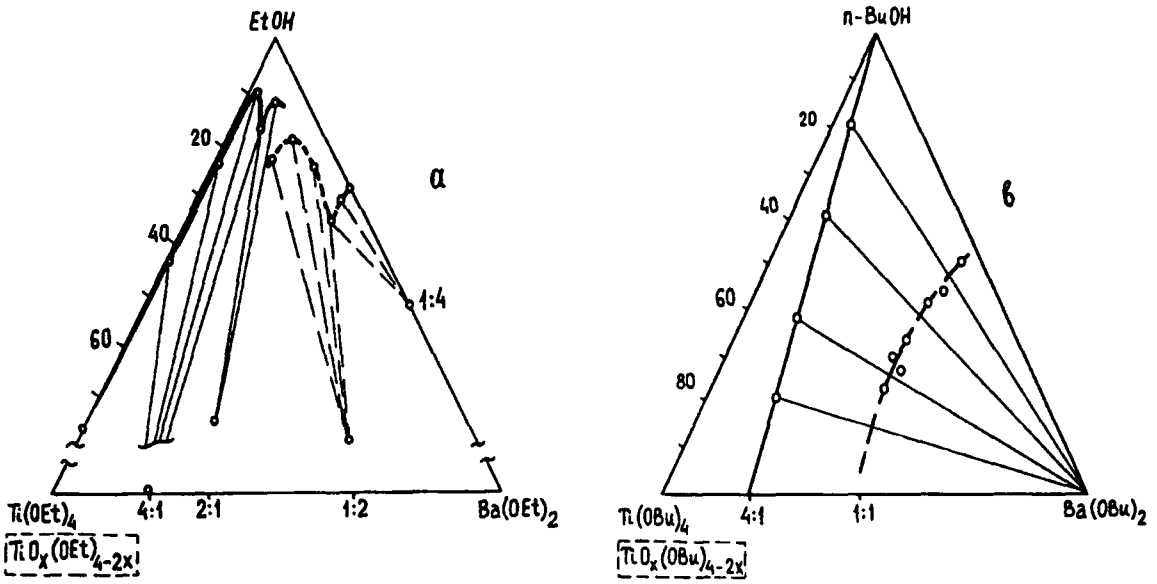


Fig.3 Solubility diagrams at 20°C in the systems
(a) $Ba(OEt)_2$ - $Ti(OEt)_4$ - EtOH
4:1=$BaTi_4(OEt)_{18}$; 2:1=$BaTi_2(OEt)_{10}\cdot 5EtOH$; 1:2=$Ba_4Ti_2O(OEt)_{14}\cdot 8EtOH$
(b) $Ba(OBu)_2$ - $Ti(OBu)_4$ - BuOH
and the products of decomposition in accordance with the following reaction:

$$nTi(OR)_4 + mBa(OR)_2 \longrightarrow Ba_nTi_mO_x(OR)_y + R_2O$$

Thermolysis of oxoalkoxides at 800°C results in tetragonal $BaTiO_3$. Formation of the oxoalkoxides in solutions determines their very good film-forming properties and stability on storage, particularly towards air moisture. The controlled hydrolysis of these precursors results in crystalline $BaTiO_3$. On the other hand hydrolysis of thealkoxide solutions which did not undergo decomposition with excess of water leads to amorphous product, crystallization of $BaTiO_3$ occurs on continued refluxing of the mixture with excess H_2O. In this variant synthesis of $BaTiO_3$ practically does not differ from the well-known method based on the interaction of aqueous solution of $Ba(OH)_2$ with $Ti(OR)_4$ [29-31]. The detailed study of all the conditions of the latter method allows us to obtain $BaTiO_3$ of very high quality, these powders are used for production of capacitors.

This method has been also extended for synthesis of a series of complex perovskites. In these cases synthesis is performed in two steps, e.g..:

$$1)\ Mg + 2Ta(OBu)_5 \xrightarrow{BuOH(or\ CH_3OC_2H_4OH)} "MgTa_2(OBu)_{12}"$$

$$2)\ Ba(OH)_2 + 1/3"MgTa_2(OBu)_{12}" \xrightarrow{80\text{-}100^oC} BaMg_{1/3}Ta_{2/3}O_3$$

Sintering of thus obtained powders gives ceramic materials with high Q-factor.

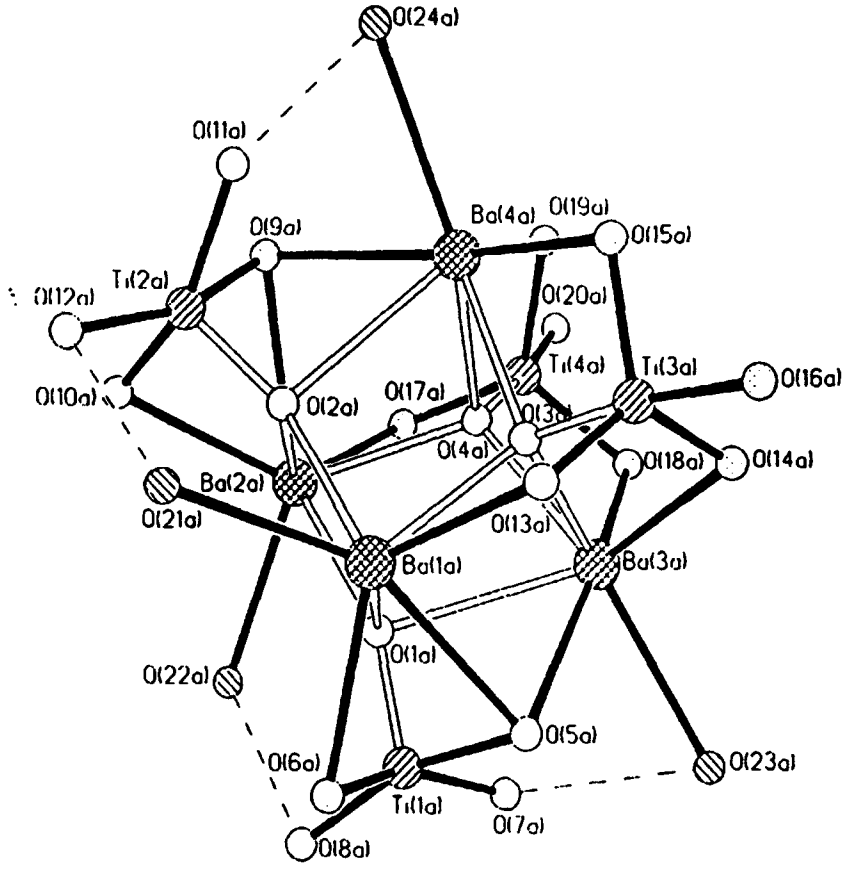


Fig.4 Molecular structure of $BaTiO(OPr^i)_4 \cdot 7/8\ Pr^iOH$ (molecule I); (There are two independent molecules in the structure which differ only in the number of Pr^iOH solvating groups: $[BaTiO(OPr^i)_4]_4 \cdot 4\ Pr^iOH$ (I) and $[BaTiO(OPr^i)_4]_4 \cdot 3Pr^iOH$ (II)).

The abovediscussed examples concerned syntheses of crystalline oxides under extremely mild conditions - practically directly in the course of hydrolysis, i.e. before evaporation of the solvent ($t \approx 100^0C$).

Formation of $LiNbO_3$ gives an example of crystallization occurring in the course of elimination of the residual alkoxide groups on thermal treatment of the hydrolysis product [5]. Minute crystallites of $LiNbO_3$ appear directly on the hydrolysis stage, which has been confirmed by electron diffraction study of the as-prepared samples. However the crystallites are distributed in the amorphous matrix which contains residual alkoxide groups. Intensive crystallization takes place in the temperature range of 300-600^{0}C which coincides with the main weight loss connected with elimination of residual alkoxide groups.

Crystallization of $LiNbO_3$ from the amorphous matrix was also studied by means of second harmonic generation of the laser beam (SHG). This method proved exceptionally fruitful for the study of crystallization of non-

centrosymmetric phases, and may be used in these cases as an indicator of crystallization.

This technique has been also used for study of crystallization of Bi_2WO_6 and Bi_2MoO_6 [6]. However the paths of crystallization of the two ferroelectric compounds differ greatly. Solutions of Bi and W ethoxides in EtOH are quite stable, on their hydrolysis amorphous precipitates are formed; residual organic groups are eliminated from the precipitates at 350-400^{0}C while crystallization of Bi_2WO_6 occurs at 450^{0}C. At this temperature SHG signal is first registered testifying to appearance of the non-centrosymmetric phase. In the case of synthesis of Bi_2MoO_6 application of ethoxide solutions proved a failure, as far as at any ratio of the initial metal alkoxide in the ethoxide solution precipitation of pseudocubic phases with different Bi:Mo ratio occurs. That is why methoxyethoxide solutions were used for synthesis of Bi_2MoO_6. Hydrolysis of such solutions which are quite stable, results in precipitation of the crystalline powder at room temperature. The powder practically does not contain residual alkoxide groups; SHG signal is registered already for the as-prepared samples.

Application of metal alkoxides proved especially fruitful in the thin films technology. Metal alkoxides solutions are used for application of thin films by dipping or spinning techniques. Just as in the case of powder synthesis the key problem is the correct choice of the alkoxide precursors.

Alkoxide derivatives of two different series $MO(OR)_4$ and $MO_2(OR)_2$ were used for preparation of molybdenum and tungsten sols [7]*). Application of these compounds allowed us to suggest a new method for preparation of stable tungsten and molybdenum sols containing no foreign electrolytes. The study of the sols by means of electronic spectroscopy and X-ray small angle scattering suggests that colloids obtained from $WO(OR)_4$ should be described as "polymeric sols" consisting of polymeric chains which in the course of hydrolysis are organized into three-dimensional network. The structure of such a network is first of all determined by the [water]:[alkoxide] ratio in solution. On the other hand molybdenum sols are "particulate" colloids with the dense polymolybdate nucleus.

The nature of the sols determines the structure and the properties of the films obtained from these solutions. Interrelation between the nature of sols and the morphology of the films is in a good agreement with the scheme suggested by

---

*)Mo alkoxides of the $MoO(OR)_4$ series decompose far more readily than the derivatives of W, that is why $MoO_2(OR)_2$ were used for preparation of stable sols.

Brinker for hydrolysis of $Si(OR)_4$. Films obtained from the tungsten and molybdenum sols demonstrate photo- and electrochromic properties.

Metal alkoxides were used for preparation of the complex oxide films. One of the first examples studied was preparation of $LiNbO_3$ crystalline films [5]. Films were applied from the ethoxide solutions of $LiNb(OEt)_6$. The main difficulties lied in preparation of high quality films without cracks and "bubbles", they have been overcome by application of dilute solutions with successive operations of solution application and thermal treatment; morphology of the films is also sensitive to the traces of moisture in solutions and its ageing.

At present films of a wide range of perovskites are being under investigations. The following films have been obtained: $BaTiO_3$, $BaM_{1/3}B_{2/3}O_3$(M=Mg,Zn; B=Nb,Ta); $PbMg_{1/3}B_{2/3}O_3$(B=Nb,Ta); $PbTiO_3$, $PbTi_xZr_{1-x}O_3$. For application of this films electrochemically prepared oxoalkoxide solutions are widely used. Crystallization of ferroelectric phases has been successfully studied by SHG technique.

With the discovery of high-temperature superconductivity a series of publications concerning synthesis of superconductors from metal alkoxides appeared. We succeeded in preparation of superconducting films of two systems $YBa_2Cu_3O_{7-x}$ and Bi-containing materials[8]. Solutions in methoxyethanol were used as precursors. After heat treatment at 950 and 800°C respectively highly oriented films $YBa_2Cu_3O_{7-x}$ (T_c=70K) and $Bi_2Sr_2CaCu_2O_x$ (T_c=80K) have been obtained. Although there are few superconducting phases in the Bi-containing system, it is usually the above-mentioned phase that crystallizes readily regardless the composition of the initial solution. Increase of the content of the $Bi_2Sr_2Ca_2Cu_3O_x$ phase with $T_c \approx 110K$ occurs with partial substitution of Bi by Pb.

The abovedescribed examples demonstrate that the proper processing makes metal alkoxides unique precursors for oxide synthesis. However only careful study of all the stages of oxide synthesis together with complete understanding of its chemical foundations may lead to oxide materials of high quality.

REFERENCES

1. M.I.Yanovskaya, N.Ya.Turova, E.P.Turevskaya et al., Izv.Akad. Nauk SSSR,Neorg.Mater.,17,No.2, 307 (1981).
2. M.I.Yanovskaya and N.Ya.Turova, Ibidem, 19, No.5, 693 (1983).
3. M.I.Yanovskaya, E.P.Turevskaya, N.Ya.Turova et al., Ibidem, 23, No.4, 658 (1987).

4. M.I.Yanovskaya, T.V.Rogova, S.A.Ivanov et al.,J. Mater. Sci. Lett., 6, 274 (1987).
5. M.I.Yanovskaya, E.P.Turevskaya, A.P.Leonov et al., J. Mater. Sci., 23, 385 (1988).
6. I.E.Obvintseva, M.I.Yanovskaya, S.I.Kucheiko et al., Izv. Akad. Nauk SSSR, Neorg. Mater., 25, No.1, 90 (1989).
7. M.I.Yanovskaya, I.E.Obvintseva, V.G.Kessler et al., J.Non-Cryst. Solids, 124, 155 (1990).
8. M.I.Yanovskaya, E.P.Turevskaya, N.Ya.Turova et al., Ferroelectrics, 105, 39 (1990).
9. E.P.Turevskaya, N.Ya.Turova, M.I.Yanovskaya et al., Sverkhprovodimost, 3, No.9 (1990).
10. D.C.Bradley in Preparative Inorganic Reactions, v.2, edited by W.L.Jolly, Interscience Publ. N-Y-London, Sydney, 1965.
11. V.A.Shreider, E.P.Turevskaya, N.I.Kozlova and N.Ya.Turova, Inorg. Chim. Acta, 53, L73 (1981).
12. T.V.Rogova, N.Ya.Turova, B.V.Zhadanov, Koord. Khim., 11, 784 (1985).
13. S.I.Kucheiko, N.Ya.Turova, V.A.Shreider, Zh.Obsh.Khim., 55, 2396 (1985).
14. N.Ya.Turova and V.G.Kessler, Ibidem, 60, 113 (1990).
15. N.Ya.Turova, T.V.Rogova, N.I.Kozlova et al., Koord. Khim., 9, 1244 (1983).
16. A.V.Novoselova, N.Ya.Turova, E.P.Turevskaya et al., Izv. Akad. Nauk SSSR, Neorg. Mater., 15, 1055 (1979).
17. E.P.Turevskaya, N.Ya.Turova and A.V.Novoselova, Koord Khim., 9, 755 (1983).
18. T.V.Rogova, N.Ya.Turova, N.I.Kozlova, Ibidem, 12, 762 (1986).
19. S.I.Kucheiko, N.Ya.Turova, Ibidem, 13, 1057 (1987).
20. E.P.Turevskaya, N.Ya.Turova, A.V.Novoselova, Dokl.Akad. Nauk SSSR, 242, 883 (1978).
21. M.I.Karpovskaya, N.Ya.Turova, N.I.Kozlova et al., Dokl. Akad. Nauk SSSR, 239, 334 (1978).
22. V.G.Kessler, N.Ya.Turova, A.I.Yanovsky et al., Zh. Obsh. Khim., 60, 2769 (1990).
23. Yu.A.Buslaev and Yu.V.Kokunov, Izv. Akad. Nauk SSSR, Neorg. Mater., 4, 537 (1968).
24. O.Poncelet, W.J.Sartain and L.Hubert-Pfalzgraf, Inorg. Chem., 28, 263 (1989).
25. J.S.Smith, R.T.Dollof and K.S.Mazdiyasni, J. Amer. Ceram. Soc., 53, 91 (1970).
26. S.Hirano and K.Kato, Advanced Ceram. Mater., 2, No 2, 142 (1987).
27. A.N.Nesmeyanov, O.V.Nogina and R.Kh Freidlina, Izv.Akad. Nauk SSSR, Ser.Khim., 1956, 373.
28. K.S.Mazdiyasni, R.T.Dolloff, J.S.Smith, J. Amer. Ceram. Soc., 52, No.10, 523 (1969).
29. S.S.Flaschen, J. Amer. Ceram. Soc., 77, No.12, 6194 (1955).
30. K.Kiss, J.Magder, M.S.Vukasovich and R.J.Lockhart, J. Amer. Ceram. Soc., 49, No.6, 291 (1966).
31. F.Chaput and J.P.Boilot, J.Mater. Sci. Lett., 6, No.9, 1110 (1987).

AD-P006 654

FERROELECTRIC THIN FILM RESEARCH IN FRANCE

P. GAUCHER*, S. P. FAURE*,**, P. BARBOUX**

* THOMSON CSF, Laboratoire Central de Recherches, Orsay

** CNRS, Université de Paris VI, Chimie de la matière condensée

Abstract : After a review of the research made on thin film deposition in France, this work presents the comparison between two chemical deposition methods for PZT films : sol-gel method based on low molecular weight precursors and solvent, and MOD (Metallo-Organic Deposition) process based on a hydrophobic solvent. The influence of the viscosity of the solvent and of the solubility of water is shown with regard to stability and drying properties. The final electrical properties of the ferroelectric films are also compared such as the hysteresis loop which characterizes the most important properties for memory application : coercive voltage and rectangularity .

INTRODUCTION

Ferroelectric materials have a lot of applications in relation with the non linearity and of the hysteresis of the internal polarisation P as a function of field E, which is described by the well known hysteresis loop P(E). Historically, the high dielectric constant of barium titanate due for a great part to the presence of domain walls, was the first industrial application for capacitors in the years 1950. About a decade later, the piezoelectric properties of poled PZT were used for ultrasonic transducers and sensors, mainly for sub-

92-16118

marine activities (sonars). The optical properties of ferroelectrics like lithium niobate are also of interest for electro-optic devices (wave modulation or frequency doubling) and the electrostrictive properties of ferroelectric relaxors like PMN are studied for actuators applications.

Unfortunately, the non linear phenomena appear at high fields (generally greater than 10^6 Vm^{-1}) and this has limited their use up to now as discrete components working (or poled) under high voltages. With the develoement of thin film deposition methods, the integration of all these devices in the semi-conductor technology is now possible with working voltages as low as 5 Volts and high surface capacitance due to the very low thickness of the layers (typically less than 1μm). During the last decade, only polymer ferroelectrics were studied as thin layers because of their high forgeability, and the technology is presently used for hydrophones and studied at THOMSON LCR for pyroelectric detectors[1] or fast computers based on a neural concept[2]. But the polymer material, because it is only partially crystallized, has a higher coercive field than the ceramic with the consequence that, despite the low coercive voltage obtainable by thinning, breakdown of the dielectric may occur before saturation. To improve cristallinity of polymer films, some experiments are presently made at Thomson LCR by thermal evaporation of copolymer on monocrystalline substrates[3].

The semi-conductor activity has a large experience in physical methods of deposition. That is the reason why these methods would be preferred by manufacturers if available. Unfortunately, the synthesis of multicomponent systems by conventional sputtering is very difficult and original methods have to be developped. For this reason, a few laboratories in France have initiated research in RF magnetron with a ceramic target (IUT Orsay[4]), facing target sputtering (CEA LETI Grenoble[4]), and Ion Beam Sputter Deposition (Institut d'Electronique Fondamentale, Orsay[5]).

Compared to the physical methods of deposition, the chemical methods are giving more and more results because of their higher versatiility concerning the chemical formulation and the better control of the exact stoichiometry which is the most important parameter in the processing of dense ceramics.

Among all of the chemical methods already published in the litterature, it is very difficult to decide, at this time, what is the best concerning the initial goal of the research : improving high surface capacitance (related to the purity of the phase) with low leakage current and high rectangularity of the hysteresis loop for a thickness as small as possible. The methods differ by the raw material used, the nature and the amount of solvent, the additives used for improving the stability and the rheological properties of the sol, and the drying and annealing step. Two kinds of methods exist for chemical processing of the liquid precursor : the "sol-gel" process is based on the concept of hydrolysis of a complex alcoxyde[6], the "MOD" process is based on the use of high molecular weight for the precursors and the solvent[7]. Some experiences have been made in France on thin film synthesis of barium titanate by an original MOD process (CNRS Orléans[8]), and by a sol gel process (Ecole Polytechnique Palaiseau[9]).

In this paper, we shall outline the differences between two different processes developped simultaneously in both laboratories of Thomson and CNRS for PZT ceramic films and based on MOD and sol-gel method.

I. LIQUID PRECURSOR PROCESSING

The chart in fig 1 describes the primary steps for both processes. The sol-gel process necessitates more operations than the MOD concerning the preparation of the sol, but the final steps are qualitatively similar. We shall detail these different steps in the following, but we can already notice the two basic differences at the top of the chart :

-in sol-gel, we speak about "dissolution" instead of "mixing" in MOD because of the nature of the lead precursor (solid for sol-gel and liquid for MOD), but also because the dissolution has to be made at high temperature during several hours, contrary to mixing which is made very easily at room temperature.

- the term "non reactive solvent" used in MOD means that no exchange reaction is likely to occur between the solvent and the dissolved species, which is unlikely in sol-gel where the alcohol can modify the environment, and so the reactivity, of the metal precursor. This assumption is in fact not verified indeed, and the chemistry of MOD is-perhaps not qualitatively different than that of sol-gel.

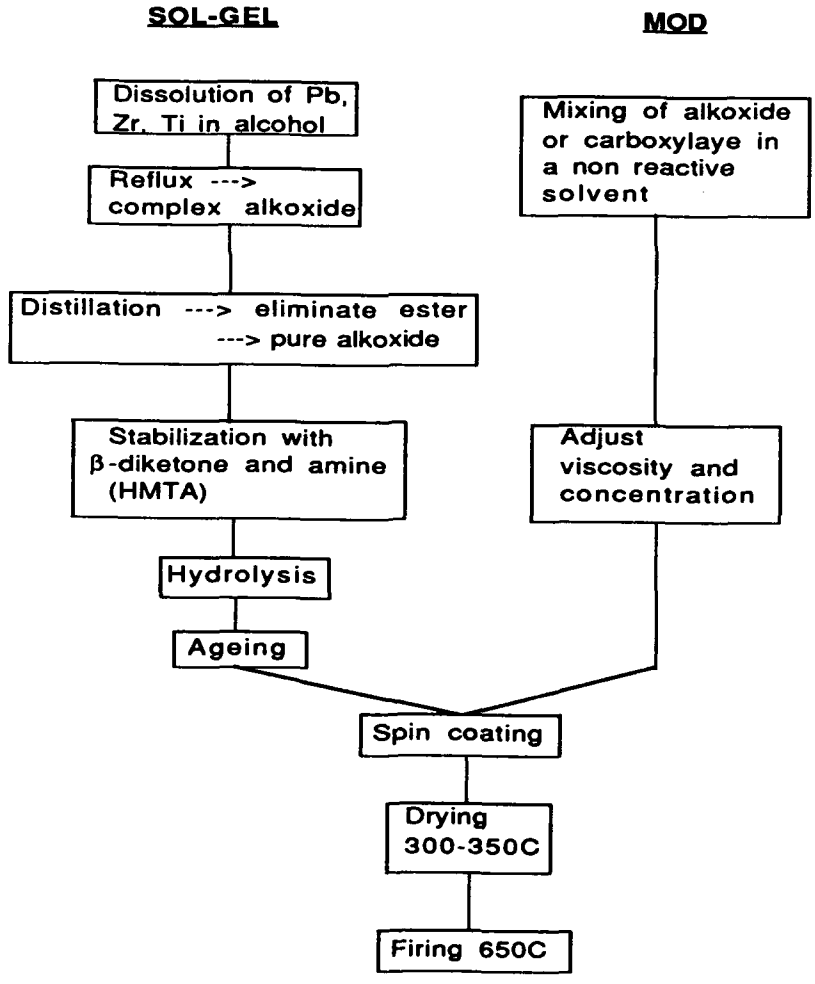


FIGURE 1 : sol-gel and MOD process chart

-1) Dissolution of metals

In both processes, titanium and zirconium are introduced as alkoxides (propoxides or butoxides) which are in liquid form (pure liquid or solution). Lead carboxylate (acetate or 2-ethyl-hexanoate) was used as a cheap commercial precursor.

In the sol-gel process, the acetate is in a solid form, and hydrated : after removal of the water in an oven, this salt cannot be dissolved in any alcohol (propanol, butanol or 2-ethyl-hexanol), but the presence of a titanium alkoxide allows dissolution. The assumed chemical reaction :

$$Pb\,(COOR)_2 + Ti\,(OR')_4 \text{ ------> } TiPbO_2\,(OR')_2 + 2R\text{-}COO\text{-}R'$$

has been made possible even with pure alkoxide (Ti n-butoxide) under reflux. The ester (butyl acetate) produced in this transesterification reaction has been separated by distillation to isolate the complex alkoxyde in a liquid form. It is pointed out that no water is formed which would lead to hydrolysis of the alkoxide. The nature of the formed species is presently studied.

In the MOD process, the lead 2-ethyl hexanoate was provided either in solution (Alpha Ventron product) or in solid form (Strem chemicals product), but can be in any case dissolved in 2-ethyl-hexanol, octanol or a mixture of them with butanol. The advantage of 2-ethyl-hexanol or octanol is in the strong limitation of the hydrolysis rate due to the very low solubility of water in these solvants. On the photo shown in fig 2, we compare qualitatively the effect of pouring upon water the following compounds :

- pure titanium butoxide
- titanium butoxide in solution with butanol (which moderately dissolves water)
- titanium butoxide in solution with octanol (hydrophobic solvant)

In the last case, the hydrolysis appears only at the interface between the water and the solvant and does not progress inside the upper phase. In the first two cases instead, there is a "bulk" hydrolysis because of the possibility for the water molecules to reach the alkoxide molecules everywhere in the solvent. This explains the apparent stability of alkoxide solution in hydrophobic solvent.



FIGURE 2 : Illustration of the difference of hydrolysis behavior of titanium n-butoxide solutions poured in pure water : pure alkoxide (left), with butanol solvent (middle) and with octanol solvent (right). The last solvent, hydrophobic, leads to 2-dimensionnal hydrolysis at the interface with water.

-2) Stabilization of the sols

Because of the instability of the alcohol based sol-gel solution towards hydrolysis, it is impossible to use it on a photoresist spinner : the ambiant moisture causes hydrolysis during the coating and before the film has reached its equilibrium thickness. It is thus necessary to stabilize the product by addition of external ligands. Acetylaceton (acac) can be used in proportions of 1 mole/mole of PZT[10]. The resulting solution is more stable, except for its color that change from clear yellow to red within a few months, but this does not seem to affect the results.

Nevertheless, the viscosity of the solution is much lower than in the MOD process, especially for the higher concentrations up to 0.5 moles/l (fig 3). For a 0.5M solution in butanol, the viscosity is only 3.5 cstokes instead of more than 6 for MOD. The thickness of the deposited film being related to kinematic viscosity[11], the films obtained by this method are thinner and more deposition steps are necessary for a given final thickness.

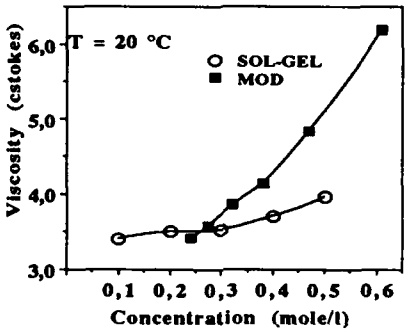


FIGURE 3 : Influence of concentration on kinematic viscosity of the sols.

A method for increasing viscosity in the sol-gel process is to add a polymerizing agent like Hexamethylene-tetramine (HMTA)[11]. The mechanism of formation of a very viscous resin (about 14 cstokes for 0.5M solution) with very good wetting properties is not well undersood. We suppose that a resin is formed by the polyaddition of amine groups to acetylaceton.

II. SPIN COATING AND DRYING

The sols are coated at 4000 rpm with a Headway photoresist spinner during 20s on platinium coated silicon substrates. Drying of the films is performed in a tunnel oven heated with Infra red lamps (Radiant Inc). The temperature on the layer is supposed to be larger than 300°C in the middle of the tunnel. Further deposition can be made after this drying step without redissolving the film.

Problems of cracking of film cracking upon drying have already been described in another paper[13] where the influence of viscosity and spin rate is pointed out. For a given viscosity, sol-gel layers give rise to more cracks because of the larger rate of gelation compared to the rate of evaporation of the solvent. As shown in fig 4, if the reticulation of the sol occurs before the evaporation of the solvent, a shrinkage parallel to the substrate is the cause of cracks. Instead, in MOD process where the solvent lowers the gela-

tion rate (mainly because of its hydrophobic nature), the film first shrinks in a direction perpendicular to the substrate during evaporation, and the reticulation occurs later. This can be easily checked by drying a drop of each sol at about 100°C : MOD leads to a very viscous and continuous resin and sol-gel leads to a dry powder.

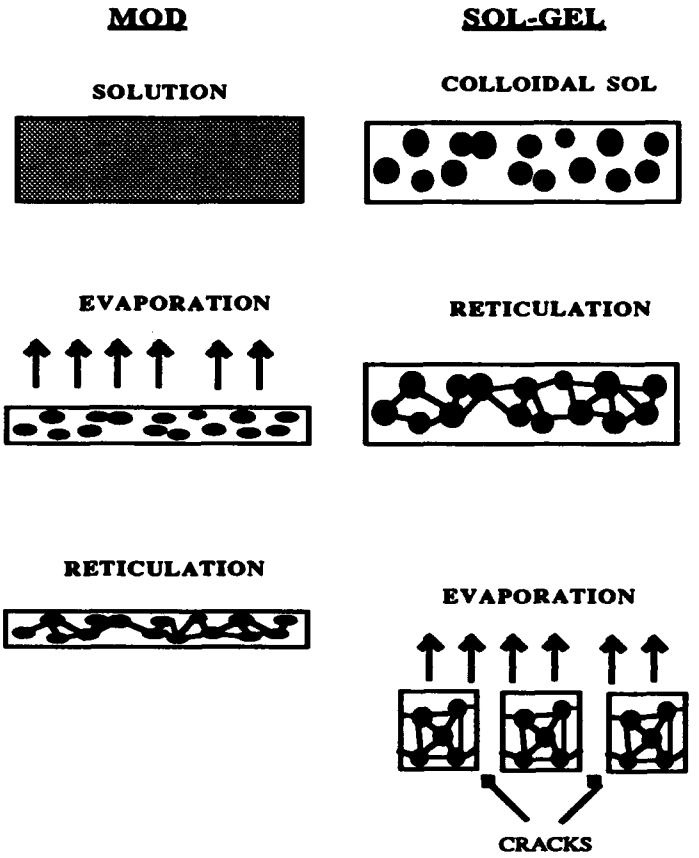


FIGURE 4 : Schematic desciption of the successive steps during drying of sols of equal concentation from MOD and sol-gel process explaining the formation of cracks for too concentrated sols in sol-gel.

III. HIGH TEMPERATURE ANNEALING

After 3 to 6 coating and drying steps, the films are heat treated in a conventionnal furnace. The temperature is raised up to 650 - 680°C in 1 hour, then maintained during 2 hours and decreased down to room temperature in 1 hour. All the firing cycle is performed under pure oxygen.

The difference of decomposition behaviour between sol-gel and MOD have been described elsewhere[12]. The main advantage of sol-gel is the lower weight loss between 200 and 500°C because of the partial hydrolysis of the complex alkoxide with either added water or ambiant moisture. In MOD process instead, a larger mass is lost during annea-

ling, but the weight loss occurs at lower temperature.

IV. ELECTRICAL MEASUREMENTS

For electrical characterizations, aluminium square dots are deposited onto the surface of the film by direct evaporation. Their size is 1.2X1.2mm^2.

Hysteresis loops are measured with a conventionnal Tower-Sayer circuit at 40 Hz. Fig 5 shows the comparison between sol-gel and MOD layer made both by 6 deposition steps of 0.5M solutions. The lower viscosity of the sol-gel solution is the cause of the lower coercive voltage, resulting from a lower thickness. The thickness measured from MEB observations are respectively 0.3 and 0.6µm.

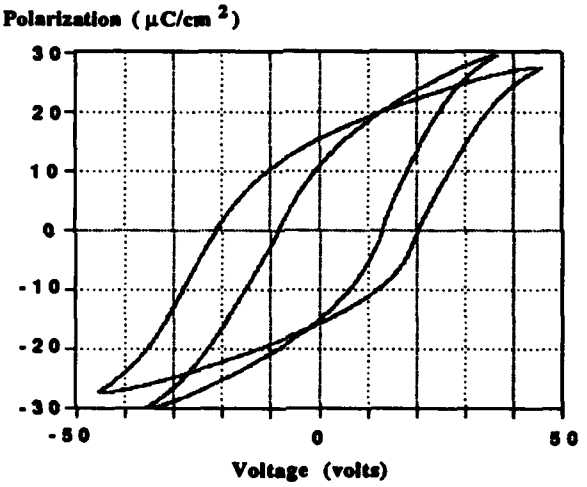


FIGURE 5 : Hysteresis loops of films made by 6 depositions of 0.5M sols by sol-gel and MOD.

For better comparison between the processes, the number of deposition for each method has been adjusted to get the same thickness (about 0.5µm for 0.5M solutions). The following results are made with these comparative samples.

The capacitance of sol-gel films are always larger than that of MOD films, whatever the concentration. The variation of capacitance shown in fig. 6 is due to the thickness variation of the film with concentration of the precursor sol. It is surprising that capacitance is not increasing when we decrease the concentration for MOD process. This is probably due to a poor crystallization of the very thin layers. About the same behaviour is seen for the coercive voltage (fig 7), with lower values obtained or MOD (between 2 and 5 Volt).

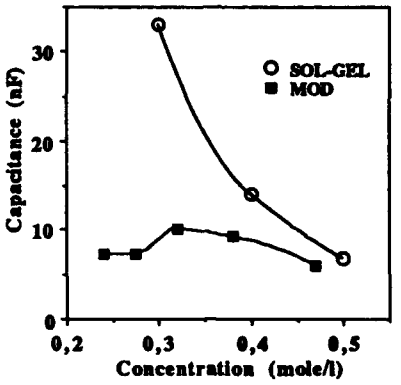


FIGURE 6 : Capacitance (1.44 mm^2 dots) for MOD and sol-gel films

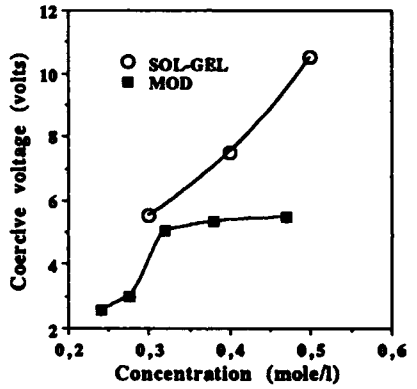


FIGURE 7 : Coercive voltage (1.44 mm^2 dots) for MOD and sol-gel films

The most important parameter for memory application is the rectangularity of the loop, given by the ratio P_r/P_s of the remanent polarization on the saturation polarization. This ratio defines the ability of the material to provide a difference during the reading of a memory cell, between a switching and a non switching pulse. A switching pulse corresponds to the reading of a bit 1 and a non switching pulse corresponds to the reading of a bit 0. When the rectangularity is equal to 1, the non switching pulse will release a null charge and the switching one a charge equal to $2P_r$. With a rectangularity equal to zero, both switching and non switching pulses will release the same charge. The discrimination between bits 0 and 1 is so related to rectangularity.

The rectangularity P_r/P_s of the loops are compared for both processes in fig 8. At low concentrations, rectangularity decreases steeply for MOD process. It remains almost constant, with higher values, for sol-gel.

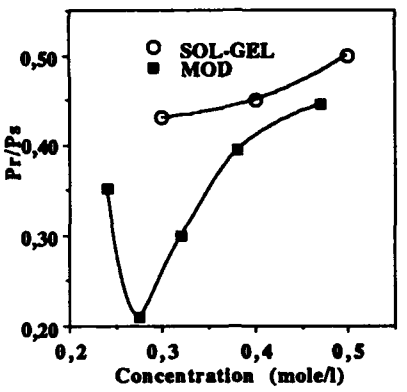


FIGURE 8 : Rectangularity (1.44mm^2 dots) for MOD and sol-gel films

V. DISCUSSION

There is an apparent contradiction between the observed results of electrical measurements : the higher capacitance of sol-gel layers should be related to a better purity and crystallinity of the phase, and this is in agreement with the better rectangularity. But the higher coercive voltage should lead to an opposite conclusion. The reason of that could be a larger concentration of lead vacancies in MOD films. This defect is well known as a coercive field depressor in bulk PZT, because of its action on the domain wall mobility[14].

The fact that the capacitance does not depend on concentration for MOD process may be attributed to a more difficult phase crystallization, especially for very thin layers. In the same conditions, sol-gel allows better cristallisation , which is not surprising because of the prereaction of the constituants during the processing of the sol.

VI. CONCLUSION

At this time, both processes can give satisfaction concerning the electrical results. MOD permits an easy processing and an easy introduction of dopants . It is suitable for thick layers with a small number of deposition steps because of the high viscosity of the solvent. The stability of the solutions is mainly due to the hydrophobic nature of this solvent which prevents the solute species from hydrolysis, except at the interface between moisture and solution. The gelation of the film might occur slowly during the evaporation of the solvent.

Sol-gel is a more sophisticated process with very promising possibilities, but physical parameters like viscosity or wettability are not easy to control and the stability of the

sols is limited. So it is necessary to add some stabilizing and polymerizing agents (acac, HMTA) at the end of the sol processing to improve these properties and prevent the film from cracking during the drying step.

The determining parameter for MOD is the solubility of water in the solvent, its viscosity and its boiling point. For sol-gel, the use of cross linking agents seems to be unavoidable to get a spinnable sol with good rheological properties and finally low coercive field and high rectangularity.

REFERENCES

1. P. ROBIN, H. FACOETTI, D. BROUSSOUX, G. VIEUX and J.L. RICAUD, Revue technique Thomson CSF, 22(1), 143-186, (1990)
2. J. M. VIGNOLES, E. de CHAMBOST and F. MICHERON, Ferroelectrics, 93, 8017, (1989)
3. B. SERVET, S. RIES, P. ALNOT, . DESBAT, Int Conf on Polymer-solid Interfaces, Namur (Belgium), Sept 1991
4. E. CATTAN, B. AGIUS, H. ACHARD, J.P. JOLY, 7th European Meeting of Ferroelectricity (EMF7), July 1991, Dijon, France (to be published in Ferroelectrics)
5. D. BOUCHIER et al, EMF7 (see ref 4)
6. C. J. BRINKER, in "Transformation of organometalics into common and exotic materials" pp 261-78, (1988)
7. R.W. WEST, Ferroelectrics, 102, 53-69, (1990)
8. C. PROUST, Doctorate Thesis, Orleans 1990
9. F. CHAPUT and J. P. BOILOT, 6th CIMTEC Milan, June 1986 (ed P. Vincenzini, 1987)
10. P. GAUCHER, S. LEQUIEN, J. P. GANNE, S. P. FAURE and P. BARBOUX, 7th Int Symp on the Appl of Ferroelectrics, Urbana (IL) June 6-8, 1990. (To be published in "IEEE ultrasonics and frequency control")
11. I. VALENTE, S. FAURE, P. GAUCHER, J. LIVAGE, French Patent n° 89 15174, Nov 20, (1989)
12. N. L. ALLINGER et al, Inorganic chemistry §25.2, Worth Publ Inc NY 1971
13. P. GAUCHER, J. P. GANNE, S. P. FAURE and P. BARBOUX, EMF7 (see ref 4)
14. T. SHROUT, A. SAFARI, W.A. SCHULZE, Ferroelectrics letters, 44, 227-33, (1983)

NOTE : This work has been made under support of french *Ministère de la Recherche et de la Technologie*.

AD-P006 655

THIN FERROELECTRIC FILMS FOR THERMAL DETECTOR APPLICATIONS

F. AINGER, A. PATEL, N.M. SHORROCKS, C. TRUNDLE, AND
R.W. WHATMORE
GEC-Marconi Materials Technology Ltd,
Caswell, Towcester, Northants, NN12 8EQ, UK

ABSTRACT

The deposition of thin films of lead scandium tantalate ($Pb(Sc_{\frac{1}{2}}Ta_{\frac{1}{2}})O_3$) have been investigated by two processing routes. In the first, progress is reviewed for chemical vapour deposition in a purpose built low pressure reactor, utilising suitable modified proprietary precursors. Deposition has been studied over the temperature range 400-800^{0}C and, in general, amorphous films result which convert to crystalline perovskites on subsequent annealing. However, inclusion of hydroxy compounds in the vapour train catalyses the crystallisation process and enhances the growth rate at above 600^{0}C. It was found that the best thin films, in terms of density and morphology, are formed at low deposition rates 1-2μm/hr. The perovskite phase is obtained if the gas phase composition is controlled throughout growth. The choice of precursors, gas compositions and growth conditions will be described. In the second process, lead scandium tantalate thin films (>1μm) were deposited using a modified sol-gel solution route. This was achieved by spin-coating a solution of metallo-organic compounds of scandium and tantalum followed by lead, onto suitable substrates and firing and annealing the films at 800-1000^{0}C. These firing temperatures gave films with grain sizes ranging from 0.5-4μm, which are single phase perovskite. Permittivity, dielectric loss and field induced pyroelectricity have been measured against field and temperature to assess the pyroelectric figure-of-merit, F_D of films obtained from both film deposition process. The F_D for sol-derived films indicates a performance similar to that of bulk ceramic material.

92-16119

INTRODUCTION

Interest in the growth of thin film ferroelectric materials has grown rapidly in recent years. The interest can primarily be attributed to the need to reduce the cost and complexity involved in thinning and polishing ceramic materials, along with the need to produce coherent layers of the material onto given substrate materials.

Much interest has centred on thin film growth of lead lanthanum zirconate titanate (PLZT), lead zirconate titanate (PZT) and lead titanate for electro-optic, piezoelectric and pyroelectric applications.

The principal techniques used for deposition of thin films for these materials have been rf and magnetron sputtering[1-3]. The sputtering of multicomponent oxide materials is complicated by the difficulty in fabricating suitable targets to obtain the correct composition.

Although several other thin film deposition techniques are available, in this present study, we will be reviewing 2 techniques in particular: (i) Metal-Organic Chemical Vapour Deposition (MOCVD), (ii) Sol-Gel deposition, for the growth of lead scandium tantalate ($Pb(Sc_{\frac{1}{2}}Ta_{\frac{1}{2}})O_3$, PST) thin films.

PST is a perovskite structured (Figure 1) relaxor ferroelectric oxide and is an important member of a class of ferroelectric compounds exhibiting diffuse ferroelectric-paraelectric phase transitions. Unlike the conventional pyro-electrics with high transition temperatures, the first order transition of ceramic PST is at 28^{0}C. It is therefore used in an induced pyroelectric mode, ie, with an applied bias field[4]. Under these conditions, a high figure of merit (F_D), $12 \times 10^{-5} Pa^{-\frac{1}{2}}$ for dielectric bolometer applications has been obtained.

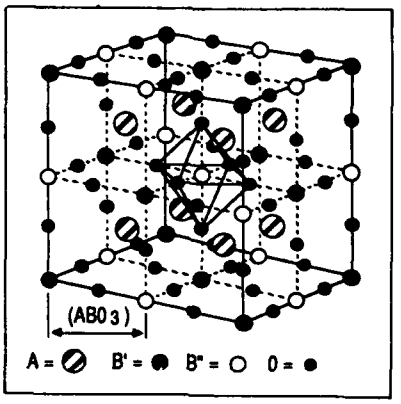


FIGURE 1 Structural model of ordered PST

i) PST Films by MOCVD Processing

MOCVD has necessitated the development of precursors with the rigorous exclusion of oxygen from their structures and in the carrier gas during growth. The metal alkyls and hydrides have been almost exclusively used. These materials have the advantage of being reasonably volatile at room temperature or below, but are also very toxic and often pyrophoric.

Metal oxide deposition clearly does not require oxygen free precursors and as a result many workers have opted to use the metal alkoxides or acetyl acetonate derivatives instead[5-6]. Although these precursors are less volatile than their alkyl equivalents, they are much easier to handle and much less toxic. The use of these precursors at atmosphere pressure tends to result in interfering homogeneous reactions, which degrade film quality through powder formation[7]. For this reason, we have used a low pressure MOCVD system, which also has the added advantage of increasing the efficiency of the process by reducing the wastage of precursor during each run.

The volatility of most metallorganic compounds is related to the molecular weight of the species, so that generally, the higher the molecular weight, the lower the vapour pressure. However, since metal alkoxides have a strong tendency to oligomerise through the co-ordination of the metal atom of one molecule with an oxygen atom on adjacent molecules, they are rarely found as monomers. The degree of oligomeristion is sensitive to steric factors such as the number and complexity of the ligands attached to the metal[8].

An alternative adduct to the alkoxides involves the β-diketonate ligand. The metal acetylacetonates are generally more stable than alkoxides to hydrolysis, whilst decomposing pyrolytically at temperatures in excess of 450°C. Kwak et al[6] report the use of $Ra(thd)_2$, (thd = $C_{11}H_{19}O_2$) in the MOCVD growth of $BaTiO_3$ thin films.

We have synthesised scandium and lead di-methyl heptofluoro acetyl acetonates (FOD) (Figures 2a and 2b). Such compounds, by increasing the co-ordination number achieved by the metal atom, are less prone than alkoxides to high degrees of oligomerisation, and with substituted fluorinated groups present, the volatility is often increased as well.

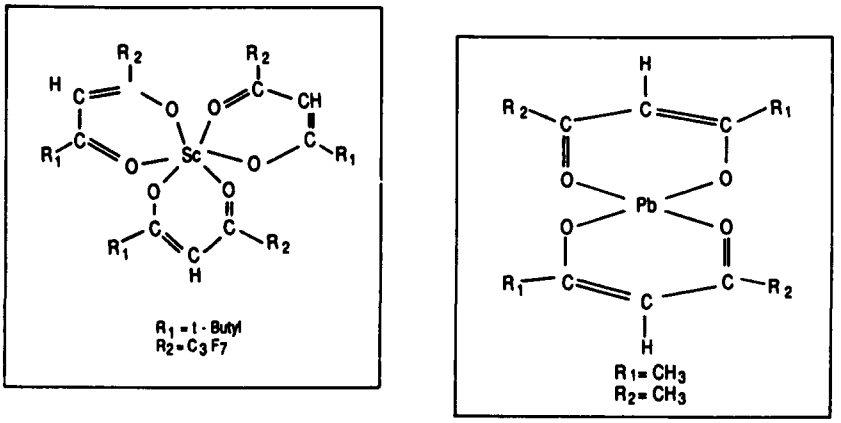


FIGURE 2 Structures of scandium and lead precursors

$Sc(FOD)_3$ is a mobile liquid at room temperature and distils at 110^0C at 0.1torr. The lead equivalent ($Pb(FOD)_2$) exists as a solid at room temperature but melts at around 70^0C and distils at 140^0C at 0.1torr. The solid nature of this lead precursor has the advantage that it is safer to handle at room temperature. Tantalum ethoxide is commercially available and is a liquid at room temperature, which can be readily volatilised at 50^0C.

DEPOSITION APPARATUS

The deposition apparatus used in this work is shown schematically in Figure 3. The apparatus consists of a quartz reactor containing an RF heated silicon carbide coated graphite susceptor.

A thermocouple placed in the susceptor is used to control the substrate temperature. Substrate temperatures of up to 900^0C can be achieved over an area of 25 x 27mm. The reactor is pumped by a rotary pump and roots blower combination with a butterfly valve controlled by a capacitance manometer to mainain a set pressure in the reactor.

The precursors are contained in quartz bubblers which are individually temperature controlled by the use of oil jackets. Mass flow controllers are used to control the helium bubbling through each precursor.

A diluting gas mixture of helium and oxygen flows along the stainless steel mixing rail (also oil heated) to carry the precursor vapour into the reactor. A hydroxyl source, such as water or n-butanol is fed into the end of the reactor between the precursor inlet and the susceptor. The hydroxyl source reservoir is temperature controlled and the flow varied using a heated needle valve. The pipework between the bubblers and the mixing

rail, and the reactor inlet are heated to prevent condensation of the precursors.

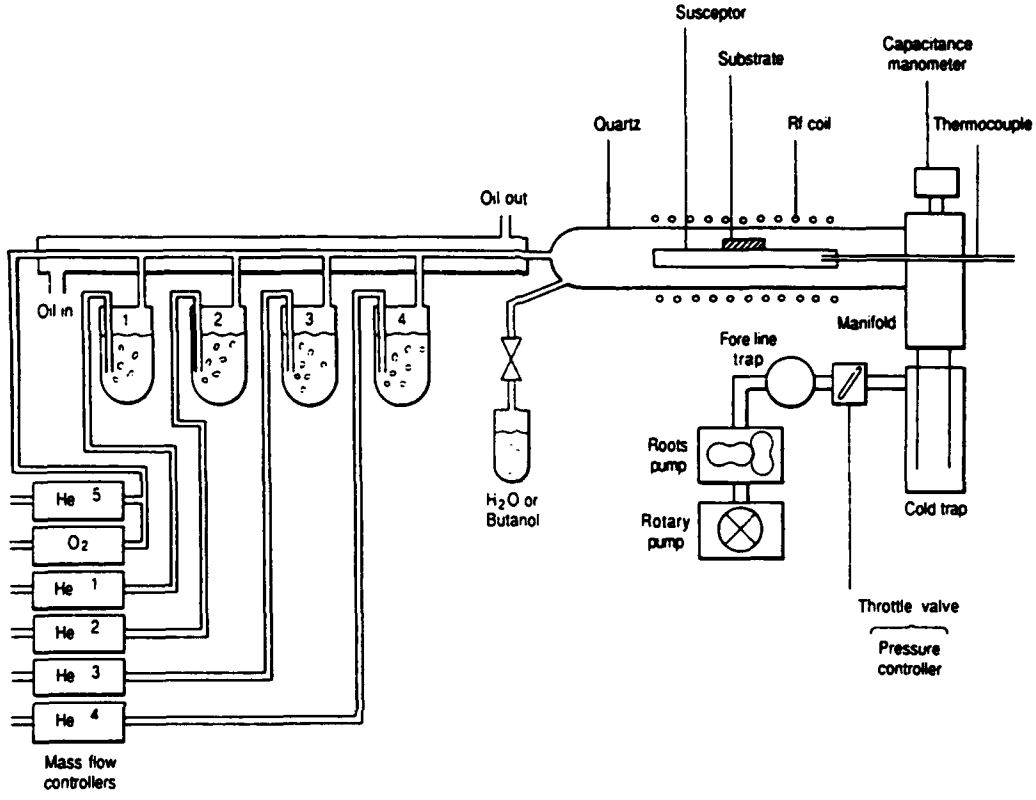


FIGURE 3 Oxide MOCVD deposition system

The temperatures and rates at which gas has been bubbled through these precursors are listed in Table 1. Substrate temperatures have been in the range 650-800^{0}C and water has been used as the hydroxyl source. The amount of water vapour entering the reactor has been controlled with a needle valve, and the temperature of the water reservoir controlled accurately as the vapour pressure of water varies significantly with temperature. Run durations from 30 minutes to 6 hours have been used.

The bubbler temperature and gas flow rate of each precursor has an influence on the quantity of all the elements in the deposited film. This makes tuning the deposition parameters to give stoichiometric films rather time consuming. The growth rate of the films can be varied from 0.5 to 10μm/hour by changing the deposition parameters. The films grown at higher growth rates are very rough and not fully dense. At low growth rates, the films are smooth and transparent.

The substrate temperature does not seem to influence significantly whether the perovskite or fcc phase is formed at temperatures in excess of 650°C, although the deposition conditions for stoichiometric films vary for different temperatures. This is due to the precise thermal breakdown behaviour of the different precursors. The substrate temperature does have a marked effect on the grain size of the film. Films grown at 650°C have a grain size of about 0.1μm (Figure 4a) and those grown at 800°C have a grain size of over 1μm (Figure 4b). The films on sapphire, particularly at the higher temperatures, show preferred orientation in the X-ray diffraction trace. The perovskite phase films prefer the (220) plane parallel to the substrate, and the fcc phase films show either (111) or (200) preferred orientation.

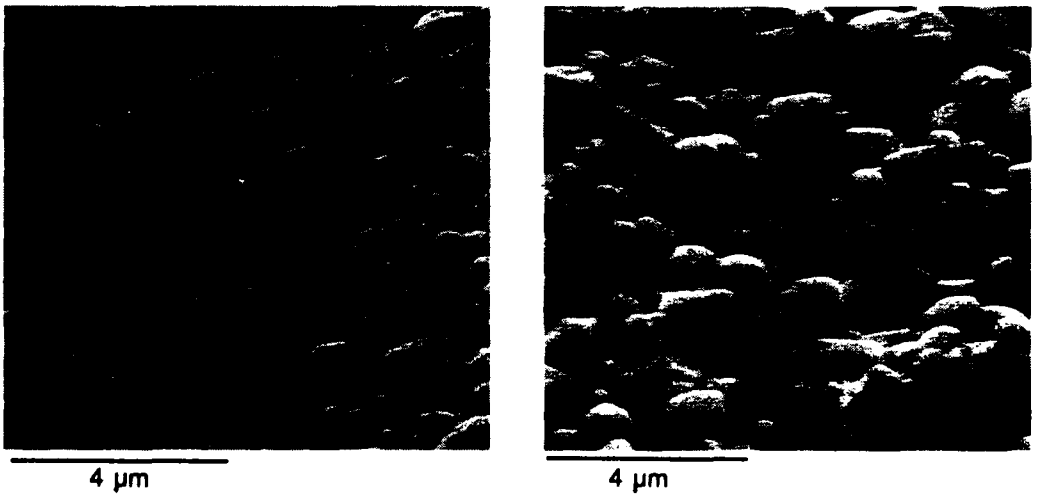


FIGURE 4 Electron micrographs of PST films on sapphire a) grown at 650°C; b) grown at 800°C

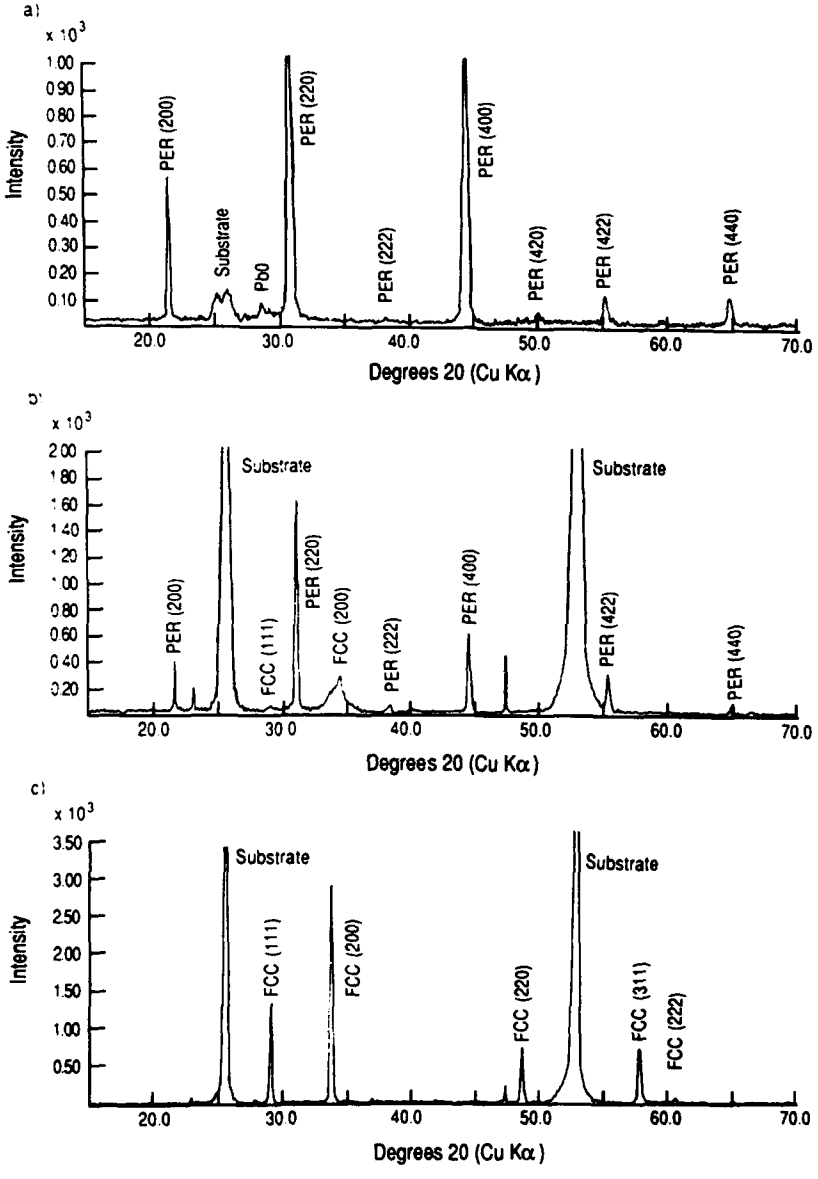


FIGURE 5 X-ray diffraction traces of PST on sapphire
a) perovskite; b) mixed perovskite and FCC; c) FCC

The phase of the films varied from perovskite (Figure 5a) through mixed perovskite/fcc (Figure 5b) to fcc phase (Figure 5c). The composition of the gas stream and the composition of the film have been found to influence whether the perovskite of the fcc phase forms.

TABLE 1 $Pb(Sc_{0.5}Ta_{0.5})O_3$ Deposition Conditions Evaluate

PRECURSOR	BUBBLER TEMPERATURE RANGE /^{0}C	BUBBLE GAS FLOW RATE RANGE/SCCM
$Pb(FOD)_2$	75 - 120	2 - 15
$Sc(FOD)_3$	60 - 105	2 - 10
$Ta(OEt)_5$	40 - 70	2 - 9

To form perovskite, the oxygen content of the gas needs to be at least 30%; the lead content of the film needs to be at, or greate than the stoichio- metric value; and the scandium content of the (atomic %) must exceed the tantalum content. If there is a large excess of lead oxide in the film, then this is often observed in X-ray pattern as PbO (litharge) peaks.

Some of the fcc phase films have been annealed for 10 hours at 90 in flowing oxygen with PST spacer powder. Subsequently, the film were found to have partially converted to the perovskite phase. has also been shown that longer annealing periods of 40 hours can convert mixed phase films into single phase perovskite.

Films have been deposited mainly on sapphire, but also on other substrates, such as MgO, silicon and Al_2O_3 on silicon. The best results have been achieved on sapphire as the films on the other substrates crack due to the thermal expansion mismatch. Reactions between the substrate and the PST have also been seen, such as the formation of silicides in the films on silicon. The composition of films deposited with the same parameters on different substrates has been found to vary. This is probably due to variations in substrate temperatures arising from differences in thermal conductivities.

ii) PST Films by Sol-Gel Processing

It is well known that if the ceramic preparation of $Pb(B'B'')O_3$ perovskites is done by conventional processing, formation of stablelsed pyrochlore-type phase(s) invariably occurs. The pyrochlore phases severely degrade the dielectric properties and the primary cause of the variation in dielectric properties reported in the literature[9].

To achieve single phase perovskite PST, a similar approach was used to that pertaining in $Pb(Mg_{1/3}Nb_{2/3})O_3$, whereby the two refractory B-site cations Sc and Ta were prereacted to form thin films of the wolframite phase $ScTaO_4$ before reaction with PbO, as shown in the flow diagram below:

$$Sc(R')_3 + Ta(OR'')_5 \xrightarrow[\Delta]{ROH} ("RO)_3Ta(OR)_2Sc(R')_3 \text{ (stock solution)}$$

R = $CH_2CH_2OCH_3$

R' = $CH_3COCHCOCH_3$

R" = $-CH_2CH_3$

A stock solution containing Pb^{2+} was also prepared using lead acetate trihydrate:

$$Pb(R'COO)_2 + 2ROH \rightarrow Pb(OR)_2 + 2R'COOH$$

R = $-CH_2CH_2CH_3$

R' = $-CH_3$

Precursor solutions were then applied to a substrate via a 0.02μm filter, followed by spin-coating on sapphire substrates at 2000rpm for 30 seconds. Thicker films were processed by multiple depositions with pyrolysis of organics between layers. $ScTaO_4$ films were typically fired at 800-1000°C for 5 hours. PST films were obtained by spin coating $Pb(OR)_2$ solution onto the $ScTaO_4$ film, and then firing at 900-1000°C in $PbZrO_3$ spacer powder.

A typical X-ray diffraction trace for a 4μm thick film after firing is shown in Figure 6. The peaks are typical for a cubic perovskite structure with a lattice parameter value of a_0 = 4.075Å, which is in accordance with earlier results[10].

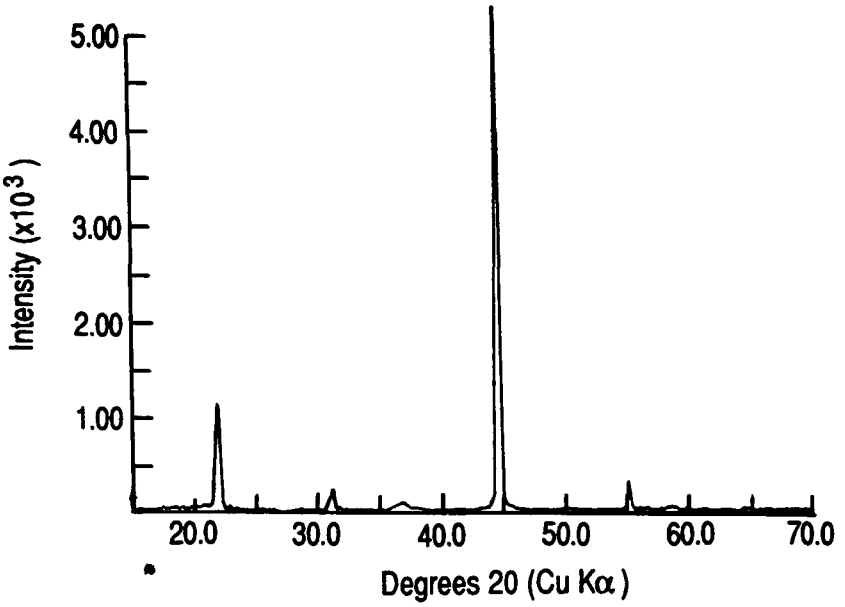


FIGURE 6 X-ray diffraction trace of PST film on sapphire

It is also evident from the X-ray trace that a high degree of orientation along the (100) axis is obtained. We believe that the degree of orientation in a particular PST film is strongly influenced by the film thickness, and the layering process which may lead to different film textures. Due to this orientation, the degree of B-site ordering cannot be estimated from the relative intensities of superlattice ((111) + (311)) and lattice reflections.

Figure 7 shows (a) surface and (B) cross-sectional SEM photographs of a 4μm PST film. The films exhibited a granular texture with an approximate grain size of 0.5μm. The films were also fully dense and exhibited none of the fine scale porosity normally observed in sol-gel films[11].



FIGURE 7 Electron micrograph of sol-derived PST film on sapphire a) surface; b) cross-section

iii) Film Dielectric Properties

The electrical properties of films from both process routes were measured using either chromium/gold interdigitated electrodes or evaporated aluminium electrodes. Contact to these electrodes was made by ultrasonic wirebonding, and dielectric and pyroelectric measurements obtained using a General Radio bridge type 1615-A and a Wayne Kerr 6425 LCR meter.

Figure 8 (a-c) show the measured properties of the MOCVD grown PST films. The films show the characteristic peak in the dielectric constant with temperature (Figure 8a). Both the films shown are on sapphire substrates, sample A is 1.2μm thick with a peak dielectric constant of $3050\varepsilon_0$ and sample B is 5μm thick with a peak of $1500\varepsilon_0$. These values are somewhat low compared to the ceramic material which has a peak of around $15{,}000\varepsilon_0$. Figure 8b shows the dielectric loss of 0.2%. Ceramic material has a loss of around 0.1%. The affect of bias on the peak in the dielectric constant for sample B is shown in Figure 8c. The resistivity of sample B at 30^0C is $2 \times 10^{10}\Omega$m and the pyroelectric coefficient at 23^0C and 2V/μm was found to be $800\mu Cm^{-2}K^{-1}$.

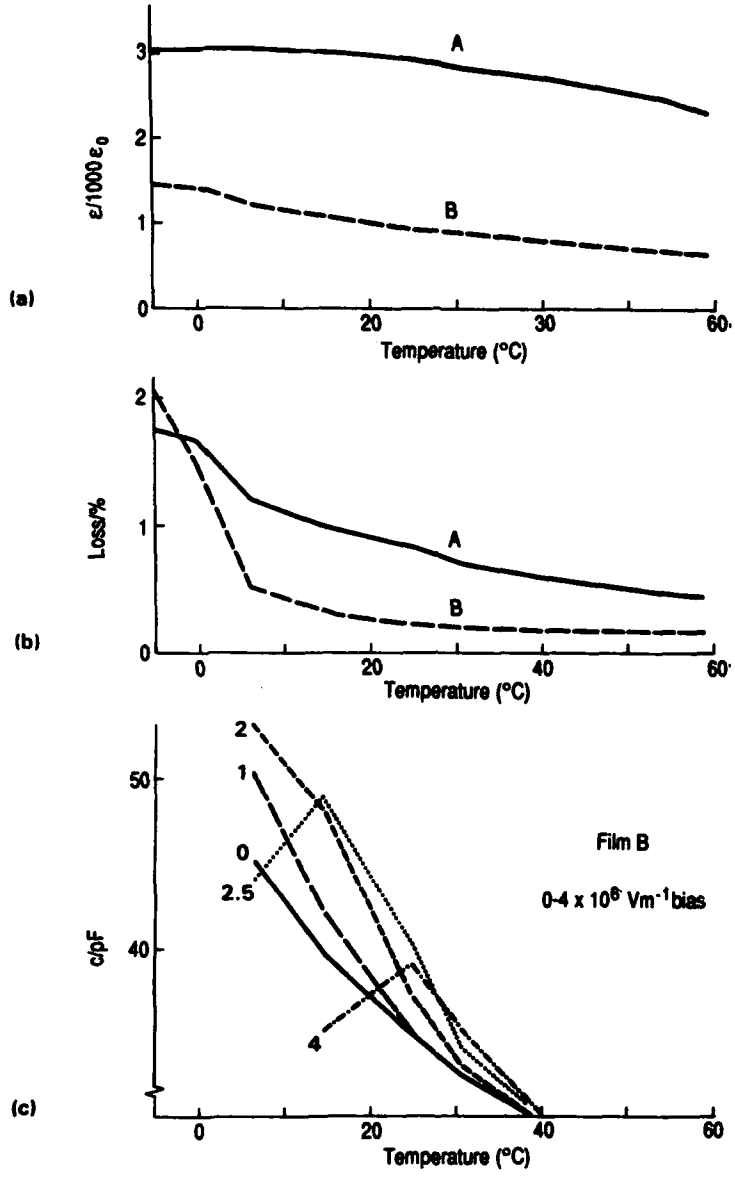


FIGURE 8 Electrical results on annealed PST films
a) dielectric constant; b) loss; c) effect of bias on dielectric constant

The variation of dielectric properties of a 4μm sol-gel derived PST film with varying bias field against temperature are shown in Figures 9(a-b) and It is evident that the behaviour is relaxor type, with a moderately high dielectric constant 4500 and a broad maxima. The dielectric con stant was lower than expected (see above); this low value may be related to the small grain size. The dissipation factor (tanδ) had a minimum value of ~0.4%; which is higher than expected. The measured induced pyroelectric coefficients ranged from 500-900μC/m^2/K for bias voltages of 1-3Vμm^{-1}, (cf bulk ceramic values of 5000 (1Vμm^{-1}), and 2000 (3Vμm^{-1})). The room temperature dc resistivity of the PST film was >10^{11}Ωm, which is comparable to that of bulk ceramic. The film also showed good dielectric strength, surviving 7 x 10^6Vm^{-1}.

For sol-gel derived films on GGG (Gadolinium Gallium Garnet) substrates a marked improvement in the induced pyroelectric coefficient was observed ranging from 3000-4000μC/m^2/K for bias voltages of 1-3Vμm^{-1}. This is well over an order of magnitude greater than the value for, eg, PZT[12]. Consequently, the figure of merit, F_D defined as $F_D = P/(C\sqrt{\varepsilon}.\tan\delta)$ are in the range 7-11 x 10^{-5}Pa$^{-\frac{1}{2}}$ for various sol-derived PST film thicknesses.

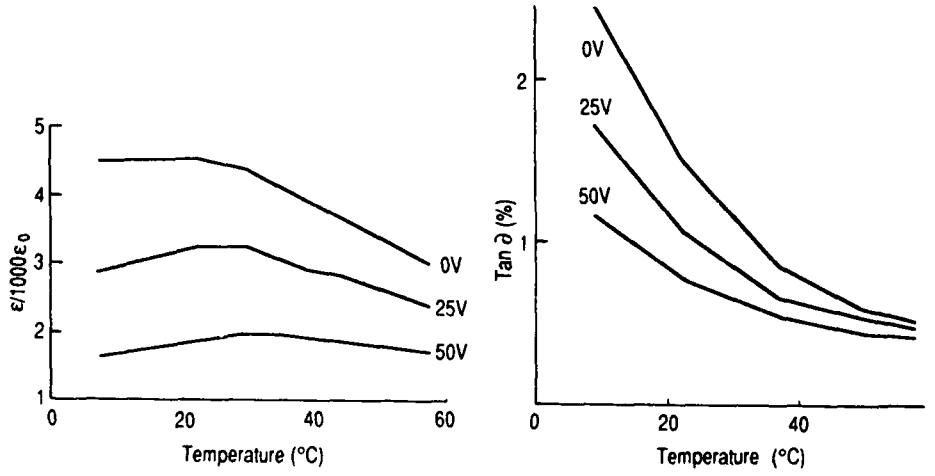


FIGURE 9 Electrical results on sol-derived PST films
a) variation of permittivity under bias vs temperature
b) variation of dissipation factor underbias vs temperature

CONCLUSIONS

It has been demonstrated that complex perovskite oxides can be deposited by MOCVD and Sol-Gel deposition, using a range of metal-organic compounds deposited by which are either commercially available or may be synthesised by standard organic synthesis procedures. MOCVD the grown films show grain sizes between 0.2 and 1.5μm and have been grown up to 5μm thick at a growth rate of 1μm/hour. Furthermore, addition of water or n-butanol to the reactant gas stream significantly enhances the breakdown of the FOD precursor to the oxide. This is particularly important for lead as this is a difficult element to form as the oxide. Also, the addition of water vapour significantly increases the lead oxide content; growth rate and the crystallinity of the films. Annealing of the PST films a 900^{0}C/10 hours has led to a peak dielectric constant of 3000 and loss of 0.2%.

The sol-gel process involves a two-stage deposition, with a film scandium tantalate prepared and fired first on a given substrate. Solutions of lead acetate are then deposited on to the surface to form a composite film which on firing, diffuses the lead oxide as liquid phase resulting in perovskite films of PST. Films obtaine show an average grain size of 0.5μm, peak dielectric constant of 4500, low dissipation factor and high resistivity. The merit figure F_D has been shown to be greater than conventional pyroelectric material,and approaching that of bulk ceramic PST.

ACKNOWLEDGEMENT

This work has been carried out with the support of Procurement Executive, Ministry of Defence.

REFERENCES

1. S.B. Krupanidhi and M. Sayer, J. Vac. Sci. Technol., A2, (2) pp303-306 (1984).
2. M. Kitabatake, T. Mitsuya, K. Hirochi and K. Wasa, Jpn. J. Appl. Phys., 22, Suppl. 22-2, pp31-34 (1978).
3. A. Okada, J. Appl. Phys., 49, (8), pp4495-4499 (1978).
4. N.M. Shorrocks, R.W. Whatmore and P.C. Osbond, Ferroelectrics 106, pp387-392 (1990).
5. B.S. Kwak, E.P. Boyd and A. Erbil, Appl. Phys. Lett., 53, pp1702 (1988).
6. B.S. Kwak, K. Zhang, E.P. Boyd and A. Erbil, J. Appl. Phys., 69, (2), pp767-772 (1991).
7. K.H. Sladek and W.W. Gilbert, in Proc. III, Int. Chem. Vapour Deposition Conferences, pp215-231 (1982).
8. D.C. Bradley, R.C. Mehrotra and D.P. Gaur, 'Metal Alkoxides' (Academic Press Inc., London, 1978).
9. T.R. Shrout and A. Halliyal, Am. Ceram. Soc. Bull., 66 (4), pp704 (1987).
10. C.G.F. Stenger, F.L. Scholton and A.J. Burggraaf, Solid State Commu., 32, pp989 (1979).
11. D.P. Partlow and J. Greggi, J. Mater. Res., 2 (5), pp595 (1987).
12. N. Tohge, S. Takahashi and T. Minami, J. Am. Ceram. Soc., 74 (1), pp67-71 (1991).

AD-P006 656

SOL-GEL DERIVED FERROELECTRIC THIN FILMS IN SILICON MICROMACHINING

C.-C. HSUEH, T. TAMAGAWA, C. YE, A. HELGESON, and D. L. POLLA
Department of Electrical Engineering
University of Minnesota
Minneapolis, Minnesota 55455

Abstract Ferroelectric thin films have been integrated with silicon micromechanical structures in the fabrication of microsensor and microactuator structures. Both the piezoelectric and pyroelectric effects in thin films of lead zirconate titanate ($Pb(Zr_xTi_{1-x})O_3$) and lead titanate ($PbTiO_3$) have been used for physical force sensing (pressure sensor), thermal heat sensing (pyroelectric infrared detector), and microactuation (mechanical positioner). Solid-state micromachining is used to form mechanical membranes on a silicon wafer for implementing easily deformable membranes of structures with a low thermal mass. This paper demonstrates the compatible simultaneous integration of 1) sol-gel deposited ferroelectric thin films, 2) surface-machined micromechanical structures, and 3) *n*-well CMOS integrated circuit technologies.

92-16120

INTRODUCTION

Ferroelectric materials show excellent properties for silicon-based piezoelectric and pyroelectric microsensor and microactuator applications [1]. In particular, the piezoelectric coefficients of the perovskite ferroelectric thin films lead zirconate titanate ($Pb(Zr_xTi_{1-x})O_3$ or PZT) and lead titanate ($PbTiO_3$) are approximately 15-30 times larger than that of previously used non-ferroelectric materials such as aluminum nitride (AlN) and zinc oxide (ZnO). The pyroelectric properties in these ferroelectric thin films are approximately 100 times larger than in previously used non-ferroelectric (ZnO) thin films. The large piezoelectric properties of PZT are therefore ideally suited for integrated microsensor applications such as 1) pressure sensing [2], 2) tactile force sensing [3], 3) acceleration measurement [4], and 4) a variety of sensing applications based on surface-acoustic wave (SAW) devices [5]. The large pyroelectric response of $PbTiO_3$ are ideally suited for 1) room temperature infrared detection

[6], 2) hot wire anemometry [7], and 3) chemical enthalpimetric detection [8]. Furthermore, the large inverse piezoelectric effect observed in ferroelectric films may be suitable for future micromechanical positioner and micromechanical motor applications [9,10].

Piezoelectric thin films have been used in microsensor applications over the last twenty years. When combined with silicon electronic circuitry [11], these films form useful integrated microsensors with 1) low-noise, 2) low power dissipation, 3) compact size, and minimal interconnection parasitic losses.

Solid-state micromachining [12] has recently been used in forming 0.5-3.0 μm-thick micromechanical membranes of such materials as polycrystalline silicon, silicon nitride, and aluminum which easily deform in response to an applied force or implement a low thermal mass structure. These membranes are often machined through lateral, selective etching techniques known as micromachining.

This paper considers the use of ferroelectric thin films in integrated microsensor and microactuator applications. A generic device structure is shown in Fig. 1. In particular, three processes are integrated on a single silicon chip: 1) sol-gel ferroelectric deposition, 2) surface-micromachining, and 3) NMOS and *n*-well CMOS integrated circuits. Materials and process integration issues are emphasized. Some case examples of ferroelectric pressure sensors, infrared detectors, and micromechanical positioners are briefly discussed.

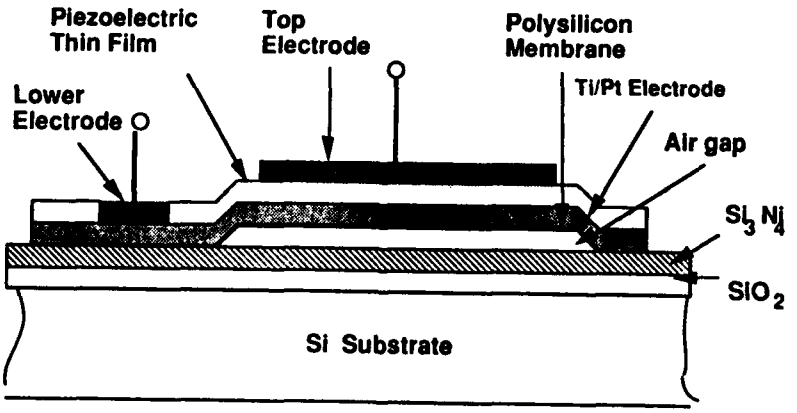


Fig.1. a) Cross section of a PZT or $PbTiO_3$ ferroelectric capacitor integrated on a surface-micromachined membrane. b) Optical photograph of PZT (54/46) microstructures (top view).

MATERIAL PROPERTIES OF SOL-GEL DEPOSITED FERROELECTRIC THIN FILMS

Several sol-gel methods have previously been reported [13-15]. The sol-gel deposited ferroelectric films used in this work start with the preparation of liquid precursors [16]. Metal-organic starting materials such as alkoxides, acetates, and inorganics are used. The "sol" is prepared by dispersing the starting materials in alcohol solvents. Water and catalysts are added to the sol solution to initiate a series of hydrolysis and polycondensation reactions resulting in the production of a viscoelastic "gel" network [17]. The sols are then partially hydrolyzed to give rise to precursor solutions with suitable viscosity for spin-casting.

Spin-casting of the sol-gel material is carried out in much the same manner as photoresist dispensing. For the microstructures used in the devices of this work, the sol-gel technique suffers the same limitations as the application of photoresist over features with varying topology [1]. Device structure design rules and processing steps were developed to take this limitation into account. Application of sol-gel films were carried out through successive 800-900 Å spin-castings on polycrystalline silicon membranes with 500-1000 Å sputtered platinum nucleation electrode. Drying and pyrolysis of the films was carried out after successive spin-castings. A final firing step at 650 °C produced PZT films with a perovskite structure.

PZT films of 0.1-0.8 μm thickness with various ratios of zirconate to titanate have been done by sol-gel methods in our laboratory. The device work discussed below used films of 54% zirconate to 46% titanate. This ratio lies near the morphotropic phase boundary and can be expected to exhibit strong piezoelectric properties, although the validity of the bulk material phase diagram for these thin film samples still requires more investigation. These films have exhibited excellent microstructure [16] and good ferroelectric properties, although some variation with deposited film thickness has been observed.

A typical x-ray diffraction spectrum is shown in Fig. 2. A transmission electron micrograph (Fig. 3) showing the presence of ferroelectric domains demonstrates that dense PZT films can be obtained by the sol-gel deposition technique. Although our devices have not been optimized for ferroelectric properties, conventional Sawyer-Tower electrical characterization techniques (and TEM and x-ray diffraction) have been used for convenience in evaluating our processed ferroelectric films. The fatigue characteristics of our films are shown in the remanent polarization and coercive field versus number of ±10 V electric cycles plot shown in Fig. 4.

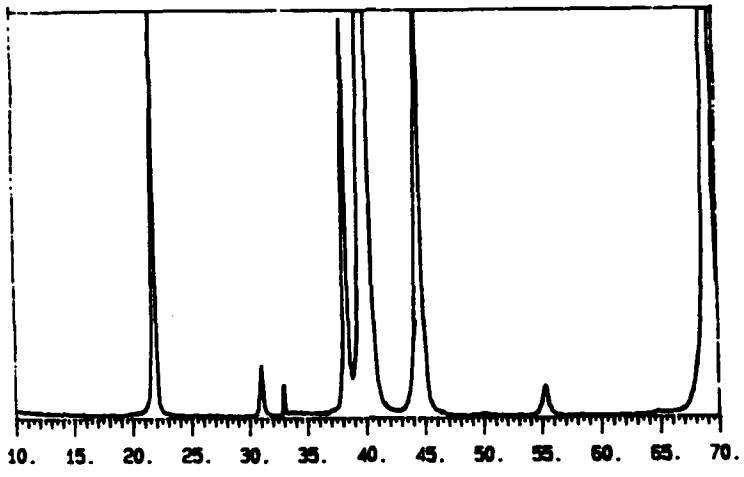


Fig. 2. Typical x-ray diffraction pattern of a sol-gel deposited PZT (54/46) thin film used for microsensor applications.

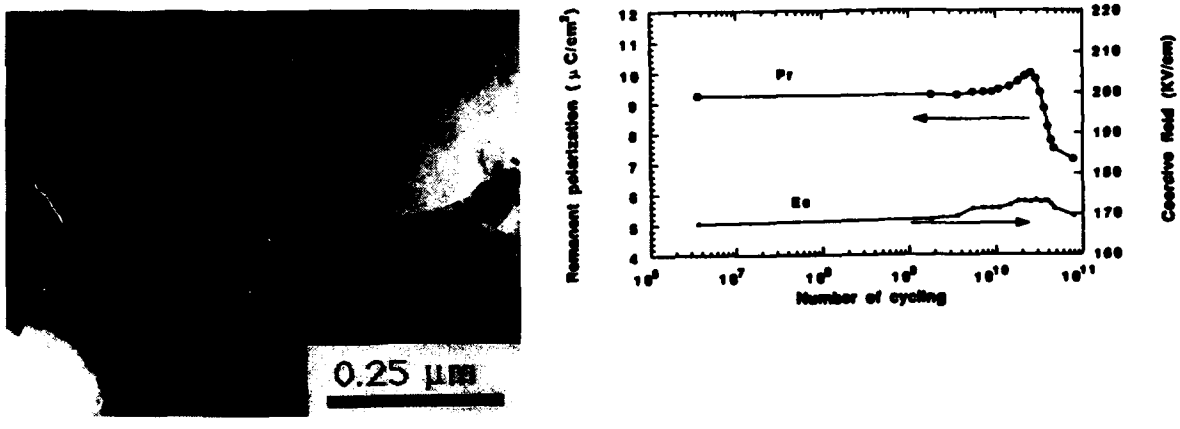


Fig. 3. Transmission electron micrograph of a sol-gel deposited PZT thin film. The observation of ferroelectric domains indicates excellent dense film quality.

Fig. 4. Dependence of remanent polarization and coercive electric field versus number of ±10 V cycles for a PZT (54/46) thin film. Area = 2.83×10^{-3} cm^2, thickness = 0.28 µm, cycling frequency = 1 MHz, measurement frequency = 500 Hz.

MICROMACHINING AND PROCESS INTEGRATION

Micromachining refers to the materials processing techniques used to form useful micromechanical structures. Two general forms are used: bulk-micromachining and surface-micromachining. The major difference lies in the

removal of the backside substrate or a sacrificial layer from the surface of the wafer. Of the two approaches, we believe surface-micromachining holds more promise for VLSI systems for the following reasons [18]: 1) no two-sided photolithography is required, 2) no non-standard chemicals are used, 3) precise dimensional control can be achieved, and 4) the mechanical integrity of the substrate is not weakened.

Ferroelectric fabrication begins with either MOS circuits processed up to the point of source-drain contact opening if integrated microsensor structures are to be made or with Si_3N_4/SiO_2 covered silicon substrates if off-chip electronics are to be used. A 0.3 μm-thick layer of low-pressure-chemical-vapor-deposited (LPCVD) silicon nitride and a 0.8 μm-thick layer of phosphosilicate glass (PSG) are first deposited at 800 ^{o}C and 450 ^{o}C, respectively. The silicon nitride layer forms an encapsulation layer to protect the almost finished CMOS circuitry from subsequent processing of the on-chip sensors and the PSG serves as the sacrificial oxide spacer used in the formation of sensor membrane structures. The PSG is patterned and chemically etched to form anchor regions for a subsequent phosphorus-doped polysilicon microstructure membrane deposition (by LPCVD). Sensor membrane regions are defined and anisotropically patterned in a SF_6/CCL_2F_2 plasma by reactive-ion-etching (RIE). A high-temperature anneal at 1050 ^{o}C for one hour is performed in a nitrogen ambient to improve polysilicon stress properties [19]. A 500-1000 Å-thick lower platinum electrode is then sputtered over the entire wafer. The platinum serves the dual purpose of providing an adhesion/nucleation surface for the subsequently deposited PZT of $PbTiO_3$ thin film and serves as the lower electrode for piezoelectric and pyroelectric microsensors.

Sol-gel spin-casting of ferroelectric PZT or $PbTiO_3$ is then carried out as previously described. The ferroelectric films are then patterned by either chemical etching or ion beam sputter etching. Photolithography is then used to protect the ferroelectric thin films in carrying out a lateral sacrificial etching step of the PSG layer. This step is commonly called surface-micromachining. Doubly-supported, suspended, structures are released using 48 wt% hydrofluoric acid to undercut the PSG spacer layer. The polysilicon membrane therefore forms an easily deformable structure desirable for force sensing or a low thermal mass structure necessary for pyroelectric detection. For pressure sensors, the open side walls of the microbridge are sealed by the directional sputtering of silicon dioxide.

A top electrode to the ferroelectric thin film is then deposited by Ti/Au evaporation. Contact openings to both the CMOS transistors and sensor bottom polysilicon electrode are then chemically etched. This is followed by sputtering aluminum (2% Si) to form interconnects and bonding pads.

Ferroelectric thin film properties are summarized in Table I.

MICROSENSOR CIRCUIT INTEGRATION

There are several key sensor-circuit integration challenges: 1) realization of properly crystallized ferroelectric thin films on micromechanical membranes, 2) compatible merging of piezoelectric thin film deposition techniques with a high performance CMOS process [18], and 3) the ability to carry out necessary micromachining techniques while ensuring the integrity of both microsensors and circuits.

The gate of a MOS transistor provides an excellent interface for piezoelectric capacitors. The high input impedance prevents piezoelectric-induced surface charge from being drained from the capacitor. A simple integration technique for PZT thin film sensors is shown in Fig. 5. An induced stress will produce a charge due to the piezoelectric effect or a change in temperature will produce an induced charge due to the pyroelectric effect. This charge (or voltage) is transduced to the gate of an on-chip NMOS transistor. The amplifiers on our test chip had one input gate connected to a reference potential for bias point control. Alternatively, a differential amplifier configuration can be used to cancel unwanted signals by fixing a second PZT element to the silicon substrate (or optically shielding it).

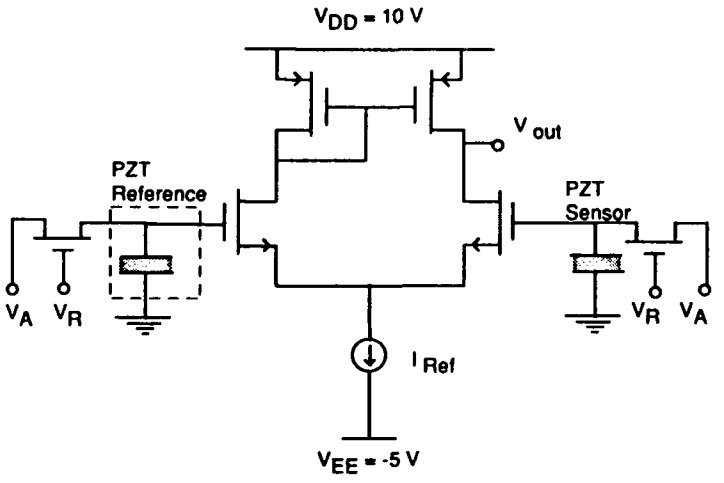


Fig. 5. Basic ferroelectric sensor integration technique.

Because these voltages are directly transduced to the gate of an on-chip MOSFET amplifier, the small-signal drain voltage or change in dc operating point voltage can be conveniently measured for both time-varying and steady-state sensing of stress and temperature change depending on the specific sensing application. In either case, for microsensor optimization this requires the highest possible piezoelectric or pyroelectric coefficients.

Pressure Sensor

As an example, in the design of a thin membrane piezoelectric pressure sensor, the change in capacitor voltage produced due to sound waves stressing the composite membrane structure can be found by determining the change in average polarization of the ferroelectric crystal. The average polarization change depends on the in-plane stress components σ_x and σ_y and is nearly independent of σ_z.

$$P_{zav} = d_{31}(\sigma'_{xav} + \sigma'_{yav})$$

Since the electrodes are formed normal to the z axis, the induced charge on the electrodes is nearly independent of σ_z. From Eqn. (1), the unamplified sensitivity of this microsensor is [2]

$$S = \frac{V_m}{q} = \frac{P_{zav}}{qC_z} = \frac{d_{31}(\sigma'_{xav} + \sigma'_{yav})}{qC_z}$$

where C_z is the capacitance per unit area between the upper and lower electrodes. The details of the solution reveal that the sensitivity is linearly dependent on the side length of the device and is maximized when the membrane is square. Representative pressure sensor data is shown in Fig. 6.

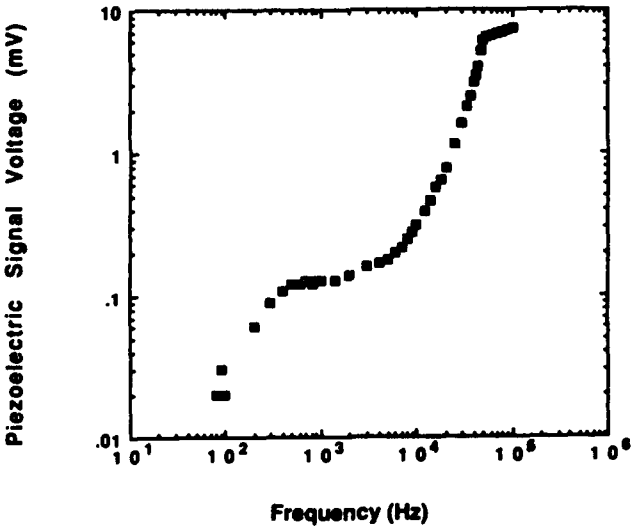


Fig. 6. PZT-on-polysilicon pressure sensor responsivity versus frequency for a 2.83×10^{-3} cm^2 acoustic sensor.

Pyroelectric Infrared Detector

Although pyroelectric sensors have previously been fabricated in a variety of configurations in both bulk and silicon-compatible forms [6,18], a pyroelectric material integrated with polysilicon microbridge technology [20] offers the possibility of achieving an extremely high infrared detectivities at room temperature. Sol-gel deposition of $PbTiO_3$ thin films on 1.0-1.5 μm-thick polysilicon membranes offers a key advantage of implementing an extremely low thermal mass for high sensitivity pyroelectric detection. Its compatibility with silicon MOS technology makes it an attractive choice for system integration with signal processing electronics.

The basic pyroelectric responsivity is given as

$$R_v = \frac{\omega p A_d R_d}{\sqrt{1 + \omega^2 \tau_E^2}} \frac{\varepsilon R_T}{\sqrt{1 + \omega^2 \tau_T^2}}$$

where ω is the chopping frequency, p is the pyroelectric coefficient, A_d is the sensor area, R_d is the detector resistance, R_T is the thermal resistance to a heat sink, ε is the emissivity, τ_E is the electrical time constant, and τ_T is the thermal time constant.

The infrared detector structure is similar to the generic microsensor shown in Fig. 1. The sensor makes use of the pyroelectric effect in $PbTiO_3$ and the extremely low heat capacity of the composite material structure and low thermal conductance between the $PbTiO_3$ element and the underlying silicon substrate. The measured voltage response is shown in Fig. 7.

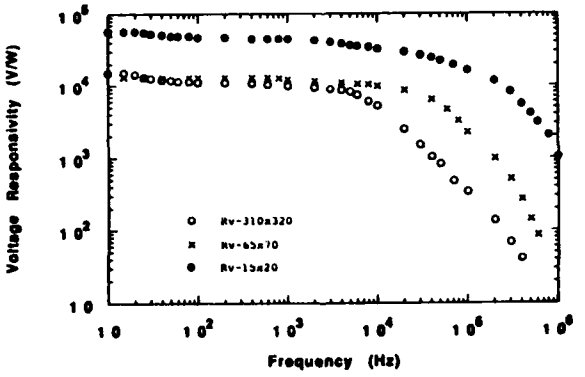


Fig. 7. Infrared responsivity of three pyroelectric $PbTiO_3$-on-polysilicon infrared detectors operating at room temperature. Active areas are 310x320 μm^2, 65x70 μm^2, and 15x20 μm^2.

MICROMECHANICAL DEVICES

Both force sensing and micromechanical actuation are physically governed by the well-known piezoelectric constitutive relations

$$D = \varepsilon^S E + eS$$

$$T = c^E S + eE$$

where D is electric displacement in an electric field E, ε^S is the dielectric constant with zero or constant strain, e is the piezoelectric stress constant, S is the macroscopic strain in the material, T is the externally applied stress, and c^E is the elastic stiffness in the presence of constant or zero electric field. Eqn. (1) relates electric flux density to the electric field strength (E) and considers induced polarization resulting from applied stress. Eqn. (2) is a form of Hooke's Law relating stress to strain and considers strain produced by an applied electric field.

Novel macro- and micro- positioning actuators has been fabricated based on the inverse piezoelectric effect. The basic device is implemented in a geometry of N piezoelectric bars connected in a meander line configuration which are mechanically in series and electrically in parallel [9]. As shown in Fig. 8, each bar is electroded on two opposing faces parallel to the length of the bar with electrical connection made to the terminals of a dc variable power supply. The films on alternating bars are poled in alternating directions to achieve linear expansion and linear contraction in adjacent bars. Because both ends of the meanderline are anchored to a silicon substrate, the center of the meander line experiences a forward displacement equal to N times the change in length of a single piezoelectric bar. An additive displacement is therefore obtained. The folded geometry allows substantially large experimental displacement (4 μm when actuated by 80 V) to be obtained on a microfabricated chip.

The positioning force obtained from the meanderline has been derived by Robbins, et. al. [9,10]. The force F_{pz} is given by

$$F_{pz} = 2 E d_{31} w V$$

where V is the applied voltage, w is the width of the piezoelectric bar, d_{31} is the piezoelectric coupling constant ($d_{31} = 2.8 \times 10^{-10}$ m-V^{-1}), and E is Young's modulus (7×10^{10} N-m^2) for PZT. Typical piezoelectric actuation forces for this device are several milli-Newtons.

Additional microactuator device concepts are being explored in our laboratory

based on ferroelectric thin films. A linear stepper motor on a chip capable of sub-micrometer controlled movement, or nano-actuation, is currently being constructed using PZT [21] as shown in Fig. 9.

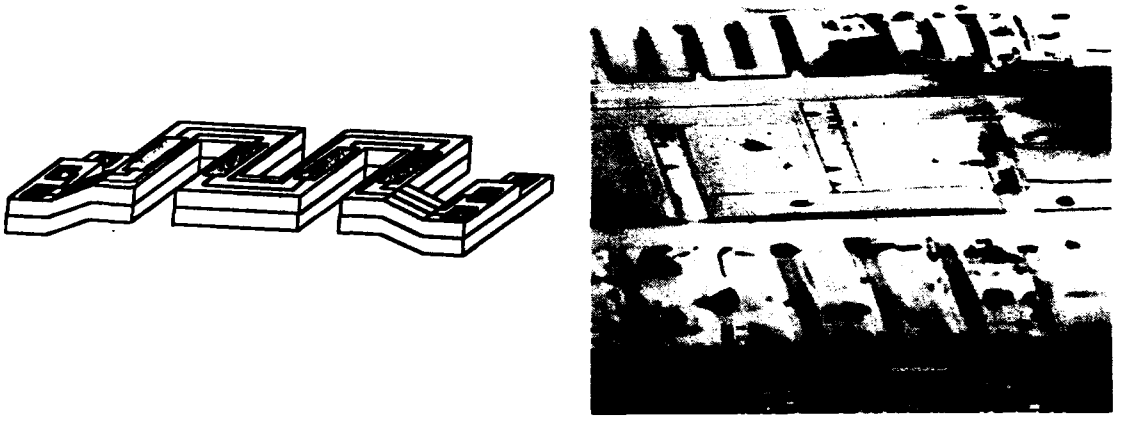


Fig. 8. a) Schematic diagram of a surface-micromachined meanderline microactuator consisting of a series of PZT-on-polysilicon bars connected mechanically in series and electrically in parallel.

b) Chip photograph of the micro-meanderline positioner.

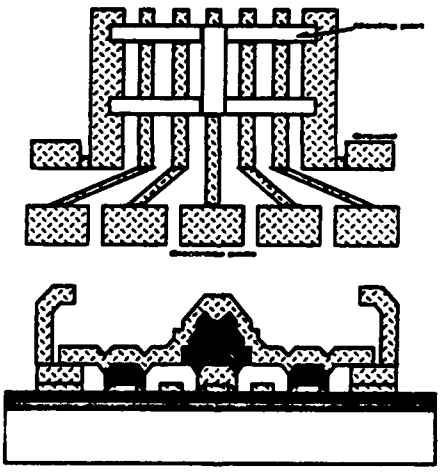


Fig. 9. Schematic diagram of a piezoelectric stepper motor on a chip currently under fabrication at the University of Minnesota.

The device is constrained by polysilicon rails to undergo motion to one dimension. An electrode on the bottom of the glider is used with an electrode on the top of the trench to implement an electrostatic clamp. Motion is implemented through a novel periodic clamping and releasing technique applied to an activated/deactivated PZT element that can be described in four steps. First, the back electrostatic clamp is activated with a large voltage (50 volts max.) to hold the glider in place. Second, the PZT element is extended by an applied voltage which moves the center of mass of the entire structure, glider and attached load, forward. Third, turning off the electrostatic clamp then releases the glider. The voltage across the PZT is held constant during this step keeping the piezoelectric material extended and the overall center of mass in the same position as at the end of the previous step. Fourth, the piezoelectric material is finally snapped back to its original size by turning off its applied voltage. This pulls the back of the glider forward by a small distance d.

Initial success in a prototype PZT macro-version of this device have demonstrated promising results. For the silicon-based micro-version, displacement steps on the order of 10 nm are expected with stepping velocities of micrometers per second.

DISCUSSION OF RESULTS

The use of ferroelectric films in physical microsensor and microactuator applications has shown promising results in the pressure sensor, infrared detector, and micro-meanderline positioner demonstrated to date however much more work needs to be done before practical integrated systems can be realized. First, for physical microsensors, the voltage (charge) responsivity is linearly proportional to the ferroelectric film thickness. Our sol-gel deposition technique has not been able to produce films with thicknesses greater than 0.8 μm without cracking taking place. We are currently experimenting with rapid annealing (firing) techniques to solve this problem. Second, the physical microstructures used in forming membranes require sol-gel spin-casting over topology variations of 1-4 μm. This is an a priori known limitation of the sol-gel method. We are therefore currently integrating recessed and fully-recessed microstructures into our basic fabrication sequence. Third, the large dielectric constants observed in these ferroelectric films limits the voltage responsivity of the sensors being studied but gives a significant enhancement in the charge sensitivity over that of

previously used non-ferroelectric active films. New sensor-circuit integration schemes are therefore being considered. Fourth, a great deal more information regarding thin film ferroelectric physics may be needed. For instance, the measured pyroelectric coefficients and dielectric constants in our $PbTiO_3$ appear to exhibit a dependence on film thickness [20]. The operative physical mechanisms here need to be determined. Finally, the long-term stability, reliability, and reproducibility of ferroelectric thin films for micromechanical applications has not been investigated. Although we believe ferroelectric films for micromechanical applications will have similar electrical reliability characteristics as ferroelectric films used in memory applications, the effects of large and repeated mechanical stressing still needs to be addressed.

CONCLUSIONS

Ferroelectric PZT and $PbTiO_3$ thin films have been integrated for the first time in micromachined, silicon-based, sensor and actuator structures. These ferroelectric films have been deposited by sol-gel deposition techniques with thicknesses ranging from 0.1 to 0.8 μm. Solid-state micromachining techniques have been used to form easily deformable membranes and low thermal mass structures for pressure sensors (based on the piezoelectric effect) and infrared detectors (based on the pyroelectric effect), respectively. A silicon-based linear micro-positioner based on the inverse piezoelectric effect in PZT has also been demonstrated.

The measured piezoelectric and pyroelectric properties of these thin films are excellent and can successfully reproduced on micromachined platinum/polysilicon membranes. Although some initial pressure sensor, infrared detector, and micro-positioner data have been presented, more work is needed in both process integration and understanding of thin films physics.

ACKNOWLEDGEMENTS

The authors would like to acknowledge helpful contributions form Professors William P. Robbins and Martha Mecartney of the University of Minnesota. The help of Messers. Peter Schiller, Wika Tjhen, and Daniel Glumac who have collectively shared in this work is also greatly appreciated. This work was supported by NSF (ECS-8906121, ECS-8821103, and Presidential Young Investigator Award ECS-8814651).

Table I. Measured pyroelectric properties of ZnO, PZT, and $PbTiO_3$ thin films at T = 300 ^{o}K.

	ZnO	PZT	$PbTiO_3$
Relative Dielectric Constant	10.8 - 11.0	800 - 1100	150 - 400
	9.9 - 11.0	500 - 3400	170 - 230
Pyroelectric Coefficient ($x10^{-9}$ C/cm^2-K)	0.95 - 1.05	50 - 70	95
	0.93 - 1.1	76*	30
Piezoelectric Coefficient [d33] (pC/N)	10.5 - 11.5	190 - 250	20
	12.4	156 - 590	42
Resistivity (Ω-cm)	3.9×10^{9}	2.2×10^{7}	$10^{7} - 10^{8}$

REFERENCES

1. T. Tamagawa, D.L. Polla, and C.-C. Hsueh, "Lead Zirconate Titanate (PZT) Thin Films in Surface-Micromachined Sensor Structures," *IEEE International Electron Devices Meeting*, San Francisco, Dec. 1990.
2. E. S. Kim and R. S. Muller, IC-Processed Piezoelectric Microphone, *IEEE Electron Dev. Lett.*, vol. EDL-7, 254(1987).
3. D. L. Polla, W.T. Chang, R.S. Muller, and R.M. White, "Integrated Zinc Oxide-on-Silicon Tactile Sensor Array," *IEEE International Electron Devices Meeting*, Washington, D.C. 1985.
4. P-L. Chen, R. S. Muller, R. D. Jolly, G. L. Halac, R. M. White, A. P. Andrews, T. C. Lim, and M. E. Motamedi, "Integrated Silicon Microbeam PI-FET Accelerometer," *IEEE Trans. Electron. Dev.*, vol. ED-29, 27 (1982).
5. S. W. Wenzel and R. M. White, "A Multisensor Employing an Ultrasonic Lamb-Wave Oscillator," *IEEE Trans. Electron Dev.*, vol. ED-35, 735 (1988).

6. D. L. Polla, R. S. Muller, and R. M. White, "Fully-Integrated ZnO on Silicon Infrared Detector Array," *IEEE International Electron Devices Meeting*, San Francisco, CA 1984.
7. D. L. Polla, R. S. Muller, and R. M. White, "Monolithic Zinc-Oxide on Silicon Pyroelectric Anemometer," *IEEE International Electron Devices Meeting*, Washington, D.C. 1983.
8. D.L. Polla, R.M. White, and R.S. Muller, "Integrated Chemical-Reaction Sensor," *Third International Conference on Solid-State Sensors and Actuators*, Philadelphia, PA 1985.
9. W.P. Robbins, D.L. Polla, and D. Glumac, "High-Displacement Piezoelectric Actuator Utilizing a Meander Line Geometry," *1990 Sonics and Ultrasonics Symposium*, Honolulu, Hawaii, 1990 and *IEEE Trans. on Ultrasonics, Ferroelectrics, and Frequency Control*, September 1991.
10. W.P. Robbins, "Theory of High-Displacement Piezoelectric Actuator Utilizing a Meander Line Geometry," *IEEE Trans. on Ultrasonics, Ferroelectrics, and Frequency Control*, September 1991.
11. D. L. Polla, R. S. Muller, and R. M. White, "Integrated Multisensor Chip," *IEEE Electron Dev. Lett.*, vol. EDL-7, 254 (1986). Reprinted in Microsensors, (R.S. Muller, R.T. Howe, S.D. Senturia, R.L. Smith, and R.M. White, eds.) IEEE Press, New York 1990.
12. K. E. Petersen, "Dynamic Micromechanics on Si: Techniques and Devices, "*IEEE Trans. Electron Dev.*, vol. ED-25, 2141(1978).
13. R. W. Vest and J. Xu, "$PbTiO_3$ Films for Metalloorganic Precursors," *IEEE Trans. on Ultrasonics, Ferroelectrics, and Frequency Control*, 35, 711 (1988).
14. G. Yi, Z. Wu, and M. Sayer, "Preparation of $Pb(Zr,Ti)O_3$ Thin Films by Sol Gel Processing: Electrical, Optical, and Electro-Optic Properties, *J. Appl. Phys.*, 64, 2717 (1988).
15. S. K. Dey and R. Zuleeg, "Integrated Sol-Gel PZT Thin-Films on Pt, Si, and GaAs for Non-Volatile Memory Applications," *Ferroelectrics*, 108, 37 (1990).
16. C.-C. Hsueh and M. L. Mecartney, "TEM Analysis of Sol-Gel Derived and Sputtered PZT Thin Films," *Mat. Res. Soc. Symp. Proc.* 200, 219 (1990).
17. B. J. J. Zelinski and D. R. Uhlmann, *J. Phys. Chem. Solids*, 45, 1069 (1984).
18. D.L. Polla, H. Yoon, T. Tamagawa, and K. Voros "Integration of Surface-Micromachined Zinc Oxide Sensors in n-Well CMOS Technology," *IEEE International Electron Devices Meeting*, Washington, D.C. 1989.
19. H. Guckel, J.J. Sniegowski, T.R. Christenson, S. Mohney, and T.F. Kelly, *Sensors and Actuators*, 20, 117 (1989).
20. C. Ye, T. Tamagawa, and D. L. Polla, "$PbTIO_3$ Pyroelectric Microsensors," *Sixth International Conference on Solid-State Sensors and Actuators*, San Francisco, CA, June 26, 1991.
21. J. Judy, D.L. Polla, and W.P. Robbins, A Linear Piezoelectric Stepper Motor with Sub-Micrometer Displacement and Centimeter Travel," *IEEE Trans. on Ultrasonics, Ferroelectrics, and Frequency Control*, **UFFC-37**, 428-437, 1990.

AD-P006 657

THIN PIEZOELECTRIC VDF-TrFE COPOLYMER FILMS FOR DATA STORAGE

PETER GÜTHNER, JOACHIM GLATZ-REICHENBACH,
DORIS SCHILLING and KLAUS DRANSFELD
Universität Konstanz, Fakultät für Physik, D-7750 Konstanz, FRG

ABSTRACT: We used the Scanning Nearfield Acoustic Microscope - a non-touching profilometer with a conducting tip - both to pole thin ferroelectric VDF-TrFE copolymer films and to subsequently monitor the resulting piezoelectrically stimulated surface motion. For thin uncovered polymer films we were able to measure simultaneously the piezoactivity and the surface topography with a lateral resolution of 1 μm.
Furthermore we used a focused electron beam to create a poling pattern of narrow lateral extension and detected the corresponding local piezoactivity by using the Scanning Nearfield Acoustic Microscope.

INTRODUCTION

In the past the piezoelectric behavior of polyvinylidenefluoride PVDF and vinylidenefluoride-trifluoroethylene VDF-TrFE copolymer films was measured only averaged over large samples[1]. These experiments determined the piezoelectric constant by applying a stress to the polymer film and detecting the generated surface charges. More recently also experiments using a Scanning Tunneling Microscope (STM) to investigate the local piezoactivity were reported[2].

For both methods it is necessary to cover the sample with metal electrodes. For very thin polymer films (< 100 nm) it is difficult to use a metal top electrode without the danger of an electrical short circuit to the bottom electrode.

The Scanning Force Microscopy (SFM)[3] is a new technique to investigate also non-conducting surfaces with an atomic resolution and to detect magnetic structures[4], localized charges[5] or ferroelectric domains[6]. For the experiments described in this paper we used the *Scanning Nearfield Acoustic Microscope* (SNAM)[7,8], a special kind of SFM. The SNAM uses the edge of a commercial tuning fork made of quartz as a distance sensor. By approaching the quartz to the sample surface the hydrodynamic interaction attenuates the oscillation of the quartz resonator leading to a reduction of the vibrational amplitude. This can be

92-16121

used to regulate the distance between the edge of the quartz and the sample surface.

For technical application, for example for ferroelectric data storage devices, it is of great advantage to work with thin polymer films. With decreasing film thickness d also the necessary poling voltage is reduced (for d = 50 nm the poling voltage is about 5 V). It is possible to produce very thin VDF-TrFE copolymer films of less than 100 nm thickness by using the spin coating technique.

Copolymer films of vinylidene fluoride and trifluoroethylene P(VDF-TrFE) show ferroelectric properties for a VDF content of more than 50 mol%. Their morphology is semi-crystalline, the ferroelectric crystallites are embedded in an amorphous matrix. Investigations of the structure of P(VDF-TrFE) films by scanning electron microscopy[9], x-ray diffraction[10] as well as synchrotron radiation experiments[11] indicate that the size of the crystallites ranges from 10 to perhaps 100 nm.

After poling in sufficiently high electric fields (> 100 MV/m) these polymers exhibit a remanent polarization and show both pyroelectric and piezoelectric behavior. The dynamic of the polarization process was studied in detail by Furukawa et. al.[12] and by Eberle et. al.[13]. Switching times below 1 μs for very high electric fields were reported for thick films (d>1 μm)[12] as well as for thin films[14]. To investigate the unknown local polarization process a microscopic method has to be used and will be described in this paper.

One approach to this problem is the use of a STM[2]. But for STM studies it is necessary to cover the film with a metal film also serving as a poling electrode. This may modify the original properties of the polymer. For the generation of polarized regions with small lateral extensions without a limiting top electrode we used a focused electron beam. This method is described elsewhere[15]. By applying the poling voltage directly to the conducting tip of the Scanning Nearfield Acoustic Microscope (SNAM) local poling can be achieved and the local poling process can be observed in situ. To read out the ferroelectrically written information we applied a small AC field between the distance sensor and the bottom electrode, thus observing the piezoelectrically induced local surface motions of our thin polymer films.

EXPERIMENTAL SETUP AND TEST OF THE INSTRUMENT

The polymer films were produced by the spin coating technique on well cleaned flat glass plates coated by a 300 nm aluminum layer. Our copolymer had a VDF content of 60 mol%. The thickness of the polymer films varied between 0.1 and 5 μm. To increase the crystallinity of the samples they were annealed up to 145°C for two hours. On top of some of the VDF-TrFE copolymer films a 50 nm thick aluminum electrode was evaporated covering only a part of the sample (0.1 cm^2).

For our experiments on these films we used a Scanning Nearfield Acoustic Microscope (SNAM)[7,8]. This microscope is a non-touching profilometer using a commercial tuning fork as a distance sensor having a lateral resolution of about 1 μm and a height resolution of 10 nm. In order to measure the piezoelectric sur-

face motion of the VDF-TrFE copolymer films, a low frequency (10 - 100 Hz) AC electric field (approx. 10 V) is applied to the polymer. The stimulated surface motion (approx. 0.4 nm) is detected by the SNAM sensor using the lock-in technique.

Interestingly it is also possible to investigate the local piezoelectric hysteresis. For this purpose we applied simultaneously a high DC electric field to polarize the polymer film and a small AC electric field (having an amplitude of 7 V and a frequency of 10 Hz) to generate a piezoelectric surface motion. From an analysis of the local hysteresis loop[16] we find a coercive field of about 40 MV/m and a piezoelectric constant of $d_{33} \cong 40$ pm/V which agree both with existing results for thick (d = 20 μm) copolymer films[17].

Using our SNAM sensor as a probe it is possible to measure the local piezoelectric activity with a lateral resolution of 1 μm. For this experiment we used a polymer film covered by a round top aluminum electrode having a thickness of about 50 nm and a diameter of 3 mm. The area of the polymer film underneath this metal layer was poled by applying a DC electric field of 100 MV/m for 5 minutes at room temperature. The area outside of the top electrode was not polarized.

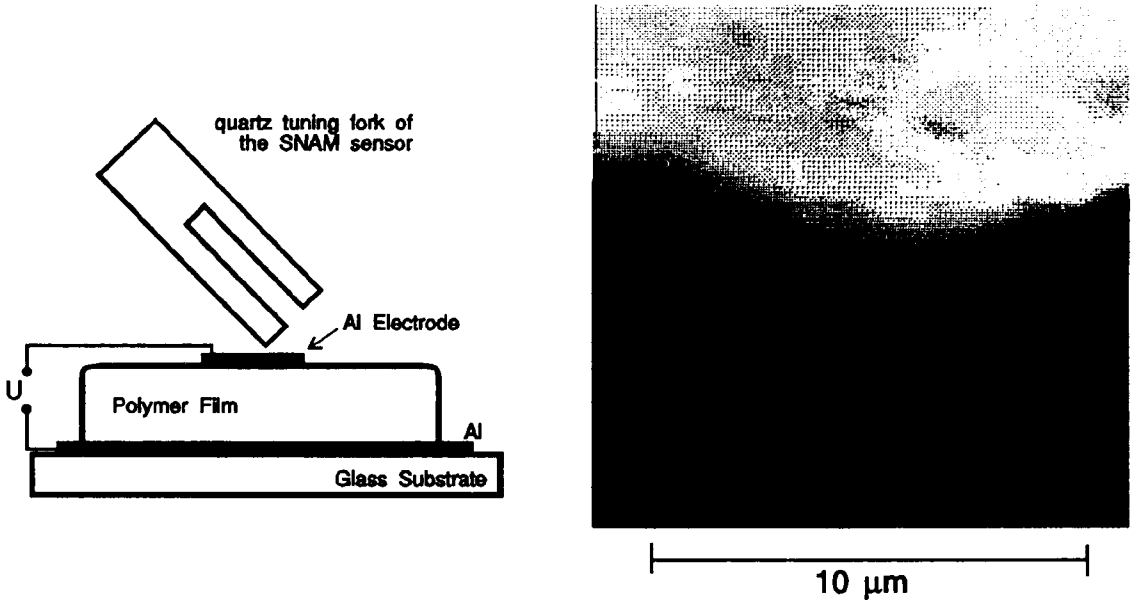


FIGURE 1: **Left side:** A polymer film (60/40 VDF-TrFE, thickness 2μm) spin coated on a metallized glass substrate was covered partly by a 50 nm aluminum layer. The surface motion - stimulated by an AC electric field - applied between the top and the bottom Al electrode - was measured with the Scanning Nearfield Acoustic Microscope (SNAM).
Right side: A two dimensional image of the piezoactivity of a partly metallized VDF-TrFE sample. After poling only the metallized region shows a high piezoactivity (bright area) whereas the non-metallized region is not piezoactive (dark area).

For imaging the locally resolved piezoactivity our SNAM was scanned over the sample in two dimensions at constant height. At the same time we applied a

small AC field (well below the coercive field) to stimulate the surface motion. The feedback signal corresponds to the topography. The vibration amplitude of the polymer film is detected by the lock-in amplifier. In this way it is possible to image the surface topography and the local piezoelectric activity simultaneously. Fig. 1 shows the image of the local piezoelectricity for the transition between the metallized and the non-metallized area of the sample. The upper part of the sample was metallized and shows a strong piezoactivity (bright), whereas the lower part is not metallized and was therefore not poled. This region is dark which indicates no piezoactivity.

DATA STORAGE IN NON-METALLIZED SAMPLES

We used a thin VDF-TrFE copolymer film spin coated onto an aluminized glass substrate without any top electrode. To polarize the film and to measure the piezoelectricity we used the SNAM sensor. The electric field is now applied between the metallized electrode of the quartz resonator and the bottom electrode of the sample. Otherwise the principle of the experiments is the same as for the metallized polymer films.

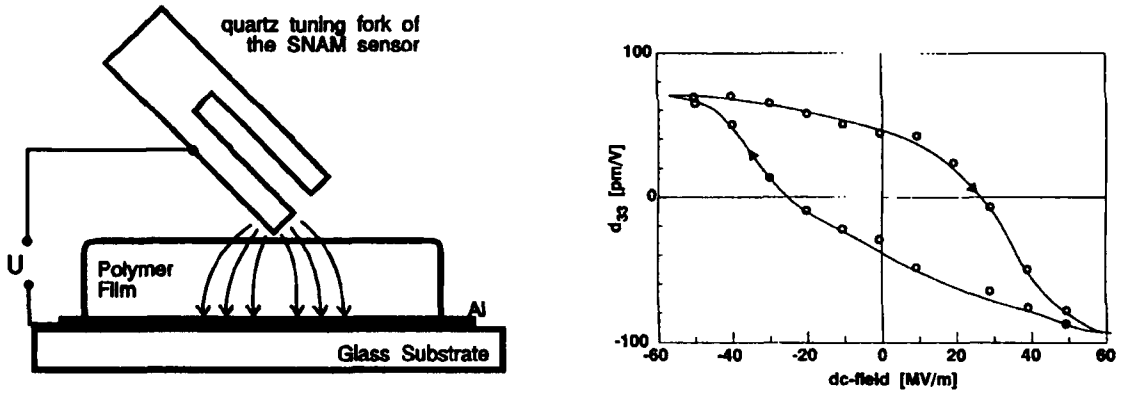


FIGURE 2: The **left side** shows the principle setup for measuring the piezoelectricity of non metallized samples with the SNAM sensor. The high DC electric field for the poling and the small AC electric field for the piezoelectric stimulation are applied between the gold electrode of the quartz and the bottom electrode of the polymer film.
On the **right side** the piezoelectric hysteresis of a previously poled polymer film is shown. The shape of the curve is caused by the inhomogeneous electric field underneath the edge of the quartz.

This setup enables us to polarize and to stimulate small areas underneath the edge of the quartz. To test the system we have measured the piezoelectric hysteresis of the uncovered polymer. Fig. 2 (right side) shows the piezoactivity of the sample as a function of the applied DC poling field. In this setup the electric field is inhomogeneous and therefore we used the averaged electric field for the scale. The shape of the hysteresis curve deviates clearly from the more rectangu-

lar loops of ferroelectric polymers measured elsewhere[2,12,16,17]. This different behavior may be caused by the inhomogeneous field such that different regions underneath the probe are polarized at different applied DC voltages.

The poling procedure by the metal edge, however, leads to a polarized region which was observed to be at least 30 μm. In order to pole smaller areas we used the method of electron beam poling[15], a technique which enables us to create smaller polarization structures on bare films. The poling structure generated in this way can be investigated on a micrometer scale by the Scanning Nearfield Acoustic Microscope.

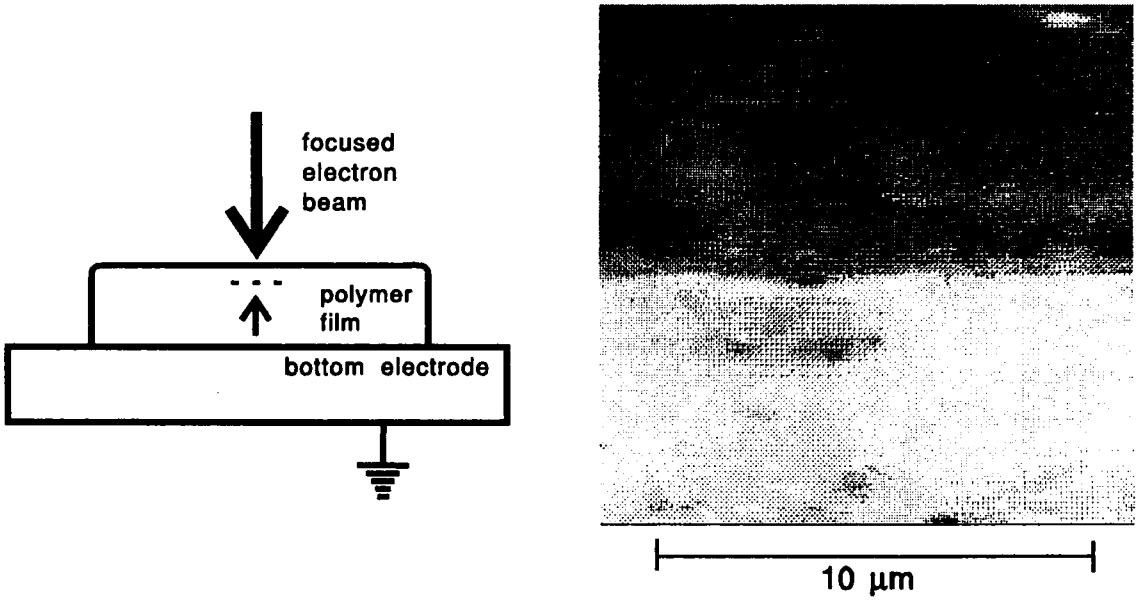


FIGURE 3: The principle of electron beam poling is shown on the **left side**. A bare polymer film is irradiated by a focused electron beam (approx. 5 keV). The penetrating electrons create an electric field towards the grounded bottom Al electrode which leads to a remanent polarization of the polymer film.
On the **right side** a two dimensional image of the piezoelectric activity of a 5 μm thick polymer film measured with the Scanning Nearfield Acoustic Microscope is shown. The lower part was poled by a focused electron beam. Bright areas have a strong piezoactivity, dark areas don't show piezoelectric motion.

We have poled small squares (50 x 50 μm^2) by the technique of electron beam poling and imaged these samples subsequently with the SNAM. The field for piezo-stimulation was applied again between quartz and bottom electrode, and the corresponding surface motion was detected by the SNAM sensor. Fig. 3 shows a two-dimensional image of the piezoactivity of a partly electron beam poled sample. The upper part was not polarized and therefore it shows no piezoactivity (dark), the lower part (bright) was irradiated by a focused electron beam and therefore a piezoactivity was measured. The achieved lateral resolution of

our technique is better than 1 μm. The minimum detectable piezoactivity in these thin films is of the order of 1 pm/V.

CONCLUSION

We have demonstrated that it is possible to polarize very thin non-metallized VDF-TrFE copolymer films locally. At the same time the direction of the polarization can be measured locally by monitoring the phase of the piezoelectric surface motion. This enables us in principle to write and read digital information on these samples.

The lateral resolution of our instrument is limited by the geometry of our tuning fork quartz and can be improved. In order to reach a higher resolution similar experiments using a Scanning Force Microscope (SFM) are in progress. The problems involving the speed of the writing and the reading process will be discussed elsewhere.

REFERENCES

1. T. Furukawa; IEEE Transactions on Electrical Insulation **24**, 375 (1989)
2. H. Birk, J. Glatz-Reichenbach, Li-Jie, E. Schreck and K. Dransfeld; J. Vac. Sc. Techn. (3/91)
3. G. Binnig, C. F. Quate and Ch. Gerber; Phys. Rev. Lett. **56**, 930 (1986)
4. D. Rugar, H. J. Mamin, P. Güthner, S. E. Lambert, J. E. Stern, I. McFayden and T. Yogi; J. Appl. Phys **68**, 1169 (1990)
5. B. D. Terris, J. E. Stern, D. Rugar and H. J. Mamin; Phys. Rev. Lett. **63**, 2669 (1989)
6. F. Saurenbach and B. D. Terrisw; Appl Phys. Lett. **56**, 1703 (1990)
7. P. Güthner, U. Ch. Fischer and K. Dransfeld; Appl. Phys. **B48**, 89 (1989)
8. P. Güthner, E. Schreck, K. Dransfeld and U. Ch. Fischer; in: R.J. Behm, N. Garcia and H. Rohrer (eds.), Scanning Tunneling Microscopy and Related Techniques; p. 507, Dordrecht 1990
9. K. Kimura and H. Ohigashi; Jpn. J. Appl. Phys. **25**, 383 (1986)
10. H. Ohigashi, S. Akama and K. Koga; Jpn. J. Appl. Phys **27**, 2144 (1988)
11. C. Leonard-Bourgaux, J.-F. Legrand, P. Delzenne and J. Lajzerowicz; Ferroelectrics **109**, 327 (1990)
12. T. Furukawa; Phase Transitions **18**, 143 (1989)
13. G. Eberle, E. Bihler and W. Eisenmenger; IEEE 1990 Anual Report Conf. Electr. Insul. and Dielectr. Phenom., p. 41 (1990)
14. Li-Jie, E. Schreck and K. Dransfeld; to be published
15. D. Schilling, Ph.D. thesis, Universität Konstanz 1988 (Hartung-Gorre, Konstanz, 1988)
16. P. Güthner, J. Glatz-Reichenbach and K. Dransfeld; J. Appl. Phys. (5/91)
17. T. Furukawa, J. X. Wen, K. Suzuki, Y. Takashina and M. Date, J. Appl. Phys. **56**, 829 (1984)

AD-P006 658

PHOTOVOLTAGES IN FERROELECTRIC FILMS

P. S. BRODY AND B. J. ROD
Harry Diamond Laboratories, U.S. Army LABCOM, Adelphi MD 20783

Abstract: Polarization-dependent steady photovoltaic currents were found in thin lead zirconate-titanate films on silicon substrate. In addition to a polarization-dependent current, there was a steady non–polarization-dependent background current. There were also transient photovoltaic currents that appeared once, in an initial response to illumination, after the remanent polarization is switched. For mercury arc illumination and a 0.25-μm-thick, sol gel process, 53/47 Zr/Ti ratio film, the polarization-dependent current was equal to 2.7 A/C per W/cm^2.

INTRODUCTION

Steady-state photocurrents that are proportional to remanent polarization are characteristic of uniformly illuminated ferroelectric ceramics [1–3]. Reversing the direction of polarization reverses the direction of the photocurrent. Open-circuit voltages are proportional to the length of ceramic between electrodes and can be very large, greatly exceeding the potential difference of the energy gap. This phenomenon is considered anomalous (the anomalous photovoltaic effect or APE), since the photovoltages do not appear to result from band bending at contacts or the Dember effect (which is due to gradients in photocarrier density). A similar high-voltage effect is found in ferroelectric single crystals [4]. The single-crystal phenomenon is also identified as an anomalous effect. There are, however, reasons to believe that the mechanism producing high voltages in ceramics differs from that producing such voltages in single crystals [5].

Steady photovoltaic currents are also seen in thin ferroelectric films. High voltages have not been observed, but a partial dependence on remanent polarization has been observed [6]. Current progress in the development of thin film integrated ferroelectric-semiconductor structures [7] has made polarization-

92-16122

dependent photovoltages in ferroelectric films a subject of interest. Such photovoltages make possible, in principle, an application to nonvolatile, nondestructive readout memory and to optical correlation [8–10]. In these applications, information is encoded in the direction and magnitude of the remanent polarization, and readout occurs in the form of polarization-dependent photocurrents. Also, polarization-dependent photovoltages have been used to study remanent polarization decay in ceramics [11], and the same technique may also be useful for studying the retention of stored memory states in thin film devices.

In this paper we present the results of a study of photovoltaic phenomena in lead zirconate-titanate (PZT) films. We observed steady photovoltaic currents that contained both a polarization-dependent component and a polarization-independent component. We also observed photovoltaic current transients comparable in magnitude to the steady currents. These appeared only in response to an initial illumination pulse. We describe our study in detail and also briefly discuss implications with respect to possible applications.

METHOD OF PRODUCING PHOTOCURRENT AND MEASURING POLARIZATION DEPENDENCE

The films studied were sol-gel process, 53/47 Zr/Ti ratio, lead zirconium-titanate spun cast onto platinum-coated silicon wafers. The platinum was sputter deposited. The wafers were passivated with a thermally grown SiO_2 layer. There was an thin sputter-deposited titanium layer intervening between the platinum and the oxide. An array of top electrodes, each 150×150 μm, was fabricated by the sputter deposition of platinum using a silicon micromachined shadow mask. The electrodes were either thick and opaque, or thin (200 Å) and semitransparent. The semitransparent electrodes transmitted roughly 10 percent of incident illumination.

Each electroded area constituted a thin film ferroelectric capacitor. An experimental arrangement, based on a probe station, allowed pulse voltages to be applied to individual ferroelectric capacitors. The arrangement places a linear measuring capacitor in series with the ferroelectric capacitor in a Sawyer-Tower configuration, so that the remanent polarization change induced by a voltage pulse can be measured. The probe station microscope was trinocular in design. Collimated light from a mercury arc passed through the trinocular

optical train and was focused onto the film. The illumination was controlled with a camera shutter.

Four probes were used in the experimental arrangement (Fig. 1). Probe 2 was used to apply a pulse voltage. Probe 1 was in contact with the electrode to measure the applied voltage. Probe 4 was in contact with the base electrode and connected the Sawyer-Tower capacitor between the ferroelectric capacitor and ground. Probe 3 contacted the base electrode to measure the voltage on the Sawyer-Tower capacitor. The charge on that capacitor divided by the area of the ferroelectric capacitor is the ferroelectric polarization. A digital oscilloscope was used to record the applied voltages and resulting changes in polarization. The contact to probe 2 could also be used to connect the ferroelectric capacitor to an electrometer. Photovoltages were recorded on a strip chart.

The steady-state photovoltaic output of the films could be characterized by a photo-emf (electromotive force) in series with a photoresistance. There was a characteristic short circuit photovoltaic current (the photovoltaic current) which did not vary with load resistance. We determined the photovoltaic current by measuring the photovoltage across a 10^7-Ω load resistor. We determined the photo-emf by measuring the photovoltage across a 10^{11}-Ω resistor which constituted effectively an open circuit.

POLARIZATION-DEPENDENT AND NON–POLARIZATION-DEPENDENT PHOTOVOLTAIC CURRENTS

We measured the changes in remanent polarization in the film capacitors that followed the application of a voltage pulse. The voltage pulses used were

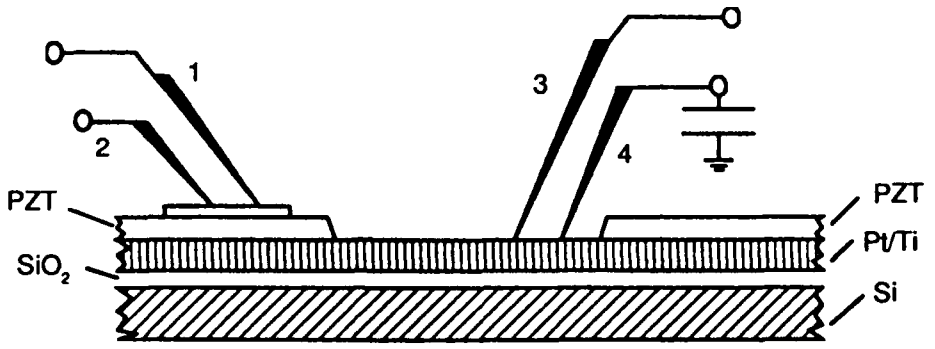


FIGURE 1. Experimental arrangement for applying voltage pulses and measuring changes in remanent polarization. Photovoltages were measured between probes 1 and 3. The top electrode is a 200-Å thick platinum layer.

positive and negative 16-V pulses, 5 μs in duration, with additional 1-μs rises and falls.

We found that the film was initially always fully polarized with a near maximum negative remanent polarization. We ascertained this by observing that the application of a negative pulse would produce only a small increase in this negative remanent polarization. The polarization goes to zero when the applied voltage goes to zero (trace 1, Fig. 2). We do not know why the capacitor elements are initially polarized. It is possible that the capacitors are polarized by accumulated negative charge during the sputter deposition of the top electrodes.

A positive pulse decreased the magnitude of the negative remanent polarization (trace 2). After being decreased with a positive pulse, it can be increased back toward its initial value with a negative pulse. We did notice, however, that the negative pulse, opposite in sign but equal in magnitude to the preceding positive pulse, did not act to restore completely the initial maximum negative remanent polarization.

Fig. 3(a) through 3(f) shows the response of capacitor elements with semitransparent electrodes to illumination pulses. Fig. 3(a) shows the photovoltaic current from a capacitor in its initial state, before any voltage pulses have been applied. Fig. 3(b) shows the response after the application of a negative pulse. There is no change in the steady photovoltaic current. The application of a positive voltage pulse, however, results in a decrease (δ_1, Fig.

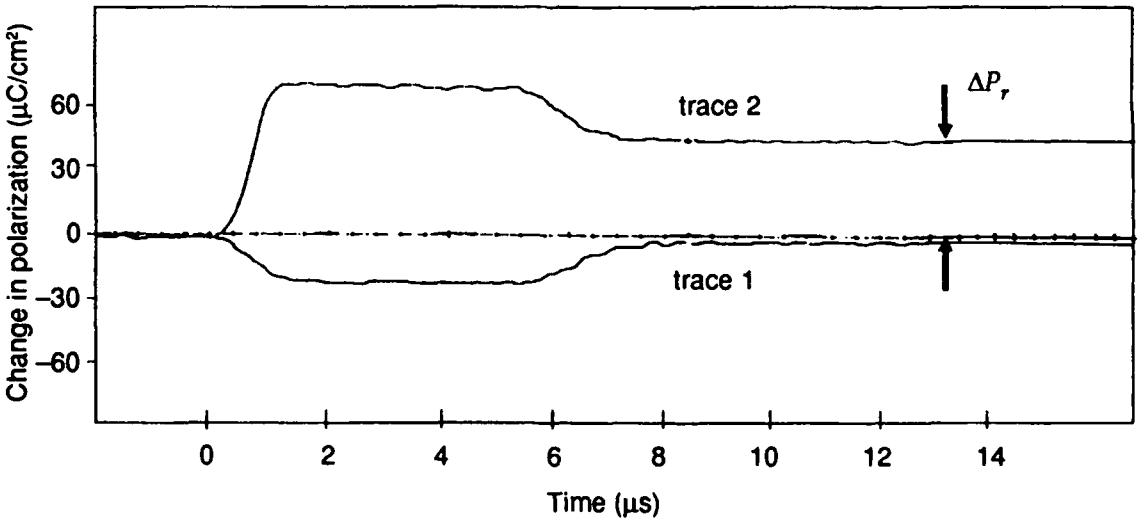


FIGURE 2. Polarization versus time for an initial negative applied pulse (trace 1) and a subsequent positive pulse (trace 2), showing the increment in remanent polarization, ΔP_r, when the positive pulse is applied.

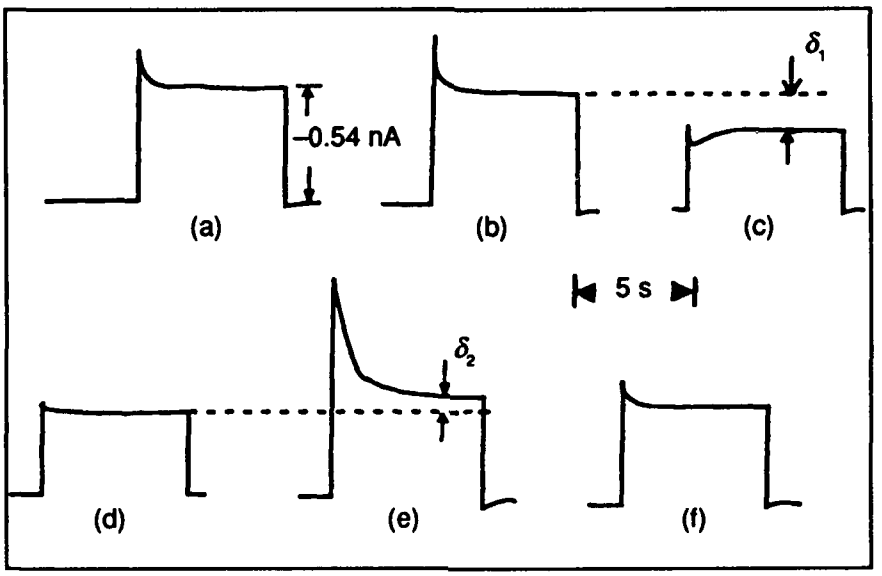


FIGURE 3. Photovoltaic currents for 6-mW/cm^2 high-pressure mercury arc illumination. After the initial transient the currents are steady: (a) initial state, (b) after a negative pulse, (c) after a positive pulse, (d) after the same positive pulse but a second illumination, (e) after a subsequent negative pulse, and (f) a second illumination.

3(c)) in the steady photovoltaic current. A subsequent negative pulse now produces an increase with respect to the last value (δ_2, Fig. 3(e)).

There are, in addition to the steady photovoltaic currents, large transient currents that are comparable in magnitude to the steady currents and that decay to the steady levels. These appear only in response to an initial illumination after remanent polarization is switched, as shown in Fig. 3(c), where the current transient is positive following the initial rise, and Fig. 3(e), where it is negative. They do not appear in response to the illumination pulse when the remanent polarization has not been changed, as in Fig. 3(a) and (b). The current discharge occurs only once, and after it decays, a subsequent illumination pulse does not produce a transient (Fig. 3 (d) and (f)). The polarity of the transient is in the direction of the applied voltage and is relatively larger after a negative pulse.

There are smaller, quickly decaying transients (obscured partially by the larger transients where they occur), which are generally seen in response to the onset of illumination and to the removal of illumination. These are in the direction of the steady current on the onset illumination and in the opposite direction when the illumination is blocked. The net integrated current (the net charge) in these transients is zero. These are most probably pyroelectric in

origin characterized by current proportional to the rate of temperature change. We believe that rapid heating by direct absorption produces the more sharply rising transients when illumination is incident, and conduction cooling to the substrate produces the less apparent transient, more slowly decaying, when illumination is removed.

Fig. 4 is a plot of the steady photovoltaic current versus change in remanent polarization. This result shows a linear relation between remanent polarization change and photocurrent. The sign of the current is the same as that of the applied voltage pulse and the induced remanent polarization. This same relation is seen for anomalous photovoltages in bulk ceramics [12].

The illumination intensity at the film measured with a calibrated thermopile was approximately 6 mW/cm^2 after the transmittivity of the electrode is taken into account. Photovoltaic current was proportional to intensity. The relation between the change in photovoltaic current and the change in remanent polarization, for this mercury arc illumination, is

$$\Delta i_{ph} = 2.7\ (\mathrm{A/C})/(\mathrm{W/cm^2}) \times \mathrm{area} \times \Delta P_r \times I_0\ .$$

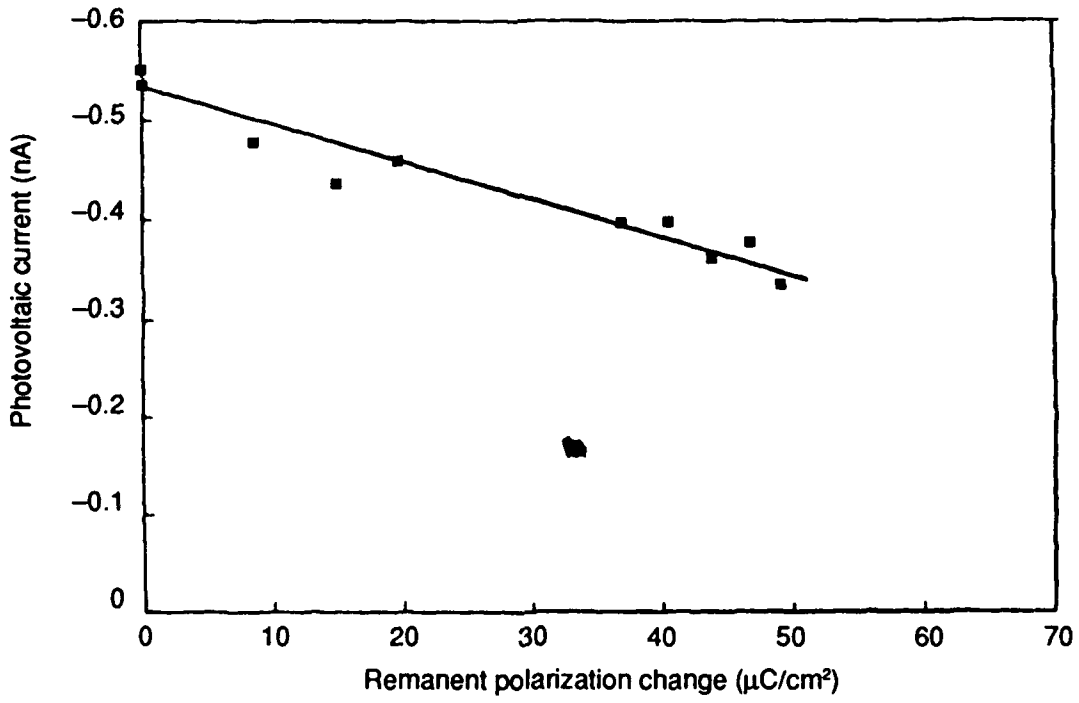


FIGURE 4. Photovoltaic current versus change in remanent polarization for mercury arc illumination of 6 mW/cm^2. The remanent polarization was changed with a switching pulse and measured. The capacitor was then illuminated and the steady photocurrent measured. A new voltage pulse was then applied and the operation repeated. The figure combines results from four capacitors.

The area is that of the electrode in square centimeters, P_r is the remanent polarization in coulombs per square centimeter, and I_0 is the intensity in watts per square centimeter.

We note that the change in remanent polarization is that determined immediately following the application of a pulse (e.g., at 1 ms). The photocurrent was measured about 10 s later. We have assumed no significant decay in remanent polarization during the 10-s interval.

In addition to the polarization-dependent photocurrent, there is a current component that is not dependent on remanent polarization. Because of this component, a large positive applied pulse sufficient to reverse the remanent polarization of the film does not reverse the direction of the photovoltaic current, but only decreases its magnitude (see Fig. 3(c)).

Hysteresis loop measurements of film capacitors (Fig. 5) show a near-saturation-level remanent polarization of 24 $\mu C/cm^2$. It is reasonable to assume that the 16-V, 5-μs-duration positive pulse applied to the film capacitor in its initial negative polarization state completely (or almost completely) switches the direction of the remanent polarization. The initial remanent polarization equal to $-P_r$ has been switched from a negative to a positive direction. From Fig. 4 the negative saturation value of remanent polarization corresponds to a photovoltaic current of –0.54 nA. The photovoltaic current corresponding to the positive saturation remanent polarization (after 50 $\mu C/cm^2$ has been switched) is –0.35 nA. The photovoltaic current midway between these

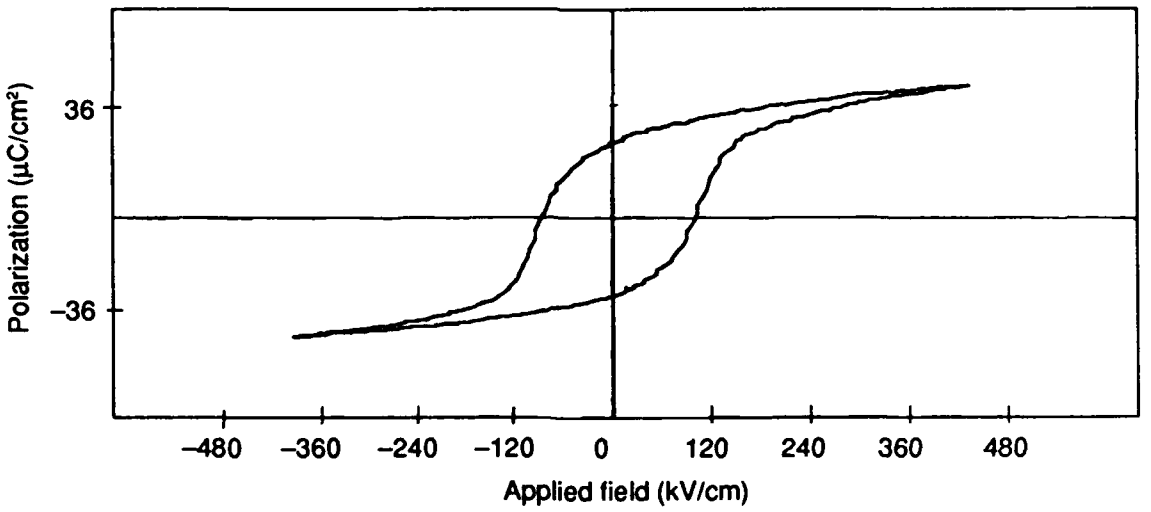


FIGURE 5. Hysteresis results for a film capacitor. The driving sinusoidal voltage is at 1000 Hz. The remanent polarization was 24 $\mu C/cm^2$ and the coercive field, 90 kV/cm.

must then correspond to zero remanent polarization. If our assumptions concerning the complete switching of the polarization are correct, then there must be a nonswitchable background of –0.44 nA.

To our surprise, steady photovoltaic current outputs were produced from capacitors with opaque electrodes as well as capacitors with thin semitransparent electrodes. Measurements of photovoltaic currents from circular opaque electrodes of three different diameters showed these currents to be proportional to the electrode diameter (and thus also perimeter) rather than to electrode area. This indicates that the electrode perimeter was collecting or generating the current.

This perimeter current must also be a component of the total current for the case of the capacitors with semitransparent electrodes. For our measurements of the change in photovoltaic current versus change in remanent polarization which used 150 × 150 μm electrodes (Fig. 4), this perimeter current was –0.20 mA. The perimeter current is thus a significant portion of the total current. Perimeter currents could be eliminated by masking, so that the perimeter region is not illuminated. We note that photocurrents originating from regions outside the electrodes would not be switchable even if they result from the APE. Voltages applied to electrodes produce only short-range fringing fields in the nonelectroded region and thus would not switch a significant amount of remanent polarization external to that region. To check this experimentally we observed photovoltaic currents from opaque electrode capacitors and found only small to nonexistent changes in the current after applications of voltage pulses.

SOURCES OF NON–POLARIZATION-DEPENDENT PHOTOVOLTAIC CURRENTS

No background currents are observed in typical measurements of APE currents in ceramics and single crystals. These measurements are made with an arrangement in which the electrodes are uniformly illuminated, and there is no gradient in optical absorption in the direction perpendicular to the electrodes. This has the effect of eliminating photovoltages from similar contacts and those from gradients in the absorption of light (Dember effect). The arrangement for the films (Fig. 1) is quite different. There is now a gradient in light absorption in the thickness direction for the strongly absorbed photocarrier-

generating wavelengths used in this study; this results in the possibility both of Dember effect photovoltages and of photovoltages from similar contacts, since the contacts are now illuminated at different intensity levels. Photovoltages from a single metal-ferroelectric contact can easily be observed. Efficient Schottky barrier photodiodes consisting of a transparent gold electrode and a barium titanate crystal with a reduced surface have been demonstrated [13].

SOURCE OF POLARIZATION-DEPENDENT PHOTOVOLTAIC CURRENTS

Whether the polarization-dependent steady photovoltaic currents and open-circuit voltages are the result of a true bulk effect [5,14] or are the result of surface layer phenomena [12] is not clear. The anomalous photovoltaic effects both in bulk ceramic and macroscopic single crystals are proportional to length in the direction of polarization and can produce large, greater than band-gap voltages. In truly single macroscopic crystals, the large voltages would have to result from a fundamental bulk effect producing greater than band-gap voltages. In ceramics, however, the voltages are also observed to be proportional to the average number of grains per unit length in the direction of the remanent polarization [12]. This suggests that the high voltage may simply be the result of the addition, grain by grain, of ordinary less than band-gap voltages, which are related to the surface regions of grains [5,12].

In limited experiments on thin films we could find no clear dependence of the photo-emf on film thickness. Otherwise similar films, of 0.25- and 0.6-μm thickness, produced open-circuit photovoltages for saturation negative remanent polarization of –0.52 and –0.46 V, respectively. Because the films are thin, the electric fields associated with these voltage are large: about 20 kV/cm for the 0.25-μm film. The total open-circuit voltages are, however, small: less than the 3-eV band gap. The large fields, therefore, do not in themselves imply a true bulk effect. We think it more likely that the polarization-dependent steady voltages and currents found in the films have the same origin as those found in ceramics, namely, the voltages are the result of band bending in space charge regions on near grain boundaries [12]. Since there is no thickness dependence in the photo-emf of the films, one must also assume that the films are only one grain thick.

TRANSIENT PHOTOVOLTAIC CURRENTS

The large initial photovoltaic current transients seen after the application of a negative applied voltage pulse has switched remanent polarization are similar in form to transients observed in single-crystal ferroelectric [15]. In these studies, an initial illumination pulse results in a large initial transient, and subsequent illumination pulses result in transients of considerably reduced magnitude. It has been suggested that these currents are produced as illumination-generated carriers form space charge fields [5]. We suggest a similar source for the transients in the films. Specifically we suggest that transients are the result of carriers generated by the illumination moving to screen the existing internal electric fields associated the existing polarization state. Once the new space charge distribution is established. there is no illumination-related transient until polarization switching produces a new internal field structure.

APPLICATIONS

Our study confirms the existence of polarization-dependent photovoltaic currents in lead zirconate-titanate films on platinum-coated silicon substrates. We believe it should be possible to take advantage of this phenomenon in device applications based on the principle of storing information as remanent polarization and accessing and retrieving it as photocurrents. Such devices would include nondestructive-readout, nonvolatile-memory RAM (random access memory) cells and correlators based on photocurrent outputs which are the product of illumination intensity and remanent polarization. Such applications should be able to use the presently developing capabilities in fabricating silicon/lead zirconate-titanate ferroelectric-semiconductor integrated circuits.

The existence of nonpolarization background currents at most limits the dynamic range of the polarization-dependent response and should not be an impediment to applications. An increase in the efficiency of producing the photovoltaic current with respect to illumination intensity is, however, probably needed if practical applications are to be realized. It is known that this efficiency can be considerably increased by doping and by using narrow-band illumination centered near the absorption edge of the film [2,16].

ACKNOWLEDGEMENTS

We would like to thank Dr. S. Bernacki of Raytheon Corporation and Dr. S. Dey of Arizona State University for providing films used in this study.

REFERENCES

1. P. S. Brody, Solid State Commun. *12* (1973), 673.
2. P. S. Brody, Solid State Chem. *12* (1975), 193.
3. K. Uchino, Y. Miyawaza, and S. Nomura, Jap. J. Appl. Phys. *2* (1982), 1671.
4. A. M. Glass, D. von der Linde, and T. J. Negran, Appl. Phys. Lett. *25* (1974), 234.
5. V. M. Fridkin, *Photoferroelectrics*, Springer-Verlag, New York (1979), pp 103, 121.
6. V. S. Dharmadhikaru and W. W. Grannemann, J. Appl. Phys. *53* (1982), 8988.
7. J.F. Scott and C. A. Paz de Aroujo, Science *246* (1989), 1400.
8. P. S. Brody, U.S. Patent No. 4,126,901 (1978), U.S. Patent No. 4,139,908 (1979), U.S. Patent No. 4,144,591 (1979).
9. P. S. Brody, Appl. Phys. Lett. *38* (1981), 153.
10. P. S. Brody and Emanuel Katzen, *New Nonvolatile Memory with RAM Capabilities and Intrinsic Radiation Hardness*, Harry Diamond Laboratories, HDL-TM-82-14 (1982).
11. B. Jiminez, R. Gomez, J. Mendiola, E. Maurer, and C. Alemany, Ferroelectrics *45* (1982), 147.
12. P. S. Brody and F. Crowne, J. Electron. Mater. *4* (1975), 955.
13. D. A. Sawyer, Appl. Phys. Lett. *13* (1969), 392.
14. M. E. Lines and A. M. Glass, *Properties and Applications of Ferroelectric and Related Materials*, Clarendon Press, Oxford (1977), p 455.
15. A. V. Guinzberg, K.D. Kochev, Yu. S. Kusminov, and T.R. Volk, Phys. Status Solidi (a) *29* (1975), 309.
16. M. Tanimura and K. Uchino, *Sensors and Materials*, vol. 1 (1988), 47.

AD-P006 659

PHOTORESPONSE FROM THIN FERROELECTRIC FILMS OF LEAD ZIRCONATE TITANATE

SARITA THAKOOR, ANIL P. THAKOOR
Center for Space Microelectronics Technology
Jet Propulsion Laboratory
California Institute of Technology
Pasadena, California 91109
and
STEPHEN E. BERNACKI
Electro-Optics and Strategic Systems Directorate
Raytheon Equipment Division
Sudbury, MA 01776

Abstract Bulk (ceramic as well as single crystal) ferroelectric materials are known for their remanent-polarization-dependent photoresponse: a photocurrent (and a photoemf), when illuminated by light with a wavelength close to the bandgap of the material. This paper reports on observation of a similar photoresponse from sol-gel derived polycrystalline thin films of lead zirconate titanate (PZT). The internal field due to the remanent polarization modulates this net photoresponse from the ferroelectric material. Thin film ferroelectric capacitors were fabricated in a sandwich geometry with a transparent top electrode. On illumination with ≈365nm wavelength (PZT bandgap ~ 3.5 eV) light pulse, photocurrent profiles from such capacitors correspond to their distinct remanent polarization memory states. Further, such a read-out has negligible effect on the magnitude of the remanent polarization and therefore it is a potential candidate as a non-destructive readout of the nonvolatile memory states. The observed photocurrent has two components: first, a transient spike coincident with the onset of the illumination pulse, and second, a steady dc photocurrent which prevails as long as the light is `ON'. The steady current response exhibits a weak dependence on the polarization whereas the transient response exhibits a distinct polarization dependence. Our study suggests that the predominant contribution to the steady photovoltaic current is due to the asymmetric pair of Schottky junctions at the two interfaces of the ferroelectric film with the top and bottom electrodes respectively.

92-16123

INTRODUCTION

With the advent of technology, to deposit ferroelectric thin films of PZT (lead zirconate titanate) with tailored stoichiometry, and to successfully integrate them with conventional silicon technology, ferroelectric non-volatile memories are now well into their development phase.[1-4] The memory element consists of a thin film ferroelectric capacitor, in which the non-volatile storage is based on the remanent polarization in the ferroelectric thin film. The established readout technique relies on the transient displacement current modulated by polarization reversal under applied switching pulse. However, such a process destroys the stored information, which necessitates a rewrite operation after every read cycle and complicates the hardware.

Alternatively, a "poled" ferroelectric element, when illuminated with a wavelength near its bandgap, generates a small photocurrent proportional to the remanent polarization (stored memory) and the incident intensity.[5,6] If radiation-hard, nonvolatile, ferroelectric memories could be read non-destructively in terms of the photo-response (photocurrent or photo-emf) with such contact-less optical addressing, they would clearly have an impact on the growing need for rugged and robust solid state memory systems. Furthermore, a strong motivation for such a readout arises from the fact that the highly parallel photoresponse output from an array of memory pixels would be ideally suited for high performance computing applications[12], especially those involving parallel processing and architectures such as large scale artificial neural networks. In addition, such a non-destructive

readout(NDRO) would allow utilization of the full potential of the ferroelectric capacitor as an analog memory.

Non-destructive readout from bulk ferroelectric ceramic elements has been demonstrated[7,10] utilizing the remanent polarization dependent photo-emf. The polarity of the photo-emf depends on the direction of the remanent polarization.

This paper reports the first unambiguous observation of polarization dependent photocurrent response generated from **ferroelectric thin film capacitors** of sol-gel deposited PZT at zero applied bias.

EXPERIMENTAL DETAILS

The sol-gel PZT thin films (~1700 Å) were deposited by a modified Sayer's Technique[8] on oxidized silicon substrates with an intermediate evaporated Ti/Pt (~ 1000 Å/1000Å) base electrode. Typically the PZT composition of (Zr/Ti = 52/48) with ~18% excess lead was investigated. The crystallization of the PZT was done at 550°C for 10 minutes in 100% oxygen.

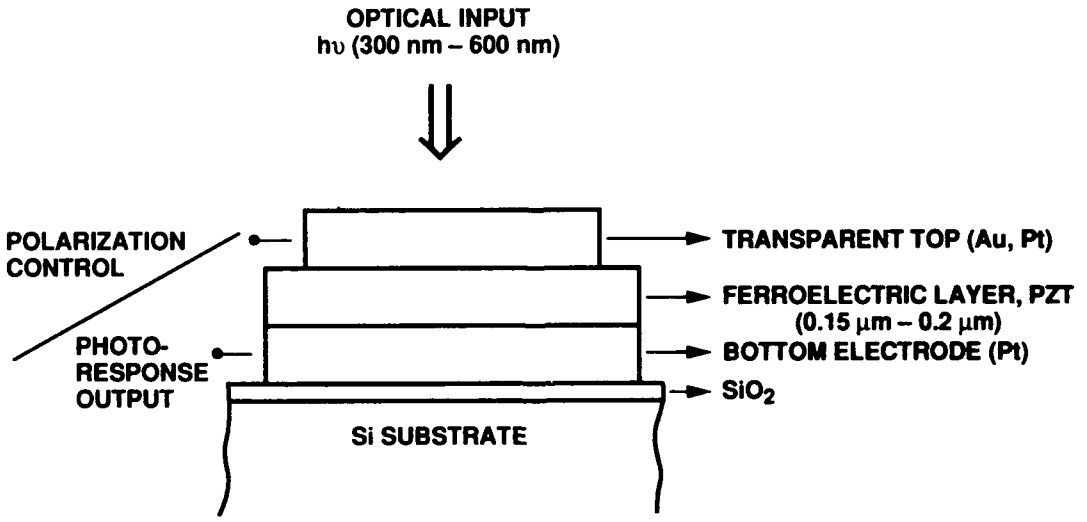


FIGURE 1 Thin film ferroelectric capacitor(TFFC) test structure for photoresponse investigation.

To complete a standard sandwich capacitor test structure as shown in Figure 1, thin transparent films of either gold or platinum were deposited as the top electrode. The top electrodes were patterned by conventional lift-off technique as dots of 100μ to 250μ diameter. The transmission from 300 nm to 800 nm through the electrode films (≈100Å Pt or ≈300Å Au) was about 30%. Platinum was significantly more robust, scratch resistant, and thus more durable than gold in our experiments with the microprobes.

In our photoresponse measurement, a short-arc mercury lamp was used as the near UV/visible(300nm to 600nm) illumination source with the strongest line at 365nm. The choice of this light source was motivated by the bandgap value of PZT (~3.5eV) that would lead to maximum photoresponse at about 354nm. The interim focussing optics delivered a 5mm divergent beam with an intensity of ~0.1 watt/cm2 onto the sample. A shutter controlled by a *solenoid valve* allowed a pulse illumination with a minimum pulse length of 1 sec and a maximum of 99 sec. IV characteristics of the ferroelectric capacitor on illumination, even in the unpoled state, exhibited an open circuit photovoltage and a short circuit current. The high impedance of the device (resistance ≈1 to 10 Gigaohms, capacitance ≈1 nf) made open circuit voltage measurement a rather slow process, over several seconds. Short circuit current measurement was thus an obvious choice. Photocurrent through a 100 K ohm resistor shorting the sample, was monitored in response to a pulse of illumination as described above. To illustrate the repetitive non-destructive readout, experiments were conducted by using light chopped by a mechanical chopper.

RESULTS AND DISCUSSION

Typical (Q-V) hysterisis loops with drive voltages ranging

from ±2V to ±10V for the ferroelectric capacitors are shown in fig. 2. The remanent polarization(P_r = 25 $\mu C/cm^2$) and coercive voltage value(V_c = 2.3V) as deduced from the hysterisis loop for ±10V drive signal confirm that the deposited films are comparable to the state of the art films used for memory devices.

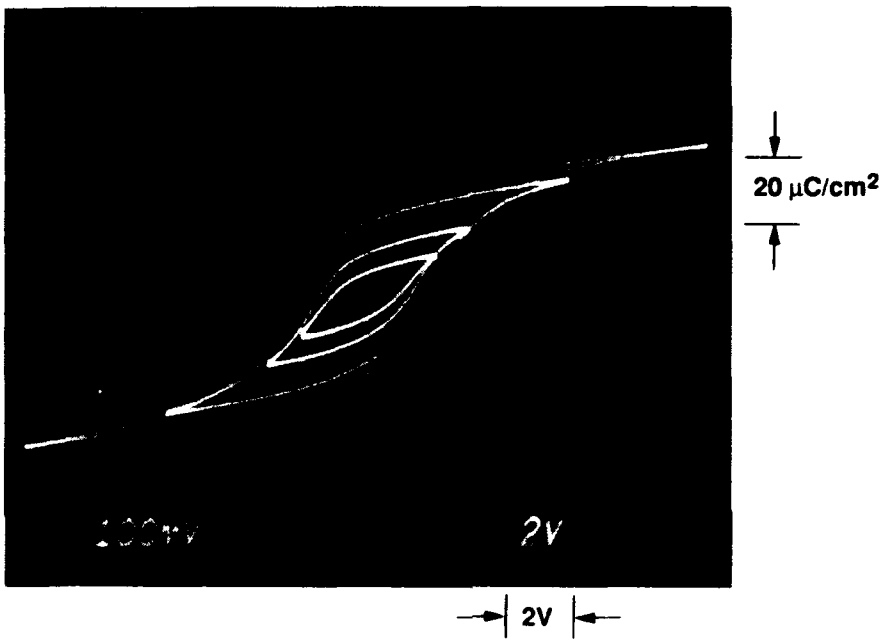


FIGURE 2 Hysterisis loops (Q versus V plots) of Pt/PZT(52/48)/Pt TFFC.

Figure 3 shows traces of the photocurrent generated from the ferroelectric capacitor in response to illumination pulses of 40sec duration for the two polarization states corresponding to ±4V poling respectively. There are two main components to the photoresponse, a transient response(J_T) at the onset of illumination, and a steady photoresponse(J_{ST}) prevailing for the entire duration of the illumination. The transient component predominantly exhibits a polarization dependent character, whereas the steady component has only a weak polarization dependence. Therefore the transient component is of prime interest for

the non-destructive readout (NDRO). The peak value of the transient essentially reflects the state of the remanent polarization value. The transient photocurrent response could be composed of displacement current arising due to: (a) localized electronic transitions (J_E), (b) space charge contributions (J_S), and (c) pyroelectric contributions (J_{PYRO}).

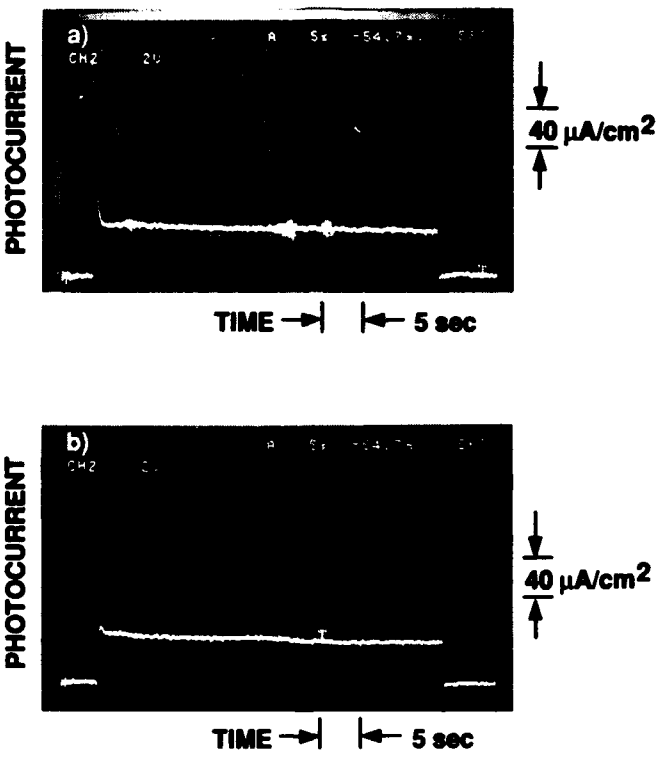


FIGURE 3 Photocurrent response from a TFFC illuminated with a 40sec light pulse. TFFC poled to (a) +4V (b) -4V.

Table 1, summarizes the typical expected rise time and relaxation time characteristics of these possible components of the photoresponse as suggested[9-11] from studies on bulk ferroelectrics. When the light is switched `ON', the transient photocurrent reaches a maximum and then falls off to a value corresponding to the steady current. The space charge component of the transient response may be

attributed to the screening of the spontaneous polarization by the photogenerated carriers[9]. The relaxation time of the transient is seen to be dependent on the amount of charge injected in the capacitor during the "writing " operation, as is suggested by its dependence on the duration of the writing pulse. This relaxation may be related to the relaxation time of the space charge current and is discussed in details elsewhere[14].

TABLE 1. Photoresponse Component Characteristics

Current Component	Rise time	Relaxation time
J_E	≈psec	≈psec-nsec
J_S	≈psec-nsec	≈ms-seconds
J_{PYRO}	≈μsec	≈seconds
J_{ST}	≈psec	*

* steady, while the light is on

If the transient photoresponse would have a pyroelectric contribution, a transient response would also be expected in opposite direction at the end of the illumination pulse. A transient, however, is not observed at the turn `OFF' of the illumination suggesting that with the illumination utilized here, the pyroelectric contribution to the photoresponse is negligible. Although, our PZT films are not intentionally doped, the trace impurities in the chemicals utilized for the sol-gel deposition may contribute to impurity centers within the formed PZT thin film that may give rise to a displacement current proportional to the polarization change due to localized electronic transitions[11]. The observed transient response is therefore mainly attributed to the contributions due to the space charge component and probably the localized

electronic transitions. Experiments are underway to further understand the nature of the transient photoresponse.

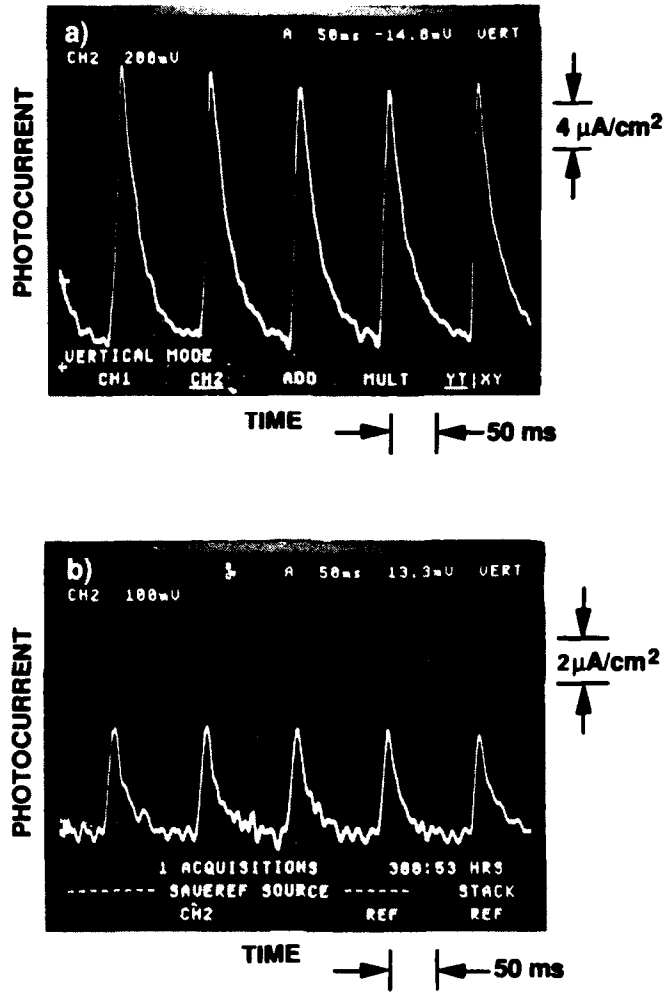


FIgure 4 Photocurrent response from a TFFC illuminated with a light, chopped at approximately 10Hz frequency. TFFC poled to (a) +4V, (b) -4V.

Figures 4a and 4b, present the photoresponse from a ferroelectric capacitor in its positively poled state and negatively poled state, respectively, when illuminated with light chopped by a mechanical chopper run at a 10 Hz frequency. A repetitive non-destructive readout clearly differentiating between the polarization states is thus

obtained, utilizing the transient photocurrent response. In fact each of the three polarization dependent components of the transient response may be useful as nondestructive readout.[12,15]

Although the transient response exhibits the dependence on polarization, the large steady photocurrent background (only weakly dependent on polarization) offsets the observed signal to the same polarity for both polarization directions. There are atleast five possible mechanisms contributing to this steady photocurrent component: (a) a pair of asymmetric Schottky junctions at the top and bottom electrode-PZT interface, (b) the Dember Effect[10], (c) the photovoltaic effect as observed in bulk ferroelectrics,[8-10] (d) built/in stress gradients within PZT, and (e) residual polarization arising due to the slow switching polarization components[12]. In the following is discussed each mechanism and its validity with respect to the present observations.

A post-top electrode anneal treatment substantially suppresses the steady photoresponse, however, the suppressed steady current still remains weakly dependent on the polarization state. This is illustrated in figure 5a and 5b, which shows the photoresponse to a 40 second pulse from a sample that was annealed (575°C for 3 hours in air) after deposition of top electrode, in its positive and negative polarization states respectively. This observation suggests that the steady current may arise due to the asymmetry in the two photovoltaic Schottky junctions at the two interfaces between PZT and the two electrode layers. The heat treatment (~550°C) provided to PZT for its crystallization probably causes formation of a photovoltaic junction between PZT and its bottom platinum electrode. The top electrode, deposited at room temperature, on the other hand does not form a photovoltaic junction until the post deposition anneal. After the post-

deposition anneal, however, the two virtually identical junctions situated in opposition to each other, tend to cancel the total photoemf thereby reducing the net photoemf. A similar suppression of the steady current enhancing the directional transient response was also accomplished by voltage soaking the sample for an extended duration of time (over few hours) with a ±(2 to 4)V drive voltage.

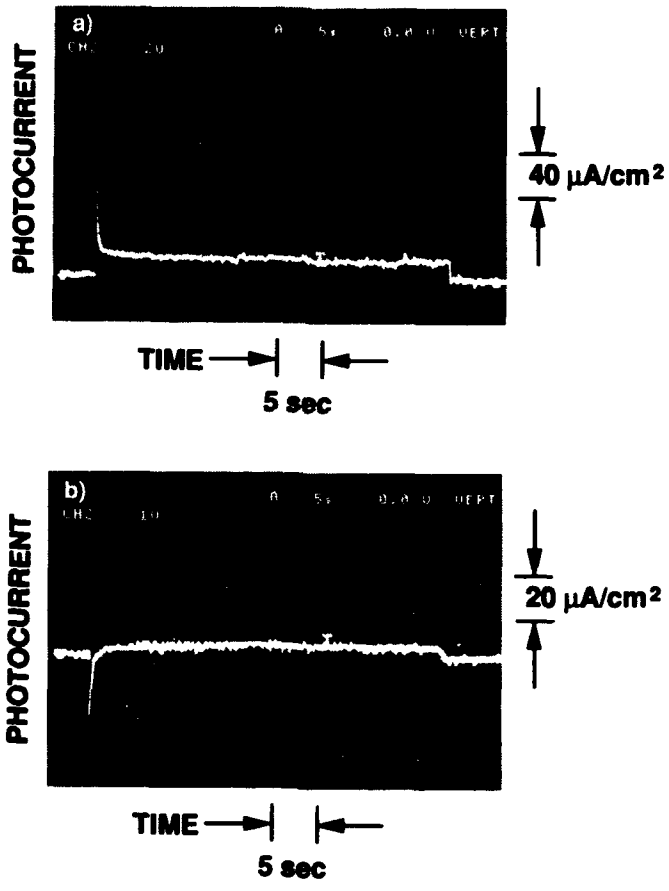


FIGURE 5 Photocurrent response from a TFFC which was annealed after top-electrode deposition to illumination with a 40sec light pulse. TFFC poled to (a) +4V (b) -4V.

The anneal treatment, or equivalently, the field triggered thermal heating in the voltage soak treatment may

be responsible for "formation" of the electrode/ferroelectric interface. C-V measurements are underway to further understand these observations in terms of the differences in the band bending at the two interfaces of the capacitor. This anneal treatment, in effect, enhances the polarization dependence of the transient response and thereby can be utilized[12] for a more efficient NDRO.

The PZT films transmit about 30% of the incident illumination at 365nm (the strongest line in the source spectrum). This implies that the resultant charge density difference along the thickness of the film could cause the Dember effect. However, the substantial suppression of the photocurrent on annealing supports the possibility of the asymmetric Schottky junction as the dominant cause over that of the Dember effect. Further measurements of the electron-hole mobilities and the diffusion lengths of the carriers within the PZT material will allow a precise assessment of the relative contribution of the Dember effect.

The steady part of the response is seen to be essentially independent of the polarization. The photovoltaic effect in bulk ferroelectrics as reported earlier[9-11] is expected to convey the sense of polarization. The weak dependence on polarization clearly suggests that this is not the most significant contribution.

Measurement by the Newton's Ring method of the radius of curvature of the silicon wafer before and after the deposition and crystallization of PZT yields $\approx 1.3 \pm 0.3$ Giga-Pascal tensile stress within the film. If this stress is non-uniformly distributed along the thickness of the film, then it could contribute to the observed steady current. Also, the annealing treatment may very well serve to relax the existing stress gradient thereby

suppressing the steady photocurrent. This possibility could be verified by applying an external stress gradient of both a tensile as well as compressive nature and observing its effect on the photoresponse.

The residual polarization in the film, attributed to slow switching components[13], could be easily reversed by application of a voltage soak treatment for about a minute at 2-4V drive voltage. However, such a single voltage soak treatment had no effect on the photoresponse characteristics from the ferroelectric capacitor, suggesting that photoresponse is not related to residual polarization. Our observations therefore suggest that primarily the asymmetric Schottky junction at the two interfaces is the dominant mechanism giving rise to the steady photoresponse.

TABLE II Effect of 99 sec continuous illumination (≈365nm) on the remanent polarization.

Sample Description	Polarization Value (in $\mu C/cm^2$) Before illumination	After Illumination
# 1	+25	+22
# 1	-25	-26
# 2	+30	+25
# 2	-30	-33
# 3	+22	+20
# 3	-20	-26
# 4	+20	+19
# 4	-20	-20

The effect of near UV/visible light illumination on the stored memory was investigated to establish the overall potential of this non-destructive readout technique. The conventional destructive readout technique was used to do this cross verification. It is noteworthy that the effect of light on the remanent polarization is directional. In TABLE II is summarized the effect, of extended cumulative exposure (≈ 99 sec) to illumination (≈ 365nm), on the remanent polarization. The remanent polarization(P_r) on negatively polarized capacitors is either unchanged or shows an increase in the negative value of the P_r in response to an exposure of about 99 sec of continuous illumination. However, positive P_r values show a definite decrease in the remanent polarization value in response to a similar illumination. This suggests that the steady

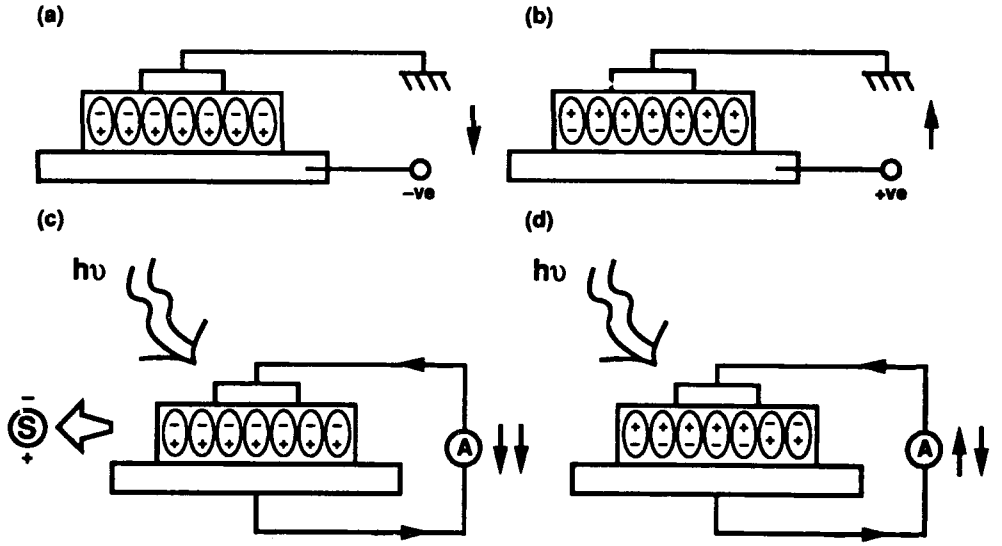


FIGURE 6 Schematic representation of effect of illumination on the memory. (a) and (b) represent the capacitor before illumination in its two states respectively, the arrow suggests the direction of polarization. (c) and (d) illustrate the status during illumination, the additional arrow indicates the direction of the photogenerated field.

photoresponse from the device is, in-fact, responsible for this effect of overwriting by the light. As illustrated schematically in figure 6, when the photogenerated field is in the same direction as the remanent polarization, it enhances the polarization value and degrades it in the opposite direction. An ideal pulsed light source with short pulses(~10ns duration), therefore, could be used to yield a substantial number of real fast non-destructive readout cycles ($>10^{10}$), with small change of the remanent polarization.[15]

CONCLUSIONS

1. Repetitive, nondestructive readout from individual ferroelectric memory pixels is indeed feasible
   (a) Photoresponse profiles from PZT thin films with no external bias applied is polarization dependent.
   (b) Extended, cumulative illumination($\approx$ 365 nm) for over 99 seconds has a directional effect on the remanent polarization such that the negative polarization values are substantiated but the positive polarization values are degraded ($\approx$ 15%).
   (c) Transient component of the photoresponse has the predominant polarization dependence.

2. Steady photocurrent is predominantly due to the pair of asymmetric Schottky junctions at the two surfaces of the PZT film. Post-top-electrode annealing suppressed the steady photocurrent and allowed observation of a transient response exhibiting sense of polarization by its direction.

ACKNOWLEDGEMENTS

Useful discussions with Dr. L. E. Cross from Pennsylvania State University and Dr. A. M. Glass from AT&T are

gratefully acknowledged. The work described in this paper was performed by the Center for Space Microelectronics Technology, Jet Propulsion Laboratory and California Institute of Technology, and was sponsored by Defense Advanced Research Projects Agency through an agreement with National Aeronautics and Space Administration(NASA).

REFERENCES

1. J. T. Evans and R. Womack, IEEE Journal of Solid-State Circuits, **23**, 1171 (1988).
2. D. Bondurant and F. Gnandinger, IEEE Spectrum, 30(1989).
3. J. F. Scott and C. A. Paz De Araujo, Science, **246**, 1400 (1989).
4. S. E. Bernacki et. al. , Proceedings Third International Symposium on Integrated Ferroelectrics, April 3-5, 1991, Colorado.
5. C. E. Land, J. Am. Ceram. Soc., **72**, 2059 (1989).
6. S. J. Martin, M. A. Butler and C. E. Land, Electronics Letters, **24**, 1486 (1989).
7. P.S. Brody, Appl. Phys. Lett., **38**, 153 (1981).
8. G. Yi, Z. Wu and M. Sayer, J. Appl. Phys. **64**, 2717 (1988).
9. V. M. Fridkin, Photoferroelectrics, Springer-Verlag (1979).
10. F. Micheron, J. M. Rouchon and M. Vergnolle, Ferroelectrics, **10**, 15 (1976).
11. A. M. Glass, D. von der Linde, D. H. Auston and T. J. Negran, J. of Electronic Mat., **4**, 915 (1975).
12. S. Thakoor (to be published), Transactions of the Ceramic Society (1991).
13. S. Thakoor, Proceedings Third International Symposium on Integrated Ferroelectrics, April 3-5, 1991, Colorado.

14. S. Thakoor, M.Lakata, and J. Maserjian, (in preparation).
15. S. Thakoor, J. Perry, and A.P. Thakoor, (in preparation).

AD-P006 660

STUDY OF THE OPTICAL PROPERTIES OF RF SPUTTERED LITHIUM NIOBATE THIN FILMS

CHARLES HUNG-JIA HUANG and THOMAS A. RABSON
Department of Electrical & Computer Engineering, Rice University
Houston, TX 77251-1892

Abstract Lithium niobate optical waveguides were fabricated on (110), and (100) sapphire by both diode and magnetron rf sputtering at 500-600°C in a flowing Ar/O_2 atmosphere. Light coupling utilizing a rutile prism coupler was demonstrated. The propagation losses were obtained by measuring the scattered light from the surface using a fiber probe. The mode angles were also measured and used to calculate the thickness and the refractive indices of each sample. X-ray diffraction studies and the birefringence observed in the films have confirmed the crystalline nature of the films. The lowest value of attenuation of the He-Ne laser light propagating in the lithium niobate waveguide sputtered on sapphire was determined to be 1.1 ± 0.1 dB/cm. In addition, the lowest attenuation in lithium niobate thin film waveguides sputtered on SiO_2/Si substrates was measured to be 2.3 dB/cm using end-fire coupling and fiber probing techniques.

INTRODUCTION

For the development of integrated optics the fabrication of low loss waveguides on various substrates is essential.[1] Since lithium niobate has excellent electro-optic, nonlinear optical, and piezoelectric properties,[2] it is considered to be a good candidate of optical materials in integrated optics for applications such as electro-optic modulation, switching, second harmonic generation, etc.[1] Titanium in-diffusion (TI) and proton exchange (PE) techniques on bulk crystals have been used for several years to make low loss optical waveguides.[3] However, guides made with these methods are difficult to integrate with semiconductor

92-16124

substrates. Fortunately, thin film technology offers a solution to this problem. Recently, significant progress has been reported in the region of rf sputtered lithium niobate on a variety of substrates. Griffel *et al.*[4] has reported the lowest attenuation (less than 2 dB/cm) and the highest electro-optic coefficient (1.34×10^{-12} m/V) obtained so far for thin film lithium niobate rf sputtered on an amorphous glass (Corning 7059) substrate. Hewig and Jain[5] also reported second harmonic generation in a lithium niobate film deposited on a sapphire substrate. We have grown high quality lithium niobate thin films on SiO_2/Si and various sapphire substrates and the values of the propagation loss in those waveguides are lower than the published data.[6] Electrical switching of lithium niobate thin film has been studied and observed by Rost and colleagues.[7] Moreover, they have successfully built a MFS (Metal-Ferroelectric-Semiconductor) transistor using ferroelectric lithium niobate as the gate material,[8] which means that the combination of the technologies of integrated optics, semiconductor microelectronics, and ferroelectrics is possible in the near future.

FABRICATION

In this paper, thin film lithium niobate rf sputtered on (110), (100) sapphire, and SiO_2/Si substrates are studied. Sapphire was chosen to be the substrate because it is transparent in the visible light region, it has a similar lattice structure to lithium niobate, the lattice mismatch between sapphire and lithium niobate is small (about 7%), and its much lower refractive index gives excellent light confinement. Therefore, sapphire is an excellent substrate on which to epitaxially grow low loss lithium niobate optical waveguides. Since $LiNbO_3$ is mainly employed in making electro-optic devices, the maximum field induced birefringence is certainly desired. For convenience, a modulating electric field parallel to the c axis of lithium niobate is usually applied, and the guided beam is excited in the direction normal to the c axis of the film. The field induced birefringence is thus given by $\Delta n = -\frac{1}{2} n_e{}^3 r_{33} E$ for a wave polarized in the direction of the c axis. Therefore, both (110) and (100) sapphire substrates are suitable for growing epitaxial thin film with the c axis in the plane of the surface. The other substrate used, SiO_2/Si, was selected simply because silicon is one of the most popular substrates in semiconductor microelectronics.

TABLE I The sputtering parameters.

Sputterer	Diode	Magnetron
Substrate	(110) Al_2O_3 & SiO_2/Si	(110) & (100) Al_2O_3
Target	$LiNbO_3$+10%Li_2O	pure $LiNbO_3$
Separation	6 cm	5 cm
Pressure	2-4 mTorr	1-2 mTorr
Temperature	500-600°C	500-600°C
Gas ratio	54% Ar + 36% O_2	70% Ar + 30% O_2
Pre-sput. time	30 min	30 min
Forw. power	150 W	50 W
Refl. power	70 W	0 W

Both diode and magnetron rf sputtering systems were used to grow lithium niobate films. Typical growth conditions are listed in Table I. For the diode rf sputtering system, the target consisted of lithium niobate powder mixed with 10% lithium oxide to compensate for lithium loss which occurs during sputtering, while pure fresh lithium niobate powder was used in each run for the magnetron system. The substrate was heated to a temperature in the region of 500°C to 600°C during the process to improve the growth of oriented film . The deposition rate under the conditions listed in Table I is about 250 Å/hr using 150 W (70 W reflected) rf power in the diode sputtering system and using 50 W in the magnetron system. Note that the magnetron rf sputtering system although operating at a lower power gives the same deposition rate as the diode one. Lithium niobate thin films fabricated at such a low rate are very uniform and optically transparent. The films were then annealed in either air or O_2 atmosphere at 600°C for a few hours to improve their crystallinity.

X-RAY DIFFRACTION

X-ray diffraction (XRD) has been done to analyze the crystallinity of the thin films. One can see in Figure 1 that the sputtered lithium niobate thin films are highly oriented crystalline with the c axis parallel to that of the sapphire substrate. The XRD peaks are listed in Table II. The lattice constants a_H of the thin film lithium niobate deposited on (110) and (100) sapphire are calculated to be 5.144 Å and 5.154 Å, respectively. These values are in close agreement with the bulk value of 5.149 Å.

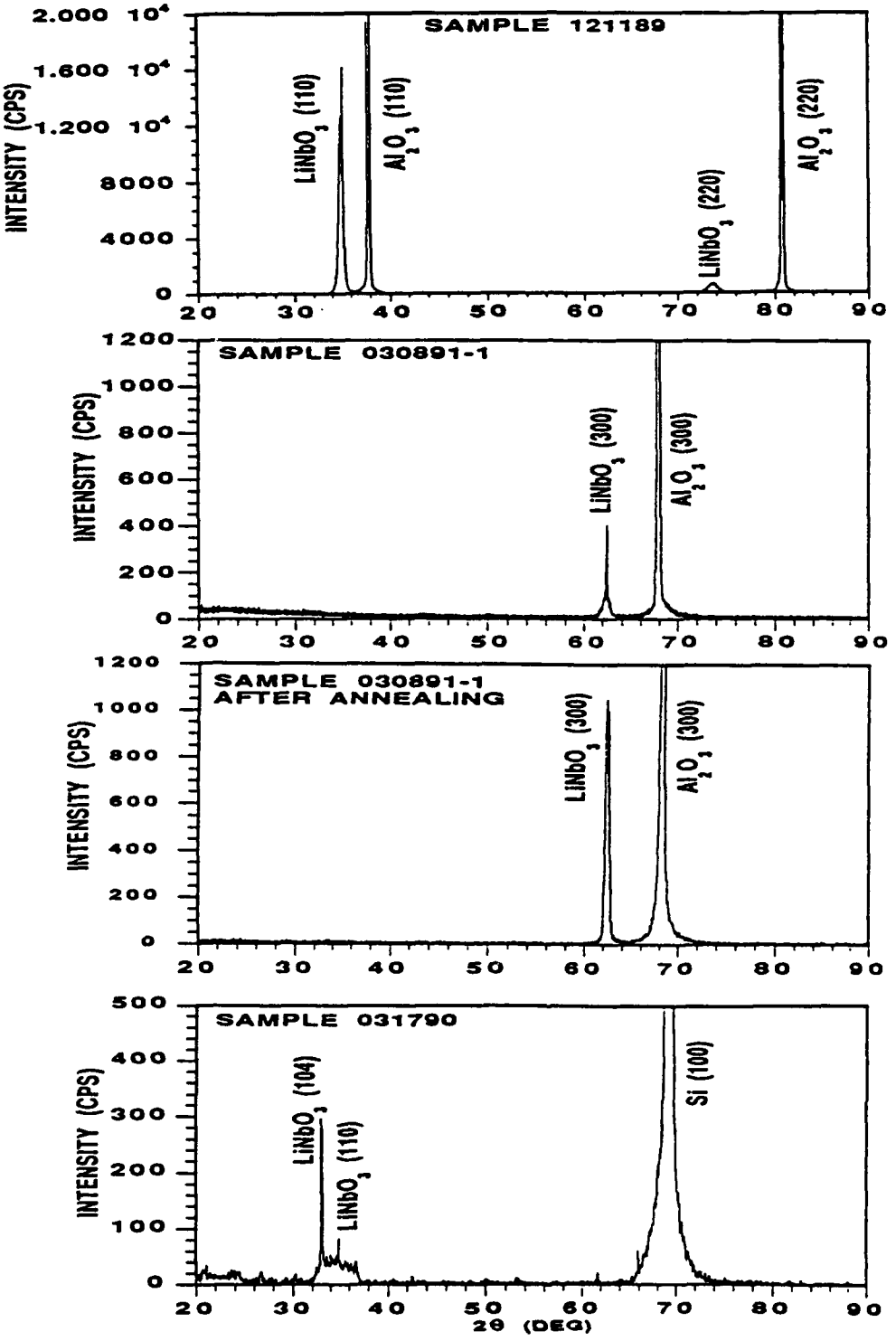


FIGURE 1 XRD of $LiNbO_3$ sputtered on various sapphire.

TABLE II X-ray diffraction data of thin film lithium niobate on sapphire.

Substrate	2θ	Identification	Lattice constant
(100) sapphire	62.42°	(300) $LiNbO_3$	a_H=5.154 Å
(110) sapphire	34.88°	(110) $LiNbO_3$	a_H=5.144 Å

Comparing the intensities of the two lithium niobate (300) peaks before and after annealing, we confirm that the annealing process has improved the crystallinity of the thin films. However, since the thickness of the thin films is only a few thousand of angstroms, a long annealing period as people used to do for bulk materials is not preferred.[9] Moreover, the temperature region from 550°C to 600°C is considered to be the optimum condition for annealing after sputtering. Higher temperatures up to 1000°C had been applied to anneal the sputtered films which then turned out white and opaque after the thermal treatment. The transparency reduction of the film indicates a higher optical scattering and propagation loss in the waveguides, which is not desirable.

X-ray diffraction of a film on an amorphous SiO_2 buffer layer, shown in Figure 1, has a sharp peak at 32.90° corresponding to a (104) orientation and another peak at 34.85° corresponding to a (110) orientation. The broadening at the bottom of these two peaks is due to the amorphous characterisitcs of the SiO_2 layer. This demonstrates that the films on SiO_2/Si substrates have a polycrystalline quality with some preferred orientation.

OPTICAL PROPERTIES

The film's optical properties, such as refractive index, thickness, and attenuation, were examined by beam-coupling into the thin film waveguide utilizing a high index rutile prism coupler,[10] as shown in Figure 2. Evaporated Al thin film spacers ($\approx$ 1000 Å) and a steel wire were used to create a tapered air gap which then increased the coupling efficiency. With this setup we are able to measure the mode angles and the attenuation in the waveguide simultaneously. Figure 3 shows the reflectivity of a 6328 Å light from a lithium niobate film on (100) sapphire substrate vs. the angles of incidence, in which the bottoms of the dips, correspond to the mode angles.

TABLE III Thicknesses and refractive indices of the lithium niobate thin films deposited on sapphire substrates.

Orientation	System	Mode angles	$n_f(\pm 0.002)$	$t\ (\pm 0.001\mu m)$
(110)	Diode	$\delta_{TE_2} = -4.90°$	$n_o = 2.324$	$t = 0.635\mu m$
		$\delta_{TE_1} = 11.96°$		
		$\delta_{TE_0} = 23.16°$		
		$\delta_{TM_2} = -0.42°$	$n_e = 2.244$	$t = 0.639\mu m$
		$\delta_{TM_1} = 20.37°$		
		$\delta_{TM_0} = 36.35°$		
(100)	Magnetron	$\delta_{TE_0} = 4.86°$	$n_o = 2.301$	$t \approx 0.2\mu m$
		$\delta_{TM_0} = 7.96°$	$n_e = 2.230$	$t \approx 0.2\mu m$

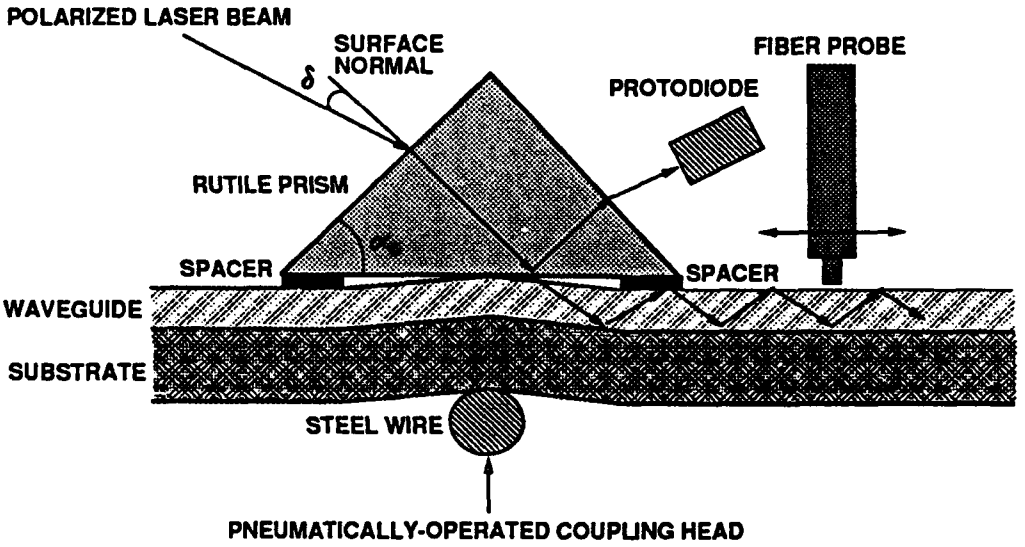


FIGURE 2 Setup of the prism coupler.

If two or more modes are observed, the thickness t and the refractive index n_f of the film can be evaluated by the mode condition given by Eq. (2.2.12) in Ref. 11. The calculated thickness and refractive indices of lithium niobate thin films deposited on sapphire substrates are tabulated in Table III. Since two different values of refractive index corresponding to TE and TM waves have been obtained in each sample and the index difference is larger than the allowed error, the thin films grown by the rf sputtering method under the conditions listed in Table I exhibit birefringence and thus are highly-oriented. Note that in the case of single mode waveguides the thickness and the refractive index

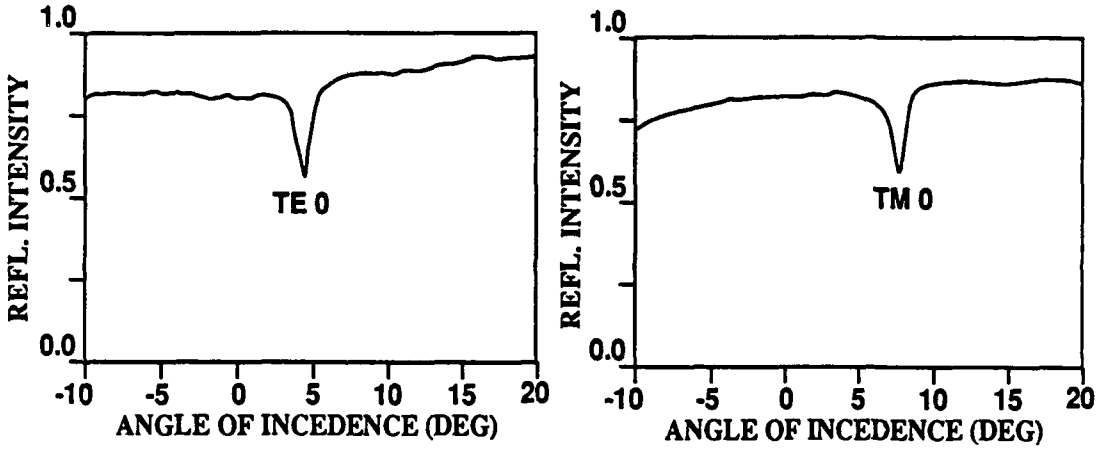


FIGURE 3 Guided modes prism coupled into $LiNbO_3$/(100) Al_2O_3.

can not be calculated at the same time. Therefore, One of the parameters has to be estimated by other techniques. For example, the thickness of the (100) sample was estimated by counting the color periodicity of the film edge, which was then used to calculate the refractive indices of the film.

Assuming the guided optical power is proportional to the intensity of the surface scattered light, we can then calculate the attenuation in the optical waveguide by measuring the surface scattered light. Conventionally, a fiber probe connected to a lock-in amplifier is used to serve this function. In our studies, another technique, namely, the photographic recording method, was also utilized. The waveguiding streak was photographed, as shown in Figure 4, for a number of different exposures. Only those taken within the linear region of the film sensitivity were used to calculate the attenuation. Figure 4 shows the attenuation of TE_0 guided mode propagating in lithium niobate waveguide sputtered on (110) sapphire. The lowest attenuation in our sputtered films was found to be 1.1 ($\pm$0.1) dB/cm which is the smallest value reported so far in the literature for sputtered lithium niobate films. Since the attenuation is caused by the scattering at the surface of the waveguide and grain boundaries and by the absorption at the defects, surface flatness and crystalline quality are very important in lowering the attenuation of the film. In general, a higher rf power creates bigger crystallites, while a lower rf power gives better surface flatness. Therefore, a trade-off must be made to optimize the deposition rate. For our magnetron system, 50 W is found to be the preferred value.

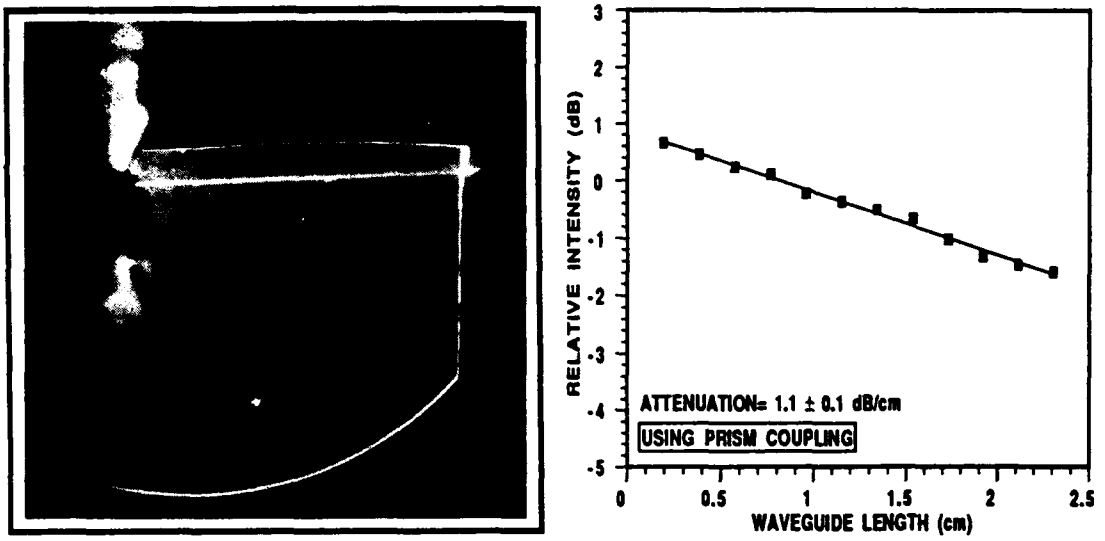


FIGURE 4 A He-Ne light guided in $LiNbO_3/(11\bar{2}0)$ Al_2O_3.

Although the attenuation obtained in our work is the lowest value reported for sputtered thin film waveguides, it is still not as low as 0.5dB/cm of waveguides made by thermal diffusion techniques.[11] To lower the attenuation of the films fabricated by rf sputtering, one must improve the optical uniformity of the film and its surface as well as reduce absorption in the film. Annealing, mechanochemical polishing, and ion-beam etching are promising techniques for further reducing the attenuation.

For the lithium niobate thin film rf sputtered on silicon substrates with a 2.5 μm SiO_2 buffer layer sandwiched in between, we have demonstrated waveguiding via end-fire coupling, which is shown in Figure 5. The attenuation is determined to be 2.3 $\pm$ 0.1 dB/cm. This is the first time that waveguiding in lithium niobate thin film on SiO_2/Si has been reported. Since the guided modes were excited by end-fire coupling, the measured attenuation was an averaged value over all of the supported modes. Therefore, it should be lower than 2.3 dB/cm for a single mode waveguide. The thick oxide layer makes the coupling much easier. However, it is not necessary to have such a thick buffer layer. Theoretically, only 0.3 μm of SiO_2 buffer layer thickness is required to reduce the leakage loss of waveguides on SiO_2/Si substrate to about 0.1 dB/cm if only coupling of the wave to the silicon substrate is considered.[12] Further research on the properties of these waveguides are currently under investigation, and the

results will be published in a later paper.

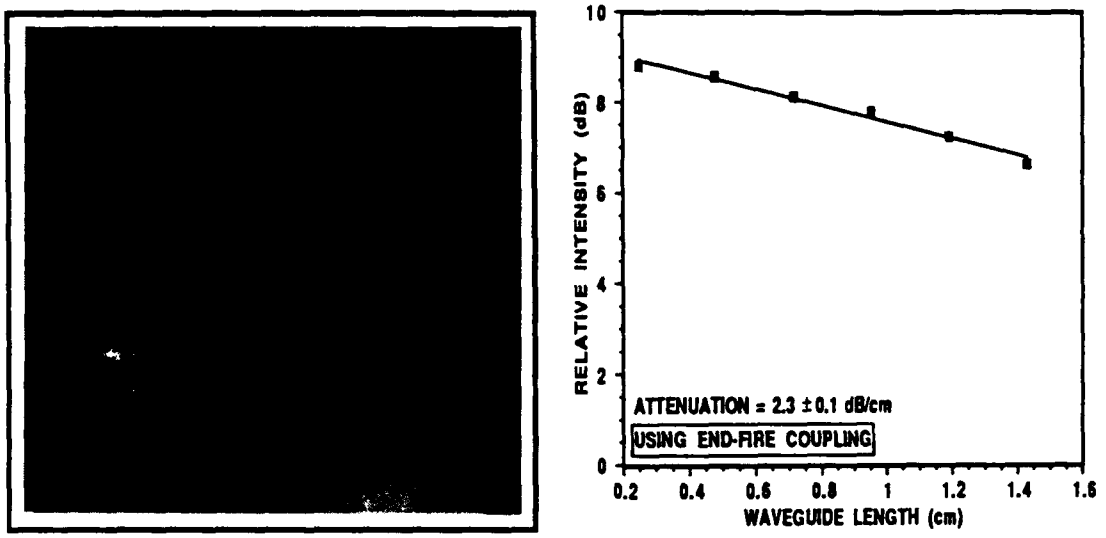


FIGURE 5 A He-Ne light guided in $LiNbO_3/SiO_2/Si$.

CONCLUSIONS

In summary, lithium niobate optical waveguides have been epitaxially deposited on sapphire and SiO_2/Si substrates by both diode and magnetron rf sputtering techniques. By Bragg x-ray diffraction analysis, these films were found to be highly oriented with their c axis parallel to the c axis of the substrates. The thickness and the refractive index of the films were determined utilizing a rutile prism coupler. The propagation losses were measured to be about 1.1 dB/cm and 2.3 dB/cm for lithium niobate thin film waveguides deposited on sapphire and SiO_2/Si substrates, respectively. The deposition parameters for sputtering shown in Table I effectively produced films with low defect density and optically smooth surfaces, thereby reducing optical attenuation in the waveguide.

ACKNOWLEDGEMENTS

This research is supported by the Texas Higher Education Advanced Technology Program under grant numbers 4075 and 3604.

REFERENCES

1. T. Tamir, Integrated Optics (Berlin, Springer-Verlag, 1979).
2. M. E. Lines and A.M. Glass, Principles and Applications of Ferroelectrics and Related Materials (Oxford. 1977).
3. T. Tamir, Guided-Wave Optoelectronics (Berlin, Springer-Verlag, 1988),
4. G. Griffel, S. Ruschin, and N. Croitoru, Appl. Phys. Lett., 54, 1385, (1989).
5. G. H. Hewig and K. Jain, J. Appl. Phys., 54, 1, 57, (1983).
6. C. H. Huang, H. C. Chui, B. A. Stone, T. A. Rost, and T. A. Rabson, to be published in the Proceedings of ISAF '90.
7. T. A. Rost, H Lin, and T. A. Rabson, to be published in the Proceedings of ISIF '91.
8. T. A. Rost, H Lin, and T. A. Rabson, to be published in the Proceedings of ISIF '91.
9. L. O. Svaasand, M. Eriksrud, G. Nakken, and A. P. Grande, J. Crystal Growth, 22, 230, (1974).
10. P. K. Tien, Applied Optics, 10, 2395, (1971).
11. T. Tamir, Guided-Wave Optoelectronics, (Berlin, Springer-Verlag, 1988).
12. N. Nishihara, M. Haruna, and T. Suhara, Optical Integrated Circuits, (New York, McGraw-Hill, 1989).

AD-P006 661

THEORY OF CONDUCTION AND BREAKDOWN IN PEROVSKITE THIN FILMS

RAINER WASER and MAREIKE KLEE

Philips GmbH Forschungslaboratorium Aachen,
D-5100 Aachen, Federal Republic of Germany

Abstract. The mechanism of the dc electrical conduction and breakdown of perovskite-type titanates was investigated by impedance analysis. Based on an acceptor doped $SrTiO_3$ model material, samples of different microstructures - ceramics, single crystals, and thin films - were employed. This approach allows us to distinguish conduction contributions of the bulk lattice, grain boundaries, and electrode interfaces. Based on defect chemistry studies, a predominant ionic contribution due to mobile oxygen vacancies and an additional p-type conduction were revealed for the bulk. At interfaces, space charge depletion layers of 100-500 nm width are formed in which the local conductivity is reduced by approx. four orders of magnitude compared to the bulk. Thin films show a similar depression of the conductivity. The combination of these facts may be indicative for considering thin films as distributed Schottky barriers. The field enhancement of the conductivity of thin films and of the interface depletion layers is compared and discussed.

1. INTRODUCTION

The extent to which properties such as the switching behaviour, the fatigue, and the retention of ferroelectric thin films can be controlled and improved will have an essential impact on a future success of these films in device applications. As pointed out in numerous contributions at the ISIF'91 conference and at earlier meetings, these electrical properties are supposed to be up to a large degree determined by the conduction and breakdown mechanism of the films (for example, see Ref. 1).

Ferroelectric thin films based on perovskite-type materials are extremely complex electrical systems. Firstly, they are *thin* films. The dielectric thickness typically ranges from 0.1 to 1 μm. Consequently, the influence of the electrode interfaces will be much more pronounced than in compact samples. In addition, the microstructure of the films usually is very different from bulk ceramics or bulk single crystals. Secondly, they are *ferroelectric*. Even in non-ferroelectric perovskite films, the charge transport and polarization properties are not yet understood. Hence, the ferroelectric behaviour superimposes an additional degree of complexity because it significantly affects the polarization and charge transport in the material. Devoting ourselves to a step-by-step research approach, we will restrict ourselves in this report to non-ferroelectric perovskite-type titanates such as $SrTiO_3$ and $BaTiO_3$ above the Curie temperature. These materials show the same crystal structure and a similar band gap as the

ferroelectric PZT (lead-zirconate-titanate) and are assumed to be governed by a comparable defect structure. Single crystals, ceramics, and thin films of the same composition will be compared in order to separate the different conduction and polarization contributions. In addition, the conductivity enhancement under high electrical fields will be considered, keeping in mind that fields across films in actual devices under operating voltages (typically 3 to 5 V) are in the range of $0.5\text{-}5 \cdot 10^5$ V/cm. Related to that aspect, the possible nature of the instantaneous dc breakdown will be discussed briefly.

Under relative low dc fields and at moderate temperatures titanates and other mixed conducting oxides are known to suffer from a long-term resistance degradation due to an ionic de-mixing process which leads to an increase of the electronic carrier concentration. While a quantitative model for the degradation kinetics of single crystals based on the defect chemistry, the charge transport properties, and the electrode interface transfer rates was presented recently [2], research concerning the degradation of titanate thin films is at its very beginning. Comprehensive studies are currently carried out at our laboratory and will be presented at a later date.

2. MOBILE SPECIES IN THE CRYSTAL LATTICE

The types and concentrations of charge carriers in the crystal lattice of barium or strontium titanate are determined by the defect chemistry and are affected by the temperature, the oxygen partial pressure during annealing, P_{O_2}, and the concentration of dopants. Lower-valent cations substitutionally accommodated on regular cation sites (e. g. Ni^{2+} on Ti^{4+} sites) act as acceptors, while higher-valent cations (e. g. Ce^{3+} on Ba^{2+} sites) are donors. The defect chemistry of undoped and acceptor doped titanates in the high temperature regime (approx. T > 900 K) were the subject of several comprehensive studies and the reader is referred to the corresponding papers [3-7] and the excellent review Ref. 8. The high temperature regime is characterized by equilibria with the P_{O_2} of the ambient atmosphere which are established within reasonable times. Undoped titanates were found to be governed by a low concentration of cation vacancies as native acceptors and acceptor-type impurities (Al, Fe, Mn, etc.). The latters have been detected even in samples of highest purity. For conductivity studies nominally undoped titanates are less suitable because of the undefined and possibly locally varying impurity concent. Slightly acceptor doped titanates (e. g. 0.1 at% Ni-doped $SrTiO_3$), instead, represent well-defined model systems and were used in the present study.

The defect chemistry of acceptor doped titanates after quenching from high temperature equilibria to temperatures at which the oxygen content is frozen-in (approx. T < 700 K) has been investigated recently by means of the impedance analysis [9]. This temperature regime is relevant for the regular operation and the accelerated life testing of electronic ceramic components. Fig. 1 is reproduced from this study and shows that annealing under conventionally oxidizing to moderately reducing atmospheres leads to a dominant ionic conductivity, σ_{ionic}, and a certain contribution by a p-type electronic conductivity, σ_p. The mobile ionic species are oxygen ions which move by a vacancy mechanism. The mobility of the oxygen vacancies, $V_{\ddot{O}}$, is thermally activated with an activation energy of 1.0 to 1.1 eV which fits well to high temperature data [5]. In titanates, the holes (and the electrons as well) can be regarded as polarons which move by a hopping process. The slight, non-activated temperature dependence supports the large-polaron model [10] although the

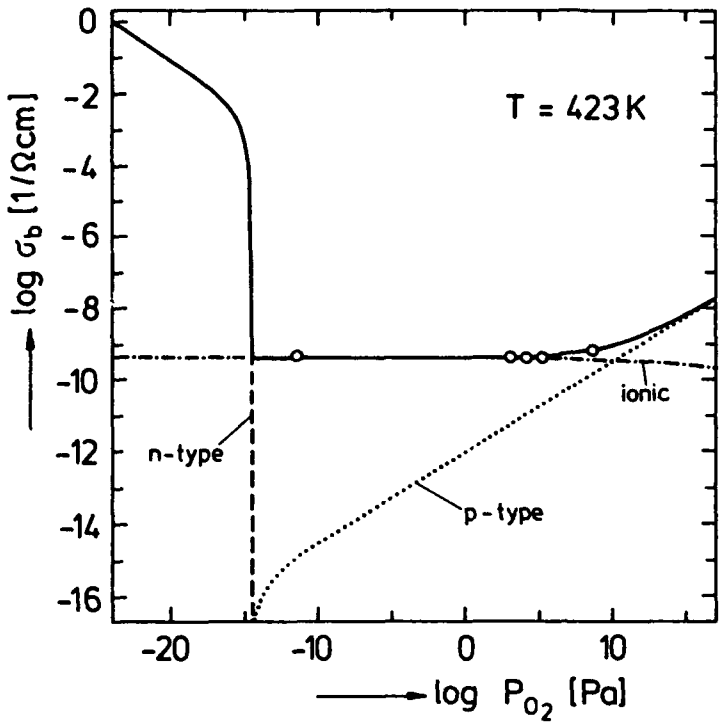


FIGURE 1
Calculated (——) and measured (o) bulk conductivity of 0.1 at% Ni-doped $SrTiO_3$ after annealing at 973 K and different P_{O_2} and subsequent quenching to 423 K [9].

mobilities are relatively small (e. g. μ_h = 0.1 cm^2/Vs for $Sr_{0.97}Ba_{0.03}TiO_3$ at 1223 K [10]) and fall close to those expected for the small-polaron model [11]. Altogether, undoped and acceptor doped alkaline earth titanates today rank among the most studied and best understood oxides from the defect chemistry's point of view. As far as the bulk crystal lattice is concerned, this does not leave much room for ambiguities in interpreting conductivity data with respect to carrier types, concentrations, and mobilities.

Donor doped titanates show a different conduction mechanism due to the very low concentration of $V_{\ddot{O}}$. Single crystal and coarse grained ceramic are semiconducting due to the electron compensation of the donor centers, while fine grained ceramic sintered under oxydizing atmospheres is highly insulating at room temperature due to the cation vacancy compensation [4]. While in both cases there is virtually no ionic transport in the lattice due to the low mobility of the cation vacancies, oxygen ions are known to show a certain motion along the grain boundaries under gradients of the oxygen activity or the electrical potential [12].

3. IMPEDANCE ANALYSIS IN THE TIME DOMAIN

The impedance of real samples is not only determined by the conductivity of the crystal lattice. The electrode interfaces (el) and - in the case of ceramics - the grain boundaries (GB) contribute to the total impedance as illustrated by the simplified equivalent network in Fig. 2. In the present study, impedance analysis in the time domain was utilized by recording the time evolution of the current response after applying a dc voltage step. Details of this method and the transformation between the time and the frequency domain are described in Ref. 13. It is well known that ionically conducting ceramics as, for instance, stabilized ZrO_2 [14] as well as mixed conducting ceramics such as titanates [15, 16] tend to build highly resistive layers at

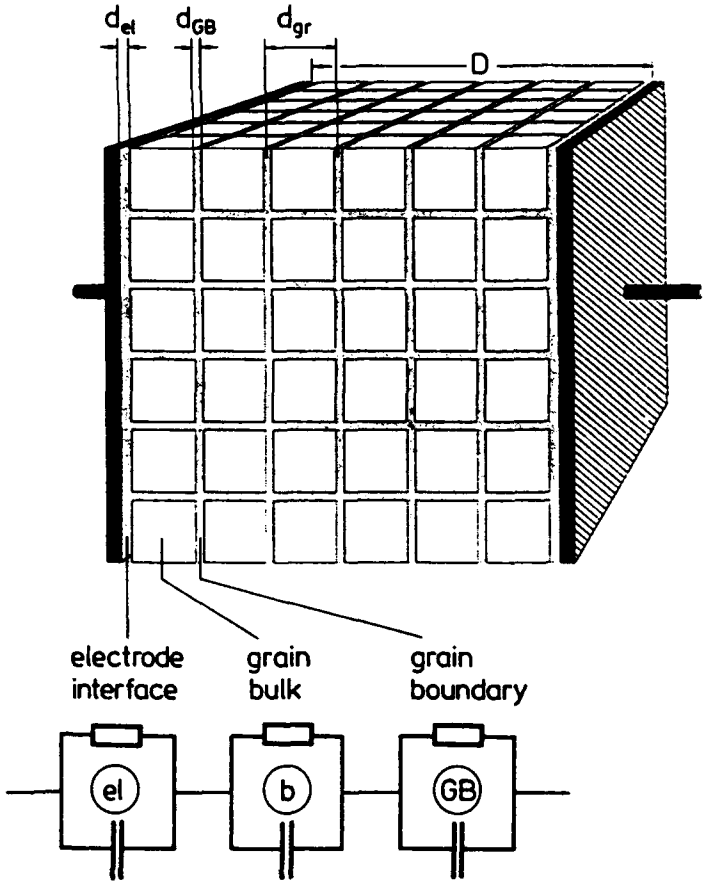


FIGURE 2
Simplified block model of a ceramic and simplified electrical equivalent network illustrating the conduction and polarization contributions. The contributions of both electrode interfaces are merged into branch 'el'. The contributions of all grains and all grain boundaries are merged into branch 'b' and branch 'GB', respectively.

electrode and GB interfaces. These are commonly interpreted as depletion space charge layers similar to Schottky barriers at semiconductor interfaces [17]. Consequently, the conductivities σ_{el} and σ_{GB} are usually very small compared to σ_b because the corresponding layers are depleted by the charge carriers. In conventional ceramics, the depletion layer thicknesses d_{GB} and d_{el} are much smaller than the grain size:

$$d_{gr} >> d_{GB}, d_{el}. \quad (1)$$

Hence, the capacities generated by the interfaces (i. e. branches 'el' and 'GB' of the equivalent network in Fig. 2) are large compared to the capacity caused by the bulk of the grains (branch 'b'). In addition, the GB contributions perpendicular to the electrodes can be neglected because of relation (1). Still, there is a certain mobility of oxygen ions **along** GBs. This becomes obvious in either donor doped titanates where the ionic conduction in the bulk of the grains is negligible [24] or in very fine grain acceptor doped ceramics where relation (1) is not valid any more (see Sec. 7).

The permittivity in the depletion layers, ε_{GB} and ε_{el}, is equal to the permittivity ε_b of the crystal lattice in paraelectric ceramics as has been shown recently for $SrTiO_3$ [18].

Applying a dc voltage step to a network (Fig. 2) with two dominating branches leads to a Maxwell-Wagner polarization. In Fig. 3, the voltage stimulation as well as the current response is shown for a charging period and a discharging period. At very short times, when the space charge polarization at the interfaces is still negligible, the current density J is determined by a short-term conductivity $\sigma_s := \sigma(t \rightarrow 0)$. If relation (1) is valid, σ_s is equal to the bulk conductivity σ_b within a good

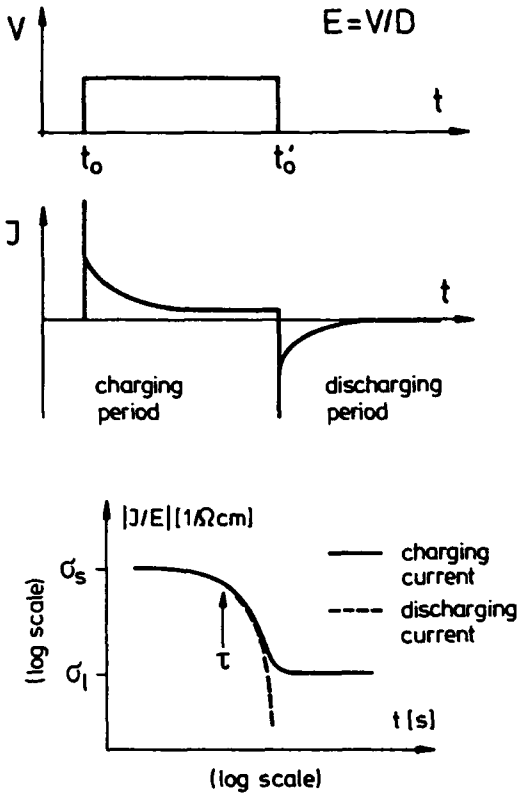


FIGURE 3
Sketch of a dc voltage step experiment. The voltage stimulation V(t) and the current density response J(t) are illustrated for a charging period starting at t_0 and a discharging period starting at t_0'. In the present paper, the response is shown on a log-log scale. Furthermore, the unsigned current density - field ratio |J/E| is used in order to obtain data in the conductivity unit and to compile the charging and discharging response in one diagram. For an explanation of the short term conductivity σ_s, Debye relaxation time τ, and the long term conductivity σ_l: see text.

approximation

$$\sigma_b \approx \sigma_s \ . \tag{2}$$

The current decays in a manner which is typical for a Debye relaxation:

$$J \sim \exp(-t/\tau) \ . \tag{3}$$

After a long time, when the polarization process is complete, the residual conductivity σ_l remains left being caused by the leakage through the depletion layers. Switching off the applied voltage leads to a depolarization current of reversed sign which proceeds until the capacitive interface elements are discharged. This discharging process has been included in all studies reported in the present paper.

For further details on the measuring principle see Ref. 13.

4. CONDUCTION THROUGH GRAIN BOUNDARIES OF CERAMICS

A ceramic of 0.1 at% Ni-doped $SrTiO_3$ was prepared using the conventional mixed-oxide technique. For details see Ref. 9. After sintering at 1613 K for 6 h in oxygen and subsequent isostatic hot-pressing at 1573 K for 1 h, a porefree ceramic with a uniform microstructure and a grain size of 2.5 ± 1.0 μm was obtained. Discs of 125 μm, 250 μm, and 500 μm thickness were cut, lapped, polished, and annealed at 973 K for 6 h in oxygen. After quenching, electrodes of NiCr alloy (thickness: 6 nm) and Au (150 nm) were applied by evaporation.

Fig. 4a shows the results of dc voltage step experiments at 423 K and different

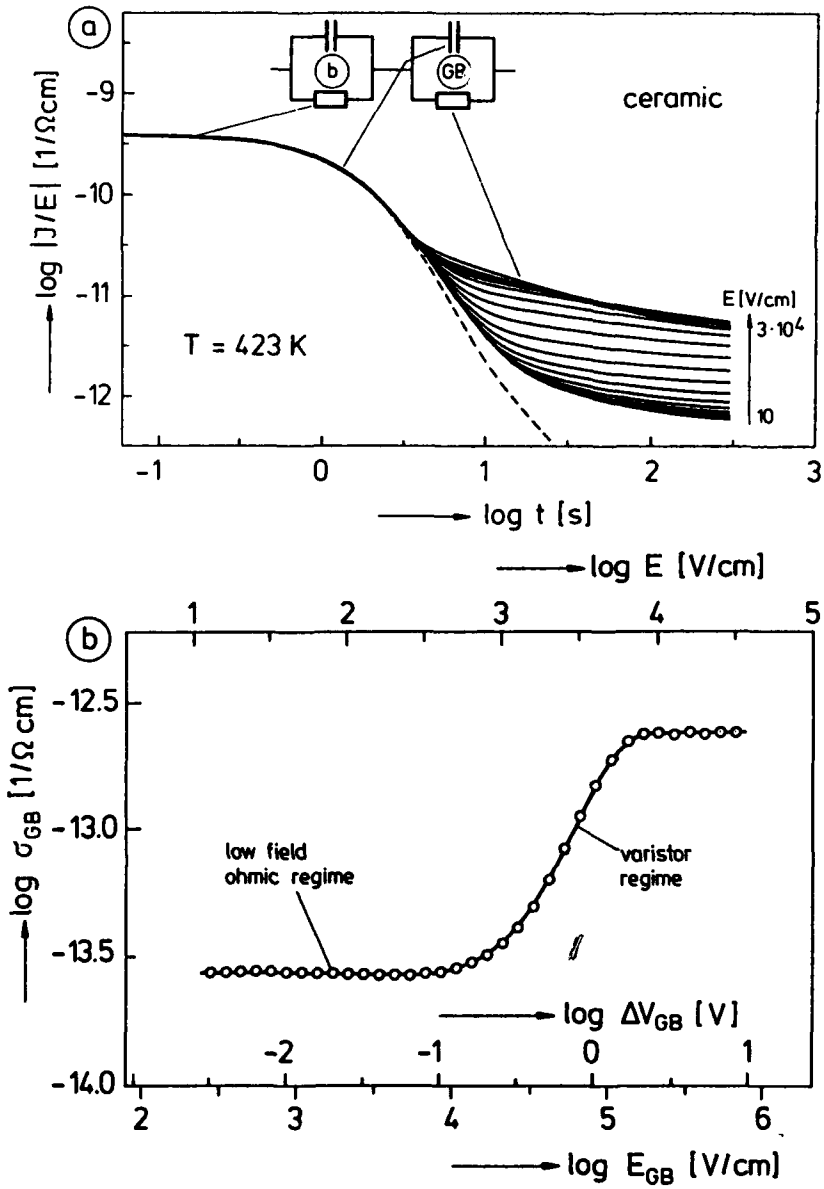


FIGURE 4

(a) Current density - field ratio |J/E| vs. time t for a fine grained, 0.1 at% Ni doped $SrTiO_3$ ceramic at T = 423 K for different dc voltage steps corresponding to dc fields in the range from E = 10 V/cm to $3 \cdot 10^4$ V/cm. The determining components of the equivalent network are sketched on top. The discharging curve (dashed line) is shown for E = 300 V/cm.

(b) Field dependence of the conductivity at t = 300 s in diagram (a), interpreted as the conductivity in the GB space charge layer σ_{GB} according to Eq. (8). Abscissa from top to bottom: applied field at the sample E = V/D, average voltage drop at a GB ΔV_{GB}, and average field across a GB depletion layer E_{GB}. Thickness of the sample: D = 500 μm. Average grain size: d_{gr} = 2.5 μm.

field strengths E. The regimes of the |J/E| curves are formally attributed to components of the schematic equivalent network (Fig. 2). These assignments are supported by additional experiments using samples of different grain sizes (prepared by varying the sintering temperature) and different sample thicknesses. It is worthwhile to note that the electrode interface branch (el) was not observed presumably due to the large number of GBs between the electrodes which outweigh the influence of the two electrode layers.

The Debye relaxation time τ of the Maxwell-Wagner polarization of the GBs is determined by

$$\tau = \varepsilon_{eff}\varepsilon_0 / \sigma_s \qquad (4)$$

where ε_{eff} denotes the effective permittivity of the material when the grains act as shorts. ε_0 is the vacuum permittivity ($8.854 \cdot 10^{-14}$ As/Vcm). Based on geometrical

considerations for the simple block model of the ceramic and relation (1), ε_{eff} obviously is determined by the ratio of the grain size d_{gr} to the GB depletion layer width d_{GB}:

$$\varepsilon_{eff}/\varepsilon_{GB} = d_{gr}/d_{GB} \tag{5}$$

Inserting (2) and (4) into (5) reveals

$$d_{GB} = d_{gr}\frac{\varepsilon_{GB}\,\varepsilon_0}{\tau\,\sigma_b} \quad . \tag{6}$$

A GB depletion layer width $d_{GB} = 115 \pm 20$ nm is evaluated from the data in Fig. 4a. The origin of the depletion layer is assumed to be due to donor-type interface states. There are indications that these interface charges are active even during the sintering process and lead to a certain segregation of acceptors at the GB [19]. For the ceramic used in the present study, a relatively high GB interface charge Q_{GB} of approx. $7 \cdot 10^{-5}$ Cb/cm^2 is determined using the Schottky approximation for depletion space charge layers [20]:

$$Q_{GB} \approx e_0\, d_{GB}\, z_{Ni,av}\, c_{Ni,av} \tag{7}$$

In this relation, $c_{Ni,av}$ is the average Ni acceptor concentration in the depletion layer taking into account the segregation. $z_{Ni,av}$ represents the average valency of the Ni centers related to the substituted Ti ions and is approx. 2. e_0 denotes the unit charge.

The magnitude of d_{GB} is almost independent of the field and of the temperature within the measured range from approx. 350 K to 750 K [21]. This is typical for a Schottky-type depletion space charge layer [17]. Due to the symmetry of a GB, the depletion layer can be regarded as a back-to-back double Schottky barrier (Fig. 5).

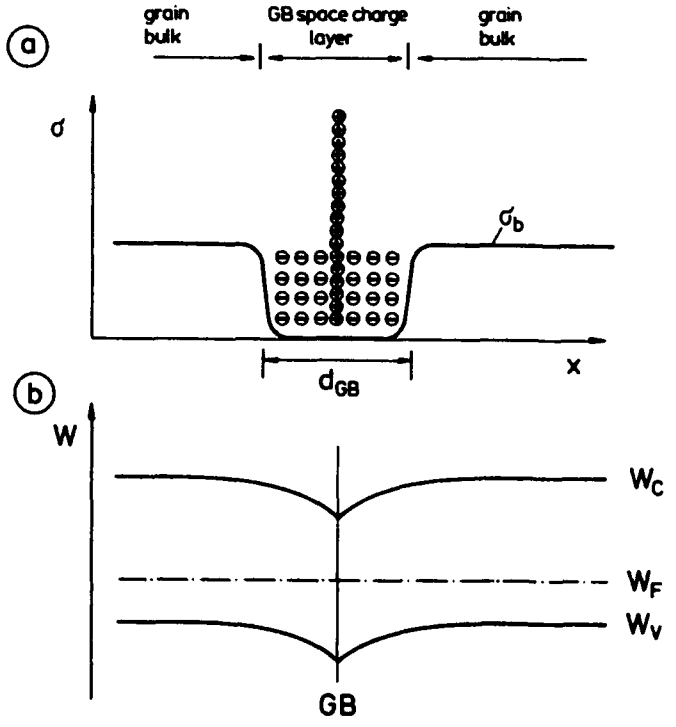


FIGURE 5
Sketch of the conductivity profile (a) and the energy band diagram (b) across a GB in acceptor doped titanate ceramics.
In (a), ⊕ indicate the positively charged (i. e. donor type) GB interface states and ⊖ illustrate the uncompensated acceptor centers forming a negative space charge region.
In (b), W_C, W_V, and W_F are the conduction and valence band edges and the Fermi level, respectively.

According to this model, donor-type GB charges lead to a depletion of the positively charged mobile carriers, oxygen vacancies $V_{\ddot{O}}$ and holes $h^{\cdot}$. In the depletion layer, the immobile acceptors form a negative space charge. The width d_{GB} of the depletion layer is established in such a way that the positive GB charges are just compensated by the negative space charge. Fig. 5b qualitatively illustrates the corresponding bending of the energy bands.

Since the bulk conductivity σ_b is thermally activated (see Sec. 2), the relaxation time τ varies by many orders of magnitude in the stated temperature range. This fact emphasizes the often neglected importance of recording the current as a function of time when it is intended to determine and to interpret the conductivity of materials. Another clear indication for the presence of GB depletion layers is the discharging current which is indistinguishable from the charging current up to approx. $t \approx \tau$ (Fig. 4a). Hence, the current at short times has to be regarded as a space charge polarization current and not as a conduction current.

The local conductivity σ_{GB} in the GB depletion layer is calculated from the long-term conductivity σ_l and the geometry shown in Fig. 2 in combination with relation (1):

$$\sigma_{GB} = \frac{d_{GB}}{d_{gr}} \cdot \frac{\sigma_l \, \sigma_b}{\sigma_b - \sigma_l} \tag{8}$$

For $\sigma_l << \sigma_b$, this equation can be approximated by

$$\sigma_{GB} = \frac{d_{GB}}{d_{gr}} \, \sigma_l \, . \tag{9}$$

For 0.1 at% Ni-doped $SrTiO_3$ at low fields and T = 423 K, σ_{GB} turns out to be more than four magnitudes below the conductivity σ_b in the bulk of the grains (Fig. 4b). Towards higher temperatures, the difference between σ_{GB} and σ_b becomes smaller due to a higher activation energy of σ_{GB} [21].

In Fig. 4b, σ_{GB} is shown as a function of the externally applied field E = V/D. After the Maxwell-Wagner polarization is settled, the grain bulk regions are virtually field free. Based on this, additional abscissa are included in Fig. 4b showing the actual field across the GB depletion layer E_{GB} and the voltage drop $\Delta V_{GB} = E_{GB} d_{GB}$. At a low voltage drop, σ_{GB} exhibits an ohmic behaviour. Above approx. ΔV_{GB} = 0.5 V, σ_{GB} starts to enhance strongly with incremented voltages. This varistor-type regime is succeeded at very high fields by another ohmic regime. A further increase of the external field E is not possible although the ceramic does not yet suffer an instantaneous breakdown. Rather, the onset of the resistance degradation is shifted to such short times at very high fields that the Maxwell-Wagner polarization of the GBs remains incomplete.

The ohmic regime at low voltages and the varistor regime of GB depletion space charge layers in n-type semiconducting ceramics has been consistently interpreted in terms of *charge transport over a Schottky barrier* (see Ref. 20 and references cited therein). In these ceramics, the energy distribution of the densities of interface states $N_{GB}(W)$ was found to affect the voltage ΔV_{GB} at which the enhancement of the conductivity sets in, the slope of the conductivity increase, and the fine structure of the J-E curve. We assume a similar process to be responsible for the charge transport across the GB depletion layers in the case of acceptor doped titanates. Further details and possible implications of the predominant ionic conduction superimposed on the p-type conduction in the titanates will be reported in Ref. 21.

5. CONDUCTION THROUGH ELECTRODE INTERFACES AT SINGLE CRYSTALS

Samples were cut from a single crystal boule of 0.1 at% Ni-doped $SrTiO_3$ (Commercial Crystals Inc.), lapped, and polished to optical quality. Sython W30 (Monsanto) was used as a polishing medium. Any mechanical damage to the surface was found to be below the detectability limit of a SEM [22]. Voltage step measurements were performed for different surface treatments (e. g. annealing at 973 K in oxygen before or after polishing) and for different electrode metals (e. g. Au, Al, Cu, Pt). In all these cases, a clear indication for a depletion space charge layer at the surface was found. An example is given in Fig. 6a. A total depletion layer width of approx. 1000 nm can be calculated from the data using Eq. (6) appropriately. For a low voltage step stimulation, we assume that the total layer width is equally distributed between both electrodes, i. e. d_{el} = 500 nm. At higher voltages, the widths at the anode and cathode may be different. This aspect has to await further clarification using samples with asymmetric electrodes. Compared to the GB depletion layer d_{GB}, the depletion layer at the electrode d_{el} is unexpectedly broad. This may either be attributed to a high surface charge or it may be enhanced by artefacts introduced during the surface preparation which are below the SEM detectibility limit.

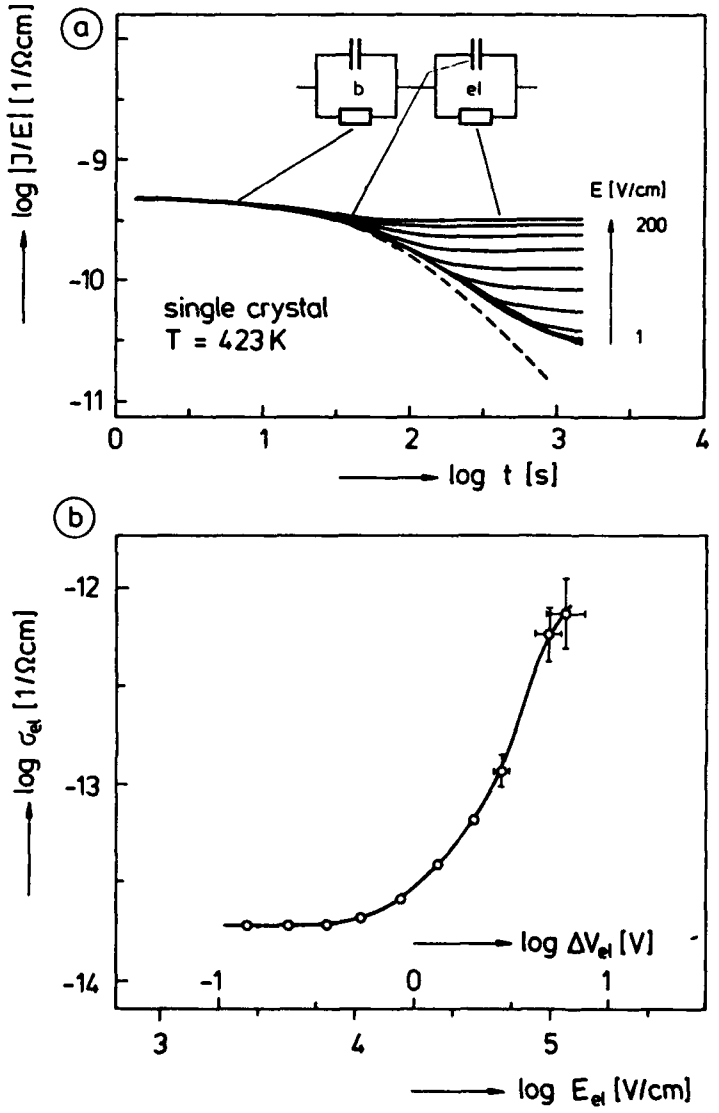


FIGURE 6

(a) Current density - field ratio |J/E| vs. time t for a 0.1 at% Ni doped $SrTiO_3$ single crystal at T = 423 K for different dc voltage steps corresponding to dc fields in the range E = 1 V/cm to 200 V/cm. The determining components of the equivalent network are sketched on top. The discharging curve (dashed line) is shown for E = 50 V/cm.

(b) Field dependence of the conductivity at t = 1500s in diagram (a), interpreted as the conductivity in the electrode interface space charge layers σ_{el}. Abscissa from top to bottom: applied field at the sample E = V/D, voltage drop at an electrode interface ΔV_{el} assuming equal distribution at both electrodes, and field across a depletion layer E_{el}. For three data points, error bars are included indicating the strong decrease in the reliability when σ_i gets close to σ_s at high fields. Thickness of the sample: D = 1500 μm.

For instance, such an artefact could be a near-surface layer of a high dislocation density possibly establishing additional donor states.

Fig. 6b illustrates the field dependence of the conductivity σ_{el} in the depletion layer evaluated in the same way as σ_{GB} of the ceramics adapting Eq. (9). A comparison of Fig. 4b and Fig. 6b shows that the conductivity in the depletion layers of grain boundaries and at electrodes are quite similar. In the low field ohmic regime, σ_{el} is in the same order of magnitude as σ_{GB} in ceramics indicating the same situation concerning the degree of depletion of charge carriers. Above a voltage drop ΔV_{el} in the depletion layer of approx. 0.5 V (as at GBs in ceramics), the conductivity departs from the ohmic behaviour and exhibits a pronounced varistor-type behaviour. At high voltages, σ_l gets close to σ_s and, hence, the reliability of the data evaluated using Eq. (9) drastically decreases (as indicated by the error bars in Fig. 6b). Based on the present data it is therefore not possible to judge whether the slope of the varistor regime of σ_{el} decreases towards high fields before σ_{el} comes close to σ_b.

Both the width of the depletion layer d_{el} as well as the conductivity σ_{el} and its field dependence are influenced by the annealing before or after the polishing and by the electrode metal. Details will be given in a forthcoming paper [23].

6. PREPARATION AND STRUCTURE OF TITANATE THIN FILMS

A modified sol-gel process has been developed to deposit doped and undoped $SrTiO_3$ and $BaTiO_3$ films on Si(100) substrates with a Ti/Pt electrode layer [37]. Solutions containing Ba, Sr, Ti, Ni, Mn, and Ce as metal alkoxides, metal carboxylates, and metal acetylacetonates dissolved in butanol were deposited by spin coating and subsequent firing at 773 to 973 K in oxygen. Perovskite films with thicknesses of 55 nm and 110 nm per coating were obtained using 0.2 M and 0.4 M solutions, respectively. To increase the thickness up to the desired value, the deposition process was repeated several times. X-ray diffraction (XRD) and scanning electron microscopy

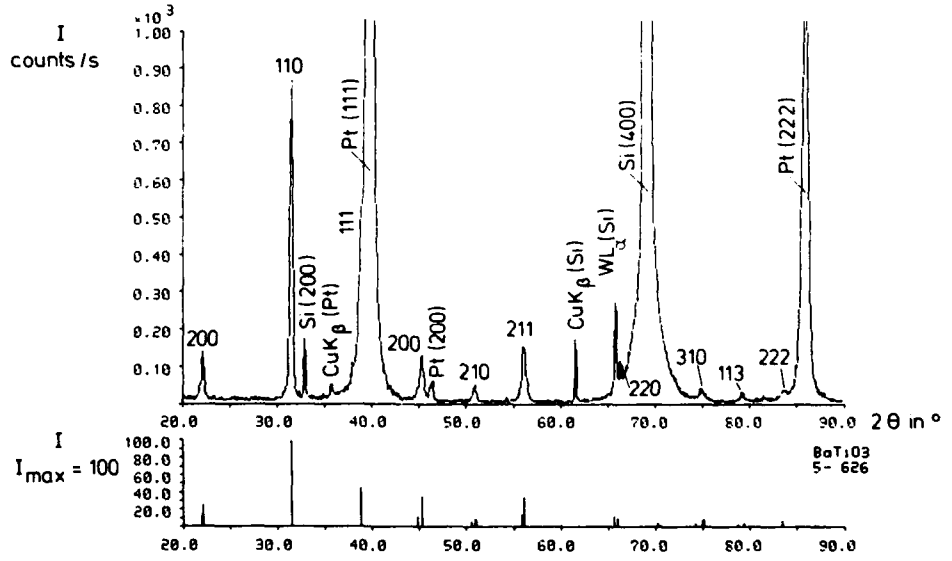


FIGURE 7 XRD pattern of a 1 μm thick $BaTiO_3$ film deposited on a Si/Ti/Pt substrate

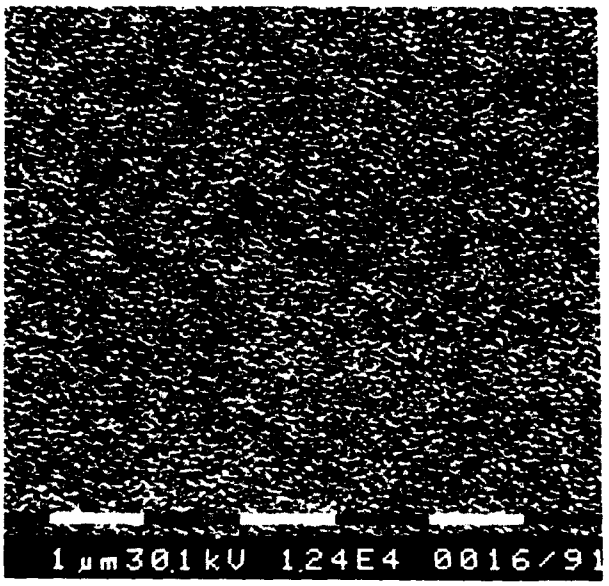


FIGURE 8
SEM micrograph of a 0.55 µm thick 0.1 at% Ni doped $SrTiO_3$ film deposited on a Si/Ti/Pt substrate. The white bar indicates a length of 1 µm.

(SEM) studies revealed that all the films reported here crystallize in a single phase perovskite structure with a random orientation of the crystals on the substrate plane (Fig. 7). Due to the low reaction temperatures of the sol-gel process extremely fine grained ceramic films with grain sizes of 40-90 nm are obtained (Fig. 8). These grain size data are supported by evaluating the broadening of the XRD lines.

Capacity measurements were carried out after evaporation of Au electrodes (area: 0.01 cm^2) on top of the films. The dielectric constants ε were 500-800 for the $BaTiO_3$ films and 140-160 for the $SrTiO_3$ films at 298 K.

7. CONDUCTION THROUGH THIN FILMS

Fig. 9 shows the charging and discharging behaviour of a 0.1 at% Ni-doped $SrTiO_3$ thin film for a voltage V = 2 V (representing $E = 3.64 \cdot 10^4$ V/cm) for different temperatures. As in the ceramic and the single crystal sample, the *polarization* current predominates in the beginning while at long times the current is determined by the *conduction* through the film. The transition times τ_T between the polarization and the conduction regime are approx. 0.0015 s (T = 603 K), 0.02 s (543 K), 0.3 s (483 K), and 4 s (423 K). An extrapolation to 298 K reveals a τ_T of approx. 10^5 s. This means that any dc measurement at room temperature has to be carried out for at least one day to determine the true conductivity with a reasonable reliability. Since PZT films (prepared along two alternative sol/gel routes) exhibit qualitatively the same dc voltage step responses [25], we expect similar amounts of time to be needed for reliable conductivity measurements at room temperature.

The eminent difference between the space charge polarization behaviour of the ceramic and the single crystal on the one hand and the thin film on the other hand is given by the fact that the first shows a Debye relaxation, Eq. (3), while the latter is described by a Curie - von Schweidler law (the so-called "universal law") [13]

$$J \sim t^{-n} . \qquad (10)$$

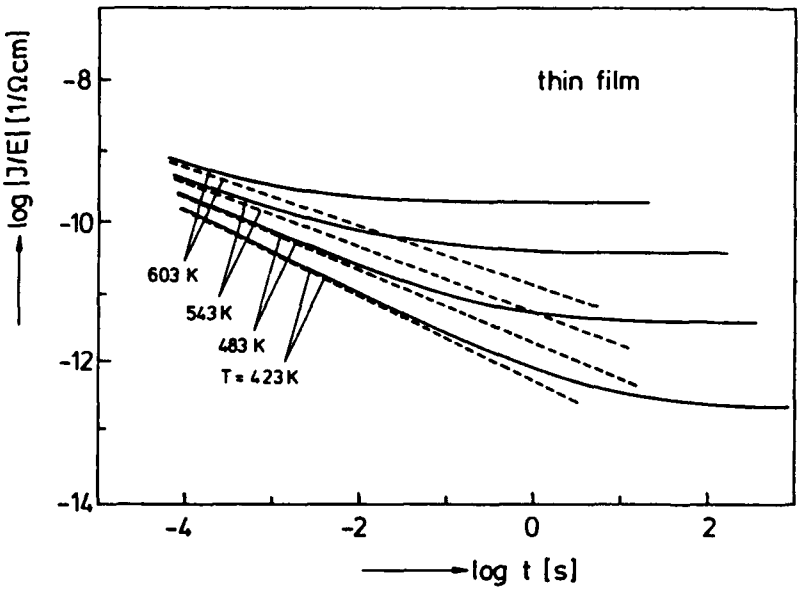


FIGURE 9
Current density - field ratio |J/E| vs. time t for a 0.1 at% Ni doped $SrTiO_3$ thin film at T = 423 K, 483 K, 543 K, and 604 K. The charging (solid lines) and discharging (dashed lines) responses for a dc voltage step of 2 V are shown. Thickness of the film: 0.55 μm. Area of an electrode dot: 0.011 cm^2.

For the discharging curves in Fig. 9 (dashed lines), n is decreasing from 0.63 to 0.44 when increasing the temperature from 423 K to 603 K.

The Curie - von Schweidler law is reported for a wide range of disordered systems such as partially or totally amorphous solid and different materials such as organic polymers and inorganic compounds. In contrast to a Debye relaxation which can be represented by an equivalent network consisting of a resistor and a capacitor in series, a Curie - von Schweidler relaxation corresponds to a distributed RC line of infinite length. Different explanations have been offered to explain the behaviour expressed by Eq. (10):

1. Applying a dc field at materials with a negligible equilibrium concentration of free carriers due to a very large band gap (e. g. SiO_2, Al_2O_3) leads to charge injection at the electrode. The decay of the injection current according to Eq. (10) was reported to be caused by a trapping of the carriers and a consequent formation of a repulsive space charge [26].

2. A distribution of Debye relaxation times over many orders of magnitude and a corresponding weigth of the underlying processes may lead to a response as described by Eq. (10). The pros and cons of distributed relaxation time approaches are discussed in Ref. 13.

3. A many-body interaction model ([13] and ref.s cited therein) explains Eq. (10) for disordered materials on the base of the interaction of individual charges with their microscopic environment and the transition of this interaction during charge transport. This leads to a mutual correlation of all transport events.

We can not yet decide which of these explanations is applicable for our ultra-fine grained titanate films. One may speculate that the situation is possibly determined by a combination of a many-body interaction and a distribution of relaxation times based on local flucations of the charge carrier concentrations proposed below.

At T = 423 K, the long-term conductivity σ_l of the 0.1 at% Ni-doped $SrTiO_3$ thin film is approx. $2 \cdot 10^{-13}$ 1/Ωcm. This more than three orders of magnitude *below* the bulk conductivity of the material $\sigma_b = 4.5 \cdot 10^{-10}$ 1/Ωcm and close to the residual conductivity in the depletion layers of the electrode interface, σ_{el}, and the GBs, σ_{GB}, which are in the range $2\text{-}3 \cdot 10^{-14}$ 1/Ωcm. This indicates unequivocally that the complete film is strongly depleted of mobile charge carriers compared to the bulk material. We suppose this depletion to be caused by the facts that the grains are

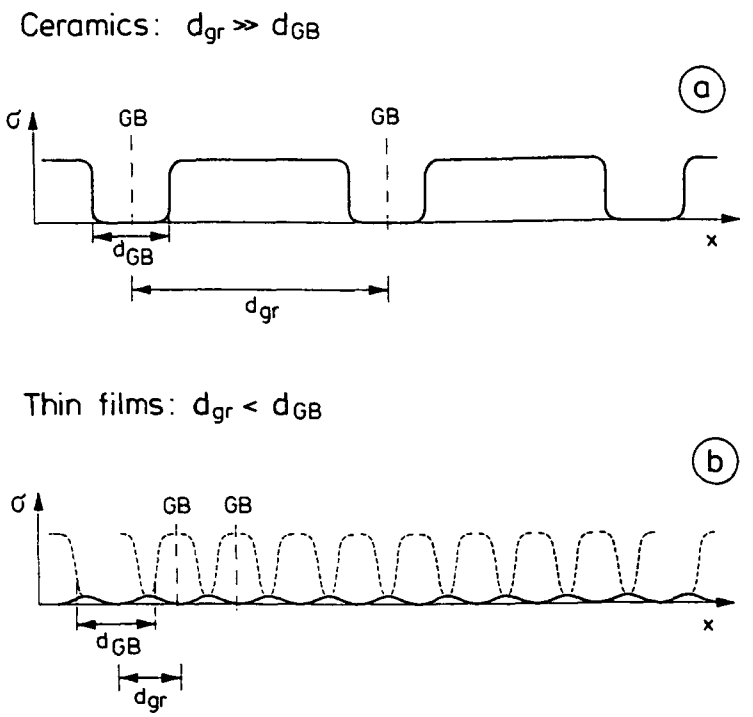


FIGURE 10
Schematic illustration of the conductivity profiles in a cross section of ceramics (a) and ultrafine grained thin films (b) as proposed to explain the different dc voltage step responses.

smaller than the GB depletion layer width in ceramics, $d_{gr} < d_{GB}$, and that the film thickness is in the same range as the electrode interface depletion layer, $D_{film} \approx d_{el}$. Each of the two facts in itself would be sufficient to cause the depletion. This aspect is important for the discussion of those PZT films which are reported to be single crystalline throughout their thickness.

The situation concerning the grain size is sketched in Fig. 10. In ceramics where $d_{gr} >> d_{GB}$, a pronounced Debye relaxation is observed due to the charging GB capacities caused by the GB depletion layers via the bulk of the grains as described in Section 4. In the ultra-fine grained thin films, there is obviously no region with a bulk conductivity anymore due to $d_{gr} < d_{GB}$, i. e. due to the overlap of the GB depletion layers. We assume a distributed spectrum of local conductivities on a level far below the bulk conductivity of the material. These conductivity fluctuations may be responsible for a polarization according to the Curie - von Schweidler law.

The approx. one order of magnitude higher long-term conductivity of the Ni-doped $SrTiO_3$ film compared to the conductivity in the depletion layers, σ_{el} and σ_{GB}, may be indicative for a charge transport (e. g. of oxygen ions) *along* the GBs. In conventional acceptor doped titanate ceramics this route plays only a minor role due to the high ionic conductivity in the bulk crystal lattice. In donor doped titanate ceramics the route was observed [24]. Due to the absence of any "bulk" in our Ni-doped $SrTiO_3$ film on the one hand and the high density of GBs on the other hand, the charge transport route along the GBs possibly becomes dominant. Another indication for this route is the activation energy of σ_i. The data given in Fig. 9 reveal a value of 0.82 ± 0.04 eV which is significantly below the activation energy for the oxygen vacancy transport in the bulk lattice of 1.05 ± 0.04 eV [9]. It is known for other polycrystalline materials as well that the diffusion along grain boundaries is less thermally activated than the corresponding diffusion in the bulk [27]. For final conclusions, however, data about the electronic and the ionic contribution to the conductivity of thin titanate films are required.

8. NATURE OF THE FIELD ENHANCED CONDUCTIVITY

In Fig. 11, the long-term conductivity σ_l of various titanate thin films at T = 423 K is displayed as a function of the applied field E. Besides Ni-doped $SrTiO_3$ which was used as a model material throughout this paper, Ce as a donor dope and Mn as an acceptor dope in $BaTiO_3$ were studied in addition. The field dependence of the conductivity of the thin films exhibits a similar characteristic as the conductivity of the depletion layers at GBs and electrode interfaces. At low fields, an ohmic regime is observed. Above a field of $1.5\text{-}3 \cdot 10^4$ V/cm for the $BaTiO_3$ films which corresponds to voltages in the range from 0.6 to 2 V, the conductivity shows an enhancement over many orders of magnitude. In the case of the Ni-doped $SrTiO_3$, the onset of the conductivity enhancement occurs at significantly higher fields ($E \approx 2 \cdot 10^5$ V/cm, corresponding to 10 - 15 V).

Reproducibility tests were performed for the Ce-doped $BaTiO_3$ films. In the ohmic regime, the scatter of σ_l is less than a factor of two for each film. In the varistor regime (c. g. at $E = 10^5$ V/cm), the scatter increases to a factor of up to five for the individual films. Due to this fact, the data reported in Fig. 11 should be regarded as showing trends. Further studies including statistical data collection are currently performed by the authors. Despite of this relatively large scatter, it can be stated that there is obviously a pronounced influence of the host material (i. e. $SrTiO_3$ and

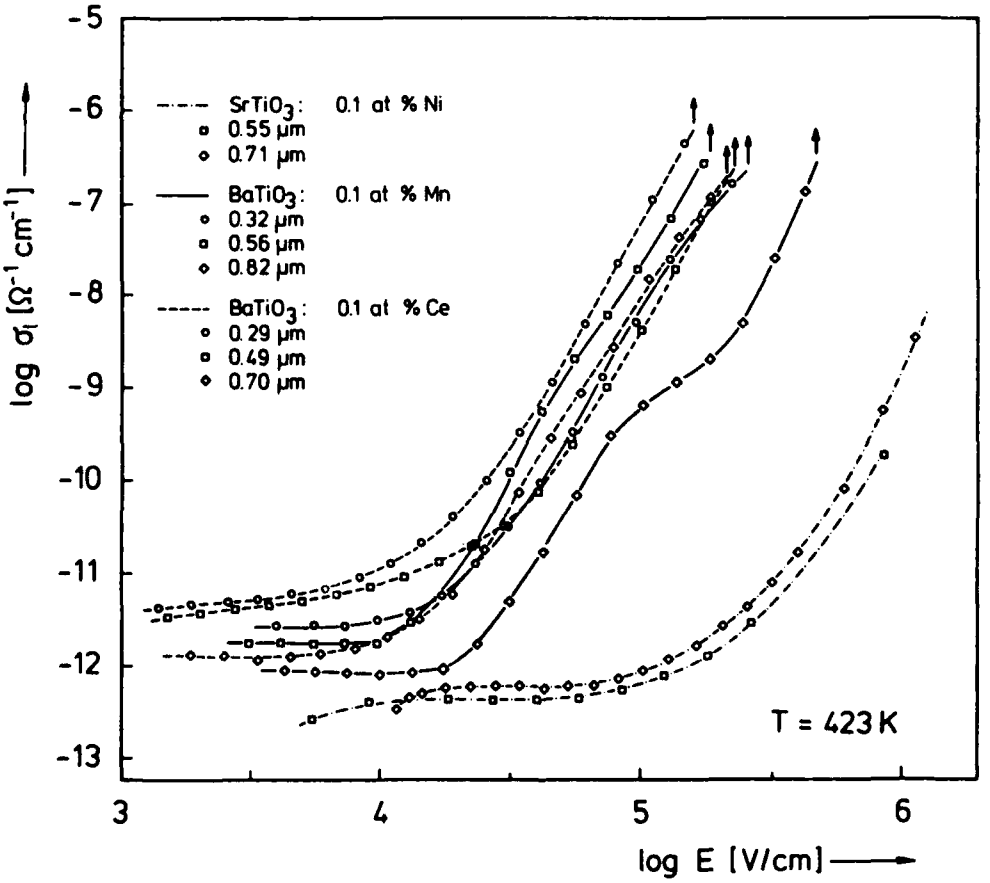


FIGURE 11 Field dependence of the long-term conductivity σ_l (recorded at t = 300 s after the dc voltage step) for 0.1 at% Ni doped $SrTiO_3$, 0.1 at% Mn doped $BaTiO_3$, and 0.1 at% Ce doped $BaTiO_3$ thin films at T = 423 K. The curves must be considered as preliminary results because no statistical evaluation was performed. The arrows indicate breakdown incidences.

$BaTiO_3$) on the onset field of the varistor regime while the type of dopant in $BaTiO_3$ (i. e. Mn and Ce) does not lead to a significant difference. The latter may be indicative for the fact that the high density of interface states suppresses the influence of small concentrations of additional donors or acceptors on the conduction process.

No final conclusion can be drawn concerning the thickness dependence of the $\sigma_I(E)$ function. Based on the present data, the film thickness seems to impose no clear influence on the conductivity at a given field in the varistor regime. Due to the scatter of the results, this statement has to be regarded as preliminary.

It can be estimated that the conductivity in the varistor regime must be predominantly of *electronic nature*. The estimation is based on the mass transfer in the case of an ionic current and the resulting time of material degradation [2]. In the ohmic regime the conduction type is not known yet.

There are various mechanisms which lead to an enhancement of the electronic conductivity at high fields. These include material effects such as the *field-dependent electron mobility* derived by Stratton [28] and the *Poole-Frenkel effect* describing the field-dependent thermoionic emission from traps in the material [29] as well as contact effects such as the *Schottky emission* of electronic carriers from a conducting phase into a dielectric [30] and the *space charge limited currents* at ohmic contacts [31]. A comprehensive comparison of these effects is given by O'Dwyer [32].

The influence of the field dependence of the electron mobility (i. e. the creation of "hot" electrons or holes) is considered as a less likely cause for the orders of magnitude increase of the conductivity in the varistor because in other polar crystals, this effect occurs at higher fields and is less pronounced [32]. The available data are insufficient to assess the impact of Poole-Frenkel phenomena.

We found that, firstly, the acceptor-doped $SrTiO_3$ thin films are strongly depleted by charge carriers compared to the bulk crystal lattice of the same composition and that, secondly, interfaces (GBs as well as electrode interfaces) give rise to such depletions. Based on these findings, we regard our titanate thin films as a kind of Schottky barriers. Compared to the Schottky barriers represented by depletion space charge layers at individual interfaces in compact samples, they presumably show a different fine structure and possibly should be named "distributed Schottky barriers". Consequently, the current through the film has to be considered as a Schottky emission across a metal / Schottky barrier / metal system. The onset of the varistor regime and the slope as well as the details of the log σ_I (log E) curve may then be determined by the energy distribution of the interface states, in a similar way as theoretically derived by Pike and Seager for GBs in semiconductors [33].

Space charge limited currents which have been proposed as the cause of the conductivity enhancement of thin perovskite films require ohmic i. e. enrichment contacts instead of depletion contacts. Because we always observed pronounced depletion contacts at titanate single crystals (see Sec. 5), we assume the metal / ceramic interface to behave similarly in the case of thin films. In addition, a model based on space charge limited currents will have to explain the strong depletion throughout the film compared to the bulk. Further studies of the conductivity dependence on the film thickness D will provide essential information since Mott and Gurney's law for space charge limited currents predicts $J \sim V^2/D^3$ (which corresponds to $\sigma \sim E/D$).

Due to the incomplete understanding of the electronic structure of the titanate thin films the statements given here should be considered as a working model which still awaits further confirmations, modifications, or disproofs.

9. BREAKDOWN PROCESS

In a simple classification, the instantaneous failure in a dielectric under very high fields may be either a purely electrical breakdown or a thermal breakdown. In the first case, an impact ionization in the material causes an avalanche of electronic carriers and/or a chemical deterioration [32, 35]. A thermal breakdown occurs when the generated Joule heating in the system determined by the product of the current and the applied voltage leads to an excessive temperature rise. Because of the positive temperature coefficient of the conductivity, this rise causes an instability and a subsequent thermal runaway.

Using the data at the upper end of the $\sigma_I(E)$ curves in Fig. 11, a calculation shows that Joule powers in the range between 3 and 100 mW are generated in the films of submicron thickness and of approx. 0.01 cm^2 area. A consideration of the heat dissipation based on the estimated thermal transfer coefficient of the films and the thermal conductivity of the substrate reveals a situation which is typical for a thermal runaway. This finding is supported by ramp voltage breakdown tests at room temperature. In contrast to Al_2O_3 thin films, the current evolution for our $BaTiO_3$ films always exhibits a field enhanced conductivity before the final breakdown sets in [36]. We conclude that titanate thin films fail by a *thermal breakdown* in contrast to a purely electrical breakdown due to the strongly enhanced high field conductivity.

10. SUMMARY

It is the aim of the present and of continuing studies to understand the behaviour of perovskite thin films under dc voltage stress. Currently, the major interest behind this aim is determined by the application of ferroelectric (e. g. PZT) films for non-volatile memory applications.

This work is based on three concepts:

1. the use of a simple non-ferroelectric model material (here: acceptor doped $SrTiO_3$),
2. the comparison between single crystals, ceramics, and thin films of the same model material in order to judge and to interpret similarities and differences,
3. the separation of polarization and conduction contributions of the current using the impedance analysis (here: over many orders of magnitude in time).

The measurements were conducted in the temperature range up to 600 K. From the results of our investigation, we draw the following conclusions.

- → In the bulk, acceptor doped $SrTiO_3$ is a mixed ionic-electronic conductor with a predominant ionic conduction due to mobile oxygen vacancies and an additional p-type conduction.
- → Highly resistive layers are formed at the grain boundaries (layer width: approx. 100 nm) and at the electrode interface (approx. 500 nm) in conventional ceramic and single crystal; they are interpreted as Schottky barrieres i. e. as depletion space charge layers generated by charged interface states.
- → The conductivity in the depletion layers is approx. 4 orders of magnitude below the bulk conductivity.
- → At low fields the leakage across the depletion layers shows an ohmic behaviour.

→ Above a voltage drop of approx. 0.5 V across a layer the conductivity becomes field enhanced as expected for the charge transport over a Schottky barrier.
→ Empirically, thin films show a similar behaviour as depletion layers with respect to the low conductivity and the enhancement of the conductivity by high fields.
→ Several mechanisms of the field enhanced conductivity in the films may be considered with some indications favoring the Schottky emission model. The breakdown mode at high fields is a thermal runaway.

ACKNOWLEDGEMENT

We appreciate valuable discussions with Prof. Dr. R. Zuleeg and Dr. P. K. Larsen about space charge limited currents. We thank W. Brand, A. Wagner, S. Hünten, B. Krafczyk and H. D. Bausen for their support in the preparation and characterization of the samples.

REFERENCES

[1] C. A. Paz de Araujo, L. D. McMillan, B. M. Melnick, J. D. Cuchiaro, and J. F. Scott, Ferroelectrics **104**, 241 (1990).
[2] R. Waser, T. Baiatu, and K. H. Härdtl, J. Am. Ceram. Soc. **73**, 1645, 1654, and 1663 (1990).
[3] N.-H. Chan and D. M. Smyth, J. Electrochem. Soc. **123**, 1584 (1976).
[4] J. Daniels, K. H. Härdtl, D. Hennings, and R. Wernicke, Philips Res. Rep. **31**, 489 (1976).
[5] N.-H. Chan, R. K. Sharma, and D. M. Smyth, J. Am. Ceram. Soc. **64**, 556 (1981).
[6] N.-H. Chan, R. K. Sharma, and D. M. Smyth, J. Electrochem. Soc. **128**, 1762 (1981).
[7] H.-J. Hagemann and D. Hennings, J. Am. Ceram. Soc. **64**, 590 (1981).
[8] D. M. Smyth, in: Microstructure and Properties of Ceramic Materials, Proceedings of the First China - U. S. Seminar, Edited by T. S. Yen and J. A. Pask, p. 399, North-Holland Publishing Co., Amsterdam, 1984.
[9] R. Waser, J. Am. Ceram. Soc. (accepted for publication).
[10] G. M. Choi, H. L. Tuller, and D. Goldschmidt, Phys. Rev. **B 34**, 6972 (1986).
[11] H. Ihrig, J. Phys. C **9**, 3469 (1976).
[12] K. Okazaki, Adv. Ceram. **1**, 23 (1979).
[13] A. K. Jonscher, "Dielectric Relaxation in Solids", Chelsea Dielectrics Press Ltd., London 1983.
[14] T. G. Stratton, D. Reed, and H. L. Tuller, Adv. Ceram. **1**, 114 (1983).
[15] H.-Y. Lee, S. S. Villamil, and L. C. Burton, IEEE Proc. of the 6th ISAF, Bethlehem, PA, June 8-11, 1986.
[16] H. Neumann and G. Arlt, Ferroelectrics **69**, 179 (1986).
[17] S. M. Sze, "Physics of Semiconductor Devices", John Wiley & Sons, New York 1981.
[18] R. Waser, G. Rosenstein, and S. Oostra, submitted to Ber. Bunsenges. Phys. Chem.
[19] Y.-M. Chiang and T. Tagaki, J. Am. Ceram. Soc. **73**, 3278 (1990).
[20] G. E. Pike and C. H. Seager, Adv. Ceram. **1**, 53 (1983).
[21] R. Waser, to be submitted to the J. Am. Ceram. Soc.
[22] H. Oepen, private communication.
[23] R. Waser, to be published.
[24] M. Kahn, Am. Ceram. Soc. Bull. **50**, 676 (1971).
[25] M. Klee, R. Eusemann, and R. Waser, to be published.
[26] D. R. Wolters and J. J. an der Schoot, J. Appl. Phys. **58**, 831 (1985).
[27] P. G. Shewmon, "Diffusion in Solids", McGraw-Hill, New York 1963.
[28] R. Stratton, Proc. R. Soc. A **246**, 406 (1958).
[29] J. Frenkel, Phys. Rev. **54**, 647 (1938).
[30] P. T. Landsberg, Proc. R. Soc. A **206**, 463 (1951).

[31] M. A. Lampert and P. Mark, "Current Injection in Solids", Academic Press, New York 1970.
[32] J. J. O'Dwyer, "The Theory of Electrical Conduction and Breakdown in Solid Dielectrics", Clarendon Press, Oxford 1973.
[33] G. E. Pike and C. H. Seager, J. Appl. Phys. **50**, 3414 (1979).
[34] J. F. Scott, ISIF'91 (see current proceedings).
[35] D. R. Wolters and A. T. A. Zegers-van Duijnhoven, J. Vac. Sci. Technol. A5, 1563 (1987).
[36] G. Greuel, unpublished results.
[37] M. Klee and R. Waser, to be published.

AD-P006 662

ON POLARIZATION REVERSALS IN FERROELECTRICS

YOSHIHIRO ISHIBASHI
Synthetic Crystal Research Laboratory,
School of Engineering, Nagoya University,
Chikusa-ku, Nagoya 464-01, Japan

ABSTRACT

Theoretical aspects of polarization reversals in ferroelectrics will be reviewed, with the emphases placed on the application of the Kolmogorov-Avrami theory and of a lattice model which the author has proposed.

INTRODUCTION

Fabrication techniques of ferroelectric thin films have shown a great deal of progress for last several years, and a considerable amount of data on polarization reversals (switchings) in ferroelectric thin films, to be utilized as memories, have been accumulated.[1,2] Under this circumstance, it is extremely important to promote understanding of the processes of polarization reversals. It is well known that the switching in ferroelectrics is a typical example of the nucleation-and-growth process, where nuclei form here and there, and switched regions grow from such nuclei. The switching takes place inhomogeneously through a specimen. One can apply the Kolmogorov-Avrami theory to such systems[3-5]. In the next section an example of the application of the Kolmogorov-Avrami theory will be shown.

In the characterizations of produced films, quite often hysteresis loops at high frequencies, not at the commercial frequency, are observed instead of the switching transient itself. However, the Kolmogorov-Avrami theory can not be applied directly for reproducing hysteresis loops. We need therefore some models for hysteresis loops. In third section, a simple lattice model is

92-16126

proposed in which the existence of nuclei is taken into account, i.e., positive and negative nuclei are distributed by using random numbers, and thus inhomogeneous nature of the switching process is well incorporated[6]. As will be clarified in what follows, in this model a set of simultaneous nonlinear rate equations has to be integrated numerically.

Concluding remarks will be presented in the final section.

THE KOLMOGOROV-AVRAMI THEORY AND ITS APPLICATION TO SWITCHING IN A FERROELECTRIC LIQUID CRYSTAL

Let us take a specimen of an infinite size, and assume that nuclei of zero size form at time at the rate R( ) per unit area per unit time and the switched area expands with a constant velocity v. Then, it is known that the fraction of the switched area is expressed as

$$q(t) = 1 - e^{-A(t)}, \qquad (1)$$

where A(t), the extended area, is calculated as follows.

In films we may have to consider two-dimensional and one-dimensional domains (Fig. 1)[5]. The latter domains should be seen in very anisotropic films. In what follows we show the quantities for such one-dimensional domains in parentheses.

There are two conceivable "mechanisms" for the switching process[5,7]. One is the (homogeneous) case where $R(\tau)$ is constant per unit area (length) per unit time, i.e., $R(\tau) = J$, and the other is the (inhomogeneous) case where nuclei exist from the beginning (we call them latent nuclei) and the domains expand from them. In the latter case let us use the nucleus density, i. e., N nuclei per unit area (length). For the constant nucleation case

$$A(t) = \pi J v^2 t^3/3, \quad (A(t) = Jvt^2), \qquad (2)$$

and for the latent nucleus case

$$A(t) = \pi N v^2 t^2, \quad (A(t) = 2Nvt). \qquad (3)$$

It should be noted that, in the above formulas, the index n to t is given as

$$n = d + 1 \tag{4}$$

for the constant nucleation case and as

$$n = d \tag{5}$$

for the latent nucleus case, where d is the dimension characterizing the shape of domains (see Fig. 1). In all q(t) can be expressed in a form as

$$q(t) = 1 - e^{-(t/t_0)^n}, \tag{6}$$

where t_0 is a time scale determined by J, N and v. In actual cases of switching two mechanisms may be mixed up, and then a non-integral n may appear as the result of analyses of experimental data.

In Fig. 2 the temporal variation of switched area in a surface stabilized ferroelectric liquid crystal is shown[8]. It is readily found that experimental data are well fitted by the curve

$$q(t) = 1 - e^{-(t/t_0)^2}, \tag{7}$$

implying that the process is either the constant nucleation case of one-dimensional domains or the latent nucleus case of two-dimensional domains. It can be discerned only by direct microscopic observations, as shown in Fig. 3, where it is seen that two-dimensional domains expand from latent nuclei.

It is needless to say that the switching current i(t) is proportional to dq(t)/dt.

A LATTICE MODEL OF POLARIZATION REVERSALS[6]

The KA-model, applied to polarization reversals, is only a very

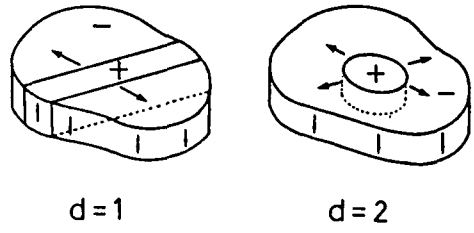


Fig.1. The dimensionality of the reversed domains.

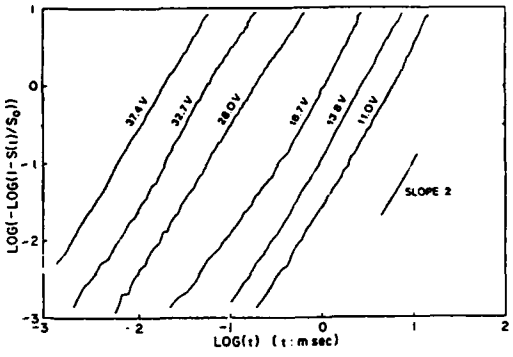


Fig.2. Temporal evolution of switched area in a surface stabilized liquid crystal DOBAMBC for various applied voltages. $S(t)/S_0$ in the ordinate corresponds to q(t).

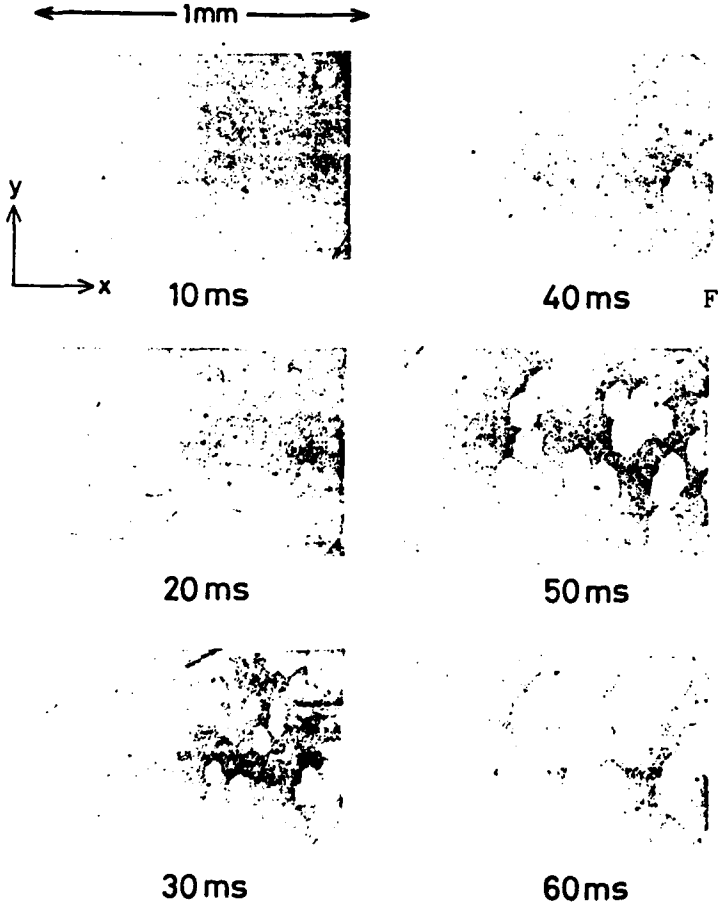


Fig. 3. The micrographs showing the switching process in a surface stabilized ferroelectric liquid crystal DOBAMBC.

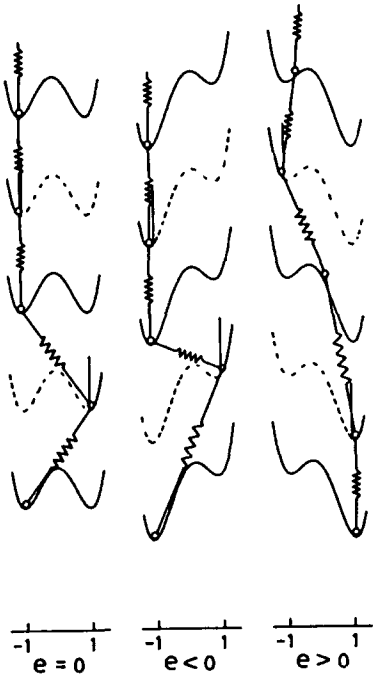


Fig. 4. A lattice model, where each "atom" lying in the double minimum potential interacts with neighbors. There are steep potential barriers at p = 1 and p = -1 for positive and negative nuclei, respectively, beyond which "atoms" can not move.

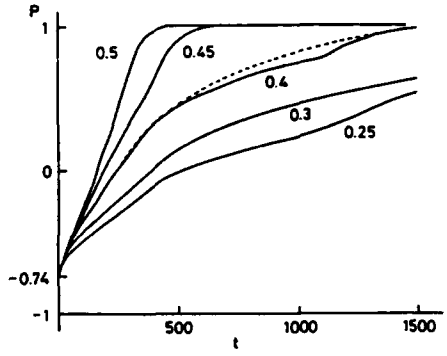


Fig. 6. Time dependences of polarization for various applied fields. t is measured with the unit of $\Delta t = 0.02$.

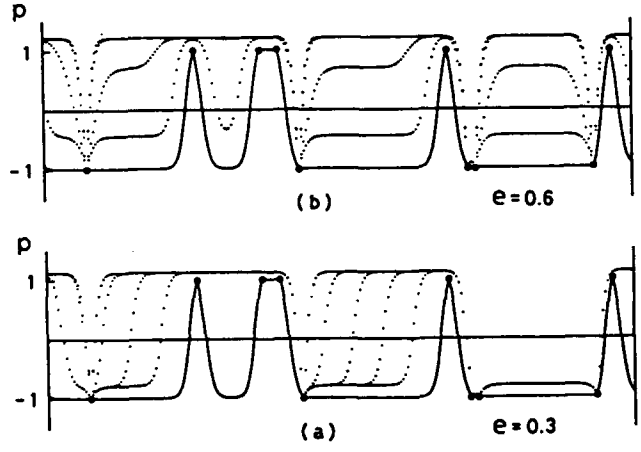


Fig. 5. Temporal evolutions of the spatial dipole distribution in polarization reversal processes. Solid lines show the negatively polarized initial state. Adopted parameter values: $\kappa = 5$, $\gamma = 1$, $\Delta t = 0.02$. (a) $e = 0.3 < e_c = 0.385$. p_n's are plotted at $t/\Delta t = 400, 800, \ldots$. (b) $\epsilon = 0.6 > e_c$. p_n's are plotted at $t/\Delta t = 100, 200, \ldots$.

simplified model of the processes. For example, in the KA-model usually only two states i.e., the initial state and the stable final state, are considered, though the extension of the model to the multi-state cases is not difficult. The boundaries between various states are considered to be of zero-thickness in the KA-model, which of course are not so in ordinary cases. The velocity of the wall (boundary) motion, v, is usually regarded as constant in the KA-model, irrespective of environment of walls. Obviously, this is not a good approximation either, because in two and three dimensional systems, the velocity of domain boundaries should be dependent on the local curvature. Even in one-dimensional systems, the wall will be accelerated or decelerated due to interactions between nearby walls, and with nuclei.

Under this circumstance, the present author has proposed a lattice model, where each atom, interacting with nearest neighbors, moves in the p^4-type double minimum potential (Fig. 4). The total energy is expressed as

$$f = \sum \left[\frac{\alpha}{2} p_n^2 + \frac{\beta}{4} p_n^4 + \frac{\kappa}{2}(p_n - p_{n-1})^2 - p_n e \right] \qquad (8)$$

where p_n denotes the displacement of the n-th atom or the dipole moment at the n-th site, e applied field, α and β are model parameters (α and β can be set to $\alpha = -1$ and $\beta = 1$ without loss of generality), and κ is a parameter denoting the magnitude of interaction between neighbors. The case $\kappa = 0$ corresponds to the homogeneous polarization switching. The motion of the n-th atom is governed by

$$\gamma \frac{\partial p_n}{\partial t} = - \frac{\partial f}{\partial p_n}, \qquad (9)$$

where γ is a viscosity coefficient, except for nucleus sites where we assume, in addition to eq. (9), that $p_i \geq 1$ and $p_i \leq -1$ if the i-th atom plays the role of a positive and a negative nucleus, respectively (i is chosen by random numbers). The eq. (9) is rewritten, by taking a discrete time step Δt, as

$$p_n(t+\Delta t) = p_n(t) - \frac{\Delta t}{\gamma}\left\{-p_n(t) + p_n(t)^3 - \kappa\left[p_{n+1}(t) - 2p_n(t) + p_{n-1}(t)\right] - e(t)\right\}. \quad (10)$$

The total polarization is, of course, given by

$$P(t) = \frac{1}{N}\sum p_n(t) , \quad (11)$$

where N is the total number of atoms.

Examples of the switching by rectangular fields are shown in Fig. 5. In the case of Fig. 5(a) the applied field e is smaller than e_c, the coercive field in the homogeneous system (e_c 0.385). Even in this case the switching proceeds, because positive nuclei "pull" atoms lying in unfavorable potential wells at the negative side to positive side. But in the region bounded by negative nuclei no atom is "pulled", and as a result it can not move beyond the potential maximum at p = 0, and so the amount of switchable polarization must be somewhat reduced. In the case of Fig. 5(b) the applied field is stronger, and switching proceeds faster.

The time dependences of polarization are shown for various applied fields in Fig. 6. The relationship of the shown time evolution of the total polarization and the one expected from the KA-model has been discussed in elsewhere.

By putting in eqs. (8) and (9)

$$e = e_0 \sin 2\pi ft, \quad (12)$$

where f is the frequency, we can simulate dielectric hysteresis loops. Details of simulations are described in ref. 9, and the properties related with hysteresis loops are also discussed there.

CONCLUDING REMARKS

In this paper, the application of the KA-model to polarization reversals in ferroelectrics has been described, and

the proposed lattice model for polarization reversals has been discussed.

As for the KA-model, it is for sure that it is a powerful tool for analyzing transient behaviors in polarization reversals. On the other hand, there remain some problems to be further studied. For example, it is necessary to derive the KA-formulas applicable to finite systems. This may be quite important, because in future memory pixcels will be getting smaller and smaller, and then the theories which take the sample size into account must be needed.

As for the lattice model, it is desirable to extend the model to two-dimensional systems. There one will be able to utilize the energy function as

$$f = \sum \Big\{ \frac{\alpha}{2} p_{m,n}^{\,2} + \frac{\beta}{4} p_{m,n}^{\,4} + \frac{K_1}{2}(p_{m,n} - p_{m-1,n})^2 + \frac{K_2}{2}(p_{m,n} - p_{m,n-1})^2 + \frac{K_3}{2}\left[(p_{m,n} - p_{m-1,n+1})^2 + (p_{m,n} - p_{m-1,n-1})^2 \right] - p_{m,n}\, e \Big\}, \tag{13}$$

and the equation of motion as

$$\gamma \frac{\partial p_{m,n}}{\partial t} = -\frac{\partial f}{\partial p_{m,n}} \quad . \tag{14}$$

Efforts towards this direction have already been done and the results will be reported shortly elsewhere.

REFERENCES

1. J. F. Scott and C. A. Araujo: Science 246, 1400 (1989).
2. K. Dimmler, M. Parris, D. Butler, S. Eaton, B. Pouligny, J. F. Scott and Y. Ishibashi: J. Appl. Phys. 61, 5467 (1987).

3. A. N. Kolmogorov: Izv. Akad. Nauk, USSR., Ser. Math. 3, 355 (1937).
4. M. Avrami: J. Chem. Phys. 7; 1103 (1939) 8: 212 (1939), 9; 177 (1941).
5. Y. Ishibashi and Y. Takagi: J. Phys. Soc. Jpn. 31, 506 (1971).
6. Y. Ishibashi: J. Phys. Soc. Jpn. 59, 4148 (1990).
7. Y. Ishibashi; Jpn. J. Appl. Phys. 24, suppl. 24-2, 126 (1985).
8. H. Orihara, Y. Ishibashi and Y. Yamada: J. Phys. Soc. Jpn. 57, 4101 (1988).
9. M. Ohmura and Y. Ishibashi: In this issue.

AD-P006 663

FAST REVERSAL PROCESS IN REAL FERROELECTRICS

V. YA. SHUR, A.L. GRUVERMAN, N. YU. PONOMAREV,
E.L. RUMYANTSEV, N.A. TONKACHYOVA
Ural State University, Sverdlovsk, 620083, USSR

Abstract On the base of comparison of domain dynamics and transient current the applicability of Kolmogorov's model for the description of current shape in real ferroelectrics is considered. The influence of electrode edges and inhomogeneity of real samples are taken into account. The computer modeling of switching process is carried out. The obtained results can be applied for the improvement of the description the change of parameters in Ferroelectric memory devices.

INTRODUCTION

It is known that switching of polarization in ferroelectrics is a result of arising and growing of domains with preferable polarization direction [1]. Usually this complicated process of domain structure evolution is investigated through the measuring of some indirect integral parameters [2]. The most informative method is a registration of transient current [3] from which one can calculate some parameters of domain dynamics [4]. However, the theoretical analysis of transient current shape is based on Kolmogorov's model, which was developed from infinite homogeneous medium [5]. The present paper is devoted to the clarification of applicability of this model for real ferroelectric samples. To solve this problem we have carried out the direct observation of domain dynamics and also the measurement of transient current in model crystal.

EXPERIMENT

It is known that fast polarization reversal with switching time less than 100 nsec is the base for creation of modern ferroelectric memory. Unfortunately, it is impossible to observe directly the fast domain dynamics in thin films, which is why we have studied as a model the

92-16127

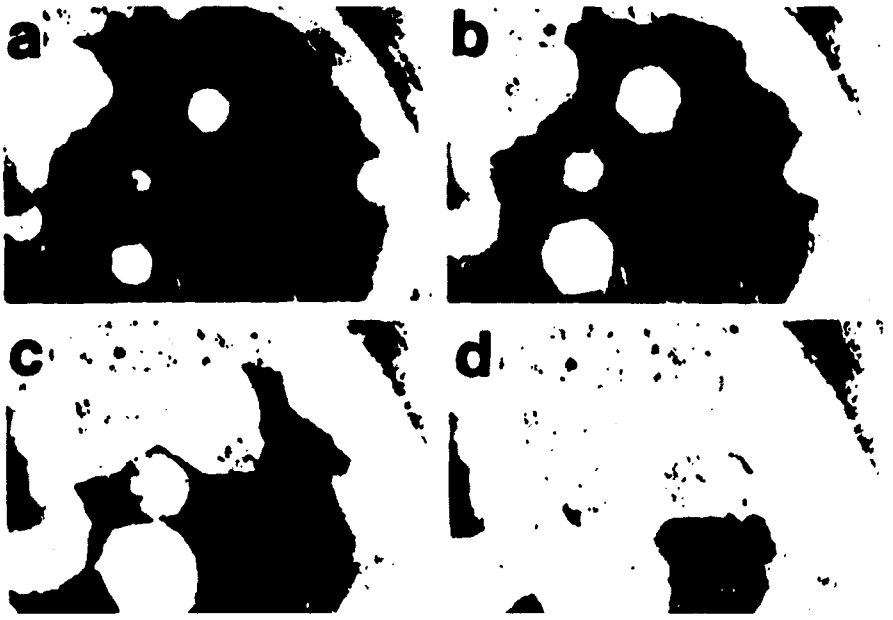


FIGURE 1 Evolution of domain structure during polarization reversal in weak field ($E = 1.8*10^5$ V/m); Delay time from the front of switching voltage pulse: a – 2.5 ms; b – 4 ms; C – 6 ms; d – 9 ms.

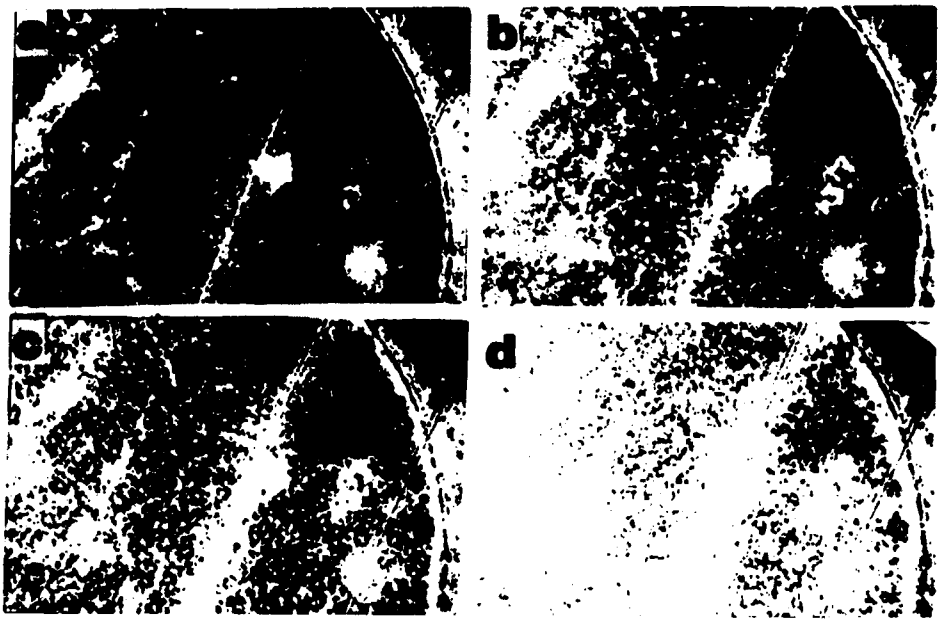


FIGURE 2 Evolution of domain structure during polarization reversal in strong field ($E = 1.1*10^6$ V/m); Delay time from the front of switching voltage pulse: a – 0.5 ms; b – 0.7 ms; c – 0.9 (ms); d – 1.1 ms.

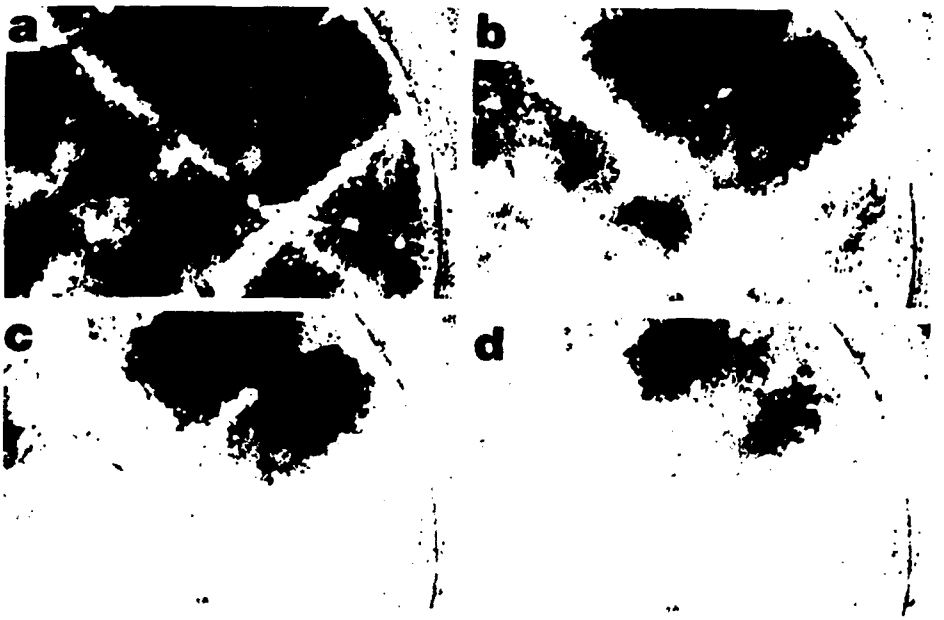


FIGURE 3 Evolution of domain structure during polarization reversal in superstrong field ($E = 1.9*10^6$ V/m); Delay time from the front of switching voltage pulse: a – 10 mcs; b – 15 mcs; c – 30 mcs; d – 49 mcs.

In this field region as in weak fields prevails the sidewise motion of the walls, but detail investigations show that mechanism of this motion qualitatively differs from the one observed in weak fields (Fig. 4).



FIGURE 4 Chain–like domain structure arising as a result of correlated nucleation near the moving domain wall in superstrong field.

Near the wall appears a lot of new small domains which organize a specific chain–like structure. As a result of correlated nucleation these arising domains are growing and coalescencing with parent domain. Then a new chain appears and this process repeats once again.

It is necessary to draw attention to some more peculiarities of domain structure evolution during switching. Firstly, the behavior of domain structure essentially depends on the quantity and space distribution of nucleation sites and residual nonthrow domains because they determine the number of newly arising domains. Secondly, the switching always starts at the electrode edges. This boundary effect is very important in real samples of small surface area when switching is achieved through the sidewise wall motion (in weak or superstrong field). Thirdly, the interaction of walls of growing domains when they are reproaching each other is observed. In weak fields (Fig. 5) this interaction reveals itself through the slowing of wall motion before the coalescence.

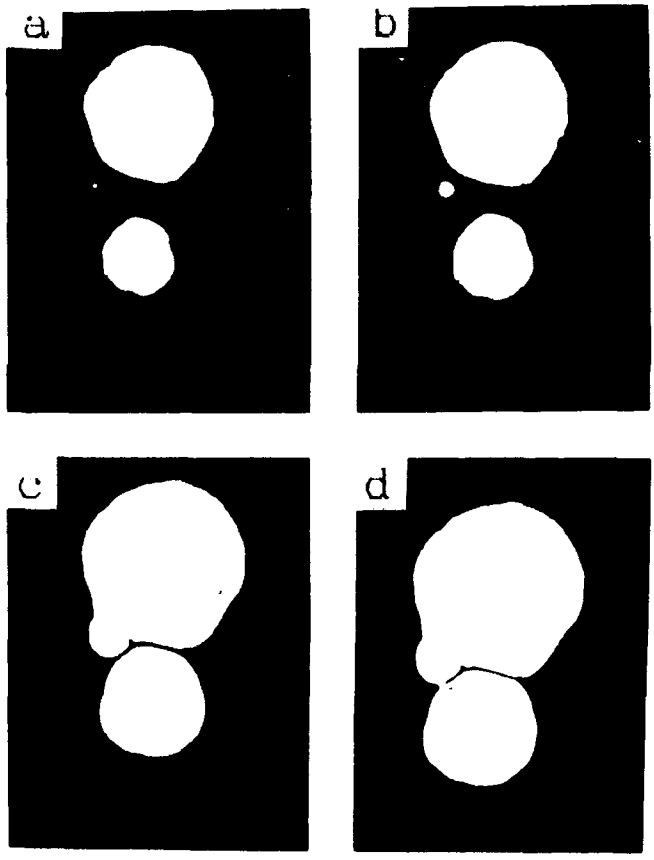


FIGURE 5 Interaction of domain walls during polarization reversal in weak field ($E = 1.8*10^5$ V/m); Delay time from the front of switching voltage pulse: a – 1.5 ms; b – 2.5 ms; c – 5.5 ms; d – 7.5 ms.

In strong fields (Fig. 6) it leads to the formation of raster–type structure of newly arising domains.

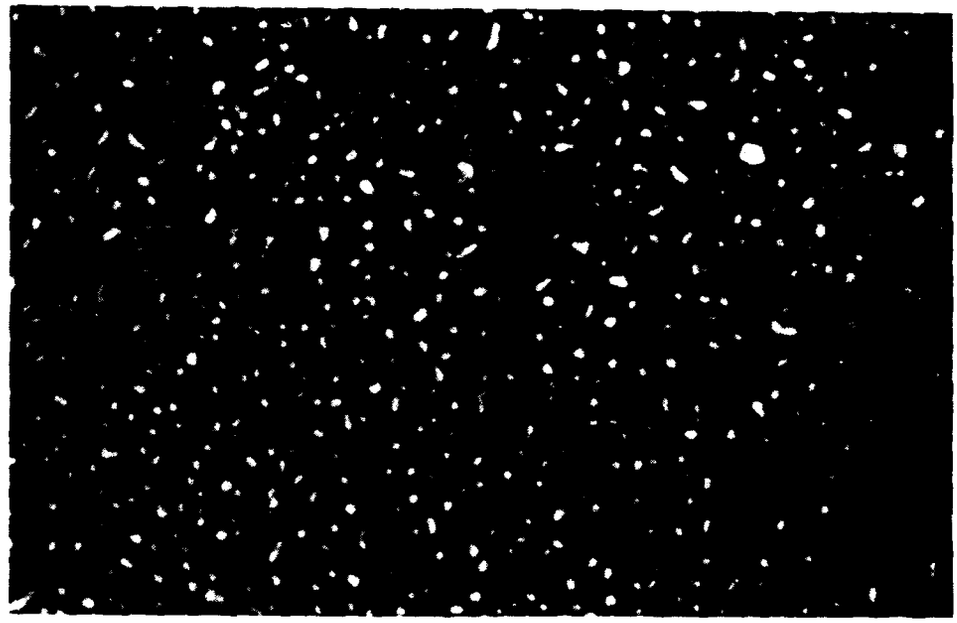


FIGURE 6 Raster–type domain structure arising in strong field.

THE QUALITATIVE EXPLANATION

In order to explain the observed peculiarities we use the fact that in broad sense, the formation and evolution of domain structure is nothing but the kinetics of new phase growth during phase transition. It is clear that nucleation probability at the given place and consequently the rate of domain growth depends on the local value of internal field. For ferroelectric capacitor this value is determined not only by the electric potential difference between electrodes but also by the sum of depolarization field of bound charges and screening fields produced by electrode charges (external screening) and bulk charges (internal screening). Due to the existence near the crystal surface of so–called dielectric gap [9] the effect of internal screening is very important and the magnitude of bound internal field produced by localized bulk charges can be up to 10^6 V/m. It was shown by us earlier that domain dynamics during switching strongly depends on the screening effects [10].

The existence of dielectric gap leads to the incomplete screening of the depolarization field in the vicinity of domain wall. The calculated space distribution of summarized internal field for staying domain wall is plotted on (Fig. 7. curve 1).

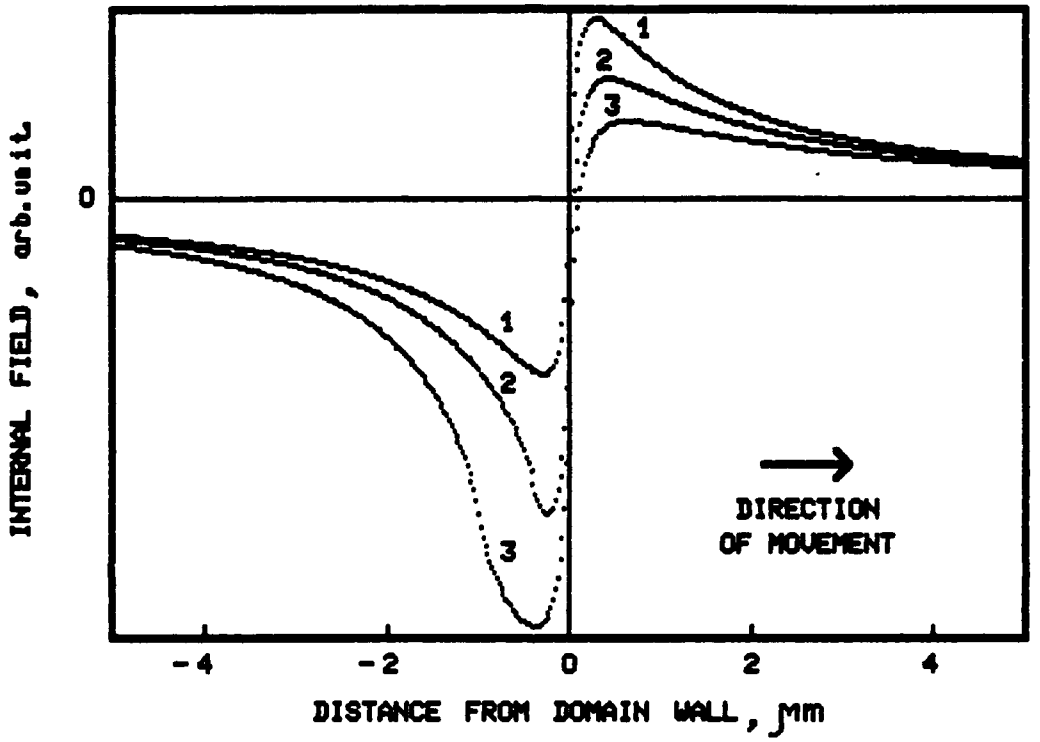


FIGURE 7 The calculated space distribution of internal electric field in the vicinity of moving domain wall: Velocity of the wall: 1 – 0; 2 – 3 m/s; 3 – 10 m/s.

It is seen that nearby domain wall electric field strength reaches its maximum value. In the case of moving wall behind it appears the so–called train of depolarization field which decreases the field on the wall and slows its motion. The length of this train is determined by the domain wall velocity and the time constant of external screening. The space distribution of summarized internal field becomes asymmetrical but even in this case (Fig. 7, curves 2, 3) in front of the wall remains the maximum of internal field. Such behavior makes it possible to explain the arising of chain–like domain structure in superstrong field.

The estimations of internal field with taking into account depolarization effects shows that it is decreasing on the walls of narrow domains. This fact permits to explain the domain interaction just before the coalescence.

The suppression of the arising of new domains in super–strong field can be explained if we take into account the delay time – the interval between the moment of voltage applying and the moment when the nuclei start to form. It is known mention that this delay time increases with increasing of nuclei dimension. The rate between delay time and time of external field action (switching time in our case) is very important. If switching time becomes less than delay time for three–dimensional nuclei the polarization reversal will be achieved through the sidewise motion of existing domain walls and arising the chains of new domains near it. It is clear that in this case the already existing domain walls in the vicinity of electrode boundary and existing residual domains will play the main role.

COMPUTER MODELING

To clarify the influence of observed phenomena on the transient current the computer modeling of domain structure evolution was carried out using matrix comprising 80*80 elements. The space distribution of newly arising domains (switching elements) was defined by Monte–Carlo method. The next stage of its evolution involved the switching of nearest elements (sidewise motion of domain walls). The edge effect was taken into account by the existence from the very beginning of already switched elements along the matrix boundary (existence of domain walls near electrode edges). This modeling permits nevertheless to explain some peculiarities observed in experiment. It was shown that the edge effect produces the initial jump in transient current in accordance with experimental results (Fig. 8 & 9). The appearance of the observed bends on transient current curve (Fig. 9) while passing from strong to superstrong fields can be explained within this model by the diminishing of the number of newly arising domains.

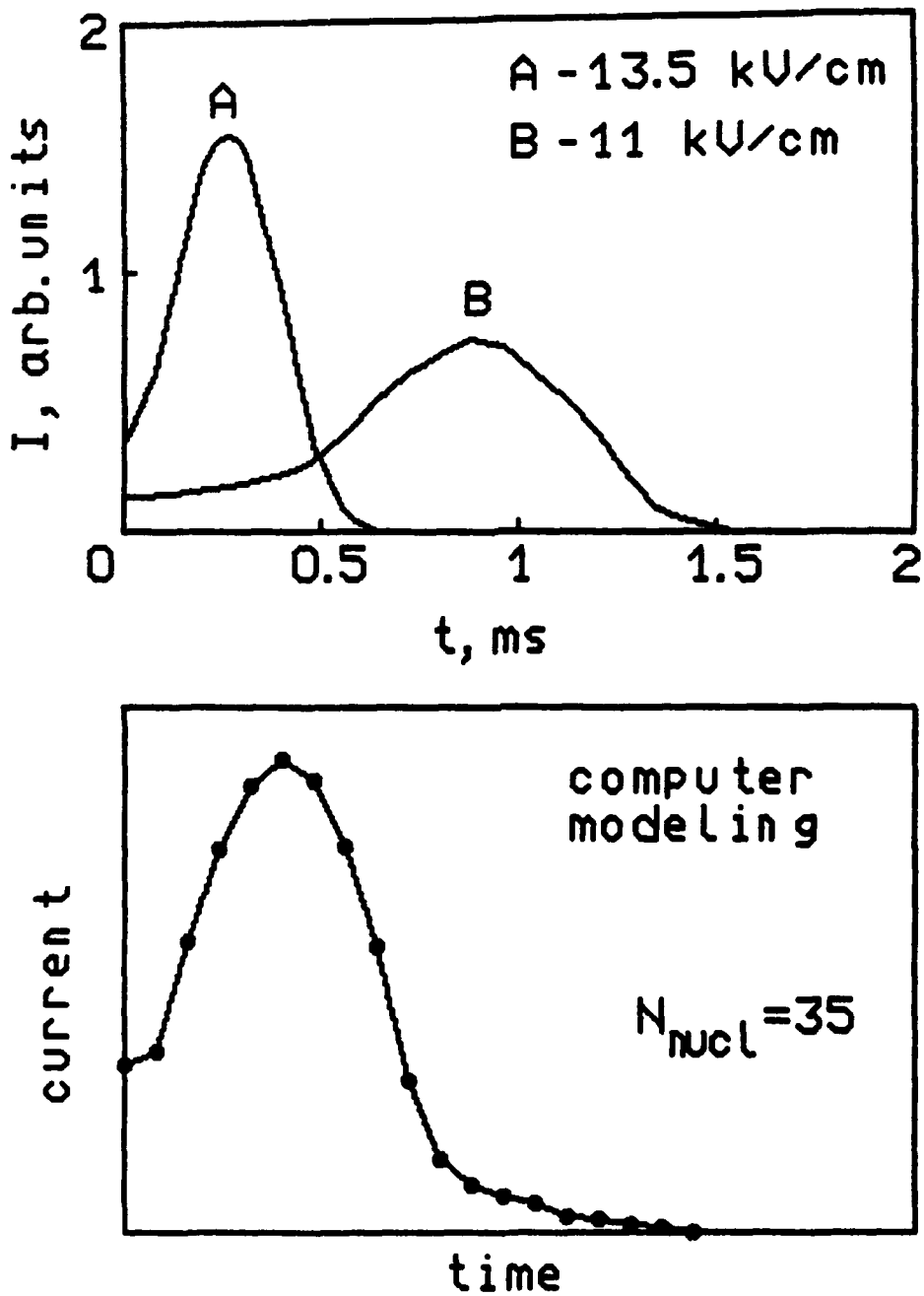


FIGURE 8 The transient currents in strong field and results of computer modeling for high density of nuclei.

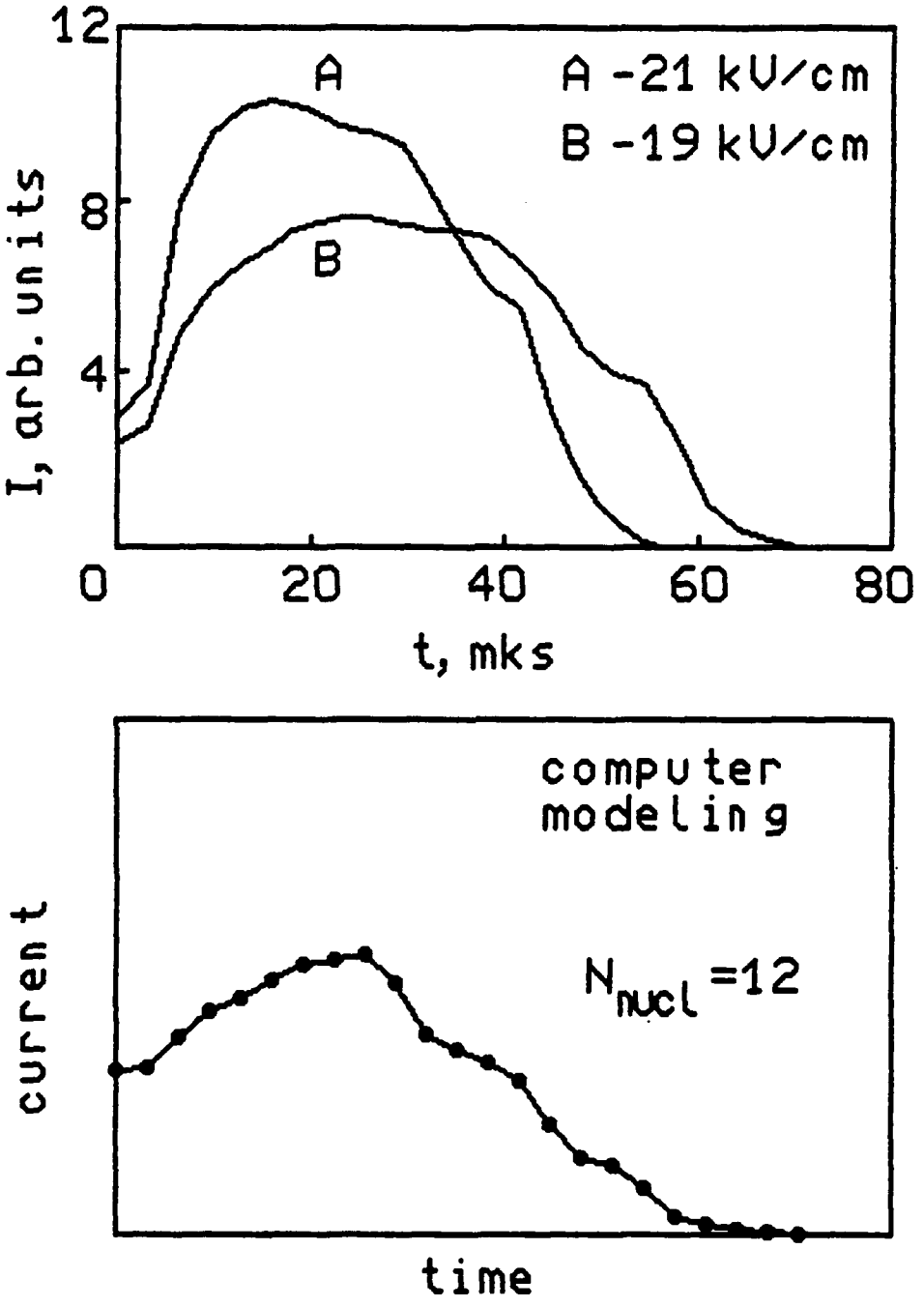


FIGURE 9 The transient currents in superstrong field and results of computer modeling for low density of nuclei.

CONCLUSIONS

We must conclude that direct observation of domain dynamics during the switching in real ferroelectrics reveals the influence of boundary effects and inhomogeneities of internal field distribution on the shape of switching current. These peculiarities can not be accounted for within the Kolmogorov's model. This can lead consequently to the misinterpretation of observed experimental results. The obtained results can be applied for the improvement of the description the change of parameters in ferroelectric memory devices due to fatigue and affect of external influences.

ACKNOWLEDGEMENTS

Authors are grateful to Prof. J.F. Scott for valuable discussions. Authors also would like to thank A. Yu. Bunkin for the crystals used in research and V.M. Kondakov for fine mechanical working of the samples.

REFERENCES

1. M.E. Lines and A.M. Glass, Principles and Application of Ferroelectrics and Related Materials, (Clarendon Press, Oxford, 1977).
2. E. Fatuzzo and W.J. Merz, Ferroelectricity, (North–Holland Publishing Co., Amsterdam, 1967).
3. C.Araujo, J.F. Scott, R.B. Godfrey, and L. McMillan, Appl. Phys. Lett., Vol. 48, No. 21, 1439–1440, (1986).
4. K. Dimmler, M. Parris, D. Butler, S. Eaton, B. Pouligny, J.F. Scott, and Y. Ishibashi, J. Appl. Phys., Vol. 61, No. 12, 5467–5470 (1987).
5. Y. Ishibashi and Y. Takagi, J. Phys. Soc. Jap., Vol. 31, No. 2, 506–510, 1971).
6. V.Ya. Shur, A.L. Gruverman, V.V. Letuchev, E.L. Rumyantsev, and A.L. Subbotin, Ferroelectrics, Vol. 98, 29–49, (1989).
7. L.D. Landau and E.M. Lifshitz, Statistical Physics, (Pergamon Press, Oxford, 1981).
8. V. Ya. Shur, A.L. Gruverman, and E.L. Rumyantsev, Ferroelectrics, Vol. 111, (1990).
9. V.M. Fridkin, Photoferroelectrics, (Springer–Verlag, Berlin, Heidelberg, N.Y. 1979).
10. V. Ya. Shur, A.L. Gruverman, V.P. Kuminov, and N.A. Tonkachyova, Ferroelectrics, Vol. 111, (1990).

AD-P006 664

NUMERICAL ANALYSES OF FERROELECTRIC CHARACTERISTICS FOR MEMORY USE BY USING A LATTICE MODEL

MASAYOSHI OMURA , HIDEO ADACHI AND YOSHIHIRO ISHIBASHI†
Research Dept., Corporate Research Div.
Olympus Optical Co.,Ltd, Hachioji-shi, Tokyo 192, Japan
†Synthetic Crystal Research Laboratory , Faculty of Engineering
Nagoya University, Chikusa-ku, Nagoya 464-01, Japan

92-16128

Abstract The numerical analyses of fundamental ferroelectric characteristics for memory use have been carried out by using a one-dimensional model of polarization reversal in ferroelectrics, in which latent nuclei are distributed randomly. Studied characteristics include pulse response, hysteresis (P-e curves), and switching current versus voltage (i-v curves) in ferroelectrics. Obtained results have been discussed.

INTRODUCTION

The polarization reversal phenomena in ferroelectric materials are very important from the view point of its application to ferroelectric memories.

The reversal process has often been analyzed on the basis of the Kolmogorov-Avrami (KA) model. [1-3] The KA -model applied to the polarization reversal is however a very simplified model.

Ishibashi has recently proposed a lattice model on polarization reversal, by which we can analyze the structure of the domain and its expansion during switching. [4]

In this paper we describe the numerical analyses of ferroelectric characteristics for memory use by using the lattice model. First the method of it will be mathematically specified. Next the obtained results will be reported and discussed.

THEORY

Let us describe the method of numerical analyses in a one-dimensional lattice system representing ferroelectrics. The total free energy of this system is written by

$$f = \sum_{n=1}^{N} \{ \frac{\alpha}{2} p_n^2 + \frac{\beta}{4} p_n^4 + \frac{\kappa}{2} (p_n - p_{n-1})^2 - p_n e \} \quad (1)$$

where p_n is the dipole moment at the nth lattice site, κ the interaction coefficient between neighboring atoms and e the applied field.

α is the function of temperature given as

$$\alpha = a (T - T_0) \ , \quad a > 0 \ , \quad (2)$$

where T_0 is the Curie temperature, and we assume that

$$\alpha < 0 , \quad \beta > 0 , \quad (3)$$

In this model, latent nuclei are assumed to exist and distributed randomly. We assume that the dipole moments at the positive nucleus sites can take only the values $p_n \geq 1$ and at the negative sites $p_n \leq -1$. The system is divided into many regions bounded by these nuclei. In the initial state we first establish the equilibrium state

where the system is negatively polarized. This state corresponds to the memory state "1".

To study the process of polarization reversal, we have to take into account the viscosity which causes the delay in motion of individual dipole moment. The time dependence of dipoles can be expressed as

$$\gamma \frac{d p_n}{d t} = - \frac{\partial f}{\partial p_n} ,$$

$$= - \{ \alpha p_n + \beta p_n^3 - \kappa (p_{n+1} - 2 p_n + p_{n-1}) - e \} , \quad (4)$$

where γ is the viscosity coefficient.

The total polarization P is obtained as

$$P = \sum_{n=1}^{N} p_n , \quad (5)$$

and current response is obtained as

$$i = \frac{d P}{d t} . \quad (6)$$

For studying the pulse response we put e as

$$e = \begin{cases} e_o & \text{for } 0 \le t < t_o , \\ 0 & \text{for } t_o \le t , \end{cases} \quad (7)$$

where t_o is the pulse width, and for studying the hysteresis characteristic, we put e as

$$e = e_o \sin (2 \pi f t) , \quad (8)$$

where f is frequency, e_o amplitude and t time.

RESULTS AND DISCUSSION

In the present numerical analyses we took a chain composed of 250 atoms (N = 250). 5 atoms are replaced by positive nuclei, 5 more atoms are also chosen and replaced by negative nuclei. A set of simultaneous equation (4) was integrated by the Runge-Kutta method.

Figure 1 shows the results for pulse response, where the parameters are chosen as $\kappa = 5$, $\gamma = 1.0\times10^{-8}$, $e_o = 1$.

Figures 1(a), 1(b) and 1(c) show the applied pulse field, polarization response and current response, respectively. The amplitude of two positive pulses for reading out memory state is about twice as large as the coercive field. The pulse width is set to 50 ns. The memory state changes from the state "1" into the state "0" when the first pulse is applied. When the second positive pulse is applied in the state "0", we will find the difference between the state "1" and the state "0" in current response as the well-known destructive read-out.

Next let us apply the present technique to study the desirable pulse shape for the nondestructive read-out.

Figures 2 and 3 show the results in the memory state "1" and in the state "0" for partial switching response, where the parameters are chosen as $\kappa = 5$, $\gamma = 1.0\times10^{-8}$, $e_o = \pm 1$ and the pulse width $t_o =$ 0.55 t_{max}. The time t_{max} is defined as the time at which the switching current (i) becomes maximum when the step-type field is applied ($e_o = 1$, $di/dt = 0$ at $t = t_{max}$).

Figures 2(b) and 3(b) show that the polarizations both in the state "1" and in the state "0" are not lost even when the read-out pulse is applied. It is also seen that the current responses are different for the state "1" and the state "0" when this narrow pulse is applied as shown in Figs. 2(c) and 3(c). Thus, it seems possible to distinguish the state "1" from the state "0". This result indicates the possibility of the nondestructive read-out.

Figures 4 and 5 show the results for P-e hysteresis curve and i-v curve, which of course depend upon chosen parameter values.

Figures 4(a) and 4(b) show the viscosity coefficient-dependence of two characteristics. The hysteresis curves show that as γ increases, both polarization and coercive field increase. The i-v curves show that as γ decreases, the peak value of current becomes larger and the slope becomes steep. The value of the field at the peak current becomes smaller. It implies that as γ decreases, the switching time becomes shorter.

Figures 5(a) and 5(b) show the interaction coefficient-dependence of two characteristics. The hysteresis curves show that as κ increases, both polarization and coercive field decrease. The i-v curves show that as κ increases, the peak value of switching current decreases and the slope does not change much.

CONCLUDING REMARKS

In this paper we have described the numerical analyses of ferroelectric characteristics performed using a proposed lattice model. Results of pulse response seem to reproduce the experimental data. Thus, the simulations based upon the lattice model will be well helpful in designing ferroelectric memories.

REFERENCES

1. A . N . Kolmogorov , Izv . Akad . Nauk . USSR . Ser Math., 3, 355, (1937).
2. M . Avrami , J. Chem . Phys ., 7, 1103, (1939) , 8 , 212, (1939) , 9, 177, (1941).
3. Y . Ishibashi and Y . Takagi , J . Phys . Soc . Jpn ., 31, 506, (1971).
4. Y . Ishibashi , J . Phys . Soc . Jpn ., 59, 4148, (1990).

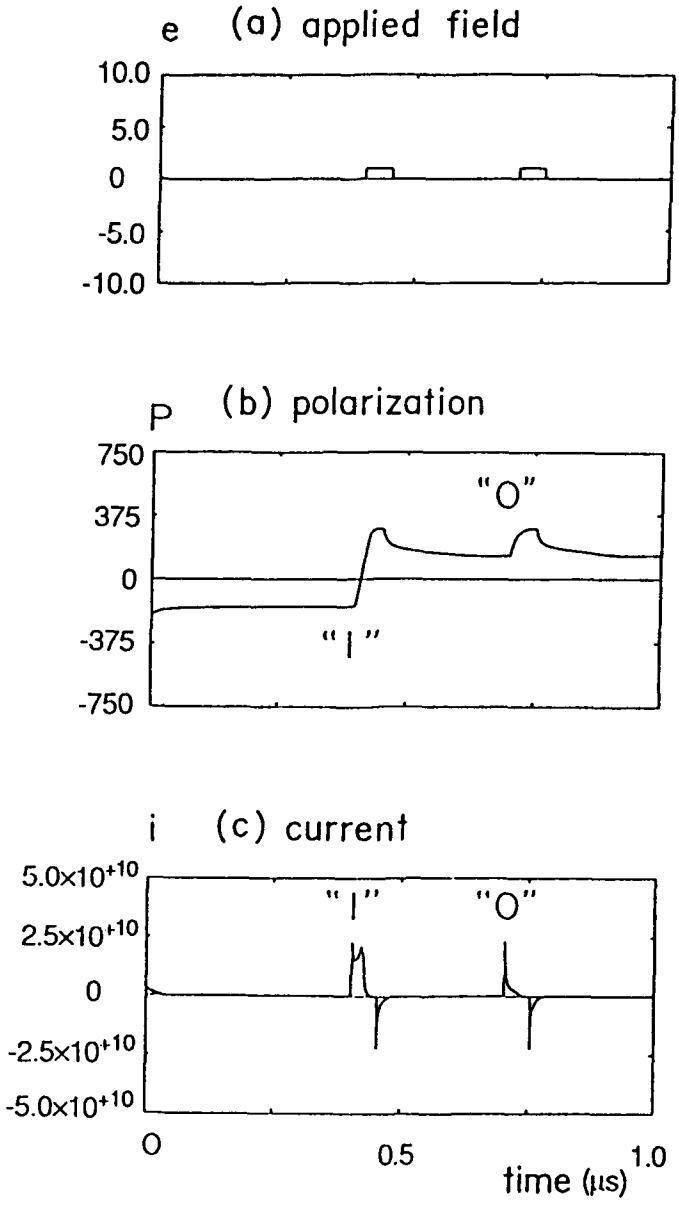


FIGURE 1 Pulse response. Adopted parameter values : $\alpha = -1$, $\beta = 1$, $\kappa = 5$, $e_0 = 1$, $\gamma = 1.0\times10^{-8}$. (a) applied field, (b) polarization response, (c) current response.

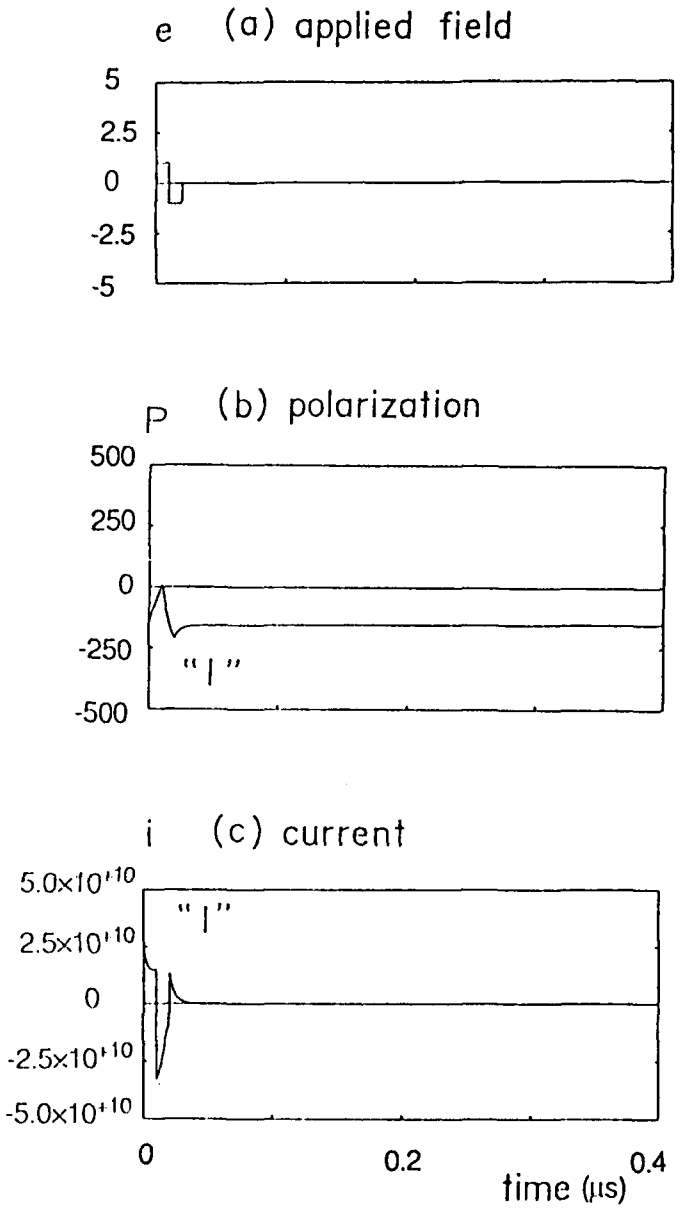


FIGURE 2 Pulse response. Adopted parameter values : $\alpha = -1$, $\beta = 1$, $\kappa = 5$, $e_o = \pm 1$, $\gamma = 1.0 \times 10^{-8}$. (a) applied field, (b) polarization response, (c) current response.

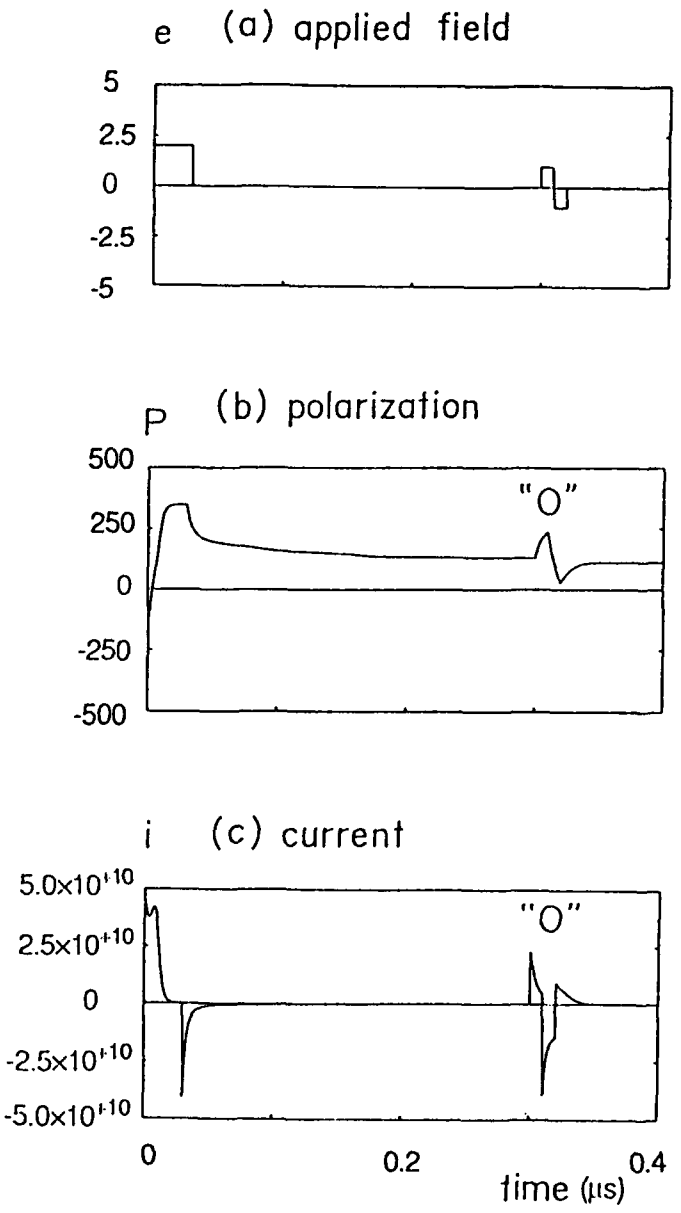


FIGURE 3 Pulse response. Adopted parameter values : $\alpha = -1$, $\beta = 1$, $\kappa = 5$, $e_o = \pm 1$, $\gamma = 1.0 \times 10^{-8}$. (a) applied field, (b) polarization response, (c) current response.

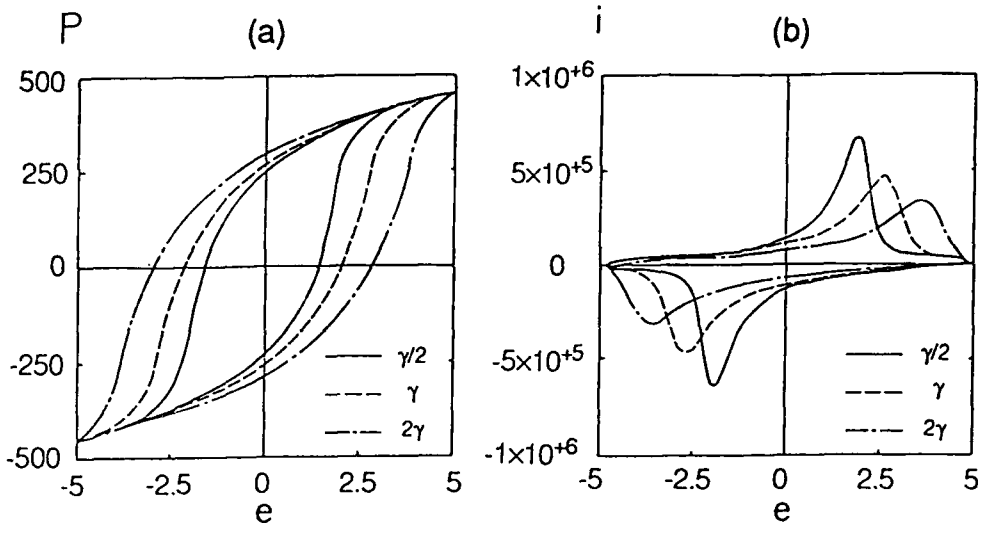


FIGURE 4 The viscosity coefficient (γ) dependences of characteristics. Adopted parameter values : $\alpha = -1$, $\beta = 1$, $\kappa = 5$, $e_o = 5$, $\gamma/2 = 0.667\times10^{-3}$, $\gamma = 1.333\times10^{-3}$, $2\gamma = 2.667\times10^{-3}$. (a) hysteresis curves (b) i-v curves.

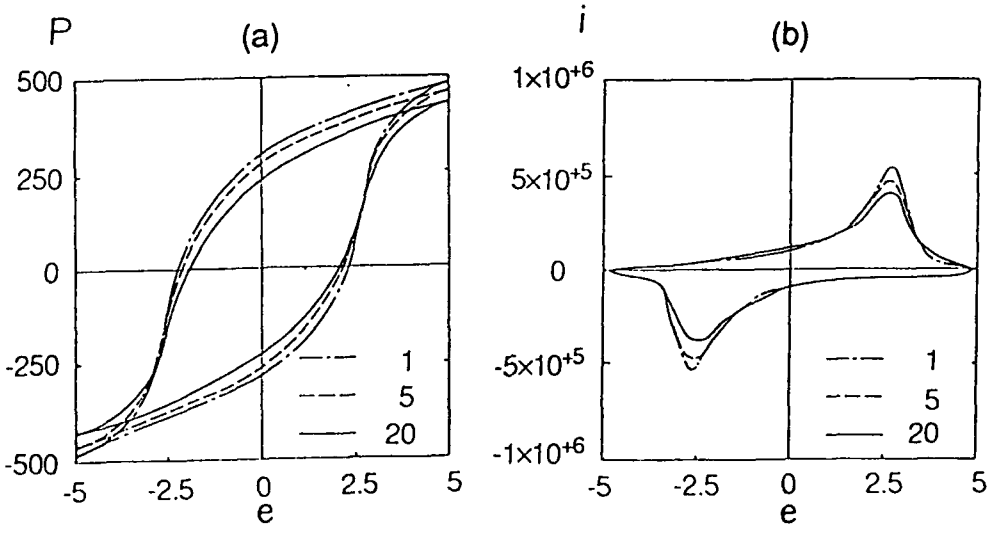


FIGURE 5 The interaction coefficient (κ) dependences of characteristics. Adopted parameter values : $\alpha = -1$, $\beta = 1$, $\kappa = 1 \sim 20$, $e_o = 5$, $\gamma = 1.333\times10^{-3}$. (a) hysteresis curves (b) i-v curves.

AD-P006 665

REJUVENATION OF FERROELECTRIC FATIGUE IN MODIFIED LEAD ZIRCONATE TITANATE CERAMICS NEAR TETRAGONAL-RHOMBOHEDRAL MORPHOTROPIC PHASE BOUNDARY

WUYI PAN and CHENG-FENG YUE
Materials and Metallurgical Engineering Department
New Mexico Institute of Mining and Technology
Socorro, NM 87801

Abstract

Rejuvenation of ferroelectric fatigue is investigated in modified lead zirconate titanate ferroelectric ceramics near the tetragonal-rhombohedral morphotropic phase boundary. Ferroelectric fatigue rejuvenates with changes in the applied electric field direction. Spontaneous rejuvenation occurs in the absence of an electric field. A coupling among the applied electric field, oxygen vacancy related defect dipoles, and spontaneous polarizations is proposed to explain ferroelectric fatigue andrejuvenation.

INTRODUCTION

In the past few years, ferroelectric switching has been considered for many potential applications[1,2,3]. The one that receives most attention is the recent use of ferroelectric lead zirconate titanate (PZT) thin films for non-volatile semiconductor memory applications. A limiting factor for the performance of the potential devices is ferroelectric fatigue. During ferroelectric fatigue, the ferroelectric polarization decreases and the coercive field increases with increasing switching cycles. This leads to unacceptable device performance.

In spite the practical importance of the problem, the mechanism of ferroelectric fatigue is not clear at the moment. Among the previous proposed mechanisms, there are the "microcracking" mechanism[4,5] the "lack of intimate electrode-ceramic contact" mechanism[6] and the "electrode charge injection" mechanism[7]. None of the investigations have shown convincing evidence for the proposed mechanisms. In this paper, we present important experimental evidences for the rejuvenation of ferroelectric fatigue and provide the mechanisms of ferroelectric fatigue and rejuvenation.

EXPERIMENTAL PROCEDURES

The lead lanthanum zirconate titanate (PLZT) 7/62.5/37.5 ceramic, compositionally at the tetragonal-rhombohedral morphotropic phase boundary, was used to study the rejuvenation of ferroelectric properties with changes in the applied electric field direction. The detailed preparation procedures are described in an earlier paper[8]. The PLZT ceramics were cut into bars 6 mm long and 0.6 mm x 0.6 mm cross section.

92-16129

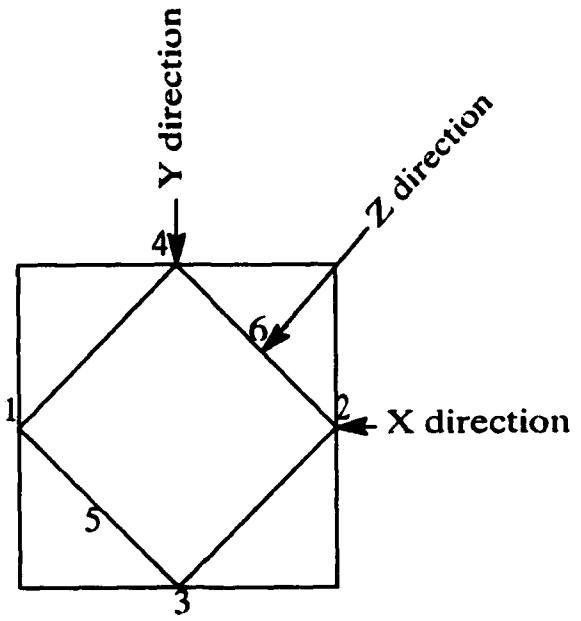


Figure 1. Schematics of the cross-section of the PLZT ceramic bar that shows the different applied electric field directions.

The small cross section and low coercive field of the ceramic composition were necessary for applying enough electric field to saturate the ferroelectric polarization. A schematic of the bar cross section is shown in Figure 1 to illustrate the direction change of the applied electric field. The X and Y directions are normal to the long faces of the bar.

A gold electrode was sputter deposited onto faces 1 and 2 of the bar. An electric field was applied in X direction to fatigue the sample. The electrodes were removed by grinding with SiC papers after the sample was fatigued in the X direction. Gold was then sputter deposited on faces 3 and 4. Dielectric hysteresis loops were measured and the sample was electrically fatigued in the Y direction. The electrodes on faces 3 and 4 were removed again and gold was sputter deposited back onto faces 1 and 2. After the ceramic sample was fatigued for the second time in the X direction, it was cut and polished to create surfaces 5 and 6 that were 45° from the X and Y directions as shown in Figure 1.

Gold was then deposited on faces 5 and 6 for fatigue measurement. Between each direction change, the electrode removal and redeposition took less than 20 minutes. The sputter deposition was confirmed to have negligible heating effect on the samples.

Commercial PZT-5 ceramic samples manufactured by Piezokinetic Inc. were used for X-ray diffraction study. The piezoelectric d_{33} coefficient of the as-received, poled ceramics was approximately 400 pC/N. Rectangular plate samples were cut from the as- received disk using a diamond blade and then ground to a size of 6mm x 4 mm x 0.3 mm. Samples were thermally depoled by heating them above the Curie temperature to 500°C for approximately four hours. X-ray diffraction analysis was performed with a computer- controlled Philips X-ray diffractometer. The samples

were mounted in the sample holder of the diffractometer in such a way that the major surface was incident to the X-ray beam.

A precise analysis of the diffraction peaks corresponding to the pseudocubic 200 indices was performed. A 2θ interval of 0.2° and 2-second photon collection time at each angle position were used. After analysis of the thermally depoled samples, the major surfaces of the samples were electroded by applying Dupont thick-film conducting paste. The samples were poled by applying a field in excess of 50 kV/cm at room temperature for about 20 minutes. The electrodes of the samples were then removed by attaching a plastic tape to the electrode and then mechanically peeling the electrode off the sample. A slow X-ray scan was then performed on the dc poled samples. The electrode was then applied to the samples again and the samples were depoled by an ac electric field for about one minute. The amplitude of the ac electric field for the ac depoling was about 40 kV/cm. The ac depoled samples were electroded and fatigued by applying an ac field of the same amplitude until less than 25% of the initial ferroelectric polarization remained. The electrodes were again removed for the slow X-ray scan. Between post-fatigue X-ray analyses, the samples were stored on the shelf at room temperature.

Dielectric hysteresis loops were measured with a Diamant- pepinsky circuit. The frequency of the ac field was 100 Hz for all fatigue measurements. A digital oscilloscope interfaced to an IBM computer was used for data acquisition. For the PZT-5 ceramic samples, the piezoelectric d_{33} coefficient was measured after fatigue using a Berlincout d_{33} meter.

RESULTS AND DISCUSSION

Rejuvenation of ferroelectric properties due to the change in the applied electric field direction is illustrated in Figure 2.A maximum field-induced polarization of 26 uC/cm^2 was initially obtained for an electric field applied in the X direction of the sample. After 7.4 x 10^6 cycles, the induced polarization was reduced to 7 μC/cm^2. After the field was changed to the Y direction, an initial polarization of 27 μC/cm^2 was measured. This is approximately equal to the initial polarization in the X direction. After 8.4 x 10^5 cycles, the polarization in Y direction was reduced to 5 μC/cm^2. When the electric field was changed back to the X direction, a polarization of 13 uC/cm^2 was observed. This is somewhat larger than 7 μC/cm^2 at the end of the first fatigue in the X direction. After the sample was fatigued for the second time in X direction, it was cut and electroded in the Z direction. An initial polarization 17 μC/cm^2 was measured. The observed rejuvenation with change in applied electric field direction does not agree with the "microcracking" mechanism proposed by Salaneck et al[4]. The "microcracking" mechanism is based upon the preferential drop of the applied field across high impedance cracks generated by the incompatible deformation of the grains in ceramics. However, there is no theoretical basis for the cracks to arrange themselves in a perfect preferred orientation so as to only block the field that causes fatigue. A possible cause of the above effects, the gradual electrode-ceramic interface decohesion was also confirmed to be not responsible for our gold sputter-deposited samples. A fatigued sample was cut parallel to the major surfaces of the sample into three thin wafers. Gold was deposited on the three wafers to test the ferroelectric polarizations in the original fatigued directions. It was found that all three wafersremained fatigued and the differences in the ferroelectric polarizations for the threewafers were within the experimental error. If a gradual decohesion of

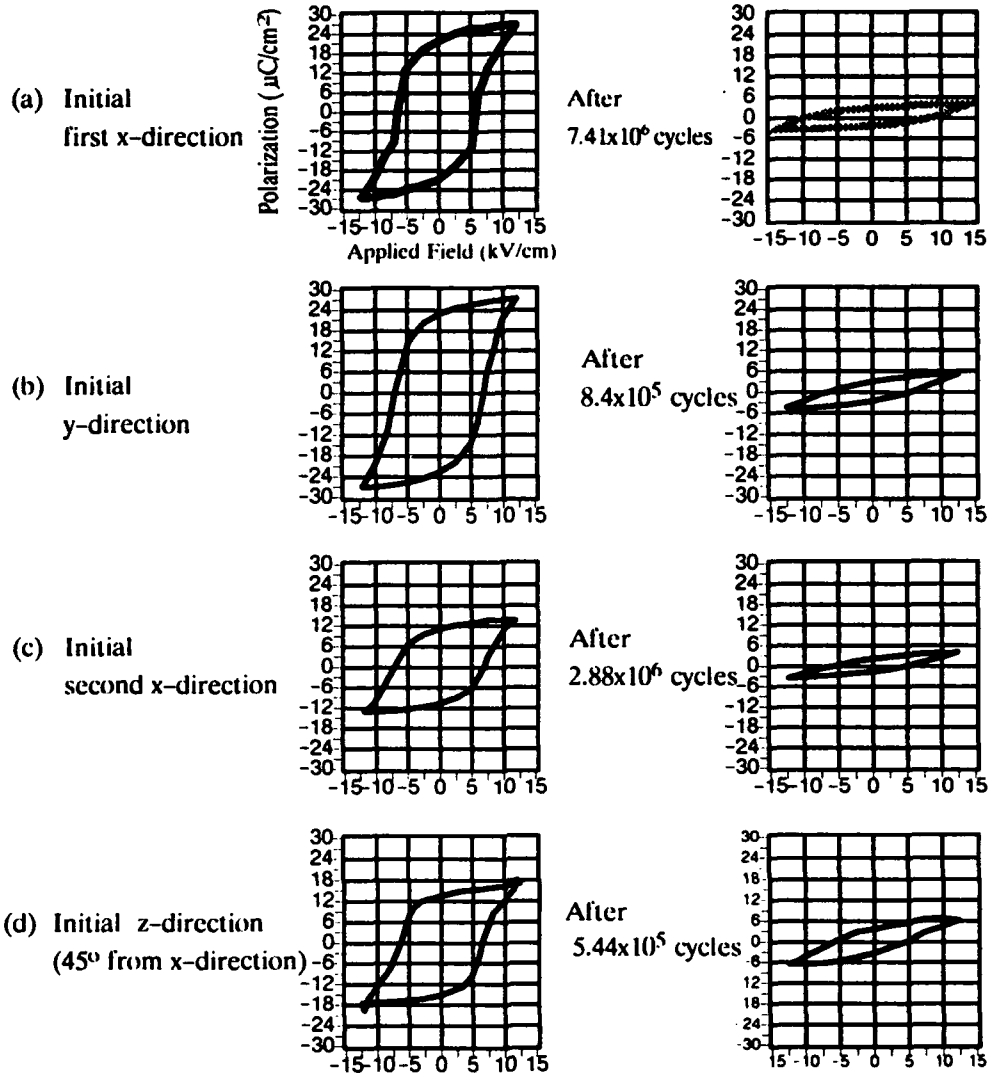


Figure 2. Dielectric hysteresis loops measured for different applied field directions. a) initial and fatigued (7.41 x 10^6 cycles) hysteresis loops for a field applied in the X direction; b) initial and fatigued (8.6 x 10^5 cycles) hysteresis loops for a field applied in the Y direction, after X direction fatigue; c) initial and fatigued (2.88 x 10^6 cycles) hysteresis loops for a field applied in the X-direction, after fatigues described in a) and b); and d) initial and fatigued (5.44 x 10^5 cycles) hysteresis loops for a field applied in the Z direction (45^o to x direciton) after fatigues described in a), b) and c).

the electrode-ceramic interfaces were responsible for the observed fatigue, the middle wafer would have an unfatigued ferroelectric polarization value.

Four different X-ray diffraction traces recorded from 43.5^o to 45.5^o range are shown in Figure 3 for PZT-5 ceramic samples. The X-ray diffraction trace in this 2θ range corresponds to the pseudocubic {200} peak. For the thermally depoled samples, the {200} peak split into (200) and (002) peaks due to tetragonal distortion.

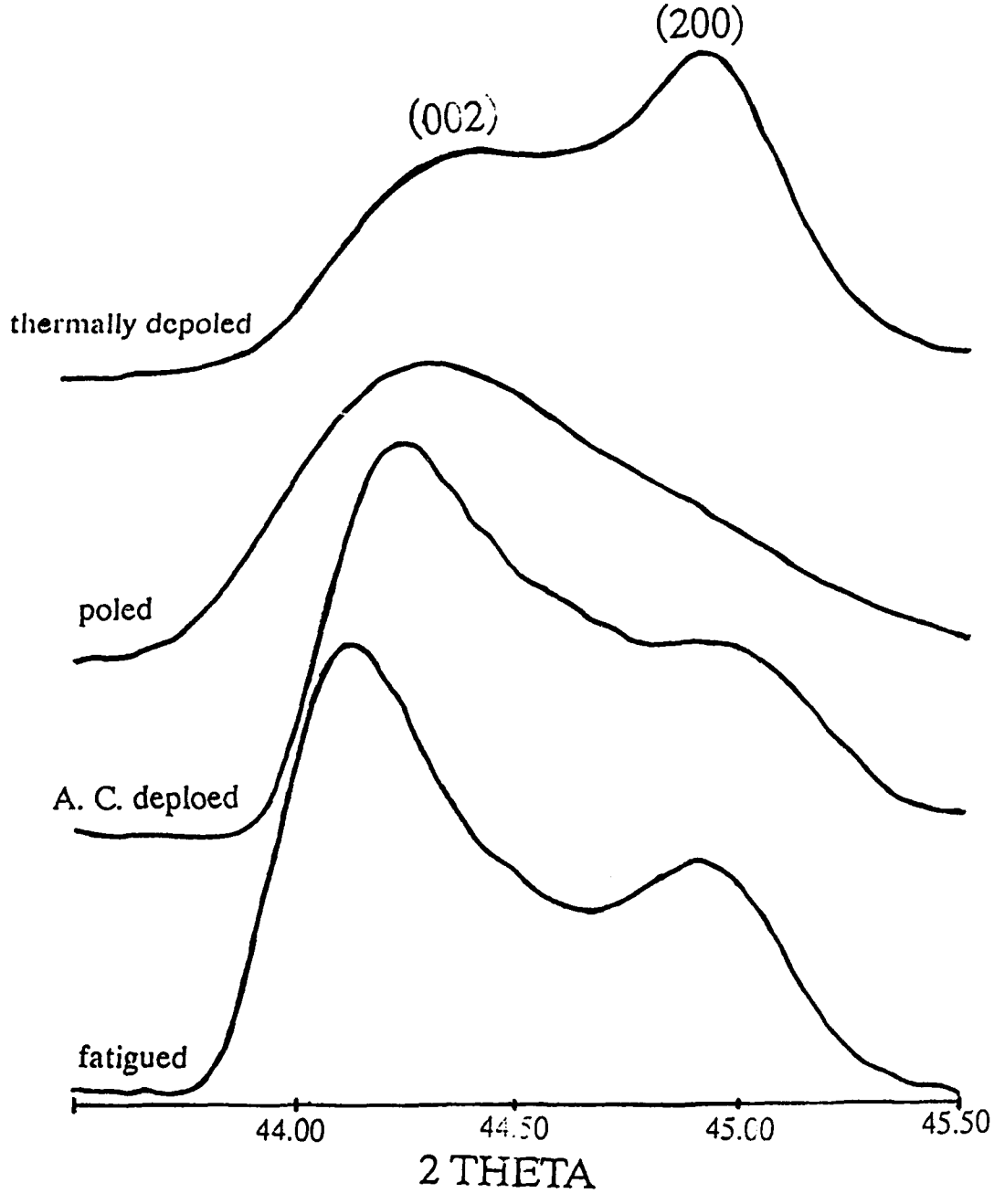


Figure 3. The Pesudocubic {200} peaks for PZT-5 ceramics after different thermal and electric treatments.

The intensity of (200) is much higher than (002), implying a random orientation of the domains and grains for the thermally depoled samples. The valley between (002) and (200) peaks is much higher than the background noise. This is due to the presence of {200} peak of the rhombohedral phase which is not resolved. After dc poling under ambient temperature and pressure, the (002) peak intensity increases at the expense of (200) due to the domain orientation induced by the poling. By contrast after ac depoling, the (200) intensity increases slightly with respect to (002), largely due to the alignment of the c axes of the tetragonal cells parallel to the major surfaces of the samples. Since (002) is still much higher than (200), the ac depoling primarily

randomizes the polar vectors in the two directions of the applied field. Note also that the two peaks are not well separated for the ac depoled samples. For the fatigued sample, 25% of the initial ferroelectric polarization remained; however, both (002) and (200) peaks are very distinct. A deep minimum appears in the middle of the two peaks to separate them. The two peaks are further separated in 2θ values after fatigue.

We feel that the observed X-ray peak changes accompanied the rhombohedral-tetragonal phase change brought about by ferroelectric fatigue. The free-energy difference between the rhombohedral phase and the tetragonal phase for the morphotropic composition is very small. A field-induced rhombohedral-to-tetragonal phase change is expected for the tetragonal phase has a larger spontaneous polarization than the rhombohedral phase.Therefore it can be more stable under the applied electric field.

As mentioned previously, the {200} planes of the rhombohedral phase are largely responsible for the high valley between the two peaks. A conversion of rhombohedral-to-tetragonal phase reduces the valley between the two peaks and further separates the peaks in 2θ values. Figure 4 shows the change of X-ray diffraction traces of the fatigued samples after the samples had been stored at room temperature for different lengths of time without electric field driving. First of all, the deep minimum between the two peaks gradually disappeared with time. Secondly, the two peaks got close to each other with time. We think that the cause of this change is the tetragonal-to-rhombohedral phase change. The tetragonal phase, which was obtained from the rhombohedral phase by fatigue, is not stable under the absence of the applied electric field. As the X-ray peak changed under the absence of the applied electric field, we observed a partial rejuvenation of ferroelectric properties. Figure 5 shows the P-E hysteresis loops for fatigued samples and samples stored at room temperature for 2.5 months. Apparently, rejuvenation of ferroelectric polarization occurred.

We think that the coupling between the defects and spontaneous polarization is responsible for the stabilization of spontaneous polarization under the applied electric field. Since the applied electric field is large, it can couple to those defects which have a dipole character. Such an orientation of the defects under a prolonged application of a dc electric field was demonstrated in an earlier paper[9]. Since a dc electric field can induce an oriented pattern of defect dipoles, an ac electric field should be able to induce a textured pattern of defect dipoles. The defects can interact with spontaneous polarizations to stabilize their positions. The fatigue is a consequence of such a stabilization. The d_{33} coefficient measured after fatigue was 130 pC/N. If we substract from it the contribution from the remanent polarization shown in Figure 5(a), the contribution to the d_{33} coefficient from the stabilized polarizations will be less than 130 pC/N. However, the intensity ratio of (002) and (200) peaks for the fatigued sample shown in Fig. 3 indicates a preferred orientation of the polar axes perpendicular the major surfaces of the samples. The polar axes must have up-down texture, otherwise, the d_{33} coefficient of the fatigued ceramic would be larger. When the applied electric field changes 90°, the defect dipoles which were textured in the first direction by fatigue cannot orient with the new electric field instantaneously.Thus, the spontaneous polarizations and defect dipoles decouple as a result, and consequently, ferroelectric properties rejuvenate. When the applied field changes less than 90°, the textured defect dipoles still have projections on the new directions of the applied electric field;therefore, ferroelectric properties only partially rejuvenate.

Pervoskite ferroelectric ceramics that contain oxygen vacancies predominantly are said to be "hard" in the sense that an oxygen vacancy easily migrates from

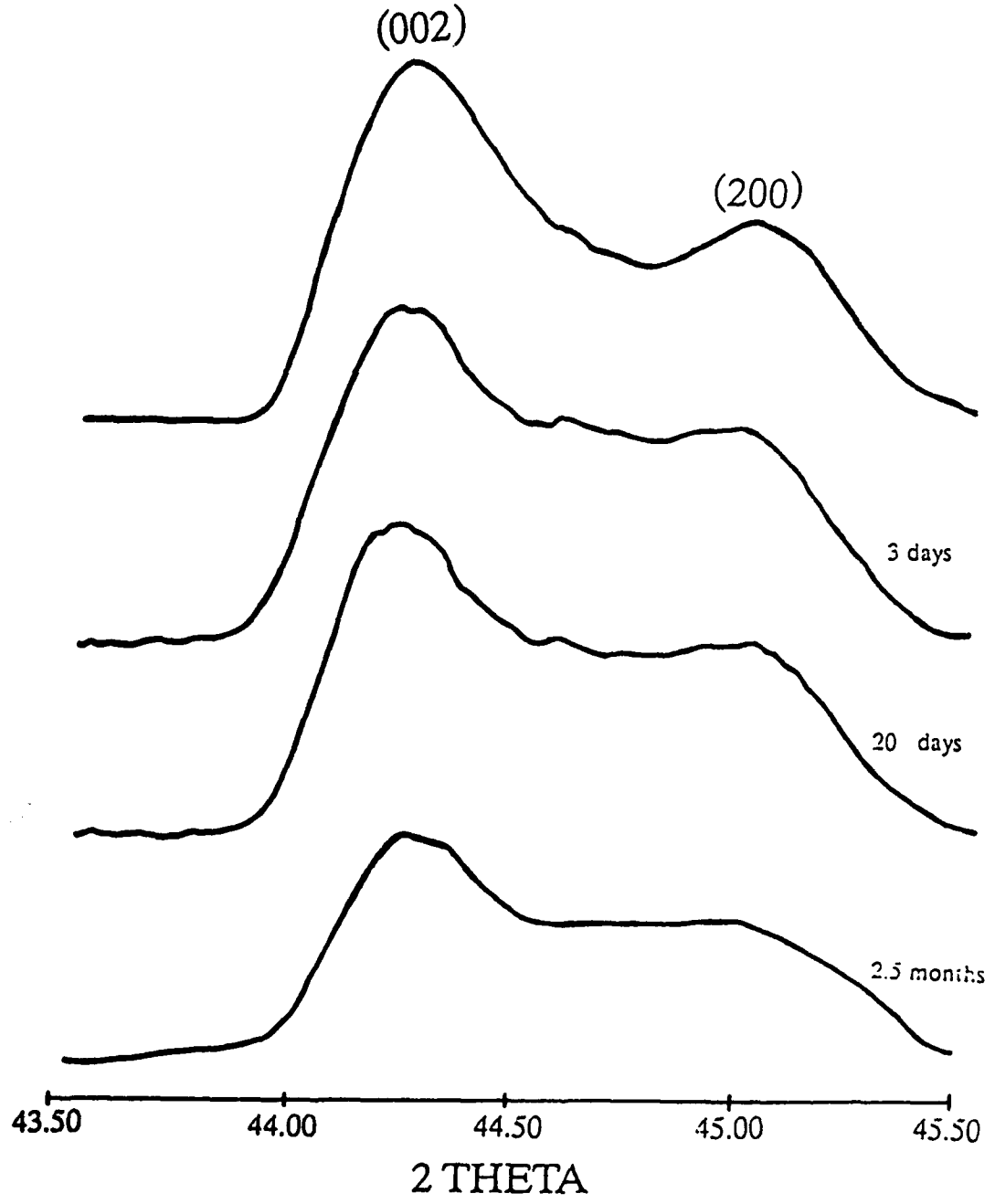


Figure 4. The Pesudocubic {200} peaks for fatigued PZT-5 ceramics different times after fatigue was terminated.

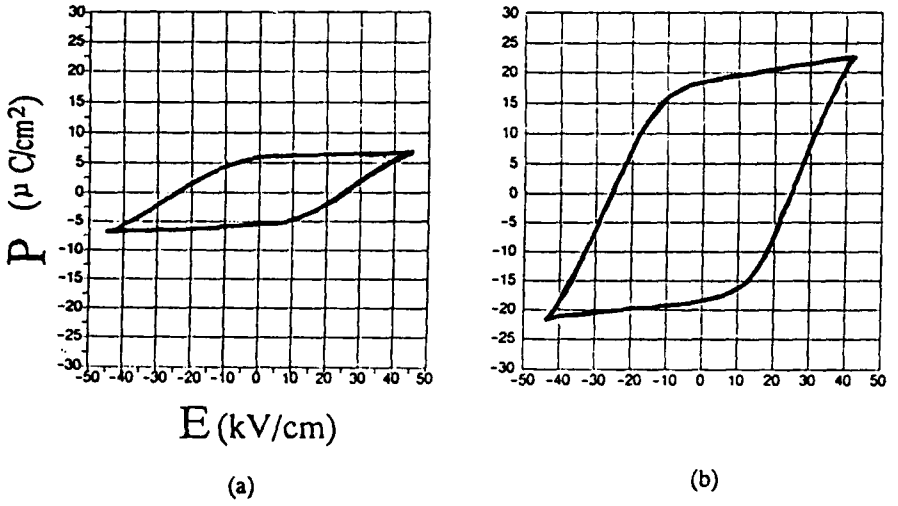


Figure 5. Dielectric hysteresis loops of the PZT-5 ceramic: a) at the end of fatigue and b) 75 days after fatigue. changes less than 90°, the textured defect dipoles still have projections on the new directions of the applied ac electric field therefore, ferroelectric properties only partially rejuvenate.

one face center to the other to pin the spontaneous polarization. Under the electric field driving, the defect dipoles associated with the oxygen vacancies can couple to the electric field and arrange themselves in a textured pattern. Apparently, there are six <100> directions in a unit cell for defect dipoles to align with. In the tetragonal phase, the coupling between the spontaneous polarizations and the defect dipoles can be perfect because the <100> directions are allowed for both. In the rhombohedral phase, the allowed directions for the spontaneous polarization are the eight <111> directions. The coupling between the spontaneous polarizations and defect dipoles due to the oxygen vacancies cannot be perfect because of the non-zero angle between the <111> and <100> directions.After a tetragonal-rhombohedral phase change in the absence of an applied electric field, the polarizations in the recovered rhombohedral phase are not strongly coupled to the defect dipoles. Consequently, the ferroelectric properties partially rejuvenate.

SUMMARY AND CONCLUSIONS

Ferroelectric fatigue in modified lead zirconate titanate rejuvenates with change in the applied electric field direction. Spontaneous rejuvenation occurs in the absence of an applied electric field. The fatigue and rejuvenation can be well explained by the coupling among the applied electric field, oxygen vacancy related defects, and spontaneous polarization.

ACKNOWLEGEMENT

Authors would like to thank Dr. B.A. Tuttle at Sandia National Lab for his kind assistance and discussions. Appreciation is extended to Dr. A.R. Miller for a critical reading of the manuscript.

REFERENCES

1. D. Bondurant, Ferroelectrics, pp 273-82 (1990).

2. W.Y. Pan, C.Q. Dam, Q.M. Zhang, and L.E. Cross, Appl. Phys, pp 6014-23, (1989).

3. C.E. Land, Amer. Ceram. Soc. pp 905-908 (1988).

4. W.R. Salaneck, Ferroelectrics, pp 23-32, (1975).

5. K. Carl, Ferroelectric, pp 97-101 (1972).

6. C.F. Pulvari and J.R. Sprour, IEEE Transaction on Electron Devices, vol. ED-16, pp 532-535 (1969).

7. D.B. Fraser and J.R. Maldonado, Appl. Phys., pp. 2172-79 (1970).

8. W.Y. Pan, Q.M. Zhang, Q.Y. Jiang and L.E. Cross, Ferroelectrics, pp. 1-15 (1988).

9. W.Y. Pan, Q.Y. Jiang and L.E. Cross, Am. Ceram. Soc., C17-C19 (1988).

AD-P000 3

A GENERALIZED FERROELECTRIC CAPACITOR MODELING METHODOLOGY

DOUGLAS E. DUNN
North Dakota State University, Fargo, North Dakota, U.S.A.

CARLOS A. PAZ de ARAUJO
University of Colorado at Colorado Springs, Colorado U.S.A.

Abstract A generalized ferroelectric capacitor modeling methodology is presented from a theoretical basis through implementation in PSPICE. The approach postulates nonspecific sources of mobile charge as the source of nonideal hysteresis characteristics. These charges are modeled as depletion capacitances in an equivalent circuit model of the ferroelectric capacitor, capable of simulating both AC and DC behavior. A parameter extraction software package is presented, the use of which establishes that the model parameters may be fit to measured hysteresis data with a high degree of accuracy. PSPICE simulation results are then produced which demonstrate the ability to simulate hysteresis and switching behavior. These results may be correlated to measured data to identify specific physical phenomenon, and speed process and device design.

INTRODUCTION

The ultimate goal of a ferroelectric model is to aid in the development of an optimal dielectric material. Therefore, the usefulness of the model must lie its ability to provide a predictive capability, rather than describe what is already known. To achieve predictive capability in a single stroke requires a detailed model, constructed at a fundamental theoretical level. However, this usually results in a model with too many degrees of freedom to be truly predictive. There are simply too many unknown variables to free the model from being an exercise in curve fitting. The problem with ferroelectric device modeling

92-16130

then is to achieve a model of sufficient detail to be useful, but simple enough to strongly correlate results to controllable physical and process variables.

Where multiple unknown physical processes are at work, the development of a model and the material must proceed jointly in an iterative fashion. Measured device characteristics may be used to infer physical processes which are then incorporated in the device model at some level. The model is then used to predict the proper direction for the next process iteration. The results produce new measured data and cycle is repeated. As the model is optimized the physical processes become better understood, predictive capability is increased, and the material more easily characterized and itself optimized.

From this ideological standpoint it is desirable to begin with a relatively simple model; one which allows for later enhancements as necessary. This paper describes a methodology which fosters such an approach. Basic theoretical descriptions are used to link material behavior to physical processes. An equivalent circuit model then extends the model to the practical level, such that it can function in the iterative process just described. Overall the methodology provides a framework for connecting the practical aspects of modeling with the theoretical in such a way that a detailed model may be built from the ground up in concert with process development.

METHODOLOGY

Assumptions are made at the theoretical, physical, and circuit modeling levels which divide the ferroelectric capacitor's behavior into ideal and nonideal components. Together these components provide both the DC and AC responses of the capacitor.

Theoretical Assumptions

The model assumes the polarization, P, and electric field, E, are related by the Landau/Devonshire polynomial,

$$E = \alpha P + \beta P^3 + \gamma P^5 \tag{1}$$

derived from a phenomenological consideration of the thermodynamic Gibbs free energy.[1] These two variables are also related by the Poisson equation. Dividing P into linear and switching components, P_l and P_s, the Poisson equation takes the form shown below, where ρ is the total charge density, and D is the displacement field.

$$\nabla \cdot D = \rho$$

$$D = \epsilon_0 E + P_l + P_s$$

$$\nabla \cdot D = \nabla \cdot \epsilon E + \nabla \cdot P_s$$

$$\nabla \cdot E = \frac{1}{\epsilon} (\rho - \nabla \cdot P_s) \tag{2}$$

Switching is assumed to follow the basic relationship shown in Eq. (3), provided the correct functional dependence of the capacitance is known.

$$i(t) = \frac{d}{dt} [\, C(v(t)) \cdot V(t)] \tag{3}$$

Physical Assumptions

Physically, an ideal ferroelectric, as described by Eq. (1) is assumed to underlie all other physical processes which

may give rise to nonideal behavior. Nonideal physical processes are assumed to be related to sources of mobile charge within the ideal ferroelectric.

Many possible sources of charge exist, including ionized impurities, mobile ions, and vacancy states. The model is completely nonspecific as to the actual source. It concentrates, rather, on the assumption that the net effects of these charges are voltage dependent depolarization fields, which appear as the divergence of Ps in Eq. (2).

Such fields may occur both within the bulk of the device at grain boundaries, and near the surface due to the effect of surface states and Schottky barriers. Determination of the relative influence of each source of these fields is left as an application for the model.

Equivalent Circuit Model

An equivalent circuit model may be constructed combining linear and nonlinear circuit elements based on the physical assumptions above. The nonideal portion of the capacitor may be modeled by voltage dependent "depletion" capacitors, appearing both in series and parallel with an ideal ferroelectric capacitor, as shown in Figure 1. To first order, the voltage dependence of the depletion devices may be characterized by a two parameters as shown in Eq. (4) below.

$$C(v) = C_0 V^n \qquad (4)$$

The ideal ferroelectric capacitor must be modeled in such a way as to reproduce both AC and DC behavior. A simple approach is shown in Figure 2. A linear capacitor is used to model the DC response, while the AC switching

response is modeled by an empirically defined current source.

This approach has several disadvantages. First, the linear capacitor does not model the nonlinear polarization charge, and would of course fail to correctly simulate hysteresis. Second, while the current source could be made to generate the correct switching current, it provides no connection to the underlying physical process, and so provides no predictive capability whatsoever.

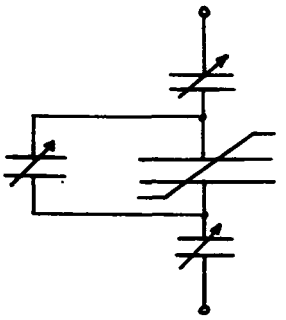


FIGURE 1 Basic DC model.

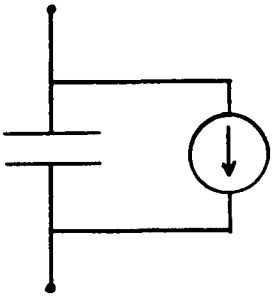


FIGURE 2 Primitive AC model.

The approach taken in this work was to model the internal structure of the ferroelectric by splitting the capacitor into three linear capacitors in series. The two internal nodes provide locations for the polarization charge to reside, corresponding to the two states of the device. The movement of charge between these nodes is regulated by a controlled voltage source.

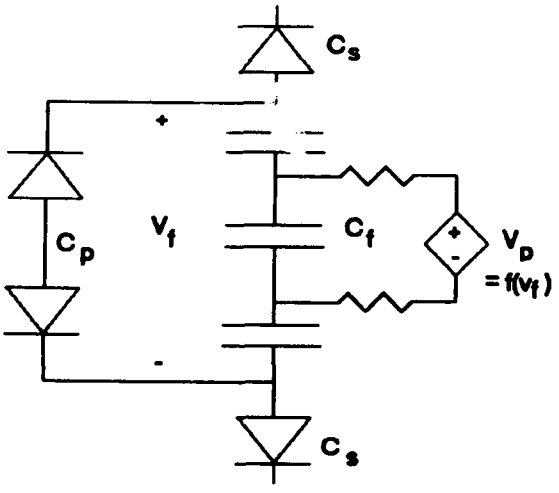


FIGURE 3 Complete model.

The complete model suitable for PSPICE implementation is shown in Figure 3, where the depletion capaci-

tors are implemented as reverse biased diodes. (The parameters C_0 and n are included in the PSPICE diode model). The controlled source V_p is a constant which reverses polarity depending on the voltage across the ideal ferroelectric, V_f.

For DC simulation, V_p effectively switches instantaneously, providing a large increase in charge when the coercive field is reached, and correctly simulating the nonlinear charge buildup evidenced in the hysteresis loop.

On short time scales this charge movement produces a displacement current pulse in the external circuit. The pulse shape is governed by an internal RC time constant, as well as the RC time constant of the external circuit. Physically, this equates dipole switching to a first order relaxation process. While simple, this approach takes the first step away from the purely empirical approach described earlier. In doing so, it provides a starting point for equating physical processes with controllable parameters.

PARAMETER EXTRACTION

A software package called FCAP (Ferroelectric Capacitor Analysis Program) was developed for this model to handle the details of linking empirical data with PSPICE simulation. This includes data I/O, parameter optimization and extraction, and creation of the PSPICE models and circuit file. The following FCAP results illustrate the parameter extraction process, and the extent to which it is possible to fit the model to measured hysteresis data.

The simplest complete version of the model contains five parameters; the three Devonshire polynomial parameters, and the C_0 parameter for the series and parallel depletion capacitors. The parameter n is assumed to be

1/2, as is the case with a step junction capacitor.

Figure 4a shows the optimum fit which can be obtained using only the three Devonshire parameters. Shown is the hysteresis curve from an actual device, measured using a Sawyer-Tower circuit. Against this, the Devonshire polynomial, Eq. (1), is presented from which the ideal hysteresis is extracted. The reader may note that the fit is deficient in two respects. First, the infinite slope of the switching region is unrealistic. Second, the slope elsewhere in the fit, which is proportional to the dielectric constant, is less than the measured dielectric constant.

Figures 4b and 4c show optimized 4 parameter fits including the parallel and series depletion capacitors

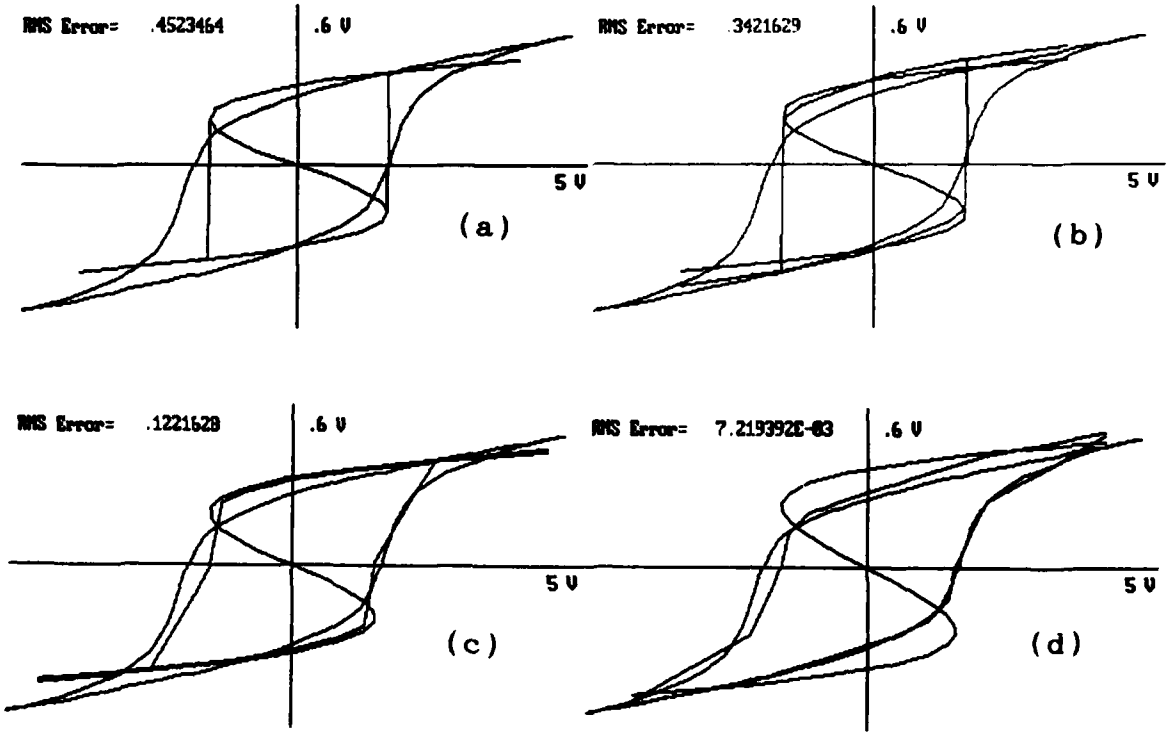


FIGURE 4 The model fitted to data using FCAP (a) ideal 3 parameter model, (b) 4 parameter model including parallel parasitics, (c) 4 parameter model including series parasitics, (d) 5 parameter model including all parasitics.

respectively. In Figure 4b, the parallel device picks up the higher dielectric constant, but the ideal transition region is still evident. In Figure 4c, the series device produces a more realistic spread in the transition region, while failing to model the high dielectric constant elsewhere.

The optimized 5 parameter model including both depletion devices is shown in Figure 4d. Both the high dielectric constant, and the transition region are fit to a high level of accuracy. Most of the remaining error may be attributed to numerical effects. A smoother fit would be obtained by fitting to a larger number of data points. Also, in this example the optimization was performed on the forward voltage sweep half of the hysteresis loop, rather than the entire loop.

The quality of the fit is compelling circumstantial evidence that the basic assumptions of the model are at least to some extent modeling the actual physical processes at work in the device. Physically, the parallel device provides an additional source of charge storage, possibly as depletion regions develop around grain boundaries in the bulk. The series device prevents the entire dipole charge from switching at the same time, since for each incremental unit of dipole charge, an equal amount of charge must first develop across the surface depletion capacitor, before other dipoles can switch. This has the effect of spreading out the switching region of the hysteresis curve.

PSPICE SIMULATION RESULTS

Figures 5 and 6 are results of PSPICE simulations using the circuit of Figure 3. These results are qualitative in that they have not been fit to data, but serve to illustrate how a nonideal hysteresis loop, and switching transient may be simulated using a single equivalent circuit.

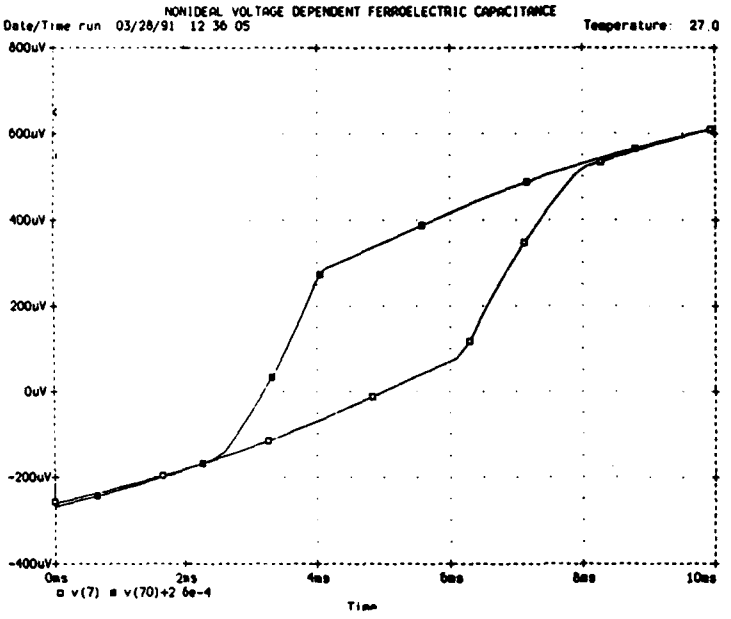


FIGURE 5 Sawyer-Tower hysteresis simulation.

Figure 5 shows the simulation of a Sawyer-Tower circuit containing the equivalent circuit model for the ferroelectric device. The resulting curve is somewhat less smooth than measured results, primarily because a linear capacitor is used to model the dielectric constant of the ideal device. Figure 6 shows the external current pulse observed when the voltage across the equivalent circuit model is switched.

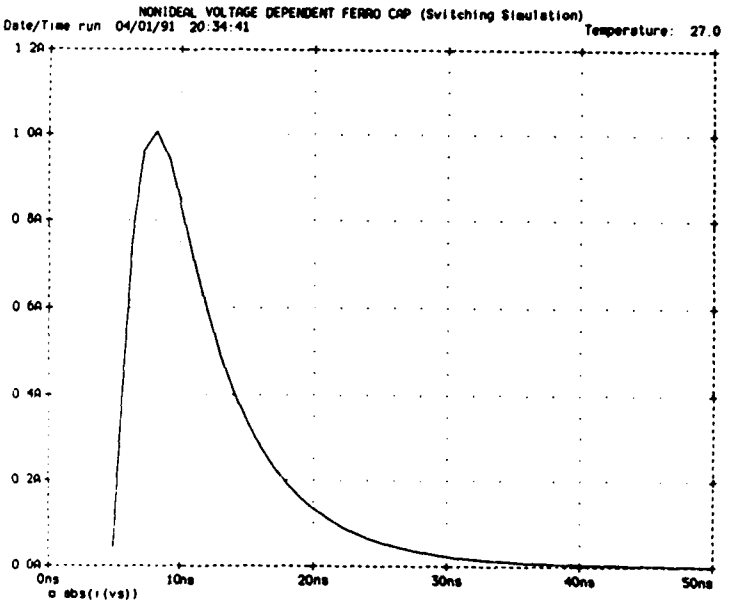


FIGURE 6 Simulation of switching transient.

SUMMARY

An integrated approach to modeling ferroelectric capacitors has been developed which

links theory and physical processes to an equivalent circuit and PSPICE simulation. In this approach, nonideal aspects of device behavior are attributed to mobile charges, which are modeled as depletion capacitances. The structure of the ideal ferroelectric is modeled to first order by an internal RC circuit. A parameter optimization program demonstrates how accurate fits to hysteresis data may be obtained. PSPICE simulations demonstrate how the same model produces both DC and AC results.

This approach may be refined and enhanced as data and new theories become available. Hopefully the result will be a basis by which device modeling may be integrated with process development in a practical way, reducing development time while providing the means to understand the physical processes at work in ferroelectric thin films.

REFERENCE

1. M.E. Lines and A.M. Glass, Principles and Applications of Ferroelectrics and Related Materials, (Oxford, New York 1977), p.72.

AD-P006 667

CHARACTERIZATION AND MODELLING OF THIN-FILM FERROELECTRIC CAPACITORS USING C-V ANALYSIS

CIARAN J. BRENNAN
The Charles Stark Draper Laboratory, Inc., 555 Technology Square, Cambridge, MA U.S.A

Abstract Advances have been made in the electronic characterization and analysis of thin-film ferroelectric (FE) memory capacitors using capacitance vs. voltage (C-V) measurements. A mathematical model of the small-signal electrical behavior of the FE capacitor has been developed. This analysis shows that the small-signal characteristics of the FE capacitor are largely determined by the space charge concentrations at the ferroelectric to contact interface. These space charge regions have an adverse effect on the permittivity, coercivity and switching characteristics of the ferroelectric capacitor. These results will contribute to improving ferroelectric processing, appraising the quality of ferroelectric devices, and developing device models of the ferroelectric memory capacitors for use in circuit design.

92-16131

INTRODUCTION

This work is focused on developing a thorough interpretation of the C-V measurements and their implications. Previous work on C-V analysis has been largely qualitative in nature[1-5]. The theory of the semiconductor behavior of thin-film ferroelectrics has been used to develop a mathematical model to explain and analyze the C-V data.

Outline:
1) The interaction between the dielectric switching of the ideal ferroelectric and the space-charge regions at the contacts are presented.
2) An analytical model for the small signal C-V characteristics is developed. The C-V behavior and the switching of the polarization are shown to be modulated by the space charges.
3) The significance of the model to ferroelectric device characterization is discussed.

FERROELECTRIC SWITCHING AND SPACE CHARGES

Simple model of switching permittivity:
This analysis employs a simplified model for the switching dielectric properties of the ferroelectric. A more rigorous and complete model of the switching dielectric properties has been derived from the free energy expression and will be presented in an upcoming article.

The ferroelectric permittivity K is very large in a small region about the coercive field value ($E_C \pm \delta$) due to the switching of the domains. This occurs

because during switching a very small change in the applied electric field results in a very large change in the ferroelectric polarization. Peak permittivity values of 5,000 or more can be obtained in high-quality samples.[6,7] In the limit that $K(E_C) \rightarrow \infty$ and $\delta \rightarrow 0$, the following expression using the Kronecker delta function describes the permittivity K. The negative sign in the delta function is used when the applied field is increasing in the positive direction; the positive sign is used in the negative direction. K_0 is a constant which approximates the non-switching permittivity.

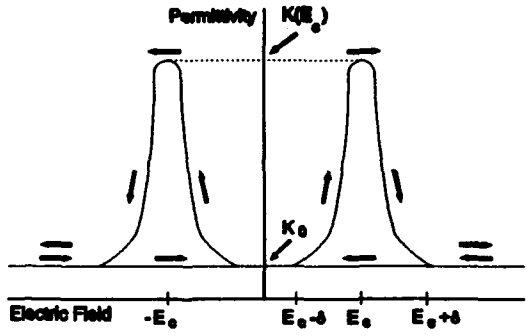


Figure 1 *Diagram of permittivity vs. electric field for the idealized ferroelectric.*

$$K = K_0 + \left[K(E_C) - K_0\right] \cdot \delta(E \pm E_C) \tag{1}$$

Space Charge Effects:

Ferroelectrics ceramics have a large bandgap (3 to 5 eV) and are normally considered insulators. However, the large value of spontaneous polarization of the ferroelectric tends to produce immense electric fields at the surface of the ferroelectric crystal. This electric field causes strong band bending and the ionization of trap states in the surface region of the ferroelectric regardless of the size of the bandgap. This ionization continues until a surface space charge develops of sufficient magnitude to screen the internal polarization of the ferroelectric.[8,9]

The metallic electrodes in a ferroelectric capacitor form Schottky contacts. The space charge accumulation at the interface is due to the band-bending caused by the Schottky potential, the spontaneous polarization, and the applied bias[9,10] (Figure 2). The depolarizing field in the ferroelectric is produced by the difference in space charge concentrations at the two junctions. Net charge neutrality is maintained by opposing electron concentrations in the metal contacts.

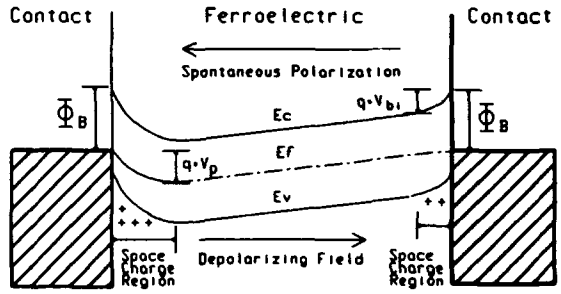


Figure 2 *Band-bending in the ferroelectric capacitor due to the Schottky barriers and the spontaneous polarization.*

Charge-Compensation Effects:

The electric field is not a linear function of distance in the ferroelectric because K is a function of the electric field. Therefore Poisson's equation must be rewritten:

$$\nabla \cdot E = \frac{\rho}{K(E)\varepsilon_0} \tag{2}$$

Integrating, we get:

$$E = \int \frac{\rho}{K(E)\,\varepsilon_0} \cdot dx \qquad (3)$$

The electric field changes slowly in the regions where K is large, i.e., when E is in the neighborhood of the coercive field value. Figure 3 is a plot of the electric field as a function of the distance through the ferroelectric as given in Equation (3).

The *neutral region* is defined as the region in which the electric field is in the vicinity of its coercive value. The *space charge regions* are defined as the areas at each contact where the electric field is large enough to saturate the ferroelectric ($E > E_C+\delta$). Ionized traps may be present in the neutral region. However, the contribution of the ionized traps to the electric field are almost completely compensated by the large polar displacement of the ferroelectric.

The compensation of the ionized charge by the ferroelectric is important; only the neutral region of the ferroelectric has a large permittivity value - the space charge regions at the contacts have the much lower saturated permittivity. The ferroelectric capacitor is a three-layer dielectric sandwich, that is, a high-permittivity layer between two low-permittivity layers. This is the primary insight in the ferroelectric model which follows. By determining the widths of the space charge under bias one can accurately predict the electrical characteristics of the ferroelectric capacitor.

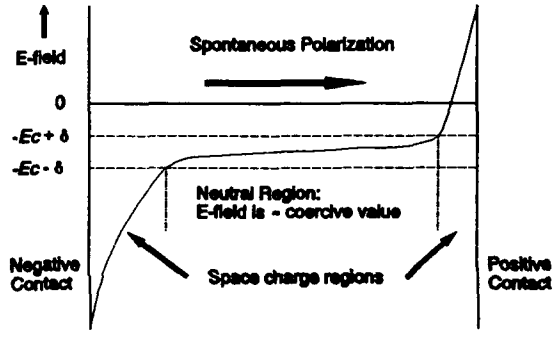


Figure 3 *Electric field as a function of distance in the ferroelectric.*

THE FERROELECTRIC C-V MODEL

Assumptions:

The assumptions for the ferroelectric model are drawn from the discussion above.

1) The ferroelectric has the properties of a wide-bandgap semiconductor. The occupancy of trap states near the band edges changes as a function of the Fermi energy.

2) A metal contact to the ferroelectric forms a Schottky contact with a characteristic Schottky barrier ϕ_B. The difference between the work function of the metal and the electron affinity of the ferroelectric make the metal the anode and the ferroelectric the cathode.

3) Any surface states at the metal-ferroelectric junction can be adequately characterized as a static shift in ϕ_B. No dynamic effects involving the change in occupancy of surface states are considered.

4) The permittivity of the ferroelectric is given by (1). The permittivity is characterized by high peak values around the coercive field E_C, hysteresis, and a lower saturated permittivity for $E >> E_C$.
5) The concentration of immobile ionized states ρ is constant.

Measurements:
All the data for the C-V measurements were taken from a commercial ferroelectric memory integrated circuit. The memory capacitors were measured by probing the integrated circuit. These ferroelectric devices employ a PZT ferroelectric with ruthenium oxide contacts. The capacitors measured 20 microns by 20 microns. All measurements were taken at room temperature.

The Model:
The small-signal C-V model simultaneously solves for the voltages across the space charge regions and the spontaneous polarization across the neutral region. We consider the applied voltage V_{ap}, the voltages across the two space charge regions V_{sc1} and V_{sc2}, and the voltage developed by the spontaneous polarization in the neutral region V_{pol}. The sum of the voltages across the two space charge regions and the voltage across the neutral region is equal to the total voltage applied.

The capacitance of the thin-film ferroelectric capacitor is modelled as the series capacitance of the two space charge and the neutral regions. Because the permittivity of the neutral region is very large compared to the space charge regions, the series capacitance of the neutral region can generally be ignored. The capacitance of the space charge regions follow the formula for Schottky contacts:

$$C_{sc} = \sqrt{\frac{q K \varepsilon_0 N}{2 (V_{sc})}} \tag{4}$$

C_{sc} is the capacitance per unit area across the space charge region, N is trap concentration which is assumed to be equal to the ionized charge density ρ, and V_{SC} is the potential across the space charge region at the junction.

The width of the space charge region W_{sc} is given by:

$$W_{sc} = \sqrt{\frac{2 V_{sc} K \varepsilon_0}{q N}} \tag{5}$$

The total capacitance C_{tot} for the ferroelectric capacitor is equal to the series capacitances of the two space charge region C_{sc1} and C_{sc2} and the capacitance of the neutral region C_{neut}:

$$C_{tot} = \frac{1}{\frac{1}{C_{sc1}} + \frac{1}{C_{sc2}} + \frac{1}{C_{neut}}} \tag{6}$$

To calculate the capacitance of the ferroelectric device as a function of voltage, the values of C_{sc1}, C_{sc2}, and C_{neut} must be determined. The capacitance values can be

calculated from the voltages V_{sc1}, V_{sc2}, and V_{pol}. The sum of these voltages must equal the applied voltage V_{ap}:

$$V_{ap} = V_{sc2} - V_{sc1} + V_{pol} \tag{7}$$

V_{sc1} and V_{sc2} have opposite polarities because the two junctions face in opposite directions.

Equation (7) serves as one constraining equation for the problem. The second constraining equation is simply charge conservation. Therefore, the problem of calculating the C-V behavior of the ferroelectric capacitor boils down to determining how the applied voltage is split between the space charge regions and the spontaneous polarization.

Obtaining the solution is simplified by examining three different voltage ranges: (1) $V_{ap} < 0$, (2) $0 \le V_{ap} \le 2 \cdot VPOL$, (3) $V_{ap} > 2 \cdot VPOL$ ($VPOL$ is the maximum value of the spontaneous polarization V_{pol}). The divisions were selected assuming that the ferroelectric capacitor has been polarized in the negative direction and that the applied voltage is increasing from a negative value to a positive value. If the capacitor was polarized in the positive direction, the three voltage ranges would be chosen with the opposite polarity.

$\underline{V_{ap} < 0:}$

Assume that the ferroelectric capacitor has been fully polarized to its negative state. The negatively biased contact (contact 1) is reverse biased by V_{ap}, V_{pol}, and the Schottky potential ϕ. The other contact (contact 2) is assumed to be at ground potential. Contact 2 is forward biased, and the voltage across it is the Schottky potential only, so its capacitance is constant. The C-V behavior in this voltage range is governed by the width of the space charge at contact 1, the only quantity affected by the applied voltage.

The voltages across the three regions of the ferroelectric are: $V_{pol} = VPOL$; $V_{sc2} = \phi$; $V_{sc1} = -V_{ap} + V_{pol} + \phi$. Using (4) and (6), the overall capacitance is given by:

$$C_{tot} = \frac{1}{\frac{1}{\sqrt{\frac{q K \varepsilon_0 N}{2(-V_{ap} + VPOL + \phi)}}} + \frac{1}{\sqrt{\frac{q K \varepsilon_0 N}{2\phi}}}} \tag{8}$$

The C-V curve of the ferroelectric capacitor follows the Schottky model closely in this region, and provides a good fit to the experimental data (given appropriate choices for $VPOL$, ϕ, and N).

Equation (8) may be used to extract values for ϕ and N from experimental data. ϕ and N are extracted by iteratively optimizing the fit between (8) and the experimental C-V data for the voltage range between the maximum applied voltage and zero.

$\underline{0 \le V_{ap} \le 2 \cdot VPOL:}$

The significant event which occurs over the voltage range $0 \le V_{ap} \le 2 \cdot VPOL$ is the

transfer of the space charge between the contacts. As the applied voltage sweeps across this range, the space charge is transferred from the first contact to the second contact. No switching of the ferroelectric occurs because the neutral region is shielded from the applied voltage by the redistributed space charge.

First, we must look at the endpoints of this voltage range. When $V_{ap} = 0$, (7) gives:

$$\begin{aligned} V_{sc1} &= \phi + VPOL \\ V_{sc2} &= \phi \end{aligned} \tag{9}$$

The spontaneous polarization *VPOL* maintains the equal and opposite space charge voltage V_{sc1}. When V_{ap} increases in the positive direction, contact 2 becomes reverse biased, and the reverse bias on contact 1 is reduced. The space charge on contact 1 shrinks while the space charge at contact 2 grows by an equal amount, as required by charge conservation. When $V_{ap} = 2 \cdot VPOL$, (7) gives:

$$\begin{aligned} V_{sc1} &= \phi \\ V_{sc2} &= V_{ap} + V_{sc1} - V_{pol} = VPOL + \phi \end{aligned} \tag{10}$$

V_{sc1} is now equal to its equilibrium voltage ϕ, and V_{pol} is still equal to its maximum value *VPOL*. Contact 1 is no longer reverse biased, and all the space charge that was at contact 1 has been transferred to contact 2. The applied voltage $2 \cdot VPOL$ is opposed both by the polarization voltage V_{pol} and an additional space charge voltage equal to *VPOL* at contact 2.

The numerical solution to this problem requires two constraints. The first is (7), which establishes the sum of the voltages. The second constraint is charge conservation; the space charge removed from contact 1 must be gained by contact 2. If the space charge regions are assumed to have a constant charge density, the total width of the space charge regions is constant over this range:

$$W_{sc1}(V_{ap}) + W_{sc2}(V_{ap}) = W_{sc1}(0) + W_{sc2}(0) \tag{11}$$

Using (5) and (11) we get an expression for the voltage across one space charge in terms of the voltage across the other:

$$V_{sc1}(V_{sc2}) = \frac{N}{C_X} \cdot \left[W_{sc1}(0) + W_{sc2}(0) - \sqrt{\frac{C_X}{N} \cdot V_{sc2}} \right]^2 \tag{12}$$

C_X is just the collection of constants in (5):

$$C_X = \frac{2 \cdot K \cdot \varepsilon_0}{q} \tag{13}$$

$W_{sc1}(0)$ and $W_{sc2}(0)$ are found by inserting the conditions for $V_{ap}=0$ given in (9) into the equation for space charge width (5). Equations (7) and (12) are combined to find V_{sc1} and V_{sc2}. This is done by numerically solving for the root of the following equation:

$$V_{sc2} = \text{ROOT}\,(V_{ap} - VPOL - V_{sc2} + V_{sc1}(V_{sc2})) \tag{14}$$

The ROOT function varies V_{sc2} until the expression in parentheses equals zero. The value found for V_{sc2} is then inserted into (12) to find V_{sc1}. After the space charge voltages have been found, the Schottky capacitance equations (4) and (6) are applied to find the small-signal capacitance.

$\underline{V_{ap} > 2 \cdot VPOL:}$

When the applied voltage exceeds $2 \cdot VPOL$, the space charge at contact 2 increases with the applied voltage, and the space charge at contact 1 remains at the minimum width established by the Schottky potential ϕ. The polarity of the ferroelectric region engulfed by space charge 2 is switched by the large electric field in the space charge. The ferroelectric in the neutral region retains its original polarity. The voltage due to spontaneous polarization V_{pol} diminishes and then reverses sign as the neutral region is engulfed by space charge 2. When the applied voltage reaches the point where the space charge extends all the way across the ferroelectric, the switching of the ferroelectric is complete.

For this voltage range, V_{sc1} is constant and equal to ϕ, so the width of space charge 1 (W_{sc1}) is constant. The width of space charge 2 (W_{sc2}) is determined by the voltage drop across that space charge.

$$\begin{aligned} W_{sc1} &= \sqrt{\frac{C_X}{N} \cdot \phi} \\ W_{sc2} &= \sqrt{\frac{C_X}{N} \cdot V_{sc2}} \end{aligned} \tag{15}$$

V_{pol} and V_{sc2} are the two unknowns. Since V_{pol} is determined by the W_{sc2}, which in turn is determined by V_{sc2}, we can write V_{pol} as a function of V_{sc2}:

$$V_{pol} = VPOL \cdot \left[\frac{W_{tot} - 2 \cdot W_{sc2}(V_{sc2})}{W_{tot} - 2 \cdot W_{sc1}} \right] \tag{16}$$

This equation calculates V_{pol} in terms of the fraction of the neutral zone which is engulfed by space charge 2. Equations (16) and (7) are combined and the root is found numerically:

$$\begin{aligned} V_{sc2} &= \text{ROOT}[V_{ap} - V_{pol}(V_{sc2}) - V_{sc2} + V_{sc1}] \\ V_{sc1} &= \phi \end{aligned} \tag{17}$$

Once the space charge voltages have been found, the overall capacitance is calculated using the equations for the Schottky junction capacitance (4) and (6).

RESULTS

The results of the C-V model for one sweep vs. the experimental data is shown in Figure 4. The fit of the calculated curve is excellent for applied voltages less than -*VPOL*. This indicates that the Schottky contact model for the capacitance is a good one for this voltage range. The following device parameters were extracted from the C-V data: ϕ = .55v, *VPOL* = .65v, $N = 4 \cdot 10^{18}/cm^3$, K_0=400.

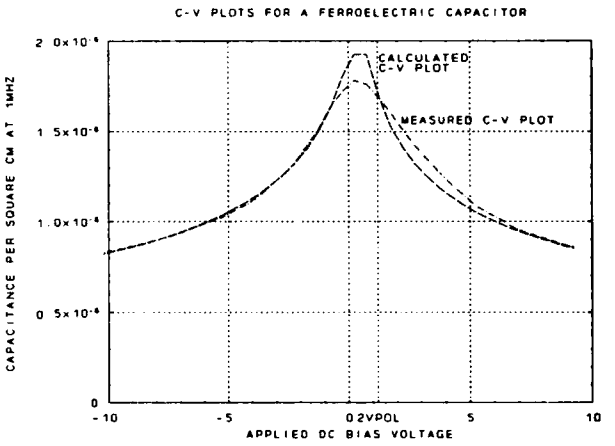


Figure 4 *The calculated C-V plot without compensation for finite permittivity.*

However, the calculated curve deviates from the experimental data for positive applied voltages. Two effects can be observed here. First, the peak calculated capacitance, which occurs in the range $-VPOL \le V_{ap} \le 2 \cdot VPOL$, is significantly greater than the measured peak capacitance. Second, the calculated capacitance is lower than the measured capacitance for much of the range $V_{ap} > 2 \cdot VPOL$.

The anomalous calculated peak capacitance is due to the fact that the series capacitance of the neutral region has been ignored in the previous calculations. When the applied bias is less than the coercive voltage, the permittivity of the ferroelectric in the neutral region declines, and the series capacitance of the neutral region cannot be ignored. The permittivity of the ferroelectric under these bias conditions can be inferred from the difference between the theoretical and measured C-V plots. The adjusted value of the permittivity (K_{eff}) for the low field condition can be calculated by adding the effective capacitance of the neutral region in series with the small signal capacitance of the two space charge regions (C_{tot}).

$$\frac{1}{\frac{1}{C_{tot}} + \frac{1}{\left[\frac{K_{eff} \cdot \varepsilon_0}{W_{tot} - W_{sc1} - W_{sc2}}\right]}} \approx C_{measured} \qquad (18)$$

This calculation yields $K_{eff} \approx 5000$ for $0 < V_{ap} < VPOL$, and $K_{eff} \approx 10{,}000$ for $-VPOL < V_{ap} < 0$ or $VPOL < V_{ap} < 2 \cdot VPOL$. This shows that the permittivity of the neutral region, though always very large, is at its minimum under low biases that are not strong enough to maintain the coercive field (Figure 5).

The second discrepancy between the calculated and measured C-V curves occurs at voltages above $2 \cdot VPOL$, where the measured capacitance values are significantly greater than the calculated values. The capacitance readings of the samples tested were observed to decrease steadily over a period of several minutes when held at a constant DC bias. The C-V plots shown here, on the other hand,

were taken with a constant bias voltage sweep rate of 50 mV per second. These preliminary observations indicate that the measured C-V plot falls much closer to the calculated curve if the capacitance measurement is allowed to stabilize for several minutes at each value of the bias voltage. The slow relaxation of the dielectric properties of the ferroelectric has been attributed to the slow thermalization of deep electron states in the ferroelectric[11-13].

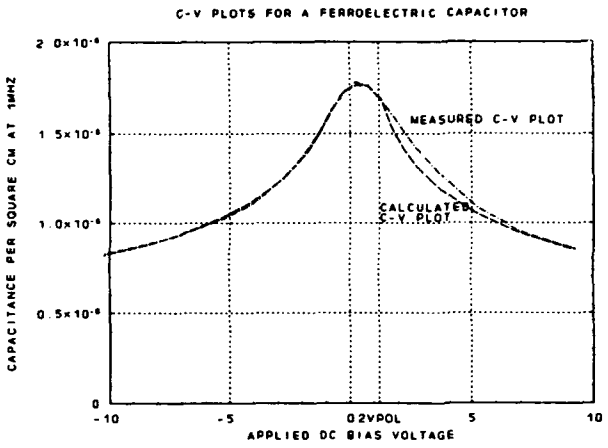


Figure 5 *C-V plot compensated for finite permittivity at low bias voltages.*

CONCLUSION

A model has been derived for the small-signal capacitance vs. voltage (C-V) characteristics of the thin-film ferroelectric capacitor. The ferroelectric capacitor is analyzed from first principles in terms of the interactions between the polar dielectric properties of the ferroelectric and the space charge regions which form due to its semiconducting properties. The ferroelectric capacitor is shown to obey the ideal Schottky contact C-V behavior over the non-switching portion of the cycle. During the switching portion of the voltage sweep, the partial switching of the ferroelectric is shown to be governed by the expansion of the space charge regions. The size of the space charge regions, in turn, is affected by the polarization of the ferroelectric.

This model has a number of immediate applications. First, the C-V model can be used to extract important device parameters: the trap concentration, which indicates the quality of the ferroelectric; the Schottky barrier potential, which permits an appraisal of the metallization quality; the maximum spontaneous polarization; and the saturated permittivity of the ferroelectric. Second, the model gives an accurate way to infer the characteristics of the space charge regions, which are thought to play a significant role in the aging and wear-out of ferroelectric devices[14-16]. Monitoring the C-V characteristics during aging and endurance cycling will provide a means to test those hypotheses. Third, this small-signal model will constitute a significant part of a more complete model in the future, which will be used for circuit-level design work.

REFERENCES

[1] B.H. Meadows, MSEE Thesis, University of Colorado, 1986.
[2] S. Narayan, MSEE Thesis, Michigan Technological University, 1987.
[3] G. Rohrer, S. Narayan, L. McMillan, and A. Kulkarni, *J. Vac. Sci. Technol. A*, **6**, 1756-1758 (1988).
[4] S.E. Adams, MSEE Thesis, Michigan Technological University, 1988.
[5] S.B. Krupanidhi, A. Mansingh, and M. Sayer, *Ferroelectrics*, **50**, 117-122, (1983).

[6] B. Jaffe, W.R. Cook, & H. Jaffe, *Piezoelectric Ceramics*. New York: Academic Press, 1971, ch. 4.
[7] G. Arlt, D. Hennings, G. de With, *J. Appl. Phys.*, **58**, 1619-1625, (1985).
[8] R.R. Mehta, B.D. Silverman, and J.T. Jacobs, *J. Appl. Phys.*, **44**, 3379-3385, (1973).
[9] Fridkin, V.M., *Ferroelectric Semiconductors*. New York: Consultants Bureau, 1980, ch. 3.
[10] V.B. Sandomirskii, S. Khalilov, and E.V. Chensky, *Ferroelectrics*, **45**, 107-115, (1982).
[11] V.M. Fridkin, et al., *Ferroelectrics*, **61**, 299-314, (1984).
[12] L. Jingde, L. Deming, and H. Di, *Ferroelectrics*, **70**, 7-13, (1986).
[13] Z. Liangyixg, Y. Xi, H.A. Mckinstry, and L.E. Cross, *Ferroelectrics*, **49**, 75-79, (1983).
[14] C. Alemany, B. Jimenez, J. Mendiola, and E. Maurer, *Ferroelectrics*, **54**, 141, (1984).
[15] J.F. Scott, and B. Pouligny, *J. Appl. Phys.*, **64**, 1547-1551, (1988).
[16] A.K. Kulkarni, G.A. Rohrer, L.D. McMillan, and S.E. Adams, *IEEE/IRPS*, (1989).

AD-P006 668

FERROELECTRIC MEMORY EVALUATION AND DEVELOPMENT SYSTEM

DAVID W. BONDURANT
Ramtron International Corporation, Colorado Springs, Colorado, U.S.A.

Abstract The Ramtron FEDS-1 is an IBM PC/AT® compatible single board 16-bit microcomputer with 8-Kbyte program/data memory implemented with nonvolatile ferroelectric dynamic RAM. This is the first demonstration of a new type of solid state nonvolatile read/write memory, the ferroelectric RAM or FRAM® memory.

FMx 1208 NONVOLATILE FERROELECTRIC RAM

At the First International Symposium on Integrated Ferroelectrics held in 1989, Ramtron described the FMx 8101 nonvolatile dynamic RAM test vehicle.[1] In January 1991, Ramtron announced the availability of the world's first nonvolatile dynamic RAM built using ferroelectric materials. The FMx 1208 ferroelectric RAM, or FRAM memory, is the first semiconductor memory to combine the read/write performance

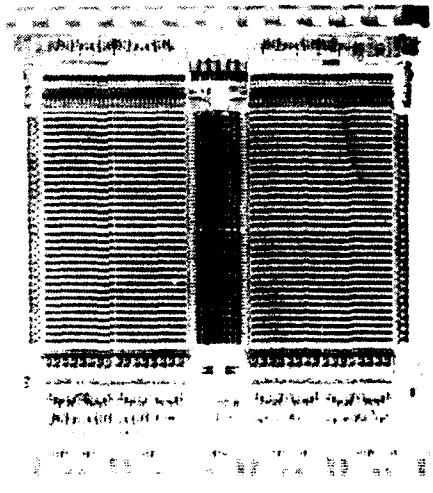


FIGURE 1 FMx 1208 DIE PHOTO

92-16132

and unlimited endurance of DRAMs with the nonvolatility of magnetic memory. The FMx 1208 is a 4,096-bit memory organized 512x8 and fabricated using a 3.0 micron CMOS technology with integrated ferroelectric storage cells.

Each memory bit consists of two transistors and two ferroelectric capacitors (two DRAM cells/bit). The memory operates in two modes: dynamic and nonvolatile. In dynamic mode, the memory uses the high linear dielectric constant of the ferroelectric capacitor to store data in the form of a charge. The memory must be periodically refreshed to restore the charge like a normal DRAM. When a system power loss is detected, the memory can be switched to its nonvolatile mode and data can be polarized into the ferroelectric capacitors to retain data without power. When power returns, the polarization state of the capacitors can be detected to restore the data and continue operation in the dynamic mode.

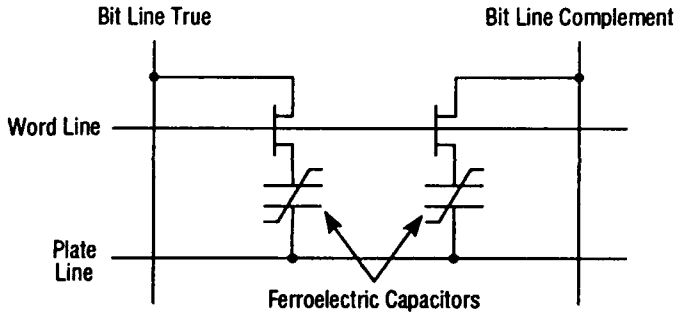


FIGURE 2 DUAL MEMORY CAPACITOR CELL

The memory operates using a single +5 volt power supply with 44mW maximum dynamic power and is TTL/CMOS compatible at all inputs and outputs. Operation is synchronous on the high to low transition of the chip enable input. Read/write cycle time is 500ns and read access is 250ns over the 0-70°C temperature range. The product has a standard bytewide SRAM pinout and is packaged in a 24-pin ceramic DIP. The FMx 1208 serves an engineering evaluation vehicle for a series of higher density ferroelectric memories to be announced later in 1991.

FRAM EVALUATION AND DEVELOPMENT SYSTEM

The FEDS-1 FRAM Evaluation and Development System is an IBM PC/AT compatible single board computer which can be used to functionally evaluate FRAM memory technology and develop the hardware and software for embedded control applications. The microcomputer includes an Intel® 8097 16-bit microcontroller and 8-Kbytes of FRAM main memory (16 FMx 1208 components). The board provides the power sequencing, refresh and memory arbitration control functions necessary to support nonvolatile DRAM operation. The main memory is a true dual port memory which arbitrates between the 8097 microcontroller and host PC processor during operation. This allows the host PC to fully evaluate the operation and data retention of the FRAM memory using its software. The host PC can use the FRAM memory for nonvolatile system storage since it is directly mapped into the PC address space. The host PC can be used to develop application software targeted for the 8097 controller using standard Intel assembler and compiler tools. The final object code can be loaded into the FRAM memory and the microcontroller can be enabled to execute the program. A public domain monitor program is available for the 8097 which allows software to be debugged using single step, software breakpoint, symbolic assembly and disassembly functions.

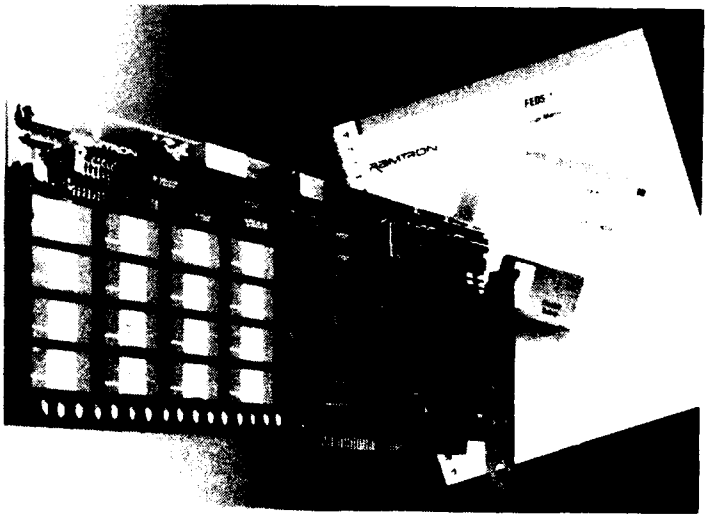


FIGURE 3 FEDS-1 BOARD

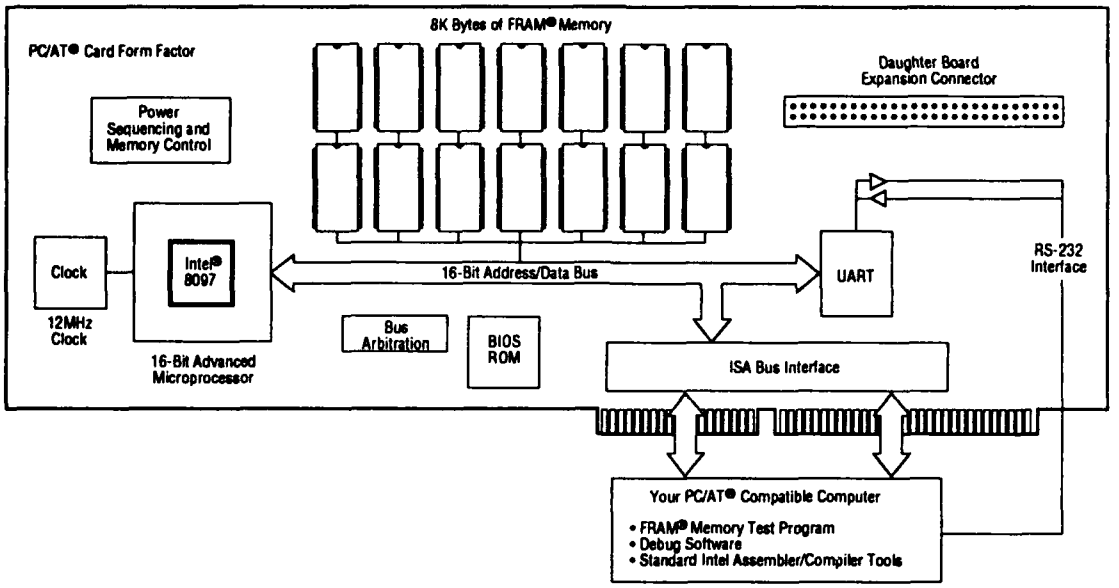


FIGURE 4 FEDS-1 BLOCK DIAGRAM

IMPACT OF THE FERROELECTRIC RAM

The impact of a nonvolatile solid state random access read/write memory with unlimited read/write endurance and a single standard +5 volt power supply on computer systems will be significant. The FMx 1208 demonstrates that a simple DRAM cell structure using a ferroelectric thin film capacitor in two storage modes (dynamic and nonvolatile) can accomplish this objective. The FEDS-1 system demonstrates the architecture for new microprocessor systems with a single ferroelectric RAM memory which stores programs and data which can be altered dynamically at the speed of the computer yet retain all data when power is removed. This flexibility will reduce the total number of memory devices in the system and potentially eliminate the need for ferromagnetic secondary memory devices in many systems.

REFERENCES

1. D. W. Bondurant, *Ferroelectronic RAM Memory Family for Critical Data Storage*, Proceedings of the First Symposium on Integrated Ferroelectrics (March 1989), pp. 212-215.

FRAM is a registered trademark of Ramtron International Corporation. IBM is a registered trademark of International Business Machines Corporation. IBM PC/AT is a product and registered trademark of International Business Machines Corporation. Intel is a registered trademark of Intel Corporation.

CHARACTERIZATION OF PZT FILMS FATIGUED AT LOW FREQUENCY

R. A. LIPELES, B. A. MORGAN, and M. S. LEUNG
Electronic Technology Center, The Aerospace Corporation, El Segundo, CA

Abstract We report a method using SEM, EDX, SIMS, and polarization-voltage hysteresis data to investigate changes that occur in PZT thin films fatigued using low (below 100 kHz) frequency square waves. Fatigue in PZT capacitors can limit the lifetime of destructive readout ferroelectric memories. Identification of physical and electronic changes that occur during fatigue will lead to understanding fatigue mechanisms and the development of improved electrode-ferroelectric interfaces.

AD-P006 669

INTRODUCTION

Fatigue in PZT capacitors can limit the lifetime of destructive readout ferroelectric memories. Identification of the physical and electronic changes that occur during cycling will lead to an understanding of fatigue mechanisms and to the development of improved electrode-ferroelectric interfaces. Reports on the material and electrical properties of thin ferroelectric capacitors,[1] and reviews of ferroelectric materials for nonvolatile random access memories[2] and dynamic random access memories[3] have advanced the understanding of fabrication, switching, and degradation issues. These reports show that the development of ferroelectric films requires a multidisciplinary approach to optimize the physical and electronic properties for memory applications. In this paper, we examine the use of scanning electron microscopy (SEM) with energy dispersive x-ray (EDX), secondary ion mass spectrometry (SIMS), and polarization-voltage hysteresis measurements to characterize the properties of ferroelectric films.

92-16133

EXPERIMENTAL

Ferroelectric lead zirconate titanate (nominal composition $PbZr_{0.5}Ti_{0.5}O_3$) films were prepared by two methods. Thick films (0.5μm thick) were prepared by the method of Lipeles et al.[4] on platinum foil substrates. Silver paint was used to make electrical contact to the film. Thin films (0.1μm thick) prepared by a method similar to Budd et al.[5] were obtained on platinum/titanium/silicon dioxide-coated silicon.[6] Films obtained during early process optimization with evident defects of specific types were selected to demonstrate the use of diagnostic techniques in improving the film properties.

We used a pulse technique to induce and measure the polarization stored in a ferroelectric capacitor. The PUND (for Positive, Up, Negative, Down) technique uses four pulses to characterize the remnant polarization.[7] Starting with the ferroelectric switched to a state of negative remnant polarization ($-P_r$), a positive pulse (P) is used to switch the ferroelectric to $+P_r$. An amount of charge equal to $2P_r$ is measured in a current integrator. Another positive voltage or up pulse, (U), is applied to detect the capacitive part of the displacement current. A negative pulse (N) is applied to switch the ferroelectric to the $-P_r$ state. Finally, another negative or down pulse, (D), is applied to measure the capacitive part of the displacement current starting from $-P_r$. Polarization-voltage hysteresis loops and pulsed

measurements of polarization taken at intervals during cycling were made using an RT66A measuring system obtained from Radiant Technologies in Albuquerque, NM.

RESULTS AND DISCUSSION

Cycling of ferroelectric capacitors results in a loss of their ability to store charge. This phenomenon, known as ferroelectric fatigue, will limit the lifetime of ferroelectric random access memory (FRAM) devices. Fatigue was evaluated in a thin PZT film[6] with a gold upper electrode and a platinum lower electrode. The P–V loops for an unswitched and fatigued capacitor are shown in Figure 1a. The saturated value of the polarization is about three times the remnant polarization due to high capacitance (6.8nF).

The effect of cycling three adjacent capacitors on the same substrate using 100 Hz, 1 kHz, and 10 kHz square waves is shown in 1b. Fatigue does not depend on the frequency or the total time under test, but only on the total number of cycles at these low frequencies.

The hysteresis loop of a fatigued capacitor is compared to the initial loop in Figure 1a. The P–V curve of the fatigued sample shows reduced remnant polarization. After heating the film to about 100°C for 2 minutes, the remnant polarization increased as shown in Figure 2a. The coercive voltage has increased and is consistent with the formation of a low dielectric layer that reduces the electric field in the ferroelectric film. The rate of the fatigue and the magnitude of the coercive energy increase after heating can be used as a rapid test to characterize ferroelectric properties of a film and its resistance to fatigue.

The net polarization, ΔP, obtained from the integrated polarization resulting from the P pulse, P_P, and from the U pulse, P_U, was fitted to the equation

$$\Delta P = (P_P - P_U) = (P_P - P_U)_o \, N^{-n} \qquad (1)$$

where N is the total number of cycles. When the data in Figure 1b were fitted to Eq. (1), the value of the exponent n was 1/4 as shown in Figure 2b.

On this sample, all of the capacitors show a decrease in P_r during fatigue. Heating the fatigued capacitors resulted in the recovery of the initial value of P_r. The changes in the shape of the P-V hystersis loop during fatigue are in agreement with the model presented by Miller et al.[8] In that model, the decrease in the value of P_r and the increase in E_c observed during fatigue is consistent with the formation and growth of low dielectric, nonferroelectric material under the electrodes or domain wall pinning. The response of the P-V loop to heating is consistent with removing defects to restore ferroelectric switching.

Scanning electron microscopy/energy dispersive x-ray (SEM/EDX) is a technique widely used for the physical and chemical characterization of coating and bonding problems. Because ferroelectric films are insulators, problems with charging can affect image quality in the SEM. Samples with very low conductivity (usually the best samples) will often need either a thin coating of carbon or gold to act as a conducting layer or a beam of ions to neutralize the charge on the surface. The micrographs in Figure 3 show the effects of annealing gold

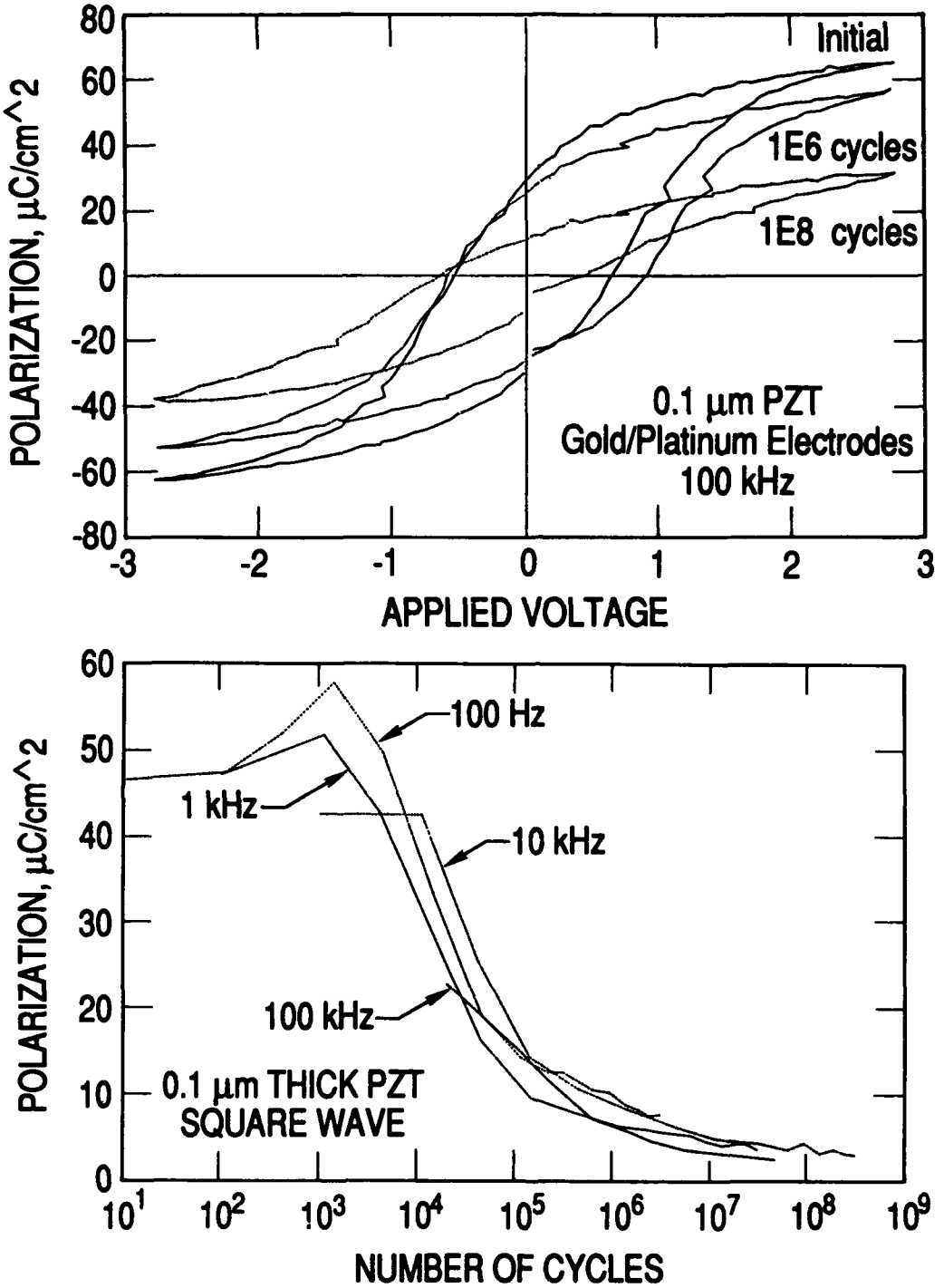


FIGURE 1. (a) Polarization-voltage hysteresis curves with gold electrodes prior to cycling and after cycling 10^6 and 10^8 cycles. (b) degradation of switched polarization.

electrodes on thin PZT films. Prior to annealing, the gold electrode shown in Figure 3a is a conformal film with a smooth edge as defined by a shadow mask. Little charging of the surface occurred. This observation can be explained by the trace amount of gold found over most of the surface by EDX. After annealing at 650°C (Figure 3b), a liquid-like flow has occurred leading to an uneven edge and more gold on the surface. These results show that gold is

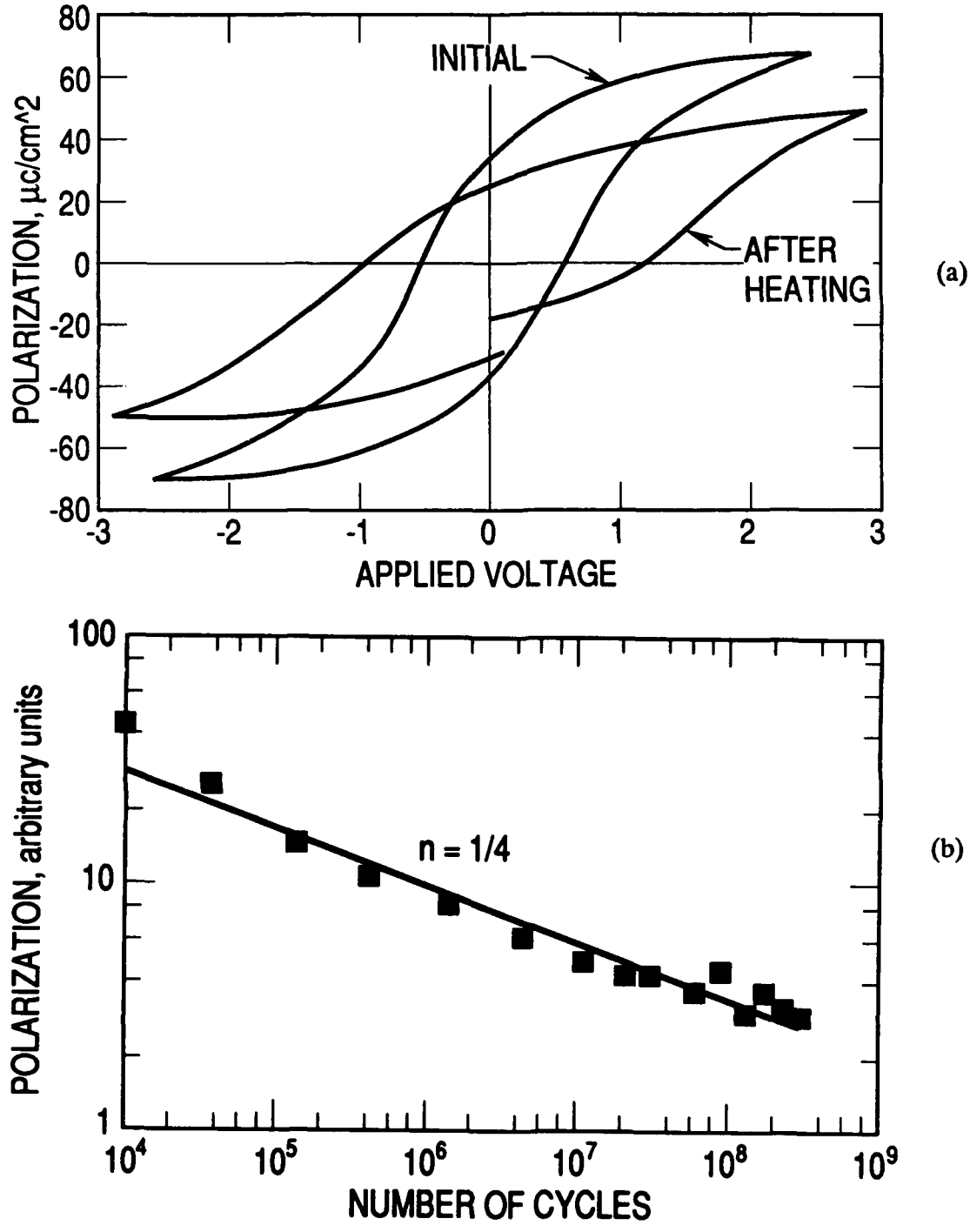
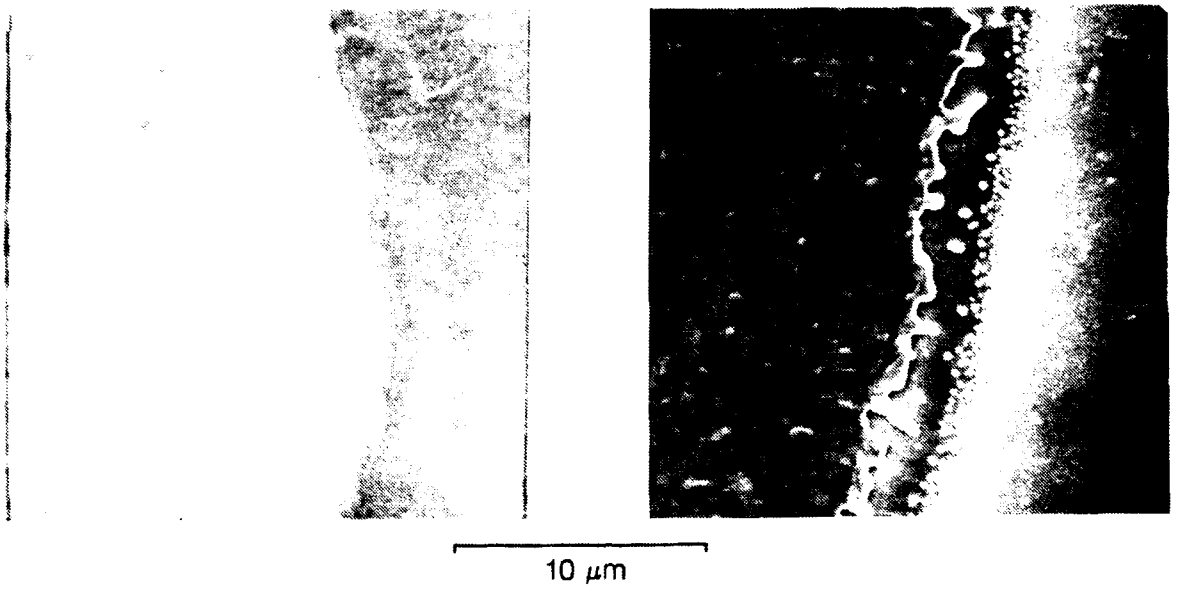


FIGURE 2. (a) Affect of heating a fatigued sample compared to original P–V curve. (b) Fit of net polarization and number of cycles to (Eq.) 1.

extremely mobile on the surface at the annealing temperature. Darkening of the film where the gold has receded indicates a reaction with the film that can alter the composition of the PZT and affect its switching properties. SEM was used to investigate the source of shorting in a capacitor. On another thin film shown in Figure 3c, cracks were observed in the underlying platinum layer. The cracking pattern indicates that the sputtered platinum film was deposited



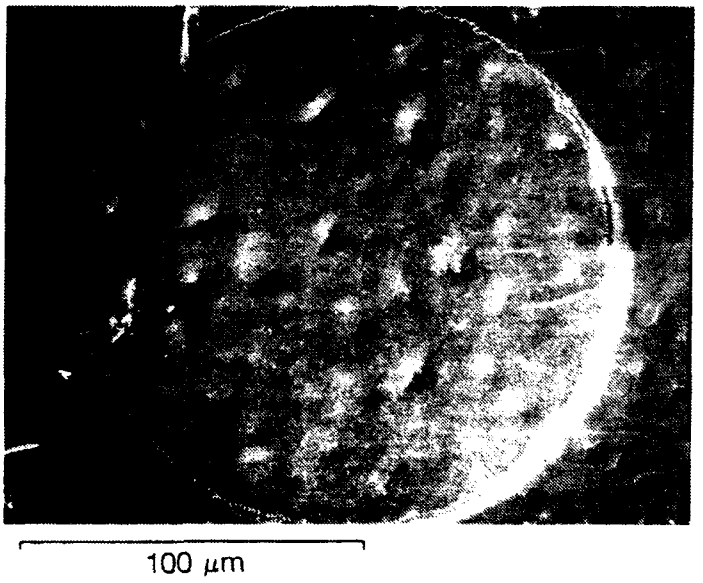


FIGURE 3. Electron micrographs of gold electrodes on PZT films: (a) unannealed, (b) annealed at 650°C for 15 minutes, (c) platinum bottom electrode cracking.

under compression. Sputtering conditions could be altered to increase tension in the film and eliminate the cracking. The effect of switching on the morphology of a thick PZT film on platinum was investigated using SEM. Silver paint electrodes were used as temporary top electrodes on a thick PZT film. After switching through about 10^6 cycles, the capacitor developed high conductivity. The silver electrodes were removed with toluene in an ultrasonic bath. The micrograph in Figure 4a showed that small areas of the PZT film pulled out, leaving

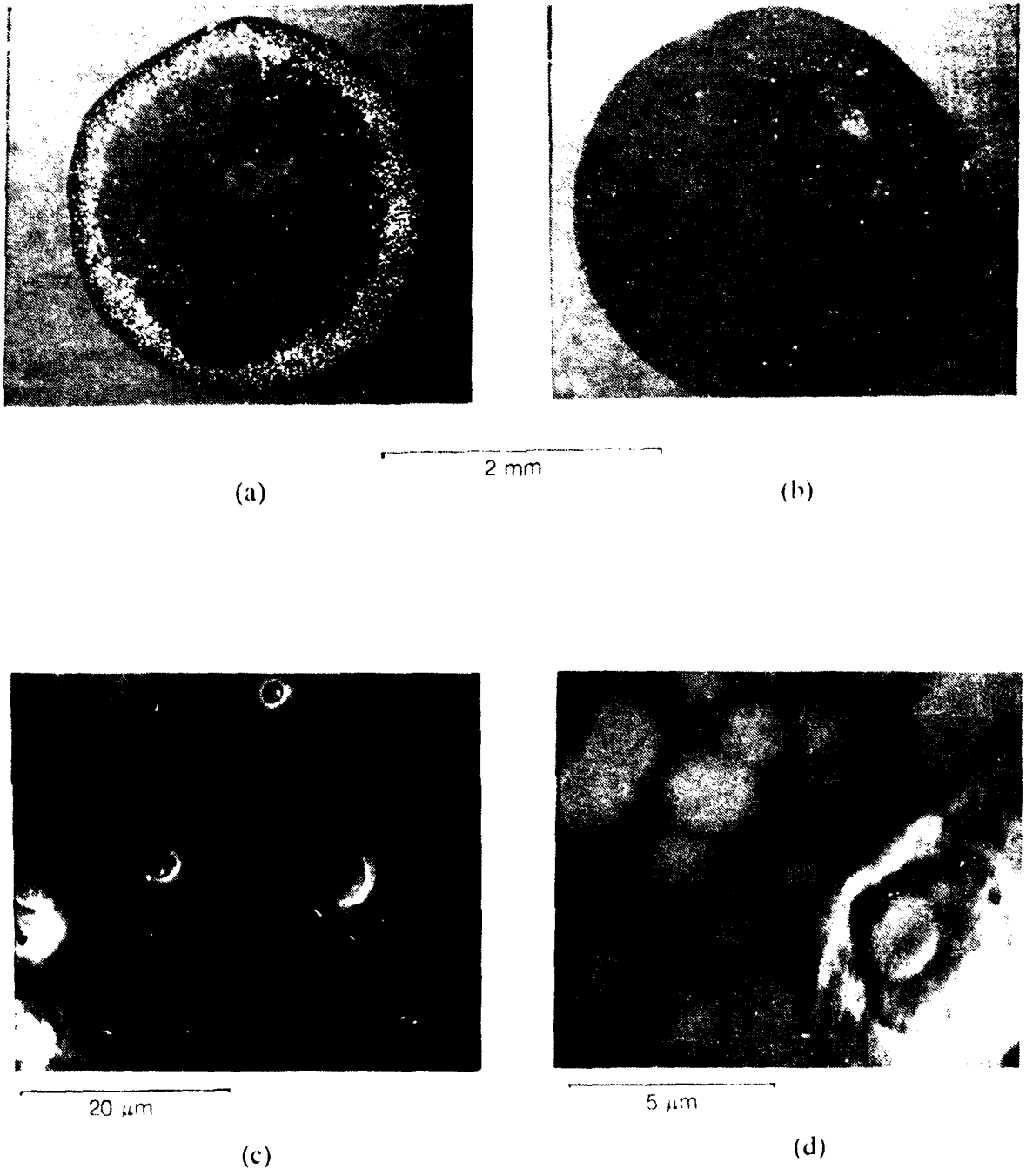


FIGURE 4. Electron micrographs of thick PZT after removal of silver paint electrodes: (a) shorted capacitor with about 10^6 cycles. (b) capacitor with about 10^4 cycles. (c) and (d) defects on cycled capacitors.

behind holes near the edge. For comparison, an area of PZT with an electrode that was not extensively cycled showed no holes after the electrode was removed (see Figure 4b). At higher magnification, holes are clearly seen in the film in Figures 4c and 4d. EDX data revealed platinum at the bottom of the holes and a trace of silver remaining on the surface. The sample also showed the gray, circular blooms reported by others.[1] The composition of these gray

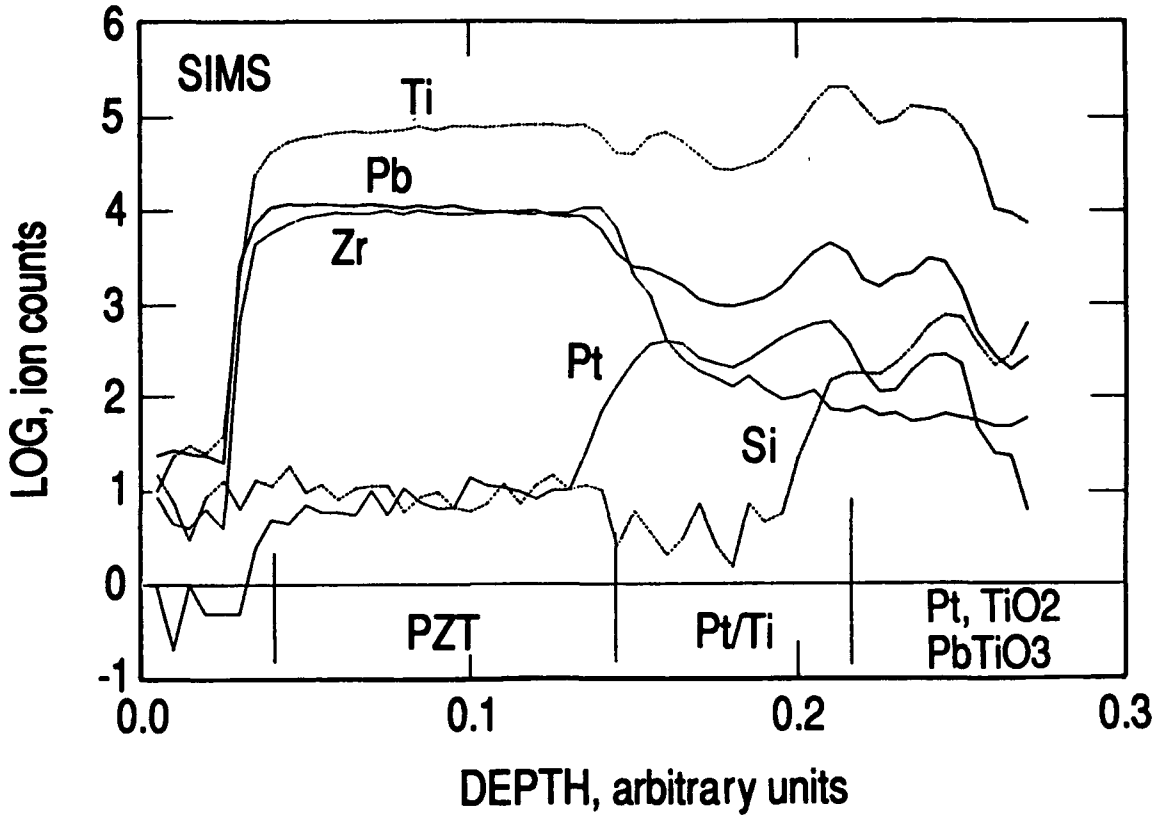


FIGURE 5. Profile of gold/PZT/platinum/titanium/silicon dioxide films on silicon obtained by secondary ion mass spectrometry. Sample was annealed at 650°C for 30 minutes. Gold was not detected due to low instrument sensitivity.

areas was analyzed by EDX and found to be the same as the surrounding film. Switching the ferroelectric film apparently developed cracks that weakened the film, caused shorting, and allowed the film to be pulled out during ultrasonic cleaning. No such spalling was observed in nonswitched areas.

Depth profiling by secondary ion mass spectrometry (SIMS) analysis of the electrode interfaces of thin, annealed PZT films was carried out to study the effects of annealing on electrode metallizations and changes in composition during fatigue. The structure of the interface of gold on PZT/platinum/titanium/silicon dioxide on silicon is shown in Figure 5. Fatigue did not affect the structure of any interfaces. The PZT layer was very uniform whether or not it was fatigued. The lead and zirconium concentrations fall simultaneously with the rise of platinum. However, extensive interdiffusion of the titanium layer and platinum occurred in the original titanium layer. A small amount of lead has also diffused into the titanium layer. Auger electron spectroscopy is being done to determine whether the platinum, titanium, and lead exist as an alloy or as lead titanate. The formation of an oxide could contribute to poor adhesion of the platinum electrode on the semiconductor. A platinum silicide (probably Pt_2Si) is formed on the silicon. The extent of the silicide formation can be used to characterize the annealed interface.

SUMMARY

Electrical and physical techniques have been discussed that are useful in characterizing ferroelectric films and capacitors. SIMS was used to characterize the PZT/platinum/silicon interfaces. Physical changes to cycled PZT capacitors were investigated with SEM/EDX. P-V hysteresis and pulse measurements were used to characterize the electrical properties of PZT films cycled at low frequency. Further investigation of the physical and electronic changes that occur during fatigue in specific structures will help to understand fatigue mechanisms and the development of improved electrode-ferroelectric interfaces.

ACKNOWLEDGMENTS

We thank N. Marquez for the SIMS data, G. Eng and G. W. Stupian for technical discussions, and L. Sanchez and I. Nauk at McDonnell-Douglas Microelectronics for some of the PZT films used in this work.

REFERENCES

1. Better Ceramics Through Chemistry, Mat. Res. Soc., San Francisco (April 1990).
2. J. F. Scott and C. A. Araujo, Science, 246, 1400-1405 (1989).
3. L. H. Parker and A. F. Tasch, IEEE Circuits And Devices, 17-26 (January 1990).
4. R. A. Lipeles, D. J. Coleman, and M. S. Leung, in Ultrastructure Processing of Advanced Ceramics, edited by J. D. Mackenzie and D. Ulrich, (Wiley Interscience) 919-924, (1986).
5. K. Budd, S. Dey, and D. A. Payne, Better Ceramics Through Chemistry II, 73, 711-716 Mat. Res. Soc (1986).
6. L. E. Sanchez, D. T. Dion, S. Y. Wu, and I. K. Naik, Ferroelec., 116, 1-17 (1991).
7. J. F. Scott, C. A. Araujo, H. B. Meadows, L. D. McMillan, and A. Shawabkeh, J. Appl. Phys., 66, 1444-1453 (1989).
8. S. L. Miller, R. D. Nasby, J. R. Schwank, M. S. Rodgers, and P. V. Dressendorfer, J. Appl. Phys., 68, 6463-6471 (1990).

AD-P006 670

ASPECTS OF FATIGUE AND RAPID DEPOLARIZATION IN THIN FILM PZT CAPACITORS *

R. D. NASBY, J. R. SCHWANK, M. S. RODGERS, AND S. L. MILLER

Sandia National Laboratories, Albuquerque, New Mexico, U.S.A., 87185

Abstract Discrepancies in switched polarization values obtained with pulse measurements and hysteresis measurements have been observed in ferroelectric PZT thin film capacitors. We attribute the differences as partially due to the effects of rapid depolarization. To measure rapid depolarization a pulse was applied to pole a ferroelectric capacitor; and then a second identical pulse of the same polarity was applied after a specified time. Significant switched charge was observed after the second pulse. This depolarization was observed to occur in the time frame from microseconds to seconds.

Secondly, the effect of cycling voltage on fatigue was studied on several samples processed by different vendors. A strong dependence on voltage was obtained for one sample which was characterized using a voltage activation approach. A second sample showed no appreciable effect of cycling voltage on fatigue. The difference in behavior demonstrates that the dependence of the fatigue mechanism on voltage can vary significantly depending on the sample.

* This work preformed at Sandia National Laboratories was supported by the Defense Advanced Research Projects Agency and by U.S. Department of Energy (DE-AC04-76DP00789).

92-16145

INTRODUCTION

Interest in nonvolatile ferroelectric, FE, memories has significantly increased in recent years[1,2]. Lead-zirconate-titanate, PZT, is the primary material for the thin film memory development. The number of detailed studies of the low frequency electrical response of PZT films, as well as the number of studies of transient or short time switching behavior of capacitors has increased. These studies are necessary in order to understand the behavior of the materials at the operational speeds of integrated circuit memories. One effect observed is that pulsed measurements of switched charge do not always agree with values of remanent polarization obtained from low frequency hysteresis data. This may be attributed to loss of polarization which occurs as a function of time after the applied field is removed or reduced. In the first section of this paper, we report on measurement of this loss of polarization, which we call rapid depolarization. This effect has also been referred to as ΔP_0[3].

We have also investigated the effect of cycling voltage on device fatigue by varying the electric field across ferroelectric thin film capacitors. Establishing the fatigue characteristics of the FE material is important to determine memory reliability and operational life performance. It is also important to identify mechanisms that may accelerate fatigue and provide the potential for accelerated life and reliability tests. Specifically, we examine whether or not the fatigue mechanism is accelerated by voltage. To date no parameter

has been identified for establishing the reliability of FE devices from accelerated life tests.

RAPID DEPOLARIZATION EFFECTS

General Discussion And Measurements Techniques

Studies of depolarization were conducted on FE capacitors at room temperature, 23°C, using a Sawyer-Tower circuit[3]. Figure 1 illustrates the applied voltage pulse train and the voltage across the integrating capacitor. The voltage across the integrating capacitor is proportional to the FE thin film polarization. Preceding this pulse sequence the capacitor had been poled in a negative direction, such that the first pulse represents the switched charge obtained during a polarization reversal. The second pulse represents the nonswitched charge measurement. The time between these two pulses was varied to vary the depolarization time.

If no depolarization occurs during this time then the voltage across the integrating capacitor should be the same after the second pulse as immediately before the pulse. No charge should switch due to the second pulse; however, this is not the case. The second pulse results in an increase in voltage on the integrating capacitor. This is indicated by the difference in voltage immediately before and immediately after the pulse returns to zero. For this paper, this difference is defined as representing the rapid depolarization occurring during the depolarization time, t. The switched charge equals $C\Delta V$. This behavior was studied by Abt^3 and the switched charge was designated as ΔP_0.

Often the depolarization effect is also apparent in the decay of the voltage across the integrating capacitor after the field becomes zero. This is also illustrated in Figure 1. This decay does not correspond to circuit RC time constants. For instance, the decay through the 1 megohm input impedance of the digitizer used to measure the capacitor voltage would be of the order of milliseconds where depolarization can be observed in tens of microseconds. The observed decay will be further discussed in a following paragraph.

For this study the pulse width was a constant value of 10 microseconds with rise and fall times of 300 nanoseconds. The integrating capacitor voltage was measured within 500 nanoseconds of the time when the applied field became zero in order to obtain depolarization data valid in the microsecond range. The shortest depolarization time measured was 0.7 microseconds.

Depolarization Data

Depolarization data is shown for two different samples in Figures 2 & 3. The samples were fabricated by solution deposition techniques by two vendors; the first by Krysalis and the second by National Semiconductor. The switched charge density on the y axis equals $C\Delta V/A$, where A equals the area of the test capacitor. This value indicates the amount of depolarization occurring in the time t. Both figures include data taken on samples which were cycled to 1E6 cycles. These data represent samples which had suffered little or no fatigue. For the second curve in Figure 2, the sample was cycled to 2.5E9 cycles

at 10 volts which caused the remanent polarization, Pr, to decrease to approximately half its original value.

As indicated, significant depolarization occurred. For the Krysalis capacitors the amount of depolarization at longer times equals 25-30% of the Pr value obtained from hysteresis curves taken a 10 kHz. The initial value of Pr equaled 8.0 $\mu C/cm^2$ and after cycling equaled 3.9 $\mu C/cm^2$. For these samples, depolarization occurs over a long time period, with an asymptote being approached in the time regime of seconds. For times less than a microsecond, little depolarization appears to take place.

The data on National capacitors in Figure 3 indicates a more rapid depolarization. Most of the depolarization has occurred by the 100 microsecond time frame. The amount of depolarization is significant when compared to the Pr value of 5.6 $\mu C/cm^2$ obtained from 10 kHz hysteresis curves. A rapidly measured Pr, before significant depolarization, would equal approximately 8.7 $\mu C/cm^2$.

The depolarization times varied considerably between the two samples. However, for both samples the data indicate little depolarization would be observed during a fast write/read at IC operational speeds and that total depolarization would occur for cases of long data retention. For intermediate times, often occurring in c apacitor testing, the measurement values could vary depending on the measurement speed.

Effects of Depolarization on Retention Analysis

The interpretation of data, such as the retention data in Figure 4, may be affected by rapid depolarization. These

results will be described to illustrate that short time retention data may include both effects of aging and depolarization. First the measurement technique is described.

The plots in Figure 4 are of the retention, depolarization, and 2Pr data for the Krysalis capacitors which exhibited the slow depolarization behavior. To obtain the data in Figure 4 the sample was tested with the retention pulse sequence shown in Figure 5. This sequence was repeated after a specified time to obtain the retetention data as a function of time. The first pulse yields the retention data, while 2Pr is obtained from the 2nd and 3rd pulses. The depolarization data was taken using a similar pulse sequence except the last pulse was positive. The first pulse then yielded the depolarization data as a function of time. Following the depolarization sequence, the retention sequence was rerun to verify sample stability. There was some drift between the retention data sets presumably due to the combined affects of aging during the time between pulses and deaging due to the pulse sequences. The agreement was sufficient, however, to illustrate the general behavior discussed in following paragraphs.

The retention data were measured following the first pulse approximately 10 microseconds after the field was zero. All subsequent measurements of 2Pr and depolarization were taken at the same time after the appropriate pulse became zero. A longer time elapsed after the pulse became zero and the measurement was taken than for the previous depolarization data, because a different and slower test set up was used. However, if you assume that the depolarization decay rate is the same

for switched and nonswitched pulses and for negative or positive pulses, all measurements would include equal amounts of depolarization. For the sample set shown this was approximately the case; however, in general, the decay behavior was not symmetric with pulse polarity. The decay behavior for the positively switched and nonswitched pulses appeared the same.

With these assumptions and referring to Figure 4, the value for 2Pr equals the sum of the retention and the depolarization values. This is shown to be the case. Note that the slope of the decay is different for the retention data than for both the retention+depolarization data and 2Pr data. This is because the retention data include both the effects of depolarization and aging, while 2Pr data include only aging. Thus, modeling the physical process of aging by using retention data could lead to erroneous conclusions. Also, the retention value is the relevant value for memory operation, and values of 2Pr can significantly overestimate the switchable charge.

VOLTAGE DEPENDENCE ON FATIGUE

The dependence of fatigue on the electric field is important for defining device operational voltage and the cycling life of a device. It is also of interest to determine if field activation of fatigue occurs, providing a means for accelerated testing of fatigue.

For fatigue tests, capacitors were cycled from 5 to 10 volts using a 300 kHz sinusoidal signal at 23°C. The hysteresis behavior was measured automatically at specified times at the cycling voltage using a 10 kHz

sinusoidal signal. Pr values were determined from the hysteresis data. Samples from two different vendors were studied and the results for the first sample are given in Figures 6 & 7 and for the second in Figure 8.

In Figure 6 the fatigue is characterized by examining the effect of the voltage during cycling on the normalized remanent polarization. After some early changes in the normalized Pr values, a region of rapid decay occurs which is approximately linear in log cycles. The data were analyzed in this region to obtain the field dependence.

The number of cycles necessary to produce a given fractional decay in Pr was determined for each voltage. In figure 7 the log of the number of cycles which results in Pr being reduced to 0.7 of its original value is plotted versus the inverse voltage. A linear dependence is obtained, which is expected if the degradation in Pr is field activated. This behavior indicates that analytical tools and techniques developed to analyze activated processes[4] may be applied to describe FE fatigue. The field dependence of diectric breakdown with time has also been described with a model based on voltage activation[5]. Such dependence has been modelled by Carlos A. Pax de Araujo, et.al. and reported at this conference[6].

A second set of samples from a different supplier was studied and the results are shown in Figure 8. For these data there appears to be no discernible effect of electric field on fatigue to within sample-to-sample variations. Thus, we observed a large difference in the effect of cycling voltage on fatigue on samples from two suppliers. These results indicate each sample type needs

to be investigated, and that using voltage for accelerated testing may not be generally applicable.

SUMMARY

Depolarization has been measured on PZT thin films from two suppliers. The results are summarized as:
(1) Significant rapid depolarization of charge has been observed; ranging from approximately 25 to 50% of Pr.
(2) The time for most of the depolarization to occur varied from milliseconds to seconds for the two sample types.
(3) Short time retention data may contain components of both aging and depolarization.
(4) Depolarization effects can produce discrepancies between slow and fast performance measurements.
(5) Because of depolarization, one detects switched charge when poling with a nonswitching pulse (i.e. write and read pulses of same polarity). This effect decreases the difference in sensed charge for detecting a stored "1" or "0" and thus decreases the sensing margin in the determination of a stored bit.

Very different response of fatigue to electric field during cycling has been observed on samples from two suppliers. One data set indicated a strong dependence of fatigue with electric field and agreed well with a voltage activation model. The second sample exhibited little or no electric field dependence. These results indicate that increasing the voltage accelerates fatigue for some materials, but not necessarily for all materials.

Acknowledgments The authors acknowledge G. Goddard for his technical assistance.

REFERENCES

1. Ferroelectric Thin Films, MRS Symposium Proceedings, 200 (1990).
2. Proceedings of the Second Symposium on Integrated Ferroelectrics, 116, 1-2 (1991).
3. N Abt, MRS Symposium Proceedings, 200, p. 303 (1990).
4. S.L. Miller, P.J. McWhorter, W.M. Miller, and P.V. Dressendorfer, submitted J. Appl. Phys.
5. J. Lee, I.C. Chen, and C. Hu, Proc. 26th IRPS, p. 131 (1988).
6. C.A. Araujo, T Mihara, A.S. Carrico, R. Zuleeg, L.D. McMillan, Third International Symposium on Integrated Ferroelectrics (1991), this conference, to be published.

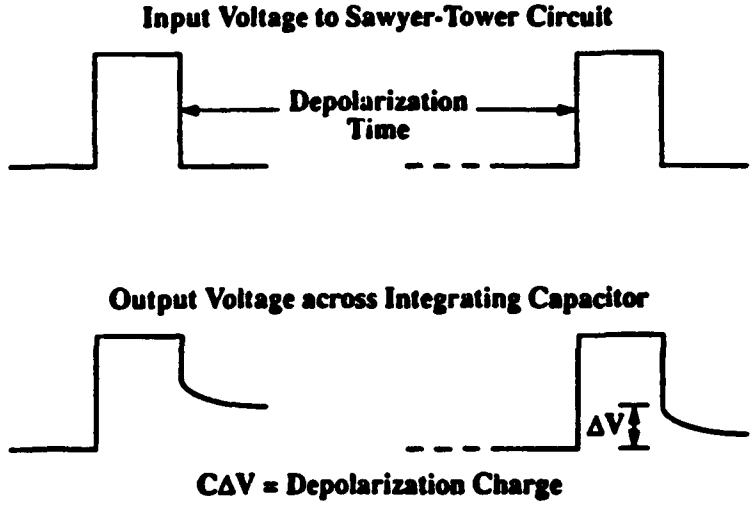


FIGURE 1. Input and output waveforms for the depolarization measurement.

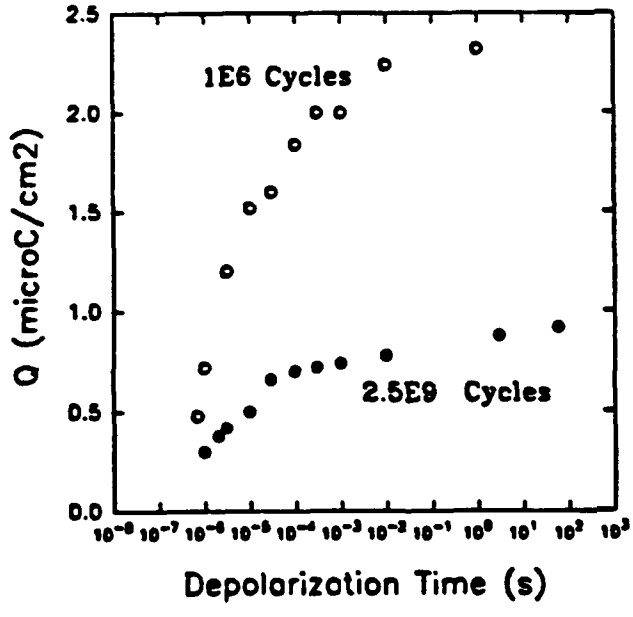


FIGURE 2. Amount of depolarization charge versus the depolarization time for a sample which had been cycled first to 1E6 cycles and then 2.5E9 cycles. The sample was fabricated by Krysalis.

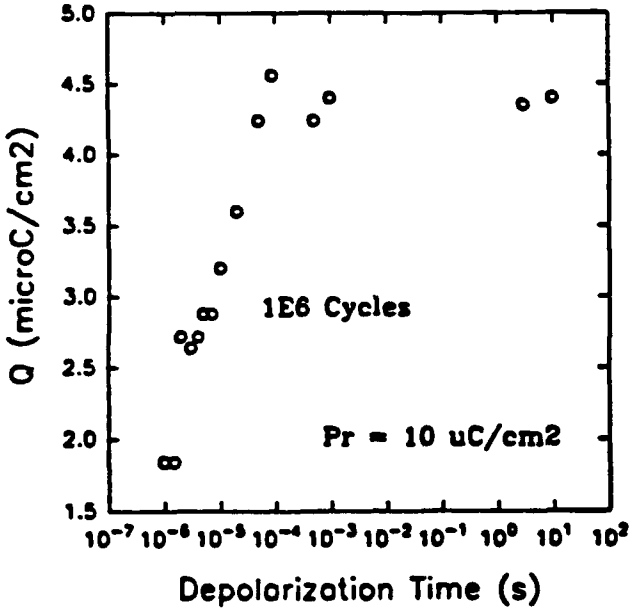


FIGURE 3. The depolarization charge versus time for a sample fabricated by National Semiconductor and cycled to 1E6 cycles.

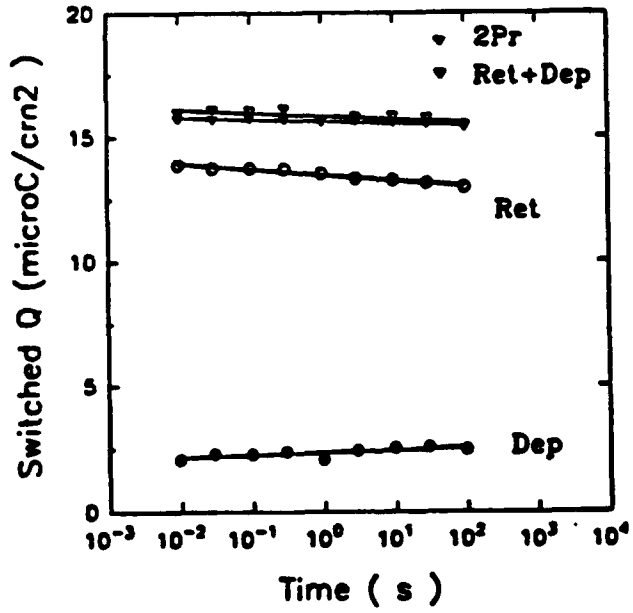


FIGURE 4. Plot of depolarization, retention, 2Pr, and the sum of the retention and depolarization. The sample was similar that shown in Fig. 2 and exhibited continued depolarization in the time frame of seconds.

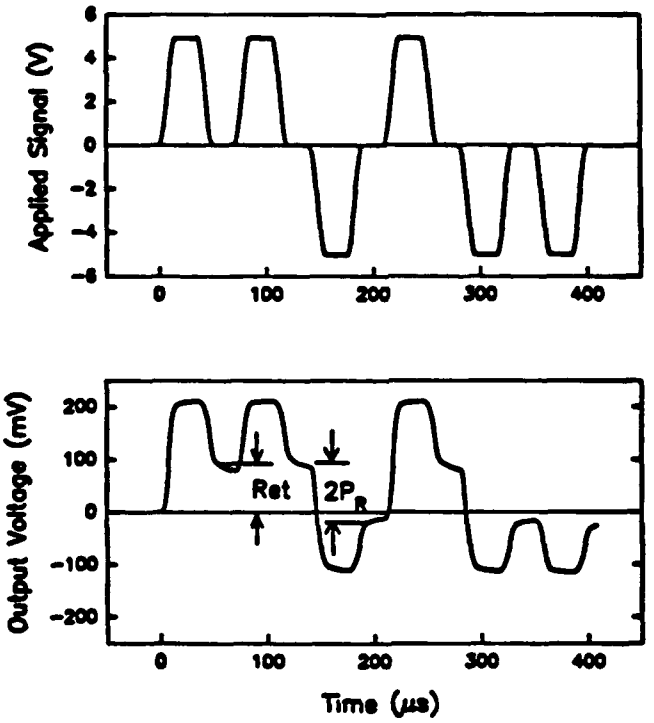


FIGURE 5. Input and output waveforms for the measurements of retention and 2Pr shown in Fig. 4.

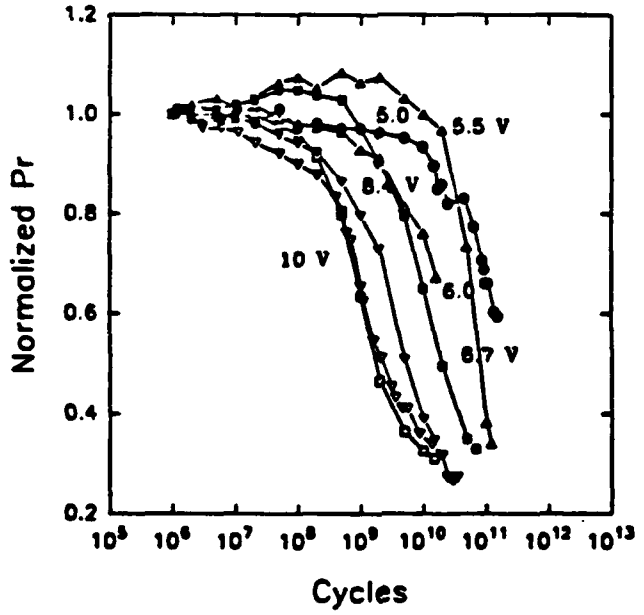


FIGURE 6. The effect of cycle voltage on fatigue. The Pr values were normalized to their value after an initial 1E6 cycles. The sample thickness was 400 nanometers.

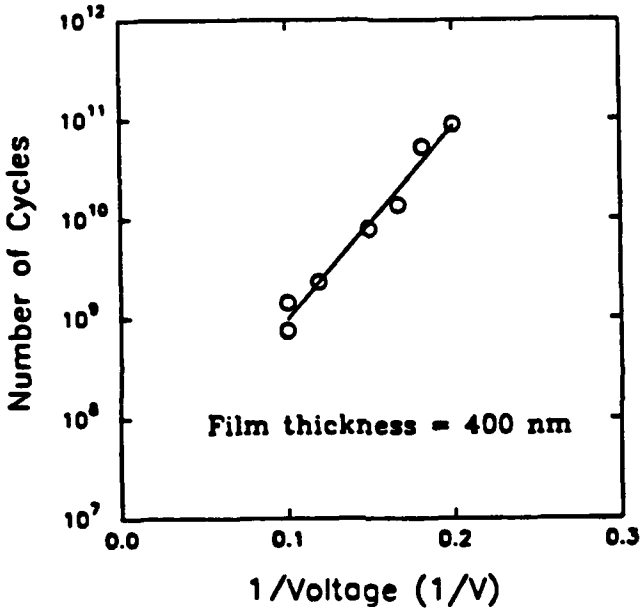


FIGURE 7. Voltage activation of fatigue. The number of cycles which produced a degradation in Pr to 0.7 of its initial value is plotted versus the reciprocal applied voltage. These data were determined from the results shown in Fig. 6.

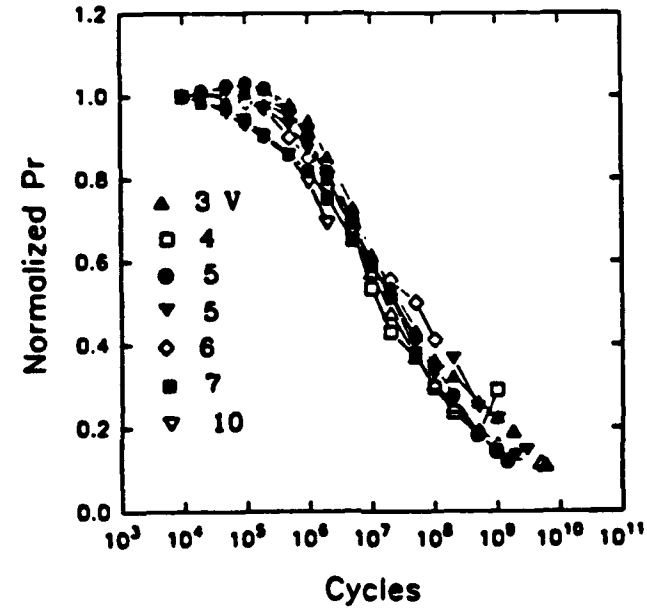


FIGURE 8. Fatigue as a function of applied voltage for a sample which was 170 nanometers thick. No discernable voltage acceleration is apparent.

AD-P006 671

INTEGRATION OF FERROELECTRIC PZT CAPACITORS WITH GaAs JFET DEVICES

S. Y. WU AND W. A. GEIDEMAN
McDonnell Douglas Electronic Systems Company, 5301 Bolsa Avenue, Huntington Beach, CA 92647

Abstract. This invited paper presents the development work on integration of ferroelectric PZT capacitors with GaAs JFET devices for the fabrication of high density nonvolatile ferroelectric random access memories at McDonnell Douglas Electronic Systems Company. The paper will start with the preparation and characterization of various properties of the PZT films deposited by a sol-gel technique. It will be followed by the two approaches investigated for the formation of the p+ gates of GaAs JFETs: zinc diffusion and zinc implantation. The process compatibility and sequence of memory fabrication incorporating these two approaches will be described. The difficulties associated with the zinc diffusion approach will be discussed. Finally, the current effort in the integration of the PZT capacitors and the implanted GaAs JFETs will be presented.

INTRODUCTION

The revived interest in the nonvolatile ferroelectric random access memory (FERRAM) incorporating a ferroelectric thin film with semiconductor technology can be reflected from a large number of papers and attendees at the two recent ferroelectric conferences (1,2). Several companies including the McDonnell Douglas Electronic Systems Company (MDESC) have been exploring, designing and fabricating various device structures and memory configurations(3-7). This invited paper intends to present the results of investigation on the integration of lead-zirconate-titanate (PZT) capacitors with GaAs junction field-effect transistor (JFET) devices performed at MDESC under a DARPA contract. We are currently developing a 4K/2K nonvolatile FERRAM (15). The basic memory cell consists of one transistor-one capacitor per cell (for the 4K memory) or two transistors-two capacitors per cell (for the 2K memory). The cross-sectional view of the one transistor-one capacitor cell structure and its equivalent circuit are illustrated in Figure 1. The PZT capacitor is fabricated alongside the GaAs JFET on the same wafer. This structure offers more flexibility for the integration and optimization of both the PZT capacitor and the GaAs JFET.

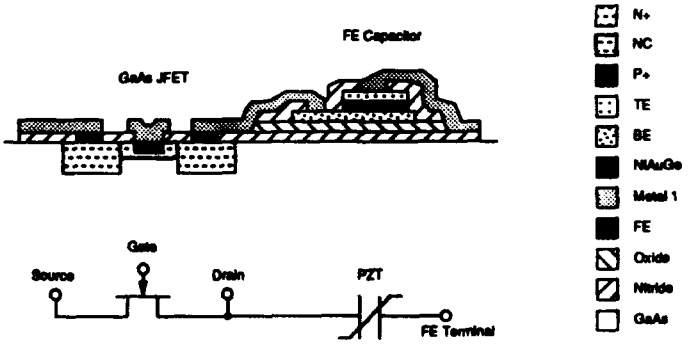


FIGURE 1. Cross-sectional view and the equivalent circuit of one transistor-one capacitor memory cell.

Several areas which require special attention in the integration of a PZT capacitor and a GaAs JFET have been investigated, namely: PZT capacitor, GaAs JFET, process compatibility and sequence of integration, and interconnects and dielectric crossovers. They are highlighted in Table 1. In this paper, we will start with the PZT film preparation

92-16146

and characterization of various properties. It will be followed by the sections describing the approaches taken to form the p+ gate, and the process compatibility and sequence of integration of the GaAs JFET with the PZT capacitor for each approach. The current status on the progress of the program will be presented in the last section.

- **PZT CAPACITOR**

  Composition, Structure, Surface Morphology, Film Thickness, Capacitor Size, Contact Electrode, Passivation Layers, Delineation Method, Polarization, Coercive Voltage, Switching Speed, Endurance, Retention, etc.

- **GaAs JFET**

  Source, Drain and Channel Implantations

  Gate Formation (Threshold Voltage = 0.2 volt)

  Ohmic Contacts

- **PROCESS COMPATIBILITY AND SEQUENCE OF FABRICATION**

- **INTERCONNECTS AND CROSS-OVER DIELECTRIC LAYER**

TABLE 1. Key considerations for PZT capacitor and GaAs JFET integration.

PZT FILM PREPARATION AND CHARACTERIZATION

The PZT films are prepared by a sol-gel technique [8]. The precursor materials used are lead acetate, titanium isopropoxide and zirconium n-propoxide. One part of the solution of lead acetate dissolved in methoxyethanol is mixed with a methoxyethanol solution containing zirconium n-propoxide. The other part of the lead acetate solution is mixed with another methoxyethanol solution containing titanium isopropoxide. The final stock solution is formed by mixing these two lead acetate solutions, boiling for a few minutes and slowly cooling to room temperature.

Before spin coating the film, a chemical additive, formamide, is added into the stock solution. Formamide modifies the hydrolysis, polymerization and crystallization processes of the film to prevent it from cracking during the drying and sintering operation [9,10]. After spin coating the film, it is dried and sintered in air at 650°C for 15 minutes. The flow diagram showing the preparation of the PZT films is given in Figure 2.

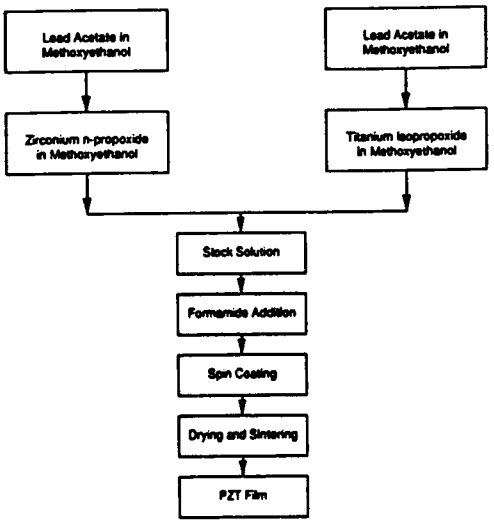


FIGURE 2. Flow diagram for the sol-gel preparation of PZT films

The properties of the PZT films are characterized by various analytical and electrical techniques. The x-ray diffraction (XRD) analysis is used to determine the structure and the phase of the films. Figure 3 shows XRD patterns of a 1200Å (top) and

a 600Å (bottom) films measured with a small angle Norelco modified x-ray system using an angle of incidence of 1.5°. The films are deposited on Pt/Ti electroded and SiO_2/SiN passivated silicon wafers. The Zr/Ti atomic ratio of the films is 60/40. The diffraction peaks characteristic of the tetragonal structure are clearly seen in these patterns. The (112) and (211) peaks of the 1200Å thick film show clearly ⁻ splitting. The broad peak corresponding to (103)/(301) reflections of the 600Å thick film indicates two side by side peaks. These XRD patterns demonstrate that our 60/40 PZT films have a tetragonal structure at room temperature. This is different from the rhombohedral structure reported in the bulk ceramics of the same Zr/Ti ratio[11,12]. The morphotropic phase boundary separating the tetragonal and the rhombohedral phases apparently has shifted from Zr/Ti ratio of 52/48 in the bulk ceramics to a higher ratio in thin films. We attribute this shift to stresses in these thin films.

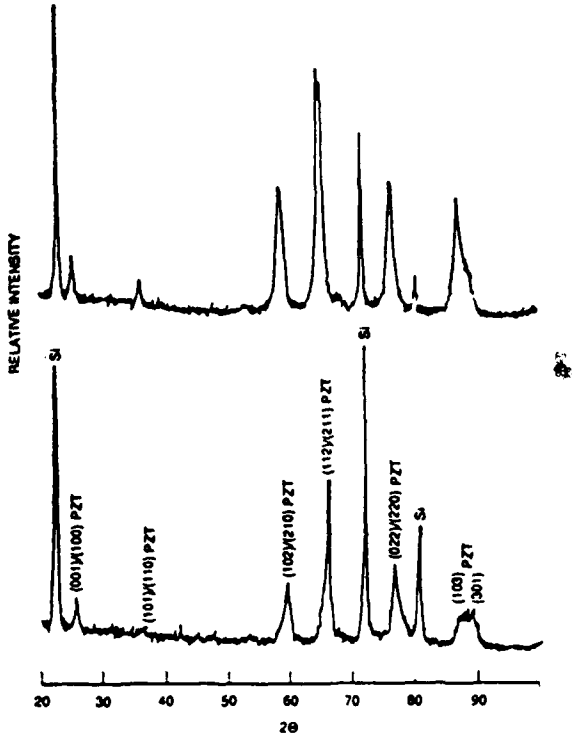


FIGURE 3. XRD patterns of 1200Å (top) and 600Å (bottom) 60/40 PZT films

The surface microstructures of the same films measured from a scanning electron microscope are illustrated in Figure 4. The films are very dense, smooth and uniform with a lateral grain size in the range of 0.2~0.5 μm, which is much smaller than those reported previously for thicker PZT films[13] and bulk ceramics[14].

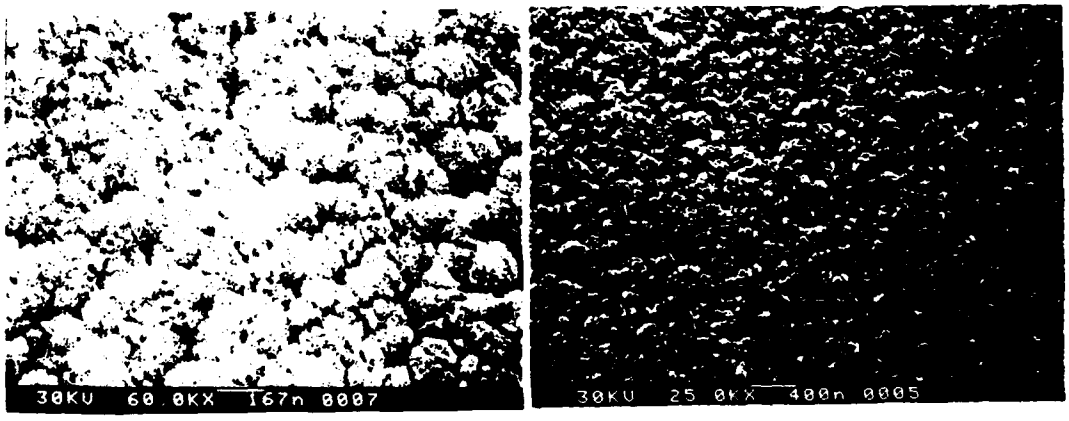


FIGURE 4. Surface microstructures of 600Å (left) and 1200Å (right) 60/40 PZT films

The chemical composition of the films is analyzed by Auger electron spectroscopy. Figure 5 shows the Auger depth profiles of the elements of two 600Å films with Zr/Ti ratios of 50/50 and 60/40. The measured Zr/Ti ratios matched very well with those of the starting sol-gel formulation. There is a disturbed region of about 50~100Å in thickness at the surface. To fabricate PZT capacitors possessing a good upper contact, we perform a heat treatment at 650°C for 15 min. to diffuse the contact metal, gold, into the films to avoid this non-stoichiometric composition region.

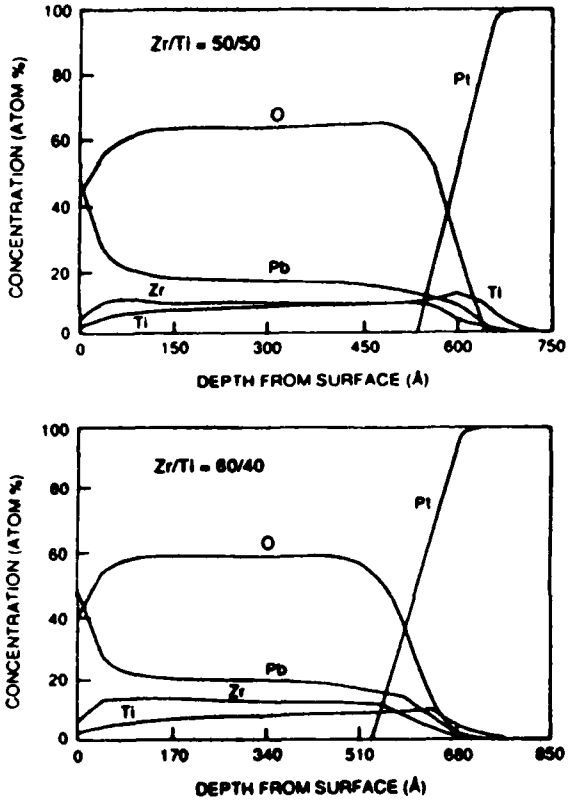


FIGURE 5. Auger electron spectroscopy depth profiles of elemental concentrations of 600Å 50/50 (top) and 60/40 (bottom) PZT films

The ferroelectric hysteretic properties of the films are studied using a Sawyer-Tower bridge circuit with a 1 KHz sine wave. The hysteresis loop of a 600Å thick capacitor is displayed in Figure 6. The remanent polarization, maximum polarization and coercive field of the film are 21 $\mu C/cm^2$, 38 $\mu C/cm^2$ and 75 KV/cm, respectively. To demonstrate that our thin PZT capacitors could be poled to saturation at 3~5 volts, we gradually increased the applied voltage in steps from 0.8 to 4 volts on a 650Å capacitor. At each voltage increment, the maximum polarization, Pmax, remanent polarization and coercive voltage were measured and plotted in Figure 7. Pmax increased from 8.2 $\mu C/cm^2$ at 0.8 volt to about 39 $\mu C/cm^2$ at 3 volts. It then increased linearly at higher voltages with the applied voltage. This indicated that the film reached saturation at 3 volts. A similar experiment on a 1000Å thick capacitor also showed that the capacitor reached saturation at 5 volts.

Figure 8 shows the switching time versus capacitor area for a 600Å thick capacitor. We have found that the switching time is linearly proportional to the capacitor area. The shortest switching time measured was 4 nsec from a 12 x 12 μm^2 capacitor, which implied that the intrinsic switching time of the film was faster.

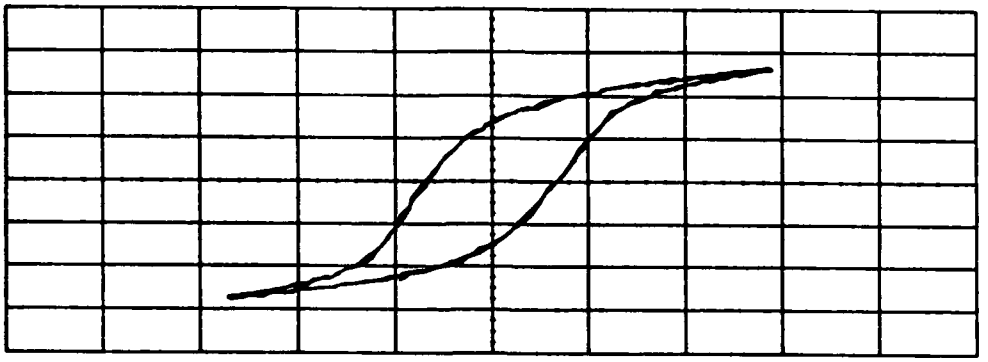


FIGURE 6. Hysteresis loop of a 600Å thick 12x12 μm^2 capacitor measured at 1 KHz (Zr/Ti = 50/50).
Scale: V: 13.9 $\mu C/cm^2$/Div. H: 167 KV/cm/Div.

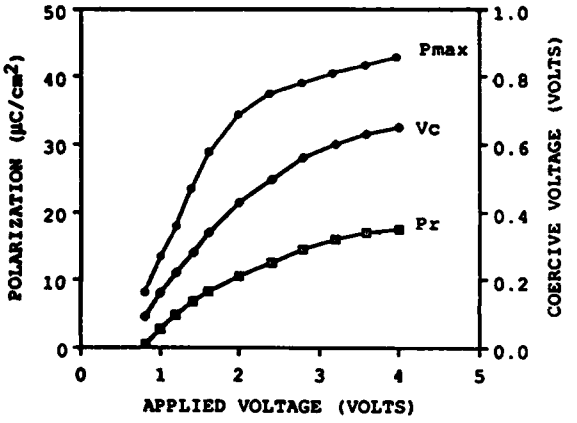


FIGURE 7. Maximum polarization, remanent polarization and coercive voltage versus applied voltage of a 650Å thick 40x40 μm^2 capacitor

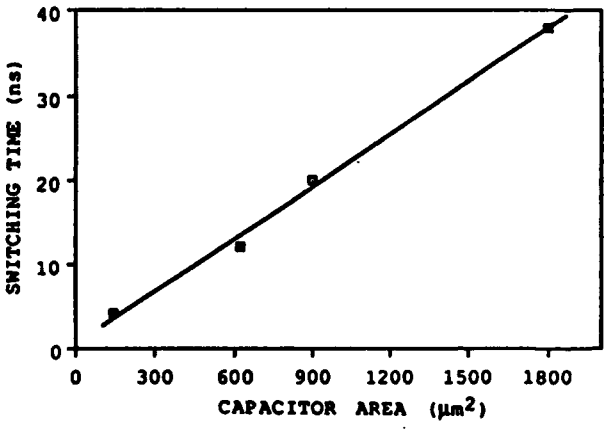


FIGURE 8. Measured switching time versus capacitor area of a 600Å thick 50/50 PZT film.

The switching endurance was measured by applying a 100 KHz square wave of a certain amplitude to the test capacitor in series with a 50 Ω resistor. The hysteresis loop was then measured at various time intervals using a Sawyer-Tower bridge circuit with a 1 KHz sine wave of the same amplitude as that of the square wave. The measured remanent polarization versus the cycling time of a 650Å capacitor is shown in Figure 9.

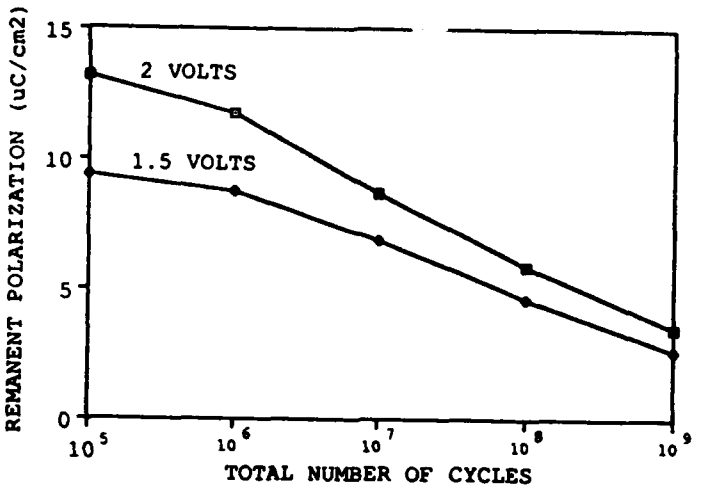


FIGURE 9. Measured remanent polarization versus cycling time of a 650Å thick 40x40 μm^2 capacitor.

After 1 x 10^9 cycles, the capacitor retained 27% (4 $\mu C/cm^2$) of the initial remanent polarization when the capacitor was cycled with 2 volt pulses. When the capacitor was cycled with 1.5 volt pulses, the remanent polarization reduced to 3 $\mu C/cm^2$, 30% of the initial value. Since the sensing circuit is capable of detecting a charge as low as 1 $\mu m/cm^2$ for the capacitor with an area of 4 x 5 μm^2, the projected life of our capacitors is estimated to be longer than 1 x 10^{10} switching cycles. The memory retention of the capacitor was also investigated. The result was very encouraging. No change in the stored charge or remanent polarization was observed after 236 days of storage without power.

Our PZT capacitors are delineated by the ion milling technique. This technique has been quite successful in delineating capacitor sizes as small as 4x4 μm^2. The uniformity of the film quality is also very good, which can be seen from the remanent polarization values measured from 40x40 μm^2 capacitors over a 1 x 0.7 in^2 area illustrated in Figure 10. The variation is 10% from the mean.

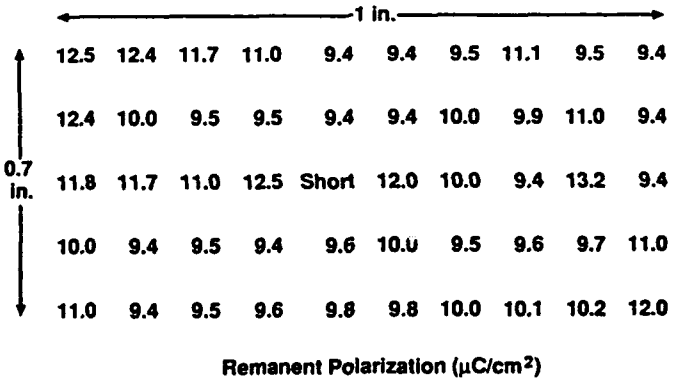


FIGURE 10. Measured remanent polarization of 40x40 μm^2 capacitors over an 1x0.7 in^2 area.

FORMATION OF P+ GATE N-CHANNEL GaAs JFETs AND INTEGRATION WITH PZT CAPACITORS

As shown in Figure 1, the GaAs JFETs are used as access transistors in the memory. These n-channel JFETs must be operated in the enhancement mode with a threshold voltage of about 0.2~0.3 volts. At MDESC we have investigated two approaches to form the p+ gate. The first approach we employed was magnesium implantation followed by zinc diffusion, which was called the zinc diffusion approach, and the other was straight zinc implantation. The process sequences of integration and the experimental results using these two approaches will be described next.

1. Zinc Diffusion Approach:

The zinc diffusion approach is employed first because this method has been well established and adopted as the standard process in our laboratory for the formation of the p+ gate enhancement mode n-channel GaAs JFETs. There are four critical high temperature treatments involved in the fabrication process employing this approach. They are given in Table 2.

1. Post-implant annealing of the source, drain and channel of the JFET at 750°C for 15 minutes in forming gas
2. Spin-coating and sintering of PZT at 650° for 15 minutes in air and alloying of gold electrode again at 650°C for 15 minutes
3. Zinc diffusion at 650°C for 1 minute in argon
4. NiAuGe ohmic contact alloying at 440°C for 3 minutes in forming gas

TABLE 2. Sequence of critical high temperature processes employing the zinc diffusion approach.

The PZT film is deposited and sintered (step 2) after the source, drain and channel post-implant annealing to avoid the PZT from being reduced at 750°C in forming gas. The zinc diffusion (step 3) is done after the PZT sintering and the gold upper electrode alloying to prevent zinc from being driven in deep by the two 650°C 15 min. heat treatments. But the zinc diffusion at 650°C for 1 min. in argon is found to be detrimental to the PZT film and the gold upper electrode. To protect the PZT film during the zinc diffusion, we cap it with a layer of diffusion barrier such as silicon nitride (SiN) layer. Figure 11 shows the sequence of the processing steps in cross-sectional view.

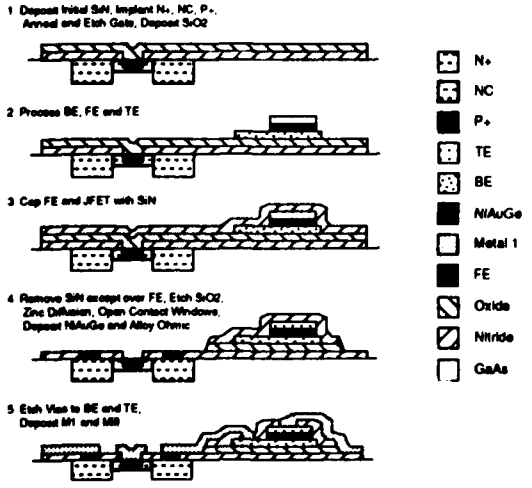


FIGURE 11. Sequence of processing steps in cross-sectional view of GaAs JFET and PZT capacitor using zinc diffusion approach.

There were several problems developed, however, during the zinc diffusion using the SiN as the capping layer. First, the SiN reacted chemically with the gold electrode at 650°C which left holes in the gold electrode. This problem was overcome by depositing a Pt layer on top of the gold electrode since Pt was found less reactive with SiN than gold at 650°C. Second, the edge coverage by the SiN was poor, which resulted in zinc penetration through the weak spots at edges of the capacitor and subsequently destroyed the PZT film. Third, the poor adhesion of the SiN on the upper contact electrode caused delamination or partial lifting of the SiN layer during the 650° zinc diffusion operation. Because of these difficulties mentioned above, the zinc diffusion approach was not further pursued in our integration study.

2. Zinc Implantation Approach:

The formation of the p+ gate of n-channel GaAs JFETs by the zinc implantation was investigated next after we encountered some difficulties with the zinc diffusion approach mentioned in the previous section. We have found that the zinc implantation has many advantages over the zinc diffusion. These advantages are:

1. Elimination of wafer exposure to zinc atmosphere.
2. Zinc implantation can be done before PZT capacitor fabrication.
3. No significant broadening of zinc profile after post-implant rapid thermal annealing and PZT capacitor heat treatments.
4. More controllable than zinc diffusion.
5. More compatible with other processing steps.

The processing sequence incorporating the zinc implantation for the integration of the PZT capacitor and the GaAs JFET is given in Figure 12. The zinc implantation (step 2) is done before the PZT capacitor fabrication (step 3). This is different from the zinc diffusion approach in which the PZT capacitor is processed before the zinc diffusion step. Our experiments have shown that the two heat treatments required for the PZT film sintering and the upper contact electrode alloying in step 3 do not degrade the implanted p+ gates processed in step 2. They also do not alter the threshold voltage of the JFETs, which will be described in the following paragraph.

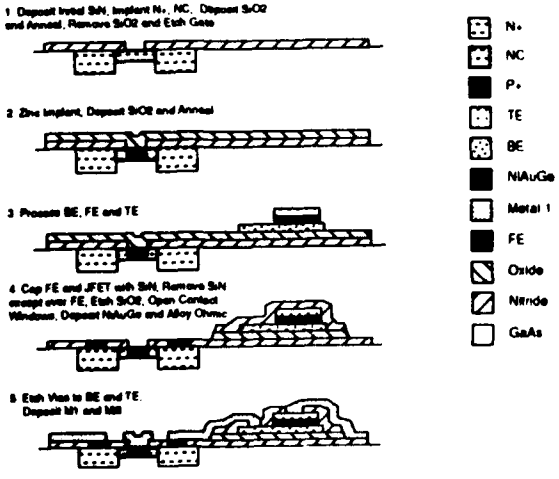


FIGURE 12. Sequence of processing steps in cross-sectional view of GaAs JFET and PZT capacitor using zinc implantation approach.

Initially we found that the threshold voltage of the JFETs varied from +0.8 volts to -0.8 volts across a 3 inch wafer after a post-implant rapid thermal annealing (RTA) at 800°C for 5 sec, which is shown in Figure 13. The JFETs in the middle of the wafer were in the enhancement mode (positive threshold voltage) while away from the center they were in the depletion mode (negative threshold voltage). The histogram illustrating the number of JFETs versus the threshold voltage across a 3 inch wafer after the RTA is given in Figure 14 (a). The wafer was next given an additional 650°C 30 min heat treatment, simulating the two heat treatments, 650°C 15 min. each, for the PZT film sintering and the upper contact electrode alloying. The histogram after the 650°C 30 min. heat treatment is illustrated in Figure 14(b), which shows no significant shift in the threshold voltage after the additional heat treatment.

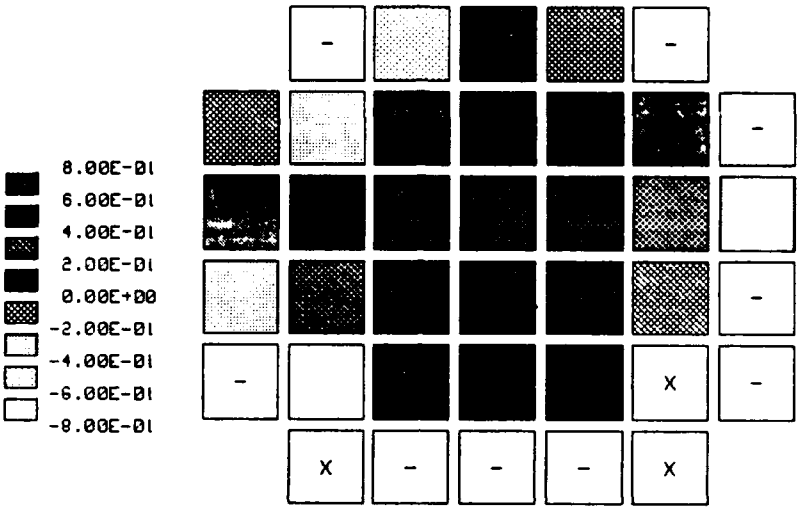


FIGURE 13. Variation on threshold voltage of JFETs across a 3 inch wafer after RTA at 800°C for 5 sec.

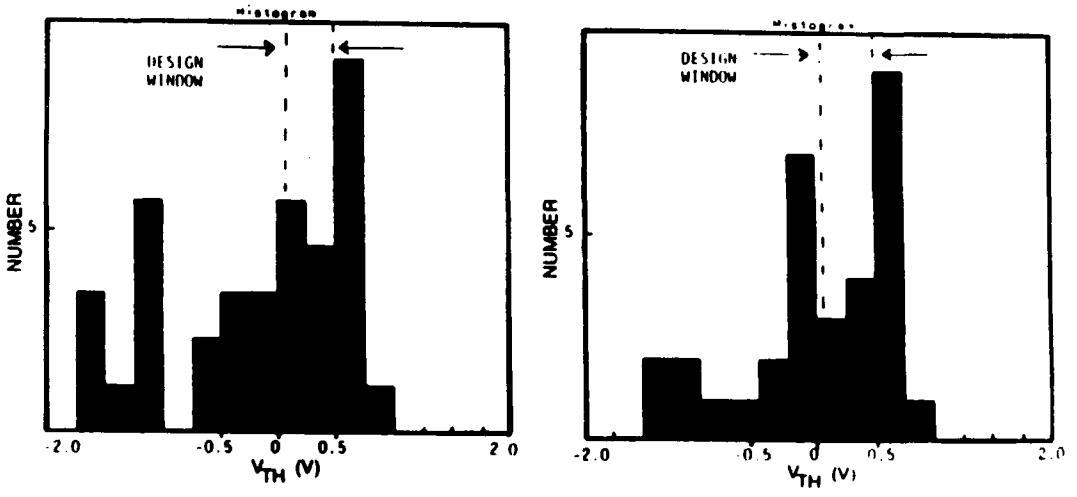


FIGURE 14. Histogram illustrating number of JFETs versus threshold voltage across 3 inch wafer after RTA only (left) and RTA plus 650°C 30 min. heat treatment (right).

The spread in the threshold voltage was due mainly to an uneven heating in the RTA system. This was taken care of after we readjusted the lamps in the RTA system. The spread in the threshold voltage was reduced to about 0.2 Volt as shown in Figure 15 after the RTA only and the RTA plus 650°C 30 min heat treatment. The mean threshold voltage was higher than the upper margin (~0.5 volt) of the design window. This was later corrected by reducing the zinc implantation energy from 40 KeV to 30 KeV. The histogram after the correction is illustrated in Figure 16.

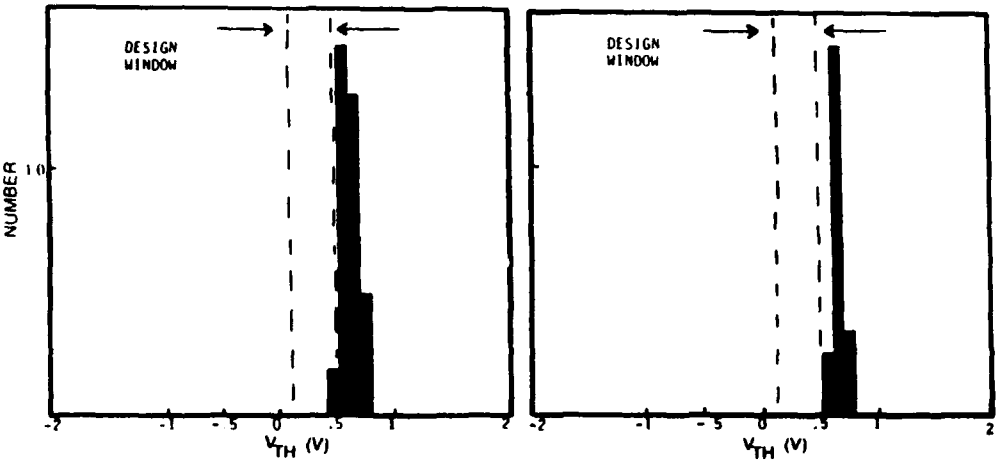


FIGURE 15. Histogram illustrating number of JFETs versus threshold voltage across 3 inch wafer following RTA after lamp adjustment (left) and RTA plus 650°C 30 min. heat treatment (right).

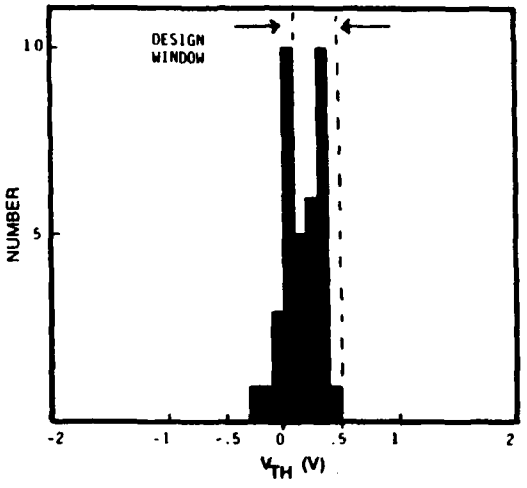


FIGURE 16. Histogram illustrating number of JFETs versus threshold voltage after correction of zinc implant energy.

INTEGRATED GaAs JFET AND PZT CAPACITOR MEMORY CELL

After the PZT capacitor is fabricated (step 3 in Figure 12) the wafer is covered with a 3000Å SiN layer. This SiN and the underlying SiO_2 layers over the JFET are next removed. The ohmic contacts for the source, drain and gate of the JFET are processed. Following this vias in the SiN for the upper and bottom contacts of the PZT capacitor are opened. After depositing and etching of the first level interconnect we complete the integration of the GaAs JFET and the PZT capacitor.

A photograph showing memory cells with integrated GaAs JFETs and PZT capacitors (after the first level interconnect delineation) is illustrated in Figure 17. The hysteresis loop of a 40x40 μm^2 capacitor and the current-voltage characteristics of the integrated GaAs JFET are demonstrated in Figure 18. The wafer is next covered with a dielectric crossover, either a SiN or a polyimide layer. Vias in the crossover are opened and the aluminum second level interconnects are deposited and delineated. A finished

4K/2K FERRAM is shown in Figure 19. We are currently working on a functional FERRAM. More detailed experimental results on the latest FERRAM development will be reported in the two companion papers[15,16].

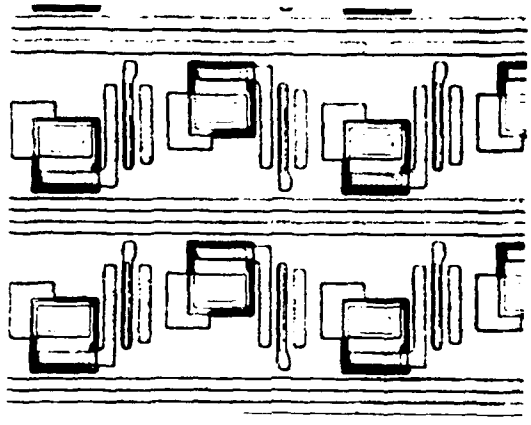
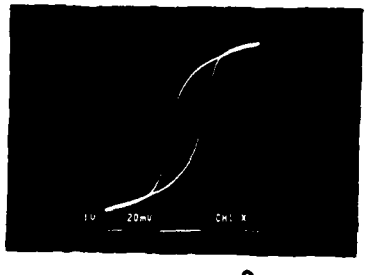


FIGURE 17. Memory cells with GaAs JFETs and PZT capacitors integrated on the same GaAs wafer (after the first level interconnect delineation)



P_r = 20 $\mu C/cm^2$

V_c = 0.65 volt

A = 40 x 40 μm^2
t = 100 nm



V_{TH} = 0.27 volt

G_m = 130 mS/mm

L = 1 μm
W = 20 μm

FIGURE 18. Hysteresis loop of 40 x 40 μm^2 capacitor and current-voltage characteristics of integrated GaAs JFET.

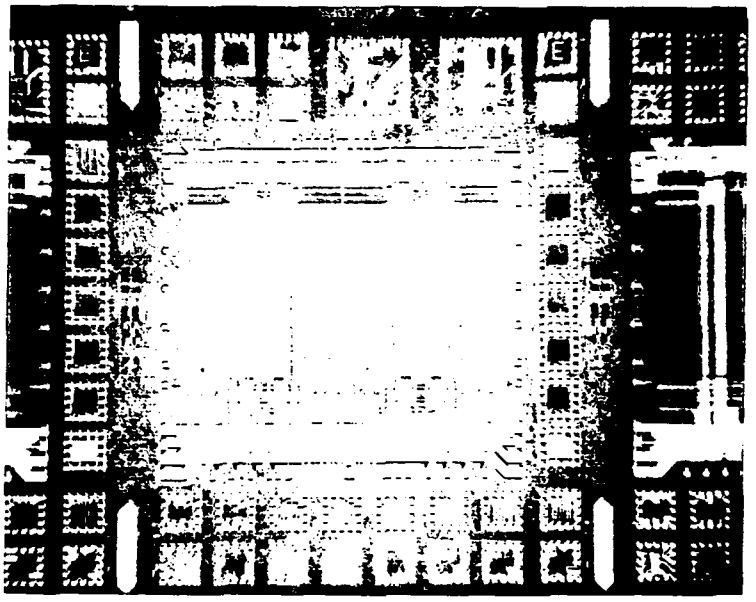


FIGURE 19. A finished 4K/2K FERRAM (after the second level interconnect delineation)

CONCLUSIONS

In this paper we have presented the results of investigation on the integration of PZT capacitors and GaAs JFETs on the same GaAs wafer for the fabrication of 4K/2K nonvolatile ferroelectric random access memories. Several areas such as the preparation and characterization of the PZT films, formation of the p+ gate, process compatibility and sequence of integration of the GaAs JFET with the PZT capacitor, and the current status on our development program have been described.

The PZT films are prepared by a sol-gel technique which uses precursor materials containing lead acetate, titanium isopropoxide and zirconium n-propoxide mixed with methoxyethanol. A chemical additive, formamide, is added in the precursor solution to prevent the films from cracking during the drying and sintering operation. Excellent structural, compositional, ferroelectric hysteretic, switching endurance and memory retention properties have been obtained in these films. They are very dense, smooth and uniform with a lateral grain size of 0.2~0.5 μm. The remanent polarization, maximum polarization and coercive field of a 600Å thick capacitor are 21 $\mu C/cm^2$, 38 $\mu C/cm^2$ and 75 KV/cm, respectively. The films with a thickness of 600~1000Å have exhibited a low saturation voltage of 3~5 volts. The switching speed of the films is very fast. The shortest switching time measured from a 12x12 μm^2 capacitor is 4 nsec. The switching endurance and memory retention of the capacitors are very encouraging. The projected life of the capacitors is estimated to be longer than $1x10^{10}$ switching cycles. No change in the stored charge or remanent polarization has been observed after 236 days of storage without power. The uniformity of the film quality is very good. The variation of the remanent polarization measured from 40x40 μm^2 capacitors over a 1 x 0.7 in^2 area is less than 10% from the mean.

Two approaches for the formation of the p+ gates of the n-channel GaAs JFETs have been investigated: one is magnesium implantation followed by zinc diffusion,

which is called the zinc diffusion approach, and the other is the zinc implantation approach. The sequence of integration and the process compatibility using these two approaches have been developed and examined., Due to the poor edge coverage and occurring of delamination and partial lifting of the SiN capping layer during the 650°C zinc diffusion process, the zinc diffusion approach was not further pursed.

The zinc implantation approach has been quite successful in forming the p+ gates of the GaAs JFETs. After the lamp adjustment in the RTA system and the correction of the zinc implantation energy, we are able to obtain a threshold voltage of 0.2 ~ 0.5 volts. Using the zinc implantation approach together with the developed processing sequence, we have successfully fabricated PZT capacitors and JFETs on the same GaAs wafer. Excellent hysteresis loops and current voltage characteristics have been demonstrated on PZT capacitors and the GaAs JFETs fabricated on the same wafer. Work on the crossover dielectric layer and the second level interconnects is being continued for making a functional 4K/2K ferroelectric random access memory.

ACKNOWLEDGEMENTS

The authors would like to thank Drs. J. Alexander and M. Yoder for their continued interest and encouragement. Work has been supported by DARPA under Contract N00014-89-C-0020.

REFERENCES

1. The Seventh International Symposium on Applications of Ferroelectrics, Urbana, Illinois, June 6-8, 1990.
2. The Third International Symposium on Integrated Ferroelectrics, Colorado Springs, Colorado, April 3-5, 1991.
3. W. A. Geideman and S. Y. Wu, "Progress in Ferroelectric Memory Technology", presented at the 7th International Symposium on Applications of Ferroelectrics, Urbana, IL, June 6-8, 1990.
4. W. A. Geideman, S. Y. Wu, L. E. Sanchez, B. P. Maderic, W. M. Liu, I. K. Naik and S. H. Watanabe, " PZT Thin Films for GaAs Ferroelectric RAM Applications", presented at the Seventh International Symposium on Applications of Ferroelectrics, Urbana, IL, June 6-8, 1990.
5. S. Bernacki, L. Jack, S. Collins, S. Bernstein, Y. Kisler, B. Armstrong, J. Shaw, J. Bullington, J. Evans, B. Bunker and B. Tuttle, "Integration of Ferroelectrics into Semiconductor Devices", presented at the 3rd International Symposium on Integrated Ferroelectrics, Colorado Springs, CO, April 3-5, 1991.
6. N. Aft, "Ferroelectrics at National Semiconductor", presented at the 3rd International Symposium on Integrated Ferroelectrics, Colorado Springs, CO, April 3-5, 1991.
7. D. Bondurant, "Ramtron's Ferroelectric RAM Evaluation and Development System", presented at the 3rd International Symposium on Integrated Ferroelectrics, Colorado Springs, CO, April 3-5, 1991.
8. L. E. Sanchez, D. T. Dion, S. Y. Wu and I. K. Naik, "Processing and Characterization of Very Thin PZT Ferroelectric Capacitors by a Sol-Gel Method", presented at the 2nd Symposium on Integrated Ferroelectrics, Monterey, CA, March 6-8, 1990.
9. G. Orcel and L. Hench, K. Non-Cryst. Solids 79, 177 (1986).
10. L. L. Hench, G. Orcel and J. L. Nogues, Mat. Res. Soc. Symp. Proc. 73, 35 (1986).
11. G. Shirane and K. Suzuki, J. Phys. Soc. Japan 7, 333 (1952).
12. E. Sawaguchi, J. Phys. Soc. Japan 8, 615 (1953).
13. K. D. Budd, S. K. Dey and D. A. Payne, Proc. Brit. Ceram. Soc. 36, 107 (1985).
14. G. H. Haertling and C. E. Land, J. Amer. Ceram. Soc. 54, 1 (1971).

15. L. E. Sanchez, I. K. Naik, S. H. Watanabe, J. H. Madok and S. Y. Wu, "Process Technology Development for GaAs Ferroelectric Nonvolatile Memory", presented at the 3rd Symposium on Integrated Ferroelectrics, Colorado Springs, CO, April 3-5, 1991.
16. I. K. Naik, L. E. Sanchez, B. P. Maderic and S. Y. Wu, "Improved Switching Endurance of Thin Film Lead-Zirconate-Titanate Capacitors for Nonvolatile Ferroelectric Memories", presented at the 3rd Symposium on Integrated Ferroelectrics, Colorado Springs, CO, April 3-5, 1991.

AD-P006 672

ANOMALOUS REMANENT POLARIZATION IN FERROELECTRIC CAPACITORS

NORMAN E. ABT
Fairchild Research Center, M/S E140
National Semiconductor Corporation, Santa Clara, CA 95052-8090

Abstract An apparent remanent signal seen by the application of voltage pulses to a Sawyer-Tower circuit is described. This 'remanent' is present for two pulses in the same direction when no remanent is expected. Variation of this signal with fatigue and ageing will be shown. Implications for memory circuits will also be discussed. Finally, several suggestions of possible mechanisms will be presented.

INTRODUCTION

Ferroelectric materials have been studied extensively since their discovery early in the century. A standard technique for analyzing ferroelectric properties is to measure an electrical hysteresis loop[1]. Recently ferroelectric materials have been prepared as thin films for use in semiconductor memory applications[2]. Hysteresis loops using sine wave excitation were measured for these films. Also, polarization was measured using single pulses. The pulses mimicked the operation of the memory circuit. The value of the remanent polarization from these two method did not agree. In addition, when two pulses of the same polarity were applied to a sample there appeared to be a remanent signal after the second pulse when in principle no switching of dipole should have occurred and no remanent should be present. In this paper we will expand on the observations of this phenomenon including its relation to the familiar ageing and fatigue. The importance of this to memory applications will be discussed

92-16147

and a new failure mechanism for memories caused by this will be described. Finally several suggestions of possible causes are made.

EXPERIMENTAL OBSERVATIONS

The phenomenon which we call ΔP0 can be most easily seen by comparing two pulse sequences shown in figure 1. The output shown is that which would be seen across the sense capacitor of a Sawyer-Tower circuit. The write and sense pulses are applied to the top of the ferroelectric capacitor. In the first sequence the pulses are of opposite polarity. The second pulse, the sense pulse, will cause the dipoles to switch producing a large remanent labeled ΔP1. In the second sequence the two pulses are in the same direction and the sense pulse should not produce switching of dipoles but immediately after the fall of the pulse a remanent can be seen, labeled ΔP0. In our work we used 8μS pulses though this is seen for all pulse durations. Examining the remanents for the two cases on longer time scales reveals a decay of the signals (figure 2). Both ΔP1 and ΔP0 follow identical decays except that the ΔP1 signal is

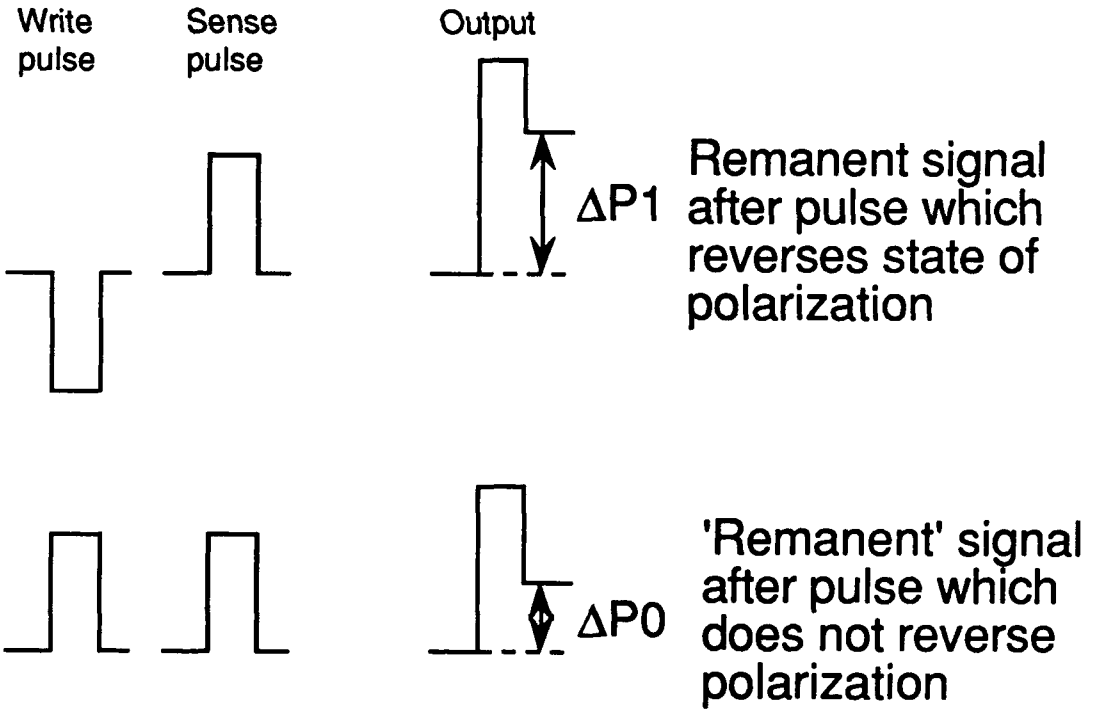


Figure 1. Pulse definitions of ΔP1 and ΔP0

offset from zero by a constant. This decay nominally takes 100mS and follows a -Log(time) dependence.

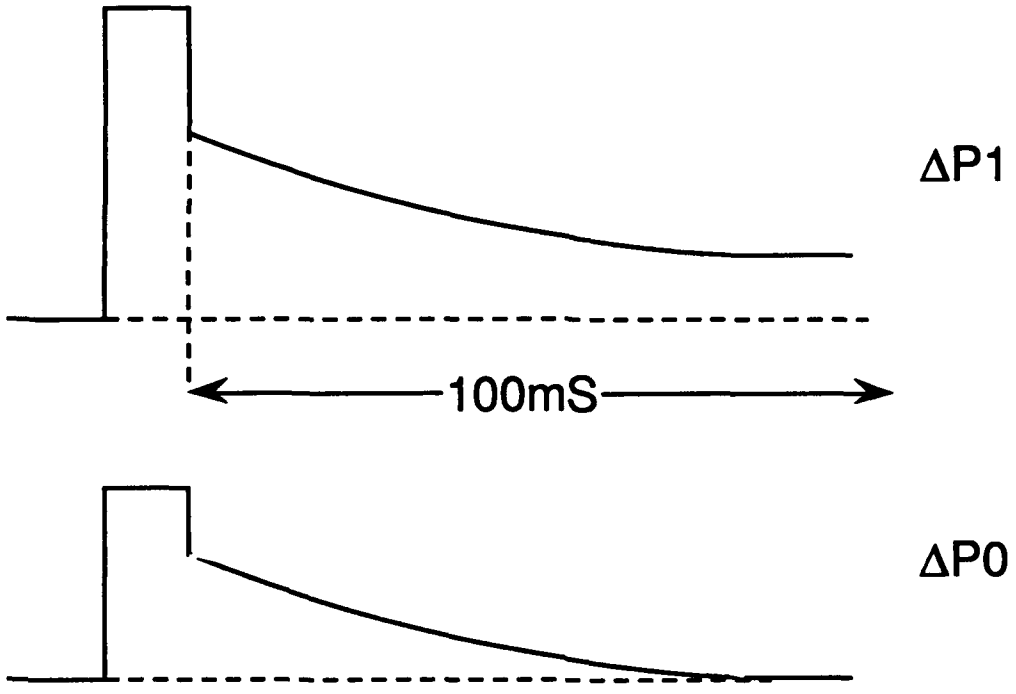


Figure 2. Decay of remanents follows Log(time)

It is important to see the relation between pulsed measurements and a hysteresis loop (figure 3). In the usual measurement, as a sine wave is applied the signal goes around the loop , A-C-B-D-A. For the pulses of the first sequence of figure 1 the write pulse places the capacitor at point A'. The sense pulse drives the capacitor following A'-C-B and during the decay in the next 100mS from B-B'. The second sequence goes B'-C-B and then during the slow decay B-B'. From the hysteresis loop Pr = A-B but from the pulses one sees only A'-B

Figure 4 shows the change in ΔP1, ΔP0, and -ΔP0 (ΔP0 for two down pulses) with fatigue. The capacitor was cycled with a 5 volt 1Mhz sine wave at room temperature. At each read point the cycling was stopped and the signals measured with pulses of the form 1- $\sin(2\pi ft-\pi/2)$ with f= 80kHz. Note ΔP0 does not equal -ΔP0 and the difference between ΔP1 and ΔP0 is decaying with fatigue faster than ΔP0 itself.

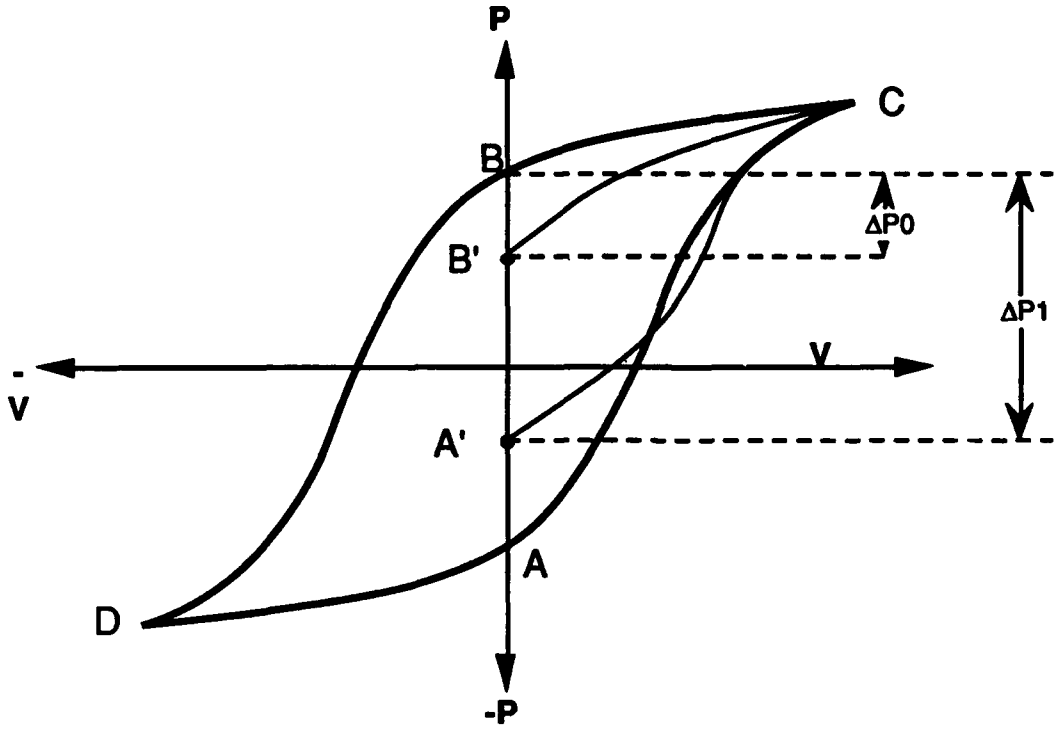


Figure 3. Relation of ΔP0 and ΔP1 to hysteresis loop

ΔP0 shows only minor changes with ageing (Figure 5). However, there is a similar test with ageing that does show dramatic change. We have called it imprint because of its effect on a memory circuit but it is a worst case ageing phenomenon. If a capacitor is placed in an up state for a prolonged period of time the opposite or down ΔP0 will increase. Similarly, if the capacitor is pulsed down and left there the up ΔP0 will increase. This memory of the previous state cause errors in data for a circuit as will be shown in the next section. A way to see this is to compare two ways of doing an ageing experiment. Two pulse sequences are shown in figure 6. In the first the capacitor is put in a down state before the ageing period and in the second it is put in an up state. At each read data point the up ΔP0 is measured. Figure 7 compares the result for the two cases. When stored down the up ΔP0 increases while for the stored down case the up ΔP0 is roughly constant.

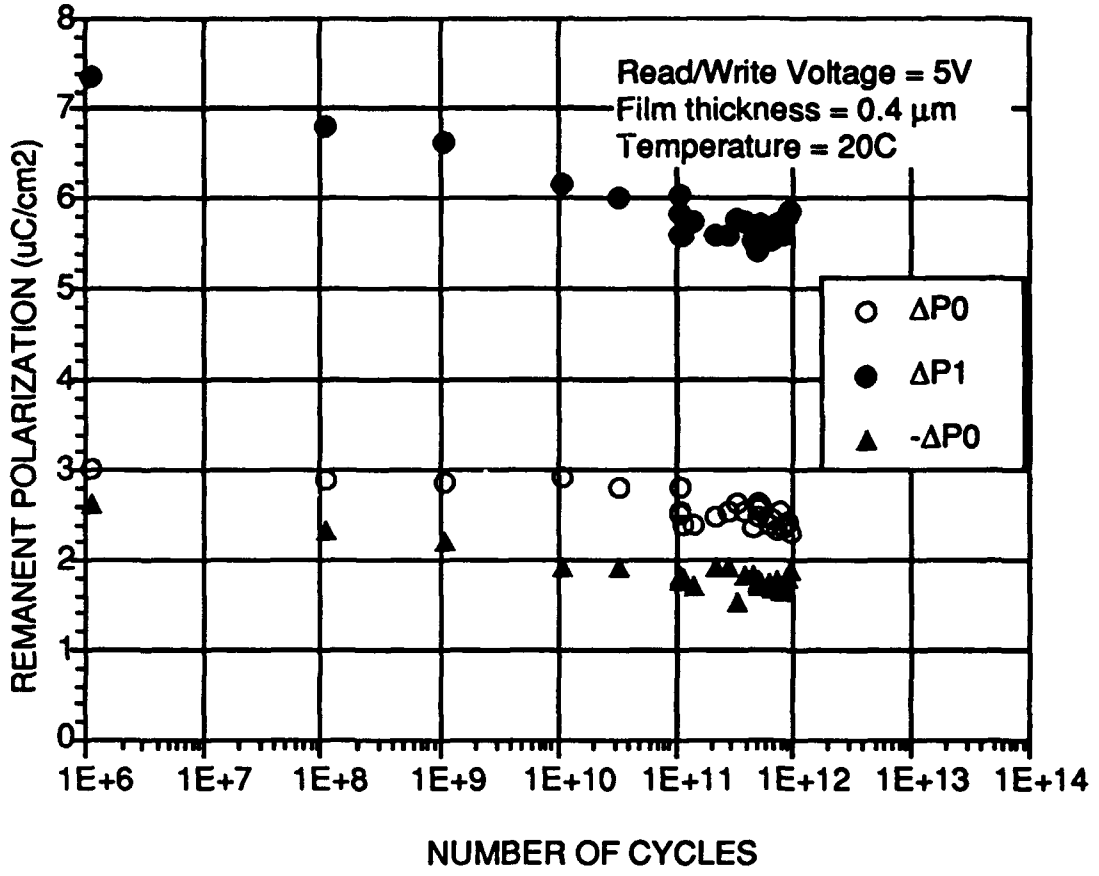


Figure 4. Fatigue of fully integrated Ferroelectric capacitor

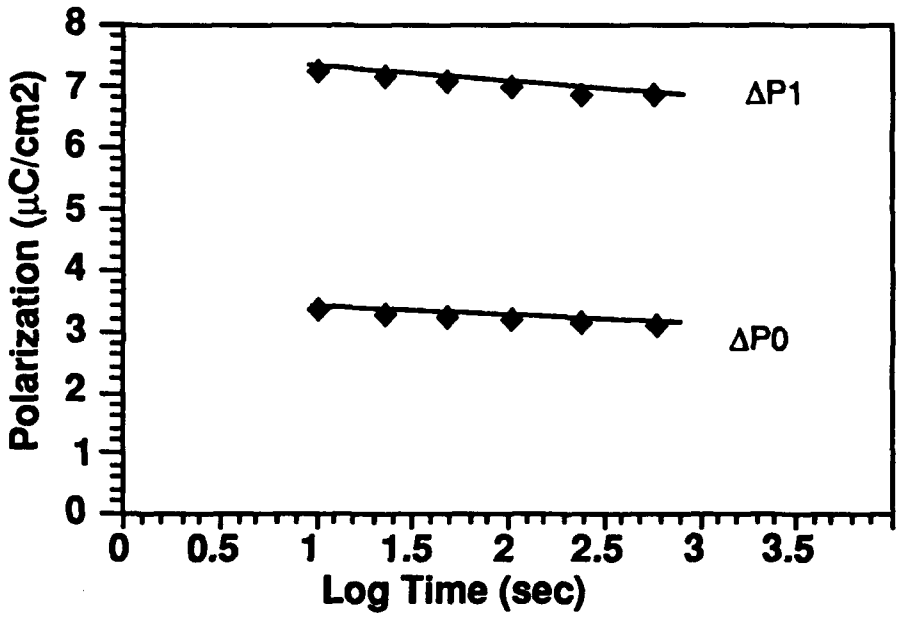


Figure 5. Ageing of ΔP1 and ΔP0

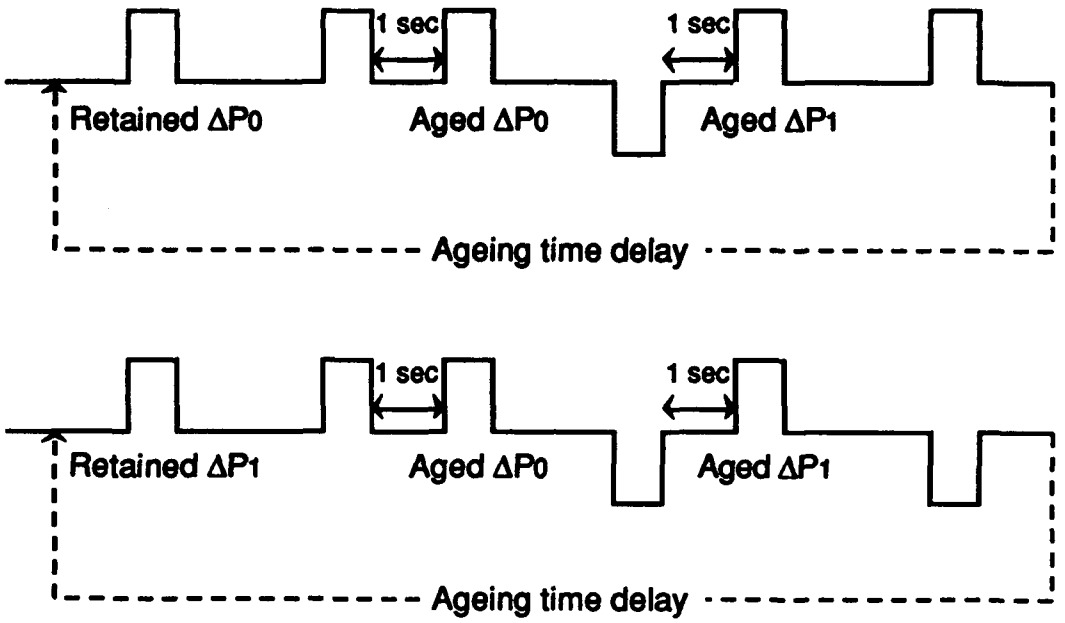


Figure 6. Two Cases of an ageing test

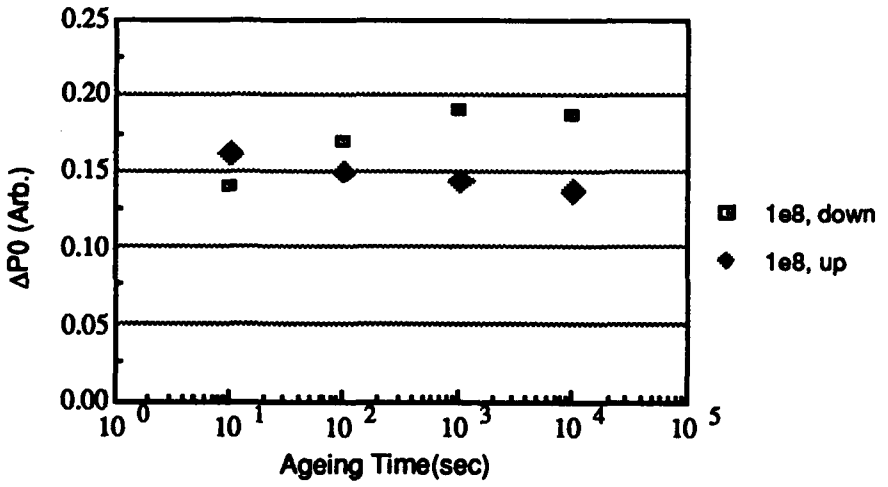


Figure 7. Change in ΔP0 during ageing with capacitor store up and down.

Effect on Measurements and Circuits

The presence of ΔP0 puts extra conditions on the measurement of ferroelectric properties. With pulses the time delay between poling and reading is critical. Note Figure 8. Two cases are shown with the time delay between poling and reading

being t_{w1} and t_{w2} respectively. Because ΔP0 has a finite decay time in the first case it has not completed its decay before being read. This produces a smaller value than in the second case where ΔP0 has had more time to decay.

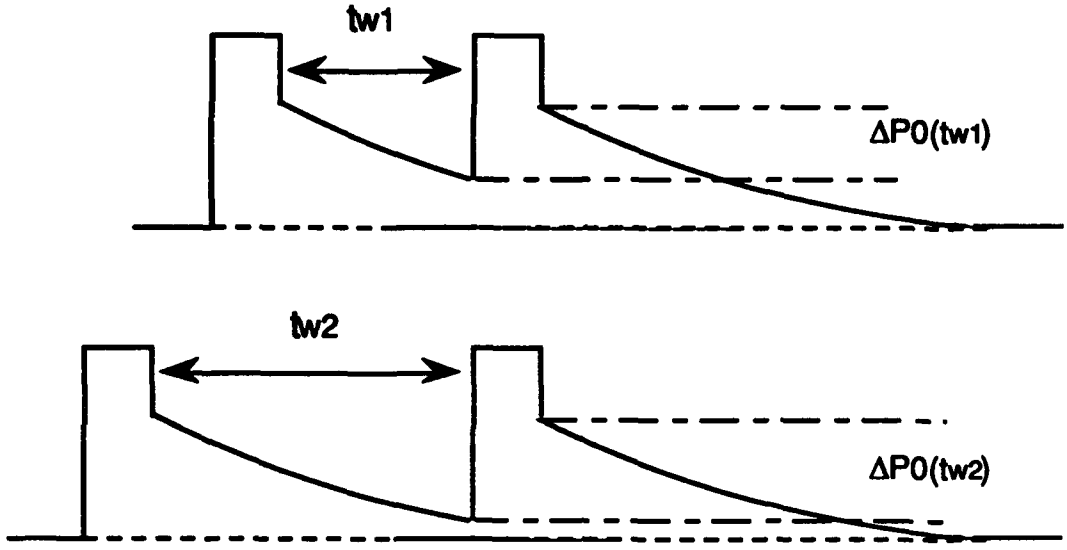


Figure 8. For tw1 < tw2 ΔP0(tw1) < ΔP0(tw2)

(The use of the term 'decay' is somewhat arbitrary. What happens during this relaxation time could also be a 'charge buildup' since the mechanism is not known. In either case, it is a charge flow that we are observing and in time the rate of flow goes to zero.)

Measurements of P_R made by a CW hysteresis loop will not agree with pulsed measurements unless ΔP0 is taken in to account. The hysteresis loop result will overstate the true remanent polarization.

One way to use ferroelectric capacitors in a memory circuit is to compare the remanent signal from two capacitors poled in opposite directions to form one data bit. These will be read by applying the same direction pulse to both (defined as an up pulse for this discussion). One will switch (that which was stored down) producing ΔP1 and the other will not switch (stored up) producing ΔP0. We can define a '1' state as the first capacitor signal greater than the second ($\Delta P1_{\text{first cap}} > \Delta P0_{\text{second cap}}$) and, conversely, a '0' state as the second signal greater than the first ($\Delta P0_{\text{first cap}} < \Delta P1_{\text{second cap}}$). If a bit is stored for a long time as a '1' and then written as a '0' the ΔP0 of the first capacitor will increase and the ΔP0 portion of the ΔP1 from the

second capacitor may decrease resulting in $\Delta P0_{\text{first cap}} > \Delta P1_{\text{second cap}}$. The circuit will read the bit as a '1', the previous data will appear 'imprinted' on that bit.

For reliable circuit operation the ferroelectric films must be optimized to reduce or stabilize ΔP0. This effect can be accelerated with temperature which helps testing.

ORIGINS OF ΔP0

Simple Tests

A few simple tests were run to begin to elucidate the source of this phenomenon. This work was done using PLZT films which covers a wide range of compositions. ΔP0 was not present or very small for paraelectric compositions. Lateral capacitors were illuminated with UV light (365nm) which produce no change in electrical results.

Four pulse sequences which attempt to vary the number of domains oriented up or down are shown in figure 9. Pulses A and B are used to set the state of the capacitor while the identical pulse C is used in all cases to read ΔP0. Resulting values can be seen in figure 10. All 3 Volts reads, independent of pulses A and B, gave the same value. Cycling increased the value slightly.

Suggested Models

Trapping is often suggested as a cause of ΔP0 but this is not expected to be the cause because of the lack of ΔP0 in the paraelectric film and the null result from the UV exposure. The presence of domains seems a necessary requirement and the following suggestions are based on that.

Depolarization due to reverse fields caused by finite electrode resistance[3] is not believed to be the cause because ΔP0 remains the same for electrodes of widely differing resistance.

We suspect it is a bulk phenomenon of ferroelectric thin films and present three possibilities.

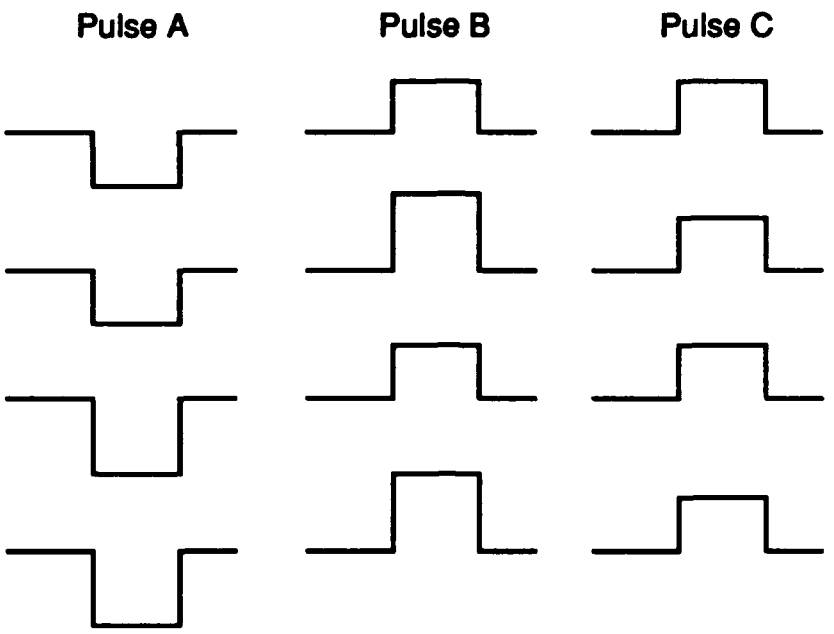


Figure 9. Pulses vary orientation of domains but ΔP0 remains the same.

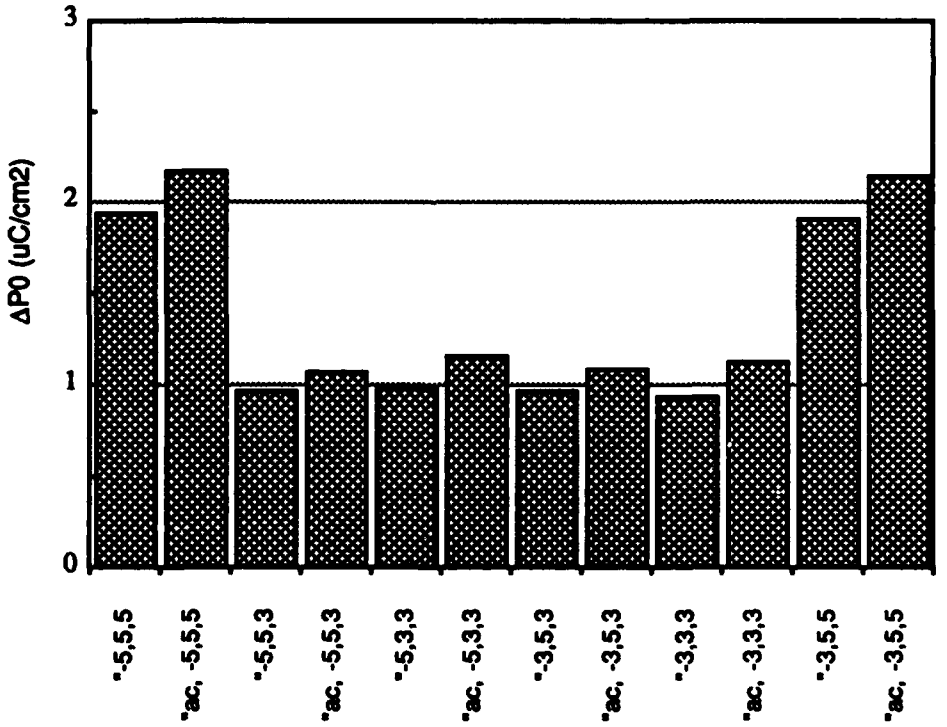


Figure 10. ΔP0 is constant for the different pulse sequences of firgure 9.

1. Many small domains (on the order of 100Å) are present. These are aligned by the applied field but become randomized by thermal energy which is comparable to the domain energy for this size domain.

2. There is a strong stress vector present in the film. The applied field causes a domain to grow but in the absence of the external field the surface energy driven by the stress exceeds the volume energy[4] and the domain collapses. This is inherently asymmetric as the stress vector add differently to the up or down field.

3. There is the possibility of a field-induced phase transition for compositions close to the morphotropic phase boundary[5]. A rhombohedral domain may adjoin a tetragonal domain and in the presence of the applied field at the boundary the rhombohedral phase may convert and contribute to the polarization. Then the field is removed it converts back.

CONCLUSIONS

We have shown an electrical measurement on a ferroelectric capacitor which we believe reveals a new behavior of thin film ferroelectric materials. This component must be taken into account in describing the remanent polarization of a ferroelectric capacitor. It can only be seen using pulsed measurement techniques.

Considerably more study of this effect is needed given the complexity of the materials used and, particularly, given its importance to the functioning of high density memories.

REFERENCES

1 C.B. Sawyer and C.H. Tower, Physical Review, 35, 269(1930).
2 J.T. Evans and R. Womack, IEEE Journal of Solid State Circuits, 23, 1171(1988).
3 B.S. Sharma, S.F. Vogel, and P.I. Prentky, Ferroelectrics, 5, 69(1973).
4 M. Avrami, Journal of Chemical Physics, 9, 177(1941).
5 E. Cross, Personal Communications.

AD-P006 673

A High-Capacitance PZT-on-Ta_2O_5 Memory cell with a Chemically Stable Electrode Suitable for Sub-Micron Processing

92-16148

M. Azuma, T. Nasu, S. Katsu, T. Otsuki and G. Kano
Electronics Research Laboratory
Matsushita Electronics Corporation

ABSTRACT A high-capacitance $Pb(Zr_x, Ti_{1-x})O_3$ (PZT)-on-Ta_2O_5 memory cell suitable for sub-micron processing is proposed, and an experimental capacitor of PZT (Zr/Ti= 52/48)-on-Ta_2O_5 with Ta electrode was prepared. The X-ray diffraction and XMA analysis of the sample showed that PZT reacted with neither Ta nor Ta_2O_5. The capacitor with 500 nm PZT thickness shows current density of 10^{-8} A/cm^2 at 4MV/cm, the breakdown field of 8MV/cm, and the effective dielectric constant of 40.

INTRODUCTION

The memory device in next generation requires a cell capacitor which has high charge density and suitability for sub-micron processing.

Conventional ferroelectric material lead zirconate titanate $Pb(Zr_x, Ti_{1-x})O_3$ (PZT) used for memory capacitors in silicon VLSI has the disadvantages of unsuitability of a Pt electrode for sub-micron processing and of undesirable reaction of poly-silicon and W electrodes with PZT. A Ta_2O_5 capacitor has no such problems, but has disadvantage of capacitance considerably smaller than that for PZT.

This paper proposes a high capacitance memory cell suitable for sub-micron processing by using poly-silicon or W electrodes under high chemical stability. The proposal is based on the finding that T_2O_5 never reacts with PZT so that a PZT-on-T_2O_5 buffer layer impudent to chemical reaction with the above electrode materials, has high capacitance.

EXPERIMENTAL DESIGN

To ensure suitability for sub-micron processing, candidate metals for electrodes of the PZT capacitor were selected from the materials in use of current silicon processing. Then, for these candidate metals, another factor of chemical stability should be considered.

Two types of undesirable chemical reaction can be occurred at PZT and the metal surface;

1. metal oxidation
2. metal-lead oxidation

The following reactions with PZT for each candidate metals are suggested from the oxidation energy of PZT and the metals shown in figure 1. Oxidation energy of PZT is calculated from that of PbO, ZrO_2 and TiO_2.

1) Silicon (poly-Si) reduces PZT.(-> SiO_2)
2) Ta can be oxidized slightly and Ta_2O_5 is hard to react with Pb and PZT.
3) W reacts with Pb in PZT easily and produce $PbWO_4$ oxide.
4) Mo reacts with Pb in PZT easily and produce $PbMoO_4$ oxide.

These studies show that PZT and Ta_2O_5 formations are more stable than any other formations, indicating suitability of a PZT-on-Ta_2O_5 layer as a chemically stable memory capacitor.

EXPERIMENT

The experimental configuration of the PZT-Ta_2O_5 capacitor sample is shown in Figure 2. Tantalum is used for the bottom electrodes and Ta_2O_5 layer is formed in natively.

SiO_2 is prepared with the thickness of 500nm by furnace oxidation.

Ta metal was deposited on a SiO_2/Si Substrate by electron beam evaporator. The substrate temperature is 120°C and the film

thickness is 200nm.

Thin film of $Pb(Zr_{0.52},Ti_{0.48})O_3$ was prepared by reactive rf diode sputtering with a sintered PZT powder containing 10 wt% excess PbO to compensate for the loss of Pb in the thermal treatment process. A sputtering gas of 90% Argon and 10% oxygen was used at the pressure of 1 Pascal. Under applying rf power of 120W, deposition rate was 10nm/min and the film thickness was 500nm. To ensure the film with smooth morphology, the substrate temperature was set to 180 °C, and after deposition, the thermal treatment process at 600 °C 15 min in O_2 gas has done. The mophology of the films before and after annealing are shown in Figure 3(a)(b). The sputtering conditions are summarized in table 1, and the sputtering system is shown in Figure 4.

Top electrode of 200nm Tantalum layer was deposited by using electron beam evaporator in same conditions with bottom electrode.

The reaction between Ta electrodes and PZT film was studied by using XRD, XMA and TEM analysis. The evaluation of electric properties has also done.

RESULTS AND DISCUSSIONS

(1) Reaction between Ta electrode and PZT film

Figure 5 shows X-ray diffraction spectrum of

(a) as sputtered PZT film on $Ta/SiO_2/Si$-substrate

(b) sample after 650°C 15min. annealing in O_2

(c) PZT powder reference

The spectrum (b) after annealing shows the clear lines of Ta_2O_5 crystal and PZT perovskite ones. From comparison to the spectrum (a) before annealing, Ta electrode surface seems to be oxidized during PZT annealing. A TEM photograph (Figure 6) of Ta-PZT interface after annealing shows that 40nm thick Ta_2O_5 layer is formed in this interface. An XMA analysis with probing depth of 400-500nm shows no particular composition change occurs during annealing (Table 2).

These results endorse that there is no reaction between Ta2O5-

PZT.

(2) Electric properties of Ta_2O_5-PZT capacitor

Figure 7 shows the temperature dependence of dielectric properties of the Ta_2O_5-PZT capacitor. The effective dielectric constant is 40 at 25°C, and temperature dependence is originated from ferroelectricity of PZT layer. The effective dielectric constant can raised by control the thickness of Ta_2O_5 layer. The slight temperature dependence of loss tangent suggests that the small lack of oxygen in PZT surface region of Ta_2O_5 side. This problem is solved by use of pre-formed thin Ta_2O_5 layer.

I-V characteristics of the Ta_2O_5-PZT capacitor are shown in Figure 8. The current density is as low as $10^{-8}A/cm^2$ at 4MV/cm, and breakdown voltage is as high as 8MV/cm.

CONCLUSIONS

To realize a high capacitance memory cell suitable for sub-micron processing, a multilayer capacitor of PZT-Ta2O5 capacitor was proposed.

Thermodynamic study of PZT-metal reactions leads chemically stable system of PZT-Ta2O5 capacitor.

Experimental results endorse that the PZT-Ta2O5 capacitor is a promising candidate as a high capacitance memory cell suitable for the silicon VLSI technology.

ACKNOWLEDGEMENTS

The authors wish to thank Dr.H.Kawamura, Dr.S.Nakajima and Dr.H.Takagi for their encouragement and support in this study.

REFERENCES

1. R.Moazzami, et al., Tech.Dig.Symp.VLSI Tech., p.15, 1990.

2. J.Carrano, et al., IEDM Tech.Dig., p.255,1989.

3. J.F.Scott, et al., J.Appl.Phys.66(3), p.1444, 1989

4. H.Shinriki, et al., Tech.Dig.Symp.VLSI Tech., p.25, 1989.

5. C.A.Araujo, et al., Ferroelectrics 104, p.241, 1990.

Figure Captions

Table 1. Sputter Deposition Conditions of PZT Film

Table 2. Results of XMA Analysis

Figure 1. Oxidation Energy of PZT and Metals

Figure 2. Configuration of PZT-Ta_2O_5 Capacitor

Figure 3. SEM Photographs of PZT Film
(a) As Sputter
(b) After Annealing

Figure 4. PZT Sputtering System

Figure 5. X-ray Diffraction Spectrum
(a) PZT As Sputter Film (on Ta Electrode)
(b) PZT Film After Annealing (650°C 15min in O_2)
(c) $Pb(Zr_{0.52}Ti_{0.48})O_3$ Powder

Figure 6. TEM Photograph of PZT-Ta_2O_5 Capacitor

Figure 7. Temperature Dependence of Dielectric Properties

Figure 8. I-V Characteristics of PZT-Ta_2O_5 Capacitor

Table 1. Sputter Deposition Conditions of PZT Film

Sputtering System	RF-Diode
Target	$Pb(Zr_{0.52}Ti_{0.48})O_2$ + PbO 10wt% Powder
Substrate	Ta/Ti on SiO_2/Si Substrate
Sputtering Gas	1Pa (Ar : O_2 = 90 : 10)
Substrate Temperature	180℃
Sputtering Power	120W
Diameter of Target	80mm
Deposition Rate	100Å/mm

Table 2. Results of XMA Analysis

Sample	Intensity (Counts)			
	Pb	Zr	Ti	O
As Sputter	5800	1450	3200	18000
After Annealing	5800	1450	2800	16000

Conditions ; Accerarate Voltage : 8 kV
Beam Current : 0.5 μA

Figure 1. Oxidation Energy of PZT and Metals

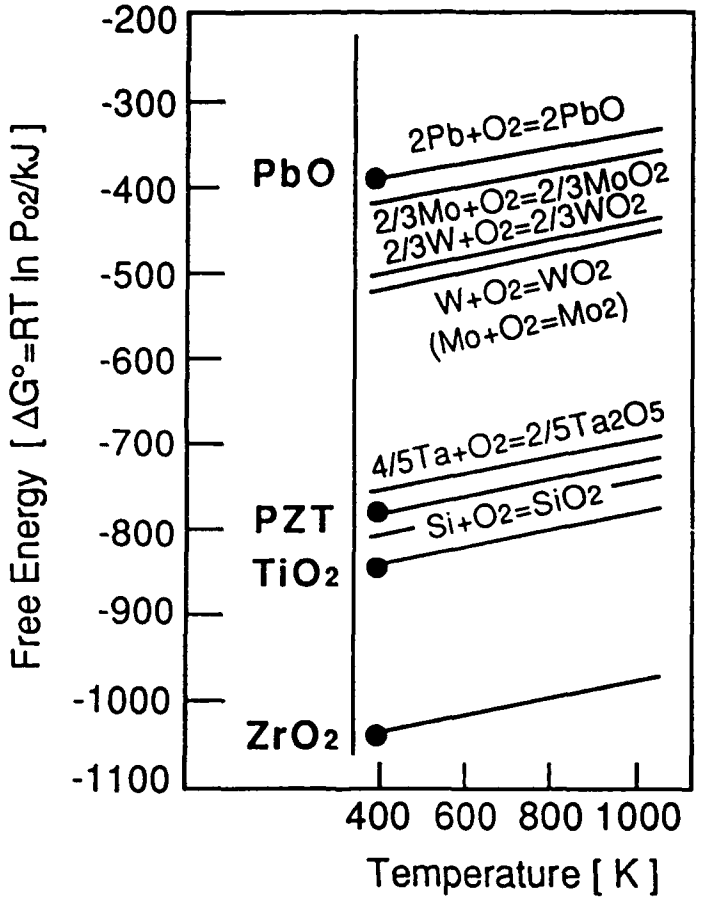


Figure 2. Configuration of PZT-Ta_2O_5 Capacitor

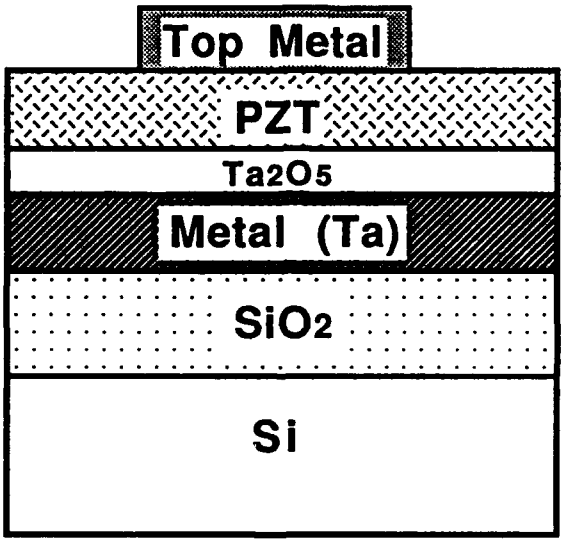


Figure 3. SEM Photograph of PZT Film (a) As Sputter

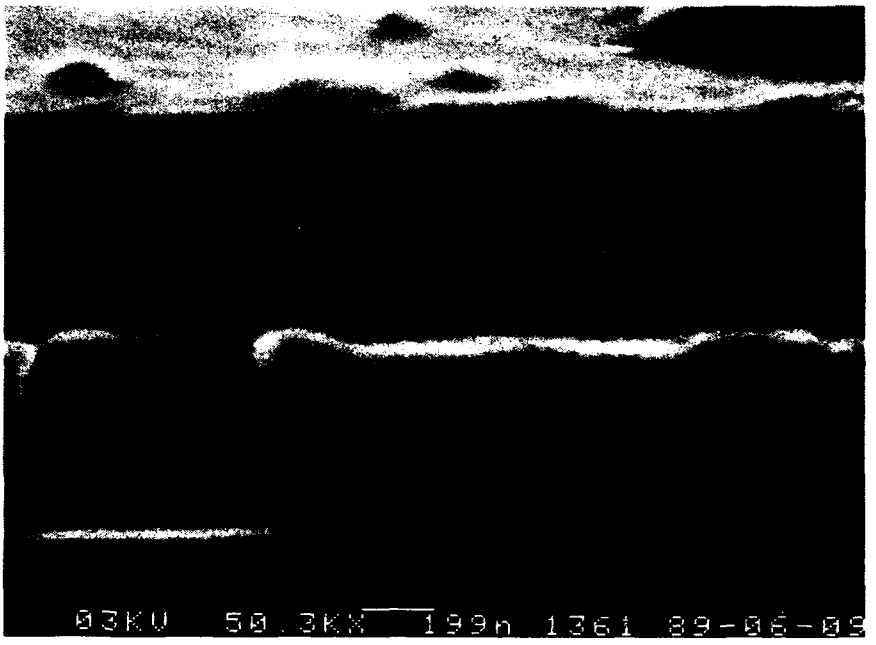


Figure 3. SEM Photograph of PZT Film (b) After Annealing

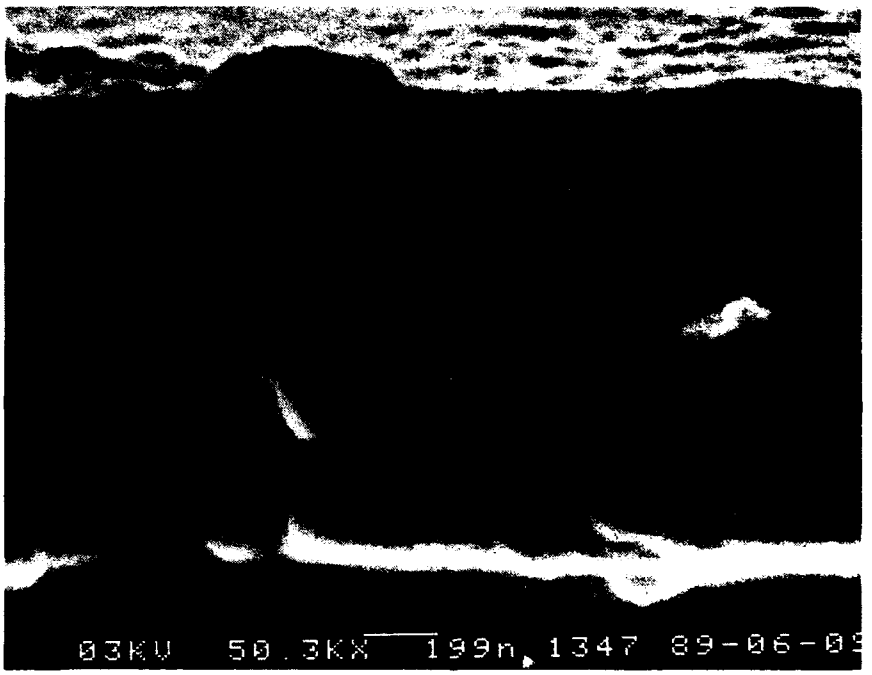


Figure 4. PZT Sputtering System

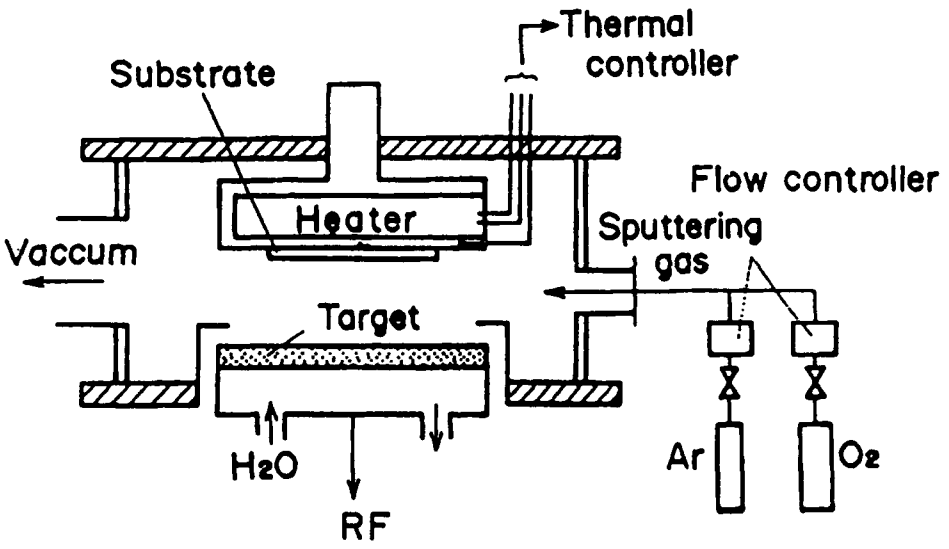


Figure 5. X-ray Diffraction Spectrum

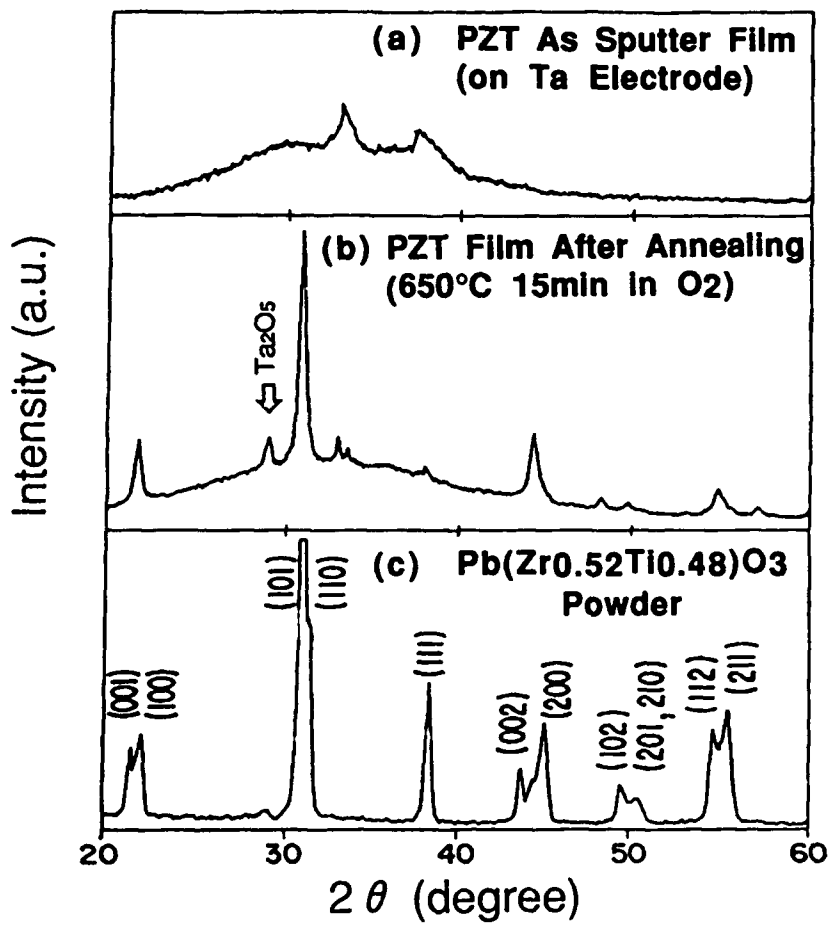


Figure 6. TEM Photograph of PZT-Ta_2O_5 Capacitor



Figure 7. Temperature Dependence of Dielectric Properties

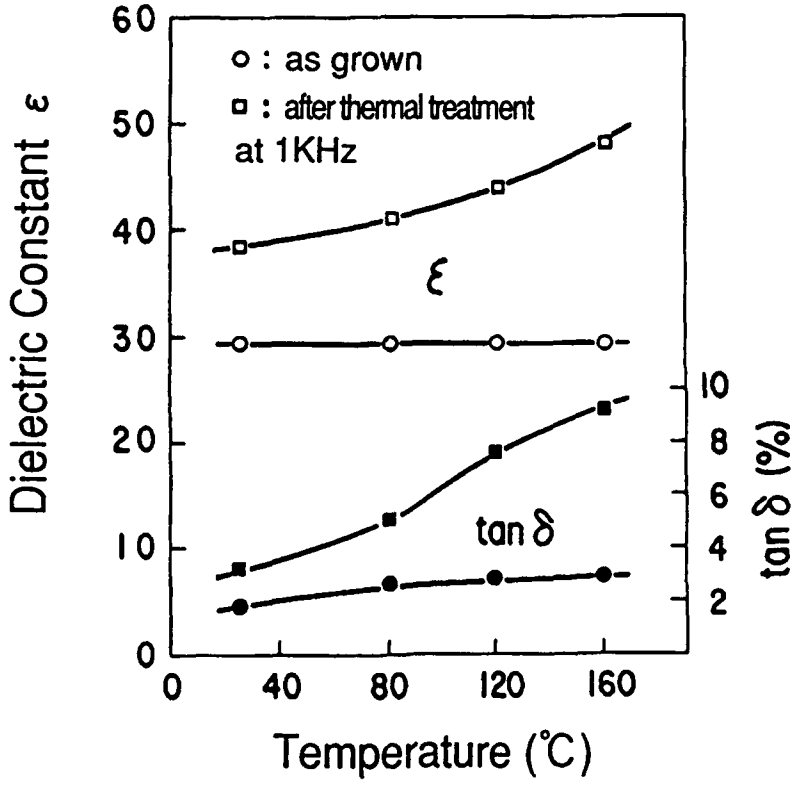
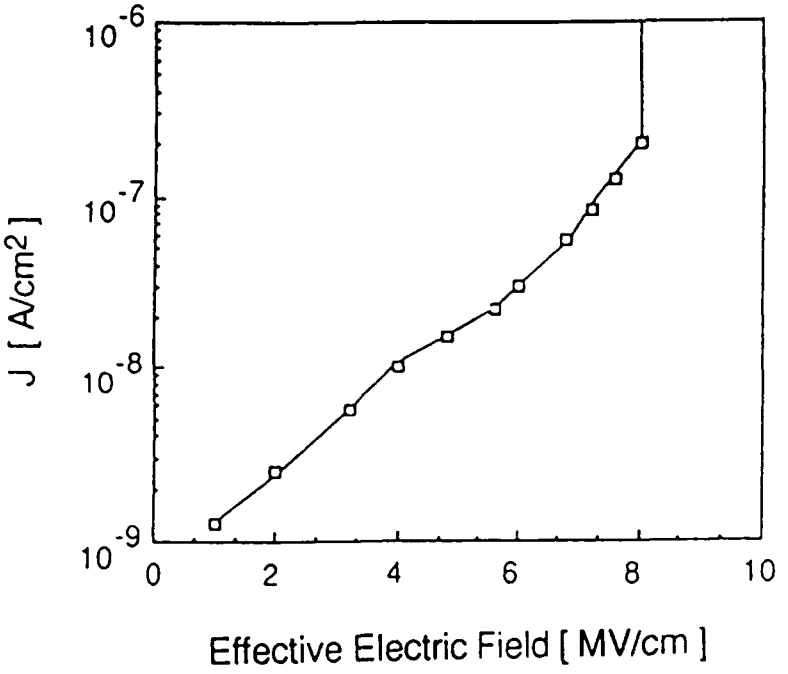


Figure 8. I-V Characteristics of PZT-Ta_2O_5 Capacitor



IMPROVED SWITCHING ENDURANCE OF LEAD ZIRCONATE-TITANATE CAPACITORS FOR NONVOLATILE MEMORY APPLICATIONS

I. K. Naik, L. E. Sanchez, S. Y. Wu and B. P. Maderic
McDonnell Douglas Electronic Systems Company
5301 Bolsa Avenue, Huntington Beach, CA 92647

Abstract. For nonvolatile memory applications, thin-film ferroelectric capacitors having high level of switching endurance (or ferroelectric fatigue limit) are required. This paper presents results that demonstrate improved endurance characteristics in our semiconductor-device quality, sol-gel derived lead zirconate-titanate (PZT) capacitors compared to other published results under comparable test conditions. These improved endurance characteristics have been obtained through continued developments in the PZT film deposition process, electrode metallization and capacitor fabrication techniques. Capacitors with top electrode of gold, platinum or palladium film and bottom electrode of platinum-titanium film were tested for endurance and related properties of transient current response, leakage current density, and small-signal capacitance-voltage and conductance-voltage characteristics. An alloying heat treatment of the gold or platinum top electrode to the PZT film significantly improved the endurance characteristics, apparently by decreasing the leakage current density. Capacitors with Pt top electrode that were alloyed at a lower than optimum temperature exhibited abnormal hysteresis loop changes after mid-10^9 cycles. Some evidence indicated that these changes were related to an increase in the leakage current density.

AD-P006 674

1. INTRODUCTION

Ferroelectric capacitors based on lead zirconate-titanate (PZT) thin films are currently being evaluated in nonvolatile memories of different designs.[1-3] This resurgence of interest in the use of the ferroelectric property for nonvolatile memory is largely due to the development of ferroelectric thin film deposition techniques that are compatible with the current semiconductor device and process technologies. The nonvolatility of these memory designs stems from the capability of storing a charge in the ferroelectric capacitor even when the applied voltage is removed, for example, as a result of turning the power off. Upon resumption of the power, the state of the memory cell is restored by a read-out of the charged state of the ferroelectric capacitor. Such scheme involving destructive read-out and rewriting entails multiple polarization reversals in the ferroelectric capacitor under high switching fields. This polarization reversal occurs via ferroelectric domain switching in the ferroelectric PZT material. With increased number of polarization reversal cycles, the polarization in the PZT film is known to decrease gradually, and this polarization degradation is generally known as fatigue in the ferroelectric material. In the terminology of semiconductor memories, the number of switching cycles that a memory device can withstand without failing as a memory is the switching endurance of the device. Thus, improved switching endurance is synonymous with better fatigue characteristic of a ferroelectric capacitor.

92-16149

Presently, sol-gel and sputter deposition processes for PZT films are the favored techniques for integrating with the semiconductor processes to develop ferroelectric nonvolative memory. Even though some limited applications are possible with the currently-available PZT capacitors, large-scale applications of

the ferroelectric memory will depend on the demonstration of high levels of switching endurance as well as reliability in the memory capacitors. This paper deals with the characterization and demonstration of improved fatigue or switching endurance in the sol-gel derived PZT capacitors for nonvolatile memory applications. The improved switching endurance has been obtained through continued developments in the PZT film processes, electrode metallization and capacitor fabrication techniques.

2. FERROELECTRIC FATIGUE/ENDURANCE

The phenomenon of ferroelectric fatigue has long been known in the bulk ferroelectric ceramics[4]. Fatigue characteristics are dependent on many parameters such as the chemistry and microstructure of the ferroelectric, electrode metallization, details of capacitor preparation techniques and details of test methods. Because of this complex nature, fatigue mechanisms are not well-understood even in the bulk ferroelectrics. In addition, since the applications of bulk ferroelectrics do not require a large number of polarization reversals as does the nonvolatile thin-film memory ($>10^{10}$ reversal cycles), fatigue of bulk ferroelectrics has not received a close examination. Recently, some experimental investigations of fatigue in PZT thin film capacitors have been reported, as discussed below.

Shepherd[5] published results of fatigue testing of PZT capacitors prepared using sol-gel deposited films. A pulse technique was used for measuring the switchable polarization remaining after various number of switching cycles, which were applied as 1 MHz sinusoidal voltage cycles. The results showed that maximum switchable remanent polarization (P_r) was 6 $\mu C/cm^2$. For capacitors designated as type I with PZT thickness of 4000Å, the fatigue limit (i.e. the switching endurance) at useful operating voltage of 5V was about 10^{10} cycles with P_r of 2 $\mu C/cm^2$ after 10^{10} cycles. For another category of capacitors designated as type II that used proprietary electrodes, P_r of 4 $\mu C/cm^2$ remained after 10^{11} cycles. Fatigue was observed to occur in two stages: an initial period characterized by a rising polarization during which the domain matrix was presumed to be undergoing restructuring and a second stage during which the polarization decreased presumably due to the formation of low dielectric constant layers adjacent to the electrodes. A more detailed correlation with the PZT microstructure, domain structure and electrode-ferroelectric interface was not possible within the scope of that study.

Johnson et al.[6] investigated the fatigue characteristics of PZT capacitors made by both sol-gel process and sputter deposition. For the sputtered films, they explained the observed fatigue behavior in terms of delamination at the electrode/PZT film interface. The fatigue limit for the sputtered films was about 10^9 cycles. For sol-gel processed films, the fatigue limit was quite low ($\sim 10^5$ cycles) and this low limit was attributed to a dielectric breakdown in the relatively poorly-prepared sample.

Melnick et al.[7] compared the fatigue characteristics of Pt/PZT/Pt capacitors with Zr/Ti ratios of 40/60 and 60/40. The PZT films of 2500Å thickness were deposited by a sol-gel technique. The fatigue cycles were applied as pulses and the switchable polarization was measured intermittently during cycling. They found that, up to 10^9 cycles, the 40/60 PZT composition had better fatigue characteristic. Beale and Duiker[8] have proposed a qualitative model for ferroelectric fatigue in thin films which involves diffusive motion of "point defects" in the film. Under repeated polarization reversal cycles, relatively high-

conductivity dendrites are presumed to grow from the electrode/ferroelectric interfaces as a result of the accumulation of charged point defects at these interfaces. This model is claimed to explain several observed features of the fatigue behavior.

In this paper, we provide some detailed experimental data on the fatigue or endurance characteristics of our PZT capacitors made with sol-gel derived very-thin PZT films. We demonstrate that the electrode metallization, heat treatment of the electrode/PZT interface, PZT microstructure and the electric field at which the capacitors are cycled all have crucial effects on the fatigue characteristics. By improving these parameters through materials and process development, we have achieved improved fatigue characteristics that make these capacitors useful for nonvolatile memory applications.

3. EXPERIMENTS

3.1 Sample Preparation

A cross-section of a typical PZT capacitor employed in this study is shown in Fig. 1. These capacitors were fabricated from thin PZT films deposited by our modified sol-gel process as published before.[9] A brief description of the processing of the PZT films and capacitors is given here. The sol-gel process uses a metallorganic liquid formulation that is spin-coated on a semiconductor wafer (Si or GaAs) in a manner similar to that used for photoresist. For capacitor fabrication, the spin-coating is applied to a wafer that already has the bottom electrode (BE) of Pt(2000Å)/Ti (200Å) and diffusion barrier films [2000Å SiO_2 and 1000Å silicon nitride (SiN)] between BE and the wafer as shown in Fig. 1. The dried metallorganic coating is then heat-treated in an oxygen-containing atmosphere at 650°C for 15 min. to crystallize and densify the PZT film. The Zr/Ti atomic ratio and excess PbO in the PZT film are controlled mainly by the sol formulation and sintering conditions.

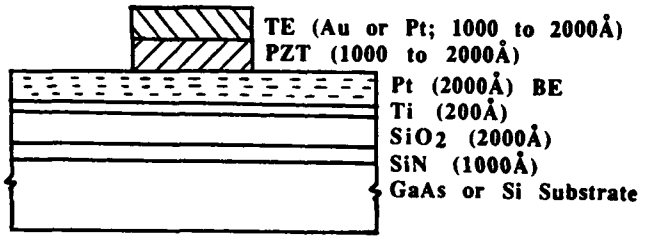


Fig. 1. Cross-section of a typical ion-beam-milled PZT capacitor used in this study. (TE: Top electrode; BE: Bottom electrode.)

In the next step, top electrode (TE) metallization is deposited over the PZT-coated wafer by electron beam evaporation technique. In the present study, following top electrode metallizations have been evaluated: Au(2000Å), Au (1000Å)/Pt(1000Å), Pt(2000Å), Pd(2000Å). Then individual capacitors ranging in areas from 4 μm x 4 μm to 40 μm x 40 μm are defined by means of standard photolithography and ion beam milling techniques. The ion beam milling is done through both the top electrode and the PZT film in the areas not covered by the photoresist and stopped at the bottom electrode. After this, the discrete capacitors are heat-treated and finally electrically tested.

3.2 Endurance and Related Measurements

We have characterized the endurance behavior in terms of the variation of the remanent polarization (P_r) as a function of the number of fatigue cycles. The remanent polarization was obtained from the measured ferroelectric hysteresis loop of the PZT capacitor under test. The hysteresis loop was measured by means of a Sawyer-Tower bridge circuit using 1 KHz sine-wave voltage signal ranging from 3 to 6 V. Endurance cycling of the capacitors was done at a frequency of 1 MHz at voltages from 3 to 6 V. To determine P_r after certain number of fatigue cycles, the cycling was interrupted and the hysteresis loop was measured at 1 KHz. Then the cycling process was resumed to accumulate additional number of cycles.

Microstructures of the fresh and endurance-cycled capacitors were examined by means of Nomarski phase contrast microscopy up to a magnification of 2000 to determine if any significant microstructural change had taken place during endurance cycling.

Complementary electrical tests were performed on the fresh and various fatigue-cycled capacitors by means of the following techniques: (1) high-precision d.c. leakage current measurements with a sensitivity of 5 pA. (2) small-signal (30 mV rms) capacitance versus voltage (C-V) and conductance versus voltage (G-V) measurements at 1 MHz. (3) high-precision transient current (I-t) measurements by means of a computer-controlled test system that provided a clean voltage signal and time-precision of better than one nanosecond.

4. RESULTS AND DISCUSSION

4.1 Effects of Zr/Ti Ratio

The dependence of the endurance characteristics on the Zr/Ti atomic ratio close to the morphotropic phase boundary composition is shown in Fig. 2. These data were obtained from 40 μm x 40 μm capacitors having 1000Å PZT thickness and 2000Å Au top electrode that was alloyed at 650°C. The capacitors with 50/50 Zr/Ti ratio films were hysteretic after 10^{10} cycles while the capacitors with 60/40 and 70/30 Zr/Ti ratio films shorted at ~10^9 and ~10^8 cycles, respectively. The film with 50/50 Zr/Ti ratio had tetragonal crystal structure as determined by x-ray diffraction and it was predominantly single phase as indicated by both x-ray diffraction and high-resolution phase contrast microscopy. The higher Zr/Ti ratio films showed lower initial P_r and slimmer hysteresis loops. In addition, the film with 70/30 Zr/Ti ratio had primarily rhombohedral crystal structure. The lower endurance limits of the capacitors with 60/40 and 70/30 Zr/Ti ratios may be related to a multiphase structure for these films. These results indicated that the PZT film with tetragonal crystal structure and 50/50 Zr/Ti ratio had the optimum endurance for our sol-gel films. Similar effect of Zr/Ti ratio on the fatigue property has also been reported recently by Melnick et al.[7] Based on the above results, the PZT composition with 50/50 Zr/Ti ratio was selected as an optimum composition with respect to high P_r (i.e. a composition close to morphotrophic boundary) and good endurance characteristics. The results discussed in the following parts are for the PZT films of 50/50 Zr/Ti ratio.

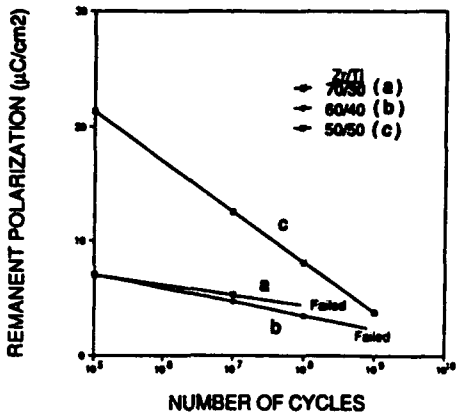


Fig. 2. Dependence of the endurance characteristics on the Zr/Ti ratio for Au/PZT (1000Å)/Pt-Ti capacitors.

4.2 Effect of Alloying Heat Treatment of Top Electrode

We have found that a simple heat treatment we call alloying of the top electrode of Au or Pt to the PZT film significantly improves the endurance characteristic of the PZT capacitor. Typical data showing the endurance improvement upon TE alloying are shown in Fig. 3 for 40 μm x 40 μm Au/PZT(1000Å)/Pt-Ti capacitors. The alloying treatment for the samples of these data was carried out at 650°C for 15 min. in a flowing O_2/N_2 atmosphere. In addition, this alloying treatment makes the hysteresis loop more symmetrical compared to that of an unalloyed capacitor and reduces the coercive voltage significantly. We believe that the alloying treatment establishes a good contact between the top electrode and the PZT film via diffusion of the TE metallization into PZT to a certain controlled extent. In addition, the diffusion reduces the effects of space charge layers at the electrode/PZT interface. This area deserves further study by means of high-resolution electron microscopy and other complementary electrical and material characterization techniques.

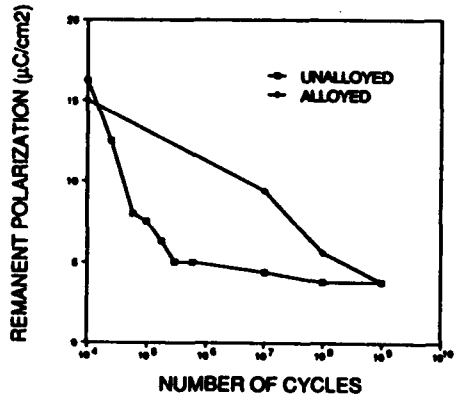


Fig. 3. Improvement in the endurance characteristics as a result of the alloying heat treatment of the top electrode for 40 μm x 40 μm Au/PZT(1000Å)/Pt-Ti capacitors.

4.3 Effects of Type of Top Electrode Metallization

We have evaluated Au, Au/Pt, Pt and Pd as top electrode metallizations. Au and Au/Pt (overlayer) essentially show the same endurance characteristics since Au is the intimate contact to PZT in both cases. Top electrode of Au alone, however, develops some porosity due to reaction between Au and excess PbO in the PZT film

during alloying which gives rise to a "fritted" top electrode as shown in Figure 4. To improve the morphology of the top electrode when Au is used, a layer of ~1000Å thick Pt is deposited over the Au film.

Fig. 4. Photomicrograph of a gold top electrode (125 μm diameter dot) alloyed at 650°C for 15 min on a PZT film of Zr/Ti ratio 50/50.

⊢ 20 μm ⊣

4.3.1 Gold Top Electrode

The endurance characteristics of Pt(1000Å)/Au(1000Å)/PZT/Pt(2000Å) -Ti(200Å) capacitors with different PZT film thicknesses are shown in Fig. 5. For the thinner PZT films (1000Å and 1400Å), P_r decreased linearly with the logarithm of the number of fatigue cycles between 10^5 and 10^8 cycles. Following the logarithmic decay, P_r reaches a stage in which it decreases very slowly. After 10^{11} cycles, P_r is ~3 μC/cm^2 for these capacitors. For the 1900Å film, P_r did not decrease significantly up to 10^{10} cycles for both voltages, 3 V and 6 V corresponding to fields of 158 kV/cm and 316 kV/cm. Typical hysteresis loops obtained during cycling are shown in Fig. 6 which show negligible change in the hysteresis loop after 10^{10} cycles at ± 3 V. After 10^{11} cycles, P_r values decreased to 3 μC/cm^2 and 5 μC/cm^2 at switching fields of 158 and 316 kV/cm, respectively. At such high switching fields, these endurance characteristics are the best published to date. For comparison, Shepherd'sresults[5] were as follows: (1) For his type I capacitors: P_r was 1 μC/cm^2 after 10^8 cycles at 150 kV/cm sine-wave cycling; P_r was 1 μC/cm^2 after 10^7 cycles at 400 kV/cm; (2) For his type II capacitors with proprietary top electrodes: P_r was ~4 μC/cm^2 after 10^{11} cycles at 125 kV/cm; P_r was ~3.5 μC/cm^2 after 10^9 cycles at 200 kV/cm.

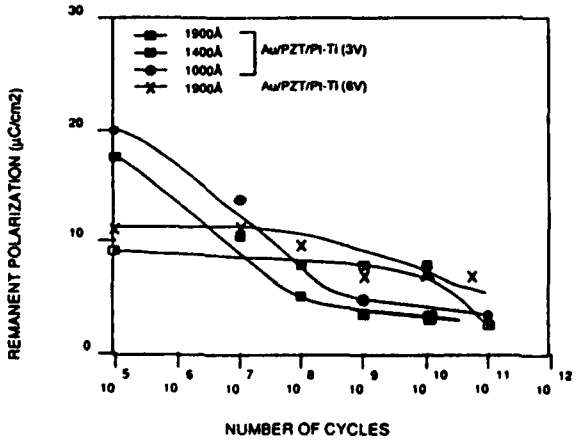
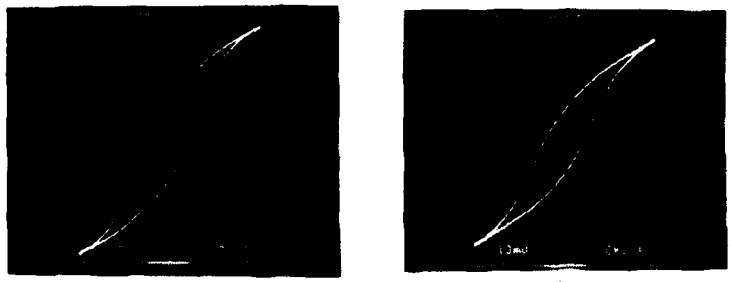


Fig. 5.

Endurance characteristics of gold-top-electroded Pt/Au/PZT/Pt-Ti capacitors with different PZT film thicknesses.



a b

Fig. 6. Hysteresis loops of Pt/Au/PZT(1900Å)/Pt-Ti capacitor at different stages in the fatigue cycling: (a) initial (~10^4 cycles) (b) after 10^{10} cycles. (Scales: x-axis: 1 V/div.; y-axis: 6.25 μC/cm^2/div.).

We believe that the improved endurance characteristics of our PZT capacitors are the result of better control of the PZT film chemistry, degree of preferred orientation of the PZT grains and microstructure of the PZT film obtained in the modified sol-gel process. These high-density PZT films have submicron grain size (0.2 to 0.7 μm range) as shown in Fig. 7 and high degree of {001} preferred orientation as shown in the x-ray diffraction pattern of Fig. 8. In addition, the alloying treatment significantly improves the electrode/PZT contact interface and thus reduces the space charge effects in the capacitors.

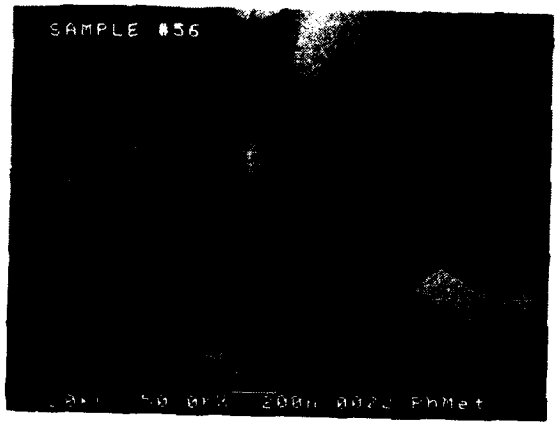


Fig. 7.

Scanning electron photomicrograph of the surface of a typical 1000Å PZT film with Zr/Ti ratio 50/50 showing the fine grain size.

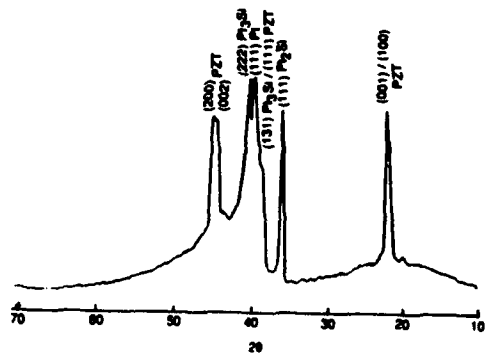
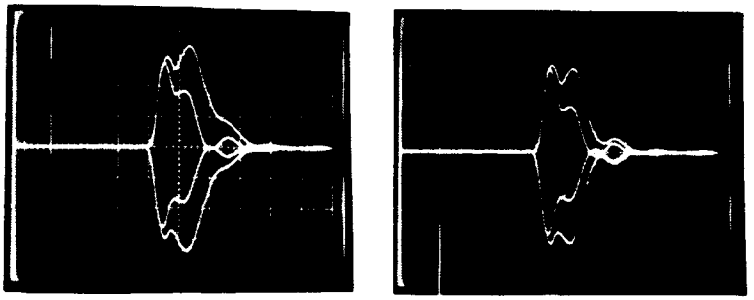


Fig. 8. X-ray diffraction pattern of a typical 1000Å PZT film with Zr/Ti ratio 50/50.

We have observed significant reduction in the leakage current density of the very-thin PZT film (2000Å or less) capacitors upon alloying of the Au top electrode. In an unalloyed capacitor, grain boundaries in the PZT film are most likely the leakage current paths as a result of impurity segregation and high defect concentration in the grain boundaries. It is conceivable that diffusion of Au (or for that matter of other similar noble metal such as Pt as described in the next section) into the grain boundaries during alloying compensates some of the charge carriers in the grain boundaries and thus reduces the leakage current density. Alternatively, diffusion of Au into the grain boundaries might be able to reduce the space charge effects at the grain boundaries and improve the endurance characteristics. To our knowledge, such improvement in the endurance characteristics by electrode alloying has not been documented before.

Transient current responses measured on fresh and endurance-cycled Pt/Au/PZT(1900Å)/Pt-Ti capacitors are shown in Fig. 9. After 1.6×10^{10} fatigue cycles at ± 3 V, the amount of charge switched in a polarization reversal (as indicated by the area between the two curves corresponding to the switching (outer) and nonswitching (inner) current responses) is more than 50% of that for the fresh capacitor. This result validates the fatigue characteristics shown in Fig. 5 which were determined using hysteresis loop as the measure of the switching property.



a b

Fig. 9. Transient current response of 40 μm x 40 μm Pt/Au/PZT (1900Å)/Pt-Ti capacitors (a) fresh capacitor (b) after 1.6×10^{10} cycles.
(Scales: x-axis: 20 ns/div: y-axis: 4 mA/div.).

Typical results of small-signal C-V and G-V measurements made on fresh and endurance-cycled 40 μm x 40 μm Pt/Au/PZT(1900Å)/Pt-Ti capacitors are shown in Fig. 10. When cycled at ± 3 V, there was little change in the C-V and G-V characteristics after 10^{10} cycles. This result was consistent with the fatigue characteristics of Fig. 5 that used hysteresis loop as the measure of the change during fatigue. When cycled at ± 6 V, as the number of cycles were accumulated, the capacitance and conductance peaks due to domain switching were reduced. This result indicated that as fatigue progressed, less number of domains responded to this small-signal (30 mV rms) voltage compared to a fresh capacitor. Such an effect can be interpreted as the result of pinning of domain walls as large number of polarization reversal cycles (~10^{10}) are applied to the capacitor.

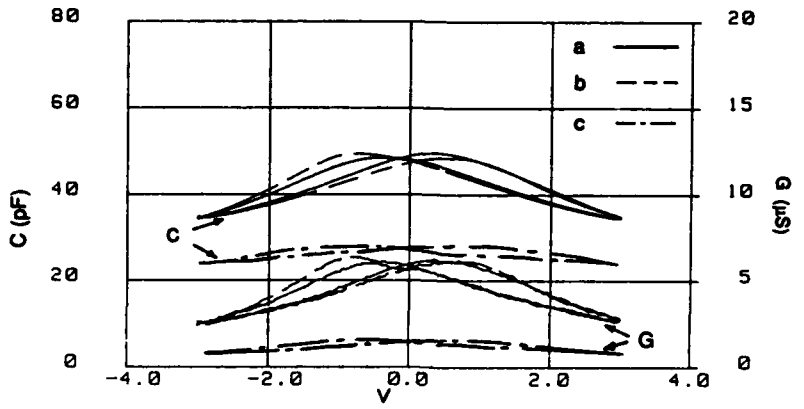


Fig. 10. Small-signal C-V and G-V characteristics of 40 μm x 40 μm Pt/Au/PZT(1900Å)/Pt-Ti capacitors: (a) fresh capacitor (b) after 10^{10} cycles at ± 3 V (c) after 10^{10} cycles ± 6 V.

Endurance-cycled Pt/Au/PZT/Pt-Ti capacitors examined after 10^{10}, 10^{11} and 10^{12} cycles did not exhibit any significant changes in the microstructures in the phase contrast microscopy up to a magnification of 2000. Based on these observations, microcracking of PZT or major delamination of the top electrode were considered unlikely. Thus, all of the above experimental results were consistent with a domain pinning model for gradual reduction in P_r with cycling.

4.3.2 Platinum Top Electrode

Capacitors with Pt top electrode showed a slightly different endurance behavior as shown in Fig. 11. After mid-10^9 cycles at ± 3 V, Pt(2000Å)/PZT(1000Å)/Pt-Ti capacitors that were alloyed at 650°C for 15 min showed a blooming-type distortion of the hysteresis loop. Such typical hysteresis loop distortion is shown in Fig. 12 (b) and (c). Small-signal C-V and G-V measurements on such cycled capacitors did not show any increase in the displacement-related capacitance or conductance; in fact, the peak capacitance and conductance were significantly lower than that for a fresh capacitor (Fig. 13). Additionally, high-precision (pA-level) d.c. leakage current measurements on such distorted-loop capacitors showed some increase in the leakage current: from ~40 pA at 4 V for a 20 μm x 20 μm fresh capacitor to ~70 pA at 4 V for a capacitor cycled to 4 x 10^9 cycles (Fig. 14). This leakage current increase corresponded to a resistivity decrease from 4 x 10^{10} Ω-cm for a fresh capacitor to 2.3 x 10^{10} Ω-cm for the cycled capacitor. Transient current responses of these Pt-electroded capacitors at different stages of the endurance cycling are shown in Fig. 15. It is seen that the amount of charge switched did not degrade significantly up to 10^9 cycles. But after 4 x 10^9 cycles, the switching transient became considerably slower. These results indicated that the distortion of the measured hysteresis loop might be due to an increase in the leakage current. Even though the absolute magnitude of the leakage current was still quite small after mid-10^9 cycles, the distortion in the hysteresis loop was quite dramatic. This observed distortion of the hysteresis loop qualitatively matches the recent modeling prediction of Miller et al.[10] based on an equivalent circuit approach.

Alloying of the Pt TE at a higher temperature (700°C, 5 min) gave capacitors that did not show significant hysteresis loop distortion until 8 $x10^{10}$ cycles (Fig. 11). Still higher temperature of alloying (800°C, 5 sec in a rapid thermal annealing equipment) gave capacitors that did not show distortion up to 2 x 10^{11} cycles. This trend of the effect of alloying temperature showed that the Pt top electrode requires higher temperature of alloying to get the equivalent improvement in endurance characteristics as the Au electrode.

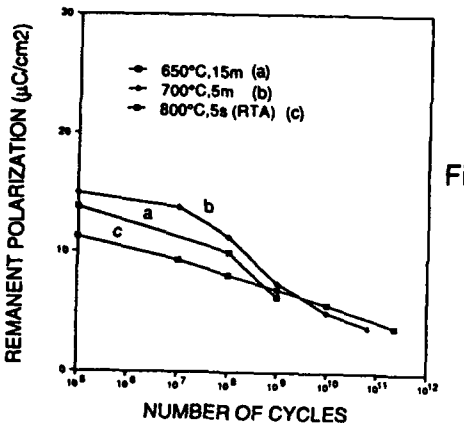


Fig. 11. Endurance characteristics of Pt-top electroded 40 μm x 40 μm Pt/PZT (1000Å)/Pt-Ti capacitors alloyed under different conditions.



a b c

Fig. 12. Hysteresis loops of 20 μm x 20 μm Pt-top-electroded Pt/PZT (1000Å)/Pt-Ti capacitors: (a) fresh capacitor (b) after $5x10^9$ cycles (c) after $1x10^{10}$ cycles. (Scales: x-axis: 1 V/div; y-axis: 12.5 $\mu C/cm^2$/div.).

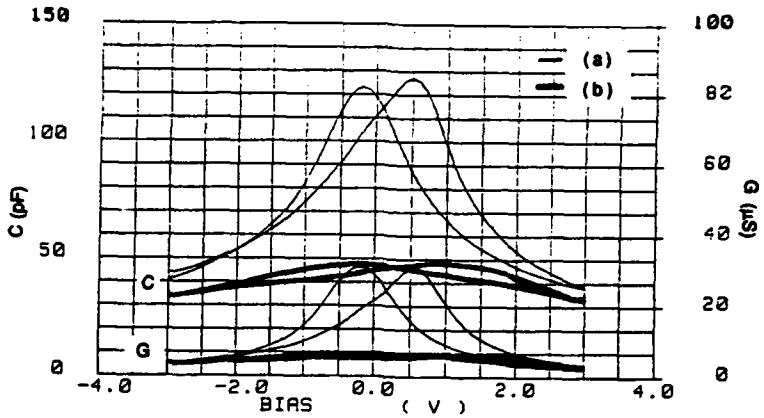


Fig. 13. Small-signal C-V and G-V characteristics of 40 μm x 40 μm Pt/PZT(1000Å)/Pt-Ti capacitors (a) fresh capacitor (b) after $6x10^9$ cycles.

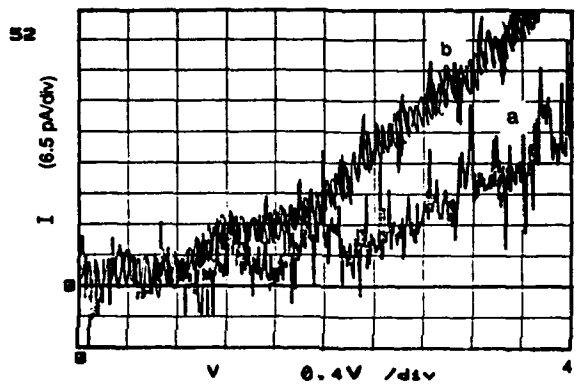


Fig. 14. D.C. leakage current versus voltage of 20 μm x 20 μm Pt/PZT (1000Å)/Pt-Ti capacitors: (a) fresh capacitor (b) after $4x10^9$ cycles.

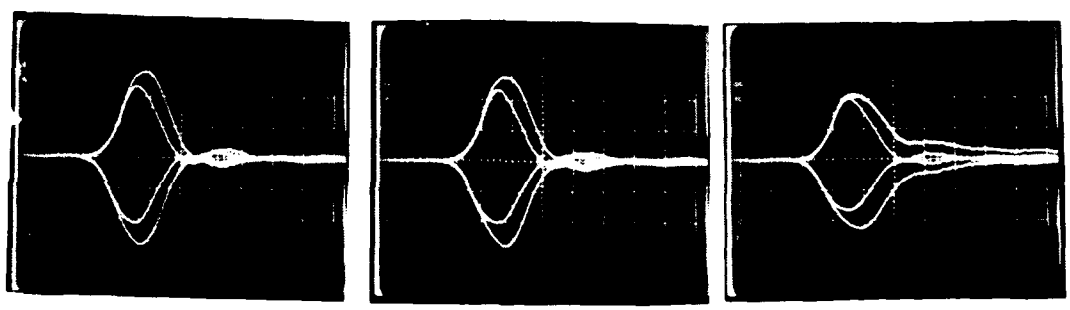
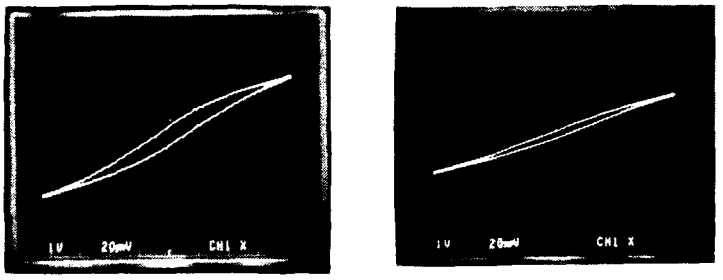


Fig. 15. Transient current response of 20 μm x 20 μm Pt-top-electroded Pt/PZT (1000Å)/Pt-Ti capacitors: (a) fresh capacitor (b) after $1x10^9$ cycles (c) after $4x10^9$ cycles (Scales: x-axis: 5 ns/div and y-axis: 4 mA/div).

4.3.3 Palladium Top Electrode

Palladium (Pd) film proved to be much inferior as a top electrode than Au and Pt films. Hysteresis loops of Pd (2000Å)/PZT(1000Å)/Pt-Ti capacitors in fresh condition and after 10^7 cycles are shown Fig. 16. This Pd TE was alloyed at 650°C for 15 min in O_2/N_2 mixture. It is known that Pd forms an oxide much more readily than Pt or Au. In our experiments, the initial silvery, mirror-finished top Pd surface turned rough and blue-black in color after the alloying treatment. This result taken in conjunction with the known results of other electrodes made of oxide-forming metals such as Cr, V or W demonstrated that any metal that tends to significantly deplete oxygen from the PZT film is a poor electrode for obtaining better endurance characteristics. By projection, conducting oxides such as indium-tin oxide (ITO), ruthenium oxide (RuO_2) or superconducting oxides (such as high T_c superconductors) should prove quite effective as electrodes if other processing requirements can be satisfied.



a b

Fig. 16. Hysteresis loops of 40 μm x 40 μm Pd-top-electroded Pd/PZT (1000Å)/Pt-Ti capacitor: (a) fresh capacitor (P_r = 5 μC/cm^2) (b) after 10^7 cycles (P_r = 1 μC/cm^2). Scales: x-axis: 1 V/div; y-axis: 12.5 μC/cm^2/div.

5. CONCLUSIONS

Compared to the results reported in the literature under similar test conditions, we have demonstrated improved switching endurance limit in the sol-gel derived, semiconductor device-quality PZT thin-film capacitors. In particular, typical endurance of better than 10^{11} polarization reversal cycles at 316 kV/cm was obtained with remanent polarization of 5 μC/cm^2 maintained after 10^{11} cycles. This endurance improvement was mainly realized through continued developments in the PZT thin film processing, electrode metallization and capacitor fabrication techniques. As a result, our PZT film with 50/50 Zr/Ti ratio sintered on Pt-Ti bottom electrode had tetragonal perovskite crystal structure, high degree of {001} preferred orientation and very fine grain size (0.2 to 0.7 μm). For capacitors with PZT film thickness between 1000Å and 2000Å, noble metal top electrodes of Au, Pt and Pd were evaluated. We determined that a heat treatment of the Au or Pt top electrode to the PZT film improved the endurance characteristics significantly, apparently by decreasing the leakage current density. Evidence indicated that the optimum heat treatment temperature was lower for Au top electrode than that for Pt electrode. Capacitors with Pt top electrode that were alloyed at a less than optimum temperature exhibited abnormal changes in the hysteresis loop after extended cycling (mid-10^9 cycles) that looked like an apparent increase in P_r. These

capacitors, however, also showed a small increase in the leakage current density after mid-10^9 cycles (from ~10 $\mu A/cm^2$ to ~18$\mu A/cm^2$ at 4 V). The endurance behavior of the well-alloyed Au-and Pt-electroded capacitors seemed to conform to a fatigue model based on the gradual clamping of the domain walls with increased number of switching cycles.

ACKNOWLEDGEMENTS

The authors acknowledge useful technical discussions and managerial support provided by W. A. Geideman and A. J. McDonald. This work was funded by the Defense Advanced Research Projects Agency.

REFERENCES

1. C. A. Paz de Araujo and G. W. Taylor, Ferroelectrics 116, 215 (1991). (Proceedings of the Second Symposium on Integrated Ferroelectrics, 1990).
2. J. F. Scott, C. A. Paz de Araujo and L. D. McMillan, Ferroelectrics, 116, 107 (1991).
3. W. A. Geideman, S. Y. Wu, L. E. Sanchez, B. P. Maderic, W. M. Liu, I. K. Naik and S. H. Watanabe, 'PZT Thin Films for GaAs Ferroelectric RAM Applications," Paper presented at the Seventh International Symposium on Applications of Ferroelectrics, Urbana, Illinois, June 1990.
4. M. E. Lines and A. M. Glass, "Principles and Applications of Ferroelectrics and Related Materials", Clarendon Press, Oxford, U.K., p. 117 (1977).
5. W. H. Shepherd, Materials Research Society Symp., Proc. Vol. 200, 277 (1990).
6. D. J. Johnson, D. T. Amm, E. Griswold, K. Sreenivas, G. Yi and M. Sayer, ibid, 289 (1990).
7. B. M. Melnick, C. A. Paz de Araujo, L. D. McMillan, D. A. Carver and J. F. Scott, Ferroelectrics, 116, 79 (1991).
8. P. D. Beale and H. M. Duiker, ibid, 111 (1991).
9. L. E. Sanchez, D. T. Dion, S. Y. Wu and I. K. Naik, Ferroelectrics, 116, 1 (1991).
10. S. L. Miller, R. D. Nasby, J. R. Schwank, M. S. Rodgers and P. V. Dressendorfer, J. Appl. Phys., 68 (12), 6463 (1990).

AD-P006 675

CRACK-FREE PZT THIN FILMS MICROPATTERNED ON SILICON SUBSTRATE FOR INTEGRATED CIRCUITS

MOTOO TOYAMA, NAOTO INOUE, MASANORI OKUYAMA*,
AND YOSHIHIRO HAMAKAWA*
Seiko Instruments Inc., Takatsuka Unit, 563 Takatsukashinden, Matsudo, Chiba 271, Japan
*Department of Electrical Engineering, Faculty of Engineering Science, Osaka University, Machikaneyama-cho 1, Toyonaka, Osaka 560, Japan

Abstract Process for getting crack-free lead zirconate titanate (PZT) thin films micropatterned on Si substrate is demonstrated. The PZT film was deposited at temperatures below 300°C by magnetron sputtering using a ceramic target, and then etched before annealing. After annealed above 500°C to get perovskite phase, the PZT films shows no crack, while PZT films, not patterned, has cracks. This result can be explained as dissipation of stress energy by reduction of the lateral size of the film. The effects of processing parameters of reactive sputtering and annealing on the morphology of the PZT thin films are presented. Photo-assist etching of the PZT thin films using KrF laser is described, too.

INTRODUCTION

Lead zirconate titanate (PZT) is a promissing material for a ferroelectric thin film used in integrated memory circuits[1]. Preparation of PZT films in a crack-free state is crucial for the applications. A report[2] was done about a method of getting crack-free PZT films by sol-gel technique. On the other hand, high temperature sputtering has been widely used to prepare PZT films[3,4] but it is a costly process. Instead, we have studied about preparing a perovskite PZT film by annealing of a low temperature (<300°C) sputtered film[5]. This paper describes some detailes about the effects of processing conditions on PZT film morphology and presents a route to suppress cracks in the PZT films processed by this method.

DEPOSITION AND ANNEALING OF PZT FILMS

Deposition and annealing of PZT films were done on (111) oriented Pt (1200Å) films sputtered beforehand on Si substrates with 1000Å SiO_2. Ti (1200Å) layer was used for better adhesion between Pt and SiO_2. Deposition conditions of PZT thin films by magnetron sputtering are summerized on Table I . Sputtering target was a hot

92-16150

pressed PZT disk of the Zr/Ti atomic ratio of 65/35. Maximum substrate temperature during deposition was limited to 300°C.

Figure 1 shows a relationship between the deposition rate of the PZT film and the oxygen partial pressure during sputtering. The deposition rate drops drastically at around 5×10^{-3} Pa. This change is explained as process of reduction of oxide metals on the ceramic target surface by the argon ions[6]. Composition was measured by AES for the PZT film deposited at room temperature in the gas composition of $Ar/O_2=72/8$ (in [ccm]). Compared with the composition of the ceramic target, the amount of lead was reduced by 20% and Zr/Ti ratio became Zr rich (74/26), while oxygen content remained unchanged. Figure 2 shows X-ray diffraction patterns of the PZT film as sputtered at room temperature and after annealed at 500-800°C in oxygen atmosphere for 3 hours in a quartz tube. By annealing at 600°C, the film becomes rhombohedral perovskite. The annealing effects were investigated on PZT films deposited under several Ar/O_2 ratios at substrate temperatures of 300°C and room temperature. The results are summerized on Table II. The structure of the film becomes perovskite by a lower temperature annealing when gas ratio of oxygen decreases and when the film is deposited at lower temperature. Lower oxygen ratio in sputtering gas composition is preferable for higher deposition speed but leads to peel-off of the PZT film by annealing. The FWHMs of the XRD peaks of (110) and (100) of the PZT films are ploted in Figure 3. These data are for those perovskite films depicted on Table II. The values of FWHMs don't chage in the perovskite films annealed at the lowest temperature and the highest temperature. According to Table II and Figure 3, higher deposition temperature is preferred for better crystallinity though it requires higher annealing temperature to obtain a perovskite phase. P-E hysteresis were measured by depositing aluminum electrodes on the annealed PZT films. Figure 4 shows an uncompensated P-E curve for the sample deposited at room temperature with the gas supply of $Ar/O_2=72/8$ (in [ccm]), annealed at 700°C. The capaciter area is 0.03 cm^2. The value of remanent polarization (3.1 $\mu C/cm^2$) is smaller than those reported for the PZT films deposited under high temperatures.

SUPPRESSION OF CRACKS IN PZT FILMS ON SILICON SUBSTRATES

Though the as-deposited films had smooth surface without crack, they grew cracks after the annealing. The examples of cracks are shown in Figure 5 for the PZT (3000Å) films annealed at 600°C on a platinum coated substrate (a) and on a Si (100) wafer (b). Typical sizes of cracks are clearly different between the two samples: 5 to 10 μm for PZT on platinum film, and 1 mm for PZT on Si. The difference of crack

scales can be attributed to difference in thermal expansion. Data of thermal expansions for platinum, silicon and PZT (50/50) are listed on Table Ⅲ. The expansion from room temperature to 600°C is about the same value between silicon and PZT (50/50), but, for platinum, the value is more than two times larger. The above results indicate that, by reducing the scale of PZT films by patterning before annealing, suppresion of cracks would be possible, because the stress energy caused by difference in thermal expansion would be dissipated in pattern edges.

Photo-assist etching of PZT films.

PZT films, as deposited at low temperature, were etched by HF solution. But the acid attacked photoresist (negative type) and adhesion of photoresist to the PZT films was weak, resulting in low fidelity to the feature of photomask. So, the authors tried photo-assist etching of PZT films. The samples of PZT films deposited on Si substrates at room temperature were dipped in KOH solution (10 mol in 1 l of water). The etching rate at 50°C was 20 Å/min. Three kinds of light sources were examined for photo-assistance: xenon lamp, KrF eximer laser 248 nm (50 mJ/cm^2/shot), and ArF laser. When a sample was irradiated by the light from xenon lamp, the etching rate became higher by two times. When a sample was irradiated by KrF laser (100 shots during 2 minutes of dipping), the etching rate became more than ten times higher. Light from ArF laser was absorbed by water and had no effect on etching. The photo-assist etching method seems quite adequate for lithography of ceramic films which has poor adhesion with photoresist, because photo-assistance doesn't depend on the adhesion.

The patterned PZT filmes after annealed

Figure 6 is a photograph of PZT films after annealed at 600°C in oxygen ambient for 3 hours. These films had been patterned before annealing. In this randomly chosen photo, larger patterns have cracks while smaller patterns don't. This result verifies our supposition that cracks would be suppressed by reducing the film size by patterning. But this tecnique is with reservation; the identical patterns shown in Figure 7 are of well reduced size, but each film has a crack at the same part (at "neck", one being indicated by an arrow). It seems that stress has concentrated in the "neck" portion. Consideration would be required in designing of PZT patterns to annihilate crackings by this method.

SUMMARY

In this paper, we have shown a process of getting crack-free PZT thin films deposited at low temperature and micropatterned on silicon substrate. The process includes

annealing of the low temperature deposited PZT thin film after patterning. The remanent polarization of the annealed PZT film was smaller (3.1 $\mu C/cm^2$) than the values reported for high temperature deposited films. In order to make the best of our method, rapid thermal annealing shouled be examined[7] for the benefit of reduction of thermal damages to the underlying devices during annealing as well as during film deposition. And relations between the pattern shapes of PZT films and growth of cracks have to be further investigated.

Also reported in this paper is photo-assist etching of PZT thin films. The etching rate was well enhanced by irradiation of KrF laser in KOH solution. The photo-assist etching is quite adequate when adhesion of photoresist to ceramic film is no good.

Efforts to improve the process demonstrated in this paper are now under way including multi-target sputtering in our laboratory.

ACKNOWLEDGEMENT

The authors are grateful to H. Kanda of Seiko I Technoresearch Co., and H Niwa for their experimental assistance.

REFERENCES

1. J. F. Scott, L. D. McMillan, and C. A. Araujo, Ferroelectrics, 116, 147 (1991).
2. L. E. Sanchez, D. T. Dion, S. Y. Wu, and I. K. Naik, Ferroelectrics, 116, 1 (1991).
3. R. Takayama and Y. Tomita, J. Appl. Phys., 65, 1666 (1989).
4. M. Adachi, T. Matsuzaki, T. Yamada, T. Shiosaki, and A. Kawabata, Jpn. J. Appl. Phys., 26, 550 (1987).
5. T. Fukami, S. Fujii, and H. Tsuchiya, Jpn, J. Appl. Phys. 24, Suppl., 24-2, 410 (1985).
6. J. Heller, Thin Solid Films, 7, 1 (1971).
7. B. R. Biswa, S. Chandratraya, and A. Pask, J. Am. Ceram. Soc., 58, 729 (1979).
8. T. S. Kalkur, J. Kulkarni, Y. C. Lu, M. Rowe, W. Han, and L. Kammerdiner, Ferroelectrics, 116, 135 (1991).

TABLE I Deposition conditions of PZT thin films.

Substrate	Pt(111)/Ti/SiO_2/Si, Si(100)
Target	PZT (65/35) Hot-press 3-in. ϕ
RF Power	100W (2.2W/cm^2)
Sputter Gas	Ar/O_2 Total Flow 80ccm
Pressure	0.35 Pa

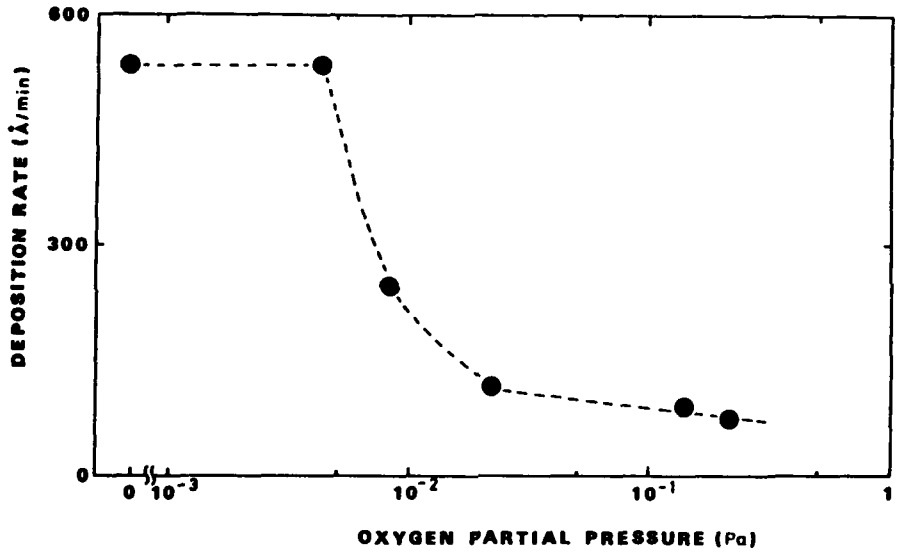


FIGURE 1 Deposition rate of PZT v.s. oxygen partial pressure.

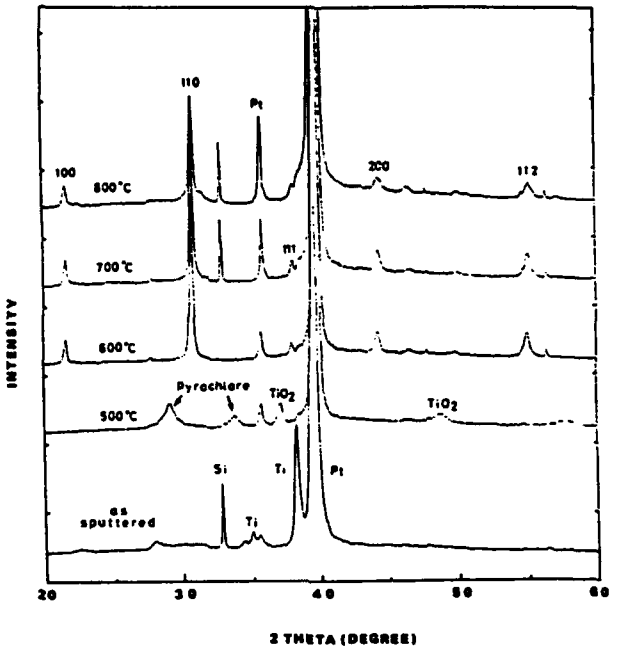
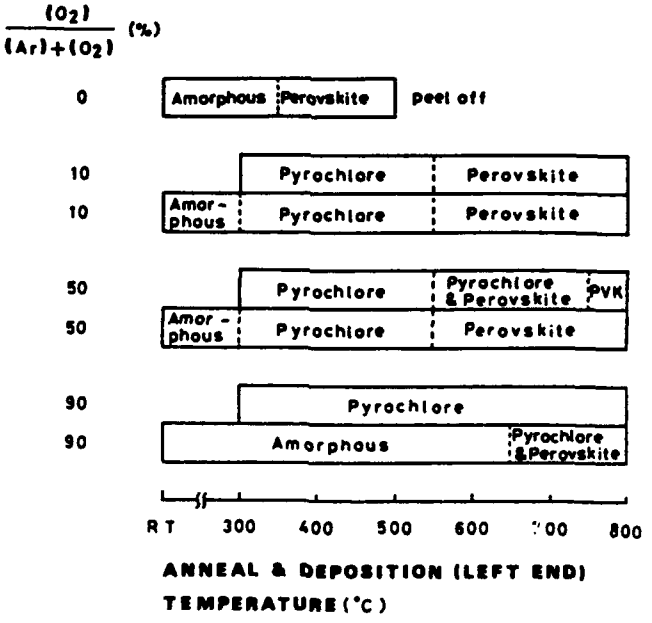


FIGURE 2 X-ray diffraction patterns for a PZT film, deposited at room temperature, annealed at 500-800°C, measured at room temperature.

TABLE II Crystallographic structures of annealed PZT thin films deposited with various gas mixing compositions of oxygen and argon. Upper columns are about the films deposited at 300°C, and lower columns are about the films deposited at room temperature.



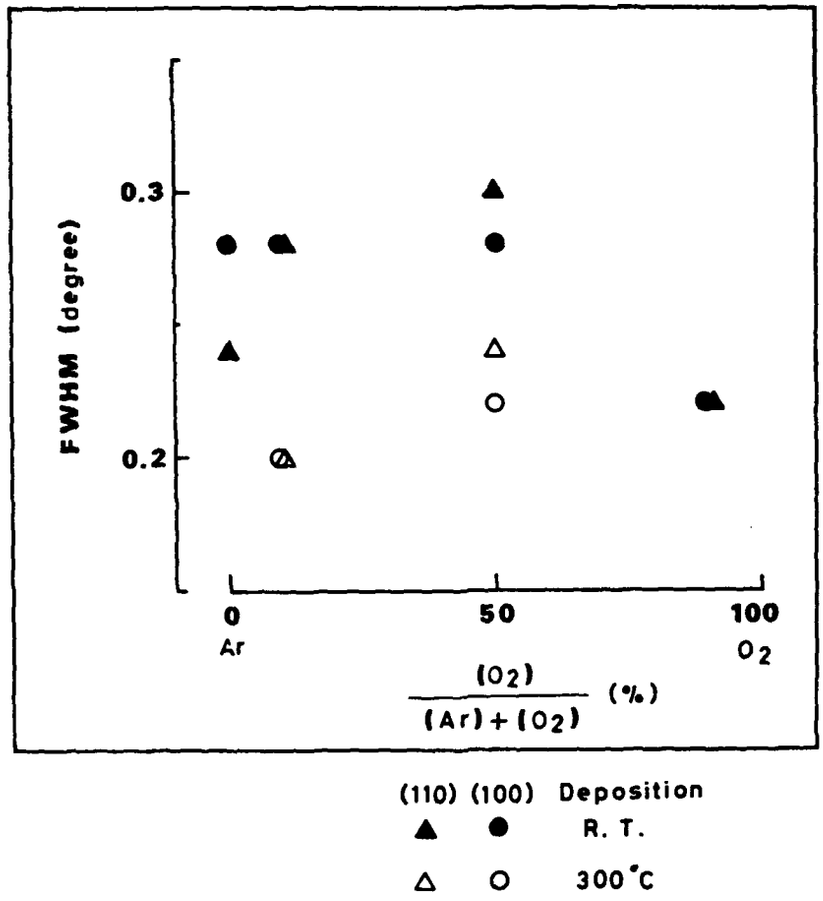


FIGURE 3 Full width at half maximum of XRD peaks for annealed PZT samples.



X: 10V/div., Y: 3.1μC/cm²/div

100Hz, Film Thickness = 540nm

FIGURE 4 A hysteresis loop of a PZT sample, deposited on Pt film at room temperature and annealed at 700°C.

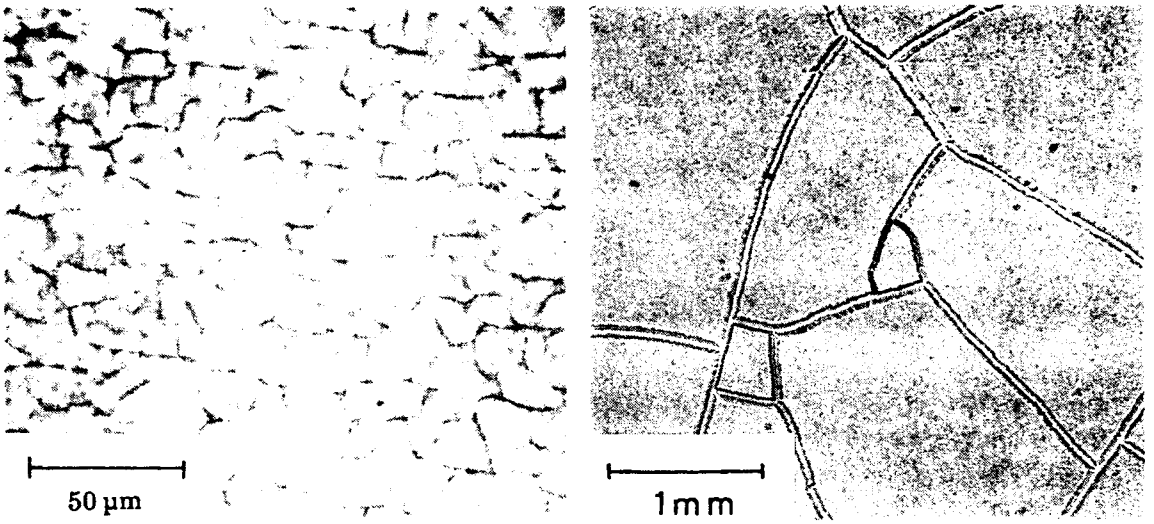


FIGURE 5 Cracks in PZT films on a Pt layer (a) and Si (100) (b).

TABLE Ⅲ Linear expansion, ε (×10-6) at 600°C; $\varepsilon = (L_{600°C} - L_{20°C})/L_{20°C}$, L being the length of the sample. *: ref. 7.

Pt	5600
Si	2100
PZT (50/50)*	2000

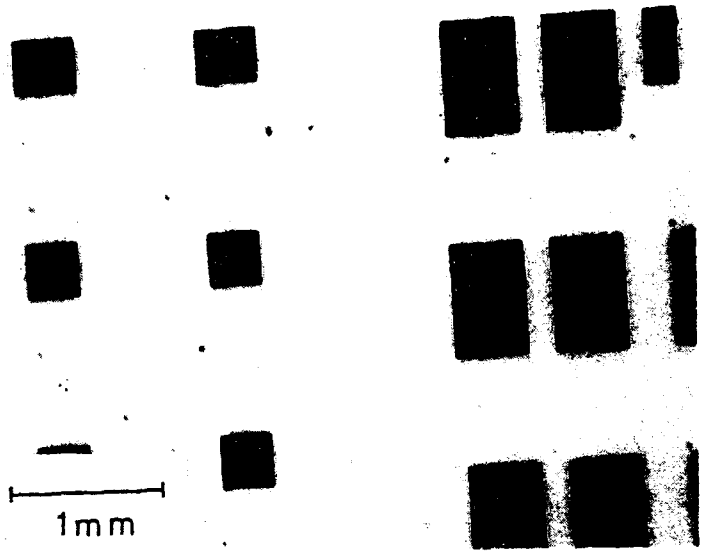


FIGURE 6 Patterned PZT films after annealing.

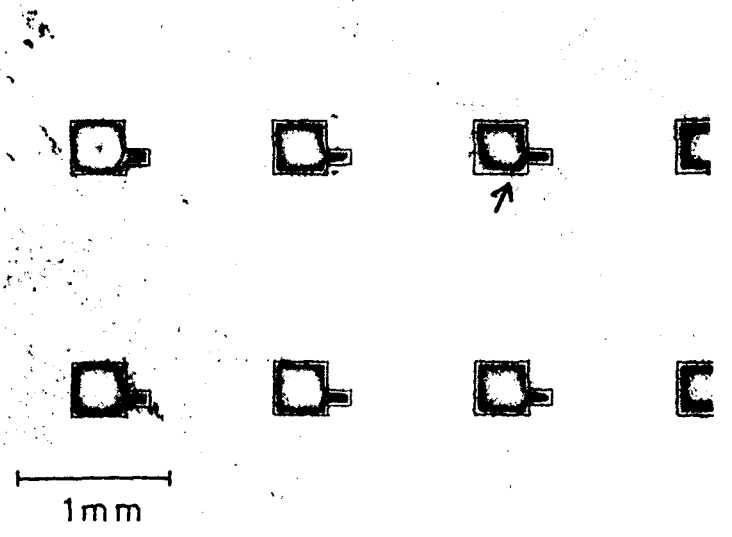


FIGURE 7 Patterned PZT films after annealing. One of the cracks at "neck"s is indicated by an arrow.

AD-P006 676

FERROELECTRIC $Pb(Zr,Ti)O_3$ THIN FILMS PREPARED BY PLANAR MULTI-TARGET SPUTTERING

R. Bruchhaus, H.Huber, D. Pitzer and W. Wersing
SIEMENS AG, Corporate Research and Development,
Munich, Germany

Abstract Lead zirconate titanate films are deposited using a planar multi-target sputtering system. This system consists of three metallic targets (Zr,Pb,Ti) and a rotating substrate holding pallet achieving a layer-by-layer growth of the material.
Substrates used in this study were oxidised (100)Si wafers with thin sputtered Pt layer. At substrate temperatures of about 450°C "in situ" (i.e. without post-deposition annealing) deposition of single phase perovskite PZT was obtained. Deposition rate is 3.5 nm/min. At substrate temperatures of more than 500°C the layers are poor in lead. $ZrTiO_4$ was identified by x-ray diffraction.
The dielectric constant and losses of the PZT films varied from 400-500 and from 0.008-0.015 respectively. The films exhibited a hysteresis loop, remanent polarization measured was 7 $\mu C/cm^2$ and coercive field strength $7.5*10^6$ V/m.

INTRODUCTION

The progress made in depositing high quality very thin ferroelectric films has opened a new era for applications. Especially their possible integration as nonvolatile storage element in a high density CMOS-process has triggered renewed interest in thin ferroelectric films. Lead zirconate titanate (PZT) has properties which makes it a potential candidate for these memory applications[1]. There are different techniques, e.g. evaporation[2], ion-beam deposition[3], some chemical routes employing sol-gel techniques[4-8], laser ablation[9] and chemical vapor deposition[10] for the fabrication of these films.

92-16151

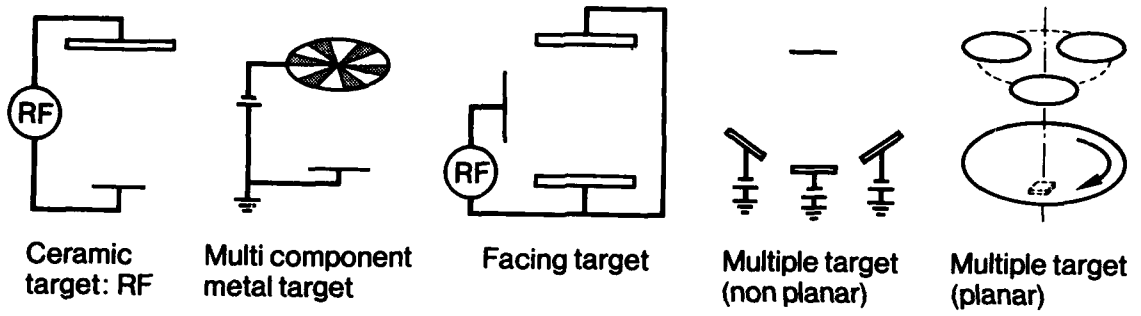


FIGURE 1. Sputtering geometry and targets for deposition of multicomponent oxid films

Besides these, sputtering seems to be a promising and with standard IC-technology compatible method. Different kinds of sputtering geometry have been used to deposit multicomponent oxide films including PZT, Figure 1[11-14]. The materials of the PZT family show a wide range of properties with changing composition (for example Zr/Ti ratio). Therefore it is advantageous to use a deposition method where composition of the films can easily be changed. By using single target methods this possibility is very limited due to fixed composition of the target. For every new composition new targets have to be manufactored individually.

With multiple target methods the stoichiometry can be varied simply by the control of power at the targets. We used a planar multi-target method with three targets where the deposition rate of each component can individually be controlled.

EXPERIMENTAL

PZT films were produced by using a modified Perkin Elmer 4400 sputter system with high vacuum load lock. A schematic diagram of the system is given in Figure 2. Films were reactively sputtered from metallic targets. Substrate was rotated during deposition continously with 10 rpm achieving a layer by layer growth of the film. Target 1 was a Zr (DC-supply), target 2 a Pb (DC-supply) and target 3 a

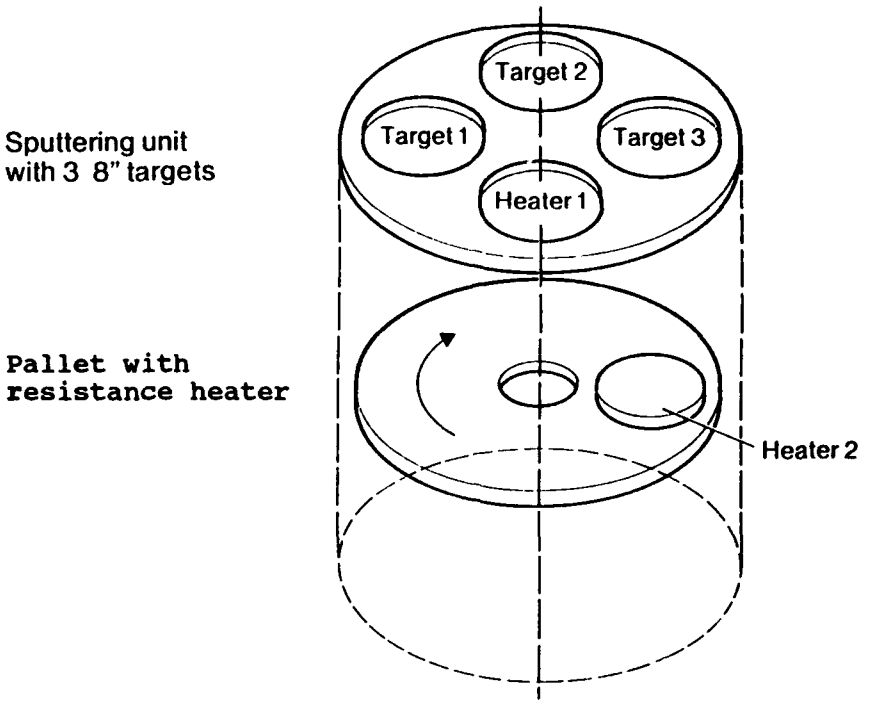


FIGURE 2. Schematic diagram of the sputtering system

Ti (RF-supply). Sequence of deposition during one rotation of the pallet is Zr - Pb - Ti. With two individually adjustable heaters we were able to sustain substrate temperatures of more than 500°C. A heater plate (heater 2) was located on the pallet the other was a lamp heater (heater 1) fixed at the upper plate of the recipient. Therefore, during every rotation after the deposition of Ti the lamps will illuminate the growing film a short period of time. Substrate temperatures given in this paper refer only to the heater plate located on the pallet. Typical sputter conditions are listed in Table 1.

TABLE 1. Sputtering conditions

	range	for PZT
Gas	50-100%O_2	50%
Pressure	1.2-3.0 Pa	1.4 Pa
Power	Pb 28-245 W	90 W
	Ti 1000-1500 W	1500 W
	Zr 150-270 W	250 W
Deposition rate	3-4 nm/min	3.5 nm/min
Substrate temp.	25->500°C	about 450°C

Substrates used were oxidised single crystal silicon wafers deposited with a sputtered bottom electrode of Pt. Upper electrodes were sputtered Pt layers patterned by standard lithographic techniques. Electrical measurements were done on MIM structures ("test capacitors"). Test capacitor area was about 50,000 μm^2.

The crystallographic structure of the PZT-films was examined by X-ray diffraction. A SIEMENS F 500 diffractometer with Cu anode, silicon primary detector and position sensitive detector was used. Dielectric constant (ϵ) measurements were made at room temperature using a Hewlett Packard 4275A multifrequency LCR meter. Measurement frequency was 100 kHz. Polarization hysteresis loops measurements were taken at room temperature at a frequency of 10 kHz by means of a Sawyer-Tower-Circuit[15]. The sine wave generator was a Hewlett-Packard 3324A function generator and storage oscilloscope a Tektronix 7834A.

RESULTS AND DISCUSSION

The crystallographic structure of the films was dependent on substrate temperature. Figure 3 shows the X-ray patterns of layers deposited at different substrate temperatures. Even at 200°C indications of crystalline phases are seen. Peaks of PZT perovskite phase do not appear, other phases have not been identified yet. At about 450°C the film consists of single phase perovskite type PZT. There is no need for a post-deposition annealing step. The structure seems to be pseudo-cubic with a lattice constant of 414 pm. At substrate temperatures above 500°C lines of PZT are no more seen. The phase exhibits to be $ZrTiO_4$. Despite an increase of power at the lead target compared to the deposition at 450°C the layers are poor in lead as confirmed by elemental analysis. It seems to be that during palett rotation at temperatures above 500°C the formation of $ZrTiO_4$ is completed before lead is sputtered on the substrate.

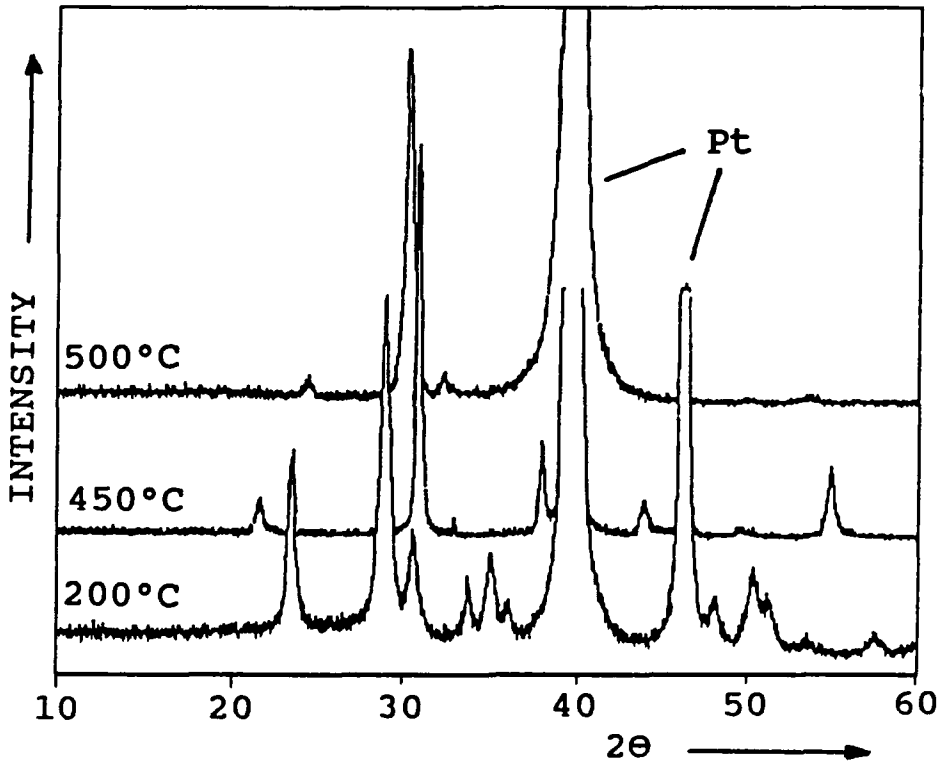


FIGURE 3. X-ray diffraction patterns of films deposited at different substrate temperatures

By the continous rotation of the substrate during deposition very thin layers of each element are sputtered achieving layer growth on an atomic scale. Therefore diffusion distances necessary to form the reaction product are minimized. The deposition rate is 3-4 nm/min, thus the film grows about one lattice constant of PZT during every rotation of the pallet. Our conditions can be compared with the results of ion beam sputtering[3]. This group also suceeded in growing "in situ" perovskite PZT films at substrate temperatures of 450-550°C.

A SEM picture of the PZT surface is shown in Figure 4. The layer consists of well defined crystallites about 100-300 nm in size. There are some pores in the microstructure. This is correlated with a DC-breakdown strength of 10^5 V/cm. No indications of microcracking are seen.



FIGURE 4. SEM microstructure of PZT deposited at about 450°C

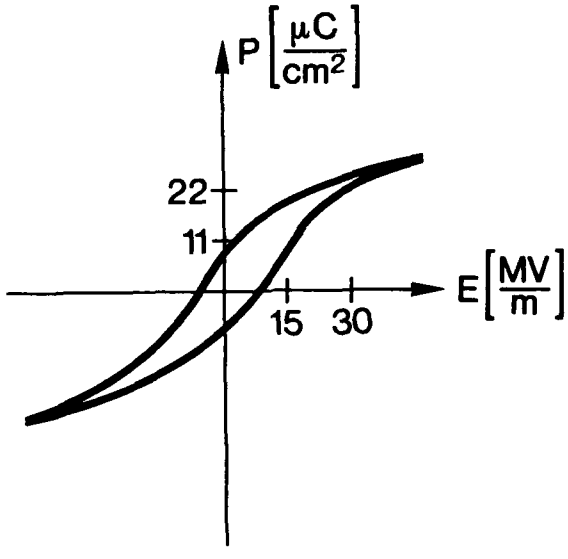


FIGURE 5. Hysteresis loop of a 400 nm thick film

Single phase "in-situ" grown films were used to investigate dielectric and ferroelectric properties. The film thickness ranged from 400 to 570 nm. Electrical results are encouraging in light of this method and of the low processing temperatures. Dielectric constant is 400-500, dielectric loss tan δ is as low as 0.008-0.015 independent of film thickness. PZT films exhibited hysteresis loops as shown in Figure 5. Remanent polarization (P_r) is 7 $\mu C/cm^2$ and coercive field strength (E_c) is $7.5*10^6$ V/m.

Conclusions

PZT films have been produced by using a planar multi-target sputtering system. At substrate temperatures as low as about 450°C "in situ" (i.e. without post-deposition annealing) growth of perovskite phase material was obtained. Deposition rate was 3.5 nm/min. Films exhibited hysteresis loops with P_r=7 $\mu C/cm^2$ and E_c=$7.5*10^6$ V/m. The dielectric constant was 400-500 and the losses 0.008-0.015. At substrate temperatures of more than 500°C the layers are poor in lead and $ZrTiO_4$ was identified by x-ray diffraction.

Acknowledgements

The authors wish to thank Mrs. Jobst for x-ray diffraction measurements, Mr. Stolz for SEM investigations and Mr. Lesti and Mr. Zurmühlen for electrical measurements.

References:

1. D.W. Bondurant and F.P. Gnadinger, IEEE Spectrum, 26,30(1989).
2. M. Oikawa and K. Toda, Appl. Phys. Lett.,29,491(1976).
3. M.S. Ameen et al. in Ferroelectric Thin Films, edited by E.R. Myers and A.I. Kingon (Mater. Res. Soc. Proc. 200, Pittsburgh, PA 1990), pp. 65-76.
4. J. Fukushima, K. Kodaira and T: Matushita, J.Mater. Sci.,19,595(1985).
5. K.D. Budd, S.K. Dey and D.A. Payne, Br. Ceram. Proc.,36,486(1985).
6. S.K. Muralidkar, Ceram.Bull.,63,486(1984).
7. S.K. Dey and R. Zuleeg, Ferroelectrics,108,37(1990).
8. G. Yi, Z. Wu and M. Sayer, J.Appl. Phys.,64,2717(1988).

9. S. Otsubo, T. Maeda, T. Minamikawa, Y. Yonezawa, A. Morimoto and T. Shimizu, Jpn. J. Appl.Phys., 29,L133(1990).
10. M. Okada, K. Tominaga, T. Araki, S. Katayama and. Y. Sakashita, Jpn. J. Appl. Phys.,29,718(1990).
11. A. Okada, J. Appl. Phys.,48,2905(1977).
12. K. Sreenivas and M. Sayer,J. Appl. Phys.,64,1484(1988).
13. R.A. Roy, K.F. Etzold and J.J. Cuomo in Ferroelectric Thin Films, edited by E.R. Myers and A.I. Kingon (Mater. Res. Soc. Proc. 200, Pittsburgh, PA 1990), pp. 77-82.
14. H. Adachi, T. Mitsuyu, T. Yamazaki and K. Wasa, Jpn. J. Appl. Phys.,24, Suppl. 24-3,13(1985).
15. C.B. Sawyer and C.H. Tower, Phys. Rev.,35,269(1930).

AD-P006 677

Electrical Results of Multilevel and Homogeneous Ferroelectric Capacitors

J.D. CUCHIARO, B.M. MELNICK, AND C.A. PAZ DE ARAUJO
Symetrix Corporation, Colorado Springs, Colorado and
University of Colorado at Colorado Springs

Abstract Sol-gel deposited ferroelectric capacitors composed of composite materials are electrically compared to homogeneous capacitors of the same nature. the composites are derivatives of PT and PZT which are all built by a standardized process. The composites consist of doped and homogeneous interfaces in layered structures. The electrical results of hysteresis, dielectric constant, switching polarization measurements are used to analyze the samples.

INTRODUCTION

Solution-gelation of metal alkoxides after spin coating as a deposition technique of ferroelectric materials, creates latitude in capacitor device construction. Layering achieves different device structures through changes in molarity (M) spin speed and time of the deposition. Therefore, thickness variations at select device levels can be tailored for most designs.

For the devices discussed in this paper, the alkoxide homogeneous capacitors were spun from .9M solutions at 1500 rpm for 20 seconds yielding an after processing thickness of approximately 2000 Å per layer. These thin films were hydrolyzed before deposition with a combination of acetic acid and water for an h factor of 2.0 $\left(h = \frac{\text{total moles metal}}{\text{total moles hydrolizer}}\right)^1$ in a glass beaker and filtered with a .2 μm syringe filter. The substrates are made from p-type <100> 5-25Ω-cm 4" silicon test grade wafers on which 2000 Å of platinum is sputtered on 200 Å of sputtered titanium on 5000 Å of thermally grown SiO_2. After ferroelectric deposition, or depositions, and thermal treatments, another 2000 Å platinum layer is sputtered to form the top plate of the capacitor. The top plate is patterned and etched using an ion-mill to form 10,000 μm^2 capacitors. To ensure contact of the top

92-16152

electrode to the ferroelectric material, the specimens were contact annealed in a diffusion furnace under a 5 liter/min O_2 flow at 650°C for 1 hour. The basic ferroelectric capacitor structure is shown in Figure 1.

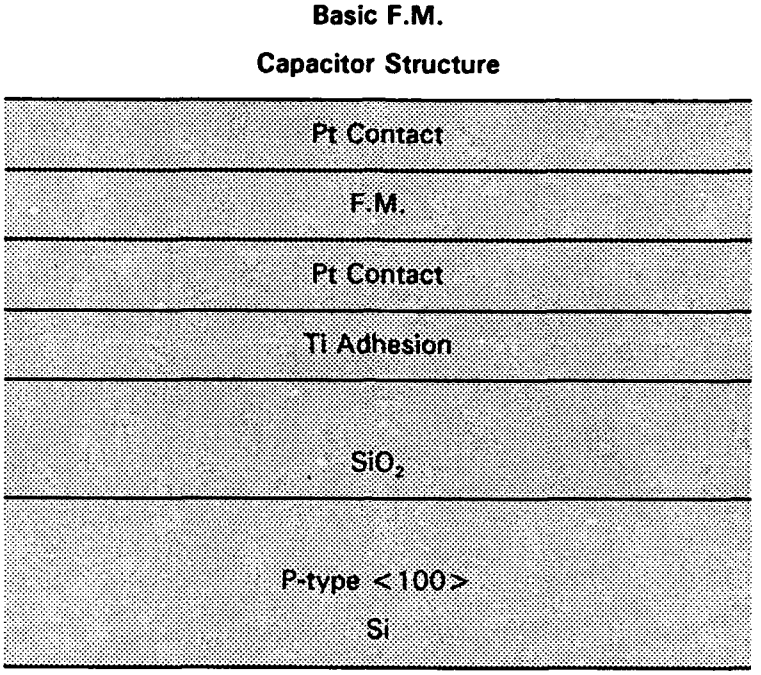


Figure 1

MONOLAYER STRUCTURES

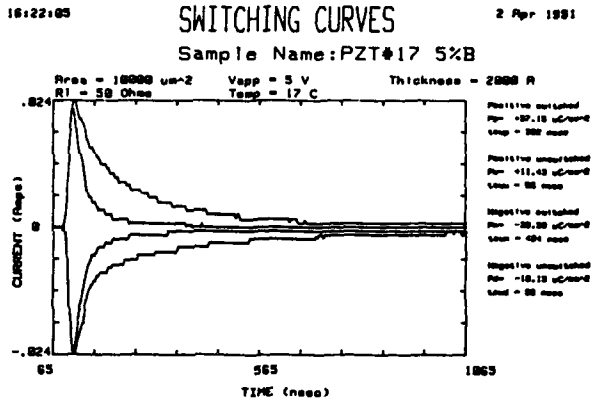
The ferroelectric capacitors built and tested resembling the structure of Figure 1 are as follows: The first two wafers contained $PZ_{.4}T_{.6}$, one doped with 5 mole percent boron and the other with 5 mole percent Iodine. The third and fourth wafers contained PT with the same doping concentrations of boron and iodine. The probed electrical data is listed in Table 1.

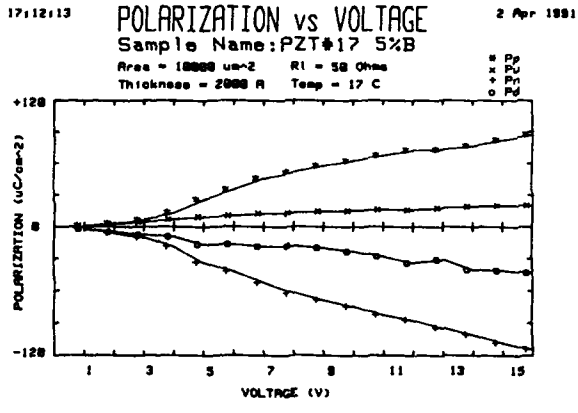
Sample	PZT #17 5% B	PZT #17 5% I	PT #3 5% B	PT #3 5% I
d	2800 Å	2900	2600	2600
Cp	157.2PF	192.3	222	230
Cs	157.2PF	192.3	221.5	229.4
D	.014	.01	.012	.019
Rs	∞	∞	∞	∞
Rp	Off Scale	Off Scale	Off Scale	Off Scale
Z	101.0 k Ω	82.7	71.9	69.5
Θ	-89.30°	-89.4	-89.32	-89.9
K	497.13	629.85	651.91	675.4
∈	4.400 X 10^{-9} F/m	5.58 X 10^{-1} F/m	5.77 X 10^{-9} F/m	5.98 X 10^{-9}

Table 1

Ferroelectric property tests were also conducted. Figures 2, 3, 4, & 5 show switching polarization vs voltage and hysteresis curves for $PZ_{.9}T_{.6}$ #17 5% B, $PZ_{.4}T_{.6}$ #17 5% I, PT #3 5% B, TP #3 5% I, respectfully. The data from the figures of both doped $PZ_{.4}T_{.6}$ samples do not saturate under the applied bias. The boron doped sample switches in approximately 650ns and the iodine doped sample switches in approximately 900ns, or 27.8% slower. However, the boron dopant yielded a 25.72 $\mu C/cm^2$ charge vs the iodine sample of 24.15, or a 6.1% increase in switched charge. The increase of switching charge is gained at the cost of 250ns switching time. It is important to note that undoped $PZ_{.4}T_{.6}$ samples are able to switch in approximately 200 ns[1].

Although the switching time is longer for the iodine doped $PZ_{.4}T_{.6}$ samples, the polarization vs voltage curves show a more consistent amount


16:22:05
SWITCHING CURVES
2 Apr 1991
Sample Name:PZT#17 5%B
Area = 10000 um^2
Vapp = 5 V
Thickness = 2000 A
Rl = 50 Ohms
Temp = 17 C
.824
0
-.824
CURRENT (Amps)
65
565
1065
TIME (nsec)


17:12:13
POLARIZATION vs VOLTAGE
2 Apr 1991
Sample Name:PZT#17 5%B
Area = 10000 um^2
Rl = 50 Ohms
Thickness = 2000 A
Temp = 17 C
+128
0
-128
POLARIZATION (uC/cm^2)
1
3
5
7
9
11
13
15
VOLTAGE (V)

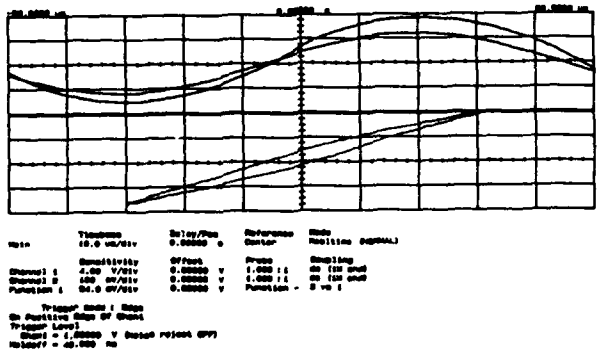
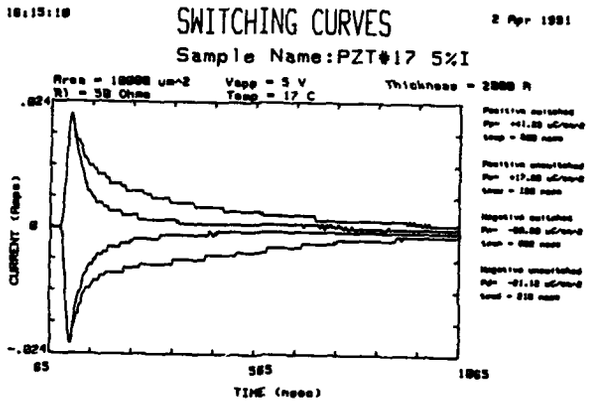
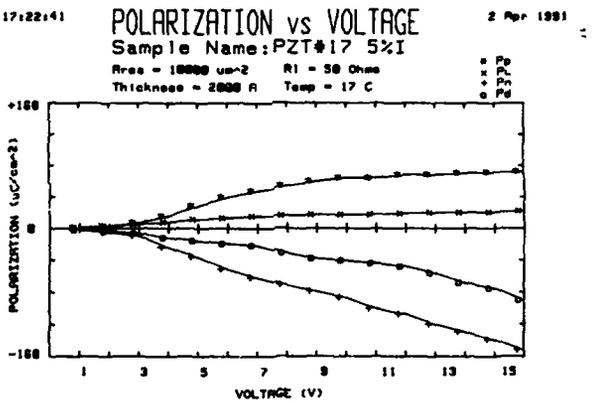


FIGURE 2


SWITCHING CURVES
Sample Name:PZT#17 5%I
CURRENT (Amps)
.024
0
-.024
65
585
1065
TIME (msec)


POLARIZATION vs VOLTAGE
Sample Name:PZT#17 5%I
Pp
Pr
Pn
Pd
+100
0
-100
POLARIZATION (uC/cm^2)
1
3
5
7
9
11
13
15
VOLTAGE (V)

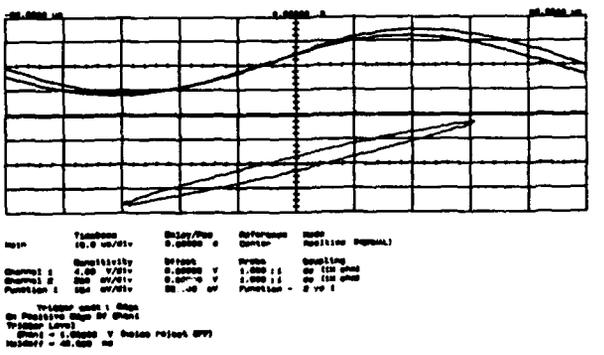
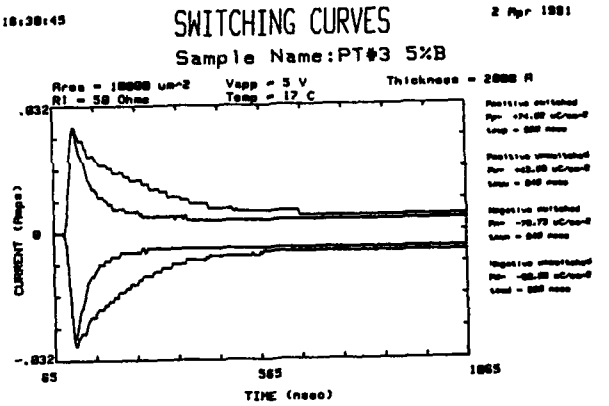
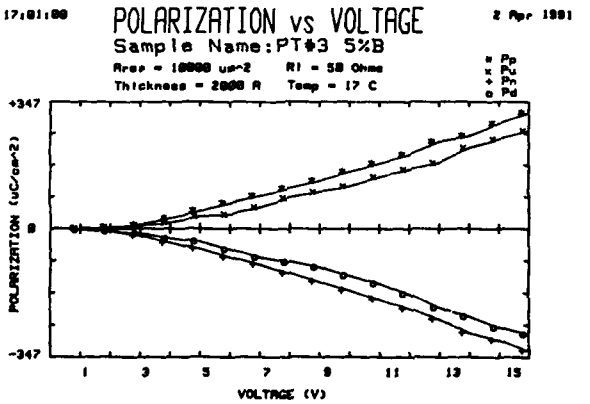


FIGURE 3


SWITCHING CURVES
Sample Name:PT#3 5%B
CURRENT (Amps)
.832
0
-.832
85
565
1065
TIME (nsec)


POLARIZATION vs VOLTAGE
Sample Name:PT#3 5%B
POLARIZATION (uC/cm^2)
+347
0
-347
1
3
5
7
9
11
13
15
VOLTAGE (V)

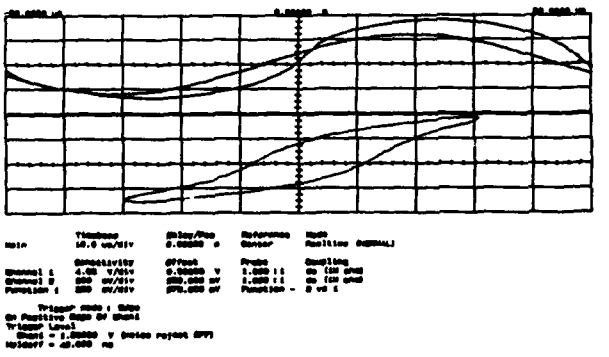
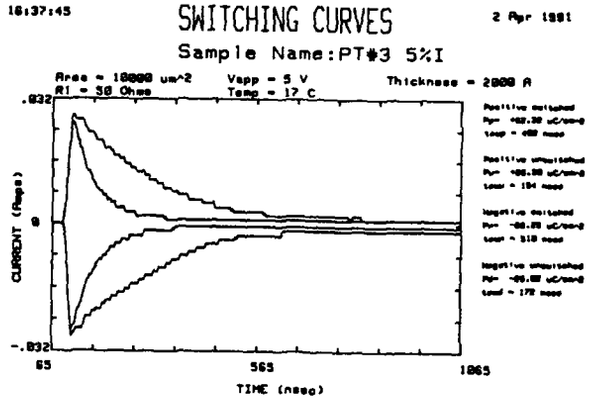
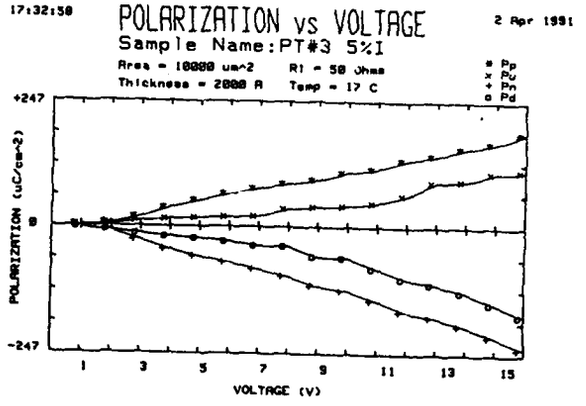


FIGURE 4


16:37:45
SWITCHING CURVES
2 Apr 1991
Sample Name:PT#3 5%I
Area = 10000 um^2
Vapp = 5 V
Thickness = 2000 A
Rl = 50 Ohms
Temp = 17 C
.832
0
-.832
CURRENT (Amps)
65
565
1065
TIME (nsec)


17:32:58
POLARIZATION vs VOLTAGE
2 Apr 1991
Sample Name:PT#3 5%I
Area = 10000 um^2
Rl = 50 Ohms
Thickness = 2000 A
Temp = 17 C
* Pp
x Pu
+ Pn
o Pd
+247
0
-247
POLARIZATION (uC/cm^2)
1
3
5
7
9
11
13
15
VOLTAGE (V)

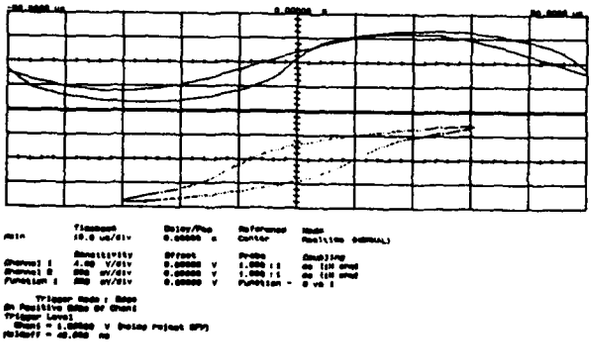


FIGURE 5

of switched charge over variable voltages with the iodine dopant (Figure 3). Both samples begin to switch at approximately the same voltage (3^+V), however, the boron doped sample switches more charge with increasing voltage (Figure 2). The cause of this phenomena are still under investigation.

The same tests applied to the B and I doped PT samples showed the following. Boron makes PT leaky and never fully switches. The leakiness, however, makes for a very consistent amount of switched charge, approximately 31 $\mu C/cm^2$, as shown by the polarization vs voltage curve of Figure 4.

Comparing the iodine sample to that of the boron doped sample, shows that more switched charge is achieved, 36 $\mu C/cm^2$ in 750ns. The switched charge curve of Figure 5 is symmetric, showing that the value of 2Pr achieved in orienting the dipoles is approximately the same, when going from a positive to a negative state or from negative to a positive state. From a materials view this is the desired behavior, however, the amount of charge required for specific device applications will have to be tailored in the future.

MIXED MATERIAL FERROELECTRIC CAPACITORS

The latitude of doping sol-gel solutions of ferroelectric compositions allows for the building of completely different ferroelectric materials, one on top of the other. The two structures shown in Figures 6 and 7 of this nature were also built and tested. The intention is to show improved electrical results over homogeneous capacitors by creating polarization and dielectric gradients near the electrodes to compensate for oxygen poor regions of the ferroelectric near the platinum interfaces. Previous investigations suggest that an increase in material coercive field (Ec) is a result of a surface and sub-surface region with lower $\in r$[2,3,4] which results in a lower value of polarization (P) by reducing the bound surface charge (Qbound = $\vec{P}A$). This concept is modeled in Figure 6.

CONCEPTUAL MODEL OF FERROELECTRIC CAPACITOR

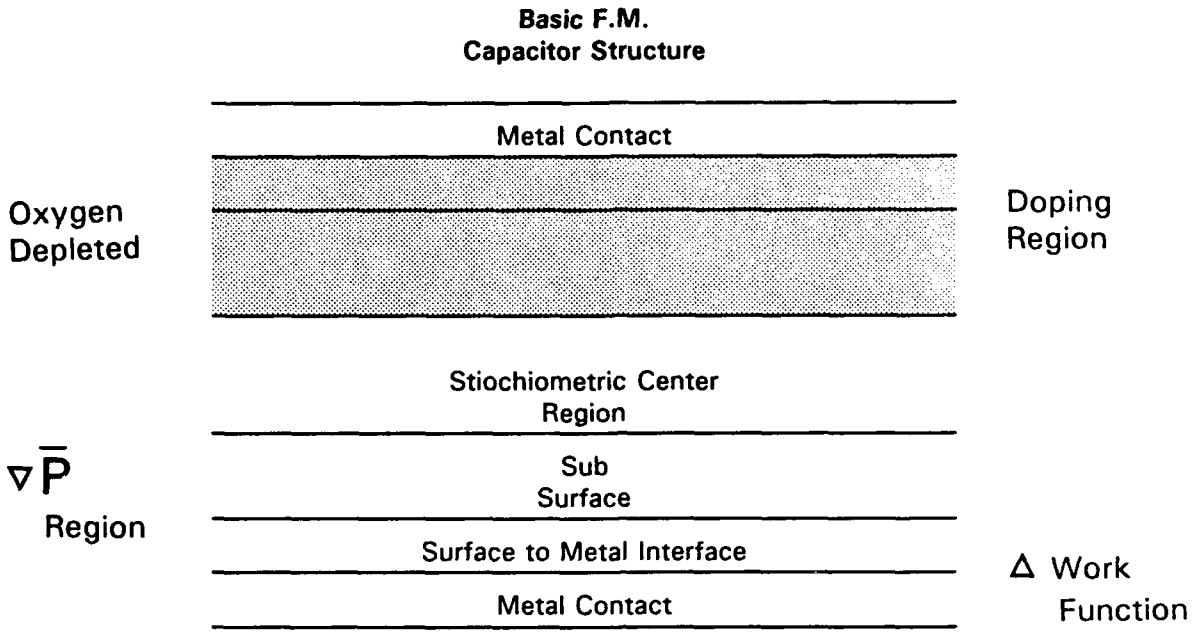
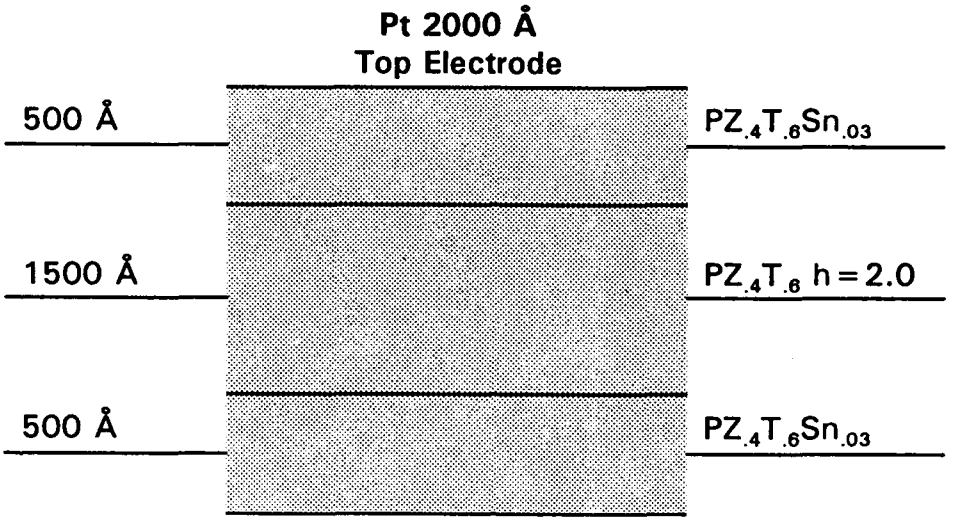


FIGURE 6

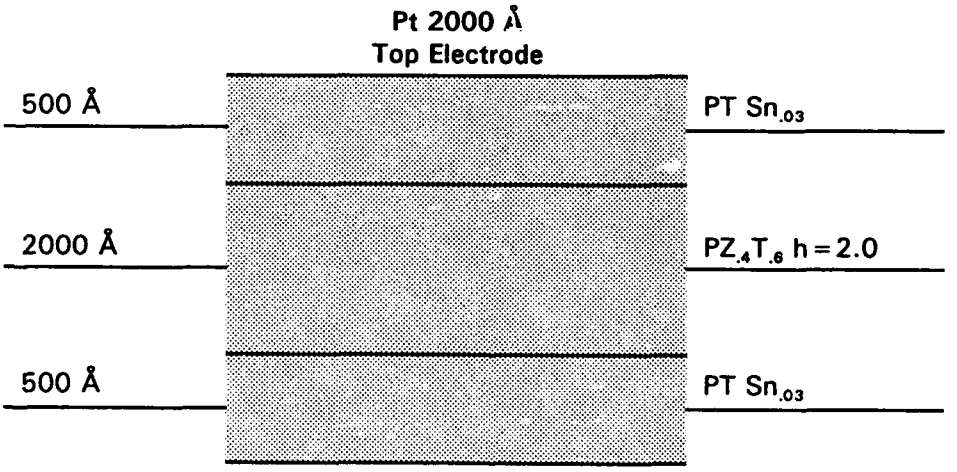
The model shows that at the surface of the doped ferroelectric/metal interface there is a ∇, in the materials work function. Immediately following is the sub surface region. This contains both changing $\in$ and $\vec{P}$ values as a function of thickness, d, reaching an equilibrium value near the stoichiometric center. To illustrate the electrical properties of the model, the two capacitor cells of Figures 7 and 8 were built and tested.

In Figure 7 the dielectric constant of sample 9-6-1 at the subsurface region was lowered by doping $PZ_{.4}T_{.6}$ with 3 mole percent Sn. The stoichiometric center was built approximately 3 times thicker with undoped $PZ_{.4}T_{.6}$. To further enhance the gradient effect sample 9-6-4 contains $PZ_{.4}T_{.6}$ with $\in r$ of approximately 900 at the stoichiometric center contacting 3 mole percent Sn doped PT with $\in r$ approximately 400 on both sides. Electrical results of hysteresis, for variable fields created by the listed applied voltages,



SAMPLE 9-6-1

FIGURE 7



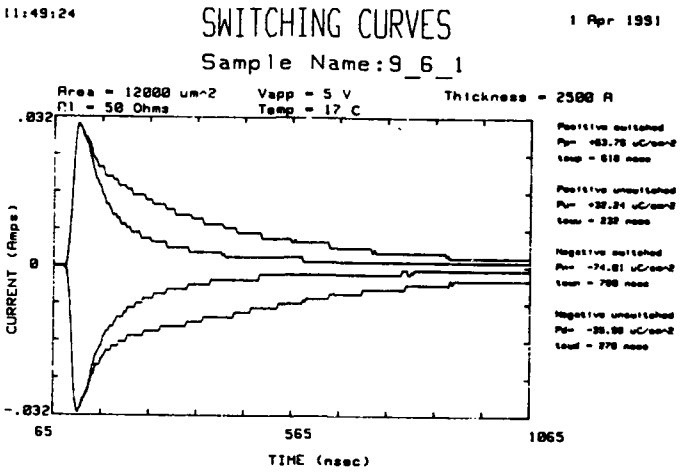
SAMPLE 9-6-4

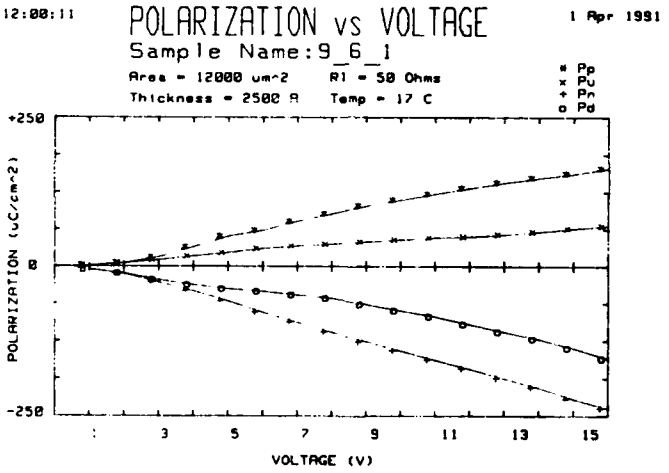
FIGURE 8

polarization vs applied voltages of 1-16V, and switching curves for 5V are shown for samples 9-6-1 and 9-6-4 in Figures 9 & 10, respectively. As can be seen from the Figures, sample 9-6-4 exhibits a better defined hysteresis at the cost of a lower $2P_r$. Sample 9-6-4 also switches approximately two times faster than 9-6-1 without a significant current leakage. This may be due to sub surface layer dielectric constant of Sn doped PZT not being low enough to create the desired gradient. In contrast, sample 9-6-4 drastically reduces the dielectric constant near the metal interface by half using PT in the sub surface region, thus yielding better measured ferroelectric results.

SUMMARY

In this paper we have shown that by doping sol-gel deposited ferroelectric $PZ_{.4}T_{.6}$ and PT with boron and iodine inherently slower switching times can be sped up by reducing switched charge. Also, the sol-gel deposition process enables mixed material capacitors to be built. A capacitor model requiring mixed materials with different dielectric constants was presented, and the electrical results of switching, polarization vs voltage, and hysteresis divulged. Consequently, ferroelectric parameters can be altered through doping and mixed material construction.


11:49:24
SWITCHING CURVES
1 Apr 1991
Sample Name:9_6_1
Area = 12000 um^2
Rl = 50 Ohms
Vapp = 5 V
Temp = 17 C
Thickness = 2500 A
.032
0
-.032
CURRENT (Amps)
65
565
1065
TIME (nsec)


12:08:11
POLARIZATION vs VOLTAGE
1 Apr 1991
Sample Name:9_6_1
Area = 12000 um^2
Rl = 50 Ohms
Thickness = 2500 A
Temp = 17 C
# Pp
x Pu
+ Pn
o Pd
+250
0
-250
POLARIZATION (uC/cm^2)
3
5
7
9
11
13
15
VOLTAGE (V)

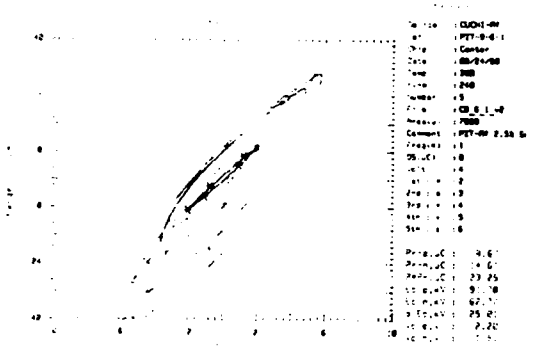
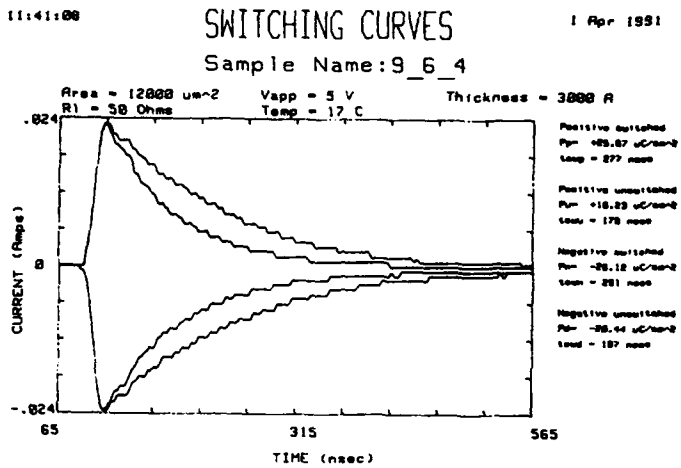
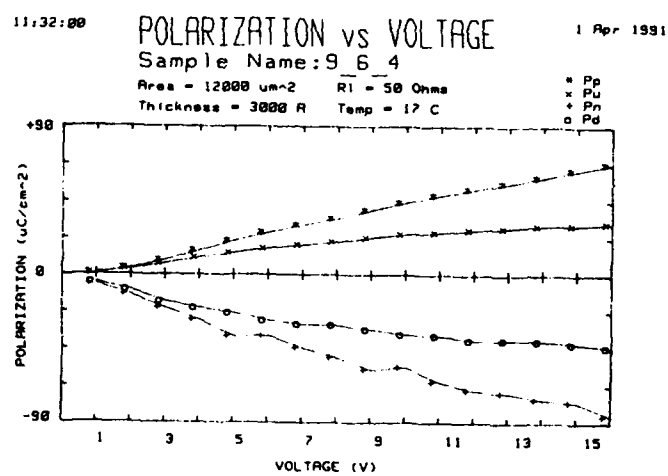


FIGURE 9


11:41:08
SWITCHING CURVES
1 Apr 1991
Sample Name:9_6_4
Area = 12000 um^2
Vapp = 5 V
Thickness = 3000 A
Rl = 50 Ohms
Temp = 17 C
.024
0
-.024
CURRENT (Amps)
65
315
565
TIME (nsec)


11:32:00
POLARIZATION vs VOLTAGE
1 Apr 1991
Sample Name:9_6_4
Area = 12000 um^2
Rl = 50 Ohms
Thickness = 3000 A
Temp = 17 C
* Pp
x Pu
+ Pn
o Pd
+90
0
-90
POLARIZATION (uC/cm^2)
1
3
5
7
9
11
13
15
VOLTAGE (V)

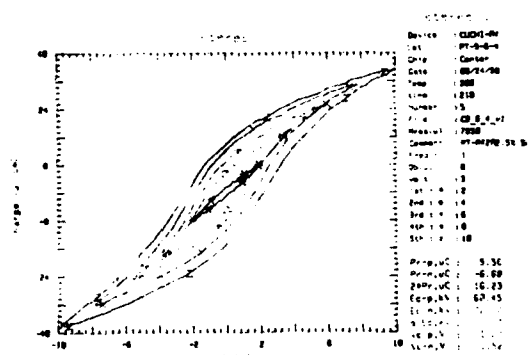


FIGURE 10

REFERENCES

1. B.M. Melnick, J.D. Cuchiaro, L.D. McMillan, C.A. Paz de Araujo and J.F. Scott, Process Optimization and Characterization of Device Worthy Sol-Gel Based PZT for Ferroelectric Memories, Ferroelectrics, 1990, Vol. 112, pp. 329-351.
2. X.T. Chen, D.N. Huang, and Z.W. Yin, Proc. 6th IEEE Intls. Symp. on Ferroelectrics, June 8-11, p. 62 (1986).
3. L.E. Cross, Ferroelectrics, 76, 262 (1987).
4. J.F. Scott et al., J. Appl. Phys., 64(2) 787 (1988).

FERROELECTRICS FOR SILICON VLSI

AD-P006 678



SHENG T HSU and ISRAEL H. KALISH
David Sarnoff Research Center, CN5300 Princeton, NJ

Abstract The application of ferroelectrics to EEPROM, non-volatile SRAMs, and sub-0.5 micron channel length MOS field effect transistors for silicon VLSI can significantly simplify device fabrication process, increase circuit density, and enhance device performance.

INTRODUCTION

The constraints to Very Large Scale Integrated (VLSI) circuits devices are; low operating voltage, small device area, thin insulator thickness, shallow junction depth, and practically no lateral diffusion of p-n junctions. Not all of these constraints can be achieved with the state-of-the-art silicon technology without a very complicated fabrication process. The high permittivity and the polarization properties of ferroelectric dielectric material can be used to solve many of VLSI and ULSI devices problems. It is shown in this paper that ferroelectric materials can be used to reduce EEPROM operation voltage, to form new non-volatile memory devices, and to improve the performance and packing density of sub-0.5 micron MOS transistors. Since the application of ferroelectrics to Dynamic Random Access Memories, (DRAM), has been discussed by many investigators [1], it will not be discussed here.

92-16153



EEPROM Cell

There are many EEPROM cell structures available. All state-of-the-art EEPROM cells consist of a thin tunnel oxide, a floating gate polysilicon layer, an inter-polysilicon dielectric, and a control gate polysilicon layer. The inter-polysilicon dielectric is either thermally grown oxide or a thermal grown oxide-nitride composite layer. The thickness of the tunnel oxide is about 80Å to 200Å. The inter-polysilicon dielectric thickness is equivalent to about 200Å to 400Å of thermal oxide. The cross-sectional view of a simple stacked gate EEPROM cell is sketched in Fig.1.

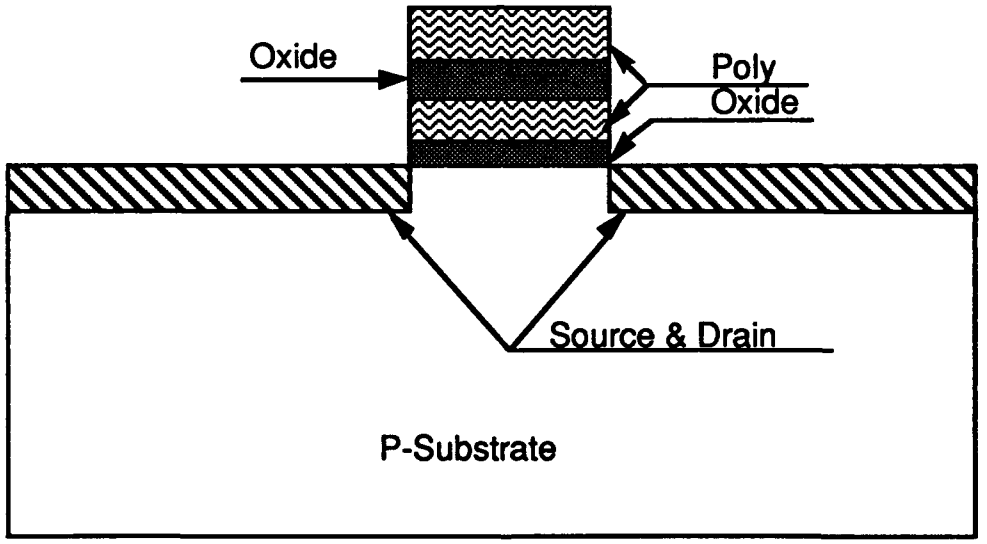


FIGURE 1 Cross-section view of an EEPROM device

When a voltage, V_{PP}, is applied to the control gate. The voltage at the floating gate, V_F, is given by:

$$V_F = \frac{C_I}{C_I + C_O} \left(V_{PP} - \frac{Q_F}{C_I}\right) \qquad (1)$$

where C_O is the tunnel oxide capacitance, C_I is the inter-polysilicon insulator capacitance, and Q_F is the charge stored in the floating gate. The coupling ratio, $C_I/(C_O+C_I)$, defines the efficiency with which the voltage at the control gate can control the field intensity at the tunnel oxide and the potential at the silicon surface. The amount of charge flowing from the silicon into the floating gate is controlled by the field intensity at the tunnel oxide. For a state-of-the-art device, the coupling ration is about 0.3 to 0.5 and the programming voltage is about 10 V to 15 V. A sub-0.5 μm VLSI circuit operates at 2.0 V to 3.5 V internal voltage and 5 V power supply for the input/output portions of the circuit. The 5 V input/output is required to interface with the existing electronics components. The high EEPROM programming voltage is either supplied externally or generated on chip internally. This high programming voltage is a serious reliability concern for the small feature size devices. The programming voltage prevents the further scaling of the memory device [2].

If the inter-polysilicon dielectric is replaced by a wide band gap ferroelectric dielectric material, the capacitance, C_I, will be very large. The coupling ratio of about one can be obtained. When the amount of charges stored at the floating gate is Q_F the threshold voltage of the device is increased by ΔV_T, such that

$$\Delta V_T = \frac{Q_F}{C_I} \tag{2}$$

Since C_I is very large for ferroelectric memory devices a very large amount of charge in the floating gate is required for a small increase in threshold voltage. A memory device with coupling ratio of nearly equal to one is, therefore, of no practical value. Probably the coupling ratio should be no larger than 0.8. A thin layer of thermal oxide of thickness between 40Å to 70Å may be grown onto the floating gate polysilicon to enhance the retention time and to reduce the coupling ratio to

0.6 to 0.8. The memory array can be programmed and read with the standard 5 V power supply voltage and 2.0 V to 3.5 V internal voltages, respectively. A ferroelectric stacked memory cell is sketched in Fig.2. The upper polysilicon layer is replaced by a refractory metal diffusion barrier layer.

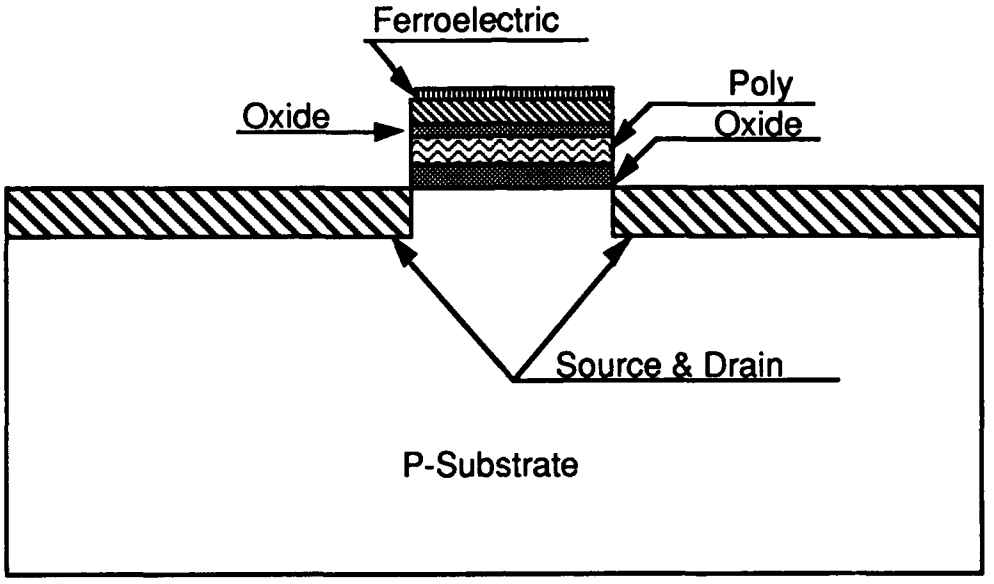


FIGURE 2 EEPROM device utilizing ferroelectric inter-polysilicon insulator.

A new ferroelectric non-volatile memory device.

The cross-sectional view of a ferroelectric n-channel memory transistor is sketched in Fig.3. The source and the substrate of the device are permanently connected together. A memory gate, MG, is inserted between the control gate, CG, and the source of an MOS transistor. The insulator of the memory gate is ferroelectric. A very thin layer of oxide may be grown onto the silicon surface prior to the ferroelectric deposition. The top electrode of the memory gate can be either refractory metal or polysilicon.

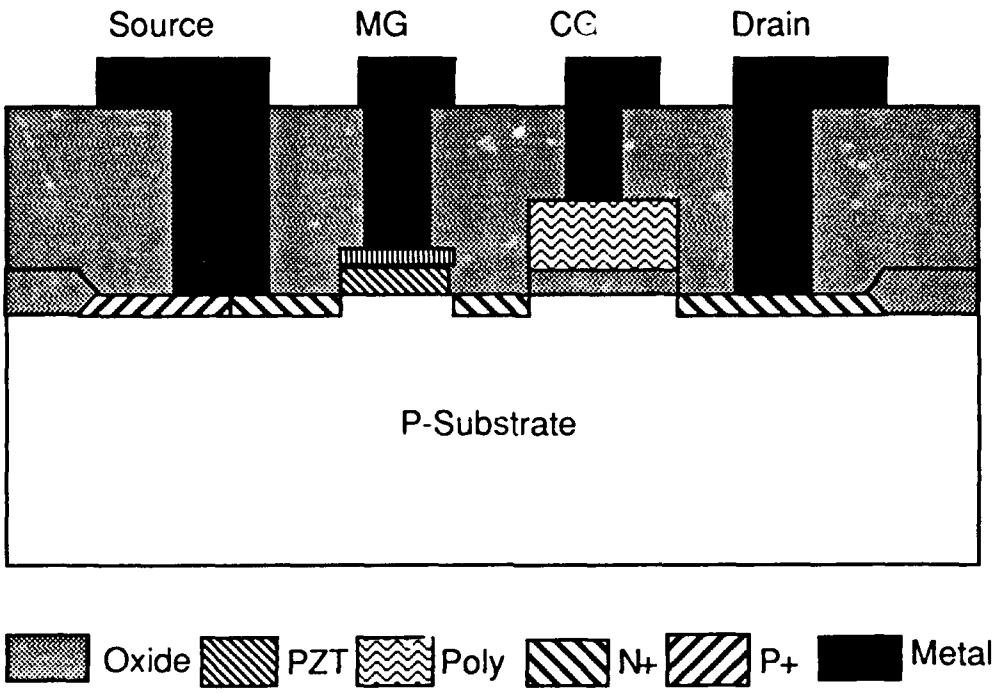


FIGURE 3 Cross-sectional View of a Ferroelectric Non-Volatile Memory

When a positive programming voltage, V_{PP}, is applied to the memory gate with respect to the source of the memory transistor the ferroelectric dielectric at the MG is polarized causing the silicon surface under the MG to invert. The channel under the MG is at the high conductive state. This is the erase operation. When the memory gate and the source of the device are grounded and positive voltages, $V_{PP}+\Delta V$ and V_{PP} are applied to the control gate and the drain of the device, respectively, the silicon surface under the control gate is very strongly inverted. The channel pinch-off is at the drain side of the memory gate. The voltage drop across the ferroelectric is about V_{PP}. The ferroelectric is polarized to the opposite polarity. The silicon surface under the memory gate is accumulated. The memory device is, therefore, programmed to the high resistivity state. The voltage ΔV can be much smaller than 1 V.

The current flow through the device during the programming process is limited by the conductivity of the surface channel

under the memory gate. This programming current is controlled by the channel dopant density of the memory section of the device and by the thickness of ferroelectric dielectric. A low voltage, $V_{PP} \leq 5$ V, write/erase is possible.

During read operation current flow through the silicon surface under the control gate and memory gate. There is no current flow through the ferroelectric. As a result the memory content is not disturbed by the read operation. Therefore it is a static memory device. There is no need for memory refreshment.

The area of this device can be minimized by eliminating the N^+ layer between the memory gate and the control gate as is shown in Fig.4. A thicker oxide on the sidewall and on the top surface of the control gate is required to reduce the coupling between the control gate and the memory gate. This thick oxide layer can be formed by a CVD oxide and etch back technique. It is

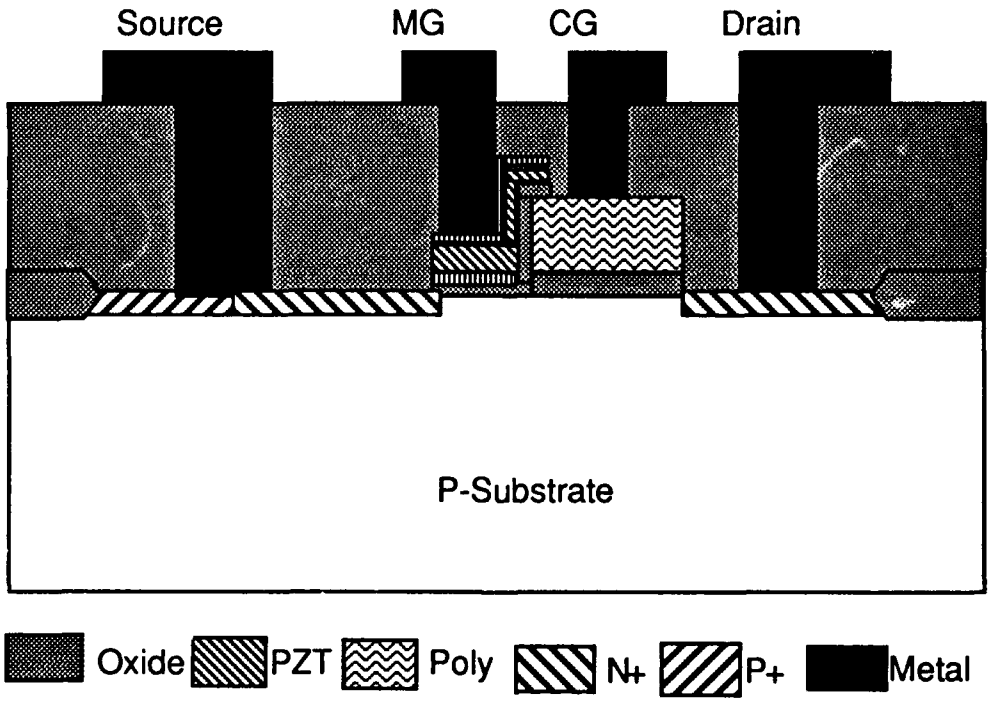


FIGURE 4 Cross-sectional view of a high density ferroelectric memory transistor

also possible to thermally grow thicker oxide on the N^+ doped polysilicon and thinner oxide on the lightly doped silicon. The ratio of these thermal oxide thicknesses can be larger than 10. The thickness of the control gate sidewall oxide must be kept thin in order to have a good coupling between the surface channel under the memory gate and the control gate.

This device can be arranged in a very large memory array. A 3x4 memory array is show in Fig.5. The memory gates of all memory cells in the array are connected together to a block erase pad. This non-volatile memory array can be programmed as follows:

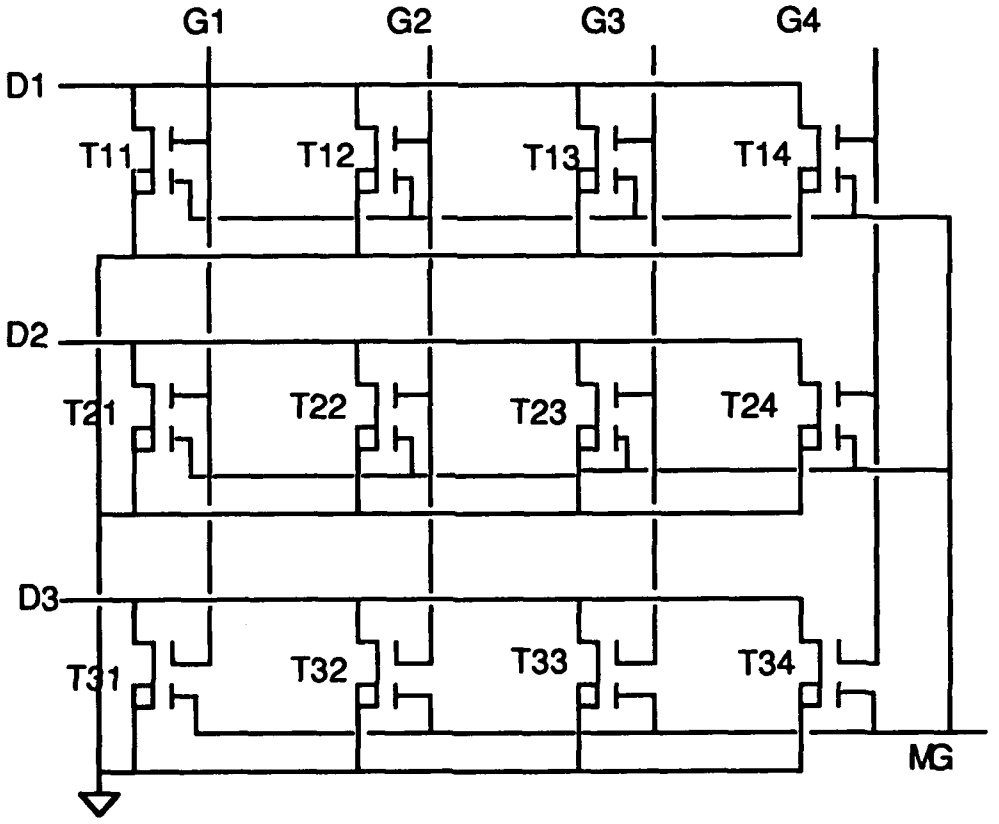


FIGURE 5 A 3x4 ferroelectric memory array

First the contents of the array are erased to the "0" state by applying V_{PP} to the memory gate, MG, while all other electrodes are grounded. This operation writes all cells in the array to their high conductive state.

Next we shall explain how to write a selected cell to the "1" state. The source and the programming gate electrodes are grounded. If the cell T_{23} is selected voltages $V_{PP}+\Delta V$ and V_{PP} are applied to the word line, G3, and the bit line, D2, respectively. The ferroelectric of the memory gate of T_{23} is polarized causing the silicon surface under the ferroelectric of the memory electrode to accumulate holes. There is no surface conduction channel under the memory gate of T_{23}. The memory cell T_{23} is written to "1" state. The gate voltage of the memory cells T_{i3}, where $i\neq2$, is equal to $V_{PP}+\Delta V$, but the drains of these memory cells are at the ground potential. The drain voltage of memory cells T_{2j}, where $j\neq3$, is equal to V_{PP} but the gate electrodes of these memory cells are at the ground potential. The gate and the drain of all other memory cells are at the ground potential. Therefore, only the content of T_{23} memory cell is affected by this write operation. To read the contents of the memory array the internal low voltage of 2.0 V to 5.0 V is applied to the selected bit line and word line.

NON-VOLATILE SRAM CELL

The equivalent circuit of a state-of-the-art non-volatile SRAM cell is sketched in Fig.6 [3], where C_1 and C_2 are non-volatile memory elements. A control line is used to control the write/erase pulses from the common plate to program the non-volatile elements, C1 and C2. Compared to a standard SRAM cell it requires an additional two non-volatile elements, two switching transistors, and a programming pulse.

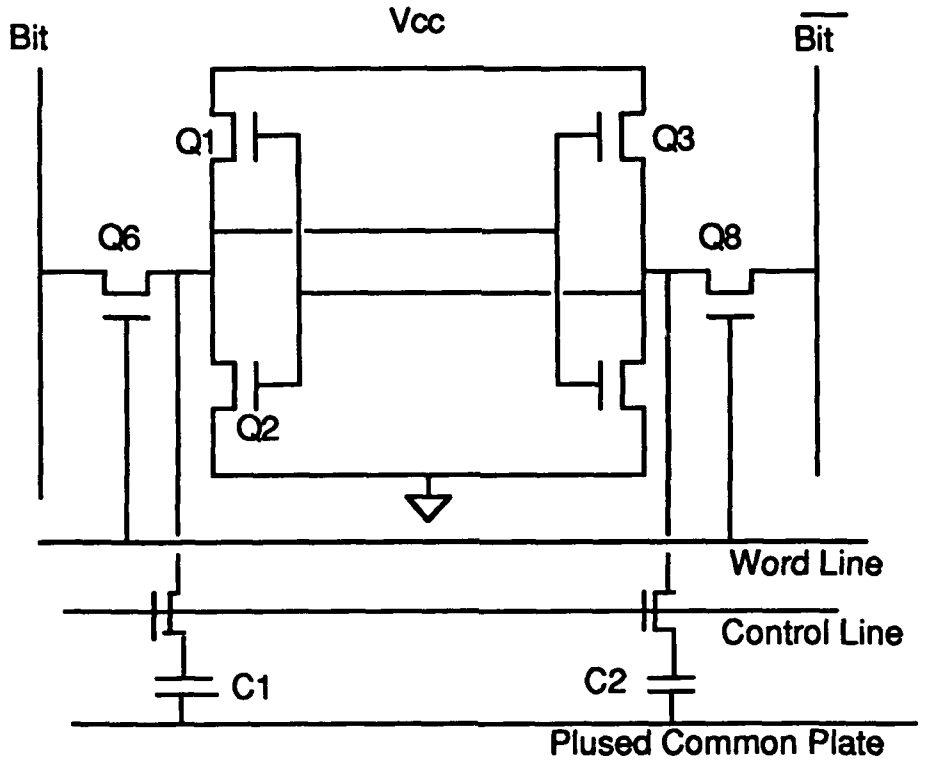


FIGURE 6 State-of-the-art Non-volatile SRAM cell.

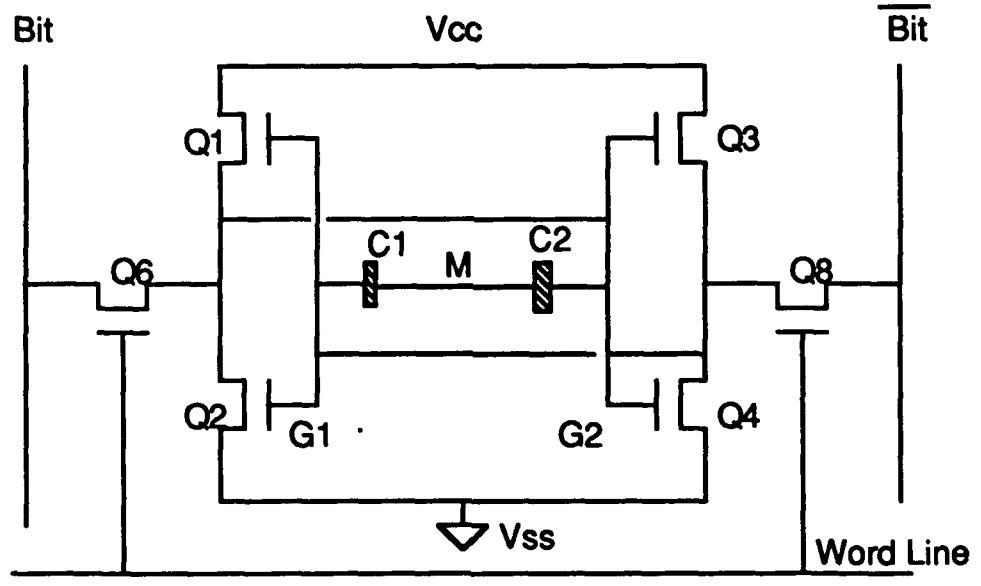


FIGURE 7 Equivalent circuit of a ferroelectric non-volatile SRAM with a floating capacitor plate.

The polarization field intensity of a ferroelectric material, such as PZT, is about 100 kV/cm. Therefore, the polarization voltage of a 3500 Å PZT film is less than 5 V [3]. It is possible to used PZT or other ferroelectric materials in a non-volatile SRAM which requires no write/erase operation.

The equivalent circuit of a ferroelectric non-volatile SRAM cell is sketched in Fig.7. The cross-sectional view of the non-volatile SRAM cell is sketched in Fig.8. The addition of the ferroelectric capacitors, C_1 and C_2, does not increase the memory cell area or alter the memory cell layout. The gate electrode of Q_1 and Q_2 is G_1 and that of Q_3 and Q_4 is G_2. The capacitors, C1 and C2, are the ferroelectric capacitors which are formed by a floating top electrode and the bottom electrode on gate G1 and G2, respectively.

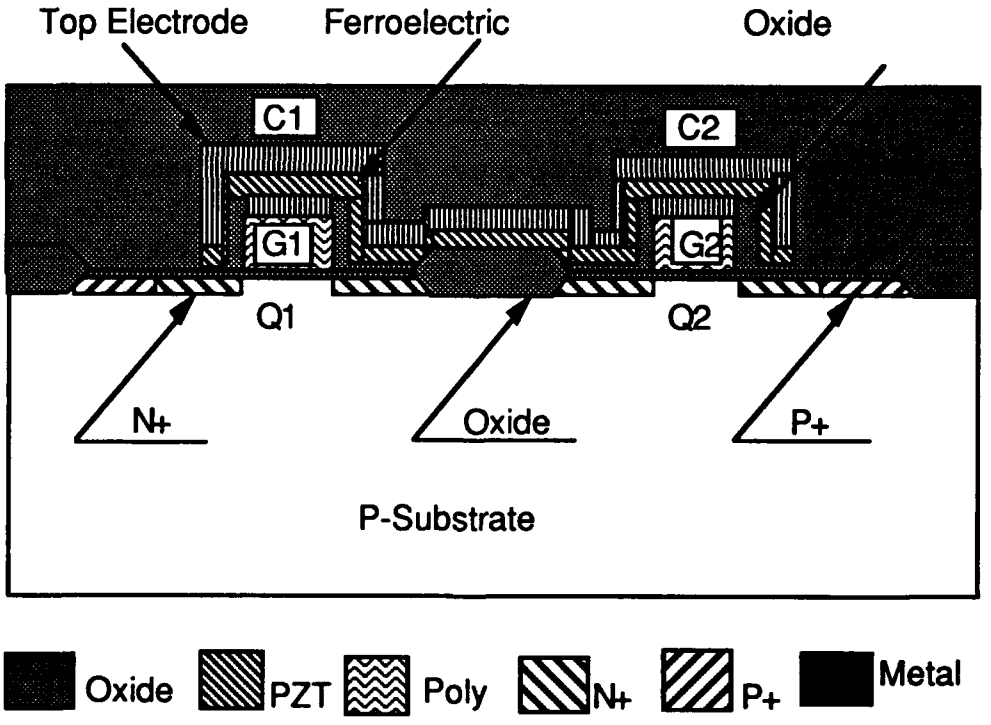


FIGURE 8 Cross-sectional view of Ferroelectric non-volatile SRAM cell.

This ferroelectric non-volatile SRAM does not require a separate write/erase operation. When the bit line is written to high voltage state the voltage at G_1 is equal to V_{SS} and that at G_2 is equal to V_{DD}. The ferroelectric dielectric in C_1 and C_2 are at least partially polarized at the SRAM operation voltage. When the power supply is shut off the charge at the capacitor is equal to the remnant polarization charge of the ferroelectric. A small imbalance of the order of a ten millivolts between the gates of the two latch inverters enables the SRAM cell to restore the memory content when the power is turned on. Therefore, full polarization of ferroelectric is not required. Since it requires only a small imbalance of charges in the storage capacitors this ferroelectric non-volatile SRAM is expected to have a very large endurance. This ferroelectric non-volatile SRAM can be operated at a supply voltage of as low as 3 V.

Sub-micron MOS Transistor.

It is well known that the gate electrode of a MOS transistor must overlap the source/drain junction otherwise the drain current would be very small. The optimum gate overlap to source/drain junction of a highly reliable and high performance MOS transistor has been simulated and experimentally proven to be as large as 0.2 μm per side by R. Izawa et. al [4]. This condition is not feasible for sub-micron MOS transistors. Even a 0.1 μm per side overlap is not acceptable for a MOS transistor having a channel length shorter than 0.4 μm. A state-of-the-art sub-0.5 micron MOS transistor is very difficult to optimize for high performance and high reliability. Several approaches, such as GOLD [4], TOPS [5], inverse T gate [6], tilted source/drain ion implanted HS-GOLD [7], and elevated source/drain structures [8,9] have been proposed to solve this problem. However, their fabrication processes are very complex and, with the exception of the elevated source/drain structure, their effective channel

length is substantially smaller than the physical width of the polysilicon gate line, hence increasing the MOS transistor area.

It is shown here that by using a very high permittivity dielectric, such as ferroelectric material, as the gate sidewall insulator no gate to source/drain junction overlap is required. A high performance, highly reliable extremely short channel length MOS transistor can be fabricated easily. The cross-sectional view of a ferroelectric sidewall MOS transistor is sketched in Fig.9. Since only high permittivity is required, the top and the bottom ferroelectric electrodes can be eliminated. A thin layer of thermal oxide between the ferroelectric and silicon surface is preferred. This thin oxide can prevent the polarization of the ferroelectric when the gate and the drain are at low an high voltages, respectively. The fabrication process is very simple and there is no scaling limitation by the gate overlap to source/drain junctions.

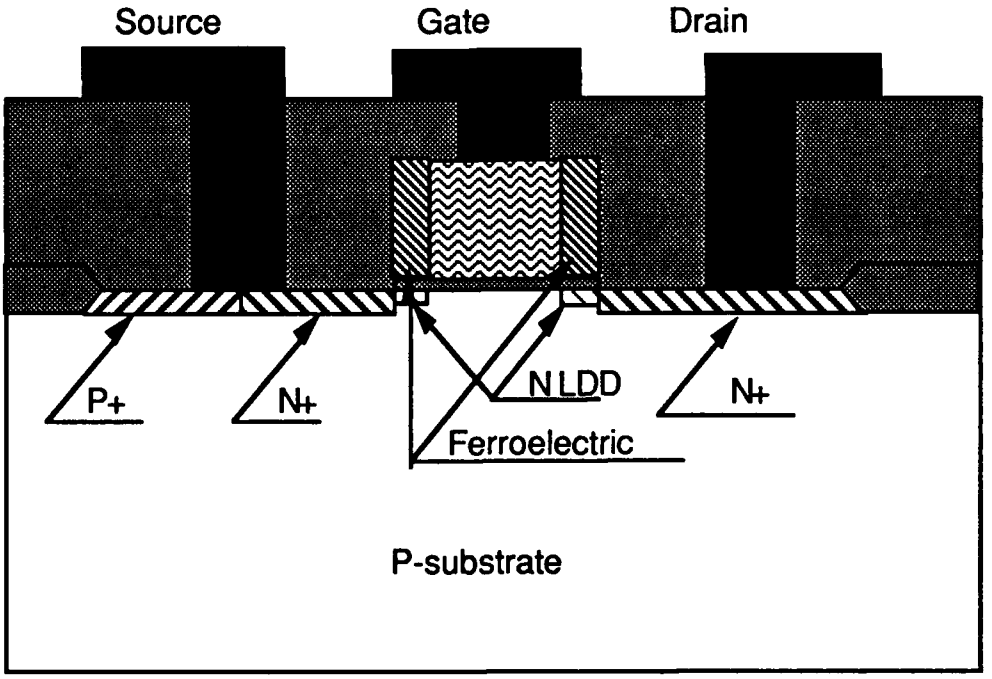
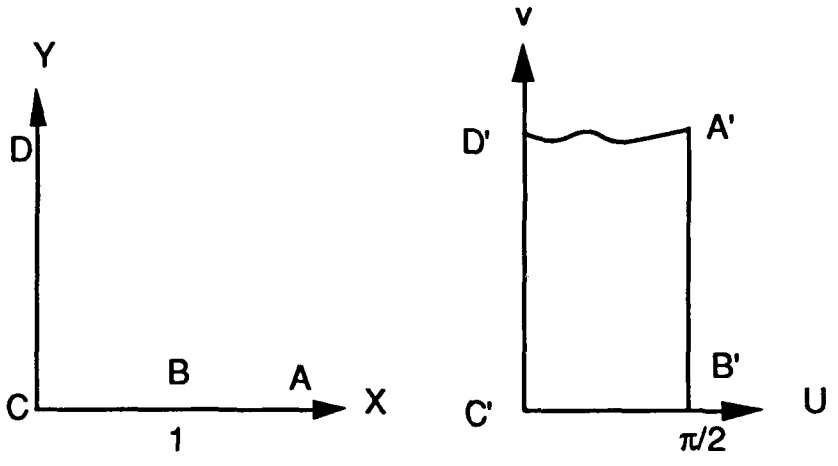


FIGURE 9 Cross-sectional view of a ferroelectric sidewall MOS transistor

The qualitative voltage distribution at the sidewall spacer region of a MOS transistor can be calculated by using the conformal mapping method. Let us locate the gate-source/drain to the x-y axes of the first quadrant of an x-y plane. The sidewall of the polysilicon is at the y-axis. The x-axis is the silicon surface of the source or the drain surface. We transfer the normalized (x,y) plane into (u,v) plane in according to the relationship of z = sin w as is shown in Fig.10.



$$z=\sin w$$
$$x=\sin u \cosh v, \quad y=\cos u \sinh v$$

FIGURE 10 Conformal Mapping of Gate-Source area.

The voltage in the w-plane is independent of v and is given by:

$$V(w) = \frac{2Vu}{\pi} \tag{1}$$

It can be shown that [10]

$$2\sin u = \sqrt{(x+1)^2+y^2} - \sqrt{(x-1)^2+y^2} \tag{4}$$

therefore,

$$V(z) = \frac{2Vg}{\pi}u = \frac{2Vg}{\pi}\,\mathrm{Arcsin}\left(\left(\frac{1}{2}\right)\left(\sqrt{(x+1)^2+y^2}-\sqrt{(x-1)^2+y^2}\right)\right) \qquad (5)$$

The field intensity at a distance y above the silicon surface is

$$F = \frac{\partial V(z)}{\partial x} = \frac{2Vg}{\pi\sqrt{(1+y^2)}} \qquad (6)$$

If there is a thin layer of oxide of thickness, Tox, on the silicon surface of the source/drain junction, then

$$F = \frac{\partial V(z)}{\partial x} = \frac{2Vg}{\pi\sqrt{(Tox^2+y^2)}} \qquad (7)$$

In this expression y has the same dimension as that of T_{ox}. The voltage drop across the thermal oxide is approximately given by:

$$V_{ox} = V_g \frac{\varepsilon_1 T_{ox}}{\varepsilon_1 T_{ox} + \varepsilon_2 x\left(\frac{\pi}{2} - \mathrm{Arctan}\left(\frac{T_{ox}}{x}\right)\right)} \qquad (8)$$

The voltage V_{ox} increases with the increase of the permittivity ε_1 of the gate polysilicon sidewall dielectric spacer.

The voltage V_{ox} in Eq. (6) is plotted as a function of distance x from the gate electrode in Fig.11 for a thickness of thermal oxide of 10 nm and a permittivity of the polysilicon sidewall dielectric of 500. The voltage across the thermal oxide is normalized to V_g. The voltage on the surface of the thermal oxide is larger than 70% of the gate voltage when the distance is less than 0.3 μm. The larger the permittivity of the sidewall dielectric the larger the voltage on the oxide at a given distance from the edge of the gate electrode will be. The voltage at the surface of the thermal oxide can be controlled by the thickness of the thermal oxide and the permittivity of the sidewall spacer material. The series resistance at the source and drain region adjacent to the gate electrode decreases with increasing gate bias voltage.

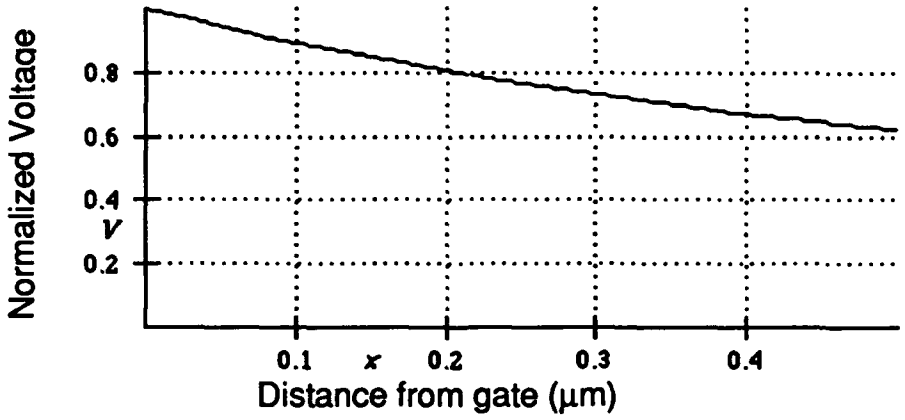


FIGURE 11 Normallized voltage drop across 10 nm of thermal oxide layer of a composite sidewall spacer with high relative dielectric constant of 500.

The series resistance can be further reduce by a low dose low energy donor (acceptor) ions implantation into the source drain area of n-channel (p-channel) MOS transistors after the gate polysilicon is etched. This ion implantation formed a depletion or a lightly doped buried surface layer under the ferroelectric sidewall spacer with practically no encroachment into the gate region. Therefore the conductivity of the sidewall region is higher than that of the channel region at all gate biases. The effective channel length of the device is practically equal to the width of the polysilicon gate line. The gate voltage may cause a portion of the ferroelectric sidewall spacers to polarize. The polarization of source side ferroelectric sidewall spacer enhances the conductivity while that of the drain side increases the series resistance of the drain sidewall section hence reducing the hot carrier effect.

For the sake of comparison we also plotted the normalized voltage in the source drain region of MOS transistors with CVD oxide spacers in Fig.12. The device structure is identical to that used in Fig.11 except that the ferroelectric thin film is replaced by CVD oxide having a relative dielectric constant of 3.9. The

voltage at a distance larger than 0.1 μm from the edge of the gate electrode is less than 10% of the gate voltage . The advantage of using a large permittivity dielectric material, such as ferroelectric, for sidewall spacer of a short channel length MOS transistor is obvious.

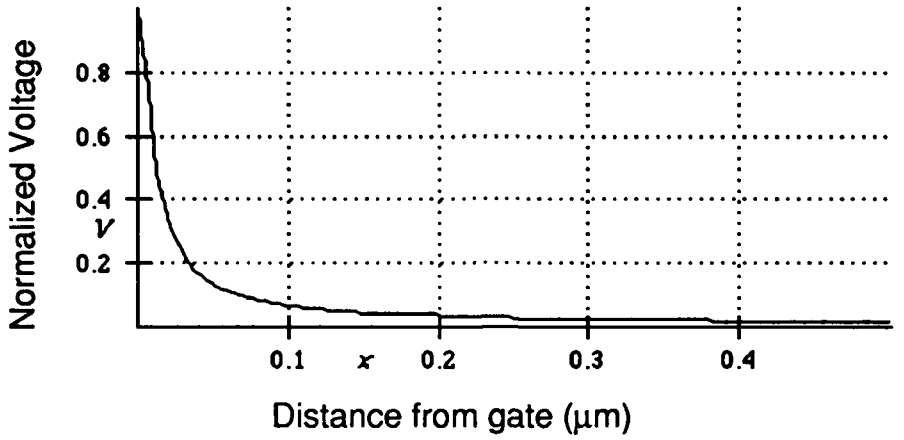


FIGURE 12 Normalized voltage drop across the 10 nm of thermal oxide of a thermal oxide/CVD oxide composite spacer. V_g = 1 V

Conclusion

There are many applications of ferroelectrics to silicon VLSI. The polarization property of ferroelectrics can be applied to many types of memory devices. The high permittivity of ferroelectrics is very useful for both large scale memory arrays such as DRAMs and EEPROMs as well as very small feature size high performance MOS transistors. A new non-volatile memory cell and a new non-volatile SRAM are shown as examples of the application of the polarization properties of ferroelectrics materals. The large linear permittivity of ferroelectric materials is applied to reduce the operating voltage of EEPROMs and to improve the performance of sub-0.5 μm channel length MOS transistors.

REFERENCES

1. J. Carrano, C. Sudhama, J. Lee, A. Tasch, and W. Miller, 1989 IEDM Technical Digest, p.255
2. See J. Caywood and S. Lai on 1990 IEDM Short Course Program on Non-Volatile Memory.
3. A. K. Goel, International Reliability Symposium, March 26, 1990
4. R. Izawa, T. Kure, S. Lijima, and E. Takada, 1987 IEDM Technical Digest p.38.
5 J. E. Moon, T. Garfinkel, J. Chung, M. Wong, P. K. Ku, and C. Hu, IEEE Electron Device Lett. p. 221, Vol. EDL-11, 1990
6. J. R. Pfiester, F. K. Baker, R. D. Sivan, N. Crain, J. H. Lin, M. Liaw, C. Seelback, C. Gunderson, and D. Denning, IEEE Electron Device Lett. p. 253, Vol. EDL-11, 1990
7. T. Buti, S. Ogura, N. Rovedo, K. Tobimatsu, and C. F. Codella, p.617, 1989 IEDM Technical digest.
8. S. T. Hsu, U/S. Patents #4,841,347 and #4,945,070
9. J. R. Pfiester, R. D. sian, H. M. Liaw, C. A. Seelbach, and C. D. Gunderson, p.365, IEEE Electron Device Lett. Vol. EDL-11, 1990.
10. See Introduction to Complex Variables and Applications. by R. V. Churchill, p.153.

AD-P006 679

INTEGRATED SAW-AO OPTICAL SWITCH ON Si

TADASHI SHIOSAKI, NAOKI KITAMURA and AKIRA KAWABATA
Department of Electronics, Faculty of Engineering,
Kyoto University, Kyoto 606, Japan

Abstract

The developments in the integration of the SAW acousto-optic Bragg deflector of guided optical waves in the ZnO thin film on a Si substrate and Schottky diode photodetectors on the same Si substrate are reported. Thin film lens has been fabricated by making use of a gradual film thickness change, the refractive index dispersion of the fundamental mode on the film thickness, and the mode cut-off property of the higher order modes in the area of the concave shaped converging lens of the ZnO film. The guided optical waves SAW-Bragg deflected, mode selected and lens focused are detected by the Schottky diode photo-detector incorporated at the boundary between the ZnO film wave guide and the Si substrate. A couple of detectors are located one for deflected and the other for undeflected waves.

92-16154

Introduction

Zinc oxide, a member of the hexagonal wurtzite class, has very strong piezoelectric effect among nonferroelectric material. It has large piezoelectric, sizable elasto-optic, electro-optic and nonlinear optic coefficients. It is also optically transparent from 0.4 to 2μm and electrically highly resistive due to the 3.3eV wide band gap. The thin film ZnO has been used extensively as a piezoelecric transducer for the generation and detection of bulk and surface acoustic waves. The ZnO thin film is usually deposited either under or over the electrode array for SAW transducers which can generate surface acoustic waves with power enough to attain high diffraction efficiency in surface acoustooptic devices on nonpiezoelectric substrates. The ZnO film is also very suitable as an optical waveguide and can be used as the interaction medium in surface acoustooptic and electrooptic devices.[1-5] Thus, using a low optical loss ZnO waveguide, it can perform a variety of active and passive operations on guided light such as have been proposed for integrated optical systems. Since optical scattering loss must be kept to a minimum in waveguides, a continued effort has been made to get low-loss ZnO films for optical applications.

We have reported the following results elsewhere.[6]

1) Although the optical intensity profile of the scattered light from the ZnO films on glass and Si was a little wavy than that on sapphire, their optical losses were around 0.5dBcm^{-1}. The minimum

loss of 0.1dBcm^{-1} was attained for one of the ZnO films on glass.
2) Diffraction ratios of 95 and 98 percent for the TE_0 mode beam (at 632.8nm) were accomplished with the surface-acoustic-wave deflectors at acoustic powers of 90mW in a ZnO film on glass and 80mW in a ZnO film on Si, respectively.[7]
3) An electrooptic Bragg diffraction modulator with high diffraction ratio was obtained using a low-loss epitaxial ZnO optical waveguide on a sapphire substrate. The unclamped electrooptic coefficient r_{33} is estimated to be 5.8×10^{-12}m/V, which is much larger than the clamped value of 2.6×10^{-12}m/V listed in the literature.[8]
4) A grating-type Schottky-barrier photo-detector was integrated with a ZnO optical wavetguide on a silicon substrate. Silicon was chosen as the base material for the future integration of optical and electronic components.
5) SHG in an as-sputtered ZnO optical waveguide on a fused-quartz substrate was performed with a Nd:YAG laser at 1.064μm wavelength. For 150mW fundamental input power, the observed conversion efficiency was about 4.9×10^{-6}. The phase-matched interaction length of 2.5mm was about 125 times larger than the previous result. The results reveal another potential use of sputtered ZnO film in integrated optical applications.[9]

In this paper we describe on the integration of a thin film optical wave guide, a surface acoustic wave guide, an AO Bragg deflector, a mode index lens, a mode filter and two Schottky photodiodes on a Si substrate, where the piezoelectric, acoustic, optic, and acousto-optic properties of ZnO are used.

Materials

A SiO_2 layer was used as a buffer layer between the ZnO film and the Si substrate to decrease the optical absorption of the guided wave in the ZnO film. When the thickness of the SiO_2 layer was about 0.5um, surface acoustic waves were not generated on Si substrates with resistivity of several Ωcm because, the applied voltage to the interdigital transducer was nearly short-circuited by the conductive Si substrate. When n-type Si substrates of 100-120 Ωcm with the (100) face and of 1250-2000Ωcm with the (111) face were used, the surface acoustic waves were observed on both substrates. The surface acoustic wave velocity depends on thicknesses of both SiO_2 and ZnO films. The SAW velocity at the thicknesses of 0.5μm for SiO_2 and 1.6um for ZnO was 3900m/s. Platinum was used as the Schottky barrier metal. This is because the platinum film fabricated by the lift-off technique was less damaged than other metals during the subsequent ZnO sputtering. The sputtering condition of the ZnO film was as follows: Substrate temperature: 380°C, atmospheric gas Ar(50%) + O_2(50%) at 1.0×10^{-2} Torr, target: Li doped ZnO ceramic disc of 100mm in diameter, RF input power: 180W, substrate-target distance: 47mm.

Acoustic and Optic Waves

He-Ne laser beam was coupled into the ZnO film with a rutile prism. The optical propagation loss for the fundamental TE mode was

about 0.5dB/cm or lower.

Fig.1 shows the measuring system of in-plane scattering and diffraction inherent in the guided optical waves before generating the surface acoustic waves. Fig.2 shows the experimental results of the measurement of the in-plane angular dependence of the guided optical wave intensity. The intensity at $\phi = 0.2^{o}$ is 20dB below the peak value at $\phi = 0^{o}$. The good value reported for a $LiNbO_3$ wave guide is 55dB. The in-plane scattering in the ZnO film on Si is higher maybe because the ZnO film is polycrystalline and the scattering takes place at the grain boundary parallel to c-axis.

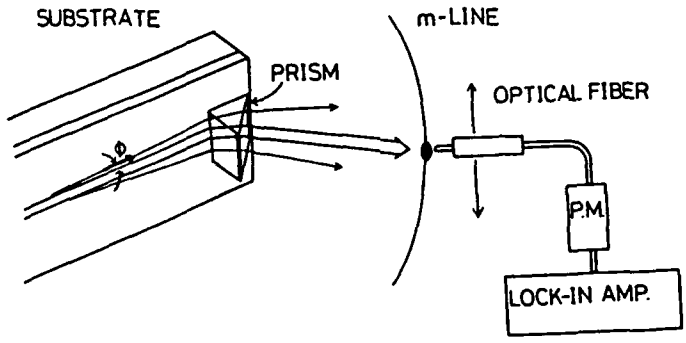


FIGURE 1 The measuring system of in-plane scattering and diffraction inherent in the guided optical waves.

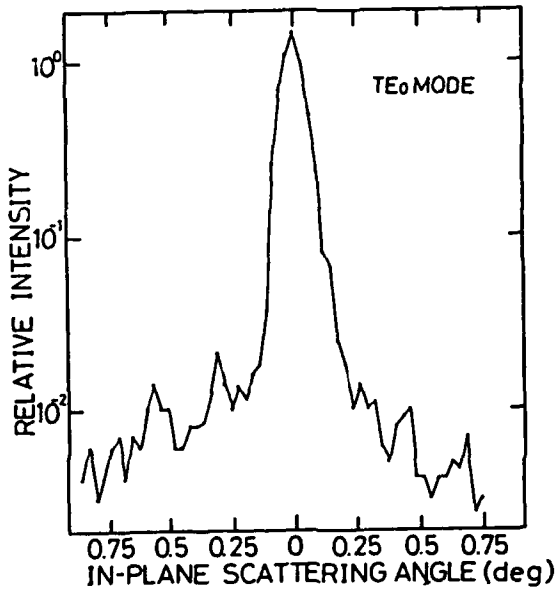


FIGURE 2 The experimental results of the in-plane angular dependence measurement of the guided optical wave.

The normal type interdigital transducers were used to generate the surface acoustic waves. Fig.3 shows the acoustic frequency dependence of the intensity of the AO-Bragg diffracted He-Ne laser beam keeping the input rf power constant. As expected, the band width increases as the number of pairs of the fingers of the interdigital transducer decreases. However, the intensity of the diffracted light decreases as it decreases.

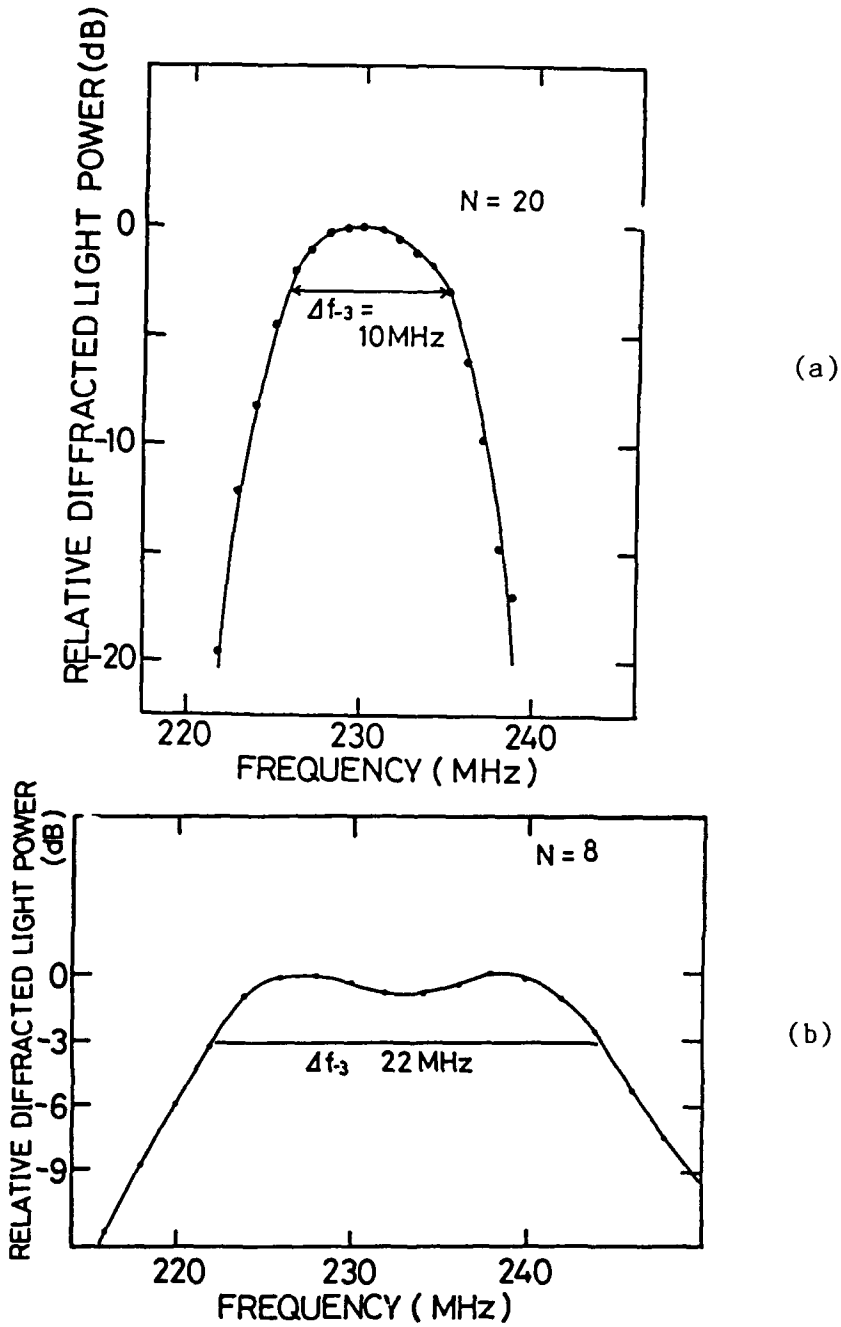


FIGURE 3 The acoustic frequency dependence of the AO-Bragg diffracted He-Ne laser intensity. The number of finger pairs is (a) 20 and (b) 8.

Integration of Devices

Figure 4 shows the integrated device. The He-Ne 632.8nm laser light is prism coupled at the right end area of this device, which is not shown in this figure. The whole dimension of the device is 9mm x 27mm. The Schematic diagram of the Schottky diode area is shown in Fig.5, and the top view of the diode Pt metal electrode is shown in Fig.6.[10] The optical grade ZnO film can be grown by the planar magnetron sputter deposition on these bare Si and sputter-deposited Pt film area as well as on the water-vapor-thermally grown SiO_2 film on Si.

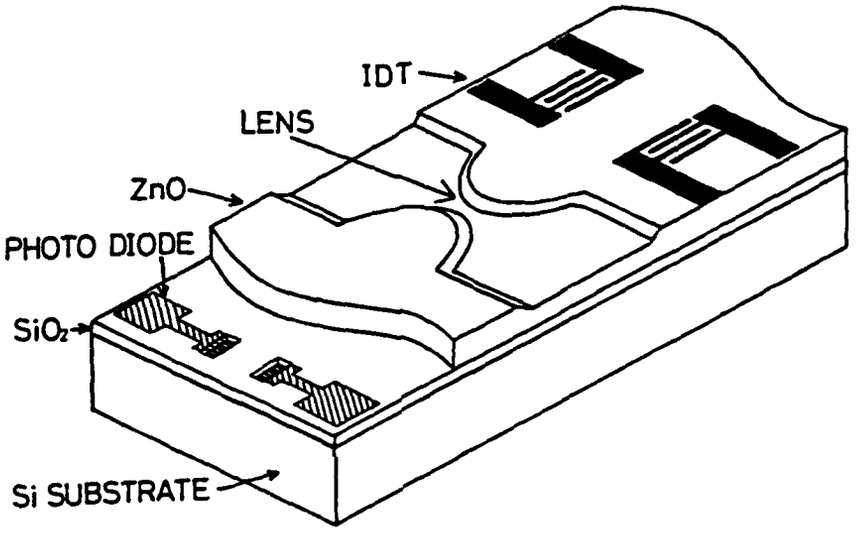


FIGURE 4 A schematic diagram of the integrated SAW-AO deflector, lens, mode filter and photo-detector on Si.

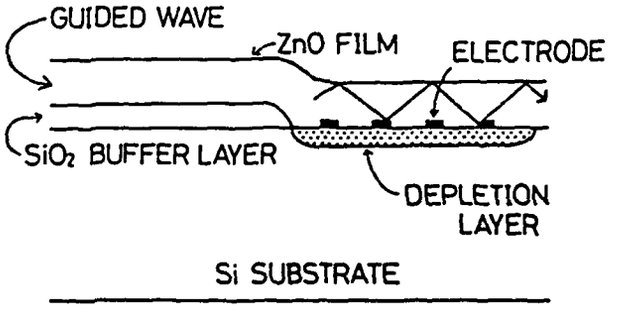


FIGURE 5 A schematic diagram of the Schottky diode photo-detector area.

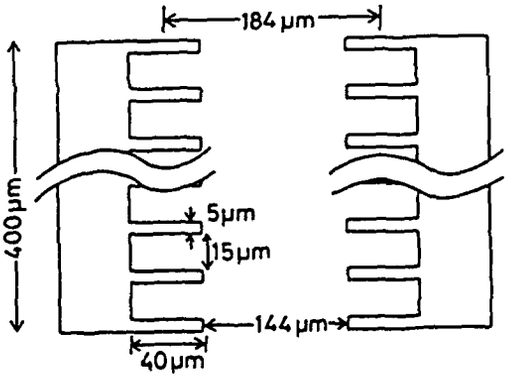


FIGURE 6 The top view of the Schottky diode Pt electrode.

The thin film mode index lens was fabricated together with the mode filter by making use of the optical properties of ZnO.[11] The dispersion relation between the effective refractive index and the film thickness of the ZnO film is shown in Fig.7. The film thicknesses T_1 and T_2 of the optical waveguide and lens areas are, for example, 0.82μm and 0.20μm, or 1.4μm and 0.2μm. The effective refractive index n_1 of the former is higher than the latter n_2 as is seen from Fig.7, and therefore a concave-shaped lens gives rise to a converging lens as shown in Fig.8. The focal length f is calculated as,[12]

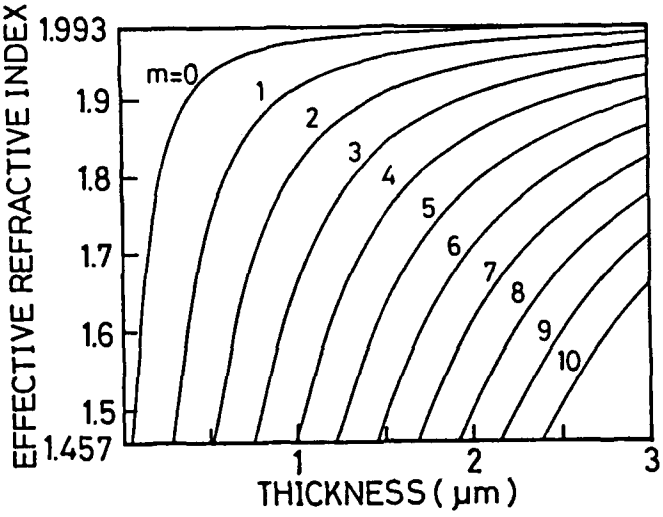


FIGURE 7 The relation between the effective refractive index and the ZnO film thickness. The SiO_2 film of infinite thickness is assumed to be between the ZnO film and Si.

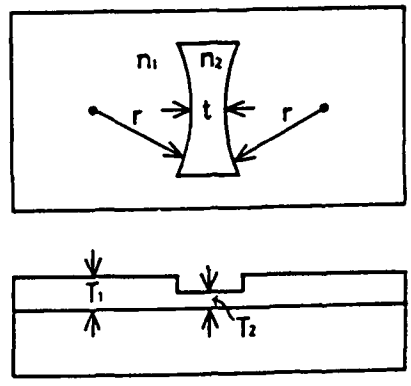


FIGURE 8 The schematic diagram of the concave-shaped converging lenses.

$$f = n_1 n_2 r^2/(n_1 - n_2)(2n_2 r - (n_1 - n_2)t) \qquad (1)$$

where r is the radius of the lens boundary and t is the thickness of the lens as shown in Fig.7. The shadow mask with r=2.5mm and t=1.2mm was used. Taking the values of n_1 and n_2 at T_1=0.82μm and T_2=0.20μm of the one of the specimen into account the theoretical value of f is 12.3mm. On the other hand, the measured focal length was 12.4mm.

The film thickness in the lens area is so designed to be thinner than the other and also thinner than the cut off thickness for the higher modes, that the area plays the role of the mode filter which passes only the fundamental TE mode and cut off the higher TE modes in addition to the role of the converging lens.

A bright technique was adopted in making the lens edge as follows. That is, a two-step sputtering deposition was used as shown in Fig.9, when making the lens. First, the 0.20μm thick ZnO film was deposited on the whole area on the SiO_2/Si substrate, then the shadow mask was kept slightly above not to contact the previously sputtered ZnO film in the lens area and the second-step ZnO film was sputter deposited in the waveguide area. By keeping the shadow mask in this way, the thickness of the ZnO film changes gradually from 0.20μm to 0.82μm orfrom 0.20μm to 1.40μm in the lens boundary area, and reflection and mode conversion are decreased.

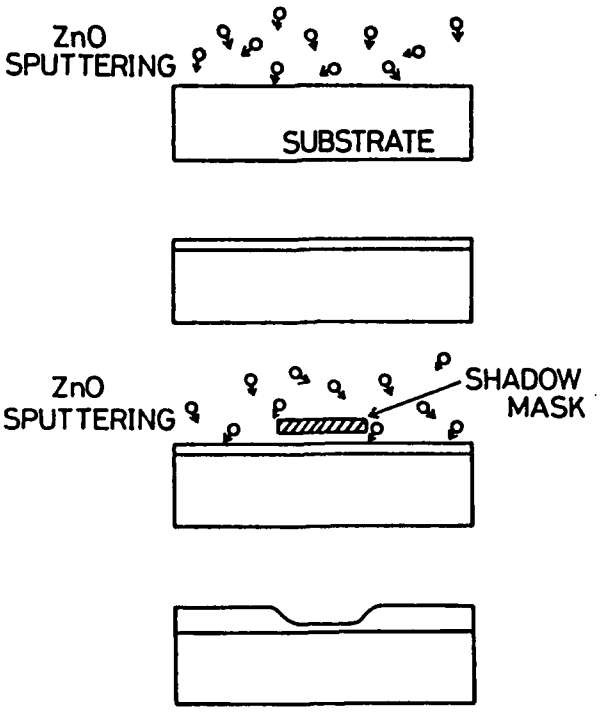


FIGURE 9 The explanation for the two step sputtering deposition of the ZnO film and non-contact shadow mask method to fabricate the mode index lens.

The interdigital transducer for the surface acoustic wave acousto-optic Bragg deflector was fabricated by lifting off of the aluminum thin film vacuum evaporated on top of the ZnO film. The spatial period of the interdigital transducer was 20μm, the aperture is 3mm, and the number of finger pairs is 20 which gives the Q number of 15 and therefore the Bragg diffraction. The ZnO film thicknesses T_1 and T_2 are 1.40μm and 0.20μm, and then the focal length is 11.6mm for the particular device described below. The separation distance d between two focusing points corresponding to the deflected and undeflected is given by the equation

$$d = 2f\tan\Theta_B \qquad (2)$$

where Θ_B is the Bragg angle. Taking the spatial period 20um of the interdigital transducer into account Θ_B is calculated as 0.455°, and then d is 184μm as f is 11.6mm. Thus center to center separation between two photodiodes are designed to be 184μm as indicated above in Fig.6.

Only one element that was not incorporated on this device is the light source. Instead, the He-Ne laser light of 632.8nm wavelength was coupled in with a rutile prism.

Results and Discussion

Figure 10 shows the photodiode outputs of the deflected and undeflected lights. The frequency of the surface acoustic wave is 195MHz. The bias voltage of the diodes is 7V and the load resistance is 200kΩ. The rf pulse duration is 1ms.

There are several problems to be solved:

1) The unwanted scattered light was detected at the photodiode for

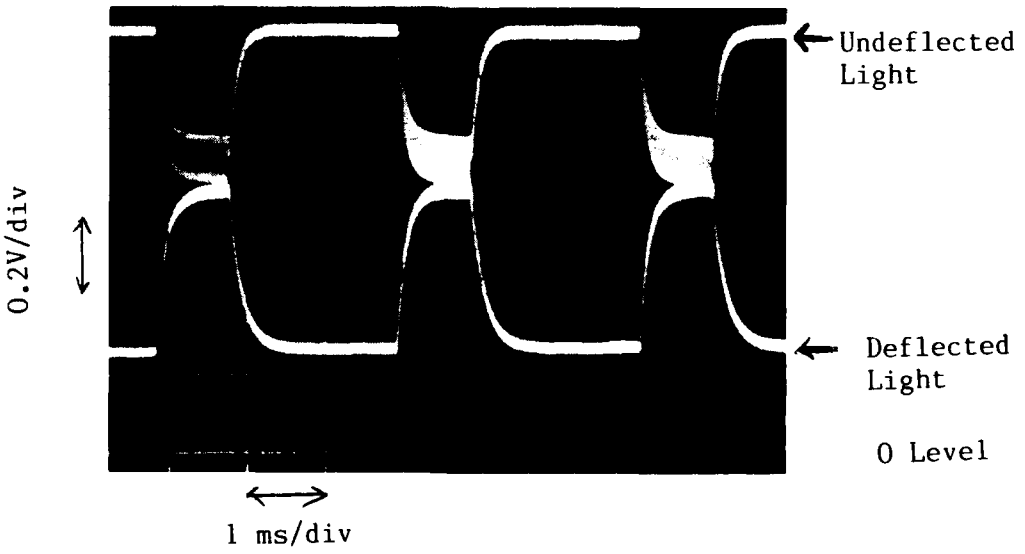


FIGURE 10 The photodiode outputs of the deflected and undeflected lights.

deflected light.
2) The electrical resistivity of Si was chosen to be high enough to give a good SAW interdigital transducer, and this the resistivity gave the slow response in the photodetectors.
3) The radio frequency noise was observed in the photodetector. This noise coupled from the interdigital transducer to the detector.
4) The band width of surface acoustic wave should be increased by using a phased array transducer, tilted-finger chirp transducer, or multi tilted-array transducer.

Rererences

1. P.K. Tien, R. Ulrich, and R.T. Martin, Appl. Phys. Lett., 14, 291 (1969).
2. J.M. Hammer, D.J. Channin, M.T. Duffy and J.P. Wittkle, Appl. Phys. Lett., 21, 358 (1972).
3. K. Setsune, T. Mitsuyu, and K. Wasa, Japan, Jpn. J. Appl. Phys., 22, Suppl.22-3, 173 (1983).
4. T. Shiosaki, S. Ohnishi, Y. Murakami and A. Kawabata, J. Cryst. Growth, 45, 346 (1978).
5. T. Shiosaki, S. Ohnishi and A. Kawabata, J. Appl. Phys., 50, 3113 (1979).
6. T. Shiosaki, Ceramic Transactions Vol.14 (The American Ceramic Society) pp.197-210.
7. M.S. Wu, A. Azuma, T. Shiosaki and A. Kawabata, IEEE Transactions on Ultrasonics, Ferroelectrics and Frequency Control, 36, 442 (1989).
8. M.S. Wu, T. Shiosaki and A. Kawabata, IEEE J. of Quantum Electronics, 25, 252 (1989).
9. T. Shiosaki, S. Fukuda, K. Sakai, H. Kuroda and A. Kawabata, Jpn. J. Appl. Phys., 19, 2391(1980).
10. C.C. Tseng and S. Wang, Appl. Phys. Lett., 26, 632 (1975).
11. B.U. Chen, E. Marom and A. Lee, Appl. Phys. Lett., 31 263(1977).
12. J.M. Hammer, D.J. Channin, M.T. Duffy and C.C. Neil, IEEE J. Quantum Electron., QE-11, 138(1975).

AD-P006 680

ELECTRON EMISSION BY NANOSECOND SWITCHING IN PLZT

HARTMUT GUNDEL

Technische Universität Berlin, Institut für Theoretische Elektrotechnik, EN 2, Einsteinufer 17, 1000 Berlin 10

ABSTRACT Copious electron emission from a PLZT ceramic surface takes place either when the surface is illuminated with laser pulses, or when short, high-voltage pulses are applied. In the latter case, charge densities of up to 5 $\mu C/cm^2$ and current densities of some ten of amperes per square centimetre have been measured. Depending on the position of the material in its phase diagram, different behaviour of the emission has been observed. Consequently the pulsed electron beam varies with respect to its pulse length, its amplitude, and its risetime. Further investigation of these data related to the corresponding material state might be a good diagnostic method, interesting for the switching dynamics in the ns-region. Moreover, a direct application as a pulsed "Ferroelectric Electron Beam Source" is envisaged, as the emission does not rely on vacuum, but also works in low pressure gas or plasma. A maximum repetition frequency of 2 MHz has been established. An improvement of all data of the emitted electron beam seems feasible.

92-16155

INTRODUCTION

Electron emission from ferroelectrics had already been observed as far back as 1964, when Belayev and Bendrikova[1] investigated the influence of the state of spontaneous polarization in triglycine sulfate and Rochelle salt on the intensity of photostimulated exoelectron emission. In the following a large number of materials has been examined by several groups in order to study the switching dynamics and the domain wall motion processes in ferroelectric single crystals as well as in ceramics. Investigations have been performed using d.c. and a.c. electric fields as well as pulsed voltage, with thermal stimulation, and under the influence of light illumination. The experiments have been undertaken at air athmosphere, in low pressure gas, and under vacuum. As a common result, it turned out, that the effiency to generate electrons seems to be correlated to the rate of polarization change in the used material. Since almost all investigations were mainly directed at the surface layers and the kinetics of the corresponding material, but not at the generation of intense beams, electron emission however had been pure. Emitted electron currents were $10^{-11} A/cm^2$ at its best[2], and mostly even less. In 1973 the thermally stimulated field emission was used by Bräunlich to illuminate a target for x-ray generation[3]. Here $10^{-9} A/cm^2$ have been achieved. A review on earlier publications concerning electron emission from ferroelectrics was given by Biedrzycki in 1986[4].

The present work describes copious electron emission, orders of magnitude higher than reported before, as it has been demonstrated recently by fast switching, using the methods of pulsed power technique and plasma physics[5-13]. Summarizing these investigations, in the following chapters a simple and tentative model of the emission process is proposed, the experimental technique is described, selected results are presented and discussed, and an outlook to possible applications and further improvements is given.

THE EMISSION PROCESS

The dielectric displacement of a ferroelectric is written as $\mathbf{D} = \epsilon_0 \mathbf{E} + \mathbf{P}$, where $\mathbf{E}$ is the applied electric field, ϵ_0 is the dielectric constant and $\mathbf{P}$ is the polarization of the material. The polarization is a sum $\mathbf{P} = \epsilon_0 \chi \mathbf{E} + \mathbf{P}_s + \mathbf{P}_d$, the first term being the polarisability of the material, the second representing the spontaneous alignment $\mathbf{P}_s$ of the dipols, and the last taking into account a polarisation $\mathbf{P}_d$ due to existing defects. χ is the dielectric suszeptibility of the material.

The dielectric displacement varies with the applied electric field and does normally not vanish at zero field, since the spontaneous polarization is permanent. Additionally the polarization $\mathbf{P}_d$ may contribute by affecting the normal hysteresis loop of a ferroelectrics[14]. Provided the polarization due to defects does not reverse in an external field, and if all defects are polarized in the same direction, a biased hysteresis loop appears . In the case of opposite directed polarization in neighbouring regions a double hysteresis loop results . It is similar to the well known double hysteresis loop of an antiferroelectric state. If $\mathbf{P}_d$ does reverse with an external field, then the coercive field depends on both the sign and magnitude of $\mathbf{P}_d$ and the field required to switch the defects.

In a steady state the ferroelectric appears neutral to its outer world because any remanent polarization is immediately compensated by free charge carriers. Thus surface charge densities of 30 $\mu C/cm^2$ or even higher can exist in a normal equilibrium state without effecting the surrounding. However, there are several possibilities to disturb this charge equilibrium for a transient time, generating a surplus of equally labelled charges at opposite faces of the affected volume. Such a mechanism which can change the polarization inside the material and which is fast enough not to be compensated instantaneously, results in a high potential at the surface. Under proper experimental conditions charged particles can be liberated and accelerated thereby. In the present case conditions are chosen in order to achieve a surplus of negative charges at the emitting surface, resulting in electron emission. The electrons are drawn from levels which are preferable from the energy point of view. These may be screening charges of $\mathbf{P}_s$, electrons trapped by the defects, or others. As the external induced change of the polarization developes, the surface potential behaves in time, and the emission is enhanced or reduced. The emission characteristic is governed by external manipulation and can be controlled up to a certain degree. Moreover, a sophisticated diagnostic method, resolving space and time, to observe the electrons may give a picture of the

polarization dynamics of the ferroelectric surface.

There are different processes to achieve a fast change of the polarization of the material (see also Ref. 5):

- heating or cooling across a phase-transition boundary from or to the ferroelectric (FE) state;
- transitions between the FE phase and the antiferroelectric (AFE) or paraelectric (PE) phases, by applying pulsed stress;
- transitions between the AFE or PE phases and the FE phase, by applying a pulsed electric field;
- (partial) reversal of P_s inside the ferroelectric phase, by high voltage pulses;
- illumination by laser light (photo assisted domain switching[15]);

or any combination of these processes.

For repetitive emission, heating across a phase boundary does not seem to be a good method. The need for periodical cooling of the sample to its original state poses problems if emission with high repetition rates is envisaged.

Phase shift caused by stress pulses is possible within less than 100 ns [16-18]. During shock-depoling experiments, released currents of up to 500 Amperes have been measured on the electrodes, when pulsed pressure (1-10 GPa) was applied[19]. However, most of these experiments were of destructive character and the release of electrons to vacuum was not investigated.

A fast change of P_s induced by high-voltage pulses, by phase shift, and/or by (partial) reversal of P_s is the main method used in the experiments presented below. Phase shift offers the advantage that the material after emission relaxes back to its state prior to the voltage pulse. Thus no resetting process has to be undertaken. Reversal inside the FE phase necessarly needs an active resetting, either by applying pulses with alternating polarity, or by pulsing from a low continous potential level to the opposite polarity. The emission dynamics in detail will be strongly correlated to the actual material under use, taking into account the kind of phase transition (1^{st} or 2^{nd} order, or DPT), nucleation and domain wall motion, grain properties, defect concentration, homogeneousity, ect.

A few experiments with laser-induced electron emission were performed. They will not be described here, since there is detailed information in Ref. 8.

EXPERIMENTAL TECHNIQUE

The composition of the PLZT ceramics used was 2/95/5 and X/65/35, with X equal 7, 8, 9 or 10. The first number refers to the percentage of the lanthanum content, and the following numbers indicate the established Zr/Ti ratio of the samples. The materials were prepared by conventional oxide sintering.*)

*) The samples were supplied by Prof. Handerek from the Institut of Physics of the University of Silesia in Katowice, Poland

At roomtemperature PLZT 2/95/5 is antiferroelectric and has an AFE-FE-PE phase sequence with rising temperature; PLZT 7/65/35 is in the rhombohedral FE state; PLZT 8/65/35 is close to the phase boundary separating the rhombohedral and tetragonal phases; the 9 and 10/65/35 materials are in the region of speudo-ferroelectricity near to the PE phase boundary. As a common feature all these materials posess the characteristics of diffuse phase transitions (DPTs). Typical values of the dielectric constant are between several hundred and several thousand, and the specific electrical resistivity is high. Comprehensive information about the mechanical, the electrical, and the optical properties, and a phase diagram can be found in Refs. 20 to 29, and in other publications.

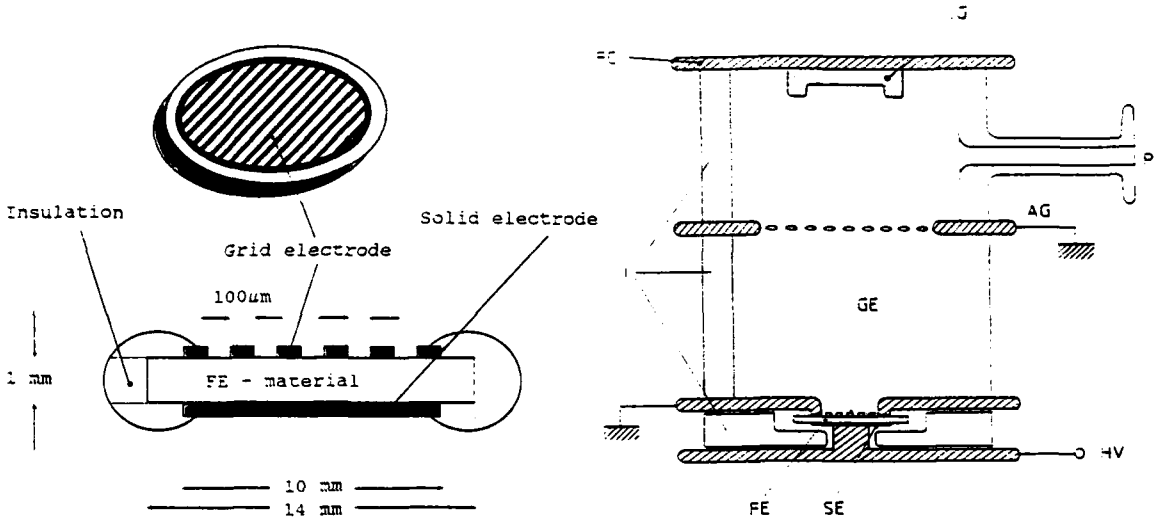


FIGURE 2: Scheme of the experimental set-up with HV-pulse induced electron emission. FE - Ferroelectric sample, SE - Solid electrode, GE - Grid electrode, FC - Measuring electrode, G - Graphite, I - Insulator, AG - Auxiliary grid, P - Pump, HV - High voltage

The disk-shaped samples, about 1 mm thick and up to 17 mm in diameter, were coated with evaporated gold electrodes of 10 mm diameter, solid on one side and in form of a striped grid on the opposite face. The interconnected 200 µm wide gold stripes were separated by bare stripes of the same width. The electroded part of the grid enables electric fields to be applied; the bare part of the sample serves as emitting surface. The sample edge and the bare-sample surface around the electrode were covered with an insulating layer. This has to be designed in such a way that high-voltage pulses up to 5 kV may be applied without danger of breakdown across the sample edges. Fig. 2 shows a scheme of the sample geometrie and a diagram of the mechanical set-up. The grid electrode (GE) of the PLZT sample (FE) is oriented towards the vacuum of the camber and was grounded during all experiments. The support for the sample is equipped with a heating element and a thermocouple which are not shown. The measuring electrode (FC) cosists of a graphite cup (G). The collected electron current was measured time-resolved with an oscilloscope. To measure

the emitted charge, the current was passively integrated on a proper condenser. Auxiliary grids (AG) could be inserted in between the PLZT sample and the measuring electrode. These grids, which consist of metal plates with a fine metallic mesh in the centre, were used for acceleration or deceleration of the emitted electrons, and served as protection against high-frequency noise from the HV-circuit components.

Prior to emission the samples were prepoled with a d.c. electric field of about 2 kV/cm, applied as negative voltage to the grid electrode. After poling for half an hour at 20 K above the corresponding Curie temperature, the samples were cooled down under the same field strength to room temperature, through the PE-FE and FE-AFE phase boundary for PLZT X/65/35 and PLZT 2/95/5 respectively.

To initiate the emission, negative high-voltage pulses were applied to the rear electrode SE. They were generated in a low impedance HV-pulse circiut, mainly consisting of a storage capacity, a fast-rising high-power transistor switch, and a transition line of low impedance into the load. In order to achieve high-current pulses to measure the emitted charge as a function of the field growth rate, up to four circuits were used parallel, resulting in charging currents of almost 500 Amperes. More details on the HV-pulse circuit, the diagnostic methods, and the mechanical set-up can be found amongst others in Refs. 9 and 13.

RESULTS

Many experiments have been performed which demonstrate electron emission from PLZT ceramics, and most of the data were already presented in previous publications. Therefore the results are only discussed briefly, and the reader finds references to special papers for more detailed information. The electron emission was investigated as a function of the applied electric field strength, of the sample temperature[7,10], of the field growth rate[10,13], of the surrounding gas pressure[9], and of the repetition frequency[13] of the pulses. The energy of the emitted electrons was estimated by applying a decelerating field[7,9].

PLZT 2/95/5 CERAMIC EMITTERS

Electron emission depends strongly on the applied electric field strength and varies with the temperature of the sample, as the ferroelectric properties also change according to the phase diagram. The influence of the applied electric field strength on the emitted charge density can be seen in Fig. 3a, measured for a few constant temperatures as a parameter. The emission process starts at a threshold field of about 7 to 11 kV/cm, which increases with decreasing temperature and reaches about 20 kV/cm at room temperature. As higher electric fields are applied, there is a strong increase in the emitted current and charge. The electron emission is also enhanced by increasing the temperature of the ferroelectric ceramics. All curves $Q(E)_T$ are clearly divided into two regions of different slope.

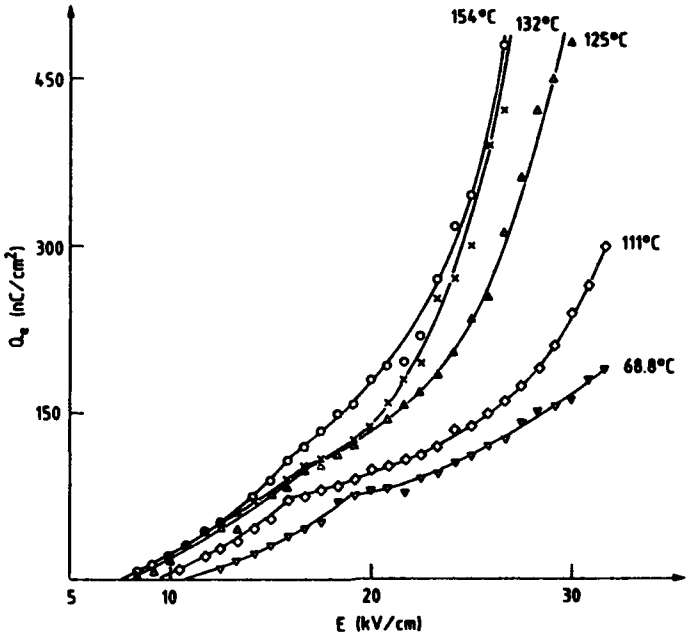


FIGURE 3a The emitted electron charge density as a function of the applied electric field strength at different temperatures near the AFE-FE phase transition.

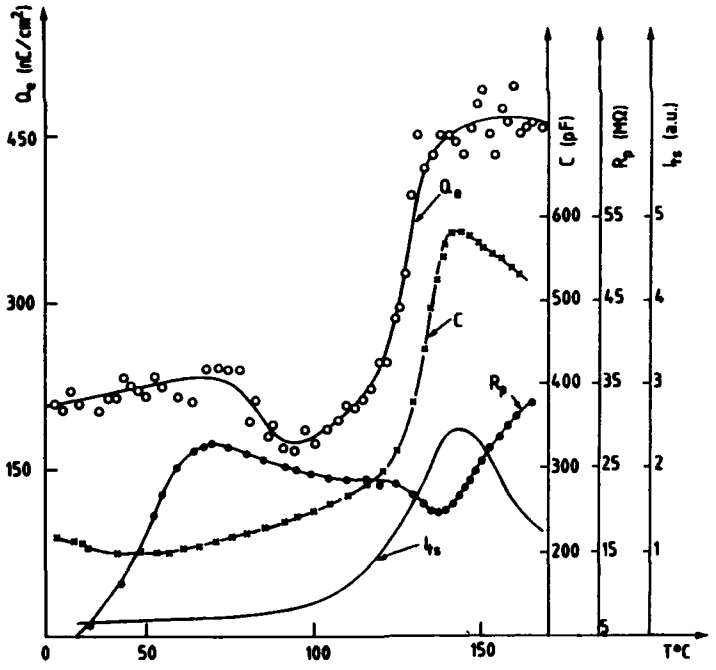


FIGURE 3b Emitted electron charge density (Q_e), capacity (C), resistance (Rp), and thermostimulated current (I_{ts}) as a function of temperature in the vicinity of the AFE-FE phase transition.

The temperature dependence of the emitted charge in relation to the dielectric properties of PLZT 2/95/5 can be seen in Fig. 3b. At a constant electric field strength, the sample was slowly heated across the AFE-FE diffuse phase-transition boundary.

This temperature region is characterized by the broad local maximum of the capacity curve C(T). At higher temperatures, the capacity of the sample increases further, and a more distinct maximum occurs at the FE-PE phase transition at 235°C, which is not shown in the figure. Near to the AFE-FE phase transition, a steep rise of the emitted charge density takes place. There is an evident correlation between the maximum of the emitted charge and the temperature dependences on the sample capacity (C) and the resistance (Rp), which was measured with an a.c. field of 1 kHz. The maximum of the thermostimulated current (Its), which was recorded during heating of the previously pre-poled sample, also coincides with the AFE-FE phase transition.

As mentioned before, the emission process relies on a change of polarization, which has to be fast enough so as not to be compensated. As a consequence, the total emitted charge as well as the current and charge density should increase, while changing the same amount of polarization in less time. The emitted charge density as a function of the field growth rate is shown in Fig. 4. Near the threshold electric field (lowest trace, 20 kV/cm), the charge density increases with the field growth-rate, but reaches saturation. With a higher electric field strength, saturation of the emitted charge density does not seem to be reached in the range investigated (upper trace, 35 kV/cm). The increase of the emitted charge is identical to an increase in the current amplitude, since the emission time decreased slightly with increasing field growth-rates.

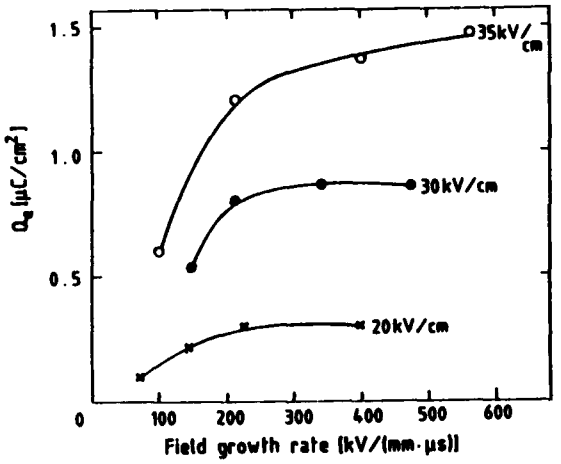


FIGURE 4

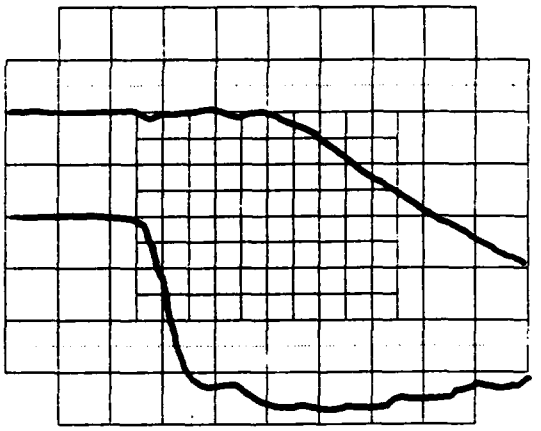


FIGURE 5

FIGURE 4 The emitted charge density (Q_e) as a function of the electric field growth rate for three different electric field amplitudes.

FIGURE 5 The begin of electron emission (upper trace) correlated to the applied negative HV pulse (lower trace). The time has been 10 ns per small division.

In Fig. 5 the time correlation between the applied negative HV pulse (lower trace) and the begin of the electron emission can be seen (integrated current, upper trace). After the voltage has reached the threshold, there is a distinct delay of about 30 ns to the start of the emission. Within the limits of experimental error, no dependence

from the applied field or from the field growth rate could be stated. As a general fact it should be noted, that the electron emission process always lastet about 50 to 100 ns (FWHM) even with electric fields applied for a much longer period. The total emitted current consists of many short current spikes[13]. The resolution of its time structure (5 to 10 ns) however has been limited by the rise time of the used Faraday Cup and by the bandwidth of the oscilloscope.

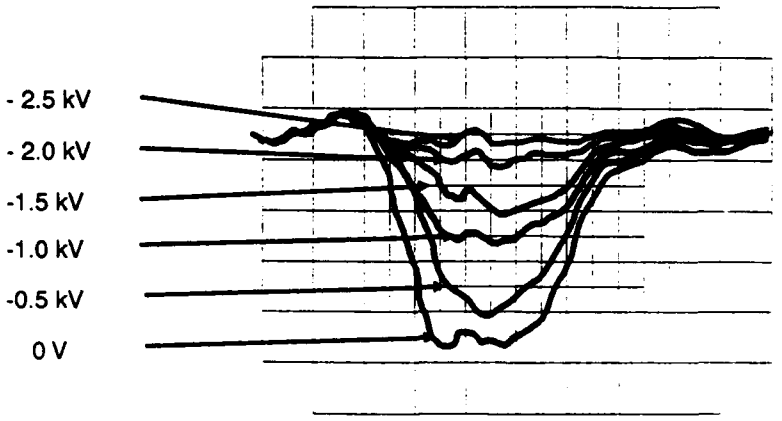


FIGURE 6 The emitted electron current at different decelerating fields

A rough information of the energy distribution of the emitted electrons can be found in Fig. 6. A deceleration potential (U_D) has been applied to an auxiliary grid between the emitting surface and the Faraday Cup. Here the current signal decreases homogeneously as the potential increases. This is evidence for all electron energies occuring during the whole emission time.

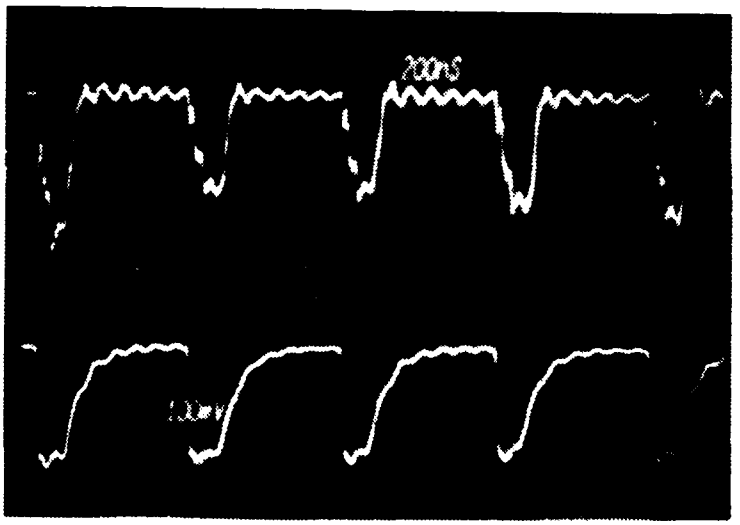


FIGURE 7 The emitted electron current (upper trace, 0.4A/cm2/small div.) induced by HV pulses (lower trace, 1 kV/small div.) of 1.1 MHz repetition rate.

The emission as a function of repetition rate of the HV pulses has been investigated up to 2 MHz, which was experimental restricted by the pulsgenerator. In Fig. 7 the first 5 pulses of a burst with 20 pulses each separated by about 900 ns can

be seen (upper trace) correlated to the HV pulses (lower trace). There is a small visible decrease of the HV amplitude, which is due to a too low charging capacity in the HV pulse circuit. One can see, that the first electron-beam pulse amplitude is about 20% higher than the following ones, which are detached with jitter values comparable to those found in all emission experiments. The emitted electron currents were about 1.5A/cm^2. The average charge density was about 250 nC/cm^2.

PLZT X/65/35 CERAMIC EMITTERS

Electron emission has been measured as a function of temperature. For PLZT 8/65/35 in Fig. 8 the emitted charge density is shown together with dielectric data, like capacity and resistance of the FE, and with the sum of pyroelectric and thermostimulated current. This resultant current has been measured separately by

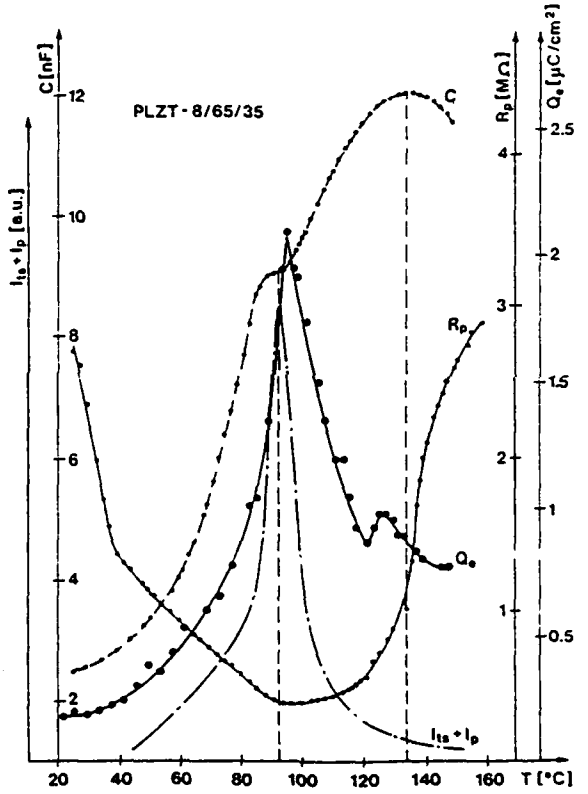


FIGURE 8 Electron emission correlated to the materials dielectric properties.

changing the temperature quickly, whereas the other results have been achieved during slow heating of the sample. A clear correlation between the maxima of electron emission and the resultant current has been found. At this temperature the resistance has a minimum and the capacity shows an anomaly which is known from other investigations as well. For the materials 7 and 9/56/35 similar behaviour was found[10], although it has not been as distinct as in the case of PLZT 8/65/35.

The emission characteristic as a function of the applied electric field has been investigated for different X/65/35 materials. In Fig. 9 three curves for a lanthanum content of 8, 9 and 10% can be seen, each having only one slope unlike in the case of

PLZT 2/95/5. No clear difference in the threshold field has been visible amongst these materials; however, as the lanthanum content increases (i.e. the distance from room temperature to the FE-PE phase boundary gets closer), the emission is stronger and the same amount of charge can be emitted with much less field applied.

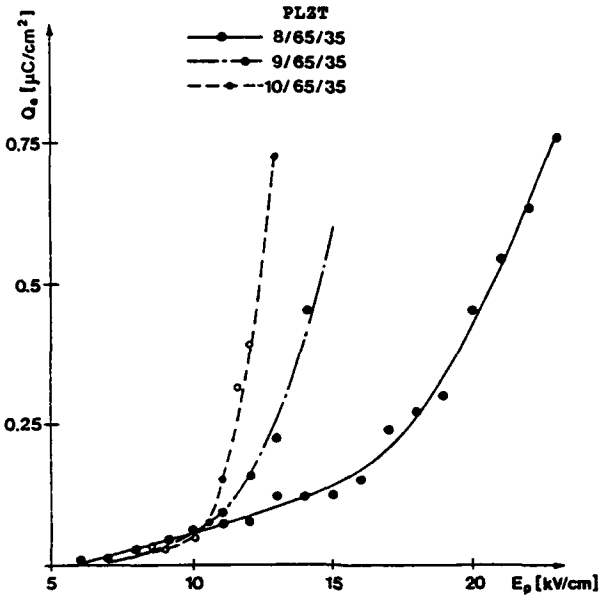


FIGURE 9 The emitted charge as a function of the applied electric field.

The influence of the field growth rate on the emitted charge density is shown in Fig. 10 for three different electric fields. Similar as for PLZT 2/95/5 the emitted charge density reaches saturation at high field growth rates only for lower applied electric fields. For higher fields no saturation effect has been observed.

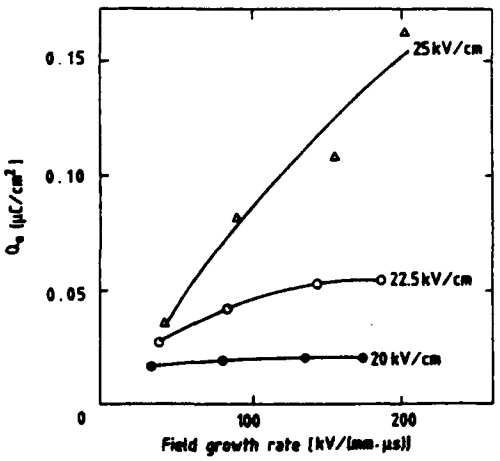


FIGURE 10

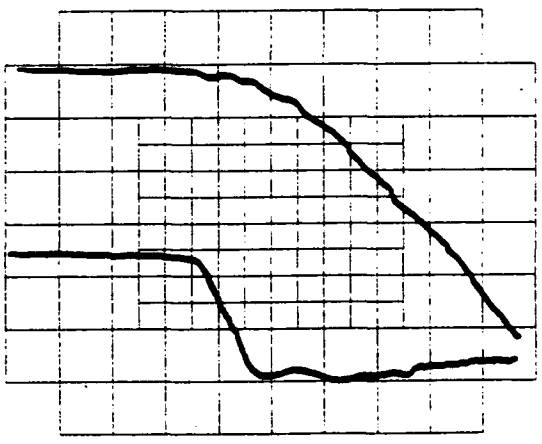


FIGURE 11

FIGURE 10 Electron emission as a function of field growth rate
FIGURE 11 Time correlation between emission and applied HV pulse

A significant difference to the results from PLZT 2/95/5 is shown in Fig. 11, where the time correlation between the applied HV pulse (lower trace) and the start of

electron emission (integrated current signal, upper trace) can be seen. In the frame of error no delay between both signals could be resolved. On the contrary to PLZT 2/95/5 the total emission time was much longer and has been determined by the HV-pulse length. Again the total pulse consisted of many short spikes. No high repetition rate experiments could be performed, since the amplitude of the second pulse decreased strongly if pulse sequences with more than a few Hz were applied.

DISCUSSION

The investigated materials can be characterized by qualitativly different emission behaviour. One the one side there is PLZT 2/95/5, showing short and very sharp electron pulses, allowing repetitive emission, but posessing a distinct delay time between the threshold electric field being applied and the start of the emission. PLZT X/65/35 on the other side emits instantaneously once the threshold field is reached and continues emitting up to the end of the HV pulse. Repetitive emission however is not possible. The reason for this different behaviour has to be found in the dynamics of polarization change in these two material groups.

To induce a phase shift AFE-FE by electric field (PLZT 2/95/5), first nucleation of FE domains in the AFE matrix is necessary, and then domain wall motion has to enlarge the FE region. The nucleation process might by correlated to the measured delay to emission; nucleation then has to be independent from the field growth rate and the absolute value of the threshold electric field which is depending on temperature, since no dependence on these parameters could be measured. At temperatures nearer to the phase transition boundary the emission increases, which is in accordance to the lowering of the coercive field.

Within the FE phase there are two regions, one with rhombohedral and the other with tetragonal structure, being refered to as 'soft' and 'hard', since they reveal different coercive field. Assumed both FE phases can be induced, the two different slopes in the Q(E) characteristic of PLZT 2/95/5 could be explained. The difference between both fields is almost constant while changing the absolute value with increasing temperature.

The apperance of many short electron spikes seem to be a successive switching of grains, each having slightly different coercive field. This is supported by the fact, that electron energies of the whole measured spectrum can be observed at any time of the pulse.

The possibility to achieve high repetition rates with pulses of only one polarity is an strong suppport that a phase shift takes place; immediately when the HV pulse is switched off, the material relaxes back to the non-polar state prior to emission and no resetting is necessary. The restorage of the emitted charge may be explained by injection from the electrodes, since the ohmic conductivity of the material is to low to generate charge equilibrium in less than 500 ns. When the polarization relaxes back however the potential between the bare-sample surface and the electrode grid is just opposite directed than during emission. For a short time thus high fields may arise,

strong enough to allow considerable currents quickly leading to a compensated surface state[30].

PLZT 8/65/35 has rhombohedral symmetry at room temperature and posesses twin domains with compensated antiparallel P_s vectors[29]. When the HV pulse is applied no nucleation process of suitable oriented domains is necessary, but domain wall motion may start immediately from one of the twins. This might be a reason for the observed lack of delay between the application of the threshold electric field and the begin of electron emission. Normally twinning of domains may be removed permanently by electical field[14], therefore emission induced by unipolar electric field should be impossible once all the material is oriented by the successive pulses. This is true for material without prepoling where no emission behaviour could be observed. The prepolarization process which is substantial for emission seems to play a double role: It may (partially) direct the twin domain perpendicular at the sample surface, and thereby increase the switchable part of the ceramics. Additionally existing defects may be separated resulting in a shift of the hysteresis loop. The internal fields generated as a result of this process might be a reason for forming twin domains again when the HV pulse excitation is over. Repetitive emission then would be possible as it has been measured with rates up to a few Hz only. Due to the complexity of the phase diagram of the investigated PLZT X/65/35 materials, however, in this case there is up to now no conclusive explanation of the phenomena of electron emission.

OUTLOOK AND APPLICATIONS

Investigations on electron emission from ferroelectrics are just in the beginning as compared to the well established conventional electron sources. From FE materials there exist compositions that emit during only a few tens of nanoseconds, which is very restricted in time, and others that emit continuously for a much longer period, as long as the HV pulse is applied. Current and charge densities vary by two orders of magnitude. The relaxation time to the previous state, which allows repetitive emission to take place, ranges from less than 500 ns to almost seconds. Up to now, the physical limits of the emission processes from ferroelectric ceramics are neither reached experimentally nor known theoretically. However, although on the one hand the big difference of results makes an extensive interpretation difficult, on the other hand it enables one to find a satisfactory material, that delivers the desired electron-beam data for many different applications. Interesting features of the so called 'Ferroelectric Electron Beam Source' (FEBS) are almost arbitrary emission cross-section, emission without external extraction fields allowing to modulate the beam easily, the lack of need of ultra-high vacuum, and the possibility to emit even in low pressure gas or plasma.

Consequently, the beam from the FEBS is well suited for example as for pre-ionization, for triggering high-power gas and vacuum switches, for generating primary electron beams for injection into linacs, and for generating secondary electron and ion

beams by sputtering from solid targets. Basic experiments have been undertaken, which demonstrate its feasibility for HV switching[31], and for electron and ion beam generation[32]. A summary of potential applications and its latest experimental results are reported in Ref. 33.

Beside possible applications a fundamental interest on electron emission arises since its behaviour is strongly correlated to the dynamics of the material. Thus a new instrument has been found to investigate phase shift and polarization reversal, provided techniques are applied which allow to measure in the pico-second region. These are already available and may be useful to find intrinsic switching and fastest relaxation times.

Particular interest is directed to emission experiments from ferroelectric thin films. Such emitters should be driven by very low voltages only and will find a wide range of applications using integrated material technologies.

ACKNOWLEDGEMENT

I am very grateful to Dr. H. Riege and to Prof. J. Handerek, with whom I have performed most of the experiments during my stay at CERN, Geneva.

LITERATURE

1. L. M. Belayev, G. G. Bendrikova, Fiz. Tverdogo Tela **6** (1964) 645
2. G. I. Rozenman, V. A. Okhapkin, Yu. L. Chepelev, V. Ya. Shur, JETP Lett. **39** (1984) 477
3. P. Braunlich, United States Patent No. 3,840,748 from Oct. 8, 1974
4. K. Biedrzycki, phys. stat. sol (a) **93** (1986) 503-508
5. H. Gundel, H. Riege, E.J.N. Wilson, J. Handerek, K. Zioutas, Nucl. Instrum. Methods A **280** (1989) 1-6
6. H. Gundel, H. Riege, E.J.N. Wilson, J. Handerek, K. Zioutas, Ferroelectrics **94** (1989) 337-341
7. H. Gundel, J. Handerek, H. Riege, E.J.N. Wilson, K. Zioutas, Ferroelectrics **109** (1990) 137
8. K. Geissler, H. Gundel, H. Riege, J. Handerek, Appl. Phys. Lett. **56** (10) (1990) 895-897
9. H. Gundel, H. Riege, E.J.N. Wilson, J. Handerek, K. Zioutas, Ferroelectrics **100** (1989) 1-16
10. H.Gundel, J. Handerek, H. Riege, E.J.N. Wilson, Ferroelectrics **110** (1990) 183
11. J. Handerek, Proc. Bendor Workshop on *Short Pulse High Current Cathodes*, Bendor 1990, p. 73, Edition Frontières 1990, ISBN 2-86332-092-0
12. H. Gundel, Proc. Bendor Workshop on *Short Pulse High Current Cathodes*, Bendor 1990, p. 305, Edition Frontières 1990, ISBN 2-86332-092-0
13. H. Gundel, J. Handerek, H. Riege, J. Appl. Phys. **69** (1991) 975-982
14. M.E. Lines, A.M. Glass, Principles and Applications of Ferroelectrics and Related Materials, Clarendon Press, Oxford 1977
15. G.H. Haertling, Ferrroelectrics **75** (1987) 25-55
16. P. C. Lysne, J. Appl. Phys. **49** (1978) 4296
17. J. J. Dick, J. E. Vorthman, J. Appl. Phys. **49** (1978) 2494
18. J. A. Mazzie, J. Appl. Phys. **48** (1977) 1368

19. W. Mock, Jr., W. H. Holt, J. Appl. Phys. 50 (1979) 2740
20. C. G. F. Stenger, A. J. Burggraaf, J. Phys. Chem. Solids 41 (1980) 17 and 25
21. K. Wojcik, J. Blaszcak, J. Handerek, Ferroelectrics 70 (1986) 1
22. Z. W. Yin, X. T. Chen, X. Y. Song, J. W. Feng, Ferroelectrics 87 (1988) 85
23. A. Sternberg, Ferroelectrics 91 (1989) 53
24. S. Miga, K. Wojcik, Ferroelectrics (1989)
25. Z. Ujma, J. Handerek, Phase Transitions 3 (1983) 121
26. J. Handerek, J. Kwapulinski, M. Pawelczyk, Z. Ujma, Phase Transitions 5 (1985)81
27. J. Handerek, J. Kwapulinski, Z. Ujma, K. Roleder, Ferroelectrics 81 (1988) 253
28. Z. Ujma, J. Handerek, Phys. Status Solidi A 28 (1975) 489
29. J. Handerek, K. Roleder, Ferroelectrics 76 (1987) 159
30. Paper in preparation
31. H.Gundel, H. Riege, J. Handerek, K.Zioutas, Appl. Phys. Lett. 54(21) (1989) 2071-2073
32. H.Gundel, H. Riege, Appl. Phys. Lett. 56(16) (1990) 1532-1534
33. H. Gundel, J. Handerek, H. Kuhn, H. Riege, E.J.N. Wilson, Proc. *2nd European Particle Accelerator Conference*, Nice 1990, p. 712, Edition Frontières 1990, ISBN 2-86332-090-4

AD-P006 681

FERROELECTRIC $Pb(Zr,Ti)O_3$ THIN FILMS PREPARED BY GAS JET DEPOSITION

C.L. HWANG, B.A. CHEN*, T.P. MA
Center for Microelectronic Materials and Structures
Yale University, New Haven, CT 06520
*Current address : IBM, Essex Junction, VT 05452

J.W. GOLZ, Y.D. DI, B.L. HALPERN, and J.J. SCHMITT
Schmitt Technology Associates, New Haven, CT 06511

Abstract Lead-zirconate-titanate thin films were successfully codeposited in a modest vacuum environment using a novel Gas Jet Deposition (GJD) process. The GJD process utilizes supersonic carrier gas jets to efficiently transfer the depositing species to substrates. High throughput, large coating area, and easy control of film stoichiometry make the GJD unique among various deposition techniques. GJD deposited PZT films exhibit excellent ferroelectric properties. Unlike other films reported in the literature, only one preferred orientation ([110]) was found in our films grown on Pt electrode. Fatigue tests show that the films are quite stable under ac voltage stress.

INTRODUCTION

Recently, the possibility of applying ferroelectric materials to new generations of integrated circuits has aroused interest in lead-zicornate-titanate (PZT) films[1-3]. The current methods employed to deposit these films include sputtering, sol-gel, and laser ablation. In this paper, we report our recent results on PZT films fabricated by a novel gas jet deposition[4-6] technique. High deposition rates and large coating areas can be achieved. Some attractive properties, such as one preferred orientation of the polycrystalline PZT films and their high endurance have been found. All of these indicate that GJD could be a viable candidate for future development of PZT films for a variety of applications.

92-16156

GAS JET DEPOSITION (GJD) TECHNIQUE

In a GJD system, depositing species are convected from the sources to the substrates by supersonic jets. The jets are formed by running gases such as helium, oxygen, or argon through a nozzle into a lower pressure environment to achieve supersonic veloc-

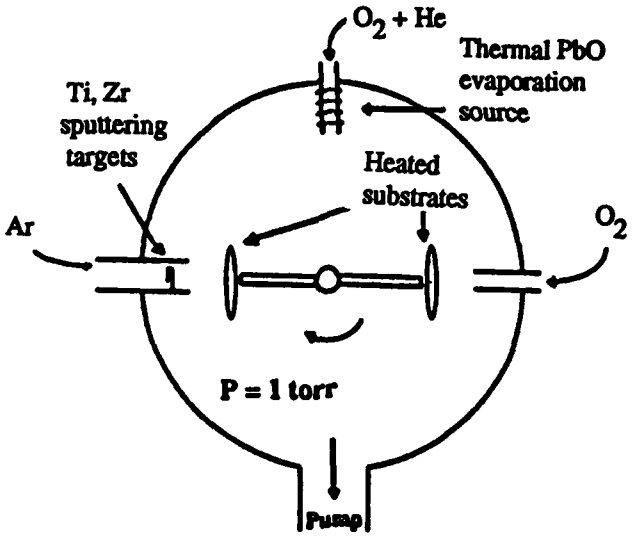


Fig. 1 Schematic diagram of Gas Jet Deposition for PZT

ity[6] above 1 km/sec. The jets are directed toward the substrates during deposition. A variety of sources derived from thermal evaporation, sputtering, gases, and chemical vapors can be incorporated in the nozzles for codeposition.

Figure 1 shows a schematic representation of the GJD system for depositing PZT films. The chamber pressure is maintained at 1 torr during deposition by a high volume mechanical pump. The pump down time is only several seconds, which is much faster than that required for a typical sputtering system. Substrates are mounted on a carousel which is spun at 2 to 3 rps, and moved up and down to enhance uniformity. Under full load condition, the total coating area can be as large as 500 cm^2.

Three jets are used to deposit PZT films : (1) He and O_2 are used to convect thermally evaporated PbO into the chamber; (2) the Zr and Ti sources come from DC sputtering of pure metal targets; (3) a third jet of pure oxygen is used to enhance the oxidation of PZT films during deposition. The deposition parameters are discussed next.

The PbO flux is controlled by its source temperature which is set between 700 ^oC to 830 ^oC. Figure 2 shows that the PbO deposition rate is an exponential function of the source temperature. Figure 3 shows the time dependence of the PbO deposition rate at 704 ^oC. It is apparent that the rate reaches a stable state after running for 5 minutes, which is the usual pre-fire time before deposition.

The deposition rates of Zr and Ti are controlled by the dc sputtering power. For a given dc voltage (set at 500-550 V), the sputtering power is proportional to the cur-

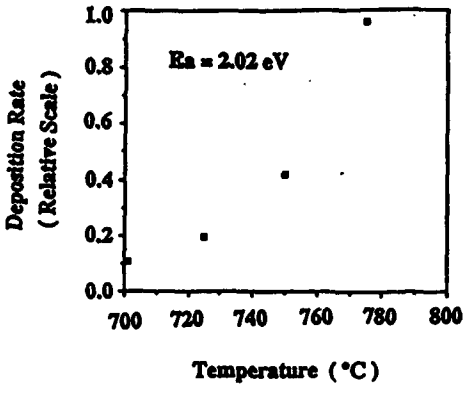


Fig 2. Deposition rate of PbO as a function of source temperature

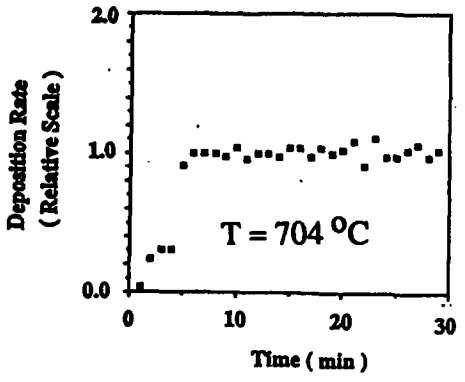


Fig. 3 Deposition rate of PbO as a function of time at a fixed temperature

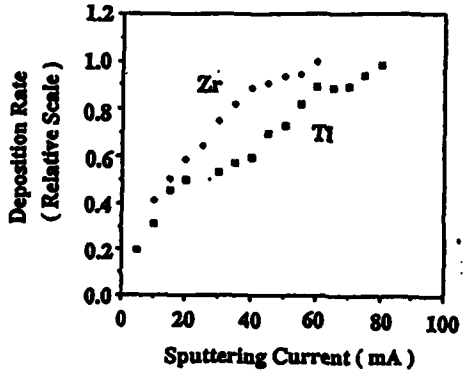


Fig 4. Deposition rate of Zr, Ti as a function of sputtering current

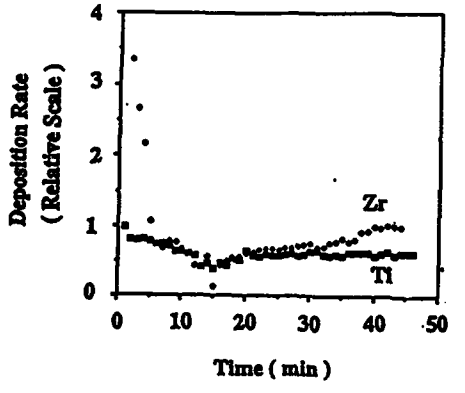


Fig. 5 Deposition rate of Zr, Ti as a function of time at a fixed temperature

rent. In our set-up Ar acts as the sputtering gas and He is used as a carrier gas. Figure 4 shows the relationship between the Zr, Ti deposition rates and sputtering current. Figure 5 indicates that both the Zr and Ti sources are stable after running for 5 minutes. A small rise in deposition rate after running for 30 minutes is observed in both Zr and Ti sources. This may be attributed to the temperature rise of the metal targets. This is not a problem for films less than 200 nm thick. For thicker films, additional cooling can be incorporated to solve the problem.

The composition of the deposited PZT film is controlled by adjusting the relative deposition rates between the PbO, Ti, and Zr sources. In principle, through proper control of these parameters, a variety of film compositions may be achieved.

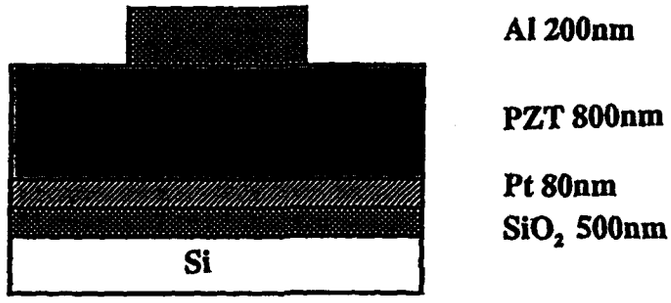


Fig. 6 PZT test capacitor structure

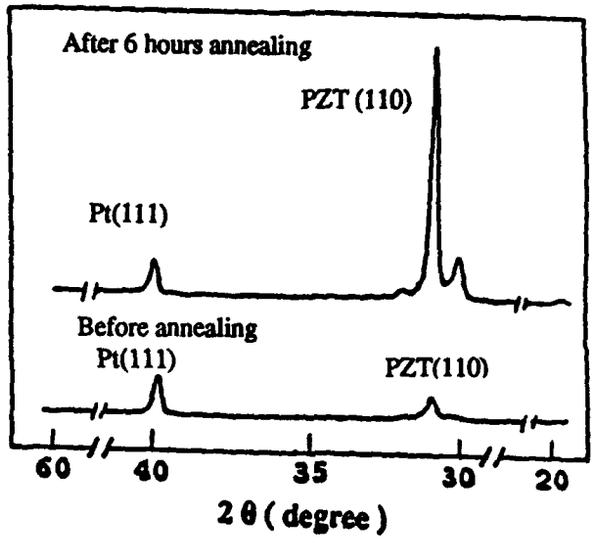


Fig. 7 X-ray diffraction patterns of PZT films

SAMPLE PREPARATION

Figure 6 shows the structure of the test PZT capacitors used in this study. A thermally grown SiO_2 layer acts as a buffer layer between the Si substrate and the Pt electrode. The Pt layer of 100 nm is sputtered onto the SiO_2 and then annealed at 400 ^{o}C to improve its crystallinity and adhesion. Since Pt tends to peel off from SiO_2, in some cases a thin (5 - 10 nm) layer of Cr or Ti is thermally evaporated on SiO_2 to improve the adhesion of Pt. The PZT film is then deposited by the GJD technique described above, with a substrate temperature ranging from room temperature to 650 ^{o}C. Post-deposition annealing is done at 400 ^{o}C to 600 ^{o}C in air for 2 to 7 hours. Al electrodes are thermally evaporated on PZT films to form the test capacitors.

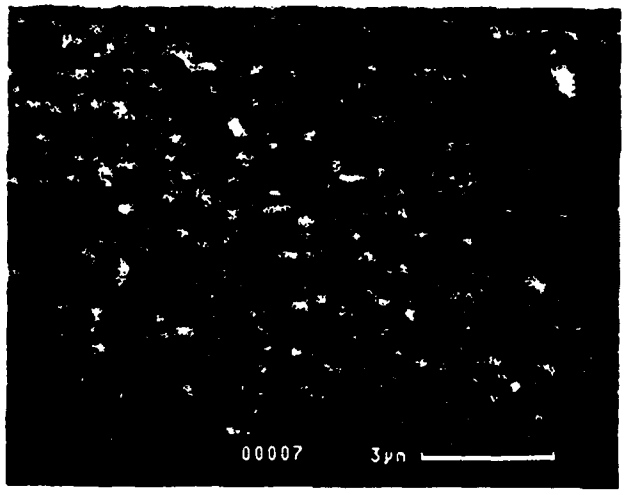


Fig. 8 SEM picture of the surface of a PZT film

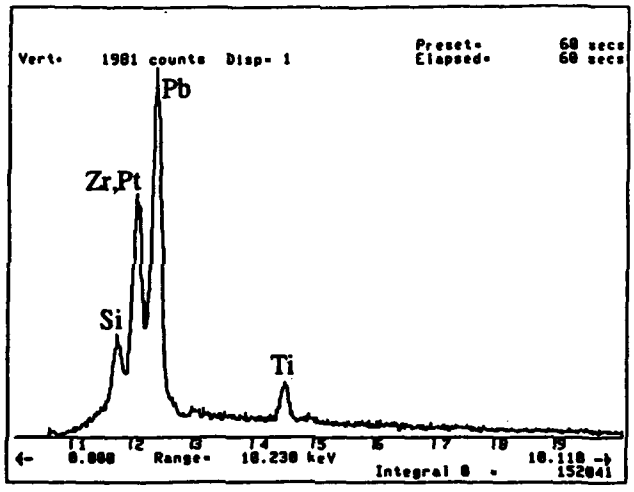


Fig. 9 EDS spectrum of a PZT film

FILM STRUCTURE

The crystalline structure of the GJD deposited PZT films are examined by x-ray diffraction (XRD). The crystallinity of the PZT films depends on the substrate temperatures during deposition and annealing as usually reported[7]. Films deposited below 400 ^{o}C are amorphous. The typical X-ray diffraction pattern of a stoichiometric PZT film deposited at 600 ^{o}C before and after annealing are shown in Fig. 7. The most striking feature is that only one preferred orientation for perovskite PZT, (110), was found either before or after annealing. The small peak at 30.2 degree in the annealed sample can be attributed to excessive lead oxide. No pyrochlore structure was found before or after annealing. We believe that the preferred orientation arises from the special way

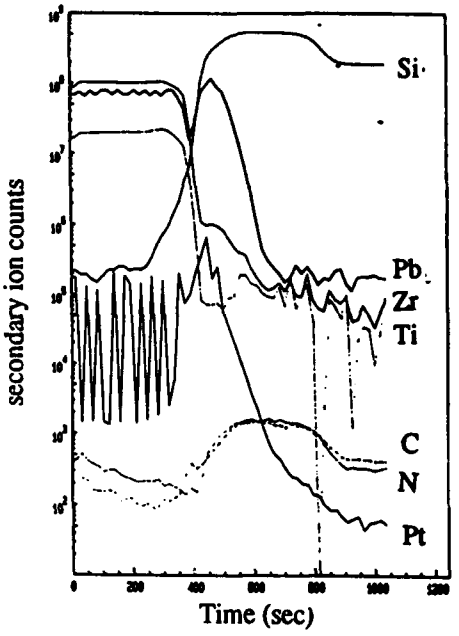


Fig. 10 SIMS data

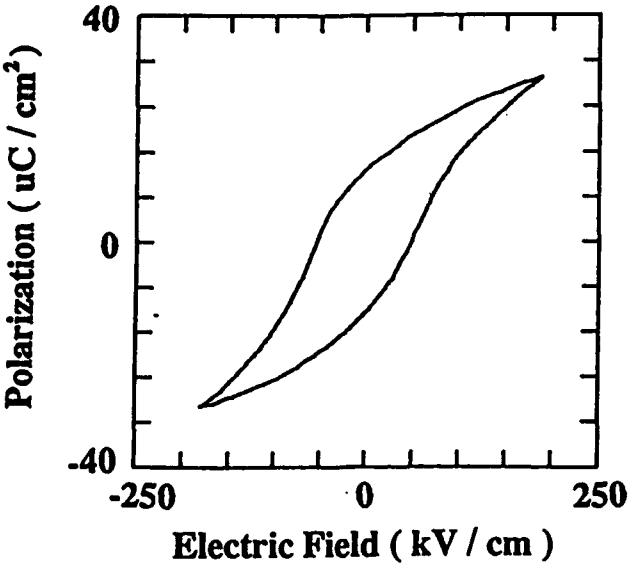


Fig. 11 P-E. hysteresis loop of PZT film

that the film is deposited in the GJD system; in particular the high speeds of the vapors arriving at the substrate may play an important role.

The average grain size as estimated from the x-ray diffraction peak width is around 150 nm. Figure 8 shows an SEM picture of the surface topography after annealing. No microcracks have ever been observed in any of GJD deposited PZT films before or after annealing.

COMPOSITION

The compositions of the PZT films were examined with a JEOL JXA-8600 electron microprobe using energy dispersive spectrometer (EDS) and wavelength dispersive spectrometer (WDS). The EDS data in Fig. 9 show the presence of only Pb, Zr, Ti, and Si. The energies of the Zr Lα line and Pt Mα line are nearly the same, and are inseparable with the resolution of the system. We then employed WDS, which possesses higher resolution, to get a quantitative ratio between Pb, Zr, and Ti. As expected the composition varies with process parameters. Stoichiometric films with Ti/Zr ratio between 0.55/0.45 to 0.45/0.55 were achieved. A detailed study of the relationship between the process parameters and the film composition remains to be carried out.

Additional analysis was done by SIMS. Figure 10 shows the SIMS data for a

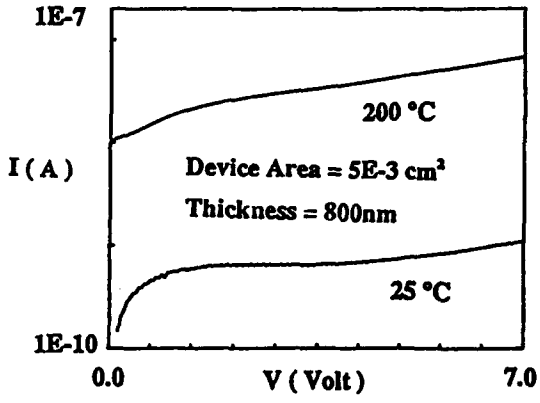


Fig. 12 Leakage current at 25 and 200 °C

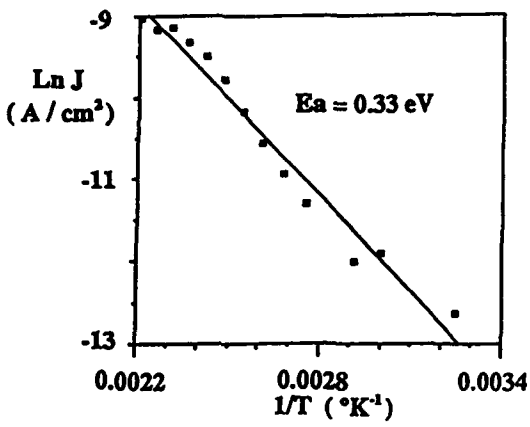


Fig. 13 Temperature dependency of leakage current

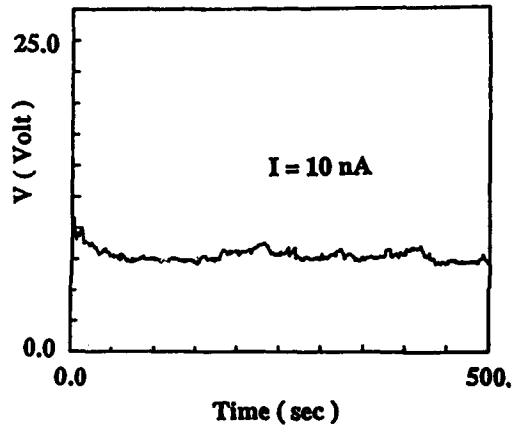


Fig. 14 Constant current stress

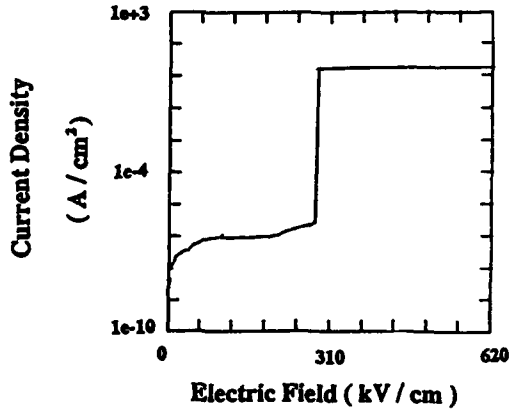


Fig. 15 Hard breakdown of PZT films

stoichiometric PZT film. It is evident that the composition is constant along the depth of the film. The levels of carbon and nitrogen contamination are very low, despite the fact that the film was deposited in a modest vacuum environment evacuated by a mechanical pump.

ELECTRICAL PROPERTIES

Figure 11 shows a typical P-E hysteresis loop using a Sawyer-Tower circuit with a 1.0 kHz triangular wave. The remnant polarizations of GJD PZT films range from 6 uC/cm^2 to 13 uC/cm^2, depending on the thickness of the film. The typical coercive field is around 140 kV/cm. The dielectric constants of the films range from 370 to 1300 among various samples.

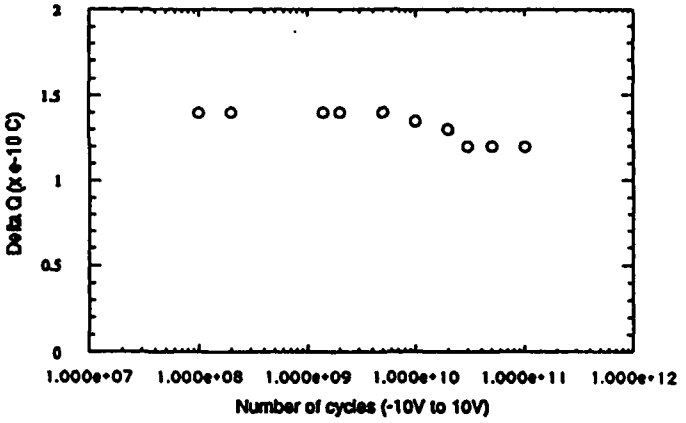


Fig. 16 Fatigue Stress

The I-V characteristics are shown in Fig. 12-15. Figure 12 shows the leakage current both at room temperature and 200 ^{o}C. The temperature sensitivity of the leakage current, which is an important consideration for device application, is further studied and shown in Fig. 13. The activation energy is found to be 0.33 eV. Constant current stress experiment was employed to study electron trapping properties. The data in Fig. 14 suggest that electron trapping is not severe in GJD PZT films. As shown in Fig. 15, hard breakdown rather than soft breakdown has been typically observed. In general, smaller devices exhibit higher breakdown fields, suggesting the breakdown event occurs at weak spots which are randomly distributed.

Fatigue stress was done with a 1 MHz sine wave of 10 V amplitude. The results are shown in Fig. 16 for a device of 20 um × 40 um in size. Although slight reduction in the remnant polarization was observed after 10^{10} cycles, it levels off and remains approximately the same up to 10^{11} cycles. Data for longer fatigue test are not yet available at the time of writing. The results indicate that GJD deposited PZT films are more stable than most PZT films made by other deposition techniques. We suspect that improved endurance may be linked to the fact that the GJD film has only one preferred orientation Further work is needed to clarify the underlying mechanism.

CONCLUSION

Gas jet deposition of ferroelectric PZT thin films has been successfully demostrated. Large coating areas and high deposition rates can be achieved by the GJD technique. Preliminary measurements show good ferroelectric properties. Two unusual features are especially worth noting : (1) the GJD PZT films exhibit only one preferred orienta-

tion, (110), and, (2) no serious degradation is observed under ac voltage stress up to 10^{11} cycles. Both features may be intimately related, and they both arise from the special way that the films are deposited. The underlying mechanisms and the relationship between these properties remain to be studied.

ACKNOWLEDGEMENT

This work was supported by grants from the Semiconductor Research Corporation, Office of Naval Research Contract No. N00014-80-C-0002, and DARPA Contract No. DAAH01-90-C-0653. The author wants to thank Dr. T. Tamagawa at U. of Minnesota and Mr. C. Beggy of Yale U. for their assistance in many parts of the work. The fatigue test was performed by Dr. Tamagawa. Also thanks to Dr. Brian Doyle of Digital Equipment Co. for the SIMS data.

REFERENCE

1. D. Bondurant and F. Gnadinger, IEEE Spectrum, 26, 30, July (1989)

2. J.F. Scott and C.A. Paz de Araujo, Science, 246, 1400 (1989)

3. L.H. Parker and Al F. Tasch , IEEE Circuits and Device Magazine, 6, 17, Jan. (1990)

4. Jerome J. Schmitt, U.S. Patent No. 4788082 (1988)

5. R. Iscoff, Semiconductor International, 14, 50, (1991)

6. J.B.Fenn, Applied Atomic Collision Vol. 5, (Academic Press, 1987), p. 349

7. A. Okada, J. of Appl. Phys., 48, 2905 (1977)

PROCESS TECHNOLOGY DEVELOPMENTS FOR GaAs FERROELECTRIC NONVOLATILE MEMORY

L. E. Sanchez, I. K. Naik, S. H. Watanabe, I. S. Leybovich, J. H. Madok and S. Y. Wu
McDonnell Douglas Electronic Systems Company
5301 Bolsa Avenue, Huntington Beach, CA 92647

AD-P006 682

Abstract. Fabrication of nonvolatile memories utilizing ferroelectric polarization charge of lead zirconate-titanate (PZT) thin film capacitors requires the integration of the PZT capacitor process with the semiconductor device processes. This paper discusses the development of enabling process technology for integration of PZT capacitors with GaAs junction field-effect transistors (JFET) on a GaAs wafer for the fabrication of a GaAs ferroelectric random access memory (FERRAM). Individual processes for PZT capacitors and GaAs JFETs are described briefly first. The PZT capacitor process utilizes sol-gel deposition of PZT thin films, while the GaAs JFET process is based on selective ion implantations of silicon and magnesium directly into the GaAs wafer. The integration of these two chemically different processes has been accomplished through process innovations in the areas of sintering of PZT film, ion implantation in GaAs, interconnect metallization and patterning of this metallization. Successful operation of the nonvolatile memory cell has been demonstrated in a memory test circuit fabricated using this integrated process technology.

1. INTRODUCTION

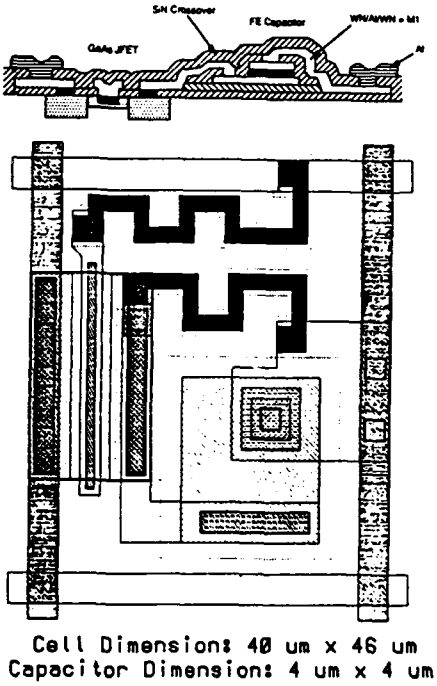
Development activities for nonvolatile memories based on the ferroelectric polarization charge of lead zirconate-titanate (PZT) thin films have seen a resurgence in recent years.[1,2] Generally, this type of memory integrates a semiconductor switch with a ferroelectric capacitor that can retain a charged state even in the absence of an applied voltage. McDonnell Douglas Electronic Systems Company (MDESC) has been developing a nonvolatile memory that integrates GaAs junction field-effect transistor (JFET) switches with ferroelectric thin-film capacitors on a GaAs wafer. The JFET used is an enhancement-mode, n-channel transistor and the capacitor has a PZT thin film as the ferroelectric material. In addition to the nonvolatility, the combination of the GaAs JFET with the PZT capacitor would offer a high-speed performance, extreme radiation hardness and low-power circuit operation. In this paper, we discuss the process technology developments for the fabrication of a 4K bit GaAs ferroelectric random access memory (FERRAM). The 4K bit FERRAM is a vehicle for developing and demonstrating the feasibility of this new technology. Our objective is to demonstrate that we have developed the required enabling process technology and that a fully-functional 4K bit GaAs FERRAM is imminent.

2. MEMORY CELL AND CIRCUIT

A single memory cell of this experimental 4Kbit FERRAM consists of one GaAs n-channel JFET pass-transistor and one PZT capacitor as shown in Fig. 1. Capacitors with four different areas (4x4, 5x5, 7.5x5 and 9x5 μm^2) have been incorporated in the 4K bit memory design to study the effect of the amount of the polarization charge on the memory performance. At the device level, the GaAs JFET technology requires that the coercive voltage of the capacitor be less than 1 V and the saturation

92-16157

voltage be 3 V or less. At the circuit level, two circuit designs are being evaluated for the 4K bit memory. The design one which is configured as 512 x 8 bits uses a cross-coupled sense amplifier. The second design uses a differential sense amplifier which is incorporated in a test module of the reticle. These device and memory circuit designs serve as the initial vehicle for developing FERRAM fabrication processes which are described in this paper.



(a)

(b)

Fig. 1. (a) Cross-section and (b) layout of a single memory cell of the experimental FERRAM.

3. INDIVIDUAL DEVICE PROCESSES

3.1 Process for PZT Capacitor Fabrication

We have adapted and modified the sol-gel process for depositing semiconductor device-quality PZT thin films (500 to 2000Å thickness) as reported recently.[3,4] The ferroelectric capacitors made with these films have demonstrated the required characteristics for nonvolatile memories.[3] This sol-gel process uses a metallorganic liquid formulation that is spin-coated on a semiconductor wafer in a manner similar to the photoresist. For capacitor fabrication, the spin-coating is applied on a wafer that already contains the bottom electrode made of Pt (2000Å)/Ti(200Å) films. The dried metallorganic coating is then heat-treated in an oxygen-containing gas atmosphere at 650 to 700°C to crystallize and densify the PZT film. The details of this process have been discussed in reference 3.

In the next step, top electrode metallization, Au (2000Å) or Au (500Å)/Pt(1500Å), is deposited over the entire wafer by the electron beam evaporation technique. Then individual capacitors ranging in size from 40 μm x 40 μm to 4 μm x 4 μm are defined by means of standard photolithography and ion beam milling techniques. The ion beam milling is done through both the top electrode and the PZT film in the field areas down to the bottom electrode. Subsequently, another photoresist mask defines the bottom electrode which is then ion milled in the same manner to complete the capacitor fabrication.

We have found that alloying of the top electrode metal to the PZT film by means of a heat treatment at 600 to 700°C improves the capacitor ferroelectric characteristics very significantly. This alloying treatment makes the hysteresis loop more symmetrical, reduces the coercive voltage[3] and improves the fatigue characteristic.[5] It was determined that, during the alloying treatment, a small amount of liquid phase is formed through a reaction between Au metallization and the excess PbO in the PZT film. This reaction appears to facilitate the formation of an intimate electrode contact with the PZT film. It also appears to reduce the effective thickness of the PZT dielectric of the capacitor through diffusion of Au into PZT which results in lower coercive voltage and saturation voltage of the capacitor. Thus, this simple alloying treatment makes the poling of the capacitor easier by the peripheral switching circuit.

Typical properties of our PZT capacitors are as follows: coercive voltage of 0.6 to 0.8 V, saturation voltage of about 3 V and remanent polarization (P_r) of 15 to 20 $\mu C/cm^2$ for capacitor area range of 4x4 μm^2 to 40x40 μm^2 (Fig. 2). The PZT film corresponding to these properties has a Zr/Ti atomic ratio of 50/50, ~3 mole percent excess PbO, and thickness of 1000 to 2000Å.

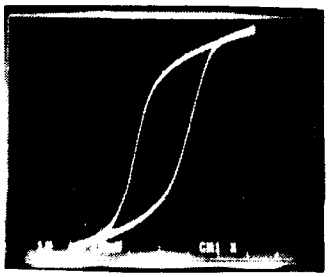


Fig. 2. A typical hysteresis loop of the sol-gel derived 10 μm x 10 μm PZT film capacitor Pt/Au/PZT (1000Å)/Pt-Ti. [X axis: voltage (one large div. = 1 V); Y axis: polarization (One large div. = 8 $\mu C/cm^2$)]

3.2 GaAs JFET Pilot Line Process

During the 1980s, MDESC developed a VLSI-capable GaAs JFET process for low-power, radiation-hard, high-speed digital ICs. This process has been used as the baseline or starting process for the development of GaAs FERRAM. The main features of the n-channel JFET process, as described in Ref. 6, are as follows: (a) selective Si+ ion implantation directly into GaAs wafer to form n-channel, source and drain (b) selective Mg+ implantation followed by zinc diffusion to form p+ gate (c) furnace annealing to activate the implants (d) standard Ni/Ge/Au metal contacts for source and drain (e) Ti/Pt/Au first-level interconnect that is patterned by means of ion beam milling (f) sputter-deposited silicon nitride (SiN) as the inter-level dielectric (g) Ti/Pt/Au second-level interconnect patterned by ion beam milling. As an example, this baseline process uses 11 mask layers for fabrication of a 4K bit GaAs static RAM that does not contain nonvolatile PZT capacitor elements.

In the following section, we discuss the developments that were necessary to integrate the PZT capacitor with GaAs JFET for the fabrication of GaAs FERRAM. Significant modifications to the baseline GaAs JFET process had to be made to achieve compatibility between the two processes.

4. PROCESS INTEGRATION

The first conceptual integration of the PZT process and the GaAs JFET pilot line process to fabricate a GaAs FERRAM is depicted in the general process sequence in Fig. 3. This process integration, however, turned out to be more difficult than anticipated. Several processing-related problems arose as the integration experiments were carried out. These problems and their solutions are discussed in this section.

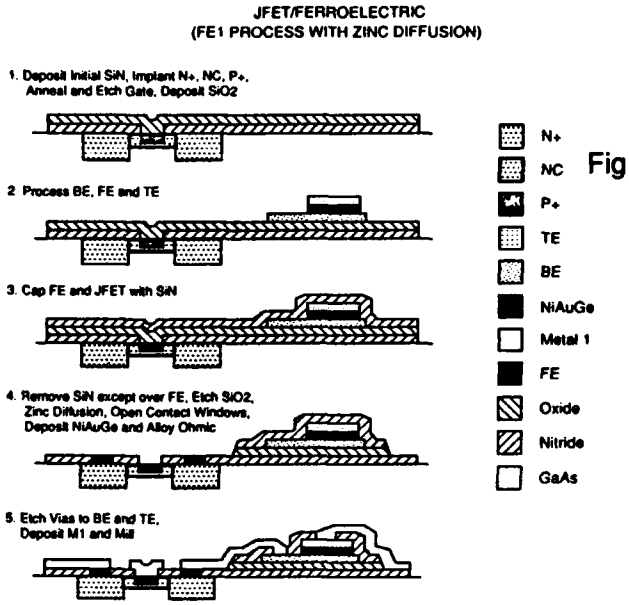


Fig. 3. General process sequence for integration of the PZT process and the GaAs JFET process using zinc diffusion approach.

4.1 Arsenic Contamination of PZT

High-quality PZT capacitors, in terms of high remanent polarization, low coercive voltage, symmetrical hysteresis loop, and low leakage current, are obtained when the PZT film has stoichiometric composition, in particular no oxygen deficiency or excess. For this reason, the PZT film has to be sintered in a high oxygen partial pressure atmosphere (≥0.2 atm) at elevated temperatures (550 to 700°C for a sol-gel film). However, GaAs is unstable in oxygen-containing atmosphere at such temperatures. In our initial experiments, it was found that arsenic-containing gaseous species evolved from the open GaAs areas when a PZT film was sintered on GaAs in an O_2/N_2 mixture. Surface chemical analyses by Auger electron spectroscopy of PZT films sintered on GaAs wafers with exposed backside revealed presence of arsenic in the PZT films. Such arsenic-contaminated PZT films yielded degraded hysteresis loop as shown in Fig. 4. This loop has lower P_r than normal (6 $\mu C/cm^2$ vs. 15 $\mu C/cm^2$) and it does not attain saturation. Further experiments showed that even a small exposed rim area of GaAs at the wafer edge could contaminate PZT in the proximity of this rim area. These observations taught us that the GaAs wafer has to be sealed completely (both faces as well as the edges) to avoid As-contamination of the PZT film during sintering. This wafer sealing is done by depositing a 1000Å thick silicon nitride (SiN) film on both faces and the edges of the GaAs wafer by means of reactive ion beam sputtering. The SiN film has proven an effective encapsulant of GaAs wafer for sintering PZT films on GaAs.

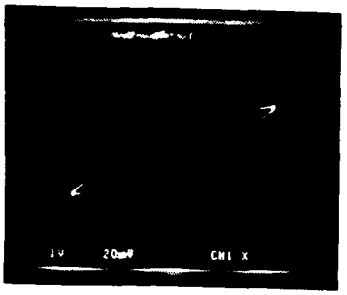


Fig. 4. Degraded hysteresis loop due to arsenic contamination of the PZT film during sintering of the PZT film on GaAs wafer.

4.2 Zinc Diffusion versus Zinc Implantation

In process integration experiments, we investigated the effects of zinc diffusion step, which is used in the baseline process for the formation of p^+ gate of the JFET, on the properties of the PZT capacitors. Individual silicon nitride (SiN) and silicon dioxide (SiO_2) layers were evaluated as the encapsulant to protect the PZT capacitors during the zinc diffusion treatment. A wafer with a blanket 4000Å thick SiN layer over the patterned PZT capacitors was subjected to argon atmosphere at 650°C for 60 sec. Another similar wafer was subjected to argon containing zinc vapor at 650°C for 60 sec, which is a typical zinc diffusion operation: done in an open tube furnace using zinc metal as the source.

The results of the wafer subjected to the argon ambient will be described first. The adhesion of the silicon nitride layer on gold (top electrode) and platinum (bottom electrode) was not completely satisfactory. Interference patterns were observed on both gold and platinum electrodes in some areas (about 50% of the wafer), indicating that lifting of the silicon nitride layer occurred. Cracking and peeling of the layer were also observed in parts of the wafer.

We noticed roughening of the gold electrode after the argon treatment. Some electrodes developed discoloration in small areas, as shown in Fig. 5(a). When the silicon nitride capping layer was removed, we discovered that there was no gold in these small areas as shown in Fig. 5(b). Apparently the silicon nitride layer reacted with gold during the 650°C 60 second heat-treatment and developed holes in the gold electrode. Ferroelectric hysteresis loops were measured on the 40 x 40 μm^2 capacitors on this wafer. A typical hysteresis loop is illustrated in Fig. 6. The

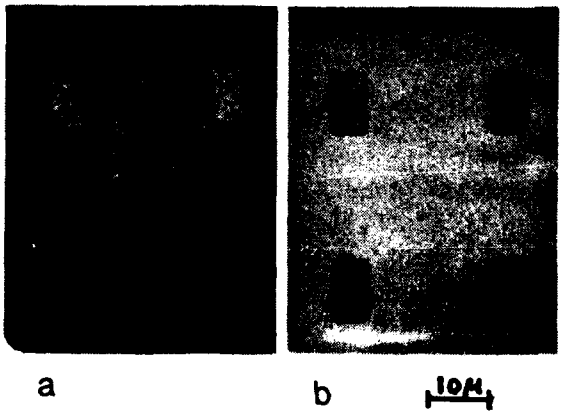


Fig. 5. Microstructures of PZT capacitors after heat treatment in argon at 650°C for 60 sec: (a) Gold top electrode area with silicon nitride capping layer (b) The same after removing the silicon nitride capping layer.

switched polarization and the remanent polarization were both lower than those before the argon heat treatment. The former was 37.5 $\mu C/cm^2$, a drop of 14%, and the latter was 16 $\mu C/cm^2$, a drop of 28%.

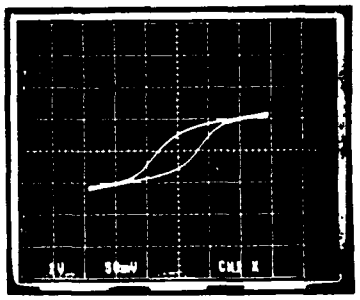


Fig. 6. A typical hysteresis loop of a 40 μm x 40 μm capacitor with gold top electrode and silicon nitride capping layer after heat treatment in argon at 650°C for 60 sec.

The wafer subjected to the zinc-argon atmosphere also developed similar surface structure on the gold electrode, as described in the previous paragraph. On a few capacitors which were not protected well by the silicon nitride capping layer, zinc entered through cracks and reacted both with the gold top electrode and the surrounding platinum electrode. The gold metal was degraded by the zinc vapor as shown in Fig. 7. Electrical testing showed that this capacitor had shorted out during the zinc-argon heat treatment. Fig. 8 shows the hysteresis loop of a capacitor around which silicon nitride had not cracked. As a result of the zinc-argon treatment, the hysteresis loop became slim, and the remanent polarization decreased to 4 $\mu C/cm^2$, which was a decrease of about 82% from the initial value.

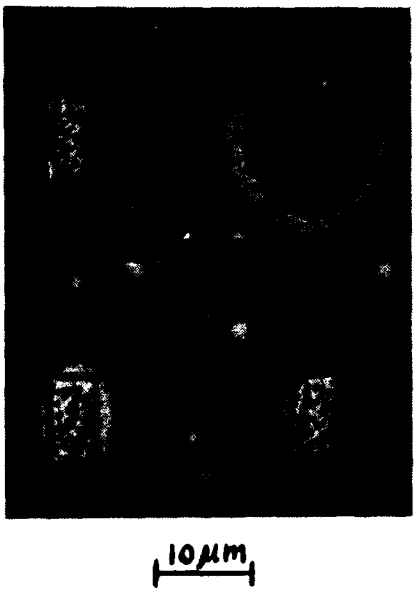


Fig. 7. Microstructure of gold electrodes of silicon nitride-capped PZT capacitors after heat treatment in zinc-argon atmosphere at 650°C for 60 sec. The capacitor at upper right was not protected well by the capping layer.

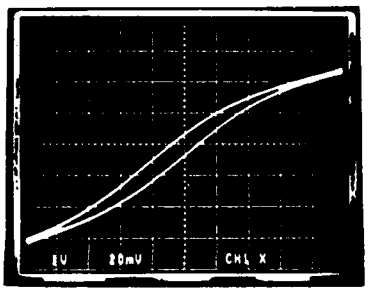


Fig. 8. Hysteresis loop of a gold-electroded capacitor with silicon nitride capping layer after heat treatment in zinc-argon atmosphere at 650°C for 60 sec.

Wafers coated with a 4000Å of sputtered SiO_2 were also subjected to the zinc-argon treatment at 650°C for 60 seconds. The adhesion of the SiO_2 on the gold and platinum electrodes seemed to be worse than that of silicon nitride. High stresses in the SiO_2 layer were believed to cause it to wrinkle and crack. During the zinc-argon heat treatment, zinc also penetrated through the cracks and reacted with the gold top electrode, as in the case with the silicon nitride layer. A similar roughening and discoloration was also observed on the gold electrodes well-covered with the SiO_2 layer. A chemical reaction might have occurred between the SiO_2 and the gold electrode.

The above results led to the conclusion that the zinc diffusion technique is not robust enough to be reliably and reproducibly used when PZT capacitors are present on the GaAs wafer. As an alternate approach, we considered zinc ion implantation in GaAs followed by a rapid thermal annealing (RTA). This approach has been shown to be a viable process for forming very thin (~1000Å) p^+ layers in GaAs without significant broadening of the zinc profile[7]. Zinc ion implantation followed by RTA in forming gas eliminates the need for exposure of the GaAs wafer with PZT capacitors to zinc vapor atmosphere which seems to be the most detrimental part of the zinc diffusion step toward PZT capacitors. Furthermore, the steps of zinc implantation and RTA can be carried out before PZT capacitor fabrication thus avoiding any problems of capacitor degradation. From the point of view of process reliability and robustness, the zinc implantation is more controllable and more compatible with other processing steps. Based on these considerations, we decided to implement zinc ion implantation and RTA for the fabrication of GaAs FERRAM. A FERRAM process sequence that uses zinc ion implantation and RTA is shown in Fig. 9. This process sequence has yielded integrated structures of enhancement-mode JFETs and PZT capacitors whose test results are discussed in section 5.

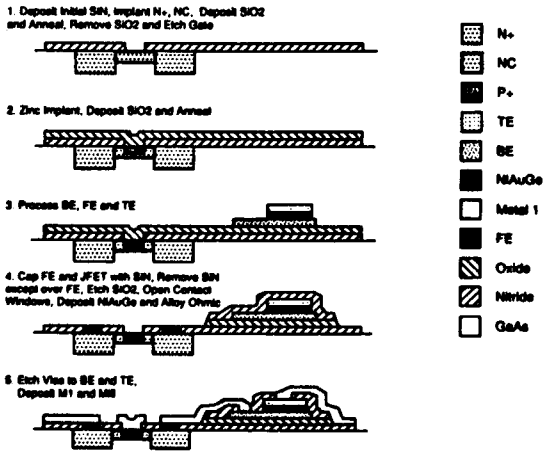


Fig. 9. General process sequence for FERRAM fabrication using zinc ion implantation and rapid thermal annealing.

4.3 New Metallization

First-level interconnect Ti/Pt/Au used in the baseline JFET process also gave problems in the integrated FERRAM processing. This noble metal interconnect was not chemically etchable and its patterning in the baseline process was done by ion beam milling. The ion beam milling worked well when the wafer topography was planar. But when it was used to pattern the Ti/Pt/Au interconnect on the GaAs wafers containing PZT capacitors, the bottom and top electrodes of the capacitors remained shorted after the patterning was completed. Even after a considerable overmilling time, these capacitor shorts could not be eliminated. Scanning electron microscopy (SEM) of the ion-milled structures showed evidence of a remanent metal film along the edges of the encapsulating SiN (Fig. 10). It appeared that ion milling was not able to completely remove the metallic layer along the edges of the SiN capping over the capacitors. Further analysis by means of an electron potential probe in conjunction with SEM conclusively proved the presence of this shorting path. These shorts occurred in spite of the precautions taken to obtain uniform ion milling through rotation of the wafer and use of an oblique (45°) angle of ion beam incidence on the wafer. From these results, it was concluded that the nonplanar topography of the FERRAM wafer at this stage prevented a successful use of ion beam milling for patterning the first-level interconnect.



Fig. 10. Back-scattered-electron-mode scanning electron micrograph of a typical shorted capacitor after ion beam milling of the first-level interconnect Ti/Pt/Au.

To solve the above problem, we decided to use an interconnect metallization that can be readily dry-etched by means of the current state-of-the-art technique of reactive ion etching (RIE). Based on our experience, we selected refractory metal tungsten(W)-base interconnect for this purpose. The metallization consisted of a two-layer sandwich: W-N (250Å)/W (2500Å). The W-N layer which was a W-nitrogen solid solution with ~30 atom percent nitrogen, provided a good ohmic contact to the p+ GaAs gate while the thicker W layer reduced the resistivity of the interconnect. This sandwich metallization was deposited as a blanket layer in a single pump-down in a magnetron sputter deposition system using a W target. The patterning was then carried out using SF_6 gas in an RIE system. This interconnect scheme has been successfully used on the GaAs FERRAM wafer. A photomicrograph of the memory cells with integrated GaAs JFETs and PZT capacitors after the first-level interconnect is shown in Fig. 11.

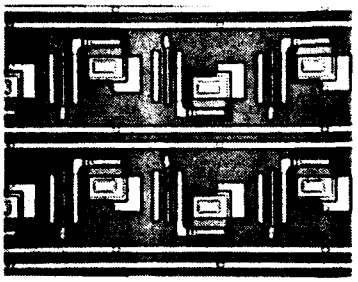


Fig. 11 A photomicrograph of the memory cells with integrated GaAs JFETs and PZT capacitors after the first-level interconnect.

To complete the wafer-level IC fabrication, the following steps are then carried out: an inter-level dielectric of 5000Å SiN or 7000Å polyimide is deposited vias are etched in the inter-level dielectric by means of RIE, second-level interconnect metal of aluminum is deposited by a sputter deposition and patterned by means of RIE. Electrical test results of the integrated devices fabricated by this process are presented in the following section.

5. ELECTRICAL TEST RESULTS

Typical hysteresis loop of the PZT capacitor (40 μm x40 μm) and current-voltage (I-V) characteristics of the GaAs JFET both fabricated on the same GaAs wafer are shown in Fig. 12. These tests were made at the first-level interconnect stage of the processing sequence. The hysteresis loop is almost identical to that obtained on individually-processed capacitors on a wafer that has not gone through the JFET process part. Also, the JFET characteristics are comparable to those of the individually-processed GaAs JFETs. This result demonstrates that the major problems of process integration for combining PZT capacitor with GaAs JFET have been resolved.

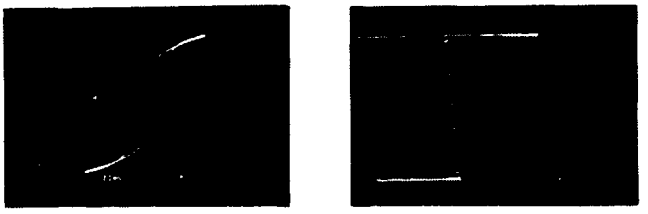


Fig. 12. (a) Typical hysteresis loop of a 40 μm x 40 μm PZT capacitor and (b) I-V characteristics of GaAs JFET (1 μm gate length x 20 μm width) both on the same GaAs wafer after completion of the first-level interconnect.

Successful operation of a nonvolatile memory cell has been demonstrated in a test circuit which is a 6-cell memory circuit shown in Fig. 13. This test circuit contains the same size PZT capacitors and GaAs JFETs as the 4k FERRAM, namely 4 μm x 4 μm and 7.5 μm x 5 μm capacitors and 1 μm gate-length x 20 μm width JFETs. The electrical test for this demonstration was carried out in the following manner. WRITE operations for the binary states 0 and 1 were performed on the memory cells using a supply voltage of 5 V. Then the power to the circuit was turned off for five minutes. Upon turning the power on again, READ operations were done on the previously-written cells. Typical results of such WRITE and READ operations are shown in Fig. 14. It is seen that the cell stored the state that was written before the power-down and maintained it when the power was off. When the cell was read again after the power-down, the same state as that written before the power-down was read back. This result demonstrated functionality of the nonvolatile memory cell.

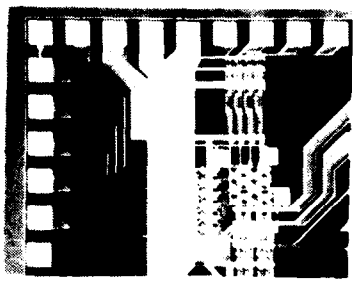


Fig. 13. Photomicrograph of a 6-cell memory test circuit after completion of second-level interconnect.

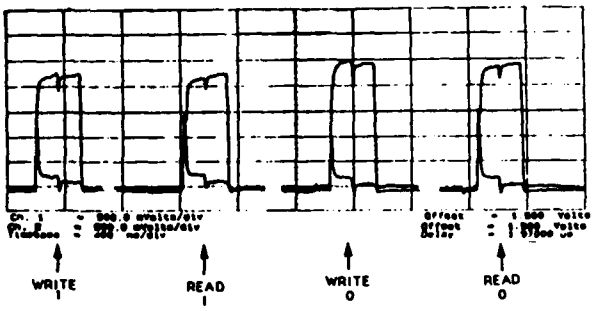


Fig. 14. WRITE and READ pulse responses with power turned off between the WRITE and READ operations demonstrating nonvolatility of the memory cell.

Four kilobit GaAs FERRAM ICs have been fabricated using the processes discussed in this paper. Detailed results of the electrical testing of this GaAs FERRAM will be presented in the near future.

6. CONCLUSION

We have demonstrated important enabling processes necessary for integrating ferroelectric PZT capacitors with GaAs JFETs on the same GaAs wafer for fabrication of a nonvolatile ferroelectric memory. Integrated process sequence developed using these individual processes has been successfully used to fabricate nonvolatile memory cells, test circuits and elements of 4K bit GaAs FERRAM. These integrated PZT capacitor-GaAs JFET structures have shown the functionality necessary for operation of a nonvolatile GaAs ferroelectric memory.

ACKNOWLEDGEMENTS

The authors acknowledge useful technical discussions and managerial support provided by W. A. Geideman, A. J. McDonald and G. L. Troeger and technical support provided by the Microelectronics Center personnel. This work was funded by the Defense Advanced Research Projects Agency.

REFERENCES

1. C. A. Paz de Araujo and G. W. Taylor, Ferroelectrics, 116, 215 (1991). (Proceedings of the Second Symposium on Integrated Ferroelectrics, 1990). Also, Ferroelectrics, 104, 241 (1990).
2. J. F. Scott, C. A. Paz de Araujo and L. D. McMillan, Ferroelectrics, 116, 107 (1991).
3. L. E. Sanchez, D. T. Dion, S. Y. Wu and I. K. Naik, Ferroelectrics, 116, 1 (1991). (Proceedings of the Second Symposium on Integrated Ferroelectrics, 1990.)
4. L. E. Sanchez, S. Y. Wu and I. K. Naik, Appl. Phys. Lett., 56 (24), 2399 (1990).
5. I. K. Naik, L. E. Sanchez, B. P. Maderic and S. Y. Wu, "Improved Switching Endurance of PZT Capacitors for Nonvolatile Memory Applications", Paper presented at the Third International Symposium on Integrated Ferroelectrics, April 1991. (Published in this volume.)
6. R. Zuleeg, J. K. Notthoff and G. L. Troeger, in Gallium Arsenide Technology, Vol. 2, D. K. Ferry, Editor, H. W.Samms and Company, Indiana, U.S.A., p. 95 (1989).
7. I. K. Naik, J. Electrochem. Soc., 134, 1270 (1987).

92-16158

SOLUTION CHEMISTRY EFFECTS IN $Pb(Zr,Ti)O_3$ THIN FILM PROCESSING

R. W. SCHWARTZ, B. C. BUNKER, D. B. DIMOS, R. A. ASSINK, B. A. TUTTLE, D. R. TALLANT, and I. A. WEINSTOCK

Materials and Process Sciences Directorate, Sandia National Laboratories, P.O. Box 5800, Albuquerque, NM 87185 U.S.A.

(Received June 14, 1991)

Ferroelectric thin films in the PZT compositional family were prepared by two different solution deposition methodologies. The approaches were based on the use of carboxylate and alkoxide precursors, and acetic acid. Solution aging and mixing order effects on thin film microstructure and ferroelectric properties were studied. Films prepared from 15 day old solutions had a lower remanent polarization (1.4 $\mu C/cm^2$) and higher coercive field (256 kV/cm) than films prepared from 1 day old solutions (P_r = 18.7 $\mu C/cm^2$; E_c = 55.2 kV/cm). Raman, FTIR, and NMR spectroscopies were employed to confirm the role of acetic acid in the process, and to begin to understand why changes in solution chemistry can so dramatically affect the resulting film microstructure and properties. FTIR spectroscopy indicated that in addition to acting as a solvent, acetic acid also serves as a chemical modifier in the two processes. That is, it reacts with the alkoxide precursors on a molecular level, replacing the alkoxy ligands. Ester formation was also observed by both FTIR and NMR spectroscopy. The formation of this by-product implies the simultaneous formation of water, and therefore, in-situ hydrolysis and condensation of the precursors.

AD-P006 683

INTRODUCTION

Ferroelectric $Pb(Zr,Ti)O_3$ (PZT) thin films have been prepared by a variety of physical and chemical deposition methods. The physical methods that have been used, include: sputtering from oxide[1] or elemental metal targets;[2] molecular beam epitaxy;[3] ion beam deposition;[4] and various laser ablation techniques.[5] Chemical solution deposition methods, including: sol-gel;[6] MOD (metallo-organic decomposition);[7,8] and hybrid approaches;[9] have also been used with success to fabricate PZT thin films. Solution deposition approaches are of interest because of the low capital investment costs, the ability to closely control composition, and the relative ease of process integration with standard Si wafer technology. Further, the films prepared by solution deposition methods have displayed ferroelectric properties comparable to those of bulk ceramics. While the thin films prepared by chemical methods are typically polycrystalline, the ability to prepare highly oriented thin films has been noted.[10,11] Solution deposited thin films have also been reported to possess high electro-optic retardations.[12]

Sol-gel, MOD, and hybrid deposition methods are based on the use of metallo-organic precursors. Three different classes of precursors have been used: (i) metal alkoxides, $M(OR)_x$; (ii) metal carboxylates, $M(OOCR)_x$; and (iii) metal acetylacetonates, $M(C_5H_7O_2)_x$; where R is an alkyl group, and x is the valence of the metal. Sol-gel methods generally use metal alkoxide precursors, and maintain close control over the reaction conditions to form mixed metal alkoxide species, which serve as molecular building blocks for the development of the desired crystalline structure.[13] Hydrolysis conditions are then manipulated to control the nature of the polymeric species in solution, prior to deposition of the thin film. In contrast to sol-gel approaches, MOD methods typically use carboxylate precursors with large organic moieties, such as 2-ethylhexanoate

and neodecanoate ligands.[7] The method is more straightforward than the sol-gel approach, since the precursors are typically water insensitive. However, due to the high organic content of the films, cracking problems are frequently encountered. Recently, Haertling has developed an alternate MOD route which utilizes precursors with smaller organic groups, which may allow for the preparation of thin films which exhibit less tendency toward cracking.[14] Hybrid solution deposition methods generally use low molecular weight carboxylate and alkoxide precursors, namely, acetates and propoxides or butoxides. In these methods, less attention is given to control of the hydrolysis conditions, due to the use of chemical modifiers, which diminish the hydrolysis rates of the alkoxides.

Although there are obvious differences between the three approaches, in general, the following steps are involved: (i) dissolution (and reaction) of the cation precursors in a common solvent; (ii) tailoring of solution characteristics, such as viscosity; (iii) deposition of the films by spin-casting or dip-coating; (iv) low temperature heat treatment for organic pyrolysis and conversion to an inorganic amorphous intermediate; and (v) higher temperature heat treatment for densification and crystallization into the desired phase. We might expect that changes in any of the processing steps outlined above could potentially affect not only the nature of the species obtained in the subsequent step, but the final film microstructure and electrical properties as well. For example, changes in the precursor reactivity or hydrolysis conditions are known to change the nature of the polymeric species in solution.[15] In turn, variations in the nature of the solution polymeric species affect the nature of the wet film, especially residual organic removal and cracking tendency during drying.[16] The resulting changes in the physical and structural properties of the dried amorphous film, i.e., its structural free volume, porosity and surface area, define the free energy of the film, and therefore, its densification and crystallization behavior, and the ceramic microstructure and associated properties which are obtained.[17] Thus, the parameters used in each step of the overall processing route, from solution preparation conditions, to heat treatment temperatures, times and ramp rates,[18] serve to define the ferroelectric properties of the film.

One problem with the use of chemical deposition methods is the lack of a fundamental understanding regarding the effects of solution chemistry variations, and structural evolution behavior, on film dielectric and ferroelectric properties. And from a review of the results reported for films prepared by different solution deposition approaches, we can see there are indeed significant differences in dielectric and ferroelectric properties, crystallization temperatures, and thin film microstructures. We have also noted similar effects of variations in solution chemistry. For films which were subjected to identical heat treatment conditions following deposition, different ceramic microstructures and electrical properties were observed for solutions prepared under different conditions. Since the reasons for these effects are, at the present time, unclear, consistent control of film microstructure and ferroelectric properties is difficult. Preparation of property-optimized films is not possible.

The focus of the present study is to begin to address the underlying reasons for the observed differences noted above, by using a variety of characterization techniques at different process points. Since the final film properties can conceivably be affected by variations at any stage in the preparation process, e.g., from variations in the nature of the solution polymeric species, or differences in the physical and structural characteristics of the amorphous film, we need to consider using characterization techniques which provide structural information on different size scales. Multinuclear NMR can provide information about the local chemical environment of different species, while SAXS (small angle x-ray scattering) can provide information on a larger size scale, describing the size and shape of the polymeric species in solution.[15] The microstructural features of the films may be characterized by SEM and TEM, and the macroscopic physical properties of the amorphous films may be determined by depositing the films onto SAW (surface acoustic wave) devices.[19]

Finally, the effects of solution chemistry variations on crystallization and densification behavior may also be determined. Raman spectroscopy may be used to study metastable and stable crystalline phase development, while ellipsometry can be used to monitor consolidation behavior. The potential use of various characterization techniques at different process points is shown in Table I. Our goal is to use these characterization techniques to understand, on a fundamental level, the effects of variations in solution chemistry on structural evolution and thin film electrical and optical properties, so that processing conditions which lead to the development of optimal properties can be determined.

Table I

Applicability of characterization techniques to the study of structural evolution in solution processing of thin films.

	Liquid			Film		
	Precursors	Rxn. Prod.	Solution	Wet	Amorphous	Crystalline
Technique						
NMR	*	*	*			
FTIR	*	*	*	*		
SAXS	*	*	*		*	
Raman			*	*	*	*
SAW				*	*	
Ellipsometry					*	*
TEM					*	*
SEM						*
Elec. Prop.						*

EXPERIMENTAL

Thin film preparation

We fabricated the thin films of the present study by using two different hybrid solution deposition approaches. Flow diagrams are shown in Figure 1. For both approaches, the film composition was PZT 53:47 with 5 mol % excess Pb. In the first approach, a sequential precursor addition (SPA) method, based on an approach reported by Sayer and co-workers,[9] was used. Lead acetate trihydrate* was dissolved in acetic acid* and dehydrated by heating to 105°C. The other precursors, zirconium butoxide-butanol§ and titanium isopropoxide,* were then added sequentially as the solution was cooled. Solution viscosity characteristics were tailored through further additions of acetic acid, water, and methanol. In the second approach, an inverted mixing order (IMO) approach

* Aldrich Chemical Company, Inc.; Milwaukee, WI

§ Alfa Products; Ward Hill, MA

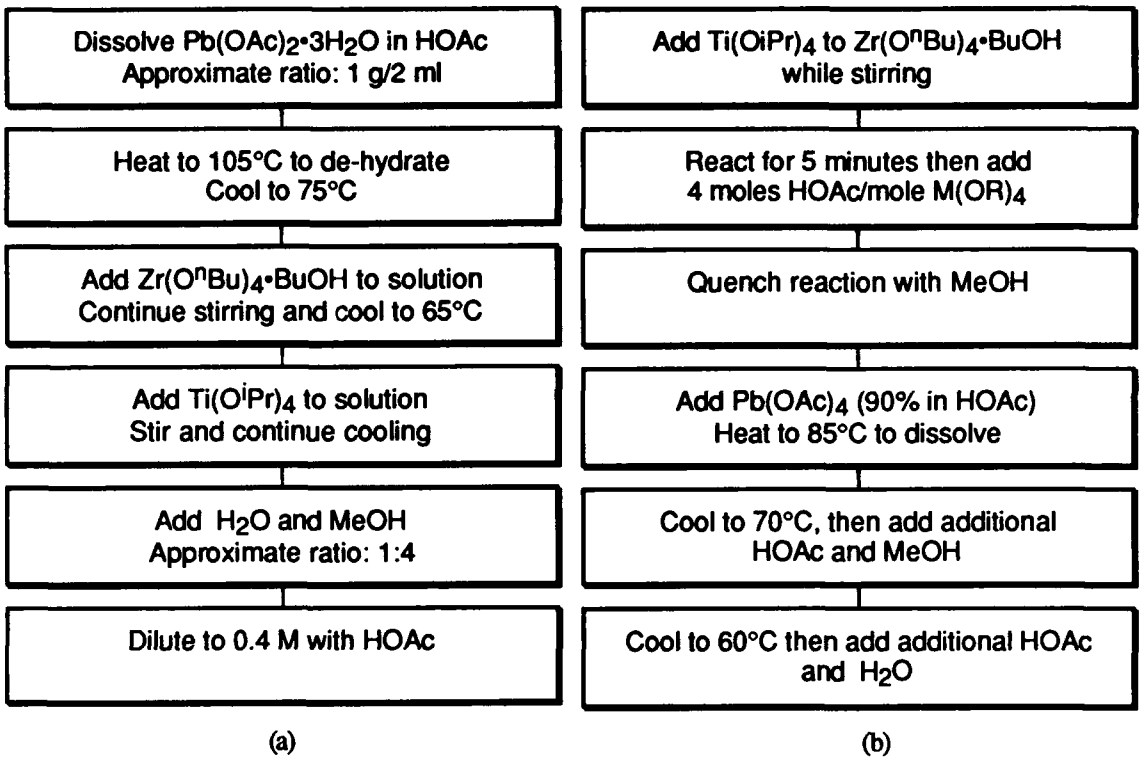


Figure 1. Flow diagrams for: (a) Sequential Precursor Addition (SPA) process; and (b) Inverted Mixing Order (IMO) process.

was used. Titanium isopropoxide was first added to zirconium butoxide-butanol. Methanol and acetic acid were then added, followed by addition of lead (IV) acetate[§]. At this point, the solution was heated to 85°C to dissolve the lead precursor. Finally, additional methanol, acetic acid and water were added. Solution concentration for both approaches was 0.4 M. Immediately before deposition, the solutions were filtered with a 0.2 μm syringe filter. The thin films were deposited onto electroded silicon substrates by spin-casting at 3000 rpm for 50 seconds. Following deposition, the films were heat treated for 5 minutes at 300°C to pyrolyze residual organic species. Typically, five layer films were prepared. Crystallization was accomplished by heat treatment at 650°C for 30 minutes. A 15°C per minute ramp rate was used. The fired film thickness, determined by ellipsometry, was approximately 0.40 μm for the SPA films and 0.45 μm for the IMO films.

Thin film characterization techniques

FTIR spectra were obtained at a resolution of 4 cm^{-1} using a Nicolet 7199 FTIR spectrometer equipped with a l-N_2 cooled HgCdTe detector. Samples were examined as capillary films between two KBr windows. The ^1H NMR spectra were accumulated on an IBM AC-200 operating at 200 MHz. Tetramethylsilane (0.0 ppm) was used as a primary reference standard with acetone (2.19 ppm) used as a secondary reference standard. Raman spectra were obtained using a computer-controlled, scanning, double monochromator equipped with holographic gratings and a photon-counting photomultiplier tube. The films were illuminated with the laser beam focused to a 0.1 x 2 mm line. The 514.5 nm argon laser line, with an intensity of 200 mW, was used for excitation. Background features (Rayleigh scatter, fluorescence) were removed by empirical fitting procedures. SEM photomicrographs were obtained with a Hitachi S-800 operating at 20 keV. Dielectric properties were measured using an HP 4194A impedance analyzer at 10 kHz. Ferroelectric hysteresis loops were obtained with a Radiant Technologies RT66A ferroelectric test system.

RESULTS AND DISCUSSION

Our interest in the characterization of solution chemistry effects was prompted by our observations on the extent of the effects which changes in solution mixing conditions, and solution aging, can have on film microstructure and ferroelectric properties. Typical results for these effects are shown in Figures 2 and 3. Figure 2 shows the effects of solution aging (1 versus 15 days) on the film microstructure and ferroelectric properties of films prepared by the SPA process. The films were prepared using identical deposition and heat treatment conditions. The film prepared from the "fresh" solution was characterized by a microstructure consisting primarily of the perovskite phase, which crystallized with a "rosette" appearance, i.e., spherulitic crystallization behavior, from a pyrochlore matrix.[20] The presence of a minor amount of a residual pyrochlore phase is also indicated. Even though the microstructure was somewhat diphasic in nature, a dielectric constant of ~ 400 and a loss tangent of 0.038 were measured at 10kHz. The ferroelectric properties of the film (Fig. 2a) were also very good. Although the loop was slightly open, a remanent polarization of 18.7 $\mu C/cm^2$ and a coercive field of 55.2 kV/cm were observed. In contrast, the film prepared from the "aged" solution (Fig. 2b) displayed a porous, poorly defined microstructure and poor electrical properties. Although the film exhibited some hysteresis, a very low remanent polarization (P_r = 1.4 $\mu C/cm^2$), and a high coercive field (E_c = 256 kV/cm), were measured. The dielectric constant at 10kHz was 80.

Shown in Figure 3 are the effects which variations in solution chemistry, i.e., SPA versus IMO processing, can have on film microstructure and ferroelectric properties. In contrast to the diphasic microstructure of the film prepared by the SPA process (Fig. 3a), the film prepared by the IMO process (Fig. 3b) was characterized by a single phase

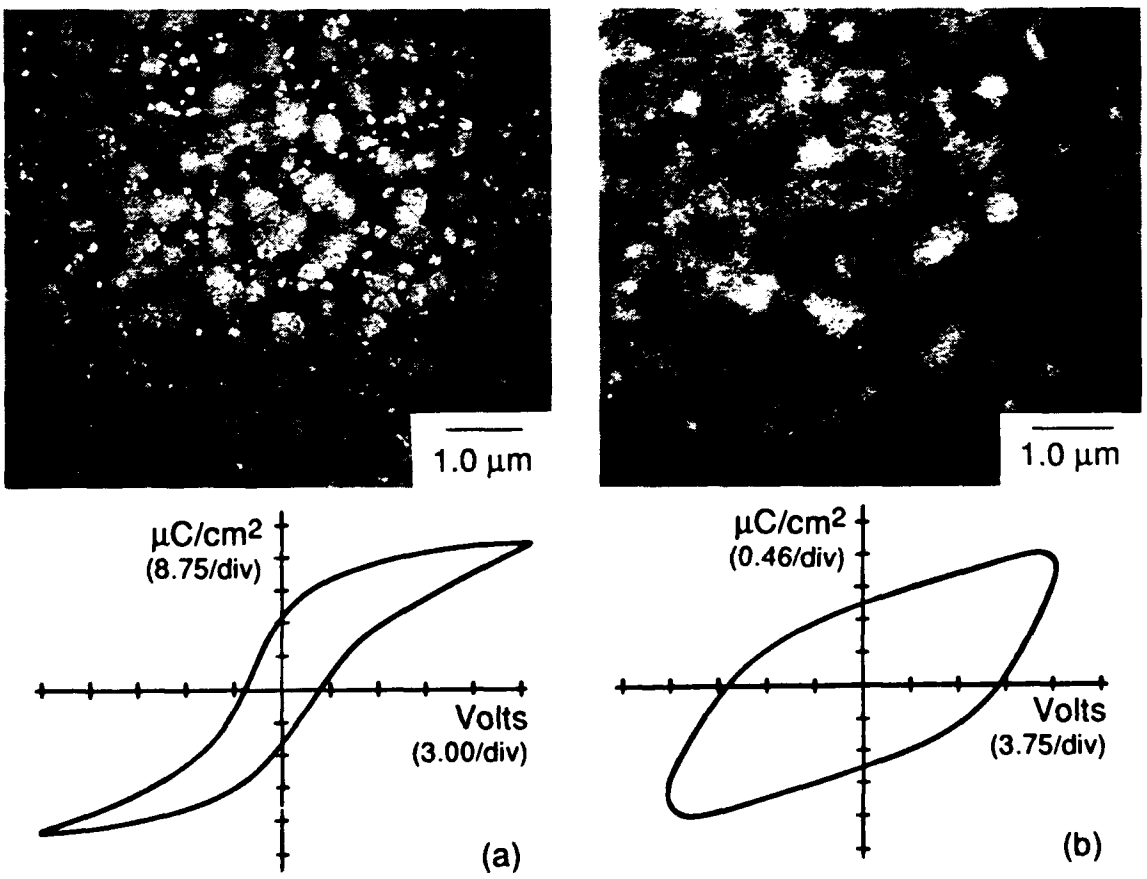


Figure 2. Effect of solution aging on thin film microstructure and ferroelectric properties for films prepared by the SPA process: (a) solution age, 1 day; and (b) solution age, 15 days.

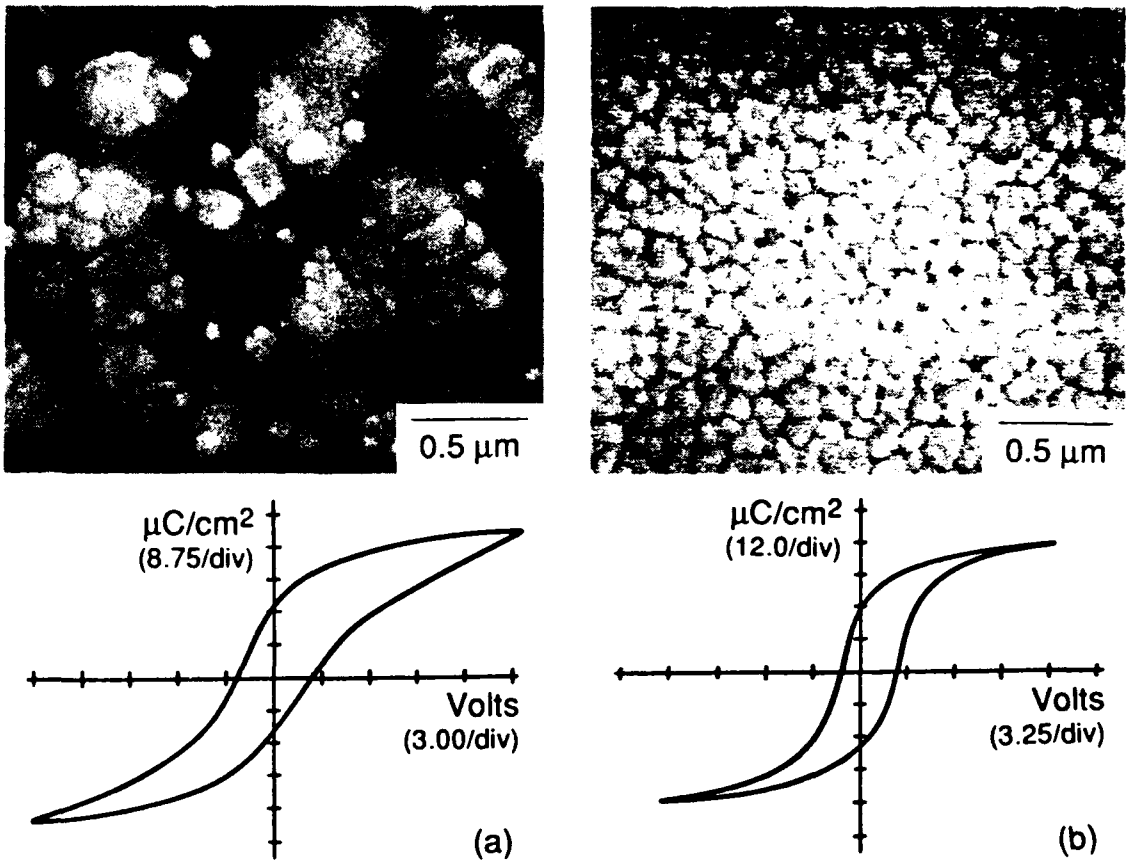


Figure 3. Effect of the solution preparation process on film microstructure and ferroelectric properties: (a) *SPA process*; and (b) *IMO process*.

perovskite, fine grain microstructure. The grain size, and overall nature, of this microstructure would seem to indicate that a different crystallization process was followed. The dielectric and ferroelectric properties of the IMO processed film were also better than those of the film prepared by the SPA process. A dielectric constant of 835 and a loss tangent of 0.030 at 10 kHz were measured. The hysteresis loop for this film displayed significantly less resistive leakage than the film prepared by the SPA process, and was characterized by a higher remanent polarization, 26.2 $\mu C/cm^2$, and a lower coercive field, 43.3 kV/cm.

We expect that one of the key aspects of both the SPA and the IMO processes is the role which acetic acid plays in the processes. From the reports of Doeuff and co-workers on the effects of acetic acid additions to titanium alkoxides,[21-23] we might predict that in these preparation procedures, acetic acid will also serve as more than a simple solvent. That is, as in the processing of bulk TiO_2 gels from titanium alkoxides,[21] in the processing of PZT films, acetic acid might act as a chemical modifying agent by reacting with the alkoxide precursors at a molecular level, replacing at least some of the alkoxy groups, and thus, altering the precursor hydrolysis and condensation characteristics. If this is indeed the case, we would also expect the production of reaction by-products, e.g., free alcohols. Other reactions involving acetic acid (which are discussed below) can lead to the formation of water and ester compounds (methyl, isopropyl or n-butyl acetate).

We have used FTIR and NMR spectroscopies to address these issues and our results are shown in Figures 4 through 6. Figure 4 shows the FTIR spectrum for a 4.0:0.5:0.5 molar mixture of acetic acid, zirconium butoxide-butanol, and titanium isopropoxide. This mixture is nearly identical to that used in the initial part of the IMO procedure. The predominant spectral features include two intense bands centered at ~ 1570 cm^{-1} and 1440 cm^{-1}, which are due to the asymmetric and symmetric COO

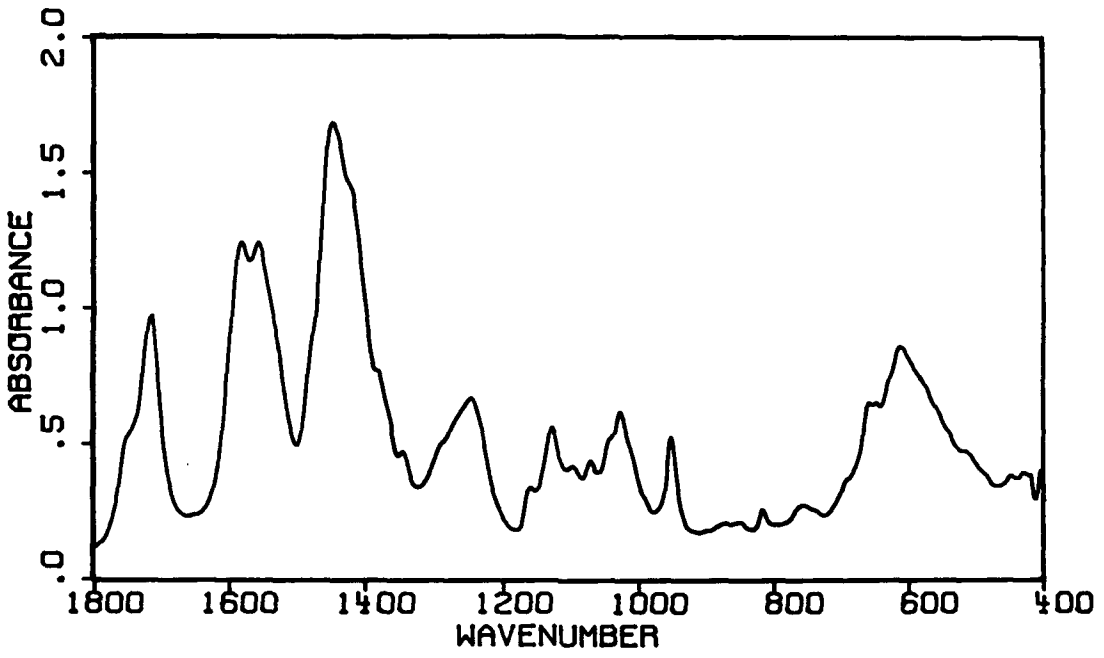


Figure 4. FTIR spectrum of a 4.0:0.5:0.5 mixture of HOAc, $Zr(O^nBu)_4$•BuOH, and $Ti(O^iPr)_4$.

stretching vibrations of the acetate ligand, respectively.[22,24,25] The band separation of ~ 130 cm^{-1} is indicative of bidentate acetate coordination.[25] From the information available, it is not possible to determine unequivocally whether the acetate groups are bridging: Zr-OAc-Zr, Zr-OAc-Ti, or Ti-OAc-Ti; or simply chelating (i.e., bound to only one metal). For titanium compounds, Von Thiele has reported that for simple bidentate chelating acetate ligands, a band separation of 80 cm^{-1} is expected, while for bidentate bridging coordination, a band separation of 160 cm^{-1}, close to the observed value of 130 cm^{-1}, is expected.[25] The fact that one of these peaks is present as a doublet, and the other peak shows a distinct shoulder, is perhaps indicative of bridging acetate groups of different nature. The mere presence of these bands, however, confirms that acetic acid reacts with the alkoxide precursors at a molecular level; i.e., it is a chemical modifier in the processing of PZT by the IMO method. We expect analogous behavior in the SPA process.

The presence of other bands in the FTIR spectrum are also of interest. The shoulder at ~ 1740 cm^{-1} and the peak at 1250 cm^{-1} are consistent with the formation of an ester compound;[21,26] in the present case, either isopropyl or n-butyl acetate. This "by-product" is possibly formed due to the reaction of acetic acid with an alcohol according to:

$$ROH + CH_3COOH \rightarrow ROOCCH_3 + H_2O \quad . \qquad (1)$$

The alcohol (ROH) may be the excess butanol associated with the zirconium alcoholate precursor, isopropanol resulting from an alkoxy exchange reaction between the titanium isopropoxide and the butanol from the alcoholate, or alcohol resulting from the replacement of the alkoxy ligands with acetate ligands, as shown in Rxn. 2:

$$CH_3COOH + M(OR)_x \rightarrow M(OR)_{x-1}(OOCCH_3) + ROH \quad . \qquad (2)$$

Rxn. 1 also indicates that we can expect the (in-situ) formation of water, which may initiate the hydrolysis and condensation of the precursor alkoxides, leading to the formation of polymeric zirconium/titanium oxo-acetate-alkoxide species in the solution.

The rate and extent of the condensation of these species will depend on the degree of replacement of the more easily hydrolyzed alkoxy ligands (of the original alkoxide precursors) by acetate groups. If the in-situ generated water does indeed initiate hydrolysis and condensation, close control of the times and temperatures utilized in PZT solution processing will be critical, since the extent of hydrolysis and condensation will be dependent on the amount of by-product (water) formed.

Finally, the peaks below 1200 cm^{-1} are most likely due to C-O and M-O stretching vibrations of the alkoxides,[27,28] indicating that all of the alkoxy groups of the precursors are not replaced under the present conditions. Some of these peaks may also possibly be assigned to free alcohols or free acetic acid, which is responsible for the peak at 1718 cm^{-1}.[21]

The results of our NMR spectroscopic investigations are shown in Figures 5 and 6. Figure 5 shows the ^1H NMR spectrum for the SPA solution. The most intense peaks are due to the solvents, H_2O and MeOH, and XOAc, where X is H, a metal cation, or an alkyl group. The XOAc resonance is split into a narrow and a broad component. Addition of acetic acid to this sample contributes to the intensity of the broad component. Thus, we believe that the broad component corresponds to free acetic acid which is exchanging with acetic acid that is complexed with a metal (i.e., chelated acetate). The observed linewidth may be the result of homogeneous broadening due to the high molecular weight of the metal clusters and/or inhomogeneous broadening due to the distribution of chemical shifts of the acetate ligand in its various bonding sites. The

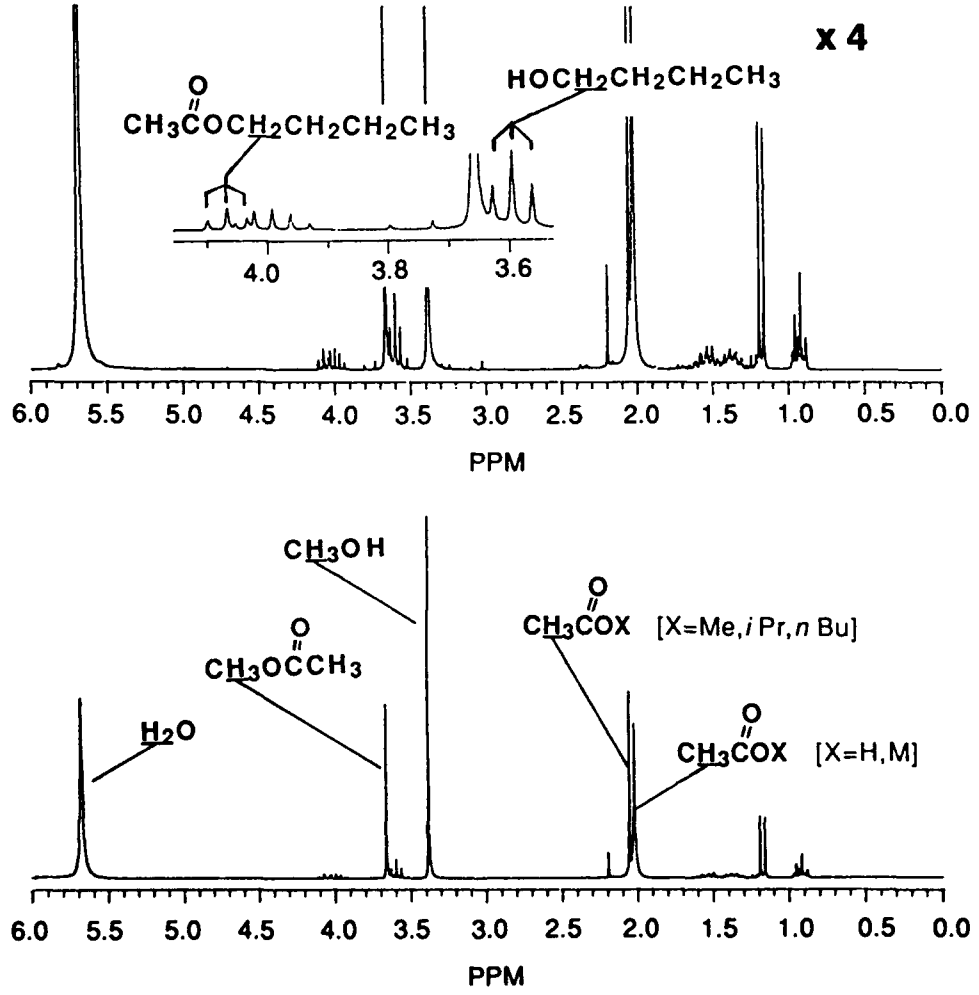


Figure 5. ^1H NMR spectrum of the SPA solution. A small amount of acetone was added as a reference.

narrow component of the XOAc resonance arises from the acetate group of the ester compounds formed by Rxn. 1, i.e., the reaction of acetic acid with alcoholic species.[29] This result is thus in agreement with the results of our FTIR studies, which indicated the probable existence of esters in these solutions.

We can also see in Figure 5 that the resonances for each of the alcohols (MeOH, Pr^iOH, and Bu^nOH) have both major and minor components. Since our FTIR results implied the formation of ester compounds, we might suspect that one component of the resonances would be due to the ester compounds. In fact, the observed chemical shifts of the minor components agree with the literature values[29,30] for their corresponding esters. Also, as would be expected, the total intensity of the alcoholic minor components is equal to the intensity of the narrow XOAc resonance. The ^1H NMR spectrum of the IMO solution displayed similar resonances, but exhibited less ester formation. This implies the formation of less water via Rxn. 1, which may potentially reduce the degree of condensation of the polymeric species which are formed.

In an attempt to further determine the nature of the (oligomeric or) polymeric $Pb(Zr,Ti)O_x(OAc)_y(OR)_z$ species present in the solution, solvents and by-products were eliminated from the solution. The sample was prepared by halting the (SPA) preparation process after adding the titanium precursor and removing any by-products which might have been formed by vacuum distillation. The dried powder thus obtained was dissolved in 99% D_2O and the ^1H NMR spectrum was then obtained. The spectrum for this sample, shown in Figure 6, was characterized by intense peaks due to water and acetate.

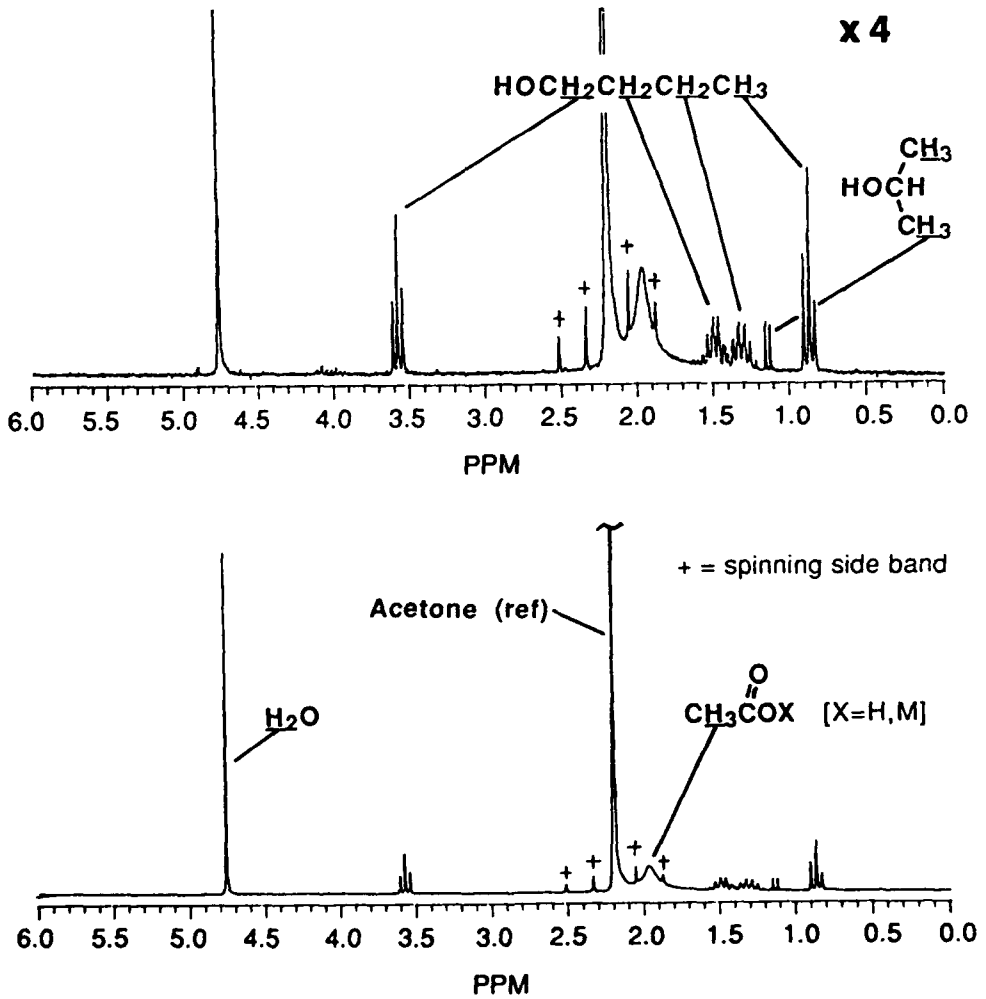


Figure 6. ^1H NMR spectrum of dried SPA solution dissolved in D_2O. A small amount of acetone was added as a reference.

The water peak is expected due to the protio impurities in the deuterium oxide and the generation of water via Rxn. 1, which was not removed by vacuum distillation. The minor components of the Me, *i*-Pr, *n*-Bu resonances are no longer present, indicating removal of the esters, due to their high vapor pressures. Free methanol has been completely removed, and through comparison of the peak intensities in Figures 5 and 6, we can see that the Pr^iOH concentration is now much less than the Bu^nOH concentration. This trend is expected, because of the relative volatilities of MeOH, Pr^iOH, and Bu^nOH. Also, in this sample, the broad XOAc resonance is much broader than in the neat solution sample. Probably, most of the free acetic acid has been removed, and the remaining acetic acid (acetate) is chelated to the metals. Addition of a small amount of acetic acid to the sample narrows and shifts the XOAc resonance considerably. Compared to the acetate resonance, the resonances for Pr^iOH and Bu^nOH are narrow. Further, the width and position of the butanol resonances do not change with the addition of butanol to the sample, indicating that the resonances are in fact due to free butanol. The NMR results thus imply that there are, at most, only a few alkoxy ligands remaining on the polymeric $Pb(Zr,Ti)O_x(OAc)_y(OR)_z$ species, i.e., the original isopropyl and n-butyl ligands have been replaced by acetate ligands. The polymeric species formed in these solutions is thus, essentially, oxo-acetate in nature, i.e., $Pb(Zr,Ti)O_x(OAc)_y$.

In addition to studying the local chemical environment of solution species, as was accomplished by NMR spectroscopy, it is possible to study the nature of the films on a larger size scale. We have used Raman spectroscopy to study the structural evolution of the films as a function of heat treatment, and the results are illustrated in Figure 7. For all samples, a heating rate of 15°C/min., and hold time of 30 minutes, were used. The amorphous films (350 and 400°C) displayed only a broad peak at a Raman shift of

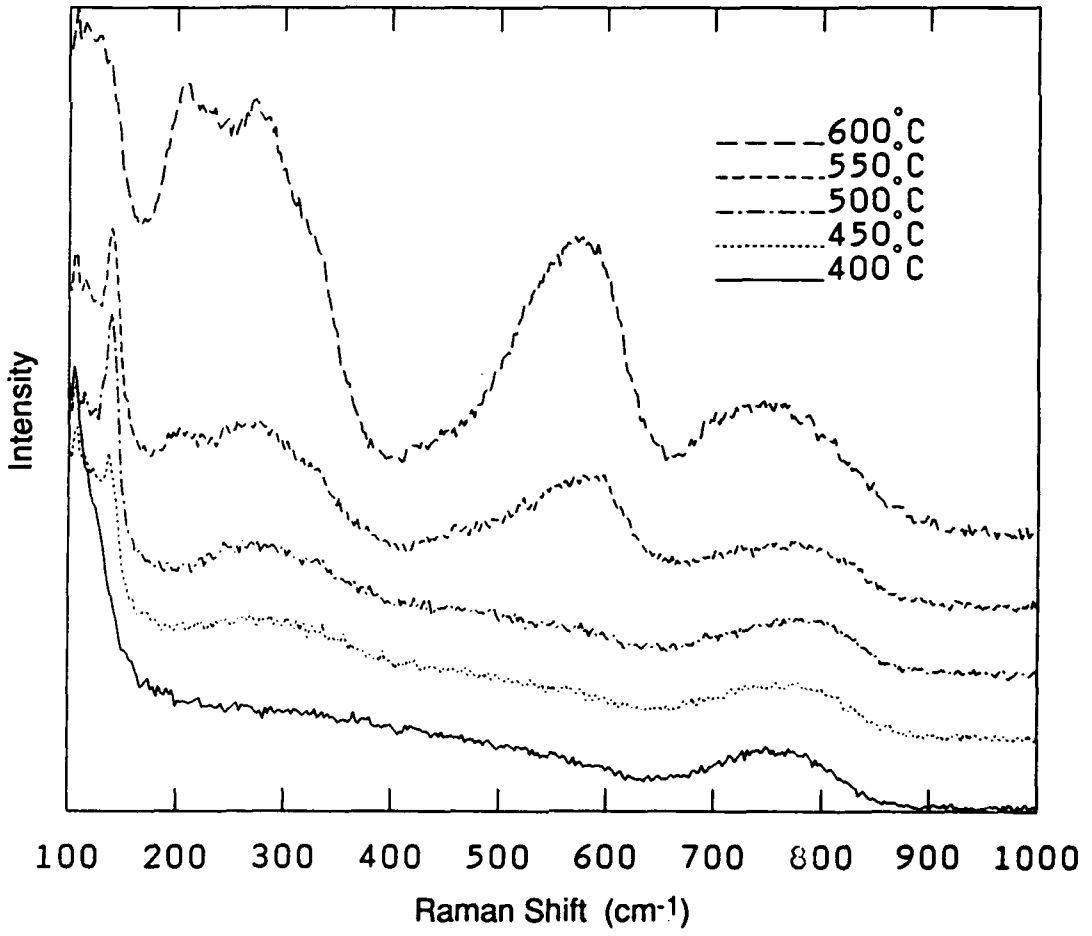


Figure 7. Effects of heat treatment on the Raman spectrum of SPA derived PZT thin films.

~ 750 cm^{-1}. The result is similar to that observed previously for sol-gel derived lead titanate powders.[26] As the heat treatment temperature was increased from 400°C to 550°C, the peak present in the amorphous films shifted to higher wavenumber; a peak at ~ 275 cm^{-1} appeared; and a sharp peak at ~ 140 cm^{-1} appeared. The intense sharp peak at ~ 140 cm^{-1} was assigned to an anatase-like structure.[31] The assignment of this peak to a PbO phase was considered, however, the spectral match was not as good as for anatase. As the heat treatment temperature was further increased, from 550°C to 600°C, the peak due to the anatase-like phase disappeared; and new bands associated with crystallization into the perovskite phase appeared at 210 cm^{-1}, 265 cm^{-1}, 560 cm^{-1}, and 740 cm^{-1}. Due to the concomitant behavior of the bands, it seems possible that the anatase-like phase is involved in a solid state reaction leading to the formation of the desired perovskite phase. Similar behavior was noted for films prepared by the IMO process, although the disappearance of the anatase-like phase, and the appearance of bands associated with the perovskite phase, were observed to occur at lower temperatures.

CONCLUSIONS

Variations in solution chemistry have been observed to cause dramatic differences in film microstructures and ferroelectric properties. As a first step to understanding the underlying reasons for these effects, we have used spectroscopic characterization techniques to: (i) define the role of acetic acid in the solution preparation process; (ii) determine the nature of the solution polymeric species; and (iii) characterize the structural evolution of the thin films into the desired crystalline phase. FTIR analysis confirmed that acetic acid serves not only as a solvent, but also as a chemical modifier in the solution processing of PZT thin films. We thus expect that the hydrolysis and condensation behavior of the resulting species will be significantly different than the initial alkoxide precursors. Further, due to the formation of water as a by-product, care needs to be taken to control to the extent and nature of in-situ hydrolysis and condensation.

NMR spectroscopy was used to study the local chemical environment of the polymeric species formed in solution. Results indicate that the acetate group from acetic acid chelates the cation precursors, and that the polymeric species formed is oxo-acetate in nature. The NMR spectra for the SPA and IMO solutions were qualitatively similar, however, the spectrum for the SPA solution indicates more extensive formation of ester compounds for this process. Therefore, we would also expect the formation of more water in this process, which could conceivably result in polymeric species of a more highly condensed nature. We hope that with further such studies, we can develop the level of understanding necessary to design a solution deposition route which has highly controllable chemistry and will lead to the fabrication of property-optimized ferroelectric thin films.

ACKNOWLEDGEMENTS

This work was supported by the U.S. Department of Energy under contract DE-AC04-76DP00789. We would like to acknowledge our technical discussions with D. M. Haaland and with J. Bullington of Radiant Technologies. We would also like to thank B. A. Dodd, C. L. Hernandez, T. J. Zender, D. A. Schneider, R. L. Simpson, and H. D. T. Jones for excellent technical support. We gratefully acknowledge the use of microscopy facilities in the Dept. of Chemical Engineering at the University of New Mexico.

REFERENCES

1. M. Adachi, et al., *Jap. J. Appl. Phys.*, Vol. 26 (4), 550 (1987).
2. K. Sreenivas, M. Sayer, and P. Garrett, *Thin Solid Films*, Vol. 172, 251 (1989).

3. A. I. Kingon, et al., in Ferroelectric Thin Films, eds., E. R. Myers and A. I. Kingon (Mat. Res. Soc., Pittsburgh, 1990) pp. 45-56.
4. M. S. Ameen, et al., in Ferroelectric Thin Films, eds., E. R. Myers and A. I. Kingon (Mat. Res. Soc., Pittsburgh, 1990) pp. 65-76.
5. K. L. Saenger, et al., in Ferroelectric Thin Films, eds., E. R. Myers and A. I. Kingon (Mat. Res. Soc., Pittsburgh, 1990) pp. 115-120.
6. K. D. Budd, S. K. Dey, and D. A. Payne, *Brit. Ceram. Soc. Proc.*, Vol. 36, 107 (1985).
7. R. W. Vest and J. Xu, *Ferroelectrics*, Vol. 93, 21 (1989).
8. J. Fukushima, K. Kodaira, and T. Matsushita, *J. Mater. Sci.*, Vol. 19, 595 (1984).
9. G. Yi, Z. Wu, and M. Sayer, *J. Appl. Phys.*, Vol. 64 (5), 2717 (1988).
10. D. S. Hagberg and D. A. Payne, in Ferroelectric Thin Films, eds., E. R. Myers and A. I. Kingon (Mat. Res. Soc., Pittsburgh, 1990) pp. 19-24.
11. K. D. Budd, Ph.D. Thesis, University of Illinois, 1985.
12. D. B. Dimos, C. E. Land, and R. W. Schwartz, to be published in Ceramic Transactions, 1991.
13. W. G. Klemperer, V. V. Mainz, and D. M. Millar, in Better Ceramics Through Chemistry II, eds., C. J. Brinker, D. E. Clark, and D. R. Ulrich (Mat. Res. Soc., Pittsburgh, 1986) pp. 3-13.
14. G. H. Haertling, *Ferroelectrics*, Vol. 116, 51 (1991).
15. K. D. Keefer, in Better Ceramics Through Chemistry, eds. C. J. Brinker, D. E. Clark, and D. R. Ulrich (North-Holland, New York, 1984) pp. 15-24.
16. C. J. Brinker, A. J. Hurd, and K. J. Wall, in Ultrastructure Processing of Advanced Ceramics, eds., J. D. Mackenzie and D. R. Ulrich (Wiley & Sons, Inc., New York, 1988) pp. 223-240.
17. C. J. Brinker, et al., in Science of Ceramic Chemical Processing, eds., L. L. Hench and D. R. Ulrich (Wiley & Sons, Inc., New York, 1986) pp. 37-51.
18. B. A. Tuttle, et al., in Ferroelectric Thin Films, eds., E. R. Myers and A. I. Kingon (Mat. Res. Soc., Pittsburgh, 1990) pp. 159-165.
19. G. C. Frye, et al., in Better Ceramics Through Chemistry II, eds., C. J. Brinker, D. E. Clark, and D. R. Ulrich (Mat. Res. Soc., Pittsburgh, 1986) pp. 349-354.
20. A. H. Carim et al., accepted for publication in *J. Am. Ceram. Soc.*, Vol. 74 (1991).
21. S. Doeuff, et al., *J. Non-Cryst. Sol.*, Vol. 89, 206 (1987).
22. S. Doeuff, M. Henry, and C. Sanchez, *Mat. Res. Bull.*, Vol. 25, 1519 (1990).
23. S. Doeuff, et al., *Inorg. Chem.*, Vol. 28, 4439 (1989).
24. K. Nakamoto, Infrared and Raman Spectra of Inorganic and Coordination Compounds (Wiley-Interscience, New York, 1963).
25. K. H. Von Thiele and M. Panse, *Z. Annorg. Allg. Chem.*, Vol. 441, 23 (1978).
26. S. Li, R. A. Condrate, and R. M. Spriggs, *Spec. Lett.*, Vol. 21 (9&10), 969 (1988).
27. R. E. Riman, et al., in Better Ceramics Through Chemistry, eds., C. J. Brinker, D. E. Clark, and D. R. Ulrich (North-Holland, New York, 1984) pp. 233-238.
28. J. V. Bell, et al., *Anal. Chem.*, Vol. 25 (11), 1720 (1953).
29. C. J. Pouchert, The Aldrich Library of NMR Spectra, Edition II (Aldrich Chemical Company, Inc., Milwaukee, 1983).
30. N. S. Bhacca, et al., NMR Spectra Catalog (Varian Associates, 1962).
31. R. J. Capwell, F. Spagnolo, and M. A. DeSesa, *Appl. Spec.*, Vol. 26 (5), 537 (1972).

STATISTICAL INVESTIGATION OF SOL-GEL LEAD TITANATE (PT) PROCESSING

B. M. MELNICK
Condensed Matter Physics Department, University of Colorado,
Microelectronics Research Laboratory, University of Colorado at Colorado Springs,
and
Symetrix Corporation.

R.GALLEGOS
Microelectronics Research Laboratory, University of Colorado at Colorado Springs.

C. A. PAZ DE ARAUJO
Microelectronics Research Laboratory, University of Colorado at Colorado Springs,
and
Symetrix Corporation.

AD-P006 684

Abstract There are three stages involved in the successful application of a thin film sol-gel oxide, (1) solution synthesis, (2) application, and (3) post application treatments. Each stage contains many processing steps that can be varied in order to optimize the thin film for various applications. This work entails a statistical investigation of a thin film sol-gel PT process for use in memory applications.

Statistical experimental design yields a maximum amount of information for a minimum amount of effort. Candidate controllable variables (factors) and responses are first identified. A screening experiment is then conducted to identify the most important factors based on the identified responses. A full-factorial experiment is then conducted to further evaluate the important factors. Finally, a response surface analysis is performed in order to optimize the important factors. Responses such as switching charge (2Pr), endurance and dielectric measurements are used to analyze the sol-gel lead titanate.

INTRODUCTION

In order to integrate ferroelectric thin films into semiconductor memories, engineers must understand how the

92-16159

various processing steps impact the electrical characteristics of the ferroelectric material. Additionally, by thoroughly understanding the interactions between processing parameters and the physical and electrical characteristics of the ceramic thin films, the devices can be designed to operate in the appropriate regimes. Statistical experimental design (known in industry as design of experiments) is ideally suited for this type of analysis.

This paper describes a design of experiments (DOE) that shows how processing steps effect the standard sol-gel lead titanate (PT) process that has been developed at the University of Colorado at Colorado Springs. Since a stable sol-gel PT stock solution process with a shelf life of one year exists at UCCS, the design focused only on steps that follow the stock solution synthesis. The VAX VMS version of RS was employed to aid in the design and analysis of the experiment.

REVIEW OF EXPERIMENTAL DESIGN

Although this paper does not discuss in any detail the fundamentals of the statistical approach used in experimental design, the overall strategy involved is summarized here. The design normally consists of several phases. Depending on the degree of information that is needed, an experimental design using all or part of the phases can be formulated.

Assuming that an objective has already been determined, candidate control variables (factors) and system responses to the changes in these factors must be identified. A phase I screening experiment may then be performed. Screening experiments are used to identify the major factors or "big knobs" of the system and should be performed whenever a large number of factors need to be examined. The most common types of screening experiments used are the Plackett-Burman and the fractional factorial. A fractional-factorial design should be used when the

number of factors does not exceed eight. For nine to twenty factors, a 20 run Plackett-Burman design is recommended[1]. Plackett-Burman designs,unlike fractional-factorial designs, will not separate main effects from all of the higher order interactions, but the most important factors for the given responses can be identified. Once the screening experiment has been performed, the major factors are further examined during Phase II and Phase III experimentation.

Phase II experimentation consists of design space exploration of the major factors determined in the first phase. Full factorials are used to separate main effects from interactions and to determine where in the design space the system should operate. Phase III experimentation utilizes central composite design to investigate linear effects, interactions, and curvature of responses. A central composite inscribed design (CCI) is implemented when the phase III factor settings are not to be exceeded. CCIs do not characterize the entire Phase II space. The information near the "corners" must be extrapolated (Figure 1a). A central composite circumscribed design (CCC) may be used if the Phase III factor settings may be slightly exceeded. The entire Phase III space is covered when using a CCC and all information within the space may be interpolated from acquired data (Figure 1b). Response surfaces (contour plots of how the responses vary due to changes in the factors) and ANOVA tables, which quantify the quality of the response surface models, are all generated from the information obtained using the central composite design. Contour plots not only show where optimum points are located, but can also aid in process control by allowing an engineer to see the trends of a response due to changes in the factors.

Verification of the optimum points should then be performed as a final phase (Phase IV) to the design. Normally, a minimum of five runs are used. All optimum points should be within a 95% confidence interval, as

determined by the models, before implementing the design into a product line.

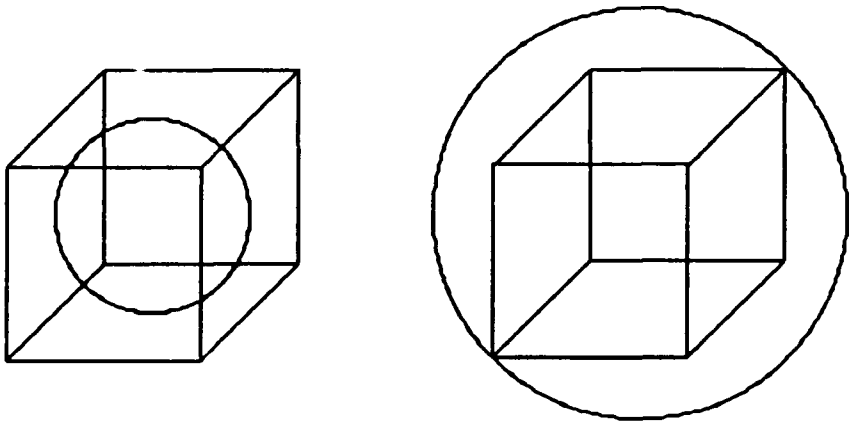


FIGURE 1 A schematic representation of the differences between a) central composite inscribed and b) central composite circumscribed Phase III designs.

EXPERIMENT

The goal of this work was to optimize an existing sol-gel lead titanate process that had been developed at the University of Colorado at Colorado Springs Microelectronics Research Laboratory. Any sol-gel thin film process is made up of several steps such as stock solution synthesis, pre-deposition hydrolization, deposition, annealing, and post anneal processing. Each of these general categories can be further broken down to the specific processes and variables contained within these processes. Due to the fact that a stable lead titanate stock solution with a known shelf life of one year was already in existence at the beginning of this work, the following design covered steps after the synthesis of the PT stock solution.

Phase I Factors and Responses

Due to limitations on time, man power, and available material, a seven factor fractional factorial was designed using the variables listed in Table 1. The variables and

high and low limits were chosen based on previous

TABLE I Phase I factors and levels.

Factor	-Level	+Level
H_2O h-factor	1	2
Acid h-factor	.75	1.25
Hot plate dry time	60 sec.	300 sec.
Hot plate dry temp.	156 C	307 C
Furnace anneal time	15 min.	60 min.
Furnace anneal temp.	550 C	750 C
Furnace anneal ambient	O_2	N_2

experience with sol-gel lead titanate processing. The hydrolyzing factor (h-factor) is defined as

$$\text{h-factor} = [\text{hydrolyzing agent}]/[\text{metal}]. \quad (1)$$

A design that investigates the effects of rapid thermal processing is planned for future work. Since this work was intended to aid in memory applications, the responses chosen were: dielectric constant, 2Pr positive, 2Pr negative, % fatigue initial (see Equation 2), and % fatigue following 1E6 switching cycles (see Equation 3).

$$\%\ \text{fatigue initial} = (2Pr_{init} - 2Pr_{1E6})/2Pr_{init} \quad (2)$$

$$\%\ \text{fatigue 1E6} = (2Pr_{1E6} - 2Pr_{1E8})/2Pr_{1E6} \quad (3)$$

The results of the 16 run Phase I fractional-factorial screening experiment determined that the most significant factors were the acid h-factor, the furnace temperature, the hot plate temperature, and the furnace ambient. Since the furnace ambient is either N_2 or O_2, this variable was set to the most favorable position which was O_2. The less significant factors were H_2O h-factor, hot plate time, and the furnace time. These variables were set to 1.5, 60 seconds, and 30 minutes respectively for the remainder of

the design.

Phase II and Phase III Design and Results

Due to limited material, manpower, time, and because previous experience had already shown that the operating space was suitable, a Phase II design space exploration was not conducted. Phase III consisted of a three factor, 20 run central composite inscribed design. The Phase III design is listed in Table II. The same responses listed

TABLE II Phase III CCI design.

Sample#	Acid h-factor	HP temp.(C)	Furn. temp.(C)
1	1.3	450	588
2	1.4	291	625
3	1.3	250	588
4	1.3	350	525
5	1.3	350	588
6	1.3	350	588
7	1.4	409	550
8	1.3	350	588
9	1.4	409	625
10	1.4	291	550
11	1.1	409	625
12	1.1	291	625
13	1.3	350	588
14	1.3	350	588
15	1.0	350	588
16	1.5	350	588
17	1.3	350	588
18	1.3	350	650
19	1.1	409	550
20	1.1	291	550

in the Phase I section were used to evaluate the Phase III samples.

Once the responses were measured for the Phase III samples, the data was used to generate statistical models and response surface plots. Table III shows a typical analysis of variance (ANOVA) for one of the measured responses. The ANOVA table allows an engineer to evaluate how well the response surface model predicts the actual data. The total (Corr.) line describes the statistics of the raw data. The regression (broken into linear and non-

linear portions) describes the statistics of the leasc

TABLE III Typical analysis of variance (ANOVA) table. The table shown describes the % fatigue between 1E6 and 1E8 cycles for the positive switching polarization.

source	DOF	Sum of Squares	Mean Square	F-ratio	Signif.
Total (Corr.)	19	3684972			
Regression	5	2491004	498201	5.84	0.0041
Linear	3	381165	127055	1.49	0.2604
Non-linear	2	2109839	1054919	12.37	0.0008
Residual	14	1193968	85283		
Lack of fit	9	867011	96335	1.47	0.3493
Pure error	5	326956	65391		

R-sq. = 0.6760
R-sq.-adj. = 0.5603

squares model generated by the RS software. The residual describes the statistics between the predicted error of the responses and the actual responses. The two most important quantities to evaluate from ANOVA tables are the significance column and the R-squared/adjusted R-squared statistics. The significance statistic determines the probability that the F-ratio will occur given the number of degrees of freedom. For the regression statistics, a smaller significance implies a better model. The sum of squares of the regression divided by the sum of squares of the total gives the R-squared. The R-squared gives an idea of how much of the total variation in the response is explained by the model. The higher the R-squared (up to a maximum of 1), the better the model. R-squared values are somewhat dependent on the degrees of freedom (DOF) of the system, so an adjusted R-squared is calculated that removes this dependence.

The actual response surface plots are shown in Figures 2-7. Since the Phase III samples used a CCI design, all data outside of the exclusion area is

extrapolated information and would not fall within a 95% confidence interval. Figures 2-4 show the percent fatigue data at constant hot plate temperatures of 325°C, 350°C and 400°C respectively, while varying the acid h-factor and furnace temperature. Figures 5-7 show the dielectric constant and switching polarizations at constant hot plate temperatures of 300°C, 350°C and 400°C respectively, while also varying the acid h-factor and furnace temperature. Three dimensional plane representations containing fatigue and switching data are shown in Figures 8 and 9.

DISCUSSION

The response surface curves presented in Figures 2-7 indicate some interesting trends. In Figures 5-7 the dielectric constant data indicates no interaction between hot plate temperature and dielectric constant. The dielectric constant does, however, interact with the furnace temperature and acid h-factors.

The switching polarizations follow the same trends as the dielectric constant, except that the switching polarizations interact with and depend on the hot plate temperature. For constant furnace temperature and acid h-factor, the switching polarizations appear to increase with increasing hot plate temperatures.

The analysis of the percent fatigue models are more complicated. The models predict a region in which the initial fatigue of the ferroelectric capacitors actually decreases at the lower furnace temperatures and acid h-factors. This effect has been observed in various other samples manufactured at the UCCS facility and published by Dey and Zuleeg for sol-gel PZT[2]. One possible explanation for this effect may be that the films are initially very defective and charge traps are being filled during the early cycling. The models which describe the percent fatigue between 1E6 and 1E8 cycles predict a decrease in

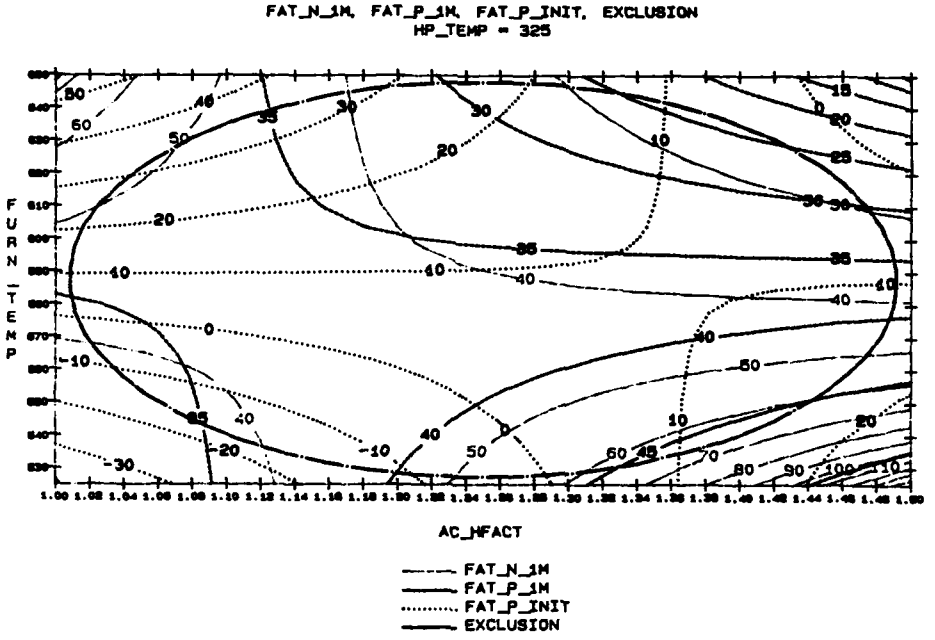


Figure 2 Percent fatigue data at constant hot plate temperature of 325°C, while varying the acid h-factor and furnace temperature.

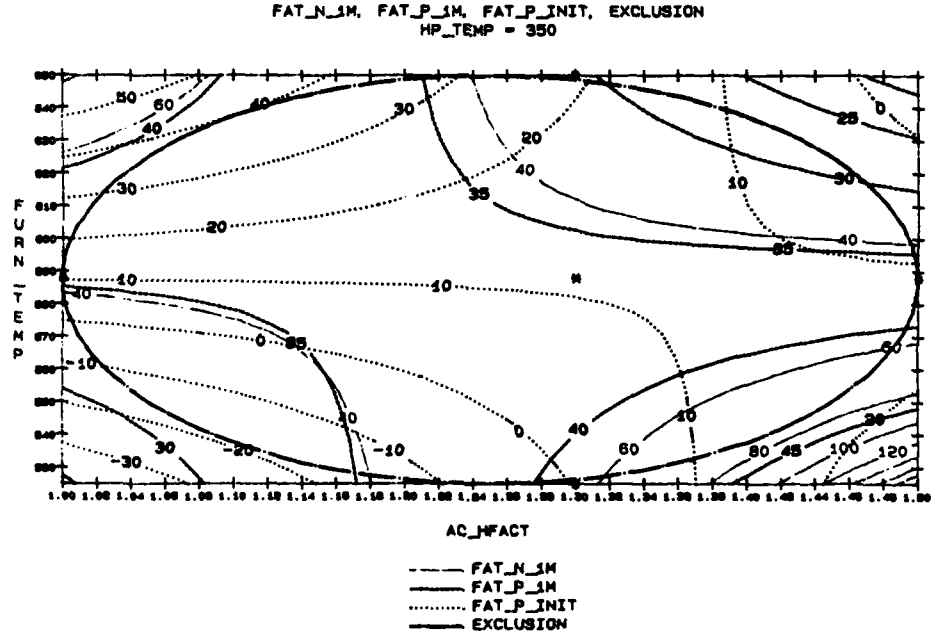


Figure 3 Percent fatigue data at constant hot plate temperature of 350°C, while varying the acid h-factor and furnace temperature.

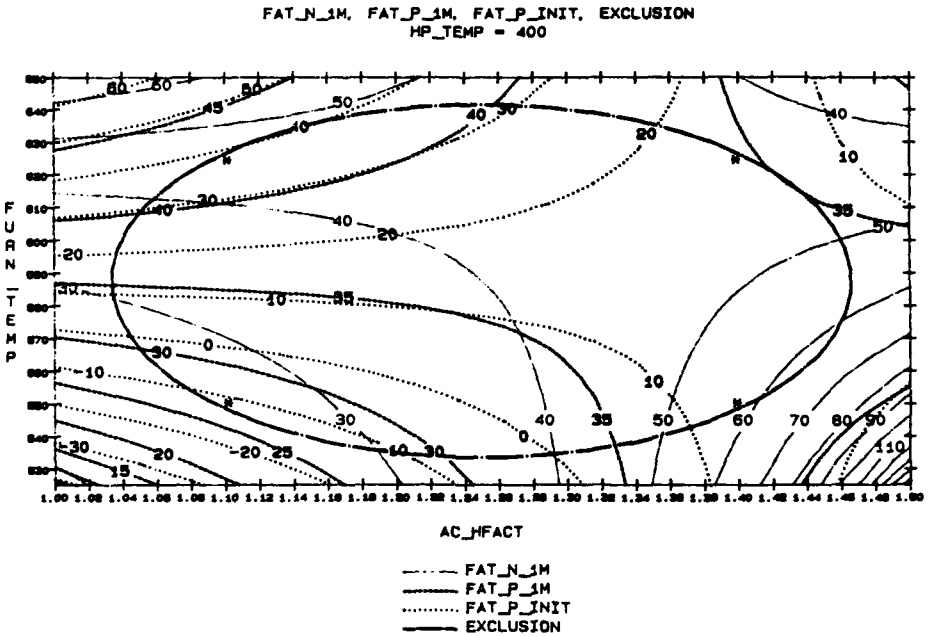


Figure 4 Percent fatigue data at constant hot plate temperature of 400°C, while varying the acid h-factor and furnace temperature.

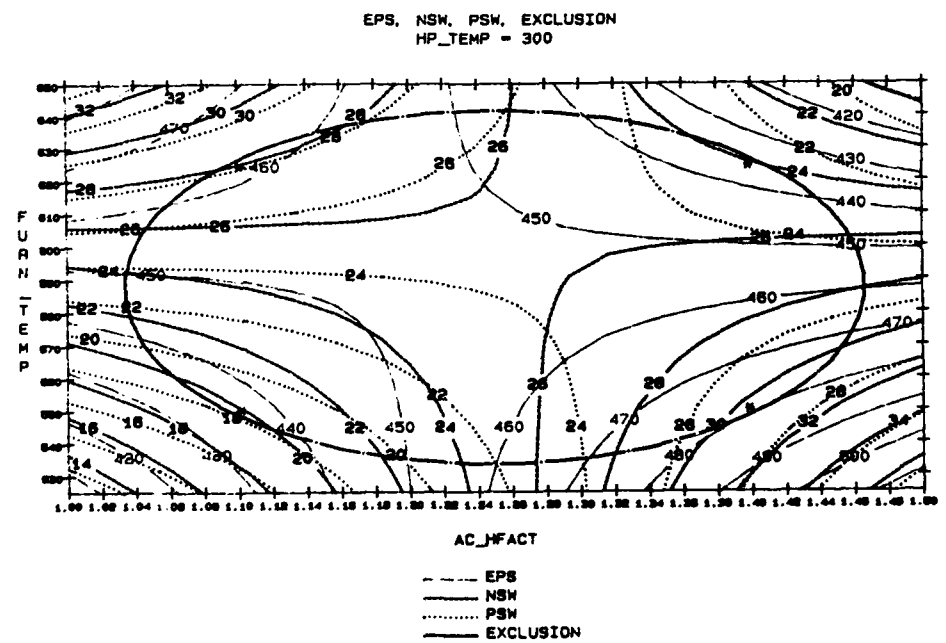


Figure 5 Dielectric and switching data at constant hot plate temperature of 300°C, while varying the acid h-factor and furnace temperature.

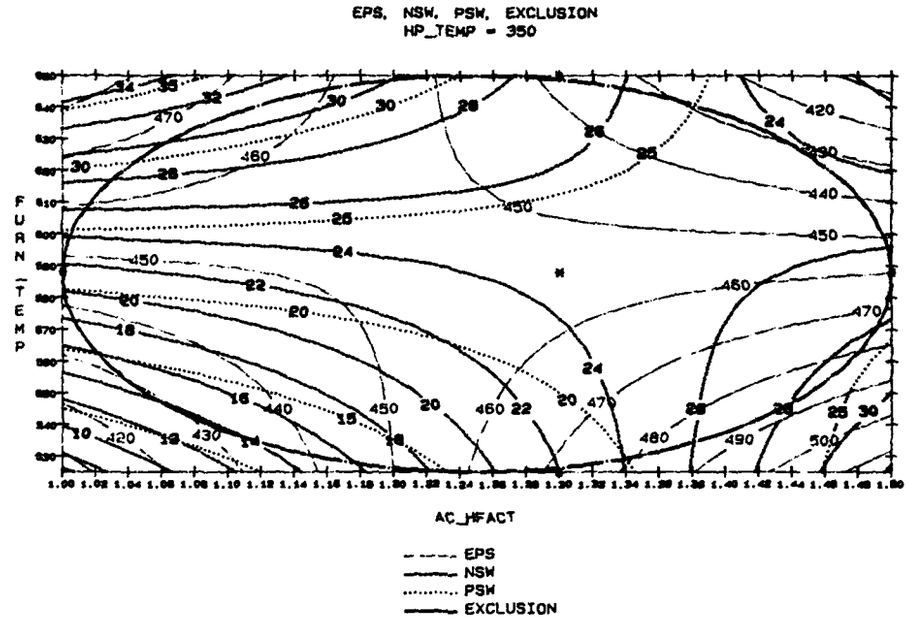


Figure 6 Dielectric and switching data at constant hot plate temperature of 350°C, while varying the acid h-factor and furnace temperature.

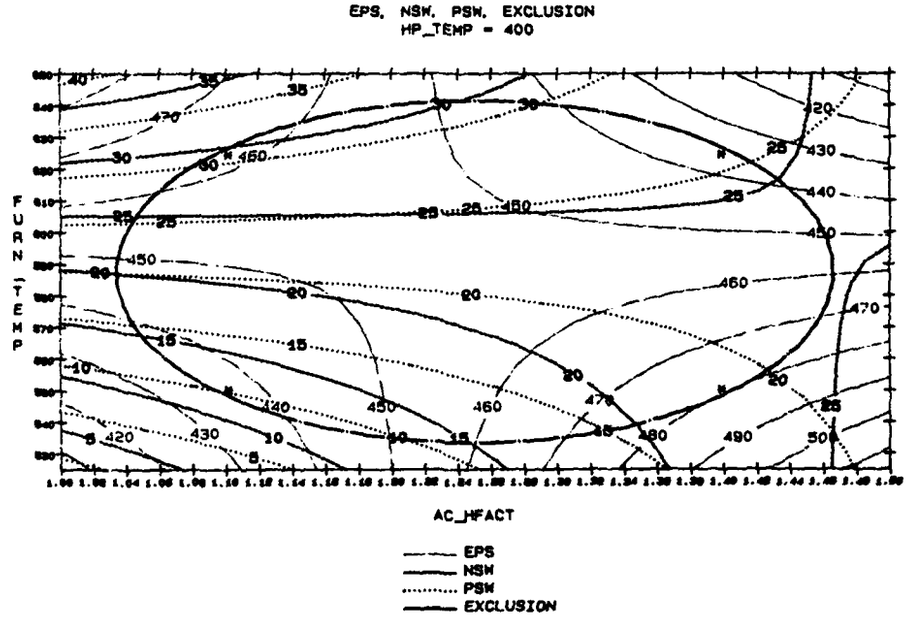


Figure 7 Dielectric and switching data at constant hot plate temperature of 400°C, while varying the acid h-factor and furnace temperature.

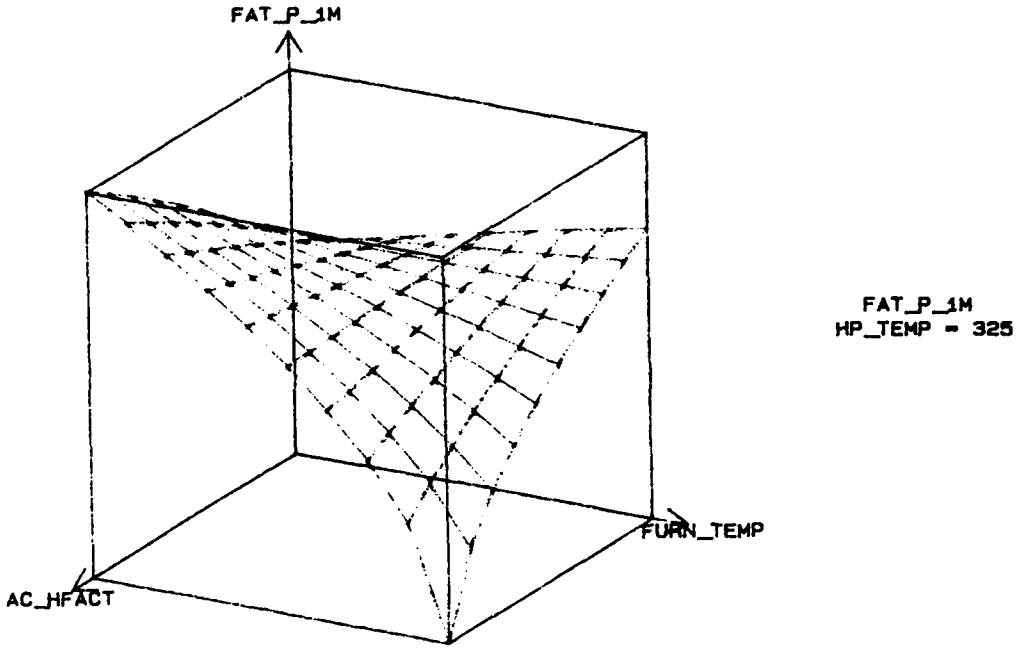


Figure 8 Three dimensional contour plot of the percent fatigue at constant hot plate temperature while varying the acid h-factor and furnace temperature.

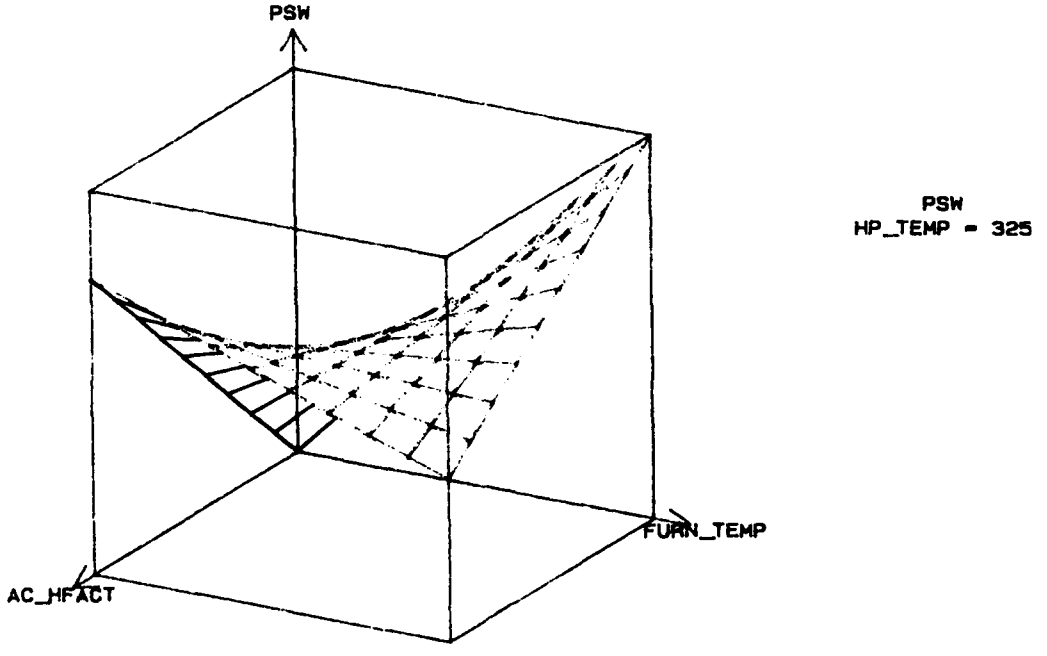


Figure 9 Three dimensional contour plot of the switching polarization at constant hot plate temperature while varying the acid h-factor and furnace temperature.

the response at two conditions; high acid h-factor/high furnace temperature, and low acid h-factor/low furnace temperature. Hot plate conditions which yield favorable percent fatigue between 1E6 and 1E8 are as follows: high acid h-factor and high furnace temperature at a hot plate temperature of 325°C or a low acid h-factor and low furnace temperature at a hot plate temperature of 400°C.

CONCLUSIONS

Statistical experimental design was used to obtain the maximum amount of information from a minimum number of samples. For the experimental design presented in this paper, the acid h-factor, furnace temperature, hot plate temperature and furnace ambient were the most significant factors as determined by screening experiments. Further response surface experimentation using a central composite design identified two optimum regions of operation. For a hot plate temperature of 325°C, a high acid h-factor combined with a high furnace temperature is recommended. For a hot plate temperature of 400°C, a low acid h-factor combined with a low furnace temperature is recommended.

This work has determined that, for memory applications using the process developed at the University of Colorado at Colorado Springs, sol-gel lead titanate should be processed under the following conditions:

1. Hot plate temperature = 325°C
2. Acid h-factor = 1.45
3. Furnace temperature = 625°C
4. Furnace ambient = O_2
5. H_2O h-factor = 1.5
6. Hot plate time = 60 seconds
7. Furnace time = 30 minutes.

REFERENCES

1. S. Wolf and R. N. Tauber, Silicon Processing for the VLSI Era, (Lattice Press, California, 1986), pp. 618-645.
2. S. K. Dey and R. Zuleeg, Ferroelectrics, 112, pp. 309-319 (1989).

LOW TEMPERATURE PROCESSING OF FERROELECTRIC THIN FILMS AND AMORPHOUS FERROELECTRICITY

REN XU, YUHUAN XU, AND JOHN D. MACKENZIE
Department of Materials Science and Engineering
University of California, Los Angeles, CA 90024

AD-P006 685

Abstract $LiNbO_3$ thin films on various substrates were fabricated from sol-gel process. Epitaxial growth of $LiNbO_3$ on sapphire(012), single crystal $LiTaO_3$(110) and single crystal $LiNbO_3$(001) were found. Water addition in the solution prior to film deposition was found to be unnecessary. Crystallization temperature was between 350°C and 450°C in air. Amorphous gel films stabilized at temperatures ranging from 25°C to 250°C at different Li/Nb ratios were also found to show P-E hysteresis loops. P_r and E_c values were in the same order of magnitude as those of single crystal $LiNbO_3$. Pyroelectric coefficients were measured. Auger and IR spectra were used to study the gel film composition and structure. X-ray and electron diffractions were used to confirm the amorphousness of these gel films. Amorphous ferroelectricity was used to account for these observations.

INTRODUCTION

Crystalline lithium niobate has attracted great interest in the past few decades because of its excellent ferroelectric, piezoelectric, acoustic, and electrooptic properties.[1] Conventional processing techniques include Czochralski method[2] for single crysstals and other thin film fabrication methods such as r.f. sputtering[3] and other techniques.[4] Sol-gel process has been applied to the lithium niobate thin film fabrications and highly oriented crystalline films were made at low temperatures.[5] These were led by investigations of solution structures and detailed analysis of the processing conditions.[6] Although the potential of epitaxial thin films of lithium niobate by sol-gel has been demonstrated,[5,7] little is known about the epitaxial relationship of this system with various single crystal substrates, nor is the epitaxial growth kinetics well understood. Water addition to the solution prior to film depositon often leads to instability and subsequent precipitaion or gelation. Therefore, stable solution or modified processing conditions are needed for viable control of its structure as well as the structure of the gel film, which in turn governs the crystallization process during heat-treatment.

92-16160

Amorphous ferroelectricity was first suggested by Lines[8] and partially experimentally demonstrated[9] on rapidly quenched $LiNbO_3$ and $LiTaO_3$ glasses, where a ferroelectric or ferroelectric like phase transitions were reported at temperatures below crystallization temperature. Other observations of ferroelectric or ferroelectric-like phase transition in $LiNbO_3$ and PZT systems[10-12] have been reported in the past where RF sputtering was also used to form amorphous films of these systems. However, there has been no report of P-E hysteresis loops and pyroelectric coefficients of these materials, mainly due to the difficulties in making these amorphous materials in large enough quantities and geometries suitable for measurements of properties. Despite these previous reports, the confirmation of amorphous ferroelectricicy still awaits more conclusive experiments. Observation of P-E hysteresis and improvement of processing technique are needed for this purpose.

In this paper we report briefly our initial attempt in utilizing sol-gel process to fabrications of both crystalline and amorphous ferroelectric thin films of the lithium niobate system. The sol-gel processing of crystalline $LiNbO_3$ resulted in nearly single crystal films, and the processing of amorphous lithium-niobium oxide system resulted in stable ferroelectric thin films that did not require heat-treatment temperature higher than 100 °C. Structural information was obtained from X-ray, electron diffractions, IR and Auger spectra. Reliability of these observations are discussed on the basis of complimentary experiments.

EXPERIMENTAL PROCEDURES

(1) Solution synthesis and gel film deposition

The crystalline ferroelectric thin films studied in this work were stoichiometric $LiNbO_3$, while the amorphous ferroelectric thin tilms were of four different compositions. As shown in Table 1, sample No.1 is stoichiometric and the same composition was used for both crystalline and amorphous film studies. Sample No.2 through No.4 were used for amorphous film studies.

Commercial lithium metal, 99.95% purity from Morton Thiokol, was used to react with absolute ethyl alcohol of appropriate volume to form $LiOC_2H_5$ solution and this was then mixed with commercial $Nb(OC_2H_5)_5$, 99.99% from Aldrich. The resulting solution was refluxed for 24 hours and then stored in dry atmosphere. Gel films were deposited onto various substrates by spin coating. H_2O were not added to the solution

TABLE 1 Summary of properties of amorphous ferroelectric thin films.

SAMPLE	No. 1	No. 2	No.3	No.4
Composition Li/Nb	1:1	1:2	1:3	0:1
Lithium Concentration (M)	0.500	0.167	0.125	0.000
Niobium Concentration (M)	0.500	0.333	0.375	0.500
Thickness (Å)	2100	2300	2560	2870
P_r ($\mu C/cm^2$)	10	14	9	18
E_c (kV/cm)	110	86	65	24
Refractive Indices	1.43	1.13	1.13	1.15
Pyroelectric Coefficient at 28 °C (nC/cm^2K)	24			8

for two reasons: (1) addition of water results in either precipitation or gelation in a relatively short period of time, while dry solutions are stable for months. (2) in the presence of ambient moisture at 50% relative humidity, full hydrolysis was estimated to take only less than a minute for a 6000 Å thick as-spun liquid film with 0.6 (M) lithium or niobium concentration. In other words, full hydrolysis is often accomplished during the spin coating process. Auger analysis of as-spun film showed less than 6% of the original alkoxy groups in $LiNb(OC_2H_5)_6$ remained in the gel film.

(2) Crystalline ferroelectric thin films

Gel films with the same composition as that of sample No.1 in Table 1. were coated on the following single crystal substrates: silicon (111), silicon (100), sapphire (012), $LiTaO_3$ (110) and $LiNbO_3$ (001). These films were heat-treated at 1 °C/min heating rate up to 450 °C in air for 5 hours. X-ray diffraction patterns are shown in Figure 1. It is readily seen that polycrystalline films of $LiNbO_3$ were formed on silicon (111) and

silicon (100). Highly preferentially oriented $LiNbO_3$ film was formed on sapphire (012). Nearly single crystal films were formed on $LiTaO_3$ (110) and $LiNbO_3$ (001).

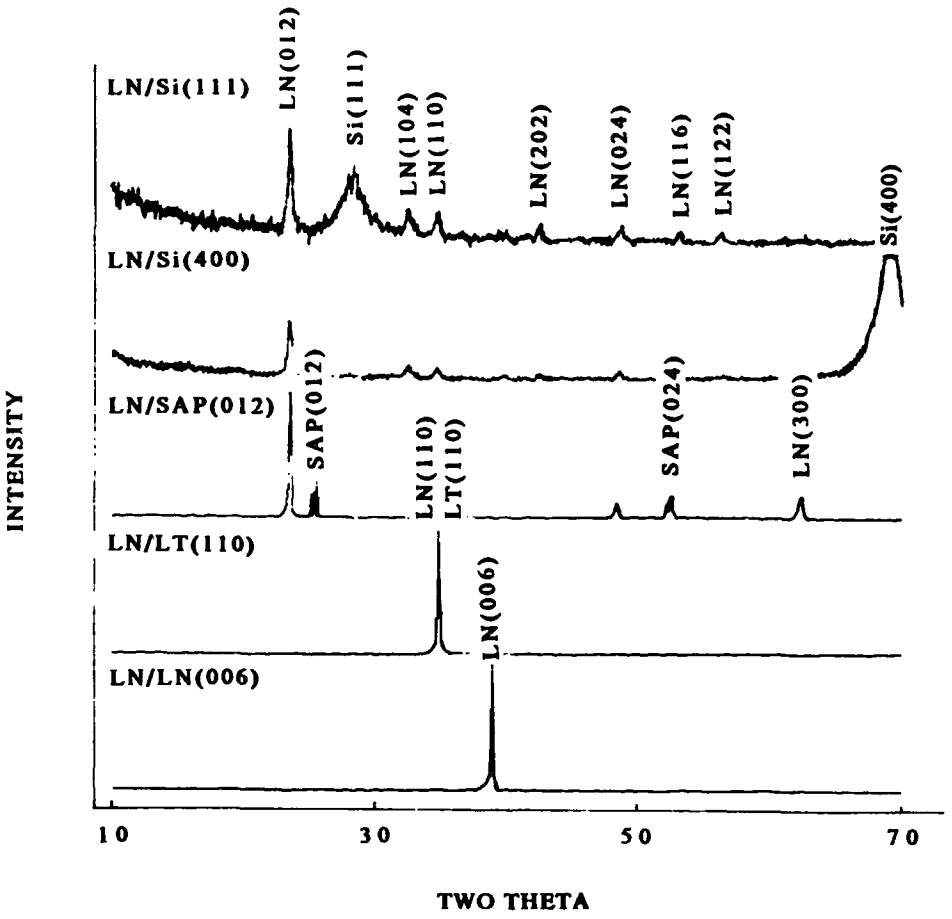


FIGURE 1 Epitaxial growth of $LiNbO_3$, heat treated in the same batch.

These epitaxial relationships are summarized in Table 2. Films deposited on silicon (111) and heat-treated up to different temperatures are shown in Figure 2., which shows that

TABLE 2 Epitaxial relations of $LiNbO_3$ on various single crystal substrates.

SINGLE CRYSTAL SUBSTRATES	silicon (111)	silicon (100)	Sapphire (012)	$LiTaO_3$ (110)	$LiNbO_3$ (001)
XRD Peaks of Substrates	(111)	(400)	(012)	(110)	(006)
XRD Peaks of $LiNbO_3$ film	poly-crystalline	poly-crystalline	(012),(300)	(110)	(006)

the crystallization temperature in our process was between 350 °C and 450 °C.

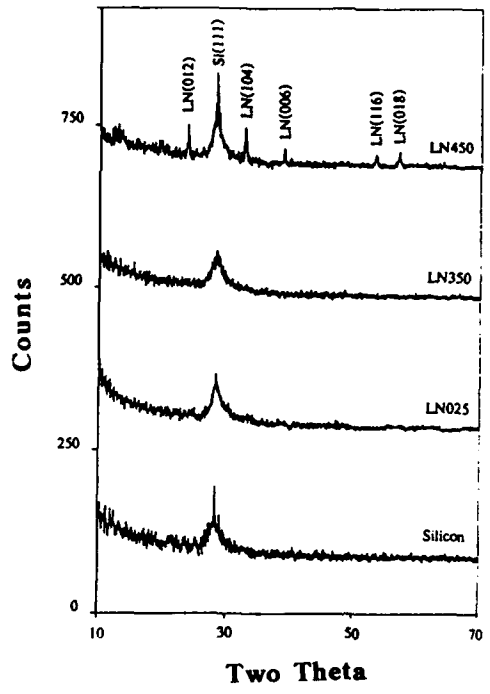


FIGURE 2 X-ray diffraction patterns of films deposited on silicon (111) and heat-treated to different temperatures.

(3) Amorphous ferroelectric thin films

The amorphous gel films with starting compositions shown in Table 1, samples No. 1

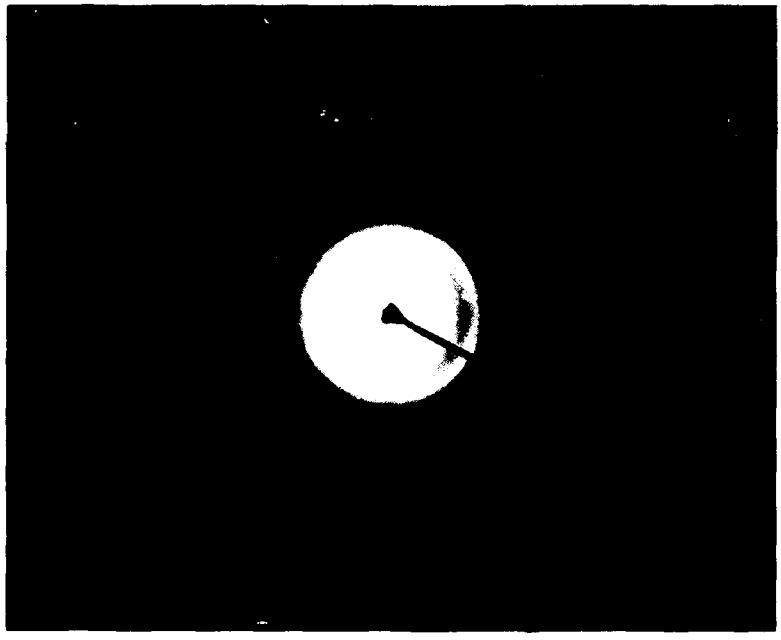


FIGURE 3 Electron diffraction pattern of sample No. 1.

through 4, were deposited on Au passivated silicon wafers and stabilized at 100 °C in air for 2 hours. X-ray diffraction showed that these were amorphous. Electron diffraction of sample No.1 is shown in Figure 3, where diffused rings also indicate the amorphous nature of the film. High resolution electron microscopy also confirmed that no crystallites with size larger than 20 Å were observed.[13] Auger profile, as shown in Figure 4, of the film stabilized at 200 °C in air for 1 hour showed nearly stoichiometric compositions with very small amount oxygen defficiency and minute residual carbon.

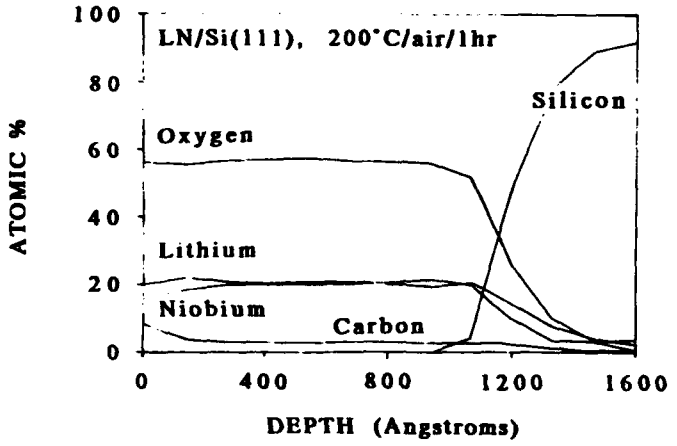


FIGURE 4 Auger compositional profile of the film stabilized at 200 °C in air for 1 hour.

Nominal formula of this film was found to be $Li_{1.01}Nb_{0.99}(OC_2H_5)_{0.06}O_{2.75}$. The exact cause of the oxygen defficiency is not clear. IR spectra of the room temperature

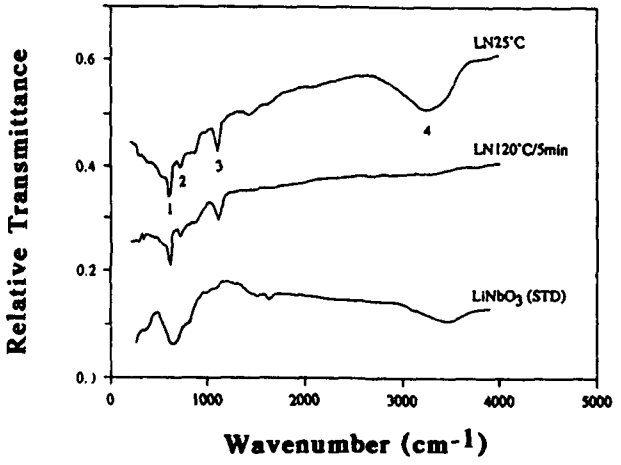


FIGURE 5 IR spectra of sample No. 1 on silicon (111), double side polished, stabilized at different temperatures.

film of sample No.1 and the same film stabilized at 120 °C for 5 minutes, both deposited on double side polished silicon wafers, are shown in Figure 5. IR spectrum of $LiNbO_3$ crystal dispersed in KBr pellet is also shown in Figure 5 for comparison. Absorption 1 and 2 are attributed to the vibrations of Nb-O octahedron.[14] Absorption 3 is attributed to the streching mode of C-O bond, while absorption 4 is the contribution of H-O bond from wither HOC_2H_5 or H_2O. Comparison between these three spectra suggested the similarity in the local atomic arrangements in these samples.

Electrical characterizations were conducted with a Pt/gel film/Au sandwitch structure. A modified Sawyer-Tower bridge was used for P-E hysteresis loop measurements. Dielectric measurements were made with an HP-4192A impedence analyser.

Figure 6 (a) through 6 (d) show the hysteresis loops of gel films No.1 through No.4 coated on Au passivated silicon wafers. Data are summarized in Table 1. P_r and E_c values were found to be in the same order of magnitude of those of single crystal $LiNbO_3$. Pyroelectric coefficients of samples No.1 and No.4 were measured and detailed disscussions will be published separately.[15]

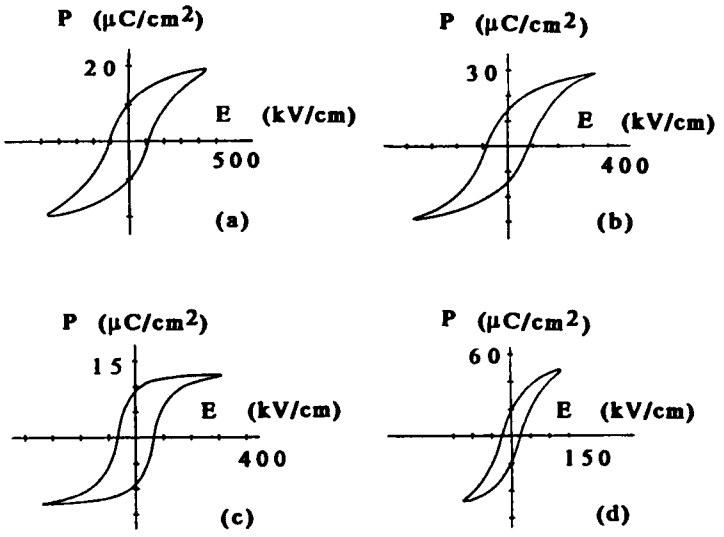


FIGURE 6 P-E hysteresis loops of sample No.1 through No.4 coated on gold, measured with a modified Sawyer-Tower bridge at 50 Hz.

The above observations strongly suggest that the observed P-E hysteresis behavior was due to amorphous ferroelectricity. Samples No.1 through No.4 have different lithium to niobium ratios and deviation from $LiNbO_3$ stoichiometry indicates that the P-E hysteresis did not pertain only to stoichiometries known to give rise to crystalline

ferroelectricity. In order to exclude any possible complications of interface effects between gel film and the substrates, ground powder of bulk gel was used to independently confirm the hysteresis loops. In this experiment, ground dry gel powder with composition same as sample No. 1 was heat-treated as 100 °C in air for 2 hours. X-ray diffraction was conducted to confirm the amorphousness of the gel powder after heat treatment. The gel powder was then dispersed in acetone and droped on to polished surface of copper plate. A second copper plate was then pressed on to the other side of the powder layer and hysteresis loops were recorded from such sample. This indicates that the observed hysteresis loops were not the result of any interface effect. Another independent experiment was conducted to estimate the characteristic Maxwell relaxation time of the 100 °C stabilized gel film coated on fused quartz by measuring its dielectric constant and electrical conductivity. The electrical conductivity was measured to be 10^{-6} Ω^{-1}-cm^{-1}, and dielectr4ic constant was 5. The relaxation time was estimated to be well in the order of 10^4 second. This is in sharp contrast with the frequency used in the hysteresis loop measurements, which was 50 Hz and some up to 12 kHz. Therefore, the hysteresis loops could not be caused by the very slow space charge effect or electronic charge effects for the very indulating films in this study. The organic content as determined by Auger profile was less than 6% for room temperature films and no more than 1% for films stabilized at 200 °C in air for 1 hour. Therefore, it was our conclusion that the residual organic groups could not have contributed to the overall observed polarizations.

Structurally we proposed[16] the importance of highly distorted metal-oxygen polyhedra which are probably the predominate structure in the amorphous gel films. This distortion, random in both magnitude and orientation, allows the existence of permenant electric dipoles pointing in random directions. These dipoles are separated from each other for less than 10 Å, smaller than the typical coherent length of 10 to 500 Å for ferroelectrics[17], and each individual dipoles are reversible, hence giving rise to ferroelectricity in the amorphous phase.

Similar observations were made on amorphous $BaTiO_3$, $Pb(Zr_{0.9}Ti_{0.1})O_3$ and $(Sr_{0.61}Ba_{0.39})Nb_2O_6$. Qualitative hysteresis loops of these systems were recorded.

CONCLUSIONS

In this work we have reported the epitaxial relationship of crystalline $LiNbO_3$ with various single crystal substrates. The processing conditions were different from

previously reported. Water addition seem to be unnecessary and the stability of the solution can be significantly enhanced by avoiding water addition.

We have established the feasibility of using sol-gel method to fabricate amorphous ferroelectric thin films for the first time. Quantitative P-E hysteresis loops of an amorphous ferroelectric material was observed also for the first time. In combination with the pyroelectric current measurement, which confirms the persistence of the polarized state, and the complimentary experiments of gel powder and Maxwell relaxation time, we conclude the existance of amorphous ferroelectricity. The successful application of sol-gel technique permits fabrication and stabilization of ferroelectric materials at near room temperatures. The low processing temperature in turn allowed deposition of ferroelectric thin films on a much larger variety of substrates than before. The independence of the chemical composition of the amorphous ferroelectric materials suggests a significantly broader range of oxide systems as possible candidates for the amorphous ferroelectric materials, thus allowing the fabrication not only of lthe amorphous counter part of known crystalline ferroelectrics, but also of amorphous oxides not known as ferroelectric in their crystalline form. The compositional deviation of mixed-oxide amorphous ferroelectrics from the crystalline stoichiometry would provide oppotunities for fin-tuning the various interdependent properties of thin films.

ACKNOWLEDGEMENT

The authors acknowledge Mr. C. H. Cheng, Mr. N. Desimone and Y. H. Kao for their help in some of the experiments, Professor L. Eyring and Dr. Z. C. Kang for their help in HREM experiments. This work was sponsored by the Air Force Office of Scientific Research, Directorate of Chemical and Atmospheric Sciences under grant No. AFOSR-88-0066.

REFERENCES

1. M. M. Abouelleil and F. J. Leonberger, J. Am. Ceram. Soc., 72 [8], 1311-21 (1989).
2. S. Abrahams, H. Levinstein and J. Reddy, J. Phys. Chem. Solids., 27, 1019-26 (1966).
3. S. Takada, M. Ohnishi, H. Hayakawa and N. Mikoshiba, Appl. Phys. Lett., 24 [10], 490-92 (1974).
4. P. K. Tien and A. A. Ballman, J. Vac. Sci. Technol., 12 [4], 892-904 (1975).
5. S. Hirano and K. Kato, Mat. Res. Soc. Symp. Proc., 155, 181-90 (1989).

6. S. Hirano and K. Kato, Adv. Ceram. Mater., 2 [2], 142-45 (1987).
7. D. P. Partlow and J. Greggi, J. Mater. Res., 2 [5], 595-605 (1987).
8. M. E. Lines, Phys. Rev. B15, 388-95 (1977).
9. A. M. Glass, M. E. Lines, K. Nassau and J. W. Shiever, Appl. Phys. Lett., 31 [4], 249-51 (1977).
10. T. Mitsuyu and K. Wasa, Japan. J. Appl. Phys., 20, L48 (1981).
11. M. Kitabatake, T. Mitsuyu and K. Wasa, J. Non-Cryst. Solid., 53, 1-10 (1982).
12. H. Engelmann, N. Kraemer and U. Gonser, Ferroelectrics, 100, 127-34 (1989).
13. R. Xu, Z. C. Kang, L. Eyring and J. D. Mackenzie, to be published.
14. J. D. Axe and D. F. O'Kane, Appl. Phys. Lett., 9, 58 (1966).
15. Y. H. Xu, R. Xu and J. D. Mackenzie, to be published.
16. R. Xu, Y. H. Xu and J. D. Mackenzie, submitted to Phys. Rev. B.
17. W. N. Lawless and A. M. Glass, Ferroelectrics, 29, 205-208 (1980).

AD-P006 686

CHEMICAL ASPECTS OF Pb-Zr-Ti OXIDE THIN FILM SYNTHESES BY PE-MOCVD BELOW 500°C

WILLIAM T. PETUSKEY and DAVID A. RICHARDSON
Department of Chemistry, Arizona State University, Tempe, AZ 85287-1604

SANDWIP K. DEY
Department of Chemical, Bio & Materials Engineering and Center for Solid State Electronics Research, Arizona State University, Tempe, AZ 85287-6006

Abstract The general features of the chemistry in synthesizing lead zirconium titanate thin films by PE-MOCVD are discussed based on a preliminary experimental investigation. A qualitative model was constructed as a guide for optimizing the formation of the perovskite phase in the as-deposited condition. This was based on concepts of crystal chemistry of the perovskite and pyrochlore structures and the observed deposition kinetics. Currently, thin films containing up to 92 vol % perovskite have been formed below 500°C in the as-deposited condition. Sufficient latitude remains in adjusting the operating parameters that the formation of phase pure perovskite is considered possible. A thermodynamic analysis of the solid state suggests that low temperature thermal equilibration will yield minority lead-rich phases. Consequently, nonequilibrium processing techniques such as plasma processing are considered necessary. Ferroelectric hysteresis was observed for films receiving post deposition anneals.

INTRODUCTION

The purpose of this paper is to discuss several issues of the chemistry in synthesizing thin films of the perovskite structured $Pb(Zr,Ti)O_3$ (or PZT) by plasma-enchanced, metal organic chemical vapor deposition (PE-MOCVD). The observations and conclusions presented are based on a combination of thermodynamic and preliminary experimental studies. Details of the latter are presented elsewhere[1,2]. We discuss here what we consider as the important characteristics in solid state chemistry, precursor chemistry and the processing parameters which control the formation of the perovskite phase in the as-deposited condition. Based upon observed experimental trends, an understanding is emerging on the conditions that are necessary for forming a phase pure perovskite. Several simple mechanistic explanations are offered based on crystal chemistry and reaction kinetics. Some of these concepts may be applicable to other fabrication techniques such as sputter deposition, e-beam deposition, laser ablation, etc.

At this early stage of research, the models and conclusions presented are preliminary and are subject to further investigation. We are primarily concerned with phase chemistry

92-16161

rather than microstructural development since without 100% of the perovskite phase, the ferroelectric properties and microstructure of these films are of little significance. Nevertheless, several details of microstructure are discussed. We also demonstrate ferroelectric hysteresis in films that have received a post-deposition anneal.

The emphasis is on forming thin-film perovskite structures below 500°C since, for the applications intended, it is desirable to avoid excessive heating of the underlying semiconductor substrate[3]. Such low temperatures may be a disadvantage for alternate fabrication processes because of the sluggishness of various reactions. This may be overcome for gas phase reactions using plasmas induced by radio-frequency coupling (13.56 MHz). Compared to thermal decomposition processes, a 10 to 40 fold increase in deposition rates can result due to the plasma. This effect is equivalent to raising the temperature of the reaction without substantially raising the temperature of the substrate. In addition, the interaction of a plasma with solid interfaces will likely stimulate surface relaxation processes. We observe that the perovskite content of the thin films is greatly influenced by the plasma power which is probably related to structural rearrangements on the solid surface. Thus, plasma power density becomes an important experimental control in achieving 100% perovskite at low temperatures.

BACKGROUND

Impetus for Research

The driving force for this work is to develop a reliable and consistent technology for synthesizing thin films of complex oxide compounds of a wide range of compositions. One interesting class of materials are based on the oxygen octahedral network represented by such structures as perovskites and tungsten bronzes. Such materials as $LiNbO_3$, $BaTiO_3$, $(Pb,La)(Zr,Ti)O_3$ (i.e., PLZT) and $(Sr,Ba)Nb_2O_6$ (i.e., SBN) are attractive for their appealing physical properties such as high permittivities, large electromechanical coupling coefficients, ferroelectricity, pyroelectricity and electro-optic effects[4,5]. In particular, $Pb(Zr,Ti)O_3$ (or PZT) thin films are being evaluated for a variety of applications including non-volatile computer memories, neural network components and integrated capacitors[6-8]. The success of these is contingent on developing a reliable thin-film technology which is IC compatible.

There are other capable techniques emerging which may meet these needs. Within our research group, work on thin films produced by polymeric solution-gelation (sol-gel) have shown promise[9,10]. Dense, crack-free ferroelectric films of $Pb(Zr_{0.52}Ti_{0.48})O_3$

have been produced on 3 inch diameter Pt-passivated silicon substrates at temperatures as low as 550°C. The dense microstructure shown in Fig. 1 represents what is currently possible. Very good electrical properties have been obtained on films 0.5 μm thick (residual polarizations of P_r = 29-32 μC/cm^2, switched polarization of P_{sp} = 44-53 μC/cm^2 and coercive fields of E_c = 50-60 kV/cm). Switching times less than 3 ns have been observed for 30 X 30 μm^2 capacitors. However, despite these successes, CVD and, particularly, PE-MOCVD may offer additional advantages.

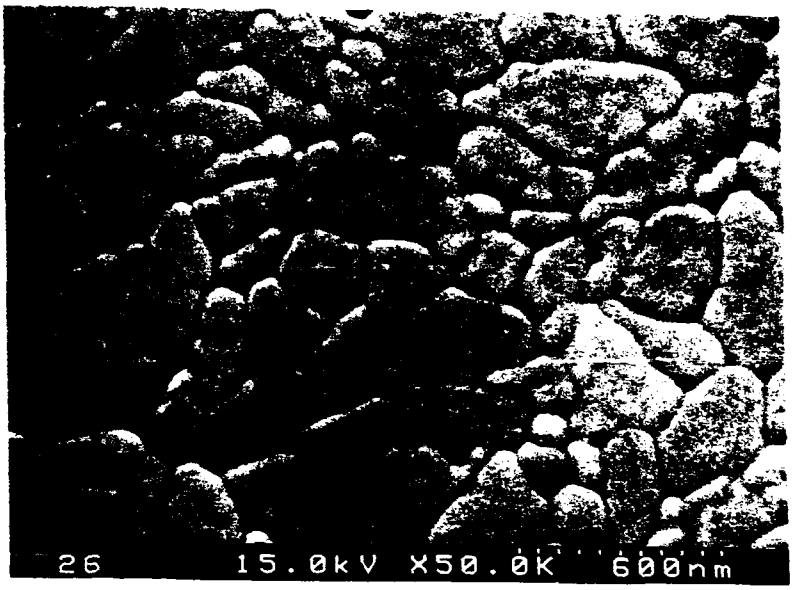


Figure 1. Microstructure of dense thin film of $Pb(Zr_{0.52}Ti_{0.48})O_3$ on Pt passivated silicon substrate. Film was fabricated by sol-gel synthesis and represents what is possible by alternative synthetic techniques.

Chemical vapor deposition has a demonstrated routine utility in the microelectronics and integrated optics industries[11]. Aside from SiO_2, CVD is usually employed for processing nonoxide semiconductor materials. Inherent advantages include high purity, low processing temperature, short processing cycle and excellent control of composition, thickness and lateral film homogeneity. In general, CVD may also offer high quality, conformal step coverage. The current challenge for PE-MOCVD is to prove these advantages for fabrication of PZT thin films.

To our knowledge, this is the first study to use rf-plasma to assist in the decomposition reactions for making PZT thin films. However, recently, there have been several investigations of thermal CVD. An early investigation of Kojima, et al[12] used volatile chlorides of lead, zirconium and titanium to produce films between 400 to 800°C. Unfortunately, the ferroelectric properties of their films were compromised by dissolved chlorine. Recent investigations have relied on commercially available metal organic compounds as volatile precusors and found them more suitable for low temperature synthesis. Many of these have concentrated on $PbTiO_3$[13-17] and only recently on the more complex PZT system[18].

Phase Thermochemistry

In approaching a new chemical system for synthesis by CVD, it is valuable to theoretically examine the solid state equilibria in terms of parameters that can be controlled or measured. Thermodynamic calculations allow the most stable state to be specified in terms of temperature, composition and partial pressures. If experimental results comply with thermodynamic predictions then the calculations provide a useful tool for predicting the outcome of experiments On the other hand, if there is a deviation, comparisons between results and calculations allows the nature of reaction mechanisms to be studied. This has been used successfully for various CVD reactions such as on nonoxide ceramics[19].

A particularly useful manner for presenting thermodynamic data for solid oxide systems are stability diagrams which plot the ranges of stability of solid phases as a function of oxygen partial pressure and cation composition. Both parameters are controllable in a thermal CVD reactor. Figure 2 plots the stability fields for solids in the Pb-Zr-Ti-O system at 480°C and with a fixed Zr:Ti ratio of 53:47. The vertical lines and shaded fields correspond to the single phases whereas the open fields refer to two and three phase equilibria.

Figure 2 was calculated for 480°C using a modified version of the computer program SOLGASMIX-PV[20] and thermodynamic data obtained from a variety of literature sources[21,22]. A number of approximations were required, however, which affects somewhat the accuracy of the diagram. First, of the two titanium zirconate compounds, Ti_2ZrO_6 has been identified as the low temperature phase although its stability has not been experimentally verified below 800°C[23]. Its stability at 480°C is simply assumed here. The free energy of forming Ti_2ZrO_6 was obtained using an enthalpy of formation of -3,010 kJ/mol which was estimated from the enthalpies of formation for the

component oxides TiO_2 and ZrO_2 and assuming a stabilization of about -27 kJ/mol. The latter accounts for 0.9% of the total free energy of formation which was judged to be reasonable considering the modest structural differences relative to TiO_2 and ZrO_2. An entropy of formation was assumed to be equal to the geometrical sum of those of the binary oxides (-558 J/mol·K). The free energy of forming $PbTi_3O_7$ was approximated by optimizing enthapy (-3,043 kJ/mol) and entropy (-575 J/mol·K) of formation so that it was consistent with the low temperature phase equilibria reported by Eisa, et al[24].

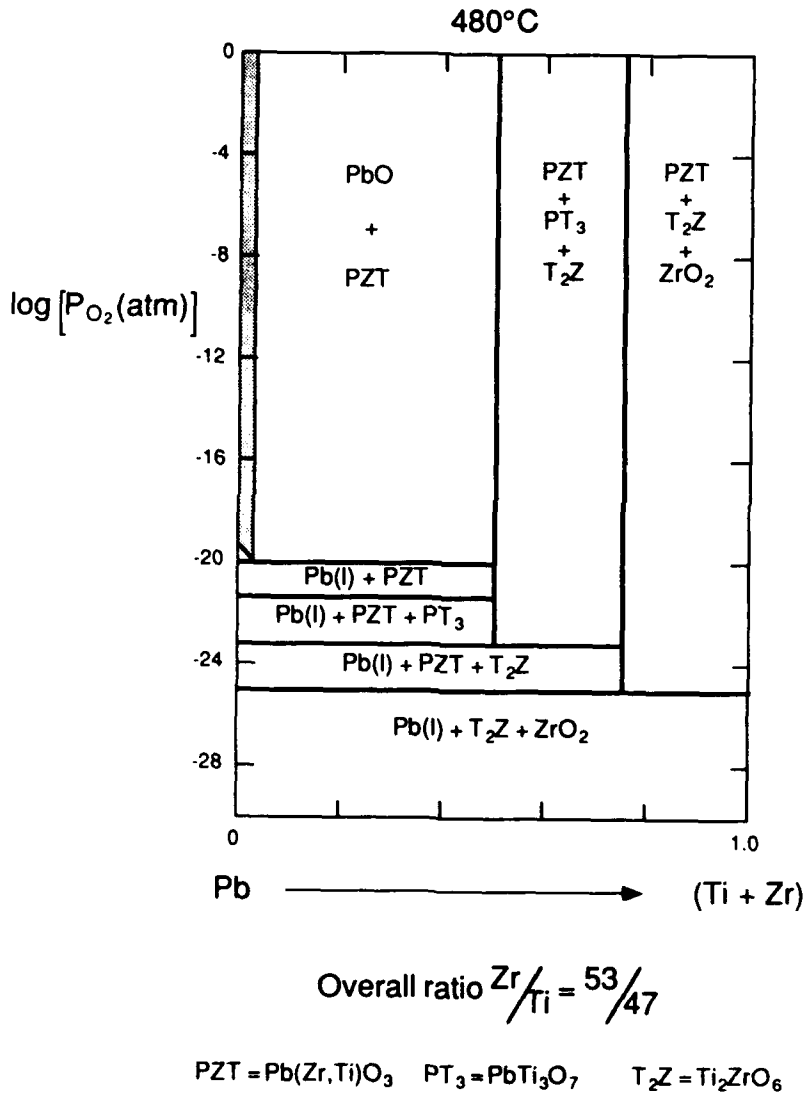


Figure 2. Calculated phase stability diagram for the Pb-Ti-Zr-O system at 480°C and a fixed ratio of Zr/Ti = 53/47 (morphotropic composition). Phase fields represent the thermodynamically most stable combination of solid phases as a function of the system cation composition and oxygen partial pressure. Calculations assumed that the pyrochlore phase was metastable for all compositions.

Only two solid solutions were thought to be of importance at 480°C, namely, $Pb(Zr,Ti)O_3$ and (Pb,Ti)O. Lacking any specific thermodynamic data, both were assumed to be ideal solid solutions relative to their pure end members. The resulting errors are expected to be small considering the large range of oxygen activities shown on the diagram. In addition, the solubility of TiO_2 in PbO is small and, therefore, has little effect on the final appearance of the diagram.

One serious concern in evaluating Fig. 2 is the omission of a "pyrochlore" phase. Several investigations on the low temperature synthesis of PZT compounds indicate the formation of a "pyrochlore-like" structure that appears over a wide range of compositions[25,26]. It seems to be metastable for most compositions since subsequent annealing causes transformation to other phases. However, it does not seem to transform easily, or even at all, for lead poor compositions where the cation fraction $X_{Pb} < 0.42$. Although this may indicate that it is thermodynamically stable under some conditions, without more definitive information, it is assumed to be metastable for all conditions. Therefore, the pyrochlore does not appear in these calculations.

In general, the perovskite structured PZT is stable at high oxygen partial pressures above about 10^{-25} atm O_2 (10^{-20} Pa). The vertical line near the center of the diagram indicates the homogeneous phase is stable. It coexists with PbO for high concentrations of lead and with $PbTi_3O_7$, Ti_2ZrO_6 and ZrO_2 for successively smaller amounts of lead. At low oxygen partial pressures, it equilibrates with liquid lead.

The zirconium and titanium fractions in the perovskite phase was also calculated as a function of oxygen partial pressure for the various multiphase equilibria shown in Fig. 2. Note that the perovskite composition does not necessarily reflect the cation ratios as that for the entire system (i.e., Zr/Ti = 53/47), since other phases may co-exist. Figure 3 summarizes those compositions for three different regimes of lead content. For high lead contents, the perovskite is slightly zirconium rich relative to the morphtropic composition PZT 53/47 because PbO has the capacity to dissolve small amounts of titanium oxide. This implies that perovskites with precisely the morphotropic composition cannot be attained at thermal equilibrium. It is only at low oxygen partial pressures in the range of about 10^{-20} to 3×10^{-22} atm O_2 that the perovskite composition of $Pb(Zr_{0.53}Ti_{0.47})O_3$ would appear to be stable by itself with no other phase. At successively lower oxygen partial pressures, the composition of the perovskite shifts increasingly to the zirconium rich side, where $PbZrO_3$ is the most stable perovskite composition at the lowest oxygen pressure.

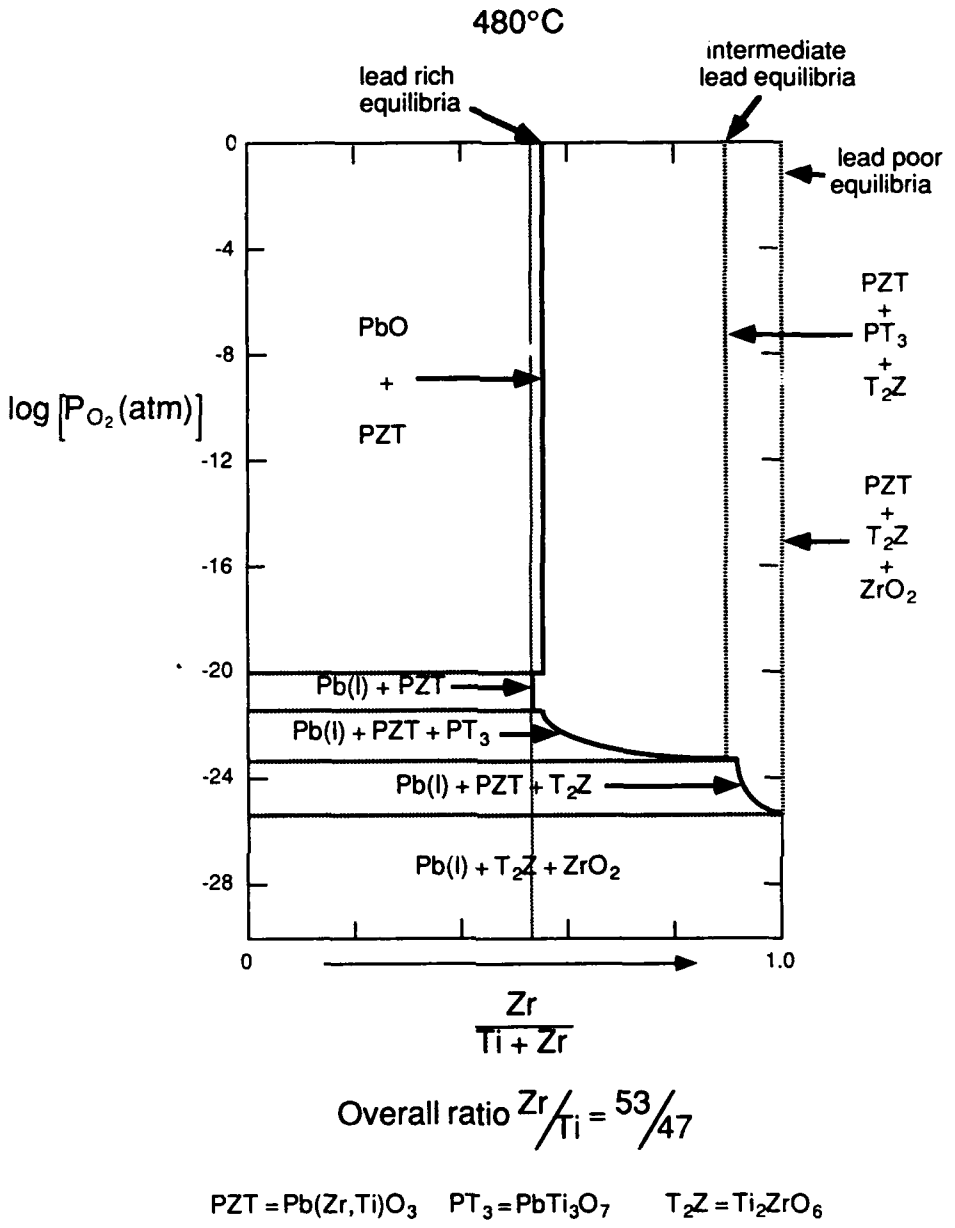


Figure 3. Relative fraction of zirconium, x, of perovskite phase, $Pb(Zr_xTi_{1-x})O_3$, in equilibrium at 480°C with various phases as a function of oxygen partial pressure. Corresponds to calculated stability diagram shown in Fig. 2 for three different composition regimes for lead, i.e., lead rich, intermediate lead and lead poor compositions.

These results suggest that it may be desirable to rely on synthetic techniques which avoid thermodynamic equilibration of the solid phases with oxygen in the gas phase.

This would be necessary in order to obtain single phase perovskites with the morphotropic composition. Most CVD reactions on this system are typically carried out between 10^{-4} to 1 atm O_2. The consequence is to produce minor quantities of a lead rich phase in contact with the perovskite if the process is entirely thermally driven. Therefore, plasma assisted CVD may reveal an additional advantage since the injection of rf energy greatly upsets the system chemistry from approaching a quasi, thermal equilibrium state.

EXPERIMENTAL SET-UP

Details of the experimental work leading to this presentation are described elsewhere[1,2], however, it is useful to review some of the special characteristics of the reactor system used. Figure 4 illustrates three cabinets housing the primary functions of the CVD apparatus. The gas reactant injection system consists of four mass flow controllers which control the supply rates of oxygen and argon. The argon gas streams are directed through bubblers containing the liquid precursors for lead, titanium and zirconium. Since the vapors of these metal organic compounds do not saturate their gas carriers in general, their concentrations were determined via a gravimetrically calibrated procedure.

The reactor cabinet consists of a furnace, the reaction chamber through which the gas reactants are conducted, rf-plasma generation equipment and susceptor. The substrate sits on a quartz platform within a quartz reaction tube (7.0 cm inner diameter, 92 cm length). This platform is itself a closed end quartz tube which isolates the graphite susceptor, rf-antenna and matching network from the reactants and substrate. The susceptor, which is connected to the end of the antenna, is radiatively heated by twelve quartz lamps (400 V, 4600 W each) arrayed parallel to the reaction tube. Substrates can be controllably heated from room temperature to greater than 1600°C.

The gas reactants were conducted individually through separate lines in a water cooled, stainless steel injector to prevent their premature, thermal decomposition. They were combined prior to the injection into the plasma, at a distance of about five centimeters from the substrate surface. To prevent premature plasma-assisted precursor decomposition, a special nozzle was designed to prevent the plasma from penetrating into the injector and down the gas lines. The plasma was generated using a 13.56 MHz frequency generator and matching network which could be tuned to minimize reflected power, that normally was no greater than 1 W. Forward plasma powers between 20 to 30 W were typically used for this study. The plasma was mostly contained in an effective

volume of about 250 cm^3 formed between injector and susceptor, because the injector was electrically grounded.

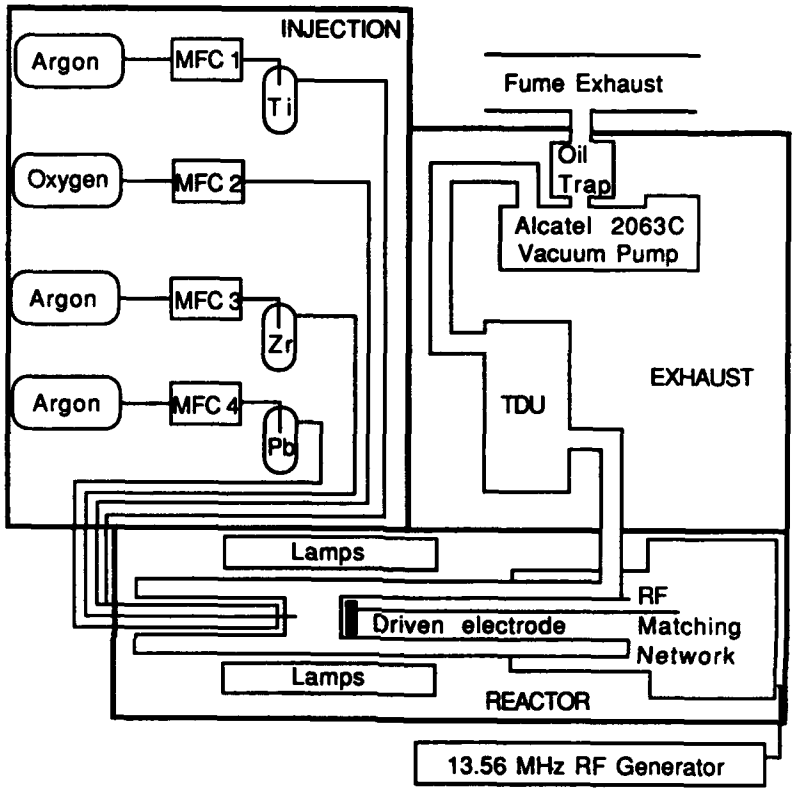


Figure 4. Schematic arrangement of PE-MOCVD apparatus which is comprised of three primary cabinets; the gas reactant injection system, the reactor with quartz lamp furnace and plasma generator, and the pumping and exhaust system.

The gas products were directed from the reactor to the pumping and exhaust cabinet through particle filters, an automatically controlled throttling valve for maintaining constant pressure, a thermal decomposition unit (TDU) for removing undecomposed toxic components and the vacuum pump. The pump itself was charged with perfluoro polyether oil (PFPE) appropriate for oxygen service and capable of pumping at a rate of 50 cfm.

Initial experimental results were found to be sensitive to the geometry and dimensions of the reactor. Therefore, great care was taken in maintaining these variables constant throughout this study.

Precursors

The precursors used include the tertiary butoxides of titanium and zirconium, tetraethyl lead, and oxygen, i.e., *tert*- $Ti(OC_4H_9)_4$, *tert*- $Zr(OC_4H_9)_4$, $Pb(C_2H_5)_4$ and O_2. Argon was used as a carrier for each of the metal components. The first three are liquid at ambient temperatures and exhibit convenient ranges of vapor pressures for CVD as shown in Fig. 5. The vapor pressures of the two *tert*- butoxides at room temperature and TEL at 0°C are similar, at about 0.06 torr, which is useful for controlling the supply of reactants. In the following paragraphs, some of the pertinent characteristics and systhesis procedure of these precursors are discussed. However, more thorough description of their characteristics are given in reviews by Bradley[27] for the metal alkoxides and Shapiro and Frey for TEL[28].

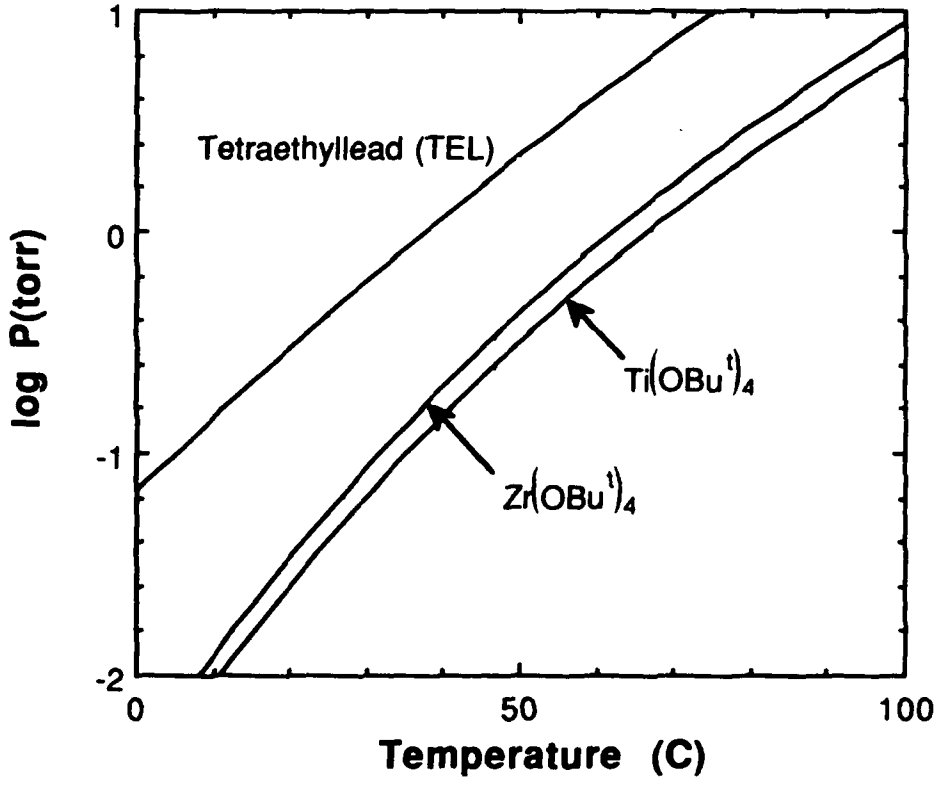
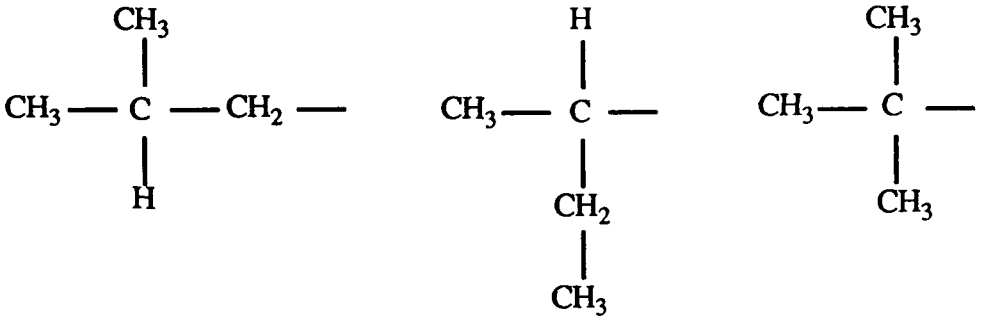


Figure 5. Vapor pressures of liquid precursors as a function of temperature.

The tertiary butoxides of zirconium and titanium exhibit the highest vapor pressures of the alkoxide series principally because they exist as monomeric species. Unlike *n*-,

iso- and *sec*-butoxides, intermolecular coordination is low due to steric hindrances. The configuration of the carbon and oxygen atoms in a butoxy group, as illustrated below,



isobutyl *sec*- butyl *tert*- butyl

essentially shields the oxygen atom from interacting with metals of neighboring molecules. This is particularly effective for tetravalent transition metals such as $Ti(OBu^t)_4$ and $Zr(OBu^t)_4$ where the surrounding arrangement of twelve methyl groups is quite dense. Another reason for the high vapor pressures of these butoxides is their low molecular weights relative to the other tertiary alkoxides. The butoxide is the smallest tertiary group possible.

The butoxides of titanium and zirconium were synthesized in our laboratory using the procedures outlined by Mehrotra[29]. The process begins with an alkoxide, such as an ethoxide or *iso*-propoxide, and an organic ester, such as *tert*- butyl acetate. The alkoxy group is exchanged yielding the *tert*- butoxide according to the reaction

$$M(OR)_4 + 4CH_3COOR' \Rightarrow M(OR')_4 + 4CH_3COOR \qquad (1)$$

where R refers to either ethyl or isopropyl and R' refers to *tert*- butyl. The reaction is driven to completion by fractionating out the volatile ester product. After a final distillation step, the *tert*-butoxide obtained was quite pure (>99%). The purity could be measured from ^1H NMR (300 MHz) spectra by the dominance of the *tert*- butyl protons (chemical shift, $\delta = 1.201$ ppm) over protons associated with organic impurities. Yields for this process varied from 20 to 85% of theoretical depending on whether the reaction began with ethoxide or *iso*-propoxide precursors, respectively.

As concerns volatile lead sources, tetraethyllead (TEL) was considered best for a number of reasons. Although at room temperature, its vapor pressure of 0.410 torr is nearly an order of magnitude greater than those of titanium and zirconium sources, it is a more practical choice relative to most other alternatives. However, its vapor pressure at

0°C is comparable to that of $Ti(OBu^t)_4$ and $Zr(OBu^t)_4$. The vapor pressure of tetramethyllead is excessively high at 40 torr and is considerably more difficult for safe handling. The vapor pressures of most oxyorganolead compounds is quite low.

Synthesis of volatile organolead compounds is hazardous due to their toxicity. Consequently, TEL was chosen as a lead source since it was desirable to reduce the number of steps necessary for purification prior to its introduction into the CVD reactor. TEL was obtained commercially (E.I. du Pont de Nemours & Co.) in the form of a 10 wt % solution in 2,2,4 trimethylpentane (for safer transport) and purified by a carefully controlled vacuum distillation procedure. (The importance in taking necessary safety precautions in distilling TEL cannot be overemphasized.) After a two stage distillation process, the purity was checked by ^1H NMR (300 MHz) where TEL is identified by a single strong peak (chemical shift, δ = 1.41 ppm)[28].

RESULTS & DISCUSSION

Our discussion focuses on explaining the variations in perovskite content found in the films. It was found to depend on the substrate, deposition rate, gas composition and plasma power. These are discussed at length in following sections but, prior to that, the operating conditions and some general characteristics of the films are described.

General Characteristics of Films

The typical operating conditions for PECVD experiments are outlined in Table I. A series of experiments were conducted for three different pressures, that is, 1000, 310 and 160 mtorr. As expected, a decrease in pressure was found to suppress the deposition rate due to lower reactant concentrations. Interestingly, the percentage of the perovskite phase was found to increase correspondingly which is discussed later. Film deposition was carried out on silicon substrates with and without platinum passivation layers. Orientation of the silicon was on the (111) planar surface. Deposition times ranged from 50 to 140 minutes which, depending on the operating conditions, yielded films anywhere from 0.5 to 12.5 μm thick. Thermal decomposition of gases without plasma gave significantly lower deposition rates. The phase content of the films were determined from x-ray diffraction peak intensities. This yielded semiquantitative values which were useful for comparative analysis. The compositions of the films were determined reliably by electron probe microanalysis since they were sufficiently thick.

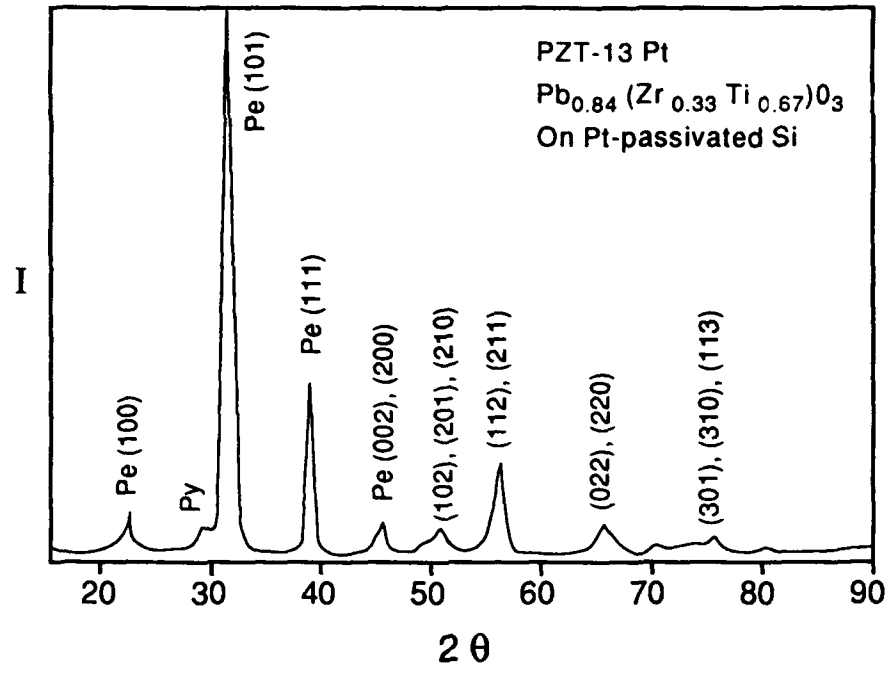
Table I. General process parameters for PE-MOCVD of PZT

Substrate temperatures:		425-495°C
Pressures:		160, 310, 1000 mtorr
Deposition times:		50-140 min
RF Power (forward):		20 or 30 W
(reflected):		1 W
Gas flow rates:	Ti carrier	4-15 sccm
	Zr carrier	1-10 sccm
	Pb carrier	2-10 sccm
	O_2	10-300 sccm
Source temperatures:	Ti	24°C
	Zr	24°C
	Pb	0°C
	O_2	24°C

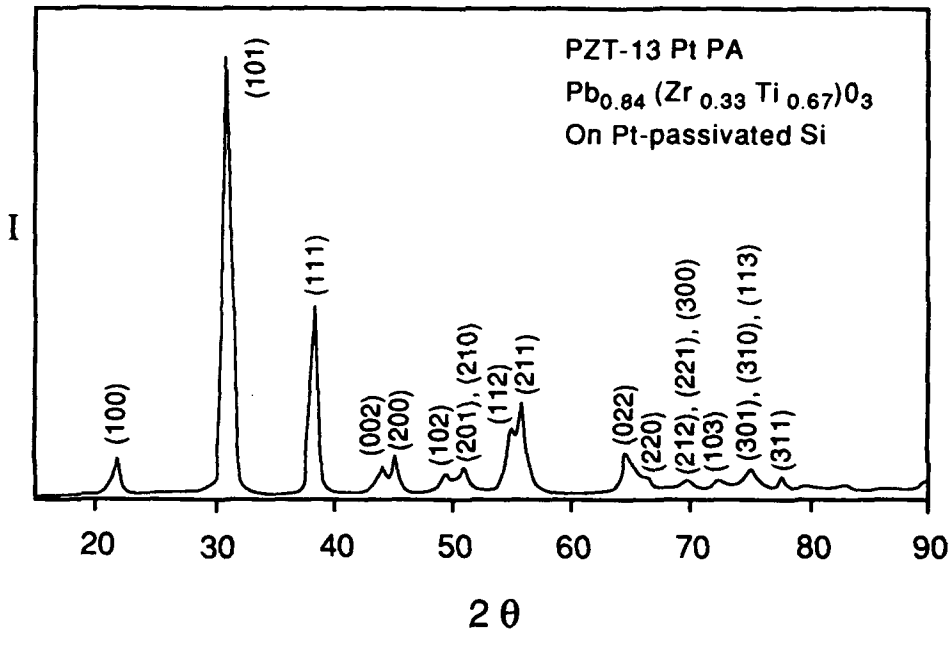
Generally, experimental runs conducted at the higher pressures did not yield films containing any perovskite phase, except at higher rf-power. These contained mostly a pyrochlore phase with other minority phases. It was only at 160 mtorr, for the 20 W rf-power series, where the perovskite appeared routinely in significant amounts. The x-ray pattern of the film which gave the highest perovskite content in the as-deposited condition (92%) is shown in Fig. 6a. The substrate was platinum-passivated silicon and the film composition corresponded nominally to the formula $Pb_{0.84}(Zr_{0.33}Ti_{0.67})O_3$. The perovskite phase appears to be fairly well developed with peak intensities that are suggestive of a random orientation of the grains.

Evidence of a second phase appears at $2\theta = 29°$ which is likely the pyrochlore phase seen under other conditions. After a post-deposition anneal at 650°C in air for 1 hour, all evidence of this second phase disappears. Tetragonal splitting of the diffraction peaks is more clearly evident in the pattern shown in Fig. 6b.

While this paper is concerned mostly with the as-deposited condition, there are a few interesting comments that can be made about films receiving a post-deposition anneal. No attempt was made to optimize annealing conditions, however, we found that films existing initially as a pyrochlore phase could be converted completely to the perovskite below 500°C for lead rich compositions. One example concerns a film with the nominal composition $Pb_{1.03}(Zr_{0.50}Ti_{0.50})O_3$. After annealling for 24 hours at 480°C in air, the



(6a)



(6b)

Figure 6. X-ray (CuKα) pattern of 1 μm thick film of $Pb_{0.84}(Zr_{0.33}Ti_{0.67})O_3$ produced by PE-MOCVD on Pt passivated silicon at 490°C, 160 mtorr and 20 W plasma power. (a) As-deposited condition. Film consists of 92 vol % perovskite and small amounts of pyrochlore phase in the as-deposited condition. (b) After receiving a post annealing treatment of 650°C for 1 hour, the pyrochlore phase has disappeared .

pyrochlore converted completely to a well formed perovskite as indicated by the diffraction pattern in Fig. 7. One important detail is that there is strong preferential orientation as is indicated by the intensity of the (100) reflection appearing at $2\theta = 21.7°$. The measured relative intensity of 40% is significantly stronger than the 12% normally associated with random orientation[30]. This was a common characteristic of such transformations in thin films after a post anneal.

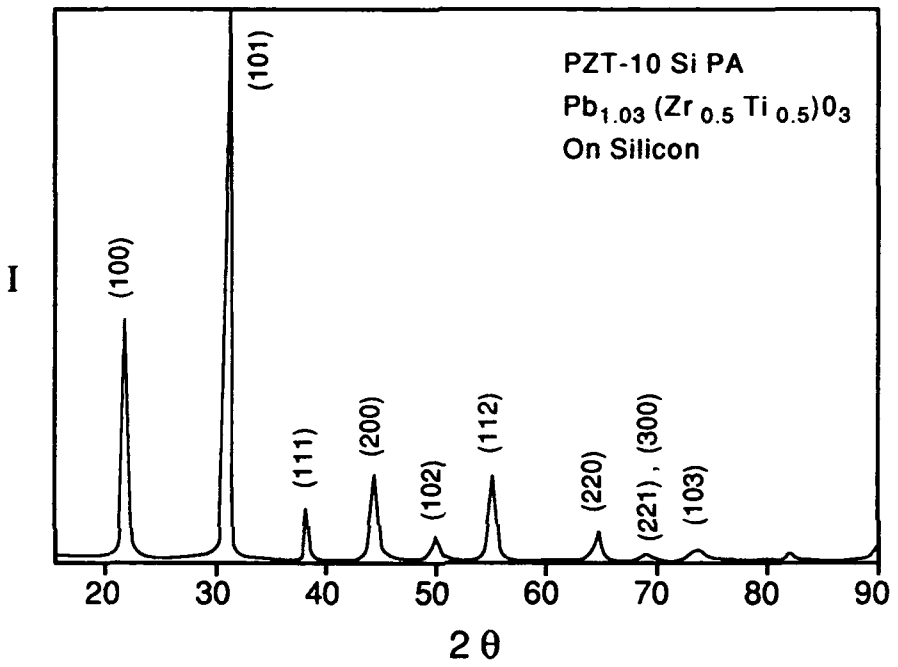


Figure 7. X-ray (CuKα) pattern of $Pb_{1.03}(Zr_{0.50}Ti_{0.50})O_3$ thin film produced by PE-MOCVD on (111)Si after receiving a low temperature post anneal treatment at 480°C for 24 hours. Shows complete conversion to the perovskite phase with a significant degree of orientation. (designation PZT-10Si PA)

The ideal microstructure would be PZT thin films that are 100% dense. So far, using PE-MOCVD, we have managed to obtain dense films of TiO_2 and ZrO_2 only. An example is shown in Fig. 8 for a 2.9 μm TiO_2 film grown at 450°C. The grains are columnar, and appearing to be about 0.3 μm in diameter. Both rutile and anatase phases were identified. However, the microstructural characteristics change when lead is introduced into the system. Figure 9 shows a section of a mixed pyrochlore-perovskite with a nominal composition of $Pb_{0.82}(Zr_{0.33}Ti_{0.67})O_3$. The film was deposited onto Pt

passivated silicon, where during a post anneal, the platinum layer separated from the film. A columnar structure that seems somewhat porous, is evident for the top 1.8 μm of the PZT layer. However, the bottom 0.8 μm appears to be more dense, exhibiting a somewhat different morphology. It is not clear what leads to this transition, although it is a characteristic typical of many films deposited on platinum.

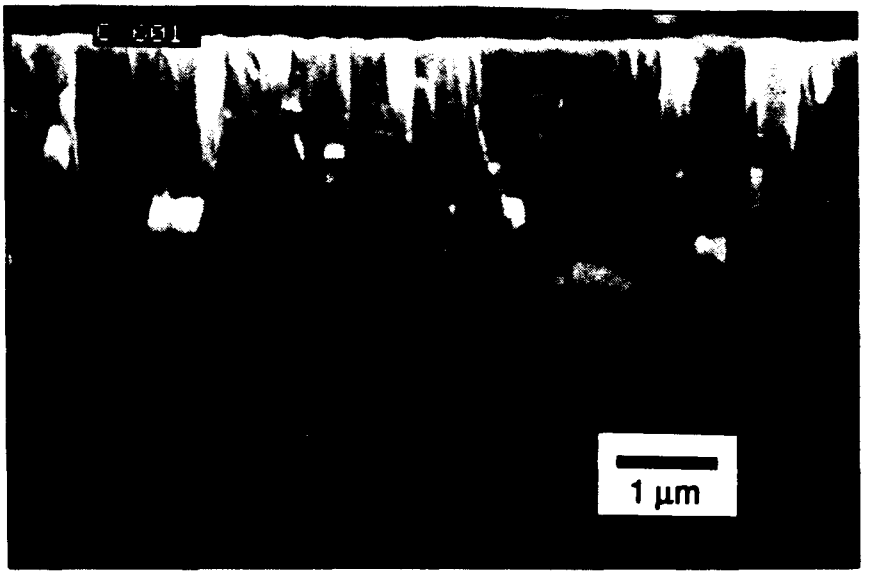


Figure 8. Dense microstructure of TiO_2 thin film produced by PE-MOCVD on silicon substrate at 450°C.

The type of substrate used was found to have a significant effect on the perovskite content in the as-deposited film. No perovskite was found to form directly on silica, polycrystalline alumina and sapphire substrates. However, films deposited directly on silicon were found to contain up to 37% perovskite in the as deposited condition. Platinum substrates were found to be most appropriate for direct perovskite formation. In all cases for the 160 mtorr series of experiments, between 8 to 92 vol % perovskite formed depending on the experimental conditions of the reactor.

The ferroelectric hysteresis properties of PZT capacitors derived from PE-MOCVD thin films were measured on a standard Sawyer-Tower circuit. Generally, none of the as deposited films exhibited hysteretic characteristics, principally because they were not phase pure perovskite. However, such behavior was observed in films receiving additional annealing. Figure 10 illustrates a 100 Hz hysteresis loop obtained on a PZT (33/67) thin film (1 μm) on Pt passivated silicon. It is the same film as discussed earlier for Fig. 6b. The magnitudes of P_r, P_{sp} and E_c were 12 $\mu C/cm^2$, 16 $\mu C/cm^2$, and 54

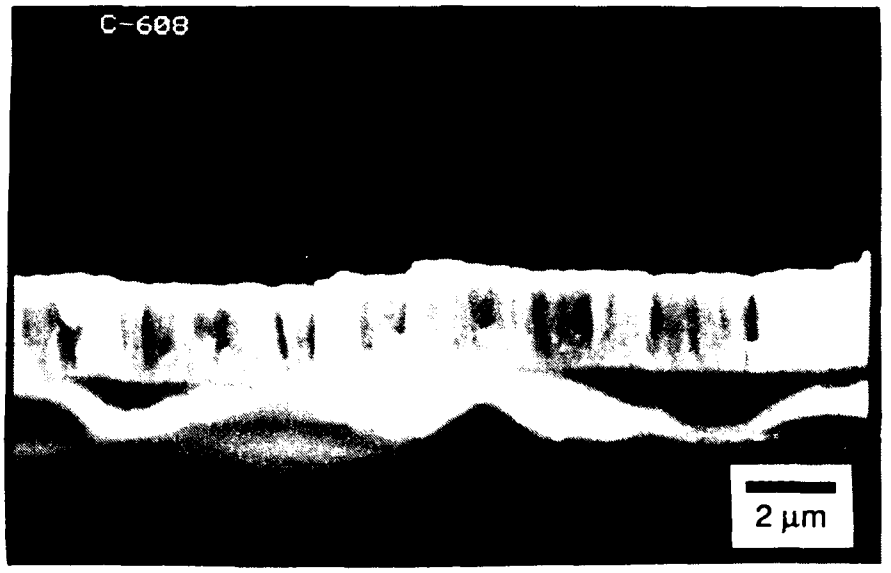


Figure 9. Columnar microstructure of $Pb_{0.82}(Zr_{0.33}Ti_{0.67})O_3$ thin film produced by PE-MOCVD on platinum passivated silicon at 425°C, 300 mtorr and 20 W rf power. Film converted to the perovskite phase after receiving a post deposition anneal treatment of 650°C for 1 hour. The platinum underlayment separated from the film during this anneal.

kV/cm, respectively. The low value of P_r is attributed to residual porosity in the films.

Control of Composition

One of the most important advantages for using a plasma for the deposition of PZT materials is compositional control. Figure 11 correlates the metal fraction of the deposit with the metal fraction in the vapor phase for experimental runs conducted at 480°C. The composition of the solid was measured by electron probe microanalysis (EPMA) and the composition of the gas phase was measured from the gravimetric losses of the bubblers containing the liquid precursors. In Fig. 11a, the lead and zirconium fractions are plotted only. The titanium fraction is not plotted since it represents redundant information. The scatter observed is associated with the uncertainties in measuring metal fraction of the gas phase.

The most striking feature of Fig. 11a is that when using a plasma there is a direct, linear correspondence between gas and solid. This is clearly shown for the compositions ranging from 10 to 42% zirconium and from about 33 to 75% lead. In contrast, the results from a single thermal CVD experiment at 480°C shows a large deviation from this one-to-one relationship. Evidently the deposition efficiency of each metal during a thermal process is not the same where zirconium deposits most efficiently and lead

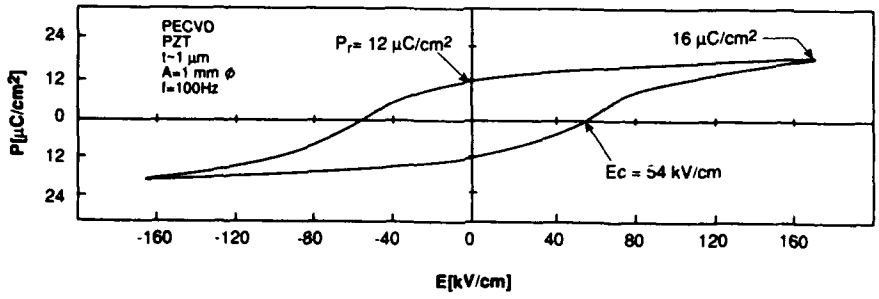


Figure 10. Sawyer-Tower ferroelectric hysteresis loop of PE-MOCVD derived PZT (33/67) thin film (1μm) shown in Fig. 6b.

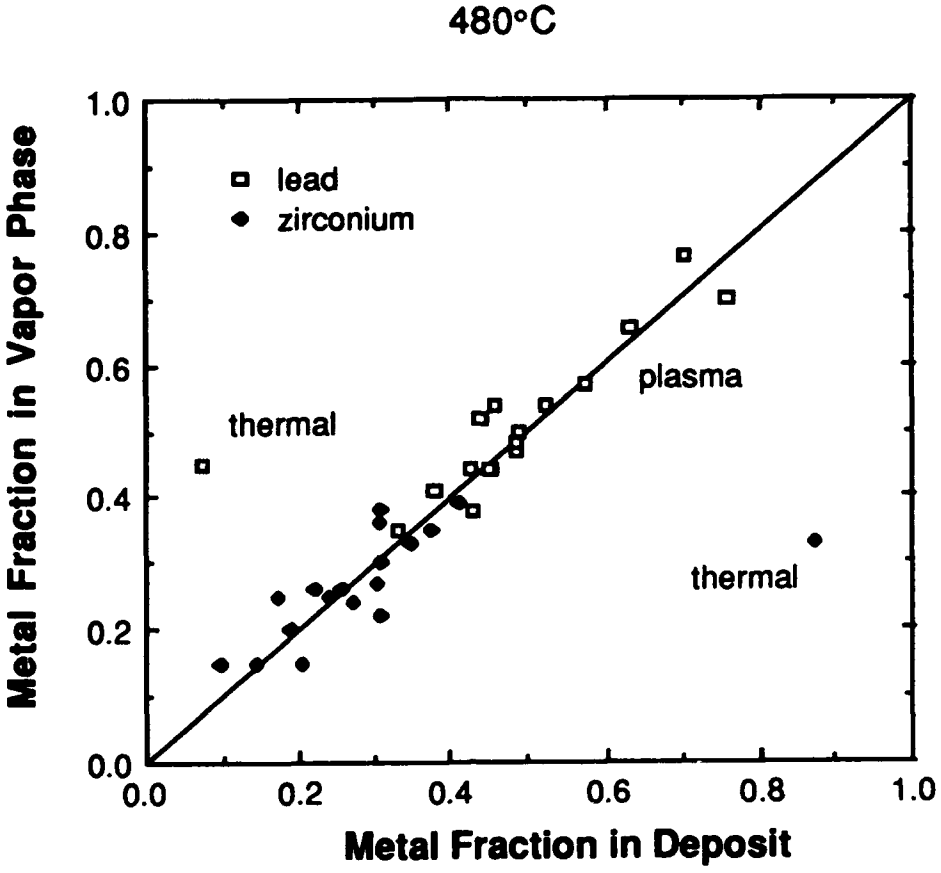
deposits least efficiently. The molecular redistribution of atoms in the gas phase is likely the reason for these diverging deposition characteristics. On the other hand, an rf plasma introduces sufficient energy to the gas to overcome the differences in stability, thus leveling the effective deposition rates.

Figure 11b shows these results redrawn schematically to emphasize the systematic trends. The degree of compositional control is indicated by the steepness of the slope of the curves. That is, a shallow slope indicates a high sensitivity of the film composition to the gas composition. This means that small variations in the gas composition leads to proportionately greater variations in the film composition. In making ferroelectric PZT's, the compositions desired for each metal is indicated by the shaded areas, where typically 50% lead, 25% titanium and 25% zirconium are sought. For their respective ranges, compositional control of both lead and zirconium for thermal decomposition processes is relatively difficult compared to plasma processes. This is indicated by their relatively shallow slopes compared to that for the plasma processes. On the other hand, titanium deposition from thermal and plasma processes are more or less equivalent.

It is to be expected that the thermal decomposition processes are more complicated than what was implied in Fig. 11 which corresponds to only one temperature. Molecular distributions in the gas phase are usually very sensitive to temperature and, therefore will influence the deposition characteristics of each metal differently. Such behavior has often been seen for thermal CVD of other compounds such as SiC[19,31]. Rf-plasma may overcome some of these temperature effects.

Effect of Plasma Power on Deposition Rate

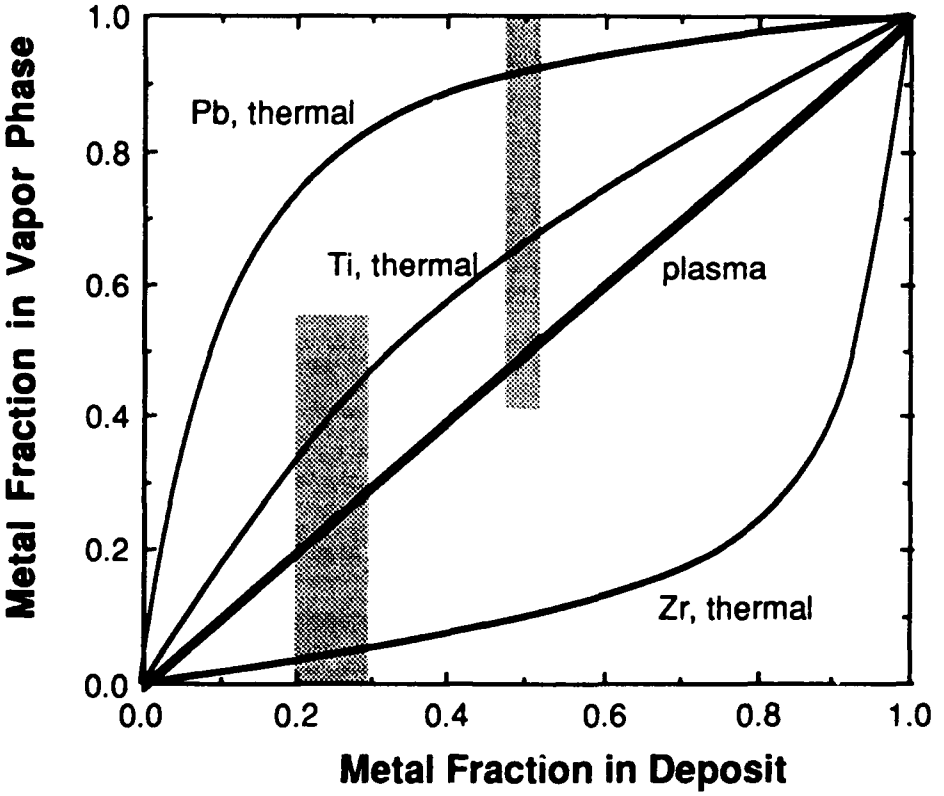
There are two effects that an rf-plasma may have on the rate of deposition. The most obvious is simply increasing the reactivity of the gas phase. This arises from the



(11a)

generation of ionized, energetic particles which, through subsequent gas phase collisions, generates reactive molecules consisting of the metal components. In this study, the plasma couples primarily with both oxygen (O_2) and argon since they are the most abundant (55-90% O_2 and 45-10% Ar depending on pressure). These are ionized producing free electrons and cationic species. In the case of oxygen, a small percentage of molecules are split into monatomic species. Presumably, these interact with molecules in the gas phase producing fragmented, ionized species carrying the metal components which are more reactive.

The increased reactivity appears as an increase in the deposition rate with plasma power. A simple comparison is made in Table II between deposition rates from thermal decomposed and plasma decomposed gases at 1000 mtorr, 450°C and approximately the same gas flow conditions. Two different deposition rates are defined. One is simply the



(11b)

Figure 11. Correlation of the metal fraction in CVD grown PZT films and the fraction metal composition of the gas reactant. (a) Shows linear relationship of experimental data for PE-MOCVD grown films and compares this to the large deviation of thermal MOCVD grown thin film. (b) Schematic representation of compositional relationships between gas and solid film compositions for both plasma and thermal MOCVD processes.

direct linear growth rate of the films. The second is the linear growth rate adjusted for the absolute concentration of reactants. In either case, the effect of a 20 W plasma is substantial, where the adjusted deposition rate is 14 times greater than without the plasma.

The principal advantage in increasing reactivity due to a plasma is that thin films can be deposited at lower temperatures than is practical for thermal processes. Although there is no direct evidence in this case, it is likely that the temperature dependence of deposition rates are not as strong for plasma processes since the intended effect of the plasma is to overcome many of the thermodynamic and activation barriers in forming reactive molecular species[32]. Presuming that this is true, thin film synthesis will become less

Table II. Deposition rates for thermal and plasma stimulated CVD at 450°C, 1000 mtorr and 22 sscfm total carrier flow rate

	Deposition Rate (μm/hr)	Adjusted Deposition Rate (μm/mol·hr)
Thermal	0.34	240
Plasma (20 W)	12.5	3300

temperature sensitive and more reproducible.

Despite these advantages, other problems arise. When deposition rates are too high, the structural reorganization at solid surfaces cannot keep pace with the rate at which more components arrive. This leads to the formation of disordered crystal structures or even metastable crystal structures which are locked by subsequent layers. More is discussed later on this issue as it pertains to the interplay of perovskite versus pyrochlore formation.

The second effect of a plasma is actually a reversal of the deposition process at sufficiently high plasma powers. Plasma etching occurs due to the high energy collision of ions on the substrate surface. Qualitatively for our reactor geometry, we observed that surfaces actually recede with plasma powers greater than about 40 to 45 W. For somewhat lower power levels, Table III compares typical deposition rates measured for experiments operated at 20 and 30 W. Both the actual and adjusted deposition rates decrease substantially with higher power settings. This is in contrast to Table II which shows deposition rates to increase at low power settings.

The combination of these two effects suggests that a maximum in the deposition rates should be evident as a function of plasma power. This is shown schematically in Fig. 12. On one hand, reactivity is expected to increase monatonically with the rf-power. On the other hand, the surface etching effect, while small at low power settings, is expected to be proportionately large at high power settings. Etching appears here as a negative deposition rate. The combination of the two effects gives a net deposition rate which is positive for low power settings but negative at high power settings.

Effect of Deposition Rate and Plasma on Crystal Structure

The perovskite content in the films is dependent on a number of factors. These include temperature, pressure, reactant concentrations and plasma power. The mechanism is

Table III. Effect of high plasma power on deposition rate and perovskite content at 480°C 300 mtorr.

RF-Power (Watts)	Perovskite Content (volume %)	Actual and Adjusted Deposition Rates (μm/hr)	(μm/mol·hr)
20	0	1-2.0	1100-1500
30	22	0.7	540

perceived to be a trade-off between the rate that components are deposited and the speed with which those components rearrange themselves on the solid surface. If deposition is too fast for surface rearrangement, then a higher entropy, metastable structure forms. These are the conditions that are thought to lead to the formation of the pyrochlore structure as opposed to the perovskite.

Referring again to Table III, the perovskite content increases with an increase in plasma power. No perovskite was found to form for any case involving 20 W plasma power for the 300 and 1000 mtorr series of experiments. Only the pyrochlore phase was found. However, a higher plasma power of 30 W served to stimulate 22 vol % perovskite formation in the as-deposited condition. This occurs concurrently with a decrease in the deposition rate as discussed previously. It would appear that the more energetic bombardment of the surface by plasma particles serves to agitate the surface, thus increasing surface mobility of the ions. Therefore, barriers in forming the perovskite structure can be overcome.

In general, the deposition rate is inversely dependent on the reactant concentration which is controlled through the mass flow controllers and hydrostatic pressure. With a plasma power of 20 W, the deposition rates decrease with decreasing pressure as was observed in proceeding from 1000 to 300 to 160 mtorr[1,2]. At this lowest pressure, significant contents of perovskite were observed in nearly all cases but no perovskite phases were observed at the higher pressures[1]. Significantly, the deposition rates on the order of 0.5 μm/hr (300 to 1000 μm/mol·hr adjusted rate) at 160 mtorr are lower than rates typically found at 300 mtorr (1.0 to 2.0 μm/hr lineal; 900 to 1500 μm/mol·hr adjusted) and at 1000 mtorr (8.3 to 12.5 μm/hr lineal; 3200 to 3300 μm/mol·hr adjusted). This supports the notion that conditions favorable for perovskite formation must correspond to sufficiently low deposition rates.

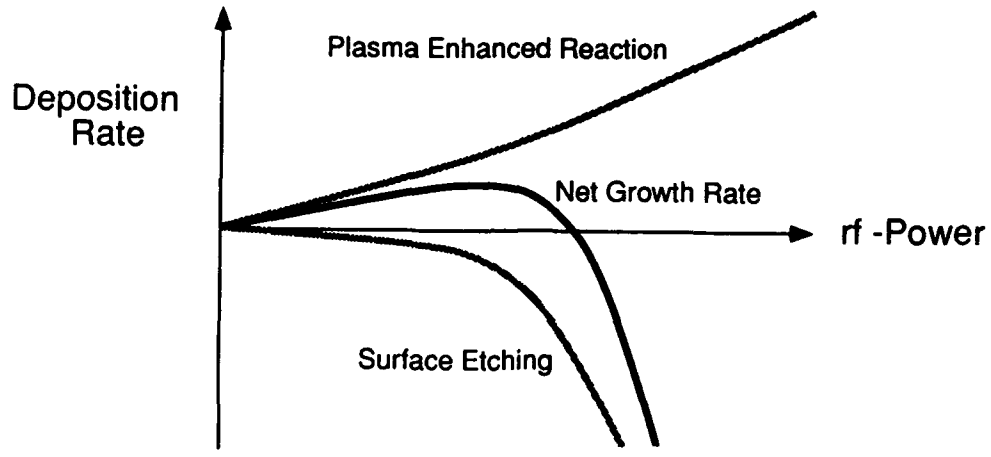


Figure 12. Schematic representation of the effects of plasma power on the deposition rate of PZT thin films by PE-MOCVD. One effect is to increase gas phase reactivity with plasma power which increases the deposition rate. Second effect is plasma etching of solid surface. Overall net effect is shown as bold line.

The evidence seen thusfar suggests that the pyrochlore structure is favored over the perovskite structure for high deposition rates. To understand this, it is worthwhile reviewing pertinent details of their crystal chemistries. The perovskite structure in the context of $Pb(Zr,Ti)O_3$ compositions is a relatively dense packing of ions. Lead is coordinated by twelve oxygen atoms, whereas the zirconium and titanium ions are coordinated by six oxygens. These two polyhedra share trigonal faces such that each lead ion is surrounded by eight nearest neighboring cations (Zr and Ti) and, similarly, zirconium and titanium are surrounded by eight lead ions.

The primary distinction between the pyrochlore and perovskite structures is the oxygen coordination about lead. The general formula for most lead based pyrochlores is $Pb_{2-\delta}(Zr,Ti)_2O_{7-x}$, where x is very near unity in many cases[32]. The stoichiometric parameter, δ, is assumed to be near zero for the sake of these arguments. Interestingly, the ionic ratios for the pyrochlore is nearly the same as that for the perovskite. As in the perovskite, both titanium and zirconium are 6-fold coordinated, although the octahedra are thought to be significantly more distorted if the structure of the pyrochlore thin film is similar to geologic pyrochlores[33]. On the other hand, lead is coordinated by only about six oxygen atoms. With an increase in the oxygen stoichiometric parameter, x, this coordination can increase to a maximum of eight which is still significantly less than the 12-fold coordination found in perovskites.

In forming a crystalline structure from the gas phase, the specific structure that is formed depends on the rate of surface structural rearrangements that can be accommodated before the next, overlying layer is deposited. It would seem here that the pyrochlore is easier to form than the perovskite since it requires lead to be surrounded by only six oxygen atoms. For sufficiently fast deposition rates and sufficiently slow surface mobilities, the pyrochlore structure is fixed in place rather than the perovskite. Conversely, it would be necessary to slow the deposition rate and increase the kinetics of surface rearrangements in order to form the perovskite structure.

This assessment suggests what is necessary to obtain 100%, phase pure perovskite in the as-deposited conditions. The most important operating parameters are pressure (or reactant concentration) and plasma power. In the extreme, it would be desirable to reduce the operating pressure to as low as is possible while still maintaining a plasma. It is also desirable to increase the plasma power as much as possible while still allowing a net positive deposition rate. The combined effect would be to give very low deposition rates but high surface mobilities. Practical growth rates will probably require that extreme conditions not be used. However, our experiences suggest this will not be necessary and that the goal of 100% perovskite can be attained. After preliminary experimentation, we have achieved 92 voi % perovskite in the as-deposited state. Much experimental latitude remains for optimizing experimental controls which leaves us with a very optimistic outlook on the ultimate success of PE-MOCVD for fabricating ferroelectric thin films below 500°C.

SUMMARY

The results of a preliminary experimental study on the plasma enhanced chemical vapor deposition of lead zirconium titanate shows that it is possible to produce thin films which are predominantly the perovskite phase below 500°C in the as-deposited condition. Most of the details of experimental procedure and results are reported elsewhere[1,2]. This paper generalizes the important features of the solid state chemistry of the thin films, the precusor chemistry and operating parameters of the plasma process. A mechanistic model is proposed which is meant as a guide for optimizing the experimental parameters for producing the ferroelectric phase. This model is constructed from an understanding of the crystal chemistries of the perovskite and pyrochlore structures and the deposition kinetics of thin films. The concepts proposed are thought to be applicable to other vacuum synthesis techniques.

The utility of a rf-plasma is two-fold in assisting deposition and perovskite formation. First, it increases the reactivity of the gas phase such that decomposition can be carried out expeditiously at temperatures lower than is practical for thermal decomposition processes. Second, it stimulates crystal reconstruction at the solid surfaces. This allows the formation of the perovskite phase which is more difficult to form than the less dense, metastable pyrochlore. In terms of deposition kinetics, it is desirable to form films at a low rate and under moderately high plasma powers. Correspondingly, the important experimental controls are pressure, reactant concentration and plasma power. Pressure should be low (approximately 100 mtorr) but not so low as to extinguish the plasma. Plasma power should be high, but not so high as to etch solid surfaces at an excessive rate.

The results indicate that the conditions necessary for producing 100% perovskite are well within practical limitations. After only a few experiments, the best results obtained thus far has been 92 vol % perovskite formed in the as-deposited condition on Pt-passivated silicon substrates at 490°C, 20 W rf-plasma power and 160 mtorr pressure. There remains considerable latitude in the adjustment of these experimental parameters to achieve the goal of phase pure perovskite. Consequently, the prospects for PE-MOCVD thin film ferroelectrics are optimistic.

A theoretical thermodynamic study was also conducted on the solid state Pb-Zr-Ti-O system. It reveals that it may be difficult to obtain the morphotropic composition PZT (53/47) due to the tendency for a lead oxide phase to form with a small solubility of titanium. That is to say, for thermally equilibrated systems, perovskite PZT's will form with minor quantities of a lead rich phase for most oxygen partial pressures for which most synthesis techniques operate. On the other hand, synthesis at oxygen partial pressures so low that lead oxides are not stable will lead to the formation of phase pure perovskites of this composition. Alternately, nonequilibrium processing techniques such as with plasma processing may also overcome this limitation.

Finally, ferroelectric hysteresis was observed of thin films produced by PE-MOCVD which had received a post deposition anneal. This was observed for films annealed below 500°C, as well as, at higher temperatures[1]. The small remanent polarizations observed were attributed to porous microstructures. However, it is thought, that the conditions proposed for improving the output of the perovskite phase in the as-deposited condition will also assist in the production of dense microstructures as well, thus improving their ferroelectric properties.

ACKNOWLEDGEMENTS

The authors would like to thank A.M. Yates, R.A. Nieman, and C.K. Barlingay for their assistance with x-ray, NMR, and electrical characterization. W.T. Petuskey gratefully acknowledges an internal grant from Arizona State University in providing the start-up funds for constructing the PE-MOCVD reactor.

REFERENCES

1. D. A. Richardson, Plasma Assisted Chemical Vapor Deposition of Lead Zirconium Titanate Thin Films, Ph.D. dissertation, Arizona State University, May, 1991.
2. D. A. Richardson, C. J. Kuo, W. T. Petuskey and S. K. Dey, in Proc. of the Symp. on Ferroelectric Films, 93rd Annual Meeting of the American Ceramic Society, Cincinnati, Ohio, April 28 - May 2, 1991. (in press).
3. C. A. P. de Araujo and G. W. Taylor, (eds.), Ferroelectrics,vol 116, pts 1&2, (spec. edition, Gordon & Breach, 1991).
4. J. C. Burfoot and G. W. Taylor, Polar Dielectrics and Their Applications, (Univ. of California, Berkeley and Los Angeles, 1979).
5. B. Jaffe, W. R. Cook and H. Jaffe, Piezoelectric Ceramics, (Academic, New York, 1970).
6. D. Bondurant, Ferroelectrics, 112,273(1990).
7. L. T. Clark, S. K. Dey and R. O. Grondin, Ferroelectrics, 116,205(1991).
8. J. Carrano, C. Sudhama, J. Lee, A. F. Tasch and W. Miller, in IEDM Tech. Dig. (1989) 255-258.
9. S. K. Dey and R. Zuleeg, Ferroelectrics, 112, 309 (1990).
10. A. R. Modak and S. K. Dey, in Ceramic Transactions, vol. 15: Materials and Processes for Microelectronic Systems, K. M Nair, R. Pohanka and R. C. Buchanan (eds.), (American Ceramic Society, Columbus, Ohio, 1990) pp. 477-487.
11. J. Hsieh, D. E. Ibbotson, J. A. Mucha and D. L. Flamm, in Mat. Res. Soc. Symp. Proc., Vol. 165, G. Lucovsky, D. E. Ibbotson and D. W. Hess, (eds.), (Materials Research Society, Pittsburgh, 1990), pp. 107-112.
12. M. Kojima, M. Okuyama, T. Nakagawa and Y. Hamakawa, Jpn. J. Appl. Phys., 22, 14 (1983).
13. B. S. Kwak, E. P. Boyd and A. Erbil, Appl. Phys. Lett., 53, 1702 (1988).
14. S. G. Yoon and H. G. Kim, J. Electrochem. Soc., 135, 3137 (1988).
15. C. J. Brierly, C. Trundle, L. Considine, R. W. Whatmore, and F. W. Ainger, Ferroelectrics, 91, 181 (1989).

16. S. L. Swartz, D. A. Seifert, G. T. Noel and T. R. Shrout, Ferroelectrics, 93, 37 (1989).
17. F. W. Ainger, C. J. Brierley, M. D. Hudson, C. Trundle and R. W. Whatmore, in Mat. Res. Soc. Symp. Proc. Vol. 200, (Materials Research Society, Pittsburgh, 1990), pp.37 - 47.
18. Y. Sakashita, T. Ono, H. Segawa, K. Tominaga and M. Okada, Proc. of Second International Ceramic Science and Technology Congress, Meeting of Electronics Division, American Ceramic Society, Orlando, Florida, Nov 12-15, 1990, to be published.
19. G. S. Fischman and W. T. Petuskey, J. Am. Ceram. Soc., 68, 185 (1985).
20. T. M. Besmann, "SOLGASMIX-PV, A Computer Program to Calculate Equilibrium Relationships in Complex Chemical Systems", Report ORNL/TM-5775, Oak Ridge National Laboratories, 1977.
21. R. A. Robie, B. S. Hemingway and J. R. Fisher, Thermodynamic Properties of Minerals and Related Substances at 298.15 K and 1 Bar Pressure and at Higher Temperatures, U. S. Geological Survey Bulletin 1452, (1979).
22. K. H. Härdtl and H. Rau, Sol. State Comm., 7, 41 (1969).
23. A. E. McHale and R. S. Roth, J. Am. Ceram. Soc.,.69, 827 (1986).
24. M. A. Eisa, M. F. Abadir and A. M. Gadalla, Trans. J. Br. Ceram. Soc., 79, 100 (1980).
25. K. Iijima, Y. Tomita, R. Takayama, I. Ueda, J. Appl Phys., 60, 361 (1986)
26. B. A. Tuttle, R. W. Schwartz, D. H. Doughty and J. A. Voigt, Mat. Res. Soc. Symp. Proc., vol. 200, (Materials Research Society, Pittsburgh, 1990) pp. 159-166.
27. D. C. Bradley, Chem. Rev., 89,. 1317 (1989).
28. H. Shapiro and F. W. Frey, The Organic Compounds of Lead, (Wiley, New York, 1968), pp. 61-70, 104-128.
29. R. C. Mehrotra, J. Am. Chem. Soc., 76, 2266 (1954).
30. K. Kakegawa, J. Mohri, T. Tkahashi, H. Yamamura and S. Shirasaki, Sol. State Comm., 24, 769 (1977).
31. A. I. Kingon, L. J. Lutz, P. Liaw and R. F. Davis, J. Am. Ceram. Soc., 66, 558 (1983).
32. O. Muller and R. Roy, Crystal Chemistry of Nonmetallic Materials, vol. 4: Major Ternary Structural Families, (Springer, New York, 1974).
33. A. F. Wells, Structural Inorganic Chemistry, 5th ed., (Oxford Univ. Press, Oxford, 1984), pp. 258, 604-605.

AD-P006 687

$PbTiO_3$ THIN FILMS GROWN BY ORGANOMETALLIC CHEMICAL VAPOUR DEPOSITION

G.J.M. DORMANS, M. DE KEIJSER AND P.K. LARSEN
Philips Research Laboratories, 5600 JA Eindhoven, The Netherlands.

Abstract We have used organometallic chemical vapour deposition (OMCVD) to deposit ferroelectric $PbTiO_3$ films on both single crystalline (001)$SrTiO_3$ and oxidized Si substrates provided with a platinum electrode, using the precursors titanium-iso-propoxide and tetra-ethyl-lead.

Epitaxial $PbTiO_3$ layers were grown on (001)$SrTiO_3$ at temperatures around 700 ℃. The epitaxial nature of the *c*-axis oriented $PbTiO_3$ is confirmed by Rutherford backscattering spectrometry including channeling, x-ray diffraction (XRD) and high-resolution electron microscopy. A minimum channeling backscatter yield of $\sim$ 3 % is obtained under optimal conditions.

Polycrystalline $PbTiO_3$ films have been deposited on the platinized Si substrates at temperatures between 400 ℃ and 550 ℃. XRD shows that the films are of a single-phase perovskite-type structure. For a layer deposited at 400 ℃ followed by an anneal at 700 ℃ we measured an E_c of $\sim$ 100 kV/cm, an P_r of $\sim$ 55 $\mu C/cm^2$, and a switching time $<$ 50 ns. This latter value was limited by the instrumental set-up.

INTRODUCTION

For a widespread application of integrated ferroelectrics an IC-compatible deposition technique is required to grow ferroelectric thin films. The deposition techniques most frequently used are sputtering and spin-coating. A promising alternative technique is chemical vapour deposition (CVD), which has the

92-16162

advantage that dense thin films of high purity can be grown at high growth rates on large-area substrates with very good step coverage. For the growth of oxidic materials CVD has the additional advantage that high oxygen pressures can be applied.

The feasibility of (OM)CVD for the growth of the ferroelectric material $PbTiO_3$ has been demonstrated by several research groups using various precursors[1–9]. Recently, we have shown[10] that hetero-epitaxial layers of $PbTiO_3$ can be grown on lattice-matched (001)$SrTiO_3$ substrates using the precursors tetra-iso-propoxy-titanium ($Ti(OC_3H_7)_4$ = TIP) and tetra-ethyl-lead ($Pb(C_2H_5)_4$ = TEL) at temperatures around 700 ℃.

The growth of $PbTiO_3$ from TEL and TIP by OMCVD can be qualitatively described by the overall chemical reactions 1-3:

$$Pb(C_2H_5)_4 + 3/2O_2 \rightarrow PbO + 2H_2O + 4C_2H_4 \quad (1)$$

$$Ti(OC_3H_7)_4 \rightarrow TiO_2 + 2H_2O + 4C_3H_6 \quad (2)$$

$$PbO + TiO_2 \rightarrow PbTiO_3 \quad (3)$$

These reactions show that TEL is oxidized by O_2 to form PbO, whereas TIP is thermally decomposed to form TiO_2. The primary reaction products are H_2O and the volatile hydrocarbons C_2H_4 and C_3H_6 which are easily removed via the gas phase. According to reaction 3, stoichiometric $PbTiO_3$ can be formed by matching the rates of formation of PbO and TiO_2.

In this paper we first extend our earlier work on the growth of $PbTiO_3$ on $SrTiO_3$ [10]. The hetero-epitaxial nature of the *c*-axis oriented films is evidenced by x-ray diffraction (XRD), Rutherford backscattering spectrometry (RBS) ,using channeling experiments, and high-resolution electron microscopy (HREM).

Next, some preliminary results are presented regarding the growth of polycrystalline $PbTiO_3$ on oxidized Si substrates with a platinum electrode. Single-phase $PbTiO_3$ films are formed at temperatures between 400 ℃ and 550 ℃.

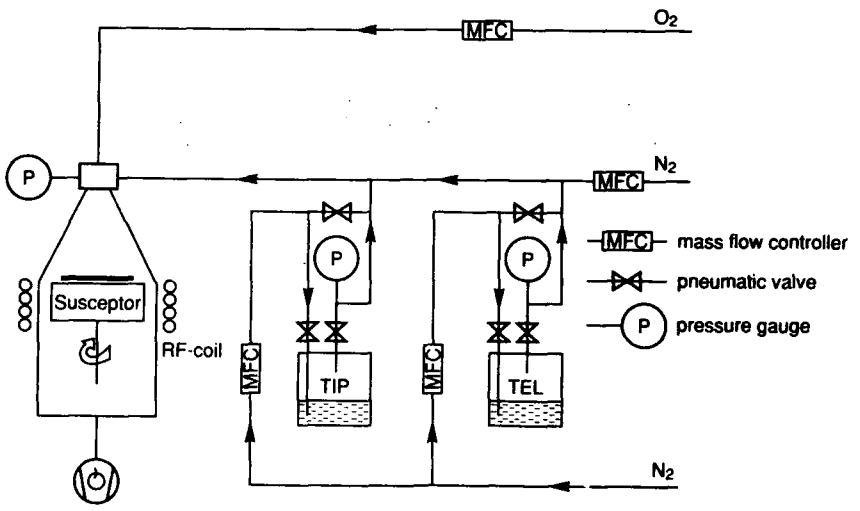


FIGURE 1 Experimental set-up for the growth of $PbTiO_3$ by OMCVD.

The layers are characterized electrically by measuring the ferroelectric hysteresis and switching behaviour.

EXPERIMENTAL

The deposition experiments were performed in a vertical quartz reactor with an inner diameter of 53 mm connected to a conventional gas mixing system (Figure 1).

Substrates are placed on an inductively heated silicon susceptor oriented perpendicular to the gas flow. The susceptor is rotated at $\sim$ 50 rpm to improve the layer homogeneity. The temperature of the susceptor is measured with a thermocouple inside the susceptor which is calibrated against the substrate temperature measured with a dual-wavelength pyrometer.

The precursors used for the growth of $PbTiO_3$ were TIP (Strem Chemicals, 99.9 %) and TEL (Billiton Precursors, 99.999 %). Dried O_2 and N_2 were used as the oxygen source and carrier gas respectively.

The partial pressures of TEL and TIP in the reactor (p_{TEL} and p_{TIP}) are

calculated from their known vapour pressures at the evaporation temperature ($p_i(T)$), the ratio of the flow through the bubbler (ϕ_i) and the total flow through the reactor (ϕ_r) and the ratio of the bubbler pressure ($p_{i,b}$) and reactor pressure (p_r). The total flow and reactor pressure were kept constant at 0.5 standard litres per minute (SLM) and 20 mbar respectively. The pressures in the bubblers are only slightly higher than the reactor pressure. They depend on the flows ϕ_i and are measured directly behind the bubblers (Figure 1).

(001)$SrTiO_3$ and oxidized Si wafers provided with a platinum electrode were used as substrates without any pre-treatment.

Layer thicknesses and growth rates were calculated from optical interference spectrometry using the wavelength-dependent index of refraction of $PbTiO_3$ and from the RBS random backscatter yield from the lead atoms (in atoms/cm^2) assuming that the layers consist of $PbTiO_3$ with a theoretical density of 7.92 x 10^{22} atoms/cm^3. With optical interference spectrometry, layer thicknesses down to $\sim$ 1000 Å can be accurately measured. Above this thickness, the results for both methods are, within the experimental accuracy, identical.

For the measurement of the ferroelectric properties of the $PbTiO_3$ layers deposited on platinized Si, gold contacts were sputtered on top of the $PbTiO_3$ layer through a shadow mask with various spot sizes.

EPITAXIAL $PbTiO_3$ ON (001)$SrTiO_3$

At room temperature, $PbTiO_3$ has a tetragonal perovskite-type crystal structure with the polarization direction along the *c* axis. The bulk values for the lattice constants of $PbTiO_3$ are 3.904 Å for the *a* axes and 4.152 Å for the *c* axis [11]. $SrTiO_3$ is a cubic perovskite at room temperature with a lattice constant of 3.905 Å, which is nearly identical to the *a* axes of $PbTiO_3$. Therefore, (001)$SrTiO_3$ is a suitable substrate for the hetero-epitaxial growth of *c*-axis

TABLE 1 Conditions for the growth of epitaxial $PbTiO_3$ on (001)$SrTiO_3$ and polycrystalline $PbTiO_3$ on platinized Si.

	$SrTiO_3$	Pt/Si
Temperature (℃)	$\geq$ 700	400 - 550
p_{O_2} (mbar)	1 - 12	1 - 4
T_{TEL} (℃)[a]	-10 - 20	-10 - 10
T_{TIP} (℃)[a]	15 - 35	18
p_{TEL} (10^{-3} mbar)[b]	0.5 - 5	0.5 - 5
p_{TIP} (10^{-3} mbar)[b]	0.5 - 5	1 - 4

[a]Temperature of evaporation. [b]Partial pressure in reactor.

oriented $PbTiO_3$.

$PbTiO_3$ layers were grown on (001)$SrTiO_3$ under the conditions given in Table 1. The growth rate was 0.1 - 0.5 μm/hour.

A general problem in the growth of multi-component materials like $PbTiO_3$ is to control the composition of the film. According to equation 3, the rates of formation of PbO and TiO_2 have to be equal to form only single-phase stoichiometric $PbTiO_3$. Therefore, the composition of the layer will depend critically on the process parameters like p_{TEL}, p_{TIP}, and the substrate temperature. However, we found [12] that for the growth of $PbTiO_3$ on $SrTiO_3$ above 700 ℃ the composition of the layer no longer depends on these parameters. This is attributed to a self-controlling mechanism in which the excess of PbO evaporates.

In Figure 2 we show the Auger spectrum of a $PbTiO_3$ layer grown at 700 ℃ after removal of a thin surface layer by Ar sputtering. There is no indication of the presence of any carbon in the layer above the Auger detection limit ($\sim$ 1 at%). Obviously, the oxidation of TEL and the decomposition of TIP (reactions 1 and 2) do not lead to incorporation of organic residues in the film.

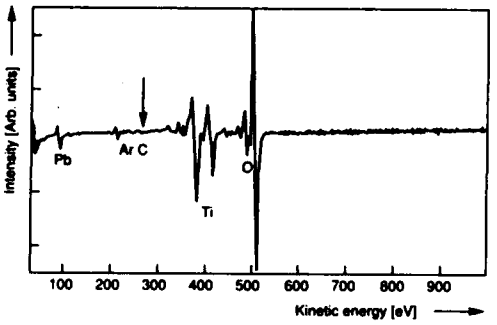


FIGURE 2 Auger spectrum of a $PbTiO_3$ layer grown on $SrTiO_3$ at 700 ℃. The spectrum is taken after removal of $\sim$ 50 Å by Ar-sputtering. There is no indication of any carbon present above the detection limit ($\sim$ 1 at%).

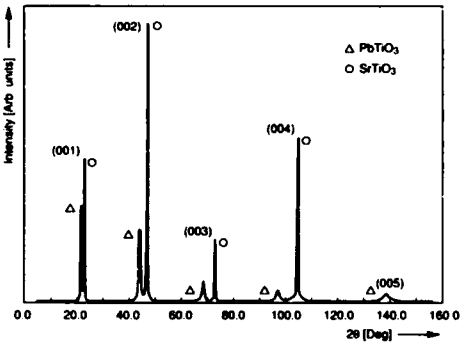


FIGURE 3 XRD pattern of a $PbTiO_3$ layer grown at 700 ℃. Only the (00l) reflections of the $PbTiO_3$ film and the (001)$SrTiO_3$ substrate are observed.

The epitaxial nature of the $PbTiO_3$ films on (001)$SrTiO_3$ is first evidenced by XRD. Figure 3 shows a characteristic XRD pattern for such a film. Besides the reflections of the (001)$SrTiO_3$ substrate, only the (00l) reflections of the $PbTiO_3$ film are observed. Because the c axis of $PbTiO_3$ is larger than the cubic axis of $SrTiO_3$, they appear at lower diffraction angles than the corresponding $SrTiO_3$ reflections. There is no indication of any other phase or orientation in the film. Note, however, that the presence of a-axis oriented $PbTiO_3$ cannot be excluded as these reflections coincide with those of the substrate.

A commonly used method for the characterization of the epitaxial quality is channeling RBS. In this method the beam of high energetic He-ions is directed along one of the crystal axes of the film and/or the substrate. The ratio of the yields (χ_{min}) of backscattered He-ions in this channeling configuration and in a random orientation is an indication of the epitaxial quality of the film.

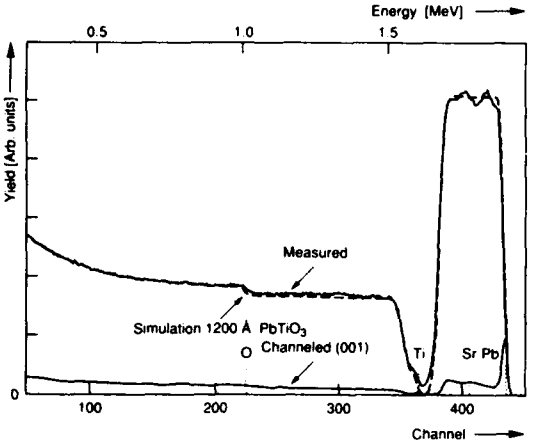


FIGURE 4 RBS spectrum of the $PbTiO_3$ layer from Figure 3. The measured spectrum is drawn with a full line, the simulated spectrum for a 1200 Å stoichiometric $PbTiO_3$ on $SrTiO_3$ with a broken line. Also, the (001) channeled spectrum is shown. The backscatter minimum yield χ_{min} is $\sim$ 3 % for this layer.



FIGURE 5 HREM picture of the $PbTiO_3/SrTiO_3$ interface. The [001] direction is indicated. The angle between the [101] direction of the $PbTiO_3$ film and the [101] direction of the $SrTiO_3$ substrate is measured to be 1.8°.

In Figure 4 we show a random and channeled RBS spectrum of a layer grown under optimal conditions. Also shown is a simulation of a spectrum of a 1200 Å thick stoichiometric $PbTiO_3$ layer on a $SrTiO_3$ substrate. This simulated spectrum coincides with the measured random spectrum. From the channeled spectrum a χ_{min} of $\sim$ 3 % can be calculated, which indicates the hetero-epitaxial nature of the $PbTiO_3$ film.

Finally, a HREM picture shows the epitaxial orientation of a $PbTiO_3$ layer grown on $SrTiO_3$ (Figure 5). The transition from the substrate to the film is nearly atomically sharp. The tetragonality of the *c*-axis oriented $PbTiO_3$ film can also be inferred from this micrograph.

To summarize, these experiments have shown that OMCVD using TEL

and TIP is a suitable technique for growing epitaxial $PbTiO_3$ thin films on lattice-matched (001)$SrTiO_3$ substrates.

POLYCRYSTALLINE $PbTiO_3$ ON Pt/Si

To exploit the ferroelectric properties of $PbTiO_3$ it is necessary to sandwich the ferroelectric film in between two electrodes. The most commonly used electrode material is platinum. When deposited on silicon or on silicon oxide at room temperature, this platinum is polycrystalline. Hence, a $PbTiO_3$ film grown on top of such an electrode will also be polycrystalline.

Here we present some preliminary results on the growth of $PbTiO_3$ on platinized Si in the temperature range of 400 ℃ to 550 ℃ (See Table 1). At higher temperatures, the recrystallization and coagulation of the Pt-layer results in the formation of pinholes and Pt-droplets. For such an incoherent layer we observed a reaction between the underlying SiO_2 and PbO or $PbTiO_3$ to form lead-silicates.

In the temperature range of 400 ℃ to 550 ℃, there is no self-regulating mechanism controlling the composition of the film as in the case of $PbTiO_3$ films on $SrTiO_3$ substrates above 700 ℃. At low temperatures, the growth rate for the formation of TiO_2 is limited by the decomposition of TIP and the formation of PbO by the oxidation of TEL. These growth rates are then temperature dependent. This temperature dependence is characterized by an activation energy which is not the same for TiO_2 and PbO. Therefore, in this kinetically controlled regime, both the thickness and the composition of the layer will depend on p_{TEL}, p_{TIP} and the substrate temperature.

At higher temperatures, the diffusion of the molecular species from the bulk of the reactor gas-phase to the substrate becomes rate-limiting. Now the temperature dependence of the growth rate is controlled by the diffusion coefficients of the diffusing species. Since these diffusion coefficients are

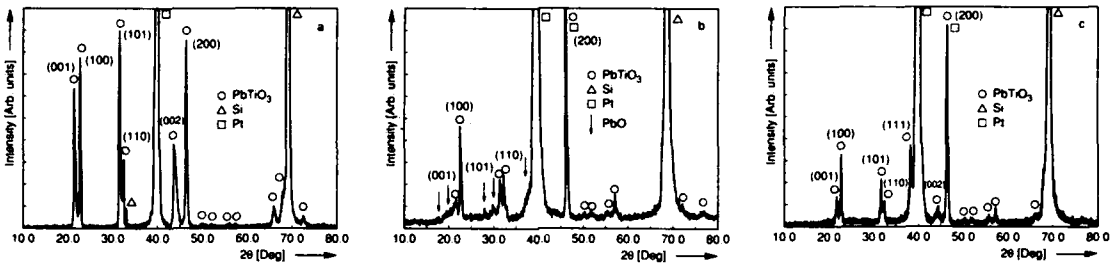


FIGURE 6 XRD patterns for $PbTiO_3$ layers grown on platinized Si at 550 ℃ (a) and at 400 ℃ (b). Pattern (c) is from the same layer as in (b) but after an anneal at 700 ℃ for 30 minutes. In (a) and (c) only reflections belonging to the substrate, the electrode and the tetragonal $PbTiO_3$ film are observed. In (b) additional reflections from an excess of PbO are observed.

hardly temperature dependent, the growth rate and composition of the layer will depend mainly on p_{TEL} and p_{TIP} (i.e. p_{TEL}/p_{TIP}) and no longer on the substrate temperature. The transition from the kinetically controlled regime to the diffusion-limited regime also depends on the flow dynamics in the reactor. Therefore, factors such as the reactor geometry, the gas-flow rate, the reactor pressure and the residence time of the precursors in the reactor are of importance. Okada et al. [9] found that in their reactor at a pressure of 8 mbar, the diffusion-controlled regimes for TiO_2 from TIP and for PbO from TEL and O_2 start at $\sim$ 550 ℃ and $\sim$ 520 ℃ respectively. In our experiments at a reactor pressure of 20 mbar we found these temperatures to be $\sim$ 400 ℃ for TiO_2 and $\sim$ 500 ℃ for PbO. Hence, the composition of the layers above 500 ℃ will depend mainly on p_{TEL}/p_{TIP}, and below this temperature also on the substrate temperature.

In Figure 6a we show an XRD pattern for an 3500 Å thick layer grown at 550 ℃ and p_{TEL}/p_{TIP}= 0.2. Only the tetragonal phase of $PbTiO_3$ is observed. It was confirmed by Auger measurements and x-ray fluorescence (XRF) that the layer consists of equal amounts of Pb and Ti. The reflections are sharp which indicates that the layer is well crystallized. The crystallites have a random orientation.



FIGURE 7 SEM pictures from the layers of which the XRD patterns are shown in Figure 6. $PbTiO_3$ grown at 550 ℃ (a), at 400 ℃ (b) and at 400 ℃ followed by an anneal at 700 ℃ (c).

Attempts to measure the ferroelectric properties of this layer failed because the size of the crystals is comparable with the layer thickness (Figure 7a). This resulted in a layer with a very rough morphology and, hence, in electrical shorting between the bottom and top electrodes.

In order to suppress the formation of these large crystals, layers were grown at lower substrate temperatures. However, below 500 ℃ the growth process is kinetically controlled. As shown before, the composition is then strongly temperature dependent. At 400 ℃ a Pb/Ti ratio of 1 is obtained for $p_{TEL}/p_{TIP} \simeq 3$. This indicates, that at these lower temperatures the oxidation of TEL is much slower than the decomposition of TIP, which is already near the diffusion limited regime. Figure 6b shows the XRD pattern of a 5000 Å thick layer deposited at 400 ℃ and $p_{TEL}/p_{TIP} = 3$. At this temperature the layer is already crystallized to $PbTiO_3$. Compared with the layer grown at 550 ℃, the reflections are smaller and broader. This indicates that the grain size of the layer grown at 400 ℃ is smaller than that of the layer grown at 550 ℃. This is confirmed by an SEM picture of this layer (Figure 7b) which shows a much smoother layer than the one grown at 550 ℃. In the XRD pattern there is also an indication of the presence of PbO.

The electrical measurements for this layer show that it is insulating. However, for this as-deposited layer no hysteresis could be measured. Therefore, the layer was post-annealed at 700 ℃ for 30 minutes in air. The XRD-pattern

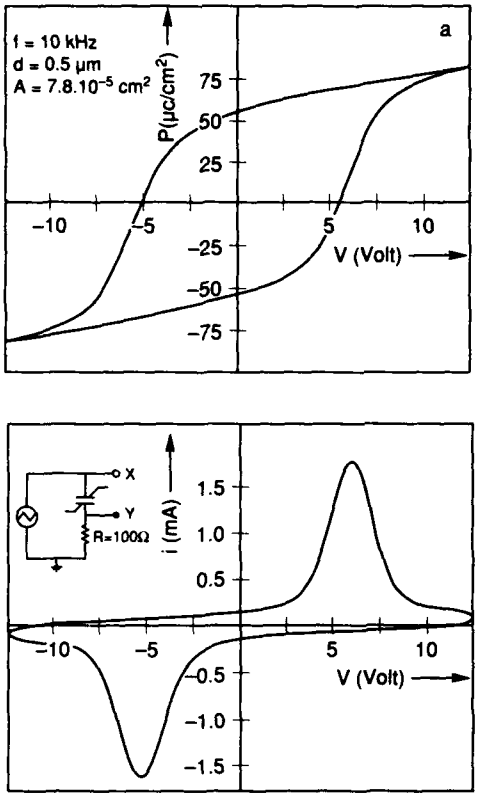


FIGURE 8 Hysteresis loop (a) and current-voltage curve (b) of a $PbTiO_3$ layer grown on platinized Si at 400 ℃ and post-annealed at 700 ℃. The XRD pattern and SEM picture of this layer are shown in Figures 6c and 7c.

of this layer is shown in Figure 6c. The only difference with the as-deposited pattern is the absence of the reflections belonging to PbO. The SEM picture of the annealed layer (Figure 7c) shows that the layer has roughened somewhat, but that it is still much denser than the layer deposited at 550 ℃.

This post-annealed layer now shows ferroelectric behaviour. The hysteresis loop and the current-voltage (i-V) curve are presented in Figure 8. The hysteresis measurement was done using a Sawyer-Tower circuit. The i-V measurements were made with triangular signals. We find a coercive field strength (E_c) of 100 kV/cm and a remanent polarization (P_r) of 55 $\mu C/cm^2$. The value of P_r mates to that of single-crystalline $PbTiO_3$ [13]. This is remarkable as the XRD pattern reveals no preferential *c*-axis orientation of the layer.

It was found that at higher electrical field strengths (> 200 kV/cm) the layer becomes conducting. This behaviour is non-linear and time-dependent.

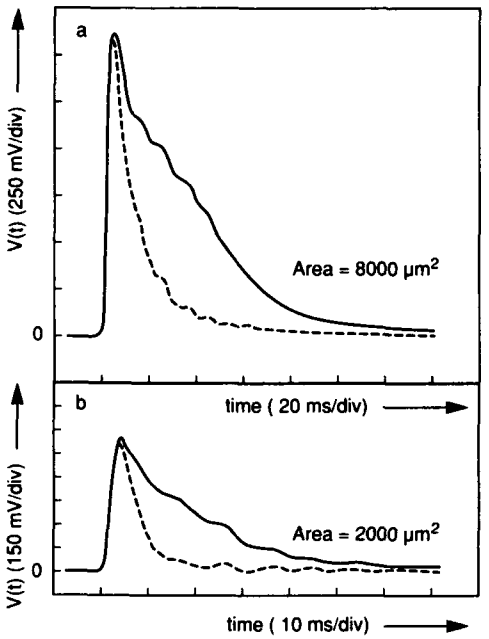


FIGURE 9 Switching behaviour of a $PbTiO_3$ layer grown on platinized Si at 400 ℃ followed by an anneal at 700 ℃. The signal V(t) is shown for the first (solid line) and second (broken line) pulse of a double pulse of 300 kV/cm. V(t) is developed over a resistance of 8 1/3 Ω in series with the ferroelectric capacitor. In (a) the switched polarization (ΔP_s) = 95 $\mu C/cm^2$ and the non-switched polarization (ΔP_{ns}) = 41 $\mu C/cm^2$. In (b), $\Delta P_s = 103\ \mu C/cm^2$ and $\Delta P_{ns} = 40\ \mu C/cm^2$.

At present we are trying to find the cause of this conductivity. The switching behaviour of the layer is presented in Figure 9. The experimental set-up for these measurements is described in detail elsewhere [14]. The measurements were performed by applying double bipolar pulses with a width of 200 ns, a delay of 1.8 μs between the two pulses of the same polarity and a delay of 12.5 ms between the first pulse of one polarity and the first following one of the other polarity (i.e. a period of 25 ms). This was done for top gold electrodes with a surface area of 8000 μm^2 and 2000 μm^2. The switching times for these areas, as determined by the time at which the current is 1/10 of the maximum current, are 80 ns and 45 ns respectively. In both cases the switching time is determined by the instrumental set-up[15]. The ratio of the displaced charge for a switching and a non-switching pulse ($\Delta P_s/\Delta P_{ns}$) is $\sim$ 2.5 for both areas.

SUMMARY

$PbTiO_3$ thin films can be grown by OMCVD using the precursors TEL and TlP. Above 700 °C on (001)$SrTiO_3$ substrates always single-phase stoichiometric $PbTiO_3$ is formed due to a self-controlling growth mechanism. The films are c-axis oriented and epitaxial with, under optimal conditions, an RBS (001) channeling minimum yield of $\sim$ 3 %.

On oxidized Si substrates with a platinum electrode, single phase polycrystalline $PbTiO_3$ films are grown at temperatures between 400 °C and 550 °C. At the higher temperatures, relatively large crystals are formed giving a rough layer morphology. No ferroelectricity is measured due to the presence of many conducting channels through this rough film causing electrical shorting between the top and bottom electrode. Layers grown at 400 °C are more dense and isolating. After a post-anneal at 700 °C they show hysteresis behaviour with a P_r of 55 $\mu C/cm^2$ and an E_c of 100 kV/cm. The layers can be switched with a time constant < 50 ns. This measured value is instrumentally limited. The ratio of switched and non-switched charge is $\sim$ 2.5. At electric fields $\geq$ 200 kV/cm non-linear and time-dependent conduction is observed.

ACKNOWLEDGEMENT

The authors wish to thank P.J. van Veldhoven for technical assistance, L. van IJzendoorn and W. Lathouwers for RBS, A. Mouwen and M. Ossekoppele for XRD, N. Bemelmans for SEM, P. Oosting and W. van de Wijgert for AES, T. Brandsma for optical interference spectrometry , H. Zandbergen (University of Delft) for HREM, J. Borstrok and M. Meulendijk for XRF and G. Kampschöer for electrical measurements.

REFERENCES

1. M. Kojima, M. Okuyama, T. Nakagawa and Y. Hamakawa, *Jpn. J. Appl. Phys.*, **24** (suppl. 22-2), 14-17 (1983).

2. M. Okuyama and Y. Hamakawa, *Ferroelectrics*, **63**, 243-252 (1985).

3. B.S. Kwak, E.P. Boyd and A. Erbil, *Appl. Phys. Lett.*, **53**, 1702-1704 (1988).

4. Soon-Gil Yoon and Ho-Gi Kim, *J. Electrochem. Soc.*, **135**, 3137-3140 (1988).

5. Soon-Gil Yoon and Ho-Gi Kim, *Thin Solid Films*, **165**, 291-302 (1988).

6. S.L. Swartz, D.A. Seifert, G.T. Noel and T.R. Shrout, *Ferroelectrics*, **93**, 37-43 (1989).

7. C.J. Brierley, C. Trundle, L. Considine, R.W. Whatmore and F.W. Ainger, *Ferroelectrics*, **91**, 181-192 (1989).

8. M. Okada, H. Watanabe, M. Murakami, A. Nishiwaki and K. Tomita, *J. Ceram. Soc. Jpn. Inter. Ed.*, **96**, 676-682 (1988).

9. M. Okada, S. Takai, M. Amemiya and K. Tominaga, *Jpn. J. Appl. Phys.*, **28**, 1030-1034 (1989).

10. M. de Keijser, G.J.M. Dormans, J.F.M. Cillessen, D.M. de Leeuw and H.W. Zandbergen, *Appl. Phys. Lett.*, in press.

11. *Landolt Börnstein*, **III/16a**, (Springer-Verlag, Berlin, Heidelberg, New York, 1981), p. 77.

12. G.J.M. Dormans, P.J. van Veldhoven and M. de Keijser, to be published.

13. V.G. Gavrilyachenko, R.I. Spinko, M.A. Martynenko and E.G. Fesenko, *Sov. Phys. -Solid State*, **12**, 1203-1204 (1970).

14. G.A.C.M. Spierings, M.J.E. Ulenaers, G.L.M. Kampschöer, H.A.M. van Hal and P.K. Larsen, *J. Appl. Phys.*, in press.

15. P.K. Larsen, G.L.M. Kampschöer, M.J.E. Ulenaers, G.A.C.M. Spierings and R. Cuppens, *Appl. Phys. Lett.*, in press.

AD-P006 688

BOTTOM ELECTRODES FOR INTEGRATED $Pb(Zr,Ti)O_3$ FILMS

PHILIP D. HREN, S. H. ROU, H. N. AL-SHAREEF, M. S. AMEEN*, O. AUCIELLO**, AND A. I. KINGON
North Carolina State University, Department of Materials Science and Engineering, Raleigh, NC 27695-7919; * Materials Research Corporation, Orangeburg, NY 10962; **Also Microelectronics Center of North Carolina, Research Triangle Park, NC, 27709-2889.

Abstract Lower electrodes for $Pb(Zr,Ti)O_3$ (PZT) used in ferroelectric random access memories must have good electrical conductivity and must interact as little as possible with the PZT film. We have evaluated a number of bottom electrodes for use with PZT films deposited by ion beam sputter deposition These electrodes include Pt, Pt/Ti, RuO_2, ReO_3, and $CoSi_2/Si_3N_4$, all on SiO_2/Si; and TiN and Pt on MgO. Films were studied by XTEM, Auger depth profiling, X-ray microanalysis, and XRD. Important issues for platinum include: a) microstructure (porous for magnetron sputtered Pt); b) rapid lead diffusion through porous Pt; c) adhesion (improved by raising deposition temperature or by adding a titanium layer); and d) hillock formation (related to compressive stress in platinum). RuO_2 has good conductivity and has no apparent interfacial layer with PZT. Each of the remaining substrates has drawbacks: $CoSi_2$ forms a surface oxide; ReO_3 has poor phase stability; TiN oxidizes and loses conductivity.

INTRODUCTION

A surge of interest in the synthesis of ferroelectric films has occurred in the last few years. A wide variety of techniques has been used to deposit the films. The history of ferroelectric films and of the various fabrication methods is described in a recent article by Roy, Etzold and Cuomo.[1] An important issue that is mentioned in this review is the interaction of the ferroelectric film with the substrate during growth or during further processing. This interaction can take the form of diffusion of substrate species into the ferroelectric film, the diffusion of film species into the substrate, or the formation of a dielectric layer at the interface. Any of these events can be harmful to the properties of the film. Considering the importance of this question, there has been relatively little

92-16163

investigation of the nature of the film/substrate reaction. In particular, only a handful of transmission electron microscopy (TEM) studies of ferroelectric film interfaces have appeared.[2,3] In this report we use TEM to study the interaction of lead zirconate titanate (PZT) films with a variety of substrates. Our emphasis is on the following issues: a) lead diffusion through the platinum layer in the system PZT/Pt/SiO_2/Si; b) the microstructure of the Pt layer, and hence its resistance to lead diffusion, depends on how the Pt layer is deposited; c) adhesion of ion-sputtered Pt on SiO_2 is highly dependent on the deposition temperature. Other substrates that are studied in less detail are the following: RuO_2/SiO_2, TiN/MgO, ReO_3/SiO_2/Si, Pd/SiO_2/Si, PtSi/Si, and $CoSi_2$/Si_3N_4/SiO_2/Si.

In order to guide our investigation of electrodes for PZT deposition,we found it useful to compile a list of all substrates mentioned in the literature. This list is given in Table I. The survey covers papers and abstracts from Jan. 1, 1990, through May 1991. A total of 72 papers and abstracts were surveyed. The list covers major meetings on ferroelectrics and major journals and is not exhaustive, but should be representative of substrates in common use.

Of the conducting substrates, several could be eliminated from consideration. Bare silicon without a buffer layer shows a tendency to oxidize during deposition of ferroelectric films, as has been observed by Matsubara *et al.*[2] during the deposition of $SrTiO_3$ on bare silicon. The interfacial layer of SiO_2 has a relatively low dielectric constant of 3.9, and even thin (4 nm) layers of SiO_2 caused the overall dielectric constant of the $SrTiO_3$/SiO_2 combination to deteriorate markedly. Platinum on silicon, Pt/Si, readily forms a silicide as low as 200°C, and this silicide in turn will oxidize, as Matsubara *et al.*[2] also observed. Indium tin oxide, or ITO, on glass has the advantage of being transparent. However Sreenivas *et al.*[4] observe that lead readily diffuses into the ITO layer, and the conductivity of ITO degrades above 300°C. Platinum and titanium foil should be good substrates, but they offer little prospect for use in circuits which integrate silicon-based electronics and ferroelectrics. Of the remaining substrates on the list, we have concentrated on Pt/SiO_2/Si, Pt/MgO, and Pt/Ti/SiO_2/Si as being the most promising. Other substrates which we have investigated which receive either one or zero mentions are RuO_2/SiO_2/Si, TiN/MgO, ReO_3/SiO_2/Si, Pd/SiO_2/Si, $CoSi_2$/Si_3N_4/SiO_2/Si, and PtSi/Si. The non-conducting substrates are listed in Table I for reference only and will not be discussed in this paper.

TABLE I Substrates for PZT, PLZT, and $PbTiO_3$ deposition, ranked by frequency of mention (out of 72 articles).

(conducting)		TiN/MgO	1	$SrTiO_3$	4
bare Si	22	$Pt/MgAl_2O_4$	1	SiO_2/Si	4
Pt/Si	19	$TiN_x/SiO_2/Si$	1	Ta_2O_5/Ta	
Pt/MgO	6	$ZrN_x/SiO_2/Si$	1	$/SiO_2/Si$	1
ITO/glass	5	poly-Si/Si	1	AlN	1
$Pt/SiO_2/Si$	5	Pt/Al_2O_3	1	Al_2O_3/Si	1
Pt foil	3	$Pt/SrTiO_3$	1	$MgAl_2O_4$	1
bare GaAs	3	Pt/glass	1	$Si_3N_4/GaAs$	1
Pt/Ti/Si	2			$SiO_2/GaAs$	1
Ti foil	1	(non-conducting)		$TiO_x/SiO_2/Si$	1
Pt/GaAs	1	Al_2O_3	21	$KTaO_3$	1
Pt/Ta/Si	1	fused qtz., glass,		$ZrO_x/SiO_2/Si$	1
Ti/glass	1	fused silica	15	ZrO_2/Si	1
PtSi	1	MgO	13		

EXPERIMENTAL

A computer-controlled ion beam sputter deposition system was used to deposit many of the films mentioned in this study. This equipment has been described elsewhere.[5,6] Specifically, the following films were deposited by this method: $Pb(Zr,Ti)O_3$ (PZT), RuO_2, Pt, ReO_3, and TiN. The deposition conditions for each of these films are listed in Table II.

The following details were common to all the depositions listed: only elemental metal targets were used (no oxides), the beam voltage was 1400 V; the beam gas was krypton. The chamber pressure was 0.6 to 1.0 x 10^{-6} Torr before a run, 2 -6 x 10^{-4} Torr during run. Flowing gases were directed at the substrate with a 0.5 cm dia. tube about 5 cm from the substrates. Typical distances used were 13.5 cm. from ion gun to target and 10 cm from target to substrate. Targets were 7 cm in diameter. Some platinum films were deposited in a Denton DESK II DC magnetron sputter deposition chamber at 50 mTorr and 20 watts.

TABLE II Deposition conditions for films produced by ion beam sputtering.

Film produced	PZT	RuO_2	Pt	ReO_3	TiN
Thickness (nm)	100	100	100	20	100
Beam current (mA)	8-20	20	20	20	20
Deposition rate (Å/min)	10	30	40	30	10
Substrate temp.(°C)	600	350	400	375	700
Gas flowing	O_2	O_2	none	O_2	N_2

The following substrates were used: single crystal Mg(001) annealed at 1200°C, 1100 Å thermally oxidized SiO_2/Si, and rapid thermal annealed Ti on SiO_2/Si (600°C for 60 sec. in flowing argon). Electron microscopy was done on a Hitachi H-800 at 200 KV. X-ray microanalysis was done on the H-800 and on a Philips EM 400. Electron microscope samples were prepared by standard dimpling and ion milling; samples on MgO were prepared following a chemical etching and milling procedure developed in our laboratory.[7]

Preliminary stress measurements were done using a Zygo Mark IV interferometer. The surface profile of a silicon piece, about 520 mm thick and 6x6 mm in area, was determined, and the stress in the thin film was determined by use of a wafer bending formula.[8]

Samples were annealed in air in a standard box furnace. Vacuum anneals were done in a quartz tube furnace; the tube was evacuated with a liquid-nitrogen trapped diffusion pump to a pressure of 10^{-6} Torr during an anneal.

ADHESION

An important requirement for a lower electrode is that it adhere well to the substrate. Lack of adhesion of the lower electrode was a problem in the case of two substrates, platinum and ruthenium dioxide. There were several factors which influenced the adhesion of the platinum, namely: a) the substrate temperature during platinum deposition; b) the mode of platinum deposition, i.e. dc magnetron sputtering vs. ion beam sputtering; c) the underlying substrate, i.e. whether the platinum was deposited onto SiO_2 or onto Ti/SiO_2; and d) whether a second ion beam was used during ion beam sputter deposition to mix atoms at the interface and improve adhesion. These factors and their effect on adhesion are given in Table III. The term "good adhesion" means that the

platinum film passed the adhesive tape test and showed no peeling, including after deposition of a PZT film on the platinum.

In general, platinum deposited with ion beam sputter deposition required that the substrate be held at elevated temperature, or that a second ion beam be used, for the platinum to adhere well. The microstructure of the platinum is described in a later section.

In the case of ruthenium dioxide, the deposition temperature was again crucial. The substrate in all cases was SiO_2/Si. For substrate temperatures above 350°C, good adhesion was observed, whereas below this temperature the RuO_2 films lost adhesion by developing blisters, which are characteristic of compressive stress in the films.

TABLE III Adhesion of platinum.

Substrate	Substrate temp.	Deposition technique	Second ion beam	Good adhesion
SiO2/Si	RT	ion beam	no	no
SiO2/Si	RT	dc magn.	no	yes
SiO2/Si	400°C	ion beam	no	yes
SiO2/Si	RT	ion beam	yes	yes
Ti/SiO2/Si	RT	ion beam	no	yes*
Ti/SiO2/Si	400°C	ion beam	no	yes
MgO	RT	ion beam	no	no
MgO	RT	dc magn.	no	yes
MgO	400°C	ion beam	no	yes

* this film lost adhesion after a PZT film was deposited.

DIFFUSION THROUGH PLATINUM

Room temperature magnetron sputtered Pt on SiO_2/Si

The properties of a platinum film are strongly dependent on their microstructure. In articles in which platinum films are used as lower electrodes for PZT films, one very seldom finds any description of how the platinum films are deposited. One must assume that many of these platinum films are deposited by magnetron sputtering at room temperature, which is a common method for depositing platinum. However, we have found through TEM examination of the microstructure of the

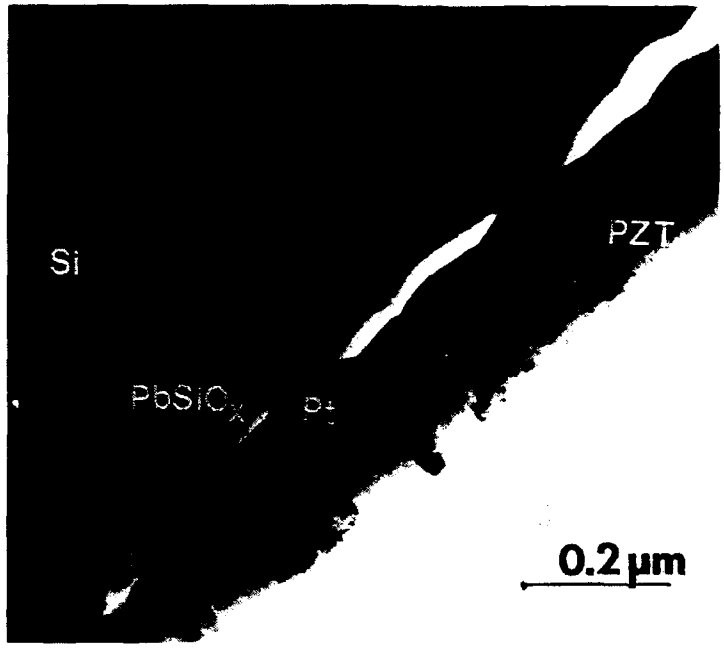


FIGURE 1 PZT film on Pt/SiO_2/Si; Pt deposited at RT in DC magnetron sputter system. Pb has diffused through Pt layer to react with SiO_2 and form amorphous lead silicate.

platinum films that magnetron sputtered films are highly porous and are very poor diffusion barriers for lead, as will be seen in the following examples.

In Fig. 1 is shown a cross-section of a PZT film on Pt/SiO_2/Si, where the platinum was deposited at room temperature in a dc magnetron. The PZT film was deposited at 500°C over a deposition time of two hours. The platinum, originally very small-grained, has coalesced into larger grains, which however have holes in between them. The SiO_2 layer below the platinum has been transformed into an amorphous lead silicate phase by the diffusion of lead during the PZT deposition. The presence of lead was detected by EDS in the electron microscope. A thicker platinum film of 7000 Å also deposited at room temperature showed the same result, namely that lead diffused through to the SiO_2 layer and converted the SiO_2 to lead silicate. The lead loss to diffusion makes control of the stoichiometry of the PZT film difficult and a denser platinum microstructure is highly desirable.



FIGURE 2 Room temperature ion beam sputtered platinum showing dense grains.

RT ion beam sputter deposited Pt on $Ti/SiO_2/Si$

At room temperature, platinum will not adhere directly to SiO_2, therefore an intermediate Ti layer is needed. For these depositions, the RTA Ti described in the experimental section is used. The microstructure of room temperature ion beam sputtered Pt on $Ti/SiO_2/Si$ is shown in Fig. 2. The grains are densely packed and no voids are visible. The microstructure of a similar ion beam sputtered Pt layer on $Ti/SiO_2/Si$ is shown in Fig. 3, where the Pt layer is still thick but the other layers have not been ion milled away. The Pt layer peeled after PZT deposition, so that no study could be made of lead diffusion through the platinum.

High temperature ion beam sputter deposited Pt on $Ti/SiO_2/Si$

If the substrate was at elevated temperature during Pt deposition, the Pt layer adhered to $Ti/SiO_2/Si$, anc continued to adhere even after a PZT layer was deposited on the platinum. The microstructure of the platinum deposited at 400°C was very similar to that of annealed room temperature deposited platinum. A PZT layer was deposited onto the high-temperature deposited platinum, and there was no trace of

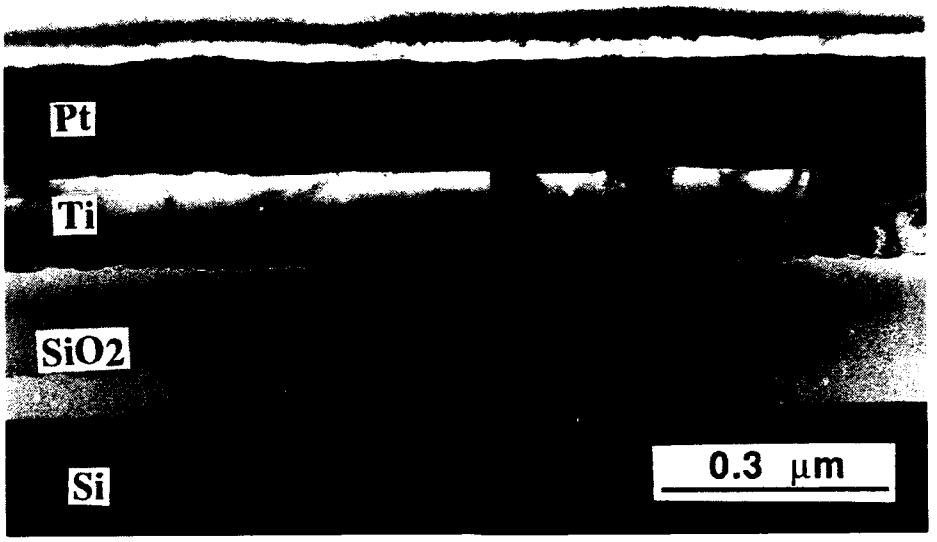


FIGURE 3 Platinum layer on $Ti/SiO_2/Si$ deposited at room temperature by ion beam sputter deposition; platinum layer is too thick for its grain structure to be imaged.

lead in the SiO_2 layer. That is, the combination of titanium and lead was sufficient to stop the diffusion of lead.

HILLOCKS IN PLATINUM

Hillocks are thin, elevated parts of a thin film which extend out from the film surface, often to a distance of several film thicknesses. They commonly form during heat treatments of metal films in which the film is in a state of compressive stress for long periods of time. They have been observed in Ni, Al, Pb, and several other metals and alloys.[9-11] However, a search of the literature revealed no published work on generation of hillocks in platinum. We have observed hillock generation during anneals of platinum films on SiO_2/Si and on MgO. In Fig. 4, which is a cross-section electron micrograph, one can see a hillock in a platinum film on $Ti/SiO_2/Si$. The platinum was deposited at room temperature by ion beam sputter deposition, then the $Pt/Ti/SiO_2/Si$ sample was annealed in air at 600°C for one hour, during

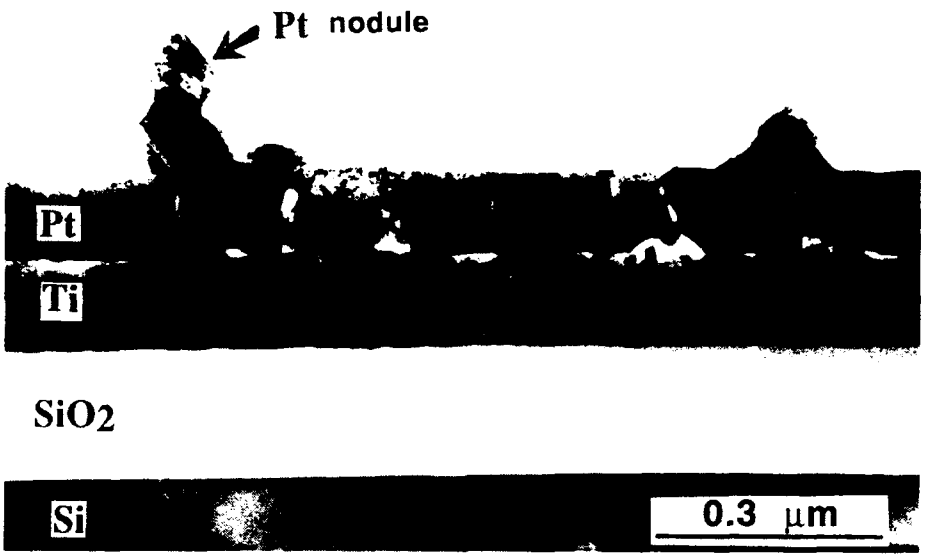


FIGURE 4 Pt/Ti/SiO_2/Si structure. Pt was deposited at room temperature, then annealed one hour in air at 600°C. During the anneal a platinum nodule or hillock was formed.

which time the appearance of the platinum surface changed from mirror-like and metallic to cloudy. Optical microscopy of the surface indicated numerous small defects on the surface, which correspond to the hillock in Fig. 4.

Another example of a hillock is shown in Fig. 5, in which a PZT film has been deposited onto a platinum film on MgO. The PZT deposition was done at 550°C for two hours. A hillock has again formed in the platinum layer, and this time it has penetrated through the PZT layer. The hillock would most likely cause a catastrophic short if this structure were part of a ferroelectric memory.

A careful study of the circumstances of the formation of hillocks in platinum would include a measurement of the state of stress in the platinum as a function of temperature. Such a study is under way as of this writing. However, two preliminary room temperature stress measurements have been made. A stress measurement was made at room temperature of two samples of Pt/SiO_2/Si. The plátinum platinum was deposited onto SiO_2/Si at 430°C. The stress in the films was determined by a wafer bending formula[8] and found to be 5×10^9 dyn/cm^2

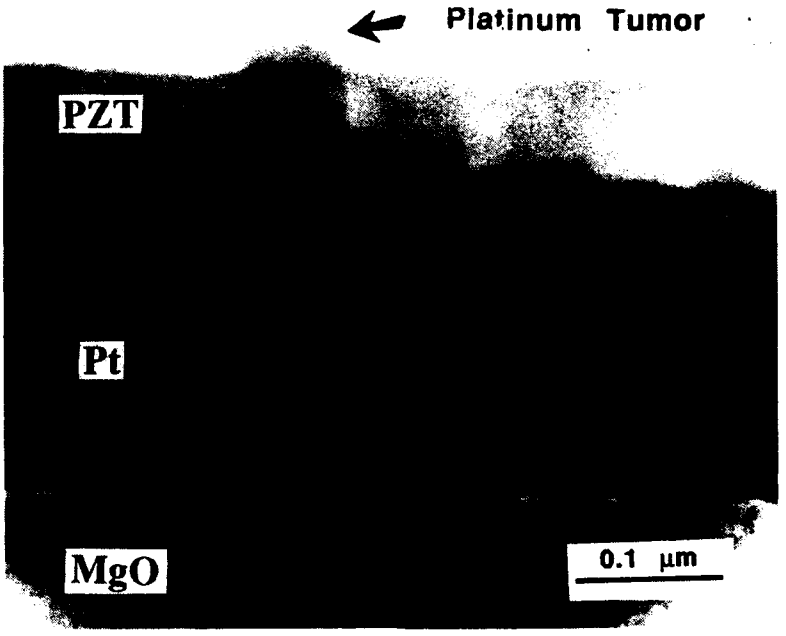


FIGURE 5 PZT film deposited on Pt/MgO. The Pt was deposited at 400°C on the MgO; the PZT film was deposited at 550°C on the Pt/MgO; both were deposited by ion beam sputter deposition. During the PZT deposition a platinum tumor or hillock formed.

for a 200 nm film and 7.4×10^9 dyn/cm^2 for a 250 nm film. If we assume bulk values for the thermal expansion coefficients of platinum and silicon[12], and bulk values for the elastic properties of platinum, then the platinum films will be in compressive stress at a temperature of 550°C, at which temperature PZT is deposited. Sputtered films are usually compressive at room temperature[13], but increasing the deposition temperature could be expected to causes them to have zero or tensile stress, as is the case for evaporated metal films.[14] The compressive stress at the PZT deposition temperature may be the cause of the hillocks.

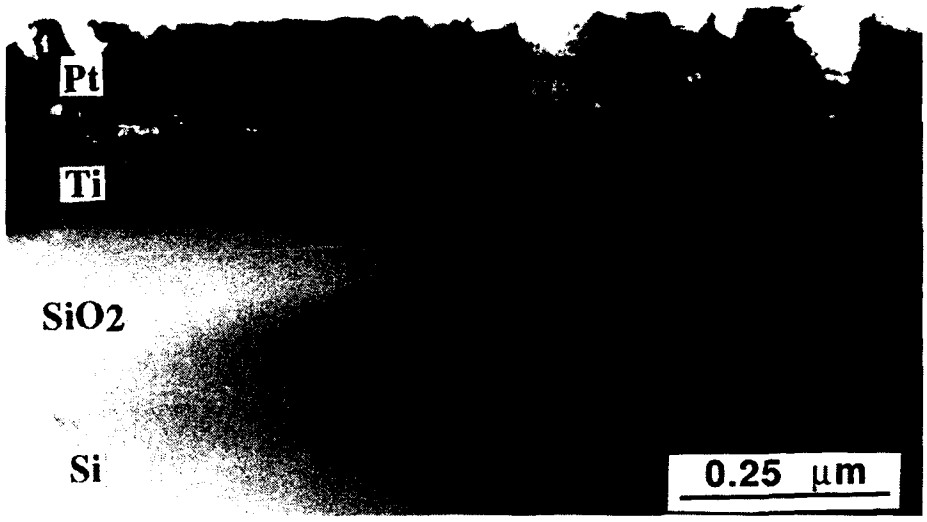


FIGURE 6 Pt/Ti/SiO_2/Si sample annealed in vacuum at 600°C for one hour; no hillocks were observed, determined by XTEM and optical microscopy.

In the case of Pt on SiO_2/Si, the annealing atmosphere had an important effect on the generation of hillocks. Three identical platinum films were annealed at 600°C for one hour, one in air, another in a vacuum furnace at $1x10^{-6}$ Torr, and the third in a vacuum chamber backfilled with oxygen to $1x10^{-3}$ Torr. The one annealed in air (shown in Fig. 4) showed a high density of hillocks, the one in vacuum showed no hillocks (seen in Fig. 6), and the one annealed in a partial pressure of oxygen showed an intermediate density of hillocks. At the moment we have no convincing explanation for this behavior, but the following facts may be noted. The surface energy of platinum oxide and platinum dioxide is considerably lower than that of platinum, based on their relative melting points (1772°C for Pt, 450 and 550°C for PtO and PtO_2).[15] Therefore, the configuration of a thin hillock leaving the surface with a high surface area causes a relatively small increase in surface energy so long as there is sufficient oxygen available to create a monolayer or two of platinum oxide. In this situation, the reduction in elastic strain in the compressed platinum film is a powerful driving force for the diffusion of platinum out of the film into the growing hillock.

One more observation was made on the hillock formation, which does not seem to fit in this picture neatly. If platinum is deposited on SiO_2/Si by ion beam sputtered

deposition at temperatures of 530°C or higher, hillocks are observed on the platinum film. The oxygen and water partial pressures during this process should be less than $1x10^{-6}$ Torr, which should not be sufficient to maintain a monolayer coverage of Pt oxide on the surface of the growing film, yet hillocks appear nonetheless. The situation is complicated by the arrival of new platinum atoms from the deposition process, which makes a comparison to a simple anneal of a platinum film less direct.

The formation of hillocks in a platinum film is clearly a complicated issue, but one of major importance for successful use of platinum as a lower electrodes. Some of the issues we are currently addressing are: a) what is the state of stress of the platinum at elevated temperature; b) how does the formation rate of hillocks depend on stress level and annealing atmosphere; c) whether platinum films deposited with different techniques and at different temperatures behave the same way with regard to hillock formation.

RUTHENIUM DIOXIDE

Ruthenium dioxide is an attractive candidate for a lower electrode for PZT films. It is a conductor with a resistivity of 50-100 μΩ-cm, its conductivity will not degrade in an oxidizing environment, and it has been shown to be a good diffusion barrier. We have deposited RuO_2 by ion beam sputter deposition at a temperature of 250 to 350°C. Improved adhesion was obtained at the higher temperature, as noted above. A cross section of PZT film on $RuO_2/SiO_2/Si$ is shown in Fig. 7. The RuO_2 is fine grained and has a smooth top surface. The composition of the structure shown in this figure was studied by EDS. No lead was observed in either the SiO_2 or in the RuO_2, and no Ru was found in the PZT film. The RuO_2 had resistivity of 50 μΩ-cm, measured by a four-point probe. As of this writing, no electrical measurements have been performed on this structure, since the optimal deposition conditions on $RuO_2/SiO_2/Si$ are different from the conditions on MgO, our usual substrate, and consequently single-phase PZT had not been formed.

OTHER SUBSTRATES

Several other substrates have been studied less intensively, and will be described below. Each has shown some deficiency making it a less promising candidate for a lower electrode for PZT.

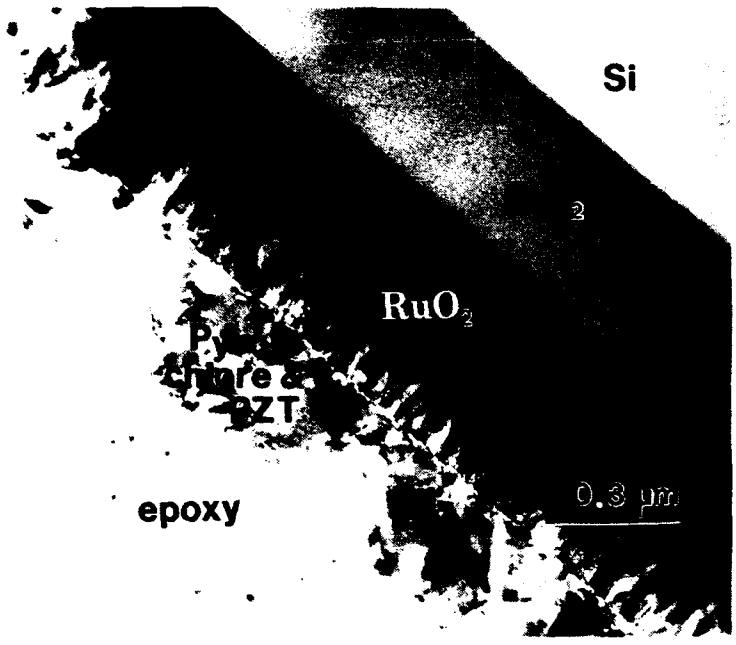


FIGURE 7 PZT film on $RuO_2/SiO_2/Si$. No interfacial phase is visible, and no diffusion into the substrate was observed by EDS.

Rhenium trioxide at first glance appears to be a good candidate, since it is a conducting oxide like RuO_2. However, the vapor pressure of ReO_3 is 120 mTorr at 300°C and 2.3 Torr at 400°C.[16] ReO_3 decomposes to ReO_2 and Re_2O_7, and Re_2O_7 is even more volatile than ReO_3. ReO_2 is stable to higher temperatures, but unfortunately neither ReO_2 nor Re_2O_7 is a conductor.[16] One ReO_3 oxide deposition was done with the conditions shown in Table II. The resistivity was about 60 μΩ-cm, indicating that most probably a mixture of Re metal and ReO_2 was formed. In general, it probably is difficult to deposit the desired ReO_3 phase, and even then its stability is highly suspect.

Cobalt disilicide showed a tendency to oxidize. This layer, as reported by Matsubara *et al.*[2] in the case of $SrTiO_3$ on bare silicon, can degrade the dielectric constant of a ferroelectric film even when only 4 nm thick.

Titanium nitride is a good conductor as deposited, but shows a tendency to oxidize to TiNO, which is a poor conductor. Auger data for a PZT film deposited on TiN/MgO, indicates that oxygen has penetrated a large distance into the TiN, and therefore created an extra dielectric layer between the TiN and the PZT.

CONCLUSION

Platinum, the most common lower electrode, shows great resistance to oxidation, but must be used with care. Adhesion to SiO_2/Si can be a problem. The microstructure of platinum is porous when deposited at room temperature in a dc magnetron. This porosity provides avenues for lead diffusion, which occurs readily and enables lead to react with an underlying SiO_2 layer to form lead silicate. Ruthenium dioxide shows promise as an electrode. Other candidates, including ReO_3, $CoSi_2$, and TiN, have serious drawbacks.

ACKNOWLEDGEMENTS

Support for this work was provided by NSF and by DARPA/ORD. We are grateful for the assistance of MCNC in providing oxidized silicon and titanium coated silicon wafers, and for the use of their electron microscope facility. Thanks also to the Analytical Instrumentation Facility at NCSU for the use of the Hitachi electron microscope and the Zygo optical interferometer for stress measurements.

REFERENCES

1. R. A. Roy, K. F. Etzold, and J. J. Cuomo, in Ferroelectric Thin Films, edited by E. R. Myers and A. I. Kingon (Mater. Res. Soc. Symp. Proc. 200, Pittsburgh, PA, 1990), p. 141.
2. S. Matsubara, T. Sakuma, S. Yamamichi, H. Yamaguchi, and Y. Miyasaka, in Ferroelectric Thin Films, edited by E. R. Myers and A. I. Kingon (Mater. Res. Soc. Symp. Proc. 200, Pittsburgh, PA, 1990), p.243.
3. K. F. Etzold, R. A. Roy, K. L. Saenger, and J. J. Cuomo, abstract presented at 93rd annual meeting of the American Ceramic Society, April 28 - May 2, 1991, Cincinnati, Ohio.
4. K. Sreenivas, M. Sayer, T. Laursen, J. L. Whitton, R. Pascual, D. J. Johnson, D. T. Amm, G. I. Sproule, D. F. Mitchell, M. M. Graham, S. C. Gujrathi, and K. Oxorn, in Ferroelectric Thin Films, edited by E. R. Myers and A. I. Kingon (Mater. Res. Soc. Symp. Proc. 200, Pittsburgh, PA, 1990), p. 255.
5. M. S. Ameen, T. M. Graettinger, S. H. Rou, H. N. Al-Shareef, K. D. Gifford, O. Auciello, and A. I. Kingon, in Ferroelectric Thin Films, edited by E. R. Myers and A. I. Kingon (Mater. Res. Soc. Symp. Proc. 200, Pittsburgh, PA, 1990), p. 65.
6. A. I. Kingon, O. Auciello, M. S. Ameen, S. H. Rou, A. R. Krauss, Appl. Phys. Lett., 55, 301 (1989).
7. S. H. Rou, in Specimen Preparation for Transmission Electron Microscopy of Materials II, edited by R. Anderson (Mater. Res. Soc. Symp. Proc. 199, Pittsburgh, PA, 1990), p. 225.
8. R. W. Vook and F. Witt, J. Appl. Phys., 36, 2169 (1965).

9. C. J. Santoro, J. Electrochem. Soc., 116, 361 (1969).
10. M. Ronay and C. F. Aliotta, Philos. Mag. A, 43, 161 1980).
11. J.Y. Kim and R. E. Hummel, Phys. Stat. Sol. A, 122, 255 (1990).
12. Y. S. Touloukian, ed., Thermophysical Properties of Matter (IFI/Plenum, New York, 1979), vol. 15.
13. J. A. Thornton, J. Tabock, and D. W. Hoffman, Thin Solid Films, 64, 111 (1979).
14. E. Klokholm, J. Vac. Sci. Technol., 6, 138 (1969).
15. R. C. Weast, ed., CRC Handbook of Chemistry and Physics (CRC Press, Boca Raton, FL, 1990), p. B-114.
16. K. B. Lebedev, The Chemistry of Rhenium (Butterworths, London, 1962), p. 15.

ELECTRICAL CHARACTERISTICS OF ALUMINUM-ZIRCONIUM OXIDE-BARIUM MAGNESIUM FLUORIDE-p SILICON MIS CAPACITORS

AD-P006 689

T.S. KALKUR, R.Y. KWOR, L. LEVENSON* AND L. KAMMERDINER**
Microelectronics Research Laboratories, Department of Electrical and Computer Engineering, University of Colorado at Colorado Springs, 80933-7150.
* Department of Physics, University of Colorado at Colorado Springs, 80933-7150
** Ramtron Corporation, Colorado Springs, CO

Abstract

The Barium Magnesium Fluoride films have been deposited on p-Si wafers at a temperature in the range of 400-450°C in an ion assisted deposition system. X-ray diffraction analysis shows that the films are polycrystalline in nature. The BMF films were encapsulated with an electron beam evaporated ZrO_2 film of thickness 300°A. The capacitance-voltage (C-V) charactersitics of Aluminum-ZrO_2-BMF-p Si MIS capacitors show hysteresis and the direction of the hysterisis correponds to ferroelectric polarization in the BMF film. The shift in threshold voltage was found to depend on bias voltage, ramp rate as well as measurement temperature.

INTRODUCTION

Recently, there has been tremendous interest in the use of ferroelectric materials like Lead Zirconate Titanate (PZT) and Bismuth titanate for non-volatile memory applications (1-3). Most of the memory elements demonstrated with these materials are based on metal-ferroelectric-metal capacitor structures. In these types of memories, whenever the memory device undergoes a read cycle, the information has to be written back immediately because the memory read out is distructive. With increase in read cycles, the memory element gets fatigued and puts limitation on its usage. A non-distructive memory element can be implemented, by incorporating the ferroelectric material as the gate

92-16164

insulator of a metal-insulator-semiconductor field effect transistor (MISFET) (4). This implementation requires the study of metal-ferroelectric-semiconductor characteristics. There were some studies on incorporating PZT and Bismuth Titanate as gate materials (5,6). Becuause of the growth of oxides at ferroelectric-semiconductor interface as well as interdiffusion of ferroelectric and semiconductor during the annealing process, it was not possible to modulate the conductivity of semiconductor at the semiconductor-ferroelectric interface. The hysteresis observed in the C-V characteristics was predominantly due to charge injection at the ferroelectric - semiconductor interface. Recently, fluoride based ferroelectrics are attracting the attention of many investigators because of the possibilty of incorporating them as gate insulators (7,8). In this paper, we are reporting the electrical characteristics of barium magnesium fluoride (BMF) based MIS capacitors.

SAMPLE PREPARATION

The silicon wafers used for the study were 4" diameter (100) p-type and had resistivities in the range of 6.8 to 10 ohm.cm. The ion-cluster beam system used for the deposition of BMF film is shown in the fig.1. Although the system had three ion sources, single ion source was used for the deposition of BMF. The vacuum in the deposition chamber before the substrate heating was 7×10^{-9} torr. Equimolar quantities of Barium flouride and magnesium fluoride was mixed in a tantalum crucible and the charge was initially heated to its melting point. The crucible was then cooled to room temperature. The substrate temperature during the film deposition was $400^{o}C$ and the barium magnesium fluoride was deposited at a rate of $2^{o}A$ per second. The vacuum during the deposition of BMF was 1×10^{-7} torr. The thickness of the film during the deposition process was monitored using quartz crystal monitor. After the film deposition, the substrates were cooled to room temperature. For some wafers, $300^{o}A$ of ZrO_2 was evaporated by electron beam evaporation with substrate at room temperature, as an encapsulation layer. The top electrode for the MIS structure was fabricated by evaporating aluminum through the shadow mask. The oxide at the backside of the wafer was etched in buffered hydrofluoric acid. A layer of aluminum of thickness $2000^{o}A$ was deposited on the backside of the wafer.

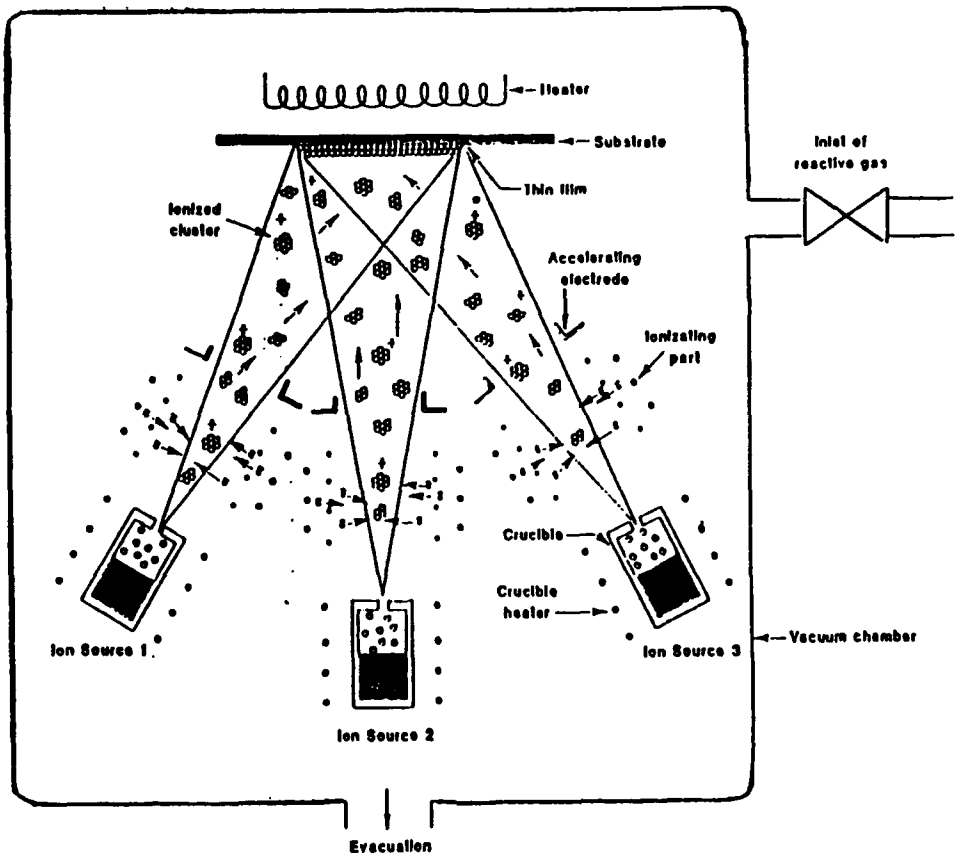


Fig.1 Ion cluster beam deposition system used to deposit BMF.

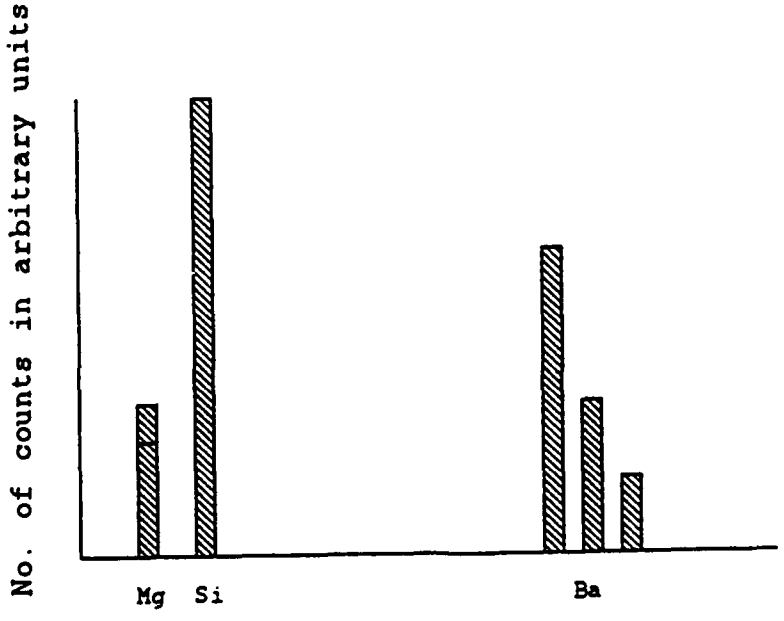


Fig.2 EDAX spectra showing the relative peak heights for Ba and Mg.

RESULTS AND DISCUSSION

The surface morphology of the as deposited BMF film was smooth and no cracking or flaking of the film was observed. When the film was etched in dilute nitric acid (20%), the surface of the silicon wafer did not show any degradation suggesting that there is negligble interaction of BMF film on silicon. The refractive index of the film as determined by an ellipsometer was found to be 1.43. The x-ray diffraction analysis of the film showed that the film is polycrystalline in nature and the diffraction peaks corresponds to orthorombic phase with a=4.130 ^{o}A, b=5.819^{o}A, and c=14.510^{o}A. The energy dispersive X-ray spectra (EDAX) of the BMF film on silicon is shown in fig.2. The EDAX spectra of the films did not show significant changes due to successive depositions with the same charge from the crucible. This shows that BMF evaporates through sublimation process without decomposition.

The device structure used for the study is shown in fig.3. The capacitance-voltage (C-V) characteristics of BMF based MIS capacitor determined at a frequency of 1 MHz is shown in fig.4. The C-V curves clearly show regions of accumulation, depletion and inversion. The hysterisis in the C-V curve was 3V for a bias change of -5V to 5V. The C-V curve determined at a frequency of 20 kHz is shown in fig.4 The thresold voltage shift did not change significantly due to the change in measurement frequency. Comparison of fig.4 and fig.5 shows that there is smearing in the C-V characteristics at high frequencies. This is due to the presence of interface states at the BMF-silicon interface. The variation of threshold shift with bias voltage swing at a measurement frequency of 1 MHz is shown in fig.6. Initially, with increase in bias voltage swing from + 3V to +11V, the threshold voltage shift was found to increase. The increase in bias voltage swing above 11 volts resulted in saturation in the threshold voltage shift. Further increase in bias voltage swing resulted in slight decrease of threslod voltage shift. This might be due to the injection of charge at Si-BMF interface. Even at a bias swing of +3V, the threslod voltage shift was 2V and this shows that with proper design of sense amplifier, it is possible to write the information at low voltages compared to that of MNOS structure. The variation in accumulation capacitance with applied bias is also shown in fig.6. With increase in applied bias voltage, the accumulation capacitance was found

to increase and this might be due to the increase in dielectric constant due to ferroelectric polarization.

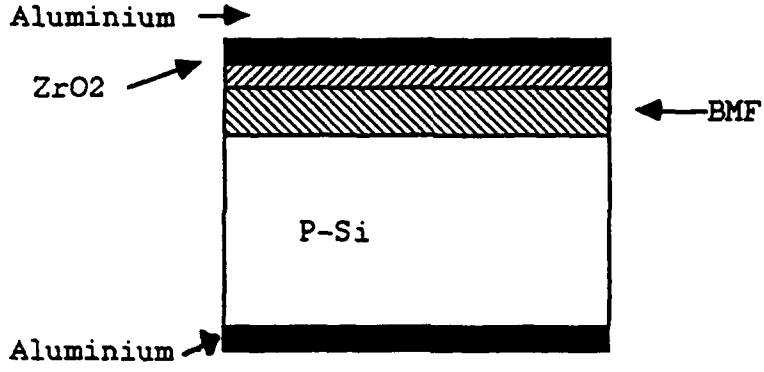


Fig.3 Device structure used for the electrical characterization.

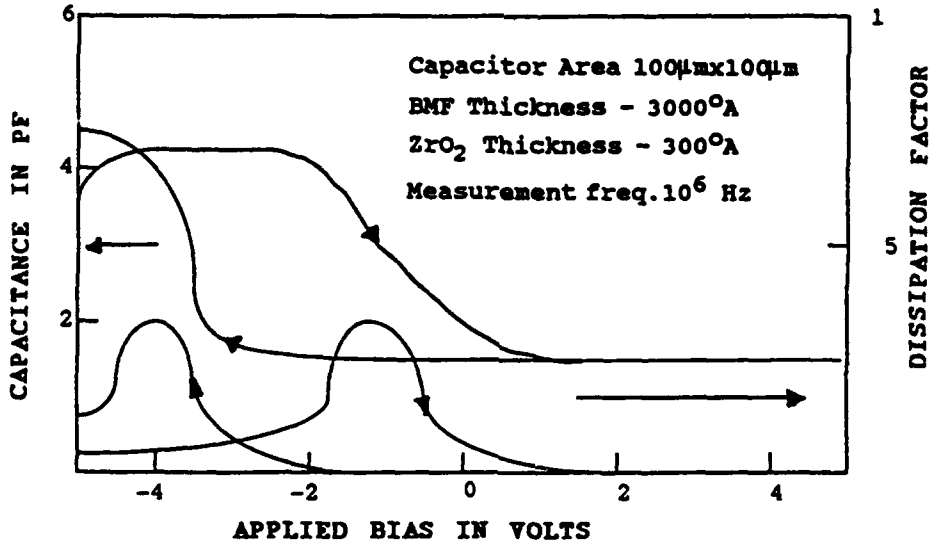


Fig.4 Capacitance-Voltage characteristics of Al-ZrO_2-BMF-p Si MIS capacitors. Time for a bias change of .2V=.1 sec. Meas. freq. 10^6 Hz.

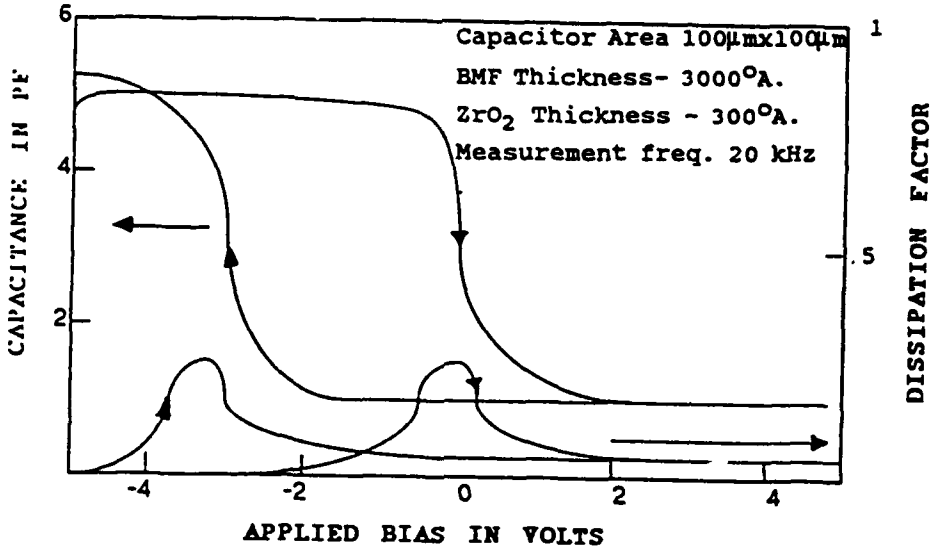


Fig.5 Capacitance-Voltage characteristics of Al-ZrO_2-BMF-p Si MIS capacitors. Meas. Freq. =20 KHz.

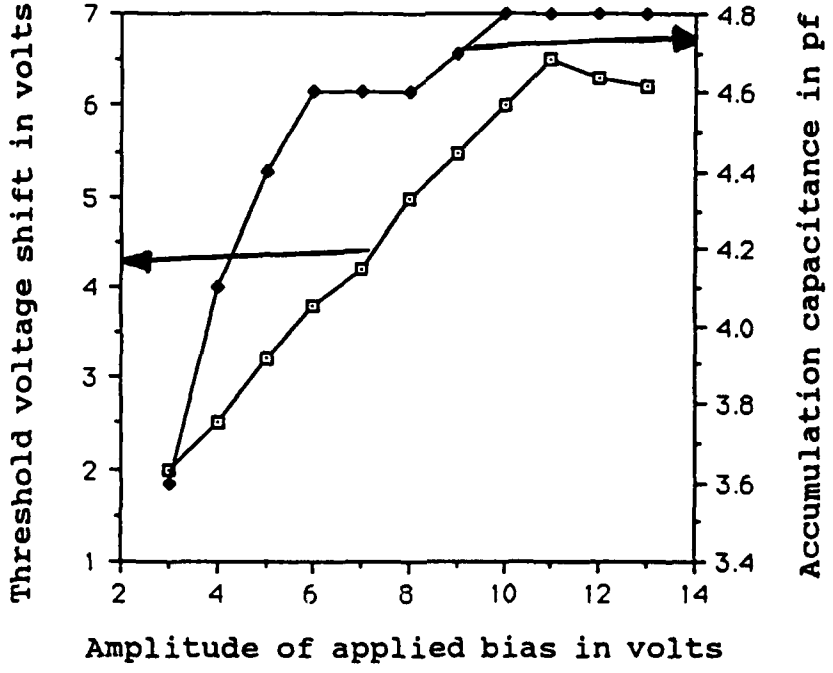


Fig.6 Variation of threshold voltage shift and accumulation capacitance with amplitude of bias voltage. Time for bias change of .2V=.1 sec.

Fig.7 shows the variation in the threshold voltage shift and accumulation capacitance with the measurement frequency between 10kHz and 2 MHz. The threshold voltage shift was not found to change significantly with the measurement frequency. But the accumulation capacitance was found to be strongly dependent on the measurement frequency and this is due to various dielectric losses taking place in the BMF or in the Si wafer at high frequencies (9).

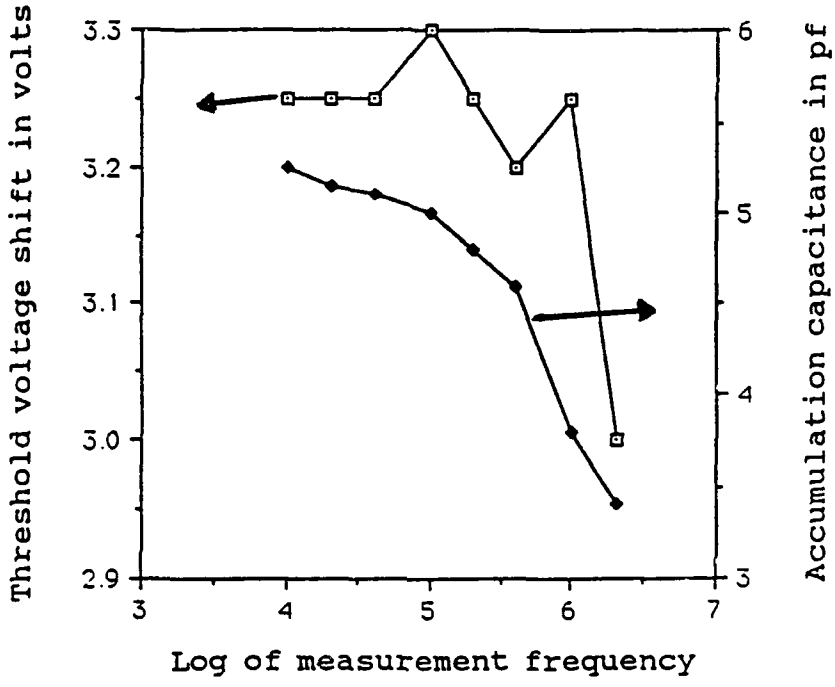


Fig.7 Variation of Threshold voltage shift and accumulation capacitance with measurement frequency.

The shape of the C-V curve was found to dependent on the time for the change in bias voltage. Fig.8 shows the C-V characteristics of BMF MIS capacitor for a bias voltage change of .2V for a time of 10 seconds. Comparison of Fig.4 and Fig.7 shows that, the C-V curve has become considerably slimmer with increase in time for the change of bias voltage. Fig.9 shows the variation in the shift in threshold voltage and accumulation capacitance with time for bias voltage change of 0.2V. The decrease in threshold voltage shift with increase in time for bias change is due to the injection of charges at the BMF-Si interface. The accumulation capacitance was found to increase with increase in time for bias change. This shows that, at faster rates of bias change, the polarization does not get saturated.

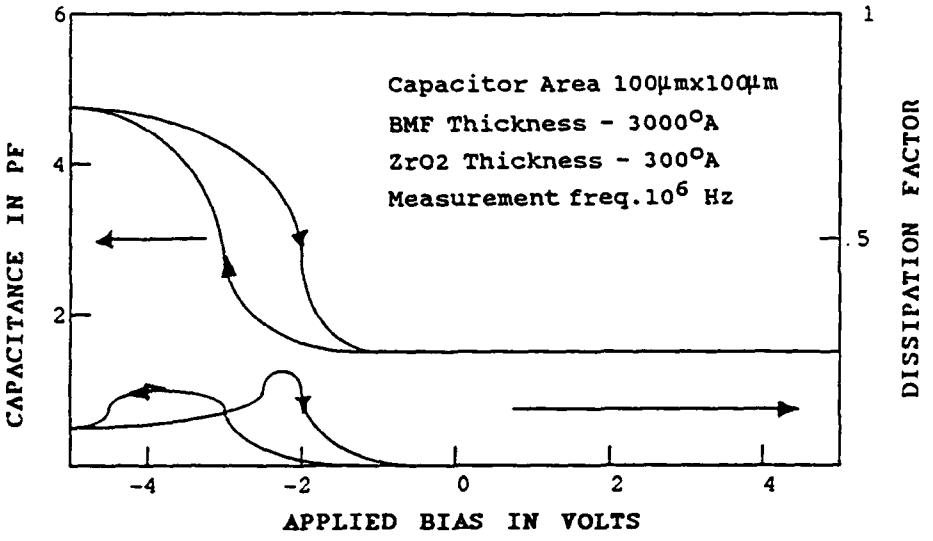


Fig.8 C-V characteristics of Al-ZrO_2-BMF-p Si MIS capacitors. Time for bias change of .2V =10 Seconds.

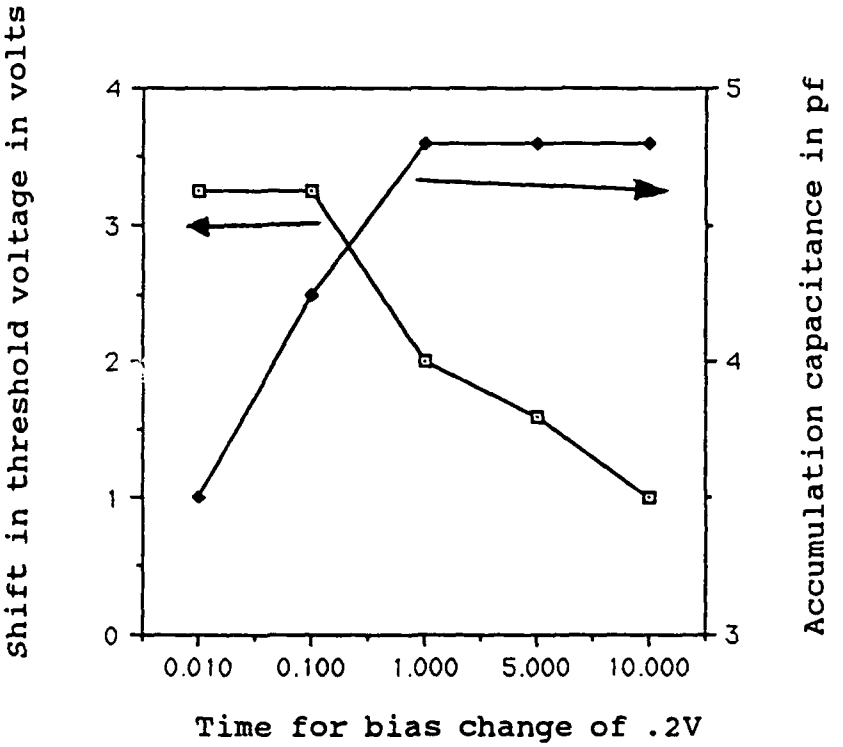


Fig.9 Variation of shift in threshold voltage and accumulation capacitance with time for bias voltage change.

Fig.10 shows the C-V curves for the MIS capacitors at a measurement temperature of 80°C. The shift in threshold voltage was found to depend on the temperature of the device. The shift in threshold voltage gets reduced with increase in device temperature. Fig.11 shows the variation in threshold voltage shift and accumulation capacitance with device temperature. The shift in threshold voltage reduces drastically when the device temperature increases above 60°C. This might be due to the ionic conduction taking place in the fluoride film.

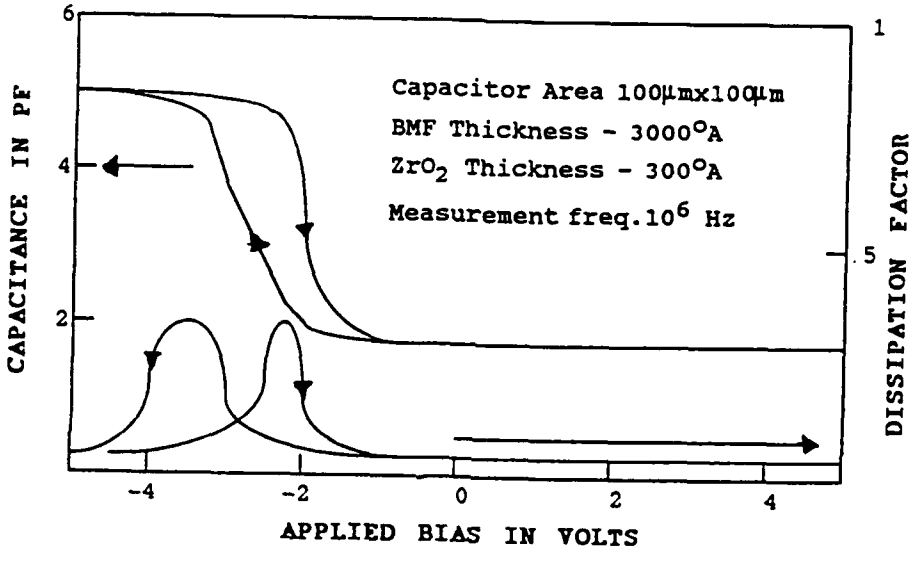


Fig.10 C-V characteristics of Al-ZrO_2-BMF-p Si MIS capacitor. Time for a bias change of .2 V is .1 sec. Measurement temperature = 80°C.

CONCLUSIONS

The MIS characteristics of ICB deposited BMF films show hysteresis in the C-V characteristics. The direction of hysteresis corresponds to ferroelectric polarization. The shift in threshold voltage was found to increase with increase in bias voltage. The shift in threshold voltage did not change significantly with measurement frequency. The hysteresis in the C-V characteristics was found to decrease with increase in time for bias voltage change as well as increase with temperature.

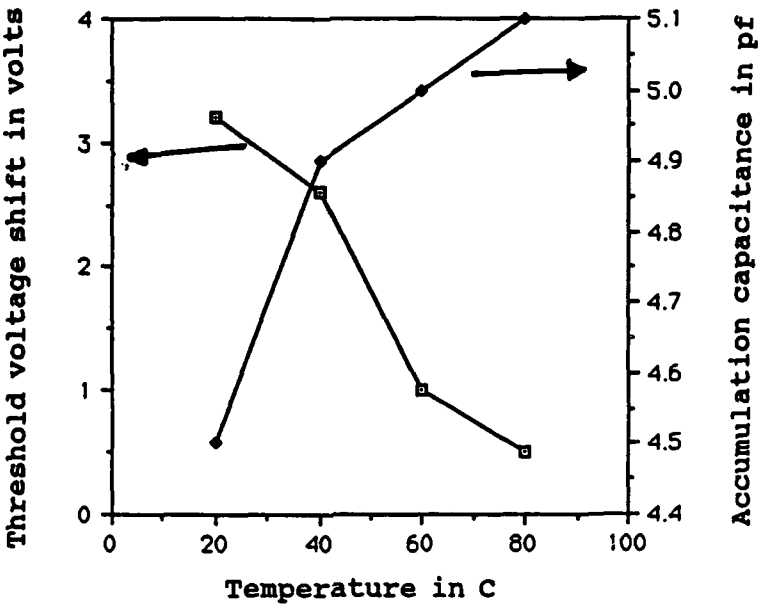


Fig.11 Variation of threshold voltage shift and accumulation capacitance with temperature.

ACKNOWLEDGEMENT

The authors are grateful to Mitsubishi Corporation for providing ICB facility.

REFERENCES

1. S.S. Eaton D.B. Butler, M. Parris,D. Wilson and H.
2. C.A. Araujo and G.W. Taylor, Ferroelectrics, vol.116, 215 (1991)
3. J.F. Scott, L. Kammerdiner, M. Parris, S. Trayner, V. Ottanbachar, A. Shawbkeh and W.C. Oliver, J. Appl. Phys. 64 (2),787 (1988)
4. Yoshio Nishi and Hisakazu IIzuka, Silicon Integrated Circuits, Part A, 121 (1981)
5. T.S. Kalkur, George Argos and L. Kammerdiner, MRS Proceedings,vol.200, 313 (1990)
6. T.S. Kalkur, J.R. Kulkarni, Y.C. Lu, M.Rowe, W.Han and L. Kammerdiner, Ferroelectrics, vol.116, 135 (1991)
7. M.H. Francombe and S.V. Krishnaswamy, MRS Proceedings, vol.200,179 (1990)
8. H. Buhay, S. Sinharoy, W.H. Kasner, M.H. Francombe, D.R. Lampe and E.Stepke, Proc.7th Symp. on Applications of Ferroelectrics, University of Illinois at Urbana-Champion, June 6-8 (1990).
9. L. Manchanda and M. Gurvitch, IEEE Electron Devices Lett., 9, 180 (1988)

THIN FILM LITHIUM NIOBATE FOR USE IN SILICON BASED DEVICES

AD-P006 690

TIMOTHY A. ROST, HE LIN and THOMAS A. RABSON
Department of Electrical and Computer Engineering, Rice University,
P.O. Box 1892, Houston, TX 77251

ROBERT C. BAUMANN and J.M. McDAVID
Texas Instruments, P.O. Box 655012, Dallas, TX 75265

Abstract The incorporation of a thin film of lithium niobate ($LiNbO_3$) in a conventional MOS (metal-oxide-semiconductor) structure gives the possibility of two fundamentally different types of computer memory architectures. One, based on ferroelectric switching involves the reorganization of charge in the transistor channel to compensate for the change in polarization. Another, based on the bulk photovoltaic effect, involves a shift in the transistor threshold with exposure to differing intensities of incident light. With the use of a molybdenum liftoff process, transistors have been fabricated in which $LiNbO_3$ replaces the usual gate oxide of an MOS transistor. Transistor parameters such as the transconductance, output conductance, and amplification for these devices are reported.

INTRODUCTION

The interest in ferroelectric thin films stems from the possibility of fabricating useful devices based on this technology. One such device, the metal-ferroelectric-semiconductor field effect transistor (MFSFET), has received attention by integrating the ferroelectric film into a conventional semiconductor device [1-4]. This MFSFET, fabricated with silicon, is shown in figure 1. This device takes advantage of the relatively mature silicon technology while introducing the novelty of the ferroelectric film. It is possible to consider this device for several different applications including nonvolatile memories [1,2], optical detection [3], and as an aid in the understanding of the band structure and interface properties of MFS devices [4].

The unique combination of optical and electrical properties of $LiNbO_3$ warrant that it also be considered for use in a MFSFET device. $LiNbO_3$ has a number of features exhibited in the bulk that could be exploited in such a device. These include the bulk photovoltaic effect, the extremely high resistivity of bulk material, and the ferroelectric properties of $LiNbO_3$. Observed switching transients and photocurrents in thin films of

92-16165

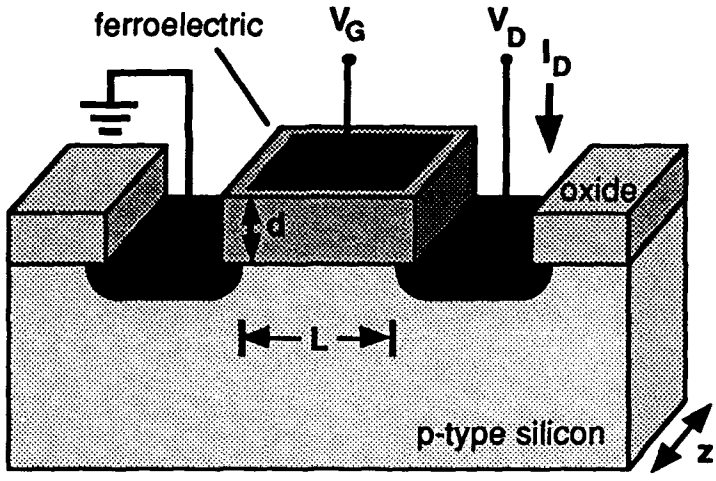


FIGURE 1 A metal-ferroelectric-semiconductor field effect transistor (MFSFET).

$LiNbO_3$ deposited on silicon [5], suggest that it is worthwhile to investigate $LiNbO_3$ in a MFSFET device, for applications in electrical switching computer memory architectures and optical-electronic computer memories. This research focuses on the first step toward that goal, the fabrication and determination of conventional MOS transistor parameters for the $LiNbO_3$ MFSFET.

EXPERIMENTAL

To fabricate a transistor it was necessary to isolate small areas of $LiNbO_3$ on silicon. This was accomplished with a molybdenum liftoff process which was developed at Texas Instruments. Thin films of lithium niobate were rf sputter deposited on the patterned silicon wafers. The details of the deposition procedure are given elsewhere [6]. After the deposition, a thin layer of gold was thermally evaporated on top of the $LiNbO_3$ film. The wafer was then subjected to several etching steps to fabricate MFS capacitors and transistors. A schematic outline of these steps is shown in figure 2. A 30% H_2O_2 etch step removes all of the molybdenum and thus all the $LiNbO_3$ not directly in contact with the silicon. This step was used to isolate MFS capacitors. A second etch step, 4.9% HF, removes the oxide, allowing electrical connection to the source and drain areas. This completes the fabrication of an MFSFET transistor. $LiNbO_3$ can be subjected to these etchants since it is very chemically unreactive.

A number of factors played an important role in yielding usable devices. These included the temperature of the wafer during deposition, $LiNbO_3$ and Au film thicknesses, and the temperature and length of the etch steps during liftoff. A photograph of two of the

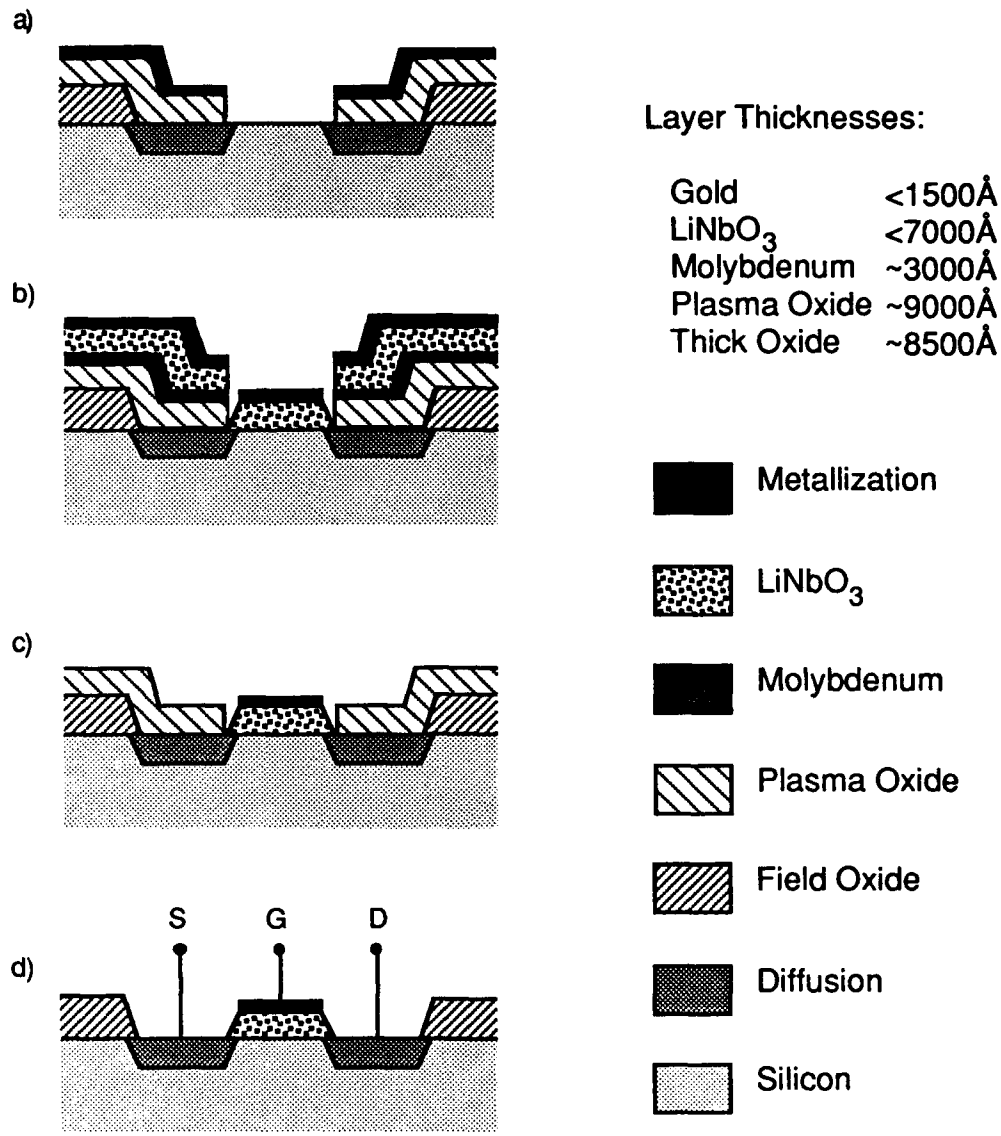
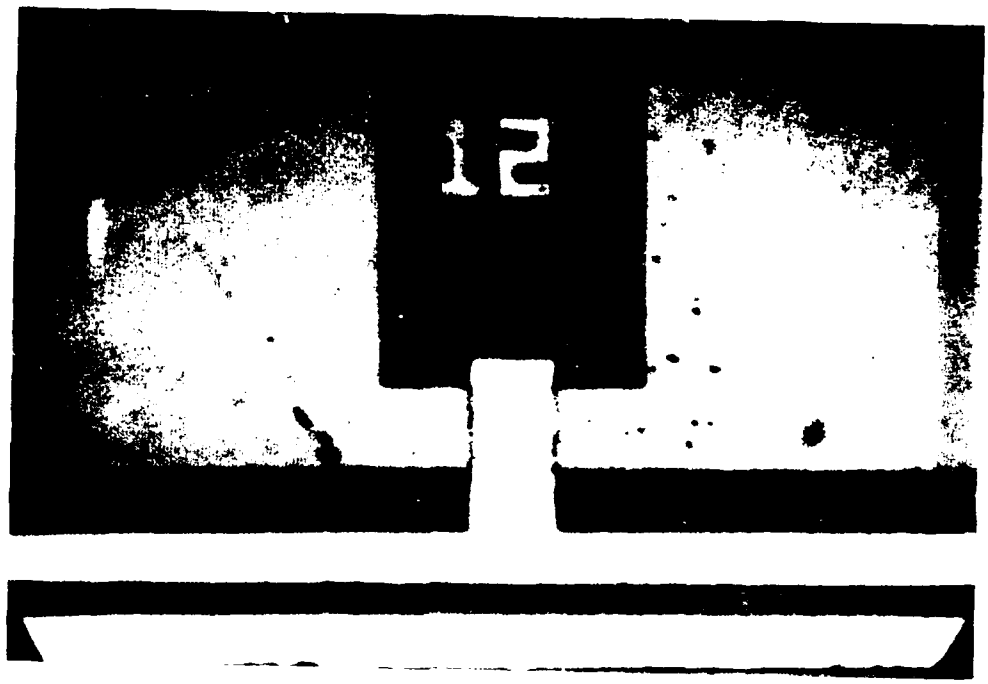


FIGURE 2 Molybdenum liftoff process for fabricating $LiNbO_3$ MFS transistors: a) prior to deposition, b) after $LiNbO_3$ and Au deposition, c) after H_2O_2 etch step, and d) after HF etch step.

best devices is shown in figure 3. Figure 3a shows a 25 × 25 μm device and figure 3b shows a 2 × 2 μm transistor gate after all the etch steps are complete. The gate area is the lighter rectangle in figure 3. As can be seen, the edges of these devices were sharply delineated. The best devices were selected for further analysis. For electrical measurements the wafer was placed on a gold-coated wafer chuck in a shielded, light tight enclosure. Small tungsten probes were positioned to make contact with the gate, and

a)



b)

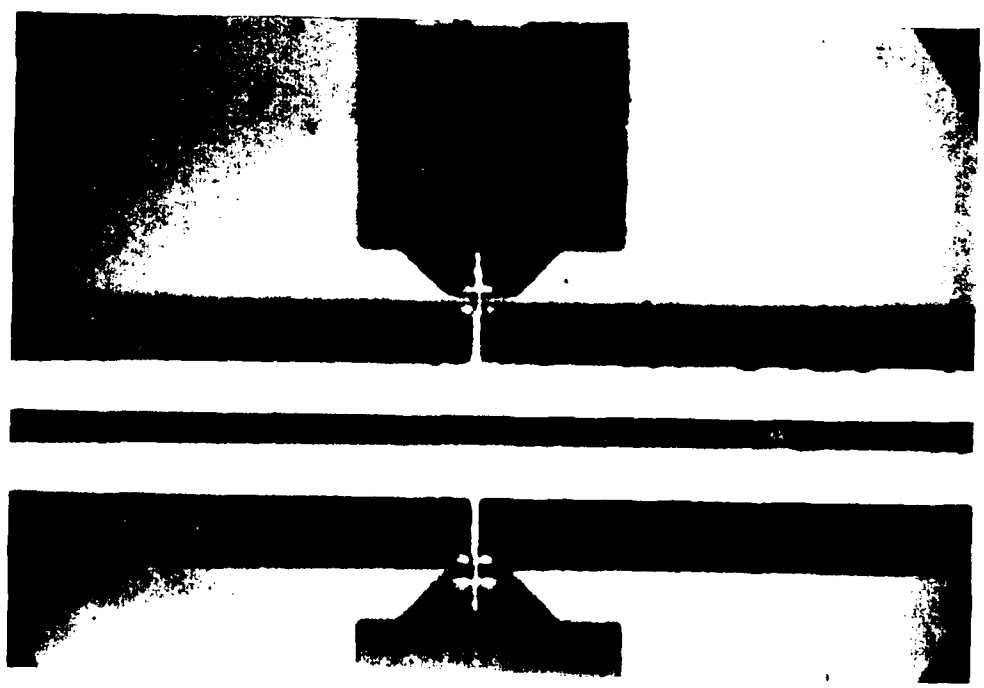


FIGURE 3 $LiNbO_3$ MFS transistors after etching is complete: a) 25 × 25 μm gate area and b) 2 × 2 μm gate area.

the source and drain areas. The gate leakage for the best devices was measured to be very low, indicating that the liftoff was successful.

TRANSISTOR PROPERTIES

The properties of the resulting transistor structures were measured with the HP4145 semiconductor parameter analyzer. This was used to provide the transistor curve traces shown in figure 4 and 5. From these curve traces, several basic transistor parameters can be determined. The transconductance is given by:

$$g_m = \left.\frac{\partial I_{DS}}{\partial V_G}\right|_{V_{DS}}$$

and the output conductance is

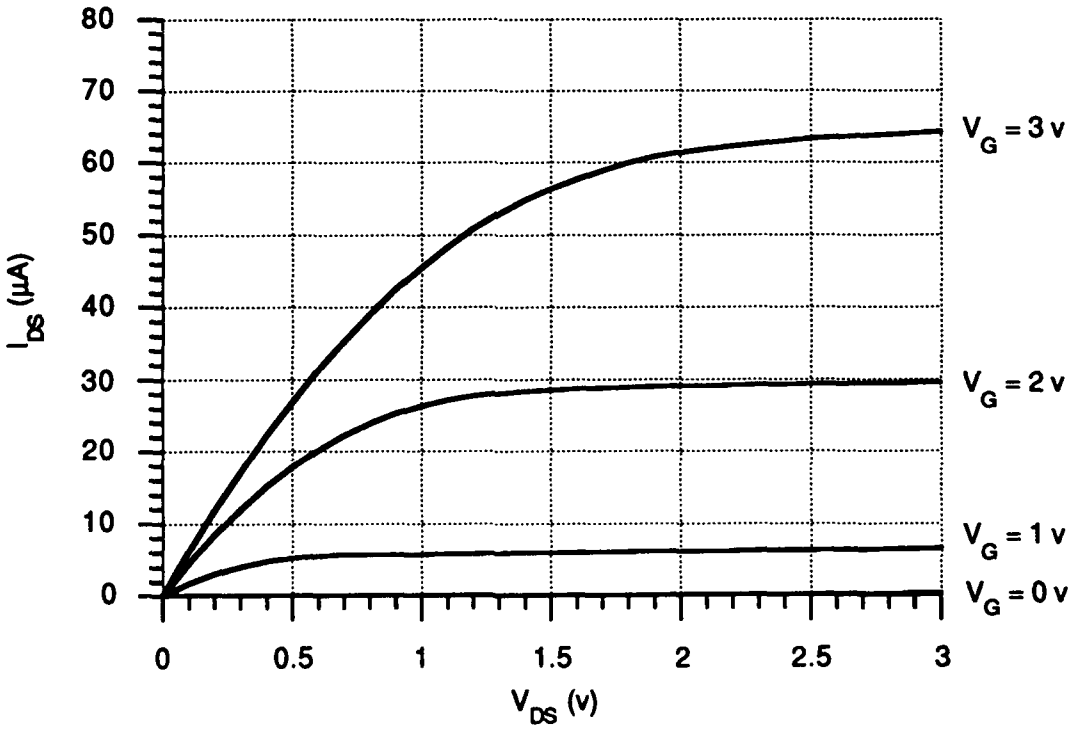


FIGURE 4 Transistor curve trace for 25 × 25 μm device.

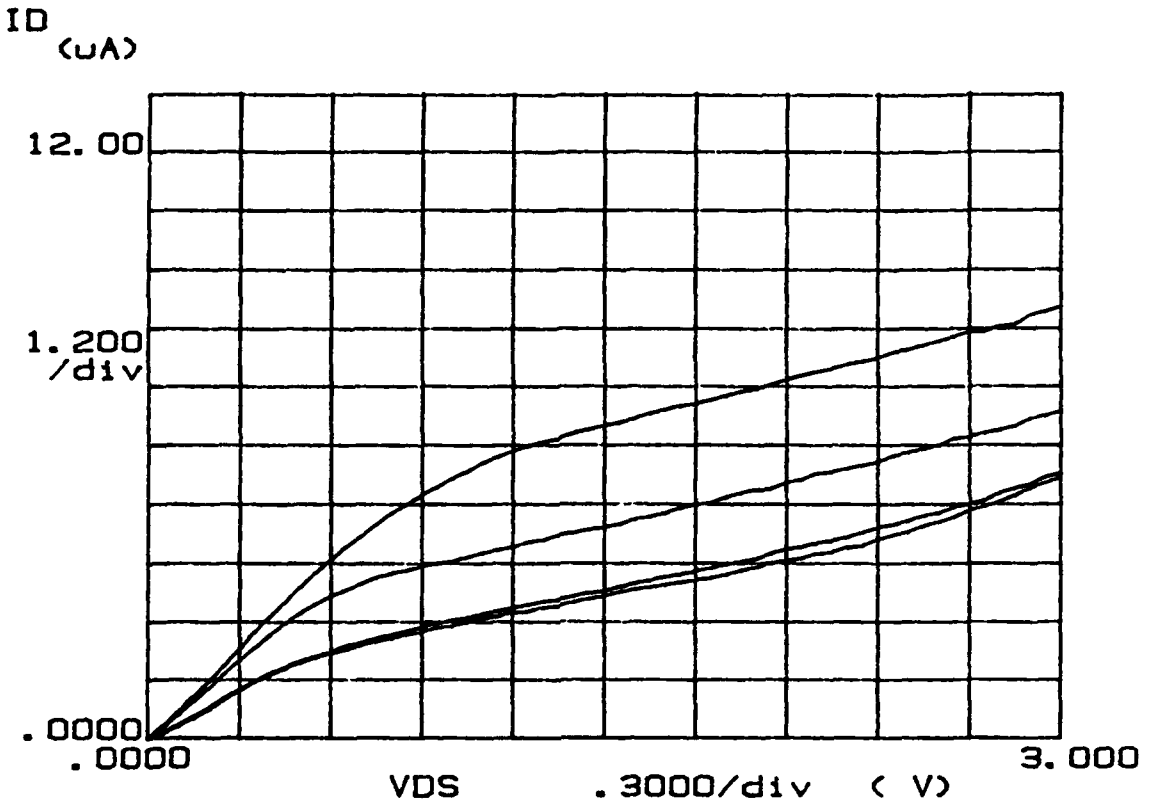


FIGURE 5 Transistor curve trace for 2 × 2 μm device.

$$g_d = \left.\frac{\partial I_{DS}}{\partial V_{DS}}\right|_{V_G}$$

By dividing the transconductance by the output conductance, the amplification factor can be determined. This is

$$\mu = \frac{g_m}{g_d}$$

These parameters give one indication of the quality of the transistor.

The gate current was extremely low, measured to be 14.0 pA at $V_G = 1$ volt, $V_{DS} = 2$ volts for the 25 × 25 μm device. The output conductance for both transistors was calculated at $V_G = 2$ volts (in saturation), and the transconductance was calculated at $V_{DS} = 2$ volts with V_G from 2 to 3 volts. The results of these measurements are shown in

TABLE 1 Summary of measured parameters for $LiNbO_3$ MFS transistors.

gate area	25×25 μm	2×2 μm
transconductance	35 μS	2.2 μS
output conductance	0.67 μS	1.3 μS
amplification factor	52.5	1.65

table 1. By dividing the transconductance by the output conductance, a rough measure of the amplification of the device can be obtained.

CONCLUSIONS

A liftoff process has been used to isolate small areas of $LiNbO_3$ on silicon in the fabrication of MFSFET devices. $LiNbO_3$ has a number of interesting properties which merit attention for this type of application. Of particular interest are the optical and ferroelectric properties of this device. $LiNbO_3$ is also compatible with the molybdenum and oxide etchants used during the liftoff process. The measured parameters of these devices indicate that $LiNbO_3$ can be used as the gate insulator of an MFSFET and that this technology is compatible with silicon based devices. The interface state density and the optical and ferroelectric switching operation of this device will be reported in forthcoming papers.

ACKNOWLEDGEMENTS

This research has been supported by the Texas Higher Education Advanced Technology Program under grant #3604 and by grants from Motorola and Texas Instruments.

REFERENCES

1. S.Y. Wu, IEEE Trans. Electron.. Devices, ED-21(8), pp. 499-503, 1974.
2. S.Y. Wu, Ferroelectrics, 11, pp. 379-383, 1976.
3. K. Sugibuchi, Y. Kurogi, and N. Endo, J. Appl. Phys., 46(7), pp. 2877-2881, 1975.
4. J. Schulz, ST. Koch, P. Würfel, W. Ruppel, U. Thiemann, and W.v. Münch, Ferroelectrics, 99, pp. 87-100, 1989.
5. R.C. Baumann, T.A. Rost, and T.A. Rabson, Materials Research Society Symposium Proceedings, 200, pp. 31-36.
6. T.A. Rost, Ph.D. Thesis, Rice University, 1991.

AD-P006 691

ELECTRICAL SWITCHING IN LITHIUM NIOBATE THIN FILMS

TIMOTHY A. ROST, HE LIN, and THOMAS A. RABSON
Department of Electrical and Computer Engineering, Rice University,
P.O. Box, 1892, Houston, TX 77251

Abstract The ferroelectric switching properties of thin films of lithium niobate ($LiNbO_3$) on silicon have been investigated. The polarization is shown to be partially reversible with an applied electric field at room temperature. The samples were films of $LiNbO_3$ which were magnetron sputter deposited on silicon substrates. A double pulse method was used to investigate the ferroelectric switching properties of the films. Evidence for partial stable switching of the $LiNbO_3$ film was observed at a field of roughly 500 kV/cm.

INTRODUCTION

Much is known about the ferroelectric lithium niobate ($LiNbO_3$). It has been one of the most intensely researched bulk materials due to its unique combination of optical, acoustic, electrical, and ferroelectric properties. Despite this attention, relatively little is known about the polarization reversal, or switching processes in $LiNbO_3$, especially at or near room temperature. This is primarily due to the previous emphasis of depositing thin film $LiNbO_3$ on insulators such as quartz and sapphire for the fabrication of thin film waveguides, and, the large coercive field of $LiNbO_3$. With the advent of techniques for depositing high quality thin films of $LiNbO_3$ on silicon substrates [1], it is possible to consider a closer examination of the switching properties of this material.

There have been several studies investigating the polarization reversal process in $LiNbO_3$. The research which produced the currently accepted value of 71 $\mu C/cm^2$ for the value of the spontaneous polarization of $LiNbO_3$ was done by Camlibel [2]. A pulsed field method was used to induce polarization reversal in 30 micron thick $LiNbO_3$ platelets at room temperature. Contact was made to the platelet with liquid electrodes consisting of a solution of LiCl. A 35 ms voltage pulse was then placed across the sample and the resulting charge flow was integrated on a capacitor. With a coercive field of 300 kV/cm the polarization in the platelet switched and the charge that flowed was used to calculate the spontaneous polarization of 71 $\mu C/cm^2$. This was the first direct measurement of the spontaneous polarization of $LiNbO_3$ at room temperature.

92-16166

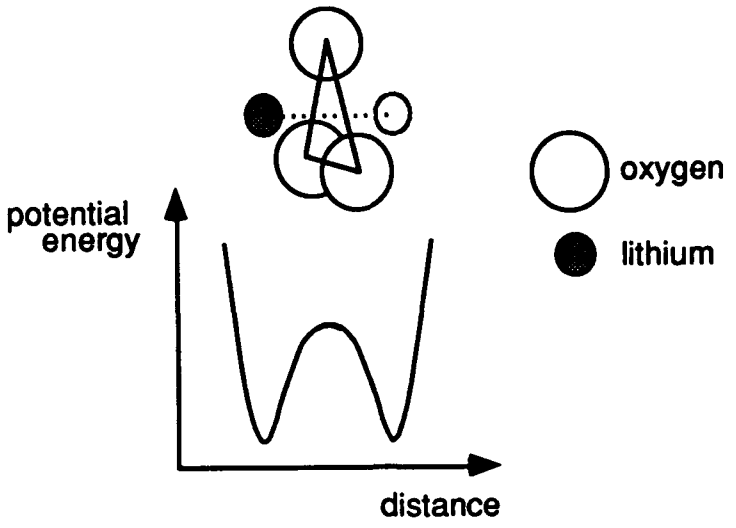


FIGURE 1 A double well potential energy diagram of the Li ion in $LiNbO_3$.

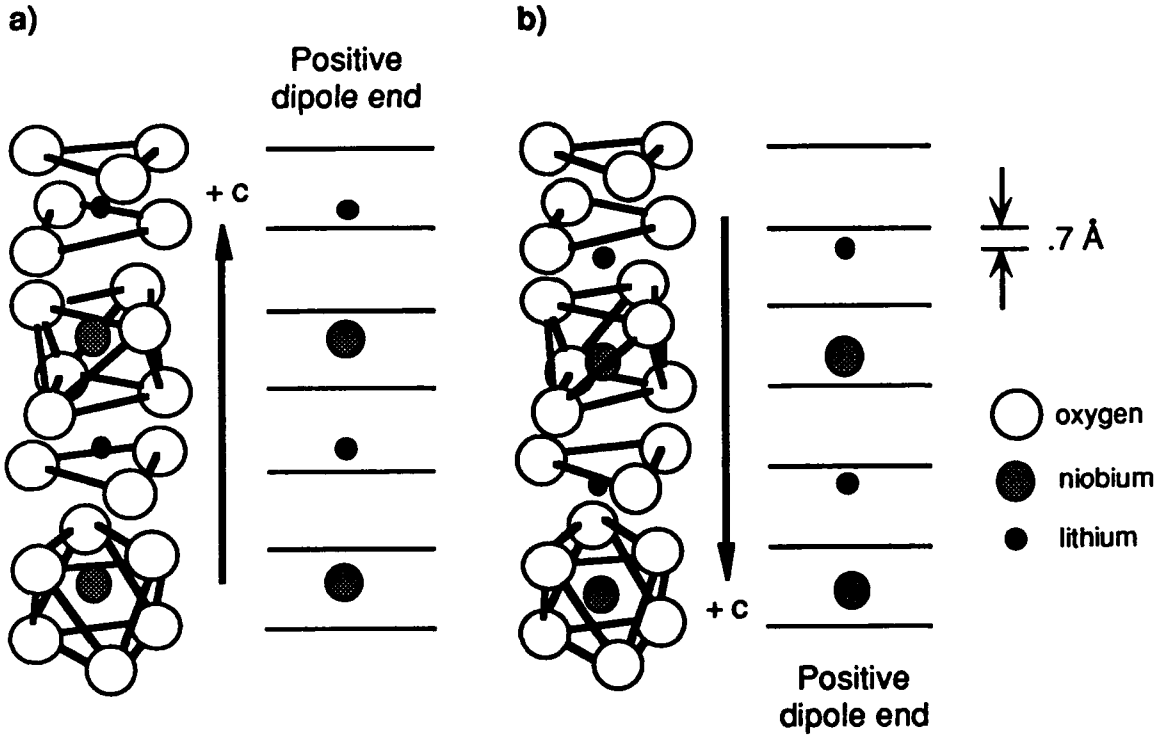


FIGURE 2 Arrangement of atoms in $LiNbO_3$ a) before, and b) after polarization reversal.

More recently, Haycock and Townsend used ionizing radiation in the form of an electron beam in the presence of an applied field to bring about permanent domain reversal at temperatures significantly below the Curie temperature [3]. This, and earlier work by Ballman and Brown on $LiTaO_3$ [4], suggest a reversal mechanism in the transport of the lithium ion across the oxygen plane as shown in figure 1. Since there are two stable positions for the Li ion, its potential energy is a double well centered about the oxygen plane. For reversal, the lithium ion must move .7 Å to cross the oxygen plane. Since $LiNbO_3$ is a 1-d ferroelectric, this action completely reverses the orientation of the c axis of the crystal, thereby reversing the polarization. This is shown in figure 2.

EXPERIMENTAL

Thin films of $LiNbO_3$ were grown on (111) silicon substrates by rf magnetron sputtering [1]. The substrates were p-type, .001 Ω-cm and were chemically etched to remove contaminants and oxides prior to sputtering. The target consisted of $LiNbO_3$ powder (99.9995%) which was replaced after every deposition. This arrangement also allowed the examination of a wide variety of target stoichiometries. X-ray diffraction and electron diffraction techniques were used to prove the films were oriented stoichiometric $LiNbO_3$ [1]. The orientation of the c axis was shown to be normal to the silicon surface. This orientation is ideal for exploiting the ferroelectric nature of the films for devices. To make electrical contact, an array of aluminum contacts was thermally evaporated on the surface of the film. The wafer was placed on a gold coated wafer chuck in a light tight enclosure for measuring the electrical and ferroelectric properties of the film.

A double pulse method was used to examine the switching properties of these films. The pulser was a model AVR-3-PN-PS-RU3 from Avtech Electrosystems which was capable of providing two positive pulses followed by two negative pulses at amplitudes of up to 150 volts. This type of setup was used to distinguish between stable and unstable full and partial switching. It is also very easy to differentiate between ferroelectric switching and dielectric breakdown with this arrangement. These pulses were applied to the sample and the resulting current was observed as a voltage across a 50 Ω current viewing resistor. The magnitude of all four pulses was kept the same and was increased until behavior other than simple charging and discharging of the linear dielectric component was observed.

The ferroelectric switching transients produced from two different films are shown in figure 3. Sample LN2/15/91 exhibited stable partial switching with pulses of 20 volts applied across the .36 μm film. This corresponds to a coercive field of roughly

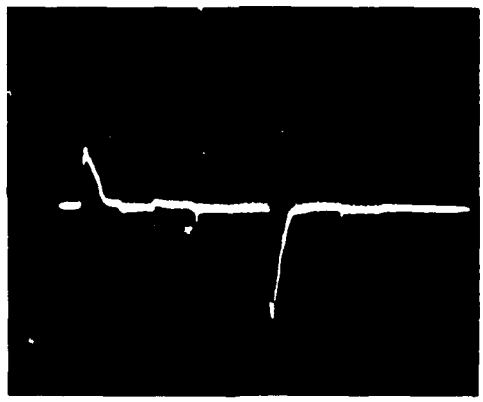


FIGURE 3 Stable switching transients produced with sample LN2/15/91. The vertical axis is 2 volts/division and the horizontal axis is 500 ns/division. The applied pulses were 500 ns in duration and 20 volts in amplitude. The magnitude was the same for both the positive and negative pulses.

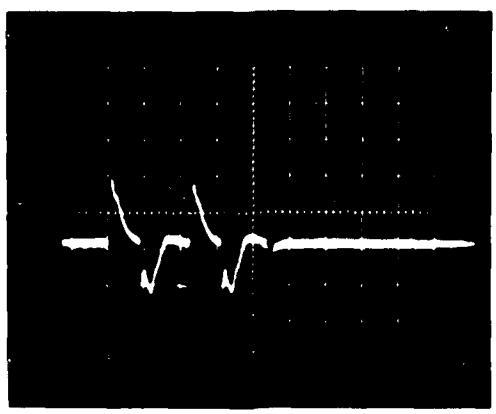


FIGURE 4 Unstable full switching transients exhibited by sample LN2/28/91. The vertical axis is 25 volts/division and the horizontal axis is 500 ns/division. The applied pulses were 500 ns in duration and 120 volts in magnitude. The magnitude was the same for both the positive and negative pulses.

500 kV/cm. The amount of switched charge was used to calculate a spontaneous polarization of roughly 5 $\mu C/cm^2$ for this sample. A second sample made under identical conditions exhibited unstable full switching as shown in figure 3b. The coercive field for this sample was 4 MV/cm^2 and the amount of charge which flowed corresponded to a spontaneous polarization of approximately 60 $\mu C/cm^2$.

CONCLUSIONS

The orientation of thin film $LiNbO_3$ on silicon is reversible with the application of an electric field at room temperature. Stable partial switching was observed at roughly 500 kV/cm with a switched charge of 5 $\mu C/cm^2$. Unstable full switching was also observed on another film with an applied field of 4 MV/cm producing a switched charge of 60 $\mu C/cm^2$. The measured coercive field is slightly higher than that obtained by Camlibel et al [2]. This is possibly due to a number of factors including depolarizing fields, interface and electrode effects, and the lower degree of crystallinity associated with thin film $LiNbO_3$.

ACKNOWLEDGEMENTS

This research has been supported by the Texas Higher Education Advanced Technology Program under grant #3604 and by grants from Motorola and Texas Instruments.

REFERENCES

1. T.A. Rost, Ph.D. Thesis, Rice University, 1991.
2. I. Camlibel, J. Appl. Phys., **40**(4), pp. 1690 - 1693, 1969.
3. P.W. Haycock and P.D. Townsend, Appl. Phys. Lett., **48**(11), pp. 698-700, 1986.
4. A.A. Ballman and H. Brown, Ferroelectrics, **4**, pp. 189-194, 1972.

AD-P006 692

LIQUID SOURCE CVD

L.D. MCMILLAN, C.A. PAZ DE ARAUJO, T. ROBERTS,
J. CUCHIARO, M. SCOTT, J. SCOTT
Symetrix Corporation, Colorado Springs, Colorado

Abstract This work entails an investigation of a new method for depositing complex thin films by injecting stoichiometrically correct liquid sources into a vacuum chamber such that thin films are formed on silicon substrates at room temperature under closely controlled conditions[1].

92-16167

INTRODUCTION

The interest in new multi-element compound thin films for various electronic, optical, and other device applications, has increased significantly over the past few years. Until recently, however, deposition of such films could be accomplished by only a rather limited number of methods, such as evaporation, sputtering, MBE, spin-coating, spray-coating, CVD, etc. All of these methods are now evolving technologically and finding applications in such a wide range of disciplines that it is quite difficult to accurately compare the merits of each system. We can, however, state the following in general terms of film complexity, stoichiometric control, purity, etc.

Most vacuum deposition techniques, such as evaporation, sputtering, MBE, etc., are well established in the IC industry. Such methods can be used to produce extremely clean thin films of single element, or in some cases, multi-component films in a controlled manner. In the case of sputtering, however, compound material target construction can be quite slow and expensive, especially if new and/or different materials are being interchangeably deposited on a regular basis.

---

[1] Funded in part by the U.S. Navy under NSWC/Symetrix SBIR contract N60921-83-C-0036.

CVD techniques, on the other hand, utilize various source (precursor) gases which are mixed and reacted under exact conditions of temperature and pressure to produce multi-element compound thin films in a closed environment.[2] Film stoichiometry can generally be changed from run to run if the proper precursor gas sources are available at reasonable costs. In many cases, however, such precursor gases are either not readily available for many of the complex compounds of interest and/or they are extremely toxic and difficult to use under normal operating conditions.

For some of the above reasons, many investigators are now turning to sol-gel, MOD or other wet chemical synthesis techniques to derive many of the new complex ferroelectric, superconductor and other materials. Such wet chemical techniques enable quick turn around of new and often very complex, multi-element compounds in a very expedient and economical manner. The sol-gel, MOD and other solutions are generally deposited by spin-coating at atmospheric pressure and room temperature. Such techniques, although quite effective, do not generally achieve the film cleanliness of vacuum depositions. It seems obvious that, even with all of the thin film deposition techniques presently available, there should be a means by which the positive merits of wet chemistry and vacuum technology could be combined in the same system. It was with this in mind that Symetrix Corporation constructed the system described in this paper and continues to develop the liquid source CVD technology.[3]

LIQUID SOURCE CVD MACHINE AND RELATED PROCESSES

The initial design for a liquid source CVD system (Figure 1) evolved from discussions at Symetrix Corporation in 1987 regarding the limitations of

---

[2] McMillan, Price and Goldman, "Deposition of Silicon Nitride," U.S. Patent No. 4,279,947 (issued 21 July 1981, Motorola).

[3] It may be inappropriate to include this technology in the family of chemical vapor deposition (CVD) methods because the source materials, reaction temperatures, etc. are considerably different than what are normally accepted as standard CVD conditions.

existing thin film deposition equipment. It was quite evident at that time that most of the commercially available thin film deposition equipment was incapable of consistently depositing stoichiometrically correct films of multi-component compounds. Even though sputtering, evaporation, CVD and other technologies were well established in the IC industry, most of these deposition techniques had inherent limitations when it came to depositing multi-element compounds containing more than three or four elements.

LIQUID SOURCE
CHEMICAL VAPOR DEPOSITION[4]

1987 Concept[5]

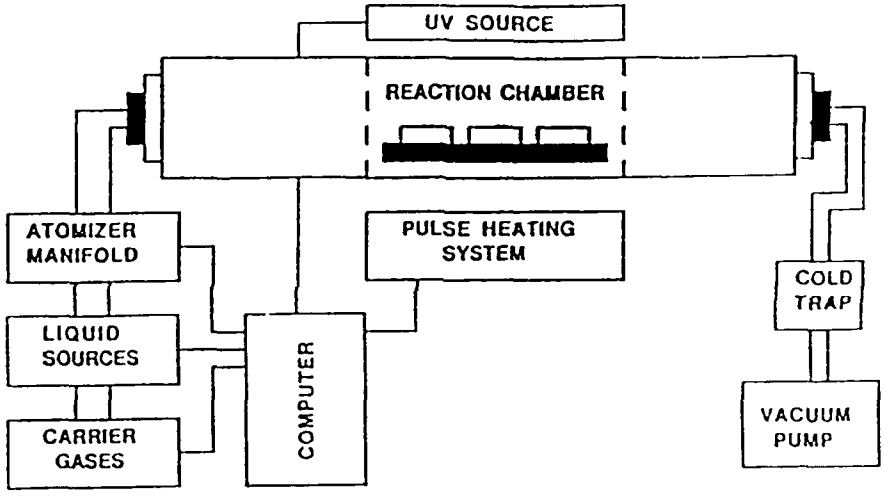


FIGURE 1: PHOTO ENHANCED CHEMICAL VAPOR DEPOSITION ACTIVATION SYSTEM

We originally believed that simply injecting a fine mist of a stoichiometrically correct compound into a vacuum chamber should enable us to deposit films (in vacuum) in much the same way that MOD and sol-

[4] U.S. Patents Pending: Serial Numbers: 290,468, 470,800, PCT/US89/605882,07/660428.
Foreign Patent's Pending: Serial Numbers: 4846990,2-502119, 90-701908.
(Symetrix: McMillan, Araujo, Roberts)

[5] McMillan & Araujo: First Presented to U.S. Government Agencies in 1988.

gel films are deposited at atmospheric pressure by spray coating. Many of the original (1987) assumptions associated with the design and construction of a system to accomplish this, however, proved to be either incorrect or extremely difficult to prove. A few of the more significant problems encountered during the execution of this project are outlined below:

O Injecting any kind of a liquid into a vacuum system is not a commonly accepted practice. Most vacuum pumping systems quickly become contaminated if moisture is present in the system. In order to solve this problem, the Symetrix engineers decided to create a very fine mist of the (sol-gel) source materials in such a way that the mist could be mixed with an inert carrier gas prior to injection into the vacuum chamber.

O Sol-gel (and other) liquid sources are not easily incorporated into a gas stream. Conventional bubblers and sprayers were considered, but subsequent experimentation indicated that such systems do not work properly in conjunction with a vacuum environment. Eventually, after considerable experimentation with various configurations of ultrasonic generators, we arrived at a design that proved to be quite efficient for creating a fine mist with small quantities of sol-gel in a vacuum connected environment (see Figure 2).

O Gassified (misted) sol-gel tends to coat (or clog up) everything that it comes into contact with. This includes valves, feed lines, vacuum chambers, pumps, etc. Solution of this problem involved utilization of inert carrier gasses, minimization of water and oxygen in the system and special valving configurations that allowed system purging with argon and/or nitrogen.

O Achieving uniform (stoichiometrically correct) film depositions onto four-inch silicon (and other) substrates, after the liquid source mist has been introduced into the vacuum chamber, proved to be one of our most difficult problems. A number of different injection nozzles, substrate heaters, exhaust (vacuum) controls, etc., were tried with little success. In

general, the mist would merely form discontinuous droplets on the substrate instead of a continuous film. We finally discovered, after considerable effort, that by placing a barrier plate in close proximity to the substrate surface, rotating the substrate and injecting the mist through a specially designed (circular) manifold such that the mist became confined to a small region of vacuum directly over the substrate, a reasonably good film could be deposited (See Figure 3).

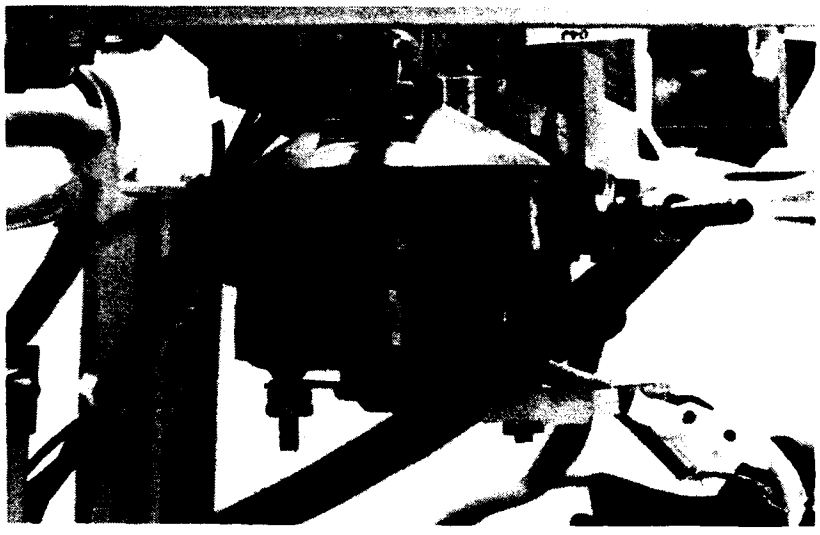


FIGURE 2: ULTRASONIC CHAMBER

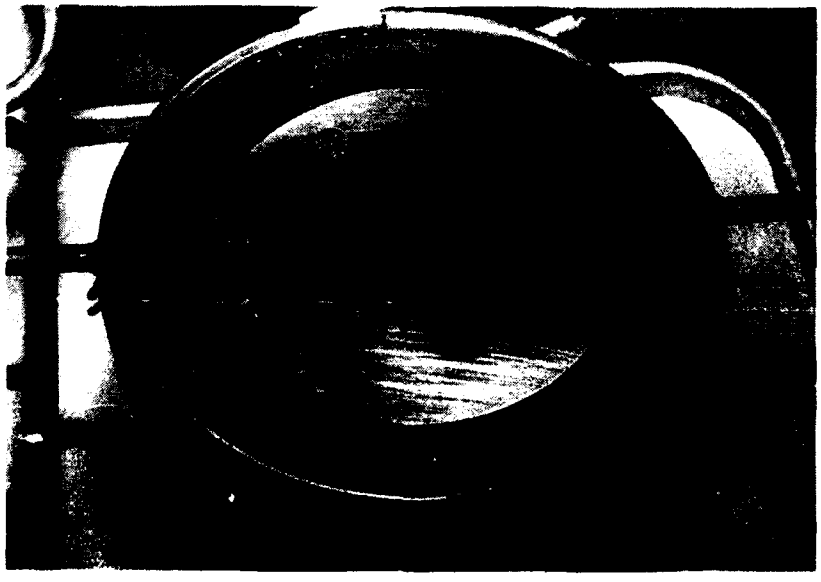


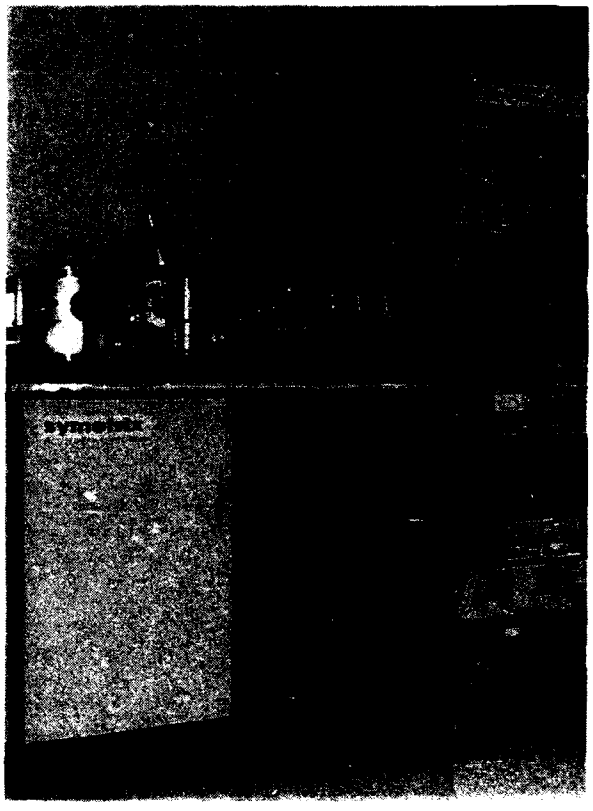
FIGURE 3: SUBSTRATE HOLDER AND INJECTION MANIFOLD (INSIDE VACUUM CHAMBER)

○ In general, sol-gels, MOD solutions, etc., that have been prepared for spin coating will not work in the machine as presently configured. As indicated above, water (commonly used for hydrolysis of sol-gel stock solutions) and viscous liquids will not form a mist in the ultrasonic generator chamber and may clog the lines, valves, etc. After experimentation with various additives such as propanol, 2-methoxyethanol, formamide, etc., we finally discovered that the addition of approximately 15% (by volume) of methanol to the sol-gel solution solved the problem.

○ Perhaps the biggest surprise came from our work with RF, ultra-violet and thermal energy sources inside the vacuum chamber. We found that the addition of RF energy to the sol-gel mist merely created carbon containing films. In like manner, ultra violet radiation during deposition formed powder deposits on the substrates and inside the vacuum chamber. Heating the substrate and/or pulsing the surface of the substrate with infrared radiation (RTA) during deposition dried the mist (droplets) before they could form a continuous film.

This difficult evolution of problems, solutions, design changes, etc., eventually led to the present machine design and the process parameters for PZT described below (refer to Figures 4 and 5).

VACUUM SYSTEM



CONTROL CONSOLE

FIGURE 4: THE SYMETRIX LSCVD MACHINE IN ITS PRESENT CONFIGURATION

TYPICAL PROCESSING PARAMETERS

○	Ultrasonic Source Temperature (DEG.C.):	40-50
○	Base Pressure Prior to Deposition (UV):	1 x 10^{-6}T
○	Base Pressure During Deposition (mm Hg[1]):	500-575
○	Substrate/Vacuum Chamber Temperature During Deposition:	RT
○	Deposition Rate (Angstroms/Min):	100-200
○	Post Processing Pressure (mm Hg):	200-300

FIGURE 5: LSCVD PROCESSING PARAMETERS FOR DEPOSITING THIN FILMS OF PZT

EXPERIMENTAL RESULTS

Figures 6 and 7 show typical hysteresis and switching curves achieved with ferroelectric capacitors built with LSCVD deposited PZT. No significant electrical differences between spin-coated and LSCVD deposited films have been noted to date.

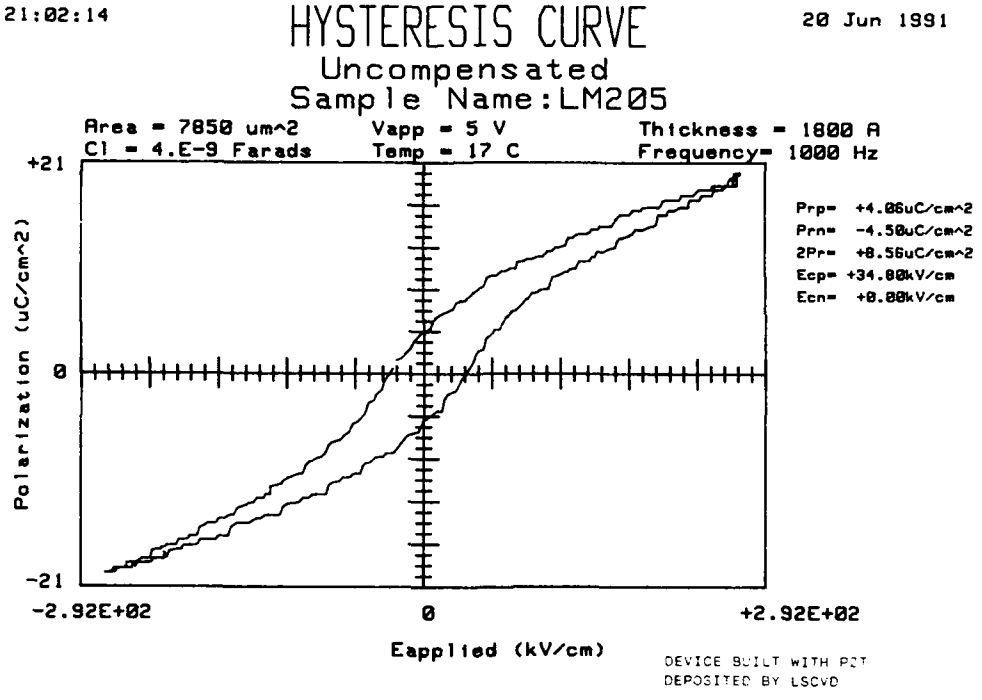


FIGURE 6: TYPICAL HYSTERESIS CURVE FOR DEVICE BUILT WITH LSCVD DEPOSITED PZT

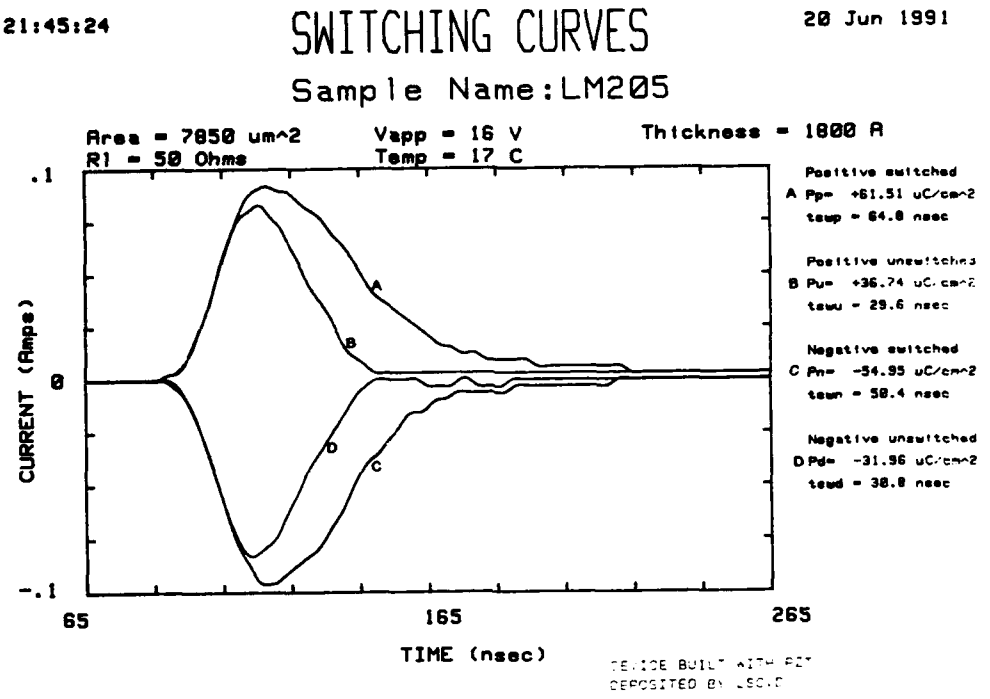


FIGURE 7: TYPICAL SWITCHING CURVES FOR DEVICE BUILT WITH LSCVD DEPOSITED PZT

CONCLUSIONS

Liquid Source CVD offers the potential for depositing extremely complex, stoichiometrically correct, thin films at low temperatures in a vacuum environment. Symetrix has deposited films of PZT and other materials, ranging in thickness from 300 to 20,000 Angstroms, with the machine described in this paper. We have, therefore, proven the feasibility of the basic concept of using liquid sources for vacuum deposition of thin films. This achievement, however, should be considered as only the basis for a much greater effort to achieve the machine capability to design and manufacture new compound materials for all kinds of new passive, as well as electrically active, devices and coatings.

Photographs by Marlene Roberts

AD-P006 693

SPUTTER DEPOSITION OF FERROELECTRIC THIN FILMS

ANGUS I. KINGON, H. N. AL-SHAREEF, K. D. GIFFORD, T. M. GRAETTINGER, S. H. ROU, P. D. HREN, O. AUCIELLO* and S. BERNACKI†
North Carolina State University, Department of Materials Science and Engineering, Raleigh, NC 27695-7919; * also Microelectronics Center of North Carolina, Research Triangle Park, NC 27709-2889; † Raytheon Company, Sudbury, MA 01776.

Abstract Ferroelectric films are typically deposited by a variety of techniques, the two most common being chemical methods (sol-gel, metalorganic decomposition) and sputtering. In this paper we briefly review the sputtering techniques, and then discuss ion beam sputter deposition in greater detail. In particular, ion beam sputter deposition of epitaxial lead zirconate titanate (PZT) films is described. It is shown that the films with compositions close to the morphotropic boundary typically show well-developed ferroelectric hysteresis loops, P_{max} around 45 $\mu C/cm^2$, and P_r around 20 $\mu C/cm^2$. In comparison with typical polycrystalline sol-gel PZT films, however, coercive fields of thin epitaxial films are large (120 - 200 kV/cm for 95 nm films). The pulsed fatigue behavior is remarkably similar to a polycrystalline non-oriented sol-gel PZT film investigated for comparison. The similarities suggest that the aging behavior may be dominated by the electrodes, which were Pt in both systems.

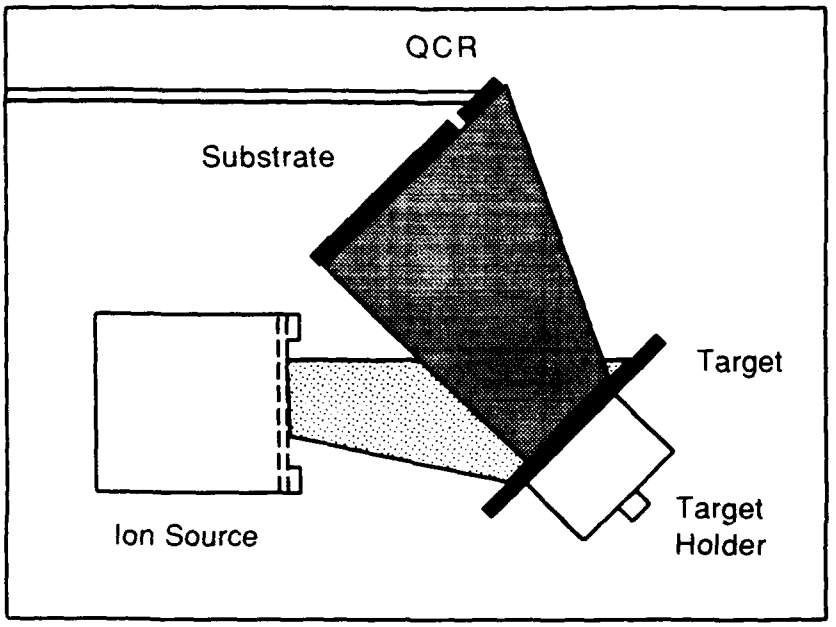
INTRODUCTION

Sputter deposition has been the most commonly used of all the vapor-phase techniques for the synthesis of ferroelectric thin films. The RF sputter deposition of $Bi_4Ti_3O_{12}$ films was reported more than twenty years ago[1], followed by a number of studies on plasma sputtered $BaTiO_3$. $Pb(Zr,Ti)O_3$ (PZT) and other ferroelectric thin films have also been synthesized by sputter deposition.[2-20]

In order to make some critical comments regarding sputter deposition, it is necessary to separate the two major categories, namely ion beam and plasma sputter deposition. The techniques are shown schematically in Figure 1a and 1b. In the plasma sputtering techniques (RF or DC), a plasma is maintained between cathode and anode. The plasma causes neutral and ionic species to be sputtered from the negatively

92-16168

a



b

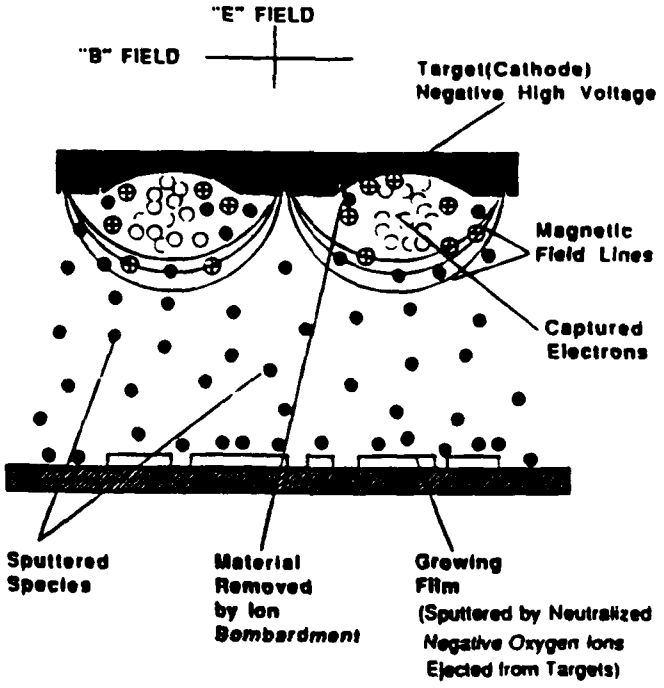


FIGURE 1 Sketch of common sputtering techniques: a) ion beam sputtering; b) magnetron sputtering; c) (next page) off-axis magnetron sputtering.

c

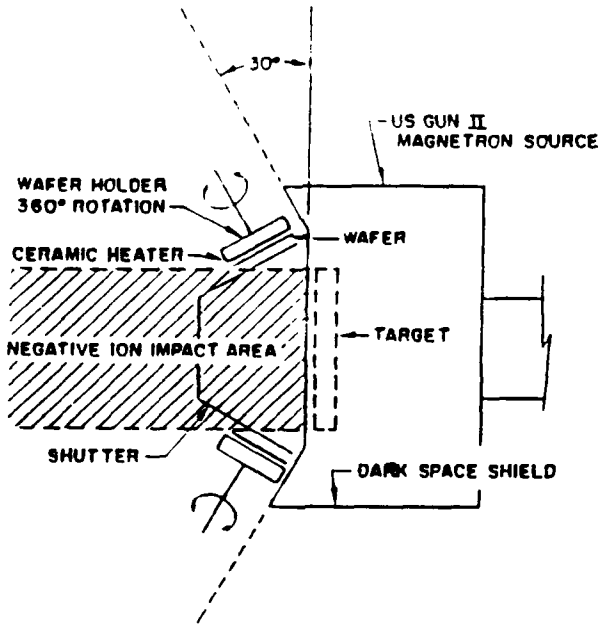


FIGURE 1 (cont.) c) off-axis magnetron sputtering.

biased target (cathode). Sputtered species are deposited on the positively biased substrate (anode). The plasma can be magnetically confined: this introduces the variant known as "magnetron" sputtering. The techniques are known collectively as plasma sputtering and all are characterized by the fact that, to a greater or lesser extent, the plasma interacts with the film growing upon the substrate.

Ion beam sputter deposition utilizes a primary ion beam, typically 500-5000 eV, which impinges upon the target, and causes sputtered species, mostly neutral atoms, to deposit onto the substrate. Salient advantages and disadvantages of the two sputtering techniques are summarized in Table I. The most important features of the two techniques will be discussed in the next sections.

PLASMA SPUTTERING

In plasma sputtering, the plasma-film interaction can have undesirable effects on the composition and structure of the films. The outstanding undesirable phenomenon in plasma sputter deposition is that known as the "negative ion effect." This effect

TABLE I Summary comments regarding ion beam and plasma sputter deposition as applied to ferroelectric oxide films.

	Ion Beam Sputter Deposition	Plasma Sputter Deposition
Variants	Ion beam assisted; multiple ion beam; multi-target	RF; DC; magnetron; multimagnetron
Advantages	• Plasma separated from substrate • Controllable ion beam energies • Variable geometries possible • Can sputter from same spatial location • Flexibility	• High rate for sputtering of metals • Has been scaled for large commercial processes • Can sputter up to pressures of 600 mTorr
Disadvantages	• Ion scattering from targets can be deleterious to film properties	• Negative ion effect • More difficult to adapt to multiple targets • Low deposition rates for oxide targets

involves the production of energetic negative oxygen ions during the sputtering of oxide targets, or their generation in an oxygen-rich plasma. Both species are accelerated towards the substrate and impact on the growing film, where they can produce sputtering and compositional changes.[21] The "negative ion effect" has been extensively investigated for the case of sputtering from $YBa_2Cu_3O_{7-x}$ targets, where it has been demonstrated that re-sputtering and compositional changes of the film are severe.[21]

Two main solutions to these problems have been investigated. The first is to sputter-deposit films in a relatively high oxygen background gas pressure, so that energetic oxygen species are thermalized by collisions with oxygen atoms in the plasma between the target and the substrate.[22] The second is to position the substrate perpendicular or at an angle to the target and outside the target's line of sight (in the off-axis position).[23] This placement minimizes the bombardment of the film by oxygen species, which are mostly moving in a direction perpendicular to the target surface (see Fig. 1c). Both solutions have the side effect of substantially reducing the deposition rate to values below those characteristic of ion beam sputter deposition. Off-axis sputtering has the additional side effect of introducing compositional variation across the substrate

because of unevenness of sputtered flux density in the off-axis position. It is important to note that the "negative ion effect" has not been specifically studied for the case of oxide ferroelectric film deposition. The effect of the energetic ions on film structures, microstructure, and defect structure are therefore not yet known.

ION BEAM SPUTTERING

A major advantage of the ion beam sputter deposition method is that the plasma used to generate the ions is confined to the ion source and is isolated from the growing film. Ions are extracted from the plasma, accelerated by biased grids, and form a high current (10-100 mA), broad ion beam with energies in the range 500-1500 eV. The most commonly used ion source is that based on the design by Kaufman.[24] The ion beam is directed at an appropriate target, where it sputters atoms and/or molecules and generates a sputtered flux of target atoms with an energy distribution peaked in the range of 3-10 eV, depending on the ion/target atom mass ratio.[25] The sputtered flux energy distribution has a tail of energetic atoms with energies up to several hundreds of eV. In addition, the beam ions can scatter off the target with energies up to a sizable fraction of the incident beam energy. These energetic sputtered and scattered ions can impact on the growing film and produce re-sputtering (leading to compositional changes) and gas incorporation.[21] The high-energy fraction of the scattered ions is larger when the ion beam is directed at a relatively large angle of incidence with respect to the target.[26] The effect of scattered ions can be reduced or eliminated by increasing the beam atomic mass relative to the target atomic mass and by optimizing the beam-target-substrate geometry. The choice of beam species and system geometry can be done effectively with the assistance of a computer model, such as the "TRIM" code.[27] Extensive calculations have been performed for the case of deposition of $YBa_2Cu_3O_{7-x}$[28]. Similar calculations have been conducted, to a lesser extent, for the case of ion beam interaction with $KNbO_3$ films.[26]

Another issue for both plasma and ion beam sputtering of multicomponent ferroelectric oxides is the choice of targets. The use of a single, multicomponent oxide target is convenient and common. However, the composition of the sputtered flux can change with time because of preferential sputtering[25], and it can require considerable presputtering to stabilize the target surface composition before a steady state sputtering flux is achieved.[29] This is a relatively minor problem for laboratory scale deposition; however it is more serious for commercial production volumes. It is for this reason, and

for ease of altering composition, that several groups have utilized multiple elemental targets.[20,30] Sreenivas and Sayer[20] used a magnetron sputtering system with a disk-shaped multi-element target containing pie-like slices of Pb, Zr and Ti metals. The composition of the flux could be altered by changing the relative size of each slice.

An advanced variant of a technique involving an ion beam and elemental targets has been described by the present authors.[31] In this case, elemental targets are sequentially sputtered by a broad ion beam generated by a Kaufman-type ion source. An important feature of this method is that the sputtered flux is monitored by a quartz crystal resonator (QCR), which sends a feedback signal to a computer that controls the amount of material sputtered from each target. This control is used to produce films of a desired stoichiometry.. The utilization of this system for ferroelectric thin films is described in the following section.

A variant of the ion beam technique involves directing a separate ion beam at each elemental target.[32] In this case, films are produced by co-deposition of elemental film components. A disadvantage, in comparison with single ion beam deposition, is that the sputtered fluxes do not originate from the same spatial location. This can be a problem if the composition of the film is not stoichiometrically "self-correcting." Our present results suggest that ferroelectric $KNbO_3$ is partially "self-correcting" (i.e. single phase $KNbO_3$ results from fluxes over some defined range of K:Nb ratios), but that PZT is not, due to the accommodation of an excess or deficiency of PbO by formation of a defect pyrochlore phase. This issue must be further investigated.

In the remainder of this paper we describe the use of the computer-controlled ion beam sputter deposition technique developed by us for the production of epitaxial PZT thin films, and the resultant film properties.

EXPERIMENTAL PROCEDURE

Ion beam sputtered PZT films prepared for this study were deposited on two types of substrate, namely, (001) MgO and Pt /(001)MgO. (Sol-gel films are described at the end of this section). The bottom electrodes (Pt) were typically 0.2 μm thick, and were also deposited using ion beam sputtering.

The deposition system used in this study was described in detail elsewhere.[31] It consists of the following components: a stainless steel chamber evacuated by a turbomolecular pump to a base pressure of ~5×10^{-7} torr, a Kaufman type ion source, a rotating target holder, a substrate holder/heater assembly, and a quartz crystal resonator

TABLE II Typical sputtering conditions.

Base Pressure	$5x10^{-7}$ torr
Deposition Pressure	$3x10^{-4}$ torr
Substrate Temperature	500-600°C
Ion Energy	1400 eV
Beam Current (Pb)	8 mA
Beam Current (Zr, Ti)	20 mA
Sputtering Gas	Kr
Kr Flow Rate	1.5 sccm
Oxygen Flow Rate	6.5 sccm

(QCR). The QCR measures the thickness of each layer of elemental species deposited and sends a feedback signal to the computer. When the programmed thickness of an elemental layer has been deposited, the computer switches the beam off, rotates the holder to position the next target in front of the ion beam and turns the beam on.. This sequence is repeated for each component of the film.

Films were deposited by sputtering Zr, Ti, and Pb metallic targets. Molecular oxygen was incorporated into the film by introducing it into the growing film from a jet directed at the substrate surface. Typical film thickness were 0.1 μm and the over all deposition rate was ~3 nm/min.

The substrate temperature was measured by a thermocouple bonded to a dummy substrate, which in turn was silver pasted on to the heater plate close to the substrate where the PZT was deposited. An optical pyrometer was used to verify the thermocouple reading. Table II shows the sputtering conditions used in a typical deposition.

The films were characterized by X-ray diffraction, scanning electron microscopy, transmission electron microscopy (TEM), Rutherford backscattering, and ferroelectric measurements. Hysteresis and fatigue measurements were performed using the RT66A Ferroelectric Tester from Radiant Technologies,[33] and the associated "Fatigue" program. Platinum contact dots of 200 μm diameter and 1000Å thickness were deposited by plasma sputtering through a contact mask.

Sol-gel films studied were obtained from the Raytheon Company. The sol-gel films have a Ti:Zr ratio of 53:47, are 1700Å thick, and were crystallized at 550°C for 10 min. in an O_2 atmosphere. The substrate used was Pt/Ti/SiO_2/Si, where the SiO_2, Pt, and Ti films were each 1000Å thick, the SiO_2 was grown by thermal oxidation, and the Pt and Ti were evaporated.

RESULTS AND DISCUSSION

Control of Perovskite/Pyrochlore Formation

The control of PZT film composition and consequently, the perovskite/pyrochlore ratio has proven to be rather difficult. The pyrochlore content of the films is a sensitive function of substrate temperature, oxygen flow rate or partial pressure and the PbO flux arriving at the substrate (relative to oxygen and Zr + Ti fluxes). The dependence of pyrochlore formation on deposition temperature has been reported by many researchers[14, 34]. Our group finds a two-phase mixture of perovskite and pyrochlore PZT in the temperature range 420-500°C. At or above 500°C we can find conditions for the formation of single phase PZT. These results are consistent with those of Castellano *et al.*[35]

The dependence of pyrochlore content on oxygen flow rate or partial pressure is illustrated in Figure 2. Figure 2a shows that the film lead content increased with increasing oxygen flow rate into the chamber. X-ray diffraction of the same films indicates that all films for which the oxygen flow rate was below about 6.5 sccm (during deposition) had a mixture of PZT and pyrochlore. Films deposited with an oxygen flow rate of 6.5 sccm or higher had single phase PZT. The oxygen partial pressure was measured as a function of flow rate for each deposition. Figure 2b shows that a linear relationship between the flow rate and the oxygen pressure exists. The oxygen partial pressure in the vicinity of the substrate has a marked effect upon the Pb sticking coefficient and hence pyrochlore content in the films. We are presently investigating whether the oxygen partial pressure additionally affects the formation of pyrochlore through the formation of Pb-rich intermediate phases at certain oxygen activities.

Microstructural Characterization of Epitaxial PZT Films on Pt/(100)MgO

The epitaxial growth of PZT films on Pt/MgO(100) has been examined by TEM. A selected area diffraction pattern for the PZT/Pt/MgO structure is shown in Figure 3a. The good alignment of the PZT, Pt and MgO diffraction spots reveals the epitaxial relationship among these multiple layers.

A dark field electron micrograph of the cross sectional microstructure of a PZT thin film on a Pt/MgO substrate is shown in Figure 3b. The MgO substrate and the platinum layer show dark contrast, because the PZT (110) reflection was used to form this image. The fairly uniform contrast indicates the epitaxial nature of the PZT thin film.

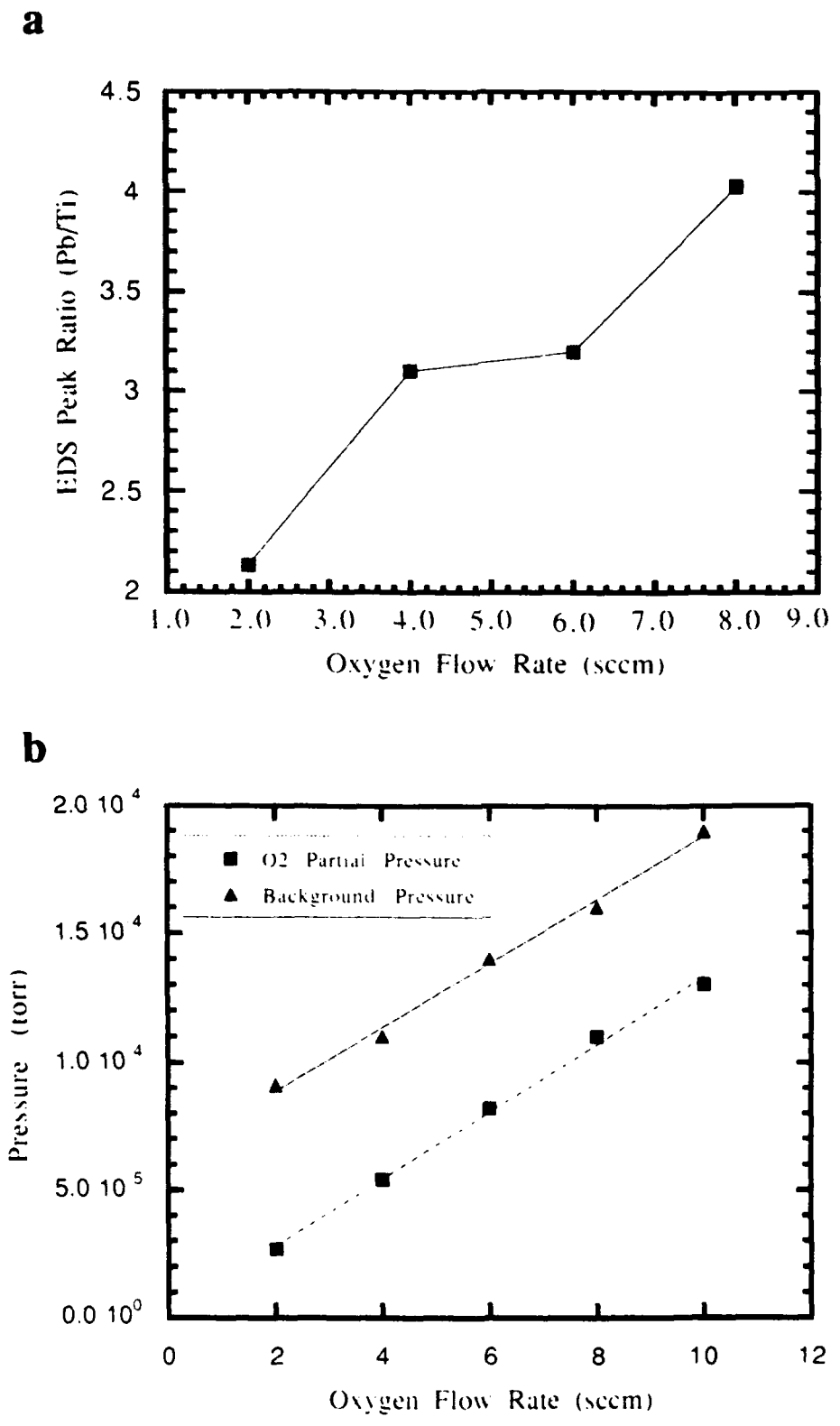


FIGURE 2 a) film lead content vs. O_2 flow rate; b) O_2 partial pressure vs. O_2 flow rate.

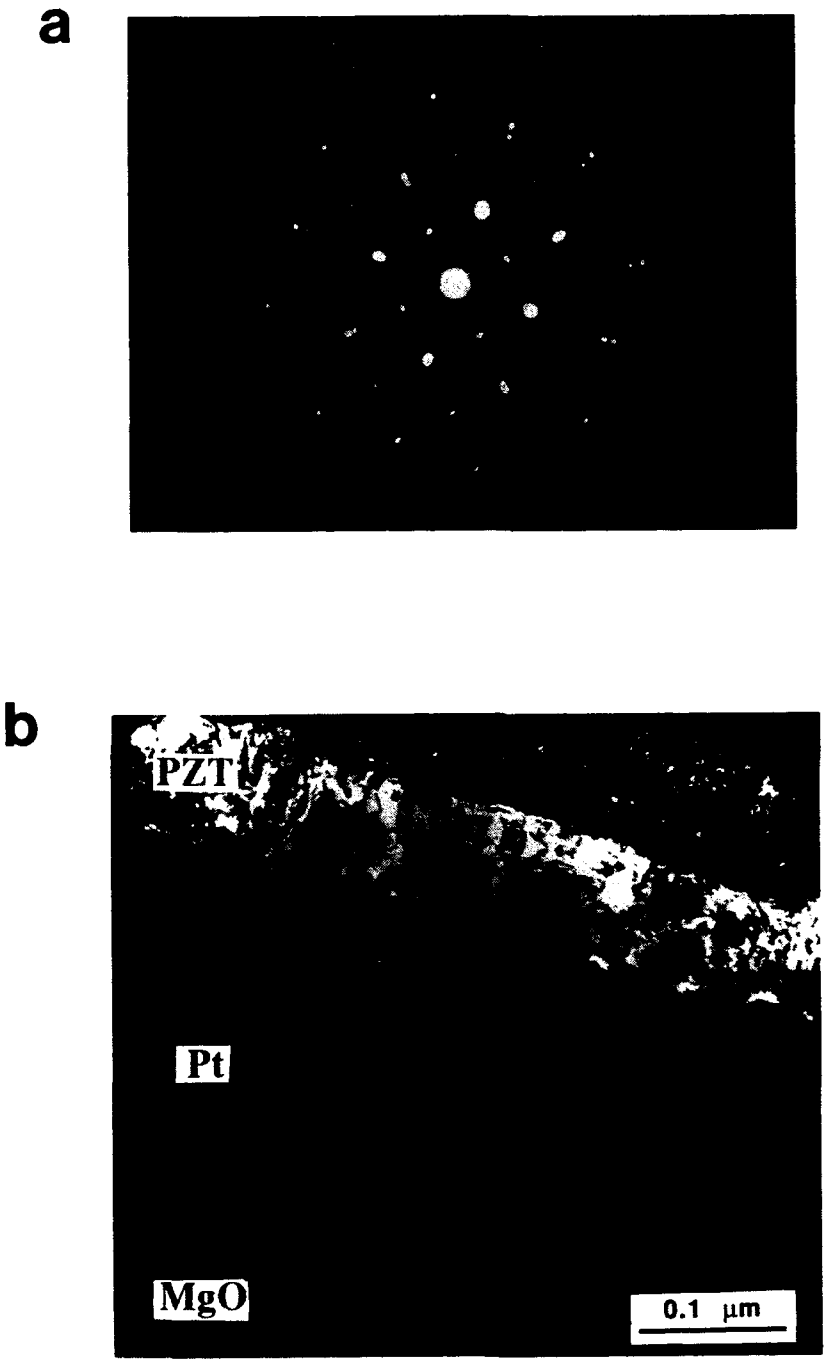


FIGURE 3 a) Electron diffraction pattern of plan-view PZT/Pt/MgO sample showing alignment of the PZT and Pt films to the substrate; b) cross-sectional dark-field electron micrograph of PZT/Pt/MgO; PZT (110) reflection is used.

The thickness of the PZT film is close to 90 nm. Note that the PZT/Pt interface is rough. This may be due to the enhanced surface diffusion of the platinum in the oxygen-rich environment during the PZT deposition. More details on the platinum surface structure are given in another report in this volume.[36]

Ferroelectric Properties of Films

Hysteresis curves for an ion beam sputter deposited PZT film (Ti:Zr ratio of 50:50, deposition temperature 600°C, thickness 1000Å), and for a sol-gel deposited film (described in the experimental section) are shown in Figures 4a and 4b. Values of P_{max}, P_r, E_c, and K_{eff} obtained for both films are in the ranges 43-50 $\mu C/cm^2$, 16-25 $\mu C/cm^2$, $5.5x10^6$-$1.4x10^7$ V/m, and 1250-1380, with differences between the films of less than a factor of two. The sputter deposited films were grown on Pt/MgO and the sol-gel films were deposited on $Si/SiO_2/Ti/Pt$ substrates. Pt top electrodes were used for both types of films. The sol-gel film showed a lower coercive field than the sputter deposited film by approximately half an order of magnitude, but the sputter deposited film displayed somewhat higher resistivity.

The fatigue results for the sputter deposited and the sol-gel film are shown in Figures 5a and 5b, respectively. P* represents the change in polarization of the sample when a square wave pulse varying from zero volts to the maximum voltage (in this case ± 5 volts) is applied to the sample. Both films show similar results in that the polarization begins a significant decrease at 10^6 cycles with the polarization being reduced to half its original value at 10^9 cycles. The need for more fatigue studies is evident since electrode effects could be playing a significant role in the fatigue of these films.

CONCLUSIONS

Sputtering techniques for deposition of ferroelectric films are reviewed, and ion beam sputter deposition is described in greater detail. The microstructure of epitaxial PZT/Pt/MgO has been examined by transmission electron microscopy. Ferroelectric properties of epitaxial ion beam sputter and polycrystalline sol-gel deposited PZT films are compared . Both types of films had well-developed hysteresis loops for compositions near the morphotropic boundary. The epitaxial films had somewhat higher coercive fields, but somewhat higher resistivity than the sol-gel film. The fatigue behavior of the two films is very similar despite the significant difference in

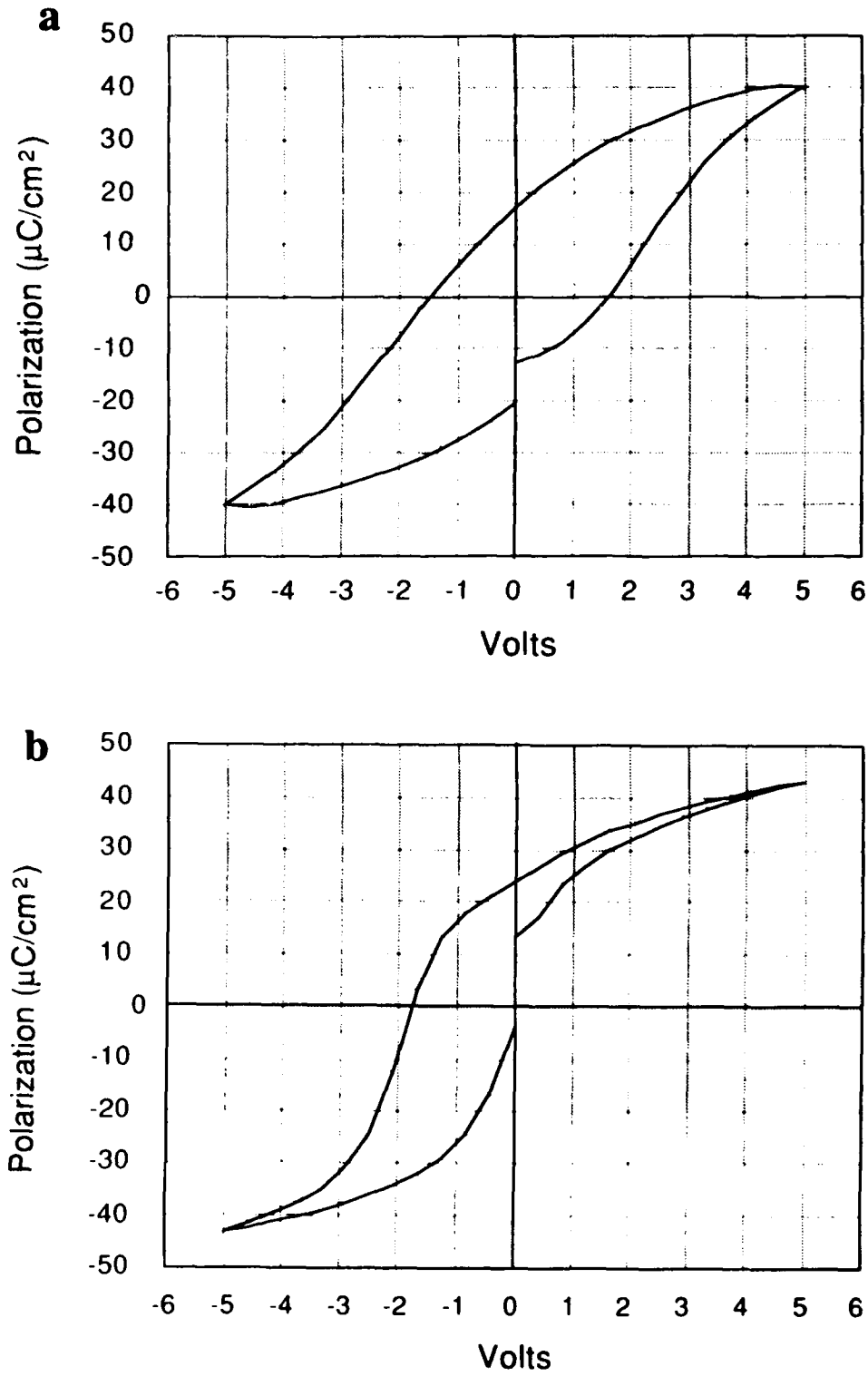


FIGURE 4 a) Hysteresis loop for ion beam sputtered PZT film; b) loop for sol-gel PZT film.

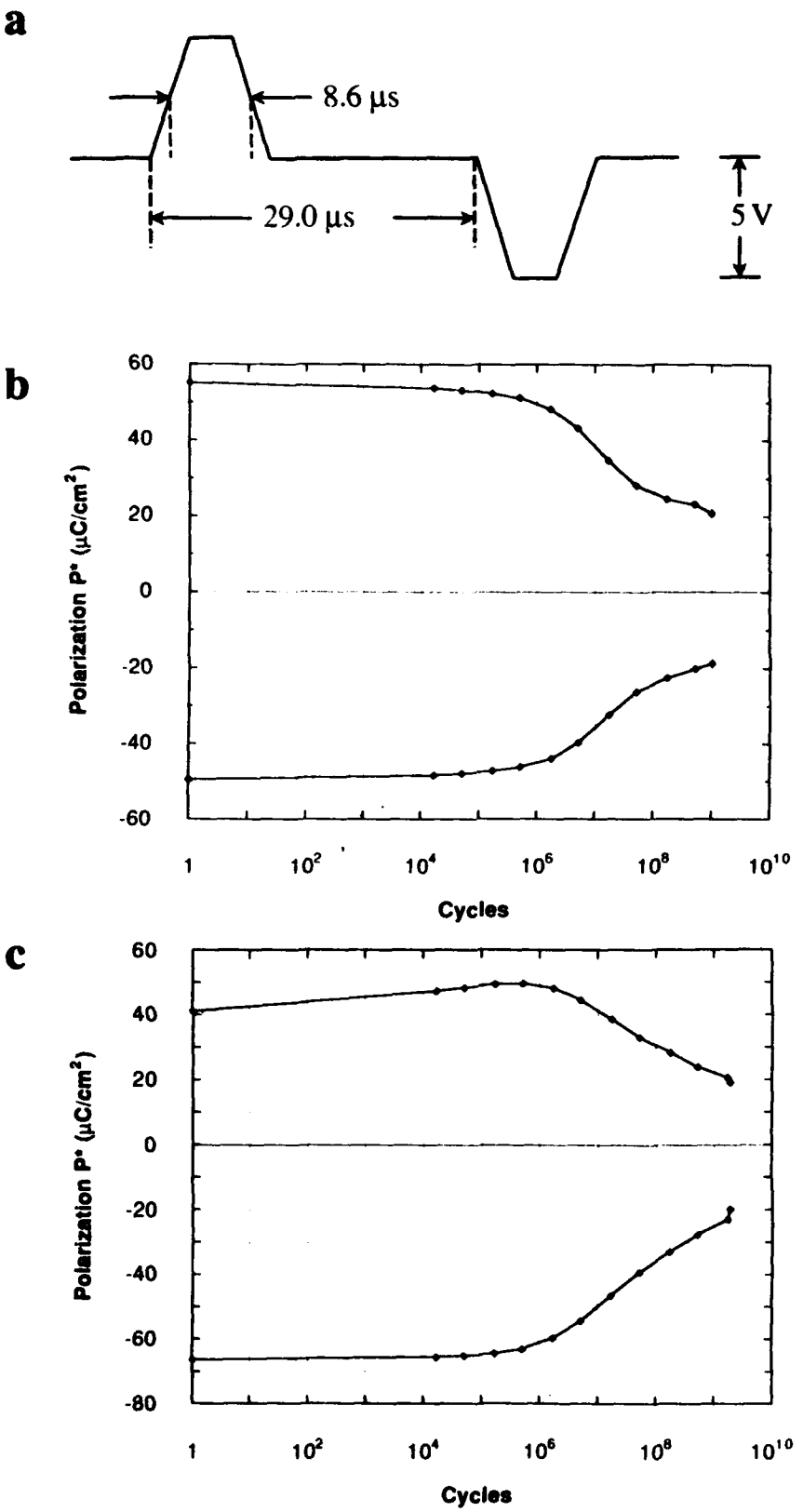


FIGURE 5 a) Pulse train for fatigue test; b) fatigue behavior for ion beam sputtered PZT film; c) fatigue behavior for sol-gel PZT film.

their crystallinity, suggesting that electrode properties may have a dominant effect on fatigue behavior.

ACKNOWLEDGEMENTS.

This project was supported by DARPA/ORD and NSF.

REFERENCES

1. W. J. Takei, N. P. Formigoni, and M. H. Francombe, Appl. Phys. Lett., 15, 256 (1969).
2. I. H. Pratt and S. Firestone, J. Vac. Sci. Techn., 8, 256 (1971).
3. Y. Shintani and O. Tada, J. Appl. Phys., 41, 2376 (1970).
4. H. Schafer and H. Schmitt, Ferroelectrics, 22, 779 (1978).
5. T. Nagatomo, T. Kosaka, S. Omori, and O. Omoto, Ferroelectrics, 37, 681 (1981).
6. J . C. Olson, D. F. Stevison, and I. Bransky, Ferroelectrics, 37, 685 (1981).
7. V. S. Dharmadhikari and W. W. Grannemann, J. Vac. Sci. Technol. A, 1, 483 (1983).
8. T. L. Rose, E. M. Kelliher, A. N. Scoville, and S. E. Stone, J. Appl. Phys., 55, 3706 (1984).
9. A. Mansingh, C. V. R. Vasanta Kumar, J. Mater. Sci. Lett., 7, 1104 (1988).
10. K. Kushida and H. Takeuchi, Appl. Phys. Lett., 50, 1800 (1987).
11. K. Iijima, Y. Tomita, R. Takayama, and I. Ueda, J. Appl. Phys., 60, 361 (1986).
12. S. Matsubara, S. Miura, Y. Miyasaka, and N. Shohata, J. Appl. Phys., 66, 5826 (1989).
13. A. Okada, J. Appl. Phys., 48, 2905 (1977).
14. A. Okada, J. Appl. Phys., 49, 4495 (1978).
15. Y. Shintani, K. Sato, M. Sakamoto, H. Fukuda, and O. Tada, Japan J. Appl. Phys., 17, 573 (1978).
16. T. Fukami, S. Fujii, and H. Tsuchiya, Japan J. Appl. Phys., 24, 410 (1985).

17. S. B. Krupanidhi, N. Maffei, M. Sayer, and K. El-Assal, J. Appl. Phys., 54, 6601 (1983).
18. M. Adachi, T. Matsuzaki, T. Yamada, T. Shiosaki, and A. Kawabata, Japan J. Appl. Phys, 26, 550 (1987).
19. K. Sreenivas, M. Sayer, D. J. Baar, and M. Nishioka, Appl. Phys. Lett., 52, 709 (1988).
20. K. Sreenivas and M. Sayer, J. Appl. Phys., 64, 1484 (1988).
21. S. M. Rossnagel and J. J. Cuomo, in Thin Film Processing and Characterization of High Temperature Superconductors, ed. by J. M. E. Harper, R. J. Colton, and L. C. Feldman (Am. Inst. of Phys., New York, 1988), AIP Conf. Proc., 165, 106.
22. H. Adachi, K. Hirochi, K. Setsune, M. Kitabatake, and K. Wasa, Appl. Phys. Lett., 51, 2263 (1987).
23. R. L. Sandstrome, W. J. Gallager, T. R. Dinger, R. H. Koch, R. H. Laibowitz, R. B. Kleinsasser, R. J. Gambino, B. Bumble, and M. F. Chisolm, Appl. Phys. Lett., 53, 444 (1988).
24. P. D. Reader and H. R. Kaufman, J. Vac. Sci. Technol., 12, 1344 (1975).
25. O. Auciello and R. Kelly, eds., Ion Bombardment Modification of Surfaces: Fundamentals and Applications (Elsevier, the Netherlands, 1984).
26. O. Auciello, M. S. Ameen, A. I. Kingon, A. R. Krauss, and M. A. Ray, Mat. Res. Soc. Conf. Proc., 157, 287 (1990).
27. J. P. Biersack and W. Eckstein, Appl. Phys. A, 34, 73 (1984).
28. M. S. Ameen, O. Auciello, A. I. Kingon, A. R. Krauss, and M. A. Ray, Amer. Inst. Phys. Conf. Proc., 200 (1990).
29. M. Hong, S. H. Liou, D. D. Bacon, G. D. Grader, J. Kwo, A. R. Kartan, and B. A. Davidson, Appl. Phys. Lett., 53, 2102 (1988).
30. T. Fukami and M. Naoe, Trans. IEE Jpn., 103A, 278 (1983).
31. A. R. Krauss, O. Auciello, A. I. Kingon, M. S. Ameen, Y.L. Liu, T.Barr, T. M. Graettinger, S. H. Rou, C. S. Soble, and D. M. Gruen, Appl. Surf. Sci., 46, 67 (1990).
32. D. Pavuna, B. J. Kellett, B. Dwir, J. H. James, A. Gauzzi, J. Faulkner, M. Affronte, and F. K. Reinhart, SPIE Conf. Proc., 1287, 166 (1990).
33. Radiant Technologies, 1009 Bradbury Dr. SE, Albuquerque, NM 87106.
34. H. Adachi, T. Mitsuya, S. Yamajaki, and K. Waso, J. Appl. Phys., 60, 736 (1986).
35. R. N. Castellano and L. G. Feinstein, J. Appl. Phys., 50, 4406 (1979).

36. P. D. Hren, S. H. Rou, H. N. Al-Shareef, M. S. Ameen, O. Auciello, and A. I. Kingon, to be published in Ferroelectrics (1991).

AD-P006 694

UHV PROCESSING OF FERROELECTRIC BARIUM MAGNESIUM FLUORIDE FILMS AND DEVICES+

S. SINHAROY, *D. R. LAMPE, H. BUHAY, and M. H. FRANCOMBE
Westinghouse Science & Technology Center, 1310 Beulah Road, Pittsburgh, PA 15235, and *Westinghouse Advanced Technology Division, Nursery and Winterson Roads, Baltimore, MD 21203

Abstract - Barium magnesium fluoride ($BaMgF_4$) has recently emerged as a strong candidate for application as the gate dielectric in ferroelectric random access memory (FERRAM) devices with nondestructive readout (NDRO). In earlier papers we reported the successful growth of oriented $BaMgF_4$ films on Si(100) and other substrates in a ultrahigh vacuum (UHV) system, as well as the results of the structural and electrical characterization of these ferroelectric films. In the present paper, we review some of the earlier results, and also examine the effect of variations in the growth temperature and various post-growth anneals on the stoichiometry, crystallinity, orientation, and electrical characteristics of the $BaMgF_4$ films. Initial attempts at integrating the ferroelectric field-effect transistor (FEMFET) with the standard CMOS VLSIC processing, as well as the effect of adding a thin capping layer of SiO_2 on the $BaMgF_4$ will also be described.

92-16169

INTRODUCTION

Recent advances in the development of high quality thin films of ferroelectric perovskite type materials (mainly lead-zirconate-titanate, PZT), have created renewed interest in ferroelectric nonvolatile random access memory (FERRAM) devices. At the present time, several groups are actively pursuing the development of capacitive FERRAM devices, where a thin film ferroelectric capacitor memory element is formed either adjacent to or directly above the standard silicon or gallium arsenide integrated circuit (IC) elements.[1] However, FERRAMs based on this concept suffer not only from the design and fabrication problems associated with the integration of the ferroelectric PZT capacitor elements to the

+Supported in part by DARPA Contract No. N00014-90-C-0159

appropriate transistor circuitry in the underlying semiconductor IC, but also from serious intrinsic problems associated with PZT, such as fatigue and endurance. In addition, these devices provide destructive readout only, i.e. the stored information must be rewritten after every read operation. The preferred memory device is a nondestructive readout (NDRO) FERRAM, where the ferroelectric thin film is integrated directly into the semiconductor memory field effect transistor (FET) as the gate dielectric in it, providing not only nonvolatility, but also nondestructive readout. We have recently proposed such a device[2,3], where a thin film of barium magnesium fluoride ($BaMgF_4$) is used as the gate dielectric.

Ferroelectricity in bulk single crystals of $BaMF_4$ (where M = Mg, Co, Ni, or Zn) was first discovered by Eibschutz et al[4] in 1969. These materials did not receive attention for capacitive memory device applications, because of their low spontaneous polarization compared to most oxide ferroelectrics, even though their low permittivity values are very attractive. However, for ferroelectric memory devices, a useful figure of merit is given by the spontaneous polarization P_s divided by the product of dielectric constant ϵ and coercive field E_c. As pointed out recently by Scott et al,[5] this dimensionless ratio, which is of the order of unity for PZT, is actually larger in ferroelectrics such as $BaMgF_4$, whose smaller spontaneous polarization (8 versus 41 $\mu C/cm^2$ for PZT) is more than compensated by its lower dielectric constant (two orders of magnitude smaller than that of PZT). We have already reported [2,3,6] the successful growth of thin films of ferroelectric $BaMgF_4$ on silicon and other substrates by evaporation in ultrahigh vacuum (UHV). As has been shown in our previous publications, UHV growth of this non-oxide ferroelectric film on a clean substrate results in very low interface state density, an essential requirement for the FET-type device application proposed by us. Structurally, the most desirable film orientation for this particular type of device is with the a-axis (the polarization axis) of the $BaMgF_4$ film perpendicular to the semiconductor substrate surface. Film growth conditions and initial structural, ferroelectric, and electrical characterization results were presented in our earlier papers.[2,3,6] In this paper, we briefly review those results, and then present some new results on the effect

of film orientation on the ferroelectric hysteresis properties, as well as the effect of a capping layer on the capacitance-voltage (C-V) hysteresis properties of $BaMgF_4$ films grown on Si(100).

EXPERIMENTAL

$BaMgF_4$ films were grown on 4-inch Si(100) wafers in a modified VG V80H molecular beam epitaxy (MBE) system. The MBE system, designed originally to accomodate 3-inch wafers, was modified to accommodate 4-inch wafers following a procedure described in a separate publication.[7] The pressure in the growth chamber was usually in the low 10^{-10} Torr range, and increased to the mid-to-upper 10^{-8} Torr range during film growth. The films were grown by evaporating an equimolecular mixture of BaF_2 (99.995%) and MgF_2 (99.99%) powders, thoroughly mixed by ball milling, and contained in a pyrolytic graphite crucible. The crucible temperature during film growth was maintained at 1075°C to 1100°C, resulting in a growth rate of about 0.2 nm/sec. Substrate cleaning in the case of silicon consisted of a modified chemical cleaning procedure immediately prior to insertion in the UHV chamber, followed by in situ thermal cleaning at 900°C for 10 to 20 minutes. Growth temperatures in the range of 250°C to 550°C, and various post-growth anneals were attempted. The films ranged in thickness from 100 nm to 500 nm.

Structural properties of the $BaMgF_4$ films were analyzed by detailed X-ray analysis. A modified Sawyer-Tower bridge was used for the ferroelectric hysteresis measurements. Capacitance and conductance measurements over the frequency range of 5 kHz to 500 kHz were performed using a Boonton model 75C direct capacitance bridge. A mercury probe was used for these measurements, as well as for capacitance-voltage (C-V) measurements on these films.

RESULTS AND DISCUSSION

A. 400°C to 550°C Growth

As has demonstrated previously[6], X-ray analysis of films grown in this temperature range confirmed that their diffraction patterns matched those of stoichiometric $BaMgF_4$, with the orthorhombic crystal structure of the ferroelectric phase. A glancing-angle X-ray

diffraction pattern for a film grown at 350°C and then vacuum-annealed at 600°C for 30 minutes, indicated a weak fiber texture. All films grown in this temperature range were found to be crystalline with preferred alignments or, at temperatures above 500°C, multiple epitaxial orientations. Details of the X-ray oscillation and Weissenberg patterns will be presented elsewhere.[8] A sketch showing the orientation typical of films grown at 500°C on Si(100), derived from the X-ray results, is shown in Figure 1.

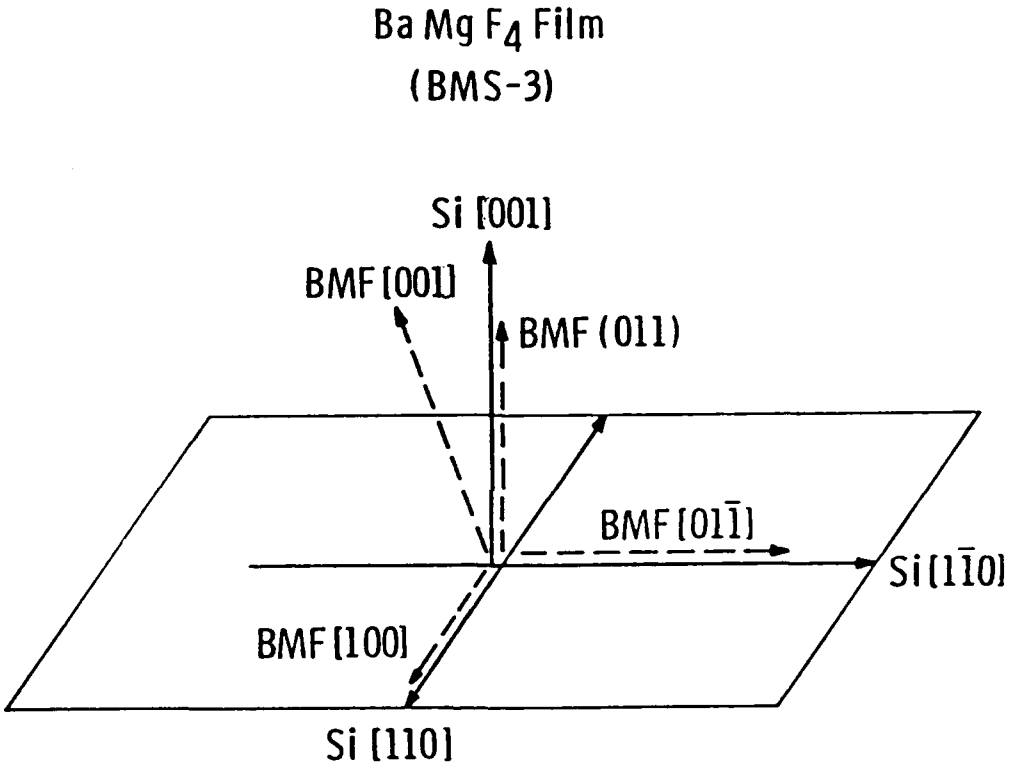


FIGURE 1 Multiple epitaxial orientations of a $BaMgF_4$ film grown on Si(100) at 500°C. Only one of the four epitaxial components derived from X-ray oscillation and Wissenberg patterns have been shown by the dashed lines in the Figure. The other components can be generated by rotating 90° about BMF(011) three times.

B. 200°C to 375°C Growth and Post-anneal

All films grown in this temperature range were found to be amorphous as grown. However, it proved possible to crystallize them by annealing at temperatures above 400°C. A summary of the X-ray analysis results for various post-annealed films is given in Table 1. Under vacuum annealing at temperatures ranging from 400°C to 700°C, crystallization led to two different results. In one case a mixed

TABLE 1 $BaMgF_4$/Si(100) post-anneal summary.
(125-300 nm films, UHV grown at 200-375°C)

Post-Anneal	Film Structure (X-ray)
None	Amorphous
Vac-anneal 1 hr each at 400, 500, 600, & 700°C	(011) multiple epi structure with some (010) fiber texture each case
Vac-anneal 600°C, 0.5 hr	Multi-epi + more (010) fiber texture or Polycrystalline + multi-epi as above
H_2-anneal 1 hr each at	
400°C	Amorphous
500°C	Poly + some (011) orientation
600°C	Poly + (100) fiber texture BaF_2
700°C	Only (100) fiber texture BaF_2

film orientation developed containing the multiple epitaxial (011) components depicted in Figure 1, together with a more pronounced (010) fiber-textured component. In the other case, the film was polycrystalline, while at the same time exhibiting some of the multiple epitaxial structure referred to above. Appearance of the epitaxial structures suggests that these may already have been present in the as-grown film, but were simply not detectable due to the poor crystallinity. The emergence of the (010) textured component is probably consistent with the known morphology of bulk crystals of $BaMgF_4$, which have been shown to exhibit a strong (010) cleavage plane. The reason for the discrepancy between these two results is not understood at this time.

Hydrogen furnace anneal for one hour at 400°C did not produce crystallinity in the amorphous films. However, 500°C anneal resulted in polycrystalline films with some (011) orientation. Partial dissociation of the polycrystalline film was observed after 600°C anneal, and after hydrogen anneal at 700°C the film appeared to have completely dissociated The dissociation process apparently involved

selective loss of MgF_2, preceded presumably by reduction to metallic magnesium. The residual BaF_2 phase was observed to develop a strong (100) fiber texture.

C. Hysteresis and Capacitance Measurements

Most of the efforts to study ferroelectric hysteresis behavior were confined to film structures grown on highly doped silicon wafers with conductivity (n-type) in the range 0.005 to 0.02 Ω-cm. Counter-electrode structures used included both vacuum-deposited metal contacts of Al, Au, or Pt, and also a mercury probe. In general, the mercury probe arrangement proved to be most successful for these measurements.

The hysteresis effects observed depended sensitively on the conditions used for film growth and/or annealing. Essentially, no signs of hysteresis were detected in highly oriented films grown at elevated temperatures. This is probably consistent with the fact that in the strong orientations observed for films grown thus far on (100) Si, the ferroelectric a-axis lies parallel to the substrate surface (see e.g. Figure 1), with no component of polarization aligned to the applied field. In those cases where a more randomly oriented crystalline structure had developed during growth (Table 1), little evidence of loop formation was seen at fields up to about 400 kV/cm, where premature breakdown usually occurred.

The clearest evidence of polarization switching was found for films grown initially in the amorphous state at 350°C and then vacuum annealed at 600°C to develop a crystalline structure (Table 1). In this case, the hysteresis loop was observed to open gradually as the switching field was increased slowly above about 400 kV/cm, and appeared to attain almost complete saturation before breakdown occured in the range 0.85 to 1.0×10^6 V/cm. The switched polarization (P_s) for such films was about 1.5 $\mu C/cm^2$, and the coercive field (E_c) about 175 kV/cm. The loop is compared with that for a 10 micron thick bulk crystal, recently studied by us,[6] in Figure 2. The discrepancy with the bulk values, of $P_s = 8.5 \mu C/cm^2$ and $E_c = 95.4$ kV/cm, can probably be attributed to crystal orientation effects and film stress respectively. In particular, the low value of P_s is qualitatively consistent[6] with the fibered film texture. This texture pattern

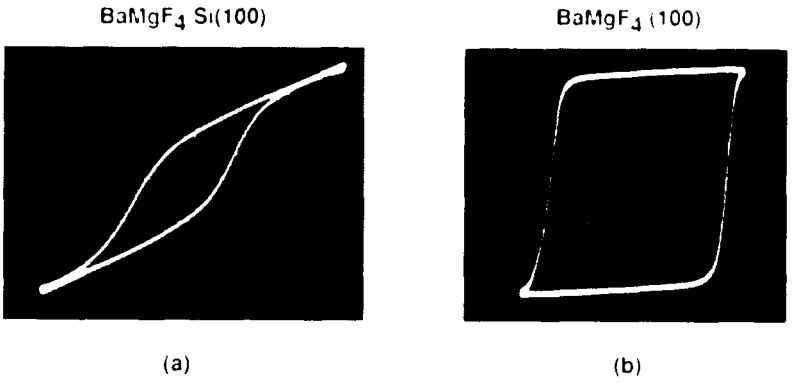


FIGURE 2 Hysteresis loop at 2kHz for a) $BaMgF_4$/Si(100) grown at 350°C and vacuum-annealed at 600°C for 30 minutes. Thickness = 200 nm. Vertical scale: 1.2 $\mu C/cm^2$ per large division; horizontal scale: 250 kV/cm per large division; b) $BaMgF_4$ single crystal along the polarization axis. Thickness = 10 μm. Vertical scale: 3.75 $\mu C/cm^2$ per large division; Horizontal scale: 47.7 kV/cm per large division.

suggests that the ferroelectric a-axes of the crystallites are distributed over an angular range of up to 20° from the substrate surface.

As we reported earlier[6], the dielectric permittivity and dissipation value for the film referred to above were fully consistent with those for bulk single crystals, and the permittivity (ϵ = 8-9) measured showed only a weak dispersion with frequency. Thus, despite the low measured value of polarization, the effective figure of merit for memory applications referred to in the introduction, still lies close to unity (i.e. almost identical to that of PZT).

D. Initial Integration with VLSIC Processing

As reported in our previous publications,[3,6] $BaMgF_4$ films grown on 4-inch diameter Si(100) wafers used in the standard one-micron CMOS VLSIC process exhibited excellent C-V hysteresis characteristics (14 volt memory window in response to $\pm$20 Volt programming voltage) that remained virtually undiminished after nearly 14 million endurance cycles of polarization reversal. We also described[3] a fabrication scheme for the integration of the ferroelectric memory field-effect transistor (FEMFET) into the standard VLSIC process.[3] The desire to achieve a more robust MISFET gate dielectric capable of handling larger electric fields to give greater breakdown resistance led to the

idea of using a well characterized "capping layer" such as SiO_2 or Si_3N_4. Additionally, the capping layer provides better memory gate adhesion and facilitates memory-gate stack photoengraving. A final reason for the capping layer was to protect the VLSIC silicon fabrication facilities from any adverse effects from the chemical constituents of the $BaMgF_4$ ferroelectric. Figure 3 is a C-V hysteresis plot obtained with a $BaMgF_4$ film capped with a low temperature SiO_2 film. The substrate in this case was a gridded Si(100) wafer as illustrated in the figure. The 12 Volt memory window observed in this case is slightly lower than that observed without the capping layer, but is still more than adequate for the memory device application. The memory window remained undiminished after 20 million endurance cycles.

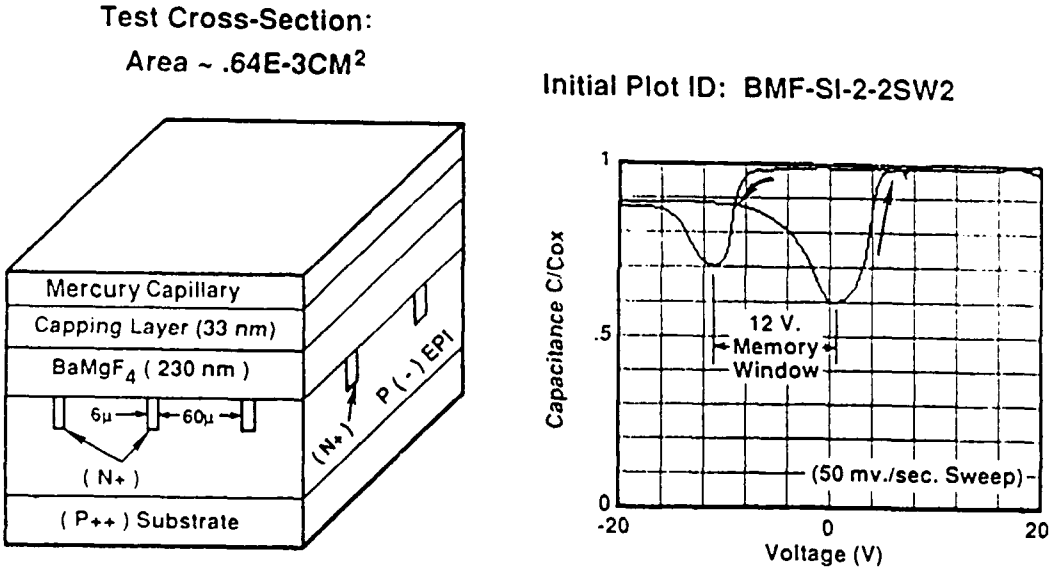


FIGURE 3 Test structure and C-V hysteresis results of a SiO_2-capped $BaMgF_4$ film on gridded Si(100).

Incorporation of the standard TiW metallization was the next processing step attempted with the $BaMgF_4$ films. Early results for wet engraving of 200 nm $BaMgF_4$ grown at 350°C, capped with 50 nm LTO followed by 300 nm TiW, with a 30 minute anneal in Forming gas were encouraging, as seen in the C-V hysteresis plot of Figure 4. The C-V plot exhibited a memory window of 10 volts in response to the same $\pm$20 Volt programming voltage that was used earlier. Thus, the $BaMgF_4$ films maintain good ferroelectric switching properties through all the

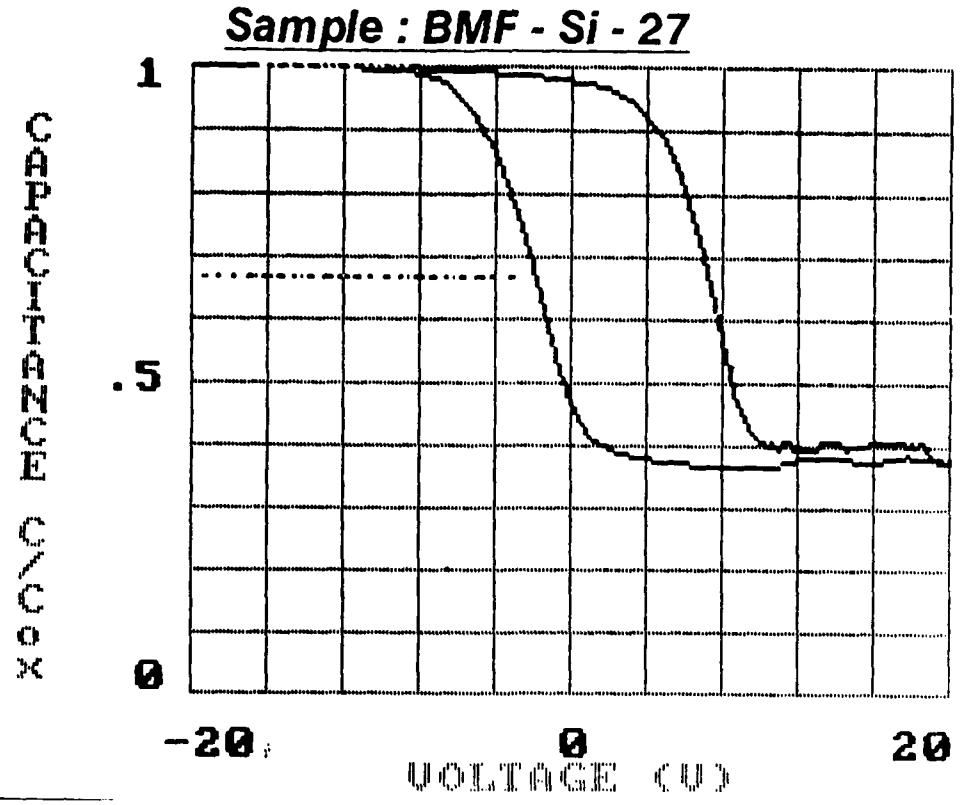


FIGURE 4 Initial C-V hysteresis results following wet engraving of a 200 nm $BaMgF_4$ film on p/p$^+$ Si(100), with a 50 nm LTO capping layer and 300 nm TiW with 30 minute anneal in Forming gas at 400°C. The $BaMgF_4$ film was grown at 350°C.

processing steps that have been attempted so far. The next step will be the fabrication of the actual transistor, allowing the measurement of switching speed, and other intrinsic properties such as fatigue and aging, radiation hardness, etc.

SUMMARY

In summary, we have reviewed the current status of UHV-grown ferroelectric $BaMgF_4$ films on Si(100), and the progress towards integrating these structures with the standard CMOS VLSIC processing for a FERRAM device. It has been shown that stoichiometric $BaMgF_4$ films can be grown by congruent evaporation from a BaF_2 and MgF_2 mixed powder source. Films grown at temperatures 400°C to 550°C possess a multiple epitaxial structure with the polarization axis (a-axis) in the Si(100) plane. Films grown in the 200°C to 375°C range are amorphous as grown, but can be crystallized into a polycrystalline form through higher temperature anneal in various atmospheres and

vacuum. The P_s is lower and the E_c is higher for these $BaMgF_4$ films compared to those measured for the bulk single crystals, because of the polycrystalline nature of the films. The films exhibit excellent C-V hysteresis characteristics which remain essentially unaffected by the incorporation of a thin SiO_2 capping layer and a TiW metallization layer as part of standard processing steps.

ACKNOWLEDGEMENTS

The authors wish to thank N. J. Doyle, W. J. Takei, and E. Stepke for valuable technical contributions, and J. M. Bogdon and J. H. Rieger for technical assistance.

REFERENCES

1. C. A. Paz de Araujo and G. W. Taylor, Ferroelectrics 116, 215 (1991).
2. S. Sinharoy, H. Buhay, M. G. Burke, D. R. Lampe, and T. M. Pollak, IEEE Transac. Ultrason. Ferroelectrics and Freq. Control, Special issue on Ferroelectric Thin Films, November 1991 (in press).
3. D. R. Lampe, S. Sinharoy, E. Stepke, and H. Buhay, Proc. 7th Int. Symp. Appl. Ferroelectrics, 1990 (in press).
4. M. Eibschutz, H. J. Guggenheim, S. H. Wemple, I. Camlibel, and M. Didomenico, Jr., Phys. Lett. 29A, 409 (1969).
5. J. F. Scott, L. D. McMillan, and C. A. Araujo, Ferroelectrics 116, 147 (1991).
6. S. Sinharoy, H. Buhay, M. H. Francombe, W. J. Takei, N. J. Doyle, J. R. Rieger, D. R. Lampe, and E. Stepke, J. Vac. Sci. Technol. A, May/June 1991 (in press).
7. J. M. Bogdon, S. Sinharoy, and A. J. Noreika, J. Vac. Sci. Technol. A, July/August 1991 (in press).
8. M. H. Francombe, S. Sinharoy, N. J. Doyle, H. Buhay, and W. J. Takei, Appl. Phys. Lett. (to be published).

A
Abt, Norman E., 404
Adachi, Hideo, 326
Ainger, F., 215
Al-Shareef, H.N., 612, 658
Ameen, M.S., 612
Assink, R.A., 535
Auciello, O., 612, 658
Azuma, M., 414

B
Barboux, P., 205
Barlingay, C.K., 30
Baumann, Robert C., 637
Benedetto, Joseph M., 44
Bennett, K.W., 87
Bernacki, Stephen E., 262, 658
Bondurant, David W., 364
Brennan, Ciaran J., 354
Brody, P.S., 87, 251
Bruchhaus, R., 453
Buhay, H., 62, 674
Bullington, J., 54
Bunker, B.C., 535

C
Carrico, A., 151
Chan, W.K., 54
Chen, Deng-Yuan, 169
Chen, B.A., 515
Chiang, C.K., 87
Chrisey, D.B., 72
Cook, L.P., 87
Cuchiaro, J.D., 461, 649

D
DeKeijser, M., 598
Dey, Sandwip K., 30, 571
Di, Y.D., 515
Dimos, D.B., 535
Dormans, G.J.M., 598
Doyle, N.J., 62
Dransfeld, Klaus, 245
Dunn, Douglas E., 344

E
Evans, J., 54

F
Faure, S.P., 205
Francombe, M.H., 62, 674

G
Gallegos, R., 547
Gaucher, P., 205
Geideman, Wm. A., 390
Gifford, K.D., 658
Glatz-Reichenbach, Joachim, 245
Gloerstad, T.K., 30
Golz, J.W., 515
Grabowski, K.S., 72
Graettinger, T.M., 658
Gruverman, A.L., 315
Gundel, Hartmut, 501
Guthner, Peter, 245

H
Halpern, B.L., 515
Hamakawa, Yoshihiro, 185, 444
Helgeson, A., 231
Horwitz, J.S., 72
Hren, Philip D., 612, 658
Hsu, Sheng T., 475
Hsueh, C.-C., 231
Huber, H., 453
Hung-Jia Huang, Charles, 278
Hwang, C.L., 515

I
Imai, Tadayuki, 185
Inam, A., 54
Inoue, Naoto, 444
Ishibashi, Yoshihiro, 306, 326

K
Kalish, Israel H., 475
Kalkur, T.S., 627
Kammerdiner, L., 627
Kano, G., 414
Kasner, W.H., 62
Katsu, S., 414
Kawabata, Akira, 492
Kessler, V.G., 195
Kingon, Angus I., 612, 658
Kitamura, Naoki, 492
Klee, Mareike, 288
Krupanidhi, S.B., 10, 100
Kwor, R.Y., 627

L
Lampe, D.R., 62, 674
Larsen, P.K., 598
Lee, J.J., 30
Leuchtner, R.E., 72
Leung, M.S., 368
Levenson, L., 627
Leybovich, I.S., 524
Lin, He, 637
Lipeles, R.A., 368

M
Ma, T.P., 515
Mackenzie, John D., 561
Maderic, B.P., 431
Madok, J.H., 524
Maffei, N., 100
McDavid, J.M., 637
McLean, F. Barry, 44
McMillan, L.D., 116, 151, 169, 176, 649
Melnick, B.M., 116, 176, 461, 547
Mihara, T., 116, 139, 151
Miller, S.L., 376
Moore, Randall A., 44
Morgan, B.A., 368

N
Naik, I.K., 431, 524
Nasby, R.D., 376
Nasu, T., 414

O
Obvintseva, I.E., 195
Okuyama, Masanori, 185, 444
Omura, Masayoshi
Otsuki, T., 414

P
Pan, Wuyi, 335
Park, B.K., 62
Patel, A., 215
Paz de Araujo, C.A., 116, 139, 151, 169, 176, 461, 547, 649
Peng, C.J., 100
Petuskey, William T., 571
Pitzer, D., 453
Polinsky, M., 62
Polla, D.L., 231
Ponomarev, N.Yu., 315

R
Rabson, Thomas A., 278, 637, 644
Ramesh, R., 54
Richardson, David A., 571
Roberts, T., 649
Rod, B.J., 87, 251
Rodgers, M.S., 376
Rost, Timothy A., 637, 644
Rou, S.H., 612, 658
Roy, D., 100
Rumyantsev, E.L., 315

S
Sanchez, L.E., 431, 524
Sands, T., 54
Sayer, Michael, 1
Schenck, P.K., 87
Schilling, Doris, 245
Schmitt, J.J., 515
Schwank, J.R., 376
Schwartz, R.W., 535
Scott, J.F., 151, 176, 649
Scott, M., 649
Shiosaki, Tadashi, 492
Shorrocks, N.M., 215
Shur, V. Ya., 315
Sinharoy, S., 62, 674
Suchicital, C.T.A., 30

T
Tallant, D.R., 535
Talvacchio, J., 62
Tamagawa, T., 231
Tarascon, J.M., 54
Thakoor, Anil P., 262
Thakoor, Sarita, 262
Tillerot, F., 54
Tonkachyova, N.A., 315
Toyama, Motoo, 444
Trundle, C., 215
Turevskaya, E.P., 195
Turova, N. Ya., 195
Tuttle, B.A., 535

V
Vaudin, M.D., 87

W
Waser, Rainer, 288
Watanabe, H., 116, 139, 151
Watanabe, S.H., 524
Weinstock, I.A., 535
Wersing, W., 453
Whatmore, R.W., 215
Wong-Ng, W., 87
Wu, S.Y., 390, 431, 524

X
Xu, Ren, 561
Xu, Yuhuan, 561

Y
Yanovskaya, M.I., 195
Ye, C., 231
Yoshimori, H., 116
Yue, Cheng-Feng, 335

Z
Zuleeg, R., 151, 176